CODEN: JASMAN 4966

THE JOURNAL of the Acoustical Society of America

Vol. 107, No. 4 April 2000

SOUNDINGS SECTION

GENERAL LINEAR ACOUSTICS [20]

(Continued)

CONTENTS—*Continued from preceding page*

NONLINEAR ACOUSTICS [25]

UNDERWATER SOUND [30]

ULTRASONICS, QUANTUM ACOUSTICS, AND PHYSICAL EFFECTS OF SOUND [35]

TRANSDUCTION [38]

STRUCTURAL ACOUSTICS AND VIBRATION [40]

ARCHITECTURAL ACOUSTICS [55]

ACOUSTICAL MEASUREMENTS AND INSTRUMENTATION [58]

(Continued)

CONTENTS—*Continued from preceding page*

(Continued)

CONTENTS—*Continued from preceding page*

LETTERS TO THE EDITOR

ERRATA

NOTES CONCERNING ARTICLE ABSTRACTS

1. The number following the abstract copyright notice is a Publisher Item Identifier (PII) code that provides a unique and concise identification of each individual published document. This PII number should be included in all document delivery requests for copies of the article.
2. PACS numbers are for subject classification and indexing. See June and December issues for detailed listing of acoustical classes and subclasses.
3. The initials in brackets following the PACS numbers are the initials of the JASA Associate Editor who accepted the paper for publication.

SOUNDINGS

Section Editor: Richard Stern

This front section of the *Journal* includes acoustical news, views, reviews, and general tutorial or selected research articles chosen for wide acoustical interest and written for broad acoustical readership.

ACOUSTICAL NEWS—USA

Elaine Moran
Acoustical Society of America, Suite 1NO1, 2 Huntington Quadrangle, Melville, NY 11747-4502

Editor's Note: *Readers of this Journal are asked to submit news items on awards, appointments, and other activities about themselves or their colleagues. Deadline dates for news items and notices are 2 months prior to publication.*

New Fellows of the Acoustical Society of America

Lynne E. Bernstein—For contributions to the understanding of communication problems of the hearing impaired.

Shigeo Ohtsuki—For contributions to diagnostic ultrasonics.

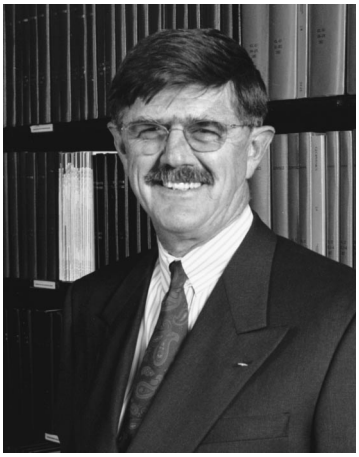

F. Michael Pestorius—For leadership in acoustic research.

Paul O. Thompson—For contributions to psychoacoustics and animal bioacoustics.

 0001-4966/2000/107(4)/1799/4/$17.00

Charles R. Steele honored by ASME International

Charles Steele, Member of the Acoustical Society of America, was awarded the Warner T. Koiter Medal by ASME International (American Society of Mechanical Engineers) for leading research accomplishments in solid mechanics and pioneering analytical work in the biomechanics of the inner ear. The medal, established in 1996, recognizes the effective blending of theory and application of applied mechanics, and leadership in the international solid mechanics community.

He has made many contributions to the theory of shells and has been involved in the development of a noninvasive technique for determining the mechanical characteristics of bone by measuring its vibrational response. Steele has published 88 scholarly articles in archive journals and is editor-in-chief of the *International Journal of Solids and Structures.*

Charles Steele received his bachelor's degree in mechanical engineering at Texas A&M College Station, in 1956 and his doctorate in engineering mechanics at Stanford University in 1960. He is a Fellow of the ASME and the American Academy of Mechanics.

USA Meetings Calendar

Listed below is a summary of meetings related to acoustics to be held in the U.S. in the near future. The month/year notation refers to the issue in which a complete meeting announcement appeared.

2000

2–5 May	Oceanic Imaging Conference, Newport, RI [E. Sullivan, Naval Undersea Warfare Center Division, Newport, RI; Fax: 401-832-2146; WWW: www.srminc.net/oceanimg/contact.html].
17–19 May	ASNE Day 2000, Arlington, VA [Andrea Zari, Meetings Department, American Society of Naval Engineers, 1452 Duke St., Alexandria, VA 22314-3458; Tel.: 703-836-6727; Fax: 703-836-7491; E-mail: azari@navalengineers.org].
30 May–3 June	139th Meeting of the Acoustical Society of America, Atlanta, GA [Acoustical Society of America, Suite 1NO1, 2 Huntington Quadrangle, Melville, NY 11747-4502; Tel.: 516-576-2360; Fax: 516-576-2377; E-mail: asa@aip.org; WWW: asa.aip.org].
22–24 June	2000 Binaural Hearing, Hearing Loss & Hearing Aids, Iowa City, IA [Richard Tyler; Tel.: 391-356-2471; E-mail: tyler@uiowa.edu; WWW: www.medicine.uiowa.edu/otolaryngology/news/news].
13–16 July	ClarinetFest 2000, Norman, OK [Dr. Keith Koons, Music Dept., Univ. of Central Florida, P.O. Box 161354, Orlando, FL 32816-1354; Tel.: 407-823-5116; E-mail: kkoons@pegasus.cc.ucf.edu].
21–23 September	Eighth Annual Conference on the Management of the Tinnitus Patient, Iowa City, IA [Rich Tyler; Tel.: 319-356-2471; Fax: 319-353-6739; WWW: www.medicine.uiowa.edu/otolaryngology/news/news].
22–25 October	IEEE Ultrasonics Symposium, San Juan, Puerto Rico [R. Almar, 896 Buttonwood Lane, Altamonte Springs, FL 32714; Fax: 407-290-5181; WWW: www.uffcsymp2000.org].
4–8 December	Joint Meeting: 140th Meeting of the Acoustical Society of America/NoiseCon 2000, Newport Beach, CA [Acoustical Society of America, Suite 1NO1, 2 Huntington Quadrangle, Melville, NY 11747-4502; Tel.: 516-576-2360; Fax: 516-576-2377; E-mail: asa@aip.org; WWW: asa.aip.org].

2001

30 April–3 May	2001 SAE Noise & Vibration Conference & Exposition, Traverse City, MI [Patti Kreh, SAE Int'l., 755 W. Big Beaver Rd., Suite 1600, Troy, MI 48084; Tel.: 248-273-2474; Fax: 248-273-2494; E-mail: pkreh@sae.org]. Deadline for submitting abstracts: 14 July 2000
4–8 June	141st Meeting of the Acoustical Society of America, Chicago, IL [Acoustical Society of America, Suite 1NO1, 2 Huntington Quadrangle, Melville, NY 11747-4502; Tel.: 516-576-2360; Fax: 516-576-2377; E-mail: asa@aip.org; WWW: asa.aip.org].
7–10 October	2001 IEEE International Ultrasonics Symposium joint with World Congress on Ultrasonics, Atlanta, GA [W. O'Brien, Electrical and Computer Engineering, Univ. of Illinois, 405 N. Mathews, Urbana, IL 61801; Fax: 217-244-0105; WWW: www.ieee-uffc.org/2001].

Revision List

New Associates

Al-Jumaily, Ahmed A., Diagnostics and Control Research Centre, Auckland University of Technology, Private Bag 92006, Auckland 1020 New Zealand

Anderson, Mark A., 610 SE 5th Street, Pompano Beach, FL 33060

Ansorge, Michael, Inst. of Microtechnology, Univ. of Neuchatel, Rue A-L. Breguet 2, Neuchatel 2000 Switzerland

Baird, Justin E., Meyer Sound, 2832 San Pablo Avenue, Berkeley, CA 94702

Barton, Robert J., Global Work Environments, Fraunhofer Center for Research in Computer Research, 321 South Main Street, Providence, RI 02903

Bass, James D., 3704 Thomasson Crossing Drive, Triangle, VA 22172

Berg, Roger O., Kockums Naval Systems, Conceptual Design, Stora Varvsgatan 11, Malmo S-20555 Sweden

Bonilha, Murilo W., 70 Middlebrook Road, West Hartford, CT 06119

Brancazio, Lawrence, Dept. of Psychology, Northeastern University, 125 NI, 360 Huntington Avenue, Boston, MA 01603

Brothers, Richard J., DERA, Environmental Acoustics, Newtons Road, Weymouth, Doreset DT4 8UR, U.K.

Busch, Rainer, Luntjenweg 59B, Oldenburg 26131, Germany

Cerjan, Jeff M., Nordam, Materials and Processes Engineering, 602 East 4th Street, Tulsa, OK 74136

Chambers, David H., Electrical Engineering, Lawrence Livermore National Lab., P.O. Box 808, L-154, Livermore, CA 94551

Chen, Geng, Inst. of Acoustics, Academy of Sciences, China, Zhong Guan Cun St. 17, Beijing 100080 P.R. China

Collins, Theodore S., Medical Research Group, Document Center, 13628 Jeff Davis Highway, #3, Woodbridge, VA 22191

Croney, Andrew P., Eurasia Architectural Products, Ltd., Unit A, 151F, Tower 2, Capitol Center 28 Joardines Crescent, Causeway Bay, Hong Kong

DeWoody, Robert T., Ingalls Shipbuilding, P.O. Box 149, Pascagoula, MS 39568-0149

Druzhinin, Alexander B., GSRG, British Geological Survey, Murchison House, West Mains Road, Edinburgh EH9 3LA, Scotland

Dube, Frederick A., IPD, One Corporate Place, Middletown, RI 02842

Frodl, Robert G., Stahlgruber Wohnpark 5, Poing D-85586, Germany

Garrett, Michael D., 1936 Mount Royal Terrace, Baltimore, MD 21217

Geers, Ann E., Central Inst. for the Deaf, 818 South Euclid, St. Louis, MO 63110

Gierlich, Hans Wilhelm, GmbH, Eberstrabe 30a, Herzogenrath 52134 Germany

Glickman, Gary M., Wilson, Ihrig & Associate, Inc., 5776 Broadway, Oakland, CA 94618-1531

Gonzalez, Julio, Carlos Albors 66, Picassent, Valencia 46220 Spain

Hankard, Michael, Hankard Environmental, Inc., 205 East Geneseo Street, Lafayette, CO 80026

Higbie, Nathan B., 59 Newcomb Road, Stoneham, MA 02180

Ho, Sze Tee Steve, Apartment Block 516, #07-244, Serangoon North Avenue 4, Singapore 550516

Hoff, Lars, Lubekkveien 46A, Oslo N-0070, Norway

Hollingshead, John S., 4941 Heather Drive, #111, Dearborn, MI 48126

Houk, Gareth M., Naval Research Lab., Acoustic Signal Processing, Code 7120, 4555 Overlook Avenue SW, Washington, D.C. 20375

Impagliazzo, John M., Signal Processing Branch, Naval Undersea Warfare Center, Code 8212, 1176 Howell Street, Newport, RI 02879

Kahn, Simon W., Bits & Pieces, Sunnymede Norlington Lane, Ringmer, Lewes, E. Sussex BN8 5SH, U.K.

Keppens, Veerle M., NCPA, Univ. of Mississippi, Coliseum Drive, University, MS 38677

Kim, Michael, 8803 Bells Mill Road, Potomac, MD 20854
King, Gregory D., 3740 Boyd Avenue, Apt. 137, San Diego, CA 92111
Kraus, Dieter, STN Atlas Elektronik, Signal and Systems Analysis, Sebaldsbrucker Heerstr. 235, Bremen 28305, Germany
Kraus, Robert P., Eastman Kodak Company, Analytical Technology Div., Rochester, NY 14652-3710
Lanza Di Scalea, Francesco, Center for Nondestructive Evaluation, Johns Hopkins University, 102 Maryland Hall, 3400 North Charles Street, Baltimore, MD 21218
Lavallee, Timothy L., Geo-Marine, Inc., 11846 Rocklanding Drive, Suite C, Newport News, VA 23606
Lavery, Andone C., Applied Ocean Physics and Engineering, Woods Hole Oceanographic Inst., Bigelow 404, MS 9, Woods Hole, MA 02543
Lenchine, Valeri V., 400 Whitney Avenue, Apt. 17, New Haven, CT 06511
Li, Dan, 55 River Drive, South, #2105, Jersey City, NJ 07310
Lilian, Chiang C. W., Blk. 522, Hougang Ave 6, #04-01, Singapore 530522
Lloyd, Daniel J., 3 Clareville Crescent, Kallaroo WA 6025, Australia
Mazzola, Salvatore, Via Villagiocosa N.9, Palermo 90146, Italy
McNeary, Michael W., Veneklasen Associates, 1711 Sixteenth Street, Santa Monica, CA 90404
Meng, Xianwe, 1041 Hemlock Hills Drive, Apt. A, Akron, OH 44313
Mills, Thomas K., 3131 Castle Leigh Road, Silver Spring, MD 20904
Mukherjee, Binu K., Physics, Royal Military College of Canada, P.O. Box 17000, Station Forces, Kingston, ON K7K 7B4, Canada
Mulet, Jordi F., Comte Borrell, 328, 6-1, Barcelona E-08029, Spain
Myungho, Han, Architectural Engineering, Seonam University, 720 Kwangchidong, Namwon, Chonbuk 590-711 Korea
Neal, Stephen R. W., Frank Hubach Associates, 2700 Rydin Road, Suite F, Richmond, CA 94804
Noca, Flavio, Microdevices Lab., Jet Propulsion Lab., M/S 302-306, 4800 Oak Grove Drive, Pasadena, CA 91109
Oligee, Louis P., Technology Services—Acoustics, GE Appliances, Appliance Park AP35-1101, Louisville, KY 40225
Olsen, Mark R., 4022 Manhattan, St. Peters, MO 63376-6544
Pellegrino, Thomas J., 283 Lakeview Avenue West, Brightwaters, NY 11718
Petrovic, Srdan, GN Resound, Research and Development, 220 Saginaw Drive, Redwood City, CA 94063
Punch, Jerry L., Audiology & Speech Sciences, Michigan State University, East Lansing, MI 48824
Ramirez, Guillermo, Civil Engineering, Univ. of Kansas, 2006 Learned Hall, Lawrence, KS 66045
Read, Robert D., The RCC Group, 429 South Cedar Road, New Lenox, IL 60451
Reeves, Efrem R., Caterpillar, Inc., Machine Research, P.O. Box 1895, Peoria, IL 61615
Rendall, Drew, Psychology and Neuroscience, Univ. of Lethbridge, 4401 University Drive, Lethbridge, AB T1K 3M4, Canada
Rodas, Ingrid E., Medical Research Group, Document Center, 13628 Jeff Davis Highway, #3, Woodbridge, VA 22191
Roozen, N. B., Philips Electronics Nederland B. V., CFT Mechatronics, Glaslaan 2, P.O. Box 218, Eindhoven 5600MD, The Netherlands
Ryder, John S., 2 Albert Road, Dorchester, Dorset DT1 1SE, England
Schlegel, Robert E., School of Industrial Engineering, Univ. of Oklahoma, 202 West Boyd, Suite 124, Norman, OK 73019
Sek, Aleksander P., Dept. of Physics, Inst. of Acoustics, A. Mickiewicz University, 85 Umultowska Street, Poznan 61614, Poland
Shiro, Ise, Dept. of Architecture and Architectural Systems, Graduate School of Engineering, Kyoto University, Yoshida-Honmachi, Sakyo-ku, Kyoto-shi, Kyoto-fu 606-8501, Japan
Shore, Susan E., Kresge Hearing Research Inst., Univ. of Michigan, Otolaryngology Dept., 1301 East Ann Street, Ann Arbor, MI 48109
Shorter, Philip J., Vibro-Acoustic Sciences, 12555 High Bluff Drive, Suite 310, San Diego, CA 92130
Sorkin, Donna L., Alexander Graham Bell Association for Deaf and Hard of Hearing, 3417 Volta Place NW, Washington, D.C. 20007-2778
Stanzani, Marco, Via San Maurizio Al Lambro 4, Brugherio MI 20047, Italy
Stover, Dennis L., The Dow Chemical Company, North End Loveridge Road, P.O. Box 1398, Pittsburg, CA 94565
Sun, Chao, Inst. of Acoustical Engineering, P.O. Box 9, Northwestern Polytechnical Univ., 127 West YouYi Road, Xi'an, Shaanxi 710072, P.R. China
Sun, Wei, Communicative Disorders & Science Dept., SUNY Buffalo, 215 Parker Hall, Buffalo, NY 14214
Surlykke, Annemarie, Dept. of Psychology, University of Maryland, College Park, MD 20742-4411
Tateno, Takashi, Graduate School of Engineering Science, Osaka University, 1-3 Machokaneyama, Toyonaka, Osaka 560-8531, Japan
Thomas, Jeanette A., Lab. of Sensory Biology, Western Illinois Univ. Regional Center, 3561 60th Street, Moline, IL 61265
Thompson, Ronald A., 1055 Nightingale Drive, Palatine, IL 60067
Tokuma, Shinichi, Dept. of English, Sagami Women's University, 2-1-1 Bunkyo, Sagami-Hara, Kanagawa 228-8533, Japan
Trainor, Laurel J., Psychology, McMaster University, 1080 Main Street West, Hamilton, ON L8S 4K1, Canada
Valenzuela, Miriam N., UC Berkeley, Psychology Dept., 3210 Tolman Hall, #1650, Berkeley, CA 94720-1650
Vance, Timothy J., Connecticut College, East Asian Languages, 270 Mohegan Avenue, New London, CT 06320-4196
Walker, John R., 31 Park Road, Portland, Dorset DT5 2AD, U.K.
Wang, Tao, Engineering Science, 104-44, California Inst. of Technology, 1200 East California Boulevard, Pasadena, CA 91125
Wayson, Roger L., Civil and Environmental Eng., Univ. of Central Florida, P.O. Box 162450, Orlando, FL 32816-2450
Weiss, Lora G., Pennsylvania State University, Applied Research Lab., N. Atherton Street, State College, PA 16804
Williams, Barry S., 1066 West 450 North, Provo, UT 84601
Woodward, Jon M., 2831 Gill Avenue, Lawrence, KS 66047
Zhou, Chunnan, 1834 Grant Street, Evanston, IL 60201

New Students

Abdelli, Wassima, 199 City Island Avenue, P.O. Box 261, City Island, NY 10464
Acosta, Guillermo, 250 Pinetree Circle, Decatur, GA 30032
Aravamudhan, Radhika, No. 820, Morris Road, Apt. 6, Kent, OH 44240
Atalla, Youssef Ya., 1464 Choquette, Sherbrooke, PQ J1K 3B8, Canada
Baskent, Deniz, 3320 Keystone Avenue, Apt. 6, Los Angeles, CA 90034
Bischel, Lillian E., 69-43 44th Avenue, 1st Floor, Woodside, NY 11377
Bissonnette, Christian M., Univ. de Sherbrooke, Mecanique, 2500 Boul. Universite, Sherbrooke, QC J1K 2R1, Canada
Bolduc, MaxiMe, Genie Mecanique, Univ. de Sherbrooke, 2500 Boul. Universite, Sherbrooke, QC J1K 2R1, Canada
Bonnoit, Alyssa C., Swarthmore College, 500 College Avenue, Swarthmore, PA 19081
Bowman, Denise M., 14 Scimitar Court, NW, Calgary, AB T3L 2B4, Canada
Carlson, John G., 2110 Warrington Court, Blenview, IL 60025
Carmena, Jose M., Div. of Informatics, Univ. of Edinburgh, 5 Forrest Hill, Edinburgh EH1 2QL, Scotland
Casper, Maureen A., 48 Tyler Circle, Rye, NY 10580
Chan, Michael T., 110 East Foster Avenue, #315, State College, PA 16801
Clarke, Cory L., Aerospace and Mechanical Engineering, Boston University, 110 Cummington Street, Boston, MA 02215
Cook, Daniel A., 332943 Georgia Tech Station, Atlanta, GA 30332-1475
Coussios, Constantin C., 7 Lambourn Close, Cambridge CB2 1RF, U.K.
Cruz, Omar, RR 8 Box 9137, Bayamon 00956, Puerto Rico
Daley, Michael J., 641 Marjorie Mae Street, State College, PA 16803
Daniels, Jeffrey A., 195 Jeffrey Drive, Sandpoint, ID 83864
Dayton, Paul A., 510 Arthur Street, #104, Davis, CA 95616
Deloach, Alana G., 99 Wyman Street, Apt. 2, Jamaica Plain, MA 02130
Dias, Vivian F., 630 East 1700 South, #9, Orem, UT 84097
Dix, Gordon R., 562 North 400 East, #14, Provo, UT 84606
Doyle, Timothy E., 3298 North 700 West, Pleasant View, UT 84414-2100
Duchassin, Franck, Genie Mecanique, Univ. de Sherbrooke, Sherbrooke, PQ J1K 2R1, Canada
Fain, Annika M., Environmental Science and Engineering, Oregon Graduate Institute, 20000 NW Walker Road, Beaverton, OR 97006
Faulds, Brandon C., 8807 Colonial Drive, Austin, TX 78758
Frisch, Katherine J., 707 Miller Avenue, Ann Arbor, MI 48103
Fuentes Cabrera, Alvaro Rodrigo, Ottawa #4383, Villa Canada San Joaquin, Santiago, Chile
Ghandi, Ahmad, American Export, Building 68 JFK, Jamaica, NY 11430
Gladden, Joseph R., Pennsylvania State University, Dept. of Physics, 104 Davey Lab., State College, PA 16802
Heake, John F., 637 East McCormick Avenue, State College, PA 16801
Hoffmann, Gustavo A., Rua Thomas Edison, 371, Ivoti RS 93900-000, Brazil

Kaschner, Kristin, Marine Mammal Research Unit, Fisheries Center, Univ. of British Columbia, Hut B-3, 6248 Biological Sciences Road, Vancouver, BC V6T 1Z4, Canada
Keane, Michael F., 144 Annwood Road, Palm Harbor, FL 34685
Kim, Daniel Y., High-Energy Physics/Cleo Group, Wilson Lab., Harvard Group, Cornell University, Ithaca, NY 14853
Knightly, Leah M., UCLA Psychology Dept., Graduate Mailroom Box 951563, Los Angeles, CA 90095-1563
Kocbach, Jan M., Kirkegaten 1C, Bergen 5009, Norway
Kumar, Aman, Program in Linguistics, Univ. of Michigan, 105 South State Street, #1076, Ann Arbor, MI 48109
Lanctot, Benoit, Genie Mecanique, Univ. de Sherbrooke, 2500 Boul. Universite, Sherbrooke, QC J1K 2R1, Canada
Langlois, Christian, 1950 rue Montagnais, App. 409, Sherbrooke, PQ J1K 2X9, Canada
Leslie, Damian M., 54 Attra Street, Perth WA 6021, Australia
Li, Chi Nin Herman, 8720 Delaware Road, Richmond, BC V7C 4Y3, Canada
Measer, Kathleen M., SUNY Buffalo, Psychology Dept., Park Hall, Amherst, NY 14260-4110
Mencik, Jean Mathieu, Genie Mecanique, GAUS, Boulevard de L'Universite, Sherbrooke, QC J1K 2R1, Canada
Moore, Geoffrey A., Experimental Psychology Dept., Cambridge University, Downing Street, Cambridge CBZ 3EB, U.K.
Narendran, Mini M., 615 West 15th Street, Apt. #8, Bloomington, IN 47404
Patel, Rupal, 276 St. George Street, #409, Toronto, ON M5R 2P6, Canada
Pavlov, Peter M., 101 Dublinwood Drive, Bellefonte, PA 16823
Pelletier, Yvan, Genie Mecanique, GAUS, Univ. de Sherbrooke, 2500 Blvd. Universite, Sherbrooke, QC J1K 2R1, Canada
Poliachik, Sandra L., Applied Physics Lab., University of Washington, 1013 NE 40th Street, Seattle, WA 98105-6698
Pouplier, Marianne, 28 Cottage Street, New Haven, CT 06511
Reich, Rebecca D., 4708 Roslyn Avenue, Montreal, PQ H3W 2L2, Canada
Richter, Melanie M., 4523 Prescott Avenue, Apt. 1, Lincoln, NE 68506
Rust, Daniel E., 5442 Brockbank Place, San Diego, CA 92115
Shafiro, Valeriy, 870 West 181st Street, #29B, New York, NY 10033
Shrivastan, Rahul, Speech and Hearing Sciences, Indiana University, 200 South Jordan Avenue, Bloomington, IN 47405
Slama, Angela L., 1515 Chandler Street, #1, Madison, WI 53711
Solberg, Stephen E., 202 East Cherry Street, Vermillion, SD 57069
Sow, Ibrahima, Genie Machanique, Univ. de Sherbrooke, 2500 Blvd. Universite, Sherbrooke, QC J1K 2R1, Canada
Summers, Jason E., 167 2nd Street, Troy, NY 12180
Teles, Sorin V., Aerospace Engineering and Engineering Mechanics, Iowa State University, 2019 Black Engineering Building, Ames, IA 50011
Thompson, Michael, 99 West 2170 North, Apt. 301, Provo, UT 84604
Thubthong, Nuttakorn, 34/166 M. 1. Ramaz Rd., Bangkok 10150, Thailand
Tuttle, Brian C., 314 West Nittany Avenue, State College, PA 16801
Ucar, Fatma Nazan, Maison Asahigaska #207, 2-17-1 Asahiganka, Hino-shi T191-8503, Tokyo, Japan
Wanis, Sameh S., School of Aerospace Engineering, Georgia Inst. of Technology, Atlanta, GA 30332-0150
Weber, Rolf, Signal Theory, IC 5/36, Ruhr Univ. Bochum, Universitaetsstr. 150, Bochum D-44780, Germany
Wysocki, Tamra M., Linguistics, Univ. of Chicago, 1010 East 59th Street, Chicago, IL 60637
Zotkin, Dmitry N., Dept. of Computer Science, Univ. of Maryland at College Park, A. V. Williams Building, College Park, MD 20742

Members Elected Fellows

M. Badiey, L. E. Bernstein, B. Ferguson, J. R. Franks, C. G. Greene, Jr., J. M. Hillenbrand, A. Hirschberg, M. Kleiner, R. S. Langley, W. K. Melville, S. Ohtsuki, F. M. Pestorius, P. O. Thompson, P. L. Tyack, P. J. Vidmar

Associates Elected Members

Z. K. Alhamdani, S. J. Allyn, M. K. Ang, A. Arvaniti, G. A. Ator, P. D. Baird, C. Bjerrum-Niese, J. F. Bridger, R. J. Brothers, D. M. Byrd, L. N. Cattafesta, III, D. J. Cheenne, S. L. Denham, T. M. Edgecock, L. J. Fradkin, L. Franck, M. A. Garces, T. Harada, A. P. Holden, C. W. Holland, T. Honkalehto, W. L. Kellermann, J-I. Kushibiki, E. Larsen, X. Lei, G. Liu, P. R. Lizana, O. I. Lobkis, L. N. Long, M. J. Lucas, R. D. Magnuson, M. J. Moore, R. M. Moroney, L. R. Moss, A. D. Munro, R. V. Murray, C. A. Negreira, J. C. Osler, V. Pallayil, C. E. Parssinen, N. R. Pennington, N. B. Roozen, M. V. Shitikova, M. Silveira, P. L. Tan, F. C. Tao, P. W. J. van Hengel, E. B. Viveiros, S. E. Voss, R. L. Wayson, C. Wong, J. Yang, C. Zhou

Students to Associates

B. A. Barker, T. K. Berger, T. A. Burnett, M. Dallal, M. J. Dapino, M. F. Dille, L. E. Dreisbach, D. G. Druker, M. L. Hawley, Y. Hirata, L. L. Holt, P. Hursky, C. M. Hurtgen, J. A. Ketterling, L. M. Lavoie, W.-S. Lee, T. C. Lieuwen, J. J. Lister, T. M. Logan, D. O. Ludwigsen, L. Max, G. R. Mellema, F. R. Ragozzine, R. J. Ruhala, J. A. Shaw, D. D. Sternlicht, S. L. Tantum, S. M. Tasko, P. Zahorik, S. E. Zeller, B. Zellner-Keller, E. M. Zettner, E. J. Zimmerman

Associate to Student

W. Soares-Filho

Reinstated

D. Boulahbal, A. K. Krishnamurthy, S. E. Voss, A. C. Walley—*Associates*

Resigned

G. S. Field, W. Rudmose—*Fellows*

O. Bergem, O. J. Bonello, P. Dalsgaard, R. K. Goodnow, J. B. Hall, Jr., W. Hong, E. P. Jensen, W. Kainz, D. Marsh, W. W. Meeks, R. Rasch, W, J, Remillard, D. O. ReVelle, P. F. D. Seitz, R. L. Sergeant, C. W. Sherry, P. T. Thawani, E. R. Writer, C-Y. Wu, M. C. Young, P. Zakelj—*Members*

R. L. Baum, B. Canlon, R. De Mori, A. Garcia, G. A. Gates, P. W. Jacobus, M. D. Prange, P. J. Price, J. T. Sherman, J. M. N. Vieira, M. J. Wilson—*Associates*

L. Fitzpatrick, J-S. S. Genot, E. Kluetz, D. T. Marks, N. C. Michel, P. A. Ryl—*Students*

Deceased

J. N. Holmes, S. N. P. Ingemansson—*Fellows*

J. W. Bray, A. C. Goodman, I. Hochberg, J. F. Keithley, E. W. McMorrow, E. S. Rogers—*Members*

Fellow	845
Members	2826
Associates	2857
Students	886
	7414

ACOUSTICAL NEWS—INTERNATIONAL

Walter G. Mayer
Physics Department, Georgetown University, Washington, DC 20057

Papers published in JASJ(E)

A listing of Invited Papers and Regular Papers appearing in the latest issue of the Englih language version of the *Journal of the Acoustical Society of Japan*, JASJ(E), was published for the first time in the January 1995 issue of the Journal. This listing is continued below.

The November issue of JASJ(E), Vol. 20, No. 6 (1999) contains the following contributions:

A review paper by M. Cohen, J. Herder, and W. L. Martens, ''Cyberspatial audio technology'' and regular papers:

T. Irino and M. Unoki, ''An analysis/synthesis auditory filterbank based on an IIR implementation of the gammachirp''
Y. Takano, ''Improved acoustical analysis method using the normal derivative form of a Helmholtz boundary integral equation''
T. Fujita and S. Ando, ''Subjective evaluations of the sound field in a piano practice room with reflective sound added using electro-acoustic technology''
S. Tsuge, T. Fukada, H. Singer, and K. K. Paliwal, ''Speaker normalized spectral subband parameters for noise robust speech recognition''
H. Mukai, S. Sakamoto, and H. Tachibana, ''Experimental study on the absorption characteristics of resonance-type brick/block walls''

The January issue, Vol. 21, No. 1 (2000) contains the following regular papers:

M. Yoshioka, K. Mizutani, and K. Nagai, ''A tomographic visualization of sound fields using laser diffraction''
S. Sakamoto, H. Mukai, and H. Tachibana, ''Numerical study on sound absorption characteristics of resonance-type brick/block walls''
R. Mochizuki, Y. Arai, and T. Honda, ''A study of the word synthesis method by using the VCV-balanced word database''

Proceedings available

Contributions to Psychological Acoustics. Proceedings of the 8th Oldenburg Symposium on Psychological Acoustics, Oldenburg, Germany, September 1999, edited by A. Schick, M. Meis, and C. Reckhardt. Contains 570 pages with 30 contributions by young scientists with innovative ideas and by internationally acclaimed experts, conveying insight into the current standing of the debate among German research groups. The English language document is published by Oldenburg University. The current list price is 25 Euro or $25, with postage included. For a listing of titles visit www.physik.uni-oldenburg.de/Docs/aku/symposium99.html

International Meetings Calendar

Below are announcements of meetings to be held abroad. Entries preceded by an * are new or updated listings with full contact addresses given in parentheses. *Month/year* listings following other entries refer to meeting announcements, with full contact addresses, which were published in previous issues of the *Journal*.

April 2000

3–4 **Structural Acoustics 2000**, Zakopane. (Fax:+48 12 423 3163; Web: www.cyf-kr.edu.pl/ghpanusz) *8/99*

17–18 ***Institute of Acoustics (UK) Spring Conference**, Liverpool, UK. (IOA, 77A St. Peter's Street, St. Albans, Herts AL1 3BN, UK; Fax: 44 1727 850 553; e-mail: ioa@ioa.org.uk)

May 2000

5–7 **Nordic Acoustics Meeting**, Rǿros. (Fax: +47 73 59 14 12; e-mail: aase@tele.ntnu.no) *2/00*

17–19 **9th International Meeting on Low Frequency Noise and Vibration**, Aalborg. (Fax: +44 1277 223 453) *6/99*

23–26 **Russia Acoustical Society Meeting**, Moscow. (Fax: +7 095 126 8411; e-mail: ras@akin.ru) *10/99*

23–26 **6th International Conference on Tactil Aids, Hearing Aids on Cochlear Implants**, Exeter. (Fax: +44 1392 264111; Web: newton.ex.ac.uk/medphys/pages/isasc.html) *2/00*

23–26 ***17th Symposium on Acoustics**, Jurata, Poland. (Fax: +48 58 625 4846; e-mail: sha@dolphin.eti.pg.gda.pl)

24–26 **Joint International Symposium on Noise Control & Acoustics for Educational Buildings** (24–25 May) and **5th Turkish National Congress on Acoustics** (25–26 May), Istanbul. (Fax: +90 212 261 0549; Web: www.takder.org) *10/99*

June 2000

5–9 **International Conference on Acoustics, Speech and Signal Processing (ICASSP-2000)**, Istanbul. (Fax: +1 410 455 3969; Web: icassp2000.sdsu.edu) *6/99*

6–9 **5th International Symposium on Transport Noise and Vibration**, St. Petersburg. (Fax: +7 812 127 9323; e-mail: noise@mail.rcom.ru) *6/99*

14–17 **IUTAM Symposium on Mechanical Waves for Composite Structures Characterization**, Chania. (Fax: +30 821 37438; Web: www.tuc.gr/iutam) *10/99*

July 2000

4–7 **7th International Congress on Sound and Vibration**, Garmisch-Partenkirchen. (Fax: +49 531 295 2320; Web: www.iiav.org/icsv7/html) *12/98*

9–13 **19th International Congress on Education of the Deaf & 7th Asia-Pacific Congress on Deafness**, Sydney, Australia. (ICED 2000 Secretariat, GPO Box 128, Sydney, NSW 2001 Australia; Fax: +61 2 9262 3135; Web: www.iced2000.com)

10–13 **5th European Conference on Underwater Acoustics**, Lyon. (Fax: +33 4 72 44 80 74; Web: www.ecua2000.cpe.fr) *12/99*

10–14 ***5th International Conference on Mathematical and Numerical Aspects of Wave Propagation**, Santiago de Compostela, Spain. (Waves2000 Secretariat, Domain de Voluceau, BP 105, 78153 Le Chesnay cedex, France; Web: www.usc.es/waves2000)

August 2000

28–30 **INTER-NOISE 2000**, Nice. (Fax: +33 1 47 88 90 60; *New Web: internoise2000/loa.espci.fr) *6/99*

31–2 **International Conference on Noise & Vibration Pre-Design and Characterization Using Energy Methods (NOVEM)**, Lyon. (Fax: +33 4 72 43 87 12; Web: www.insa-lyon.fr/laboratories/lva.html) *6/99*

September 2000

3–6 **5th French Congress on Acoustics—Joint Meeting of the Swiss and French Acoustical Societies**, Lausanne. (Fax: +41 216 93 26 73) *4/99*

13–15 **International Conference on Noise and Vibration Engineering (ISMA 25)**, Leuven. (Fax: +32 16 32 24 82; e-mail: lieve.notre@mech.kuleuven.ac.be) *12/99*

17–21 **Acoustical Society of Lithuania 1st International Conference**, Vilnius. (Fax: +370 2 223 451; e-mail: daumantas.ciblys@ff.vu.lt) *8/99*

18–22 ***47th Seminar on Acoustics (OSA2000)**, Zalew Solinski, Poland. (e-mail: osa@atena.univ.rzeszow.pl)

 0001-4966/2000/107(4)/1805/2/$17.00

October 2000

3–5 **WESTPRAC VII**, Kumamoto. (Fax: +81 96 342 3630; Web: cogni.eecs.kumamoto-u.ac.jp/others/westprac7) *6/98*

3–6 **EUROMECH Colloquium on Elastic Waves in NDT**, Prague. (Fax: +420 2 858 4695; e-mail: ok@bivoj.it.cas.cz) *10/99*

12–14 **International Conference on Newborn Hearing Screening**, Milan. (Fax: +39 2 23993367/.60; Web: www.biomed.polimi.it/nh2000) *2/00*

16–18 **2nd Iberoamerican Congress on Acoustics, 31st National Meeting of the Spanish Acoustical Society, and EAA Symposium**, Madrid. (Fax: +34 91 411 7651; e-mail: ssantiago@fresno.csic.es) *12/98*

16–20 **6th International Conference on Spoken Language Processing**, Beijing. (Fax: 86 10 6256 9079; Web: www.icslip2000.org) *10/98*

August 2001

28–30 **INTER-NOISE 2001**, The Hague. (Web: internoise2001.tudelft.nl) *6/99*

September 2001

2–7 **17th International Congress on Acoustics (ICA)**, Rome. (Fax: +39 6 4424 0183; Web: www.uniromal.it/energ/ica.html) *10/98*

10–13 **International Symposium on Musical Acoustics (ISMA 2001)**, Perugia. (Fax: +39 75 577 2255; e-mail: perusia@classico.it) *10/99*

October 2001

17–19 **32nd Meeting of the Spanish Acoustical Society**, La Rioja. (Fax: +34 91 411 76 51; Web: www.ia.csic.es/sea/index.html) *10/99*

September 2002

16–21 **Forum Acusticum 2002 (Joint EAA-SEA-ASJ Meeting)**, Sevilla. (Fax: +34 91 411 7651; Web: www.cica.es/aliens/forum2002) *2/00*

BOOK REVIEWS

P. L. Marston
Physics Department, Washington State University, Pullman, Washington 99164

These reviews of books and other forms of information express the opinions of the individual reviewers and are not necessarily endorsed by the Editorial Board of this Journal.

Editorial Policy: *If there is a negative review, the author of the book will be given a chance to respond to the review in this section of the Journal and the reviewer will be allowed to respond to the author's comments. [See "Book Reviews Editor's Note," J. Acoust. Soc. Am.* ***81****, 1651 (May 1987).]*

Ultrasonic Waves in Solid Media

Joseph L. Rose

Cambridge University Press, 1999.
Price: $90.00 (hardcover), ISBN: 0521640431.

This new book by Joseph L. Rose of The Pennsylvania State University is a comprehensive review of ultrasonic wave propagation in solid media with special emphasis on ultrasonic nondestructive evaluation (NDE) and quantitative materials characterization. During the last 20–30 years, NDE in general, and ultrasonic NDE in particular, has become a mature engineering principle that is taught at both undergraduate and graduate levels at many of the leading academic institutions all over the world. Still, there have been very few successful efforts to write a textbook connecting the fundamental physics of elastic wave propagation to practical engineering applications and, in particular, the inherently rather elaborate analytical methods to the design and evaluation of experimental measurements. Rose's new textbook provides a seamless connection between the two conventional, often unnecessarily separated, poles of theory and experiments. Throughout the book, the author presents a rigorous summary of the relevant fundamentals, that can be found only in the best theoretical works that have been used as textbooks by graduate students and practicing researchers for years, like B. A. Auld's *Acoustic Fields and Waves in Solids* (Krieger, Malabar, 1990) or J. D. Achenbach's *Wave Propagation in Elastic Solids* (Elsevier Science, Amsterdam, 1984). Still, his approach is clearly that of somebody who is ultimately interested in the experimental aspects of acoustic wave propagation in solids, like K. F. Graff's widely used textbook of similar inception, *Wave Motion in Elastic Solids* (Dover, New York, 1991). However, Rose focuses on the high-frequency aspects of acoustic wave propagation and his main goal is to lay down the foundations for applied research in ultrasonic nondestructive evaluation and materials testing. This practicality is unparalleled in other basic textbooks written on the subject and could be found previously only in textbooks specifically written for experimentalists, such as J. Krautkramer and H. Krautkramer's celebrated *Ultrasonic Testing of Materials* (Springer, Berlin, 1990). The book is organized into 20 chapters followed by five appendices containing additional information that might be especially valuable in graduate studies. Parts of the book could serve as reading material for senior-level undergraduate or dual-level graduate courses, but the bulk of the material is more suitable for advanced graduate courses and could easily support a three-quarter or two-semester series on ultrasonic wave propagation and nondestructive evaluation.

After a short Introduction in Chap. 1, the following two chapters present the fundamental dispersion principles and wave equations in both isotropic and anisotropic media. As in most standard texts, the distinction between phase and group velocities is brought out and the most important anisotropic wave propagation phenomena are discussed in detail. In Chaps. 4 through 6, acoustic reflection, refraction, and scattering are reviewed. Chapter 4 starts with the simple case of normal incidence reflection/transmission at a plane interface separating semi-infinite media and continues with the discussion of the basic concepts of oblique incidence wave refraction including Snell's Law, critical angles, and mode conversion. Chapter 5 builds on these concepts and demonstrates how the reflection and transmission coefficients can be calculated generally for different boundary conditions. Chapter 6 briefly introduces the most important methods used in wave-scattering calculations. With the exception of the normal-mode decomposition technique, which is well demonstrated through the example of shear horizontal wave scattering from a cylindrical cavity, the rest of this short summary dealing with the boundary element method, the Born approximation, and the *T*-matrix approach, is perhaps a bit ambitious and is merely introduced in order to make the reader aware of the different possibilities.

Chapters 7 through 13 deal with different types of guided waves that represent the main area of focus in this book. The topics include the fundamental Rayleigh-type surface mode propagating on the free surface of a solid half-space, Lamb-type guided modes propagating in thin plates, Stoneley-type interface waves propagating along the interface separating two elastic half-spaces, Scholte-type interface waves propagating along the surface of a fluid-loaded solid half-space, both vertically and horizontally polarized surface modes propagating on a layered half-space, longitudinal, torsional, and flexural waves in cylindrical rods, both circumferential and axial guided waves in hollow cylinders, leaky guided waves along immersed shells, and generalized guided waves in multiple-layer structures such as coated plates, adhesively bonded and diffusion-bonded plates. Although the presentation of the fundamental dispersion relationship is fairly straightforward in each particular case, the sheer number of the elements in the corresponding characteristic matrix and the algebraic complexity of the resulting dispersion equation is sometimes overwhelming. Possibly, it would have been beneficial to present all the explicit expressions for the characteristic matrices separately in one of the appendices so that the underlying physics could be more apparent for less experienced readers who do not necessarily want to experiment with numerical evaluation of a six-by-six or even higher-order secular determinant.

The one minor difficulty this reviewer experienced while otherwise thoroughly enjoying reading through this part of the book was the rather casual, alternating use of the $e^{i(kx-\omega t)}$ and $e^{i(\omega t-kx)}$ complex amplitude conventions for harmonic waves. Undoubtedly, either convention is as good as the other, since only the real part of the complex quantity is assumed to represent the actual physical quantity. However, inexperienced students might be confused by a sign that changes from chapter to chapter and, in some cases, even within the same chapter. Furthermore, the sign convention does make an important physical difference in some cases, for example, in choosing between the first and second kind of Hankel functions for the appropriate leaky field produced by axial guided waves in an immersed cylinder or whether the attenuation coefficient of the guided wave is equal to the imaginary part of the wave number or to its negative value.

Chapter 14 deals with the influence of nonideal sources, a topic of great practical importance that is entirely missing from almost all textbooks written about ultrasonic wave propagation in solid media. The two particular examples discussed in greater detail include dispersive guided wave generation and detection in traction-free plates and bulk wave generation and detection in three-dimensional anisotropic media. In the first case, the selectivity of an ultrasonic angle-beam transducer for a particular plate mode is analyzed by the normal-mode expansion technique and the role of the transducer's size, through its effect on the directivity pattern, is shown to be as important as its center frequency and bandwidth. In the case of an anisotropic medium, beam skewing in other than principal directions often results in specific problems such as apparent energy loss, anomalous focusing, beam splitting, etc. A simple numerical integration method using Green's functions is shown to accurately predict the previously mentioned anisotropic distortions of the acoustic beam in transversely isotropic materials as well as in more generally anisotropic media.

Following the main line of the book, Chaps. 15 and 16 continue the discussion of different types of guided waves in plates. First, the family of horizontally polarized guided modes is presented. Traditionally, the Rayleigh–Lamb modes of sagital polarization are primarily associated with wave propagation in plates. These modes, which are combinations of longitudinal and vertically polarized shear partial waves, can be readily generated

 0001-4966/2000/107(4)/1807/2/$17.00

and detected via normal surface tractions in either immersion or contact inspection and they allow a more complete characterization of material properties than the horizontally polarized family, which contains only shear partial waves. However, with the recent development of electromagnetic acoustic transducers (EMATs), horizontally polarized plate modes can also be relatively easily exploited for flaw detection or texture assessment in sheet metal, and these guided modes are expected to play an increasing role in future ultrasonic NDE applications. As a final note on guided wave propagation, ultrasonic waves propagating in a free anisotropic layer, such as a composite lamina, are considered in Chap. 16. The main differences between the isotropic and anisotropic cases are briefly explained and the characteristic anisotropic features are demonstrated through the example of a typical unidirectional composite plate. It would have been beyond the scope of Rose's book to extent this discussion to the case of multilayered composite laminates; interested readers are referred to A. H. Nayfeh's recent book on this subject, *Wave Propagation in Layered Anisotropic Media with Applications to Composites* (North-Holland, Amsterdam, 1995).

The following three chapters of the book are dedicated to three special topics of great interest in ultrasonic materials characterization. Chapter 17 discusses the most crucial issues of data inversion, i.e., how the sought elastic moduli of the material can be obtained from the actually measured velocity data. This inversion is particularly difficult in the case of anisotropic media, when often as many as five to nine independent constants need to be determined and sufficient accuracy cannot be achieved unless the measurements are made not just arbitrarily based on the convenience of the experimental arrangement but more systematically based on the sensitivity of given modes to a limited number of elastic moduli. Chapter 18 outlines the basic concepts of viscoelasticity and briefly reviews its impact on ultrasonic wave propagation. The well-known Maxwell and Kelvin–Voight models are analyzed in detail, but the readers are advised that overwhelming experimental evidence suggests that the actual behavior of most viscoelastic materials, such as plastics, adhesives, and epoxy matrix composites, appear to be best modeled at ultrasonic frequencies by assuming that both the real and imaginary parts of the elastic moduli are independent of frequency. Finally, Chap. 19 discusses the influence of stress on the velocity of ultrasonic waves propagating in solid media. This so-called acousto-elastic effect is arguably the most important nonlinear phenomenon that can be exploited for ultrasonic materials evaluation and plays a unique role in nondestructive residual stress assessment.

The last chapter of the book presents a short introduction to the most efficient analytical tool available for numerical modeling of ultrasonic wave propagation in solid media, namely the boundary element method. By its nature, Chap. 20 belongs a little more to the following excellent and very useful appendices rather than to the rest of the book, which is focused mainly on the physical concepts of ultrasonic wave propagation. These appendices include a short review of the special methods and instrumentation used in ultrasonic NDE, a list of basic formulas from the theory of elasticity, that are particularly relevant to ultrasonic wave propagation, a very useful introduction to the use of complex variables, some examples of Schlieren imaging and dynamic photoelasticity, and a series of key wave propagation experiments. This last appendix contains seven basic experiments that provide the students with sufficient laboratory experience not only to better understand the theoretical concepts learned from this textbook but also to start individual graduate research in ultrasonic NDE. Along with the excellent series of questions and problems presented in the exercise sections at the end of each chapter, this extensive set of appendices makes this textbook especially valuable for both graduate students and educators. Overall, Rose's *Ultrasonic Waves in Solid Media* is clearly the product of many years of combined experience in teaching and research in the subject area and it will undoubtedly serve as one of the most influential textbooks for generations of graduate students in ultrasonic nondestructive testing and materials characterization all over the country as well as in other parts of the world.

PETER B. NAGY
Department of Aerospace Engineering and Engineering Mechanics
University of Cincinnati
Cincinnati, Ohio 45221-0070

Acoustics of Layered Media I: Plane and Quasi-plane Waves (Springer Series on Wave Phenomena Volume 5) *Second, Updated Printing (softcover)*

L. M. Brekhovskikh and O. A. Godin

Springer-Verlag, New York, 1998.
x+242 pp. Price: $59.95.

Acoustics of Layered Media II: Point Sources and Bounded Beams (Springer Series on Wave Phenomena Volume 10) *Second, Updated and Enlarged Edition*

L. M. Brekhovskikh and O. A. Godin

Springer-Verlag, New York, 1999.
xv+524 pp. Price: $139.00.

These two monographs, which we will refer to as ALM I and II, are revised versions of books first published in 1990 and 1992, respectively. The publisher does not actually refer to ALM I as a second edition but rather as a second, softcover, printing of the first edition. While the revisions to ALM I are minor, the revisions and additions to ALM II are extensive and resulted in a 33% increase in the number of pages.

The books originated from a single body of work devoted to a summary review of sound-wave propagation in inhomogeneous media. Since it clearly would not have been practical to publish the material in a single book, it was divided according to the nature of the acoustic source. In ALM I monochromatic plane waves, both homogeneous and inhomogeneous, are treated, as well as pulsed plane waves. ALM II treats point sources and bounded wave beams. There are other divisions as well. Elastic wave propagation is discussed in ALM I and propagation in a range-dependent waveguide is treated in ALM II. While the two books are self-contained, the material in the first three chapters of ALM II, devoted to the refraction and reflection of spherical waves, the reflection of bounded beams, and to an excellent discussion of lateral waves, has more in common with ALM I than with the rest of the material in ALM II. I have found that there is a degree of continuity and ease of reading if these three chapters are read after having read ALM I.

Any summary review of wave propagation in layered media must necessarily build on the material in Acad. Brekhovskikh's earlier books and at first glance, it might seem ALM I and II simply represent a more mathematical treatment of old topics. These books actually provide a comprehensive survey of contemporary research in acoustical wave propagation. Many of the citations are to material published in 1999. Older topics are treated, of course, but with such thoroughness and from such an original point-of-view that new, interesting results are often obtained.

Even though there is an emphasis on the authors' own research contributions, the treatment of topics is balanced and contributions by others are thoroughly discussed. In addition, summaries are included, with references, of topics not considered in detail. These summary paragraphs are a valuable feature of the books. The books do not treat several of the research themes that have preoccupied U.S. underwater acousticians during the last two decades including propagation through random media, ocean acoustic tomography, and global propagation problems. They do deal with some of the fundamentals upon which these subjects are based.

ALM I and II were written in English by the authors; they are not translations by a native English speaker of earlier Russian editions. Most of the minor language and typographical errors have been corrected in the new versions but a few remain. In general, they do not hinder readability.

Before surveying the material chapter by chapter, it is worthwhile mentioning some of the significant features of these books. They contain a detailed treatment of acoustic propagation in moving media. Throughout both books a topic is first studied for a medium at rest and then generalized to a moving one. The authors derive new equations for linear propagation in moving media that include, as special cases, many of the equations derived by others. Modal, geometric acoustics, and parabolic approximation descriptions of propagation in moving media are developed.

The Reciprocity Principle and the Flow Reversal Theorem are central themes of ALM II. These symmetry relations state that an acoustic quantity is invariant under interchange of source and receiver and, if the medium is moving, reversal of the flow. They are of both practical and theoretical importance. These relations are derived and studied for many different situations and used to obtain general constraints on propagation processes and to develop new, approximate, propagation models.

Chapter 8 of ALM II is new in this edition and contains a discussion of a new, fundamental reformulation of the theory of both acoustic and acoustic-gravity waves in three-dimensional, inhomogeneous moving media. The focus is the study of reciprocity and energy conservation using a hybrid Eulerian–Lagrangian description. This description, which has been used in a somewhat different form by other researchers, leads to simplified equations of motion and boundary conditions and is used to obtain, under very general conditions, the Flow Reversal Theorem as well as other conservation laws. A number of applications of this new approach have already been published.

These books are characterized by a high degree of thoroughness in the treatment of the topics considered. It is this thoroughness as much as anything else that allows the authors to discover interesting results even when they consider old topics. Two illustrative examples are the treatment of boundary conditions and of source terms. The authors not only consider the usual types of rigid boundary and interface conditions but also investigate, starting from first principles, how the conditions change when the medium is in motion or the boundary is deformable. As a consequence, some new results are obtained. In ALM II source terms are included from the beginning in the Euler and continuity equations is a form based on physical considerations. Because of this approach, the authors are able to show, for example, that the acoustic quantity invariant under interchange of source and receiver positions (Reciprocity Principle) depends on the nature of the source. If the authors had been less thorough in their treatment of source terms, they would have missed this fascinating result.

The lists of references is a valuable feature of the books. There are over 1700 citations in the two books. The majority of these are to material originally published in English (67%) or translated into English from Russian (15%). Another 15% of the citations are to references in Russian that have not been translated—typically books, conference proceedings, and older research articles. About 2% are to references published in German or French. The authors went to great effort to make the lists comprehensive, up-to-date, correct, and useful.

In Chapter 1 of ALM I the linear wave equations are derived for acoustic waves in an inhomogeneous moving media and for elastic waves in isotropic solids. This derivation is repeated in Chapter 4 of ALM II but there sound sources are included. We see in Chapter 1 the first example of a technique used throughout. The wave equation is transformed to some desirable form by introducing a new independent (vertical) variable and by scaling the field. In this case the equation for a plane wave in a medium with density and flow field stratification is reduced to a Helmhotz-like equation. The same technique is used to show the similarity between a horizontally polarized shear wave propagating in a layered solid and a sound wave propagating in a layered fluid. Chapter 2 considers monochromatic plane waves propagating in stationary and moving discretely layered media. The emphasis is on calculating the reflection and transmission coefficients. Chapter 3 considers exact solutions to the wave equation for continuously layered media. By transforming the equation to a general, solvable form, essentially all the possible solvable models are constructed and several are discussed in detail. In Chapter 4 reflection of waves from discretely layered solid media is studied. Various cases are considered—elastic media with free boundaries, two or more solids in contact with one another, and a solid in contact with a fluid. Rayleigh, Stonely, and other types of waves that can exist near the boundary of an elastic medium are also discussed.

Reflection of pulsed sound waves from discrete and continuous layered media is discussed in Chapter 5 based on the law of conservation of integrated pulse. We see here another characteristic of the books. Through their analysis the authors are able to clear up confusion resulting from errors in the literature. In this case, the error relates to the change in shape of a pulse as it propagates in a waveguide. Chapter 6 is an interesting chapter in which the universal properties of reflection and transmission coefficients are discussed—those properties that are independent of the detailed nature of the stratification. Chapter 7 considers viscoelastic media and absorptive fluids, anisotropic elastic media and fine layered media. The discussion of the case when the modulus of the reflection coefficient is greater than unity for two viscoelastic media in contact has been improved in this printing. Chapters 8 and 9 treat the WKB approximation, its range of validity, and methods

 0001-4966/2000/107(4)/1809/2/$17.00

for estimating the sound field when the approximation is not adequate. Chapter 10 discusses the determination of the reflection coefficient and the impedance for an arbitrary layered media. It is suggestive of Chapter 6 and contains some improvements over the first printing. The focus is on the use of equations satisfied by the reflection coefficient rather than those satisfied by the sound field.

Turning now to ALM II, we have already mentioned the material in its first three chapters and in Chapter 8. After deriving the linear equations that determine the sound field, Chapter 4 continues with a discussion of reciprocity relations and exact solutions to the wave equation. The discrete spectral (modal) representation of the field in layered media is derived. This is done not by using separation of variables and expanding the sound field in a complete set of eigenfunctions of the one-dimensional wave equation but by associating modes with the residue of poles in an integral representation of the field. This 40-page discussion is full of useful techniques and interesting results. For example, the discrete spectrum of the sound field of a point source in a moving medium cannot, in general, be represented in terms of a superposition of modes, unlike the case of a medium at rest. Chapter 5 develops the geometric optics approximation and Chapter 6 is devoted to a discussion of the sound field in the neighborhood of a caustic. This chapter is somewhat unsatisfying. The line diagrams are not particularly informative and the chapter is full of tedious algebraic details. This is certainly not the place to look if one is interested in learning about the geometric structure of caustics. On the positive side the chapter does discuss how to calculate the sound field in the vicinity of a few types of caustics and this, after all, is what is ultimately important.

Chapter 7, devoted to wave propagation in a range-dependent waveguide, is one of the more important chapters in the books. Representation in terms of local modes is discussed as is the use of horizontal rays and vertical modes. The section on rays in range-dependent waveguides centers about the use of the ray invariant. The last part of this chapter is devoted to parabolic equation methods. The introductory material is somewhat dated but the authors make up for this shortcoming in their discussion of the parabolic approximation for a field in a moving medium.

Appendix A reminds one of Chapter 4 of *Radiation and Scattering of Waves*, by Felsen and Marcuvitz (IEEE Press, 1994). It contains a useful discussion of the classes of integrals that are typically approximated by the method of steepest descent. These integrals are encountered throughout the text. Uniform asymptotic approximations are also discussed.

Appendices B and C are new with this edition and could have been included as separate chapters in the body of the book. Appendix B is concerned with a modal description of propagation in a waveguide having range-dependent boundaries or interfaces. This is a difficult and subtle problem because the boundary conditions satisfied by the acoustic field differ from those satisfied by the local modes. The series expansion of the field in terms of modes can be so poorly convergent that it is not always possible to interchange differentiation and series summation and substitution of the series into the wave equation leads to coupled-mode equations that are unphysical. The authors address this problem by using energy conservation and reciprocity rather than by using the wave equation. They are able to derive coupled-mode equations that correct or extend the work done by others.

In Appendix C parabolic equations are derived starting with the constraints imposed by energy conservation and reciprocity. The authors begin by rigorously defining what is meant by these concepts in the context of the parabolic approximation. Using an inductive rather than a deductive process, they develop improved, wide-angle parabolic equations. There are some gems here for aficionados of the parabolic approximation: for the case considered, energy conservation and reciprocity are equivalent; self-adjointness of the vertical operator in a parabolic equation generally leads to a conservation law that is different from and incompatible with the energy conservation law; and reciprocal, wide-angle parabolic equations typically require range-derivatives of the medium parameters in their coefficients.

With a very careful choice of topics to be covered, I think these books could be used as texts for an advanced graduate course. (The authors' statement that senior undergraduate courses were taught using the books refers to the Soviet system where an undergraduate was someone working toward a degree roughly equivalent to a MS degree.) It should be noted these books require a motivated reader; one does not gain much from a superficial reading.

For the researcher, these books could not only provide a valuable source of reference material and a useful introduction to the literature on a given topic, but could also be the source of new research ideas.

In summary, ALM I and II represent an impressive achievement on the part of the authors as well as a great deal of ordinary hard work. They are recommended for anyone interested in the theoretical aspects of wave propagation.

DAVID R. PALMER
Office of the Director
NOAA Atlantic Oceanographic and Meteorological Laboratory
Miami, Florida 33173

REVIEWS OF ACOUSTICAL PATENTS

Lloyd Rice
11222 Flatiron Drive, Lafayette, Colorado 80026

The purpose of these acoustical patent reviews is to provide enough information for a Journal reader to decide whether to seek more information from the patent itself. Any opinions expressed here are those of reviewers as individuals and are not legal opinions. Printed copies of United States Patents may be ordered at $3.00 each from the Commissioner of Patents and Trademarks, Washington, DC 20231.

Reviewers for this issue:

GEORGE L. AUGSPURGER, *Perception, Incorporated, Box 39536, Los Angeles, California 90039*
DAVID PREVES, *Songbird Medical, Inc., 5 Cedar Brook Drive, Cranbury, New Jersey 08512*
KEVIN P. SHEPHERD, *M.S. 463, NASA Langley Research Center, Hampton, Virginia 23681*
ERIC E. UNGAR, *Acentech, Incorporated, 33 Moulton Street, Cambridge, Massachusetts 02138*

5,886,264

43.20.Rz SYSTEM AND METHOD FOR PREDICTING SOUND RADIATION AND SCATTERING FROM AN ARBITRARILY SHAPED OBJECT

Quiang Hu and Sean F. Wu, assignors to Wayne State University
23 March 1999 (Class 73/646); filed 5 May 1997

Prediction of the acoustic pressure radiated from a vibrating object into an unbounded fluid is accomplished via a surface integral of the particle velocity. That velocity is determined nonintrusively via a Doppler laser velocimeter. The computed solutions are unique and can be obtained with high numerical efficiency by use of standard Gaussian quadratures.—EEU

5,901,231

43.38.Fx PIEZO SPEAKER FOR IMPROVED PASSENGER CABIN AUDIO SYSTEMS

Michael J. Parrella *et al.*, assignors to Noise Cancellation Technologies, Incorporated
4 May 1999 (Class 381/86); filed 25 September 1995

Small, flat, piezoelectric modules are attached to the sides and roof of a vehicle cabin to reproduce mid and high frequencies. ''Since midrange and high-frequency sounds are the most readily attenuated by the materials in the automobile..., placing these sound sources close to the listener improved the perceived sound quality.''—GLA

5,884,254

43.38.Hz METHOD AND APPARATUS FOR RESTRICTING MICROPHONE ACCEPTANCE ANGLE

Melih Uear, assignor to Sensimetrics Corporation
16 March 1999 (Class 704/231); filed 2 August 1995

The patent describes a method of limiting the width of microphone system's pickup lobe. Secondary mics on either side of the primary mic are turned away from each other, leaving only a narrow angle of pickup overlap. When both side mics are receiving a signal, the main mic is turned on. The patent does not discuss smoothing of the side-mic control signals, either before or after the AND gate which controls the main mic.—DLR

5,793,877

43.38.Ja THROUGH-WINDOW SPEAKER/ MICROPHONE

James Peter Tagg, assignor to Moonstone Technology Limited
11 August 1998 (Class 381/156); filed 19 May 1995

A conventional loudspeaker voice coil is used to drive a small flat glass plate. This motor assembly is then mounted to a larger sheet of glass, such as a shop window. The object is, ''...to efficiently transfer plate movements to the window for causing the window to directly radiate sound as a result of speaker coil motion.''—GLA

5,818,950

43.38.Ja SPEAKER SYSTEM AND ITS SUPPORT LEGS

Yoshio Sakamoto *et al.*, assignors to Kabushiki Kaisha Kenwood
6 October 1998 (Class 381/201); filed in Japan 25 February 1994

A rigid, portable projection screen might easily be 2 in. thick without impairing its utility as a screen. The resulting internal cavity could then be used to house built-in stereo speakers. However, it is obvious that unusual speakers and baffling means must be employed. The patent describes a fairly elaborate scheme to generate low frequencies. This is combined with more conventional mid- and high-frequency transducers to cover a frequency range from about 50 to 20 000 Hz.—GLA

5,850,460

43.38.Ja BASS SPEAKER

Shoji Tanaka *et al.*, assignors to Matsushita Electric Industrial Company, Limited
15 December 1998 (Class 381/186); filed in Japan 1 September 1994

A single-ended bandpass system consists of a loudspeaker, a sealed rear cavity, and a vented front cavity. If the vent is replaced by a passive radiator, total volume can be slightly reduced and unwanted sound radiation from the vent is greatly attenuated. The patent suggests that if two identical systems are mounted back to back, then inertial forces are canceled and enclosure vibrations are reduced accordingly.—GLA

 0001-4966/2000/107(4)/1811/7/$17.00

5,875,255

43.38.Ja HIGH POWER ELECTROACOUSTIC SPEAKER SYSTEM HAVING WIDE BAND FREQUENCY RESPONSE

Paul G. Campbell, Detroit, MI
23 February 1999 (Class 381/345); filed 28 August 1997

Every few years someone gets the idea of making a loudspeaker enclosure function like a bass viol. Enclosure panel resonances are deliberately heightened rather than suppressed. The patent describes an otherwise conventional vented loudspeaker system having at least two novel features: (1) a low-pass filter located in the vent (an absorptive ring), and (2) a sound post connecting the front and back panels. The goal is to provide wideband response at very high sound levels for amplified musical instruments.—GLA

5,884,194

43.38.Si HANDS-FREE TELEPHONE

Koichi Shiraki, assignor to Mitsubishi Denki Kabushiki Kaisha
16 March 1999 (Class 455/570); filed in Japan 16 May 1997

This hands-free telephone system is similar to prior applications of this type of circuit in making use of signal-level measurements, threshold comparisons, and voice-detection systems. Various embodiments of the present

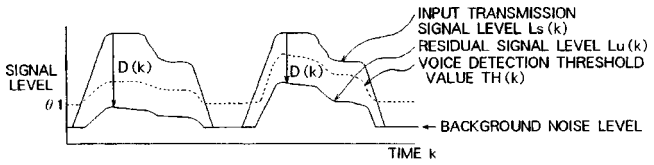

invention arrange these elements in different ways to improve the system's performance in handling all four combinations of neither end, one end, or both ends talking, while reducing clicks and cutouts.—DLR

5,889,843

43.38.Si METHODS AND SYSTEMS FOR CREATING A SPATIAL AUDITORY ENVIRONMENT IN AN AUDIO CONFERENCE SYSTEM

Andrew Jay Singer *et al.*, assignors to Interval Research Corporation
30 March 1999 (Class 379/202); filed 4 March 1996

The invention is concerned with multiple-site audio teleconferencing. It relies on binaural pickup and includes user control of ''metaphorical representations'' of each site. ''It...provides a new model for creating virtual spaces of communication through coherent audio and conceptual representation.'' Although the terminology is rarified, the patent is clearly written and the concept is interesting.—GLA

5,799,094

43.38.Vk SURROUND SIGNAL PROCESSING APPARATUS AND VIDEO AND AUDIO SIGNAL REPRODUCING APPARATUS

Tomohiro Mouri, assignor to Victor Company of Japan, Limited
25 August 1998 (Class 381/18); filed in Japan 26 January 1995

Conventional two-channel stereo reproduction relies on a phantom center image to fill the space between the two speakers. Relatively simple signal processing can also create the illusion of images lying beyond, rather than between, the loudspeakers. Recent work with more elaborate head-

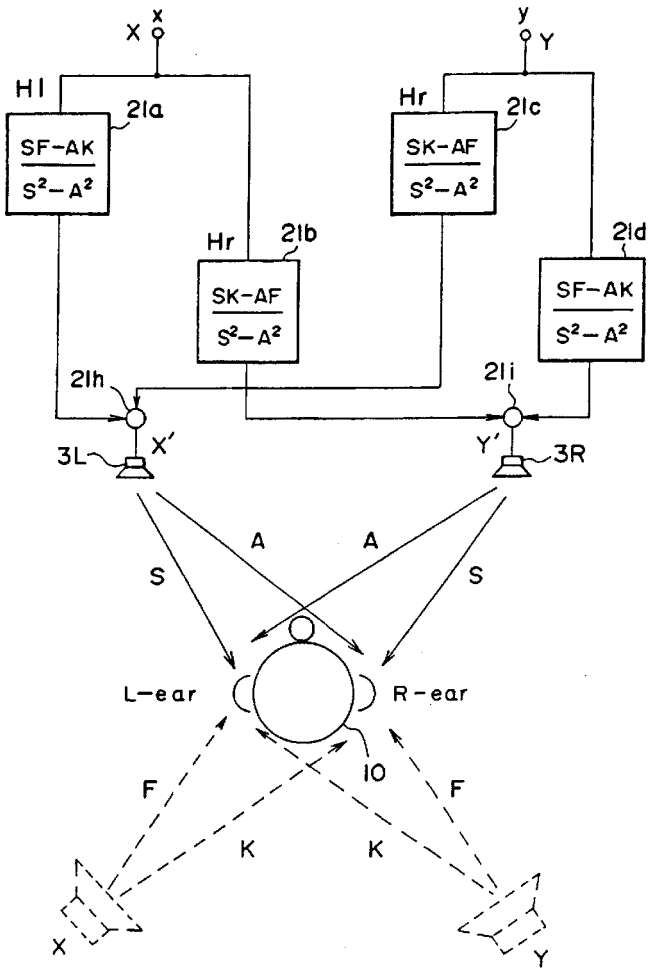

transfer functions can generate well-localized left and right rear phantom channels, allowing five-channel stereo recordings to be reproduced through two loudspeakers. The invention falls into this category. Symmetrical pairs of localizing filters are used to create the two rear channels.—GLA

5,809,150

43.38.Vk SURROUND SOUND LOUDSPEAKER SYSTEM

Steven J. Eberbach, Ann Arbor, MI
15 September 1998 (Class 381/24); filed 12 October 1995

A pair of loudspeakers in a conventional enclosure can be connected through phase-shift networks to function as a gradient source over a fairly wide range of frequencies. The penalty is 6 dB per octave of low-frequency rolloff which must be made up by equalization. Some home theater systems use dipole loudspeakers to reproduce surround channels; however, the patent suggests that a skewed hypercardioid pattern may be superior because of the narrow angle between principal lobe and null. ''Rear'' surround speakers can be located in the front of the listening room.—GLA

5,812,676

43.38.Vk NEAR-FIELD REPRODUCTION OF BINAURALLY ENCODED SIGNALS

Edwin C. Johnson, Jr., assignor to Bose Corporation
22 September 1998 (Class 381/24); filed 31 May 1994

The invention is the audio equivalent of an old-fashioned stereoptican viewer. A chin support 20 is provided to position the listener's head correctly in relation to near-field loudspeakers 28 and 30. The device may also

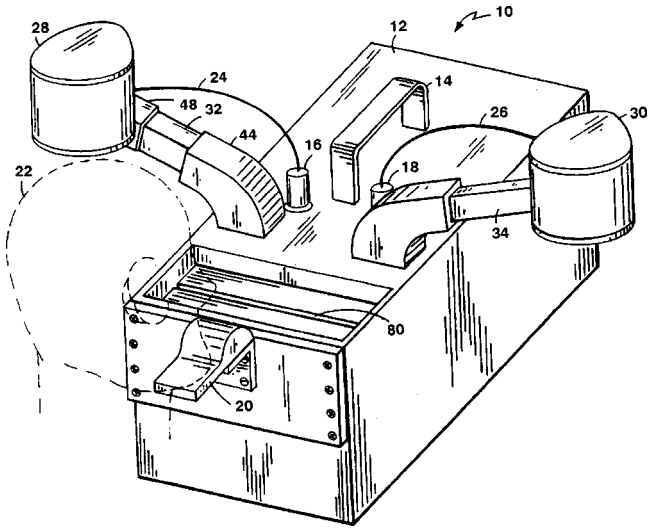

incorporate a video screen. ''When reproducing binaurally encoded signals, it creates a three-dimensional auditory illusion that is more realistic than the illusions produced by headphones or by far-field loudspeakers.''—GLA

5,822,438

43.38.Vk SOUND–IMAGE POSITION CONTROL APPARATUS

Satoshi Sekine *et al.*, assignors to Yamaha Corporation
13 October 1998 (Class 381/17); filed in Japan 3 April 1992

In a conventional two-channel stereo mixing console, individual sources can be panned anywhere between full left and full right. The pan pot simply adjusts relative levels between left and right channels. The patent describes a more sophisticated position control incorporating variable delay and interaural crosstalk cancellation, enabling virtual images to be located beyond, as well as between, the two loudspeakers.—GLA

5,907,880

43.40.Tm METHOD FOR PROVIDING ACTIVE DAMPING OF THE VIBRATIONS GENERATED BY THE WASHING ASSEMBLY OF WASHING MACHINES AND WASHING MACHINE IMPLEMENTING SAID METHOD

Piero Durazzani and Lucio Valent, assignors to Electrolux Zanussi S.p.A.
1 June 1999 (Class 8/159); filed in Italy 15 May 1997

The central feature of this patent consist of replacement of the conventional shock absorbers that connect between a washing machine's wash drum and the machine housing by shock absorbers whose damping is adjusted automatically as the drum's rotational speed changes. The latter shock absorbers contain an electrorheological fluid, whose viscosity depends on the magnetic field to which it is subjected. Here, this field is provided by an electromagnet whose strength is adjusted in accordance with the drum's speed on the basis of a signal provided by a tachometer or similar device.—EEU

5,924,261

43.40.Tm METHOD AND APPARATUS FOR DAMPING STRUCTURAL VIBRATIONS

J. Robert Fricke, assignor to Massachusetts Institute of Technology
20 July 1999 (Class 52/720.1); filed 12 June 1996

Damping of hollow structural members is accomplished by filling them with granular material; damping of open structural members is achieved by placing granular material in intimate contact with them. Unlike relatively heavy granular materials like sand or lead shot, which have been used similarly, the granular materials described in this patent are such lightweight materials as polyethylene beads and glass microspheres. The patent states that the size, shape, material properties, and composition of these materials may be engineered to meet performance criteria for specific applications.—EEU

5,859,856

43.40.Yq ELECTROMAGNETIC ACOUSTIC TRANSDUCER AND METHODS OF DETERMINING PHYSICAL PROPERTIES OF CYLINDRICAL BODIES USING AN ELECTROMAGNETIC ACOUSTIC TRANSDUCER

Ward L. Johnson, George A. Alers, and Bertram A. Auld, assignors to the United States of America as represented by the Secretary of Commerce
20 April 1999 (Class 73/643); filed 2 August 1994

A plurality of magnets is distributed circumferentially inside a tubular housing, with the magnets extending radially and adjacent magnets having opposite polarities. The cylindrical body to be tested is inserted axially in the circular space remaining near the center of the housing. Coils are provided in the space between the magnets and the test object, with some coils' wires extending axially and others circumferentially (in solenoid fashion). Current flowing in the coils produce eddy currents in the test object; interaction of these with the magnetic field result in Lorentz forces acting on the test object. Depending on the coils configuration used and on the current supplied to them, these forces can be made to induce radial, axial shear, compressional, or torsional vibrations in the test object. The responses, sensed via wire coils, are claimed to be useful for the determination of the temperature, dimensions, elastic constants, damping coefficients of a cylindrical object, or the texture and grain orientation of its material.—EEU

5,870,483

43.40.Yq SOUND-INSULATING CAP FOR SOUND LEVEL METERS

George S. K. Wong and Noland L. Lewis, assignors to National Research Council of Canada
9 February 1999 (Class 381/189); filed 24 February 1997

This patent pertains to a cap intended to fit over a microphone, so as to shield the microphone from ambient acoustic noise. The purpose of a measurement made in this manner is to determine the sensitivity of the microphone/sound-level-meter system to electromagnetic interference. The cap is made of a number of layers with different properties and is vented to prevent damage to the microphone membrane during installation and removal of the cap.—EEU

5,905,803

43.40.Yq FLUSH-PORTING METHOD AND DEVICE FOR REDUCTION OF WIND-INDUCED NOISE IN A MICROPHONE

Xinyu Dou *et al.*, assignors to Motorola, Incorporated
18 May 1999 (Class 381/359); filed 14 March 1997

According to this patent, a microphone for a two-way radio, cellular phone, or similar device is mounted in a cavity so that its sensing surface is flush with the outer edge of an opening in the device's housing. The microphone is covered with a detachable film that is no thicker than is required to maintain its structural integrity and that contains one or more apertures which permit sound to impinge on the microphone transducer.—EEU

5,872,853

43.50.Gf NOISE-ABATEMENT DEVICE

Stanley Lynn Marquiss, Plymouth, CA
16 February 1999 (Class 381/73.1); filed 10 December 1993

A multitude of loudspeakers placed adjacent to a highway is designed to actively control road traffic noise in the 10–40-Hz region. Detailed design of the cylindrically radiating loudspeakers is given and various geometric arrangements are described.—KPS

5,878,704

43.50.Gf ELECTROMAGNETIC ACTUATOR, INCLUDING SOUND-MUFFLING MEANS, FOR OPERATING A CYLINDER VALVE

Michael Schebitz and Franz Pischinger, assignors to FEV Motorentechnik GmbH & Company, Germany
9 March 1999 (Class 123/90.11); filed in Germany 4 January 1997

An electromagnetic actuator designed for the operation of a cylinder valve in an internal combustion engine is described in which layers of a temperature resistant material having elastic properties are attached to the actuator in order to reduce transmission of vibration from the electromagnet.—KPS

5,904,318

43.50.Gf PASSIVE REDUCTION OF AIRCRAFT FUSELAGE NOISE

Foad Towfiq, Oceanside, CA
18 May 1999 (Class 244/1.N); filed 18 December 1996

A design for an aircraft fuselage sidewall is described in which the outer skin **52** is attached to frame members **56** and a damping rod **54** is attached to adjacent frame members to reduce relative vibration. An additional damping rod may be provided between the outer skin **52** and the rod

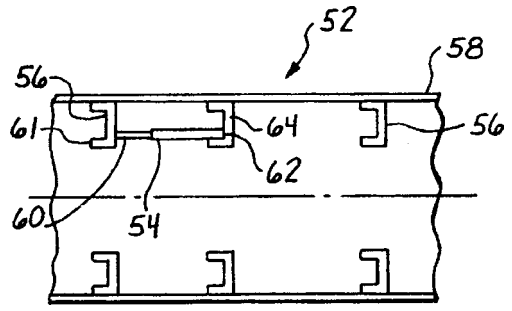

54. The inner trim panel is structurally isolated from the outer skin assembly. Several arrangements of septa and insulation blankets within the sidewall are described.—KPS

5,919,029

43.50.Gf NOISE ABSORPTION SYSTEM HAVING ACTIVE ACOUSTIC LINER

William C. Van Nostrand *et al.*, assignors to Northrop Grumman Corporation
6 July 1999 (Class 415/119); filed 15 November 1996

An active acoustic liner for absorption of fan and turbine noise in an aircraft engine is described. A conventional acoustic liner consisting of a honeycomb core **105** and porous facesheet **110** is most effective over a narrow frequency range. An arrangement is described which enables a conventional liner to be tuned to changing engine conditions. A piezoresonator **100** is composed of a piezoelectric actuator **125** attached to a sheet of metal

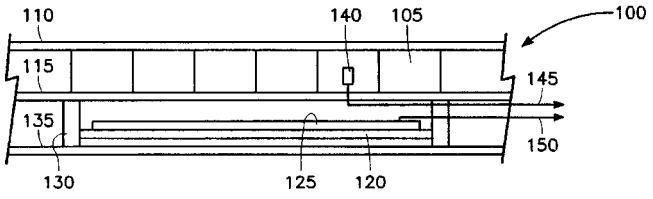

120 and the backing skin **135**. An acoustical pressure sensor **140** mounted inside one of the honeycomb cells is used to determine the control signal which drives the piezoresonator. Each piezoresonator covers an area containing several honeycomb cells and may be placed at various locations within the engine.—KPS

5,923,003

43.50.Gf EXTENDED REACTION ACOUSTIC LINER FOR JET ENGINES AND THE LIKE

Noe Arcas *et al.*, assignors to Northrop Grumman Corporation
13 July 1999 (Class 181/292); filed 9 September 1996

An acoustic liner for application to aircraft engines is described in which a conventional liner consisting of a porous facesheet **14** and a honeycomb core **20** is modified to allow fluid communication between some of

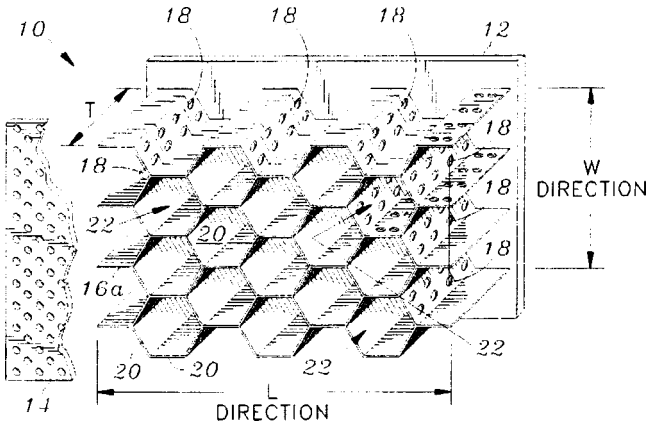

the cells of the honeycomb via openings **18**. Viscous acoustic losses occur due to these openings, the size and number of which may be tailored to provide the desired acoustic resistance.—KPS

5,845,236

43.50.Ki HYBRID ACTIVE–PASSIVE NOISE AND VIBRATION CONTROL SYSTEM FOR AIRCRAFT

Mark R. Jolly *et al.*, assignors to Lord Corporation
1 December 1998 (Class 702/195); filed 16 October 1996

A hybrid active–passive system for reducing noise within a passenger compartment and vibration of a fuselage of a vehicle such as a turboprop aircraft or helicopter is described. Loudspeakers for active noise control, active vibration absorbers, and passive tuned vibration absorbers are used in combination to provide both noise and vibration reduction. This combination remedies the drawbacks of each technique when applied individually. Various transducer arrangements are described for turboprop and helicopter applications and test results are given for both noise and vibration reduction.—KPS

5,873,559

43.50.Ki ADAPTIVELY TUNED VIBRATION ABSORBER FOR REDUCTION OF AIRCRAFT CABIN NOISE

Andreas H. von Flotow *et al.*, assignors to Applied Power, Incorporated
23 February 1999 (Class 248/557); filed 17 April 1997

Adaptively tuned vibration absorbers are incorporated into an aircraft engine mount to reduce transmitted vibration along two orthogonal axes. A sensor placed on the engine is used to determine the speeds of two rotating spools in the engine. Two additional sensors detect vibration along the two axes. The resonant frequencies of four vibration absorbers attached to the mounting structure are dynamically tuned to track the variation in vibrations due to changes in engine speed. Mechanical details of the absorbers are described, as is the control circuit.—KPS

5,905,234

43.55.Dt SOUND ABSORBING MECHANISM USING A POROUS MATERIAL

Kouji Tsukamoto *et al.*, assignors to Mitsubishi Electric Home Appliance Company, Limited; Mitsubishi Denki Kabushiki Kaisha
18 May 1999 (Class 182/286); filed in Japan 31 August 1994

This patent pertains to a sound-absorbing plate or panel that may be used as a barrier or as part of an enclosure for a noise source. The patent in essence describes a thin absorptive plate of a porous material that is mounted at some distance from an acoustically reflective surface, resulting in an air space between the porous plate and the backing surface. Within this air space additional hard-surfaced volumes are attached to the porous plate, with their open ends touching that plate. These additional volumes are claimed to serve as resonators that broaden the frequency range over which the assembly exhibits enhanced acoustic absorption performance.—EEU

5,879,283

43.66.Ts IMPLANTABLE HEARING SYSTEM HAVING MULTIPLE TRANSDUCERS

Theodore Adams and Kai Kroll, assignors to St. Croix Medical, Incorporated
9 March 1999 (Class 600/25); filed 7 August 1996

A middle ear implantable hearing aid is described in which the outputs of several piezoelectric input or output transducers having different frequency responses are combined to produce an improved frequency response. The transducers may be made of different materials and their outputs may be coupled to the ossicles at different locations or to the tympanic membrane.—DAP

5,881,158

43.66.Ts MICROPHONES FOR AN IMPLANTABLE HEARING AID

S. George Lesinski and Armand Neukermans, assignors to United States Surgical Corporation
9 March 1999 (Class 381/174); filed 23 May 1997

Construction details are provided for one or more electret microphones intended for use in a fully implantable middle-ear hearing aid. The microphone is packaged in a sealed housing with an amplifier and battery. Several signal-processing strategies and implementations of the housing are suggested. The amplifier output is coupled through a sealed connector cable to a microactuator output transducer.—DAP

5,892,836

43.66.Ts DIGITAL HEARING AID

Ryuuichi Ishige *et al.*, assignors to NEC Corporation
6 April 1999 (Class 381/316); filed in Japan 26 October 1995

In this invention, coefficients for a transposed transversal filter are derived from the input signal and the hearing loss of the person being fitted. Further described is a bank of linear phase filters with different passbands corresponding to audiometric test frequencies whose coefficients are used in

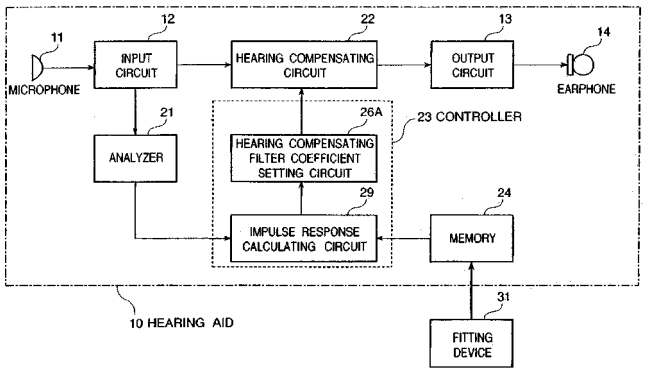

the calculation of the transposed transversal filter coefficients. This implementation is said to reduce filter order while improving signal-to-noise ratio and reducing distortion.—DAP

5,864,806

43.72.Ar DECISION-DIRECTED FRAME-SYNCHRONOUS ADAPTIVE EQUALIZATION FILTERING OF A SPEECH SIGNAL BY IMPLEMENTING A HIDDEN MARKOV MODEL

Chafie Mokbel *et al.*, assignors to France Telecom
26 January 1999 (Class 704/234); filed in France 6 May 1996

This speech spectral equalization system associates a filter with each state of a hidden Markov model (HMM). Each speech frame is then filtered prior to its spectral evaluation to determine a probable path of phonetic characteristics according to the HMM state sequence. Utterance probabilities are determined in the usual manner, also according to the HMM state sequence.—DLR

5,878,391

43.72.Ar DEVICE FOR INDICATING A PROBABILITY THAT A RECEIVED SIGNAL IS A SPEECH SIGNAL

Ronaldus M. Aarts, assignor to U.S. Philips Corporation
2 March 1999 (Class 704/233); filed in Belgium 26 July 1993

This speech signal detector is intended primarily for distinguishing speech signals from music signals. To this end, it is based on detecting patterns of power level changes at midrange frequencies, where speech would exhibit significant power levels. Within such bands, speech signal

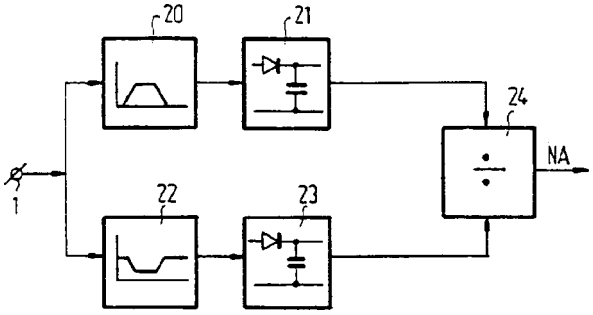

power levels should tend to decay more rapidly than those of a music signal. The device detects the ratio of the rate of midband power decrease to the rate of power decrease outside of this band.—DLR

5,884,260

43.72.Ar METHOD AND SYSTEM FOR DETECTING AND GENERATING TRANSIENT CONDITIONS IN AUDITORY SIGNALS

Frank Uldall Leonhard, Lyngby, Denmark
16 March 1999 (Class 704/254); filed in Denmark 22 April 1993

Speech signal spectrum analyzers often use both zeroth-order (steady-state) and first-order (rate of change) derivatives to represent the spectral vector data. The analysis device in this patent differs in using only the rate-of-change detectors. Applications cited include speech analysis for recognition and coding, speech synthesis, and equipment testing. A substantial part of the patent text consists of an argument for the presence of transient detectors in biological hearing systems.—DLR

5,884,261

43.72.Ar METHOD AND APPARATUS FOR TONE-SENSITIVE ACOUSTIC MODELING

Peter V. de Souza *et al.*, assignors to Apple Computer, Incorporated
16 March 1999 (Class 704/255); filed 7 July 1994

The patent describes a method of speech signal analysis in which a tone frequency value is included with each analysis frame acoustic vector. If the frame signal is voiced, the pitch value is extracted and serves as the frame tone value. If no pitch is detected, a tone value is obtained from either the preceding or succeeding frame. Intended for use in a recognizer, the frame tone value can be used for prosodic detection or, in a tone language, phoneme identification.—DLR

5,864,803

43.72.Bs SIGNAL PROCESSING AND TRAINING BY A NEURAL NETWORK FOR PHONEME RECOGNITION

Paul A. Nussbaum, assignor to Ericsson Messaging Systems, Incorporated
26 January 1999 (Class 704/232); filed 24 April 1995

This system allows the user to implement and train neural networks to perform speech segmentation and phoneme classification. The user specifies the method of acoustic analysis to obtain feature vectors and several parameters describing the neural network architecture. A speech database with

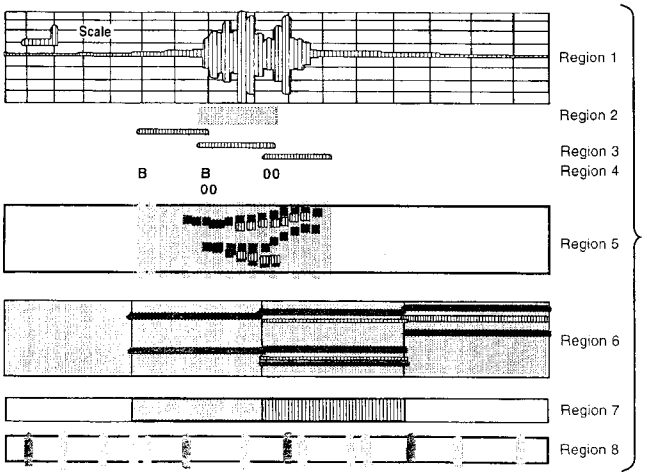

phonemically labeled segments is also required. The system then trains the networks and evaluates the performance of the resulting segmenter/classifier.—DLR

5,878,389

43.72.Dv METHOD AND SYSTEM FOR GENERATING AN ESTIMATED CLEAN SPEECH SIGNAL FROM A NOISY SPEECH SIGNAL

Hynek Hermansky *et al.*, assignors to Oregon Graduate Institute of Science & Technology
2 March 1999 (Class 704/226); filed 28 June 1995

The patent describes a method of reducing the level of noise in a noisy speech signal. Incoming speech frames are analyzed by Fourier transform and separated into magnitude and phase spectra. The magnitude spectrum is compressed by a nonlinear operation, such as an nth-order root extraction. The compressed spectrum is first filtered and then expanded by the inverse nonlinear operation. Filtering methods may include all-pole Wiener filtering or feed-forward neural networks. Recombining the processed magnitude and original phase spectra produces the output speech signal.—DLR

5,859,914

43.72.Gy ACOUSTIC ECHO CANCELER

Yoshihiro Ono and Shigeru Ono, assignors to NEC Corporation
12 January 1999 (Class 381/66); filed in Japan 23 July 1996

This echo canceler generates a replica of the incoming signal by producing locally controlled echoes of subbands of the estimated clean signal and adaptively adjusting the delay and gain of the replica subbands which are then combined to match the characteristics of the arriving signal. A set of subband subtractors can then produce a new estimated clean signal.—DLR

5,862,234

43.72.Gy ACTIVE NOISE CANCELLATION SYSTEM

Chris Todter *et al.*, San Diego, CA
19 January 1999 (Class 381/71.6); filed in Australia 11 November 1992

The patent describes an acoustic transducer which can function simultaneously as loudspeaker and microphone for use in cancellation applications such as speakerphone or conference microphone. Several methods of deriving the microphone signal are covered, including listening during pulsed output silences and by processing the speaker drive signal.—DLR

5,865,626

43.72.Ne MULTI-DIALECT SPEECH RECOGNITION METHOD AND APPARATUS

Valerie L. Beattie *et al.*, assignors to GTE Internetworking, Incorporated
2 February 1999 (Class 434/185); filed 30 August 1996

This speech recognizer constructs spectral density functions for speech frame matching according to a model which combines spectral characteristics for multiple dialects or background acoustic environments. The frame matching may be done using either hidden Markov or statistical word models. Initial matches use a generic spectral density model, but can then switch to a more specific model as recognition proceeds.—DLR

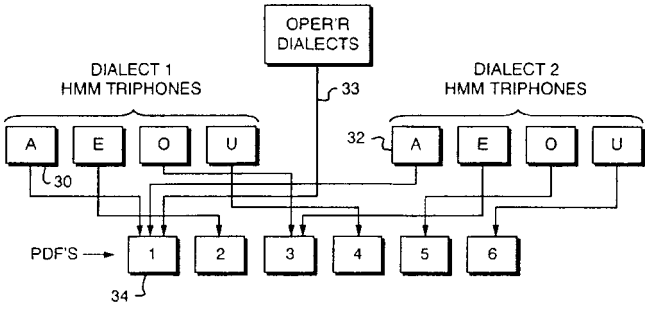

5,873,061

43.72.Ne METHOD FOR CONSTRUCTING A MODEL OF A NEW WORD FOR ADDITION TO A WORD MODEL DATABASE OF A SPEECH RECOGNIZER SYSTEM

Reinhold Haeb-Umbach *et al.*, assignors to U.S. Philips Corporation
16 February 1999 (Class 704/254); filed in European Patent Office 3 May 1995

This system for automatically building speech-recognition word models works by subdividing an initial, generic, utterance-length word model into subword portions. The initial model is generated from a transcription of the new word or by averaging existing models, e.g., from other speakers. As the new word is pronounced by current or new speakers, subword portions are selected by analysis of the matches with the generic model.—DLR

A new formalism for time-dependent wave scattering from a bounded obstacle

Eleonora Mecocci[a] and Luciano Misici[b]
Dipartimento di Matematica e Fisica, Università di Camerino, Via Madonna delle Carceri, 62032 Camerino (MC), Italy

Maria C. Recchioni[c]
Istituto di Teoria delle Decisioni e di Finanza Innovativa (DE.FIN), Università di Ancona, Piazza Martelli 8, 60121 Ancona, Italy

Francesco Zirilli[d]
Dipartimento di Matematica ''G. Castelnuovo,'' Università di Roma ''La Sapienza,'' Piazzale Aldo Moro 5, 00185 Roma, Italy

(Received 4 January 1999; revised 17 November 1999; accepted 23 November 1999)

A time-dependent three-dimensional acoustic scattering problem is considered. An incoming wave packet is scattered by a bounded, simply connected obstacle with locally Lipschitz boundary. The obstacle is assumed to have a constant boundary acoustic impedance. The limit cases of acoustically soft and acoustically hard obstacles are considered. The scattered acoustic field is the solution of an exterior problem for the wave equation. A new numerical method to compute the scattered acoustic field is proposed. This numerical method obtains the time-dependent scattered field as a superposition of time-harmonic acoustic waves and computes the time-harmonic acoustic waves by a new ''operator expansion method.'' That is, the time-harmonic acoustic waves are solutions of an exterior boundary value problem for the Helmholtz equation. The method used to compute the time-harmonic waves improves on the method proposed by Misici, Pacelli, and Zirilli [J. Acoust. Soc. Am. **103**, 106–113 (1998)] and is based on a ''perturbative series'' of the type of the one proposed in the operator expansion method by Milder [J. Acoust. Soc. Am. **89**, 529–541 (1991)]. Computationally, the method is highly parallelizable with respect to time and space variables. Some numerical experiments on test problems obtained with a parallel implementation of the numerical method proposed are shown and discussed from the numerical and the physical point of view. The website: http://www.econ.unian.it/recchioni/w1 shows four animations relative to the numerical experiments. © *2000 Acoustical Society of America.* [S0001-4966(00)05603-4]

PACS numbers: 43.20.Bi, 43.20.Fn [ANN]

INTRODUCTION

Let us consider $\mathbb{R}^3$ filled with a homogeneous nonviscous fluid at rest in an equilibrium state at constant pressure $P>0$, no source terms are present, and let $u^i(\underline{x},t)$ be the perturbation of the pressure field at point $\underline{x}\in\mathbb{R}^3$ and time $t\in\mathbb{R}$ associated to the incoming acoustic field (see Ref. 1, Chap. 6, p. 243). Let $\Omega\subset\mathbb{R}^3$ be a bounded, simply connected open set with locally Lipschitz boundary $\partial\Omega$ and let $\overline{\Omega}$ be its closure. Let $B_a=\{\underline{x}\in\mathbb{R}^3 \,|\, \|\underline{x}\|<a\}$ be the sphere of center the origin and radius a, ∂B_a be the boundary, and $\overline{B_a}$ be the closure of B_a respectively. Instead of B_1, ∂B_1, $\overline{B_1}$, we use B, ∂B, $\overline{B}$, respectively.

Without loss of generality in the following, we assume that there exists $a>0$ such that $\overline{B_a}\subset\Omega$; that is, we assume that Ω contains the origin. We observe that domains with locally Lipschitz boundary include for example polyhedra and that for these domains the outward unit normal vector to $\partial\Omega$, $\underline{n}(\underline{x})=(n_1(\underline{x}),n_2(\underline{x}),n_3(\underline{x}))^T\in\mathbb{R}^3$, $\underline{x}\in\partial\Omega$, exists almost everywhere in $\underline{x}$ when $\underline{x}\in\partial\Omega$ (see Ref. 2, Lemma 2.42, p. 88).

The set Ω represents the obstacle that scatters the incoming acoustic field and we assume that $\partial\Omega$ is characterized by a constant boundary acoustic impedance $\chi\in\mathbb{R}$, $\chi\geqslant 0$.

When the obstacle Ω is present and the incoming wave hits the obstacle Ω, a scattered acoustic wave is generated and we denote with $u^s(\underline{x},t)$ its acoustic pressure at $(\underline{x},t)\in(\mathbb{R}^3\backslash\overline{\Omega})\times\mathbb{R}$. Then, we have that $u^s(\underline{x},t)$ is a solution of the following problem:

$$\Delta u^s(\underline{x},t)-\frac{1}{c^2}\frac{\partial^2 u^s}{\partial t^2}(\underline{x},t)=0,\quad (\underline{x},t)\in(\mathbb{R}^3\backslash\overline{\Omega})\times\mathbb{R}, \quad (1)$$

where $c>0$ is the wave propagation velocity, with the boundary condition (see Ref. 3, p. 66)

$$-\frac{\partial u^s}{\partial t}(\underline{x},t)+c\chi\frac{\partial u^s}{\partial \underline{n}(\underline{x})}(\underline{x},t)=g(\underline{x},t),\quad (\underline{x},t)\in\partial\Omega\times\mathbb{R}, \quad (2)$$

with

$$g(\underline{x},t)=\frac{\partial u^i}{\partial t}(\underline{x},t)-c\chi\frac{\partial u^i}{\partial \underline{n}(\underline{x})}(\underline{x},t),\quad (\underline{x},t)\in\partial\Omega\times\mathbb{R}, \quad (3)$$

[a]Electronic mail: misici@camars.unicam.it
[b]Electronic mail: misici@camars.unicam.it
[c]Electronic mail: recchioni@posta.econ.unian.it
[d]Electronic mail: f.zirilli@caspur.it

and the following boundary condition at infinity:

$$u^s(\underline{x},t)=O\left(\frac{1}{r}\right),\quad r\to+\infty,\quad t\in\mathbb{R}, \tag{4}$$

and the radiation condition:

$$\frac{\partial u^s}{\partial r}(\underline{x},t)+\frac{1}{c}\frac{\partial u^s}{\partial t}(\underline{x},t)=o\left(\frac{1}{r}\right),\quad r\to+\infty,t\in\mathbb{R}, \tag{5}$$

where $r=\|\underline{x}\|$, $\underline{x}\in\mathbb{R}^3$, and $O(\cdot)$ and $o(\cdot)$ are the Landau symbols.

We note that $g(\underline{x},t)$, $(\underline{x},t)\in\partial\Omega\times\mathbb{R}$ in general is defined almost everywhere and that the boundary condition (2) contains as limit cases the acoustically soft obstacle; that is, $\chi=0$, and the acoustically hard obstacle; that is, $\chi=\infty$.

The boundary condition at infinity (4) and the radiation condition (5) imply that $u^s(\underline{x},t)$ as $r\to+\infty$ is made to leading order of outgoing waves (see Ref. 4, p. 485).

Let us recall that since $u^i(\underline{x},t)$ solves (1) in $\mathbb{R}^3\times\mathbb{R}$, we have

$$u^i(\underline{x},t)=\frac{1}{(2\pi)^4}\int_{\partial B}ds(\underline{\alpha})\int_{\mathbb{R}}d\omega\, W(\omega,\underline{\alpha})\times\exp\left(i\frac{\omega}{c}(\underline{x},\underline{\alpha})-i\omega t\right),\quad(\underline{x},t)\in\mathbb{R}^3\times\mathbb{R}, \tag{6}$$

where $ds(\underline{\alpha})$ is the surface measure on ∂B, i is the imaginary unit, and $W(\omega,\underline{\alpha})$, $(\omega,\underline{\alpha})\in\mathbb{R}\times\partial B$, is a suitable distribution. In particular, when $W(\omega,\underline{\alpha})$ has support in $\{(\omega,\underline{\alpha})\in\mathbb{R}\times\partial B|\,\underline{\alpha}=\underline{\gamma},\underline{\gamma}\in\partial B\}$, the integral (6) reduces to a one-dimensional integral, that is

$$u^i(\underline{x},t)=\int_{\mathbb{R}}d\omega\,\tilde{W}(\omega,\underline{\gamma})\exp\left(i\frac{\omega}{c}(\underline{x},\underline{\gamma})-i\omega t\right),\quad(\underline{x},t)\in\mathbb{R}^3\times\mathbb{R}, \tag{7}$$

for a suitable $\tilde{W}(\omega,\underline{\gamma})$. The integral (7) gives an incoming wave $u^i(\underline{x},t)$ of the form

$$u^i(\underline{x},t)=S(\rho(\underline{x},t)),\quad(\underline{x},t)\in\mathbb{R}^3\times\mathbb{R}, \tag{8}$$

where $\rho(\underline{x},t)=(\underline{\gamma},\underline{x})-ct$, and $S(\cdot)$ is the Fourier transform with respect to ω of $\tilde{W}(\omega,\underline{\gamma})$. That is, the wavefront associated to $u^i(\underline{x},t)$ is a plane. When the incoming wave is given by Eq. (6), we assume that the scattered acoustic wave has an expression analogous to the one in Eq. (6); that is

$$u^s(\underline{x},t)=\frac{1}{(2\pi)^4}\int_{\partial B}ds(\underline{\alpha})\int_{\mathbb{R}}d\omega\, W(\omega,\underline{\alpha})\times\exp(-i\omega t)u^s_{\omega,\underline{\alpha}}(\underline{x}),\quad(\underline{x},t)\in(\mathbb{R}^3\backslash\overline{\Omega})\times\mathbb{R}. \tag{9}$$

In Eq. (9) $W(\omega,\underline{\alpha})$ is used as a normalization factor and $u^s_{\omega,\underline{\alpha}}(\underline{x})$ is the wave scattered by the obstacle when hit by an incident plane wave of frequency ω and amplitude 1 that propagates in the direction $\underline{\alpha}$. When the incoming wave is given by Eq. (7), we assume that the scattered acoustic wave has an expression analogous to the one in Eq. (7); that is, in Eq. (7) $\exp(i(\omega/c)(\underline{x},\underline{\gamma}))$ is substituted with $u^s_{\omega,\underline{\gamma}}(\underline{x})$. In the development of the numerical method proposed here, we consider only the case given by Eqs. (6) and (9); that is, the general case. The case given by Eq. (7) and the corresponding formula for the scattered acoustic wave can be treated in a similar way.

It is easy to see that from (1), (2), and (5) it follows that for $\omega\in\mathbb{R}$, $\underline{\alpha}\in\partial B$, $u^s_{\omega,\underline{\alpha}}(\underline{x})$ satisfies the following exterior boundary value problem:

$$\left(\Delta u^s_{\omega,\underline{\alpha}}+\frac{\omega^2}{c^2}u^s_{\omega,\underline{\alpha}}\right)(\underline{x})=0,\quad \underline{x}\in\mathbb{R}^3\backslash\overline{\Omega}, \tag{10}$$

that is, the Helmholtz equation with the boundary condition

$$i\omega u^s_{\omega,\underline{\alpha}}(\underline{x})+c\chi\frac{\partial u^s_{\omega,\underline{\alpha}}}{\partial\underline{n}(\underline{x})}(\underline{x})=b_{\omega,\underline{\alpha}}(\underline{x}),\quad \underline{x}\in\partial\Omega, \tag{11}$$

where

$$b_{\omega,\underline{\alpha}}(\underline{x})=i\exp\left(i\frac{\omega}{c}(\underline{x},\underline{\alpha})\right)[-\omega-\omega\chi(\underline{n}(\underline{x}),\underline{\alpha})],\quad \underline{x}\in\partial\Omega, \tag{12}$$

and the Sommerfeld radiation condition at infinity

$$\frac{\partial u^s_{\omega,\underline{\alpha}}}{\partial r}-\frac{i\omega}{c}u^s_{\omega,\underline{\alpha}}(\underline{x})=o\left(\frac{1}{r}\right),\quad r\to+\infty. \tag{13}$$

We note that the function $b_{\omega,\underline{\alpha}}(\underline{x})$ in general is defined only almost everywhere in $\underline{x}$ for $\underline{x}\in\partial\Omega$. We remark that when the obstacle is acoustically soft, that is, $\chi=0$, we must divide both sides by $\omega\neq0$ in the boundary condition (11) so that the new boundary condition obtained makes sense even when $\omega=0$ while Eq. (11) as it is when $\chi=0$ and $\omega=0$ reduces to $0=0$. When the obstacle is acoustically hard, that is, $\chi=\infty$, the boundary condition (11) is rewritten dividing both sides by χ and using the fact that in this case $\chi^{-1}=0$. We note that if $\partial\Omega$ is locally Lipschitz, the boundary value problem (10), (11), and (13) for each $\omega\in\mathbb{R}$, $\underline{\alpha}\in\partial B$ has an unique solution when $\chi\geqslant0$ (see Ref. 5, Lemma 9, p. 37 and Appendix 1 §7, p.325). We note that we assume $\chi\in\mathbb{R}$ since we work in the time domain [see (1), (2), (4), and (5)] where the acoustic impedance χ, i.e., the ratio between the pressure and the normal fluid velocity at a point, is a real constant and that basic physics implies $\chi\geqslant0$ (see Ref. 3, p. 67). In the frequency domain [see Eqs. (10), (11), and (13)] the acoustic impedance can be defined as a complex constant. Moreover, we note that in the previous hypotheses (13) implies that $u^s_{\omega,\underline{\alpha}}(\underline{x})=O(1/r)$, $r\to+\infty$ (see Ref. 3, Theorem 3.6, p. 72); that is (13) implies (6) when the integral appearing in Eq. (9) is well-behaved.

In this paper we propose a numerical method to solve problems (1), (2), (4), and (5) based on two ingredients: a quadrature rule to approximate the integrals (6) and (9) and a perturbative series of the ''operator expansion'' type introduced by Milder in Ref. 6 in order to solve the resulting boundary value problems (10), (11), and (13).

Let N_1, N_2, N_3 be three positive integers, $\underline{\omega}^{N_1}=(\omega_1,\ldots,\omega_{N_1})^T\in\mathbb{R}^{N_1}$, $\underline{\phi}^{N_2}=(\phi_1,\ldots,\phi_{N_2})^T\in\mathbb{R}^{N_2}$, $\underline{z}^{N_3}$

$=(z_1,...,z_{N_3})^T \in \mathbb{R}^{N_3}$, such that (ω_i,ϕ_j,z_k), $i=1,2,...,N_1$, $j=1,2,...,N_2$, $k=1,2,...,N_3$ are the nodes of a quadrature rule, and let

$$\underline{\alpha}_{j,k}=(\sin\cos^{-1} z_k \cos\phi_j, \sin\cos^{-1} z_k \sin\phi_j, z_k)^T,$$
$$j=1,2,...,N_2, \quad k=1,2,...,N_3. \tag{14}$$

Moreover, the multilinear transformation $A \in \mathbb{R}^{N_1\times N_2\times N_3}$ contains the weights of the quadrature rule; that is $(A)_{i,j,k}=a_{i,j,k}$, $i=1,2,...,N_1$, $j=1,2,...,N_2$, $k=1,2,...,N_3$, are the weights of the quadrature rule. That is, for any smooth function $f(\omega,\underline{\alpha})$ sufficiently well-behaved to make the following integral convergent, we write

$$\int_{\partial B} ds\,(\underline{\alpha}) \int_{\mathbb{R}} d\omega\, w(\omega) f(\omega,\underline{\alpha})$$
$$= \int_0^{2\pi} d\phi \int_{-1}^{1} dz \int_{\mathbb{R}} d\omega\, w(\omega)\tilde{f}(\omega,\phi,z)$$
$$= Q(f,A,\underline{\omega}^{N_1},\underline{\phi}^{N_2},\underline{z}^{N_3}) + E(f,A,\underline{\omega}^{N_1},\underline{\phi}^{N_2},\underline{z}^{N_3}), \tag{15}$$

where $\tilde{f}(\omega,\phi,z)=f(\omega,\underline{\alpha}(\cos^{-1}z,\phi))$ and $w(\omega)$, $\omega\in\mathbb{R}$ is a positive weight function which makes the integral in Eq. (15) convergent when $\tilde{f}$ is a polynomial in the variable ω; moreover, $Q(f,A,\underline{\omega}^{N_1},\underline{\phi}^{N_2},\underline{z}^{N_3})$ is the quadrature rule used to approximate the integral in Eq. (15), and $E(f,A,\underline{\omega}^{N_1},\underline{\phi}^{N_2},\underline{z}^{N_3})$ is the error term. We have

$$Q(f,A,\underline{\omega}^{N_1},\underline{\phi}^{N_2},\underline{z}^{N_3}) = \sum_{i=1}^{N_1}\sum_{j=1}^{N_2}\sum_{k=1}^{N_3} a_{i,j,k} f(\omega_i,\underline{\alpha}_{j,k}). \tag{16}$$

We assume that the quadrature rule (16) has positive weights and that it is of order ν; that is, it is exact for polynomials in the three variables (ω,ϕ,z) of degree less than or equal to ν. In this case, let $\tilde{f}(\omega,\phi,z)$ be the function specified previously whose derivatives of each order are assumed to be continuous functions, absolutely integrable on $\partial B\times\mathbb{R}$ after being multiplied by $w(\omega)$, μ_i, $i=1,2,3$ be non-negative integers, let $\underline{\mu}=(\mu_1,\mu_2,\mu_3)^T$ be a multi-index, $|\mu|=\Sigma_{i=1}^3\mu_i$ be the length of $\underline{\mu}$, and $D^{\mu}\tilde{f}=(\partial^{\mu_1}/\partial\omega^{\mu_1})(\partial^{\mu_2}/\partial\phi^{\mu_2})\times(\partial^{\mu_3}/\partial z^{\mu_3})f$, we have

$$|E(f,A,\underline{\omega}^{N_1},\underline{\phi}^{N_2},\underline{z}^{N_3})|$$
$$\leqslant C \sup_{(\phi,z)\in[0,2\pi]\times[-1,1]} \sum_{\substack{\underline{\mu}\\ |\underline{\mu}|=\nu+1}} \int_{\mathbb{R}} d\omega\, w(\omega)$$
$$\times |D^{\mu}\tilde{f}(\omega,\phi,z)| \prod_{i=1}^{N_1} |\omega-\omega_i| (1-\delta_{\mu_1,0}), \tag{17}$$

where C is a positive constant depending on the quadrature rule (16) (see Ref. 7, Theorem 2.1I, p. 29), $\delta_{\mu_1,0}=1$ if $\mu_1=0$, and $\delta_{\mu_1,0}=0$ otherwise.

The choice of the quadrature formula depends on the function W appearing in Eqs. (6) and (9).

In the numerical experience shown later, we solve problems (1), (2), (4), and (5) when the incoming acoustic wave is a time-harmonic plane wave or is given by Eq. (8) so that the integrals (6) and (9) reduce to one-dimensional integrals [such as (7)]; this fact reduces the computational cost of the solution of problems (1), (2), (4), and (5).

For $(\omega,\underline{\alpha})=(\omega_i,\underline{\alpha}_{j,k})$, $i=1,2,...,N_1$, $j=1,2,...,N_2$, $k=1,2,...,N_3$, we compute the solution $u^s_{\omega,\underline{\alpha}}$ of the boundary value problems (10), (11), and (13); that is, we propose a method which approximates the solution of the time-dependent three-dimensional acoustic scattering problems (1), (2), (4), and (5) with the combination of the solutions of $N_1\cdot N_2\cdot N_3$ time-harmonic acoustic scattering problems obtained using a quadrature rule. The idea of computing the scattered field $u^s(\underline{x},t)$ as a superposition of time-harmonic waves has been used before by several authors, see for example Heyman,[8] and Bucci, D'Elia, and Migliore.[9]

The computation of the numerical quadrature, that is the computation of a sum such as (16), can be done in parallel. The time-harmonic scattering problems are independent from each other and can be solved in parallel. Moreover, the computation of each time-harmonic scattered wave $u^s_{\omega,\underline{\alpha}}(\underline{x})$, $(\omega,\underline{\alpha})=(\omega_i,\underline{\alpha}_{j,k})$, $i=1,2,...,N_1$, $j=1,2,...,N_2$, $k=1,2,...,N_3$ is highly parallelizable with respect to the space variables by virtue of the so-called operator expansion method that we use. The method proposed here to solve (1), (2), (4), and (5) avoids the explicit assumption of the Courant, Friedrichs, and Levy stability condition on the space and time steps required, for example, by the finite difference methods. In fact, the stability condition is implicitly contained in the expression of $u^s(\underline{x},t)$ given by formula (9). The computation of a time-harmonic scattered wave $u^s_{\omega,\underline{\alpha}}(\underline{x})$ with the operator expansion method for acoustically soft bounded scatterers has been considered by Misici, Pacelli, and Zirilli in Ref. 10. In this paper we develop a new operator expansion method to compute the wave $u^s_{\omega,\underline{\alpha}}(\underline{x})$ scattered by the acoustically soft obstacle cheaper than the one proposed in Ref. 10. Moreover, we generalize the method proposed in Ref. 10 to bounded obstacles with nonzero constant acoustic impedance, including the limit case of acoustically hard obstacles. The idea of solving the boundary value problems for the Helmholtz equation using a ''perturbative series'' known as operator expansion method was introduced by Milder (Refs. 6 and 11). Milder, in Refs. 6 and 11, studied the time-harmonic scattering of acoustic waves from an acoustically soft unbounded surface. Milder[12] and Piccolo, Recchioni, and Zirilli[13] extended the previous formalism to the electromagnetic time-harmonic scattering from an unbounded perfectly conducting surface; Smith[14] extended the formalism to the scattering of time-harmonic electromagnetic waves from a dielectric surface. Later, Fatone *et al.*[15] generalized Milder's formalism to the scattering of electromagnetic waves from a perfectly conducting bounded obstacle. A method that can be related to the operator expansion method was presented by Bruno and Reitich.[16] These authors have considered analytic solutions of the Helmholtz equation in the exterior of an acoustically soft, three-dimensional bounded obstacle with analytic boundary and they expand these solutions in term of a real parameter that represents a ''measure'' of the distance of the obstacle boundary from the boundary of a soft sphere taken as a reference surface. We remark that using the operator expansion method we expand the solu-

tions of the Helmholtz equations through the expansion of an integral operator so that by using the operator expansion method it is possible to deal with obstacles whose boundary is only locally Lipschitz so that is there is no need to require obstacles with analytic boundary. In particular, the method proposed here allows us to deal very naturally with obstacles with edges and corners. These obstacles are interesting from the physical point of view since some phenomena such as the ''dispersion'' due to the presence of corners (see Figs. 3 and 4) or the ''resonance'' due to the presence of cavities (see Fig. 5) can be shown. This kind of obstacle is not easily treated with other methods such as the boundary integral methods, since singular integral equations should be solved, or by finite differences or finite elements methods where a challenging grid generation problem should be considered.

The operator expansion method proposed here to solve the boundary value problems (10), (11), and (13) is based on the following assumptions:

(i) Ω is a bounded obstacle whose boundary is a starlike surface with respect to the origin, that is

$$\Omega=\{\underline{x}=r\hat{\underline{x}}\in\mathbb{R}^3|0\leqslant r<\xi(\hat{\underline{x}}),\quad \hat{\underline{x}}\in\partial B\},\tag{18}$$

$$\partial\Omega=\{\underline{x}=r\hat{\underline{x}}\in\mathbb{R}^3|r=\xi(\hat{\underline{x}}),\quad \hat{\underline{x}}\in\partial B\},\tag{19}$$

where $\xi(\hat{\underline{x}})>0$, $\hat{\underline{x}}\in\partial B$ is a single-valued sufficiently regular function defined on ∂B. In particular, $\Omega\supset B_a$ for some $a>0$;

(ii) For each ω there exists B_a with $a=a(\omega)>0$ such that $\Omega\supset B_{a(\omega)}$, $\overline{\cup_{\omega\in\mathbb{R}}B_{a(\omega)}}\subset\Omega$ and the solution $u^s_{\omega,\underline{\alpha}}$ of Eqs. (10), (11), and (13) defined for $\underline{x}\in\mathbb{R}^3\backslash\Omega$ can be extended to $\underline{x}\in\mathbb{R}^3\backslash B_a$ remaining a solution of the Helmholtz equation. Moreover, the extension $F_{\omega,\underline{\alpha}}(\underline{x})$ of $u^s_{\omega,\underline{\alpha}}$ can be represented as follows:

$$F_{\omega,\underline{\alpha}}(\underline{x})=\int_{\mathbb{R}^3}\Phi_\omega(\underline{x},\underline{y})v_{\omega,\underline{\alpha}}(\underline{y})\,\delta(\|\underline{y}\|-a)\,d\underline{y},\tag{20}$$

where

$$\Phi_\omega(\underline{x},\underline{y})=\frac{e^{i\omega/c\|\underline{x}-\underline{y}\|}}{4\pi\|\underline{x}-\underline{y}\|}\tag{21}$$

is the fundamental solution of the Helmholtz equation in $\mathbb{R}^3$ with the Sommerfeld radiation condition at infinity, $\delta(\|\underline{y}\|-a)$ is a ''Dirac's delta'' concentrated on ∂B_a and $v_{\omega,\underline{\alpha}}(\underline{y})$ is a density function to be determined. In the following, with abuse of notation we denote with $\delta(\cdot)$ the Dirac's delta as a distribution on $\mathbb{R}^3$, or on $\mathbb{R}$, or on ∂B. Later, we show that without loss of generality we can assume $0<a_0<a(\omega)<a_1<1$, $\omega\in\mathbb{R}$.

The density function $v_{\omega,\underline{\alpha}}(\underline{y})$ appearing in Eq. (20) is determined imposing the boundary condition (11); that is, imposing that $F_{\omega,\underline{\alpha}}(\underline{x})$ extends $u^s_{\omega,\underline{\alpha}}(\underline{x})$, and solving the resulting equation with a formal power series using $\partial B=\{\underline{x}\in\mathbb{R}^3|\|\underline{x}\|=1\}$ as the base point of the power series. We note that we can develop our numerical method in a coordinate system different from the spherical coordinates and that we can choose the base point of the ''power series'' to be a more general surface than the surface of the unit sphere. The previous assumptions are made only to keep the exposition simple and the method described later can be adapted to many other different circumstances. Moreover, we remark that the terms of the series expansion in powers of $\xi-1$ are integrals independent one from another so that they can be computed in parallel. That is, the solution of the boundary value problems (10), (11), and (13) via the ''perturbative series'' is very well suited for parallel computation.

The highly parallelizable structure of the method proposed to solve problems (1), (2), (4), and (5) makes it a practical tool.

Finally, we present some numerical results on test problems when the incoming wave is given by

$$u^i(\underline{x},t)=\exp\left(i\frac{\omega^*}{c}[(\underline{\gamma},\underline{x})-ct]\right),\quad (\underline{x},t)\in\mathbb{R}^3\times\mathbb{R},\tag{22}$$

or

$$u^i(\underline{x},t)=\exp\left(-\frac{1}{4\zeta^2}[(\underline{\gamma},\underline{x})-ct]^2\right),\quad (\underline{x},t)\in\mathbb{R}^3\times\mathbb{R},\tag{23}$$

where $\underline{\gamma}\in\partial B$ is a given vector, ω^*, $\zeta>0$ are given constants and the acoustic impedance of the obstacle Ω is chosen to be $\chi=0$, $\chi=+\infty$, $\chi=2$, or $\chi=8$. Some interesting phenomena due to the presence of faces, edges, and vertices in locally Lipschitz boundaries $\partial\Omega$ or ''resonances'' when we consider surfaces $\partial\Omega$ with cavities are shown. The quantitative character of the numerical results obtained is established.

In Sec. I we describe the perturbative series used to determine the density function $v_{\omega,\underline{\alpha}}(\hat{\underline{y}})$ that appears in Eq. (20). The series determines the solutions of the $N_1\cdot N_2\cdot N_3$ time-harmonic scattering problems of the form (10), (11), and (13) associated to the nodes (ω_i,ϕ_j,z_k), $i=1,2,...,N_1$, $j=1,2,...,N_2$, $k=1,2,...,N_3$ that are related through (14) to $(\omega,\underline{\alpha})=(\omega_i,\underline{\alpha}_{j,k})$, $i=1,2,...,N_1$, $j=1,2,...,N_2$, $k=1,2,...,N_3$ in the quadrature rule. Moreover, we give an approximation formula for the time-dependent scattered wave u^s solution of Eqs. (1), (2), (4), and (5), via the quadrature rule (16). In Sec. II we give explicit formulas to compute the ''formal series'' in powers of $\xi-1$ of the solution u^s of problems (1), (2), (4), and (5). These formulas are obtained by expanding the density functions $v_{\omega,\underline{\alpha}}(\hat{\underline{y}})$, $\hat{\underline{y}}\in\partial B$ in Eq. (20), $(\omega,\underline{\alpha})=(\omega_i,\underline{\alpha}_{j,k})$, $i=1,2,...,N_1$, $j=1,2,...,N_2$, $k=1,2,...,N_3$ on the basis of the real spherical harmonic functions $\{\{Y_{\sigma,l,m}(\hat{\underline{y}})\}_{\sigma=0,1,l=\sigma,\sigma+1,...,m=\sigma,\sigma+1,...,l},\underline{y}\in\partial B\}$, and using the quadrature rule (16). The choice of the spherical harmonic functions as a basis to represent the integral operators of Sec. I seems appropriate since these operators become diagonal in this basis and it is very effective when relatively simple obstacles are considered and only a few terms of the expansions in spherical harmonics need to be computed. In Sec. III we show some numerical results obtained with the numerical method proposed in Secs. I and II on some test problems. Quantitative and qualitative results are shown and the numerical experience is discussed both from the computational and the physical point of view. Some animations relative to the numerical experiments discussed can be seen on the website: http://www.econ.unian.it/recchioni/w1

I. EXPANSION OF THE TIME-HARMONIC ACOUSTIC FIELD

Let us start solving problems (10), (11), and (13) for a given value of the wave number $\omega/c \neq 0$ and for a given direction $\underline{\alpha}$ of the incoming plane wave. We recall that when $\omega/c=0$ and $\chi \neq 0$ is finite we have $F_{0,\underline{\alpha}}(\underline{x}) \equiv 0$, for any $\underline{\alpha} \in \partial B$. When $\chi=\infty$ or $\omega/c=0$ and $\chi=0$, the boundary condition (11) must be changed as discussed in the Introduction and $F_{0,\underline{\alpha}}(\underline{x})$ will not be equal to zero in general. In the following, we treat explicitly only the case χ equal to a nonzero constant; the remaining cases $\chi=0$ and $\chi=\infty$ can be treated analogously and are omitted for simplicity. Let $0<a<1$, B_a and $\partial\Omega$ be as specified in the Introduction; in particular we assume that $\overline{B_a} \subset \Omega$ and that (18) holds. We note that we take $a<1$ since we want to be able to choose $\Omega=B$. We use spherical coordinates. We assume that the solution $u^s_{\omega,\underline{\alpha}}$ of the boundary value problems (10), (11), and (13) can be extended to $\mathbb{R}^3 \backslash \overline{B_a}$ and that this extension $F_{\omega,\underline{\alpha}}(\underline{x})$ can be represented using formula (20); that is

$$F_{\omega,\underline{\alpha}}(\underline{x}) = a^2 \int_{\partial B} \Phi_\omega(\underline{x}, a\underline{\hat{y}}) v_{\omega,\underline{\alpha}}(\underline{\hat{y}}) ds(\underline{\hat{y}}), \quad \underline{x} \in \mathbb{R}^3 \backslash \overline{B_a}, \tag{24}$$

for a suitable choice of the density function $v_{\omega,\underline{\alpha}}(\underline{\hat{y}})$. Differentiating (24) under the integral sign, it is easy to see that the function $F_{\omega,\underline{\alpha}}(\underline{x})$ satisfies

$$\left(\left(\Delta + \frac{\omega^2}{c^2}\right) F_{\omega,\underline{\alpha}}\right)(\underline{x}) = 0, \quad \underline{x} \in \mathbb{R}^3 \backslash \overline{B_a}, \tag{25}$$

and the radiation condition (13). Since $\overline{B_a} \subset \Omega$, Eq. (25) implies that (10) holds. In order to determine $v_{\omega,\underline{\alpha}}(\underline{\hat{y}})$, we impose that $F_{\omega,\underline{\alpha}}(\underline{x})$ extends $u^s_{\omega,\underline{\alpha}}(\underline{x})$; that is, that the density function $v_{\omega,\underline{\alpha}}(\underline{\hat{y}})$ must be such that

$$i\omega a^2 \int_{\partial B} \Phi_\omega(\underline{x}, a\underline{\hat{y}}) v_{\omega,\underline{\alpha}}(\underline{\hat{y}}) ds(\underline{\hat{y}}) + c\chi a^2 \frac{\partial}{\partial \underline{n}(\underline{x})} \int_{\partial B} \Phi_\omega(\underline{x}, a\underline{\hat{y}}) v_{\omega,\underline{\alpha}}(\underline{\hat{y}}) ds(\underline{\hat{y}}) = b_{\omega,\underline{\alpha}}(\underline{x}), \quad \underline{x} \in \partial\Omega, \tag{26}$$

where $b_{\omega,\underline{\alpha}}(\underline{x})$, $\underline{x} \in \partial\Omega$ is given by Eq. (12). We note that the numerical solution of Eq. (26) in the unknown $v_{\omega,\underline{\alpha}}(\underline{\hat{y}})$ using a boundary integral method implies the solution of a computationally expensive linear system. We prefer to solve Eq. (26) with a formal power series. To fix the ideas we use $\partial B = \{\underline{x} \in \mathbb{R}^3 \,|\, \|\underline{x}\| = 1\}$ as base point of the power series; that is, we assume that the density $v_{\omega,\underline{\alpha}}(\underline{\hat{y}})$ has the following formal series expansion:

$$v_{\omega,\underline{\alpha}}(\underline{\hat{y}}) = \sum_{s=0}^{+\infty} \frac{(\xi(\underline{\hat{y}})-1)^s}{s!} v_{s,\omega,\underline{\alpha}}(\underline{\hat{y}}), \quad \underline{\hat{y}} \in \partial B, \tag{27}$$

where we have defined $0!=1$ and the ''coefficients'' of the expansion $v_{s,\omega,\underline{\alpha}}(\underline{\hat{y}})$, $\underline{\hat{y}} \in \partial B$, $s=0,1,...$, are functions to be determined. Since $0<a<1$, that is $B_a \subset B$, the choice ∂B as base point of the power series expansion (27) is legitimate. However, it is possible to develop a formalism analogous to the one developed here choosing ∂B_R, $0<a<R$, $R \neq 1$ as base point of the expansion instead of ∂B or any starlike surface which is the boundary of a bounded region of the form (18) containing B_a; that is, $r=\xi_1(\hat{\underline{x}}(\theta,\phi))$, $\hat{\underline{x}} \in \partial B$ such that $(\partial\xi_1/\partial\theta)(\hat{\underline{x}}(\theta,\phi))$, $(\partial\xi_1/\partial\phi)(\hat{\underline{x}}(\theta,\phi))$ exist almost everywhere. In a similar way the choice of ∂B_a as support of $v_{\omega,\underline{\alpha}}(\underline{\hat{y}})\,\delta(\|\underline{\hat{y}}\|-a)$ is made only to fix the ideas and keep the exposition simple. When necessary, other choices are possible.

Let $e(\hat{\underline{x}})$ be an absolutely integrable function with respect to the surface measure defined on ∂B; for $0<a<1$ we define the operators $p_{\omega,s}$, $p^\theta_{\omega,s}$, $p^\phi_{\omega,s}$, $s=0,1,...$, as follows:

$$(p_{\omega,s}e)(\underline{x}) = a^2 \int_{\partial B} \frac{\partial^s}{\partial \|\underline{x}\|^s} \Phi_\omega(\underline{x}, a\underline{\hat{y}}) e(\underline{\hat{y}}) ds(\underline{\hat{y}}), \quad \|\underline{x}\| > a, \ s=0,1,..., \tag{28}$$

$$(p^\theta_{\omega,s}e)(\underline{x}) = \frac{\partial}{\partial\theta}[(p_{\omega,s}e)(\underline{x})] = a^2 \int_{\partial B} \frac{\partial}{\partial\theta} \frac{\partial^s}{\partial \|\underline{x}\|^s} \Phi_\omega(\underline{x}, a\underline{\hat{y}}) e(\underline{\hat{y}}) ds(\underline{\hat{y}}), \quad \|\underline{x}\| > a, \ s=0,1,..., \tag{29}$$

$$(p^\phi_{\omega,s}e)(\underline{x}) = \frac{\partial}{\partial\phi}[(p_{\omega,s}e)(\underline{x})] = a^2 \int_{\partial B} \frac{\partial}{\partial\phi} \frac{\partial^s}{\partial \|\underline{x}\|^s} \Phi_\omega(\underline{x}, a\underline{\hat{y}}) e(\underline{\hat{y}}) ds(\underline{\hat{y}}), \quad \|\underline{x}\| > a, \ s=0,1,..., \tag{30}$$

and the operators $\hat{p}_{\omega,s}$, $\hat{p}^\theta_{\omega,s}$, $\hat{p}^\phi_{\omega,s}$, are defined as follows:

$$(\hat{p}_{\omega,s}e)(\hat{\underline{x}}) = (p_{\omega,s}e)(\hat{\underline{x}}), \quad \hat{\underline{x}} \in \partial B, \ s=0,1,..., \tag{31}$$

$$(\hat{p}^\theta_{\omega,s}e)(\hat{\underline{x}}) = (p^\theta_{\omega,s}e)(\hat{\underline{x}}), \quad \hat{\underline{x}} \in \partial B, \ s=0,1,..., \tag{32}$$

$$(\hat{p}^\phi_{\omega,s}e)(\hat{\underline{x}}) = (p^\phi_{\omega,s}e)(\hat{\underline{x}}), \quad \hat{\underline{x}} \in \partial B, \ s=0,1,.... \tag{33}$$

Finally, we define the operator $\hat{l}_\omega$ acting on the function e via the following equation:

$$i\omega(\hat{p}_{\omega,0}(\hat{l}_\omega e))(\hat{\underline{x}}) + c\chi(\hat{p}_{\omega,1}(\hat{l}_\omega e))(\hat{\underline{x}}) = e(\hat{\underline{x}}), \quad \hat{\underline{x}} \in \partial B. \tag{34}$$

We note that $(\hat{l}_\omega e)$ is a function defined on ∂B and that Eq. (34) defines $\hat{l}_\omega e$ for any absolutely integrable function $e(\underline{x})$ defined on ∂B. We recall that for simplicity in the following we treat only the case χ equal to a nonzero constant and that Eq. (34) must be slightly modified when $\chi=0$ or $\chi=\infty$ as shown in the Introduction. We note that when $\partial\Omega=\partial B$ and $e(\hat{\underline{x}}) = b_{\omega,\underline{\alpha}}(\hat{\underline{x}})$, $\hat{\underline{x}} \in \partial B$, Eq. (34) reduces to Eq. (26) and that Eq. (26) reduces to Eq. (11). The numerical solution of Eq. (34), that is the computation of $\hat{l}_\omega e$ given e, corresponds in our method to the numerical solution of the linear integral equation that appears in the boundary integral methods. We note that Eq. (34) holds on ∂B, while the integral equation of the boundary integral methods holds on $\partial\Omega$. This fact and the character of the operators involved, that is $\hat{p}_{\omega,0}$, $\hat{p}_{\omega,1}$, makes it possible to reduce the solution of Eq. (34) to the solution

of a diagonal linear system choosing the appropriate basis where the integral operators $\hat{p}_{\omega,0}$, $\hat{p}_{\omega,1}$ are represented (see Sec. II). This is the basis of the spherical harmonics; a similar simple choice is not possible when boundary integral methods are used and $\partial\Omega \neq \partial B$. When we choose the base point of the power series not equal to the surface of a sphere, we must use a new basis instead of the spherical harmonics that makes it possible to reduce the solution of Eq. (34) to the solution of a lincar system with some special properties that make the solution ''easy.''

Substituting (27) into (24) and using the power-series expansion of $\Phi_\omega(\underline{x},a\underline{\hat{y}})$ as a function of $\|\underline{x}\|$ with base point $\|\underline{x}\|=1$, the Cauchy product rule between series, and (31), we have

$$F_{\omega,\underline{a}}(\underline{x})=\sum_{s=0}^{+\infty}\sum_{l=0}^{s}\frac{(\|\underline{x}\|-1)^{s-l}}{(s-l)!}\times\left(\hat{p}_{\omega,(s-l)}\left(v_{l,\omega,\underline{a}}\frac{(\xi-1)^l}{l!}\right)\right)(\underline{\hat{x}}),\quad \underline{x}\in\mathbb{R}^3\backslash\overline{B_a}, \tag{35}$$

$$\frac{\partial}{\partial\theta}F_{\omega,\underline{a}}(\underline{x})=\sum_{s=0}^{+\infty}\sum_{l=0}^{s}\frac{(\|\underline{x}\|-1)^{s-l}}{(s-l)!}\times\left(\hat{p}^{\theta}_{\omega,(s-l)}\left(v_{l,\omega,\underline{a}}\frac{(\xi-1)^l}{l!}\right)\right)(\underline{\hat{x}}),\quad \underline{x}\in\mathbb{R}^3\backslash\overline{B_a}, \tag{36}$$

$$\frac{\partial}{\partial\phi}F_{\omega,\underline{a}}(\underline{x})=\sum_{s=0}^{+\infty}\sum_{l=0}^{s}\frac{(\|\underline{x}\|-1)^{s-l}}{(s-l)!}\times\left(\hat{p}^{\phi}_{\omega,(s-l)}\left(v_{l,\omega,\underline{a}}\frac{(\xi-1)^l}{l!}\right)\right)(\underline{\hat{x}}),\quad \underline{x}\in\mathbb{R}^3\backslash\overline{B_a}. \tag{37}$$

We note that the field $F_{\omega,\underline{a}}(\underline{x})$ is known when the following functions are known:

$$\left(\hat{p}_{\omega,(s-l)}\left(v_{l,\omega,\underline{a}}\frac{(\xi-1)^l}{l!}\right)\right)(\underline{\hat{x}}),\quad \underline{\hat{x}}\in\partial B,\quad l=0,1,...,s,\quad s=0,1,.... \tag{38}$$

That is, the densities $v_{l,\omega,\underline{a}}(\underline{\hat{y}})$, $l=0,1,...$, are only auxiliary unknowns and $F_{\omega,\underline{a}}(\underline{x})$ can be determined knowing only the result of the action of $\hat{p}_{\omega,(s-l)}$ on $v_{l,\omega,\underline{a}}[(\xi-1)^l/l!]$, $l=0,1,...,s$, $s=0,1,...$, without knowing the functions $v_{l,\omega,\underline{a}}(\underline{\hat{y}})$, $\underline{\hat{y}}\in\partial B$, $l=0,1,...$, themselves. Equation (35) reduces the problem of determining a formal power series of $F_{\omega,\underline{a}}(\underline{x})$ solution of Eqs. (10), (11), and (13) to the problem of determining $(\hat{p}_{\omega,(s-l)}(v_{l,\omega,\underline{a}}[(\xi-1)^l/l!]))(\underline{\hat{x}})$, $\underline{\hat{x}}\in\partial B$, $l=0,1,...,s$, $s=0,1,...$, imposing Eq. (26). Letting (r,θ,ϕ) be the canonical spherical coordinates of $\underline{x}\in\mathbb{R}^3$, we have

$$r=\|\underline{x}\|,\quad \underline{x}\in\mathbb{R}^3, \tag{39}$$

$$\underline{\hat{x}}(\theta,\phi)=\frac{\underline{x}}{r}=(\sin\theta\cos\phi,\sin\theta\sin\phi,\cos\theta)^T,\quad 0\leqslant\theta\leqslant\pi,\quad 0\leqslant\phi<2\pi,\quad \underline{x}\neq\underline{0}, \tag{40}$$

$$\underline{\hat{x}}_\theta=\frac{\partial\underline{\hat{x}}}{\partial\theta}(\theta,\phi)=(\cos\theta\cos\phi,\cos\theta\sin\phi,-\sin\theta)^T,\quad 0\leqslant\theta\leqslant\pi,\quad 0\leqslant\phi<2\pi, \tag{41}$$

$$\underline{\hat{x}}_\phi=\frac{\partial\underline{\hat{x}}}{\partial\phi}(\theta,\phi)=(-\sin\theta\sin\phi,\sin\theta\cos\phi,0)^T,\quad 0\leqslant\theta\leqslant\pi,\quad 0\leqslant\phi<2\pi; \tag{42}$$

moreover, where $\xi(\underline{\hat{x}}(\theta,\phi))$ is sufficiently regular, we define

$$\underline{\tilde{n}}(\underline{x})=\underline{\hat{x}}(\theta,\phi)-\frac{\underline{\hat{x}}_\theta(\theta,\phi)}{\xi(\underline{\hat{x}}(\theta,\phi))}\frac{\partial\xi}{\partial\theta}(\underline{\hat{x}}(\theta,\phi))-\frac{1}{\sin^2\theta}\frac{\underline{\hat{x}}_\phi(\theta,\phi)}{\xi(\underline{\hat{x}}(\theta,\phi))}\frac{\partial\xi}{\partial\phi}(\underline{\hat{x}}(\theta,\phi)),$$
$$\underline{x}=\xi(\underline{\hat{x}}(\theta,\phi))\underline{\hat{x}}(\theta,\phi)\in\partial\Omega,\quad 0\leqslant\theta\leqslant\pi,\quad 0\leqslant\phi<2\pi. \tag{43}$$

We assume that (43) holds almost everywhere in $\underline{x}$ for $\underline{x}\in\partial\Omega$. So that almost everywhere $\underline{n}(\underline{x})$, $\underline{x}\in\partial\Omega$, the outward unit normal vector to $\partial\Omega$, is given by

$$\underline{n}(\underline{x})=\frac{\underline{\tilde{n}}(\underline{x})}{\|\underline{\tilde{n}}(\underline{x})\|},\quad \underline{x}\in\partial\Omega. \tag{44}$$

We note that, for example, when $\partial\Omega$ is the boundary of a polyhedron (43) holds almost everywhere. We recall that the gradient operator in spherical coordinates is given by

$$\nabla=\underline{\hat{x}}(\theta,\phi)\frac{\partial}{\partial r}+\frac{\underline{\hat{x}}_\theta(\theta,\phi)}{r}\frac{\partial}{\partial\theta}+\frac{\underline{\hat{x}}_\phi(\theta,\phi)}{r\sin^2\theta}\frac{\partial}{\partial\phi},\quad r\geqslant 0,\quad 0\leqslant\theta\leqslant\pi,\quad 0\leqslant\phi<2\pi. \tag{45}$$

Using (43), (44), and (45), Eq. (26) can be rewritten as follows:

$$i\omega F_{\omega,\underline{a}}(\underline{x})+\frac{c\chi}{\|\underline{\tilde{n}}(\underline{x})\|}\left\{\frac{\partial}{\partial r}F_{\omega,\underline{a}}(\underline{x})-\frac{1}{\xi^2(\underline{\hat{x}}(\theta,\phi))}\times\frac{\partial\xi}{\partial\theta}(\underline{\hat{x}}(\theta,\phi))\frac{\partial}{\partial\theta}F_{\omega,\underline{a}}(\underline{x})-\frac{1}{\xi^2(\underline{\hat{x}}(\theta,\phi))}\times\frac{1}{\sin^2\theta}\frac{\partial\xi}{\partial\phi}(\underline{\hat{x}}(\theta,\phi))\frac{\partial}{\partial\phi}F_{\omega,\underline{a}}(\underline{x})\right\}=b_{\omega,\underline{a}}(\underline{x}),$$
$$\underline{x}=\xi(\underline{\hat{x}}(\theta,\phi))\underline{\hat{x}}(\theta,\phi)\in\partial\Omega,\quad 0\leqslant\theta\leqslant\pi,\quad 0\leqslant\phi<2\pi. \tag{46}$$

In the following, with abuse of notation we use ξ as an independent variable so that for example we use the notation: $O((\xi-1)^\nu)$, $\nu\geqslant 0$ when $\xi\to 1$. We define

$$D_2(\xi)=\left[\frac{\partial}{\partial\theta}(\xi-1)\right]^2+\frac{1}{\sin^2\theta}\left[\frac{\partial}{\partial\phi}(\xi-1)\right]^2,\quad 0\leqslant\theta\leqslant\pi,\quad 0\leqslant\phi<2\pi; \tag{47}$$

we have

$$\frac{1}{\xi^2}=\sum_{s=0}^{+\infty}(-1)^s(s+1)(\xi-1)^s\ \text{ when }\ |\xi-1|<1. \tag{48}$$

Let

$$\eta_0(\hat{\underline{x}})=1, \quad \hat{\underline{x}}\in\partial B, \tag{49}$$

$$\eta_s(\hat{\underline{x}})=\sum_{l=0}^{[s/2]}\frac{(-1)^{s-l}(2l-1)!!}{2^l l!}(\xi(\hat{\underline{x}})-1)^{s-2l}\times[D_2(\xi(\hat{\underline{x}}))]^l\prod_{j=1}^{s-2l}\left(\frac{2l+j-1}{j}\right),$$

$$\hat{\underline{x}}\in\partial B, \quad s=1,2,..., \tag{50}$$

where we define $(-1)!!=1$ and $[\cdot]$ denotes the integer part of $\cdot$. Moreover, in formula (50) we define $\Pi_{l=n_1}^{n_2}\cdot=1$ when $n_2<n_1$. We note that $\eta_s(\hat{\underline{x}})=O((\xi(\hat{\underline{x}})-1)^s)$, when $\xi\to1$, $s=0,1,...$. We have

$$\frac{1}{\|\tilde{\underline{n}}(\hat{\underline{x}})\|}=\sum_{s=0}^{+\infty}\eta_s(\hat{\underline{x}}),$$

$$\hat{\underline{x}}\in\partial B, \quad \underline{x}=\xi(\hat{\underline{x}})\hat{\underline{x}}\in\partial\Omega,$$

$$\text{when } |\xi-1|D_2(\xi)<1. \tag{51}$$

The terms $\partial\xi/\partial\theta$, $\partial\xi/\partial\phi$ are considered to be $O((\xi-1))$ when $\xi\to1$, in fact, we have $\partial\xi/\partial\theta=(\partial/\partial\theta)(\xi-1)$ and $\partial\xi/\partial\phi=(\partial/\partial\phi)(\xi-1)$. Moreover, using (44) the function $b_{\omega,\underline{\alpha}}(\underline{x})$ in Eq. (12) can be rewritten as

$$b_{\omega,\underline{\alpha}}(\underline{x})=i\exp\left(i\frac{\omega}{c}\xi(\hat{\underline{x}})(\hat{\underline{x}},\underline{\alpha})\right)\left[-\omega-\frac{\omega\chi}{\|\tilde{\underline{n}}(\underline{x})\|}(\tilde{\underline{n}}(\underline{x}),\underline{\alpha})\right],$$

$$\underline{x}=\xi(\hat{\underline{x}})\hat{\underline{x}}\in\partial\Omega, \tag{52}$$

so that we can consider the formal power-series expansion for $b_{\omega,\underline{\alpha}}(\underline{x})$; that is

$$b_{\omega,\underline{\alpha}}(\xi(\hat{\underline{x}})\hat{\underline{x}})=\sum_{s=0}^{+\infty}b_{s,\omega,\underline{\alpha}}(\hat{\underline{x}}), \quad \hat{\underline{x}}\in\partial B, \tag{53}$$

where $b_{s,\omega,\underline{\alpha}}(\hat{\underline{x}})=O((\xi(\hat{\underline{x}})-1)^s)$ when $\xi\to1$, $s=0,1,...$, is given by

$$b_{s,\omega,\underline{\alpha}}(\hat{\underline{x}})=i\exp\left(i\frac{\omega}{c}(\hat{\underline{x}},\underline{\alpha})\right)\left\{-\omega\frac{(\xi(\hat{\underline{x}})-1)^s}{s!}\left(i\frac{\omega}{c}(\hat{\underline{x}},\underline{\alpha})\right)^s+\omega(\hat{\underline{x}},\underline{\alpha})\sum_{p=0}^{s}\left\{\frac{(\xi(\hat{\underline{x}})-1)^p}{p!}\left(i\frac{\omega}{c}(\hat{\underline{x}},\underline{\alpha})\right)^p\eta_{s-p}(\hat{\underline{x}})\right\}\right.$$
$$-\omega\chi\sum_{\nu=0}^{s-1}\left\{\frac{(\xi(\hat{\underline{x}})-1)^{s-1-\nu}}{(s-\nu)!}\left(i\frac{\omega}{c}(\hat{\underline{x}},\underline{\alpha})\right)^{s-1-\nu}\sum_{p=0}^{\nu}\left\{\eta_{\nu-p}(\hat{\underline{x}})(-1)^{p-1}(\xi(\hat{\underline{x}})-1)^p\right.\right.$$
$$\left.\left.\left.\times\left[(\hat{\underline{x}}_\theta,\underline{\alpha})\frac{\partial\xi}{\partial\theta}(\hat{\underline{x}})+\frac{1}{\sin^2\theta}(\hat{\underline{x}}_\phi,\underline{\alpha})\frac{\partial\xi}{\partial\phi}(\hat{\underline{x}})\right]\right\}\right\}\right\}, \quad \underline{x}\in\partial B, \quad s=0,1,.... \tag{54}$$

The coefficients in Eq. (54) are obtained using (51), the Taylor expansion of $\exp(i(\omega/c)\|\underline{x}\|(\hat{\underline{x}},\underline{\alpha}))$ with respect to $\|\underline{x}\|$ with base point $\|\underline{x}\|=1$ and the Cauchy product rule.

We solve Eq. (46) order by order and we must take the expansion in powers of $\xi-1$ of the datum $b_{\omega,\underline{\alpha}}(\underline{x})$, $\underline{x}\in\partial\Omega$. We consider two cases: the first case when the boundary value problems (10), (11), and (13) come from a time-dependent scattering problem such as the one described in the Introduction and the datum $b_{\omega,\underline{\alpha}}(\underline{x})$, given by Eq. (12) [i.e., Eq. (52)] is known on any closed Lipschitz continuous surface so that we can use the expansion (53) to solve Eq. (46) order by order, and the second case when we solve the boundary value problem like (10), (11), and (13) and the datum $b_{\omega,\underline{\alpha}}(\underline{x})$ is known only when $\underline{x}\in\partial\Omega$ so that we consider the datum $\tilde{b}_{\omega,\underline{\alpha}}(\hat{\underline{x}})=b_{\omega,\underline{\alpha}}(\xi(\hat{\underline{x}})\hat{\underline{x}})$, $\hat{\underline{x}}\in\partial B$ as a fixed zero-order term in the expansion in powers of $\xi-1$. Taking these two cases in mind, let us define

$$\tilde{b}_{s,\omega,\underline{\alpha}}(\hat{\underline{x}})=b_{s,\omega,\underline{\alpha}}(\hat{\underline{x}}), \quad \hat{\underline{x}}\in\partial B, \quad s=0,1,..., \tag{55}$$

in the first case and

$$\tilde{b}_{s,\omega,\underline{\alpha}}(\hat{\underline{x}})=\begin{cases}\tilde{b}_{\omega,\underline{\alpha}}(\hat{\underline{x}}), & s=0\\ 0, & s=1,2,...,\end{cases} \quad \hat{\underline{x}}\in\partial B, \tag{56}$$

in the second case. Now, let $\chi\in\mathbb{R}$, $\chi>0$, $\omega\in\mathbb{R}$, $\underline{\alpha}\in\partial B$, and let $(\hat{p}_{\omega,(s-l)}(v_{l,\omega,\underline{\alpha}}[(\xi-1)^l/l!]))(\hat{\underline{x}})$, $\hat{\underline{x}}\in\partial B$, $l=0,1,...,s$, $s=0,1,...$, be the functions defined on ∂B such that the corresponding function $F_{\omega,\underline{\alpha}}(\underline{x})$ given by Eq. (35) coincides with the solution of the boundary value problems (10), (11), and (13) in $\mathbb{R}^3\backslash\Omega$ and let $\hat{l}_\omega$ be the operator defined in Eq. (34). Substituting formulas (35), (36), (37), (48), and (51) in Eq. (46) and using the Cauchy rule in the product of the series expansions in powers of $(\xi-1)$ of $\tilde{\underline{n}}$, $F_{\omega,\underline{\alpha}}(\underline{x})$, $(\partial/\partial\theta)F_{\omega,\underline{\alpha}}(\underline{x})$, $(\partial/\partial\phi)F_{\omega,\underline{\alpha}}(\underline{x})$, $b_{\omega,\underline{\alpha}}(\xi(\hat{\underline{x}})\hat{\underline{x}})$ and $1/\xi^2$, and equating the terms that multiply the same powers of $\xi-1$, we obtain

$$\left(\hat{p}_{\omega,(s-l)}\left(v_{l,\omega,\underline{\alpha}}\frac{(\xi-1)^l}{l!}\right)\right)(\hat{\underline{x}})=(\hat{p}_{\omega,(s-l)}(\hat{l}_\omega z_{l,\omega,\underline{\alpha}}))(\hat{\underline{x}}),$$

$$\hat{\underline{x}}\in\partial B, \quad l=0,1,...,s, \quad s=0,1,..., \tag{57}$$

and formulas analogous to (57) hold for $\hat{p}^{\theta}_{\omega,l}$ and $\hat{p}^{\phi}_{\omega,l}$, $l=0,1,...$, where

$$z_{0,\omega,\underline{\alpha}}(\hat{\underline{x}})=\tilde{b}_{0,\omega,\underline{\alpha}}(\hat{\underline{x}}),\quad \hat{\underline{x}}\in\partial B, \tag{58}$$

$$z_{l,\omega,\underline{\alpha}}(\hat{\underline{x}})=-i\omega\sum_{\nu=0}^{l-1}\left\{\frac{(\xi-1)^{l-\nu}}{(l-\nu)!}(\hat{p}_{(l-\nu)}(\hat{l}_\omega z_{\nu,\omega,\underline{\alpha}}))(\hat{\underline{x}})\right\}-c\chi\sum_{\nu=0}^{l-1}\left\{\eta_{l-\nu}(\hat{\underline{x}})\sum_{\mu=0}^{\nu}\left\{\frac{(\xi-1)^{\nu-\mu}}{(\nu-\mu)!}(\hat{p}_{(\nu+1-\mu)}(\hat{l}_\omega z_{\mu,\omega,\underline{\alpha}}))(\hat{\underline{x}})\right\}\right\}$$
$$+c\chi\sum_{\nu=0}^{l-1}\left\{\eta_{l-1-\nu}(\hat{\underline{x}})\sum_{q=0}^{\nu}\{(-1)^{\nu-q}(\nu-q+1)(\xi-1)^{\nu-q}\nu_q(\hat{\underline{x}})\}\right\}+\tilde{b}_{l,\omega,\underline{\alpha}}(\hat{\underline{x}}),\quad \hat{\underline{x}}\in\partial B,\quad l=1,2,..., \tag{59}$$

with

$$\nu_q(\hat{\underline{x}})=\sum_{\mu=0}^{q}\left\{\frac{(\xi-1)^{q-\mu}}{(q-\mu)!}\left[\frac{\partial\xi}{\partial\theta}(\hat{p}^{\theta}_{(q-\mu)}(\hat{l}_\omega z_{\mu,\omega,\underline{\alpha}}))(\hat{\underline{x}})+\frac{1}{\sin^2\theta}\frac{\partial\xi}{\partial\phi}(\hat{p}^{\phi}_{(q-\mu)}(\hat{l}_\omega z_{\mu,\omega,\underline{\alpha}}))(\hat{\underline{x}})\right]\right\}$$
$$\hat{\underline{x}}\in\partial B,\quad q=0,1,..., \tag{60}$$

and $\tilde{b}_{\omega,\underline{\alpha},s}(\hat{\underline{x}})$, $\hat{\underline{x}}\in\partial B$, $s=0,1,...$, are given by (55) or (56), and $\eta_s(\hat{\underline{x}})$, $\hat{\underline{x}}\in\partial B$, $s=0,1,...$, are given by (49), (50).

Formulas (58) and (59) imply that $z_{l,\omega,\underline{\alpha}}(\hat{\underline{x}})=O((\xi(\hat{\underline{x}})-1)^l)$, $\hat{\underline{x}}\in\partial B$, $\xi\to1$, $l=0,1,...$. Formulas (57), (58), and (59) show that the solution of Eq. (26) via the perturbative series (35) is very efficient when a parallel architecture is used to carry out the corresponding computation. In fact, for $s=0,1,...$, the functions $(\hat{p}_{\omega,(s-l)}(v_{l,\omega,\underline{\alpha}}[(\xi-1)^l/l!]))(\hat{\underline{x}})$, $(\hat{p}^{\theta}_{\omega,(s-l)}(v_{l,\omega,\underline{\alpha}}[(\xi-1)^l/l!]))(\hat{\underline{x}})$, $(\hat{p}^{\phi}_{\omega,(s-l)}(v_{l,\omega,\underline{\alpha}}[(\xi-1)^l/l!]))(\hat{\underline{x}})$, $\underline{x}\in\partial B$, $l=0,1,...,s$ are defined by recursive formulas involving double integrals which are independent from each other so that they can be computed in parallel.

Let

$$q^S_{\underline{x},t}(\omega,\underline{\alpha})=\frac{W(\omega,\underline{\alpha})}{w(\omega)(2\pi)^4}\exp(-i\omega t)\times\sum_{s=0}^{S}\sum_{l=0}^{s}\frac{(\|\underline{x}\|-1)^{s-l}}{(s-l)!}(\hat{p}_{\omega,(s-l)}(\hat{l}_\omega z_{l,\omega,\underline{\alpha}}))(\hat{\underline{x}}),$$
$$\underline{\alpha}\in\partial B,\quad \omega\in\mathbb{R},\quad (\underline{x},t)\in(\mathbb{R}^3\backslash\overline{\Omega})\times\mathbb{R}, \tag{61}$$

and

$$R_{S,\underline{x},t}(\omega,\underline{\alpha})=\frac{\exp(-i\omega t)W(\omega,\underline{\alpha})}{w(\omega)(2\pi)^4}\times\left(\sum_{s=S+1}^{+\infty}\sum_{l=0}^{s}\frac{(\|\underline{x}\|-1)^{s-l}}{(s-l)!}\times(\hat{p}_{\omega,(s-l)}(\hat{l}_\omega z_{l,\omega,\underline{\alpha}}))(\hat{\underline{x}})\right),$$
$$\underline{\alpha}\in\partial B,\quad \omega\in\mathbb{R},\quad (\underline{x},t)\in(\mathbb{R}^3\backslash\overline{\Omega})\times\mathbb{R}. \tag{62}$$

From formulas (57), (58), and (59) we have $R_{S,\underline{x},t}(\omega,\underline{\alpha})=o((\xi-1)^S)$ when $\xi\to1$; hence, for $\chi\in\mathbb{R}$, $\chi>0$, we approximate $u^s(\underline{x},t)$, $(\underline{x},t)\in(\mathbb{R}^3\backslash\overline{\Omega})\times\mathbb{R}$, solution of problems (1), (2), (4), and (5) and represented by formula (9) with $v^S(\underline{x},t)$ given by

$$v^S(\underline{x},t)=Q(q^S_{\underline{x},t},A,\underline{\omega}^{N_1},\underline{\phi}^{N_2},\underline{z}^{N_3}),\quad (\underline{x},t)\in(\mathbb{R}^3\backslash\overline{\Omega})\times\mathbb{R}, \tag{63}$$

where $Q(q^S_{\underline{x},t},A,\underline{\omega}^{N_1},\underline{\phi}^{N_2},\underline{z}^{N_3})$ is given by Eq. (16) and $q^S_{\underline{x},t}$ is given by Eq. (61). Moreover, we have

$$|u^s(\underline{x},t)-v^S(\underline{x},t)|\leqslant|E(q^S_{\underline{x},t},A,\underline{\omega}^{N_1},\underline{\phi}^{N_2},\underline{z}^{N_3})|+\int_{\partial B}ds(\underline{\alpha})\int_{\mathbb{R}}d\omega\,w(\omega)|R_{S,\underline{x},t}(\omega,\underline{\alpha})|,$$
$$(\underline{x},t)\in(\mathbb{R}^3\backslash\overline{\Omega})\times\mathbb{R}, \tag{64}$$

where $E(q^S_{\underline{x},t},A,\underline{\omega}^{N_1},\underline{\phi}^{N_2},\underline{z}^{N_3})$ can be estimated by Eq. (17) and $R_{S,\underline{x},t}$ is given by Eq. (62).

II. COMPUTATIONAL METHOD

Let $\partial\Omega$ be given by Eq. (19), and we recall that $\partial\Omega$ is a starlike surface with respect to the origin and that we use a formal power-series expansion with ∂B as the base point and that for simplicity we treat only the case $\chi\neq0$ and $\chi\neq\infty$; that is, χ equal to a nonzero positive constant. Let $L^2(\partial B)$ be the space of square integrable functions defined on ∂B with respect to the surface measure. The real spherical harmonics $Y_{\sigma,l,m}(\underline{y})$, $\sigma=0,1$, $l=\sigma,\sigma+1,...$, $m=\sigma,\sigma+1,...,l$, (see Ref. 3, p. 77) is an orthonormal complete set of functions in $L^2(\partial B)$. This basis consists of the following functions:

$$Y_{\sigma,l,m}(\hat{\underline{x}})=\begin{cases}\gamma_{l,m}P^m_l(\cos\theta)\cos m\phi, & \sigma=0,\\ \gamma_{l,m}P^m_l(\cos\theta)\sin m\phi, & \sigma=0,\end{cases}$$
$$m=\sigma,\sigma+1...,l,\quad l=\sigma,\sigma+1,...,\quad \hat{\underline{x}}\in\partial B, \tag{65}$$

where $P^m_l(\cos\theta)$, $m=0,1,...,l$, $l=0,1,...$, are the Legendre polynomials and $\gamma_{l,m}$ are normalization factors; that is

$$\gamma_{l,m}=\left[\epsilon_m\frac{2l+1}{4\pi}\frac{(l-m)!}{(l+m)!}\right]^{1/2},\quad m=0,1...,l,\quad l=0,1..., \tag{66}$$

with $\epsilon_m=2$ when $m=0$ and $\epsilon_m=1$ when $m\neq0$. Using this basis of functions we can represent the action of the operators $\hat{l}_\omega$, $\hat{p}_{\omega,s}$, $\hat{p}^{\theta}_{\omega,s}$, $\hat{p}^{\phi}_{\omega,s}$, $s=0,1,...$, as infinite matrices and the datum $b_{\omega,\underline{\alpha}}(\hat{\underline{x}})=b_{\omega,\underline{\alpha}}(\xi(\hat{\underline{x}})\hat{\underline{x}})$, $\hat{\underline{x}}\in\partial B$ of Eq. (46) as an infinite vector.

We note that the choice of the spherical harmonics is appropriate to study scattering from obstacles with ''simple'' geometries. In fact, this choice makes the matrices representing the operators mentioned above that appear in the computation simple (i.e., diagonal), and when the obstacles consid-

ered are simple, only a few terms are necessary in the series expansions in spherical harmonics to obtain a good approximation. However, when the scattering from obstacles with complicated geometries is considered, the need to use many terms in the series expansion to obtain a good approximation makes the choice of the spherical harmonics as basis functions inappropriate since the computation of expressions involving $Y_{\sigma,l,m}(\hat{\underline{x}})$ when l and m are large is difficult. In this paper, we restrict our attention to the spherical harmonics choice. This choice is sufficient to study the numerical examples considered in Sec. III. Now, let $e(\hat{\underline{x}})$ be a locally integrable function defined on ∂B and let $e(\hat{\underline{x}})$ be given by the following expansion:

$$e(\hat{\underline{x}})=\sum_{\sigma=0}^{1}\sum_{l=\sigma}^{+\infty}\sum_{m=\sigma}^{l} e_{\sigma,l,m}Y_{\sigma,l,m}(\hat{\underline{x}}),\quad \hat{\underline{x}}\in\partial B, \tag{67}$$

where $\{e_{\sigma,l,m}\}_{\sigma=0,1,l=\sigma,\sigma+1,\ldots,m=\sigma,\sigma+1,\ldots,l}$ are the generalized Fourier coefficients of e, and let $\hat{p}_{\omega,s}$, $\hat{p}^{\theta}_{\omega,s}$, $\hat{p}^{\phi}_{\omega,s}$, $s=0,1,\ldots,\hat{l}_{\omega}$ be the operators given by Eqs. (31), (32), (33), and (34). Then, using formulas (28), (29), (30), and (34), and the following expansion of $\Phi_{\omega}(\underline{x},\underline{y})$:

$$\begin{aligned}\Phi_{\omega}(\underline{x},\underline{y})=&i\left(\frac{\omega}{c}\right)\sum_{\sigma=0}^{1}\sum_{l=\sigma}^{+\infty}\sum_{m=\sigma}^{l} h_l\left(\left(\frac{\omega}{c}\right)\|\underline{x}\|\right)\\&\times j_l\left(\left(\frac{\omega}{c}\right)\|\underline{y}\|\right)Y_{\sigma,l,m}(\hat{\underline{x}})Y_{\sigma,l,m}(\hat{\underline{y}}),\\&\|\underline{x}\|>\|\underline{y}\|,\end{aligned} \tag{68}$$

for $\omega\in\mathbb{R}$, we have

$$\begin{aligned}(\hat{p}_{\omega,s}e)(\hat{\underline{x}})=&ia^2\left(\frac{\omega}{c}\right)\sum_{\sigma=0}^{1}\sum_{l=\sigma}^{+\infty}\sum_{m=\sigma}^{l} e_{\sigma,l,m}\left(\frac{\omega}{c}\right)^s h_l^{(s)}\\&\times\left(\left(\frac{\omega}{c}\right)\right)j_l\left(\left(\frac{\omega}{c}\right)a\right)Y_{\sigma,l,m}(\hat{\underline{x}}(\theta,\phi)),\\&\hat{\underline{x}}(\theta,\phi)\in\partial B,\quad s=0,1,\ldots,\end{aligned} \tag{69}$$

$$\begin{aligned}(\hat{p}^{\theta}_{\omega,s}e)(\hat{\underline{x}})=&ia^2\left(\frac{\omega}{c}\right)\sum_{\sigma=0}^{1}\sum_{l=\sigma}^{+\infty}\sum_{m=\sigma}^{l} e_{\sigma,l,m}\left(\frac{\omega}{c}\right)^s h_l^{(s)}\\&\times\left(\left(\frac{\omega}{c}\right)\right)j_l\left(\left(\frac{\omega}{c}\right)a\right)\frac{\partial Y_{\sigma,l,m}}{\partial\theta}(\hat{\underline{x}}(\theta,\phi)),\\&\hat{\underline{x}}(\theta,\phi)\in\partial B,\quad s=0,1,\ldots,\end{aligned} \tag{70}$$

$$\begin{aligned}(\hat{p}^{\phi}_{\omega,s}e)(\hat{\underline{x}})=&ia^2\left(\frac{\omega}{c}\right)\sum_{\sigma=0}^{1}\sum_{l=\sigma}^{+\infty}\sum_{m=\sigma}^{l} e_{\sigma,l,m}\left(\frac{\omega}{c}\right)^s h_l^{(s)}\\&\times\left(\left(\frac{\omega}{c}\right)\right)j_l\left(\left(\frac{\omega}{c}\right)a\right)\frac{\partial Y_{\sigma,l,m}}{\partial\theta}(\hat{\underline{x}}(\theta,\phi)),\\&\hat{\underline{x}}(\theta,\phi)\in\partial B,\quad s=0,1,\ldots,\end{aligned} \tag{71}$$

$$(\hat{l}_{\omega}e)(\hat{\underline{x}})=\sum_{\sigma=0}^{1}\sum_{l=\sigma}^{+\infty}\sum_{m=\sigma}^{l}\frac{e_{\sigma,l,m}Y_{\sigma,l,m}(\hat{\underline{x}})}{i\left(\frac{\omega}{c}\right)a^2 j_l\left(\left(\frac{\omega}{c}\right)a\right)\omega\left(ih_l\left(\left(\frac{\omega}{c}\right)\right)+\chi h_l^{(1)}\left(\left(\frac{\omega}{c}\right)\right)\right)},\quad \hat{\underline{x}}\in\partial B, \tag{72}$$

and

$$(\hat{p}_{\omega,s}(\hat{l}_{\omega}e))=\sum_{\sigma=0}^{1}\sum_{l=\sigma}^{+\infty}\sum_{m=\sigma}^{l}\frac{\left(\frac{\omega}{c}\right)^s h_l^{(s)}\left(\left(\frac{\omega}{c}\right)\right)e_{\sigma,l,m}Y_{\sigma,l,m}(\hat{\underline{x}}(\theta,\phi))}{\omega\left(ih_l\left(\left(\frac{\omega}{c}\right)\right)+\chi h_l^{(1)}\left(\left(\frac{\omega}{c}\right)\right)\right)},\quad \hat{\underline{x}}(\theta,\phi)\in\partial B,\ \ \omega\in\mathbb{R},\ \ s=0,1,\ldots, \tag{73}$$

$$(\hat{p}^{\theta}_{\omega,s}(\hat{l}_{\omega}e))=\sum_{\sigma=0}^{1}\sum_{l=\sigma}^{+\infty}\sum_{m=\sigma}^{l}\frac{\left(\frac{\omega}{c}\right)^s h_l^{(s)}\left(\left(\frac{\omega}{c}\right)\right)e_{\sigma,l,m}(\partial Y_{\sigma,l,m}/\partial\theta)(\hat{\underline{x}}(\theta,\phi))}{\omega\left(ih_l\left(\left(\frac{\omega}{c}\right)\right)+\chi h_l^{(1)}\left(\left(\frac{\omega}{c}\right)\right)\right)},\quad \hat{\underline{x}}(\theta,\phi)\in\partial B,\ \ \omega\in\mathbb{R},\ \ s=0,1,\ldots, \tag{74}$$

$$(\hat{p}^{\phi}_{\omega,s}(\hat{l}_{\omega}e))=\sum_{\sigma=0}^{1}\sum_{l=\sigma}^{+\infty}\sum_{m=\sigma}^{l}\frac{\left(\frac{\omega}{c}\right)^s h_l^{(s)}\left(\left(\frac{\omega}{c}\right)\right)e_{\sigma,l,m}(\partial Y_{\sigma,l,m}/\partial\phi)(\hat{\underline{x}}(\theta,\phi))}{\omega\left(ih_l\left(\left(\frac{\omega}{c}\right)\right)+\chi h_l^{(1)}\left(\left(\frac{\omega}{c}\right)\right)\right)},\quad \hat{\underline{x}}(\theta,\phi)\in\partial B,\ \ \omega\in\mathbb{R},\ \ s=0,1,\ldots, \tag{75}$$

where $h_l(z)$, $j_l(z)$, $l=0,1,...$, are the spherical Hankel and the spherical Bessel functions, respectively (Ref. 17, p. 439) and $h_l^{(\nu)}$ $\nu=0,1,...$, are the derivatives of $h_l(z)$; that is

$$h_l^{(\nu)}(z)=\frac{d^\nu}{dz^\nu}h_l(z), \quad \nu=0,1,2,.... \tag{76}$$

We note that when ω goes to zero, the operators in Eqs. (69), (70), (71), and (72) are well-defined and not zero since the limits $\lim_{\omega\to 0}\omega^{\nu+1}h_l^{(\nu)}((\omega/c))j_l((\omega/c)a)$, $\nu=0,1,...$, and $\lim_{\omega\to 0}(\omega/c)j_l((\omega/c)a)\omega(ih_l((\omega/c))+\chi h_l^{(1)}((\omega/c)))$ are finite and not zero in general; moreover, it is easy to see that when $\chi\geqslant 0$, we have

$$\left(ih_l\left(\left(\frac{\omega}{c}\right)\right)+\chi h_l^{(1)}\left(\left(\frac{\omega}{c}\right)\right)\right)\neq 0, \quad l=0,1,..., \tag{77}$$

for every real value of (ω/c) (see Ref. 17, p. 439).

We note that when ω goes to zero and $\chi=0$, formula (72) must be slightly modified as shown in the Introduction, that is, the right-hand side of Eq. (72) must be multiplied by ω. Also, when $\chi=\infty$ formula (72) must be modified as suggested in the Introduction.

We note that formulas (73), (74), and (75) are independent of a, so that the computational method in reality does not require the choice of the sphere B_a.

Let $\chi\in\mathbb{R}$, $\chi>0$, let $z_{s,\omega,\underline{\alpha}}(\hat{\underline{x}})$, $\hat{\underline{x}}\in\partial B$, $\underline{\alpha}\in\partial B$, $\omega\in\mathbb{R}$, $s=0,1,...$, be the functions given by Eqs. (58), (59), and let

$$z_{s,\omega,\underline{\alpha}}(\hat{\underline{x}})=\sum_{\sigma=0}^{1}\sum_{l=\sigma}^{+\infty}\sum_{m=\sigma}^{l} z_{s,\omega,\underline{\alpha},\sigma,l,m}Y_{\sigma,l,m}(\hat{\underline{x}}),$$

$$\hat{\underline{x}}\in\partial B, \quad s=0,1,..., \tag{78}$$

be the expansion in spherical harmonics of the functions $z_{s,\omega,\underline{\alpha}}(\hat{\underline{x}})$; then, using formulas (68), (73), (74), and (75) we can see that the function $F_{\omega,\underline{\alpha}}(\underline{x})$ given by Eq. (24) solution of Eqs. (10), (11), and (13) has the following expansion:

$$F_{\omega,\underline{\alpha}}(\underline{x})$$
$$=\sum_{s=0}^{+\infty}\sum_{\sigma=0}^{1}\sum_{l=\sigma}^{+\infty}\sum_{m=\sigma}^{l}\frac{h_l\left(\left(\frac{\omega}{c}\right)\|\underline{x}\|\right)z_{s,\omega,\underline{\alpha},\sigma,l,m}Y_{\sigma,l,m}(\hat{\underline{x}})}{\omega\left(ih_l\left(\left(\frac{\omega}{c}\right)\right)+\chi h_l^{(1)}\left(\left(\frac{\omega}{c}\right)\right)\right)},$$

$$\underline{x}=\|\underline{x}\|\hat{\underline{x}}, \quad \hat{\underline{x}}\in\partial B, \quad \|\underline{x}\|>a. \tag{79}$$

When $\chi=0$, the right-hand side of Eq. (79) must be modified multiplying it by ω, also, when $\chi=\infty$, Eq. (79) needs some modifications.

Note that for every fixed value of $s\geqslant 0$, $\omega\in\mathbb{R}$, $\underline{\alpha}\in\partial B$, the generalized Fourier coefficients $z_{s,\omega,\underline{\alpha},\sigma,l,m}=\int_{\partial B}z_{s,\omega,\underline{\alpha}}(\hat{\underline{x}})Y_{\sigma,l,m}(\hat{\underline{x}})ds(\hat{\underline{x}})$, $\sigma=0,1$, $l=\sigma,...,$ $m=\sigma,...,l$ are double integrals independent from each other. Morever, let S, $L_{\max}$ be two positive integers and $W(\underline{\alpha},\omega)$ appearing in Eqs. (6) and (9) be a function; we define $q_{\underline{x},t}^{S,L_{\max}}(\omega,\underline{\alpha})$ to be

$$q_{\underline{x},t}^{S,L_{\max}}(\omega,\underline{\alpha})$$
$$=\frac{\exp(-i\omega t)W(\omega,\underline{\alpha})}{w(\omega)(2\pi)^4}$$
$$\times\sum_{\sigma=0}^{1}\sum_{l=\sigma}^{L_{\max}}\sum_{m=\sigma}^{l}\frac{h_l\left(\left(\frac{\omega}{c}\right)\|\underline{x}\|\right)Y_{\sigma,l,m}(\hat{\underline{x}})\sum_{s=0}^{S}z_{s,\omega,\underline{\alpha},\sigma,l,m}}{\omega\left(ih_l\left(\left(\frac{\omega}{c}\right)\right)+\chi h_l^{(1)}\left(\left(\frac{\omega}{c}\right)\right)\right)},$$

$$\underline{\alpha}\in\partial B, \quad \omega\in\mathbb{R}, \quad (\underline{x},t)\in(\mathbb{R}^3\backslash\overline{\Omega})\times\mathbb{R}, \tag{80}$$

then $u^s(\underline{x},t)$ solution of problems (1), (2), (4), and (5) can be approximated with $v_{L_{\max}}^{S,N_1,N_2,N_3}(\underline{x},t)$ given by

$$v_{L_{\max}}^{S,N_1,N_2,N_3}(\underline{x},t)=Q(q_{\underline{x},t}^{S,L_{\max}},A,\underline{\omega}^{N_1},\underline{\phi}^{N_2},\underline{z}^{N_3}),$$
$$(\underline{x},t)\in(\mathbb{R}^3\backslash\overline{\Omega})\times\mathbb{R}, \tag{81}$$

where $Q(q_{\underline{x},t}^{S,L_{\max}},A,\underline{\omega}^{N_1},\underline{\phi}^{N_2},\underline{z}^{N_3})$ is given by Eq. (16). Moreover, we have

$$|u^s(\underline{x},t)-v_{L_{\max}}^{S,N_1,N_2,N_3}(\underline{x},t)|$$
$$\leqslant|Q(q_{\underline{x},t}^{S}-q_{\underline{x},t}^{S,L_{\max}},A,\underline{\omega}^{N_1},\underline{\phi}^{N_2},\underline{z}^{N_3})|$$
$$+|E(q_{\underline{x},t}^{S},A,\underline{\omega}^{N_1},\underline{\phi}^{N_2},\underline{z}^{N_3})|$$
$$+\int_{\partial B}ds(\underline{\alpha})\int_{\mathbb{R}}d\omega\, w(\omega)|R_{S,\underline{x},t}(\omega,\underline{\alpha})|,$$
$$(\underline{x},t)\in(\mathbb{R}^3\backslash\overline{\Omega})\times\mathbb{R}, \tag{82}$$

where $|E(q_{\underline{x},t}^{S},A,\underline{\omega}^{N_1},\underline{\phi}^{N_2},\underline{z}^{N_3})|$ is given by Eq. (17), and $R_{S,\underline{x},t}(\omega,\underline{\alpha})$ is given by Eq. (62).

In Sec. III we use the form assumed by formulas (80) and (81) when $w(\omega)=\exp(-\omega^2)$, $W(\omega,\underline{\alpha})=(2\pi^4/\sqrt{\pi})\zeta\exp(-\zeta^2\omega^2)\delta(\underline{\gamma}-\underline{\alpha})$ and a particular choice of the quadrature rule is made.

III. NUMERICAL RESULTS

In this section we use the computational method proposed previously to solve the time-dependent acoustic scattering problem of the Introduction in some test cases. These test cases are discussed both from the physical point of view and from the numerical point of view. We consider the scattering phenomenon generated by an incident acoustic wave that hits an obstacle Ω when the incident acoustic wave is of the form (22); that is, a time-harmonic plane wave

$$u^i(\underline{x},t)=\exp\left(i\frac{\omega^*}{c}[(\underline{\gamma},\underline{x})-ct]\right), \quad (\underline{x},t)\in\mathbb{R}^3\times\mathbb{R}, \tag{83}$$

or the incident acoustic wave is of the form (23); that is

$$u^i(\underline{x},t)=\exp\left(-\frac{1}{4\zeta^2}[(\underline{\gamma},\underline{x})-ct]^2\right), \quad (\underline{x},t)\in\mathbb{R}^3\times\mathbb{R}, \tag{84}$$

where $\underline{\gamma}\in\partial B$, $\zeta>0$, $\omega^*\in\mathbb{R}$ are given. Since $\underline{\gamma}\in\partial B$, we have

TABLE I. Cube: $\chi=0$, $\max_{\hat{\underline{x}}\in\partial B}|\xi(\hat{\underline{x}})-1|=0.4$.

ω/c	e_{16}^1	e_{16}^2	e_{16}^3	e_{16}^4	e_{16}^5	e_{16}^6	e_{16}^7	e_{16}^8	e_{16}^9
0.5	4.09E−01	8.36E−02	2.55E−02	5.65E−03	5.95E−03	1.66E−03	1.34E−03	6.45E−04	2.75E−04
1	5.07E−01	1.51E−01	4.58E−02	1.34E−02	8.50E−03	3.11E−03	2.11E−03	1.01E−03	5.26E−04
2	6.79E−01	3.48E−01	1.19E−01	4.22E−02	1.87E−02	8.03E−03	4.47E−03	2.33E−03	1.26E−03
4	8.65E−01	9.82E−01	4.66E−01	1.84E−01	7.88E−02	3.21E−01	1.40E−02	6.78E−03	3.86E−03
8	9.63E−01	1.17E+00	1.72E+00	1.77E+00	1.01E+00	6.14E−01	3.21E−01	1.31E−01	4.91E−02

$$\underline{\gamma}=(\sin\alpha\cos\beta,\sin\alpha\sin\beta,\cos\alpha)^T,$$
$$0\leqslant\alpha\leqslant\pi,\quad 0\leqslant\beta<2\pi, \tag{85}$$

for some choice of α and β. In the following, we use $\alpha=\pi$, β arbitrary, so that $\underline{\gamma}=(0,0,-1)^T$. When $u^i(\underline{x},t)$ is given by Eq. (84), the integral (7) becomes

$$u^i(\underline{x},t)=\frac{1}{\sqrt{\pi}}\int_{\mathbb{R}}\exp(-\omega^2)\exp\left(\frac{i\omega}{c\xi}[(\underline{x},\underline{\gamma})-ct]\right)d\omega,$$
$$(\underline{x},t)\in\mathbb{R}^3\times\mathbb{R}, \tag{86}$$

and in correspondence we assume

$$u^s(\underline{x},t)=\frac{1}{\sqrt{\pi}}\int_{\mathbb{R}}\exp(-\omega^2)\exp(-i\omega t)u^s_{\omega/\xi,\underline{\gamma}}(\underline{x})d\omega,$$
$$(\underline{x},t)\in(\mathbb{R}^3\backslash\overline{\Omega})\times\mathbb{R}. \tag{87}$$

In all the experiments we choose $c=1$, and ∂B as the base point of the expansion [see (35)] and $\tilde{b}_{s,\omega,\underline{\alpha}}(\hat{\underline{x}})$, $\hat{\underline{x}}\in\partial B$, $s=0,1,...$, the functions given by Eq. (55). We remark that no choice of the sphere B_a [see (79)] is required by the computational method. In the experiments involving the incident wave (84) we choose the quadrature rule (16) to be the Gauss Hermite quadrature formula (see Ref. 7, p.114) with $N_2=N_3=1$, $\underline{\alpha}_{1,1}=\underline{\gamma}$, with ω_i, $i=1,2,...,N_1$, to be the zeros of the Hermite polynomial of degree N_1 and $a_{i,1,1}$, $i=1,2,...,N_1$, to be the weights of the Gauss Hermite quadrature formula. Let us consider the problem of how to choose the number N_1 of the nodes ω_i, $i=1,2,...,N_1$ of the quadrature rule. Let M, T be two integers and $(\underline{x}_j,t_k)\in\mathbb{R}^3\times\mathbb{R}$, $j=1,2,...,M^3$, $k=1,2,...,T$ be a rectangular grid of the set $[-2,2]\times[-2,2]\times[-2,2]\times[-3,7]$ with constant step size with respect to the spatial variables (i.e., the first three variables) equal to $4/M$ and with constant step size with respect to the time variable (i.e., the last variable) equal to $10/T$, and let u_a^i be the approximation of the incoming wave given by

$$u_a^i(\underline{x},t)=\sum_{i=1}^{N_1}a_{i,1,1}\exp\left(\frac{i\omega_i}{c\xi}[(\underline{x},\underline{\gamma})-ct]\right),\quad(\underline{x},t)\in\mathbb{R}^3\times\mathbb{R}. \tag{88}$$

We choose N_1 to be the smallest integer such that the following condition is satisfied:

$$\frac{[\Sigma_{j=1}^{M^3}\Sigma_{k=1}^{T}|u_a^i(\underline{x}_j,t_k)-u^i(\underline{x}_j,t_k)|^2]^{1/2}}{[\Sigma_{j=1}^{M^3}\Sigma_{k=1}^{T}|u^i(\underline{x}_j,t_k)|^2]^{1/2}}\leqslant 10^{-3}. \tag{89}$$

In the numerical experiments considered here, we have $M=20$ $T=40$ and (89) is satisfied choosing $N_1=400$.

When we use the incident wave (83), no quadrature rule in the variable ω is involved since the incident wave is a time-harmonic plane wave, the scattered wave will be assumed to be time harmonic with the same frequency ω^*; that is

$$u^s(\underline{x},t)=\exp(-i\omega^* t)u^s_{\omega^*,\underline{\gamma}}(\underline{x}),\quad(\underline{x},t)\in(\mathbb{R}^3\backslash\overline{\Omega})\times\mathbb{R}, \tag{90}$$

where $u^s_{\omega^*,\underline{\gamma}}(\underline{x})$ is the space-dependent part of the scattered time-harmonic wave. We note that when the time-harmonic incoming wave (83) hits a sphere of radius one and center, the origin the time-harmonic scattered wave generated coincides with the zero-order term of the expansion in powers of $\xi-1$ given by Eq. (61) when $W(\omega,\underline{\alpha})=(2\pi)^4\delta(\underline{\alpha}-\underline{\gamma})\delta(\omega-\omega^*)$. Moreover, we must consider the problem of where to truncate the series expansion (79); that is, how to choose the integer $L_{\max}$ of (80) to have in the region of the $\underline{x}$ variable considered a good approximation of the solution $u^s_{\omega,\underline{\alpha}}(\underline{x})$ of the boundary value problems (10), (11), and (13). In the numerical experience presented here, the region of the $\underline{x}$ variable where we want a good approximation is $\underline{x}\in[-2,2]\times[-2,2]\times[-2,2]$. To do this we use the results of the analysis presented in Ref. 10, Sec. IV where it is shown that the integer $L_{\max}$ must increase when the geometry of the obstacle is of increasing complexity. In particular, in the numerical experience shown here we choose $L_{\max}=16$ for obstacles with simple geometry (i.e., the sphere, and the corrugated sphere) and $L_{\max}=24$ for more complicated objects (i.e., the cube and the holed sphere).

Let us consider the computational cost of the method proposed in Secs. I and II in terms of the number of double integrals that given N_1 and $L_{\max}$ must be computed in order

TABLE II. Cube: $\chi=\infty$, $\max_{\hat{\underline{x}}\in\partial B}|\xi(\hat{\underline{x}})-1|=0.4$.

ω/c	e_{16}^1	e_{16}^2	e_{16}^3	e_{16}^4	e_{16}^5	e_{16}^6	e_{16}^7	e_{16}^8	e_{16}^9
0.5	1.79E+00	4.52E−01	8.73E−02	2.99E−02	2.84E−03	8.57E−03	1.53E−03	2.02E−03	4.97E−04
1	1.28E+00	3.25E−01	3.55E−02	2.11E−02	5.25E−03	8.74E−03	1.91E−03	1.85E−03	6.03E−04
2	8.01E−01	2.16E−01	8.24E−02	3.19E−02	1.14E−02	9.93E−03	4.45E−03	3.01E−03	1.27E−03
4	8.25E−01	6.17E−01	2.49E−01	1.26E−01	8.40E−02	7.60E−02	7.53E−02	7.44E−02	7.61E−02
8	9.55E−01	1.05E+00	1.52E+00	2.97E+00	1.07E+00	8.73E−01	9.79E−01	1.07E+00	1.13E+00

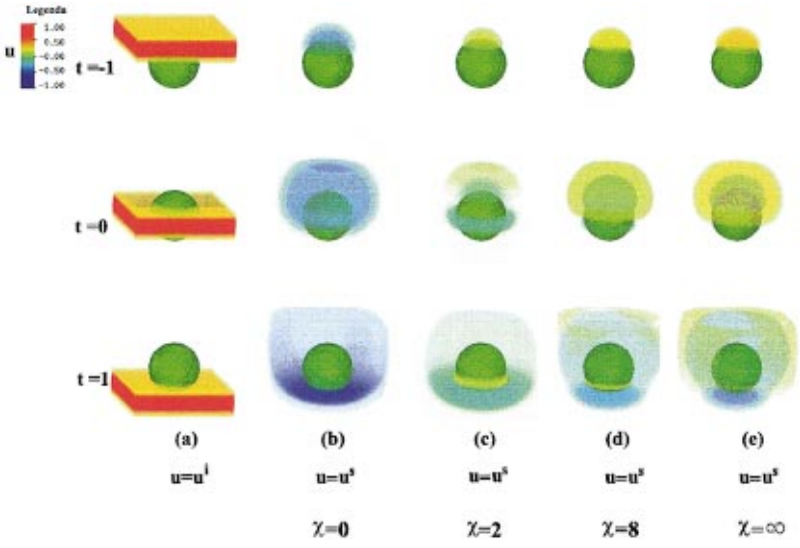

FIG. 1. The incoming wave $u^i(\zeta^2=1/32)$ and the corresponding scattered wave u^s generated by a sphere when the acoustic boundary impedance takes the values $\chi=0$ (b), $\chi=2$ (c), $\chi=8$ (d), $\chi=\infty$ (e).

to evaluate the approximate series expansion of the scattered wave $u^s(\underline{x},t)$ up to order S; that is, to evaluate $v^{S,N_1,1,1}_{L_{\max}}(\underline{x},t)$ given by Eq. (81), a simple computation gives

$$\text{Number of integrals}=\tfrac{3}{2}N_1S(S+1)(L_{\max}+1)^2. \qquad (91)$$

Formula (91) shows that the computational cost of the method proposed in Secs. I and II consists of a polynomial in N_1 times a polynomial in S times a polynomial in $L_{\max}$. We can use relatively large values of N_1, S, and $L_{\max}$ since we make the computation of the approximations up to order S of the terms $u^s_{\omega,\underline{\alpha}}$, $\omega=\omega_i$, $i=1,2,...,N_1$, $\underline{\alpha}=\underline{\gamma}$, in parallel. That is, chosen $\underline{\alpha}=\underline{\gamma}$ for $\omega=\omega_i$, $i=1,2,...,N_1$ we compute for $s_1=0,1,...,S$ the s_1th order term of the expansion of $u^s_{\omega_i,\underline{\gamma}}$ and the computation of s_1th order term of the expansion (79) is fully parallelizable with respect to the number $L_{\max}$ of spherical harmonics involved; that is, it is fully parallelizable with respect to $\sigma=0,1$, $l=\sigma,\sigma+1,...,L_{\max}$. We note that for $s_1=0,1,...,S$ the computation of the (s_1+1) order term in the perturbation theory involves the knowledge of the s_1 order term. Indeed, the computation of the terms $u^s_{\omega_i,\underline{\gamma}}$, $i=1,2,...,N_1$ is fully parallelizable in i, and for each value of i at each order in the perturbation theory the computation is fully parallelizable in l. Finally, the summation that defines the quadrature rule can be computed in parallel. That is, several different parallel architectures can be used profitably to reduce the time of the computation of the approximation $v^{S,N_1,1,1}_{L_{\max}}$ in Eq. (81) of the solution u^s of problems (1), (2), (4), and (5).

The algorithm previously described has been coded in FORTRAN 90 language and tested on a cluster of four Alpha Digital workstations, each one having four processors, and on a Cray T3E machine with 256 processors in ''single program multiple data'' programming mode using MPI as ''message passing'' library.

In the numerical experiments presented, we consider the following obstacles:

(1) Sphere $\xi(\hat{\underline{x}}(\theta,\phi))=1$, $0\leqslant\theta\leqslant\pi$, $0\leqslant\phi<2\pi$;
(2) Cube;
(3) Holed sphere;
(4) Corrugated sphere $\xi(\hat{\underline{x}}(\theta,\phi))=1+h\sin^2 2\theta|\cos 2\phi|$, $0\leqslant\theta\leqslant\pi$, $0\leqslant\phi<2\pi$,

where $h>0$ is a real parameter. The cube, the holed sphere, and the corrugated sphere are obstacles with Lipschitz continuous boundary; in particular, these boundaries are not continuously differentiable. The last three obstacles are interesting from the physical point of view for the presence of edges and corners. In the numerical experience, two different cubes are considered. We omit the analytical expressions of $\xi(\hat{\underline{x}}(\theta,\phi))$ for the cube and the holed sphere, since they are involved. We only remark that the origin is the center of mass of the cube and that the largest sphere contained in the first cube has radius equal to 0.6 (Tables I and II) and the

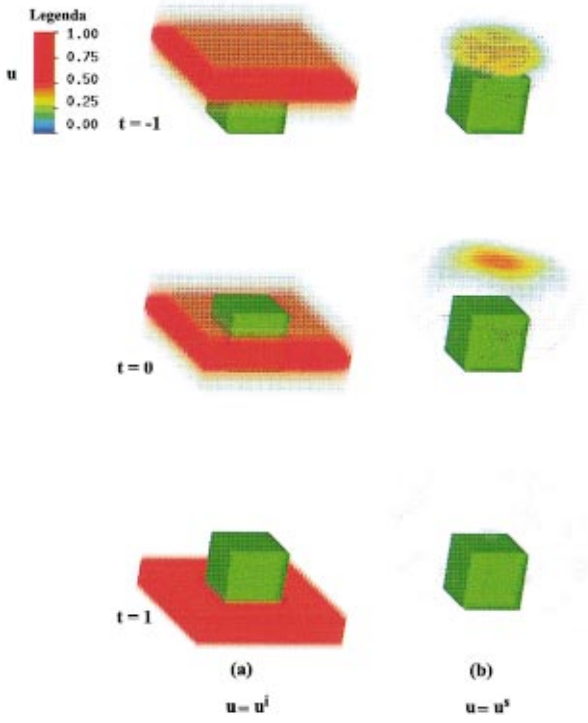

FIG. 2. The incoming wave u^i $(\zeta^2=1/16)$ and the corresponding scattered wave u^s generated by an acoustically hard cube.

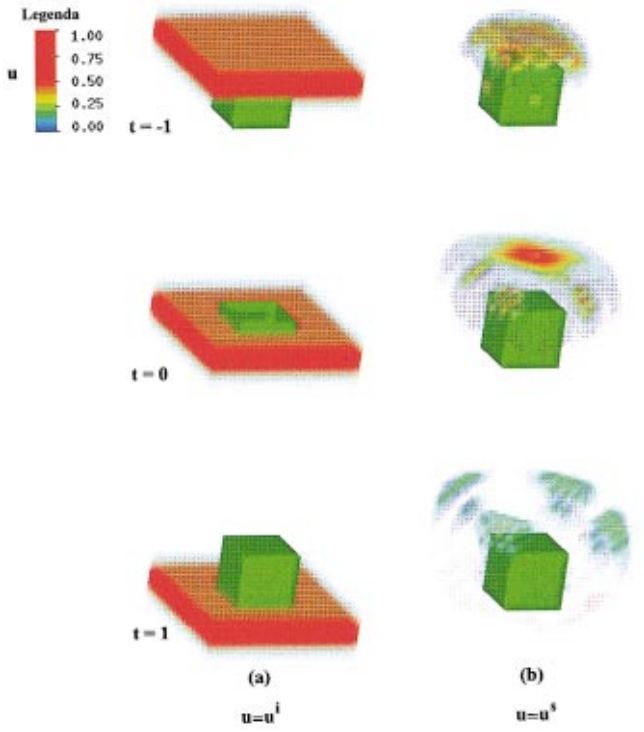

FIG. 3. The incoming wave u^i ($\zeta^2=1/32$) and the corresponding scattered wave u^s generated by an acoustically hard cube.

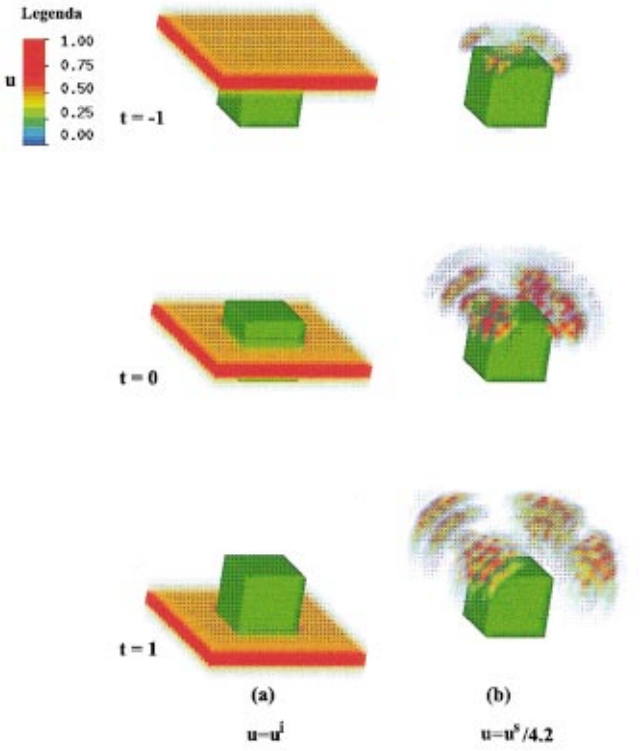

FIG. 4. The incoming wave u^i ($\zeta^2=1/64$) and the corresponding scattered wave u^s generated by an acoustically hard cube.

largest sphere contained in the second cube has radius equal to one (Figs. 2, 3, 4, Table V). Moreover, the holed sphere is made of a sphere of center the origin and radius one with a cavity. The cavity is obtained removing from the sphere of radius one and center the origin its intersection with the sphere with center $(\tan \pi/10 \sin \pi/10+\cos \pi/10,0,0)^T$ and radius $\sin \pi/10\sqrt{\tan^2 \pi/10+1}$.

First, we discuss the numerical experiments from the numerical point of view and we show some evidence of the quantitative character of the results obtained with the expansion introduced in the previous sections. The following tables (Tables I, II, and III) concern the convergence of the formal series expansion in power of $\xi-1$ of the function $F_{\omega,\underline{\alpha}}$ given by Eq. (79), where $\underline{\alpha}=\underline{\gamma}=(0,0,-1)^T$. From (79), we have

$$F_{\omega,\underline{\gamma}} \approx \sum_{\sigma=0}^{1} \sum_{l=\sigma}^{L_{\max}} \sum_{m=\sigma}^{l} \frac{h_l\left(\left(\frac{\omega}{c}\right)\|\underline{x}\|\right) Y_{\sigma,l,m}(\hat{\underline{x}})}{\omega\left(ih_l\left(\left(\frac{\omega}{c}\right)\right)+\chi h_l^{(1)}\left(\left(\frac{\omega}{c}\right)\right)\right)} \times \sum_{s=0}^{S} z_{s,\omega,\underline{\gamma},\sigma,l,m}, \tag{92}$$

so that we study the convergence of the series $\Sigma_{s=0}^{+\infty} z_{s,\omega,\underline{\gamma},\sigma,l,m}$, $\sigma=0,1$, $l=\sigma,\sigma+1,...,L_{\max}$, $m=\sigma,\sigma+1,...,l$. Let

$$e_{L_{\max}}^{S}=\frac{[\Sigma_{\sigma=0}^{1}\Sigma_{l=\sigma}^{L_{\max}}\Sigma_{m=\sigma}^{l}|z_{S,\omega,\underline{\gamma},\sigma,l,m}|^2]^{1/2}}{[\Sigma_{\sigma=0}^{1}\Sigma_{l=\sigma}^{L_{\max}}\Sigma_{m=\sigma}^{l}|\Sigma_{s=0}^{S} z_{s,\omega,\underline{\gamma},\sigma,l,m}|^2]^{1/2}}. \tag{93}$$

In Tables I, II, and III we show the behavior of $e_{L_{\max}}^{S}$ with $S=1,2,...,9$ and $L_{\max}=16$ when the obstacles are the cube and the corrugated sphere. In Tables I and II we show the behavior of $e_{L_{\max}}^{S}$ for different values of the wave number $\omega/c=0.5$, 1, 2, 4, 8 for an ''acoustically soft'' (i.e., $\chi=0$) cube (Table I) and ''acoustically hard'' (i.e., $\chi=\infty$) cube (Table II). In Table III we consider a corrugated sphere with acoustic impedance $\chi=2$ and we show the behavior of $e_{L_{\max}}^{S}$ at a fixed value of the wave number $\omega/c=10$ for different values of the height h of the corrugation.

From Tables I, II, and III we can see that the convergence of the series expansion in powers of $\xi-1$ in Eq. (79) depends on the magnitude of $(\omega/c)\max_{\hat{\underline{x}}\in\partial B}|\xi(\hat{\underline{x}})-1|$, and in

TABLE III. Corrugated sphere: $\xi(\theta,\phi)=1+h \sin^2 2\theta|\cos 2\phi|$, $\omega/c=10$, $\max_{\hat{\underline{x}}\in\partial B}|\xi(\hat{\underline{x}})-1|=h$.

h	e_{16}^{1}	e_{16}^{2}	e_{16}^{3}	e_{16}^{4}	e_{16}^{5}	e_{16}^{6}	e_{16}^{7}	e_{16}^{8}	e_{16}^{9}
1/100	$3.42E-02$	$1.01E-03$	$2.47E-05$	$5.11E-07$	$5.57E-08$	$8.01E-12$	$5.55E-24$	$5.50E-27$	$5.00E-32$
1/10	$6.08E-02$	$1.41E-02$	$4.95E-04$	$2.08E-04$	$5.54E-03$	$2.19E-03$	$1.36E-03$	$5.60E-04$	$3.60E-04$
1/5	$5.18E-01$	$3.23E-01$	$1.73E-01$	$1.03E-02$	$5.54E-03$	$2.19E-03$	$1.36E-03$	$5.60E-04$	$3.60E-04$
1/3	$6.83E-01$	$6.23E-01$	$6.03E-01$	$1.03E-02$	$5.54E-03$	$2.19E-03$	$1.36E-03$	$5.60E-04$	$3.60E-04$
1/2	$7.92E-01$	$8.11E-01$	$8.85E-01$	$1.72E-01$	$1.67E-01$	$1.53E-01$	$1.58E-01$	$1.57E-01$	$1.62E-01$

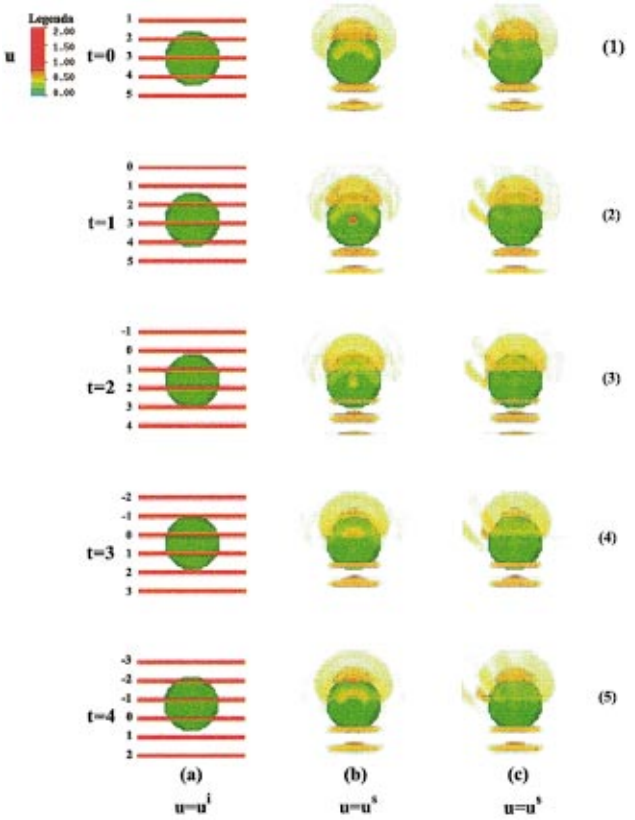

FIG. 5. The incoming wave u^i and the corresponding scattered wave u^s generated by an acoustically hard holed sphere.

the examples considered the convergence is satisfactory roughly when $(\omega/c)\max_{\underline{\hat{x}}\in\partial B}|\xi(\underline{\hat{x}})-1|\leqslant 1.5$. Moreover, in favorable circumstances such as those considered in the first row of Table III the series expansion considered can give very accurate results. That is, the operator expansion method used to compute the time-harmonic waves ''converges'' in many significant situations and sometimes gives very accurate results. Of course, there is no reason to discuss here the convergence of the ''Fourier integral'' (9) that gives $u^s(\underline{x},t)$ or the validity of the Gauss–Hermite quadrature rule used to approximate it, since these are standard topics in mathematics.

Similar results can be obtained considering the series $\Sigma_{s=0}^{+\infty} z_{s,\omega,\gamma,\sigma,l,m}$, $\sigma=0,1$, $l=\sigma,\sigma+1,...,L_{\max}$, $m=\sigma,\sigma+1,...,l$, obtained starting from (56) rather than starting from (55).

We show now three experiments which are interesting from the physical point of view. Let

$$Z_\nu=\left\{(x,y,z)^T\in\mathbb{R}^3,\ x=-2+\frac{4}{\nu}i,\ y=-2+\frac{4}{\nu}j,\ z=-2+\frac{4}{\nu}k,i,j,k=0,1,...,\nu\right\}$$
$$\nu=20,40,80. \tag{94}$$

In the figures shown in this section (i.e., Figs. 1–5), the incident wave $u^i(\underline{x},t)$ is shown in the first column and in the other columns the scattered wave $u^s(\underline{x},t)$ solution of Eqs. (1), (2), (4), and (5) on the spatial grid Z_{80} (Fig. 1), or Z_{20} (Figs. 2–4), or Z_{40} (Fig. 5) is shown. When the incident wave is given by Eq. (84), i.e., Figs. 1–4, this is done for three values of the time t, $t=-1$, $t=0$, $t=1$ (i.e., see the three rows of Figs. 1–4). That is: $t=-1$, a time when the incident wave $u^i(\underline{x},t)$ is beginning to hit the obstacle, $t=0$, a time such that $u^i(\underline{x},t)$ is passing through the obstacle, and $t=1$, a time such that $u^i(\underline{x},t)$ is almost passed through the obstacle. When the incident wave is given by Eq. (83); that is, when the time-harmonic problem is considered (see Fig. 5), we choose five values of the time t, that is, $t=0$, $t=1$, $t=2$, $t=3$, $t=4$ (i.e., see the five rows of Fig. 5). We note that in the experiments where the obstacle is the sphere of center the origin and radius one, we use $S=0$ in (61), in fact, in this case only the zero-order term of the expansion (35) is nonzero.

Let us discuss the numerical experiments from the physical point of view.

The first experiment (see Fig. 1) shows the qualitative behavior of the scattered wave $u^s(\underline{x},t)$ solution of Eqs. (1), (2), (4), and (5) generated by a sphere of radius one hit by the incident wave $u^i(\underline{x},t)$ given in Eq. (84) with $\zeta^2=1/32$, when the impedance χ of the sphere takes the values $\chi=0$ [column (a)], $\chi=2$ [column (b)], $\chi=8$ [column (c)], $\chi=\infty$ [column (d)]. We note that when $\chi=0$, that is, the case of the acoustically soft obstacle, the reflected wave has opposite sign with respect to the sign of the the incident wave [see Fig. 1(b)]; when $\chi=2$ it has the same sign as the sign of the incident wave [see Fig. 1(c)], and when $\chi=8$ [see Fig. 1(d)] the reflected wave is very similar to the reflected wave generated by an acoustically hard obstacle, i.e., $\chi=\infty$ [see Fig. 1(e)]. The second experiment (see Figs. 2, 3, and 4) shows the behavior of the scattered wave $u^s(\underline{x},t)$ solution of Eqs. (1), (2), (4), and (5) generated by the acoustically hard cube, that is, the cube with $\chi=\infty$, when hit by the incident wave $u^i(\underline{x},t)$ given by Eq. (84) with $\zeta^2=1/16$ (Fig. 2), $\zeta^2=1/32$ (Fig. 3), $\zeta^2=1/64$ (Fig. 4). In this experiment we use $S=5$ in (61) and in Fig. 4 the scattered wave is divided by a factor of 4.2 to represent the incident wave and the scattered wave on

TABLE IV. Cube: $\chi=\infty$, $\max_{\underline{\hat{x}}\in\partial B}|\xi(\underline{\hat{x}})-1|=0.7$.

ω/c	e_{24}^1	e_{24}^2	e_{24}^3	e_{24}^4	e_{24}^5	e_{24}^6	e_{24}^7	e_{24}^8	e_{24}^9
0.5	3.52E−01	1.93E−01	2.79E−02	4.21E−02	2.01E−02	3.51E−02	2.77E−02	8.54E−02	2.03E−01
1	3.27E−01	1.86E−01	4.18E−02	4.65E−02	2.69E−02	3.93E−02	3.83E−02	9.68E−02	2.35E−01
2	4.34E−01	2.49E−01	1.30E−01	1.12E−01	5.45E−02	5.11E−02	6.06E−02	1.11E−01	1.98E−01
4	4.89E−01	2.33E−01	2.40E−01	1.93E−01	2.40E−01	2.27E−01	3.49E−01	4.04E−01	5.21E−01
8	7.97E−01	8.03E−01	8.27E−01	8.40E−01	8.52E−01	7.69E−01	8.07E−01	1.18E+00	1.13E+00

TABLE V. Quadrature formula error.

ζ^2	$\epsilon^{200,100}$	$\epsilon^{300,200}$	$\epsilon^{400,300}$
16	$6.47E-02$	$6.07E-03$	$2.71E-03$
64	$7.16E-01$	$5.85E-02$	$2.06E-02$

the same reference scale. We can see that when ζ^2 is large (i.e., $\zeta^2=1/16$) only the facets of the cube irradiate energy (see Fig. 2, animation 1) while for intermediate values of ζ^2 (i.e., $\zeta^2=1/32$) we can see that not only the facets but also the edges of the cube irradiate energy (see Fig. 3, animation 2), and finally when ζ^2 is small (i.e., $\zeta^2=1/64$) we can see that almost all the energy is irradiated by the vertices of the cube (see Fig. 4, animation 3). This phenomenon is a consequence of the fact that when ζ^2 decreases, the components of high frequency of the incident wave packet become more relevant. This phenomenon is a kind of ''dispersion'' phenomenon due to the presence of edges and vertices. This phenomenon is coherent with the observation made in Refs. 10 and 15, where the acoustic and electromagnetic time-harmonic problem for acoustically soft and perfectly conducting obstacles is treated. In Refs. 10 and 15, in the case of the octahedron the authors show that when the wave number of the time-harmonic incident wave increases, the energy is irradiated first from the facets, then from the edges, and finally almost entirely from the vertices (see Ref. 10, Fig. 8 and Ref. 15, Fig. 7). The authors show that a similar phenomenon takes place in the case of obstacles with multiscale corrugations such as corrugated spheres where all the corrugations become visible for high-frequency scattering (see Ref. 10, Figs. 5, 6, and 7 and Ref. 15, Figs. 2 and 3). In Figs. 2, 3, and 4 we have considered the cube that circumscribes the sphere of radius one. In this case, a typical value of $(\omega/c)\max_{\underline{\hat{x}}\in\partial B}|\xi(\underline{\hat{x}})-1|$ involved is about 2. That is, the results obtained with the series constructed with the operator expansion method are poor from the quantitative point of view (Table IV) but they are very satisfactory from the qualitative point of view. Finally, we analyze some quantitative aspects of the second experiment (Figs. 2, 3, and 4). Let $\underline{x}_j \in \mathbb{R}^3$, $j=1,2,...,M$, $t_k\in\mathbb{R}$, $k=1,2,...,T$ be given as in Eq. (89), we denote with $\epsilon^{\nu,\mu}$, $\nu>\mu>0$ the following quantity:

$$\epsilon^{\nu,\mu}=\frac{[\Sigma_{j=1}^{M^3}\Sigma_{k=1}^{T}|v_{L_{\max}}^{S,\nu,1,1}(\underline{x}_j,t_k)-v_{L_{\max}}^{S,\mu,1,1}(\underline{x}_j,t_k)|^2]^{1/2}}{[\Sigma_{j=1}^{M^3}\Sigma_{k=1}^{T}|v_{L_{\max}}^{S,\nu,1,1}(\underline{x}_j,t_k)|^2]^{1/2}},$$

$$\nu>\mu. \tag{95}$$

The quantity $\epsilon^{\nu,\mu}$, $\nu>\mu$ is a measure of the accuracy of the numerical evaluation of the integral in the ω variable. In Table V we show the values of $\epsilon^{\nu,\mu}$ for different values of $\nu=200$, 300, 400 and $\mu=100$, 200, 300 relative to the experiment of the cube of Fig. 2 ($1/\zeta^2=1/16$) and of Fig. 4 ($1/\zeta^2=1/64$).

Table VI shows the time required by the algorithm on the Cray T3E machine to compute $\Sigma_{s=0}^{5}z_{s,\omega_i,\underline{\gamma},\sigma,l,m}$, with $\underline{\gamma}=(0,0,-1)^T$, $i=1,2,...,N_1$, $\sigma=0,\ 1$, $l=\sigma,\ldots,L_{\max}$, $m=\sigma,\ldots,l$, $N_1=400$, $L_{\max}=24$ relative to Fig. 3 versus the number of processors used. The time is measured using the (FORTRAN) routine rtc() of the Cray T3E machine that gives the real-time clock in clicks where a click corresponds to $3.333E-09$ s. In the last experiment (see Fig. 5) the obstacle is the acoustically hard holed sphere; that is, $\chi=\infty$, and the incident wave $u^i(\underline{x},t)$ is given by Eq. (83) with $\underline{\gamma}=(0,0,-1)^T$, and $\omega^*=9$. We use $S=4$ in Eq. (61). In the first column of Fig. 5 we show the incident wave, in the second and third columns we show the scattered wave form from two different points of view; that is, looking in front [i.e., column (b), animation 4) or looking on the side of the hole [i.e., column (c)]. We can see that when the time-harmonic incident wave hits the obstacle first, the energy is irradiated by the edge of the hole [see Fig. 5(b)(column)(1)], then the energy is captured by the hole [Fig. 5(c)(column)(2)] then it is irradiated by the hole [Fig. 4.5(b)(column)(3)]. Since the incident wave is time harmonic, we can observe that as t goes on the energy is alternatively trapped and irradiated by the hole. That is, some kind of ''resonance'' phenomenon takes place. This resonance phenomenon is of the same nature of the one observed in Ref. 15, Figs. 4 and 5. In those figures the authors show the results of an experiment where the obstacle is a corrugated sphere; that is, a sphere of radius one and center the origin with a certain number of corrugations along the ϕ direction and θ direction. In particular, the authors show that as a function of the wave number of the incident wave the far field generated by this obstacle, plotted at $\theta=\pi/2$ as function of ϕ, $0\leqslant\phi<2\pi$, first presents a number of peaks equal to the number of corrugations in the ϕ direction, then becomes similar to the far field of a sphere of radius one and center the origin, without corrugations; finally, valleys take the place of the previously observed peaks and then the entire phenomenon takes place again. The sequence peak, far field of the sphere, valley, peak that is visible for increasing values of the wave number of the incident wave is what in Ref. 15 we have called ''resonance'' phenomenon.

TABLE VI. Time versus number of processors.

Processors	Seconds
3	24.03
6	12.13
12	6.20
24	3.26
30	2.67
60	1.51
120	0.96

The animations relative to the previous numerical experiments can be found on the website http://www.econ.unian.it/recchioni/w1/

ACKNOWLEDGMENTS

The numerical experience shown in this paper has been made possible by the support and sponsorship of CINECA—Casalecchio di Reno (BO)—Italy through a grant account at the T3E computer facility.

[1] P. M. Morse and K. V. Ingard, *Theoretical Acoustics* (McGraw-Hill, New York, 1968).
[2] J. Nečas, *Les Méthodes Directes en Théorie des Équations Elliptiques* (Masson & Cie., Paris, 1967).
[3] D. Colton and R. Kress, *Integral Equation Methods in Scattering Theory* (Wiley, New York, 1983).
[4] J. A. Stratton, *Electromagnetic Theory* (McGraw-Hill, New York, 1941).
[5] A. G. Ramm, *Scattering by Obstacles* (Reidel, Dordrecht, 1986).
[6] D. M. Milder, ''An improved formalism for wave scattering from rough surface,'' J. Acoust. Soc. Am. **89**, 529–541 (1991).
[7] A. Ghizzetti and A. Ossicini, *Quadrature Formulae* (Birkhäuser, Basel, 1970).
[8] E. Heyman, ''Time-dependent plane-wave spectrum representations for radiation from volume source distributions,'' J. Math. Phys. **37**, 658–681 (1996).
[9] O. M. Bucci, G. D'Elia, and M. D. Migliore, ''Optimal time domain field interpolation from plane-polar samples,'' IEEE Trans. Antennas Propag. **45**, 989–994 (1997).
[10] L. Misici, G. Pacelli, and F. Zirilli, ''A new formalism for wave scattering from a bounded obstacle,'' J. Acoust. Soc. Am. **103**, 106–113 (1998).
[11] D. M. Milder, ''Role of the admittance operator in rough-surface scattering,'' J. Acoust. Soc. Am. **100**, 759–768 (1996).
[12] D. M. Milder, ''An improved formalism for electromagnetic scattering from a perfectly conducting rough surface'' Radio Sci. **31**, 1369–1376 (1996).
[13] S. Piccolo, M. C. Recchioni, and F. Zirilli, ''The time harmonic electromagnetic field in a disturbed half-space: An existence theorem and a computational method,'' J. Math. Phys. **37**, 2762–2786 (1996).
[14] R. A. Smith, ''The operator expansion formalism for electromagnetic scattering from rough dielectric surfaces,'' Radio Sci. **31**, 1377–1385 (1996).
[15] L. Fatone, C. Pignotti, M. C. Recchioni, and F. Zirilli, ''Time harmonic electromagnetic scattering from a bounded obstacle: An existence theorem and a computational method,'' J. Math. Phys. **40**, 4859–4887 (1999).
[16] O. P. Bruno and F. Reitich, ''Boundary-variation solutions for bounded-obstacle scattering problems in three dimensions,'' J. Acoust. Soc. Am. **104**, 2579–2583 (1998).
[17] M. Abramowitz and I. A. Stegun, *Handbook of Mathematical Functions* (Dover, New York, 1970).

Edge diffraction of creeping rays

S. J. Chapman,[a] J. R. Ockendon, and V. H. Saward[b]
OCIAM, Mathematical Institute, 24-29 St. Giles, Oxford OX1 3LB, United Kingdom

(Received 3 June 1999; revised 19 January 2000; accepted 20 January 2000)

Explicit formulas are derived for waves modeled by the scalar two-dimensional Helmholtz equation for the field that is diffracted when surface creeping rays encounter an infinitely sharp edge. Both Neumann and Dirichlet boundary conditions are analyzed, and the diffracted field is found to be an order to magnitude smaller in the latter case. © *2000 Acoustical Society of America.*
[S0001-4966(00)04504-5]

PACS numbers: 43.20.Bi, 43.20.Dk, 43.20.El [ANN]

INTRODUCTION

Creeping rays are real rays that exist in the shadow region of a finite scatterer that is illuminated by waves of sufficiently short wavelength. These rays describe the lowest order field in the shadow, which, for smooth scatterers, is exponentially small compared to the incident field. They are initiated at the scatterer horizon, where the incident rays are tangential, and they propagate repeatedly around the scatterer, progressively radiating diffracted rays tangentially to the surface, thus contributing to the scattered field in all directions. The energy lost by radiating these rays explains the exponential attenuation of the creeping field as it propagates into the shadow zone.

However, corners or edges in the shadow region may enhance the scattered field produced by the creeping rays, and this can be important in radar technology. This paper aims to describe a simple case of edge diffraction of a two-dimensional creeping ray field described by the dimensionless Helmholtz equation

$$\nabla^2\psi + k^2\psi = 0, \quad k \gg 1, \tag{1}$$

with

$$\psi \sim e^{ikx} \quad \text{as} \quad x \to -\infty, \tag{2}$$

together with a radiation condition and either

$$\frac{\partial\psi}{\partial n} = 0 \quad \text{or} \quad \psi = 0 \tag{3}$$

on the scatterer.

The geometry may be as shown in Fig. 1, which indicates the boundary layer structure that gives rise to the creeping ray field at the horizon H, where the scatterer is assumed to be analytic. We will not consider here the field generated at the lower tangency point.

Note that the scatterer forms a caustic for the radiating creeping rays and hence, for clarity, we refer to these rays as ''shed creeping rays'' when we are not close to the boundary and as ''the surface creeping field'' when we are in the caustic region, whose transverse dimension is $k^{-2/3}$. As usual in caustic regions, the amplitude in the surface creeping field is a factor of $k^{1/6}$ larger than in the shed creeping ray region (following a particular ray) due to the focusing effect, but this factor is dwarfed by the exponential decay of the creeping field as it propagates around the boundary.

Fortunately the mechanics of the initiation of the shed and surface creeping rays at the so-called ''Fock–Leontovič'' region near H need not concern us here, but they can be found, for example, in Refs. 1–4. However, in order to set up our diffraction problem near E, we do need to know the details of the surface creeping field solution.

The relevant boundary layer analysis is complicated, and can be found in Refs. 4–8. The key idea is to use the ansatz

$$\psi \sim e^{iks + ik^{1/3}v(s)} \sum_{j=0}^{\infty} \frac{A_j(s,n)}{k^{j/3}} \tag{4}$$

in a region in which s, the distance along the scatterer from H, is $O(1)$ as $k \to \infty$, but n, the distance normal to the scatterer, is $O(k^{-2/3})$, where the phase-function $v(s)$ is to be determined along with the amplitude coefficients A_j. The leading-order terms give that

$$\frac{\partial^2 A_0}{\partial\hat{n}^2} - 2\frac{dv}{ds}A_0 + 2\hat{n}\kappa(s)A_0 = 0, \tag{5}$$

$$\frac{\partial^2 A_1}{\partial\hat{n}^2} - 2\frac{dv}{ds}A_1 + 2\hat{n}\kappa(s)A_1 = -2i\frac{\partial A_0}{\partial s}, \tag{6}$$

where κ is the curvature, which we assume is positive, as in Fig. 1 from H to E, and $n = k^{-2/3}\hat{n}$. The solution for A_0 that is outgoing as $\hat{n} \to \infty$ is

$$A_0 = \alpha_m(s)\mathrm{Ai}\left(-2^{1/3}e^{2i\pi/3}\kappa^{-2/3}\left(\hat{n}\kappa - \frac{dv}{ds}\right)\right), \tag{7}$$

and we first apply the Neumann condition $\partial\psi/\partial\hat{n} = 0$ on $\hat{n} = 0$, which implies that

$$v = v_m(s) = \xi_m e^{-2i\pi/3}2^{-1/3}\int_0^s \kappa(s')^{2/3}\,ds', \tag{8}$$

and ξ_m is the mth zero of $\mathrm{Ai}'(z)$. The amplitude α_m can be found from the solvability condition for A_1, which, after some algebra, reduces to

$$\frac{d\alpha_m}{ds} = \frac{\alpha_m}{6\kappa}\frac{d\kappa}{ds}, \tag{9}$$

[a]Electronic mail: chapman@maths.ox.ac.uk
[b]Current address: Smith Group Limited, Surrey Research Park, Guildford, Surrey GU2 5YP, United Kingdom.

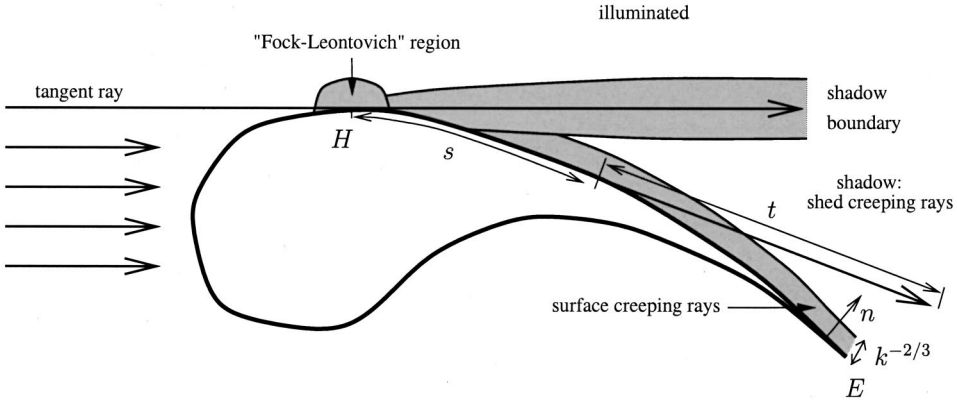

FIG. 1. Edge diffraction of creeping rays.

giving

$$\alpha_m = \alpha_{m0}\kappa(s)^{1/6}, \tag{10}$$

where α_{m0} is constant. Hence the surface creeping field solution is the superposition

$$\psi = e^{iks}\sum_{m=0}^{\infty} \alpha_{m0}\kappa(s)^{1/6}\,\mathrm{Ai}(\xi_m - 2^{1/3}e^{2i\pi/3}\kappa(s)^{1/3}\hat{n}) \times \exp\left(ik^{1/3}\xi_m e^{-2i\pi/3}2^{-1/3}\int_0^s \kappa(s')^{2/3}\,ds' \right), \tag{11}$$

where α_{m0} are determined by matching to the solution near H as described in Ref. 4. Note that because $\kappa > 0$ each term in the sum is exponentially smaller than its predecessor outside the Fock–Leontovič region near H (i.e., for $s \gg k^{-1/3}$). (Indeed, as discussed in Ref. 4, if we work to exponential accuracy and take account of Stokes phenomenon, we may find that α_{m0} may exhibit sudden rapid changes across Stokes lines.) Hence, for the purposes of this paper, we retain only the first term α_{00}.

A similar scenario applies with Dirichlet data $\psi = 0$ on $n = 0$. Equation (11) is replaced by

$$\psi = e^{iks}\sum_{m=0}^{\infty} \beta_{m0}\kappa(s)^{1/6}\,\mathrm{Ai}(-2^{1/3}e^{2i\pi/3}\kappa(s)^{1/3}\hat{n} + \eta_m) \times \exp\left(ik^{1/3}\eta_m e^{-2i\pi/3}2^{-1/3}\int_0^s \kappa(s')^{2/3}\,ds' \right), \tag{12}$$

where η_m is a zero of $\mathrm{Ai}(z)$ and the β_{m0} may also be determined by matching with the Fock–Leontovich region, subject to the same proviso about Stokes phenomenon.

Either Eqs. (11) or (12) will give rise to shed creeping rays that are described by superpositions of terms

$$\psi \sim \frac{e^{ik(s+t)}}{\sqrt{t}k^{1/6}\kappa(s)^{1/6}}\exp\left(ik^{1/3}\zeta_m e^{-2i\pi/3}2^{-1/3}\int_0^s \kappa(s')^{2/3}\,ds' \right), \tag{13}$$

where s is the position on the boundary from which the ray is shed, t is distance along the shed ray, and ζ_m is ξ_m or η_m, respectively. Because the amplitude decays only algebraically along these shed creeping rays, they will always be exponentially dominant over the field diffracted from E, which is where s takes its maximum value. Nevertheless, this diffracted field is of interest because of its possible importance on the ''underside'' of the scatterer, and because of the field that it transmits back along the body to H.

Clearly the edge diffracted field will be smaller in the case of Dirichlet data than it is with Neumann data, and we begin with the latter case, which is much the easier mathematically.

I. EDGE DIFFRACTION OF CREEPING RAYS

A. Neumann boundary data

If the end of the plate is given by $s = S$ then we need to rescale near the edge by writing

$$s = S + k^{-1}\overline{s}, \tag{14}$$

$$n = k^{-1}\overline{n}, \tag{15}$$

where n is still the unscaled coordinate normal to the plate (extended by a straight line tangent to it at the edge). An enlarged diagram of the tip region of the plate is shown in Fig. 2. We may expand the field in the surface creeping layer in terms of these inner coordinates to obtain that the leading-order incoming field is

$$\psi \sim C_N e^{i\overline{s}}, \tag{16}$$

where

$$C_N = \alpha_{00}\kappa_S^{1/6}\,\mathrm{Ai}(\xi_0) \times \exp\left(ikS + ik^{1/3}\xi_0 2^{-1/3}e^{-2i\pi/3}\int_0^S \kappa(s')^{2/3}\,ds' \right). \tag{17}$$

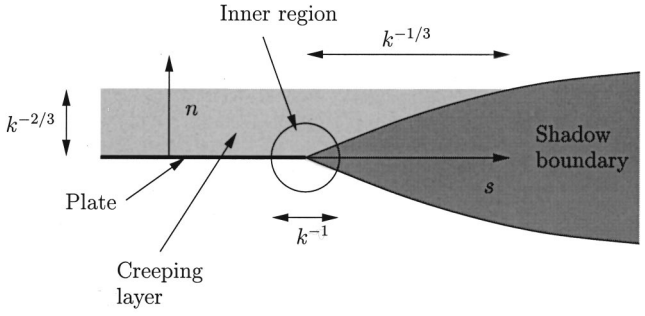

FIG. 2. An enlarged diagram of the tip region, showing the creeping ray layer, the inner region, and the shadow boundary region produced when the creeping rays are diffracted from the tip.

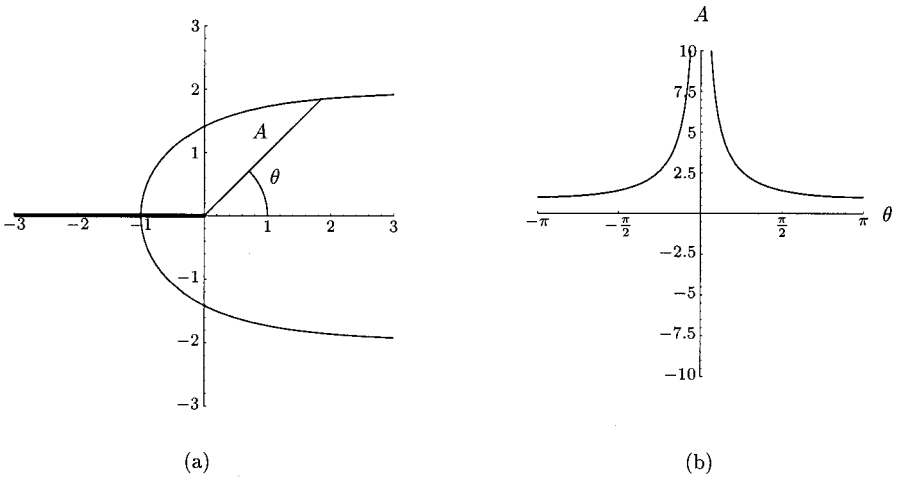

FIG. 3. The directivity of the diffracted field for Neumann boundary data. (a) The amplitude in any direction corresponds to the distance from the origin to the curve. (b) The amplitude plotted as a function of θ.

Hence the inner problem in the vicinity of the edge is

$$\frac{\partial^2\psi}{\partial\bar{s}^2}+\frac{\partial^2\psi}{\partial\bar{n}^2}+\psi=0, \tag{18}$$

$$\frac{\partial\psi}{\partial\bar{n}}=0, \quad \bar{n}=0, \quad \bar{s}<0, \tag{19}$$

$$\psi\sim C_N e^{i\bar{s}}, \text{ as } \bar{n}^2+\bar{s}^2\to\infty, \text{ for } \bar{n}>0. \tag{20}$$

This inner problem is just the Sommerfeld problem[9] with the incident field parallel to the plate, with solution

$$\psi=\frac{C_N e^{-i\pi/4+i\bar{r}}}{\sqrt{\pi}}\mathrm{Fr}\left(-\sqrt{2\bar{r}}\sin\frac{\bar{\theta}}{2}\right), \tag{21}$$

where $\mathrm{Fr}(z)$ is the Fresnel integral

$$\mathrm{Fr}(z)=e^{-iz^2}\int_z^\infty e^{iu^2}\,du\,,$$

and $\bar{r}$ and $\bar{\theta}$ are local polar coordinates with the $\bar{\theta}=0$ axis parallel to the scatterer. For $\bar{\theta}\gg\bar{r}^{-1/2}$, the far-field behavior of this inner solution is given by

$$\psi\sim C_N e^{i\bar{r}\cos\bar{\theta}}+C_N\frac{e^{i\bar{r}-3i\pi/4}}{2\sqrt{2\pi\bar{r}}\sin\bar{\theta}/2}, \quad 0<\bar{\theta}<\pi, \tag{22}$$

$$\psi\sim C_N\frac{e^{i\bar{r}-3i\pi/4}}{2\sqrt{2\pi\bar{r}}\sin\bar{\theta}/2}, \quad -\pi<\bar{\theta}<0. \tag{23}$$

Therefore the amplitude of the diffracted field at the tip is given by

$$A=C_N\frac{e^{-3i\pi/4}}{2\sqrt{2\pi kr}\sin\theta/2}, \tag{24}$$

where $r=\bar{r}/k$ and $\theta=\bar{\theta}$ are unscaled polar coordinates centred on the tip. There is a boundary layer of thickness $k^{-1/2}$ near $\theta=0$ (the shadow boundary), whose structure is discussed in Sec. III. The amplitude directivity pattern is shown in Fig. 3.

B. Dirichlet boundary data

Now the leading-order incoming field is given by

$$\psi\sim C_D\bar{n}e^{i\bar{s}}, \tag{25}$$

where

$$C_D=-k^{-1/3}2^{1/3}e^{2i\pi/3}\beta_{00}\kappa_S^{1/2}\,\mathrm{Ai}'(\eta_0)\times\exp\left(ikS+ik^{1/3}\eta_0 2^{-1/3}e^{-2i\pi/3}\int_0^S\kappa(s')^{2/3}\,ds'\right). \tag{26}$$

The inner problem is

$$\frac{\partial^2\psi}{\partial\bar{s}^2}+\frac{\partial^2\psi}{\partial\bar{n}^2}+\psi=0, \tag{27}$$

$$\psi=0, \quad \bar{n}=0, \quad \bar{s}<0, \tag{28}$$

$$\psi\sim C_D\bar{n}e^{i\bar{s}}, \text{ as } \bar{n}^2+\bar{s}^2\to\infty \text{ for } \bar{n}>0, \tag{29}$$

and the presence of the amplitude $\bar{n}$ in Eq. (29) means that we cannot apply the Sommerfeld solution directly. If we make the substitution $\Phi=\partial\psi/\partial\bar{n}$, then Φ satisfies Helmholtz equation with the far-field matching condition $\Phi\sim C_D e^{i\bar{s}}$ as $\bar{s}\to-\infty$. In addition the boundary data on the plate implies that $\partial^2\psi/\partial\bar{s}^2=0$ on $\bar{n}=0,\bar{s}<0$, and therefore $\partial\Phi/\partial\bar{n}=0$ on the plate. Hence Φ satisfies the problem Eqs. (18)–(20), so that

$$\Phi=\frac{C_D e^{-i\pi/4+i\bar{r}}}{\sqrt{\pi}}\mathrm{Fr}\left(-\sqrt{2\bar{r}}\sin\frac{\bar{\theta}}{2}\right). \tag{30}$$

Hence the solution to the inner problem Eqs. (27)–(29) has the form

$$\psi=\int_0^{\bar{n}}\Phi(\bar{s},\nu)\,d\nu+B(\bar{s}), \tag{31}$$

where $B(\bar{s})$ is zero for $\bar{s}<0$. By substituting the expression for the Fresnel integral into Eq. (31) the solution may be written as

$$\psi=\int_0^{\bar{n}}\int_{((\bar{s}^2+\nu^2)^{1/2}-\bar{s})^{1/2}}^\infty e^{i\bar{s}}e^{iu^2}\,du\,d\nu+B(\bar{s}). \tag{32}$$

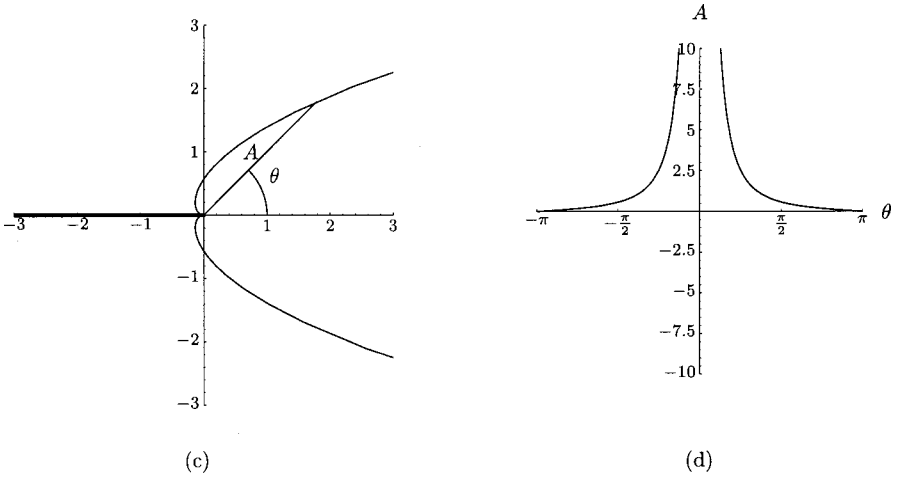

FIG. 4. The directivity of the diffracted field for Dirichlet boundary data. (a) The amplitude in any direction corresponds to the distance from the origin to the curve. (b) The amplitude plotted as a function of θ. The amplitude has been scaled with 0.2 as a representative value of $k^{-1/3}$, to aid in comparisons with Fig. 3.

This solution may then be simplified further by making the substitution $\lambda^2=\bar{s}^2+\nu^2$ and interchanging the order of integration. After some manipulation this yields that for $\bar{s}<0$ the field is given by

$$\psi=\frac{C_D e^{-i\pi/4}}{\sqrt{\pi}}\left(\bar{n}e^{i\bar{r}}\,\mathrm{Fr}\left(-\sqrt{2\bar{r}}\sin\frac{\bar{\theta}}{2}\right)+\frac{ie^{i\bar{r}}\sqrt{\bar{r}}}{\sqrt{2}}\cos\frac{\bar{\theta}}{2}+\frac{ie^{i\bar{r}}}{2}\mathrm{Fr}\left(\sqrt{2\bar{r}}\cos\frac{\bar{\theta}}{2}\right)-\frac{e^{-i\bar{s}}e^{3i\pi/4}\sqrt{\pi}}{4}\right), \tag{33}$$

while for $\bar{s}>0$ the field is given by

$$\psi=\frac{C_D e^{-i\pi/4}}{\sqrt{\pi}}\left(\bar{n}e^{i\bar{r}}\,\mathrm{Fr}\left(-\sqrt{2\bar{r}}\sin\frac{\bar{\theta}}{2}\right)+\frac{ie^{i\bar{r}}\sqrt{\bar{r}}}{\sqrt{2}}\cos\frac{\bar{\theta}}{2}+\frac{ie^{i\bar{r}}}{2}\mathrm{Fr}\left(\sqrt{2\bar{r}}\cos\frac{\bar{\theta}}{2}\right)-\frac{ie^{i\bar{s}}\sqrt{\bar{s}}}{\sqrt{2}}-\frac{ie^{i\bar{s}}}{2}\mathrm{Fr}(\sqrt{2\bar{s}})\right)+B(\bar{s}). \tag{34}$$

The solution for $\bar{s}>0$ differs from the solution for $\bar{s}<0$ only by an arbitrary function of $\bar{s}$. Since ψ is analytic in $\bar{r}>0$, and Eq. (33) is an analytic expression for the field in $\bar{s}<0$, we must have

$$B(\bar{s})=\frac{C_D e^{-i\pi/4}}{2\sqrt{\pi}}\left(i\sqrt{2\bar{s}}e^{i\bar{s}}+i\,\mathrm{Fr}(\sqrt{2\bar{s}})e^{i\bar{s}}-\frac{e^{-i\bar{s}}e^{3i\pi/4}\sqrt{\pi}}{4}\right), \tag{35}$$

for $\bar{s}>0$. However, the solution Eq. (33) does not satisfy the radiation condition for $s>0$, since the last term represents an incoming wave. Thus we must subtract off the solution corresponding to this incoming wave, giving finally

$$\psi=\frac{C_D e^{-i\pi/4}}{\sqrt{\pi}}\left(\bar{n}e^{i\bar{r}}\,\mathrm{Fr}\left(-\sqrt{2\bar{r}}\sin\frac{\bar{\theta}}{2}\right)+\frac{ie^{i\bar{r}}\sqrt{\bar{r}}}{\sqrt{2}}\cos\frac{\bar{\theta}}{2}\right),\quad -\infty<s<\infty. \tag{36}$$

For $\bar{\theta}\gg\bar{r}^{-1/2}$ the far-field behavior is given by

$$\psi\sim C_D\bar{n}^{\bar{t}s}+\frac{C_D e^{3i\pi/4}}{\sqrt{\pi}}\frac{e^{i\bar{r}}\sin\bar{\theta}}{8\sqrt{2\bar{r}}\sin^3\bar{\theta}/2},\quad 0<\bar{\theta}<\pi, \tag{37}$$

$$\psi\sim\frac{C_D e^{3i\pi/4}}{\sqrt{\pi}}\frac{e^{i\bar{r}}\sin\bar{\theta}}{8\sqrt{2\bar{r}}\sin^2\bar{\theta}/2},\quad -\pi<\bar{\theta}<0. \tag{38}$$

Note that the term of order $\bar{r}^{\frac{1}{2}/2}$ in the far-field expansion of Eq. (36) has zero coefficient. The amplitude of the diffracted field is given by

$$A=\frac{C_D e^{3i\pi/4}}{\sqrt{\pi}}\frac{\sin\theta}{8(2kr)^{1/2}\sin^3\theta/2}; \tag{39}$$

its directivity is shown in Fig. 4. As in Sec. II A there is a boundary layer of thickness $k^{-1/2}$ near $\theta=0$, which we discuss in Sec. III. Note that $C_D=O(k^{-1/3}C_N)$, so that the amplitude of the diffracted field is $O(k^{-1/3})$ smaller with Dirichlet data than with Neumann data.

II. DISCUSSION

The directivity patterns in Figs. 3, 4 indicate the expected nonuniformity at the ''shadow boundaries'' near the tangent to the scatterer at E. In general, in the far field of the inner region with $s=k^m\tilde{s}$, where $-1<m\leqslant 0$, scaling in the shadow boundary is $n=k^{(m-1)/2}\tilde{n}$, corresponding to θ of order $k^{-(m+1)/2}$. With Neumann boundary data the shadow boundary transition function is the usual one, namely

$$\psi\sim\frac{C_N e^{-i\pi/4}e^{iks}e^{i\tilde{n}^2/(2\tilde{s})}}{\sqrt{\pi}}\mathrm{Fr}\left(-\frac{\tilde{n}}{\sqrt{2\tilde{s}}}\right). \tag{40}$$

With Dirichlet boundary data, because the incoming field is not a simple plane wave, the transition function changes to

$$\psi\sim\frac{k^{(m-1)/2}C_D e^{-i\pi/4}e^{iks}e^{i\tilde{n}^2/(2\tilde{s})}}{\sqrt{\pi}}\left(\tilde{n}\,\mathrm{Fr}\left(-\frac{\tilde{n}}{\sqrt{2\tilde{s}}}\right)+\frac{i\sqrt{\tilde{s}}}{\sqrt{2}}\right). \tag{41}$$

Note that the transverse scaling of the shadow boundary is such that it lies within the surface creeping layer, so that the approximation of the incoming field as either constant or linear in $\bar{n}$ is valid, only for $(m-1)/2 < -2/3$, i.e., for $m < -1/3$. At this scale in s the shadow boundary starts to notice that the field on the ''illuminated'' side is not simply a plane wave. The full structure of the surface creeping field becomes relevant, but we will not discuss this further here.

We also remark that the diffracted field sends a ray back along the upper surface of the body, which will generate creeping rays propagating in an anticlockwise direction from E as described in Refs. 1, 10, 11.

Finally we remark that we expect similar diffraction patterns when the ''trailing edge'' at E has nonzero included angle and when the body is modeled by a mixed boundary condition $\partial\psi/\partial n + \alpha\psi = 0$.

ACKNOWLEDGMENTS

The authors would like to thank the referees for their valuable comments and to acknowledge the stimulation we received from discussions with Dr. C. Sillence.

[1] V. A. Fock, *Electromagnetic Diffraction and Propagation Problems* (Pergamon, New York, 1965).
[2] J. B. Keller, ''Diffraction by a convex cylinder,'' in *URSI Michigan Electromagnetic Wave Theory Symposium*, pp. 312–321 (1955).
[3] M. Leontovič and V. A. Fock, ''Solution of the problem of the proagation of electromagnetic waves along the Earth's surface by the method of the parabolic equation,'' J. Phys. (Moscow) **10**, 13–24 (1946).
[4] R. H. Tew, S. J. Chapman, J. R. King, J. R. Ockendon, B. J. Smith, and I. Zafarullah, ''Scalar wave diffraction by tangent rays,'' Wave Motion (to be published).
[5] V. M. Babič and V. S. Buldyrev, *Short-Wavelength Diffraction Theory—Asymptotic Methods*, Vol. 4 of *Springer Series on Wave Phenomena* (Springer-Verlag, New York, 1991).
[6] J. B. Keller and R. M. Lewis, *Asymptotic Methods for Partial Differential Equations: The Reduced Wave Equation and Maxwell's Equations*, of *Surveys in Applied Mathematics* (Plenum, New York, 1995), Vol. 1, pp. 1–82.
[7] B. R. Levy and J. B. Keller, ''Diffraction by a smooth object,'' Commun. Pure Appl. Math. **12**, 159–209 (1959).
[8] E. Zauderer, ''Wave propagation around a convex cylinder,'' J. Math. Mech. **13**, 171–186 (1964).
[9] D. S. Jones, *The Theory of Electromagnetism* (Pergamon, New York, 1964), p. 470.
[10] S. J. Chapman and V. H. Saward, ''Generation of creeping rays by acoustic sources on boundaries'' (unpublished).
[11] V. H. Saward, ''Some Problems in Diffraction,'' Ph.D. thesis, University of Oxford, 1997.

Enhancement and inhibition of acoustic radiation in spherical cavities

Zhen Ye
Department of Physics and Center for Complex Systems, National Central University, Chung-li, Taiwan, Republic of China

(Received 15 October 1997; accepted for publication 2 December 1999)

Acoustic radiation from a source located inside layered cavities is studied using the transfer matrix method. It is shown that the radiation can be either enhanced or inhibited, depending on the characteristics and the material composition of the cavities. The analysis predicts well-defined spectral peaks and nodes in some cavities. It is found that significant enhancement and inhibition are possible by varying acoustic parameters. The results also show that the strength of the radiating source can be significantly modified due to the presence of layered structures. The link to the similar phenomena in the optical cavities is discussed. © *2000 Acoustical Society of America.* [S0001-4966(00)02103-2]

PACS numbers: 43.20.Fn [DEC]

INTRODUCTION

When an electromagnetic source is placed in a cavity, its radiation will be modulated. It has long been known that the radiative decay of excited atoms through spontaneous emission can be modified significantly by the atoms' interaction with the surrounding environment.[1,2] The coupling of the source radiation to the cavity has profound effects on the radiated strength, damping rate and frequency shift.

During the last few years, much interest has been revived in the cavity electrodynamics. Many studies have been focused on the effects of metal and dielectric interfaces, forming a certain type of waveguide, on atomic radiation.[3–7] As summarized by Haroche and Kleppner,[8] the experiments have shown that spontaneous radiation from excited atoms can be greatly suppressed or enhanced by placing the atoms between mirrors or in cavities, depending on the characteristics of the atom and the cavity, which may be constructed in planar, cylindrical or spherical forms. It has been pointed out that the investigation has potential applications to waveguide devices, such as surface-emitting semiconductor laser resonators, quantum well lasers and amplifiers.[2] In addition, cavity wave studies also provide a useful bridge between microscopic and macroscopic physics.[8]

A question may naturally arise, that is, whether such radiation enhancement or inhibition phenomena can be observed in acoustic systems. Moreover, if similar phenomena do exist, what features would be expected? In this communication, we pursue these problems. As a first step, we consider a unit acoustic point source in spherical cavities which are situated in water. The cavities are allowed to be coated with spherically layered structures, in the same way as in the optical cavities. The present paper provides a systematic approach to compute the acoustic transmission and reflection in the cavities. The results will show that in certain situations, the radiation and reflection can be either greatly enhanced or suppressed, depending on the composition of individual cavities. In these situations, the cavities act as a filter which selects particular frequencies for emission. The problems considered here also draw some similarities to that of the acoustic waves in a duct or room and in musical pipes.[9,10]

I. THE FORMULATION OF THE PROBLEM

In general, consider a unit point source located inside a layered cavity. For simplicity, the cavity is assumed spherical and the source is put at the center. We would like to point out, however, that other shapes of cavities can also be studied in the same manner. A conceptual layout of the system is given in Fig. 1. The most inner and outer radii of the cavity are denoted as R_1 and R_N. Between R_1 and R_N there are $N-1$ interfaces. The boundary at R_i $(i=1,2,...,N)$ is denoted as the ith interface. The sound speed and the mass density inside the cavity, i.e., located insider the sphere of radius R_1, are c_1 and ρ_1, while the sound speed and mass density of the surrounding medium, i.e., outside the sphere of radius R_N, are denoted by c and ρ, respectively. The sound speed and mass density between the ith and the $(i+1)$-th interfaces are c_{i+1}, ρ_{i+1}. We define $g_i=\rho_i/\rho$ and $h_i=c_i/c$. The parameters g_i and h_i are called acoustic contrast parameters representing the contrast in mass density and sound speed between two materials. The case with g_i and h_i greater than 1 may represent the situation of a hard cavity in liquids and the case with g_i and h_i less than the unity may refer to the situation of a soft cavity in hard media.

The Helmholtz wave equation inside the cavity can be written as

$$(\nabla^2+k_1^2)p(\vec{r})=-4\pi\delta(\vec{r}), \quad \text{for } |\vec{r}|=r<R_1, \tag{1}$$

where ∇^2 is the Laplacian operator, k_1 is the wave number which equals ω/c_1, and $\delta(\cdot)$ is the Dirac delta function, representing the unit source located at the origin. Here, the acoustic angular frequency is taken as ω. The wave equation outside the cavity is written as

$$(\nabla^2+k^2)p(\vec{r})=0, \quad \text{for } r>R_N, \tag{2}$$

 0001-4966/2000/107(4)/1846/6/$17.00

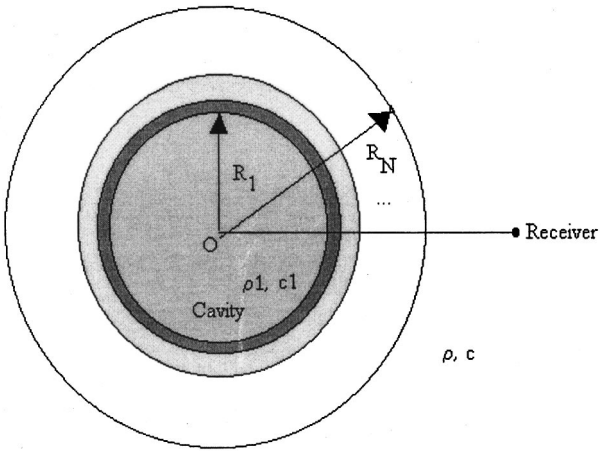

FIG. 1. Conceptual layout of the acoustic radiation from a source inside a spherical cavity.

where k is the wave number in the medium, $k=\omega/c$. Similar wave equations can be written down for the media between R_1 and R_N, e.g.,

$$(\nabla^2+k_i^2)p(\vec{r})=0, \quad \text{for } i=1,2,3,...,N-1, \quad \text{for } R_i<r<R_{i+1}. \tag{3}$$

The wave radiation and reflection coefficients at the interfaces can be calculated by the transfer matrix technique (e.g., Ref. 3). The core of this technique is to relate the coefficients of the outward- and inward-propagating waves at the interfaces. Following Refs. 2, and 3 and considering the spherical symmetry, the general solution to the wave equations (3) may be written as

$$p_i(r)=A_i\frac{e^{ik_ir}}{r}+B_i\frac{e^{-ik_ir}}{r}, \quad \text{for } R_i<r<R_{i+1} \quad (i=1,2,3,...,N). \tag{4}$$

The first and second terms refer to the outward- and inward-going waves, and A's and B's refer to the transmission (radiation) and reflection coefficients. The waves in $r<R_1$ and $r>R_N$ regions will be discussed later.

Before going any further, we consider an arbitrary spherical interface located at distance R from the origin. The interface separates two media with different sound speeds and mass densities. Suppose that the outgoing wave and incoming wave on the inner side of the interface, i.e., R^-, is

$$P_<(r)=A_<\frac{e^{ik_<r}}{r}+B_<\frac{e^{-ik_<r}}{r}, \tag{5}$$

and the outgoing and incoming wave on the outer side of the interface, i.e., R^+, is

$$P_>(r)=A_>\frac{e^{ik_>r}}{r}+B_>\frac{e^{-ik_>r}}{r}, \tag{6}$$

where $k_{<,>}=\omega/c_{<,>}$ and $A_{<,>}, B_{<,>}$ refer to the outward-going and inward-going coefficients on the inner and outer side of the interface, respectively, also called the transmission and reflection coefficients.

To solve for A's and B's, the usual boundary conditions must be invoked. These conditions state that the field and the displacement must be continuous across the interface. Explicitly, the boundary conditions can be written as

$$p_<(R)=p_>(R), \quad \frac{1}{\rho_<}\frac{\partial p_<}{\partial r}\bigg|_{r=R}=\frac{1}{\rho_>}\frac{\partial p_>}{\partial r}\bigg|_{r=R}. \tag{7}$$

In the above, $c_{<,>}$ and $\rho_{<,>}$ refer to the sound speed and density on the inner and outer side of the interface separately. The boundary equations lead to the relation

$$\begin{pmatrix}A_<\\B_<\end{pmatrix}=T(R)\begin{pmatrix}A_>\\B_>\end{pmatrix}, \tag{8}$$

where $T(R)$ is the 2 by 2 transfer matrix relating the coefficients on the inner side to that on the outer side, and is given by

$$T(R)=\begin{pmatrix} e^{ik_<R} & e^{-ik_<R} \\ \dfrac{e^{ik_<R}}{\rho_<}(ik_<R-1) & \dfrac{-e^{-ik_<R}}{\rho_<}(ik_<R+1)\end{pmatrix}^{-1} \times\begin{pmatrix} e^{ik_>R} & e^{-ik_>R} \\ \dfrac{e^{ik_>R}}{\rho_>}(ik_>R-1) & \dfrac{-e^{-ik_>R}}{\rho_>}(ik_>R+1)\end{pmatrix}. \tag{9}$$

For a system consisting of multiple interfaces, the transmission and reflection coefficients can be related through a consecutive product of the transfer matrix at each interface. The resulting transfer matrix is denoted by **M**. Therefore, the waves outside and inside the layered cavity are related through

$$\begin{pmatrix}A_{\text{in}}\\B_{\text{in}}\end{pmatrix}=\mathbf{M}\begin{pmatrix}A_{\text{out}}\\B_{\text{out}}\end{pmatrix}, \tag{10}$$

where

$$\mathbf{M}=\prod_{i=1}^{N}T(R_1)T(R_2)\cdots T(R_N)=\begin{pmatrix}m_{11}&m_{12}\\m_{21}&m_{22}\end{pmatrix}.$$

We notice that since there is no reflected wave outside the cavity, i.e., beyond R_N, we have

$$B_{\text{out}}=0, \quad \text{for } r>R_N. \tag{11}$$

Therefore, the final radiated field outside the cavity is

$$p_{\text{out}}(r)=A_{\text{out}}\frac{e^{ikr}}{r}, \quad \text{for } r>R_N. \tag{12}$$

Moreover, for $r<R_1$, the total wave can be written as

$$p_{\text{in}}(r)=\frac{e^{ik_1r}}{r}+p_R(r), \quad \text{for } 0<r<R_1, \tag{13}$$

where the first term represents the emitted wave without reflecting boundaries. The second term is the wave arising from reflection at boundaries and can be generally written as

$$p_R(r)=-Q\frac{e^{ik_1r}}{r}+Q\frac{e^{-ik_1r}}{r}, \quad \text{for } 0<r<R_1, \tag{14}$$

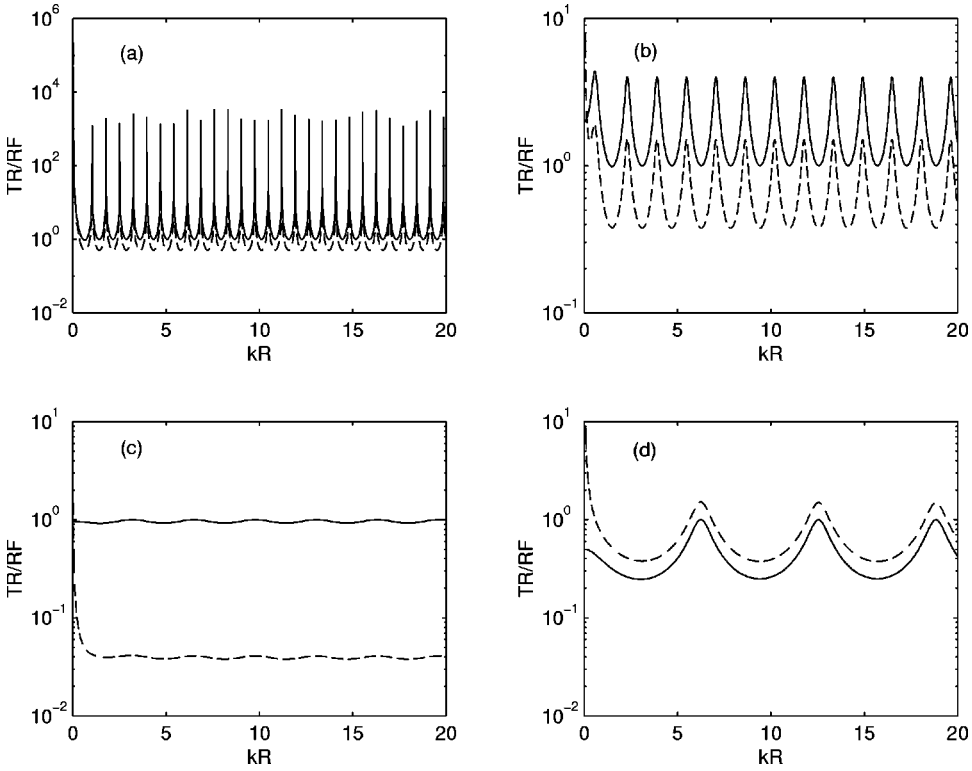

FIG. 2. Transmission and reflection coefficients as a function of kR for the cavity filled with various materials. (a) Air, $g=0.001\,29$, $h=0.23$. (b) Fluid, $g=h=\frac{1}{2}$. (c) Weak fluid: $g=h=1.04$. (d) Fluid: $g=h=2$. The transmission and reflection are represented by the solid and broken lines, respectively.

The reflection coefficient Q is to be determined. This equation is obtained by considering that the reflected wave must be finite at the center. Equation (14) indicates that a standing wave is set up in the cavity. In the presence of the surrounding materials, the wave transmitted from the source is effectively, from Eqs. (13) and (14), $(1-Q)e^{ik_1 r}/r$ and the effective source strength is therefore $1-Q$, which, as will be shown below, can differ significantly from the original source strength of unity.

From Eq. (14) we have

$$A_{\text{in}}=1-Q, \quad B_{\text{in}}=Q. \tag{15}$$

Plugging Eqs. (11) and (15) into Eq. (10), we obtain

$$\begin{pmatrix} 1-Q \\ Q \end{pmatrix}=\begin{pmatrix} m_{11} & m_{12} \\ m_{21} & m_{22} \end{pmatrix}\begin{pmatrix} A_{\text{out}} \\ 0 \end{pmatrix}. \tag{16}$$

This equation leads to solutions

$$Q=\frac{m_{21}}{m_{11}+m_{21}}, \tag{17}$$

$$A_{\text{out}}=\frac{1}{m_{11}+m_{21}}. \tag{18}$$

Consider the special case in which there is only one interface. After certain manipulation, the solutions can be simplified as

$$Q=\frac{M-M'}{(M-N)-(M'-N')}, \tag{19}$$

$$A_{\text{out}}=\frac{MN'-M'N}{(M-N)-(M'-N')}, \tag{20}$$

in which

$$M=e^{ikR/h}-e^{ikR},$$

$$N=e^{-ikR/h}-e^{ikR},$$

$$M'=\frac{1}{g}(e^{ikR/h}-e^{ikR})\left(\frac{ikR/h-1}{ikR-1}\right),$$

$$N'=-\frac{1}{g}(e^{-ikR/h}-e^{ikR})\left(\frac{ikR/h+1}{ikR-1}\right),$$

with $g=\rho_1/\rho$ and $h=c_1/c$.

From these solutions, the radiated acoustic intensity I_{out} can be related to the radiated field as

$$I_{\text{out}}(r)=\frac{1}{2\rho c}|p_{\text{out}}|^2=\frac{1}{2\rho c}\frac{|A_{\text{out}}|^2}{r^2}. \tag{21}$$

The reflected intensity I_R is

$$I_R=\frac{2}{\rho_1 c_1}\frac{|Q|^2}{r^2}. \tag{22}$$

From Eqs. (13) and (14), we know the effective transmitted intensity from the source I_s has now become

$$I_s=\frac{2}{\rho_1 c_1}\frac{|1-Q|^2}{r^2}.$$

The energy conservation states that

$$I_s=I_{\text{out}}+I_R. \tag{23}$$

In the following we will study the wave transmission and reflection strengths. For convenience, we examine the transmission (TR) and reflection (RF) coefficients,

$$\text{TR}=|A_{\text{out}}|, \quad \text{RF}=|Q|. \tag{24}$$

When no reflecting boundaries are present, $A_{out}=1$ and $Q=0$.

II. NUMERICAL ANALYSIS

In this section we inspect the radiated and the reflected acoustic intensity of a unit source in terms of the transmission and reflection coefficients in various cavities.

A. Single interface case

First, for simplicity, we consider the case that the source is located in cavities without coating.

In Fig. 2, we plot the absolute value of the transmission and the reflection coefficients as a function of frequency (measured by kR) for various situations for an air-filled cavity with $g=0.001\,29$ and $h=0.23$, and three fluid cavities with g,h equal to $\frac{1}{2}$, 1.04 and 2, respectively. Note here that the air cavities in water can be either naturally formed air bubbles in an underwater environment or a balloon with an unimportant thin elastic shell. From these figures, we observe the following. (1) The enhancement and inhibition of acoustic radiation appear in acoustic cavities, drawing many similarities to the electrical emission in dielectric cavities, where the emission is modulated by modifying cavity parameters. Overall, under the condition that the acoustic contrast parameters, i.e., $g\ (=\rho_1/\rho)$ and $h\ (=c_1/c)$, deviate away from the unity, there appear sharp frequency bands, as illustrated by the cases in Fig. 2(a) and (b). The node and peak positions are determined by the acoustic contrast parameters. At the peak positions, the radiation is enhanced, while the transmission is inhibited at the nodes. As g and h deviate further away from the unity, the peaks (enhancement) and nodes (inhibition) become more and more pronounced. The separation between the peaks and nodes is well defined and seems to be constant in each cavity. (2) Specifically in the case of air-filled cavity, the ratio between the resonance peak and the node can be as large as the order of magnitude of 4. This indicates that the acoustic radiation at the resonance peaks is greatly enhanced while the emission at the node frequencies is highly suppressed. In the air-filled cavity, the backscattering is also appreciably enhanced at the resonance frequencies and comparable to the transmission. (3) As g and h increase from the values for the air, the resonance peaks decreases, seen by comparing Fig. 2(a) and (b). The oscillatory feature, however, can still be seen. (4) When g and h are only slightly larger than 1 [Fig. 2(c)], corresponding to the weak fluid case, the oscillatory structure almost diminishes. At the low frequencies, the reflection is rather weak, as expected. In this case the transmission coefficient is close to 1, the value when no cavity is present. (5) When g and h are further increased, the oscillatory feature becomes noticeable again. The separation between peaks and nodes increases [Fig. 2(d)].

From the above we conclude that the resonance peaks and the nodes depend on the contrasts g and h. The peak amplitude increases and the separation decreases, as g and h decrease from 1. When g and h increase from 1, the peak-to-node ratio increases and the separation between nodes and peaks increases as well. The node-peak structure may be explained in analogy with the standing wave on a string of length L, where the separation of two adjacent harmonics is calculated as $c/2L$, with c being the sound speed of the string. In the present case the separation between two peaks or two node in terms of the nondimensional kR is almost equal to $c_1/2R$, or equivalently $\Delta kR=(c_1/c)\,\pi=h\pi$. For example, in the air cavity situation, calculation of ΔkR $[=(c_1/c)\,\pi=h\pi]$ gives 0.7226, which is close to the value estimated from Fig. 2(a). From this relation, it is clear that as the radius increases, the separation between peaks or nodes decreases in the frequency domain. Another important feature is that the strength of the source is renormalized to an effective value. In the presence of the interface, the effective strength is $1-Q$. The original energy conservation

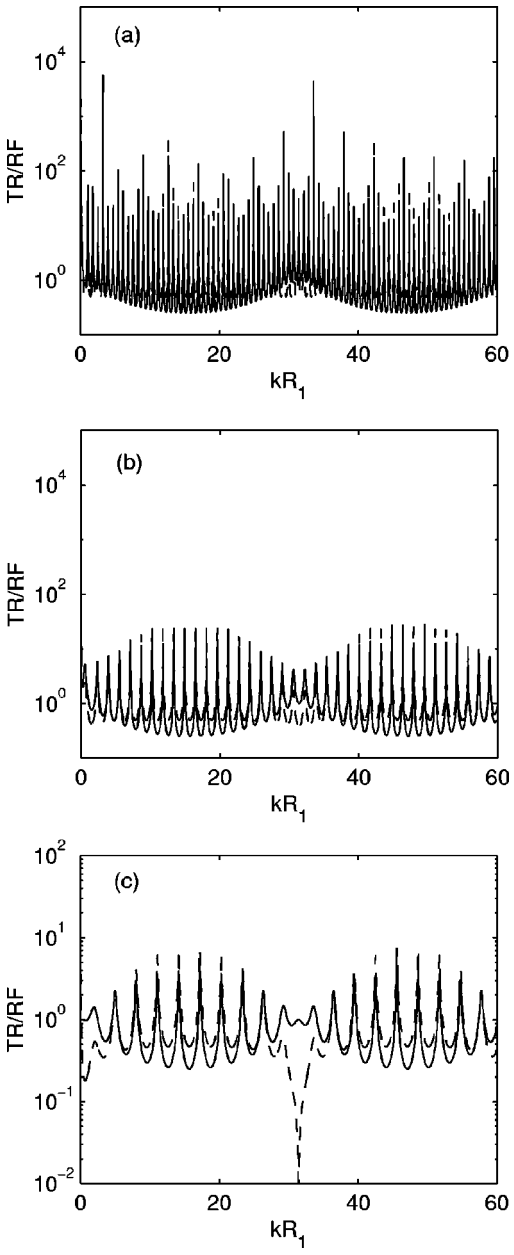

FIG. 3. Transmission and reflection coefficients as a function of kR_1 for the cavity coated with a thick layer. (a) Air cavity, $g=0.001\,29$, $h=0.23$. (b) Fluid cavity, $g=h=\frac{1}{2}$. (c) Water: $g=h=1$. The layer is made up of material with $g_2=h_2=2$. The thickness amounts to $0.2R_1$; R_1 is the cavity radius. The transmission and reflection are represented by the solid and broken lines, respectively.

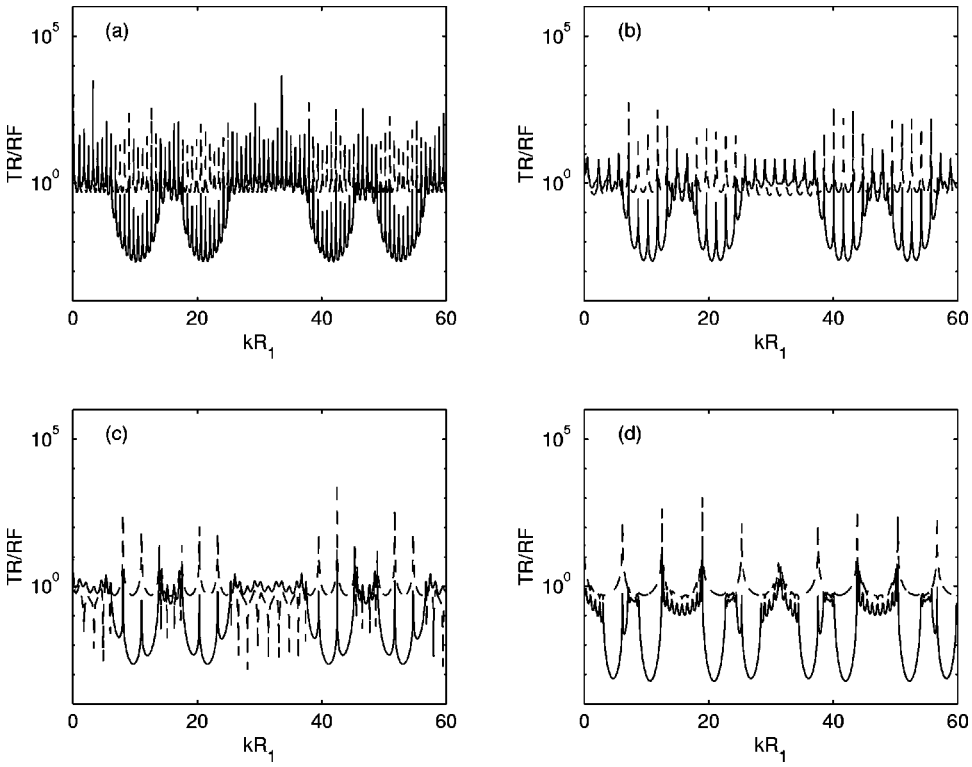

FIG. 4. Transmission and reflection coefficients as a function of kR_1 for the cavity coated with multi-layer. (a) Air cavity, $g_1=0.001\,29$, $h=0.23$. (b) Fluid cavity, $g_1=h_1=\frac{1}{2}$. (c) Water: $g_1=h_1=1$. (d) Fluid cavity: $g_1=h_1=2$ and $g_2=h_2=\frac{1}{2}$. The layer is made up of material with $g_2=h_2=2$ and water, except the case in (d). The structure is stated in the text. The thickness amounts to $0.2R_1$; R_1 is the cavity radius. The transmission and reflection are represented by the solid and broken lines, respectively.

$gh|A_{\text{out}}|^2+|Q|^2=1$ is not valid anymore, as indicated by Fig. 2. Rather, the new energy conservation takes the form

$$|1-Q|^2=|Q|^2+gh|A_{\text{out}}|^2,$$

where the factor gh is the acoustic impedance, in accordance with the definitions in Eqs. (21) and (22).

B. Spherically layered structures

When a cavity is coated with layered structures, its sound transmission and reflection can be modified significantly mainly due to wave interference. For simplicity yet not losing generality, we consider two particular cases: the cavity is coated by one layer of material and by ten equally spaced layers in the water ambient.

First consider the cavities coated with a thin layer of material. In Fig. 3, the transmission and reflection coefficients are plotted against frequency (in terms of kR_1) for several situations. Here R_1 is the radius of the cavity. The thickness of the layer is taken as $0.2R_1$. The layer is assumed to be made of material with g and h values being 2. For the three cases considered, the shell is harder than the cavity, i.e., the mass density and sound speed are greater than that inside the cavity and that of the ambient medium. It shows here that while the pattern follows the typical transmission/reflection spectra shown in Fig. 2, one interesting feature is the appearance of the modulation of the resonance peaks and the nodes. This feature is particularly prominent in the transmission. In addition to the well-defined spectral peaks and nodes, there appears a low-frequency envelope. This is due to the coherence of the multiple reflection in the layer. As the thickness increases, more envelopes are expected to appear. We also notice that there appear several sharp resonance peaks [Fig. 3(a)] and deep nodes [Fig. 3(c)].

Figure 4 plots the transmission and reflection coefficients as a function of kR_1 for ten layers of materials. The layered structure is constructed as follows. The inner portion of the cavity has radius R_1 and is filled with material which has density and sound speed contrasts g_1,h_1, coated by layers in the pattern as M-W-M-W-M-W-M-W-M-W. Here M stands for the coating material with $g_2=h_2=2$, except for the case in (d) in which $g_2=h_2=\frac{1}{2}$, whereas W stands for the ambient medium, e.g., the water. Note that all the g and h values are relative to the ambient medium. The thickness of each layer is identical and taken as $0.2R_1$. The results in Fig. 4 show that when the multiple layers are present, spectral valley regions appear and group in pairs in the transmission. For cases (a) and (b), in which the cavity is filled by air and by a fluid with $g_1=h_1=\frac{1}{2}$, respectively, the multiple layers have relatively insignificant effects on the reflection coefficient. At certain frequencies, the transmission and reflection are enhanced, while at some other frequencies the radiation and reflection are inhibited. Particularly, the transmission at the valleys is significantly reduced. For these two cases, the transmission valleys seem to show up in almost the same range of frequency. The contrast of the resonance peaks between the valley regions and other regions may be used as an efficient signal filter.[2,3] Furthermore, since the contrast between the peak and valley is of more than four orders of magnitude, acoustic cavities may be effectively used in signal devices if the frequency of a source can be modulated at two different frequencies. The present results draw many similarities to that of optical cavities. Therefore, the optical applications may lend a hand to their counterparts in possible acoustic applications. In case (c), where the cavity is filled with water, it shows fewer resonance peaks, but the frequency valleys still appear. In transmission, several resonance peaks are in the valley. Compared to other cases dis-

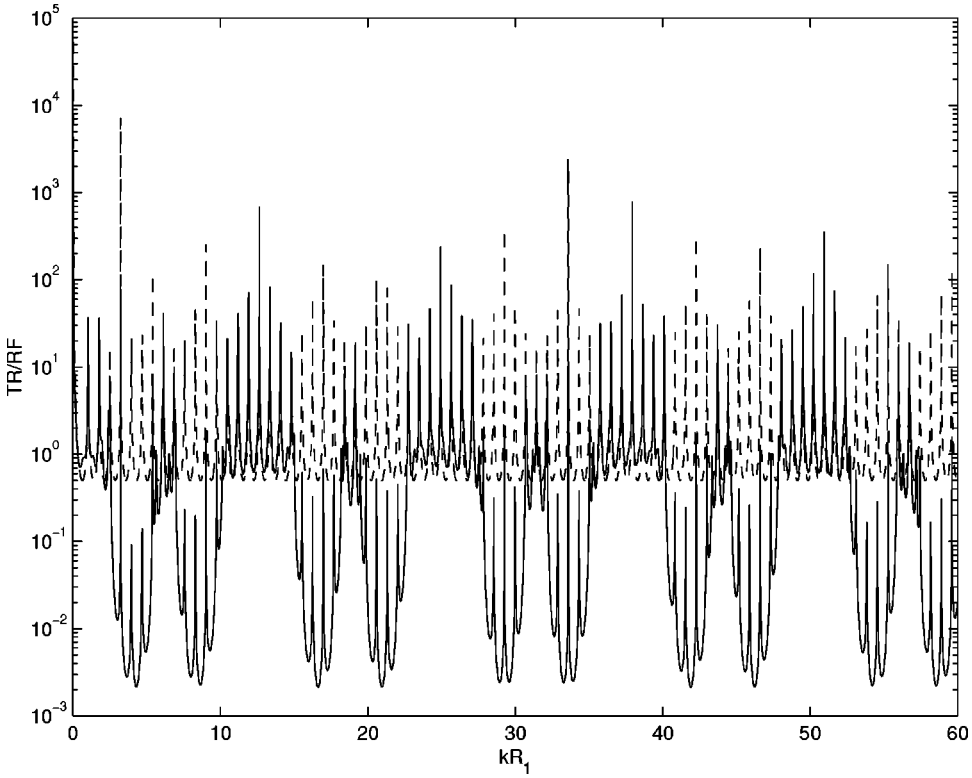

FIG. 5. Transmission and reflection coefficients as a function of kR_1 for the cavity coated with multi-layer. $g_1 = 0.001\,29$, $h_1 = 0.23$. The parameters used here are identical to those in Fig. 4(a) except that the thickness is $0.5R_1$.

cussed above, the reflection is significantly reduced. For case (d), some interesting features show up. In addition to the large valleys, some small valleys appear, e.g., at just before $kR_1 = 20$ and at kR_1 just bigger than 40. In this case, the number of resonance peaks is considerably reduced. Significant transmission is only possible at a few frequencies.

When the thickness of the layers is increased, more spectral valleys appear. Other features remain similar to that in the situation with smaller thickness. These properties are illustrated by Fig. 5. Comparing Fig. 5 to Fig. 4(a), we may conclude that the spectral valleys and the positions of the frequency bands are more sensitive to the thickness of the layers, while the rapid oscillation is more sensitive to the cavity size once the values for g,h are given.

III. CONCLUDING REMARKS

In this paper, we considered acoustic radiation from a source inside various cavities. The results show that the acoustic emission can be significantly affected by the presence of the cavities. Depending on the characteristics and material composition of the cavity, the emission can either be enhanced or inhibited. For the cavities filled with air, resonant transmission is predicted. At the resonance, the emission is greatly enhanced, and well-defined sharp spectral peaks appear. In this situation, the cavity behaves like a filter which allows amplified transmission at certain frequencies. It is also shown that the backscattering can also be modulated by the cavity. Due to the presence of the cavity, the backscattering can be enhanced. Furthermore, the effects of coating the cavities with layers of different materials were also studies. It was found that in the presence of many layers, some spectral valleys appear and at these valleys the transmission is inhibited. Finally, we point out that in this paper we only considered the case in which the source is located at the center of a cavity. When the source is placed away from the center, the problem becomes mathematically more tedious, but it can be solved using the theory developed in, for example, Ref. 3. In this case, anisotropic transmission will be expected. The present work may hint at using acoustic cavities in underwater communications.

ACKNOWLEDGMENTS

Useful discussions with Er-xuan Ping (Micron Technology, Inc., USA), and Alberto Alvarez are greatly appreciated. The useful comments from two anonymous referees were helpful in revising the manuscript. This work received support from the National Science Council through Grant No. NSC 87-2112-M008-008.

[1] E. M. Purcell, Phys. Rev. **69**, 681 (1946).
[2] T. Erdogan, K. G. Sullivan, and D. G. Hall, J. Opt. Soc. Am. B **10**, 391 (1993).
[3] Z. Ye and E. Ping, Solid State Commun. **100**, 351 (1996); C.-C. Wang and Z. Ye, Phys. Status Solidi A **174**, 527 (1999).
[4] D. Kleppner, Phys. Rev. Lett. **47**, 233 (1981).
[5] R. G. Hulet, E. S. Hilfer, and D. Kleppner, Phys. Rev. Lett. **55**, 2137 (1985).
[6] M. Toda, IEEE J. Quantum Electron. **26**, 473 (1990).
[7] T. Erdogan and D. G. Hall, J. Appl. Phys. **68**, 1435 (1990).
[8] S. Horache and D. Kleppner, Phys. Today **42**(1), 24–30 (1989).
[9] P. M. Morse and K. U. Ingard, *Theoretical Acoustics* (Princeton U.P., Princeton, 1986).
[10] L. E. Kinsler, A. R. Frey, A. B. Coppens, and J. V. Sanders, *Fundamentals of Acoustics* (Wiley, New York, 1982).

In-plane elastic property characterization in composite plates

O. I. Lobkis,[a] D. E. Chimenti, and Han Zhang
Center for Nondestructive Evaluation and Aerospace Engineering and Engineering Mechanics Department, Iowa State University, Ames, Iowa 50011-3020

(Received 2 June 1999; revised 11 October 1999; accepted 14 December 1999)

This article presents a method to deduce the in-plane elastic properties of multilayered composite plates. Drawing on a synthetic-aperture technique developed for the elucidation of materials properties in air-coupled ultrasonics, this new method exploits the high elastic anisotropy of composite materials to permit an accurate measurement of directional in-plane stiffness. It is found that comparisons of experimental measurements with plate stiffnesses calculated on the basis of lamination theory agree to within several percent for uniaxial and biaxial laminates and to within 10 percent for quasi-isotropic laminates. It is further shown that the method is largely insensitive to transducer deployment angle within a range related to the transducer beamwidth. © *2000 Acoustical Society of America.* [S0001-4966(00)05703-9]

PACS numbers: 43.20.Gp, 43.20.Jr, 74.25.Ld [ANN]

INTRODUCTION

In the elastic property characterization of composite laminates with liquid-coupled ultrasound, the stiffnesses that are most easily and accurately measured in conventional single-sided reflection geometries are those of least interest to structural design engineers. Typical elastic wave measurements produce detailed maps of out-of-plane longitudinal stiffnesses, average laminate shear constants, and even mixed stiffnesses, such as C_{13}, C_{23}, etc., although these latter can be difficult to infer accurately.[1–7] (Further background on this topic can be found in recent reviews.)[8,9] This portion of the stiffness matrix is, however, of relatively little interest to most designers of composite structure. Of far greater interest is the longitudinal in-plane stiffness, since this property controls the effect of tensile and compressive forces on the laminate structure. Additionally, the laminate bending stiffness is another useful material property. The purpose of this article is to report experiments and analytical modeling on the measurement of in-plane longitudinal stiffnesses in several directions in composite laminates.

Prior works performed to deduce in-plane elastic behavior in composites and other plate media fall principally into two groups: those exploiting point-source/receiver techniques, whether using physical contact or thermoelastic coupling,[10–17] and those where an extended source and receiver are brought into contact with the plate,[18,19,7,20,21] A smaller, third group includes fluid-coupled measurements designed to retain sensitivity to the very high in-plane stiffness,[22–25] These latter are mostly goniometric methods.

The point-source methods, relying on propagation of rays from transmitter to receiver, generally require a complicated inversion scheme to sort out ray arrivals and reconstruct elastic stiffnesses from inferred group velocities. This procedure is not straightforward, especially in an anisotropic medium, because of the complicated nature of the ray surface and the need for an elastodynamic Green's function for the plate.[26] This same difficulty can arise when the source is extended, although in some of those cases—particularly those involving ''acousto-ultrasonics''—a rigorous analysis of the influence of the extended source/receiver geometry is often absent. Because the lowest-order symmetric plate mode along material symmetry axes in a composite plate has relatively little dispersion at low frequency, a detailed source/receiver analysis is sometimes not essential if only a rough estimate of stiffness is desired. We, too, will exploit this property in the current study. In some of the transducer contact studies, however, very careful analysis is made of the effect of an extended source.[19,27] The third group of measurements consists of fluid-coupled experiments, configured to maintain sensitivity to this elastic property.

Phase-matched experiments performed with fluid coupling are sensitive to those elastic stiffnesses that influence the plate modes to which the incident acoustic beam couples. The difficulty in assessing the in-plane elastic properties in fluid-coupled experiments arises for two reasons: the in-plane stiffness C_{11} influences a relatively small portion of the reflection spectrum (incident angles less than 10°, and because the C_{11}-sensitive region of the lowest-order symmetric Lamb mode S_0 is nearly nondispersive. Ironically, swept frequency measurements cannot easily sample this portion of the S_0 mode because of its weak frequency dependence. Either the frequency must be held constant and the angle swept,[23,24] or a wave number measurement must be performed.[22] The former method relies on a transmission geometry and is suitable only for laboratory measurements on coupons. We adopt the latter approach, which is an extension of our earlier work on air-coupled ultrasonics,[28] where the experimental bandwidth was limited and information was acquired using a synthetic aperture. A preliminary version of this work has appeared elsewhere.[29]

For the special case of highly anisotropic media, such as composite laminates, the S_0 phase velocity at low frequency depends almost exclusively on C_{11}. We designate a generic inplane stiffness as C_{11}, although we clearly mean *any* in-

[a]Present address: Department of Theoretical and Applied Mechanics, University of Illinois, Urbana, IL 61808-2935. Electronic mail: lobkis@uiuc.edu

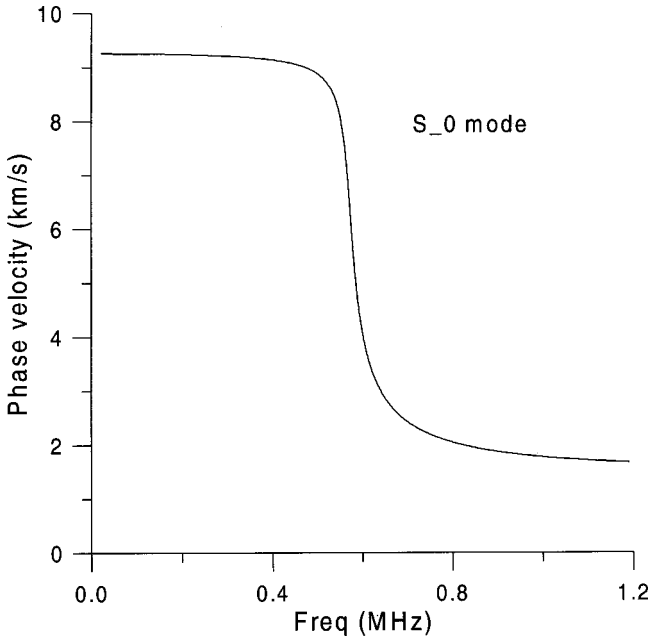

FIG. 1. Dispersion curve for the S_0 Lamb mode of a uniaxial composite laminate showing the nearly dispersionless behavior below $fd \approx 0.5$ mm MHz. In a composite this plateau depends almost exclusively on C_{11}.

plane longitudinal stiffness. The exact lay-up geometry of the laminate under study will determine the effective symmetry of the composite and therefore which of the in-plane stiffnesses are independent and require measurement. The case is illustrated in Fig. 1. Below $fd \approx 0.5$ mm MHz the S_0 wave speed is nearly constant and strongly dependent only on the in-plane stiffness. This fortunate circumstance can be exploited to infer C_{11} from a synthetic aperture liquid-coupled, one-sided reflection measurement.

I. THEORETICAL SUMMARY

For the geometry of the experiment, we assume the laminate lies in the x_1x_2 plane with the origin of coordinates at the center of the plate. The x_3 direction then is normal to the plane of the laminate. In the typical Lamb wave problem, tractions are taken to vanish only at the two free laminate surfaces $x_3 = \pm h$, where h is the laminate half-thickness. In the low-frequency limit, however, the particle motion will be dominated by in-plane displacements, and the x_3 tractions become negligible by comparison throughout the laminate. For any of the ply lay-up schemes examined here, we use the constitutive equations for an orthotropic laminate,

$$\begin{bmatrix} \sigma_{11} \\ \sigma_{22} \\ \sigma_{33} \\ \sigma_{23} \\ \sigma_{13} \\ \sigma_{12} \end{bmatrix} = \begin{bmatrix} C_{11} & C_{12} & C_{13} & 0 & 0 & 0 \\ C_{12} & C_{22} & C_{23} & 0 & 0 & 0 \\ C_{13} & C_{23} & C_{33} & 0 & 0 & 0 \\ 0 & 0 & 0 & C_{44} & 0 & 0 \\ 0 & 0 & 0 & 0 & C_{55} & 0 \\ 0 & 0 & 0 & 0 & 0 & C_{66} \end{bmatrix} \begin{bmatrix} \epsilon_{11} \\ \epsilon_{22} \\ \epsilon_{33} \\ 2\epsilon_{23} \\ 2\epsilon_{13} \\ 2\epsilon_{12} \end{bmatrix}, \tag{1}$$

and adopt a 2-D partial wave analysis for wave motion in the plate with particle displacement confined to the x_1x_3 plane only. For orthotropic media with propagation along a material symmetry axis, this assumption is well satisfied. Then, we have for the stresses,

$$\sigma_{13} = C_{55}\left(\frac{\partial u_1}{\partial x_3} + \frac{\partial u_3}{\partial x_1}\right) \approx 0,$$
$$\sigma_{33} = C_{13}\frac{\partial u_1}{\partial x_1} + C_{33}\frac{\partial u_3}{\partial x_3} \approx 0, \qquad x_3 \in [-h, +h]. \tag{2}$$

Together, these approximate equations imply that relations exist between the x_1 and x_3 displacement gradients,

$$\frac{\partial u_3}{\partial x_1} = -\frac{\partial u_1}{\partial x_3}, \qquad \frac{\partial u_3}{\partial x_3} = -\left(\frac{C_{13}}{C_{33}}\right)\frac{\partial u_1}{\partial x_1}, \tag{3}$$

where again, these relations apply throughout laminate thickness. The linear elastic wave equation for u_1, with wave motion confined to the x_1x_3 plane, is

$$\rho\frac{\partial^2 u_1}{\partial t^2} = C_{11}\frac{\partial^2 u_1}{\partial x_1^2} + C_{55}\frac{\partial^2 u_1}{\partial x_3^2} + C_{55}\frac{\partial^2 u_3}{\partial x_1 \partial x_3} + C_{13}\frac{\partial^2 u_3}{\partial x_3 \partial x_1}. \tag{4}$$

The results of Eqs. (3) can be inserted into Eq. (4), eliminating all but the dependence on u_1 and on its x_1 gradient. Assuming a harmonic time dependence of $\exp(-i\omega t)$, where ω is the angular frequency, the result is a simple differential equation for u_1

$$-\rho\omega^2 u_1 \approx C_{11}\frac{\partial^2 u_1}{\partial x_1^2} - \frac{C_{13}^2}{C_{33}}\frac{\partial^2 u_1}{\partial x_1^2}, \tag{5}$$

that can be solved by substitution in Eq. (5) of the formal solution $u_1 = U_1 \exp(i\xi x_1)$, where ξ is the x_1 wave number, and U_1 is the undetermined amplitude of the x_1 displacement. The above derivation is essentially identical to the one given for waves in a membrane by Landau and Lifshitz.[30] Moreover, it is completely equivalent to the low-frequency limiting behavior of the anisotropic Lamb wave equation for dilatational waves. The difference is that the calculation above is much simpler.

The substitution referred to above leads to a condition on the plate wave speed $V_{\mathrm{pl}}(=\omega/\xi)$, in terms of the elastic properties of the laminate,

$$\rho V_{\mathrm{pl}}^2 = C_{11} - \frac{C_{13}^2}{C_{33}}. \tag{6}$$

The relation in Eq. (6) is particularly fortuitous for composite laminates, where the elastic anisotropy can lead to ratios of 8 or 10 between C_{11} and C_{33}, accompanied by proportionately even smaller values of C_{13}. For the case of a uniaxial laminate (x_1 is the fiber direction) of 65% AS/4 fibers in 3501 epoxy, $C_{11} \approx 140$ GPa, $C_{13} \approx 2.7$ GPa, and $C_{33} \approx 10$ GPa, the error in ignoring the second term in Eq. (6) compared to the first is less than 1%. Because of this special circumstance that occurs only in elastically highly anisotropic media such as composites, where the in-plane stiffness dominates the elastic matrix, we may take V_{pl} to be wholly dependent on C_{11} with negligible loss of accuracy. In other

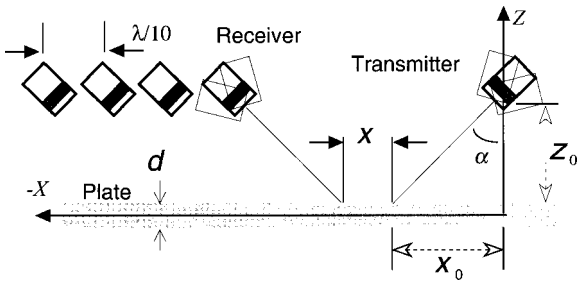

FIG. 2. Schematic diagram showing the in-plane property measurement procedure. The transducer separation parameter is x.

laminate lay-up configurations, as we shall see below, the error incurred by neglecting this term can be larger, but essentially never exceeding 10%. The major advantage of this approach is to simplify the measurement and analysis greatly. Only a single measurement is sufficient to obtain accurate in-plane longitudinal elastic stiffness information.

II. MEASUREMENT METHOD

The handy result in Eq. (6) above can be exploited only if we can find a way to make an accurate local measurement of the low-frequency S_0 plate wave speed. As we have seen above, time/frequency domain methods do not yield a sensitive measurement since the mode is nearly dispersionless (constant velocity with frequency) in the regime of interest. This means the swept-frequency approach will not work here. Instead, we take advantage of the spatial spectrum of the finite-beam transducer over a limited, but information-rich, zone of the dispersion curve. We construct a synthetic aperture by performing a spatial scan of the receiver with respect to the transmitter, as illustrated in Fig. 2, where the voltage is measured at each of 60 or 80 discrete positions. The only important criterion is that the step size should be much less than the guided mode wavelength in the plate ($\lambda_{\mathrm{pl}}=2\pi V_{\mathrm{pl}}/\omega$). The figure illustrates the transmitter and receiver (at several positions x_j) and their rotation to different incident angles. The plate and related variables are also shown.

At the low frequencies we use in this work, this step size works out to about 1 mm. It is important, however, that all geometric parameters, other than the transducer separation parameter x (shown in Fig. 2) be held constant during the scan. An example of a stepped scan in x, showing the real and imaginary parts of the transducer voltage for a uniaxial composite laminate with an incident angle of 10°, is shown in Fig. 3. These processed experimental data are the result of the Fourier transform operation described above. The two curves are nearly identical except for a $\pi/2$ phase shift.

Once the data are acquired, a spatial frequency spectrum can be constructed from the voltages measured at stepped values of x according to

$$S(\theta;\alpha)=\int_{-\infty}^{\infty} V(x;\alpha)\exp[-i(\kappa_f \sin\theta)x]dx, \tag{7}$$

or more to the point, because our data are discrete,

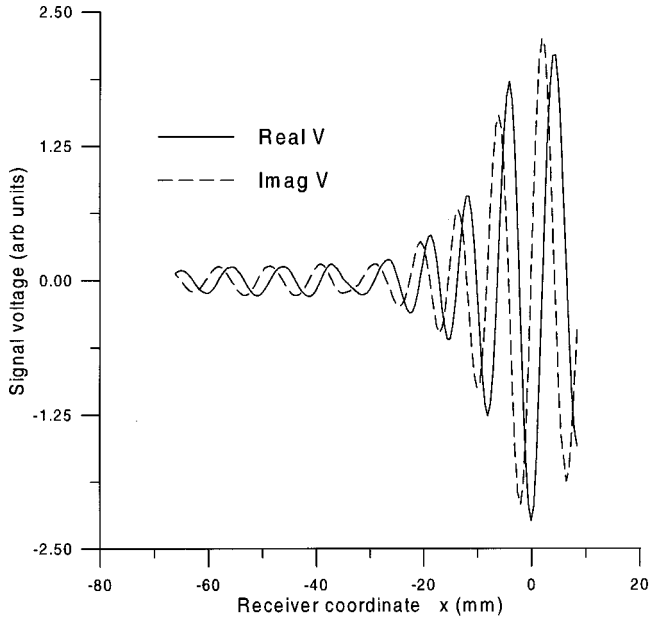

FIG. 3. Receiver position scan performed according to Fig. 2 showing real and imaginary parts of voltage for a uniaxial composite laminate with an incident angle of 10°.

$$S(\theta;\alpha)=\sum_{j=1}^{n} V(x_j;\alpha)\exp[-i(\kappa_f \sin\theta)x_j]. \tag{8}$$

Here, θ is the phase-match angle (explained below), α is the beam incident angle, x [or x_j in Eq. (8)] is the transducer separation parameter (shown in Fig. 3), and κ_f is the wave number in the fluid. In acquiring the voltage data it is critical to preserve the phase information; this task is accomplished by collecting the entire time-domain signal and performing a time–frequency Fourier transform on it, extracting only the particular frequency component of interest. Because the transducers are reasonably wideband and the signal level is high, we excite the transmitter with a one-cycle tone burst at about 1 MHz, giving us some concentration of power in the frequency band of 0.5 to 2 MHz. All data were acquired with this excitation. The result at every x_j receiver position is the term $V(x_j;\alpha)$ in the equations above. The real and imaginary parts of this voltage are illustrated in Fig. 3. The complex voltages for all the positions in the scan are then subjected to a spatial Fourier transform, as indicated in Eqs. (7) and (8).[28]

The voltage function itself is given by[28,31]

$$V(x,f,\alpha)=i\kappa_f a^4\int_0^{\pi/2-i\infty} R(\theta_i)D^T(\gamma)D^R(\gamma) \times\exp[i\kappa_f(2z_0)\cos\theta_i + i\kappa_f(2x_0+x)\sin\theta_i]\sin\theta_i\, d\theta_i, \tag{9}$$

where z_0 is the vertical distance from the transducers to the plate, x is the transducer separation, the position x_0 ($=z_0\tan\alpha$) is shown in Fig. 3, κ_f is the sound wave number in a fluid, a is the radius of the transducers, f is the frequency, and α is the incident angle The reflection coefficient $R(\theta_i,d,\{C_{ij}^*\})$, is a function of complex viscoelastic material properties, $D^T(\,)$ and $D^R(\,)$ are the transducer beam directivity functions. The plate thickness is d, and γ is the

angle between transmitter acoustical axis and each incident plane-wave direction of propagation in the incident plane, that is $\gamma = \theta_i - \alpha$.

The result of this transform operation is dependent on the transducer beam spread.[31] Were the plate to be perfectly *rigid* (unity reflection coefficient), then the resulting function $S(\theta;\alpha)$ would be exactly the spatial beam spectrum, or a function equivalent to the product of the individual transducer directivity functions of the transmitter and receiver. With an *elastic* plate the plate reflection properties will be superimposed onto the beam function. In this case, the guided wave reflection zero gives rise to a sharp decrease in the function $S(\theta;\alpha)$ at the phase-match angle corresponding to the mode phase velocity through Snell's law, $\kappa_f \sin\theta = \omega/V_{\mathrm{pl}}$. It is from this relationship and Eq. (6) that we extract our in-plane C_{11} property information. Depending on the transducer geometry, the frequency, and the initial estimate of C_{11}, however, more than one spatial beam scan at different incident angles α_m may be needed to cover the angular range of interest. In that case, the data for each angle can simply be summed incoherently over all M values of the incident angle,[28]

$$S(\theta) = \sum_{m=1}^{M} S(\theta, \alpha_m), \tag{10}$$

obtaining only in the magnitude of the $S(\theta)$ function.

More typically, and as demonstrated in this article, the beam parameters can be chosen to minimize the spatial scanning to a single instance, where only one data set suffices to provide an accurate estimate of C_{11}. Because the directivity function of a 9-mm transducer is broadly peaked at low frequency, the angular range of plane waves with sufficient energy to provide acceptable signal-to-noise ratios can be fairly large for small probes. As we show below, this aspect of the measurement also has implications for measurement sensitivity to transducer angle misalignment.

III. RESULTS AND DISCUSSION

In this section we present the results of experimental measurements and compare them to theoretical predictions based on the calculations outlined above. We also demonstrate, with examples of spatial beam scans according to the method outlined in this article, the in-plane elastic property estimation and illustrate its capabilities and advantages. To provide a realistic set of laminates to examine, uniaxial, biaxial, and quasi-isotropic lay-ups have been measured and their in-plane properties estimated. The laminates have all been produced using hand-lay-up techniques, and their volume fractions have been independently characterized. The intrinsic properties of AS/4 fibers and neat 3501-6 resin are well enough known that we feel confident in the accuracy of the calculated estimates of the in-plane stiffnesses for these plates.

Spatial Fourier transforms according to Eq. (8) of data taken at a single incident angle $\alpha = 10°$ for a uniaxial T300/CG-914$[0]_8$ graphite–epoxy laminate are shown in Fig. 4. The ultrasonic frequency is 1.0 MHz. The overall behavior in this curve is determined by the transducer geometry and frequency. The broad peak is the combined transducer directivity function of the two 9-mm radiators. Note that it shows essentially no sidelobes characteristic of a piston radiator at 1 MHz. This is because we are measuring the combined effects of the trasmitter *and* receiver together, as discussed by Lobkis *et al.*[31] The result is an effective beam function that behaves remarkably like a Gaussian beam, complete with the suppression of sidelobes and essentially no near-field/far-field boundary.

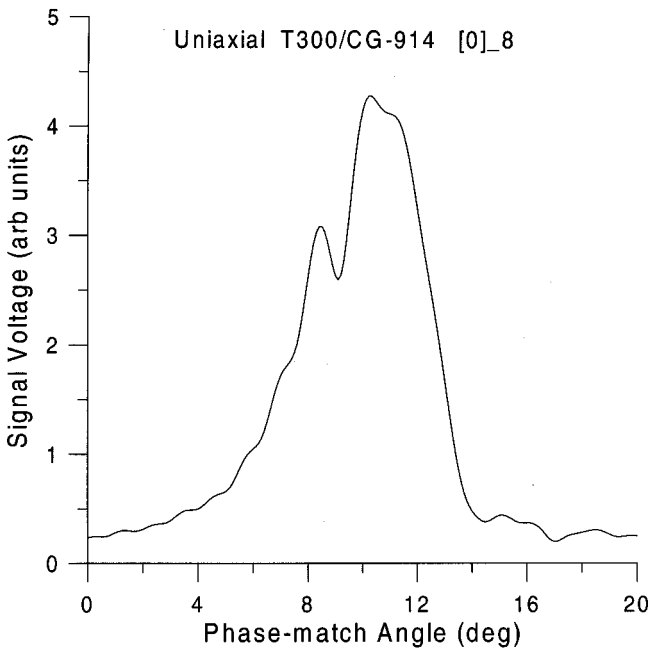

FIG. 4. Reflection function $S(\theta)$ versus phase-match angle for a uniaxial $[0]_8$ graphite–epoxy laminate of T300/CG-914. The minimum in the curve near 9° result from phase-matching incident wave to S_0 guided wave mode. Data are shown for $\alpha = 10°$; the rf is 1.0 MHz.

The dip on the left side of the peak near a phase-match angle of 9° is caused by the presence of the S_0 guided wave mode, whose reflection zero causes the signal decrease. The estimate of C_{11} (along the fiber direction) from these data is 142 GPa. The value inferred for this laminate from related, but rather different experiments, is 145 GPa, which compares favorably with our current measurement, although both these values are somewhat low when compared to generic tabular data for a similar material system, T300/5208.[32]

To verify the in-plane properties homogeneity, one more X scan has been performed for another position on the plate surface. The scanner has been shifted to 20 mm in the Y direction and the measurements have been repeated for the same geometrical setup. Figure 5, which presents the phase-matched angle of the S_0 mode for these two scans versus frequency, shows that the in-plane elastic properties are not completely identical. The estimate of C_{11} for the second scan is 147 GPa. It should be noted that the frequency-swept experiments for the same two positions have not revealed any differences of the measured signals. This example illustrates the higher sensitivity of the synthetic-aperture technique in comparison with the frequency-swept measurements for the in-plane properties determination.

The formalism developed above is generally applicable

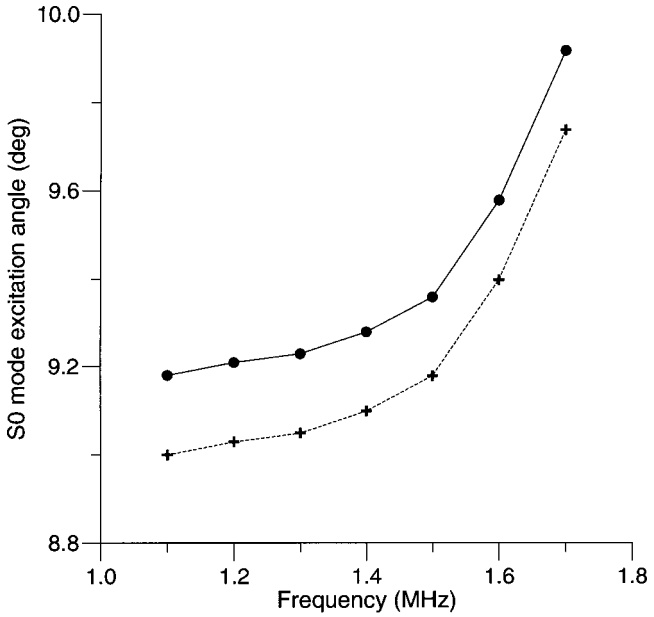

FIG. 5. The S_0 mode phase-match angle for a uniaxial $[0]_8$ graphite–epoxy laminate of T300/CG-914 versus frequency for two positions on the plate surface.

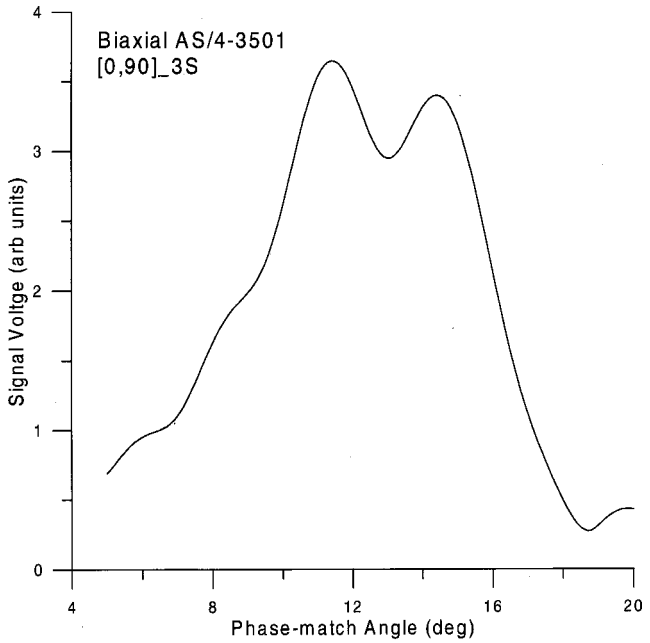

FIG. 6. Reflection function $S(\theta)$ versus phase-match angle for a biaxial $[0,90]_{3S}$ graphite–epoxy laminate of AS/4-3501. The minimum in the curve near 13° is the result of phase matching of the incident wave to the S_0 guided wave mode. Data are shown summed for $\alpha=11°$, 12°, and 13°. The frequency is 0.5 MHz.

beyond uniaxial laminates, because at low ultrasonic frequencies ($fd \lesssim 1$) only the average through-thickness (TT) properties of the laminate are important in determining the propagation characteristics. A goal of this work is to demonstrate that the more complicated, industrially relevant, lay-ups can also be accurately measured using this method. Therefore, we have examined a biaxial graphite–epoxy laminate $[0,90]_{3S}$ of AS/4-3501, whose fiber fraction has been independently characterized by fiber burnoff. The results are shown in Fig. 6 for 0.5 MHz with scanning in the one of the axial directions. Here, the clear indication of the S_0 mode is a minimum near 13°.

From lamination theory,[32] the in-plane longitudinal stiffness of a biaxial laminate is given by

$$A_{11}=U_1+(v_0-v_{90})U_2+U_3, \tag{11}$$

where the U_i are tabulated linear combinations of single-ply stiffness matrix elements, v_ϕ is the volume fraction of fibers in the ϕ direction, and A_{IJ} is the in-plane property matrix. For balanced laminates, such as we study here, (v_0-v_{90}) vanishes. Using the tabular data (our actual fiber volume fraction is close to that assumed in the table), we obtain an estimate of 73.9 GPa. This result is quite close to our measured value of 71.3 GPa, although in this case the ratio of C_{13}^2/C_{33} is a larger fraction of C_{11} than for the uniaxial laminate and can be expected to increase the systematic error. The absolute size of the out-of-plane normal stiffness C_{33} for a given material system does not, of course, change with lay-up sequence.

The last example is perhaps the most ubiquitous lay-up sequence, since it approximates the familiar properties of monolithic structural materials. The stacking sequence of $[0,+45,-45,90]_{2S}$ leads to in-plane properties that are approximately isotropic, and this sequence is called quasi-isotropic. In this case, the value of C_{13} may be slightly larger and C_{13}^2/C_{33} will be proportionately larger than C_{11}, which is decreasing as the fibers become distributed in several directions. Nonetheless, the intrinsic stiffness ratios are large enough that the error in ignoring the C_{13} contribution will still generally be acceptable for engineering estimates.

Figure 7 shows the summed results at 0.5 MHz for three measurements at incident angles of $\alpha=14°$, 15°, and 16°.

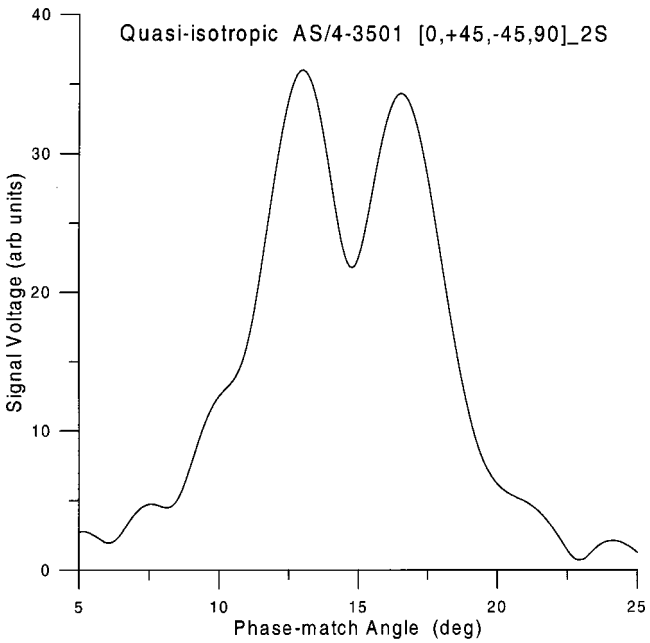

FIG. 7. Reflection function $S(\theta)$ versus phase-match angle for a quasi-isotropic $[0,+45,-45,90]_{2S}$ graphite–epoxy laminate of AS/4-3501. The minimum in the curve near 14.8° is the result of phase matching of the incident wave to the S_0 guided wave mode. Data are shown summed for $\alpha=14°$, 15°, and 16°. The frequency is 0.5 MHz.

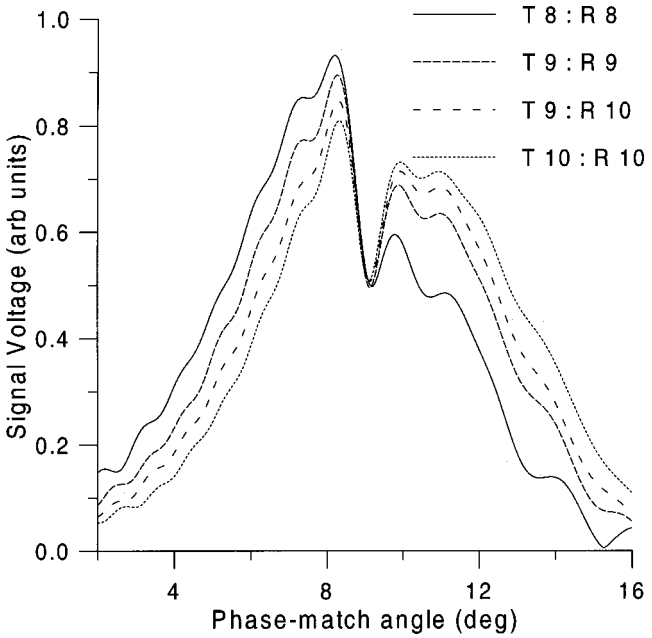

FIG. 8. Reflection functions $S(\theta;\alpha)$ versus phase-match angle for uniaxial $[0]_8$ AS/4-3501 laminate at $f=1.5$ MHz. Curves correspond to different transmitter–receiver setup, indicated in legend. Minima in curves near 9° show phase matching to S_0 guided wave. Same minima for all curves indicates method's robustness.

The material system is again AS/4-3501. Here, the sharp minimum is near a phase-match angle of 14.8°, leading to an experimental determination of C_{11} of 54.9 GPa. This value is, in fact, about 10% different from the estimate of lamination theory, $A_{11}=59.7$ GPa. But, such an outcome might be expected, since we consciously ignore the contribution to C_{11} of C_{13}^2/C_{33}, although this term should still be small. Another possibility is that the ply angles in the lay-up sequence are not precise, leading to variations in the in-plane stiffness. It would be possible, in principle, to improve the in-plane stiffness estimate; it is necessary, however, to know in advance the laminate stacking sequence. This information is almost always available for manufacturing inspections.

Finally, let us consider the robustness of the procedure. To show that neither the precise choice of angle, nor the exact equality between transmitter angle and receiver angle are critical to reproducible results, we present in Fig. 8 the results of several scans performed on the uniaxial specimen. The different curves of $S(\theta)$ are shown individually and not summed for transmission and reception at 8°, 9°, and 10°, as indicated in the figure legend. The data recorded as the wide-dash curve, however, have been acquired with the transmitter at 9° and the receiver at 10°. In all cases the minimum is reproducibly located at the angle used to derive the estimate of 142 GPa from Fig. 4 above. This important result implies that our method has significant application potential in the industrial environment, where precise transducer alignments are not always feasible.

IV. CONCLUSIONS

The method outlined in this article is a simple, effective means to infer the in-plane elastic properties of all kinds of composite laminates. We have demonstrated the utility and reproducibility of our method on uniaxial, biaxial, and quasi-isotropic laminates, and find in each case acceptable agreement with estimates from lamination theory. The method is based on the fundamental assumption of a dominant in-plane stiffness over other related stiffnesses. In cases of technological significance, this assumption will likely be well satisfied. Consequently, such an estimate of in-plane stiffness as a parameter to assure postmanufacture and in-service quality can be quite useful.

[1] D. E. Chimenti and A. H. Nayfeh, ''Leaky Lamb waves in fibrous composite laminates,'' J. Appl. Phys. **58**, 4531–4538 (1985).
[2] V. Dayal and V. K. Kinra, ''Leaky Lamb waves in an anisotropic plate. An exact solution and experiments,'' J. Acoust. Soc. Am. **85**, 2268–2276 (1989).
[3] D. E. Chimenti and A. H. Nayfeh, ''Ultrasonic reflection and guided waves in fluid-coupled composite laminates,'' J. Nondestruct. Eval. **9**, 51–69 (1990).
[4] R. A. Kline, ''Quantitative NDE of advanced composites using ultrasonic velocity measurements,'' J. Eng. Mater. Technol. **112**, 218–222 (1990).
[5] M. Deschamps and B. Hosten, ''The effects of viscoelasticity on the reflection and transmission of ultrasonic waves by an orthotropic plate,'' J. Acoust. Soc. Am. **91**, 2007–2015 (1992).
[6] Y. Bar-Cohen, A. K. Mal, and S. S. Lih, ''NDE of composite materials using ultrasonic oblique insonification,'' Mater. Eval. **51**, 1285–1296 (1993).
[7] J. L. Rose, A. Pilarski, and J. J. Ditri, ''An approach to guided wave mode selection for inspection of laminated plates,'' J. Reinf. Plast. Comp. **12**, 536–544 (1993).
[8] A. H. Nayfeh, *Wave Propagation in Layered Anisotropic Media* (North-Holland, Amsterdam, 1995).
[9] D. E. Chimenti, ''Guided waves in plates and their use in materials characterization,'' Appl. Mech. Rev. **50**, 247–284 (1997).
[10] M. Veidt and W. Sachse, ''Ultrasonic point-source/point-receiver measurements in thin specimens,'' J. Acoust. Soc. Am. **96**, 2318–2326 (1994).
[11] W. H. Prosser and M. R. Gorman, ''Plate mode velocities in graphite/epoxy plates,'' J. Acoust. Soc. Am. **96**, 902–907 (1994).
[12] H. Park and C. Calder, ''Laser-generated Rayleigh waves in graphite/epoxy composites,'' Exp. Mech. **34**, 148–154 (1994).
[13] R. L. Weaver and W. Sachse, ''Asymptotic viscoelastic rays in a thick plate,'' J. Appl. Mech. **61**, 429–433 (1994).
[14] T. T. Wu and J. F. Chai, ''Propagation of surface waves in anisotropic solids: Theoretical calculation and experiment,'' Ultrasonics **32**, 21–29 (1994).
[15] A. N. Norris, ''On the acoustic determination of the elastic moduli of anisotropic solids and acoustic conditions for the existence of symmetry plates,'' Q. J. Mech. Appl. Math. **42**, 413–420 (1989).
[16] M. D. Seale, B. T. Smith, and W. H. Prosser, ''Lamb wave assessment of fatigue and thermal damage in composites,'' J. Acoust. Soc. Am. **103**, 2416–2424 (1998).
[17] F. L. Degertekin and B. T. Khuri-Yakub, ''Hertzian contact transducers for nondestructive evaluation,'' J. Acoust. Soc. Am. **99**, 299–308 (1996).
[18] A. Minachi, D. K. Hsu, and R. B. Thompson, ''Single-sided determination of elastic constants of thick composites using acousto-ultrasonic technique,'' J. Acoust. Soc. Am. **96**, 353–362 (1994).
[19] J. J. Ditri, ''Phase and energy velocities of cylindrically crested guided waves,'' J. Acoust. Soc. Am. **97**, 98–107 (1995).
[20] G. L. Petersen, B. B. Chick, and C. M. Fortunko, ''Resonance techniques and apparatus for elastic-wave velocity determination in thin metal plates,'' Rev. Sci. Instrum. **65**, 192–198 (1994).
[21] R. B. King and C. M. Fortunko, ''Acoustoelastic evaluation of arbitrary plane residual stress states in non-homogeneous, anisotropic plates,'' Ultrasonics **21**, 256–258 (1983).
[22] T. Pialucha, C. C. H. Guyott, and P. Cawley, ''Amplitude spectrum method for the measurement of phase velocity,'' Ultrasonics **27**, 270–279 (1989).
[23] S. I. Rokhlin and W. Wang, ''Measurements of elastic constants of very thin anisotropic plates,'' J. Acoust. Soc. Am. **94**, 2721–2730 (1993).
[24] S. I. Rokhlin and W. Wang, ''Double through-transmission bulk wave method for ultrasonic phase velocity measurement and determination of

elastic constants of composite materials,'' J. Acoust. Soc. Am. **91**, 3303–3312 (1992).
[25] T. Kundu and B. W. Maxfield, ''A new technique for measuring Rayleigh and Lamb wave speeds,'' J. Acoust. Soc. Am. **93**, 3066–3073 (1993).
[26] A. G. Every and K. Y. Kim, ''Determination of elastic constants of anisotropic solids from elastodynamic Green's functions,'' Ultrasonics **34**, 471–472 (1996).
[27] J. J. Ditri and J. L. Rose, ''Excitation of guided waves in generally anisotropic layers using finite sources,'' J. Appl. Mech. **61**, 330–338 (1994).
[28] A. Safaeinili, O. I. Lobkis, and D. E. Chimenti, ''Air-coupled ultrasonic estimation of viscoelastic stiffness in plates,'' IEEE Trans. Ultrason. Ferroelectr. Freq. Control **43**, 1171–1180 (1996).
[29] O. I. Lobkis, D. E. Chimenti, H. Zhang, and M. Rudolph, ''In-plane elastic property characterization in composite plates,'' in *Review of Progress in Quantitative NDE*, edited by D. O. Thompson and D. E. Chimenti (Plenum, New York, 1998), Vol. 17, pp. 1139–1146.
[30] L. D. Landau and E. M. Lifschitz, *Theory of Elasticity*, 3rd ed. (Pergamon, Oxford, 1986) [translated by J. B. Sykes and W. H. Reid], p. 39.
[31] O. I. Lobkis, A. Safaeinili, and D. E. Chimenti, ''Precision ultrasonic reflection studies in fluid-coupled plates,'' J. Acoust. Soc. Am. **99**, 2727–2736 (1996).
[32] S. W. Tsai and H. T. Han, *Introduction to Composite Materials* (Technomic, Lancaster, PA, 1980).

Acoustic wave motion along a narrow cylindrical duct in the presence of an axial mean flow and temperature gradient

Keith S. Peat and Ray Kirby[a)]
Department of Mathematical Sciences, Loughborough University, Loughborough, Leicestershire LE11 3TU, United Kingdom

(Received 9 August 1999; revised 26 October 1999; accepted 29 October 1999)

A numerical solution is presented to the problem of nonisentropic acoustic wave motion in a circular capillary tube in the presence of both axial mean flow and a background axial temperature gradient. The effects of the radial components of the acoustic velocity are included in the analysis. The main application area is in the study of the acoustic effects of catalytic converters. The solution makes use of a series expansion and is valid for small relative changes in the background temperature, which are typical of this application area. Various solutions to the problem have been obtained previously, using different simplifications to the complete problem which is considered here. It is shown that each of the simplifications results in errors for the predicted attenuation of at least 20 dB/m, using conditions typical for catalytic converters. In particular, the isentropic assumption is shown to be invalid. © *2000 Acoustical Society of America.* [S0001-4966(00)03502-5]

PACS numbers: 43.20.Hq, 43.20.Mv, 43.20.Bi [ANN]

LIST OF SYMBOLS

a	speed of sound
c_p, c_v	specific heats
f,g	nondimensional steady flow variables
i	$\sqrt{-1}$
k	mean wave number, $\omega L/\bar{a}$
K	thermal conductivity
L	half-length of the duct section with a temperature gradient
M	Mach number of the steady flow
p	pressure
Q	steady-state heat generation per unit volume
r	radial coordinate
R	radius of a capillary tube
R_e	mean Reynolds number of the steady flow, $\bar{\rho}\bar{M}\bar{a}R/\bar{\mu}$
R_0	gas constant
s	mean shear wave number, $s=R\sqrt{\bar{\rho}\omega/\bar{\mu}}$
t	time
T	temperature
u	axial velocity
v	radial velocity
x	axial coordinate
α	linearization parameter
γ	c_p/c_v
Γ	dimensionless axial wave number
η	r/R
μ	dynamic viscosity
ρ	density
σ^2	mean Prandtl number, $\bar{\mu}c_p/K$
τ	temperature change parameter
ω	radian frequency
ξ	x/L

Subscripts

0,1,2	zeroth-, first-, and second-order terms in τ
A,B,C	zeroth-, first-, and second-order terms in ξ, of the first-order τ solution

Superscripts

$-$	value of a variable at $\xi=0$
$\sim$	dimensioned variable
$'$	acoustic fluctuation (dimensionless)

INTRODUCTION

Although the prime purpose of a catalytic converter is to reduce the levels of noxious gases emitted into the atmosphere from an engine's exhaust duct, it also has a small but noticeable effect upon the acoustic performance of the exhaust system. An acoustic model of the entire exhaust system must therefore include a representative model of the acoustic effect of a catalytic converter. The exhaust gas flow from a multicylinder engine may be considered as the sum of a steady flow component and an unsteady flow component, the sound. Thus within a catalytic converter, one can consider the acoustic waves as being convected by the steady flow, see Fig. 1. The catalyst, with which the pores of a catalytic converter are coated, creates an exothermic reaction within the gas flowing through the pores, as oxygen is stripped from the nitrous oxides and is used to completely burn the carbon dioxide and the hydrocarbons. This exothermic reaction causes a very rapid increase with distance in the steady, background value of the gas temperature. Experiments have shown that a temperature increase of the order of 100 °C occurs within the first 10–20 mm of axial distance along the

[a)]Present address: Department of Mechanical Engineering, Brunel University, United Kingdom.

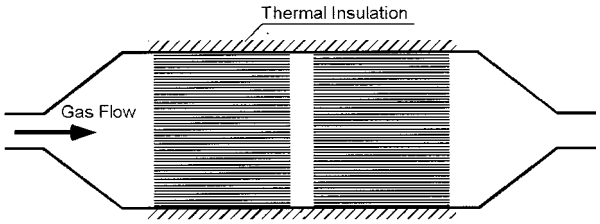

FIG. 1. A section through a two-brick catalytic converter.

capillary pore, which typically has a total length of 150 mm. The temperature after the first 20 mm is virtually constant, as is the temperature throughout any further bricks downstream of the first. Thus the temperature gradient is very localized, but of such a magnitude that its effect may be significant.

From an acoustic viewpoint, therefore, the catalytic converter is an element within which the acoustic pulsations from the exhaust ports are convected by a mean flow through capillary tubes and, over a short entry region, are subjected to large increases in mean temperature resulting from the exothermic reaction.

Analytical solutions for the acoustic wave propagation through cylindrical capillary tubes in which the background medium is stationary and isothermal have been obtained for both isentropic[1] and nonisentropic[2] cases. Variational/numerical solutions in which the acoustic waves are convected by an isothermal, fully developed laminar mean flow, for both isentropic and nonisentropic cases, were developed later.[3–6] It has been shown that results for tubes of circular cross section are a close approximation to those for tubes of other cross sections with the same hydraulic mean radius.[7] It has also been demonstrated that inclusion of the radial component of the acoustic velocity within the analysis has a small but observable effect upon the wave attenuation.[6]

A numerical solution to the problem of acoustic wave motion along a cylindrical capillary duct in the presence of an axial temperature gradient has been presented previously,[8] but for the convected wave case it was assumed that the acoustic fluctuations were isentropic. More recently, an analytical solution to this problem has been developed,[9] but in addition to the isentropic assumption it was also restricted to convection by a steady flow of very low Mach number, and also radial components of the acoustic velocity were ignored.

An analytical solution to the problem of nonconvected wave motion in capillary tubes in the presence of an axial temperature gradient has also been found.[10] In this case it was possible to use the complete nonisentropic equations and to retain radial velocity components. Results were given which compared the wave attenuation in the isentropic and nonisentropic cases. It was shown that the differences increased with increasing temperature gradient and shear wave number and were greater for the forward-going than for the backward-going wave. For temperature gradients appropriate to catalytic converters, and shear wave numbers corresponding to frequencies of 0–2 kHz, it was shown that differences in attenuation of 20 dB/m were commonplace for both waves, and in the worst cases for the forward wave were as high as 50 dB/m. The effect of the temperature gradient was to greatly increase the magnitude of the error caused by the isentropic assumption, but also to make the error less uniform with respect to the shear wave number. The conclusion is that for wave motion in the presence of a temperature gradient, the isentropic assumption is so poor as to render the results invalid.

In this paper, we consider convected, nonisentropic, acoustic wave motion through a capillary tube of circular cross section in which there is a large, constant gradient of background temperature. Radial components of the acoustic velocity are included. The steady flow Mach number is restricted to some degree, because the steady flow is assumed to be incompressible, but it can sensibly be as high as 0.3, a value which would never be exceeded in catalytic converter applications. This is in contrast to the analytical, isentropic solution,[9] which uses a low-order expansion in the Mach number and becomes noticeably inaccurate as its value approaches 0.1. In common with earlier works,[8–10] the analysis in this paper makes use of an order expansion in the temperature change parameter, defined as the temperature increase divided by twice the mean temperature. A catalytic converter typically operates at 1000 °K with a temperature increase of 100 °K over 10–20 mm. Thus although the temperature gradient is very large, the temperature change parameter is only 0.05–0.1. In common with all of the earlier works which consider convected acoustic waves, the steady flow is here assumed to be laminar and fully developed. The Reynolds number in catalytic converter applications is low enough for the assumption of the laminar flow to be valid. The assumption of fully developed flow[8–10] is of greater concern, since the large temperature gradients which are being considered actually occur within about the first 10–20 diameters of flow entry, and thus the developing flow region is a significant proportion of the full domain under consideration. This is an area which might be worthy of further study.

I. GOVERNING EQUATIONS

The equations of continuity, momentum, and energy for axisymmetric flow of a homogeneous gas through a narrow cylindrical duct can be written as[3]

$$\frac{\partial \tilde{\rho}}{\partial t}+\tilde{u}\frac{\partial \tilde{\rho}}{\partial x}+\tilde{\rho}\left[\frac{\partial \tilde{u}}{\partial x}+\frac{1}{r}\frac{\partial(r\tilde{v})}{\partial r}\right]=0, \tag{1}$$

$$\tilde{\rho}\left(\frac{\partial \tilde{u}}{\partial t}+\tilde{u}\frac{\partial \tilde{u}}{\partial x}+\tilde{v}\frac{\partial \tilde{u}}{\partial r}\right)=-\frac{\partial \tilde{p}}{\partial x}+\frac{\mu}{r}\frac{\partial}{\partial r}\left(r\frac{\partial \tilde{u}}{\partial r}\right), \tag{2}$$

$$\frac{\partial \tilde{p}}{\partial r}=0, \tag{3}$$

and

$$\tilde{\rho}c_p\left(\frac{\partial \tilde{T}}{\partial t}+\tilde{u}\frac{\partial \tilde{T}}{\partial x}+\tilde{v}\frac{\partial \tilde{T}}{\partial r}\right)=\frac{K}{r}\frac{\partial}{\partial r}\left(r\frac{\partial \tilde{T}}{\partial r}\right)+\frac{\partial \tilde{p}}{\partial t}+\tilde{u}\frac{\partial \tilde{p}}{\partial x}+\tilde{v}\frac{\partial \tilde{p}}{\partial r}+\mu\left(\frac{\partial \tilde{u}}{\partial r}\right)^2+Q. \tag{4}$$

The gas is assumed to obey the equation of state for an ideal gas, namely

$$\tilde{p}=\tilde{\rho}R_0\tilde{T}. \tag{5}$$

A linear change in the steady-state temperature T_s is assumed to occur over a length $2L$ of duct, such that

$$T_s(\xi)=(1+\tau\xi)\overline{T}, \quad -1\leqslant\xi\leqslant 1, \tag{6}$$

where τ is a constant, the temperature change parameter. The fluid variables are now expanded as the sum of a steady-state component and a small harmonic acoustic fluctuation, in the form

$$\tilde{\rho}=\overline{\rho}[(1-\tau\xi)+\alpha\rho'(\xi,\eta)e^{i\omega t}], \tag{7}$$

$$\tilde{u}=\overline{a}[\overline{M}(1+\tau\xi)f(\eta)+\alpha u'(\xi,\eta)e^{i\omega t}], \tag{8}$$

$$\tilde{v}=\frac{\overline{a}R}{L}[0+\alpha v'(\xi,\eta)e^{i\omega t}], \tag{9}$$

$$\tilde{p}=\overline{p}[1+\overline{M}^2 g(\xi)+\alpha p'(\xi,\eta)e^{i\omega t}], \tag{10}$$

and

$$\tilde{T}=\overline{T}[(1+\tau\xi)+\alpha T'(\xi,\eta)e^{i\omega t}], \tag{11}$$

where $\alpha\ll 1$.

A. Steady flow solution

It remains to be shown that the steady flow terms assumed in Eqs. (7)–(11) are consistent with the governing equations (1)–(5). The equations of continuity and state are satisfied[9] if terms of $O[\tau^2]\ll 1$ and $O[\overline{M}^2 g(\xi)]\ll 1$. The steady rate of heat release, $Q(x,r)$, from the exothermic reaction in the pore of the catalytic converter, has a distribution which gives rise to the assumed linear change in the steady-state temperature, such that the steady-state form of the energy equation is satisfied. Finally the axial momentum equation reduces to

$$\tau f^2=-\frac{1}{\gamma}\frac{dg}{d\xi}+\frac{(1+\tau\xi)(1+\tau\xi/2)}{R_e(R/L)}\frac{1}{\eta}\frac{d}{d\eta}\left(\eta\frac{df}{d\eta}\right). \tag{12}$$

With reference to the properties of gases, it is assumed that the variation of absolute viscosity with temperature is of the form $\mu=\overline{\mu}(1+\tau\xi/2)$ and that the ratio of specific heats is essentially invariant with temperature. The variation of viscosity with temperature was wrongfully ignored in the earlier isentropic analysis. Consider a series solution of Eq. (12) in terms of the temperature change parameter τ, with

$$f(\eta)=f_0(\eta)+\tau f_1(\eta)+\tau^2 f_2(\eta)+\ldots, \tag{13a}$$

$$g(\xi)=g_0(\xi)+\tau g_1(\xi)+\tau^2 g_2(\xi)+\ldots. \tag{13b}$$

Equation (12), written to zeroth- and first-order terms in τ, respectively, gives

$$\frac{R_e(R/L)}{\gamma}\frac{dg_0}{d\xi}=\frac{1}{\eta}\frac{d}{d\eta}\left(\eta\frac{df_0}{d\eta}\right)=\text{constant}, \tag{14a}$$

$$\frac{R_e(R/L)}{\gamma}\frac{dg_1}{d\xi}+12\xi=\frac{1}{\eta}\frac{d}{d\eta}\left(\eta\frac{df_1}{d\eta}\right)-4R_e(R/L)\times(1-\eta^2)^2=\text{constant}. \tag{14b}$$

The solutions to Eqs. (14a) and (14b) which satisfy the no-slip condition at the wall are

$$f_0=2(1-\eta^2), \tag{15a}$$

$$dg_0/d\xi=-8\gamma/[R_e(R/L)] \tag{15b}$$

and

$$f_1=-R_e(R/L)\left[\frac{\eta^2}{2}(\eta^2-1)+\frac{1}{9}(1-\eta^6)\right], \tag{16a}$$

$$dg_1/d\xi=-2\gamma-12\gamma\xi/[R_e(R/L)], \tag{16b}$$

where the zeroth-order τ solution of Eq. (15) is simply that of Poiseuille flow.

B. Acoustic equations

The linearized acoustic equations follow from substitution of Eqs. (7)–(11) into Eqs. (1)–(5), with retention of only first-order terms in α, to give

$$ik\rho'+\overline{M}f(\eta)\left[(1+\tau\xi)\frac{\partial\rho'}{\partial\xi}+\tau\rho'\right]-\tau u'+(1-\tau\xi)\left[\frac{\partial u'}{\partial\xi}+\frac{1}{\eta}\frac{\partial(\eta v')}{\partial\eta}\right]=0, \tag{17}$$

$$ik(1-\tau\xi)u'+\overline{M}f(\eta)\frac{\partial u'}{\partial\xi}+\overline{M}\tau f(\eta)u'+\overline{M}\frac{df}{d\eta}v'=-\frac{1}{\gamma}\frac{\partial p'}{\partial\xi}+\frac{k(1+\tau\xi/2)}{s^2}\frac{1}{\eta}\frac{\partial}{\partial\eta}\left(\eta\frac{\partial u'}{\partial\eta}\right), \tag{18}$$

$$\partial p'/\partial\eta=0, \tag{19}$$

$$ik(1-\tau\xi)T'+\overline{M}f(\eta)\frac{\partial T'}{\partial\xi}+\tau u'+\tau\overline{M}f(\eta)\rho'=\frac{k(1+\tau\xi/2)}{\sigma^2 s^2}\frac{1}{\eta}\frac{\partial}{\partial\eta}\left(\eta\frac{\partial T'}{\partial\eta}\right)+\frac{ik(\gamma-1)}{\gamma}p'+\overline{M}\frac{(\gamma-1)}{\gamma}(1+\tau\xi)f(\eta)\frac{\partial p'}{\partial\xi}+\frac{k\overline{M}}{s^2}(\gamma-1)\times\left(1+\frac{3\tau\xi}{2}\right)\left[2\frac{df}{d\eta}\frac{\partial u'}{\partial\eta}+\frac{u'}{\eta}\frac{d}{d\eta}\left(\eta\frac{df}{d\eta}\right)\right], \tag{20}$$

and

$$p'=(1-\tau\xi)T'+(1+\tau\xi)\rho'. \tag{21}$$

The acoustic variables are written in series expansions of τ as

$$p'=e^{k\Gamma\xi}\{p_0'+\tau p_1'(\xi)+\ldots\}=p_0' e^{k\Gamma\xi}\{1+\tau p_1(\xi)+\ldots\}, \tag{22}$$

$$\rho'=e^{k\Gamma\xi}\{\rho_0'+\tau\rho_1'(\xi)+\ldots\}, \tag{23}$$

$$u'=e^{k\Gamma\xi}\{u_0'(\eta)+\tau u_1'(\xi,\eta)+\ldots\}=(\Gamma s^2 p_0'/\gamma)e^{k\Gamma\xi}\{u_0(\eta)+\tau u_1(\xi,\eta)+\ldots\}, \tag{24}$$

$$v'=e^{k\Gamma\xi}\{v_0'(\eta)+\tau v_1'(\xi,\eta)+\ldots\}=(k\Gamma p_0'/\gamma)e^{k\Gamma\xi}\{v_0(\eta)+\tau v_1(\xi,\eta)+\ldots\}, \tag{25}$$

and

$$T'=e^{k\Gamma\xi}\{T_0'+\tau T_1'(\xi)+\ldots\}=T_0' e^{k\Gamma\xi}\{T_0+\tau T_1(\xi)+\ldots\}. \tag{26}$$

C. Acoustic equations of zeroth order in τ

When the series expansions of Eqs. (13) and (22)–(26) are substituted into Eqs. (17), (18), and (20) and only the terms of zeroth order in τ are retained, then the continuity, axial momentum, and energy equations can be written as

$$\frac{1}{\eta}\frac{d}{d\eta}(\eta\nu_0)=\gamma(i/\Gamma+\bar{M}f_0)(T_0-1)-\Gamma s^2u_0, \tag{27}$$

$$\frac{1}{\eta}\frac{d}{d\eta}\left(\eta\frac{du_0}{d\eta}\right)-s^2(i+\bar{M}f_0\Gamma)u_0=1+\bar{M}\frac{df_0}{d\eta}\nu_0, \tag{28}$$

and

$$\frac{1}{\eta}\frac{d}{d\eta}\left(\eta\frac{dT_0}{d\eta}\right)-\sigma^2s^2(i+\bar{M}f_0\Gamma)T_0 =\left(\frac{\gamma-1}{\gamma}\right)\sigma^2s^2\left[8\bar{M}\Gamma\frac{d}{d\eta}(\eta u_0)-(i+Mf_0\Gamma)\right], \tag{29}$$

respectively, where Eq. (21) has been used to eliminate the density.

D. Acoustic equations of first order in τ

When the series expansions of Eqs. (13) and (22)–(26) are substituted into Eqs. (17), (18), and (20) and only the terms of first order in τ are retained, then the continuity, axial momentum, and energy equations can be written as

$$\begin{aligned}\frac{1}{\eta}\frac{\partial}{\partial\eta}(\eta\nu_1)=\gamma\Bigg\{&\left(\frac{i}{\Gamma}+\bar{M}f_0\right)(T_1-p_1)-\bar{M}f_0\xi\\&+\frac{\bar{M}f_0}{k\Gamma}\left[\frac{d}{d\xi}(T_1-p_1)-T_0\right]-\frac{i\xi T_0}{\Gamma}\\&+\bar{M}f_1(T_0-1)\Bigg\}\\&+s^2\left[\left(u_0-\frac{\partial u_1}{\partial\xi}\right)\Big/\,k-\Gamma u_1\right],\end{aligned} \tag{30}$$

$$\begin{aligned}&\frac{1}{\eta}\frac{\partial}{\partial\eta}\left(\eta\frac{\partial u_1}{\partial\eta}\right)-s^2(i+\bar{M}f_0\Gamma)u_1\\&=\left[p_1+\frac{1}{k\Gamma}\frac{dp_1}{d\xi}\right]+\bar{M}\left(\frac{df_1}{d\eta}\nu_0+\frac{df_0}{d\eta}\nu_1\right)\\&\quad+s^2\left[\frac{\bar{M}f_0}{k}\left(u_0+\frac{\partial u_1}{\partial\xi}\right)+(\bar{M}f_1\Gamma-i\xi)u_0\right]\\&\quad-\frac{\xi}{2\eta}\frac{d}{d\eta}\left(\eta\frac{du_0}{d\eta}\right),\end{aligned} \tag{31}$$

and

$$\begin{aligned}&\frac{1}{\eta}\frac{\partial}{\partial\eta}\left(\eta\frac{\partial T_1}{\partial\eta}\right)-\sigma^2s^2(i+\bar{M}f_0\Gamma)T_1\\&=\left(\frac{\gamma-1}{\gamma}\right)\sigma^2s^2\Bigg\{8\bar{M}\Gamma\frac{\partial(\eta u_1)}{\partial\eta}-(i+\bar{M}f_0\Gamma)p_1\\&\quad-\frac{\bar{M}f_0}{k}\frac{dp_1}{d\xi}+\bar{M}\Gamma\Bigg[12\xi\frac{d(\eta u_0)}{d\eta}-\xi f_0-f_1\\&\quad-2\frac{df_1}{d\eta}\frac{du_0}{d\eta}-\frac{u_0}{\eta}\frac{d}{d\eta}\left(\eta\frac{df_1}{d\eta}\right)\Bigg]\Bigg\}\\&\quad-\frac{\xi}{2\eta}\frac{d}{d\eta}\left(\eta\frac{dT_0}{d\eta}\right)+\sigma^2s^2\Bigg[\frac{\bar{M}f_0}{k}\left(1-T_0+\frac{\partial T_1}{\partial\xi}\right)\\&\quad+(\bar{M}f_1\Gamma-i\xi)T_0+\frac{\Gamma s^2}{k\gamma}u_0\Bigg],\end{aligned} \tag{32}$$

respectively, where once again Eq. (20) has been used to eliminate the density.

II. SOLUTION OF THE ACOUSTIC EQUATIONS

A. Solution of the equations of zeroth order in τ

It is assumed that the walls of the duct are rigid and that they have a much greater thermal conductivity than the fluid. Since these boundary conditions are valid in the limit $\tau\to 0$, it follows that

$$u_0=\nu_0=T_0=0 \quad \text{at} \quad \eta=1, \tag{33}$$

and, from symmetry considerations on the center line,

$$\partial u_0/\partial\eta=\nu_0=\partial T_0/\partial\eta=0 \quad \text{at} \quad \eta=0. \tag{34}$$

The zeroth-order equations (27)–(29) and the above boundary conditions are exactly those considered by Jeong and Ih[6] and the following scheme for solution is only a slight adaptation of the one they proposed:

(i) A guess is made for the value of the propagation constant Γ and the distribution of the radial velocity component ν_0.

(ii) The axial momentum equation (28) is solved by a fourth-order Runge–Kutta shooting method for the axial velocity profile u_0, and then the energy equation (29) is solved in a similar way for the temperature profile T_0.

(iii) An integral form of the continuity equation (27), namely

$$i\langle T_0\rangle+\bar{M}\Gamma\langle f_0T_0\rangle-(i+\bar{M}\Gamma)-\Gamma^2s^2\langle u_0\rangle/\gamma=0, \tag{35}$$

is then used to find a better approximation to Γ. [The notation $\langle h(\eta)\rangle=2\int_0^1\eta h(\eta)d\eta$ is used throughout for the cross sectionally averaged value of a general function $h(\eta)$.]

(iv) A better approximation to the radial velocity profile is then obtained by numerically integrating, by Simpson's rule, the continuity equation (27), which can be

rwritten as

$$\nu_0=\frac{\gamma}{\Gamma\eta}\int_0^\eta \eta[(i+\bar{M}f_0\Gamma)(T_0-1)-\Gamma^2 s^2 u_0/\gamma]d\eta. \tag{36}$$

(v) Steps (ii) to (iv) are repeated iteratively until convergence is obtained.

B. Solution of the equations of first order in τ

Solutions of the form

$$\begin{aligned} p_1&=p_A+p_B\xi+p_C\xi^2,\\ u_1&=u_A(\eta)+\xi u_B(\eta)+\xi^2 u_C(\eta),\\ \nu_1&=\nu_A(\eta)+\xi\nu_B(\eta)+\xi^2\nu_C(\eta),\\ T_1&=T_A(\eta)+\xi T_B(\eta)+\xi^2 T_C(\eta), \end{aligned} \tag{37}$$

are sought, where p_A, p_B, and p_C are constants. Substitution of these expressions into Eqs. (29) and (30), followed by separation of the zeroth-, first-, and second-order terms in ξ, leads to a set of continuity, momentum, and equations for the zeroth-order terms in ξ,

$$\begin{aligned} \frac{1}{\eta}\frac{d}{d\eta}(\eta\nu_A)=\gamma\Bigg\{&\left(\frac{i}{\Gamma}+\bar{M}f_0\right)T_A+\frac{\bar{M}f_0}{k\Gamma}(T_B-p_B-T_0)\\ &+\bar{M}f_1(T_0-1)\Bigg\}-s^2[\Gamma u_A+(u_B-u_0)/k], \end{aligned} \tag{38}$$

$$\begin{aligned} &\frac{1}{\eta}\frac{d}{d\eta}\left(\eta\frac{du_A}{d\eta}\right)-s^2(i+\bar{M}f_0\Gamma)u_A\\ &\quad=\frac{p_B}{k\Gamma}+\bar{M}\left(\frac{df_1}{d\eta}\nu_0+\frac{df_0}{d\eta}\nu_A\right)+\frac{\bar{M}f_0 s^2}{k}(u_0+u_B)\\ &\qquad+\bar{M}f_1\Gamma s^2 u_0, \end{aligned} \tag{39}$$

$$\begin{aligned} &\frac{1}{\eta}\frac{d}{d\eta}\left(\eta\frac{dT_A}{d\eta}\right)-\sigma^2 s^2(i+\bar{M}f_0\Gamma)T_A\\ &\quad=\left(\frac{\gamma-1}{\gamma}\right)\sigma^2 s^2\Bigg\{8\bar{M}\Gamma\frac{d(\eta u_A)}{d\eta}-\frac{\bar{M}f_0}{k}p_B\\ &\qquad+\bar{M}\Gamma\left[-f_1-2\frac{df_1}{d\eta}\frac{du_0}{d\eta}-\frac{u_0}{\eta}\frac{d}{d\eta}\left(\eta\frac{df_1}{d\eta}\right)\right]\Bigg\}\\ &\qquad+\sigma^2 s^2\left[\frac{\bar{M}f_0}{k}(1-T_0+T_B)+\bar{M}f_1\Gamma T_0+\frac{\Gamma s^2}{k\gamma}u_0\right], \end{aligned} \tag{40}$$

the first-order terms in ξ,

$$\begin{aligned} \frac{1}{\eta}\frac{d}{d\eta}(\eta\nu_B)=\gamma\Bigg\{&\left(\frac{1}{\Gamma}+\bar{M}f_0\right)(T_B-p_B)-\bar{M}f_0\\ &+\frac{2\bar{M}f_0}{k\Gamma}(T_C-p_C)-iT_0/\Gamma\Bigg\}\\ &-s^2[\Gamma u_B+2u_C/k], \end{aligned} \tag{41}$$

$$\begin{aligned} &\frac{1}{\eta}\frac{d}{d\eta}\left(\eta\frac{du_B}{d\eta}\right)-s^2(i+\bar{M}f_0\Gamma)u_B\\ &\quad=p_B+\frac{2p_C}{k\Gamma}+\bar{M}\frac{df_0}{d\eta}\nu_B+\frac{2\bar{M}f_0 s^2 u_C}{k}-is^2u_0\\ &\qquad-\frac{1}{2\eta}\frac{d}{d\eta}\left(\eta\frac{du_0}{d\eta}\right), \end{aligned} \tag{42}$$

$$\begin{aligned} &\frac{1}{\eta}\frac{d}{d\eta}\left(\eta\frac{dT_B}{d\eta}\right)-\sigma^2 s^2(i+\bar{M}f_0\Gamma)T_B\\ &\quad=\left(\frac{\gamma-1}{\gamma}\right)\sigma^2 s^2\Bigg\{-ip_B-\bar{M}f_0\Gamma\left(p_B+1+\frac{2p_C}{k\Gamma}\right)\\ &\qquad+8\bar{M}\Gamma\left[\frac{d(\eta u_B)}{d\eta}+\frac{3}{2}\frac{d(\eta u_0)}{d\eta}\right]\Bigg\}\\ &\qquad-\sigma^2 s^2\left(iT_0-2\frac{\bar{M}f_0}{k}T_C\right)-\frac{1}{2\eta}\frac{d}{d\eta}\left(\eta\frac{dT_0}{d\eta}\right), \end{aligned} \tag{43}$$

and the second-order terms in ξ,

$$\frac{1}{\eta}\frac{d}{d\eta}(\eta\nu_C)=\gamma(i/\Gamma+\bar{M}f_0)(T_C-p_C)-\Gamma s^2 u_C, \tag{44}$$

$$\frac{1}{\eta}\frac{d}{d\eta}\left(\eta\frac{du_C}{d\eta}\right)-s^2(i+\bar{M}f_0\Gamma)u_C=p_C+\bar{M}\frac{df_0}{d\eta}\nu_C, \tag{45}$$

$$\begin{aligned} &\frac{1}{\eta}\frac{d}{d\eta}\left(\eta\frac{dT_C}{d\eta}\right)-\sigma^2 s^2(i+\bar{M}f_0\Gamma)T_C\\ &\quad=\left(\frac{\gamma-1}{\gamma}\right)\sigma^2 s^2\left\{8\bar{M}\Gamma\frac{d(\eta u_C)}{d\eta}-(i+\bar{M}f_0\Gamma)p_C\right\}. \end{aligned} \tag{46}$$

The boundary conditions on all of the first-order variables are exactly the same as for the respective zeroth-order variables, as given in Eqs. (33) and (34). Thus from comparison of Eqs. (44)–(46) with Eqs. (27)–(29), it follows that

$$u_C/p_C=u_0,\quad T_C/p_C=T_0,\quad \nu_C/p_C=\nu_0. \tag{47}$$

Integral forms of the continuity equations (38) and (41) can now be written as

$$\begin{aligned} \gamma\Bigg\{&\frac{i}{\Gamma}\langle T_A\rangle+\bar{M}\langle f_0T_A\rangle+\frac{\bar{M}}{k\Gamma}(\langle f_0T_B\rangle-p_B-\langle f_0T_0\rangle)\\ &+\bar{M}\langle f_1T_0\rangle\Bigg\}=s^2[\Gamma\langle u_A\rangle+(\langle u_B\rangle-\langle u_0\rangle)/k] \end{aligned} \tag{48}$$

and

$$\begin{aligned} &\frac{2p_C}{k\Gamma}[\Gamma s^2\langle u_0\rangle-\bar{M}\gamma(\langle f_0T_C\rangle-1)]\\ &\quad=\gamma\left\{\frac{i}{\Gamma}(\langle T_B\rangle-p_B)+\bar{M}(\langle f_0T_B\rangle-p_B)-\bar{M}-i\langle T_0\rangle/\Gamma\right\}\\ &\qquad-s^2\Gamma\langle u_B\rangle. \end{aligned} \tag{49}$$

The following iterative solution scheme has been used. The shear wave number s and the temperature change parameter τ are specified, together with the choice of forward- or backward-going wave. Solutions are found under these con-

ditions for a range of Mach numbers of the mean steady flow, up to a specified maximum and increasing by a specified increment. Since the steady flow is assumed to be incompressible, it would be unwise to exceed a maximum Mach number of 0.3. An increment of 0.05 or less has always been found to result in convergent solutions. The iterative solution proceeds as follows:

(i) The Mach number is set to zero. The analytical solution for this case[10] is then found, to give initial values for the propagation constant Γ, the complex constants p_B and p_C, and the radial velocity distribution ν_0. The radial velocity distribution ν_1 and ν_2 are set to zero.

(ii) The Mach number is incremented and the zeroth-order τ solution is found as stated in Sec. II A. (For the first increment, the initial guessed values of the propagation constant Γ and the radial velocity distribution ν_0 are taken from (i), the analytical solution for $\bar{M}=0$. For subsequent increments of the Mach number, the initial guessed values are those from the previous step.)

(iii) The axial momentum equation (39) is solved by a Runge–Kutta shooting method for the axial velocity profile u_A, and then the energy equation (40) is solved in a similar way for the temperature profile T_A.

(iv) The energy equation (43) is solved by a Runge–Kutta shooting method for the temperature profile T_B.

(v) Substitution for $\langle u_B \rangle$ from Eq. (48) into Eq. (49) now allows for solution of p_C from Eq. (49).

(vi) The axial momentum equation (42) is solved by a Runge–Kutta shooting method for the axial velocity profile u_B.

(vii) The radial velocity distributions ν_1 and ν_2 are evaluated by numerically integrating Eqs. (38) and (41) using Simpson's rule.

(viii) The residual of Eq. (48) is evaluated. The error results from the fact that the value of p_B which was assumed throughout steps (iii) to (viii) is incorrect. Let this value be termed p_{B0}, say.

(ix) Steps (iii) to (viii) are repeated for eight further values of p_B, namely $p_B = p_{B0} \pm h \pm ih$, for a chosen mesh size h.

(x) The residual evaluated at step (viii) will have a least value for one of the trial values of p_B, say $p_B = p_{B0} + mh + inh$, where $m,n = -1,0$ or $+1$. If $m=n=0$, $(p_B = p_{B0})$, gives the least error, the interval h is halved. The value of p_B corresponding to the least resultant error is used for the next step of the iteration.

(xi) Steps (iii) to (x) are repeated until convergence to the desired accuracy has been achieved.

(xii) Steps (ii) to (xi) are repeated for each Mach number value.

(xiii) Steps (i) to (xii) are repeated for each shear wave number.

At steps (iii), (iv), and (vi), a fourth-order Runge–Kutta method was used. When solving for a given variable $f(\eta)$, say, the shooting scheme involved using two separate guesses for $f(0)$, namely $f(0)=0$ and 1, evaluating the resultant value of $f(1)$ in each case, and then using linear interpolation to find the required value of $f(0)$ to satisfy the known boundary condition $f(1)$.

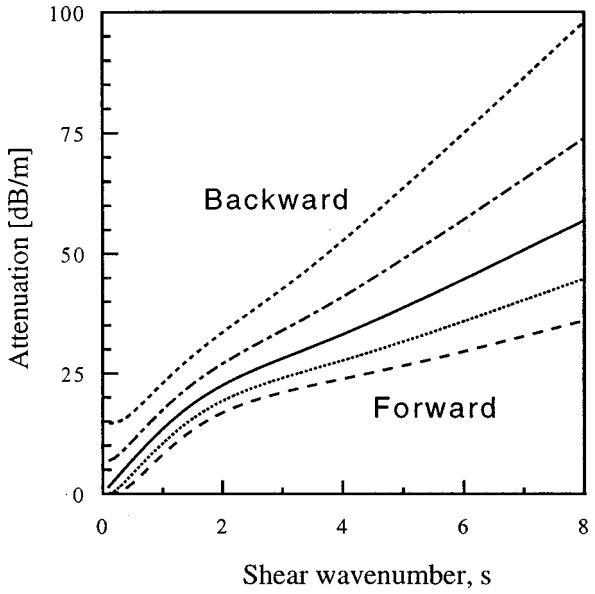

FIG. 2. Attenuation of convected waves with constant background temperature, $\tau=0$. —— $\bar{M}=0$; ····· $\bar{M}=0.1$, forward; ----- $\bar{M}=0.2$, forward; – – – – $\bar{M}=0.1$, backward; · · · · $\bar{M}=0.2$, backward.

Convergence to five significant figure accuracy of the zeroth-order τ solution, step (ii), occurs in the order of ten iterations. Convergence to five significant figure accuracy of the first-order τ solution, step (xi), occurs in the order of 100 iterations. The iteration was slowest at very low shear wave numbers. The scheme given above was found to converge stably in all cases, unlike alternative procedures which have been attempted. In particular, it should be noted that attempts to specify the Mach number and then iterate on the shear wave number, a seemingly simpler alternative to the process given above, have proved unsuccessful in that convergence was not always obtained.

III. RESULTS

The average attenuation of the pressure wave is defined here as

$$\text{Attenuation} = \{20 \log_{10}[p(\xi = \mp 1)/ p(\xi = \pm 1)]\}/2L \quad [\text{dB/m}],$$

which can be rewritten as

$$\text{Attenuation} = \mp 8.686(\omega/\bar{a}) R_e\{\Gamma + \tau p_B/k\} \quad [\text{dB/m}],$$

where the upper sign relates to the forward-going wave. All of the results in Figs. 2–5 refer to nonisentropic solutions derived from the numerical scheme presented above. Figures 2 and 3 show results for nongeneral cases, and have been found to be identical to results from earlier solutions to these simplified problems. These results, which show the influence of convective flow and a temperature gradient separately, are useful for comparison with the results of Figs. 4 and 5, where

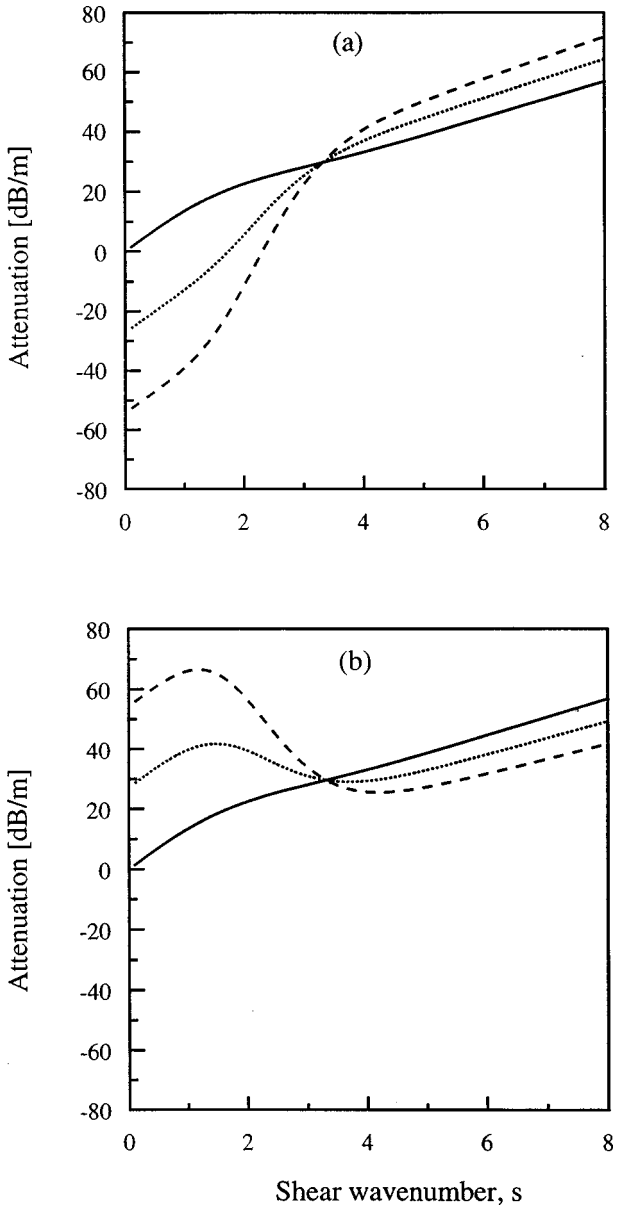

FIG. 3. Attenuation of unconvected waves, $\bar{M}=0$, with a background temperature gradient. (a) Forward-going waves, (b) backward-going waves, $\tau=0$; ····· $\tau=0.05$; ----- $\tau=0.1$.

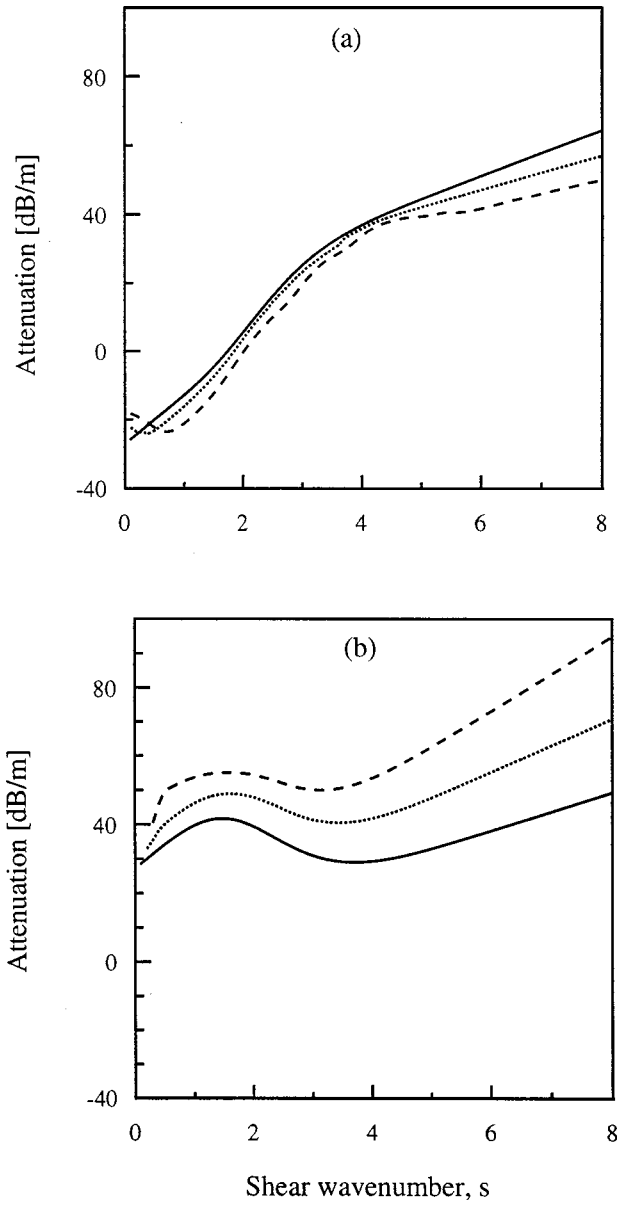

FIG. 4. Attenuation of convected waves with a background temperature gradient, $\tau=0.05$. (a) Forward-going waves, (b) backward-going waves, —— $\bar{M}=0$; ····· $\bar{M}=0.1$; ----- $\bar{M}=0.2$.

both effects are considered concurrently. They also formed basic checks on the numerical scheme and gave an indication of the required step sizes to be used in the Runge–Kutta algorithms.

Figure 2 shows results for attenuation with varying shear wave number for the case of zero temperature gradient, $\tau=0$. For a Mach number $\bar{M}=0$, the result is that of the analytical solution,[2] while in the convected cases the results follow from the earlier numerical solution.[6] In particular it is seen that the attenuation of the forward wave is decreased by flow convection and the attenuation of the backward wave is correspondingly increased. In both cases, the effect increases with increasing shear wave number.

Figure 3 shows results for attenuation with varying shear wave number for the case of zero Mach number $\bar{M}=0$. Once again, for a zero temperature gradient, $\tau=0$, the result is that of the analytical solution,[2] while for nonzero temperature gradients the results are those of the later analytical solution.[10] In contrast to the effects of flow convection, it is seen that the influence of a temperature gradient is greatest at low shear wave numbers, where the effect is to reduce the attenuation of the forward wave and increase the attenuation of the backward wave. At higher shear wave numbers the influence is less noticeable and the effect is reversed, in that the attenuation of the forward wave is increased while that of the backward wave is reduced. The attenuation of the forward wave at low shear wave numbers is highly negative, i.e., the sound is amplified rather than attenuated. Low shear wave numbers correspond to low frequencies and it would appear that the background temperature increase feeds energy into the acoustic wave, through excess dilation, and that this process occurs fast enough to dominate over viscous

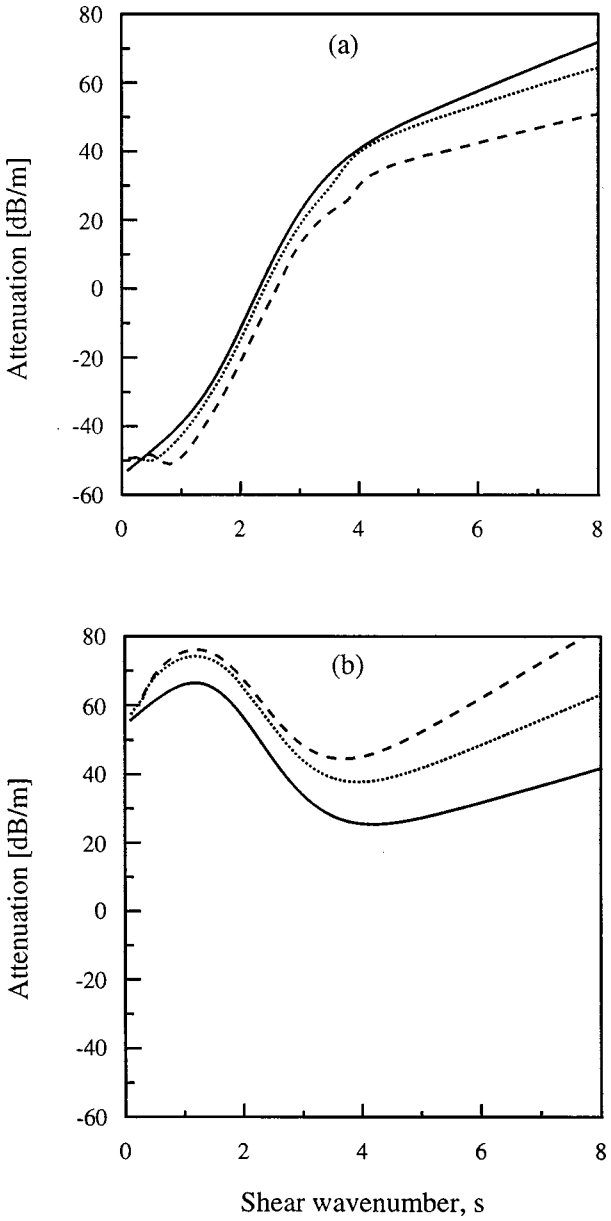

FIG. 5. Attenuation of convected waves with a background temperature gradient, $\tau=0.1$. (a) Forward-going waves, (b) backward-going waves, —— $\bar{M}=0$; ····· $\bar{M}=0.1$; ----- $\bar{M}=0.2$.

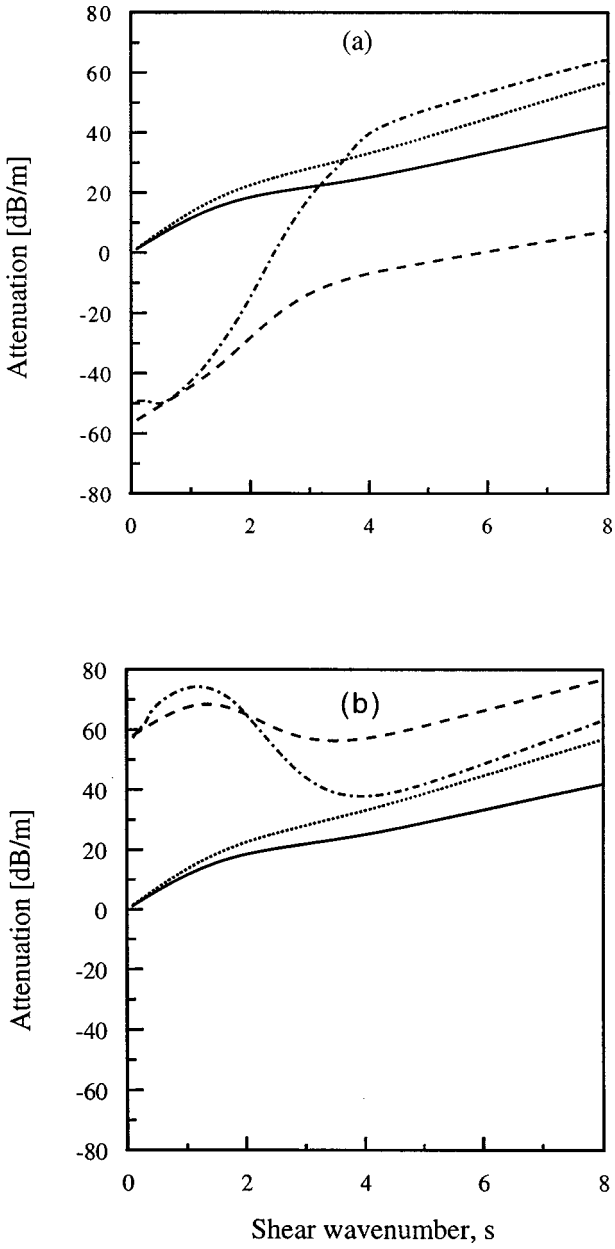

FIG. 6. Comparison of wave attenuation with and without the isentropic assumption. (a) Forward-going waves, (b) backward-going waves, $\tau=0$, $\bar{M}=0$: —— isentropic; ····· nonisentropic; $\tau=0.1$, $\bar{M}=0.1$: ----- isentropic; -·-·-·- nonisentropic.

dissipation when the wave is slowly changing, i.e., for low frequencies.

Figures 4 and 5 show results for attenuation with varying shear wave number when both flow convection and a temperature gradient are present simultaneously. Figure 4 is for the case when the temperature change parameter $\tau=0.05$ and Fig. 5 is for $\tau=0.1$. The latter may be regarded as the maximum value which is ever encountered in catalytic converter applications. In both cases, the curves for $\bar{M}=0$ are identical to those of the analytical solution.[10] The same general remarks are valid for both figures. The general form of the attenuation curves remains the same as that for the unconvected case of the same temperature gradient, i.e., the effect of the temperature gradient is dominant. The basic effect of flow convection remains the same whether or not there is a background temperature gradient. Thus the attenuation of the forward wave is reduced, i.e., at low shear wave numbers there is a further increase of amplification, and the attenuation of the backward wave is increased by flow convection. The influence of flow generally becomes greater with increasing shear wave number, for both forward and backward waves, but this effect only becomes uniform at high shear wave numbers, especially for the forward wave.

A comparison of attenuation results with[8] and without the use of the isentropic assumption is shown in Fig. 6, contrasting the differences in the absence of flow convection and a temperature gradient, $\tau=0$, $\bar{M}=0$, with those when both effects are present, $\tau=0.1$, $\bar{M}=0.1$. In the latter case, for the forward wave, the isentropic assumption is seen to result in very large errors at moderate to high shear wave numbers.

The errors are even greater than those observed for the unconvected case with a temperature gradient.[10] In contast, the errors on the backward wave are much smaller, but nonuniform with respect to shear wave number. The same nonuniformity was observed in the unconvected case,[10] but the magnitude of the discrepancy was larger in that case. Thus the effect of flow is to increase the error introduced by the isentropic assumption for the forward wave and to reduce it for the backward wave.

The numerical solution does, of course, yield complete details of all aspects of the wave propagation. In particular, results for the phase speed ratio, the radial profiles of axial velocity, temperature and radial velocity, and the axial variation of pressure, velocity, and temperature, can be determined. Detailed results are not presented here, since they have already been given for the unconvected case[10] and the zero temperature gradient case,[6] and the same general remarks for the combined case as given in the above discussion of attenuation remain valid. Thus in all cases the two separate effects are seen to add in a rational manner, without any surprising interactive effects.

IV. CONCLUSIONS

A numerical solution for nonisentropic, convected acoustic wave propagation along a capillary tube in the presence of a linear increase of steady-state temperature has been developed. A convergent iterative routine for solution has been established, although in certain circumstances the rate of convergence is extremely slow. The isentropic assumption results in very large errors, particularly for the forward wave, and must be deemed invalid when there is a background temperature gradient, whether or not the waves are convected by a steady flow. The effect of a temperature gradient dominates over the effect of flow convection at low shear wave numbers. Both effects are of similar magnitude at higher shear wave numbers. For accurate analysis of the problem, it is vital that both effects are considered simultaneously and that the isentropic assumption is not utilized.

[1] W. Kerris, Zentralblatt für Wissenschaftliches Berichtwesen, Berlin-Alderhof F.B. (1939), 1140.
[2] C. Zwikker and C. Kosten, *Sound Absorbing Materials* (Elsevier, Amsterdam, 1949).
[3] K. S. Peat, J. Sound Vib. **175**, 475–489 (1994).
[4] J.-G. Ih, C.-M. Park, and H.-J. Kim, J. Sound Vib. **190**, 163–173 (1996).
[5] R. J. Astley and A. Cummings, J. Sound Vib. **188**, 635–65 (1995).
[6] K.-W. Jeong and J.-G. Ih, J. Sound Vib. **198**, 67–79 (1996).
[7] A. Cummings, J. Sound Vib. **162**, 27–42 (1993).
[8] K. S. Peat and R. Kirby, Inter-Noise 96 Proceedings, Liverpool, U.K., 1996, pp. 1003–1006.
[9] K. S. Peat, J. Sound Vib. **203**, 855–866 (1997).
[10] K. S. Peat, Acust. Acta Acust. **84**, 57–65 (1998).

Acoustic hybrid junction in a rectangular waveguide

Jae Y. Kwon and Hyo J. Eom[a)]
Department of Electrical Engineering, Korea Advanced Institute of Science and Technology, 373-1, Kusong Dong, Yusung Gu, Taejon, Korea

(Received 5 October 1999; accepted for publication 15 December 1999)

Acoustic scattering from a hybrid junction in a rectangular waveguide is studied. The Fourier transform and mode matching is used to represent the scattered wave and the simultaneous equations for the modal coefficients are formulated. A residue calculus is utilized to obtain a solution to the simultaneous equations in fast-converging series. Numerical computations are performed to show the behavior of transmission in terms of junction geometry and operating frequency. The utility of acoustic hybrid junction is discussed in terms of its decoupling characteristics. © *2000 Acoustical Society of America.* [S0001-4966(00)05803-3]

PACS numbers: 43.20.Mv [ANN]

INTRODUCTION

The electromagnetic hybrid junction in a rectangular waveguide (magic-*T*) has been widely used as a microwave passive component (duplexer) due to its decoupling characteristics between the *E*-plane and *H*-plane arms. The decoupling characteristics of the electromagnetic hybrid junction was extensively studied and well understood.[1] It would be interesting to examine if such a decoupling behavior exists in a similar hybrid junction for acoustic waves. In this paper, we propose an acoustic hybrid junction (see Fig. 1) and investigate its transmission and reflection characteristics to assess its utility as an acoustic passive element. The theoretical technique to analyze the scattering behavior of hybrid junction is based on the Fourier transform/series and mode matching as used in Ref. 2. A residue calculus is utilized to represent the scattered field in rigorous series which is amenable to numerical computation. In the next two sections, we discuss scattering from the hybrid junction consisting of a hard and soft surface, respectively. The notations used in the paper closely follow those in Ref. 2.

I. HARD-SURFACE HYBRID JUNCTION

Consider a hybrid junction in a rectangular waveguide consisting of a hard surface (surface boundary condition: $\nabla\Phi\cdot\hat{n}=0,\hat{n}$: unit normal to the surface) in Fig. 1. In region (I) $(0<x<a,0<z<b)$, an incident field (velocity potential) Φ_1^i, propagating along y direction, impinges on a junction. The velocity potential Φ satisfies the Helmholtz equation $(\nabla^2\Phi+k^2\Phi=0)$. The wave number is k $(=\omega/c$, ω: angular frequency, c: sound speed) and an $e^{-i\omega t}$ time-harmonic convention is suppressed. In region (I) the total field is a sum of the incident and scattered components

$$\Phi_1^i(x,y,z)=\cos(A_1x)\cos(B_1z)e^{i\beta_1 y}, \tag{1}$$

$$\Phi_2^i(x,y,z)=\cos(A_2x)\cos(B_2z)e^{-i\beta_2 y}, \tag{2}$$

$$\Phi^{\mathrm{I}}(x,y,z)=\frac{1}{2\pi}\int_{-\infty}^{\infty}\sum_{m=0}^{\infty}[\tilde{A}_m(\zeta)\cos(\kappa_m x)\cos(b_m z)+\tilde{B}_m(\zeta)\cos(a_m x)\cos(\eta_m z)]e^{-i\zeta y}\,d\zeta, \tag{3}$$

where $A_1=\alpha\pi/a$, $B_1=\mu\pi/b$, $\beta_1=\sqrt{k^2-A_1^2-B_1^2}$, $A_2=\rho\pi/a$, $B_2=\nu\pi/b$, $\beta_2=\sqrt{k^2-A_2^2-B_2^2}$ $(\alpha,\mu,\rho,\nu=0,1,2,...,)$, $a_m=m\pi/a$, $b_m=m\pi/b$, $\kappa_m=\sqrt{k^2-\zeta^2-b_m^2}$, and $\eta_m=\sqrt{k^2-\zeta^2-a_m^2}$. Note that the Fourier transform of $\Phi^{\mathrm{I}}(x,y,b)$ is $\int_{-\infty}^{\infty}\Phi^{\mathrm{I}}(x,y,b)e^{i\zeta y}\,dy$ given by $\Sigma_{m=0}^{\infty}[\tilde{A}_m(\zeta)\times\cos(\kappa_m x)(-1)^m+\tilde{B}_m(\zeta)\cos(a_m x)\cos(\eta_m b)]$.

In region (II) $(0<x<a,-w/2<y<w/2,b<z)$, the incident and transmitted fields through port 3 are

$$\Phi_3^i(x,y,z)=\cos(A_3x)\cos W_3\left(y+\frac{w}{2}\right)e^{-i\beta_3 z}, \tag{4}$$

$$\Phi^{\mathrm{II}}(x,y,z)=\sum_{p=0}^{\infty}\sum_{q=0}^{\infty}a_{pq}\cos(a_p x)\cos w_q\left(y+\frac{w}{2}\right)e^{i\xi_{pq}z}, \tag{5}$$

where $A_3=\phi\pi/a$, $W_3=\tau\pi/w$, $\beta_3=\sqrt{k^2-A_3^2-W_3^2}$ $(\phi,\tau=0,1,2,...,)$, $w_q=q\pi/w$, and $\xi_{pq}=\sqrt{k^2-a_p^2-w_q^2}$.

In region (III) $(a<x,-g/2<y<g/2,0<z<b)$, the incident and transmitted fields through port 4 are

$$\Phi_4^i(x,y,z)=\cos G_4\left(y+\frac{g}{2}\right)\cos(B_4z)e^{-i\beta_4 x}, \tag{6}$$

$$\Phi^{\mathrm{III}}(x,y,z)=\sum_{p=0}^{\infty}\sum_{q=0}^{\infty}b_{pq}\cos g_p\left(y+\frac{g}{2}\right)\cos(b_q z)e^{i\gamma_{pq}x}, \tag{7}$$

where $G_4=\psi\pi/g$, $B_4=\chi\pi/b$, $\beta_4=\sqrt{k^2-G_4^2-B_4^2}$ $(\psi,\chi=0,1,2,...,)$, $g_p=p\pi/g$, and $\gamma_{pq}=\sqrt{k^2-g_p^2-b_q^2}$.

We use the boundary conditions on the field continuities at $z=b$ and $x=a$ to find the unknown modal coefficients a_{pq} and b_{pq}. Enforcing the velocity continuity condition at $z=b$ gives

[a)]Electronic mail: hjeom@ee.kaist.ac.kr

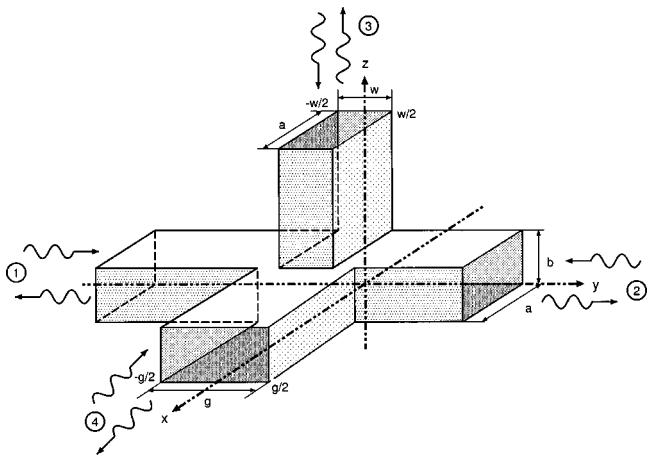

FIG. 1. Acoustic wave scattering from hybrid junction in rectangular waveguide.

$$\left.\frac{\partial[\Phi_1^i(x,y,z)+\Phi_2^i(x,y,z)+\Phi^{\mathrm{I}}(x,y,z)]}{\partial z}\right|_{z=b} = \begin{cases} \left.\dfrac{\partial[\Phi_3^i(x,y,z)+\Phi^{\mathrm{II}}(x,y,z)]}{\partial z}\right|_{z=b} \\ \quad \text{for } 0<x<a,\ |y|<w/2, \\ 0 \qquad \text{otherwise.} \end{cases} \tag{8}$$

Taking the Fourier transform of (8) results in

$$\begin{aligned} &-\sum_m^\infty \tilde{B}_m(\zeta)\,\eta_m \cos(a_m x)\sin(\eta_m b) \\ &\quad = -\beta_3\zeta\cos(A_3x)F_\tau^w(\zeta)e^{-i\beta_3 b} \\ &\qquad +\sum_p^\infty\sum_q^\infty a_{pq}\xi_{pq}\zeta\cos(a_p x)F_q^w(\zeta)e^{i\xi_{pq}b}, \end{aligned} \tag{9}$$

where

$$F_q^w(\zeta)=\frac{(-1)^q e^{i\zeta w/2}-e^{-i\zeta w/2}}{\zeta^2-w_q^2}. \tag{10}$$

Multiplying (9) by $\cos(a_m x)$ and performing integration with respect to x from 0 to a yields

$$\begin{aligned} \tilde{B}_m(\zeta) &= \frac{\zeta\beta_3}{\eta_\phi\sin(\eta_\phi b)}F_\tau^w(\zeta)e^{-i\beta_3 b} \\ &\quad -\sum_{q=0}^\infty a_{mq}\frac{\zeta\xi_{mq}}{\eta_m\sin(\eta_m b)}F_q^w(\zeta)e^{i\xi_{mq}b}. \end{aligned} \tag{11}$$

Similarly, taking the Fourier transform of the velocity continuity condition at $x=a$, multiplying $\cos(b_m z)$ and performing integration with respect to z from 0 to b yields

$$\begin{aligned} \tilde{A}_m(\zeta) &= \frac{\zeta\beta_4}{\kappa_\chi\sin(\kappa_\chi a)}F_\psi^g(\zeta)e^{-i\beta_4 a} \\ &\quad -\sum_{p=0}^\infty b_{pm}\frac{\zeta\gamma_{pm}}{\kappa_m\sin(\kappa_m a)}F_p^g(\zeta)e^{i\gamma_{pm}a}. \end{aligned} \tag{12}$$

Enforcing the pressure-continuity condition at $z=b$, $0<x<a$, $|y|<w/2$ gives

$$\begin{aligned} &\Phi_1^i(x,y,b)+\Phi_2^i(x,y,b)+\Phi^{\mathrm{I}}(x,y,b) \\ &\quad =\Phi_3^i(x,y,b)+\Phi^{\mathrm{II}}(x,y,b). \end{aligned} \tag{13}$$

Rewriting (13),

$$\begin{aligned} &\cos(A_1x)(-1)^\mu e^{i\beta_1 y}+\cos(A_2x)(-1)^\nu e^{-i\beta_2 y} \\ &\quad +\frac{1}{2\pi}\int_{-\infty}^{\infty}\sum_{m=0}^{\infty}[\tilde{A}_m(\zeta)\cos(\kappa_m x)(-1)^m \\ &\quad +\tilde{B}_m(\zeta)\cos(a_m x)\cos(\eta_m b)]e^{-i\zeta y}\,d\zeta \\ &\quad =\cos(A_3x)\cos W_3\left(y+\frac{w}{2}\right)e^{-i\beta_3 b} \\ &\qquad +\sum_{p=0}^\infty\sum_{q=0}^\infty a_{pq}\cos(a_p x)\cos w_q\left(y+\frac{w}{2}\right)e^{i\xi_{pq}b}. \end{aligned} \tag{14}$$

Substituting (11) and (12) into (14), and performing $\int_{-w/2}^{w/2}\int_0^a$ (14) $\cos(a_s x)\cos w_t(y+w/2)dx\,dy$ $(s=0,1,\ldots,\ t=0,1,\ldots)$, we obtain

$$\begin{aligned} &-i(-1)^\mu\frac{a}{2}\beta_1\varepsilon_\alpha\delta_{\alpha s}F_t^w(\beta_1)+i(-1)^\nu\frac{a}{2}\beta_2\varepsilon_\rho\delta_{\rho s}F_t^w(-\beta_2) \\ &\quad +\frac{a}{2}\delta_{\phi s}e^{-i\beta_3 b}\left(i\varepsilon_s\beta_3 I_{1\phi\tau t}^{baw}-\frac{w}{2}\varepsilon_\phi\varepsilon_\tau\delta_{\tau t}\right) \\ &\quad +i(-1)^{\chi+s}\beta_4 e^{-i\beta_4 a}I_{2s\chi\psi t}^{gw} \\ &\quad =\sum_{p=0}^\infty\sum_{q=0}^\infty\left[a_{pq}\frac{a}{2}\varepsilon_s\delta_{ps}e^{i\xi_{pq}b}\left(i\xi_{pq}I_{1pqt}^{baw}+\frac{w}{2}\varepsilon_t\delta_{qt}\right)\right. \\ &\qquad \left.+b_{pq}i(-1)^{q+s}\gamma_{pq}e^{i\gamma_{pq}a}I_{2sqpt}^{gw}\right], \end{aligned} \tag{15}$$

where δ_{ms} is the Kronecker delta and

$$\varepsilon_s=\begin{cases} 2 & \text{when} \quad s=0, \\ 1 & s=1,2,3,\ldots. \end{cases} \tag{16}$$

Enforcing the pressure-continuity condition at $x=a$, $|y|<g/2$, $0<z<b$ gives

$$\begin{aligned} &\Phi_1^i(a,y,z)+\Phi_2^i(a,y,z)+\Phi^{\mathrm{I}}(a,y,z) \\ &\quad =\Phi_4^i(a,y,z)+\Phi^{\mathrm{III}}(a,y,z). \end{aligned} \tag{17}$$

Substituting (11) and (12) into (17), and performing $\int_{-g/2}^{g/2}\int_0^b$ (17) $\cos(b_h z)\cos g_n(y+g/2)dz\,dy$ $(h=0,1,\ldots,\ n=0,1,\ldots)$, we obtain

$$-i(-1)^{\alpha}\frac{b}{2}\beta_1\varepsilon_\mu\delta_{\mu h}F_n^g(\beta_1)+i(-1)^{\rho}\frac{b}{2}\beta_2\varepsilon_\nu\delta_{\nu h}F_n^g(-\beta_2)$$
$$+i(-1)^{\phi+h}\beta_3 e^{-i\beta_3 b}I_{2\phi h\tau n}^{wg}$$
$$+\frac{b}{2}\delta_{\chi h}e^{-i\beta_4 a}\left(i\varepsilon_h\beta_4 I_{1\chi\psi n}^{abg}-\frac{g}{2}\varepsilon_\chi\varepsilon_\psi\delta_{\psi n}\right)$$
$$=\sum_{p=0}^{\infty}\sum_{q=0}^{\infty}\left[a_{pq}i(-1)^{p+h}\xi_{pq}e^{i\xi_{pq}b}I_{2phqn}^{wg}\right.$$
$$\left.+b_{pq}\frac{b}{2}\varepsilon_h\delta_{qh}e^{i\gamma_{pq}a}\left(i\gamma_{pq}I_{1qpn}^{abg}+\frac{q}{2}\varepsilon_n\delta_{pn}\right)\right], \tag{18}$$

where

$$I_{1pqt}^{baw}=\frac{1}{2\pi}\int_{-\infty}^{\infty}\frac{\zeta^2\cot(b\sqrt{k^2-\zeta^2-a_p^2})}{\sqrt{k^2-\zeta^2-a_p^2}}F_q^w(\zeta)F_t^w(-\zeta)d\zeta, \tag{19}$$

$$I_{2sqpt}^{gw}=\frac{1}{2\pi}\int_{-\infty}^{\infty}\frac{\zeta^2}{\beta_{sq}^2-\zeta^2}F_p^g(\zeta)F_t^w(-\zeta)d\zeta. \tag{20}$$

The integrand of I_{1pqt}^{baw} has simple poles at $\zeta=\pm\omega_q$ and an infinite number of poles associated with $\sin(b\sqrt{k^2-\zeta^2-a_p^2})=0$. The integrand of I_{2sqpt}^{gw} has simple poles at $\zeta=\pm\beta_{sq}$ and simple poles at $\zeta=\pm g_p,\pm w_t$ (double poles in case of $g_p=w_t$). Utilizing a technique of contour integration, we transform I_{1pqt}^{baw} and I_{2sqpt}^{gw} into rapidly converging series. The results are in the Appendix. It is possible to solve (15) and (18) for the modal coefficients a_{pq} and b_{pq} by truncating the infinite system of equations. The truncated system of equations must include at least every propagation mode of each port to achieve numerical accuracy.

The scattered fields for $y\leqslant -g/2$ and $y\geqslant g/2$ are obtained with a residue calculus.

$$\Phi^{\mathrm{I}}\left(x,y\geqslant\frac{g}{2},z\right)=\sum_{u=0}\sum_{m=0}K_{um}^{+}\cos(a_u x)\cos(b_m z)e^{i\beta_{um}y}, \tag{21}$$

$$\Phi^{\mathrm{I}}\left(x,y\leqslant-\frac{g}{2},z\right)=\sum_{u=0}\sum_{m=0}K_{um}^{-}\cos(a_u x)\cos(b_m z)e^{-i\beta_{um}y}, \tag{22}$$

where

$$K_{um}^{\pm}=\mp\sum_{q=0}^{\infty}\left[a_{uq}e^{i\xi_{uq}b}-e^{-i\xi_{\beta_3}b}\delta_{u\phi}\delta_{q\tau}\right]\times\frac{i\xi_{uq}F_q^w(\mp\beta_{um})}{b\varepsilon_m(-1)^m}$$
$$\mp\sum_{p=0}^{\infty}\left[b_{pm}e^{i\gamma_{pm}a}-e^{-i\beta_4 a}\delta_{p\psi}\delta_{m\chi}\right]\times\frac{i\gamma_{pm}F_p^g(\mp\beta_{um})}{a\varepsilon_u(-1)^u}, \tag{23}$$

$0\leqslant u,0\leqslant m,u,m$: integer.

II. SOFT-SURFACE HYBRID JUNCTION

Consider a hybrid junction in a rectangular waveguide consisting of a soft surface (surface boundary condition: $\Phi=0$) in Fig. 1. An analysis for the soft-surface case is somewhat similar to the hard case considered in the previous section. In region (I) the total field is a sum of the incident and scattered components

$$\Phi_1^i(x,y,z)=\sin(A_1x)\sin(B_1z)e^{i\beta_1 y}, \tag{24}$$

$$\Phi_2^i(x,y,z)=\sin(A_2x)\sin(B_2z)e^{-i\beta_2 y}, \tag{25}$$

$$\Phi^{\mathrm{I}}(x,y,z)=\frac{1}{2\pi}\int_{-\infty}^{\infty}\sum_{m=1}^{\infty}\left[\tilde{A}_m(\zeta)\sin(\kappa_m x)\sin(b_m z)\right.$$
$$\left.+\tilde{B}_m(\zeta)\sin(a_m x)\sin(\eta_m z)\right]e^{-i\zeta y}d\zeta, \tag{26}$$

where $\alpha,\mu,\rho,\nu=1,2,3,\ldots$.

In regions (II) and (III), the incident and transmitted fields are

$$\Phi_3^i(x,y,z)=\sin(A_3x)\sin W_3\left(y+\frac{w}{2}\right)e^{-i\beta_3 z}, \tag{27}$$

$$\Phi^{\mathrm{II}}(x,y,z)=\sum_{p=1}^{\infty}\sum_{q=1}^{\infty}a_{pq}\sin(a_p x)\sin w_q\left(y+\frac{w}{2}\right)e^{i\xi_{pq}z}, \tag{28}$$

$$\Phi_4^i(x,y,z)=\sin G_4\left(y+\frac{g}{2}\right)\sin(B_4z)e^{-i\beta_4 x}, \tag{29}$$

$$\Phi^{\mathrm{III}}(x,y,z)=\sum_{p=1}^{\infty}\sum_{q=1}^{\infty}b_{pq}\sin g_p\left(y+\frac{g}{2}\right)\sin(b_q z)e^{i\gamma_{pq}x}, \tag{30}$$

where $\phi,\tau,\psi,\chi=1,2,3,\ldots$.

Enforcing the pressure-continuity conditions at $z=b$ and $x=a$ gives

$$\tilde{B}_m(\zeta)=\frac{W_3}{\sin(\eta_\phi b)}F_\tau^w(\zeta)e^{-i\beta_3 b}+\sum_{q=1}^{\infty}a_{mq}\frac{w_q}{\sin(\eta_m b)}F_q^w(\zeta)e^{i\xi_{mq}b}, \tag{31}$$

$$\tilde{A}_m(\zeta)=\frac{G_4}{\sin(\kappa_\chi a)}F_\psi^g(\zeta)e^{-i\beta_4 a}+\sum_{p=1}^{\infty}b_{pm}\frac{g_p}{\sin(\kappa_m a)}F_p^g(\zeta)e^{i\gamma_{pm}a}. \tag{32}$$

Enforcing the velocity continuity condition at $z=b$ and $x=a$, respectively,

$$B_1(-1)^{\mu}\frac{a}{2}w_t\delta_{\alpha s}F_t^w(\beta_1)+B_2(-1)^{\nu}\frac{a}{2}w_t\delta_{\rho s}F_t^w(-\beta_2)$$
$$+\frac{a}{2}\delta_{\phi s}e^{-i\beta_3 b}\left(W_3 w_t I_{3\phi\tau t}^{baw}+i\frac{w}{2}\beta_3\delta_{\tau t}\right)$$
$$+(-1)^{\chi+s}a_s B_4 G_4 w_t e^{-i\beta_4 a}I_{4s\chi\psi t}^{gw}$$
$$=\sum_{p=1}^{\infty}\sum_{q=1}^{\infty}\left[a_{pq}\frac{a}{2}\delta_{ps}e^{i\xi_{pq}b}\left(-w_q w_t I_{3pqt}^{baw}+i\frac{w}{2}\xi_{pq}\delta_{qt}\right)\right.$$
$$\left.-b_{pq}(-1)^{q+s}a_s b_q g_p w_t e^{i\gamma_{pq}a}I_{4sqpt}^{gw}\right], \tag{33}$$

$$A_1(-1)^{\alpha}\frac{b}{2}g_n\delta_{\mu h}F_n^g(\beta_1)+A_2(-1)^{\rho}\frac{b}{2}g_n\delta_{\nu h}F_n^g(-\beta_2)$$
$$+(-1)^{\phi+h}A_3 b_h g_n W_3 e^{-i\beta_3 b}I_{4\phi h\tau n}^{wg}$$
$$+\frac{b}{2}\delta_{\chi h}e^{-i\beta_4 a}\left(G_4 g_n I_{3\chi\psi n}^{abg}+i\frac{g}{2}\beta_4\delta_{\psi n}\right)$$
$$=\sum_{p=1}^{\infty}\sum_{q=1}^{\infty}\left[-a_{pq}(-1)^{p+h}a_p b_h g_n w_q e^{i\xi_{pq}b}I_{4phqn}^{wg}\right.$$
$$\left.+b_{pq}\frac{b}{2}\delta_{qh}e^{i\gamma_{pq}a}\left(-g_p g_n I_{3qpn}^{abg}+i\frac{g}{2}\gamma_{pq}\delta_{pn}\right)\right], \tag{34}$$

where $q\neq 0$, $t\neq 0$, $h\neq 0$, $n\neq 0$, and

$$I_{3pqt}^{baw}=\frac{1}{2\pi}\int_{-\infty}^{\infty}\frac{\sqrt{k^2-\zeta^2-a_p^2}}{\tan(b\sqrt{k^2-\zeta^2-a_p^2})}F_q^w(\zeta)F_t^w(-\zeta)d\zeta, \tag{35}$$

$$I_{4sqpt}^{gw}=\frac{1}{2\pi}\int_{-\infty}^{\infty}\frac{1}{\beta_{sq}^2-\zeta^2}F_p^g(\zeta)F_t^w(-\zeta)d\zeta. \tag{36}$$

An evaluation of (35) and (36) is somewhat similar to the one of (19) and (20). The rapidly convergent series for I_{3pqt}^{baw} and I_{4sqpt}^{gw} are in the Appendix. The scattered fields for $y\leqslant -g/2$ and $y\geqslant g/2$ are

$$\Phi^{\mathrm{I}}\left(x,y\geqslant\frac{g}{2},z\right)=\sum_{u=1}\sum_{m=1}K_{um}^{+}\sin(a_u x)\sin(b_m z)e^{i\beta_{um}y}, \tag{37}$$

$$\Phi^{\mathrm{I}}\left(x,y\leqslant-\frac{g}{2},z\right)=\sum_{u=1}\sum_{m=1}K_{um}^{-}\sin(a_u x)\sin(b_m z)e^{-i\beta_{um}y}, \tag{38}$$

where

$$K_{um}^{\pm}=-\sum_{q=1}^{\infty}\left[a_{uq}e^{i\xi_{uq}b}+e^{-i\beta_3 b}\delta_{u\phi}\delta_{q\tau}\right]\times\frac{iw_q b_m F_q^w(\mp\beta_{um})}{b\beta_{um}(-1)^m}$$
$$-\sum_{p=1}^{\infty}\left[b_{pm}e^{i\gamma_{pm}a}+e^{-i\beta_4 a}\delta_{p\psi}\delta_{m\chi}\right]\times\frac{ig_p a_u F_p^g(\mp\beta_{um})}{a\beta_{um}(-1)^u}, \tag{39}$$

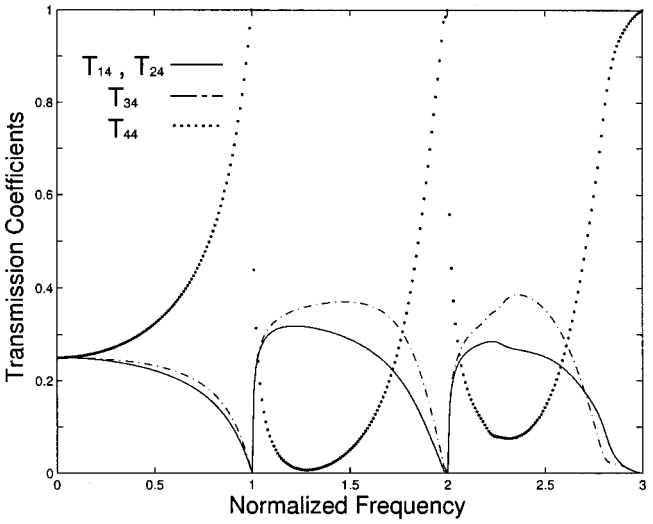

FIG. 2. Behavior of transmission coefficients ($T_{14}, T_{24}, T_{34}, T_{44}$) versus the normalized frequency (ka/π) for the hard-surface hybrid junction ($b/a=1/2$, $g=a$, $w/a=1/2$, $\psi=0$, $\chi=0$).

$0<u,0<m,u,m$: integer.

III. NUMERICAL COMPUTATIONS

The transmission coefficient (T_{ij}) is defined as a ratio of the time-averaged power transmitted through port i to the time-averaged power incident on port j.

$$T_{ij}=\frac{\int \mathrm{Re}[p_i^* v_i]ds_i}{\int \mathrm{Re}[p_j^* v_j]ds_j}, \tag{40}$$

where the acoustic pressure $p_i=i\omega\rho_0\Phi_i$ (ρ_0: constant equilibrium density), the velocity $v_i=\nabla\Phi_i$, and the symbols Re( ) and ( )* denote the real part and the complex conjugate of ( ). In order to check the numerical accuracy of our computation, we plot in Fig. 2 the transmission coefficients of the hard-surface hybrid junction when port 4 is excited with the incident wave [(6), $\psi=0$, $\chi=0$]. We used nine modes in computation to achieve numerical accuracy to better than

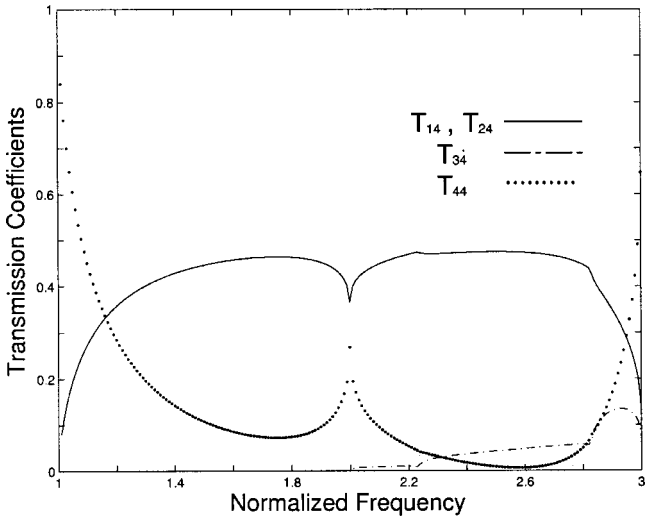

FIG. 3. Behavior of transmission coefficients ($T_{14}, T_{24}, T_{34}, T_{44}$) versus the normalized frequency (ka/π) for the hard-surface hybrid junction ($b/a=1/2$, $g=a$, $w/a=1/2$, $\psi=1$, $\chi=0$).

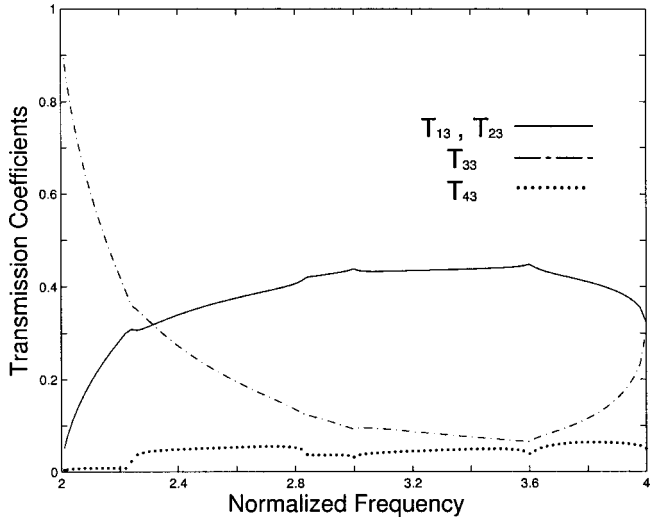

FIG. 4. Behavior of transmission coefficients ($T_{13}, T_{23}, T_{33}, T_{43}$) versus the normalized frequency (ka/π) for the hard-surface hybrid junction ($b/a=1/2$, $g=a$, $w/a=1/2$, $\phi=0$, $\tau=1$).

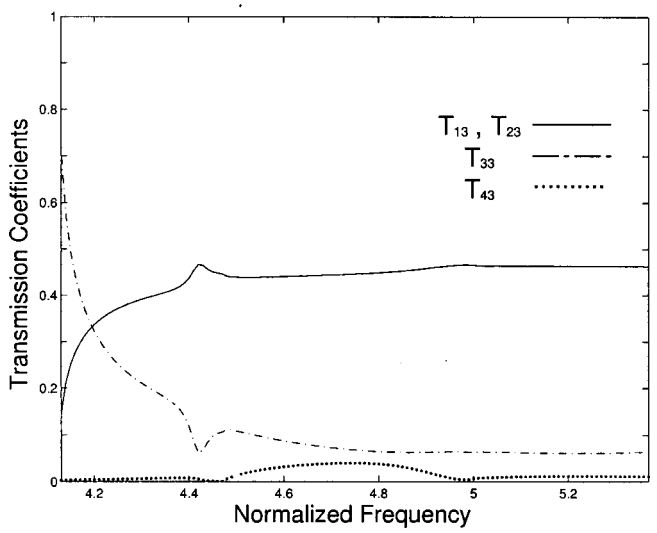

FIG. 5. Behavior of transmission coefficients ($T_{13}, T_{23}, T_{33}, T_{43}$) versus the normalized frequency (ka/π) for the soft-surface hybrid junction ($b/a=1/2$, $g=a$, $w/a=1/2$, $\phi=1$, $\tau=2$).

0.01% error in energy conservation ($T_{14}+T_{24}+T_{34}+T_{44}=1$). The number of the modal coefficients used in (15), (18), (33), and (34) is at least the propagation plus one or two higher evanescent modes to achieve numerical accuracy. This means that the series expression for a_{pq} and b_{pq} is fast convergent and numerically efficient. In Fig. 3, we show the behavior of transmission coefficient versus normalized frequency (ka/π). The field incident on port 4 is assumed to be (6) with $\psi=1$, $\chi=0$. It is interesting to note that ports 4 and 3 are almost decoupled ($T_{34}\simeq 0$) for the normalized frequency from 1 to 2. Above the normalized frequency 2, T_{34} gradually increases due to higher modes generated in port 3. Figure 4 illustrates the transmission coefficients when the incident wave [(4), $\phi=0$, $\tau=1$] impinges on the hard-surface hybrid junction from port 3. It is seen that coupling to port 4 is less than 0.06 over the normalized frequency 2–3.5. T_{33} is shown to be less than 0.1 for the normalized frequency from 3 to 3.7. In Figs. 3 and 4, the acoustic hybrid junction reveals characteristics somewhat similar to the electromagnetic magic-T (hybrid-T) which is widely used as a microwave duplexer due to its decoupling between E and H arms. In Fig. 5 we show the transmission coefficient of the soft-surface hybrid junction when port 3 is excited with an incident wave [(27); $\phi=1$, $\tau=2$]. It is seen that T_{43} is less than 0.05, but T_{33} is less than 0.1 over a frequency range 4.54–5.37. This implies that the soft-surface hybrid junction seems useful as a duplexer as much as the hard-surface hybrid junction considered in Fig. 3.

IV. CONCLUSION

Acoustic scattering from a hybrid junction in a rectangular waveguide is investigated using the Fourier transform and mode-matching technique. The closed-form solutions for the scattered fields are obtained using a residue calculus. Numerical computations are performed to illustrate the scattering behavior of a hybrid junction. The acoustic hybrid junction in a rectangular waveguide is found to have useful decoupling characteristics when its ports are appropriately excited.

APPENDIX

$$I^{baw}_{1pqt}=\frac{w\varepsilon_q\cot(b\sqrt{k^2-w_q^2-a_p^2})}{2\sqrt{k^2-w_q^2-a_p^2}}\,\delta_{qt}-\frac{i}{b}\sum_{v=0}^{\infty}\left.\frac{\zeta[(-1)^{q+t}-(-1)^q e^{i\zeta|w|}-(-1)^t e^{i\zeta|w|}+1]}{\varepsilon_v(\zeta^2-w_q^2)(\zeta^2-w_t^2)}\right|_{\zeta=\sqrt{k^2-a_p^2-b_v^2}}, \tag{A1}$$

$$I^{gw}_{2sqpt}=X_1(\zeta)+\begin{cases} iP_1(\zeta)|_{\zeta=g_p}+iQ_1(\zeta)|_{\zeta=w_t}, & g_p\neq w_t,\\ \left.\dfrac{i}{\varepsilon_p}\dfrac{f_1'(\zeta)s(\zeta)-f_1(\zeta)s'(\zeta)}{s^2(\zeta)}\right|_{\zeta=g_p}, & g_p=w_t, \end{cases} \tag{A2}$$

$$I^{baw}_{3pqt}=\frac{w\sqrt{k^2-w_q^2-a_p^2}}{2w_q^2\tan(b\sqrt{k^2-w_q^2-a_p^2})}\,\delta_{qt}-\frac{i}{b}\sum_{v=1}^{\infty}\left.\frac{(k^2-\zeta^2-a_p^2)[(-1)^{q+t}-(-1)^q e^{i\zeta w}-(-1)^t e^{i\zeta w}+1]}{\zeta(\zeta^2-w_q^2)(\zeta^2-w_t^2)}\right|_{\zeta=\sqrt{k^2-a_p^2-b_v^2}} \tag{A3}$$

$$I^{gw}_{4sqpt} = X_2(\zeta) + \begin{cases} iP_2(\zeta)\big|_{\zeta=g_p} + iQ_2(\zeta)\big|_{\zeta=w_t}, & g_p \neq w_t, \\ i\left.\dfrac{f_2'(\zeta)s(\zeta) - f_2(\zeta)s'(\zeta)}{s^2(\zeta)}\right|_{\zeta=g_p}, & g_p = w_t, \end{cases} \tag{A4}$$

where $(\,)'$ denotes the differentiation and

$$X_j(\zeta) = \left.\frac{-if_j(\zeta)}{(\beta_{sq}+\zeta)(\zeta^2-g_p^2)(\zeta^2-w_t^2)}\right|_{\zeta=\beta_{sq}}, \quad j=1,2, \tag{A5}$$

$$P_j(\zeta) = \frac{f_j(\zeta)}{(\beta_{sq}^2-\zeta^2)(\zeta+g_p)(\zeta^2-w_t^2)}, \tag{A6}$$

$$Q_j(\zeta) = \frac{f_j(\zeta)}{(\beta_{sq}^2-\zeta^2)(\zeta+w_t)(\zeta^2-g_p^2)}, \tag{A7}$$

$$s(\zeta) = \begin{cases} (\beta_{sq}^2-\zeta^2)(\zeta+g_p)^2, & g_p = w_t \neq 0, \\ \beta_{sq}^2-\zeta^2, & g_p = w_t = 0, \end{cases} \tag{A8}$$

$$f_1(\zeta) = \begin{cases} \zeta^2[(-1)^{p+t}e^{i\zeta|g-w|/2} - (-1)^p e^{i\zeta|g+w|/2} - (-1)^t e^{i\zeta|-g-w|/2} + e^{i\zeta|-g+w|/2}] & \text{for } g_p = w_t \neq 0, \\ e^{i\zeta|g-w|/2} - e^{i\zeta|g+w|/2} - e^{i\zeta|-g-w|/2} + e^{i\zeta|-g+w|/2} & \text{for } g_p = w_t = 0, \end{cases} \tag{A9}$$

$$f_2(\zeta) = [(-1)^{p+t}e^{i\zeta|g-w|/2} - (-1)^p e^{i\zeta|g+w|/2} - (-1)^t e^{i\zeta|-g-w|/2} + e^{i\zeta|-g+w|/2}]. \tag{A10}$$

[1] T. Sieverding and F. Arndt, ''Modal analysis of the magic tee,'' IEEE Microwave Guid. Wave Lett. **3**, 150–152 (1993).
[2] J. Y. Kwon, H. H. Park, and H. J. Eom, ''Acoustic scattering from two junctions in a rectangular waveguide,'' J. Acoust. Soc. Am. **103**, 1209–1212 (1998).

A study of the influence of mean flow on the acoustic performance of Herschel–Quincke tubes

A. J. Torregrosa, A. Broatch, and R. Payri
CMT, Departamento de Máquinas y Motores Térmicos, Universidad Politécnica de Valencia, Apartado 22012, E-46071 Valencia, Spain

(Received 15 April 1999; accepted for publication 2 December 1999)

In this paper, a simple flow model is used in order to assess the influence of mean flow and dissipation on the acoustic performance of the classical two-duct Herschel–Quincke tube. First, a transfer matrix is obtained for the system, which depends on the values of the Mach number in the two branches. These Mach numbers are then estimated separately by means of an incompressible flow calculation. Finally, both calculations are used to study the way in which mean flow affects the position and value of the characteristic attenuation and resonances of the system. The results indicate the nontrivial character of the influence observed. © *2000 Acoustical Society of America.* [S0001-4966(00)01903-2]

PACS numbers: 43.20.Mv [DEC]

INTRODUCTION

The Herschel–Quincke tube is a simple implementation of the interference principle with attenuation purposes: two ducts of arbitrary length and section (within reasonable limits) in a parallel arrangement. A thorough study of the acoustics of Herschel–Quincke tubes was presented by Selamet *et al.*,[1] indicating that, removing the classical restriction of equal cross section for both ducts, the attenuation obtained is not limited to narrow spikes, but may be interesting even for automotive exhaust applications, as an alternative to other resonant devices, such as concentric resonators. This is supported by the fact that numerous patents have been proposed which are based on the two-duct or the multiple-duct configurations. A list of these patents may be found in Ref. 2, as well as a complete study of the multiple-duct Herschel–Quincke tube.

Considering the application of the Herschel–Quincke tube to systems such as compressors and the intake and exhaust systems of internal combustion engines, it should be noted that, in all these cases, the effect of the mean flow may not be negligible.[3] Therefore, it is necessary to assess the importance of the effects of mean flow on the acoustic characteristics of the Herschel–Quincke tube. This effect could be particularly interesting, since the flow repartition between the branches depends on the geometry (mainly cross sections and lengths) and therefore each of the branches will be affected in a different way. Hence, not only the behavior of each branch will be modified, but also the interference between the branches, which is the actual attenuation mechanism of the system.

In this paper, the effect of mean flow on the acoustic behavior of a Herschel–Quincke tube is studied for the classical two-duct configuration. The mean flow and the acoustic field are considered to be decoupled, as usual within linear theory. With respect to the acoustics, a transfer matrix with mean flow is obtained which depends explicitly on the geometry and on the Mach number in each branch. These Mach numbers, which are also a function of the geometry, are obtained from a steady flow calculation, so that in the end one has a general expression which is only a function of the geometry and the Mach number in the inlet main duct. This expression is used in order to check the influence of mean flow in cases of interest according to the general no-flow solution, considering both the values of the characteristic frequencies and the attenuation levels achieved. The results show that the influence of mean flow arises in both senses, that is, modifying the attenuation levels, as could be expected, but also changing qualitatively the shape of the attenuation curve.

I. THEORY

In order to evaluate the influence of mean flow on the acoustic behavior of the Herschel–Quincke tube, first an expression for the transfer matrix of a system consisting of two arbitrary interfering branches will be obtained. This will permit the use of the well-known expression of the transfer matrix of a duct with flow[4] to obtain the transfer matrix of the Herschel–Quincke tube, from which the transmission loss will be evaluated. Then, a simple steady flow calculation will be performed in order to determine the Mach number in each branch. Regarding this, it should be noted that, although it is possible to consider an inviscid moving medium when describing the acoustic field inside each of the branches, it is not possible to neglect friction effects when determining the mean flow repartition between them. Therefore, in order to provide a consistent approach to the problem, viscothermal losses and friction effects will be considered in the acoustic description.

A. Acoustics

A general expression for the transfer matrix of a system consisting of an arbitrary number of subsystems connected in parallel is available for the case in which all the systems are reciprocal.[5] This expression could be applied to the *n*-duct Herschel–Quincke tube with no mean flow or dissipation, as considered in Ref. 2. However, when mean flow is present, a duct is no longer symmetrical nor reciprocal,[6] and therefore a

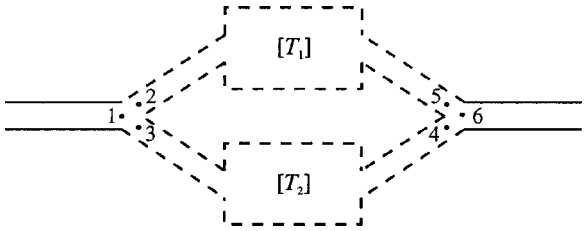

FIG. 1. A general two-branch system.

more general expression must be sought. For brevity, only the case of two branches will be considered here.

Consider a system consisting of two arbitrary branches with common endpoints, as shown in Fig. 1. Assuming one-dimensional propagation, each branch is characterized by its transfer matrix. Denote the transfer matrices of the two branches as $\mathbf{T}_1$ and $\mathbf{T}_2$, with

$$[\mathbf{T}_1]=\begin{bmatrix} A_1 & B_1 \\ C_1 & D_1 \end{bmatrix}; \quad [\mathbf{T}_2]=\begin{bmatrix} A_2 & B_2 \\ C_2 & D_2 \end{bmatrix}. \tag{1}$$

Then, according to the notation in Fig. 1, the state variables at the two ends of each branch are related by

$$\begin{bmatrix} p_3 \\ v_3 \end{bmatrix}=[\mathbf{T}_2]\begin{bmatrix} p_4 \\ v_4 \end{bmatrix}; \quad \begin{bmatrix} p_2 \\ v_2 \end{bmatrix}=[\mathbf{T}_1]\begin{bmatrix} p_5 \\ v_5 \end{bmatrix}, \tag{2}$$

where p is the pressure fluctuation and v is the mass velocity fluctuation. Now, continuity of pressure and mass velocity fluctuations at the junctions gives

$$\begin{aligned} &p_1=p_2=p_3, \quad p_4=p_5=p_6, \\ &v_1=v_2+v_3, \quad v_6=v_4+v_5. \end{aligned} \tag{3}$$

Solving simultaneously Eqs. (2) and (3) yields

$$\begin{bmatrix} p_1 \\ v_1 \end{bmatrix}=\begin{bmatrix} A & B \\ C & D \end{bmatrix}\begin{bmatrix} p_6 \\ v_6 \end{bmatrix}, \tag{4}$$

where the terms of the global transfer matrix are given by

$$\begin{aligned} A&=(A_1B_2+A_2B_1)/(B_1+B_2), \\ B&=B_1B_2/(B_1+B_2), \\ C&=C_1+C_2+(D_2-D_1)(A_1-A_2)/(B_1+B_2), \\ D&=(D_1B_2+D_2B_1)/(B_1+B_2). \end{aligned} \tag{5}$$

Considering the case of the Herschel–Quincke tube, both branches are uniform ducts. The transfer matrix of a duct of cross section S_j and length l_j with mean flow Mach number M_j may be written as[4]

$$\frac{1}{2\tilde{\alpha}_j\vartheta_j}\begin{bmatrix} \tilde{\phi}_j & a_0/\tilde{S}_j \\ \tilde{S}_j/a_0 & \tilde{\phi}_j \end{bmatrix}. \tag{6}$$

Here, a_0 is the speed of sound and $\tilde{S}_j$ is defined as

$$\tilde{S}_j=S_j/[1-i\xi(M_j)/k], \tag{7}$$

where i is the imaginary unit, $k=\omega/a_0$ is the wave number, and $\xi(M_j)$ is the flow-corrected attenuation constant (see Ref. 4 for details), while

$$\tilde{\alpha}_j=\frac{e^{-i\tilde{k}_jl_j}}{1-e^{-2i\tilde{k}_jl_j}}, \quad \tilde{\phi}_j=\frac{1+e^{-2i\tilde{k}_jl_j}}{1-e^{-2i\tilde{k}_jl_j}}, \quad \vartheta_j=e^{iM_j\tilde{k}_jl_j}, \tag{8}$$

where $\tilde{k}_j$ is the flow-corrected wave number given by

$$\tilde{k}_j=[k-i\xi(M_j)]/(1-M_j^2). \tag{9}$$

Incidentally, it can be checked that the determinant of the matrix in Eq. (6) is ϑ_j^{-2}, which is different from unity even in the absence of dissipation, indicating the nonreciprocal character of the uniform duct with flow.

Upon substitution of Eq. (6) into Eq. (5), the transfer matrix for the Herschel–Quincke tube with flow is obtained as

$$\begin{aligned} A&=\frac{\tilde{S}_1\tilde{\phi}_1+\tilde{S}_2\tilde{\phi}_2}{2(\tilde{S}_1\tilde{\alpha}_1\vartheta_1+\tilde{S}_2\tilde{\alpha}_2\vartheta_2)}=D, \\ B&=\frac{a_0}{2(\tilde{S}_1\tilde{\alpha}_1\vartheta_1+\tilde{S}_2\tilde{\alpha}_2\vartheta_2)}, \\ C&=\frac{\tilde{S}_1\tilde{S}_2}{2a_0\tilde{\alpha}_1\vartheta_1\tilde{\alpha}_2\vartheta_2}\left[\frac{\tilde{\alpha}_1\vartheta_1}{\tilde{S}_1}+\frac{\tilde{\alpha}_2\vartheta_2}{\tilde{S}_2}\right. \\ &\quad \left.-\frac{(\tilde{\alpha}_2\vartheta_2\tilde{\phi}_1-\tilde{\alpha}_1\vartheta_1\tilde{\phi}_2)^2}{\tilde{S}_1\tilde{\alpha}_1\vartheta_1+\tilde{S}_2\tilde{\alpha}_2\vartheta_2}\right]. \end{aligned} \tag{10}$$

Now, the transmission loss of the system, assuming that the areas of the inlet and outlet ducts are the same and equal to S_0, is given by

$$\mathrm{TL}=20\log_{10}\left|\frac{1}{2}\left[A+\frac{S_0}{a_0}B+\frac{a_0}{S_0}C+D\right]\right|. \tag{11}$$

Combining Eqs. (10) and (11), and after some algebra, one obtains

$$\mathrm{TL}=20\log_{10}\left|\frac{(S_0+\tilde{S}_1\tilde{\phi}_1+\tilde{S}_2\tilde{\phi}_2)^2}{4S_0(\tilde{S}_1\tilde{\alpha}_1\vartheta_1+\tilde{S}_2\tilde{\alpha}_2\vartheta_2)}\right. \\ \left.-\frac{(\tilde{S}_1\tilde{\alpha}_1+\tilde{S}_2\tilde{\alpha}_2)^2+\tilde{S}_1\tilde{\alpha}_1\tilde{S}_2\tilde{\alpha}_2(\vartheta_1-\vartheta_2)^2/(\vartheta_1\vartheta_2)}{S_0(\tilde{S}_1\tilde{\alpha}_1\vartheta_1+\tilde{S}_2\tilde{\alpha}_2\vartheta_2)}\right|. \tag{12}$$

For the particular case of zero mean flow and no losses [$M=0$ and $\xi(M)=0$], one has $\tilde{S}_j=S_j$ and $\tilde{k}_j=k$, so that Eqs. (8) reduce to

$$\tilde{\alpha}_j=\frac{e^{-ikl_j}}{1-e^{-2ikl_j}}\equiv\alpha_j, \quad \tilde{\phi}_j=\frac{1+e^{-2ikl_j}}{1-e^{-2ikl_j}}\equiv\phi_j, \quad \vartheta_j=1 \tag{13}$$

for $j=1,2$, and substitution into Eq. (12) yields

$$\mathrm{TL}=20\log_{10}\left|-\frac{S_1\alpha_1+S_2\alpha_2}{S_0}+\frac{(S_0+S_1\phi_1+S_2\phi_2)^2}{4S_0(S_1\alpha_1+S_2\alpha_2)}\right|, \tag{14}$$

that is, the same expression obtained in Ref. 1, which will be used later for comparison and analysis purposes.

B. Mean flow

Now the calculation of the Mach number in the two branches of the Herschel–Quincke tube for a given Mach number in the main duct will be addressed. Consistently with the consideration of the mean flow in the foregoing acoustic description, the simple approach of incompressible mean flow will be adopted in the following. In this way, a simple parallel flow problem must be solved.

The conditions to be satisfied are (i) equality of pressure drop across the two branches and (ii) conservation of mass. Regarding the first condition, it should be noted that the pressure drop of each branch depends on the geometrical details of the junction, and so will the flow repartition between the two branches.[7] Therefore, only the case in which the influence of the junction details is the same for both branches will be considered. In this way, since the flow is assumed to be incompressible, this first condition is expressed, making use of the Darcy-Weisbach equation, as

$$\Delta p = \frac{1}{2}\rho \frac{f_1 l_1}{D_1} u_1^2 = \frac{1}{2}\rho \frac{f_2 l_2}{D_2} u_2^2, \tag{15}$$

where D is the diameter and f is the friction factor. Since the temperature is assumed to be the same in both branches, Eq. (15) reduces to

$$(M_1/M_2)^2 = (f_2/f_1)(l_2/l_1)(D_1/D_2). \tag{16}$$

Under the same assumptions, conservation of mass is expressed as

$$M_0 D_0^2 = M_1 D_1^2 + M_2 D_2^2, \tag{17}$$

where subscript 0 makes reference to the main duct. Now, for the Reynolds numbers to be expected one may assume a Blasius-type dependence of the friction factor f on Re,[8] so that

$$(f_2/f_1) = (\mathrm{Re}_1/\mathrm{Re}_2)^{1/4} = [(D_1 M_1)/(D_2 M_2)]^{1/4}, \tag{18}$$

and then from Eqs. (16) and (17) one finally gets

$$M_1 = \frac{M_0 D_0^2}{\Gamma D_1^2 + D_2^2}, \quad M_2 = \frac{M_0 D_0^2 \Gamma}{\Gamma D_1^2 + D_2^2}, \tag{19}$$

with

$$\Gamma = (l_2/l_1)^{4/7}(D_1/D_2)^{5/7}. \tag{20}$$

A first assessment of the eventual importance of the difference between the Mach numbers of the branches is given in Fig. 2, where the ratio $M_1/M_2 = \Gamma^{-1}$ is plotted against the ratio D_1/D_2 for different values of l_2/l_1. As can be seen, considerable differences may be expected for usual design values, so that an additional asymmetry between the two branches is introduced, thus affecting the interference between them.

II. DISCUSSION OF RESULTS

Now, the influence of mean flow on the behavior of the Hershel–Quincke tube will be studied in several relevant cases by comparison with the no-flow results. A simple case in which this influence arises is when $l_1 = l_2$. When no mean flow is present, the transmission loss as given by Eq. (14) for the two-duct configuration reduces to the well-known expression for an expansion chamber with cross-section $S_1 + S_2$; the same applies for the modified n-duct configuration, the equivalent cross-section being now ΣS_i.[2] In the case of mean flow, however, such a simple behavior is not found in general. Actually, the way in which the terms related to mean flow arise makes it impossible to find an expression which is a function only of the addition of the sections of the two branches.

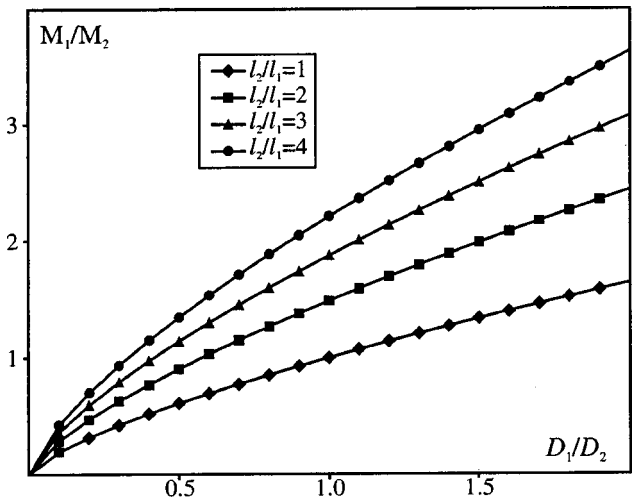

FIG. 2. Influence of geometry on flow repartition.

Only in the case that one has also $D_1 = D_2$, one has $\Gamma = 1$ from Eq. (20), and then Eqs. (19) reduce to

$$M_1 = M_2 = M_0 S_0/(S_1 + S_2), \tag{21}$$

which expresses mass conservation in a simple area change. Equation (21) allows us to set $\tilde{\alpha}_1 = \tilde{\alpha}_2 = \tilde{\alpha}$, $\tilde{\phi}_1 = \tilde{\phi}_2 = \tilde{\phi}$, $\tilde{S}_1 = \tilde{S}_2 = \tilde{S}$ and $\vartheta_1 = \vartheta_2 = \vartheta$, so that from Eq. (12) the transmission loss is given by

$$\mathrm{TL} = 20 \log_{10}\left|\frac{1}{2\tilde{\alpha}\vartheta}\left[\tilde{\phi} + \frac{1}{2}\left(\frac{S_0}{\tilde{S}} + \frac{\tilde{S}}{S_0}\right)\right]\right|, \tag{22}$$

which is the expression which would have been obtained directly from Eqs. (6) and (11). This simple case illustrates the difficulty in performing any analysis from the analytical expression obtained. The main difficulty lies in the fact that, except for the case with $\Gamma = 1$, according to Eq. (9) the complex wave number is different for each branch, $\tilde{k}_1 \neq \tilde{k}_2$, so that the dissipative terms arising from friction cannot be easily handled. Therefore, a parametric study was performed in order to assess the influence of mean flow for different geometrical arrangements and to identify the main features, which were then analyzed on the basis of the analytical solution.

The transmission loss computed from Eq. (12) has been represented as contour plots in order to get a global view of the influence of mean flow. Following the hints given by Selamet *et al.*[1] for the case without flow, both the influence of diameter ratio for given length ratios and the influence of the length ratio for fixed diameter ratio have been explored. First, in Fig. 3 the influence of the mean flow is studied for the case $l_1 = 2l_2$, for values of D_2/D_1 ranging from 0.5 to 2.

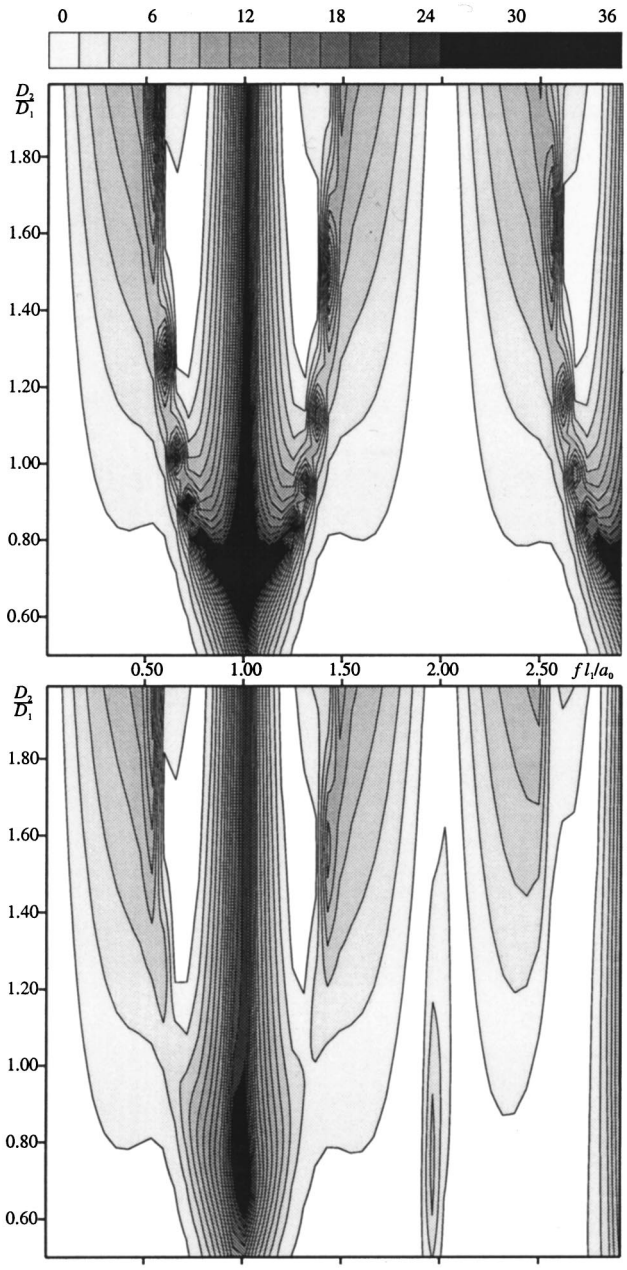

FIG. 3. Transmission loss contours: $l_1=2l_2$. Top: $M=0$; bottom: $M=0.15$.

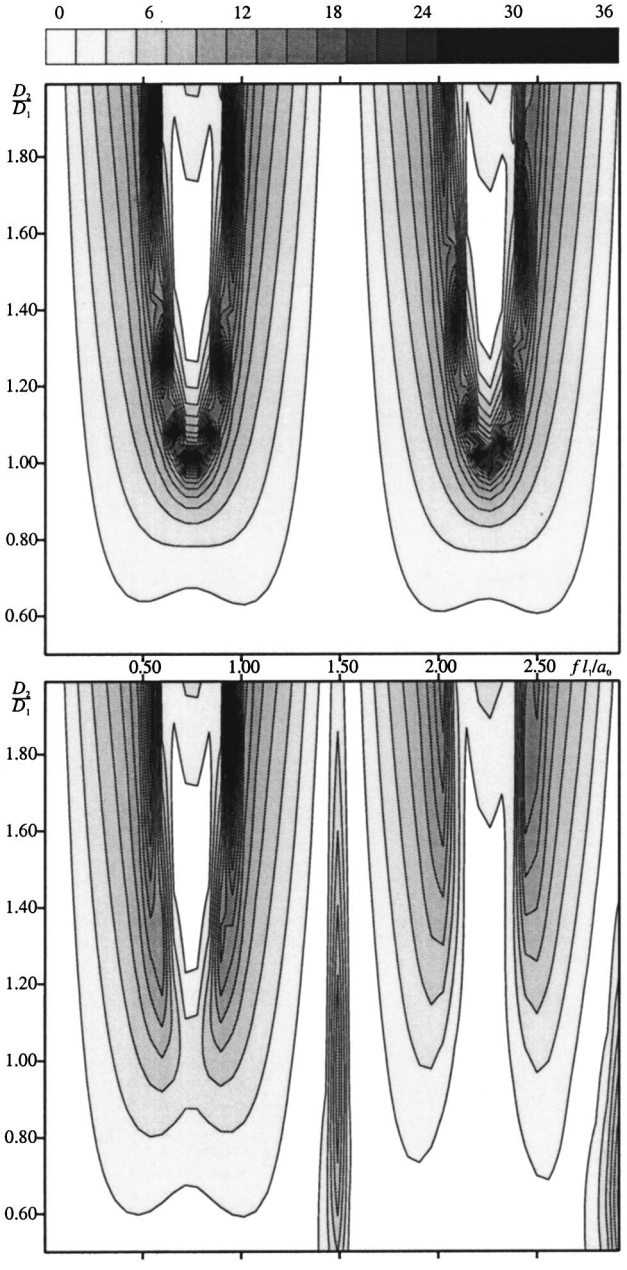

FIG. 4. Transmission loss contours: $l_1=3l_2$. Top: $M=0$; bottom: $M=0.15$.

This range of variation may be considered reasonable, bearing in mind the hypothesis that the details of the junction should not affect the flow repartition. When observing the plots, it is clear that, although the main trends seem not to be affected by the presence of the mean flow, several interesting features appear. First, it can be seen that the main resonance spike occurring at $fl_1/a_0=1$ for $M=0$ is also present for $M\neq 0$, though with a small shift in frequency due to the effect of the difference in Mach number between the branches. In fact, for diameter ratios above 1.5 only quantitative differences are observed for $fl_1/a_0<2$. For lower diameter ratios, however, it can be seen that, while for $M=0$ there appear secondary attenuation spikes around the main resonance, these secondary spikes do not appear for $M\neq 0$.

The second issue to note is the resonance spike appearing for $M\neq 0$ near $fl_1/a_0=2$ for diameter ratios below 1.5, while near this frequency the attenuation with $M=0$ is almost null regardless of the diameter ratio. These attenuation spikes appear approximately at

$$f=ma_0/(l_1-l_2), \quad m=1,2,\ldots . \tag{23}$$

For frequencies above the first occurrence ($m=1$), moreover, the influence of mean flow is more evident, except for the highest values considered of the diameter ratio.

In the case $l_1=3l_2$, represented in Fig. 4, similar features are observed. Now, the attenuation without flow exhibits a two-spike pattern for $D_2/D_1>1$, with higher spikes at precise values of the diameter ratio, and a clear single spike for $D_2/D_1=1$. With some quantitative differences, the mean flow preserves this two-spike pattern, but inhibits the appearance of the single spike for $D_2/D_1=1$, while giving rise to additional attenuation spikes at the frequencies defined by

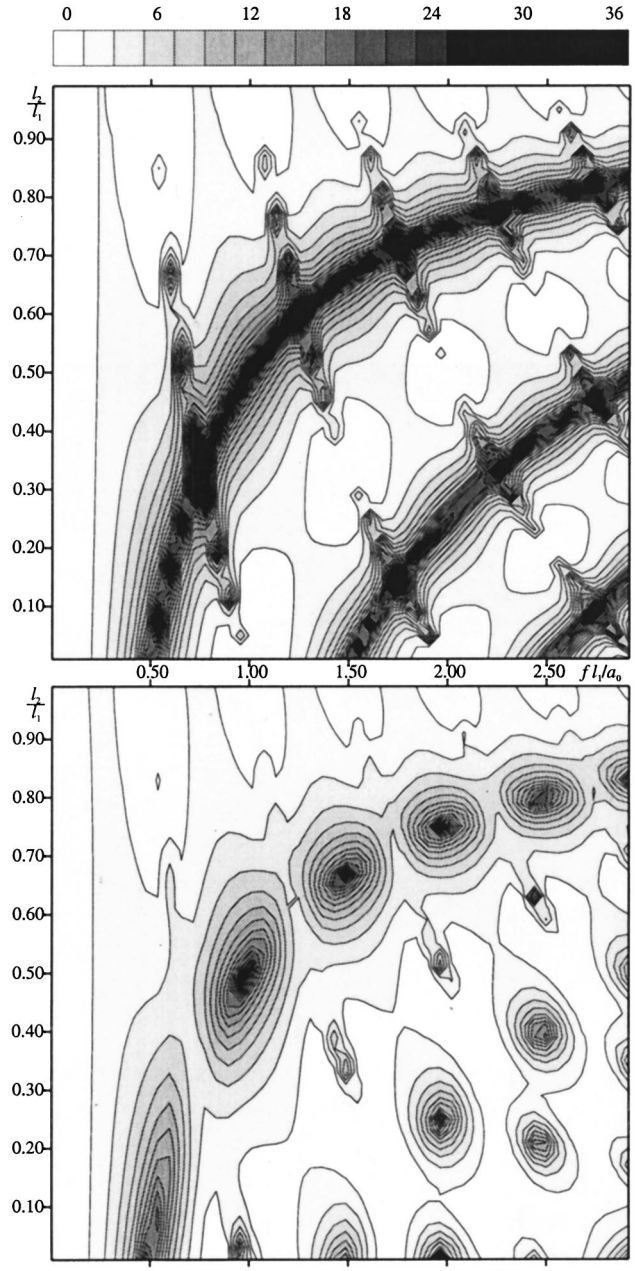

FIG. 5. Transmission loss contours: $D_1=D_2=D_0$. Top: $M=0$; bottom: $M=0.15$.

Eq. (23). Again, for frequencies above the first occurrence ($m=1$) the differences due to the presence of the flow are more apparent.

Obviously, it is not easy to find a general justification of the behavior observed. A case which is particularly well studied in the case without flow[1] is the equal-area arrangement, $S_1=S_2$, which, according to the results commented above, gives a good illustration of all the relevant facts associated with the presence of mean flow. This case is the one represented in Fig. 5, where now transmission loss contours are plotted for different length ratios. The results without mean flow illustrate the concept established by Selamet *et al.*[1] related to the existence of two different types of resonances: the attenuation spikes corresponding to the first type lie on the curve

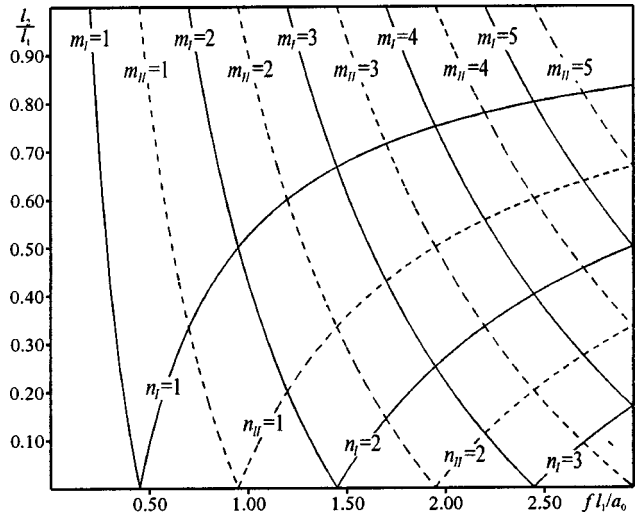

FIG. 6. Location of attenuation spikes for $D_1=D_2$: first type (solid) and second type (dashed) resonances.

$$l_2/l_1=1-(n-\tfrac{1}{2})/(fl_1/a_0), \quad n=1,2,\ldots, \tag{24}$$

while those corresponding to the second type lie on the curve

$$l_2/l_1=m/(fl_1/a_0)-1, \quad m=1,2,\ldots. \tag{25}$$

Anyway, there is a clear difference between the two types, since Eq. (24) leads always to a relatively high attenuation, while this is not the case with Eq. (25). Actually, the intersections of Eq. (25) with the curve defined by Eq. (23), that is,

$$l_2/l_1=1-m/(fl_1/a_0), \quad m=1,2,\ldots, \tag{26}$$

correspond to a null attenuation. This difference is even more clear when mean flow is considered, since it affects each type of resonance in a different way, as discussed in the following. It can be observed from Fig. 5 that, in a general sense, the attenuation patterns with mean flow are also determined (only approximately in this case) by Eqs. (24)–(26). Within this approximation, one can state that in the presence of flow the resonances of the first type result in an attenuation spike only if

$$l_2/l_1=1-(n_I-\tfrac{1}{2})/(fl_1/a_0)=(m_I-\tfrac{1}{2})/(fl_1/a_0)-1, \quad n_I,m_I=1,2,\ldots, \tag{27}$$

and hence the attenuation spikes are obtained for frequencies such that

$$fl_1/a_0=(n_I+m_I-1)/2, \quad n_I,m_I=1,2,\ldots. \tag{28}$$

The condition for the resonances of the second type is

$$l_2/l_1=1-n_{II}/(fl_1/a_0)=m_{II}/(fl_1/a_0)-1, \quad n_{II},m_{II}=1,2,\ldots, \tag{29}$$

and the attenuation frequencies are given by

$$fl_1/a_0=(n_{II}+m_{II})/2, \quad n_{II},m_{II}=1,2,\ldots. \tag{30}$$

Equations (27)–(30) provide a simple way to choose, in the case considered of equal branch sections, the values of the length ratio l_2/l_1 which produce a resonance at a given frequency of interest. In Fig. 6 the curves defined by these

equations for different values of n and m are represented, and comparison with Fig. 5 indicates that in general the best attenuation behavior for a given frequency is obtained from a resonance of the first type with $n_I=1$. Anyway, the behavior at other frequencies may also determine the best choice. For instance, for $fl_1/a_0 \sim 2.5$, one may choose four different values of l_2/l_1, corresponding to the resonances defined by $(n_I=1, m_I=5)$, $(n_I=2, m_I=4)$, $(n_{II}=1, m_{II}=4)$ and $(n_{II}=2, m_{II}=3)$. In all the cases, apart from the frequency of interest, one obtains attenuation at other frequencies which depend on the values of n and m chosen. Therefore, the final choice may be determined by the possibility to exploit these additional features in the attenuation curve, and thus no general rule may be given.

III. CONCLUSIONS

The potential applications of Herschel–Quincke tubes to duct systems with mean flow require that the effect of mean flow on the acoustic performance is assessed. With this purpose, a transfer matrix for the Herschel–Quincke tube with mean flow has been derived, which depends on the values of the Mach number in each branch. This matrix has been supplemented by a decoupled steady flow calculation which, under certain assumptions regarding the geometry of the junctions, allows us to compute the flow repartition between the branches and hence the respective Mach numbers. The combined results of the flow and the acoustic calculations have been used to explore the influence of mean flow on the transmission loss. In view of the difficulties of a purely analytical approach, a parametric study has been performed following the hints obtained from previously published work on the case without flow. From this study, it has been possible to obtain, by comparison with the results without flow, an assessment of the influence of mean flow, mainly in terms of the position of attenuation spikes. Finally, some guidelines about the behavior to be expected for the equal branch section case have been obtained.

ACKNOWLEDGMENTS

This work has been supported by CICYT through Project No. TAP97-1270-C02-01.

[1] A. Selamet, N. S. Dickey, and J. M. Novak, ''The Herschel–Quincke tube: A theoretical, computational, and experimental investigation,'' J. Acoust. Soc. Am. **96**, 3177–3185 (1994).
[2] A. Selamet and V. Easwaran, ''Modified Herschel–Quincke tube: Attenuation and resonance for *n*-duct configuration,'' J. Acoust. Soc. Am. **102**, 164–169 (1997).
[3] P. O. A. L. Davies, ''Practical flow duct acoustics,'' J. Sound Vib. **124**, 91–115 (1988).
[4] M. L. Munjal, *Acoustics of Ducts and Mufflers* (Wiley, New York, 1987).
[5] J. Y. Ha and K. J. Kim, ''Analysis of MIMO mechanical systems using the vectorial four pole parameter method,'' J. Sound Vib. **180**, 333–350 (1995).
[6] V. H. Gupta, ''On independence of reciprocity, symmetry and conservativeness of one-dimensional linear systems,'' J. Sound Vib. **179**, 547–552 (1995).
[7] F. Payri, A. J. Torregrosa, and A. Broatch, ''Pressure loss characterisation of perforated ducts,'' SAE Paper 980282.
[8] A. J. Ward-Smith, *Internal Fluid Flow* (Clarendon, Oxford, 1980).

Physical source realization of complex source pulsed beams

Ehud Heyman[a] and Vitality Lomakin
Department of Electrical Engineering-Physical Electronics, Tel-Aviv University, Tel-Aviv 69978, Israel

Gerald Kaiser[b]
The Virginia Center for Signals and Waves, 1921 Kings Road, Glen Allen, Virginia 23060

(Received 24 June 1999; accepted for publication 21 December 1999)

Complex source pulsed beams (CSPB) are exact wave-packet solutions of the time-dependent wave equation that are modeled mathematically in terms of radiation from a pulsed point source located at a complex space–time coordinate. In the present paper, the physical source realization of the CSPB is explored. This is done in the framework of the acoustic field, as a concrete physical example, but a similar analysis can be applied for electromagnetic CSPB. The physical realization of the CSPB is addressed by deriving exact expressions for the acoustic source distribution in the real coordinate space that generates the CSPB, and by exploring the power and energy flux near these sources. The exact source distribution is of finite support. Special emphasis is placed on deriving simplified source functions and parametrization for the special case where the CSPB are well collimated. © *2000 Acoustical Society of America.* [S0001-4966(00)00804-3]

PACS numbers: 43.20.Px, 43.20.Bi, 41.20.Jb, 03.50.−z [ANN]

INTRODUCTION

Complex source pulsed beams (CSPB) [also termed pulsed beams (PB) or isodiffracting PB] are exact wave-packet solutions of the time-dependent wave equation that can be modeled mathematically in terms of radiation from a pulsed point source located at a complex space–time coordinate.[1–3] Their properties, namely their direction, collimation, and space–time width, are determined by the complex source coordinates. Physically, however, these solutions are generated by physical source distributions (derived in this paper); hence, the complex source model may be considered as a mathematical trick to obtain compact field solutions due to these source distributions. This complex source approach has been originally introduced in the context of time-harmonic fields.[4–7] Another approach to derive the CSPB has been derived independently in Ref. 8.

The CSPB have many properties that make them favorable wave objects within a general wave-based approach for forward and inverse problems:

(1) They are convenient wavelets for high-resolution probing of the propagation environment, and may be used to selectively excite local scattering and diffraction phenomena (see items 2 and 4 below).
(2) They provide benchmark solutions for scattering of collimated wave packets by canonical configurations,[9–11] for propagation in inhomogeneous media,[12,13] in dispersive media,[14–16] and in random media,[17,18] or can used to model practical systems involving collimated short-pulse fields.[19–22]
(3) They furnish a complete basis for local observable-based spectral synthesis of general transient fields, providing *a priori* localization (since only those PB propagators that pass near the space–time observation point need to be accounted for). Several expansion schemes which apply to different source configurations have been derived in Refs. 23–28.
(4) Finally, in view of these properties the CSPB are well-suited to wave-based data processing and local inverse scattering.[29,30]

The *space–time localization* described above provides a systematic wave-based approach for dealing with global complexity. Concentrating on localized solutions permits the use of specific well-defined ''simpler'' problems from which global solutions are assembled. The CSPBs not only provide simple local wave solutions, but may also be directed in space–time to interrogate a particular subenvironment or wave phenomenon in the global conglomerate.

Other classes of wave-packet solutions *in free space* have been introduced in various disciplines. The basic ones are: solutions based on Brittingham's ''focus wave modes,'' [31–34] ''nondiffracting beams'' or ''*X*-waves'' [35,36] and ''bullet''-type solutions.[37,38] These solutions have not yet been utilized in a full ''wave-based architecture'' as described above.

As has been pointed out previously, the CSPB can be generated by a finite distribution of *physical sources*.[2] Our aim in the present paper is to explore this physical source realization. This is done here within the framework of the acoustic field which provides a concrete physical example, but a similar analysis can be applied for electromagnetic CSPB. The physical realization of the CSPB is addressed by deriving expressions for the acoustic source distributions and by exploring the power and energy flux around these sources. The finite support source functions obtained give rise to the *globally exact* CSPB. Yet, from a practical point of view, as discussed in the preceding paragraph, special emphasis is given to the parameter range where the CSPB are well collimated so that they maintain their localized wave-packet structure while propagating in the ambient en-

[a]Electronic mail: heyman@eng.tau.ac.il
[b]Electronic mail: kaiser@wavelets.com

vironment. In this special case the CSPB can be realized effectively by a truncated source distribution whose spatial support is much smaller than that of the exact CSPB. The collimated PB fields generated by the truncated aperture resemble the exact CSPB near the beam axis, but deviate from it in far off-axis region, where they are both negligible anyway.

The presentation starts with a brief summary of the relevant acoustic field equations (Sec. I) and of the basic properties of the CSPB (Sec. II). The physical realization is then explored in Sec. III from the point of view of the power and energy flow. The expressions for the source distributions are then derived in Secs. IV and V, starting with the formulation of general schemes for constructing source realizations and then applying them to calculate the CSPB sources. The presentation ends with a summary and conclusions.

I. ACOUSTIC FIELDS AND SOURCES

The linear acoustic equations for the pressure field $p(\mathbf{r},t)$ and velocity field $\mathbf{v}(\mathbf{r},t)$ at the space–time point $\mathbf{r}=(x,y,z)\in\mathbb{R}^3$ and time $t\in\mathbb{R}$ are

$$\frac{1}{c^2\varrho}\partial_t p+\nabla\cdot\mathbf{v}=\sigma, \tag{1.1a}$$

$$\varrho\,\partial_t\mathbf{v}+\nabla p=\mathbf{f}, \tag{1.1b}$$

where $\sigma(\mathbf{r},t)$ and $\mathbf{f}(\mathbf{r},t)$ represent the scalar particle injection source distribution and the force distribution, respectively. Here, $c=1/\sqrt{\kappa\varrho}$ is the wave speed in the medium, with κ and ϱ being the compressibility and density, respectively. In this paper we consider radiation in a uniform medium and, without loss of generality, we assume that $\varrho=1$. Henceforth, we use boldface type to denote vector constituents and a $\circ$ over a vector to denote a unit vector.

Assuming sources bounded in a volume V of finite support, the integral solution of (1.1) is

$$p=\int_V d^3\,\tau'\frac{1}{4\pi R}\left[[\dot\sigma]+\frac{1}{c}[\dot{\mathbf{f}}]\cdot\mathring{\mathbf{R}}+\frac{1}{R}[\mathbf{f}]\cdot\right], \tag{1.2}$$

where $\mathbf{R}=\mathbf{r}-\mathbf{r}'=R\mathring{\mathbf{R}}$ and $[F]$ denotes the retarded value $F(\mathbf{r}',t')|_{t'=t-R/c}$ for any function $F(\mathbf{r}',t')$. Here and henceforth, overdots and overcircles denote time derivatives and unite vectors, respectively. The solution for $\mathbf{v}$ is readily inferred from p.

II. COMPLEX SOURCE PULSED BEAMS (CSPB)

A. The complex source coordinates

Let the source in (1.1) be

$$\mathbf{f}=0,\quad \dot\sigma=4\pi\delta(\mathbf{r}-\mathbf{r}')\psi(t-t'), \tag{2.1}$$

where $\mathbf{r}'\in\mathbb{R}^3$ and $t'\in\mathbb{R}$ define the space–time source coordinates and ψ is a given time signal. From (1.2), the solution is

$$p(\mathbf{r},t)=\psi(t-t'-R/c)/R. \tag{2.2}$$

The CSPB is modeled analytically by extending the source coordinates $(\mathbf{r}',t')$ in (2.1) into the complex domain. These coordinates may be expressed in general as

$$\mathbf{r}'=\mathbf{r}_0+i\mathbf{b},\quad |\mathbf{b}|=b, \tag{2.3a}$$

$$t'=t'_r+it'_i,\quad t'_i\geqslant b/c, \tag{2.3b}$$

where $\mathbf{r}_0$ is a *real* coordinate point that defines the center of the beam waist, $\mathbf{b}$ is a *real* vector that defines the beam direction, and $b>0$ is a constant which is interpreted as the collimation distance of the beam [see the discussion after (2.19)]. The condition on t'_i in (2.3b) will be explained after (2.13). Without loss of generality, we shall assume henceforth that

$$\mathbf{r}_0=0\ \text{ and }\ \mathbf{b}=\mathring{\mathbf{z}}b,\ \text{ i.e.,}\quad \mathbf{r}'=(0,0,ib), \tag{2.4a}$$

$$t'=ib/c. \tag{2.4b}$$

B. Properties of the complex distance $s(\mathbf{r})$

In order to extend (2.2) to the complex source case, we must first extend the definition of the distance R of the observer from the source. We define this distance as

$$s(\mathbf{r})\equiv\sqrt{(x-x')^2+(y-y')^2+(z-z')}, \tag{2.5a}$$

$$=\sqrt{\rho^2+(z-ib)^2}, \tag{2.5b}$$

$$=s_r+is_i, \tag{2.5c}$$

where (2.5a) is the general definition while (2.5b) corresponds to the special choice of the complex source coordinates in (2.4a), with $\rho=\sqrt{x^2+y^2}$. The branch of the complex root in (2.5) is chosen with

$$\mathrm{Re}\,s>0. \tag{2.6}$$

This choice implies that $s\to r$ as $b/r\to 0$ [see (2.21)]. Other properties of s will be discussed next, where without loss of generality we consider the choice of $(\mathbf{r}',t')$ in (2.4).

The set of branch points of s in $\mathbb{R}^3$ is the circle $\mathcal{B}$ in the $z=0$ plane, defined by $\sqrt{x^2+y^2}=b$. In order for $s(\mathbf{r})$ to be a single-valued function of $\mathbf{r}$, we choose a branch cut in $\mathbb{R}^3$. The choice implied by (2.6) is a flat disk (Fig. 1)

$$\mathcal{E}_0=\{\mathbf{r}:x^2+y^2\leqslant b^2,z=0\}, \tag{2.7}$$

although any continuous deformation of $\mathcal{E}_0$ leaving its boundary $\mathcal{B}$ invariant will do the same.

The real and imaginary parts of $s=s_r+is_i$ have distinct physical roles. They can also be used as the natural coordinate system for the CSPB. For a given point $\mathbf{r}\in\mathbb{R}^3$, one finds

$$(\rho,z)=b^{-1}(\sqrt{b^2+s_r^2}\sqrt{b^2-s_i^2},-s_rs_i),$$

$$\text{where}\ \ s_r>0,-b<s_i<b. \tag{2.8}$$

Equation (2.8) defines an oblate spheroidal (OS) system (s_r,s_i,ϕ) with $\phi=\tan^{-1}(y/x)$ (see Fig. 1): The surfaces $s_r=$const are spheroids $\mathcal{E}_{s_r}$

$$\mathcal{E}_{s_r}:\frac{x^2+y^2}{b^2+s_r^2}+\frac{z^2}{s_r^2}=1,\quad s_r>0. \tag{2.9}$$

In the limit $s_r\to 0$, $\mathcal{E}_{s_r}$ shrinks to $\mathcal{E}_0$, whereas for $s_r\gg b$ it tends to a sphere with radius $s_r=r$. Similarly, $s_i=$const. define a family of one-sided hyperboloids $\mathcal{H}_{s_i}$

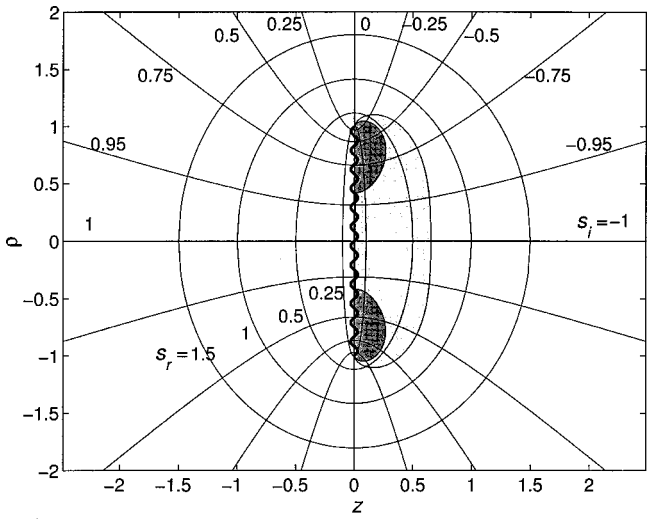

FIG. 1. The oblate spheroidal (OS) coordinate system. The shaded areas are the regions $D_{\text{in}}(\omega)$ defined in (3.16) where the energy flows inward with respect to the OS system. The light- and dark-shaded areas correspond to frequencies $kb=0.7$ and $kb=1.1$, respectively.

$$\mathcal{H}_{s_i}: \frac{x^2+y^2}{b^2-s_i^2}-\frac{z^2}{s_i^2}=1, \quad -b\leqslant s_i\leqslant b. \tag{2.10}$$

These hyperboloids intersect the $z=0$ plane at $\mathcal{E}_0$, and are discontinuous there with

$$s_i\big|_{z=\pm 0}=\mp\sqrt{b^2-\rho^2}. \tag{2.11}$$

For $-b\leqslant s_i\leqslant 0$, $\mathcal{H}_{s_i}$ covers the domain $z>0$: It shrinks to the positive z axis for $s_i=-b$ and as $s_i\to 0$, it tends to the complement of $\mathcal{E}_0$ in the plane $z=0$. For $0\leqslant s_i\leqslant b$, it likewise covers the domain $z<0$.

Other properties of the OS system are mentioned in (2.16), (2.21), and in Appendix B.

C. The CSPB solution

The field due to the complex source in (2.3) is obtained as an analytic extension of the real source solution in (2.2). In order to deal with the complex propagation delays from the complex source coordinate to the real space–time observation point, one should use analytic signals that can accommodate complex time variables (see Appendix A). Henceforth, analytic signals will be denoted by the symbol $+$. The real field is then obtained by taking the real part of the analytic field solution [in fact, one may also take the imaginary part of the analytic field; see discussion after (A3)].

The analytic pressure field at a *real* space–time observation point $(\mathbf{r},t)$, obtained as an analytic extension of (2.2), is given by

$$\overset{+}{p}(\mathbf{r},t)=\overset{+}{\psi}(\tau)/s, \quad \tau=t-\gamma(\mathbf{r}), \tag{2.12}$$

with

$$\gamma=t'+s/c, \tag{2.13a}$$

$$=s_r/c+i(b+s_i)/c=\gamma_r+i\gamma_i, \tag{2.13b}$$

where (2.13b) applies for the choice of t' in (2.4b). The functions $\gamma_{r,i}(\mathbf{r})$ are the *real and imaginary time delays*. Since $-b\leqslant s_i\leqslant b$ [see (2.10)] it follows that $\text{Im}\,\tau\leqslant 0$ for all real $(\mathbf{r},t)$ as required by the analyticity of $\overset{+}{\psi}$. Recalling further that $s(\mathbf{r})$ is continuous everywhere in $\mathbb{R}^3$ except across the disk $\mathcal{E}_0$ [see the discussion in connection with (2.7)], it follows that $\overset{+}{p}$ is an exact homogeneous solution of the time-dependent wave equation everywhere except for $\mathcal{E}_0$, which is henceforth referred to as the ''source disk'' since it represents the location of the *real* sources that give rise to the solution in (2.12) (see Sec. V).

The solution in (2.12) has the general properties of a PB (a collimated space–time wave-packet) that emerges from $\mathbf{r}_0$ (here, the origin) and propagates along the beam axis $\mathbf{b}$ (here, the positive z-axis). Confinement along the beam axis is affected by the pulse shape of $\overset{+}{\psi}$ while transverse confinement is due to the general property of analytic signals which decay in the lower half of the complex τ plane as the imaginary part of τ becomes negative. Thus, the beamwidth depends on: (a) the rate of decay of $\overset{+}{\psi}$ in the lower half of the complex τ plane (that typically depends on the pulse length), and (b) on the rate of increase of $\text{Im}\,\tau$ in (2.13) away from the z axis [following the discussion in (2.10), $\text{Im}\,\tau$ vanishes *on* the positive z axis and increases away from it]. The weakest signal is obtained along the negative z axis where $\text{Im}\,\tau=-2b/c$.

Thus, the ellipsoids $\mathcal{E}_{s_r}$ of (2.9) are the *wavefronts* associated with the time-delay $\gamma_r=s_r/c$, while the hyperboloids $\mathcal{H}_{s_i}$ of (2.10) are *equi-amplitude* surfaces.

1. Parametrization of the real signal

To further understand the properties of the *real* PB field, we introduce the real signal $\psi_{\gamma_i}(t)$ and its Hilbert transform $\overline{\psi}_{\gamma_i}(t)$ via [see (A3)]

$$\overset{+}{\psi}(t-i\gamma_i)=\psi_{\gamma_i}(t)+i\overline{\psi}_{\gamma_i}(t), \quad t\in\mathbb{R}. \tag{2.14}$$

One finds that

$$p=\text{Re}\,\overset{+}{p}=[s_r\psi_{\gamma_i}(t-\gamma_r)+s_i\overline{\psi}_{\gamma_i}(t-\gamma_r)]/|s|^2, \tag{2.15}$$

where from (2.13b) $\gamma_r=s_r/c$ and $\gamma_i=(b+s_i)/c$. Thus, along a given hyperboloid $\mathcal{H}_{s_i}$ [see (2.10)], the signal is gradually Hilbert transformed from $\overline{\psi}_{\gamma_i}(t-\gamma_r)/s_i$ in the near zone, where $s_r\to 0$, to $\psi_{\gamma_i}(t-\gamma_r)/s_r$ in the far zone, where $s_r\sim r\gg b$.

2. Paraxial parametrization for collimated PBs

Points near the positive beam axis, where the PB is strong, are of particular importance. From (2.5b) and (2.6) we have for $\rho\ll\sqrt{z^2+b^2}$,

$$s\simeq+[(z-ib)+\tfrac{1}{2}\rho^2/(z-ib)], \quad z\lesssim 0 \tag{2.16}$$

(note the discontinuity at $\mathcal{E}_0$). Substituting this into (2.12), the field near the positive z axis is given by

$$\overset{+}{p}(\mathbf{r},t)=\overset{+}{\psi}(t-z/c-\tfrac{1}{2}\rho^2/c(z-ib))/(z-ib). \tag{2.17}$$

To parametrize this field, we write $1/(z-ib)=1/R(z)+i/I(z)$, where

$$R(z)=z+b^2/z, \quad I(z)=b(1+(z/b)^2), \tag{2.18}$$

thereby obtaining from (2.13)

$$\gamma_r=z/c+\rho^2/2cR(z), \quad \gamma_i=\rho^2/2cI(z). \tag{2.19}$$

Thus, $R(z)$ is identified as the radius of curvature of the PB wavefront, while $I(z)$ controls the paraxial decay away from the axis. For $z\ll b$, $I(z)$ is to leading order independent of z and the PB propagates essentially without decay or spreading, while for $z\gg b$, $\gamma_i\sim(b/2c)(\rho/z)^2$, and the wave packet diverges along the cones $\rho/z=$const. [see (2.25)].

The *real* PB field along the z axis is given now by

$$p=[z\psi_{\gamma_i}(t-\gamma_r)-b\overline{\psi}_{\gamma_i}(t-\gamma_r)]/[z^2+b^2], \tag{2.20}$$

where $\gamma_{r,i}$ are now given in (2.19). Thus, in the near zone, the real signal is dominated by $-b^{-1}\overline{\psi}_{\gamma_i}(t-\gamma_r)$, but as z increases, it is gradually Hilbert transformed, and finally for $z\gg b$ it is dominated by $z^{-1}\psi_{\gamma_i}(t-\gamma_r)$.

3. Far-field pattern

Another important limit occurs in the far zone for $r\gg b$ where from (2.5b)

$$s\simeq r-ib\cos\theta, \quad \cos\theta=z/r. \tag{2.21}$$

Substituting this into (2.12), we obtain

$$\overset{+}{p}(\mathbf{r},t)=r^{-1}\overset{+}{\psi}(t-r/c-i\gamma_i(\theta)), \quad \gamma_i(\theta)=(1-\cos\theta)b/c. \tag{2.22}$$

The function $\mathrm{Re}\,\psi_+(t-\gamma_i(\theta))$ is the *time-dependent radiation pattern*. It is strongest for $\theta=0$ and decays to a minimum at $\theta=\pi$ [see the diffraction angle Θ in (2.27)].

4. Example: Analytic δ PB

The PB solutions may accommodate any analytic pulse shape. It is useful at this stage to consider an example of a particular pulse shape, namely the n-times differentiated analytic-δ pulse

$$\overset{+}{\psi}(t)=\overset{+}{\delta}{}^{(n)}(t-i\tfrac{1}{2}T)=\frac{(-)^n n!}{\pi i(t-i\frac{1}{2}T)^{n+1}}, \quad T>0. \tag{2.23}$$

It is sometimes convenient to multiply the pulses in (2.23) by $e^{i\alpha}$ with $0\leqslant\alpha<\pi$ in order to change the balance between the signal and its Hilbert transform when one considers the real part of the field.

The parameter T in (2.23) is a measure of the pulse length. The spectrum of these pulses is $\hat{\psi}(\omega)=(-i\omega)^n e^{-\omega T/2}$ for $\omega>0$. The derivatives suppress the low frequencies and thus create a more localized (faster-decaying) PB in both the axial and transversal directions. In many applications, using $n\geqslant 2$ is required because of the higher collimation properties of the resulting PB.[26,30] Furthermore, as will be discussed in Sec. III [see (3.16)], PB with frequency components below $\omega<c/b$ are difficult to excite.

For simplicity, however, we discuss here the PB properties for the case $n=0$ and $\alpha=0$. The real waveforms in (2.14) are given by

$$\psi_{\gamma_i}(t)=\mathrm{Re}\,\overset{+}{\delta}(t-i(\tfrac{1}{2}T+\gamma_i))=\pi^{-1}\frac{\frac{1}{2}T+\gamma_i}{t^2+(\frac{1}{2}T+\gamma_i)^2}, \tag{2.24a}$$

$$\overline{\psi}_{\gamma_i}(t)=\mathrm{Im}\,\overset{+}{\delta}(t-i(\tfrac{1}{2}T+\gamma_i))=-\pi^{-1}\frac{t}{t^2+(\frac{1}{2}T+\gamma_i)^2}. \tag{2.24b}$$

For a given γ_i, the half-amplitude pulse width in (2.24a) is $(T+2\gamma_i)$ and the peak amplitude (at $t=0$) is $\pi^{-1}(\frac{1}{2}T+\gamma_i)^{-1}$. Thus, the waveform is strongest and shortest for $\gamma_i=0$ (the beam axis), and decays as γ_i grows away from the axis. The half-amplitude beamwidth is therefore obtained when $\gamma_i=\frac{1}{2}T$. Substituting (2.19) for γ_i in the paraxial zone, the beam diameter is found to be

$$W(z)=W_0\sqrt{1+(z/b)^2}, \quad W_0=2\sqrt{cTb}. \tag{2.25}$$

One observes that for $0<z<b$ the beamwidth remains essentially constant, while for $z\gg b$ it opens up along a diffraction cone whose angle $\Theta\equiv W(z)/z$ is parametrized by $\Theta=2\sqrt{cT/b}$. Collimated PB with $\Theta\ll 1$ are obtained when

$$cT/b\ll 1. \tag{2.26}$$

Note also that, under this *collimation condition*, the effective width of the source distribution, which is roughly given by W_0 [see (2.25)], is much narrower than the ''exact'' source disk $\mathcal{E}_0$ whose radius is b. One obtains the following rule of thumb for the relation between the pulse length T, the beamwidth at the waist W_0, the diffraction angle Θ, and the collimation distance b

$$(W_0/b)^2=\Theta^2=4cT/b\ll 1. \tag{2.27}$$

Thus, the field properties are controlled by the PB parameter cT/b. Similar properties are obtained for other pulse types, such as nonmodulated or modulated Gaussian pulses or modulated δ pulses.

Figure 2 depicts cross sectional snapshots in the (z,ρ) plane of the axially symmetric p field of (2.12). The pulse used is a differentiated analytic delta pulse $\overset{+}{\psi}(t)=-e^{i\alpha}\overset{+}{\delta}{}^{(1)}(t-i\frac{1}{2}T)$ of type (2.23) and a PB parameter $cT/b=10^{-3}$ that yields a collimated PB [see (2.26)]. (Recall that it is advantageous to deemphasize the low frequencies further by using $\overset{+}{\delta}{}^{(2)}$ and a smaller parameter cT/b.) As mentioned in (2.23), the term $e^{i\alpha}$ is used to change the balance between the signal and its Hilbert transform. Here, α has been chosen to be $\pi/3$, which provides the ''nicest'' result (this value also provides the clearest results of the power flux analysis in Fig. 3).

The field in Fig. 2 is plotted at times $ct/b=0.2$, 1, and 2, where the PB is localized, respectively, in the near zone $z=0.2b$, at the collimation distance $z=b$, and in the ''far'' zone $z=2b$. Note the Hilbert transform exhibited by the waveforms in the transition from the near to the far zones [recall (2.15) and (2.20)]. To demonstrate the effect of the collimation parameter cT/b, we also show in Fig. 2(d) the

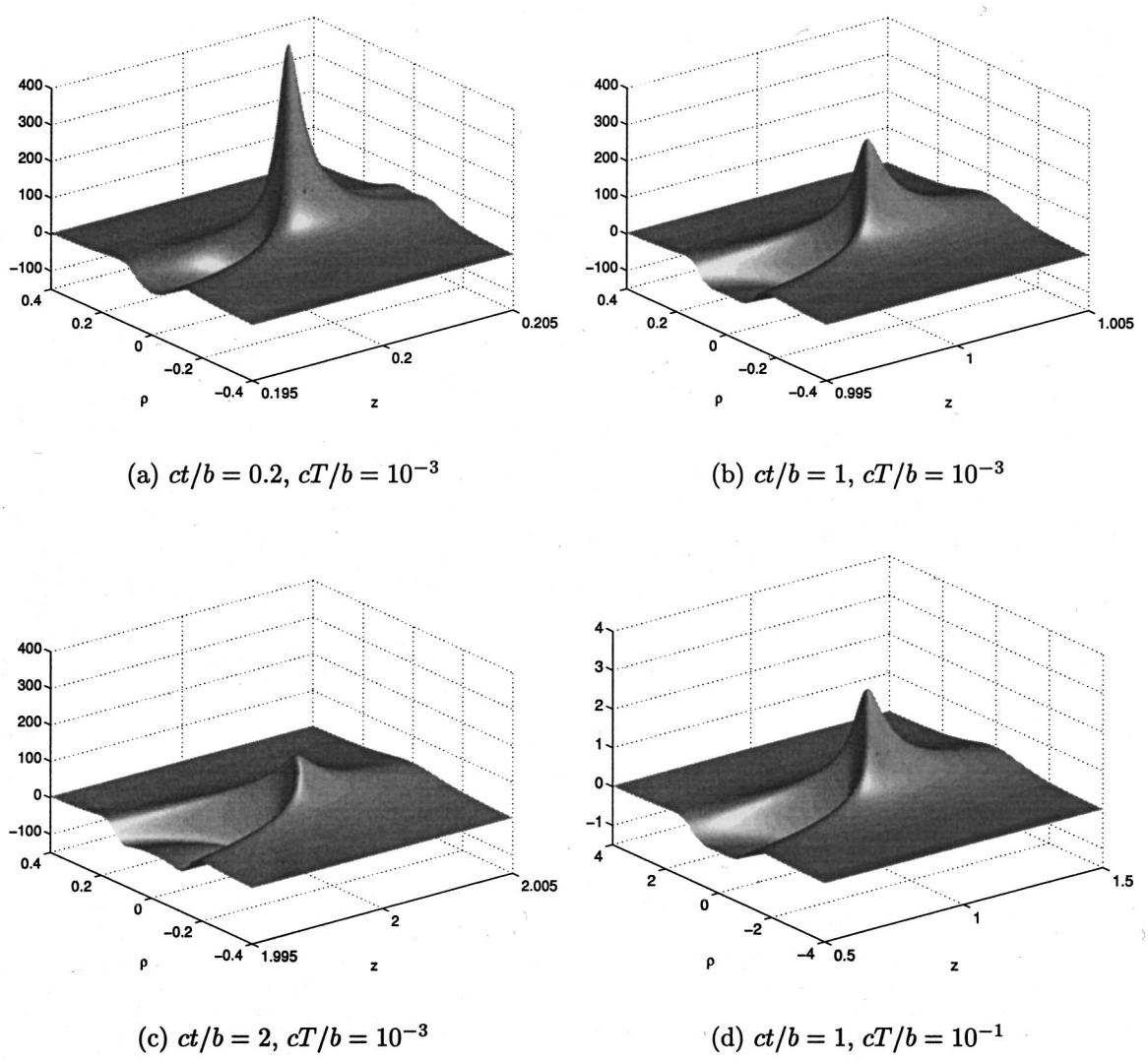

FIG. 2. Snapshots of the p field of (2.12) for a pulse $\overset{+}{\psi}(t) = -e^{i\alpha}\overset{+}{\delta}^{(1)}(t - i\frac{1}{2}T)$ with $\alpha = \pi/3$. The plots show cross-sectional cuts of the axially symmetric field in the (z,ρ) plane where all axes are normalized with respect to b. PB parameter: $cT/b = 10^{-3}$ in subfigures (a)–(c) (collimated PB), and $cT/b = 10^{-1}$ in (d) (noncollimated PB). Observation times: (a) $ct/b = 0.2$ (near zone); (b) $ct/b = 1$ (intermediate zone); (c) $ct/b = 2$ (far zone); (d) $ct/b = 1$.

CSPB field for the parameter $cT/b = 10^{-1}$. In this case the solution in (2.12) is still exact but the parametrization in (2.25)–(2.27) is not valid (note the different space–time and field-amplitude scales used in this case).

III. THE POWER AND ENERGY FLUX

A. The v field

The **v** field is needed in the calculation of the power flux [see (3.7)]. Outside the source domain, **v** is calculated from p of (2.12) via $\mathbf{v} = -\partial_t^{(-1)}\nabla p$, giving

$$\overset{+}{\mathbf{v}}(\mathbf{r},t) = \nabla s\{\overset{+}{\psi}(\tau)/cs + \overset{+}{\psi}^{(-1)}(\tau)/s^2\}, \tag{3.1}$$

$$\nabla s = (\mathbf{r} - i\mathbf{b})/s, \tag{3.2}$$

where $\psi^{(-1)}(t) = \int_{-\infty}^{t} dt'\ \psi(t')$ and τ is defined in (2.13). The real (physical) expression for **v** is [cf. (2.15)]

$$\mathbf{v} = \nabla s_r\{p/c + [(r^2 - b^2)\psi_{\gamma_i}^{(-1)} - 2zb\,\overline{\psi}_{\gamma_i}^{(-1)}]/|s|^4\} - \nabla s_i\{\overline{p}/c + [2zb\,\psi_{\gamma_i}^{(-1)} + (r^2 - b^2)\,\overline{\psi}_{\gamma_i}^{(-1)}]/|s|^4\}, \tag{3.3}$$

where $p = (s_r\psi_{\gamma_i} + s_i\overline{\psi}_{\gamma_i})/c|s|^2$ is the real p field [see (2.15)], the overbars denote Hilbert transforms of the respective waveforms [see (2.14)], and ψ_{γ_i} stands for $\psi_{\gamma_i}(t - \gamma_r)$, etc. Note in (3.3) that ∇s_r represents *outward* power flow lines *normal* to the wavefronts $\mathcal{E}_{s_r}$, while ∇s_i represents *transverse* flow lines along the wavefronts, leading from the positive z axis to the negative z axis. In deriving (3.3) we used the relations in (B1). Expressions for $\nabla s_{r,i}$ are given in (B2)–(B4).

In order to estimate the role of the various terms in (3.1) and (3.3) we assume that ψ is a short pulse with pulse length T, so that near the positive z axis where $\gamma_i \simeq 0$ we have $\overset{+}{\psi}^{(-1)}(\tau)/\overset{+}{\psi}(\tau) \sim O(T)$. Recalling from (2.16) that near the axis $s \simeq z - ib$, we find that the ratio between the second and first terms inside the braces in (3.1) is

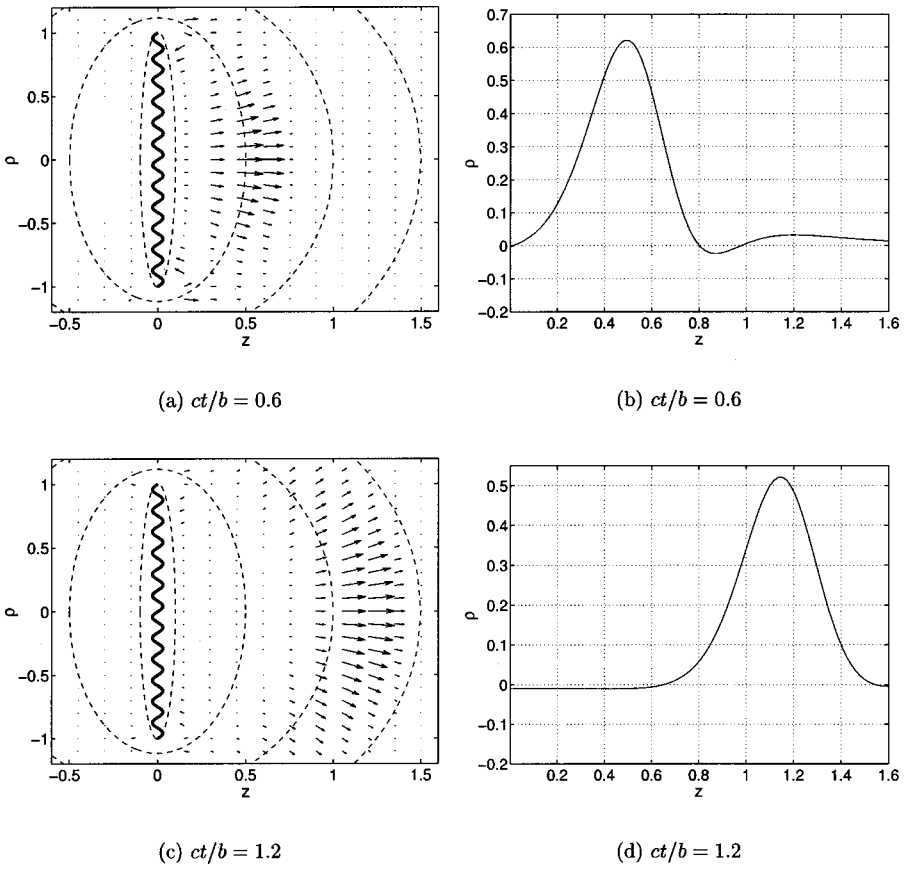

FIG. 3. Snapshots of the power flow **P** at times $ct/b=0.6$ and 1.2. Here, $\overset{+}{\psi}(t)=e^{i\alpha}\overset{+}{\delta}^{(1)}(t-i\frac{1}{2}T)$ as in Fig. 2, but with $cT/b=1.2$ (highly noncollimated PB) and $\alpha=\pi/3$. (a) and (c): Distributions of **P** in the (z,ρ) plane (all axes are normalized with respect to b). For clearer interpretation, the results are superimposed on the ellipsoidal wavefront corresponding to the coordinate system of Fig. 1. The arrows describe the size and direction of **P**. (b) and (d): snapshot of P_z on the z axis at the same times.

$$[\overset{+}{\psi}^{(-1)}(\tau)/s^2]/[\overset{+}{\psi}(\tau)/cs]\sim O[cT/|z-ib|]. \tag{3.4}$$

In the far zone, the ratio on the right-hand side of (3.4) is much smaller than unity. Under the collimation condition $cT\ll b$ in (2.26), this term is much smaller than unity also in the near zone (i.e., along the entire z axis). Under these conditions, the terms containing $\psi^{(-1)}$ in (3.1) may be neglected for all $z>0$ so that (3.3) becomes

$$\mathbf{v}\simeq(\nabla s_r)p/c-(\nabla s_i)\overline{p}/c, \tag{3.5}$$

where p is given by (2.20) for points near the z axis. Note from (2.16) with (2.18) that near the z axis $\nabla s_r\simeq\mathring{\mathbf{z}}+\boldsymbol{\rho}/R(z)\to\mathring{\mathbf{z}}$ and $\nabla s_i\simeq\boldsymbol{\rho}/I(z)\to\mathbf{0}$, where $\boldsymbol{\rho}=(x,y)$. Recall also that ∇s_r is orthogonal to the wavefronts whose local radius of curvature is $R(z)$.

In the far zone, we note from (2.21) that $\nabla s\simeq\nabla s_r\to\mathring{\mathbf{r}}$, hence

$$\mathbf{v}\simeq\mathring{\mathbf{r}}p/c, \tag{3.6}$$

where here p is given in (2.22).

B. The power and energy flux

The power flux is defined as

$$\mathbf{P}(\mathbf{r},t)=p(\mathbf{r},t)\mathbf{v}(\mathbf{r},t). \tag{3.7}$$

The expression obtained by inserting (2.15) and (3.3) is quite complicated. It is therefore convenient to explore the energy flux

$$\mathbf{E}(\mathbf{r})=\int_{-\infty}^{\infty}dt\,\mathbf{P}(\mathbf{r},t). \tag{3.8}$$

One finds that

$$\mathbf{E}(\mathbf{r})=\nabla s_r\|\psi_{\gamma_i}\|^2/c|s|^2+\langle\psi_{\gamma_i},\overline{\psi}_{\gamma_i}^{(-1)}\rangle(s_i\nabla s_r-s_r\nabla s_i)/|s^4|, \tag{3.9}$$

where $\langle f,g\rangle=\int_{-\infty}^{\infty}dt\,f(t)g(t)$ for any two real functions f and g. In deriving (3.9) we used the following relations which apply for any real f and its Hilbert transform $\overline{f}$: $\langle f,f\rangle=\langle\overline{f},\overline{f}\rangle=\|f\|^2$, $\langle f,\overline{f}\rangle=\langle\overline{f},f\rangle=0$, and $\langle f,\dot{f}\rangle=0$ (since f vanishes at $t=\pm\infty$).

In the far zone, the second term in (3.9) vanishes and the outward radiative energy is described only by the first term. Both terms are large in the near zone, in particular near $\mathcal{B}$ where s vanishes, and the field there dominated by strong reactive fields. The concept of *time-dependent reactive field and energy* has been introduced and analyzed in Ref. 39 in the context of electromagnetic fields. Using time-dependent spherical wave (multipole) expansion, it has been shown that the time-dependent power radiated by an antenna consists of radiative and reactive pulses. The radiative power is a *positive outgoing pulse* and is unchanged as it propagates away from the source (carries the same energy). The reactive power pulse, on the other hand, is strong in the near zone and vanishes in the far zone. It carries no net energy: at early times it propagates out and builds up a transient energy near the source, but after the radiative pulse has passed it discharges the energy back to the source region.

This phenomenology is demonstrated in Fig. 3, which depicts snapshots of **P**. In order to be able to discern the off-axis properties of **P** and the low-frequency phenomena discussed in (3.16) below, the PB parameters have been cho-

sen to yield a highly noncollimated field. Specifically, $\overset{+}{\psi}(t)$ is the differentiated analytic δ used in Fig. 2, but with the PB parameter $cT/b=1$. Figure 3(a) and (c) show the distribution of $\mathbf{P}$ in the (z,ρ) plane at times $ct/b=0.6$ and 1, while 3(b) and (d) show plots of P_z along the z axis at the same observation times. Note from Fig. 3(a) and (c) that the flow lines in the near zone deviate from the normal to the wavefronts $\mathcal{E}_{s_r}$ [see, e.g., (3.9)], and in particular the relatively strong ''inward'' flow near $\mathcal{B}$. As discussed in (3.16) below, this inward flow is strong near $\mathcal{B}$, but the low-frequency components propagate inward also in front of the entire source disk $\mathcal{E}_0$ (see the shaded zones in Fig. 1). Indeed, in view of the relatively low-frequency content of the signal $\overset{+}{\psi}$ chosen, the inward flow of reactive energy is readily observed as the negative part of P_z behind the leading part of the signal in Fig. 3(d).

C. Frequency-domain analysis of the energy flow

We shall explore the constituents discussed above in the frequency domain (FD). The FD expressions corresponding to the field solutions in (2.12) and (3.1) are

$$\hat{p}(\mathbf{r},\omega)=\hat{\psi}(\omega)s^{-1}e^{iks+i\omega t'}=\hat{\psi}(\omega)s^{-1}e^{i\omega(\gamma_r+i\gamma_i)}, \tag{3.10a}$$

$$\hat{\mathbf{v}}(\mathbf{r},\omega)=\nabla s[c^{-1}-(i\omega s)^{-1}]\hat{p}(\mathbf{r},\omega), \tag{3.10b}$$

where $k=\omega/c$ and the carets denote field constituents with a suppressed time dependence $e^{-i\omega t}$ with $\omega>0$ (for $\omega<0$, one should take the complex conjugate of these expressions). Here $\hat{\psi}(\omega)$ is the (rather arbitrary) spectrum of the pulse $\psi(t)$. In the high-frequency regime such that $kb\gg1$, the solution in (3.10) has the characteristics of a time-harmonic Gaussian beam (see, e.g., Refs. 4–7 and 2) but we shall not dwell here on this interpretation.

Using (3.10) in conjunction with (3.7) and (3.8), we obtain

$$\begin{aligned}\mathbf{E}(\mathbf{r})&=\frac{1}{\pi}\mathrm{Re}\int_0^\infty d\omega\,\hat{p}(\mathbf{r},\omega)\hat{\mathbf{v}}^*(\mathbf{r},\omega)\\&=\frac{1}{\pi}\mathrm{Re}\int_0^\infty d\omega|\hat{\psi}|^2|s|^{-2}e^{-2\omega\gamma_i}(c^{-1}+(i\omega s^*)^{-1})\nabla s^*,\end{aligned} \tag{3.11}$$

where the asterisks denote a complex conjugate.

Next, we consider the total energy radiated out of the spheroidal wavefront $\mathcal{E}_{s_r}$,

$$E_{\mathrm{rad}}(s_r)=\oint_{\mathcal{E}_{s_r}}\mathbf{E}\cdot d\mathbf{S}, \tag{3.12}$$

where $d\mathbf{S}$ is an area element on $\mathcal{E}_{s_r}$. Substituting (3.11), we note that on $\mathcal{E}_{s_i}$ we have $\nabla s\cdot d\mathbf{S}=|\nabla s_r|dS$, where $|\nabla s_r|$ is given in (B2) and $dS=h_{s_i}h_\phi\,ds_i\,d\phi$, where the metric coefficients are given in (B5). The ϕ-integration yields 2π. Recalling that s_i changes from $-b$ on the positive z axis to b on the negative axis, we end up with

$$E_{\mathrm{rad}}(s_r)=\int_0^\infty d\omega\int_{-b}^{b}ds_i\,E_{s_r}(s_r,s_i,\omega) \tag{3.13a}$$

with

$$E_{s_r}(s_r,s_i,\omega)=\frac{2}{bc}|\hat{\psi}|^2e^{-2k(b+s_i)}\frac{b^2+s_r^2}{s_r^2+s_i^2}\left[1+\frac{s_i/k}{s_r^2+s_i^2}\right]. \tag{3.13b}$$

E_{s_r} is the spectral density of the ''outward'' (i.e., the s_r) component of $\mathbf{E}$.

The s_i integral in (3.13) may readily be evaluated by rewriting (3.13b) in the form

$$E_{s_r}(s_r,s_i,\omega)=\frac{-1}{\omega b}|\hat{\psi}|^2(b^2+s_r^2)\frac{\partial}{\partial s_i}\left[\frac{e^{-2k(b+s_i)}}{s_r^2+s_i^2}\right], \tag{3.14}$$

which provides a closed-form result for the outward flow between any two hyperbolas $\mathcal{H}_{s_i}$. Integrating over the full domain (i.e., from $s_i=-b$ to b), we end up with

$$E_{\mathrm{rad}}=\int_0^\infty d\omega|\hat{\psi}|^2\frac{1-e^{-4kb}}{\omega b}, \tag{3.15}$$

i.e., $E_{\mathrm{rad}}>0$ and is independent of s_r as expected. Note that under the collimation condition in (2.26), most of the signal energy is concentrated in the high-frequency range $kb\gg1$ where the exponent in (3.15) is negligible.

While the *total* energy E_{rad} flows outward, the *local* energy flux E_{s_r} may, in some regions, flow inward. From (3.13b) the region $\mathcal{D}_{\mathrm{in}}(\omega)$ of inward energy flow is described by

$$\mathcal{D}_{\mathrm{in}}(\omega):\ \frac{s_i/k}{s_r^2+s_i^2}<-1. \tag{3.16}$$

In general, $\mathcal{D}_{\mathrm{in}}(\omega)$ is located in front of $\mathcal{E}_0$ (where $s_i<0$). A detailed analysis of (3.16) reveals that for frequencies such that $kb>1$, $\mathcal{D}_{\mathrm{in}}(\omega)$ has the shape of a ring in front of $\mathcal{E}_0$ whose boundary on $\mathcal{E}_0$ is given by $-k^{-1}<s_i<0$ (see the dark-shaded region in Fig. 1). In particular, in the high-collimation range where $kb\gg1$, this ring becomes concentrated near $\mathcal{B}$. For low frequencies such that $kb<1$, on the other hand, $\mathcal{D}_{\mathrm{in}}(\omega)$ covers the entire front face of $\mathcal{E}_0$ (see the light-shaded region in Fig. 1). Recall though that at any given frequency, the *total* energy flows outward through $\mathcal{E}_{s_r}$, as implied by (3.15). It follows that at low frequencies, the energy is emitted by the back face of $\mathcal{E}_0$: part of it flows around $\mathcal{E}_0$ and is absorbed by the front face, while the other radiates outward through $\mathcal{E}_{s_r}$.

The analysis above implies that for practical synthesis of the CSPB, the frequency spectrum of ψ should be concentrated at frequencies such that $kb\gg1$. Recalling that the effective width of the aperture in this range is $W_0(\omega)=\sqrt{b/k}$ [cf. (2.25) and Ref. 2], it follows that for $kb>2$, W_0 is narrower than the inner radius of $\mathcal{D}_{\mathrm{in}}(\omega)$ which is given by $s_i=-k^{-1}$ [see (3.16)]. Under these conditions the aperture can be truncated about the effective aperture W_0 of (2.25), giving essentially the same field as the *exact* CSPB which is generated by the entire source disk $\mathcal{E}_0$.

IV. SURFACE SOURCES AND EQUIVALENT SOURCES

We start by recalling the field discontinuity conditions implied by (1.1). Let $\mathcal{S}$ be a given surface carrying surface sources (σ_s, f_s), i.e.,

$$\sigma = \sigma_s(\mathbf{r}_s, t)\,\delta(n), \quad \mathbf{f} = \mathring{\mathbf{n}} f_s(\mathbf{r}, t)\,\delta(n), \tag{4.1}$$

where $\mathbf{r}_s \in S$, $\mathring{\mathbf{n}}$ is the normal to $\mathcal{S}$ at $\mathbf{r}_S$, pointing from side 1 to side 2 of $\mathcal{S}$, and n is the coordinate along $\mathring{\mathbf{n}}$. The field discontinuities implied by these sources are found from (1.1) to be

$$\mathring{\mathbf{n}} \cdot (\mathbf{v}_2 - \mathbf{v}_1) = \sigma_s, \quad p_2 - p_1 = \mathring{\mathbf{n}} \cdot \mathbf{f}_s \equiv f_s, \tag{4.2}$$

where $(\mathbf{v}_i, p_i)$ are the limiting value of $(\mathbf{v}, p)$ at side i of $\mathcal{S}$.

Next, let $\mathcal{S}$ be a closed surface that encloses all the sources to the field. We would like to synthesize the field outside $\mathcal{S}$ due to the sources inside $\mathcal{S}$ in terms of surface sources on it. As will be shown, there exist various realizations of these sources; of particular interest are those involving only σ or $\mathbf{f}$ sources. These alternative realizations are obtained by choosing inside $\mathcal{S}$ an *arbitrary solution* of the homogeneous field equation, denoted as $(p^{\text{in}}, \mathbf{v}^{\text{in}})$. Using (4.2), the surface sources are now given by

$$\sigma_s = \mathring{\mathbf{n}} \cdot (\mathbf{v} - \mathbf{v}^{in})|_S, \quad f_s = (p - p^{in})|_S, \tag{4.3}$$

where $\mathring{\mathbf{n}}$ is an outward normal to $\mathcal{S}$. Substituting (4.3) into (1.2), we obtain

$$p = \int_S dS' \frac{1}{4\pi R} [[\dot{\sigma}_s] + (c^{-1}[\dot{f}_s] + R^{-1}[f_s]) \mathring{\mathbf{n}}' \cdot \mathring{\mathbf{R}}]. \tag{4.4}$$

This integral synthesizes the true field $(p, \mathbf{v})$ at points outside $\mathcal{S}$ and the arbitrarily chosen field $(p^{\text{in}}, \mathbf{v}^{\text{in}})$ at points inside $\mathcal{S}$.

A. Kirchhoff realization

As mentioned before, different source realizations are generated by choosing different homogeneous solutions $(p^{\text{in}}, \mathbf{v}^{\text{in}})$ in (4.3). One such choice,

$$p^{\text{in}} = 0, \quad \mathbf{v}^{\text{in}} = \mathbf{0}, \tag{4.5}$$

gives rise to what will be identified below as the Kirchhoff realization. Using (4.5) and (4.3), the Kirchhoff sources are

$$\sigma_s = \mathring{\mathbf{n}} \cdot \mathbf{v}|_S = -\partial_n \partial_t^{-1} p|_S, \quad f_s = p|_S, \tag{4.6}$$

where in the second expression for σ_s we used (1.1b) to replace the limiting value of $\mathbf{v}$ outside $\mathcal{S}$ by the value of p there. When the sources in (4.6) are substituted into (4.4), we obtain the true field outside $\mathcal{S}$ and a null contribution inside $\mathcal{S}$.

Using (4.6) in (4.4), one obtains the conventional Kirchhoff integral representation for the radiating field in terms of the values of p and $\partial_n p$ on $\mathcal{S}$, which is usually obtained by using the scalar wave equation for p in conjunction with Green's theorem.[40] Thus, Eq. (4.6) provides the surface source realization of this formula.

B. Integral equations for alternative source realizations

Equation (4.4) synthesizes the field outside $\mathcal{S}$ due to the sources inside $\mathcal{S}$ in terms of both σ_s and f_s sources. Alternative formulations are obtained if one chooses different values for $(p^{\text{in}}, \mathbf{v}^{\text{in}})$. We shall look, in particular, for realizations such that either f_s or σ_s in (4.3) vanishes identically on $\mathcal{S}$. These sources are determined via an integral equation as described below.

We start by expressing the field (4.4) for the special case of the sources in (4.6) as a sum of two terms: $p = p^{\sigma} + p^{f}$ denoting, respectively, the fields due to the f_s and σ_s sources in (4.6). Substituting (4.6) in (4.4), these fields may be expressed in terms of the known field p outside $\mathcal{S}$

$$\begin{aligned} p^{f} &= \int_S dS' \frac{1}{4\pi R} (c^{-1}[\dot{p}] + R^{-1}[p]) \mathring{\mathbf{n}}' \cdot \mathring{\mathbf{R}}, \\ p^{\sigma} &= \int_S dS' \frac{-1}{4\pi R} [\partial_{n'} p]. \end{aligned} \tag{4.7}$$

The σ_s-only realization involves the σ_s sources in (4.6) plus an additional term denoted as σ_s^f that gives rise to the *known* field p^f outside $\mathcal{S}$. σ_s^f is therefore calculated via the integral equation on $\mathcal{S}$

$$\int_S dS' \frac{1}{4\pi R} [\dot{\sigma}_s^f] = p^f(\mathbf{r}, t), \quad \mathbf{r}, \mathbf{r}' \in \mathcal{S}, \tag{4.8}$$

where p^f is given in (4.7) in terms of the known field p on the outer side of $\mathcal{S}$. Note that the kernel on the left-hand side of (4.8) is singular at $\mathbf{r}' = \mathbf{r}$, but this singularity can be extracted explicitly using principal value integration.

The solution of (4.8) is not unique. Recalling from (4.3) that the internal field $(p^{\text{in}}, \mathbf{v}^{\text{in}})$ in the σ_s-only realization satisfies $p^{\text{in}}|_S = p|_S$ where p is the known pressure field outside $\mathcal{S}$, it follows that the null space of (4.8) is described by internal field solutions that satisfy $p^{\text{in}}|_S = 0$. Such solutions are possible at discrete frequencies ω_n, $n = 1,2,...$, which are the *internal resonance frequencies* of $\mathcal{S}$ for the ''soft'' boundary condition $p^{\text{in}}|_S = 0$. The solution of (4.8) can therefore be augmented by a discrete set of eigensolutions of the form $\sigma_s^f(\mathbf{r}, t) = \Sigma_n \operatorname{Re} a_n \sigma_{s_n}(\mathbf{r}) e^{-i\omega_n t}$, which do not affect the field outside $\mathcal{S}$. A unique solution is obtained by imposing another criterion, say a minimum energy condition. We shall not consider this subject here.

Similarly, the f_s-only realization involves the f_s sources of (4.6) plus an additional term f_s^{σ} that generates the p^{σ} field outside $\mathcal{S}$. f_s^{σ} is found via the integral equation on $\mathcal{S}$

$$\int_S dS' \frac{1}{4\pi R} (c^{-1}[\dot{f}_s^{\sigma}] + R^{-1}[f_s^{\sigma}]) \mathring{\mathbf{n}}' \cdot \mathring{\mathbf{R}} = p^{\sigma}(\mathbf{r}, t), \quad \mathbf{r}, \mathbf{r}' \in S, \tag{4.9}$$

where p^{σ} is given in (4.7) in terms of the known field p on the outer side of $\mathcal{S}$. As discussed after (4.8), the solution of (4.9) is not unique: its null space is described by the internal resonance frequencies associated the ''hard'' boundary condition $\partial_n p^{\text{in}}|_S = 0$.

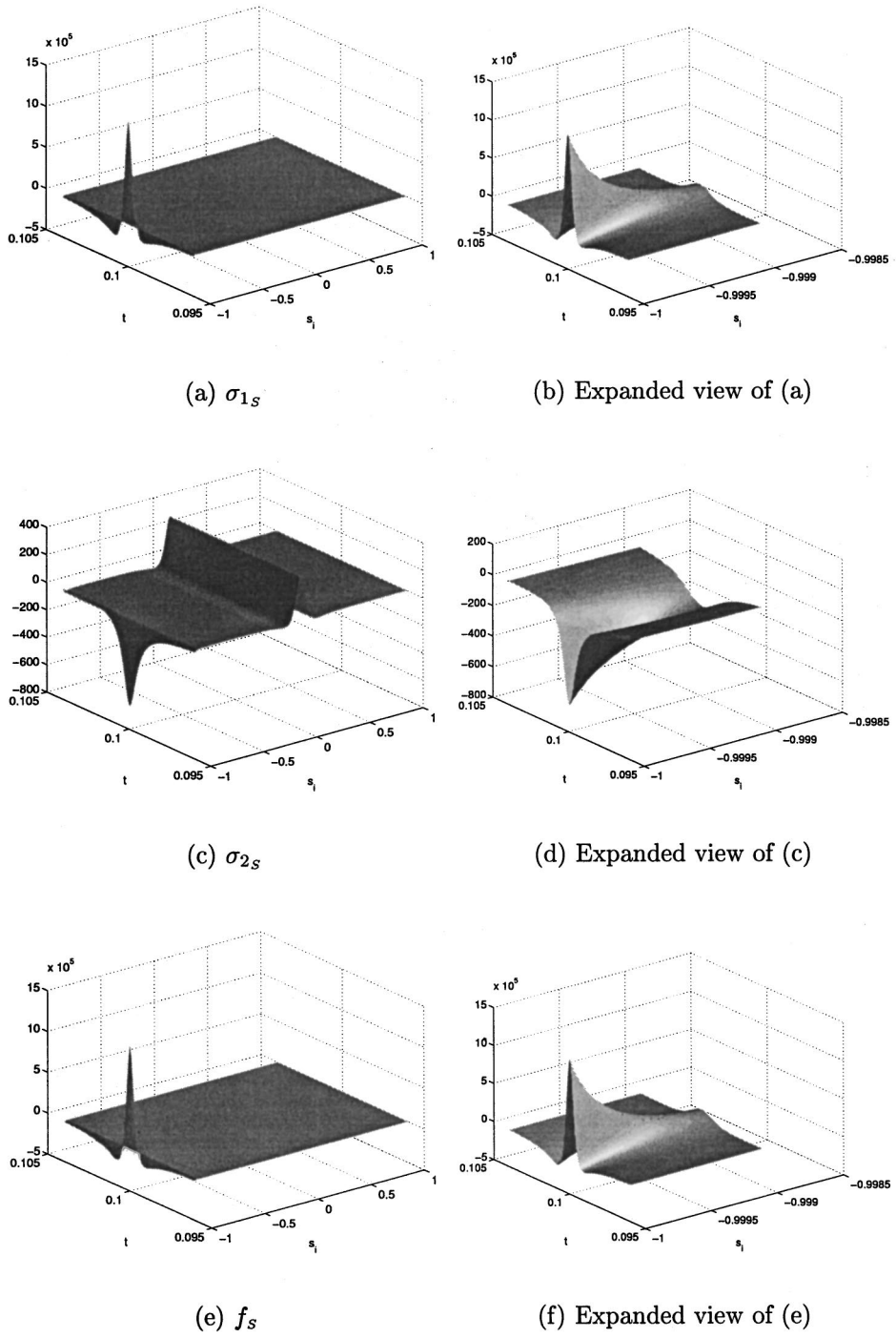

(a) σ_{1s} (b) Expanded view of (a)

(c) σ_{2s} (d) Expanded view of (c)

(e) f_s (f) Expanded view of (e)

FIG. 4. Waveforms of the surface sources in (5.1) on $\mathcal{S}=\mathcal{E}_{s_r}$ with $s_r=0.1b$. The waveforms are depicted in the (ct,s_i) plane with s_i, the coordinate along $\mathcal{E}_{s_r}$ varies from $-b$ on the positive z axis to b on the negative axis. (a) and (b): σ_{1_s}; (c) and (d): σ_{2_s}; (e) and (f): f_s. The pulse $\overset{+}{\psi}$ is the differentiated analytic δ used in Fig. 2 with high-collimation parameter $cT/b=10^{-3}$.

V. SOURCE DISTRIBUTIONS FOR THE CSPB

It is convenient to consider a source realization on the ellipsoid $\mathcal{E}_{s_r}$ of (2.9) for a given $s_r>0$. Substituting (2.12) and (3.1) into (4.6), we obtain

$$\sigma_s=|\nabla s_r|\mathrm{Re}\{\overset{+}{\psi}(\tau)/cs+\overset{+}{\psi}^{(-1)}(\tau)/s^2\}, \tag{5.1a}$$

$$f_s=\mathrm{Re}\{\overset{+}{\psi}(\tau)/s\}, \tag{5.1b}$$

where s, τ, and $|\nabla s_r|$ are given in (2.5b), (2.12), and (B2), respectively. These expressions are functions of s_i, which serves as a coordinate along $\mathcal{E}_{s_r}$.

Explicit expressions are obtained for the special case when $\mathcal{E}_{s_r}$ shrinks to the source disk $\mathcal{E}_0$ of (2.7). Denoting values on the front and back faces of $\mathcal{E}_0$ by the superscript $\pm$, respectively, we find that

$$s^{\pm}=\mp i\eta, \quad \gamma^{\pm}=i(b\mp\eta)/c, \quad \text{where} \quad \eta=\sqrt{b^2-\rho^2}. \tag{5.2}$$

Substituting (2.12) and (3.1) into (4.6), we obtain

$$\sigma_s^{\pm}=\frac{b}{\eta}\mathrm{Re}\{\pm i\overset{+}{\psi}[t-i(b\mp\eta)]/\eta c-\overset{+}{\psi}^{(-1)}[t-i(b\mp\eta)]/\eta^2\}, \tag{5.3a}$$

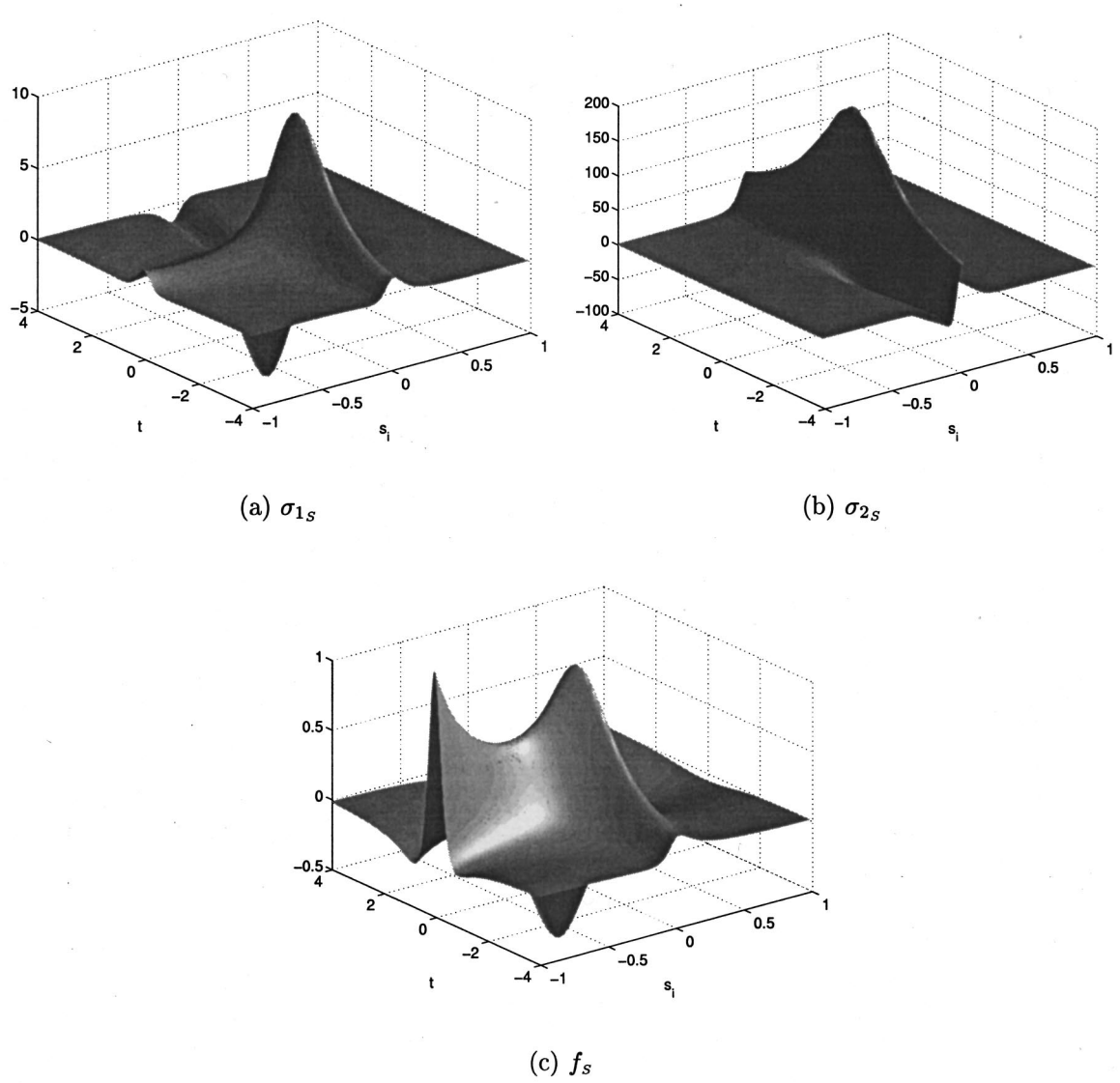

(a) σ_{1s} (b) σ_{2s}

(c) f_s

FIG. 5. Same as Fig. 4, but for noncollimated source with $cT/b=1$.

$$f_{z_s}^{\pm}=\pm p|_{\mathcal{E}_0^{\pm}}=\mathrm{Re}\{\overset{+}{i\psi}[t-i(b\mp\eta)]/\eta\}, \tag{5.3b}$$

where the upper and lower signs correspond to sources on the front and back face of $\mathcal{E}_0$, respectively, while $f_{z_s}^{\pm}$ in the last expression denotes the z component of the $\mathbf{f}_s$ source on the front and back faces of $\mathcal{E}_0$. Note also the algebraic singularity of the sources at $\rho=b$ on the circle $\mathcal{B}$.

Special attention should be given to the collimated case (2.26) which is the most important one for practical applications. We note that in this case the relevant part of the source is concentrated within the *effective aperture* W_0 (2.25) on the front face of $\mathcal{E}_0$, which is much narrower than the entire disk $\mathcal{E}_0$ [see (2.27)]. Furthermore, under the collimation condition the contribution of the second term in σ_s is negligible [see the discussion in (3.4)]. Finally, from (5.2) it follows that for $\rho\ll b, \gamma_i^+\approx\rho^2/2cb$, while $\gamma_i^-\approx 2ib/c$, hence in (5.3) $\sigma_s^+ \gg\sigma_s^-$ and $f_{z_s}^+\gg f_{z_s}^-$. Thus, Eq. (5.3) reduces to the simplified explicit expression for effective sources

$$c\sigma_s=f_{z_s}=b^{-1}\,\mathrm{Re}\{\overset{+}{i\psi}(t-i\rho^2/2cb)\},\quad \rho\sim O(W_0). \tag{5.4}$$

These simplified sources generate a strong PB field along the positive z axis that behaves paraxially like the PB in (2.17) [or (2.20)]. In all other directions, the resulting field is weak but due to the approximation in (5.4) it does not have the exact known form of (2.12).

Alternatively, one may use *only* the σ_s or the f_s sources in (5.4). This generates collimated PB along both the positive and the negative z directions: From (4.4), the σ_s source radiates symmetrically in both directions while the f_s source radiates antisymmetrically. Taken together, the contributions of σ_s and of f_s enhance each other in the positive direction and cancel each other in the negative direction, thereby radiating a strong PB field only along the positive z axis and a weak field elsewhere.

Figures 4 and 5 depict the surface sources of the CSPB realized on an ellipsoidal wavefront $\mathcal{S}=\mathcal{E}_{s_r}$ as in (5.1). Here, s_r is taken to be $0.1b$ so that $\mathcal{E}_{s_r}$ is close to the branch disk $\mathcal{E}_0$ (see Fig. 1). The waveforms are depicted in the (ct,s_i) plane with s_i being a coordinate along $\mathcal{E}_{s_r}$ (s_i varies from $-b$ on the positive z axis to b on the negative axis). The first and

second terms in (5.1a) are termed σ_{1_s} and σ_{2_s}, respectively. The pulse $\overset{+}{\psi}$ is the differentiated analytic δ used in Figs. 2 and 3. In Fig. 4 we use a short pulse with $cT/b=10^{-3}$ which yields a collimated PB, while in Fig. 5 $cT/b=1$, yielding a noncollimated field. Note that the *effective* width of the source distribution in Fig. 4 agrees with the estimates for W_0 in (2.25); hence, the sources there can be truncated and described by the simpler expressions in (5.4). In Fig. 5, on the other hand, the source distribution is much wider. In this case one also observes the relatively strong sources at points near $\mathcal{B}(s_i \simeq 0)$, which are insignificantly small under the collimation condition in Fig. 4. These sources become stronger for smaller s_r, and become singular when $\mathcal{S}$ shrinks to the branch disk $\mathcal{E}_0$, yet their contribution is insignificant in the collimation condition.

VI. SUMMARY AND CONCLUSIONS

Our aim in the present paper has been to explore this physical source realization of the CSPB. This has been done within the framework of the acoustic field, by deriving expressions for the acoustic source distributions and by exploring the power and energy flux near these sources. The surface sources have been derived via the field equivalence theorems in Sec. IV. The exact source solutions derived in (5.1) [or (5.3)] generate the *globally exact* CSPB. Yet, from a practical point of view special emphasis has been given to the parameter range $cT \ll b$ [see (2.26)]; T is the pulse length and b is the collimation distance) where the CSPB is well collimated: in this special case the CSPB can be realized effectively by the simple truncated source distribution in (5.4) whose spatial support W_0 of (2.25) is much smaller than the source support of the exact CSPB.

In order to further clarify the properties of source realization, we have also explored the power flux near the sources. It has been shown [see (3.16)] that at high frequencies such that $kb \gg 1$ (k is the wave number) the energy is emitted by a narrow aperture on the front face of the source disk $\mathcal{E}_0$. At low frequencies, on the other hand, the energy is emitted by the back face of $\mathcal{E}_0$: part of it flows around $\mathcal{E}_0$ and is absorbed by the front face, while the rest radiates outward through $\mathcal{E}_{s_r}$. Thus, for practical synthesis the frequency spectrum of the CSPB should be concentrated in the high-frequency regime, which supports the conclusions of the preceding paragraph.

ACKNOWLEDGMENTS

This work is supported in part by the U.S. Air Force Office of Scientific Research under Grant No. F49620-98-C-0013, managed by The Virginia Center for Signals and Waves, and in part by the Israel Science Foundation under Grant No. 404/98.

APPENDIX A: ANALYTIC SIGNALS

In order to deal with the complex propagation delays implied by the complex sources, one needs to use analytic signals that can accommodate complex time variables. For a given real signal $\psi(t)$, $t \in \mathbb{R}$, with frequency spectrum $\hat{\psi}(\omega)$, the dual analytic signal $\overset{+}{\psi}(\tau)$ is defined via the one-sided inverse Fourier transform

$$\overset{+}{\psi}(\tau)=\frac{1}{\pi}\int_0^\infty d\omega\, e^{-i\omega\tau}\hat{\psi}(\omega), \quad \mathrm{Im}\,\tau \leqslant 0. \tag{A1}$$

It follows that $\overset{+}{\psi}(\tau)$ is an analytic function in the lower half of the complex τ plane. This function may also be defined directly from the *real* data $\psi(t)$ for real t via

$$\psi(\tau)=\frac{1}{\pi i}\int_{-\infty}^{\infty} dt\,\frac{\psi(t)}{\tau - t}, \quad \mathrm{Im}\,\tau \leqslant 0. \tag{A2}$$

From (A2), the limit of ψ on the real t axis is related to the real signal $\psi(\tau)$ via

$$\overset{+}{\psi}(t)=\psi(t)+i\overline{\psi}(t), \quad t \ \text{real}, \tag{A3}$$

where

$$\overline{\psi}(t)=\frac{-1}{\pi}\int_{-\infty}^{\infty} dt'\,\mathcal{P}\frac{\psi(t')}{t-t'}$$

is the Hilbert transform, with $\mathcal{P}$ denoting Cauchy's principal value. The real signal for real t can therefore be recovered via $\psi(t)=\mathrm{Re}\,\overset{+}{\psi}(t)$.

Thus, if $\overset{+}{p}(\mathbf{r},t)$ is an analytic solution of the time-dependent wave equation, then both $p_r=\mathrm{Re}\,\overset{+}{p}$ and $p_i=\mathrm{Im}\,\overset{+}{p}$ are real solutions of the wave equation. Henceforth, we shall only consider p_r since p_i or any other linear combination of p_r and p_i can be obtained by multiplying $\overset{+}{p}$ by a complex constant and then taking the real part.

APPENDIX B: ADDITIONAL PROPERTIES OF THE OS SYSTEM

From (2.8), one may readily infer the following relations:

$$s_r^2-s_i^2=r^2-b^2, \quad s_r s_i=-zb, \tag{B1}$$

$$\nabla s_r=(\mathbf{r}s_r-\mathbf{b}s_i)/|s|^2, \quad |\nabla s_r|=\sqrt{b^2+s_r^2}/|s|, \tag{B2}$$

$$\nabla s_i=-(\mathbf{r}s_i+\mathbf{b}s_r)/|s|^2, \quad |\nabla s_i|=\sqrt{b^2-s_i^2}|s|, \tag{B3}$$

$$\nabla s_r \cdot \nabla s_i=0, \tag{B4}$$

and the metric coefficients[40] along the (s_r, s_i, ϕ) coordinates are

$$h_{s_r}=|s|/\sqrt{b^2+s_r^2}, \quad h_{s_i}=|s|/\sqrt{b^2-s_i^2},$$
$$h_\phi=b^-\sqrt{b^2+s_r^2}\sqrt{b^2-s_i^2}. \tag{B5}$$

[1] E. Heyman and B. Z. Steinberg, ''A spectral analysis of complex source pulsed beams,'' J. Opt. Soc. Am. A **4**, 473–480 (1987).
[2] E. Heyman and L. B. Felsen, ''Complex source pulsed beam fields,'' J. Opt. Soc. Am. A **6**, 806–817 (1989).
[3] E. Heyman, B. Z. Steinberg, and R. Ianconescu, ''Electromagnetic complex source pulsed beam fields,'' IEEE Trans. Antennas Propag. **AP-38**, 957–963 (1990).
[4] G. A. Deschamps, ''Gaussian beams as a bundle of complex rays,'' Electron. Lett. **7**, 684–685 (1971).

[5] J. W. Ra, H. Bertoni, and L. B. Felsen, ''Reflection and transmission of beams at dielectric interfaces,'' SIAM (Soc. Ind. Appl. Math.) J. Appl. Math. **24**, 396–412 (1973).
[6] L. B. Felsen, ''Complex-source-point solutions of the field equations and their relation to the propagation and scattering of Gaussian beams,'' in *Symposia Matematica, Istituto Nazionale di Alta Matematica* (Academic, London, 1976), Vol. XVIII, pp. 40–56.
[7] S. Y. Shin and L. B. Felsen, ''Gaussian beam modes by multipoles with complex source points,'' J. Opt. Soc. Am. **67**, 699–700 (1977).
[8] G. Kaiser, *A Friendly Guide to Wavelets* (Birkhauser, Boston, 1994), pp. 276–279.
[9] E. Heyman, R. Strachielevitz, and D. Koslof, ''Pulsed beam reflection and transmission at a planar interface: Exact solutions and approximate local models,'' Wave Motion **18**, 315–343 (1993).
[10] R. Ianconescu and E. Heyman, ''Pulsed beam diffraction by a perfectly conducting wedge. I. Exact solution,'' IEEE Trans. Antennas Propag. **AP-42**, 1377–1385 (1994).
[11] E. Heyman and R. Ianconescu, ''Pulsed beam diffraction by a perfectly conducting wedge. Part II: Local scattering models,'' IEEE Trans. Antennas Propag. **AP-43**, 519–528 (1995).
[12] E. Heyman, ''Pulsed beam propagation in an inhomogeneous medium,'' IEEE Trans. Antennas Propag. **AP-42**, 311–319 (1994).
[13] A. N. Norris, B. S. White, and J. R. Schrieffer, ''Gaussian wave packets in inhomogeneous media with curved interfaces,'' Proc. R. Soc. London, Ser. A **412**, 93–123 (1987).
[14] E. Heyman, A. G. Tijhuis, and J. Boersma, ''Spherical and collimated pulsed fields in conducting media,'' Proceedings of URSI Trianum International Symposium on Electromagnetic Theory, St. Petersburg, 1995, pp. 643–645 (unpublished).
[15] T. Melamed and L. B. Felsen, ''Pulsed beam propagation in lossless dispersive media. I. Theory,'' J. Opt. Soc. Am. A **15**, 1268–1276 (1998).
[16] T. Melamed and L. B. Felsen, ''Pulsed beam propagation in lossless dispersive media. Part II. Applications,'' J. Opt. Soc. Am. A **15**, 1277–1284 (1998).
[17] J. Oz and E. Heyman, ''Modal theory for the two-frequency mutual coherence function in random media. Beam waves,'' Waves Random Media **8**, 159–174 (1998).
[18] J. Gozani, ''Pulsed beam propagation through random media,'' Opt. Lett. **21**, 1712–1714 (1996).
[19] S. Zeroug, F. E. Stanke, and R. Burridge, ''A complex-transducer-point model for finite emitting and receiving ultrasonic transducers'' Wave Motion **24**, 21–40 (1996).
[20] S. Feng and H. G. Winful, ''Spatiotemporal transformations of isodiffracting ultrashort pulses by nondispersive quadratic phase media,'' J. Opt. Soc. Am. A **16**, 2500–2509 (1999).
[21] M. A. Porras, ''Ultrashort pulsed Gaussian light beams,'' Phys. Rev. E **58**, 1086–1093 (1998).
[22] M. A. Porras, ''Nonsinusoidal few-cycle pulsed light beams in free space,'' J. Opt. Soc. Am. B **16**, 1468–1474 (1999).
[23] E. Heyman, ''Complex source pulsed beam expansion of transient radiation,'' Wave Motion **11**, 337–349 (1989).
[24] B. Z. Steinberg, E. Heyman, and L. B. Felsen, ''Phase space beam summation for time dependent radiation from large apertures: Continuous parametrization,'' J. Opt. Soc. Am. A **8**, 943–958 (1991).
[25] B. Z. Steinberg and E. Heyman, ''Phase space beam summation for time dependent radiation from large apertures: Discretized parametrization,'' J. Opt. Soc. Am. A **8**, 959–966 (1991).
[26] T. Melamed, ''Phase space beam summation: A local spectrum analysis of time dependent radiation,'' J. Electromagn. Waves Appl. **11**, 739–773 (1997).
[27] E. Heyman and I. Beracha, ''Complex multipole pulsed beams and Hermite pulsed beams: A novel expansion scheme for transient radiation from well collimated apertures,'' J. Opt. Soc. Am. A **9**, 1779–1793 (1992).
[28] T. B. Hansen and A. N. Norris, ''Exact complex source representations of transient radiation,'' Wave Motion **26**, 101–115 (1997).
[29] T. Melamed, E. Heyman, and L. B. Felsen, ''Local spectral analysis of short-pulse-excited scattering from weakly inhomogeneous media. I. Forward scattering,'' IEEE Trans. Antennas Propag. **AP-47**, 1208–1217 (1999).
[30] T. Melamed, E. Heyman, and L. B. Felsen, ''Local spectral analysis of short-pulse-excited scattering from weakly inhomogeneous media. II. Inverse scattering,'' IEEE Trans. Antennas Propag. **AP-47**, 1218–1227 (1999).
[31] J. N. Brittingham, ''Focus wave modes in homogeneous Maxwell's equations: Transverse electric mode,'' J. Appl. Phys. **54**, 1179–1189 (1983).
[32] R. W. Ziolkowski, ''Exact solutions of the wave equation with complex source locations,'' J. Math. Phys. **26**, 861–863 (1985).
[33] A. M. Shaarawi, I. M. Besieris, R. W. Ziolkowski, and S. M. Sedky, ''The generation of approximate focus wave mode pulses from wide-band dynamic Gaussian apertures,'' J. Opt. Soc. Am. A **12**, 1954–1964 (1995).
[34] E. Heyman, ''The focus wave mode: A dilemma with causality,'' IEEE Trans. Antennas Propag. **AP-37**, 1604–1608 (1989).
[35] J. Durnin, J. J. Miceli, Jr., and J. H. Eberly, ''Diffraction free beam'' Phys. Rev. Lett. **58**, 1499–1452 (1987).
[36] J.-y. Lu and J. F. Greenleaf, ''Nondiffracting X waves—exact solutions to free space scalar wave equation and their finite aperture realizations,'' IEEE Trans. Ultrason. Ferroelectr. Freq. Control **39**, 19–31 (1992).
[37] H. E. Moses and R. T. Prosser, ''Initial conditions, sources, and currents for prescribed time-dependent acoustic and electromagnetic fields in three dimensions. I. The inverse initial value problem. Acoustic and electromagnetic ''bullets,'' expanding waves, and imploding waves,'' IEEE Trans. Antennas Propag. **AP-34**, 188–196 (1986).
[38] H. E. Moses and R. T. Prosser, ''Acoustic and electromagnetic bullets. New exact solutions of the acoustic and Maxwell's equation,'' SIAM (Soc. Ind. Appl. Math.) J. Appl. Math. **50**, 1325–1340 (1990).
[39] A. Shlivinski and E. Heyman, ''Time domain near field analysis of short pulse antennas. Part I: Spherical wave (multipole) expansion;'' ''Part II Reactive energy and the antenna *Q*,'' IEEE Trans. Antennas Propag. **AP-47**, 271–279 (1999); **AP-47**, 280–286 (1999).
[40] J. A. Stratton, *Electromagnetic Theory* (McGraw-Hill, New York, 1941).

Calculation of surface wave motions due to a subsurface point force: An application of elastodynamic reciprocity

J. D. Achenbach[a)]
Center for Quality Engineering and Failure Prevention, Northwestern University, Evanston, Illinois 60208

(Received 9 September 1999; revised 15 January 2000; accepted 18 January 2000)

The elastodynamic reciprocity theorem for two time-harmonic elastodynamic states of the same body is used to determine the surface wave motions generated by a subsurface point load of arbitrary direction in an isotropic, homogeneous, elastic half-space. The actual surface wave motions due to the point load expressed in a suitably general form represent one of the states, while the other one is an appropriately selected auxiliary solution consisting of incoming and outgoing surface waves. A direct application of the reciprocity theorem yields the desired information on the generated surface wave motion. © *2000 Acoustical Society of America.* [S0001-4966(00)04304-6]

PACS numbers: 43.20.Rz, 43.20.Bi [ANN]

INTRODUCTION

Reciprocity theorems in elasticity theory provide an integral relation between displacements, stress components, and body forces for two different loading states of the same body. The various forms of reciprocity theorems, together with applications, have been discussed in some detail by deHoop.[1] As discussed by Love,[2] for the elastostatic case the principal theorem is due to Betti.[3] A more general theorem, which includes the elastodynamic case, was given by Rayleigh.[4] Statements of elastodynamic reciprocity theorems using a contemporary notation can be found, among others, in the books by Achenbach,[5] Achenbach, Gautesen, and McMaken,[6] and deHoop.[1]

Reciprocity theorems are generally used to check the consistency of elastodynamic solutions or to derive systems of integral equations. The purpose of the present paper, however, is to give a direct application to the computation of elastodynamic displacement fields generated by time-harmonic concentrated forces.

In earlier work, a reciprocity theorem was used to determine the coefficients in the wave mode expansion produced in an elastic layer by a time-harmonic point load applied in an arbitrary direction, see Achenbach and Xu.[7] Point-load problems are usually solved by an application of the Hankel transform technique with an evaluation of the inverse transform by contour integration and residue calculus. That approach does in fact result in displacement expressions that are superpositions of wave modes by considering the contributions from poles. In Ref. 7 the displacements are, however, directly expressed as wave mode expansions, and the coefficients are obtained by applying the reciprocity theorem to the wave mode expansions and a suitably selected auxiliary solution.

In the present paper, we use the reciprocity theorem to calculate the surface wave motion generated by a time-harmonic point load applied in an arbitrary direction in the interior of a half-space. The calculation does not include a consideration of the body waves generated by the point load. For a point load applied normal to a half-space, it is shown that the surface wave motion is the same as that obtained in the conventional manner by use of the integral transform approach.

The general formulation of the wave fields follows a recent paper by Achenbach.[8] In a Cartesian coordinate system (x_1,x_2,z), the displacement components are expressed in terms of products such as $v_i(z)\varphi(x_1,x_2)\exp(i\omega t)$, where $\varphi(x_1,x_2)$ satisfies a simple reduced wave equation. The function $\varphi(x_1,x_2)$ acts as a carrier wave for propagation parallel to the x_1,x_2 plane. The carrier wave supports motions that depend on the z coordinate only and that are represented by $v_i(z)$. This formulation is particularly suited for Lamb waves in a layer and surface waves on a half-space. For the specific problems considered in this paper, Hankel functions represent the appropriate carrier waves, but any solution of the reduced wave equation for $\varphi(x_1,x_2)$ can be used. The analysis of the variation of motion with depth results in the Rayleigh equation for the velocity of surface waves on a half-space.

It is well-known that the dynamic response to a time-harmonic point load normal to a half-space was solved by Lamb,[9] who also gave explicit expressions for the generated surface wave motion. The surface wave motion can be obtained as the contribution from the pole in integral representations of the displacement components that involve Hankel functions. The analogous transient time-domain problem for a load normal to a half-space was solved by Pekeris.[10] The displacement solutions for a transient tangential point load applied to the surface of a half-space were worked out by Chao.[11]

I. FORMULATION

Figure 1 shows a half-space of homogeneous, isotropic, linearly elastic material, referred to a Cartesian coordinate system such that the x_1x_2 plane coincides with the surface of the half-space. The half-space is subjected to a time-harmonic point load at $x_1=x_2=0$, $z=z_0$ pointing in an arbitrary direction. Without loss of generality, the coordinate system is chosen such that the load acts in the x_1z plane. The

a)Electronic mail: achenbach@nwu.edu

 0001-4966/2000/107(4)/1892/6/$17.00

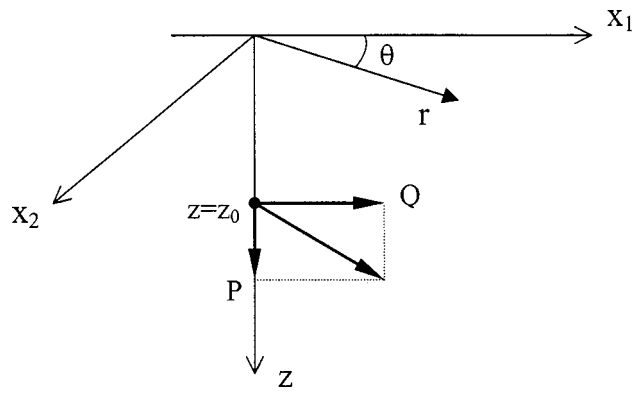

FIG. 1. Homogeneous, isotropic, linearly elastic half-space subjected to a subsurface time-harmonic point load.

surface wave response of the half-space is sought as the superposition of the responses to the vertical component, P, and the horizontal component, Q.

Following an earlier paper by Achenbach,[8] we seek solutions for the displacement components in the general forms

$$u_\alpha(\mathbf{x},t)=\frac{1}{k}V(z)\frac{\partial\varphi}{\partial x_\alpha}(x_1,x_2)e^{i\omega t}, \tag{1}$$

$$u_z(\mathbf{x},t)=W(z)\varphi(x_1,x_2)e^{i\omega t}, \tag{2}$$

where $\alpha=1,2$, and k is a wave-number-like quantity

$$k=\omega/c. \tag{3}$$

In the following analysis, the harmonic time factor $\exp(i\omega t)$ will be omitted, and Greek indices will exclusively refer to the x_1 and x_2 axes.

Solutions of the forms (1) and (2) were considered by Achenbach,[8] who showed that these expressions satisfy the elastodynamic equations of motion if the dimensionless function $\varphi(x_1,x_2)$ is taken as the solution of

$$\varphi_{,\alpha\alpha}+k^2\varphi=0, \tag{4}$$

where repeated suffices indicate a summation, and $V(z)$ and $W(z)$ are solutions of the following system of ordinary differential equations:

$$(\lambda+\mu)\frac{dW}{dz}+\frac{\mu}{k}\frac{d^2V}{dz^2}+\frac{\rho\omega^2}{k}V(z)=k(\lambda+2\mu)V(z), \tag{5}$$

$$(\lambda+2\mu)\frac{d^2W}{dz^2}+\rho\omega^2W(z)=(\lambda+\mu)k\frac{dV}{dz}+\mu k^2W(z). \tag{6}$$

Here, λ and μ are Lamé's elastic constants and ρ is the mass density. Solutions of the forms (1) and (2) are particularly convenient for bodies with one or more free surfaces or interfaces parallel to the x_1x_2 plane. Examples are Lamb waves in a layer or surface waves on a half-space. For such cases the function $\varphi(x_1,x_2)$, which can be any solution of Eq. (4), acts as a carrier wave for the propagation in planes parallel to the x_1x_2 plane, while the functions $V(z)$ and $W(z)$ describe the thickness motions for Lamb waves and the depth variations for surface waves.

For the half-space $z\geqslant 0$, we seek solutions of (5) and (6) that decay exponentially with depth. Such solutions can be written as

$$V(z)=[d_1e^{-pz}+d_2e^{-qz}]A, \tag{7}$$

$$W(z)=[d_3e^{-pz}-e^{-qz}]A. \tag{8}$$

Here, A is a multiplying constant of length dimension, and

$$p^2=k^2-\frac{\omega^2}{c_L^2},\quad \text{where } c_L^2=\frac{\lambda+2\mu}{\rho}, \tag{9a}$$

while

$$q^2=k^2-\frac{\omega^2}{c_T^2},\quad \text{where } c_T^2=\frac{\mu}{\rho}. \tag{9b}$$

Also,

$$d_1=-\frac{1}{2}\frac{k^2+q^2}{kp},\quad d_2=\frac{q}{k}, \tag{10}$$

$$d_3=\frac{1}{2}\frac{k^2+q^2}{k^2}. \tag{11}$$

It can be verified that Eqs. (7) and (8) satisfy the system of ordinary differential equations (5)–(6).

II. SURFACE WAVE MOTION GENERATED BY Q

Let us first consider the wave motion generated by a time-harmonic point load applied in the direction of the x_1 axis. In cylindrical coordinates $(x_1=r\cos\theta, x_2=r\sin\theta, z)$, Eqs. (1) and (2) can be rewritten as

$$u_r=\frac{1}{k}V(z)\frac{\partial\varphi}{\partial r}(r,\theta), \tag{12}$$

$$u_\theta=\frac{1}{k}V(z)\frac{1}{r}\frac{\partial\varphi}{\partial\theta}(r,\theta), \tag{13}$$

$$u_z=W(z)\varphi(r,\theta), \tag{14}$$

and Eq. (14) becomes

$$\frac{\partial^2\varphi}{\partial r^2}+\frac{1}{r}\frac{\partial\varphi}{\partial r}+\frac{1}{r^2}\frac{\partial^2\varphi}{\partial\theta^2}+k^2\varphi=0. \tag{15}$$

The first point of consideration now is to select the right solution of Eq. (15) for $\varphi(r,\theta)$. For this, we take guidance from the displacement in an unbounded solid when a time-harmonic point force in the x_1 direction, F, is applied at the origin. In a Cartesian coordinate system, this solution can be written as

$$u_i=\frac{1}{k_T^2}\frac{F}{\mu}\frac{\partial}{\partial x_i}\frac{\partial}{\partial x_1}[-G(k_LR)+G(k_TR)]+\frac{F}{\mu}G(k_TR)\delta_{i1}, \tag{16}$$

where δ_{i1} is the Kronecker delta, and

$$G(k_\gamma R)=e^{-ik_\gamma R}/4\pi R, \tag{17}$$

where γ is L or T, and

$$k_L^2=\omega^2/c_L^2, \tag{18a}$$

$$k_T^2=\omega^2/c_T^2, \tag{18b}$$

$$R^2 = x_1^2 + x_2^2 + z^2. \tag{19}$$

The displacements in cylindrical coordinates follow from Eq. (16) as

$$u_r = \frac{F}{\mu}\left\{\frac{1}{k_T^2}\frac{\partial^2}{\partial r^2}[-G(k_L R)+G(k_T R)]+G(k_T R)\right\}\cos\theta, \tag{20}$$

$$u_\theta = \frac{F}{\mu}\left\{\frac{1}{k_T^2}\frac{1}{r}\frac{\partial}{\partial r}[G(k_L R)-G(k_T R)]-G(k_T R)\right\}\sin\theta, \tag{21}$$

$$u_z = \frac{F}{\mu}\frac{1}{k_T^2}\frac{\partial^2}{\partial z\,\partial r}[-G(k_L R)+G(k_T R)]\cos\theta, \tag{22}$$

where

$$R^2 = r^2 + z^2. \tag{23}$$

These solutions show a simple dependence on θ. It is to be expected that the presence of a traction-free surface parallel to the plane of r and θ does not change this dependence. This has been shown to be true by Chao[11] for a point load applied tangentially to the surface of the half-space. By comparing Eqs. (12)–(14) with Eqs. (20)–(22), it then immediately follows that we should take

$$\varphi(r,\theta) = \Phi(kr)\cos\theta, \tag{24}$$

where according to Eq. (15), $\Phi(kr)$ must be the solution of

$$\frac{d^2\Phi}{dr^2}+\frac{1}{r}\frac{d\Phi}{dr}+\left(k^2-\frac{1}{r^2}\right)\Phi = 0. \tag{25}$$

The solution to Eq. (25) for an outgoing wave compatible with the time factor $\exp(i\omega t)$ is

$$\Phi(kr) = H_1^{(2)}(kr). \tag{26}$$

We can equally well consider an incoming wave, i.e., a wave which converges on the origin

$$\overline{\Phi}(kr) = H_1^{(1)}(kr). \tag{27}$$

For simplicity of notation, we will use $\Phi(kr)$ and $\overline{\Phi}(kr)$ in subsequent expressions rather than the Hankel functions. The notation of $\Phi'(kr)$ is used for the derivative with respect to the argument: $\Phi'(\xi) = d\Phi/d\xi$.

For outgoing surface waves, the corresponding displacements and stresses are

$$u_r = V(z)\Phi'(kr)\cos\theta, \tag{28}$$

$$u_z = W(z)\Phi(kr)\cos\theta, \tag{29}$$

$$u_\theta = V(z)\left(\frac{-1}{kr}\right)\Phi(kr)\sin\theta, \tag{30}$$

$$\sigma_{rz} = \Sigma_{rz}(z)\Phi'(kr)\cos\theta, \tag{31}$$

$$\sigma_{zz} = \Sigma_{zz}(z)\Phi(kr)\cos\theta, \tag{32}$$

$$\sigma_{rr} = \Sigma_{rr}(z)\Phi(kr)\cos\theta - \overline{\Sigma}_{rr}(z) \times\left[\frac{1}{kr}\Phi'(kr)-\frac{1}{(kr)^2}\Phi(kr)\right]\cos\theta, \tag{33}$$

$$\sigma_{\theta z} = \Sigma_{\theta z}(z)\left(\frac{1}{kr}\right)\Phi(kr)\sin\theta, \tag{34}$$

$$\sigma_{r\theta} = \Sigma_{r\theta}(z)\left[\frac{1}{kr}\Phi'(kr)-\frac{1}{(kr)^2}\Phi(kr)\right]\sin\theta, \tag{35}$$

where $V(z)$ and $W(z)$ are defined by Eqs. (7) and (8), and

$$\Sigma_{rz}(z) = \mu\left[\frac{dV}{dz}+kW\right], \tag{36}$$

$$\Sigma_{zz}(z) = -\mu\left[\frac{c_L^2}{c_T^2}\left(kV-\frac{dW}{dz}\right)-2kV\right], \tag{37}$$

$$\Sigma_{rr}(z) = -\mu\left[\frac{c_L^2}{c_T^2}\left(kV-\frac{dW}{dz}\right)+2\frac{dW}{dz}\right], \tag{38}$$

$$\overline{\Sigma}_{rr}(z) = 2\mu kV, \tag{39}$$

$$\Sigma_{\theta z}(z) = -\mu\left[\frac{dV}{dz}+kW\right], \tag{40}$$

$$\Sigma_{r\theta}(z) = -2\mu kV. \tag{41}$$

Substitution of the expressions for $V(z)W(z)$ yields

$$\Sigma_{rr}(z) = \mu[d_4 e^{-pz}+d_5 e^{-qz}]A, \tag{42}$$

$$\Sigma_{rz}(z) = \mu[d_6 e^{-pz}+d_7 e^{-qz}]A, \tag{43}$$

$$\Sigma_{r\theta}(z) = 2\mu[d_1 e^{-pz}+d_2 e^{-qz}]A, \tag{44}$$

$$\Sigma_{zz}(z) = \mu[d_8 e^{-pz}+d_9 e^{-qz}]A, \tag{45}$$

$$\Sigma_{\theta z}(z) = -\mu[d_6 e^{-pz}+d_7 e^{-qz}]A, \tag{46}$$

$$\overline{\Sigma}_{rr}(z) = -2\mu[d_1 e^{-pz}+d_2 e^{-qz}]A, \tag{47}$$

where

$$d_4 = \frac{1}{2}(k^2+q^2)\frac{2p^2+k^2-q^2}{pk^2}, \quad d_5 = -2q, \tag{48}$$

$$d_6 = -\frac{k^2+q^2}{k}, \tag{49a}$$

$$d_7 = \frac{k^2+q^2}{k}, \tag{49b}$$

$$d_8 = -\frac{1}{2}\frac{(k^2+q^2)^2}{pk^2}, \tag{50a}$$

$$d_9 = 2q\,. \tag{50b}$$

The surface $z=0$ should be free of surface tractions. It is immediately seen that $\Sigma_{rz}(0)=0$ and $\Sigma_{\theta z}(0)=0$, while $\Sigma_{zz}(0)=0$ requires that

$$F(k) = (k^2+q^2)^2 - 4k^2pq = 0. \tag{51}$$

By substituting p and q from Eqs. (9a) and (9b) using $\omega = kc$, Eq. (51) assumes the better-known form

$$\left(2-\frac{c^2}{c_T^2}\right)^2 - 4\left(1-\frac{c^2}{c_L^2}\right)^{1/2}\left(1-\frac{c^2}{c_T^2}\right)^{1/2} = 0. \tag{52}$$

Equation (52) is the equation for the phase velocity, $c = c_R$, of Rayleigh surface waves. As is well-known, only

one mode of surface wave motion, with wave number $k_R = \omega/c_R$, can propagate along the surface of a half-space.

In addition to the displacements defined by Eqs. (1) and (2), we may also consider wave motions that are equivoluminal, with displacements that are parallel to the x_1x_2 plane. The corresponding wave motions are horizontally polarized. They may be represented by

$$u_1 = \frac{1}{l} U(z) \frac{\partial \psi}{\partial x_2}, \tag{53}$$

$$u_2 = -\frac{1}{l} U(z) \frac{\partial \psi}{\partial x_1}, \tag{54}$$

and $u_z \equiv 0$, where $\psi(x_1, x_2)$ is a solution of

$$\nabla^2 \psi + l^2 \psi = 0. \tag{55}$$

Substitution into the displacement equations of motion shows that the displacements given by Eqs. (53) and (54) are elastodynamic displacement solutions provided that

$$\frac{d^2U}{dz^2} + q^2 U = 0, \tag{56}$$

where $q^2 = (\omega/c_T)^2 - l^2$. There are no solutions of Eqs. (53)–(56) that represent surface waves. Hence, horizontally polarized waves are not further considered in this paper.

III. USE OF ELASTODYNAMIC RECIPROCITY

The reciprocal identity relates two elastodynamic states of the same body. For two distinct time-harmonic states, labeled by superscripts A and B: f_i^A, u_i^A, σ_{ij}^A, and f_i^B, u_i^B, σ_{ij}^B, where f_i^A and f_i^B are body forces, we have for a region V with boundary S (Ref. 6, p. 34)

$$\int_V (f_i^A u_i^B - f_i^B u_i^A)\, dV = \int_S (u_i^A \sigma_{ij}^B - u_i^B \sigma_{ij}^A) n_j \, dS, \tag{57}$$

where n_j are the components of the outward normal.

Equation (57) will now be applied to the problem of a time-harmonic point load applied inside a half-space. The point load generates surface waves, and we will determine the amplitude of these surface waves by using Eq. (57). For V, we take the region defined by $0 \leqslant r \leqslant b$, $0 \leqslant z < \infty$, $0 \leqslant \theta \leqslant 2\pi$. For state A we take the displacements

$$u_r^A = C V^R(z) \Phi'(k_R r) \cos\theta, \tag{58}$$

$$u_z^A = C W^R(z) \Phi(k_R r) \cos\theta, \tag{59}$$

$$u_\theta^A = C V^R(z) \left(\frac{-1}{k_R r}\right) \Phi(k_R r) \sin\theta, \tag{60}$$

where C is an unknown amplitude factor, k_R is the solution of Eq. (51), and $V^R(z)$ and $W^R(z)$ are defined by Eqs. (7) and (8), but with $k = k_R$, while $\Phi(k_R r)$ is given by Eq. (26). For state B we take a dummy solution consisting of the sum of an outgoing and a converging wave

$$u_r^B = \tfrac{1}{2} V^R(z) [\Phi'(k_R r) + \overline{\Phi}'(k_R r)] \cos\theta, \tag{61}$$

$$u_z^B = \tfrac{1}{2} W^R(z) [\Phi(k_R r) + \overline{\Phi}(k_R r)] \cos\theta, \tag{62}$$

$$u_\theta^B = \frac{1}{2} V^R(z) \left(\frac{-1}{k_R r}\right) [\Phi(k_R r) + \overline{\Phi}(k_R r)] \sin\theta, \tag{63}$$

where $\overline{\Phi}(k_R r)$ is defined by Eq. (27).

The displacements defined by Eqs. (61)–(63) are bounded at $r = 0$. It can be verified that the left-hand side of Eq. (57) becomes

$$Q u_r^R(0,0,z_0) = \tfrac{1}{2} Q V^R(z_0). \tag{64}$$

Hence, we obtain

$$\frac{1}{2} Q V^R(z_0) = b \int_{2\pi}^0 \int_{-\infty}^0 \{[u_r^A \sigma_{rr}^B - u_r^B \sigma_{rr}^A] + [u_z^A \sigma_{rz}^B - u_z^B \sigma_{rz}^A] + [u_\theta^A \sigma_{r\theta}^B - u_\theta^B \sigma_{r\theta}^A]\} d\theta \, dz. \tag{65}$$

In Eq. (65) all field variables are evaluated at $r = b$.

We now define an integral I as

$$I = \frac{1}{A^2} \int_0^\infty [\Sigma_{rr}^R(z) V^R(z) + \Sigma_{rz}^R(z) W^R(z)] dz. \tag{66}$$

Upon substitution of the pertinent displacements and stresses in Eq. (65), we then obtain

$$Q V^R(z_0) = C A^2 I T, \tag{67}$$

where I is defined by Eq. (66), and

$$T = \pi b [\Phi'(k_R b) \overline{\Phi}(k_R b) - \overline{\Phi}'(k_R b) \Phi(k_R b)]. \tag{68}$$

This expression can be further simplified by using the following identity for Hankel functions (Ref. 12, p. 198):

$$\frac{d}{d\xi} H_\nu^{(1)}(\xi) H_\nu^{(2)}(\xi) - H_\nu^{(1)}(\xi) \frac{d}{d\xi} H_\nu^{(2)}(\xi) = \frac{4i}{\pi \xi}. \tag{69}$$

We obtain

$$T = -\frac{4i}{k_R}, \tag{70}$$

and Eq. (67) yields

$$C = -\frac{k_R}{4i} \frac{Q V^R(z_0)}{I A^2}. \tag{71}$$

Substitution of the expressions for $\Sigma_{rr}^R(z)$, $\Sigma_{rz}^R(z)$, $V^R(z)$, and $W^R(z)$, given by Eqs. (42)–(43) and (7) and (8), but with $k = k_R$, into Eq. (66) yields a relative simple integral over z which can easily be evaluated. The parameter k_R appearing in the integral is the solution of Eq. (51).

To simplify subsequent expressions, we introduce the dimensionless Rayleigh wave velocity by

$$\xi = \frac{\omega}{c_T} \frac{1}{k_R}. \tag{72}$$

We also introduce

$$q_R^2 = 1 - \xi^2, \tag{73}$$

and

$$p_R^2 = 1 - \frac{\xi^2}{\kappa^2}, \tag{74}$$

where

$$\kappa^2=\frac{c_L^2}{c_T^2}=\frac{2(1-\nu)}{1-2\nu} \tag{75}$$

here ν is Poisson's ratio. Carrying out the integration of Eq. (66) yields after some further manipulation

$$I=\mu J, \tag{76}$$

where Eq. (66) yields

$$J=-\frac{1+3q_R^2}{2q_R}+(1+q_R^2)\left[\frac{1+q_R^2}{2p_R}+\frac{q_R}{p_R}(p_R-q_R)+\frac{1}{p_R}\right] -\frac{(1+q_R^2)^2}{8p_R^3}(1+4p_R^2-q_R^2). \tag{77}$$

By using (59), (26), and (71), the vertical displacement at position (r,θ,z_1) may then be written as

$$\frac{\mu}{Q}\frac{u_z^R}{k_R}=-\frac{1}{4i}\frac{1}{J}\frac{V^R(z_0)}{A}\frac{W^R(z_1)}{A}H_1^{(2)}(k_Rr)\cos\theta, \tag{78}$$

where

$$V^R(z_0)=[d_1e^{-p_Rk_Rz_0}+d_2e^{-q_Rk_Rz_0}]A, \tag{79}$$

$$W^R(z_1)=[d_3e^{-p_Rk_Rz_1}-e^{-q_Rk_Rz_1}]A. \tag{80}$$

IV. SURFACE WAVE MOTION GENERATED BY P

For the axially symmetric case, the relevant solution $\varphi(k_Rr)$ of Eq. (15) is

$$\varphi(k_Rr)=H_0^{(2)}(k_Rr). \tag{81}$$

Analogously to Eqs. (58) and (59) the displacements for state *A*, which are the surface wave displacements generated by *P*, are

$$u_r^A=-DV^R(z)H_1^{(2)}(k_Rr), \tag{82}$$

$$u_z^A=DW^R(z)H_0^{(2)}(k_Rr), \tag{83}$$

where $V^R(z)$ and $W^R(z)$ follow from Eqs. (7) and (8), and D is the unknown amplitude factor. The relevant corresponding stresses may be written as

$$\sigma_{rz}^A=-D\Sigma_{rz}(z)H_1^{(2)}(k_Rr), \tag{84}$$

$$\sigma_{rr}^A=D\left[\Sigma_{rr}(z)H_0^{(2)}(k_Rr)+\overline{\Sigma}_{rr}(z)\frac{1}{k_Rr}H_1^{(2)}(k_Rr)\right], \tag{85}$$

where $\Sigma_{rz}(z)$, $\Sigma_{rr}(z)$, and $\overline{\Sigma}_{rr}(z)$ are defined by Eqs. (43), (42), and (47), respectively. For state *B*, we select the dummy solution

$$u_r^B=-\tfrac{1}{2}V^R(z)[H_1^{(2)}(k_Rr)+H_1^{(1)}k_Rr)],$$

$$u_z^B=\tfrac{1}{2}W^R(z)[H_0^{(2)}(k_Rr)+H_0^{(1)}(k_Rr)].$$

Equation (57) now yields

$$PW^R(z_0)=-\frac{4i}{k}DI, \text{ or } D=-\frac{k}{4i}\frac{PW^R(z_0)}{IA^2}, \tag{86}$$

where Eq. (69) has been used, and I is defined by Eq. (66).

By using Eqs. (82), (83), and (86), the displacements at position (r,θ,z_1) may then be written as

$$\frac{\mu}{P}\frac{u_r^R}{k_R}=\frac{1}{4i}\frac{1}{J}\frac{W^R(z_0)}{A}\frac{V^R(z_1)}{A}H_1^{(2)}(k_Rr), \tag{87}$$

$$\frac{\mu}{P}\frac{u_z}{k_R}=-\frac{1}{4i}\frac{1}{J}\frac{W^R(z_0)}{A}\frac{W^R(z_1)}{A}H_0^{(2)}(k_Rr). \tag{88}$$

Here, $V^R(z_1)$and $W^R(z_0)$ are given by Eqs. (79) and (80), but with z_0 and z_1 interchanged.

V. DISCUSSION

As shown in this paper, the surface wave displacements due to a subsurface time-harmonic point load are relatively easy to obtain by using the reciprocity theorem. It will, however, be of interest to verify the results for internal consistency, and by comparison with analogous results obtained by the use of Hankel transform techniques. First, we will check the reciprocity of the solutions given by Eqs. (78) and (87). The simplest check of reciprocity is for the case that a vertical unit load is applied at $r=0$, $z=z_0$, and a horizontal unit load is applied at $r=r$, $z=z_1$. In that case, the displacement u_r at $r=r$, $z=z_1$, $\theta=0$ due to the vertical load should be just the same as the displacement u_z at $r=r$, $z=z_0$, $\theta=\pi$ due to the horizontal load. It is easily verified that this equality is indeed satisfied.

For the special case of a vertical point load applied at $r=0$, $z=0$ the vertical surface wave displacement at $(r,0)$ is available from a number of sources. It has been shown that the solution may be expressed as

$$u_z(r,0)=\frac{-P}{4\pi}\frac{1}{\mu}\frac{\omega^2}{c_T^2}\int_{-\infty}^{\infty}\frac{p(k)}{F(k)}kH_0^{(2)}(kr)\,dk. \tag{89}$$

The Rayleigh wave is the contribution from the pole at the point $k=k_R$, where k_R is the solution of Eq. (51), i.e., $F(k)=0$. We find

$$u_z=\frac{P}{2}\frac{i}{\mu}\frac{\omega^2}{c_T^2}\frac{(k_R^2-\omega^2/c_L^2)^{1/2}}{F'(k_R)}k_RH_0^{(2)}(k_Rr), \tag{90}$$

where

$$F'(k_R)=\left.\frac{dF(k)}{dk}\right|_{k=k_R}. \tag{91}$$

It is convenient to recast Eq. (90) in the form

$$\frac{\mu}{P}\frac{u_z}{k_R}=U_z(\xi)H_0^{(2)}(k_Rr). \tag{92}$$

Here,

$$U_z(\xi)=\frac{i\xi^2(1-\xi^2/\kappa^2)^{1/2}}{8F'(\xi)}, \tag{93}$$

where ξ is defined by Eq. (22) and

$$F'(\xi)=2(2-\xi^2)-2p_Rq_R-\frac{q_R^2+p_R^2}{p_Rq_R}. \tag{94}$$

Casting (78) in the form (92) for $z_0=0$ and $z_1=0$ yields

$$U_z(\xi)=\frac{i}{16}\frac{(1-q_R^2)^2}{J}. \tag{95}$$

Equations (93) and (95) both represent the surface wave generated by a time-harmonic point load applied normal to the surface of a homogeneous, isotropic, linearly elastic half-space. The question of interest is whether they do in fact give the same numerical result. This can easily be checked by a simple calculation. Let us consider the case of Poisson's ratio $\nu=0.25$. For this case, Eq. (75) yields $\kappa^2=3$, and the solution of $F(\xi)=0$ is

$$\xi=0.919\,402. \tag{96}$$

Substitution of this value in Eqs. (93) and (95) yields for both cases exactly the same value, namely,

$$U_z=-0.917\,429i. \tag{97}$$

The author believes that it is in fact possible to manipulate the two expressions for U_z and show analytically that they are the same, but he has not succeeded in doing so.

The method presented here also applies to layered half-spaces, to a transversely isotropic half-space with the symmetry axis normal to the free surface, and to certain cases of continuous inhomogeneity in the z direction.

ACKNOWLEDGMENT

This work was carried out in the course of research sponsored by the Office of Naval Research under Contract No. N00014-89-J-1362.

[1] A. T. de Hoop, *Handbook of Radiation and Scattering of Waves* (Academic, London, 1995).
[2] A. E. H. Love, *A Treatise on the Mathematical Theory of Elasticity* (Dover, New York, 1944).
[3] E. Betti, ''Teori della elasticita,'' Nuovo Cimento 7–10 (1872).
[4] Lord Rayleigh, ''Some general theorems relating to vibration,'' London Math. Soc. Proc. **4**, 366–368 (1873).
[5] J. D. Achenbach, *Wave Propagation in Elastic Solids* (North Holland/Elsevier, Amsterdam, 1973).
[6] J. D. Achenbach, A. K. Gautesen, and H. McMaken, *Ray Methods for Waves in Elastic Solids* (Pitman Advanced, Boston, 1982).
[7] J. D. Achenbach and Y. Xu, ''Wave motion in an elastic layer generated by a time-harmonic point load of arbitrary direction,'' J. Acoust. Soc. Am. **106**, 83–90 (1999).
[8] J. D. Achenbach, ''Lamb waves as thickness vibrations superimposed on a membrane carrier wave,'' J. Acoust. Soc. Am. **103**, 2283–2285 (1985).
[9] H. Lamb, ''On the propagation of tremors over the surface of an elastic solid,'' Philos. Trans. R. Soc. London, Ser. A **203**, 1–42 (1904).
[10] C. L. Pekeris, ''The seismic surface pulse,'' Proc. Natl. Acad. Sci. USA **41**, 469–480 (1955).
[11] C. C. Chao, ''Dynamical response of an elastic half-space to tangential surface loadings,'' J. Appl. Mech. **27**, 559–567 (1960).
[12] N. W. McLachlan, *Bessel Functions for Engineers* (Oxford University Press, London, 1961).

Wave-number-based assessment of the doubly asymptotic approximation. I. Frequency domain wet surface impedance

Jerry H. Ginsberg[a)]
G. W. Woodruff School of Mechanical Engineering, Georgia Institute of Technology, Atlanta, Georgia 30332-0405

(Received 4 November 1996; revised 23 August 1998; accepted 14 December 1999)

The doubly asymptotic approximation (DAA) is a canonical relationship for the interaction between surface normal velocity and pressure. Its validity for a slender hemicapped cylinder is examined by formulating a frequency domain version of DAA using the global basis functions employed in the wave-number-based formulation of the surface variational principle [K. Wu and J. H. Ginsberg, ASME J. Vib. Acoust. **120**, 392–400 (1998)]. The wet surface impedance matrix, which relates the spectral representation of normal velocity to a corresponding representation of pressure, is obtained according to a second-order version of DAA and according to the surface variational principle. Comparison and interpretation of the results reveals that DAA fails to account for highlights associated with transition from supersonic to subsonic surface waves as the surface wavelength decreases with frequency held constant. © *2000 Acoustical Society of America.* [S0001-4966(00)05303-0]

PACS numbers: 43.20.Tb, 43.30.Jx, 43.40.Qi, 43.40.Ey [ANN]

INTRODUCTION

Most analyses of the response of submerged and surface vessels to underwater shock have relied on the doubly asymptotic approximation (DAA) to describe the surface interaction. The time domain relation between surface pressure and normal velocity is described in a DAA approximation by a set of coupled linear differential equations. The literature on DAA is rich. The method was developed by Geers as an outgrowth of analyses of the response of infinitely long cylindrical shells,[1,2] and spherical shells[3] to an incident wave having a step discontinuity. In essence, the original development examined the Laplace transform of the response to identify two asymptotic limits. For early times (large s), the equations governing structural response were found to be dominated by the plane-wave limit, in which the pressure is proportional to the local normal velocity. The late time (small s) relations were found to be essentially the incompressible limit, in which the pressure is proportional to the normal acceleration through an added mass impedance that is obtained as a global property. Further developments introduced improvements by correcting the plane wave limit to account for surface curvature,[4] and to extend the asymptotic matching to higher order.[3] Application of DAA to treat submerged structures with internal fluid domains is discussed by Geers and Zhang,[5] which also describes derivation of the various levels to which the asymptotic approximations may be carried.

The remarkable aspect of DAA is that, despite its wide application, it has not been fully validated. The exterior acoustic radiation problem for spheres and infinite cylinders may be represented as separable wave functions, whereas no closed form solution is possible for a capped cylinder, which is the shape of primary concern for most submerged structures. Thus, application of DAA to the finite geometry represents a fundamental assumption that the overall quality of the technique is independent of decoupling phenomena inherent to a separation of variables solution. Because analytical solutions for finite geometries do not exist, predictions obtained from DAA models have been compared in numerous studies to data obtained from small scale and full scale tests. It is difficult in such situations to ascertain whether discrepancies are due to the assumptions in DAA, shortcomings of the structural aspect of the model, or problems with the experiment.

Nicholas-Vullierme[6] performed a study in the frequency domain in order to provide a rational basis for the various DAA versions. The Fourier transform of a time derivative is an $(-ika)$ factor (based on time being nondimensionalized as ct/a, where a is a cross-section dimension). As a result, the DAA time domain equations relating surface pressure and normal displacement correspond in the frequency domain to a linear matrix equation for the corresponding transformed amplitudes; the coefficients of the transfer matrix are functions of ka. The present implementations of DAA are truncated at second derivatives, so these coefficients were considered by Nicholas-Vullierme to be quadratic in k. The terms characterizing the transfer relations were obtained by expanding the surface Helmholtz integral equation in powers of k for the low frequency (late-time) asymptotic, and in powers of $1/k$ for the high-frequency (early-time) asymptotic. Various levels of DAA approximation were identified, depending on how many terms in each asymptotic expansion are used to represent the frequency dependence of the pressure-displacement equation coefficients. Subsequently, Gears and Toothaker[7] examined the quality of various DAA levels of approximation for spheres and infinite cylinders.

Nicholas-Vullierme's work is the starting point for the present study, whose purpose is to provide an analytical as-

a)Electronic mail: jerry.ginsberg@me.gatech.edu

sessment of the validity of DAA for slender bodies. The overall concept is to use a validated structural acoustics formulation as the reference solution over a broad range of frequencies. Then the fluid-structure interaction aspects of that formulation, which will be seen to be the wet surface impedance, are replaced by the relations obtained from a DAA formulation. It is important that the only aspect that is modified is the physical law governing the surface interaction—the structural dynamics laws are not altered, nor are the basis functions associated with fluid and structural responses.

The structural acoustic solution used here as the reference is obtained from the work of Wu and Ginsberg,[8–10] in which the surface variational principle (SVP) was refined and coupled to a Ritz expansion of the shell response. The former governs the surface pressure stemming from a specified normal velocity, while the latter yields equations for the structural displacement corresponding to a specified surface pressure. This method is selected as the reference for several reasons. As described by Wu and Ginsberg, the method provides one with self-contained error estimates, and it has been thoroughly validated against standard structural acoustics programs. In addition, unlike the standard boundary or finite element formulations, the response variables in SVP have physical significance as amplitudes of waves. Correspondingly, an assessment of the degree to which DAA deviates from the reference solution indicates the spatial scales over which DAA is valid.

The first step, which is the topic of the present paper, is a derivation of the DAA wet surface impedance corresponding to the global basis function representation of surface response used previously for SVP. Typical results for this quantity are compared with those obtained from SVP. The second part of the work will present the methodology for assessing the correctness of DAA for structural motion, and the results of that assessment.

I. SVP REFERENCE SOLUTION

Wu and Ginsberg[9,10] coupled the surface variational principle and a Ritz expansion of the displacement field of a capped cylindrical shell. In doing so, they extended to asymmetric excitation Chen and Ginsberg's wave-number-based formulation[11] for axisymmetric situations. The overall procedure entails selecting individual series expansions representing the positional dependence of the surface pressure, the surface normal velocity, and the shell's displacement field. The focus here is on derivation of the wet-surface impedance.

The body to be used for the assessment is a cylindrical shell of length L and radius a capped at both ends by hemispherical shells. Position along the wetted surface is measured by the azimuthal angle measured along a slice transverse to the longitudinal axis, and arclength s is measured along a meridian obtained from a cutting plane containing the longitudinal axis. One apex is defined as $s=0$, and the arclength to the other apex, $s_0=L+\pi a$, is used to define a nondimensional meridional distance, $\alpha=s/s_0$. The azimuthal dependence of each response variable is represented by a complex Fourier series over $-\pi\leqslant\theta\leqslant\pi$. The α dependence of surface pressure and normal velocity associated with each azimuthal harmonic is represented by half-range Fourier series extending over $0\leqslant\alpha\leqslant 1$. For response to an excitation at frequency ω, all time dependencies are represented by an $\exp(-ika\tau)$ factor that is suppressed, where $\tau=ct/a$ is nondimensional time. Thus,

$$p=\frac{1}{2}\rho c^2\sum_{m=-\infty}^{\infty}\sum_{j=1}^{N}P_j^m\psi_j^m(\alpha)\exp(im\theta),$$
$$v_\perp=\frac{1}{2}c\sum_{m=-\infty}^{\infty}\sum_{j=1}^{N}V_j^m\psi_j^m(\alpha)\exp(im\theta). \tag{1}$$

Different series functions ψ_j^m are selected for the axisymmetric harmonic $m=0$, and for $m\neq 0$, in order to satisfy continuity conditions at the apexes,

$$\psi_j^m=\begin{cases}\cos(j\pi\alpha), & j=0,1,\ldots \quad \text{if } m=0,\\ \sin(j\pi\alpha), & j=1,\ldots \quad \text{if } m\neq 0.\end{cases} \tag{2}$$

In view of the trigonometric nature of Eqs. (1) and (2), the coefficients P_j^m and V_j^m may be interpreted as the surface trace of the acoustic waves that radiate and evanesce into the fluid field. On the cylindrical segment of the surface, these are a helical wave set, whose trace wavelength in the axial direction is $2s_0/j$.

To obtain equations governing the pressure coefficients P_j^m one substitutes Eq. (1) into the SVP functional, which is a double integral over the wetted surface. This functional reduces to a quadratic sum after integration. The functional is stationary with respect to infinitesimal changes of the pressure coefficients when these pressure coefficients have the value appropriate to a specified set of velocity coefficients. Requiring this stationarity leads to

$$[A^m]\{P^m\}=ika[B^m]^T\{V^m\}, \tag{3}$$

where $[A^m]$ and $[B^m]$ are coefficients involving double surface integrals at each ka. An important consequence of the axisymmetry of the wetted surface is decoupling of the azimuthal harmonics, which is manifested here by the superscript m denoting that the associated array contains only the quantities associated with harmonic m. Solution of Eq. (3) yields the wet surface impedance according to SVP, $[Z_{\mathrm{SVP}}^m]$, where

$$\{P^m\}=[Z_{\mathrm{SVP}}^m]\{V^m\}, \quad [Z_{\mathrm{SVP}}^m]=ik\alpha[A^m]^{-1}[B^m]^T. \tag{4}$$

II. DAA FREQUENCY DOMAIN REPRESENTATION

The wet surface impedance embodies the physical laws describing the interaction between the vibrating wetted surface and the surrounding fluid. The present test of DAA is based on replacing the SVP impedance by the corresponding relation associated with a DAA approximation. This relation must be based on using Eq. (1) to represent the surface response. The foundation for the development is provided by Nicholas-Vullierme,[6] whose analysis expanded the surface Helmholtz integral in power series of k for low frequency excitation, and power series of $1/k$ for high frequency excitation. To employ Nicholas-Vullierme's work, which used an $\exp(+i\omega t)$ factor, his quantities are converted to their com-

plex conjugate, and the potential function used previously is replaced by $p/i\omega\rho$. The resulting expression for low frequency excitations is

$$p(\mathbf{x}) = i\omega\rho[T_0(v_\perp(\mathbf{x})) + kT_1(v_\perp(\mathbf{x}))], \tag{5}$$

where $p(\mathbf{x}) = i\omega\rho T_0(v_n(\mathbf{x}))$ is the limiting relation for $k \to 0$, and $T_1(v_\perp(\mathbf{x}))$ is associated with monopole radiation of the vibrating surface,

$$T_1(v_\perp(\mathbf{x})) = -\frac{i}{4\pi}\int\int v_\perp(\mathbf{x})\,dS. \tag{6}$$

The high frequency expansion is a local curved wave representation,

$$v_\perp(\mathbf{x}) = \frac{p(\mathbf{x})}{\rho c} - \frac{1}{i\omega}\kappa(\mathbf{x})p(\mathbf{x}), \quad ka \gg 1, \tag{7}$$

where $\kappa(\mathbf{x})$ is the mean curvature of the surface, $\kappa(\mathbf{x}) = \frac{1}{2}(\kappa_1 + \kappa_2)$, with κ_1 and κ_2 being the principal curvatures.

For the present application, these relations must be converted to relations between $\{P^m\}$ and $\{V^m\}$. This is obtained by introducing the series expansions for pressure and normal velocity, Eq. (1), into Eqs. (5)–(7), then employing a Galerkin procedure, in which $\psi_j^{(m)}$ are weighting functions and the integration extends over the entire wetted surface. The result obtained from Eq. (5) for low frequencies is

$$\{P^m\} = ika[[T_0^m] + ka[T_1^m]]\{V^m\}, \quad ka \ll 1. \tag{8}$$

The term $[T_0^m]$ refers to the wet-surface impedance in the limit as $ka \to 0$, so it may be interpreted as the added mass at zero frequency. (How this quantity is determined will be discussed later.) The monopole term only contributes to the $m = 0$ harmonic, because only that term has a nonzero mean value over the surface. Specifically,

$$[T_1^m] = \begin{cases} [W^0]^{-1}[U] & \text{if } m = 0 \\ 0 & \text{if } m \neq 0, \end{cases} \tag{9}$$

where

$$W_{jn}^m = \int_0^1 \psi_j^m \psi_n^m R\,d\alpha, \quad U_{jn} = \int_0^1 \psi_j^0 R\,d\alpha \int_0^1 \psi_n^0 R\,d\alpha, \tag{10}$$

with $aR(\alpha)$ being the radial distance from the cylinder axis to a point on the meridian at arclength $s_0\alpha$. A similar Galerkin procedure applied to the high frequency approximation, Eq. (7), leads to

$$\{V^m\} = \{P^m\} - \frac{1}{ika}[H^m]\{P^m\}, \quad ka \gg 1, \tag{11}$$

where

$$[H^m] = [W^m]^{-1}[\kappa^m], \quad \kappa_{jn}^m = \int_0^1 a\kappa(\alpha)\psi_j^m\psi_n^m R\,d\alpha. \tag{12}$$

The last phase of the development is to derive a relation between $\{P^m\}$ and $\{V^m\}$ whose expansions for low and high ka, respectively, match Eqs. (8) and (11). This is achieved by noting that the coefficient matrices $[A^m]$ and $[B^m]$ are frequency dependent. If one assumes that they are analytic in ka, then they may be expanded in power series of that variable. The number of terms retained in the series indicates the DAA order. Because the pressure should vanish in the limit as $ka \to 0$, a truncation at quadratic terms gives

$$[[I] + ika[A_1^m] - (ka)^2[A_2^m]]\{P^m\} = [ika[B_1^m] - (ka)^2[B_2^m]]\{V^m\}, \tag{13}$$

where $[I]$ denotes the identity matrix. Equations for the elements of $[A_j^m]$ and $[B_j^m]$ are obtained by solving Eq. (13) for $\{P^m\}$, then matching to Eq. (8) the expansion of that result in powers of ka. Additional equations are obtained by solving Eq. (13) for $\{V^m\}$, then expanding the result in powers of $1/ka$, and matching it to Eq. (11). Nicholas-Vullierme categorized the order of the DAA approximation by the number of terms on either side of Eq. (13) that are actually required to match. The present assessment of DAA uses the highest order approximation identified by Nicholas-Vullierme, DAA-2, for which

$$\begin{aligned} [A_1^m] &= [[T_0^m] + i[T_1^m][H^m]][\Theta^m]^{-1}[T_0^m]^{-1}, \\ [A_2^m] &= [B_2^m] = [[T_0^m] - i[T_1^m][T_0^m]^{-1}][\Theta^m]^{-1}, \\ [B_1^m] &= [T_0^m], \end{aligned} \tag{14}$$

with

$$[\Theta^m] = [T_0^m]^{-1} + [H^m]. \tag{15}$$

Solution of Eq. (13) yields the DAA-2 version of the wet surface impedance,

$$[Z_{\mathrm{DAA}}^m] = [[I] + ika[A_1^m] - (ka)^2[A_2^m]]^{-1} \times [ika[B_1^m] - (ka)^2[B_2^m]]. \tag{16}$$

The only quantity undefined at this juncture is the added-mass matrix, $[T_0^m]$. Its evaluation corresponding to a boundary element formulation was described by deRuntz.[12] For the present purpose, using such as evaluation would not be suitable because the discrete nature of the boundary element formulation is unlike the series representations of p and $v_\perp$ used here. One could convert the boundary element representation to the present variables. However, to do so would still lead to ambiguity, because differences between DAA and SVP predictions could be attributed to discrepancies in their low frequency behavior. In order to avoid this, $[T_0^m]$ is derived from the SVP surface impedance evaluated at $ka = 0$,

$$[T_0^m] = \lim_{ka \to 0}\left\{\frac{1}{ika}[Z_{\mathrm{SVP}}^m]\right\}. \tag{17}$$

It is readily verified that as a consequence of this selection, $[Z_{\mathrm{DAA}}^m] \to [Z_{\mathrm{SVP}}^m]$ as $ka \to 0$.

The issue of spurious resonances associated with acoustic interaction formulations relying on a boundary integral arises in the computation of $[T_0^m]$ according to Eq. (17). As shown by Wu and Pierce,[13] the surface variational principle fails to give a unique solution at the Neumann eigenfrequencies of the interior domain (zero velocity at the surface). The fundamental Neumann eigenfrequency of any interior domain is $ka = 0$; the corresponding eigenmode is a constant

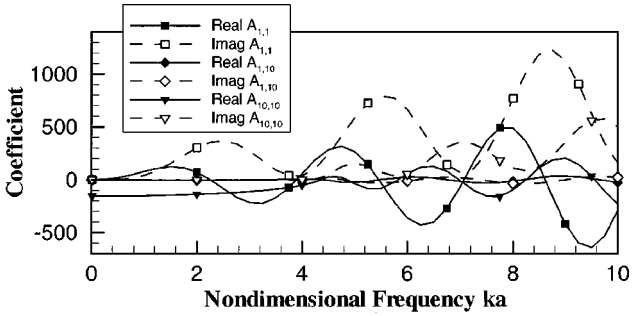

FIG. 1. Selected coefficients in the SVP equations, $L/2a=5$, $m=0$.

pressure. Hence, a spurious resonance situation is encountered when SVP is used to compute $[T_0^m]$ for $m=0$. The remedy is offered by Wu,[14] who showed that adding an interior point constraint in the manner employed for the CHIEF program[15] leads to well behaved solutions when *ka* matches any interior eigenfrequency. [At any frequency, proximity of *ka* to a resonance is indicated in the SVP formulation by a rapid rise in the condition number of $[A^m]$ appearing in Eq. (3), which marks a potential difficulty with invertibility. None of the nonzero frequencies for the present computations were found to be problematic, but the interior point constraint could have been used if necessary.]

An interesting sidebar to this development of DAA arises from comparing Eqs. (3) and (13), which shows that the DAA-2 representation is equivalent to a quadratic fit to the actual *ka* dependence of the elements of $[A^m]$ and $[B^m]$. The dependence on *ka* of a few representative coefficients of $[A^0]$ for a hemicapped cylinder whose aspect ratio is $\beta \equiv L/2a=5$ appears in Fig. 1. The curves display a highly oscillatory behavior, which is vastly different from the quadratic behavior associated DAA in Eq. (13). From this perspective, it would seem unlikely that DAA results will match solutions obtained from SVP.

III. COMPARISON OF WET SURFACE IMPEDANCE

A column Z_{nj}^m, fixed *j*, of either wet surface impedance represents the spectrum of wave amplitudes P_n^m that would be generated if the sole contribution to the surface velocity were $V_j^m=1$. Each P_j^m and V_j^m corresponds to a surface distribution whose half-wavelength in the meridional direction is s_0/j. Hence, an examination of the wet surface matrix provides an indication of the range of spatial scales over which DAA yields a valid description for the surface interaction. Such information may be displayed in terms of contour maps. To construct such a map, one must recognize that the hemicapped cylinder is symmetric about its transverse midplane. Consequently, Z_{nj}^m is composed of symmetric and antisymmetric contributions, in which *j* and *n* have the same parity, even or odd. The terms for which *j* and *n* have different parity are zero. The results displayed here are for symmetric interactions, which are indicated by Eq. (1) to be *j* and *n* even for $m=0$, and *j* and *n* odd for $m\neq 0$. In view of the discrete nature of the wave-number spectrum, the impedance values (real and imaginary) will be displayed as contours using 2×2 cells whose value is Z_{nj}^m for *j* and *n* at the lower left corner of the cell.

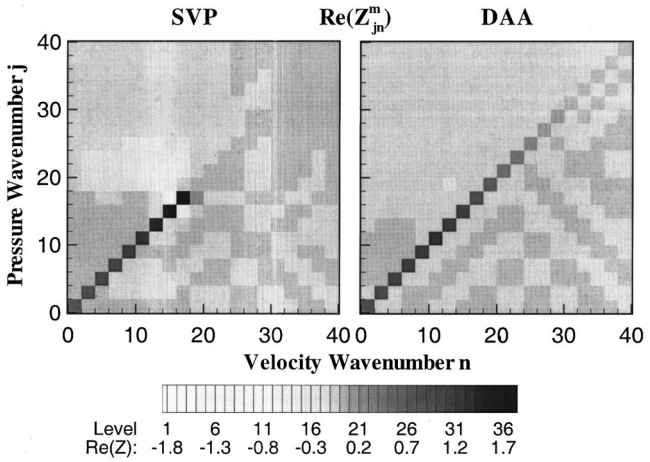

FIG. 2. Real part of the wet surface impedance, $L/2a=2$, $ka=7$, $m=0$.

Results for $[Z_{\mathrm{DAA}}^m]$ and $[Z_{\mathrm{SVP}}^m]$ were computed for $\beta=L/2a=2$ and 5, $ka=1$, 4, 7, and 10, and $m=0$ to 5. The results for $\beta=2$ and $ka=7$ yield a general picture. Figure 2 compares the real parts for $m=0$, while Fig. 3 provides the corresponding comparison of the imaginary parts. Note that the lower left-hand corner of the contour maps corresponds to the (1, 1) element of the matrix. The impedance terms for which $j=n$ are termed self-impedances, because they describe the pressure amplitude generated by a normal velocity wave having the same wavelength. Cross-impedance shall refer to pressure waves generated by velocity waves having different wavelength. Also, it is useful to recall that the real part of the impedance is the resistive effect responsible for acoustic radiation. When the imaginary part is positive, it corresponds to an added-mass effect, whereas a negative value is spring-like.

It is evident in Figs. 2 and 3 that either description leads to self-impedances that are much larger than the cross impedances. Both analyses indicate the maximum values occur in the vicinity of $j=n=16$. These maxima are indicated by SVP to be larger, and to vary more abruptly away from the maxima. Also, all cross impedances are very small according to DAA, with the largest cross impedance having a magni-

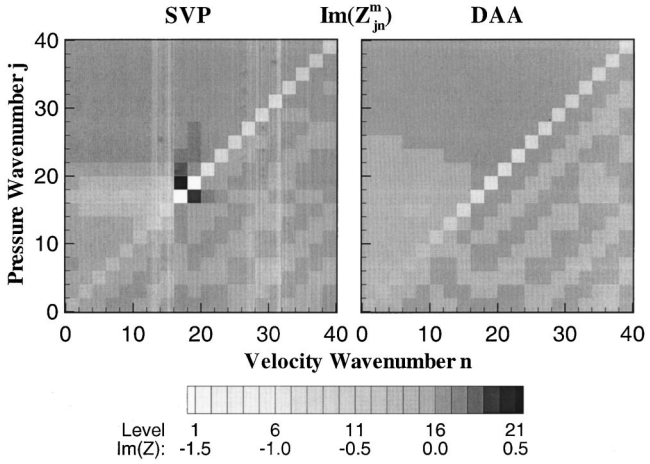

FIG. 3. Imaginary part of the wet surface impedance, $L/2a=2$, $ka=7$, $m=0$.

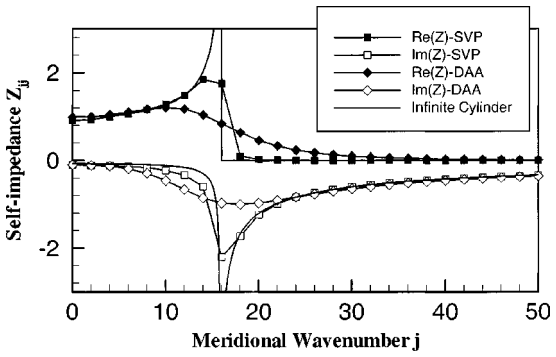

FIG. 4. Self-impedance, $L/2a=2$, $ka=7$, $m=0$.

tude of 0.03, while the largest self-impedance magnitude is 1.31. In comparison, the SVP cross-impedance magnitudes in the vicinity of $n=j=16$ are approximately 20% of the adjacent self-impedances. Particularly noteworthy in this regard is $Z_{18,16}$, which is essentially a positive imaginary value corresponding to an elastic impedance, while the imaginary part of the self-impedances are all negative and therefore mass-like.

A more detailed view of the self-impedances is provided by Fig. 4. It can be seen that the SVP prediction of the real part begins from a nearly unit value for small j, rises to a maximum around $j=14$ and 16, then essentially vanishes for larger j. DAA yields a real part that is close to the SVP values away from the peak, but it significantly underpredicts the peak values. Also, the DAA prediction falls off quite gradually beyond the peak. For the imaginary part, SVP starts from a small negative value at small j, quickly decreases to a minimum at $j=16$, then ascends monotonically toward zero for larger j. As in the case of the real part, the imaginary part of the self-impedance matches the SVP value quite well away from the peak, and the peak DAA value is much smaller in magnitude.

The variability in the SVP values is due to a transition from supersonic to subsonic waves on the cylindrical surface. To see why, consider Fig. 5, which depicts the trace on the cylindrical surface of a wave at azimuthal harmonic m. The wave vector $\mathbf{k}_{mj}$ indicates the direction in which this wave spirals relative to the meridional direction $\mathbf{s}$. The wavelength measured in the direction of $\mathbf{k}_{mj}$ is λ_s; the trace of this wavelength in the circumferential direction is the periodicity length $2\pi a/m$, while the trace in the meridional direction is $2s_0/j$. A geometrical evaluation shows that the spiral wavelength is

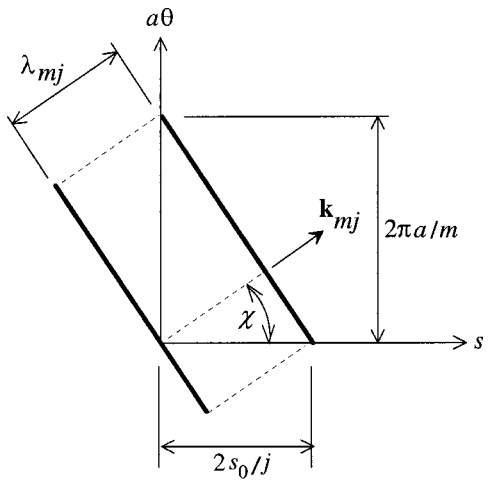

FIG. 5. Trace of a wave along the cylindrical surface.

$$\lambda_s = 2s_0 \frac{(\pi a)}{[(j\pi a)^2 + (ms_0)^2]^{1/2}}. \tag{18}$$

When the spiral wavelength is greater than the acoustic wavelength, $\lambda_s > 2\pi/k$, the wave is supersonic, while $\lambda_s < 2\pi/k$ corresponds to subsonic waves. The transition occurs when

$$j_{\mathrm{tr}} = \left(\frac{2}{\pi}\beta + 1\right)[(ka)^2 - m^2]^{1/2}. \tag{19}$$

For the parameters associated with Figs. 2–4, this yields $j=16$, which matches the transition of the SVP self-impedances.

As a further illustration of the manifestation of helical wave phenomena, consider the case of an infinite cylinder, whose solution is provided by Junger and Feit.[16] In that solution a surface normal velocity in the form of a single helical velocity wave generates only a pressure wave whose trace along the surface is comparable. Specifically, if the surface velocity is

$$v_\perp(z,\theta) = c\,\mathrm{Re}\{V \exp[i(k_z z + m\theta - \omega t)]\}, \tag{20}$$

then the pressure field will be

$$p(R,z,\theta) = \rho c^2\,\mathrm{Re}\{P H_m(k_R R) V_j^m \times \exp[i(k_z z + m\theta - \omega t)]\},$$

where $H_m(\,)$ denotes the first Hankel function. The impedance factor obtained from this solution is

$$Z \equiv \frac{p(a,z,\theta)}{v_\perp(z,\theta)} = \frac{ikaH_m(k_R a)}{k_R a H_m'(k_R a)}, \quad k_R = (k^2 - k_z^2)^{1/2}. \tag{21}$$

Note that cases where $k_z < k$ correspond to supersonic helical waves, and Z_{jj} is complex. In the subsonic case, $k_z > k$, one must select the branch cut that yields a positive imaginary value for k_R. The corresponding value of Z_{jj} is purely imaginary.

To apply Eq. (21) to the capped cylinder one equates the axial wave number k_z to the dimensional meridional wave number $j\pi/s_0$. The spectrum for the capped cylinder is discrete, whereas that for the infinite cylinder is continuous. For this reason Fig. 5 depicts Eq. (21) as a continuous line, whereas markers are used to denote the impedance values obtained from SVP and DAA. The self-impedance values obtained from the SVP analysis are in extraordinarily close agreement with the values obtained from an infinite cylinder model.

Consideration of Eq. (19) leads to insight as to how the patterns in Figs. 2 and 3 are altered by changing the azimuthal harmonic, excitation frequency, and aspect ratio. Figures 6 and 7 are the analogs to Figs. 2 and 3 for $m=5$. Increasing m in Eq. (19) yields $j_{\mathrm{tr}}=11$. The self-impedance plot in Fig. 8 shows that this falls in the range where both parts of Z_{jj}^5 obtained from SVP show a maximum. The over-

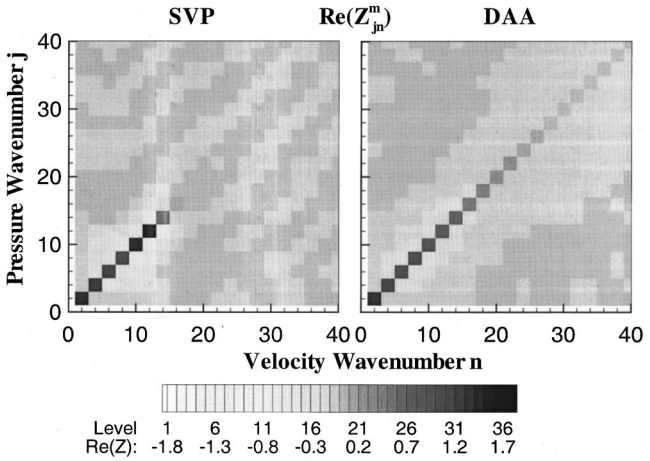

FIG. 6. Real part of the wet surface impedance, $L/2a=2$, $ka=7$, $m=5$.

all nature of both the SVP and DAA contours remains the same as for $m=0$, with the exception that all cross impedances obtained from SVP are small, so that the only important terms obtained from SVP and DAA in this case are the self-impedances.

In comparison to the self-impedances in Fig. 4 for $m=0$, the SVP values are less like the infinite cylinder values, until the wave number exceeds j_{tr}. Also, the peak in the SVP data are lower and more spread out. As was true for $m=0$, the DAA self-impedances away from j_{tr} are in good agreement with SVP, and the peak values are underpredicted by DAA. In fact, DAA only barely indicates the presence of the peak. This shortcoming of DAA was previously noted by Geers and Felippa.[17]

According to Eq. (19), the supersonic spectrum is cutoff for $m>ka$. This was confirmed in the computations. For example, when $\beta=2$ and $ka=4$, the SVP self-impedances for $m=5$ are essentially negative imaginary values that asymptotically approach zero with increasing j, which is a trend that can be anticipated by moving the peaks in Fig. 8 to the left beyond the origin.

The wet-surface impedances for other frequencies and aspect ratios behave qualitatively in the same manner as the cases displayed thus far. The primary change is the location

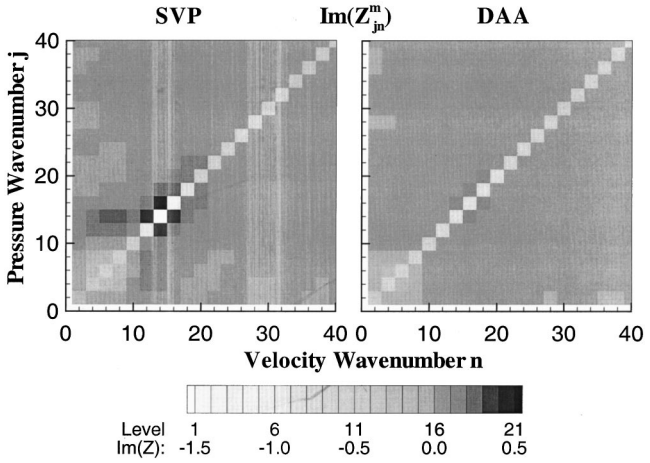

FIG. 7. Imaginary part of the wet surface impedance, $L/2a=2$, $ka=7$, $m=5$.

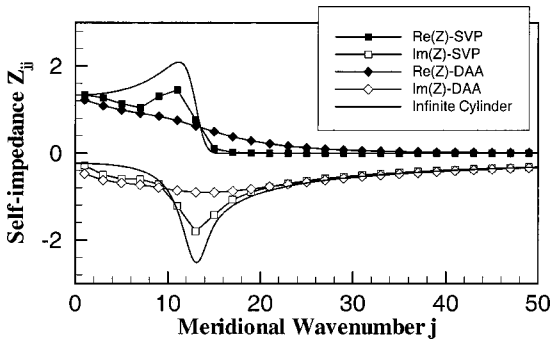

FIG. 8. Self-impedance, $L/2a=2$, $ka=7$, $m=5$.

of the supersonic to subsonic transition, as described by Eq. (19). This shifts the highlights of the contours, which occur whenever $m<ka$, and essentially rescales the self-impedances to match the new location of the transition. To illustrate this, Figs. 9 and 10 describe the case $\beta=5$, $ka=7$, $m=1$. The corresponding maximum value of $\mathrm{Re}(Z^1_{jj})$ occurs at $j=29$, which agrees with the value of j_{tr} obtained from Eq. (19). One noteworthy difference relative to the lower aspect ratio is that the cross impedances in Figs. 9 and 10 show more rapid and larger excursions in the vicinity of j_{tr}. In comparison, DAA continues to give negligibly small values for all cross impedances, and it underpredicts the peak values of the self-impedances.

To further demonstrate the common features of the wet-surface impedance for different system parameters, the self-impedances for $\beta=5$ and $ka=4$ are displayed in Fig. 11 for $m=0$ ($j_{\mathrm{tr}}=17$) and Fig. 12 for $m=2$ ($j_{\mathrm{tr}}=14$). The SVP results in Figs. 11 and 12 strongly resemble those in Fig. 4 for the lower aspect ratio, and they are quite close to the infinite cylinder values. The trends for the DAA self-impedances also are like those in Fig. 4. Specifically, DAA matches the SVP values away from j_{tr}, and it underpredicts the impedance values in the vicinity of j_{tr}.

IV. SUMMARY AND CONCLUSIONS

The surface pressure and normal velocity associated with the frequency domain response of a submerged, hemicapped cylindrical shell were represented as series whose

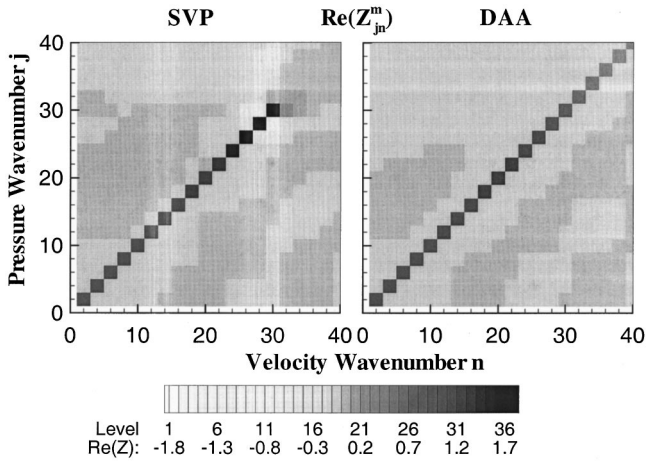

FIG. 9. Real part of the wet surface impedance, $L/2a=5$, $ka=7$, $m=1$.

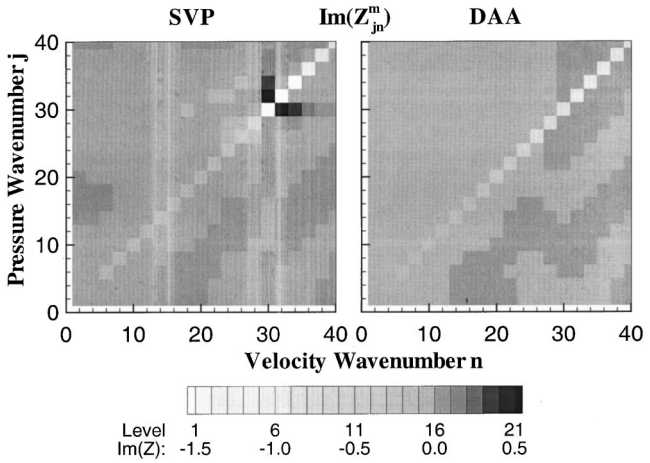

FIG. 10. Imaginary part of the wet surface impedance, $L/2a=5$, $ka=7$, $m=1$.

basis functions are globally defined. The series representation may be interpreted as a superposition of helical-like waves traversing the wet surface, which are the surface trace of the waves radiated into the surrounding fluid. The surface variational principle led to a description of the wet-surface impedance giving the pressure wave amplitudes that are generated by a set of normal velocity amplitudes. The SVP description of this quantity contains no approximations other than those contained in the basic model, specifically ideal fluid theory. The same series representation was used to derive a DAA rule for the surface interaction at a specified frequency. The rule was obtained by matching power series expansions of the surface Helmholtz integral equation to a series expansion of a standard form of the relation between pressure and normal velocity. The derived result was an expression for the wet-surface impedance according to DAA-2 (a quadratic truncation). This impedance relates the same variables as the impedance obtained from SVP. Furthermore, it was constructed to match the SVP wet surface impedance in the low frequency limit.

Comparisons of the DAA and SVP results lead to some general observations. Two types of impedance effects were identified. Self-impedances describe the pressure wave generated by a velocity wave having the same wave vector. It was shown that DAA is indeed doubly asymptotic, in that for a specified aspect ratio, azimuthal wave number, and frequency, the self-impedance obtained from DAA does match

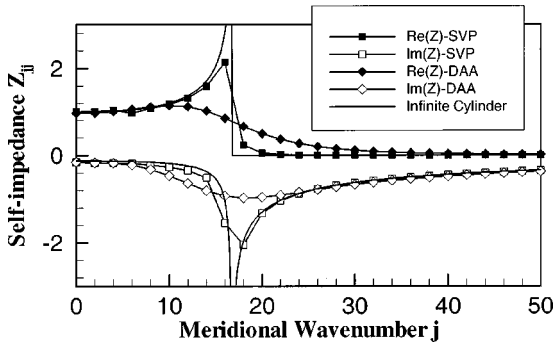

FIG. 11. Self-impedance, $L/2a=5$, $ka=4$, $m=0$.

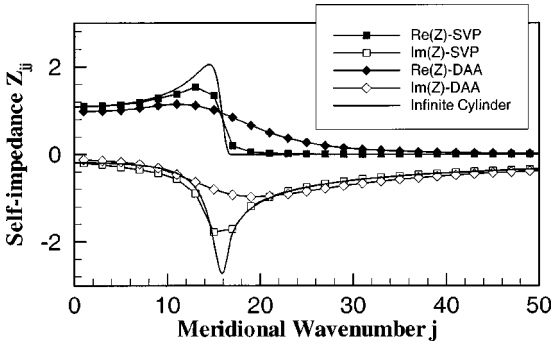

FIG. 12. Self-impedance, $L/2a=5$, $ka=4$, $m=2$.

the dependence obtained from SVP for low and high wave numbers. For intermediate wave numbers the SVP wet surface impedance is dominated by a supersonic to subsonic transition that is well-described by helical wave theory for infinite cylinders. Below the cutoff wave number, the wave is supersonic and the specific radiation impedance seen by this wave is essentially resistive; the self-impedance is essentially mass-like above this wave number. The self-impedances obtained from SVP near the cutoff wave number exhibit extrema and change rapidly. These values are closely approximated by the infinite cylinder model, but they are significantly underpredicted by DAA-2.

Cross impedances describe the pressure wave generated by a surface velocity whose wave vector is different. Such coupling does not exist for an infinite cylinder. The cross impedances are predicted by DAA-2 to be negligibly small for all wave-number pairs. The cross impedances obtained from SVP also are negligible, except for wave-number pairs in the vicinity of the supersonic-subsonic cutoff. In that region there is significant coupling between waves whose wave numbers are adjacent. This is the primary effect of the finite length of the cylinder.

The observations that DAA-2 underpredicts the self-impedances in the vicinity of the supersonic-subsonic cutoff, and that it completely misses the cross impedances in that range have the same explanation. The concept of any DAA is to match the low and high frequency behavior, which in the frequency domain is equivalent to the short and long wavelength spectra. The degree to which it matches phenomena at an intermediate wave number depends on the degree to which such phenomena are manifested at either extreme. The peak value of the SVP self-impedances in the vicinity of the cutoff is confined to a small interval of wave numbers. Furthermore, SVP indicates that coupling effects described by the cross impedances are negligible for low and high wave numbers. In this view it is not surprising that DAA-2, by interpolating the intermediate wave numbers from both extremes, fails to recognize the transition phenomena at cutoff. It has been shown by Geers[7] that a DAA based on retaining cubic terms in the low and high frequency asymptotic expansions does a better job in matching the self-impedances for an infinite cylinder. However, it is unlikely that any level of DAA approximation could ever correctly predict the cross impedances, which are only significant in the region around the cutoff wave number.

It is reasonable at this juncture to consider the significance of the foregoing phenomena for an investigation of response. For an analysis of the displacement of a submerged body due to a specified force excitation, underprediction of the wet surface impedance in a spectrum of wave numbers is likely to result in an overprediction of the response in that spectrum. This suggests that if an excitation generates significant displacement patterns over spatial scales matching the wavelengths where the transition from supersonic to subsonic waves occurs, then DAA will overpredict the response. On the other hand, if the response is dominated by either long or short wavelength patterns, DAA should provide reasonably good results. The correctness of this hypothesis is explored in the second part of this investigation.

The present analysis discloses the limitations of DAA from an acoustic viewpoint. Although DAA is intended to be employed as a tool for evaluating structural response, a few investigations have overlooked the limitation.[18,19] Ille[20,21] has used the present SVP data to show that even very small cross impedances must be retained if one wishes to correctly predict radiated power. For example, completely ignoring cross-impedance effects in an axisymmetric response can lead to errors of 10 dB in radiated power. As noted, DAA does not accurately represent the highlights of the interaction phenomena at the supersonic-subsonic transition. Given Ille's findings, it is likely that the radiated field obtained from a DAA formulation would be seriously in error.

ACKNOWLEDGMENTS

The support of the Office of Naval Research was instrumental to the performance of this work. The author is much indebted to Dr. J. Gregory McDaniel of Boston University for pointing out the similarity of the self-impedance values obtained from SVP to those of an infinite cylinder. In addition, the author would like to thank Tom Geers for identifying an inconsistency that was due to a computational error.

[1] T. L. Geers, ''Excitation of an elastic cylindrical shell by a transient acoustic wave,'' J. Appl. Mech. **36**, 459–469 (1969).
[2] T. L. Geers, ''Residual potential and approximate methods for three-dimensional fluid–structure interaction problems,'' J. Acoust. Soc. Am. **49**, 1505–1510 (1970).
[3] T. L. Geers, ''Doubly asymptotic approximations for transient submerged structures,'' J. Acoust. Soc. Am. **64**, 1500–1508 (1978).
[4] B. Bedrosian and F. L. DiMaggio, ''Acoustic approximations in fluid shell interaction,'' J. Eng. Mech. Div. ASCE **98**, 731–742 (1972).
[5] T. L. Geers and P. Zhang, ''Doubly asymptotic approximations for submerged structures with internal fluid volumes: Formulation,'' J. Appl. Mech. **61**, 893–899 (1994).
[6] B. Nicholas-Vullierme, ''A contribution to doubly asymptotic approximations: An operator top-down derivation,'' *Numerical Techniques in Acoustic Radiation*, edited by R. J. Bernhard and R. F. Keltie [Trans. ASME **NCA-6**, 7–13 (1989)].
[7] T. L. Geers and B. J. Toothaker, ''Evaluation of doubly asymptotic approximations for boundary elements,'' *Fundamental Solutions in Boundary Elements*, edited by F. G. Benitez, SAND (Camas), Sevilla, 1997 (unpublished), pp. 139–156.
[8] J. H. Ginsberg and K. Wu, ''Nonaxisymmetric acoustic radiation and scattering from rigid bodies of revolution using the surface variational principle,'' ASME J. Vib. Acoust. **120**, 95–103 (1998).
[9] K. Wu and J. H. Ginsberg, ''Progress in applying the surface variational principle to analyze acoustic radiation from slender elastic bodies,'' Proceedings of the Symposium on Acoustics of Submerged Structures and Transduction Systems, ASME 15th Biennial Conference on Mechanical Vibration and Noise, Boston, MA, 17–19 September 1995 (unpublished).
[10] K. Wu and J. H. Ginsberg, ''Mid-frequency range acoustic radiation from slender elastic bodies using the surface variational principle,'' ASME J. Vib. Acoust. **120**, 392–400 (1998).
[11] P. T. Chen and J. H. Ginsberg, ''Variational formulation of acoustic radiation from submerged spheroidal shells,'' J. Acoust. Soc. Am. **94**, 221–233 (1993).
[12] J. A. deRutz and T. L. Geers, ''Added mass computation by the boundary element integral,'' Int. J. Numer. Methods Eng. **12**, 531–549 (1978).
[13] X.-F. Wu and A. D. Pierce, ''Uniqueness of solutions to variationally formulated acoustic radiation problems,'' *Numerical Techniques in Acoustic Radiation*, edited by R. J. Bernhard and R. F. Keltie [Trans. ASME **NCA-6**, 7–13 (1989)].
[14] K. Wu, ''Extension of surface variational principle to nonaxisymmetric racoustic radiation and scattering problems,'' Ph.D. thesis, Georgia Institute of Technology, 1995.
[15] H. Schenck, ''Improved integral formulation for acoustic radiation,'' J. Acoust. Soc. Am. **75**, 363–375 (1968).
[16] M. C. Junger and D. Feit, *Sound, Structures, and Their Interaction* (MIT, Cambridge, 1986), pp. 166–173.
[17] T. L. Geers and C. A. Felippa, ''Doubly asymptotic approximations for vibration analysis of submerged structures,'' J. Acoust. Soc. Am. **73**, 1152–1159 (1983).
[18] D. E. Lesar and R. F. Jones, Jr., ''SWEEP-STAGS fluid element grid requirements for accurate representation of acoustic fluid impedance,'' Proceeding ASME Pressure Vessel and Piping Conference, 1985 (unpublished), pp. 269–276.
[19] S. Ortola, ''Acoustic radiation from submerged structures. Doubly asymptotic and iterative solutions,'' Rech. Aerosp. **6**, 55–65 (1993).
[20] J.-F. Ille, ''Interaction of spatial scales in acoustic radiation from hemi-capped capped cylinders,'' M.S. thesis, Georgia Institute of Technology, 1998.
[21] J.-F. Ille and J. H. Ginsberg, ''Interaction between wave-number pairs for a capped cylinder,'' J. Acoust. Soc. Am. (to be published).

Wave-number-based assessment of the doubly asymptotic approximation. II. Frequency and time domain response

Jerry H. Ginsberg[a)]
G. W. Woodruff School of Mechanical Engineering, Georgia Institute of Technology, Atlanta, Georgia 30332-0405

(Received 4 November 1996; revised 18 November 1998; accepted 14 December 1999)

In part I, the surface variational principle (SVP) and the doubly asymptotic approximation (DAA) were used to generate alternative descriptions of the frequency domain wet surface impedance. These are used here to obtain alternative descriptions of the displacement field in slender hemicapped cylindrical shells. This field is represented as a decomposition into a two-dimensional wave-number space. The responses that are obtained are frequency domain transfer functions for a point force at the midplane, evaluated for a discrete set of frequencies. Solutions obtained from first- and second-order versions of DAA are compared to the SVP result. Then temporal responses are obtained by using an inverse fast Fourier transform to evaluate the convolution of the transfer functions with a prototypical temporal excitation. The results reveal that DAA and SVP differ most in the vicinity of fluid-loaded resonances. The largest disagreement is encountered for the axisymmetric portion of the response. It is shown that DAA often greatly underpredicts peak displacements and accelerations, but a few cases lead to overprediction. © *2000 Acoustical Society of America.* [S0001-4966(00)05403-5]

PACS numbers: 43.20.Tb, 43.30.Jx, 43.40.Qi, 43.40.Ey [ANN]

INTRODUCTION

The doubly asymptotic approximation (DAA) is a canonical relationship for the time-domain interaction between surface normal velocity and pressure. It is widely used to predict the dynamic displacement of ships and submarines to an incident shock wave. The initial derivations of DAA by Geers[1–3] followed from trends observed in analyses using the Laplace transform to determine the shock response of a spherical shell and an infinitely long cylindrical shell. The term ''doubly asymptotic'' stems from the fact that the approximation matched the behavior of the Laplace transform solution in the early and late time limits, which correspond in the frequency domain to high and low frequencies, respectively. The lack of analytical solutions for other geometries has inhibited efforts to validate DAA for the types of configurations encountered in practice, specifically, slender bodies having finite length. The present work addresses this shortcoming.

The first part of the present investigation derived a frequency domain representation of DAA.[4] The basis for that derivation was the general treatment of the Kirchhoff surface integral performed by Nicholas-Vullierme,[5] in which the integral was expanded in power series of k for low frequency and of $1/k$ for high frequency, $(k=\omega/c)$. The development in part I applied the general formulation to the case where the surface response (pressure and normal velocity) is described by the wave-number-based representation associated with a recent application of the surface variational principle (SVP),[6,7] which yields a consistent representation having a self-contained *a posteri* error estimate. The outcome of part I was a description of the wet-surface impedance describing the spectrum of pressure waves generated by a spectrum of normal velocities at a specified frequency. It was shown in part I that the DAA wet-surface impedance fails to match the SVP values in the range of wave numbers at which the surface waves transition from supersonic to subsonic relative to the fluid. Away from this range, DAA was found to match SVP reasonably well.

As noted in part I, one consequence of the shortcoming of DAA in predicting wet-surface impedance in the vicinity of the cutoff wave number is that it should not be used to predict the surface pressure, as one would do in a structural acoustic evaluation of acoustic radiation and scattering. However, the purpose of DAA is to compute the dynamic displacement of the structure, rather than the acoustic field in the surrounding fluid. It is possible that the errors in the surface pressure are unimportant when they are applied as loads on the structure. In addition, errors at any specific frequency may be smeared out in the time domain, in view of the convolution theorem properties associated with the Fourier transform.

These issues are explored here. The frequency domain response of a shell in the shape of a cylinder with hemispherical caps is formulated using the method of assumed modes. The excitation is taken to be a point normal force applied at the midplane. Although such a force is unrealistic, it serves well as a diagnostic tool. Specifically, by exciting a broad spectrum of spatial wave numbers it allows for assessment of DAA over the wide range of spatial scales.

The structural displacement components are represented in the analysis by a Ritz expansion using basis functions that subtend the entire wetted surface, following the formulation of Wu and Ginsberg.[6,7] This leads to a set of Lagrange equations for the amplitudes of the basis functions. The loading associated with the surface pressure is described in terms of

a)Electronic mail: jerry.ginsberg@me.gatech.edu

 0001-4966/2000/107(4)/1906/9/$17.00

the wet surface impedance. Structural responses are evaluated by using first- and second-order DAA theories, as well as SVP, as alternative descriptions of the impedance. The variables that are examined are the amplitudes of surface displacement in wave-number space. In addition to comparing these variables over a broad range of frequencies, the inverse fast Fourier transform is used to construct alternative time responses of these amplitudes. An extensive set of data is used to deduce the quality of DAA.

I. FREQUENCY DOMAIN FLUID-STRUCTURE EQUATIONS

The structure under consideration is a cylindrical shell of length L, radius a, and thickness h capped at both ends by hemispherical shells of the same thickness. Position along the wetted surface is measured by the azimuthal angle θ measured along a slice transverse to the longitudinal axis and arclength s measured along a meridian obtained from a cutting plane containing the longitudinal axis. One apex is defined as $s=0$, and the arclength to the other apex, $s_0=L+\pi a$, is used to define a nondimensional meridional distance, $\alpha=s/s_0$, $0\leqslant\alpha\leqslant 1$. The azimuthal dependence of surface pressure and normal velocity for the fluid are represented by a complex Fourier series.

The shell's response is modeled using Love's assumptions, which includes the effects of extension of the midsurface and flexure, but omits the effects of transverse shear and rotatory inertia. Each azimuthal harmonic of the displacement vector is represented by a Ritz series that describes the manner in which that harmonic varies in the α direction. The basis functions for displacement components u, v, and w in the meridional, circumferential, and normal directions, respectively, are formed by mapping the natural mode functions of a spherical shell into the meridian. Specifically, the polar angle ϕ for the spherical shell mode functions is replaced by $\pi\alpha$ to obtain the appropriate terms for the capped cylinder. Such functions are selected as a convenient device for satisfying continuity conditions at the apexes for the shell, which are much more complicated than they are for the fluid. The resulting displacements are

$$\begin{aligned} u(\alpha,\theta,\tau)&=\frac{1}{2}a\sum_{m=-\infty}^{\infty}\sum_{n=m}^{N}\sum_{j=1}^{3}q_{nj}^{m}C_{mnj}\Phi_{mnj}^{u}(\alpha)\\ &\quad\times\exp(im\theta),\\ v(\alpha,\theta,\tau)&=\frac{1}{2i}a\sum_{m=-\infty}^{\infty}\sum_{n=m}^{N}\sum_{j=1}^{3}q_{nj}^{m}D_{mnj}\Phi_{mnj}^{v}(\alpha)\\ &\quad\times\exp(im\theta),\\ w(\alpha,\theta,\tau)&=\frac{1}{2}a\sum_{m=-\infty}^{\infty}\sum_{n=m}^{N}\sum_{j=1}^{2}q_{nj}^{m}\Phi_{mnj}^{w}(\alpha)\exp(im\theta). \end{aligned} \tag{1}$$

The functions Φ_{mnj}^{u}, Φ_{mnj}^{v}, and Φ_{mnj}^{w} are formed from spherical harmonics $\pounds_n^m(\cos\pi\alpha)$, and j refers to the branch number for the spherical shell vibration mode. In this representation $q_{nj}^{m}(\tau)$, where time is nondimensionalized as $\tau=ct/a$, may be interpreted as the modal amplitude for the shell vibration. However, the only configuration in which these variables are inertially and elastically uncoupled is a spherical shell. Expressions for the basis functions Φ_{mnj}^{r} and the coefficients C_{mnj} and D_{mnj} are given by Naghdi and Kalnins,[8] as well as Wu and Ginsberg.[6,7]

The structural dynamic formulation invokes Hamilton's principle, with Eq. (1) used to form the kinetic and potential energies, and the contributions of an exciting force and surface pressure to the virtual work. After integration over the surface of the shell, the energy expressions reduce to quadratic sums in the modal amplitudes. Because of the axisymmetry of the shell, the azimuthal harmonics uncouple. Thus, the coefficients in the kinetic energy quadratic sum are the inertia coefficients M_{npjl}^{m} for the harmonic, and the corresponding coefficients in the strain energy are the stiffness coefficients K_{npjl}^{m}. Explicit expressions for these terms as integrals over $0\leqslant\alpha\leqslant 1$ containing products of the basis functions Φ_{mnj}^{r} and their derivatives are given by Wu.[9]

Equations of motion for the modal amplitudes are those of Lagrange. For steady-state response, the dependence on nondimensional time may be represented by an $\exp(-ika\tau)$ factor, which is factored out. The resulting structural dynamic equations are

$$[[K^m]-(ka)^2[M^m]]\{q^m\}=\{Q_f^m\}+\{Q_p^m\}. \tag{2}$$

In the above, $\{q^m\}$ are the set of modal amplitudes for azimuthal harmonic m grouped by sector number,

$$\begin{aligned} \{q^0\}&=[q_{11}^0\quad q_{12}^0\quad q_{21}^0\quad q_{22}^0\quad q_{31}^0\quad\cdots\ ]^{\mathrm{T}},\\ \{q^m\}&=[q_{11}^m\quad q_{12}^m\quad q_{13}^m\quad q_{21}^m\quad q_{22}^m\quad q_{23}^m\quad\cdots\ ]^{\mathrm{T}};\\ &\quad m>0, \end{aligned} \tag{3}$$

where the special form of the $m=0$ case stems from the fact that there are only two vibration branches because the circumferential displacement mode is not excited in that case.

The term $\{Q_f^m\}$ represents the generalized forces associated with an external excitation. The present study considers a concentrated force at frequency ω whose amplitude is $2\pi a^2\rho c^2 f$. This force acts normally to the wetted surface at $\alpha=\alpha_f$, and its location is considered to define $\theta=0$. To construct the corresponding generalized forces the third of the displacement series in Eq. (1) is used to describe the virtual displacement field δw in the integral expression for the virtual work. Collecting the coefficients of δq_{nj}^m leads to

$$(Q_f^m)_{nj}=f\Phi_{mnj}^{w}(\alpha_f). \tag{4}$$

A construction of virtual work also leads to the generalized forces $\{Q_p^m\}$ associated with the surface acoustic pressure. In the wave-number version of SVP, the surface pressure and normal velocity are expanded in complex Fourier series representing the θ dependence, combined with half-range Fourier series that describe the α dependence of each azimuthal harmonic. The combined series are

$$\begin{aligned} p&=\frac{1}{2}\rho c^2\sum_{m=-\infty}^{\infty}\sum_{j=1}^{N}P_j^m\Psi_j^m(\alpha)\exp(im\theta),\\ v_\perp&=\frac{1}{2}c\sum_{m=-\infty}^{\infty}\sum_{j=1}^{N}V_j^m\Psi_j^m(\alpha)\exp(im\theta). \end{aligned} \tag{5}$$

The terms $\Psi_j^m(\alpha)$ are sinusoidal functions that are defined in Eq. (2) of part I. As explained there, Eq. (5) may be interpreted as a superposition of waves running along the surface, with meridional wavelength $2s_0/j$ and circumferential wavelength $2\pi R(\alpha)/m$, where $R(\alpha)$ is the radial distance from the axis of symmetry to a midsurface point. Along the cylindrical surface, these wavelengths are the traces in the respective directions of a wave that travels in a helical manner. Likewise, the spectrum of surface waves described by Eq. (5) are the trace along the wet surface of the propagating and evanescent waves shed into the surrounding fluid.

Axisymmetry of the wetted surface leads to uncoupling of the azimuthal harmonics for surface interaction, as it did for the structural displacement. The transfer matrix giving the pressure amplitudes P_j^m corresponding to a set of normal velocity amplitudes V_j^m is the wet surface impedance $[Z_{\mathrm{SVP}}^m]$, such that

$$\{P^m\}=[Z_{\mathrm{SVP}}^m]\{V^m\}. \tag{6}$$

For a given shape of the wetted surface, this impedance depends only on ka. The evaluation of this term was treated in part I, which also used the doubly asymptotic approximation to obtain an alternative description. Actually, there are several versions of DAA that one may use. These were shown by Nicholas-Vullierme[5] to correspond to different levels of approximation of the Kirchhoff surface integral. Truncation at powers of quadratic powers of k for low frequency and quadratic powers of $1/k$ for high frequency correspond to DAA-2, which is the highest order version in present use. (Nicholas-Vullierme refers to this as the two-high, two-low version). The form of DAA-2 corresponding to the wave amplitude variables was found in part I to be

$$[Z_{\mathrm{DAA\text{-}2}}^m]=[[I]+ika[A_1^m]-(ka)^2[A_2^m]]^{-1}\times[ika[T_0^m]-(ka)^2[A_2^m]]. \tag{7}$$

The coefficient matrices, which are defined in Eqs. (9)–(15) of part I, are independent of ka.

It also is useful here to consider the lowest order version, DAA-1, which has often been employed in the past. (This is referred to by Nicholas-Vullierme as the 1-high, 1-low version of DAA.) It corresponds to first order truncations of the low- and high-frequency expansions of the surface integral. Consequently, its form is simpler, which makes its time domain version easier to program and quicker to execute than DAA-2. To obtain the DAA-1 relation, one merely zeros out $[A_2^m]$ in Eq. (7), and replaces $[A_1^m]$ by $[T_0^m]$, which is proportional to the limiting surface impedance at very low ka values. Thus,

$$[Z_{\mathrm{DAA\text{-}1}}^m]=ika[[I]+ika[T_0^m]]^{-1}[T_0^m]. \tag{8}$$

It is possible to eliminate the pressure variables from the structural equations of motion. The first step is to substitute the pressure series, Eq. (5), into the generalized forces associated with the surface pressure. This leads to

$$\{Q_p^m\}=-[\Lambda^m]\{P^m\}, \tag{9}$$

where $[\Lambda^m]$ is formed from inner products of Ψ_j^m and Φ_{mnj}^w,

$$\Lambda_{njl}^m=\int_0^1 \Phi_{mnj}^w(\alpha)\psi_l^m(\alpha)R(\alpha)d\alpha. \tag{10}$$

Let $[Z^m]$ denote the wet surface impedance associated with SVP or either DAA version. Substituting $\{P^m\}=[Z^m]\{V^m\}$ into Eq. (9) then requires elimination of $\{V^m\}$, which is achieved by enforcing velocity continuity at the interface. This entails matching the series for $\dot{w}$ derived from Eq. (1) to the expansion for $v_\perp$ in Eq. (5). These operations yield

$$\{V^m\}=-ika[\Gamma^m]\{q^m\}. \tag{11}$$

The coupling matrix $[\Gamma^m]$ is obtained from the orthogonality properties of the azimuthal and meridional Fourier series used to represent $v_\perp$ in Eq. (5), which leads to

$$\Gamma_{lnj}^m=\frac{1}{2}\epsilon_l\int_0^1 \Phi_{mnj}^w(\alpha)\psi_l^m(\alpha)d\alpha, \tag{12}$$

where $\epsilon_l=2$ unless $l=0$, in which case $\epsilon_l=1$. Equation (11) then leads to an expression for $\{Q_p^m\}$ in terms of $\{q^m\}$. When that expression is substituted into the equations of motion, Eq. (2) becomes

$$[[K^m]-(ka)^2[M^m]-ika[\Lambda^m][Z^m][\Gamma^m]]\{q^m\}=\{Q_f^m\}. \tag{13}$$

These algebraic equations are readily solved for the modal amplitudes at any frequency. The specifics of the relationship between surface pressure and velocity appear in Eq. (13) solely in $[Z^m]$. Comparing solutions obtained from the DAA relations in Eqs. (7) and (8) to the SVP results associated with Eq. (6) provides a picture of the errors entailed in using either form of DAA at any specified frequency.

II. TIME DOMAIN RECONSTRUCTION

The developments in Sec. I yield a frequency domain perspective for the spatial response scales. The Fourier transform of a Dirac delta function at $t=0$ is unity, so the results for $\{q^m\}$ obtained from Eq. (13) in the case of a point force of unit amplitude independent of frequency constitute frequency domain transfer functions, or equivalently, Fourier transforms of modal amplitude impulse responses. Viewing the results as transfer functions will be seen to be very meaningful in assessing the quality of DAA. However, DAA is intended primarily as a tool for evaluating shock response in the time domain. Errors in the frequency response might not have significant effect, depending on the spectral content of the excitation. For this reason, time responses obtained from DAA and SVP also will be compared. Toward this end, Eq. (13) is considered to define a transfer matrix $[D^m(ka)]$ for the modal amplitudes associated with the Fourier transform of the impulse response,

$$[D^m(ka)]=[[K^m]-(ka)^2[M^m]-ika[\Lambda^m][Z^m]\times[\Gamma^m]]^{-1}. \tag{14}$$

The quantities of interest in shock response are displacement and acceleration. Although each variable consists of three components, it is sufficient for the present purpose to

restrict attention to the direction normal to the wetted surface. Furthermore, it is physically meaningful to view the results in terms of the meridional wave-number amplitudes. To obtain these variables the value of $\{V^m\}$ corresponding to a solution for $\{q^m\}$ is obtained by applying Eq. (11), after which dividing or multiplying by $-ika$, respectively, yields displacement and acceleration, so that

$$\{W^m(ka)\}=[\Gamma^m][D^m(ka)]\{Q_f^m(ka)\},$$
$$\{\ddot{W}^m(ka)\}=-(ka)^2[\Gamma^m][D^m(ka)]\{Q_f^m(ka)\}. \tag{15}$$

These are the frequency domain representations of the modal amplitude response to an impulsive force. Now suppose that the time domain dependence of the exciting force is $f(\tau)$, corresponding to Fourier transform $F(ka)$. The frequency domain displacement and acceleration for each wave number is then given by

$$\{w^m(ka)\}=F(ka)\{W^m(ka)\},$$
$$\{\ddot{w}^m(ka)\}=F(ka)\{\ddot{W}^m(ka)\}. \tag{16}$$

Both of these relations correspond to Fourier transforms of convolution integrals in the τ domain, which are readily computed as inverse fast fourier transforms (FFTs).

Several factors require consideration prior to implementing the FFT. The first issue is the nature of the excitation. The force should excite the structure over a broad range of azimuthal and meridional wave numbers, in order to obtain a complete assessment. Also, one should recognize that computing the transfer matrix $[D^m(ka)]$ according to DAA or SVP involves considerable computational effort. To address these issues the point force excitation is placed at the midpoint of the meridian. Because the basis functions for normal displacement have unit values at $\alpha=0.5$, the generalized forces associated with the excited mode functions are comparable in magnitude, see Eq. (4). Also, because the force is applied at the transverse midplane, the response is symmetric about that plane. Symmetry permits the number of variables to be halved because only the symmetric basis functions participate. Specifically, it is possible to zero out the odd meridian wave numbers for $m=0$, and the even numbers for $m\neq 0$.

Another issue pertaining to the force is selection of its temporal behavior, which should be reasonably similar to what would be obtained in an actual shock event. Doing so ensures that errors in DAA in a limited range of frequencies are not biased excessively in the convolution process. Accordingly, the temporal wave form of the force is taken in the examples to be a decaying exponential $f=\exp(-\tau/\tau')h(\tau)$, where $h(\tau)$ denotes a step function. The time constant for the examples is selected as the value obtained from Rogers' analysis[10] of spherical shock waves in the case of 500 kg of TNT at a radial distance of 99 m, specifically, $\tau'=0.384$. The Fourier transform of the excitation is

$$F(ka)=\frac{\tau'}{1-ika\tau'}. \tag{17}$$

As shown in Fig. 1, the spectrum of this excitation is quite broad, which means that the transfer matrix needs to be computed for rather high values of ka. However, the quality of standard structural acoustics computations for very high frequencies is an ongoing question. The surface variational principle has been validated only for values up to $ka=15$. Furthermore, examination of Eq. (17) for the above-given value of τ' would show that $|F|$ at $ka=10$ is approximately 25% of the peak value, which occurs at $ka=0$, and the spectrum $ka<10$ contains 88% of the total energy in the wave form. Setting the transform of the excitation to zero for $ka>10$, as is done for the examples appearing later, permits usage of a relatively small model for the fluid-structure system. The shortest meridional wavelength captured by the analysis will be $s_0/120$, which corresponds to using 61 symmetric basis functions for pressure, normal velocity, and each of the shell displacement components.

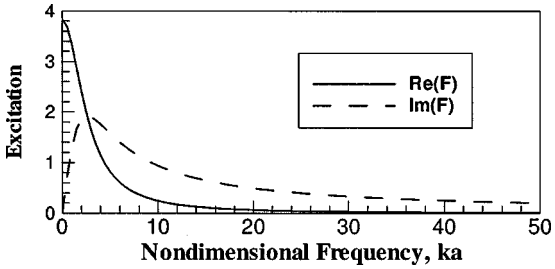

FIG. 1. Frequency spectrum of the excitation.

It should be noted that cutting off the response above $ka=10$ is equivalent to applying a step low pass filter to the frequency window, which is noncausal. The consequence of such a process is temporal responses that do not have zero initial values at $\tau=0$. In principle, a causal filter, which gradually tapers off as ka approaches 10 could be used. However, the purpose of the present study is to ascertain the quality of DAA across the entire spectrum associated with a shock event, rather than actually determining the time domain response. Using a causal filter would mask the degree to which differences between DAA and SVP in the high frequency range are significant.

In the FFT formulation presented by Press *et al.*,[11] the time window is $-T/2\leqslant\tau\leqslant T/2$, where the window width is related to the frequency increment Δka by $T=\pi/\Delta ka$. Sampling of the DAA and SVP data for several elements of $\{q^m\}$ vs ka indicated that all frequency domain features of the plots are captured with a frequency increment $\Delta ka=0.25$. However, this leads to a maximum (nondimensional) time of $T/2=12.57$, which would not be sufficient to see inverse FFTs for the termporal response fully decay. (In the usual application, applying a FFT to time domain data that are not taken over a sufficiently long time window leads to aliasing of the transform.) Rather than carrying out the frequency domain computations for a smaller frequency increment, the frequency domain results were interpolated from $\Delta ka=0.25$ to $\Delta ka=0.0625$ using a cubic spline fit, which yields $T/2=50.27$ as the time window. In other words, frequency domain responses $\{W^m\}$ were computed according to Eq. (15) using SVP and both DAA versions for $ka=0$, 0.25, 0.5,.., 10. The cubic spline routine then gave values for each element of $\{W^m\}$ at three equally spaced frequencies within each interval. Finally, the $\{\ddot{W}^m\}$ data set was obtained by

multiplying each $\{W^m\}$ by the corresponding value of $-(ka)^2$. It should be noted here that although the transfer functions displayed below seem to be rather coarsely scanned using $\Delta ka = 0.25$, the data satisfy the Nyquist sampling criterion. This was verified by comparing inverse FFTs using the interpolated data to the corresponding results using the original data. In each case, the wave forms were found to be nearly identical for $\tau < 10$.

The last issue requiring consideration is convolution wraparound, which also is discussed by Press *et al.* This numerical artifice arises from replication in the adjacent time window due to periodicity implicit to the FFT algorithm. Zero padding enables one to move the temporal values affected by wraparound outside the original time window. Press *et al.* suggest padding the frequency domain data set with a number of zeros that at least matches the number of original values. After application of the spline fit interpolation, the data set contains 161 frequency values. The most efficient FFT algorithms require that the number of data points be an integer power of 2. The nearest such value exceeding twice the number of original data values is 512, so the computed frequency data was padded with 351 zeros. The maximum frequency associated with the zero-padded data is $ka_{\max} = 32$, which corresponds to temporal responses from the inverse FFT having a time increment $\Delta\tau = \pi/ka_{\max} = 0.098\,17$.

III. RESULTS

The comparisons presented here consider a steel shell whose thickness is 1/50 of the radius. Two different aspect ratios, $L/2a = 5$ and 2, are considered. The cylinder length in the first case is sufficiently large to expect that its behavior will resemble that of an infinite cylinder, which is one of the models used to develop the DAA concept. In contrast, the shorter length is sufficiently small to anticipate that end effects are significant. It also is sufficiently long to expect that the behavior is quite different from a sphere, which is the other model used initially to develop DAA.

Contrary to the preceding expectations, the higher aspect ratio was found to exhibit the greatest degree of disrcepancy between DAA and SVP. Hence, that case will be examined in detail. The first set of data is the wave amplitude transfer functions W_j^m when $L/2a = 5$. Representative results for azimuthal harmonics $m = 0$ to 5 are displayed in Figs. 2–7. The issue addressed by Figs. 2–7 is the degree to which a DAA model agrees with the SVP result for a specific pair of wave numbers (m,j). The relative magnitude of the response at each (m,j) is not significant, because the spectral response in an actual shock environment will strongly depend on the temporal and spatial attributes of the excitation. Proper interpretation of this set of graphs requires that one be cognizant of the logarithmic scale used to span the range of amplitude values, which tends to mask the magnitude to which results disagree. An overview of these results reveals several trends.

(1) From the standpoint of overall agreement with SVP, DAA-2 is much better than DAA-1.

(2) For all m, the largest discrepancies between either DAA and SVP occurs in frequency ranges where the wave-

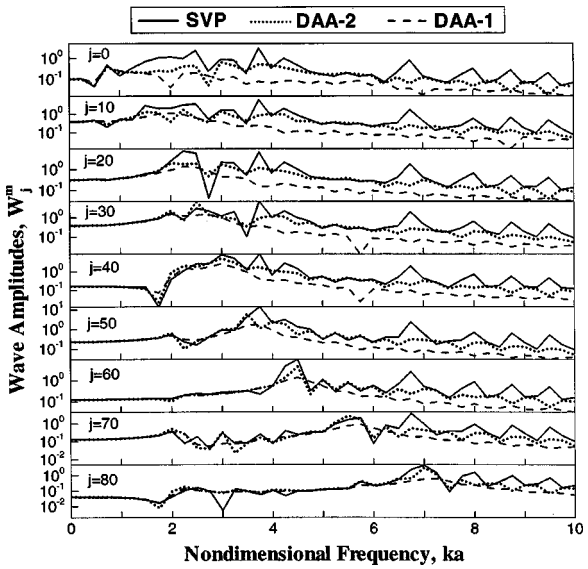

FIG. 2. Wave amplitude transfer functions, $L/2a = 5$, $m = 0$.

number amplitude shows a peak or minimum. The tendency is for DAA to underpredict the transfer function values at peaks, and to overpredict the minima.

(3) Both DAA versions agree well with SVP in the low-frequency range $ka < 1$, for any m.

(4) The axisymmetric case, $m = 0$, indicates that both DAA versions underpredict the peak transfer functions for all wave numbers. The lower limit of the frequency range in which these peaks occur increases with increasing wave number. Away from the peaks, DAA-2 is in good agreement with SVP.

(5) For $m > 0$, DAA-2 generally agrees quite well with SVP. The exception to this trend occurs for $m = 3$, where there are significant differences between DAA and SVP values for the lower frequency peaks at all wavenumbers.

(6) Although space limitations prevent showing the results, the phase of the peak transfer functions, which is ob-

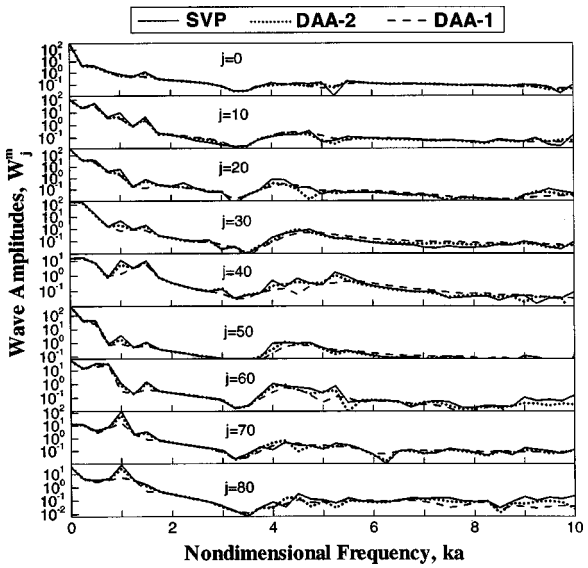

FIG. 3. Wave amplitude transfer functions, $L/2a = 5$, $m = 1$.

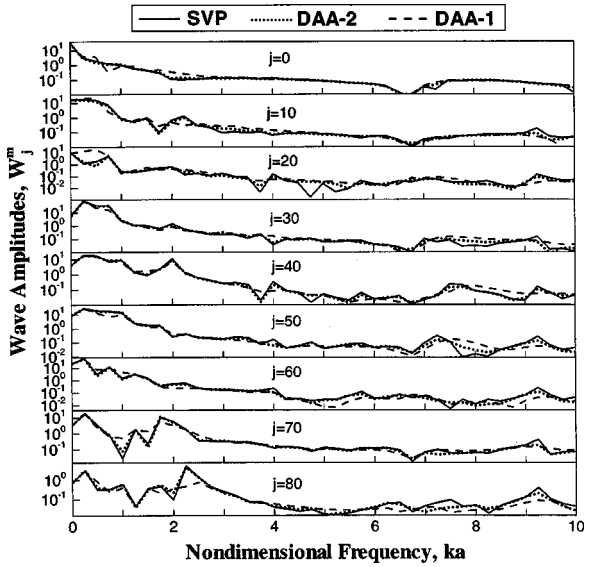

FIG. 4. Wave amplitude transfer functions, $L/2a=5$, $m=2$.

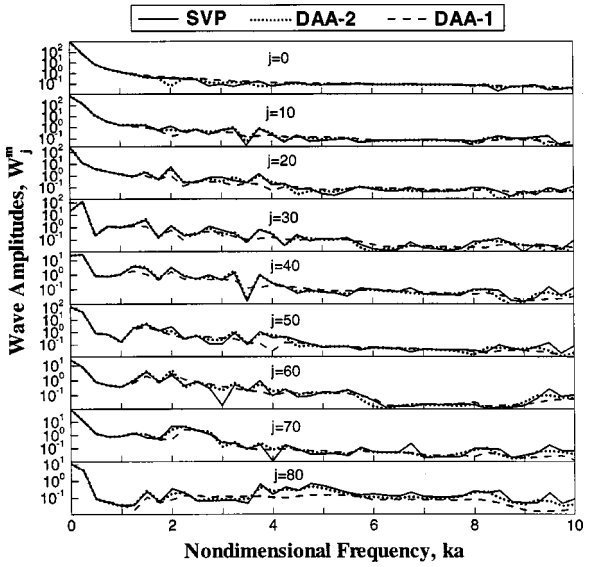

FIG. 6. Wave amplitude transfer functions, $L/2a=5$, $m=4$.

tained by considering the ratio of the real to imaginary parts, drastically differs between either DAA model and SVP whenever the magnitudes disagree.

Discrepancies for the shorter aspect ratio, $L/2a=2$, tend to follow the above-noted patterns. In particular, away from frequency intervals in which the transfer functions display peaks and minima, DAA-2 is in reasonably close agreement with SVP, while DAA-1 is less satisfactory. Peak transfer function values tend to be underpredicted, and minima are generally overpredicted. These trends are typified by Fig. 8 for $m=3$, which displays the greatest level of discrepancy for any $m\leqslant 5$ when $L/2a=2$.

Differences between both DAA versions and SVP for the transfer functions will obviously strongly influence the prototypical time domain responses obtained from the convolution procedure described in Sec. II. The major trends may be seen by considering the cases $m=0$, 3, and 5 for $L/2a=5$, which are described by Figs. 9–11. Note that differences between the alternative analyses appear to be greater for the temporal responses than for the corresponding frequency responses. In part, this is a consequence of the fact that although the spectral content of the excitation, $F(ka)$, is much lower in the region $ka>1$ (see Fig. 1), there are significant differences between DAA and SVP in that frequency range. Furthermore, the linear scale used here tends to highlight differences much more than the logarithmic scale used to display the transfer functions.

Figure 9 shows that the axisymmetric motions of the shell are poorly predicted for the longer wavelengths. At the higher wave numbers, $j>50$, DAA-2 does much better than DAA-1. Overall, both DAA analyses seem to overdamp the response. In Fig. 10 for $m=3$, the SVP response at all wave numbers $j\leqslant 70$ oscillates more rapidly than either DAA result. This is attributable to underestimation of the transfer function peak at $ka=1.5$, see Fig. 5. Figure 11 for $m=5$ exhibits the tendency of the time responses to show greater

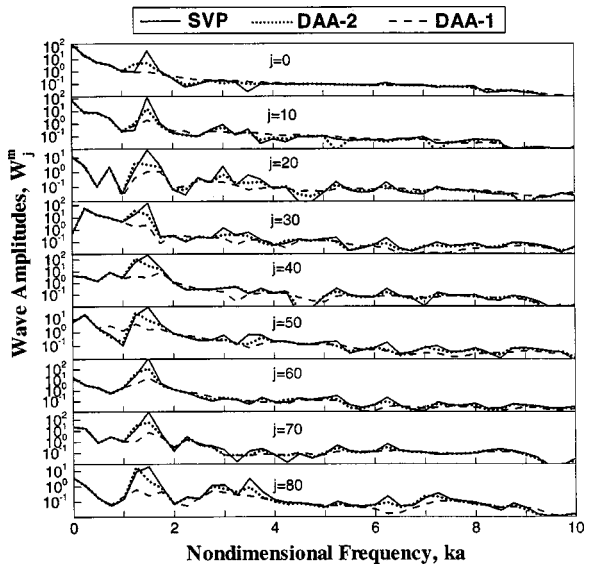

FIG. 5. Wave amplitude transfer functions, $L/2a=5$, $m=3$.

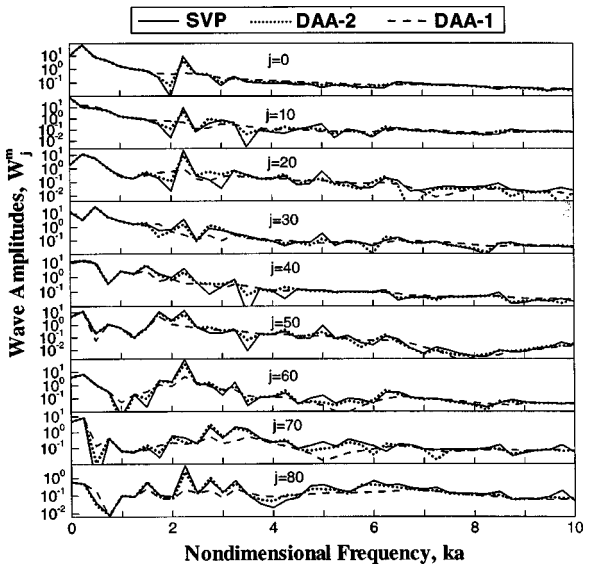

FIG. 7. Wave amplitude transfer functions, $L/2a=5$, $m=5$.

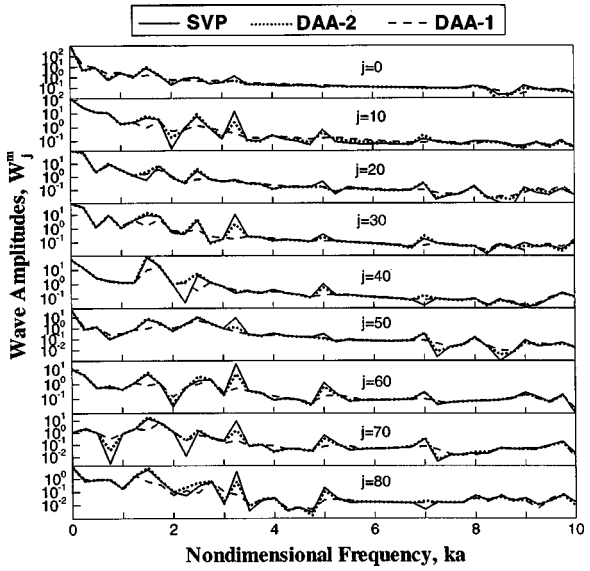

FIG. 8. Wave amplitude transfer functions, $L/2a=2$, $m=3$.

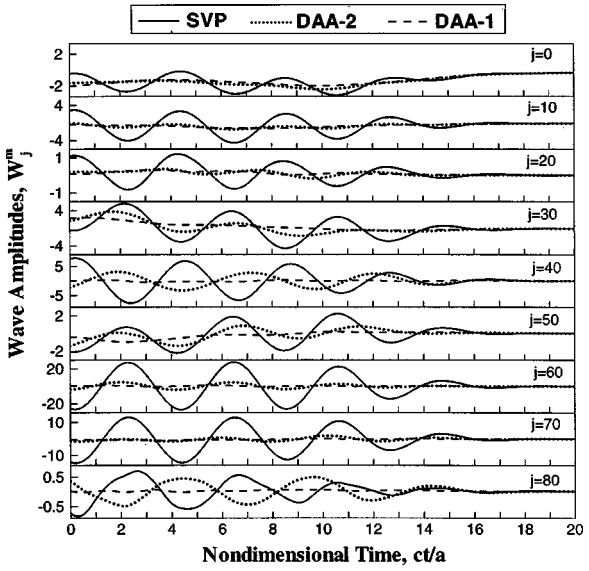

FIG. 10. Prototypical response to a point force, $L/2a=5$, $m=3$.

discrepancies than the corresponding transfer functions. It also highlights a trend hinted at by the transfer function comparisons, particularly that the greatest degree of difference is likely to be encountered in the midfrequency range. The longer wavelength scales, $j \leqslant 40$, are predominantly low frequency motions, and DAA-2 agrees well with SVP in that range.

Recall that the DAA and SVP transfer functions are in closer agreement for the shorter shell than they are for the longer one. This is reflected in the temporal responses, which are generally well predicted for each (m,j) pair at $L/2a=2$. The greatest level of disagreement is encountered in Fig. 12 for $m=3$, but unlike Fig. 9, the differences are primarily in the phase of the oscillation.

The issue of acceleration has not been addressed yet. A qualitative picture of this parameter in the frequency domain may be obtained by multiplying any of the transfer functions by $(ka)^2$, see Eq. (15). It follows that errors in prediction of the high frequency peaks for displacement will be magnified for acceleration. In order to summarize these results in a brief manner, Figs. 13 and 14 present errors in peak displacement and acceleration values in the frequency and time domain, respectively, as a function of meridional wave number for each azimuth harmonic. To obtain these curves the frequency or time range is scanned for the maximum value of the associated variable at each wave number, without regard for the frequency or time value at which it occurs. The maximum obtained from DAA is then ratioed to the maximum obtained from SVP. Only the case $L/2a=5$ is presented, because the trends for the shorter aspect ratio are similar. Also, only DAA-2, which generally does better, is described here. Both figures display the same trends. For $m=0$ and $m=3$, DAA-2 greatly underpredicts maxima for most j. For the other azimuthal harmonics, DAA-2 gives reasonably good agreement for most meridional wavenumbers, especially for peak displacement. In the few cases where DAA-2

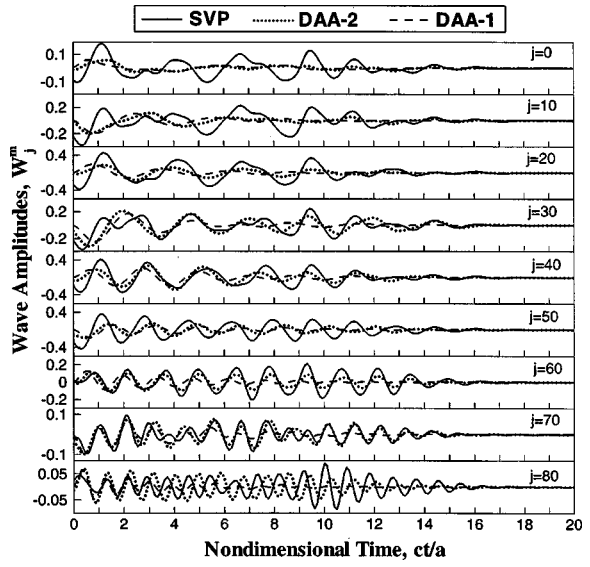

FIG. 9. Prototypical response to a point force, $L/2a=5$, $m=0$.

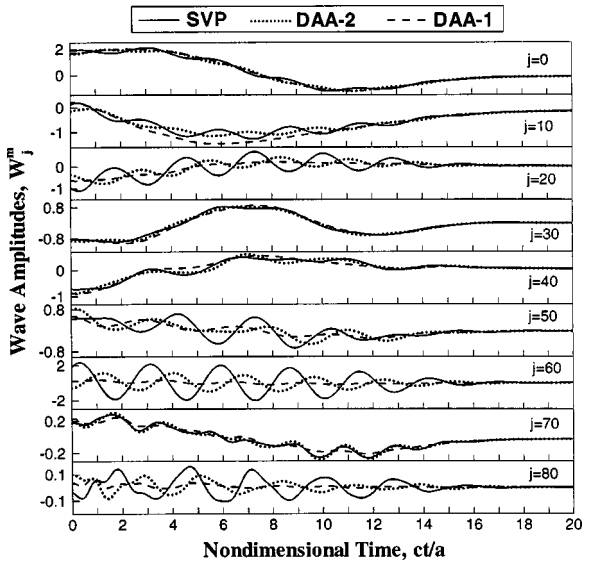

FIG. 11. Prototypical response to a point force, $L/2a=5$, $m=5$.

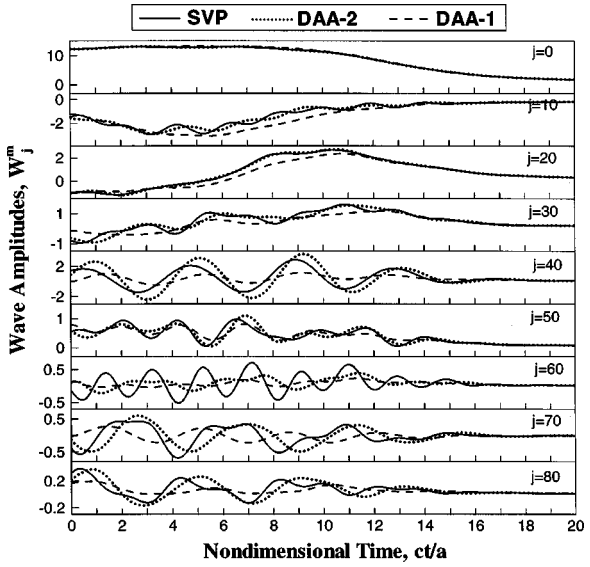

FIG. 12. Prototypical response to a point force, $L/2a=2$, $m=3$.

overpredicts a maximum, such discrepancies are confined to small intervals in the upper range of wavenumbers.

IV. SUMMARY AND CONCLUSIONS

The first part of this paper developed frequency domain descriptions of the surface impedance for a hemicapped cylinder. This quantity, which gives the surface pressure corresponding to a specified normal velocity, was evaluated according to the second-order DAA and according to SVP. It was shown there that DAA-2 does not fully capture a fundamental physical phenomenon, specifically the transition of surface waves from supersonic to subsonic, which changes the impedance from being primarily resistive to inertial. Coupling of helical waves was shown to be most evident in the vicinity of the cutoff for axisymmetric responses. In the present study, the alternative descriptions of the impedance were incorporated into a frequency domain analysis of structural response. The structural analysis was founded on the assumed modes method; the corresponding displacement variables were amplitudes of basis functions that map the modes of a spherical shell onto the shape generator for the

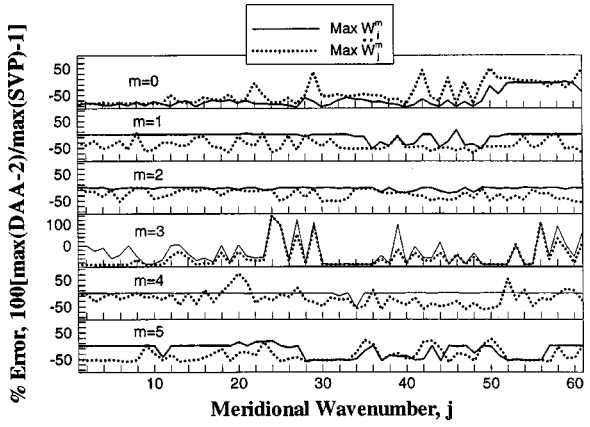

FIG. 13. Maximum error in the frequency domain transfer functions W_j^m and $\ddot{W}_j^m$, $L/2a=5$.

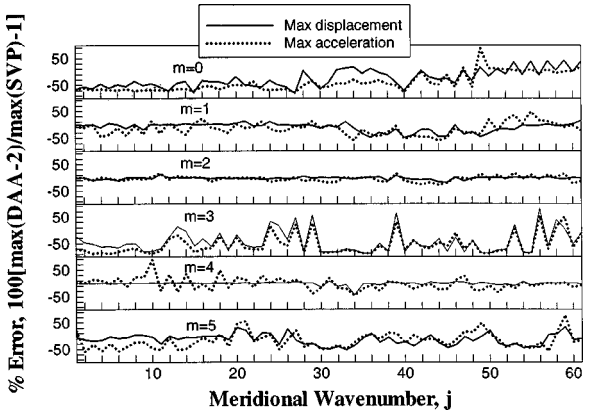

FIG. 14. Maximum error in the time domain displacement and acceleration, $L/2a=5$..

capped cylinder. These variables were converted to a spectral description in a wave-number space composed of azimuthal harmonics and meridional wave numbers, based on Fourier series decompositions along the circumference and the arclength of a meridian of the shape generator. Results for a point force at the midplane were computed over a broad frequency range according to SVP, and according to DAA formulated to two levels of approximation. Because the amplitude of the excitation was taken to be independent of frequency, the computed amplitudes as a function of frequency for a specific pair of azimuthal (m) and meridional (j) wave numbers constitutes a frequency domain transfer function, which is the Fourier transform of the impulse response associated with each helical wave.

DAA and SVP predictions for the transfer functions were compared for a slender configuration, $L/2a=5$ (tip to tip length six times the diameter), and for $L/2a=2$ (tip to tip length three times the diameter). These comparisons revealed several general features. It was observed that the second-order DAA generally does better than the first-order DAA in tracking the SVP data. It also was observed that there is much closer agreement between DAA and SVP in the case of the shorter shell. For any azimuthal harmonic m, both DAA versions were found to agree well with SVP for low frequencies, $ka<1$, and in any frequency range where a wavenumber amplitude does not display a maximum or minimum. Such maxima and minima are associated with resonances and antiresonances. Note in this regard that the lower aspect ratio leads to higher nondimensional natural frequencies for *in vacuo* vibration, so resonance phenomena are less evident in that case. The increased deviations between DAA and SVP therefore seem to reflect the fact that details of the fluid loading are most important at resonances, where the inertial and elastic contributions to dynamic stiffness tend to cancel. With very few exceptions, both DAA versions underestimated the peak amplitudes in the transfer function for a specific pair of wavenumbers.

In order to gain an indication of the significance of the transfer functions for time domain evaluations, they were convolved with a prototypical time dependence of the driving force, whose wave form was taken to be that of a strong explosion in water. The convolution process was carried out

using inverse FFTs to determine the displacement and acceleration as a function of time.

For most wave-number pairs it was found that DAA-2 gives temporal responses that are reasonably close to the SVP result. However, in a few cases where peaks in the associated transfer function were not well predicted, there were large differences in the fundamental form of the temporal response. It also was noted that DAA usually attenuates the response more rapidly than SVP.

A key application of DAA models for shock response is to generate the base structural motion to be input to dynamic models of equipment mounted internally to the structure. In such an application, it is important to predict the peak base displacement and acceleration in the frequency band(s) where the equipment is most sensitive. Such properties were evaluated for the frequency domain transfer functions, as well as the temporal response to the prototypical excitation. The results were displayed by referencing DAA-2 to SVP as a function of meridional wave number at fixed azimuthal harmonic. Displacement maxima were better predicted than acceleration maxima. In most cases where there was not agreement, DAA-2 underpredicted the value, in some cases by an order of magnitude. However, some instances where DAA-2 overpredicts the response were observed to occur for the higher wave numbers.

Past works comparing DAA to analysis have generally not indicated discrepancies as large as the worst cases reported here, probably because none have decomposed the results into the present dual wave-number spectrum. Such decomposition tends to highlight individual features. Another factor to consider in weighing the present results against previous works is the excitation arising from an actual shock event. The point force used here excites an extremely broad range of wavenumbers at nearly equal levels. In contrast, the wave form of an incident shock wave is distributed spatially, which results in the lower end of the wavenumber spectrum being excited most. Once again, the objective of the present work is to identify scales over which DAA is accurate, rather than to assess the quality of a particular response calculation.

Finally, one should note that the present structural model was an unstiffened shell. Stiffeners and internal structure produce a much richer modal environment. The present observation that the greatest discrepancies occur in the vicinity of modal resonances suggests that DAA will lose accuracy with increasing structural complexity. The underlying concepts developed here, specifically alternative descriptions of the wet surface impedance in the frequency domain, evaluation of impulse response transfer functions, and synthesis of time response using FFTs, should be directly applicable to analyses addressing this question.

ACKNOWLEDGMENT

This work was supported by the Office of Naval Research.

[1] T. L. Geers, ''Excitation of an elastic cylindrical shell by a transient acoustic wave,'' J. Appl. Mech. **36**, 459–469 (1969).
[2] T. L. Geers, ''Residual potential and approximate methods for three-dimensional fluid-structure interaction problems,'' J. Acoust. Soc. Am. **49**, 1505–1510 (1970).
[3] T. L. Geers, ''Doubly asymptotic approximations for transient submerged structures,'' J. Acoust. Soc. Am. **64**, 1500–1508 (1978).
[4] J. H. Ginsberg, ''Wave-number-based assessment of the doubly asymptotic approximation. I. Frequency domain wet surface impedance,'' J. Acoust. Soc. Am. **107**, 1898–1905 (2000).
[5] B. Nicholas-Vullierme, ''A contribution to doubly asymptotic approximations: An operator top-down derivation,'' in *Numerical Techniques in Acoustic Radiation*, edited by R. J. Bernhard and R. F. Keltie (ASME 1989), NCA-6, pp. 7–13.
[6] K. Wu and J. H. Ginsberg, ''Progress in applying the surface variational principle to analyze acoustic radiation from slender elastic bodies,'' Proceedings of the Symposium on Acoustics of Submerged Structures and Transduction Systems, ASME 15th Biennial Conference on Mechanical Vibration and Noise, Boston, MA, 17–19 September 1995.
[7] K. Wu and J. H. Ginsberg, ''Mid-frequency range acoustic radiation from slender elastic bodies using the surface variational principle,'' ASME J.Vib. Acoust. **120**, 392–400 (1998).
[8] P. M. Naghdi and A. Kalnins, ''On vibrations of elastic spherical shells,'' ASME J. Appl. Mech. **29**, 65–72 (1962).
[9] K. Wu, ''Extension of surface variational principle to nonsymmetric acoustic radiation and scattering problems,'' Ph.D. thesis, Georgia Institute of Technology, 1995.
[10] P. H. Rogers, ''Weak-shock solution for underwater shock waves,'' J. Acoust. Soc. Am. **62**, 1412–1419 (1977).
[11] W. H. Press, B. P. Flannery, S. A. Teukolsky, and W. T. Vetterling, *Numerical Recipes*, 2nd ed. (Cambridge University Press, Cambridge, UK, 1992), pp. 490–535.

Experimental investigations of nonlinear acoustic phenomena in polycrystalline zinc

Veniamin E. Nazarov
Institute of Applied Physics, Russian Academy of Sciences, 46 Uljanov Street, 603600, Nizhny Novgorod, Russia

Andrei B. Kolpakov
Department of Physics, Architectural and Civil-Engineering Institute, 65 Ilinskaya Street, 603600, Nizhny Novgorod, Russia

(Received 10 April 1997; revised 30 October 1998; accepted 7 December 1999)

The results of experimental and theoretical investigations of nonlinear acoustic phenomena (nonlinear losses, shift of resonance frequency, generation of the third harmonic, and nonlinear sound-by-sound damping) in polycrystalline zinc nonannealed and annealed resonating rods are presented. The measurements were carried out in the $10^{-7}-10^{-5}$ strain range at a frequency of about 3 kHz; the frequency of the weak ultrasonic pulse was about 270 kHz. The experimentally observed phenomena are described in frames of phenomenological equations of state containing elastic hysteresis and dissipative nonlinearity. The nonlinear acoustic parameters of these equations are determined by comparison between theoretical dependencies and experimental results. The influence of structural changes in zinc due to annealing on the nonlinear acoustic phenomena is shown. © *2000 Acoustical Society of America.* [S0001-4966(00)03803-0]

PACS numbers: 43.25.Ba, 43.25.Jh [MAB]

LIST OF SYMBOLS

σ	stress
ϵ	strain
$\dot{\epsilon}$	velocity of the strain
ε_m	amplitude of the strain of acoustic pump wave
L	length of the rod
U	displacement
γ_{1-4}	parameters of the hysteresis nonlinearity
ΔC	change of the sound velocity
p	number of the longitudinal mode resonator
F_p	resonance frequency of the longitudinal mode with number p
c_0	velocity of the longitudinal waves in rod
$Q_{1,2}$	quality factor for the first and second modes
u_0	amplitude of the electric voltage on pump radiator
E	Young's modulus
α	coefficient of the linear losses
ρ	density of the medium
A_0	amplitude of the wave on the pump radiator
Ω	cyclic frequency of the pump wave
δ	linear shift of the resonance frequency
δ_h	$2\pi\Delta F_p$ nonlinear shift of the resonance frequency
μ_p	value of the linear losses
μ_h	coefficient of the amplitude-dependent nonlinear losses
$\Delta\Omega_p$	shift of the third harmonic frequency from resonance
U_0	the amplitude of the pulse without the pump wave
$U(L)$	amplitude of the received pulse
$\chi(L)$	coefficient of the pulse nonlinear damping
g	coefficient of the dissipative nonlinearity
s	exponent of the dissipative nonlinearity
ω	the frequency of the pulse
k	ω/c_0
Γ	gamma-function

INTRODUCTION

There is great interest in nonlinear phenomena of solids due to the possibility of studying acoustic nonlinearity mechanisms characteristic of these solids and the prospect of application of nonlinear methods for nondestructive testing. The feasibility of these methods is based on the known fact of strong dependence of acoustic properties on structural defects (cracks, grains, dislocations, etc.).[1] At present, the polycrystalline diagnostic methods based on the internal friction phenomenon manifested in the amplitude dependence of damping and propagation velocity of the acoustic wave have been carefully studied and widely applied.[2,3] This phenomenon is caused by dislocation motion and has been known for more than 50 years. The study of the internal friction phenomenon deals with the analysis of the polycrystalline dislocation structure, the determination of dislocation density, and their interaction with impurity atoms, etc. To account for such phenomena as internal friction, the dislocation theory of damping[2,3] was proposed by Granato and Lucke in 1956. In this theory, the equation of the polycrystalline state $\sigma=\sigma(\epsilon,\dot{\epsilon})$ (where σ is the stress and ϵ and $\dot{\epsilon}$ are the strain and the strain velocity, respectively) is characterized by the hysteresis function: the hysteresis loop area determines amplitude-dependent losses and the value of the derivative $[\sigma'_\epsilon(0)-\sigma'_\epsilon(\varepsilon_m)]$ the defect of elasticity modulus [or change of sound velocity $\Delta C(\varepsilon_m)$], where ε_m is the amplitude of strain of an acoustic wave. For media described by such an equation of state, the strain amplitude ε_m dependen-

 0001-4966/2000/107(4)/1915/7/$17.00

cies of the decrement of the wave and its propagation velocity change are identical in character, and their relation is constant, which is not dependent on the amplitude ε_m. In addition to the phenomena outlined above, the nonlinearity of the dependence $\sigma=\sigma(\epsilon,\dot{\epsilon})$ leads to generation of higher harmonics during excitation of the harmonic acoustic wave[4] in polycrystalline materials. When the equation of state is hysteretic, these spectral components (harmonics) differ qualitatively from that of a smooth $\sigma=\sigma(\epsilon,\dot{\epsilon})$ dependence (that can be determined, for example, by the five-constant elasticity theory[4,5]). It is important to note that the smooth dependence of $\sigma=\sigma(\epsilon,\dot{\epsilon})$ is characteristic of the same polycrystalline materials at small strain amplitudes which are not sufficient to break dislocations from their fastening points (impurity atoms). The Granato–Lucke model does not always adequately describe the amplitude dependencies of nonlinear behavior[3,6–9] during experimental observation. However, the law $\sigma=\sigma(\epsilon,\dot{\epsilon})$ can be modeled empirically by the analysis of experimentally determined dependencies of nonlinear losses, modulus defect, and higher harmonic amplitudes on the initial acoustic wave amplitude.[10]

In order to study nonlinear phenomena of dislocation absorption, it is necessary to use intense sound waves which are easily realized using resonance oscillations in acoustic resonators. Analogous experiments with the resonators made from polycrystalline copper subjected to a different degree of annealing[11–16] and experiments using several rocks (granite, marble, and river sand[17]) have been carried out, and both highly reactive (elastic) and dissipative (inelastic) acoustic nonlinearity was discovered. Theoretical description of the observed phenomena was carried out in the framework of phenomenological equations of state containing elastic, hysteretic, and dissipative nonlinearity.

In this paper, experimental results of nonlinear acoustic phenomena in rod-like resonators made of polycrystalline zinc (99.95% Zn) are presented. We used two rods 35 cm in length and with square cross section 8 mm cut from the same plate. The first rod (1) was considered a control specimen. The second rod (2) was annealed preliminarily for about 6 h at a temperature of 350 °C. In these experiments, in the course of the excitation of a low-frequency pump wave and a weak ultrasonic impulse, the following phenomena were observed and studied:

(i) amplitude-dependent losses, shift of the resonance frequency, and generation of the third harmonic of the pump frequency;
(ii) nonlinear damping of the ultrasonic impulse in the presence of the powerful low-frequency wave (sound-by-sound damping).

All measurements were carried out at room temperature.

I. PROCEDURE OF THE EXPERIMENT

The block diagram of the experimental setup is shown in Fig. 1. The piezoceramic pump wave radiator 1 used to excite the sample 2 was cemented to a massive metallic loading 3 so that the boundary condition at one end was considered close to that of an absolutely rigid one. The piezoceramic

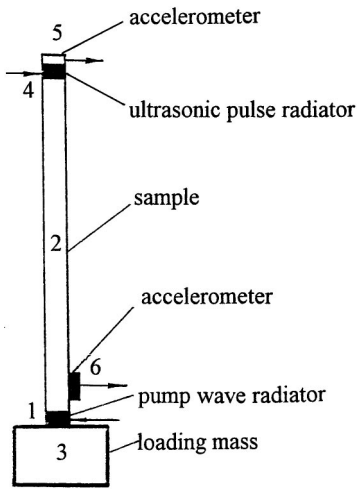

FIG. 1. Setup of the experiment.

radiator 4, used to excite the ultrasonic impulse, and the accelerometer 5, used to measure the pump wave amplitude, were cemented to the free rod end. Their total mass was sufficiently small so that the corresponding rod boundary was considered acoustically soft. In the vicinity of the pump radiator, an accelerometer 6 used to receive and measure the amplitude of the ultrasonic pulse was cemented on the lateral rod surface. The rods (1) and (2) were excited at the first longitudinal modes ($p=1$) with resonance frequencies $F_1=2765$ Hz and $F_1=2770$ Hz, respectively. The resonance frequencies F_2 of the second longitudinal modes ($p=2$) were equal to 8040 and 8000 Hz, respectively. Such frequencies correspond to the resonator with acoustic-rigid and -soft boundaries. For this resonator, fundamental frequencies F_p can be determined by the expression

$$F_p=F_1(2p-1), \quad F_1=c_0/4L, \quad p=1,2,..., \tag{1}$$

where the number p refers to the longitudinal mode number and c_0 is the velocity of longitudinal waves in the rod. From Eq. (1) follows the estimate for the velocity of the longitudinal wave in the zinc rod: $c_0\simeq 3.9\cdot 10^5$ cm/s.

For small amplitudes of the pump wave (when nonlinear losses are not observed), the quality factors $Q_{1,2}$ of the first and second modes were equal to $Q_{1,2}=138$; 210 and $Q_{1,2}=293$; 275 for each of the rods, respectively.

To study the structure of zinc, its metallographic analysis [Fig. 2(a) and (b)] was carried out. It is seen in Fig. 2(a) that the nonannealed zinc structure has reasonably small grains of dimension of about 50 μm. The 350 °C-temperature zinc annealing causes an increase of grain sizes to about 500 μm [Fig. 2(b)]. In the next sections, we consider the zinc structural change's influence on the character of the nonlinear acoustic phenomena observed in resonators.

II. PHENOMENA OF HYSTERESIS NONLINEARITY

In the first series of experiments, the pump radiator 1 was used to excite the longitudinal harmonic oscillations in the sample 2. The signal coming from the accelerometer 5 was received by analysis apparatus where measurement of its characteristics was carried out.

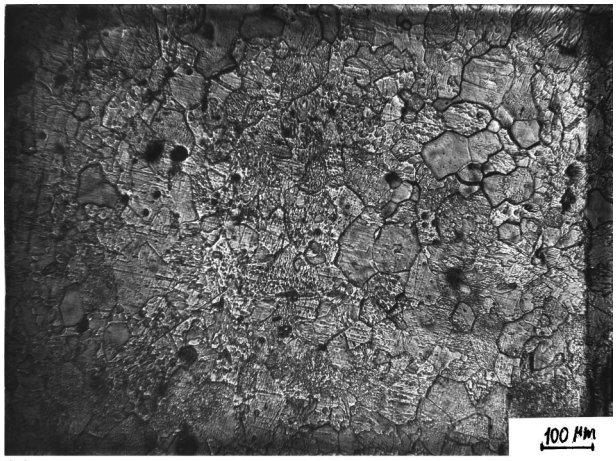

(a)

(b)

FIG. 2. (a) Microstructure of nonannealed zinc. (b) Microstructure of zinc annealed at 350 °C.

Figure 3 gives the strain amplitudes ε_m of rods (at resonance frequency) in relation to the electric voltage amplitude u_0 at the pump radiator (in dB *re* 1 μV). From the figure, it follows that for the rods under investigation, dependencies $\varepsilon_m = \varepsilon_m(u_0)$ are essentially nonlinear and differ in nature. This means that there are amplitude-dependent losses. In addition, the losses begin to manifest themselves at the strain amplitude $\varepsilon_m \simeq 10^{-6}$ for the nonannealed zinc rod and at $\varepsilon_m \simeq 4 \cdot 10^{-7}$ for the annealed sample. Further, for nonannealed zinc, nonlinear loss saturation is observed at $\varepsilon_m \geqslant 7 \cdot 10^{-6}$ (beginning with these amplitudes we can see that $\varepsilon_m \sim u_0$), i.e., the losses again become amplitude independent (however, those become more than at $\varepsilon_m \leqslant 10^{-6}$). For annealed zinc, such a clear saturation of nonlinear losses is not observed. We will return to this problem in the discussion of Fig. 7.

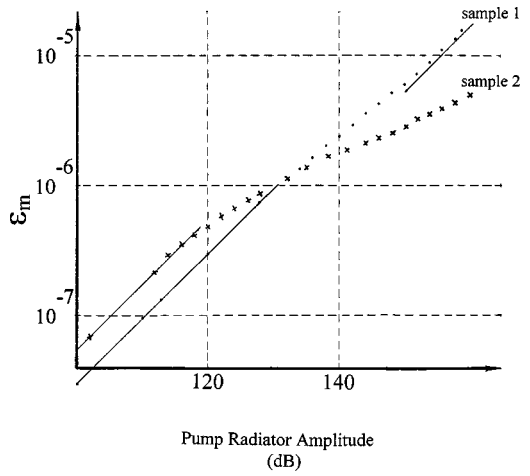

FIG. 3. The rod deformation amplitude ε_m in relation to the radiator voltage amplitude u_0 for the rods 1 and 2. The straight lines correspond to the dependences $\varepsilon_m \sim u_0$.

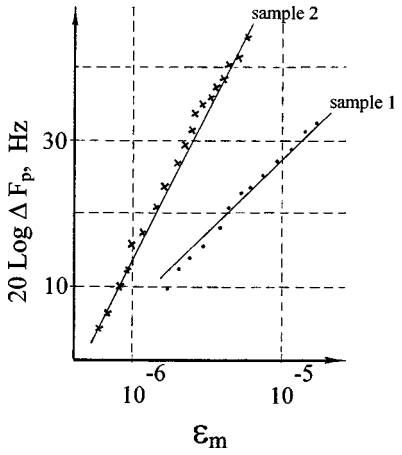

FIG. 4. The shift of resonance frequency ΔF_p in relation to the strain amplitude ε_m for the rods 1 and 2. The straight lines correspond to the dependences: 1—$\Delta F_p \sim \varepsilon_m$; 2—$\Delta F_p \sim \varepsilon_m^2$.

Figure 4 presents the shift of the resonance frequency ΔF_p vs ε_m amplitude of strain for rods (1) and (2). For the nonannealed rod $\Delta F_p \sim \varepsilon_m$, and $\Delta F_p \sim \varepsilon_m^2$ for the annealed one.

Under intensive excitation of the resonator, its oscillating spectrum has components at odd harmonic frequencies which are multiples of the pump wave frequency. [For the resonator with acoustic-rigid and -soft boundary, as follows from expression (1), even harmonics are not at resonance. Thus, the level of even harmonics was very small and those were not observed in experiments.] Figure 5 shows the strain amplitudes ε_3 of the third harmonic as a function of the fundamental frequency strain amplitude ε_m. It is seen from the figure that $\varepsilon_3 \sim \varepsilon_m^2$ for the rod (1) and $\varepsilon_3 \sim \varepsilon_m^3$ for the rod (2).

The measurement errors for frequency and strain amplitudes, were, respectively, ± 0.5 Hz and ± 0.05 dB. Experimental dependences of ΔF_p and ε_3 on ε_m were constructed in logarithmic coordinates (with identical scales along both axes). Using these coordinates, graphic presentations of functions: $\Delta F_p = C_1 \varepsilon_m^r$, $\varepsilon_3 = C_2 \varepsilon_m^q$ (where C_1 and C_2 = constants) are straight lines for which the tangents of inclination angles equal, respectively, r and q, and those can be determined by comparison between experimentally determined dependencies and the straight lines shown.

We note that the above-mentioned collection of nonlinear observations cannot be described by the five- (or nine-) constant elasticity theory[4] because it does not determine nonlinear losses. The observed nonlinear losses also cannot be explained by a decrease of pump wave energy as a result of

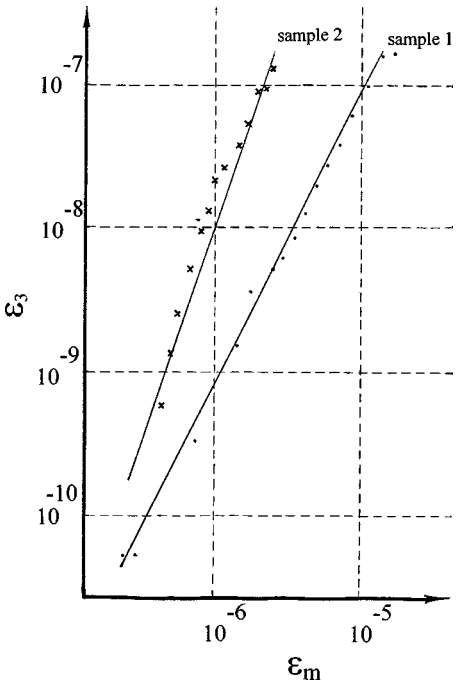

FIG. 5. The third harmonic frequency strain amplitude ε_3 in relation to the strain amplitude ε_m for the rods 1 and 2. The straight lines correspond to the dependences: 1—$\varepsilon_3 \sim \varepsilon_m^2$; 2—$\varepsilon_3 \sim \varepsilon_m^3$.

its transformation into higher harmonics because their levels are considerably less than the fundamental frequency wave amplitude. This circumstance enables us to solve Eqs. (2)–(5) by the perturbation method.

To theoretically describe the observed phenomena and the determined amplitude dependencies, we will assume that the equation of the metal state has the form[10,18]

$$\sigma(\epsilon,\dot{\epsilon}) = E[\epsilon - f(\epsilon,\dot{\epsilon})] + \alpha\rho\dot{\epsilon}, \tag{2}$$

$$f(\epsilon,\dot{\epsilon}) = \begin{cases} \gamma_1\epsilon^n/n, & \epsilon>0, \quad \dot{\epsilon}>0 \\ [(\gamma_1+\gamma_2)\epsilon\varepsilon_m^{n-1} - \gamma_2\epsilon^n]/n, & \epsilon>0, \quad \dot{\epsilon}<0 \\ -\gamma_3\epsilon^n/n, & \epsilon<0, \quad \dot{\epsilon}<0 \\ [(-1)^n(\gamma_3+\gamma_4)\epsilon\varepsilon_m^{n-1} + \gamma_4\epsilon^n]/n, & \epsilon<0, \quad \dot{\epsilon}>0 \end{cases} \tag{3}$$

where E is Young's modulus ($E=\rho c_0^2$), ρ is the density of the medium, α is the coefficient of linear losses, $|\gamma_1\varepsilon_m^{n-1}| \ll 1$, $n>1$ and γ_{1-4} are the nonlinearity parameters.

The plot of the function $\sigma=\sigma(\epsilon,\dot{\epsilon})$ (in the quasistatic case, i.e., when the term $\alpha\rho\dot{\epsilon}$ may be omitted) is given in Fig. 6; it corresponds qualitatively to the hysteresis curve of the modified Granato–Lucke model.[18] Under intensive excitation of the resonator, the spectral components arise at odd harmonic frequencies, being multiples of the pump wave frequency. It is evident that the clockwise movement along the diagram $\sigma=\sigma(\epsilon,\dot{\epsilon})$ corresponds to a medium with hysteresis losses.

Equations (2) and (3) contain five free parameters: the exponent n and four parameters of nonlinearity γ_{1-4}; Eqs. (2) and (3) can describe a wide range of media depending on

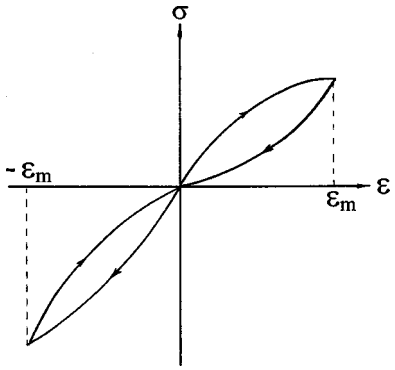

FIG. 6. General form of the hysteresis dependence $\sigma=\sigma(\epsilon)$ for the polycrystalline in modified Granato–Lucke model.

the relationship between these parameters: when $n=2$ and $\gamma_1=-\gamma_2=-\gamma_3=\gamma_4$, we have an equation of the five-constant elasticity theory,[4,5] at $\gamma_2=\gamma_4=0$ we obtain the model with the linear return (as in the Granato–Lucke model). Below, in theoretical calculations, we will assume that the parameters γ_{1-4} differ in value. Such supposition reflects the asymmetry of the equation of state for the solid during its compression and tension. Numerical values of parameters γ_1 will be determined by comparison between results of theoretical calculation and experiments. However, to do this would require us first to determine the exponent n [in Eq. (3)] for both nonannealed and annealed zinc. This exponent can be found by the condition of agreement between experimentally determined amplitude dependencies and their qualitative behavior which follows immediately from the analysis of the nonlinear part $f(\epsilon,\dot{\epsilon})$ of Eq. (3). From physical considerations expounded in the Introduction, it follows that for such agreement it is necessary to take: for nonannealed zinc $n=2$; for annealed zinc $n=3$.

Together with the motion equation[4,5]

$$\rho U_{tt} = \sigma_x'(\epsilon,\dot{\epsilon}), \tag{4}$$

and the boundary conditions at the resonator ends[4]

$$U(x=0,\ t) = A_0\cos\Omega t, \qquad U_x'(x=L,\ t) = 0 \tag{5}$$

(where U is the displacement, $\epsilon=U_x'$, A_0 and Ω are, respectively, the amplitude and the frequency of the wave produced by the pump radiator). Equations (2) and (3) adequately describe all the of phenomena discussed in both nonannealed and annealed rods.

The procedure of the solution of Eqs. (2)–(5) has been provided in papers[10,19] before and, thus, we will use the result of these papers to determine parameters γ_{1-4} below.

The rod strain amplitude is determined by the expression

$$\varepsilon_m = \frac{A_0(\Omega_p/L)}{[(\delta+\delta_h)^2 + (\mu_p+\mu_h)^2\Omega_p^4/4]^{1/2}}, \tag{6}$$

where $\delta=\Omega-\Omega_p$; $\mu_p=(\Omega_p Q_p)^{-1}$; $\delta_h=2\pi\Delta F_p$ is the nonlinear shift of the resonance frequency; μ_h is a coefficient of amplitude-dependent losses:

for nonannealed zinc

$$\delta_h = -2a_1\varepsilon_m\Omega_p/3\pi, \quad \mu_h = 4b_1\varepsilon_m/3\pi\Omega_p, \tag{7}$$

$$a_1 = 2(\gamma_1 - \gamma_2 + \gamma_3 - \gamma_4)/3\pi + (\gamma_1 + \gamma_2 + \gamma_3 + \gamma_4)/4,$$
$$b_1 = (\gamma_1 + \gamma_2 + \gamma_3 + \gamma_4)/6\pi, \tag{8}$$

for annealed zinc

$$\delta_h = -a_1 \varepsilon_m^2 \Omega_p/8, \quad \mu_h = b_1 \varepsilon_m^2/4, \tag{9}$$

$$a_1 = (\gamma_1 + \gamma_2 - \gamma_3 - \gamma_4)/4 + 3(\gamma_1 - \gamma_2 - \gamma_3 + \gamma_4)/16,$$
$$b_1 = (\gamma_1 + \gamma_2 - \gamma_3 - \gamma_4)/4\pi. \tag{10}$$

From Eqs. (7) and (9) it follows that the value of the relation of the nonlinear shift of the resonance frequency to a coefficient of amplitude-dependent losses (it is equivalent to the relation of elastisity modulus defect to amplitude-dependent losses) does not depend on the strain amplitude ε_m for both rods (as it was noted in the Introduction): $\delta_h/(\mu_h \Omega_p^2) = -a_1/2b_1$.

The rod strain amplitude ε_3 at the third harmonic frequency (in the process of resonance excitation at the fundamental frequency) can be determined by the following expressions:

for nonannealed zinc

$$\varepsilon_3 = \frac{4\Omega_p \varepsilon_m^2 [a_3^2 + b_3^2]^{1/2}}{15\pi[(\Omega_p/Q_{3p-1})^2 + 4(\delta_h + \Delta\Omega_p/3)^2]^{1/2}}, \tag{11}$$

$$a_3 = 2(\gamma_1 - \gamma_2 + \gamma_3 - \gamma_4)/15\pi,$$
$$b_3 = (\gamma_1 + \gamma_2 + \gamma_3 + \gamma_4)/30\pi, \tag{12}$$

for annealed zinc

$$\varepsilon_3 = \frac{\Omega_p \varepsilon_m^3 [a_3^2 + b_3^2]^{1/2}}{24[(\Omega_p/Q_{3p-1})^2 + 4(\delta_h + \Delta\Omega_p/3)^2]^{1/2}}, \tag{13}$$

$$a_3 = (\gamma_1 + \gamma_2 - \gamma_3 - \gamma_4)/2\pi,$$
$$b_3 = -(\gamma_1 - \gamma_2 - \gamma_3 + \gamma_4)/16. \tag{14}$$

In Eqs. (11)–(14), the term $\Delta\Omega_p = \Omega_p - \Omega_{3p-1}$ takes into account the third harmonic departure from resonance as a result of wave dispersion in the rod because of the finite dimension in its cross section and the difference of boundary conditions from ideal ones.

Having measured the resonance amplitude of the rod (at $\delta = \delta_h$) and the resonance frequency shift, we may determine the coefficients a_1 and b_1 for both resonators. By assuming A_0 changes proportionally to the voltage μ_0 of radiator, we obtain from expression (6)

$$\varepsilon_{m1}/\varepsilon_{m2} = (A_{01}/A_{02})[1 + \mu_h(\varepsilon_{m2})/\mu_p], \tag{15}$$

where ε_{01} and ε_{02} are the rod strain amplitudes at its excitation by the radiator with the amplitude A_{01} and A_{02}, respectively. (Here, ε_{01} and A_{01} are the rod strain amplitude and the radiator excitation amplitude, respectively, for which the amplitude-dependent losses are not observed in resonator.) Equation (15) determines the dependence of nonlinear losses $\mu_h(\varepsilon_{m2})$ on the strain amplitude ε_{m2}

$$\mu_h(\varepsilon_{m2})/\mu_p = (\varepsilon_{m1} A_{02})/(\varepsilon_{m2} A_{01}) - 1. \tag{16}$$

Figure 7 illustrates these dependences, which were determined from Fig. 3. It is seen that for nonannealed zinc, the dependence (7) [where $\mu_h(\varepsilon_{m2}) \sim \varepsilon_{m2}$] takes place in the range $\varepsilon_m \leqslant 7 \cdot 10^{-6}$, and at the greater strains the nonlinear loss saturation occurs: $\mu_h(\varepsilon_{m2}) = \text{const}$. For the annealed zinc, the dependence (9) [where $\mu_h(\varepsilon_{m2}) \sim \varepsilon_{m2}^2$] takes place at $\varepsilon_{m2} \leqslant 4 \cdot 10^{-6}$ and, further, the trend has only been toward nonlinear loss saturation.

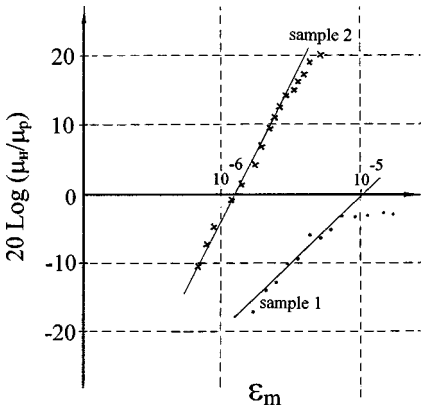

FIG. 7. Dependence of nonlinear losses $\mu_h(\varepsilon_{m2})$ on the strain amplitude ε_{m2} for the rods 1 and 2. The straight lines correspond to the dependences: 1—$\mu_h(\varepsilon_{m2}) \sim \varepsilon_{m2}$; 2—$\mu_h(\varepsilon_{m2}) \sim \varepsilon_{m2}^2$.

As it follows from Eqs. (8) and (10) the coefficients a_1 and b_1 uniquely determine the parameters $\gamma_1 + \gamma_3$ and $\gamma_2 + \gamma_4$ for nonannealed zinc and the parameters $\gamma_1 - \gamma_3$ and $\gamma_2 - \gamma_4$ for the annealed sample. By knowing these parameters, we may calculate the coefficient $(a_3^2 + b_3^2)^{1/2}$ by using Eqs. (12) and (14) for each rod. The same coefficient can be independently determined from Eqs. (11) and (13) by using the third harmonic strain amplitude ε_3. The values of these parameters for nonannealed and annealed zinc are given in Table I.

As it is seen from this table, the values of coefficients $[a_3^2 + b_3^2]^{1/2}$ determined independently by using the shift of the resonance frequency, nonlinear losses, and the third harmonic do not contradict each other; this may indicate that the chosen (on the basis of conducted measurements) approximation for the hysteresis equation of state is satisfactory enough. From Fig. 2(a) and (b) it also follows that the grain-size increases from annealing occur with a change in character hysteresis nonlinearity of zinc, primarily, with the change of the exponent n in Eq. (3): $n = 2$ for nonannealed zinc and $n = 3$ for annealed zinc.

TABLE I. The parameters of nonlinearity.

Sample	a_1 / b_1	$\gamma_1 + \gamma_3$ / $\gamma_2 + \gamma_4$	$\gamma_1 - \gamma_3$ / $\gamma_2 - \gamma_4$	$(a_3^2 + b_3^2)^{1/2}$ by the shift of frequency and losses	$(a_3^2 + b_3^2)^{1/2}$ by the third harmonic
Nonannealed zinc	$3.9 \cdot 10^3$	$6.3 \cdot 10^3$		900	700
	$1.7 \cdot 10^3$	$25.9 \cdot 10^3$			
Annealed zinc	$1.5 \cdot 10^{10}$		$1.6 \cdot 10^{10}$	$2.3 \cdot 10^{10}$	$1.9 \cdot 10^{10}$
	$1.1 \cdot 10^{10}$		$12.3 \cdot 10^{10}$		

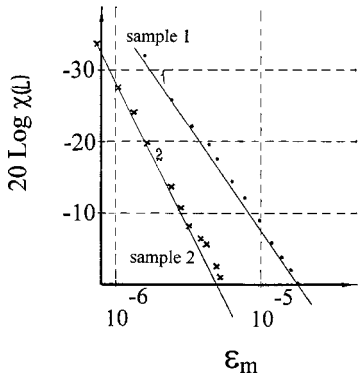

FIG. 8. Damping coefficient $\chi(L)$ versus the strain amplitude ε_m for the rods 1 and 2. The straight lines correspond to the dependences: $1-\chi(L)\sim\varepsilon_m^{3/2}$; $2-\chi(L)\sim\varepsilon_m^2$.

III. NONLINEAR SOUND-BY-SOUND DAMPING

In the second series of experiments, a weak ultrasonic pulse of $\tau\simeq 100$ μs duration and $f\simeq 270$ kHz frequency was excited by radiator 4 in the rod simultaneously with the low-frequency pump wave. The pulse was received by piezoaccelerometer 6 after its passage through the rod. To exclude the influence of the low-frequency pump signal, a low-frequency passive filter with coefficient of suppression 40 dB at the pump frequency was applied at the output of piezoaccelerometer 6.

When the strain amplitude ε_m of the pump wave in the resonator increases, a decrease of the received impulse amplitude $U(L)$ was also observed, in addition to the above-described phenomena of internal friction. [Such a phenomenon was also discovered in annealed copper,[13–16] lead, granite, marble, and river sand.[17] In most other materials (glass, steel, molybdenum, nickel, titanium, duralumin, tin), the sound-by-sound damping was not observed.]

Figure 8 presents the nonlinear damping coefficient $\chi(L)=Ln[U_0/U(L)]$ (where U_0 is the amplitude of the pulse without the pump wave) for the high-frequency pulse as the function of the pump wave strain amplitude ε_m. It is seen from these figures that $\chi(L)$ are governed by the following laws:

$$\text{for nonannealed zinc } \chi(L)\sim\varepsilon_m^{3/2}, \tag{17}$$

$$\text{for annealed zinc } \chi(L)\sim\varepsilon_m^{2}. \tag{18}$$

In the experiment, the [ε_m and $U(L)$] amplitudes measurement errors are ± 0.05 dB and 1%, respectively; the exponents in the dependencies (17) and (18) being determined with error $\pm 5\%$.

The phenomenon is inertia less, i.e., the impulse amplitude change is simultaneous with the strain amplitude change of the pump wave; therefore, this phenomenon cannot be explained by thermal processes which are associated with the sound-damping coefficient increase because of the rod temperature increase as a result of the pump wave absorption. It also cannot be explained by the acoustic waves interaction on hysteresis elastic nonlinearity (3) either, because such interaction would simultaneously cause the additional pulse delay which depends on the pump wave amplitude ε_m.[13–16] However, it is not observed in the experiment.

To explain the effect of sound-by-sound damping in annealed copper and some rocks, the phenomenological equation of state containing the dissipative nonlinearity[13–17] is used. Here, by following these papers and the above-described results, let us assume that the equation of state has the following form:

$$\sigma(\epsilon,\dot{\epsilon})=E\epsilon+\alpha\rho[1+g|\epsilon|^s]\dot{\epsilon}, \tag{19}$$

where g and s are dimensionless positive coefficients. Such a dissipative nonlinearity leads to an increase in the effective viscosity of the medium with increase in wave strain amplitude. In this case, the dissipative nonlinearity does not lead to the dependence of the velocity of the wave on its amplitude.

From Eqs. (4) and (19) we will obtain the wave equation with nonlinear dissipation for the strains $\epsilon=U_x$

$$\epsilon_{tt}-c_0^2\epsilon_{xx}=\alpha\epsilon_{txx}+\delta(|\epsilon|^s\epsilon_t)_{xx}, \tag{20}$$

where $\delta=\alpha g$.

By substituting in Eq. (20)

$$\begin{aligned}&\epsilon(x,t)=\epsilon_1(x,t)+\epsilon_2(x,t), \quad |\epsilon_1|\gg|\epsilon_2|,\\ &\epsilon_1(x,t)=\varepsilon_m\cos K_p x\sin\Omega_p t, \quad K_p=\Omega_p/c_0,\\ &\epsilon_2(x,t)=[\varepsilon_2(x)\exp[j(\omega t-kx)]+\text{c.c.}]/2,\end{aligned} \tag{21}$$

and taking into account that $\omega=c_0k\gg\Omega_p$, $K_pL=\pi(p-1/2)$, $\varepsilon_{2x}\ll k\varepsilon_2$, we will obtain the equation for the ultrasonic impulse amplitude $\varepsilon_2(x)$

$$d\varepsilon_2/dx=-æ[1+a_0g\varepsilon_m^s|\cos K_px|^s]\varepsilon_2, \tag{22}$$

where $æ=\alpha\omega^2/2c_0^3$ is the coefficient of linear (without the pump wave) dumping of the ultrasonic impulse,

$$\begin{aligned}a_0&=\pi^{-1}\int_0^{\pi}|\sin\theta|^s d\theta\\ &=\pi^{-1/2}\Gamma[(s+1)/2)]/\Gamma[(s+2)/2],\end{aligned}$$

$\theta=\Omega_p t$, $\Gamma(s)$ is the gamma-function.

From solution of Eq. (22) we find the expression for coefficient $\chi(L)$ of the nonlinear dumping of the ultrasonic impulse

$$\chi(L)=(gæL/\pi)\cdot\left(\frac{\Gamma[(s+1)/2)]}{\Gamma[(s+2)/2)]}\right)^2\cdot\varepsilon_m^s. \tag{23}$$

From comparison between theoretical (23) and experimental (17), (18) dependencies, we determine parameters s and g of the dissipative acoustic nonlinearities in the equation of state (19) (at $æL\simeq 2\cdot 10^{-1}$)

for nonannealed zinc: $s\simeq 3/2$, $g\simeq 9.2\cdot 10^8$,

for annealed zinc: $s\simeq 2$, $g\simeq 7.5\cdot 10^{11}$.

Here, as well as in the first experiment series, the polycrystalline (grain) structure change of zinc causes variation of the dissipative nonlinearity power.

IV. CONCLUSION

The present work deals with two series of experiments where the nonlinear acoustic phenomena (amplitude-dependent losses, shift of resonance frequency, generation of the third harmonic, and sound-by-sound damping) taking

place in nonannealed and annealed polycrystalline zinc rods were investigated. The theoretical description of these phenomena is carried out in the frame of phenomenological equations of state containing hysteresis and dissipative nonlinearities. The results of nonlinear acoustic investigations, which were carried out in this work and in earlier ones[11–17] alike, support the existence of high acoustic hysteresis and/or dissipative nonlinearity for some polycrystalline materials (such as copper, lead, zinc, granite, and marble) and river sand. Metallographic analysis demonstrates that the structure change of metals (at least, copper and zinc) corresponds to variation of nonlinear acoustic properties. This gives us hope that nonlinear acoustic phenomena may be used for realizing structure-sensitive methods for acoustic diagnostics of metals as well as other polycrystalline media.

ACKNOWLEDGMENT

The research was done with partial financial support of Russian Fund of Fundamental Investigations (No. 98-05-64683, 98-02-17686).

[1] ''The effect of imperfections, in *Physical Acoustics. Principles and Methods*, edited by W. Mason (Academic, New York and London, 1966), Vol. 3, p. A.
[2] A. Granato and K. Lucke, ''Theory of mechanical damping due to dislocation,'' J. Appl. Phys. **27**, 583–593 (1956).
[3] A. Granato and K. Lucke, ''String model of dislocations and dislocation absorption,'' in *Physical Acoustics. Principles and Methods*, edited by W. Mason (Academic, New York and London, 1966), Vol. 4, p. A.
[4] L. K. Zarembo and V. A. Krasil'nikov, *An Introduction to Nonlinear Acoustics* (Nauka, Moscow, 1966).
[5] L. D. Landau and E. M. Lifshitz, *Theory of Elasticity* (Pergamon, New York, 1986).
[6] A. S. Novick, ''Vibration of amplitude-dependent internal friction in single crystals of copper with frequency and temperature,'' Phys. Rev. **80**, 249–257 (1950).
[7] H. L. Caswell, ''Investigation of low-temperature internal friction,'' J. Appl. Phys. **29**, 1210–1214 (1958).
[8] D. N. Beshers, ''Internal friction of copper and copper alloys,'' J. Appl. Phys. **30**, 252–258 (1959).
[9] V. V. Lomakin, L. M. Pal'-Val', V. Ya. Platkov, and A. M. Rochchupkin, ''Nature of dislocation hysteresis losses and nonlinear effect in lead at high vibration amplitudes,'' Sov. Phys. Solid State **24**, 1915–1918 (1982).
[10] V. E. Nazarov, L. A. Ostrovsky, I. A Soustova, and A. M. Sutin, ''Nonlinear acoustics of microinhomogeneous media,'' Phys. Earth Planet. Inter. **50**, 65–73 (1988).
[11] V. E. Nazarov, ''The effect of structure on the acoustic nonlinearity of copper,'' Fiz. Met. Metalloved. **3**, 172–178 (1991).
[12] V. E. Nazarov and S. V. Zimenkov, ''Sound-by-sound modulation in metallic resonators,'' Acoust. Lett. **16**, 198–201 (1993).
[13] V. E. Nazarov, ''Nonlinear sound by sound damping in metals,'' Acoust. Phys. **37**, 1177–1182 (1991).
[14] V. E. Nazarov, ''Sound damping by sound in metals,'' Acoust. Lett. **15**, 22–25 (1991).
[15] S. V. Zimenkov and V. E. Nazarov, ''Dissipative acoustic nonlinearity of copper,'' Phys. Met. Metallogr. **3**, 242–244 (1992).
[16] V. E. Nazarov, ''Sound damping by sound in metals,'' in *Advances in Nonlinear Acoustics*, edited by H. Hobæk (Bergen, Norway, 1993), 13th ISNA, pp. 508–512.
[17] S. V. Zimenkov and V. E. Nazarov, ''Nonlinear acoustic effects in rock samples,'' Izv., Acad. Sci., USSR, Phys. Solid Earth **1**, 12–18 (1993).
[18] J. S. Swartz and J. Weertman, ''Modification of the Koehler–Granato–Lucke dislocation damping theory,'' J. Appl. Phys. **32**, 1860–1865 (1961).
[19] V. E. Nazarov, L. A. Ostrovsky, I. A Soustova, and A. M. Sutin, ''Anomalous acoustic nonlinearity in metals,'' Sov. Phys. Acoust. **34**, 284–289 (1988).

A method for estimating time-dependent acoustic cross-sections of bubbles and bubble clouds prior to the steady state

J. W. L. Clarke and T. G. Leighton
Institute of Sound and Vibration Research, University of Southampton, Highfield, Southampton SO17 1BJ, United Kingdom

(Received 16 November 1998; revised 11 August 1999; accepted 21 September 1999)

Models for the acoustic cross-sections of gas bubbles undergoing steady-state pulsation in liquid have existed for some time. This article presents a theoretical scheme for estimating the cross-sections of single bubbles, and bubble clouds, from the start of insonation onward. In this period the presence of transients can significantly alter the cross-section from the steady-state value. The model combines numerical solutions of the Herring–Keller model with appropriate damping values to calculate the extinction cross-section of a bubble as a function of time in response to a continuous harmonic sound field (it is also shown how the model can be adapted to estimate the time-dependent scatter cross-section). The model is then extended to determine the extinction cross-section area of multiple bubbles of varying population distributions assuming no bubble–bubble interactions. The results have shown that the time taken to reach steady state is dependent on the closeness of the bubble to resonance, and on the driving pressure amplitude. In the response of the population as a whole, the time to reach steady state tends to decrease with increasing values of the driving pressure amplitude; and with the increasing values of the ratio of the numbers of bubbles having radii much larger than resonance to the number of resonant bubbles. The implications of these findings for the use of acoustic pulses are explored. [S0001-4966(00)01801-4]

PACS numbers: 43.25.Ts, 43.35.Ei, 43.30.Lz [DLB]

INTRODUCTION

It has long been recognized that the high impedance mismatch between an air-filled bubble and the surrounding water provides an excellent acoustic target owing to strong inert scattering. It is also well understood that enhanced scatter and dissipation result from the pulsations into which the bubble will be driven by the sound field. To a first order, this response can be modeled as that of a single degree of freedom system with a resonance frequency, which is dependent on bubble size, where the bubble response is a maximum. It has been convenient to define acoustic extinction and scatter cross-sections for single bubbles, given, respectively, by the ratio of the power lost or reradiated by the bubble to the intensity of an incident plane wave. These have been calculated for the steady state[1] showing that, for a given bubble size, they are maximal at the resonance frequency. It should be noted that the cross-sections are only local maxima at resonance if considered as a function of bubble size for a given insonification frequency. This is because the contribution due to inert scattering will steadily increase with bubble size.

The resonant and off-resonant scattering characteristics of bubbles are well defined and are utilized in a wide number of applications including measurement of oceanic bubble populations[1–4] and research into upper ocean dynamics.[5] However, it is these same characteristics which make acoustic detection of nonbubble targets in areas with high bubble populations (such as the surf-zone) difficult.

One possible solution to this problem utilizes the bubble ''ring-up'' time, based on the time taken for a bubble to reach steady-state oscillation. Theory suggests that, owing to inertial effects, this ring-up time will be finite and that prior to reaching steady-state oscillation the acoustic scattering will be greatly reduced. A reduction in scattering attributed to ''ring-up'' time effects was first detected by Akulichev[6] in 1985. However two more recent studies[7,8] have failed to measure any reduction in scattering.

This letter outlines a theoretical scheme which enables the investigation of ring-up times of gas bubbles in fresh water. The model has also been used to determine the extinction cross-section area of bubble clouds of varying population distributions in a 150-kHz sound field assuming no bubble–bubble interactions. This model has been used to help ascertain a possible reason why Suiter[7] and Pace *et al.*[8] did not detect any reduction in scattering.

I. THEORETICAL MODELING OF THE RESPONSE OF A BUBBLE

As discussed in the Introduction, a gas bubble in water, when insonified by a plane wave, will pulsate. The oscillation is, at least to a first approximation, that of a single degree of freedom system, assuming small amplitude oscillations. In this case the restoring force is the elasticity of the gas and the mass is the effective inertia of the liquid component of the oscillating bubble. Damping, and thus energy loss, is introduced into the system by three distinct mechanisms:[9] energy radiated away from the bubble as acoustic waves (radiation damping); energy lost through thermal conduction between the gas and the surrounding liquid (thermal damping); and work done against viscous forces at the bubble wall (viscous damping).

Therefore a simple equation of motion, in the radius-force frame, for such a system driven at a single frequency would be

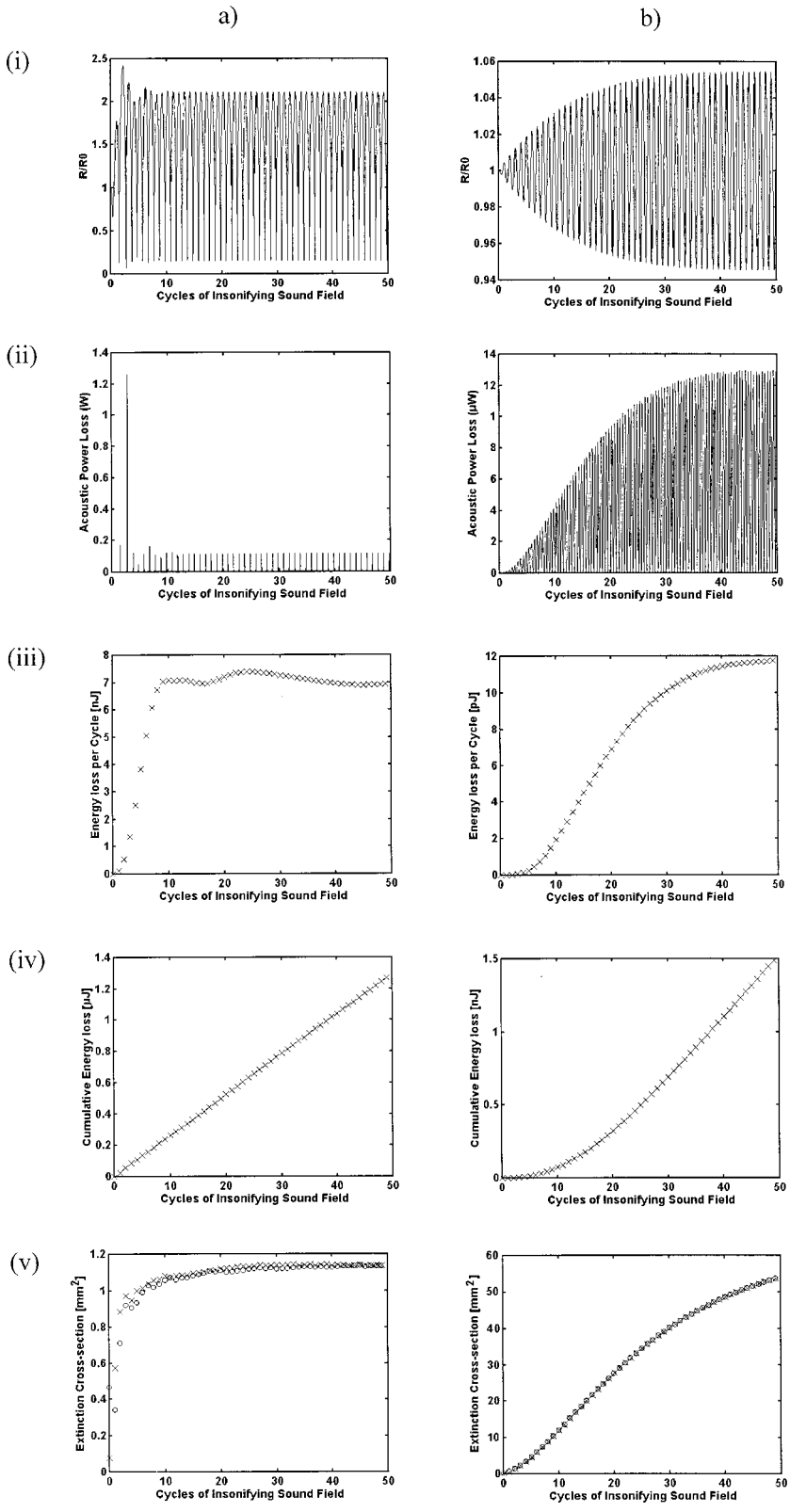

FIG. 1. Simulations of a 20-μm radius bubble in a 150-kHz (a) 1×10^5 Pa, (b) 500 Pa sound field. (i) Bubble wall displacement; (ii) the instantaneous power loss; (iii) energy loss over each cycle of the insonifying sound field; (iv) cumulative total energy loss; (v) extinction cross-sectional area of the bubble over each cycle of the insonifying sound field. For comparison the extinction cross-section calculated using the Gilmore model is also plotted in part (v) (''$\bigcirc$'' Gilmore, ''$\times$'' Keller–Miksis). The steady-state extinction cross-sectional area for a 20-μm bubble driven at resonance according to linear theory (Ref. 16) is 6.68×10^{-5} m^2.

$$m_{\rm rad}^{\rm RF}\ddot{R}+b_{\rm tot}^{\rm RF}\dot{R}+kR=-P_A\times4\pi R_0^2\cos(\omega t), \tag{1}$$

where $m_{\rm rad}^{\rm RF}$ is the inertia of the system, $b_{\rm tot}^{\rm RF}$ is the total damping in the radius-force frame, k is the stiffness, R is the radius of the bubble, R_0 is the equilibrium radius, P_A the acoustic pressure amplitude, and ω is the angular frequency of the driving sound field.[10] This is appropriate for bubble pulsations of small amplitude.

The rate of loss of energy (power loss) subtracted from the incident wave by the bubble is:

$$\text{Power}=b_{\rm tot}^{\rm RF}\dot{R}^2. \tag{2}$$

Twice during each bubble oscillation, $\dot{R}=0$. Consider two consecutive times, t_n and t_{n+1} when this occurs. The energy lost from an incident plane wave through viscous, thermal

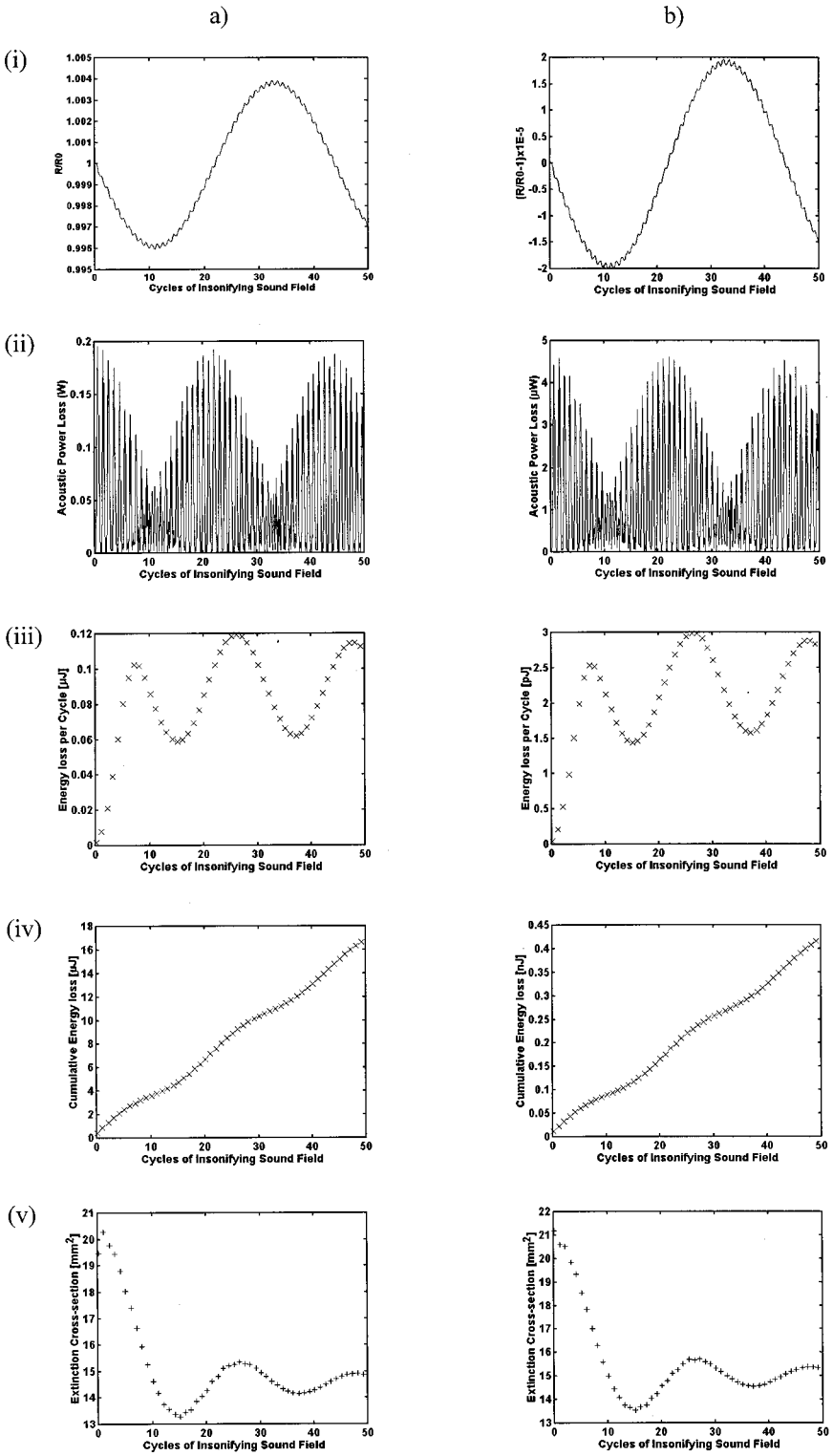

FIG. 2. Simulations of a 1-mm radius bubble in a 150-kHz (a) 1×10^5 Pa, (b) 500 Pa sound field. (i) Bubble wall displacement [for (b) the *y*-axis has been changed to show (R/R_0-1) so that the axis values can be more clearly shown]; (ii) the instantaneous power loss; (iii) energy loss over each cycle of the insonifying sound field; (iv) cumulative total energy loss; (v) extinction cross-sectional area of the bubble over each cycle of the insonifying sound field. The steady-state extinction cross-sectional area for a 1-mm bubble driven at resonance according to linear theory (Ref. 16) is 1.03×10^{-5} m^2.

and scattering losses in the interval $t=t_n$ to $t=t_{n+1}$ is:

$$\Phi_n=\int_{t=t_n}^{t=t_{n+1}} b_{\mathrm{tot}}^{\mathrm{RF}}\dot{R}^2\,dt, \tag{3}$$

and the average power loss in this interval is:

$$\langle W_n\rangle=\frac{\Phi_n}{t_{n+1}-t_n}. \tag{4}$$

It is then a simple matter to calculate the extinction cross-sectional area, Ω_n, appropriate to the time interval $t=t_n$ to $t=t_{n+1}$. This is given simply by the ratio of the average power loss in this period to the intensity of the incident plane wave:

$$\Omega_n=\frac{\langle W_n\rangle}{I}=\frac{\int_{t=t_n}^{t=t_{n+1}} b_{\mathrm{tot}}^{\mathrm{RF}}\dot{R}^2\,dt}{I(t_{n+1}-t_n)}. \tag{5}$$

It should be noted that if, instead of the total energy loss from the incident beam, it was the power scattered by the

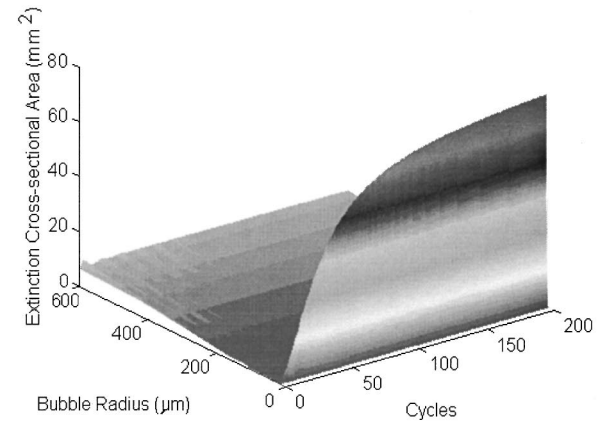

a)

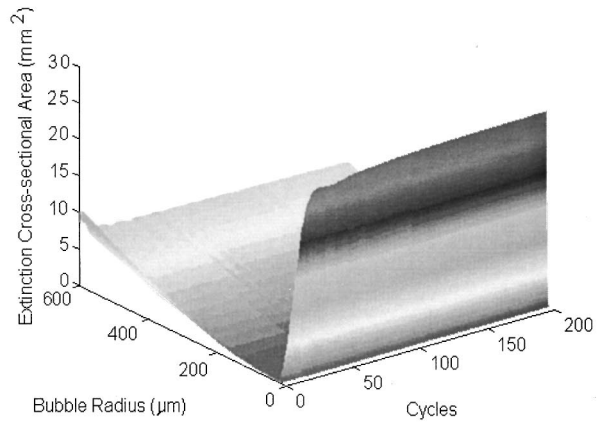

b)

FIG. 3. Extinction cross-sectional area of a single bubble of radius up to 600 μm in a 150-kHz sound field of amplitude (a) 500 Pa, (b) 5000 Pa. For clarity in plotting, the discrete function Ω_n shown in part (v) of Figs. 1 and 2 has been interpolated to provide line plots for the cross-sections shown in this figure and subsequent ones.

bubble which was of interest, then the above formulation can be simply adapted by employing only that component of the damping term $b_{\mathrm{tot}}^{\mathrm{RF}}$ which relates to radiated losses ($b_{\mathrm{rad}}^{\mathrm{RF}}$). This would give the acoustic scattering cross-section. However, a more exact form can be obtained by rewriting the scattered power in Eq. (5) in terms of the emitted pressure field, which can be formulated[10] in terms of the bubble wall motion:

$$\Omega_n = \frac{\langle W_n \rangle}{I} = \frac{4\pi r^2 \int_{t=t_n}^{t=t_{n+1}} \frac{\left(\frac{\rho R}{r}(\ddot{R}R + 2\dot{R}^2)\right)^2}{\rho_0 c} dt}{I(t_{n+1} - t_n)}, \quad (6)$$

where r is the distance from the bubble, ρ_0 is the fluid density, and c is the speed of sound.

Bubbles are nonlinear oscillators and as the following analysis shows the ring-up time is dependent on the bubble equilibrium radius, the driving frequency, and the sound pressure level.

II. TIME-DEPENDENT EXTINCTION CROSS-SECTION OF A SINGLE BUBBLE

To calculate the time-dependent extinction cross-sectional area from Eq. (5), it is necessary to calculate the velocity of the bubble wall over time as well as the total damping in the radius-pressure frame. Although several options are available,[11] in this paper $\dot{R}$ was found using the nonlinear bubble wall velocity determined from the Keller and Miksis equation[12] a form of the equations of motion first introduced by Herring.[13]

The damping term $b_{\mathrm{tot}}^{\mathrm{RF}}$ is obtained using Prosperetti's 1977 analysis.[14] This is a linearized theory for the small amplitude forced pulsation of a bubble, describing the thermal effects in terms of the effective polytropic index and thermal damping constant. This analysis assumes a linear regime. Therefore the only expression of the bubble nonlinearity in this system comes from the Keller–Miksis equation (or equivalent). The resultant is therefore an approximation only. Thus care should be taken when considering the absolute values of $b_{\mathrm{tot}}^{\mathrm{RF}}\dot{R}^2$, especially for higher sound pressure levels when bubble motion is highly nonlinear, as a significant error in the calculation is likely. As discussed in Sec. I, computation of the scattering cross-section need not be limited by such linearizations, since small amplitude expressions for viscous and thermal losses are not required.

Figures 1 and 2 show four illustrative cases, and each figure is subdivided into five subsections [(i)–(v)] showing, against a common time axis, the following: (i) the normalized bubble radius; (ii) the instantaneous power loss determined from Eq. (2); (iii) the energy loss per cycle of the insonifying sound field as determined from Eq. (3) (plotted discretely for each cycle); (iv) a cumulative plot of the energy loss; (v) the time-dependent extinction cross-section area for a single bubble, Ω_n, as calculated by Eq. (5). Plot (iv) is particularly interesting. Were a bubble to immediately attain steady state, this plot would be a straight line of constant positive gradient. However, if the energy loss is less in the ring-up period, the plot will dip below the straight line which would be drawn if the eventual steady-state behavior were extrapolated to time zero.

Figure 1 shows the time-dependent extinction cross-sectional area of a resonant bubble in a 150 kHz sound field of amplitude 10^5 Pa [Fig. 1(a)] and 500 Pa [Fig. 1(b)]. Figure 2 shows the response of a 1-mm radius, off-resonant, bubble in the same sound fields. Further discussion of these results is included in Sec. IV below.

III. TIME-DEPENDENT EXTINCTION CROSS-SECTIONAL AREA OF A BUBBLE CLOUD

The above analysis can be expanded to give a first-order estimation of the time-dependent extinction cross-section of a bubble cloud. It is assumed that the number density is sufficiently small that bubble–bubble interactions can be neglected, as is the reduction in intensity of the incident wave as it propagates through the cloud (although a second-order calculation could include this). This article is restricted to a first-order calculation and thus will underestimate the extinction cross-section near to resonance.[15] After calculating the

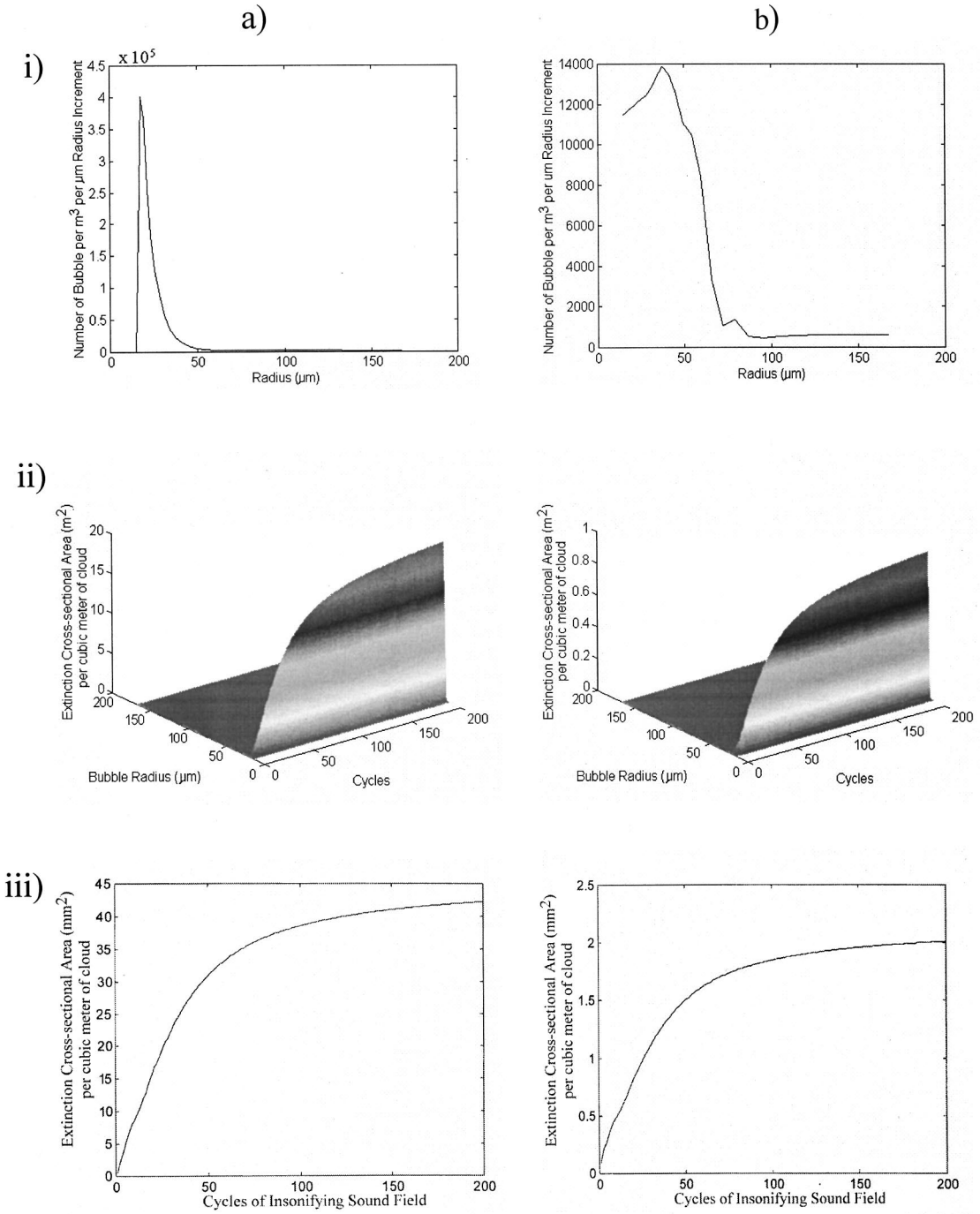

FIG. 4. Response of (a) an example oceanic bubble population (based on the measurements of Phelps and Leighton, Ref. 15); and (b) a laboratory bubble population (based on the measurements of Pace *et al.*, Ref. 8) in a 500-Pa, 150-kHz sound field. Plot (i) shows the bubble population distribution, (ii) is the extinction cross-sectional area oif a 1 m^3 cloud, resolved for each radius bubble assuming no interactions, and (iii) is the extinction cross-sectional area of the 1 m^3 cloud (i.e., summed for all radii for each cycle of the sound field).

extinction cross-sectional area of a single bubble of varying radii and compiling the results as in Fig. 3, the effective response of a bubble layer with a given population distribution can be calculated. The density of the population is used as a scaling quantity given the limitations discussed above.

Therefore the response of a nonuniform bubble distribution can be investigated by multiplying the response [calculated as for Fig. 1(a) and (b)] by a population distribution. In addition the total response of the bubble cloud can be ascertained by integrating to find the area under the extinction cross-section radius curve for each cycle of the insonifying sound field. Figures 4 and 5 show the response for a bubble population typical of an oceanic bubble cloud[16] and an artificially produced bubble cloud (taken from the population measurements of Pace *et al.*[8]) in sound fields of 500 Pa and 5000 Pa amplitude. Since the acoustic attenuation method used for measuring the laboratory population proved unreliable for larger bubble sizes in the data of Pace *et al.*,[8] their population has been extrapolated in Fig. 6, up to a radius of 600 μm, to investigate the effect that this could have on the time dependent extinction cross-sectional area (this is for illustrative purposes only and in no way suggests that this

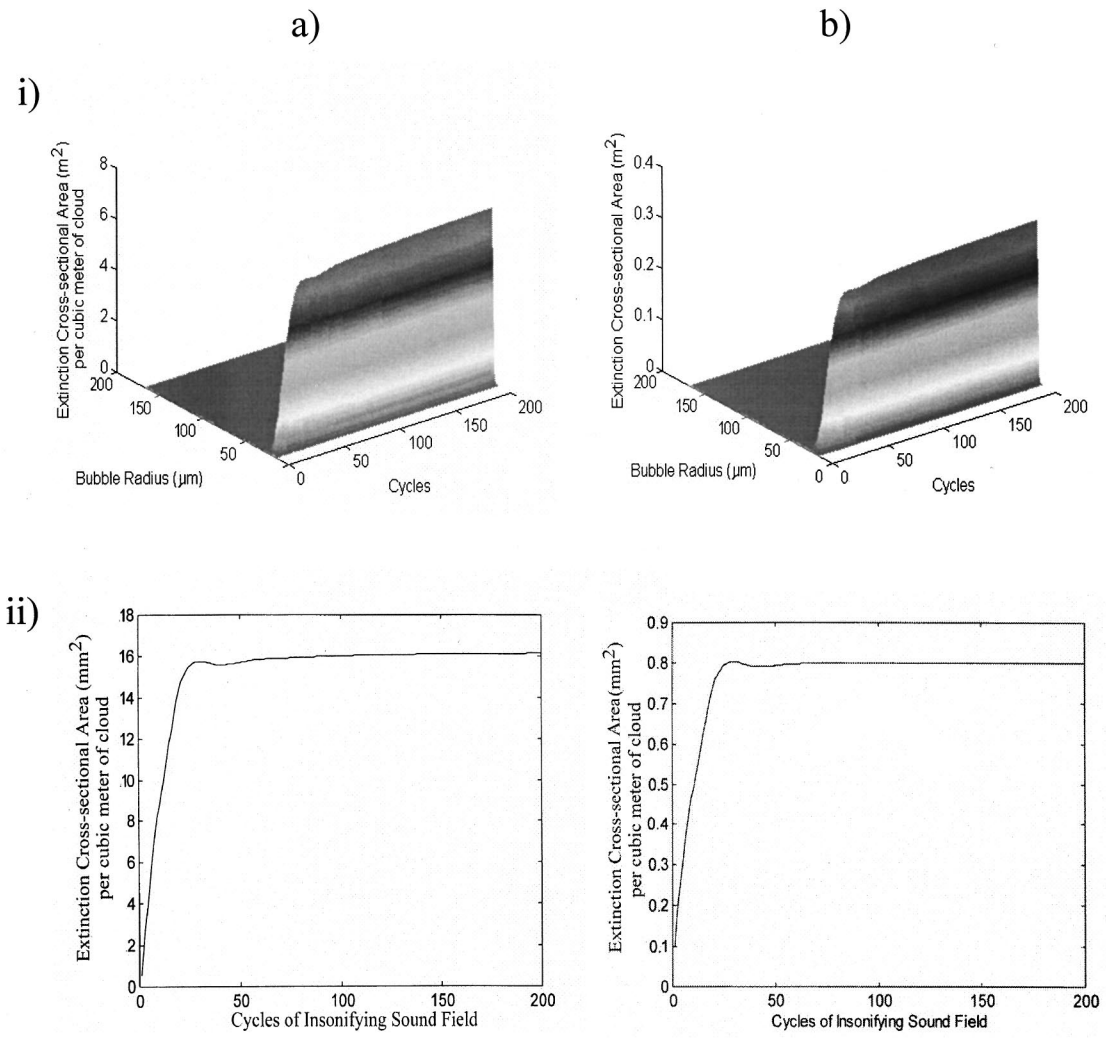

FIG. 5. Response of (a) an example oceanic bubble population (based on the measurements of Phelps and Leighton, Ref. 15) and (b) a laboratory bubble population (based on the measurements of Pace *et al.*, Ref. 8) in a 5000-Pa, 150-kHz sound field. (i) The extinction cross-sectional area of a 1 m^3 cloud, resoved for each radius bubble assuming no interactions. (ii) The extinction cross-sectional area of the 1 m^3 cloud (i.e., summed for all radii for each cycle of the sound field).

extrapolation reflects the true nature of the population).

IV. DISCUSSION

A simple comparison of the bubble wall displacements depicted in Figs. 1 and 2 provides an intuitive guide as to the effect of sound pressure level and the closeness to resonance on ring-up time. It can clearly be seen that the time taken to reach steady state is by far the longest for a resonant bubble in a low amplitude sound field. A gentle build-up to steady state is observed [Fig. 1(b)]. Conversely a resonant bubble in a high amplitude sound field exhibits a distinctly nonlinear response with significant initial transient activity before quickly achieving a steady-state response [Fig. 1(a)]. Examination of the off-resonant bubble wall displacement plots shows a reduced dependence on sound pressure level and a rapid rise time with subsequent reduction and oscillation (Fig. 2).

In the case of the resonant bubbles, the graphs of the extinction cross-sectional area shown in Fig. 1 tend to follow the mean bubble wall response exhibiting a brief, transient, ring-up at high sound pressure levels and a gradual build-up for low sound pressure levels. The latter indicates potential for reducing losses by using short pulses of ultrasound, an effect confirmed by noting that in Fig. 1(b) (iv), in the first 30 cycles the curve dips below a straight line which might be extrapolated back from the steady state (as predicted in Sec. II).

A superposition of natural and driving frequencies is evident in the radius plots [Fig. 2(i)]. The extinction cross-sectional area for these off-resonant bubbles [Fig. 2(v)] is more complicated and can be more easily understood by examining the plots of the acoustic power loss determined from Eq. (2) [Fig. 2(ii)].

Although transients are more evident at the lower driving pressures [Fig. 2(b) (ii)], the tendency in both plots is for the energy loss [Fig. 2(iii)] and extinction cross-section [Fig. 2(v)] to oscillate around the steady-state value at twice the bubble natural frequency, although the cross-section takes much higher values for the first few cycles. Clearly the presence of such bubbles would not be conducive to enhancing acoustic transmission using pulsed fields. Figure 3 summarizes the time-dependent cross-section of single bubbles. A

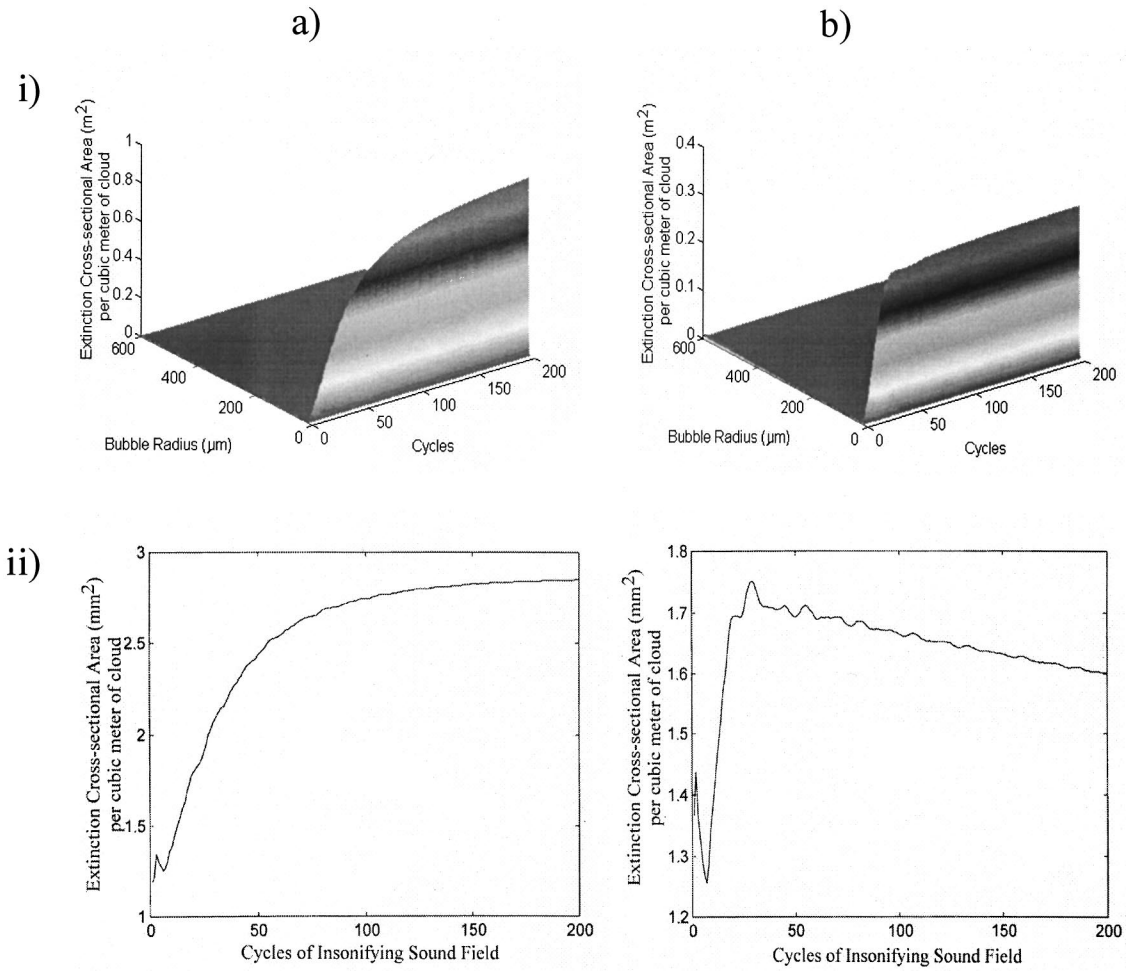

FIG. 6. Response of the laboratory bubble population (based on the measurements of Pace *et al.*, Ref. 8) extrapolated to include potential large bubbles in a 150-kHz, (a) 500 Pa and (b) 5000 Pa sound field. Plot (i) is the extinction cross-sectional area of a 1 m^3 cloud, resoved for each radius bubble assuming no interactions, and (ii) is the extinction cross-sectional area of a 1 m^3 cloud, summed for all radii for each cycle of the sound field.

''geometrical'' contribution is seen from the large bubbles, which oscillate for a few tens of cycles following the onset of insonation around the eventual steady-state value. Smaller bubbles contribute a lesser amount except around the resonance condition. Here there is a peak, with a ring-up time which tends to decrease with increasing driving amplitude. Figure 7 shows how the extinction cross-section of a 20-μm radius bubble changes with increasing sound pressure levels. The bubble response quickly deviates from an exponential ring-up with a corresponding decrease in ring-up time. Thus for the simulated response of a bubble cloud, which contain large numbers of small bubbles, to a 150-kHz sound field the response of the resonant bubble is dominant with a well defined ring-up time for low sound pressure levels (Fig. 4). It is evident that an increase in the sound pressure level can significantly reduce the ring-up time. The results shown in Fig. 5 demonstrate this effect. In the case of the extrapolated bubble populations shown in Fig. 6, despite the numbers of large bubbles being relatively few, their presence has a significant effect on the response of the cloud as a whole, particularly during the first few cycles of the insonifying sound field. In this epoch, the early motion of these large bubbles (characterized above as being a fall in the first few cycles following oscillation toward steady state) appears to dominate. Thus the presence of large bubbles and/or high sound pressure levels can be counter-indicative for the enhanced efficiency of penetration of sonar through bubble clouds.

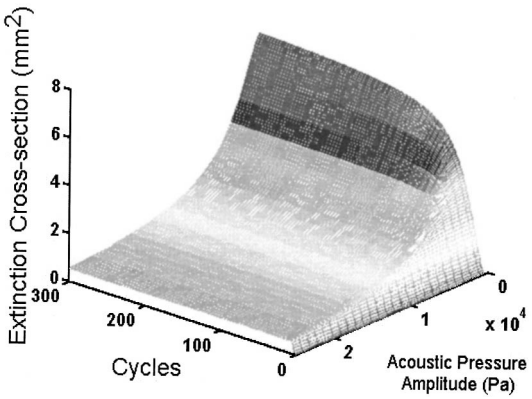

FIG. 7. Extinction cross-sectional area of a single bubble of radius 20 μm in a 150-kHz sound field of varying sound pressure level between 500 and 25 000 Pa.

V. CONCLUSIONS

A theoretical study into the time dependence of the response of air bubbles in fresh water to a continuous wave of 150-kHz sound field has shown that the ring-up time of a bubble is affected by its closeness to resonant oscillation and the amplitude of the driving sound field. Expansion of this theory to investigate the response of a low density bubble cloud of oceanic and laboratory origins has shown that a significant ring-up time should be detectable if the predominant smaller bubbles are insonified at their resonant frequency. Furthermore, higher sound pressure levels can obscure the ring-up time of the resonant bubbles, and the presence of large off-resonant bubbles even in relatively small quantities can enhance this effect significantly.

ACKNOWLEDGMENTS

The authors wish to acknowledge funding from the Defence Evaluation Research Agency (Contract No. SSDW1/647) and are very grateful to G. J. Heald and H. A. Dumbrell of DERA Bincleaves for invaluable scientific and technical input.

[1] H. Medwin, ''Counting bubbles acoustically: A review,'' Ultrasonics **15**, 7–14 (1977).
[2] D. M. Farmer and S. Vagle, ''Bubble measurements using a resonator system,'' in *Natural Physical Processes Associated with Sea Surface Sound*, edited by T. G. Leighton (University of Southampton, 1997), pp. 155–162.
[3] W. K. Melville, E. Terrill, and F. Veron, ''Bubbles and turbulence under breaking waves,'' Natural Physical Processes Associated with Sea Surface Sound, University of Southampton, edited by T. G. Leighton (1997), pp. 135–145.
[4] A. D. Phelps, D. G. Ramble, and T. G. Leighton, ''The use of a combination frequency technique to measure the surf zone bubble population,'' J. Acoust. Soc. Am. **101**, 1981–1989 (1997).
[5] S. A. Thorpe, ''Bubble clouds and the dynamics of the upper ocean,'' Q. J. R. Meteorol. Soc. **118**, 1–22 (1992).
[6] V. A. Akulichev, V. A. Bulanov, and S. A. Klenin, ''Acoustic sensing of gas bubbles in the ocean medium,'' Sov. Phys. Acoust. **32**, 177–180 (1986).
[7] H. R. Suiter, ''Pulse length effects on the transmissivity of bubbly water,'' J. Acoust. Soc. Am. **91**, 1383–1387 (1992).
[8] N. G. Pace, A. Cowley, and A. M. Campbell, ''Short pulse acoustic excitation of microbubbles,'' J. Acoust. Soc. Am. **102**, 1474–1479 (1997).
[9] C. Devin, Jr., ''Survey of thermal, radiation, and viscous damping of pulsating air bubbles in water,'' J. Acoust. Soc. Am. **31**, 1654 (1959).
[10] T. G. Leighton, *The Acoustic Bubble* (Academic, New York, 1994), Sections 3.3.1(b), 3.2.1, and 4.1.2.
[11] For comparison the Gilmore equation was also used to determine $\dot{R}$ with, as Fig. 1(v) illustrates, negligible effect for the parameter range indicated here.
[12] J. B. Keller and M. Miksis, ''Bubble oscillations of large amplitude,'' J. Acoust. Soc. Am. **68**, 628–633 (1980).
[13] C. Herring, ''Theory of the pulsations of the gas bubble produced by an underwater explosion,'' OSRD, Rep. No. 236 (1941).
[14] A. Prosperetti, ''Thermal effects and damping mechanisms in the forced radial oscillations of gas bubbles in liquids,'' J. Acoust. Soc. Am. **61**, 17–27 (1977).
[15] Z. Ye and L. Ding, ''Acoustic dispersion and attenuation relations in bubbly mixture,'' J. Acoust. Soc. Am. **98**, 1629–1636 (1995).
[16] A. D. Phelps and T. G. Leighton, ''Oceanic bubble population measurements using a buoy deployed combination frequency technique,'' IEEE J. Ocean Eng. **23**, 400–410 (1998).

Backscattering enhancements associated with subsonic Rayleigh waves on polymer spheres in water: Observation and modeling for acrylic spheres

Brian T. Hefner and Philip L. Marston
Department of Physics, Washington State University, Pullman, Washington 99164-2814

(Received 29 January 1999; revised 3 January 2000; accepted 7 January 2000)

Unlike most common solids, ''plastic'' polymer solids typically have shear and Rayleigh wave phase velocities less than the speed of sound in water. Subsonic Rayleigh waves on smooth objects in water are not classified as leakey waves and it is necessary to reexamine backscattering mechanisms. Also the intrinsic material dissipation of the Rayleigh wave can be significant. Backscattering by acrylic or polymethlmethacrylate (PMMA) spheres in water is analyzed and measured in the region $ka=1.5-7$ and it is found that prominent low-lying resonance peaks of the form function $|f|$ exist. The peaks can be modeled with quantitative ray theory as the result of coupling of subsonic Rayleigh waves with sound through acoustic tunneling. The most prominent maximum of $|f|=5.63$ occurs at $ka=1.73$ and is associated with the quadrupole (or $n=2$) partial wave. In addition to explaining the scattering, the target strength is found to be sufficiently large that such spheres may be useful for passive low frequency targets. © *2000 Acoustical Society of America.* [S0001-4966(00)03104-0]

PACS numbers: 43.30.Ft, 43.20.Fn, 43.35.Mr [DLB]

INTRODUCTION

This paper examines the backscattering response of an acrylic or polymethylmethacrylate (PMMA) sphere in water. Solid–polymer ''plastic'' objects have not received much attention in the study of backscattering primarily due to the large absorption that tends to limit the response at high frequencies. In addition to intrinsic attenuation, plastic objects have other properties which make them interesting from the standpoint of scattering theory: Plastics typically have shear and Rayleigh velocities which are less than the speed of sound in water.[1,2] Plastic scatterers have been examined in various computational studies although the detailed scattering mechanisms were not analyzed.[3–5] Previous studies have examined the role of subsonic surface waves in backscattering enhancements, however, these studies have dealt with scattering from metallic spherical and cylindrical shells.[6–12] In the modal spectrum of such shells, certain portions of the lowest antisymmetric Lamb wave are subsonic and plane waves incident on these shells can couple into these modes by tunneling through the evanescent field adjacent to the shell. The present work indicates that coupling via tunneling can be important in the scattering by solid PMMA spheres. Examination of the backscattering form function for a solid PMMA sphere (Fig. 1) reveals a large backscattering enhancement which is shown here to be associated with the subsonic Rayleigh wave. Because this enhancement occurs at low frequencies, the attenuation due to material absorption is small as can be seen from the solid line in Fig. 1 where absorption is included in the calculation of the form function as discussed in Sec. I. Figure 2 shows experimental evidence of the excitation of an enhancement for a PMMA sphere with a radius of $a=25.4$ mm. In this experiment, the incident 10-cycle tone burst has a frequency of 16.0 kHz which corresponds to the lowest resonance of the sphere. The resonance affects the peak amplitude and stretches out the decaying portion of the echo. Details of this and related experiments are given in Sec. IV. The presence of this large resonance suggests that solid plastic spheres may make good candidates for use as passive sonar targets for certain applications. This may provide an alternative to the thin fluid-filled spherical shells which have typically been used to give enhanced backscattering. These targets depend on a large velocity mismatch between the interior fluid and the surrounding fluid to enable glory scattering (Sec. 4.8 of Ref. 13). In the past this was achieved by using chlorofluorocarbon (CFC), however, the production of this substance has been banned and alternative fluids are being considered.[14,15] The simplicity and availability of plastic spheres may make them a good alternative to fluid-filled shells for narrow-band low frequency applications and this is considered in Sec. V.

To understand the role of the subsonic Rayleigh wave, a ray approximation was used to model the backscattering enhancement. The ray approximation, discussed in Sec. II, is identical to the method previously used to model subsonic guided waves on spherical shells.[8,9] In the present research, however, attention is given to the introduction of material absorption into the Watson methodology to find the phase velocity and damping of the Rayleigh wave on the PMMA sphere. This is discussed in Sec. III. Examination of the results of the Watson methodology supports an approximate *ad hoc* means of introducing material absorption into the phase velocity and damping coefficients for a Rayleigh wave on the sphere. Comparisons with partial wave series calculations support the ray approximation modified so as to include material absorption.

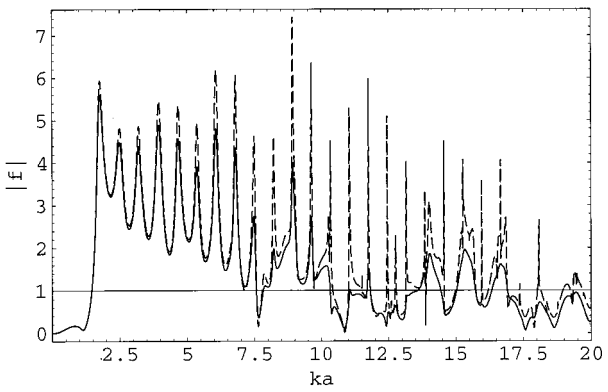

FIG. 1. Exact form function calculated with the addition of material absorption in the partial wave series (solid line) for a PMMA sphere. The exact form function without material absorption is also given for comparison (dashed line). The first resonance is associated with the $n=2$ partial wave.

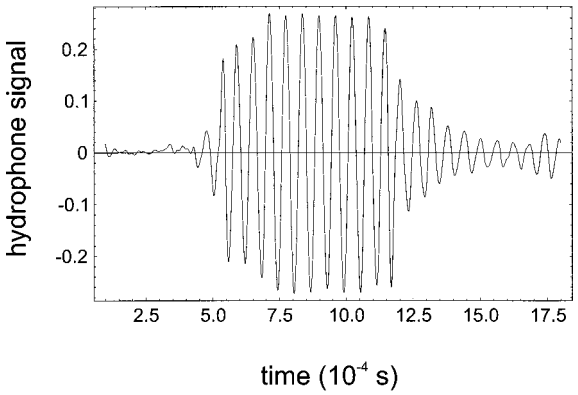

FIG. 2. Backscattered response of a PMMA sphere ($a=25.4$ mm) to a 10-cycle tone burst at 16.0 kHz ($ka=1.72$). Because the individual circumnavigations are closely spaced in time, they cannot be easily resolved. The slowly decaying tail at 120 ms indicates the presence of the resonance and the associated scattering enhancement.

I. EXACT FORM FUNCTION WITH THE ADDITION OF MATERIAL ABSORPTION

Typically material absorption is neglected in the study of backscattering from elastic objects. These absorption mechanisms are usually much less than those due to radiation damping and contribute little to an understanding of the dominant processes. However, for PMMA and other plastics a significant portion of the acoustic energy could be absorbed. Before examining the approximate ray synthesis for the scattering enhancement of interest, the exact partial wave series solution will be modified to include material absorption to examine the extent to which this will alter and possibly suppress the backscattering amplitude. The steady-state scattered pressure in the far field from an elastic sphere has the form

$$p_{\text{scat}}=p_{\text{inc}}\frac{af}{2r}e^{ikr}, \tag{1}$$

where p_{inc} is the pressure amplitude of the incident acoustic wave, a is the sphere radius, and r is the distance from the center of the sphere to some distance observation point. The wave number k of the incident plane wave is defined as $k=\omega/c$, where ω is the angular frequency and c is the speed of sound in water. The time dependence $\exp(-i\omega t)$ has been suppressed. The complex scattering amplitude or form function can be expressed by the exact partial wave series representation

$$f(x=ka)=\frac{2}{ix}\sum_{n=0}^{\infty}(-1)^n(2n+1)\frac{B_n(x)}{D_n(x)}, \tag{2}$$

where $x=ka=2\pi a/\lambda$ and λ is the wavelength of the incident plane wave. The functions $B_n(x)$ and $D_n(x)$ are 3×3 determinants the elements of which are given in Ref. 16. These functions depend on the material parameters of the sphere which are the longitudinal sound speed c_L, the shear or transverse sound speed c_S, and the density ρ_e. The density of water is denoted by ρ.

To examine the effects of material absorption, the form function was modified by introducing complex wave numbers into the determinants B_n and D_n.[4,5] These complex wave numbers are given by

$$k_L'=\frac{\omega}{c_L}(1+i\gamma_L), \tag{3a}$$

$$k_s'=\frac{\omega}{c_S}(1+i\gamma_S), \tag{3b}$$

where γ_S and γ_L are the shear and longitudinal normalized absorption coefficients given in Table I. These were derived from ultrasonic measurements made by Hartmann and Jarsynski.[2] By introducing complex wave numbers, the elements of the determinants are now expressions of complex spherical Bessel functions and complex spherical Hankel functions of the first kind. A comparison of the form functions with and without the introduction of material absorption is given in Fig. 1. As expected the sharper resonances at large ka are suppressed and the magnitudes of the broader structures in this region have decreased as well. The large enhancement for $1<ka<10$ is still prominent with only the magnitudes of the resonances having decreased. The Q of these resonances now depends on both the radiation damping

TABLE I. Material parameters used in calculations. The absorption values for PMMA were derived from ultrasonic measurements made by Hartmann and Jarsynski.[2]

Material	Density (g/cm^3)	Longitudinal velocity (km/s)	Shear velocity (km/s)	Rayleigh velocity (km/s)	Longitudinal absorption $\text{Im}(k_L')/\text{Re}(k_L')$	Shear absorption $\text{Im}(k_s')/\text{Re}(k_s')$
PMMA	1.19	2.690	1.340	1.250	0.0034	0.0053
water	1.00	1.479				

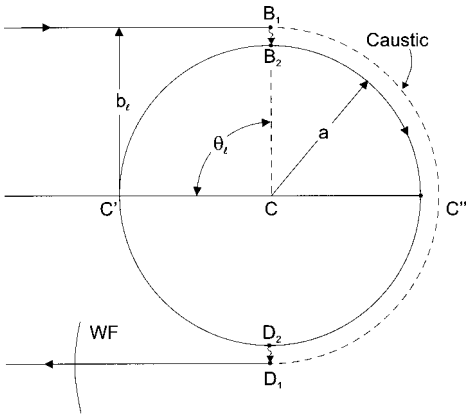

FIG. 3. Ray diagram for the subsonic Rayleigh wave propagating around the sphere. On the caustic, the projected tangential velocity of the Rayleigh wave equals the speed of sound in water. Evanescent coupling to and from the sphere is designated by the wiggly arrows at B_1B_2 and D_1D_2. WF denotes a section of the wavefront that appears to be radiated from the caustic.

and the material absorption and indicates that any approximate ray synthesis of this enhancement must incorporate both of these effects. A secondary consequence of absorption is to introduce a weak frequency dependence of c_L and c_S. This dispersion is estimated to have a negligible effect for $1<ka<10$.

II. RAY APPROXIMATION WITHOUT MATERIAL ABSORPTION

Previous studies have examined ray approximations for scattering contributions due to subsonic guided waves on spherical and cylindrical shells.[8–10] The antisymmetric a_{0-} was found to have a phase velocity along the shell surface that is less than the speed of sound in the surrounding water. For PMMA, the Rayleigh wave speed is less than the surrounding water and the ray approximation for subsonic guided waves becomes applicable for the solid PMMA sphere. Figure 3 shows the modified ray picture for subsonic Rayleigh waves on a solid sphere. Neglecting material absorption, the resulting contribution to the form function by the *m*th circumnavigation of the counterpropagating waves may be written[9]

$$f_{mR}=-G_R\ \exp[-\pi\beta_R-2\pi m\beta_R + i(\eta_R-m\pi+2\pi mxc/c_R)], \tag{4}$$

where the subscript R indicates that this is the contribution due to the Rayleigh wave and $m=0,1,2...$. The coupling coefficient G_R accounts for the interaction of the surface wave with the surrounding water and is related to the radiation damping parameter β_R by the approximation[17] $|G_R| \approx 8\pi\beta_R c/c_R$. Each term in the complex exponent has a simple geometric significance. The terms proportional to β_R describe the radiation damping as the surface wave travels around the sphere. The phase terms proportional to m describe the phase shifts due to polar caustics and propagation due to each complete circumnavigation. The phase $\eta_R = \pi xc/c_R-\pi/2$ is associated with the first partial circumnavigation and crossing of the polar caustic at C''. The contributions due to repeated circumnavigations may be summed giving

$$f_R=\sum_{m=0}^{\infty} f_{mR}=\frac{-G_R\ \exp(-\pi\beta_R+i\eta_R)}{[1+\exp(-2\pi\beta_R+i2\pi xc/c_R)]}. \tag{5}$$

In the absence of material absorption, the properties of the Rayleigh wave on a solid sphere are calculated using the Watson methodology which yields

$$c_R/c=x/(\alpha_R+1/2), \tag{6a}$$

$$v_R=\alpha_R+i\beta_R, \tag{6b}$$

$$D_{v_R}(x)=0, \tag{6c}$$

where Eq. (6c) is defined by replacing the partial-wave index by the complex number v_R everywhere in the definition of $D_n(x)$.[18] The results of this calculation are given Figs. 4 and 5 as the solid curves. As expected the Rayleigh phase velocity is subsonic and asymptotes to the fluid-loaded half-space phase velocity with increasing *ka*. Note that the free half-space Rayleigh velocity is $c_R/c=0.845$ which is signifi-

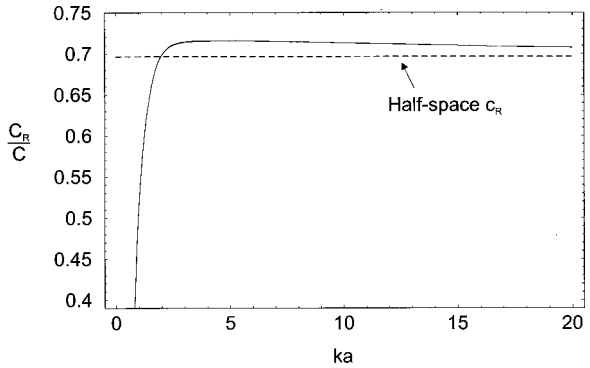

FIG. 4. Normalized phase velocity of the Rayleigh wave on a PMMA sphere with and without the addition of material absorption. The differences between these two curves are so slight that they cannot be distinguished. The dashed line ($c_R/c=0.696$) is the Rayleigh speed on a fluid-loaded PMMA half-space. The Rayleigh speed on a free PMMA half-space is $c_R/c=0.845$.

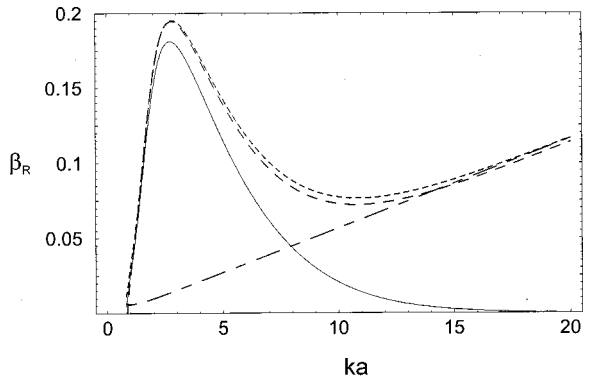

FIG. 5. Damping of the Rayleigh wave on a fluid-loaded PMMA sphere calculated by three methods. The radiation damping with no material absorption (solid line). The damping calculated for a sphere with the addition of material absorption in D_{v_l} (long dashes). An approximation calculated by the addition of the result with no material absorption and the material damping for a fluid-loaded PMMA half-space as in Eq. (8b) (short dashes). Also displayed is the material absorption for a fluid-loaded PMMA half-space which is the second term in Eq. (8b) (long–short dashes).

cantly larger than for a water-loaded half-space[19] ($c_R/c = 0.695$). The density of PMMA is very close to water ($\rho/\rho_e = 0.839$) and this may account for the difference in the fluid-loaded and free Rayleigh velocities. For Rayleigh waves on fluid-loaded flat surfaces having[19] $c_R/c > 1$ the phase velocity increases with increasing ρ/ρ_e. However, we find that if $c_R/c < 1$ (as in the case of PMMA), increased fluid loading causes the Rayleigh velocity to decrease. This is consistent with recent studies of PVC–water and Plexiglass–water interfaces.[20] In the limit of $\rho/\rho_e \to \infty$, the surface can be considered to have mixed boundary conditions (normal displacement $u = 0$, vanishing shear stress $\tau_{zx} = \tau_{zy} = 0$, where z is normal to the surface). It may be that this decreasing velocity follows the transition from a free boundary ($\rho/\rho_e = 0$) to a mixed boundary ($\rho/\rho_e \to \infty$) where $c_R/c \to 0$. In the limit $\rho/\rho_e \to 0$ the root we study evolves to the free surface Rayleigh root.

An example of this type of subsonic surface wave was examined by Guzhev.[21] In that work, a surface wave, which was classified as a Stoneley wave, at a flat fluid–solid interface was studied as a function of sound speed in the fluid. When the sound velocity in the fluid becomes larger than the Rayleigh wave speed, the speed of the wave studied approaches the Rayleigh wave speed. For this wave, the majority of the strain energy was found to reside in the solid in the aforementioned limit. The wave studied by us has a similar asymptotic behavior for the speed and is classified for the purposed of our discussion as a generalization of the Rayleigh wave.

The solid line in Fig. 5 gives the corresponding radiation damping β_R. The *ka* dependence can be qualitatively explained in terms of the evanescent field coupling as is done in Refs. 8 and 12. As $ka \to 0$, c_R/c decreases rapidly and consequently the caustic separation $(b_R - a) = (ac/c_R)(1 - c_R/c)$ increases rapidly as well (Sec. 2.16 in Ref. 13). The increasing value of $k(b_R - a)$ causes the evanescent leakage of radiation to decrease and the associated value of β_R decreases. For large *ka*, the value of c_R/c asymptotes to a fixed value and $b_R = ac/c_R \to 1.44a$. The value of $k(b_R - a) = 0.44ka$ now increases monotonically with *ka*. This decreases the amount of evanescent leakage of radiation from the sphere and the value of β_R. This differs significantly for the a_{0-} wave on steel spherical shell.[8] For that wave, the phase velocity asymptotically approaches the speed of sound in water, the caustic separation vanishes, and the coupling between the shell and water becomes very large. Following Felsen,[11,12] highly subsonic waves having small radiation damping are termed ''trapped,'' while waves that are only slightly subsonic are termed ''creeping.'' Unlike the a_{0-} wave, which makes a transition from trapped to creeping wave, the subsonic Rayleigh wave goes from being a trapped wave to a creeping wave and then back to a trapped wave. This behavior accounts for the *ka* dependence of β_R.

III. RAY APPROXIMATION WITH MATERIAL ABSORPTION

To modify the root calculation to incorporate material absorption, the complex wave numbers in Eq. (3) are used in Eq. (6c) and the roots are recalculated to yield c_R'/c and β_R'.

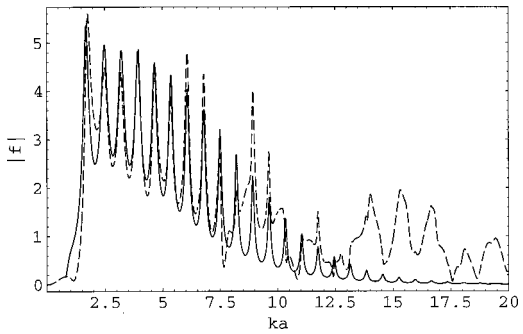

FIG. 6. The dashed curve gives $|f_{\text{sub}}|$, a background subtracted form function for a PMMA sphere. The solid curve gives the ray approximation $|f_R|$ for the Rayleigh wave using c_R'/c and β_R' as discussed in Sec. III. Both curves incorporate material absorption. The ray approximation using an approximate phase velocity and damping coefficient is not discernible from $|f_R|$ on the scale of this graph.

In Fig. 4, c_R'/c and c_R/c are both displayed, however, the two curves are indistinguishable at the scale of the graph. Material absorption has only a slight effect on the phase velocity, decreasing its value by a maximum of $\Delta(c_R/c) = 7.5 \times 10^{-4}$ at $ka = 2.6$. In Fig. 5, there is a significant change in the total damping parameter β_R' which reflects the combined damping due to radiation losses and due to material absorption. Comparing β_R' (long dashes) to β_R (solid line), for low *ka* the dominant mechanism is the radiation damping as expected since the material absorption is linear in frequency. As *ka* increases, the material absorption dominates the damping.

Care must be taken in the incorporation of c_R'/c and β_R' into the ray approximation for the backscattering form function. Recall that the coupling coefficient G_R depends on the radiation damping parameter β_R. This coefficient accounts for the degree of coupling between the acoustic fields and the Rayleigh waves on the sphere. It follows that even with material absorption, the coupling coefficient should be approximated by $|G_R| \approx 8\pi\beta_R c/c_R'$. In the rest of the expression for f_R, the remaining terms with β_R describe the exponential damping of the Rayleigh wave as it travels around the sphere. Since this damping is affected by the material absorption, it is reasonable to replace β_R by β_R' in the exponent in Eqs. (4) and (5).

The ray approximation $|f_R|$ using c_R'/c and β_R' is compared to a background-subtracted contribution $|f_{\text{sub}}|$ in Fig. 6. This contribution is calculated as $f_{\text{sub}} = f - f_{sp}$, where f_{sp} is the specular contribution to the form function. This is approximated by $f_{sp} = \Re \exp(-i2x)$, where $\Re = (\rho_e c_L - \rho c)/(\rho_e c_L + \rho c)$ is the unimodular reflection coefficient of a water–PMMA interface. The ray approximation describes the enhancement well for $ka < 7.5$ where other mechanisms such as whispering gallery modes begin to contribute to the backscattering. The agreement is remarkable at low *ka*: even as low as $ka = 1.5$ there is near agreement between the ray approximation and $|f_{\text{sub}}|$. A plausible explanation for this agreement is that the incident wave actually couples at a larger radius than the sphere itself due to the tunneling mechanism (Fig. 3). For example, the ratio of the caustic radius to sphere radius is $b_R/a = 1.53$ at $ka = 1.5$ and the fre-

quency of the incident wave normalized to the caustic radius becomes $kb_R = 2.29$.

The quality factors of the resonances can be determined from the decay rate of the echo amplitudes as done in Refs. 22 and 23. The mth echo can be expressed as $A_m \approx B \exp(-T\beta_R c_{gR}/c)$, where $T \equiv (ct-R)/a$, c_{gR} is the group velocity, and R is the source distance, and from this expression, $Q \approx ka/(2\beta_R c_{gR}/c)$. For the lowest resonance at $ka = 1.73$ which corresponds to the quadrupole $(n=2)$ partial wave, the quality factor was calculated to be $Q = 7.7$. This compares with the measured quality factor from Fig. 2 which was found to be $Q = \omega\tau/2 \approx 9.9$ where $1/\tau$ is the free decay rate. As expected the addition of material absorption has only a small affect on the lowest resonances where the difference in the calculated Q with and without material absorption is $\Delta Q = -0.51$. This difference increases significantly for the higher modes where the material absorption is the dominant dissipative mechanism.

The previous discussion of the structure of β'_R suggests that it may be possible to approximate β'_R by treating the material absorption as simply being additive to β_R. Straightforward numerical calculation yields the wave number for a fluid-loaded PMMA half-space with material absorption:[19] $k'_R = k_R(1 + i\gamma_R)$ where γ_R is the normalized damping parameter for the Rayleigh wave and $\gamma_R = 0.004\,19$ for the parameters given in Table I. Because Fig. 4 indicates that α'_R is negligibly different from α_R, we can use the approximation $\alpha'_R \approx \alpha_R$. Equation (6b) becomes

$$v'_{R(\text{approx})} \approx \alpha_R \left(1 + i\left(\frac{\beta_R}{\alpha_R} + \gamma_R \right) \right) \tag{7}$$

and, using Eq. (6a),

$$\alpha'_{R(\text{approx})} \approx \alpha_R, \tag{8a}$$

$$\beta'_{R(\text{approx})} \approx \beta_R + \gamma_R \left(\frac{x}{c_R/c} - \frac{1}{2} \right). \tag{8b}$$

In this approximation, $D_n(x)$ does not need to be modified by introducing complex wave numbers and a relatively simple numerical calculation is required to find γ_R. The result of this approximation is given as the short dashed line in Fig. 5. The approximate β'_R is slightly larger in the region where there is a transition from radiation to material loss.

When the parameters in Eqs. (8) are used to calculate the backscattering contribution $|f_{R(\text{approx})}|$, the resulting curve is barely distinguishable from the original ray prediction $|f_R|$ on the scale of Fig. 6 and the greatest error occurs at the resonances where material damping is most important. It appears that the approximations in Eq. (8) are useful for determining whether absorption effects will significantly modify form functions without doing a detailed analysis.

IV. EXPERIMENTAL RESULTS

To confirm the presence of the Rayleigh wave backscattering enhancement, the backscattering for different PMMA spheres were measured. For the PMMA sphere, the backscattering enhancement occurs near $ka \approx 1.73$ for the quadrupole term. The specular return and the echoes due to repeated circumnavigations are separated in time by only a few cycles making them difficult to measure individually, as can be seen in Fig. 2. The individual circumnavigations and the specular reflection typically appear as the staircasing of the tone burst at the beginning of the response.[3] This build-up to steady state was exploited by using sufficiently long tone bursts and by measuring the total response from which the form function could be extracted.

In this experiment two PMMA spheres were used. They were composed of solid, clear acrylic with no visible seam. The large sphere had a radius of $a = 25.4$ mm and was obtained from a juggling supply company. The smaller sphere had a radius of $a = 12.7$ mm and was obtained from Industrial Tectonics, Inc. Each of these spheres was attached to a length of fishing line via a small piece of kapton tape and lowered to depth of 121 cm. The experimental setup is very similar to that used by Gipson and Marston[24] with a different selection of transducers. Against one wall of the tank, a 10.16×10.16 cm 1–3 piezocomposite transducer built by Material Systems, Inc. was lowered to the same depth and aligned such that it ensonified the submerged sphere with 30 cycle tone bursts. The sphere and source were separated by a distance of 1.87 m. To measure the response of the sphere, an Edo spherical hydrophone was placed between the source and the PMMA sphere at a distance of 1.18 m from the sphere. The frequency range of interest for these spheres was 30–60 kHz and in this frequency range both the sphere and the hydrophone were in the far field of the source and sphere, respectively. For the large sphere, this frequency range corresponds to $ka = 3.2$–6.4 and for the small sphere this corresponds to $ka = 1.6$–3.2.

To obtain the normalized form function for each sphere, the following calibration procedure was used. The voltage response of the hydrophone was measured and recorded with the sphere in place. The sphere was removed and a background signal was then recorded and subtracted from the previous record to give the steady-state backscattered voltage amplitude V_{scat}. In order to normalize the response, the hydrophone was placed in the position of the sphere and the incident tone burst was recorded using the same source level for the scattering records. Since the resulting voltage amplitude V_{inc} is portional to the incident pressure, the normalized form function becomes $|f| = (V_{\text{scat}}/V_{\text{inc}})(2R/a)$, where $(2R/a) = 92.91$ and 185.82 for the large and small spheres, respectively. The results of this measurement are compared to the calculated form function in Fig. 7. The triangles are data points taken with the smaller sphere and the diamonds are points taken with the larger sphere over the frequency range discussed above. The measurements are in good agreement with the calculations presented earlier, however, in the frequency range used here, it is difficult to resolve the extent to which the material absorption of these spheres affects the backscattering at higher frequencies. This choice of frequencies was mitigated by several factors. The lower bound was determined primarily by the dimensions of the tank in which the experiment was performed. The upper bound was determined by the Rayleigh distance of the source and diffractive effects on the incident beam due to the hydrophone.

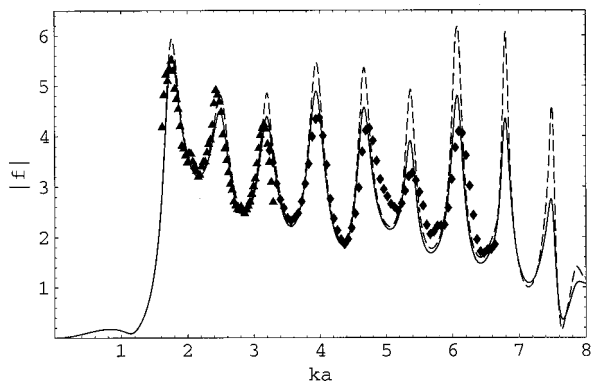

FIG. 7. The exact form function with material absorption (solid line) and without material absorption (dashed line) is compared to experimental data. The data are based on the normalization procedure discussed in Sec. IV. The triangles are data taken using a PMMA sphere with $a=1.27$ cm. The diamonds are data taken using a PMMA sphere with $a=2.54$ cm.

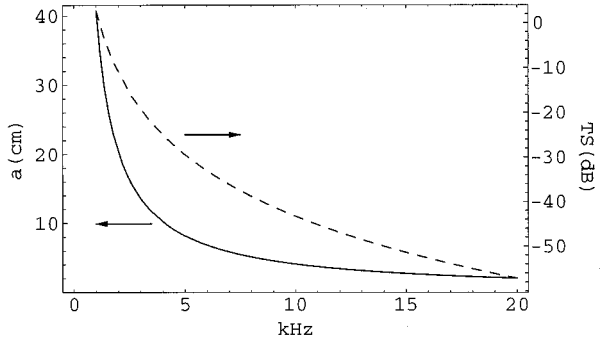

FIG. 8. Radius (solid line) and target strength (dashed line) as a function of frequency for a PMMA sphere in fresh water at the first Rayleigh resonance, $ka=1.73$.

V. DISCUSSION

These results indicate that a solid PMMA sphere exhibits a large, low frequency backscattering enhancement which was shown to be associated with tunneling to a subsonic Rayleigh wave. The enhancement is not removed by PMMA's material absorption. Although many of the features at higher frequencies are strongly affected by the attenuation, it is worth mentioning here some observations pertaining to the whispering gallery modes. It was noted earlier that the density of PMMA was very close to water ($\rho/\rho_e=0.839$) and this was seen to have a significant effect on the velocity of the Rayleigh wave. Studies of Lamb waves on plates have found that increased fluid-loading produces interactions between the various modes which can have a significant effect on the modal spectrum of the plate.[25,26] Calculations not presented here for the PMMA sphere have found similar interactions between whispering gallery waves and Stoneley waves that may be mediated by the density of the surrounding medium. The consequences of these interactions may not have as pronounced an effect on the backscattered response of the plastic spheres due to the high material absorption of these waves, however, this indicates that for low-density materials, some interesting features may be present.

As stated earlier, the presence of this backscattering enhancement may make PMMA spheres a potential candidate as passive sonar targets for situations where the narrow resonances may be used to advantage. To evaluate this possibility, the target strength[27] can be calculated for the largest resonance which occurs as at $ka=1.73$. The radius of the sphere at this particular value of ka is $a(\mathrm{m})=407/F(\mathrm{Hz})$, where F is the frequency for the parameters listed in Table I. The target strength can be written as

$$TS=20\log\left(|f|\frac{1.73c}{4\pi R_{\mathrm{ref}}F}\right), \tag{9}$$

where $R_{\mathrm{ref}}=1$ m is the reference distance, $c=1479$ m/s, and at the resonance $|f|=5.63$. The peak resonance value of $|f|$ does not depend on F because the normalized coefficients γ_L and γ_S in Eq. (3) are, to a good approximation, independent of F. This calculation is displayed in Fig. 8 as well as the radius of the PMMA sphere required for this frequency. For low frequencies, the target strength is substantial supporting the possibility of creating a simple target having an enhanced cross section. Certain other low-dissipation polymers[1,2,20] such as polysterene may also be useful for this application.

It is noteworthy that Hay and Schaafsma[28] previously observed ''giant resonances'' in the *attenuation of sound* in monodisperse suspensions of polystyrene spheres having $1<ka<6$. Our analysis of the effect of fluid loading on Rayleigh waves on polymers, Sec. II, indicates that these resonances are like those we have studied in backscattering. They are properly identified as associated with subsonic Rayleigh waves.

ACKNOWLEDGMENT

This work was supported by the Office of Naval Research.

[1] B. Hartmann and J. Jarzynski, ''Immersion apparatus for ultrasonic measurements in polymers,'' J. Acoust. Soc. Am. **56**, 1469–1477 (1974).
[2] B. Hartmann and J. Jarzynski, ''Ultrasonic hysteresis absorption in polymers,'' J. Acoust. Soc. Am. **43**, 4304–4312 (1972).
[3] W. E. Howell, S. K. Numrich, and H. Uberall, ''Complex-frequency poles of the acoustic scattering amplitude, and their ringing,'' IEEE Trans. Ultrason. Ferroelectr. Freq. Control **34**, 22–28 (1987).
[4] L. W. Anson and R. C. Chivers, ''Ultrasonic scattering from spherical shells including viscous and thermal effects,'' J. Acoust. Soc. Am. **93**, 1687–1699 (1993).
[5] R. H. Vogt, L. Flax, and W. G. Neubauer, ''Monostatic reflection of a plane wave from an absorbing sphere,'' J. Acoust. Soc. Am. **57**, 558–561 (1975).
[6] M. Talmant, H. Uberall, R. D. Miller, M. F. Werby, and J. W. Dickey, ''Lamb waves and fluid-borne waves on water-loaded, air-filled thin spherical shells,'' J. Acoust. Soc. Am. **86**, 278–289 (1989).
[7] G. S. Sammelmann, D. H. Trivett, and R. H. Hackman, ''The acoustic scattering by a submerged shell. I: The bifurcation of the dispersion curve for the antisymmetric Lamb wave,'' J. Acoust. Soc. Am. **85**, 114–124 (1989).
[8] L. G. Zhang, N. H. Sun, and P. L. Marston, ''Midfrequency enhancement of the backscattering of tone bursts by thin spherical shells,'' J. Acoust. Soc. Am. **91**, 1862–1874 (1992).
[9] P. L. Marston and N. H. Sun, ''Resonance and interference scattering near the coincidence frequency of a thin spherical shell: An approximate ray synthesis,'' J. Acoust. Soc. Am. **92**, 3315–3319 (1992).
[10] P. L. Marston and N. H. Sun, ''Backscattering near the coincidence frequency of a thin cylindrical shell: Surface wave properties from elastic theory and an approximate ray synthesis,'' J. Acoust. Soc. Am. **97**, 777–783 (1995).
[11] J. M. Ho and L. B. Felsen, ''Nonconventional traveling wave formulations and ray-acoustic reductions for source-excited fluid-loaded thin elastic

spherical shells,'' J. Acoust. Soc. Am. **88**, 2389–2414 (1990).
[12] L. B. Felsen, J. M. Ho, and I. T. Lu, ''Three-dimensional Green's function for fluid-loaded thin elastic cylindrical shell: Formulation and solution,'' J. Acoust. Soc. Am. **87**, 543–553 (1990).
[13] P. L. Marston, ''Geometrical and catastrophe optics methods in scattering,'' in *Physical Acoustics*, edited by A. D. Pierce and R. N. Thurston (Academic, New York, 1992), Vol. XXI, Chap. 1, pp. 1–234.
[14] G. Kaduchak and C. M. Loeffler, ''Relationship between material parameters and target strength of fluid-filled spherical shells in water: Calculations and observations,'' IEEE J. Oceanic Eng. **23**, 26–30 (1998).
[15] H. Boehme and J. E. Stockton, ''Alternate focusing fluids for passive acoustic targets,'' J. Acoust. Soc. Am. **88**, 2484–2485 (1990).
[16] G. C. Gaunaurd and H. Uberall, ''RST analysis of monostatic and bistatic acoustic echoes from an elastic sphere,'' J. Acoust. Soc. Am. **73**, 1–12 (1983).
[17] P. L. Marston, ''GTD for backscattering from elastic spheres and cylinders in water and the coupling of surface elastic waves with the acoustic field,'' J. Acoust. Soc. Am. **83**, 25–37 (1988).
[18] K. L. Williams and P. L. Marston, ''Synthesis of backscattering from an elastic sphere using the Sommerfeld–Watson transformation and giving a Fabry–Perot analysis of resonances,'' J. Acoust. Soc. Am. **79**, 1702–1708 (1986).
[19] H. Uberall, ''Surface waves in acoustics,'' in *Physical Acoustics*, edited by W. P. Mason and R. N. Thurston (Academic, New York, 1973), Vol. X, Chap. 1, pp. 1–60; I. A. Viktorov, *Rayleigh and Lamb Waves* (Plenum, New York, 1967), pp. 25–29, 46–57.
[20] F. Padilla, M. de Billy, and G. Quentin, ''Theoretical and experimental studies of surface waves on solid-fluid interfaces when the value of the fluid sound velocity is located between the shear and the longitudinal ones in the solid,'' J. Acoust. Soc. Am. **106**, 666–673 (1999).
[21] S. N. Guzhev, ''Study of phase velocity and energy distribution of Stoneley waves at a solid–liquid interface,'' J. Acoust. Soc. Am. **95**, 661–667 (1994).
[22] L. R. Dragonette, D. M. Drumheller, C. F. Gaumond, D. H. Hughes, B. T. O'Conner, N. Yen, and T. J. Yoder, ''The application of two-dimensional signal transformations to the analysis and synthesis of structural excitations observed in acoustical scattering,'' Proc. IEEE **84**, 1249–1263 (1996).
[23] D. H. Hughes, ''Backscattering of sound by spherical shells in water,'' Ph.D. dissertation, Washington State University, Department of Physics (1998).
[24] K. Gipson and P. L. Marston, ''Backscattering enhancements due to retroreflection of ultrasonic leaky Rayleigh waves at corners of solid elastic cubes in water,'' J. Acoust. Soc. Am. **105**, 700–710 (1999).
[25] S. I. Rokhlin, D. E. Chimenti, and A. H. Nayfeh, ''On the topology of the complex wave spectrum in a fluid-cooled elastic layer,'' J. Acoust. Soc. Am. **85**, 1074–1080 (1989).
[26] A. Freedman, ''Effects of fluid-loading on Lamb mode spectra,'' J. Acoust. Soc. Am. **99**, 3488–3496 (1996).
[27] A. D. Pierce, *Acoustics: An Introduction to its Physical Principles and Applications* (Acoustical Society of America, New York, 1991), pp. 428–429.
[28] A. E. Hay and A. S. Shaafsma, ''Resonance scattering in suspensions,'' J. Acoust. Soc. Am. **85**, 1124–1138 (1989).

A mapping approach for handling sloping interfaces

Michael D. Collins and Dalcio K. Dacol
Naval Research Laboratory, Washington, D.C. 20375

(Received 17 June 1999; accepted for publication 21 December 1999)

A mapping approach for handling sloping interfaces in parabolic equation solutions is developed and tested. At each range, the medium is rigidly translated vertically so that a sloping interface becomes horizontal. To simplify the approach, the slope is assumed to be small and the extra terms that arise in the wave equation under the mapping are neglected. The effects of these terms can be approximately accounted for by applying a leading-order correction to the phase. The mapping introduces variations in topography, which are relatively easy to handle for the case of a pressure-release boundary condition. The accuracy of the approach is demonstrated for problems involving fluid sediments. The approach should also be accurate for problems involving elastic sediments and should be useful for solving three-dimensional problems involving variable topography. © *2000 Acoustical Society of America.* [S0001-4966(00)00204-6]

PACS numbers: 43.30.Bp, 43.30.Ma [SAC-B]

INTRODUCTION

Parabolic equation techniques are useful for solving range-dependent wave propagation problems.[1] They are based on factoring and approximating operators to obtain one-way wave equations that handle outgoing energy accurately and efficiently. The development of parabolic equation techniques has been an active area since the early 1970s. Many of the key issues have been resolved for acoustics problems.[2–8] There has also been progress on the elastic case,[9–14] but significant limitations in accuracy still exist for some range-dependent problems. In this paper, we present a mapping approach that can be used to obtain accurate parabolic equation solutions for problems in involving sloping interfaces between fluid and elastic layers.

Coordinate mappings can be used to simplify problems involving variable boundaries and interfaces. For example, conformal mappings have proved to be useful for handling rough ocean surfaces.[15,16] Some mappings trade off complicated geometry for additional terms in the wave equation, which may be difficult to handle. We consider a vertical translation of the medium at each range, which has been applied to problems involving rough surfaces.[17] To simplify the approach, we assume that slopes are small and either discard or approximate the additional terms in the wave equation. In Sec. I, we describe the mapping solution and confirm its accuracy for problems involving fluid layers. In Sec. II, we describe a correction to the mapping solution. In Sec. III, we apply the mapping approach to problems involving fluid and elastic layers. In Sec. IV, we apply the mapping solution to problems involving variable topography.

I. THE MAPPING SOLUTION

In this section, we describe the mapping solution and confirm its accuracy for problems involving fluid layers. We obtain reference solutions using an energy-conserving parabolic equation model.[5] We work in cylindrical coordinates, where the range r is the horizontal distance from a source, z is the depth, and θ is the azimuth. We apply the uncoupled azimuth approximation[18] to reduce to two dimensions and work with the far-field wave equation,

$$\frac{\partial^2 \psi}{\partial r^2} + \frac{\partial^2 \psi}{\partial z^2} + k^2 \psi = 0, \tag{1}$$

$$[\psi] = \left[\frac{1}{\rho} \frac{\partial \psi}{\partial n} \right] = 0, \tag{2}$$

where $p = r^{-1/2}\psi$ is the complex pressure, $k = \omega/c$ is the wave number, ω is the circular frequency, c is the sound speed, ρ is the density, $\partial/\partial n$ is the normal derivative, and the bracket notation indicates quantities that are continuous across an interface at $z = d(r)$. The pressure-release boundary condition $\psi = 0$ applies at $z = 0$.

We assume that the slope of the interface is small and apply the change of variables,

$$\begin{pmatrix} \tilde{r} \\ \tilde{z} \end{pmatrix} = \begin{pmatrix} r \\ z - d(r) \end{pmatrix}, \tag{3}$$

where $\tilde{r}$ and $\tilde{z}$ are the mapped coordinates. This mapping replaces a sloping interface with a sloping surface, which is easier to handle since the pressure-release condition is nondirectional.[19] We neglect terms involving the slope to obtain

$$\frac{\partial^2 \psi}{\partial \tilde{r}^2} + \frac{\partial^2 \psi}{\partial \tilde{z}^2} + k^2 \psi = 0, \tag{4}$$

$$[\psi] = \left[\frac{1}{\rho} \frac{\partial \psi}{\partial \tilde{z}} \right] = 0. \tag{5}$$

The combination of the mapping and the neglect of slope terms is equivalent to physically distorting the waveguide, which conserves energy. The adiabatic mode solution[20] is invariant under this distortion since it involves rigid vertical translations.

Example A illustrates that the mapping solution is superior to the adiabatic mode solution since it accounts for mode coupling. This mode cutoff problem[21] involves a

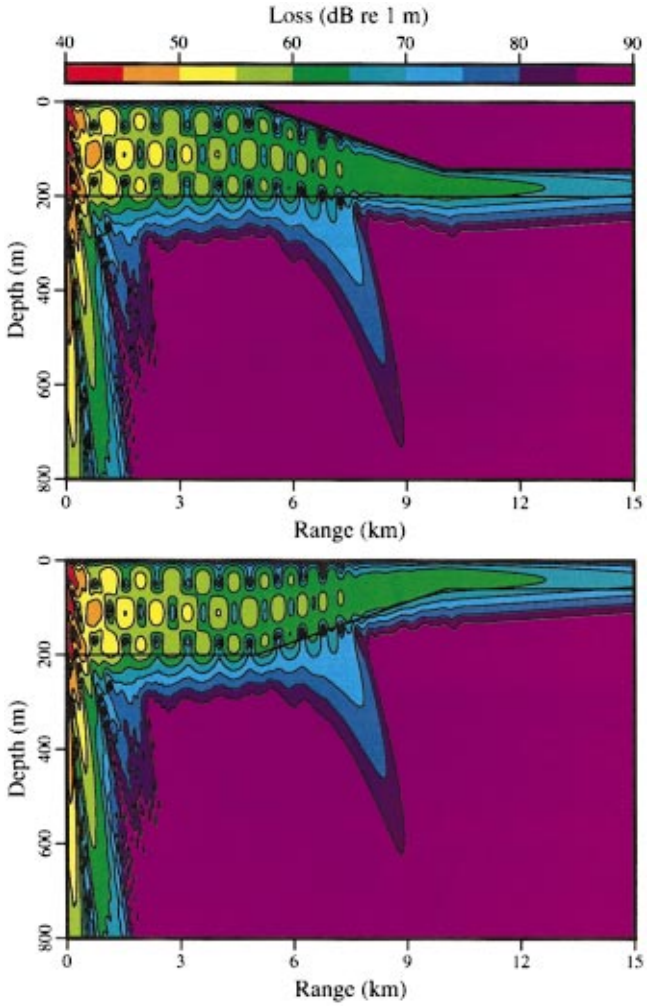

FIG. 1. Transmission loss for example A, which involves a 25-Hz source and a mode cutoff in an ocean with a sloping bottom. The mapping solution is obtained by first solving the problem in mapped coordinates (top image), where the ocean bottom is horizontal. This solution is then mapped back to the original coordinates to obtain a solution to the original problem (bottom image).

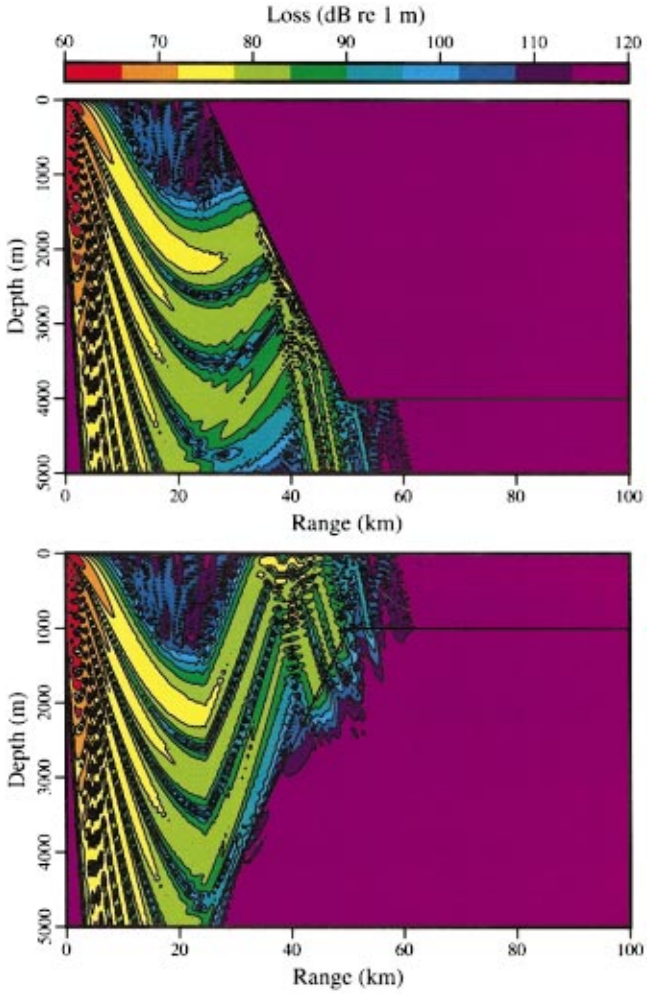

FIG. 2. Transmission loss for example B, which involves a 25-Hz source and the reflection of Lloyd's mirror beams from a sloping bottom. The mapping solution is obtained by first solving the problem in mapped coordinates (top image), where the ocean bottom is horizontal. This solution is then mapped back to the original coordinates to obtain a solution to the original problem (lower image). The beams are smooth in the mapped coordinates. When the solution is mapped back to the original coordinates, sharp bends are erroneously introduced into the beams at $r=25$ km.

25-Hz source at $z=112$ m. The bathymetry is 200 m for $r<5$ km, 60 m for $r>10$ km, and linearly sloping for 5 km $<r<10$ km. The sound speed is 1500 m/s in the water column. In the sediment, the sound speed is 1704.5 m/s, the density is 1.15 g/cm^3, and the attenuation is 0.5 dB/λ. The mapping solution appearing in Fig. 1 is in agreement with the reference solution (which is not shown). In particular, the mapping solution accurately handles the beam in the sediment, which corresponds to the release of energy from the third mode at cutoff. The adiabatic mode solution does not handle this feature properly.[22]

II. A LEADING-ORDER CORRECTION

In this section, we describe a correction to the mapping solution. Example B illustrates that the correction is required for some problems. This deep water problem involves a 25-Hz source at $z=400$ m and the canonical sound speed profile,[23]

$$c(z)=c_*\left(1+\alpha\left(\frac{z-z_*}{H}+\exp\left(\frac{z-z_*}{H}\right)-1\right)\right), \tag{6}$$

where $c_*=1500$ m/s, $H=600$ m, $z_*=1000$ m, and $\alpha=0.007$. The bathymetry is 5 km for $r<25$ km, 1 km for $r>50$ km, and linearly sloping for 25 km$<r<$50 km. In the sediment, the sound speed is 1550 m/s, the density is 1.15 g/cm^3, and the attenuation is 0.5 dB/λ. The mapping solution appearing in Fig. 2 contains sharp bends in the Lloyd's mirror beams at $r=25$ km, which are artifacts of neglecting the additional terms that arise in going from Eqs. (1) and (2) to Eqs. (4) and (5). The beams are smooth in the plot of the solution in mapped coordinates appearing in Fig. 2. The bends are introduced when the solution is mapped back to the original coordinates.

The error associated with the bends can be reduced by approximately introducing equal but opposite bends with the leading-order correction,

$$\psi(\tilde{r},\tilde{z})\rightarrow\exp(-ik_0\tilde{z}\,\sin\,\delta)\psi(\tilde{r},\tilde{z}), \tag{7}$$

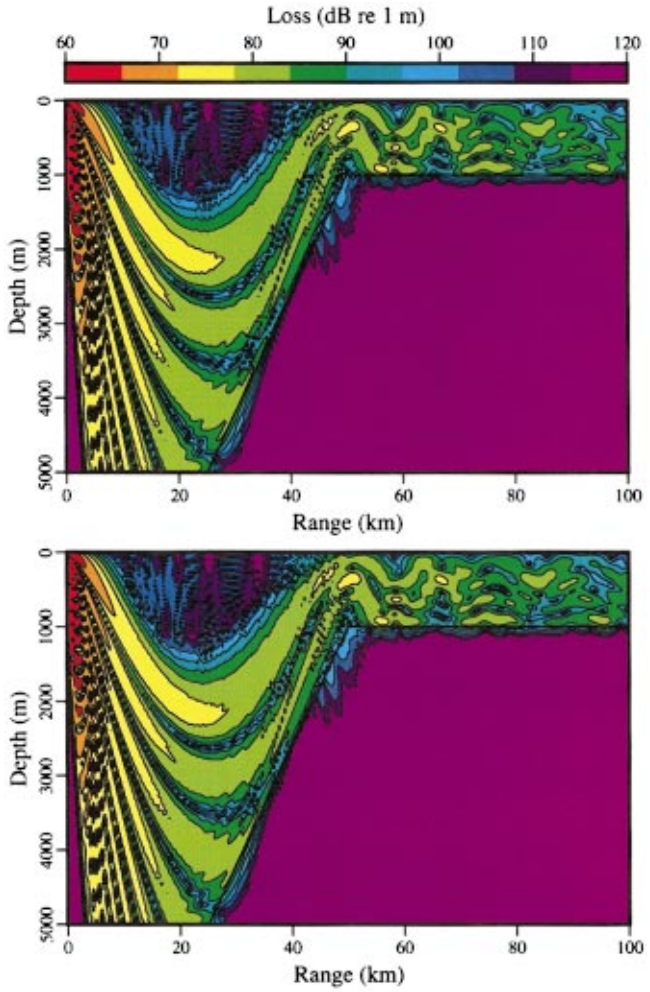

FIG. 3. Transmission loss for example B, which involves a 25-Hz source and the reflection of Lloyd's mirror beams from a sloping bottom. The corrected mapping solution (top image) is in agreement with the reference solution (lower image).

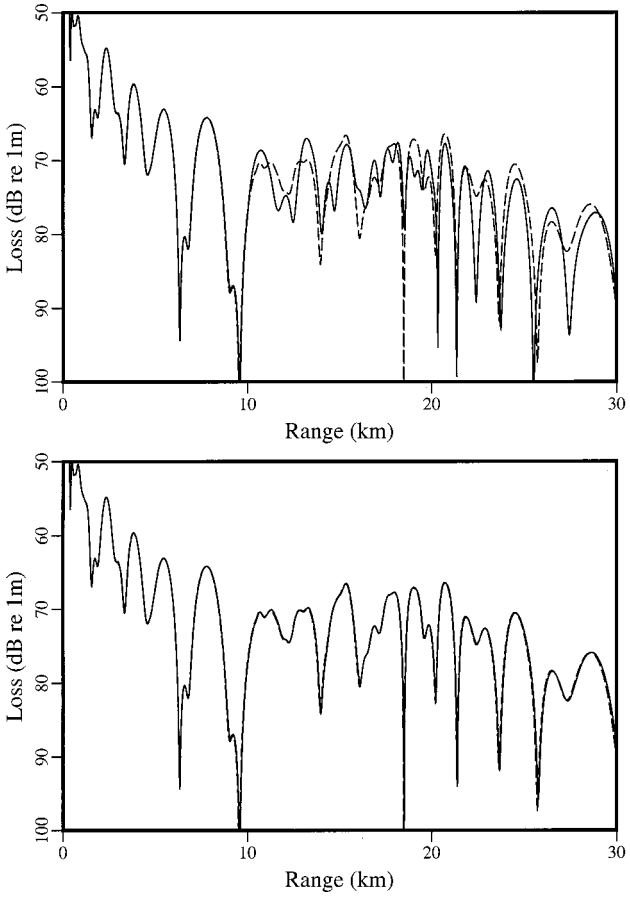

FIG. 4. Transmission loss at $z=30$ m for example C, which involves a 25-Hz source in shallow water and changes in the slope of the ocean bottom at $r=10$ and $r=20$ km. In the top frame, the uncorrected mapping solution (solid curve) is in agreement with the reference solution (dashed curve) for $r<10$ km. In the bottom frame, the corrected mapping solution (solid curve) is in agreement with the reference solution (dashed curve) for all ranges.

each time the slope changes, where $k_0=\omega/c_0$ is a representative wave number, c_0 is a representative wave speed, and δ is the change in slope. We take $c_0=1500$ m/s for each of the examples. Since the waveguide distortion conserves energy, the leading-order correction in Eq. (7) only affects the phase. In contrast, the leading-order energy-conservation correction in Eq. (19) of Ref. 13 only affects the amplitude since phase is handled properly by the higher-order parabolic equation. Based on the analogy between these corrections, we would expect the leading-order phase correction to provide accurate solutions for many problems since the leading-order amplitude correction provides accurate solutions for many problems. The corrected solution appearing in Fig. 3 does not contain the sharp bends and is in agreement with the reference solution.

Example C quantitatively illustrates the accuracy of the corrected mapping solution. This problem involves a 25-Hz source at $z=100$ m. The bathymetry is 200 m at $r=0$ and $r=20$ km, 40 m at $r=10$ km and $r=30$ km, and linear between these points. The sound speed is 1500 m/s in the water column. In the sediment, the sound speed is 1700 m/s, the density is 1.5 g/cm^3, and the attenuation is 0.5 dB/λ. Parabolic equation solutions appear in Fig. 4. The corrected mapping solution is in agreement with the reference solution. The uncorrected mapping solution is accurate for $r<10$ km but breaks down for $r>10$ km.

The mapping solution is related to the rotated parabolic equation solution,[24] which involves a rotated coordinate system in which the range parallels the interface. Although coordinate rotations do not give rise to additional terms in the wave equation, handling changes in slope is relatively complicated with the rotated parabolic equation. At a transition between regions of constant slope, the incident field at the end of the old region must be rotated to obtain the transmitted field at the beginning of the new region. Rotating using the local approximation,

$$\psi(r+\Delta r,z)\cong\exp(ik_0\Delta r)\psi(r,z), \tag{8}$$

is analogous to using the correction in Eq. (7). It should be possible to achieve improved accuracy by interpolating and extrapolating the incident field.

III. SLOPING FLUID–SOLID INTERFACES

The mapping solution, including the correction in Eq. (7), can be applied to problems involving elastic bottoms. Examples D and E involve a 10-Hz source at $z=390$ m. The bathymetry is 400 m for $r<4$ km, 100 m at $r=10$ km, and

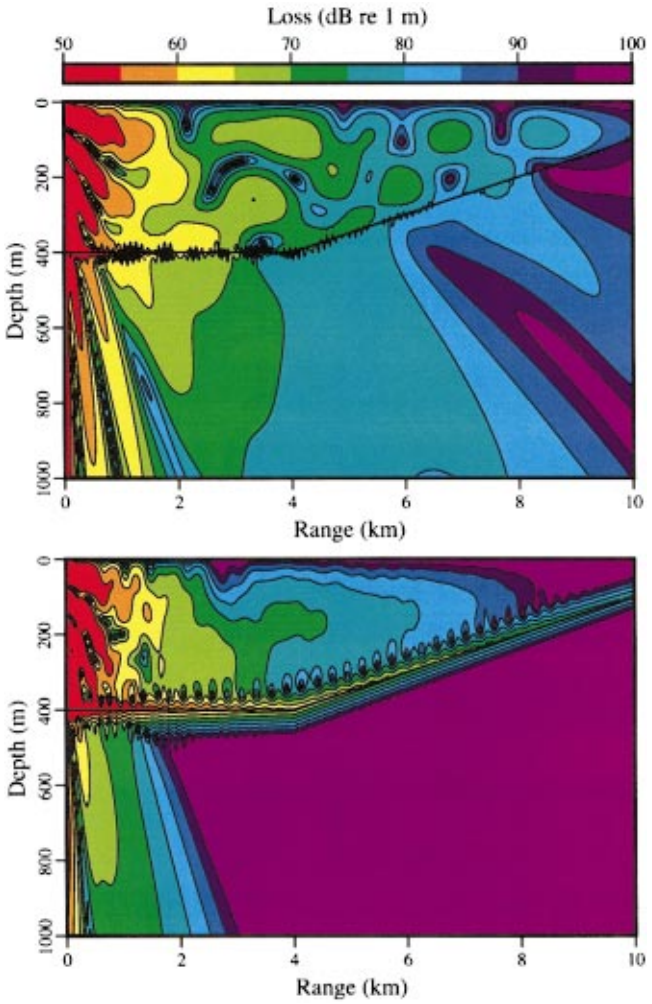

FIG. 5. Compressional wave transmission loss for examples D and E, which involve a 10-Hz source in shallow water and an elastic sediment. The compressional and shear wave speeds are 1700 and 800 m/s for example D (top) and 2400 and 1200 m/s for example E (bottom).

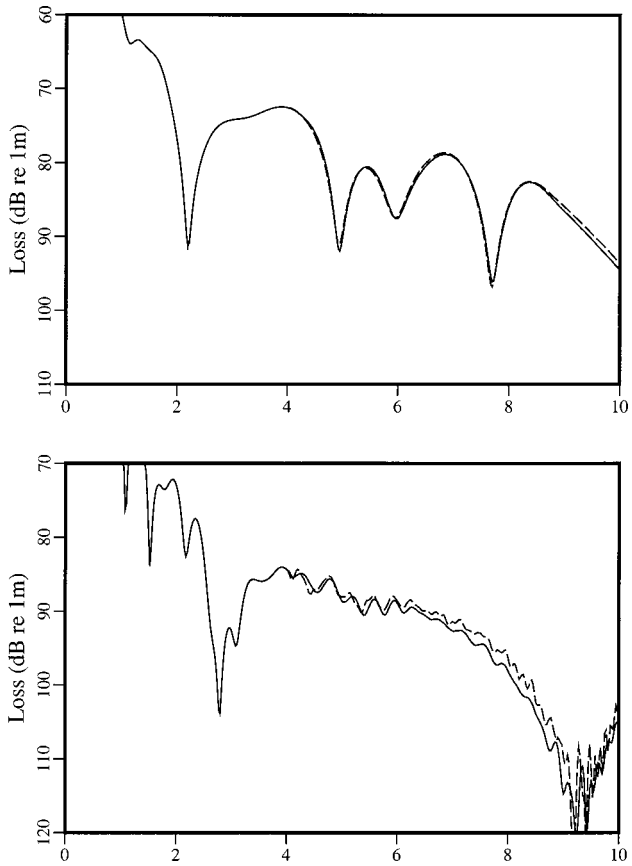

FIG. 6. Transmission loss at $z=30$ m for examples D and E, which involve a 10-Hz source in shallow water and an elastic sediment. Comparison of corrected mapping solutions (solid curves) and solutions that approximately conserve energy (dashed curves). The compressional and shear wave speeds are 1700 and 800 m/s for example D (top) and 2400 and 1200 m/s for example E (bottom).

linearly sloping for 4 km$<r<$10 km. The sound speed is 1500 m/s in the water column. In the sediment, the density is 1.5 g/cm^3, the compressional attenuation is 0.1 dB/λ, and the shear attenuation is 0.2 dB/λ. For example D, the compressional speed is 1700 m/s and the shear speed is 800 m/s. For example E, the compressional speed is 2400 m/s and the shear speed is 1200 m/s. We solve these problems using the correction in Eq. (7). We compare the corrected mapping solution with an elastic parabolic equation solution that approximately conserves energy.[13]

Results for examples D and E appear in Figs. 5 and 6. Energy from the water column couples into compressional waves in the bottom at all ranges for example D but only at short ranges for example E. The interface wave is strong for example E but weak for example D. The differences between the transmission loss curves corresponding to the corrected mapping solution and the energy-conserving solution are relatively small for example D but relatively large for example E. This is consistent with the results in Fig. 1 of Ref. 13, which indicate that the errors in the energy-conserving solution are relatively small for wave speeds of 1700 and 800 m/s and relatively large for wave speeds of 2400 and 1200 m/s.

IV. VARIABLE TOPOGRAPHY

An effective approach for solving two-dimensional problems involving variable topography is to allow the location of the boundary of the computational grid to depend on range.[19] It would be relatively complicated and inefficient to apply this approach to three-dimensional problems. The azimuthal step of the splitting solution of the three-dimensional parabolic equation involves the equation,[25,26]

$$\frac{\partial \psi}{\partial r} = \frac{i}{2k_0 r^2} \frac{\partial^2 \psi}{\partial \theta^2}, \tag{9}$$

which must be solved over azimuth for each depth grid point at each range step. If the topography is relatively complicated, the domain of Eq. (9) is a circle at fixed range and depth that may pass through the surface several times. At each crossing point, the pressure-release boundary condition must be incorporated into the matrix that discretizes the operator on the right side of Eq. (9). The decomposition of this matrix must be repeated each time the locations of the crossing points change, which may occur many times at each range. Greater simplicity and efficiency can be achieved by mapping the surface to a horizontal plane. With this ap-

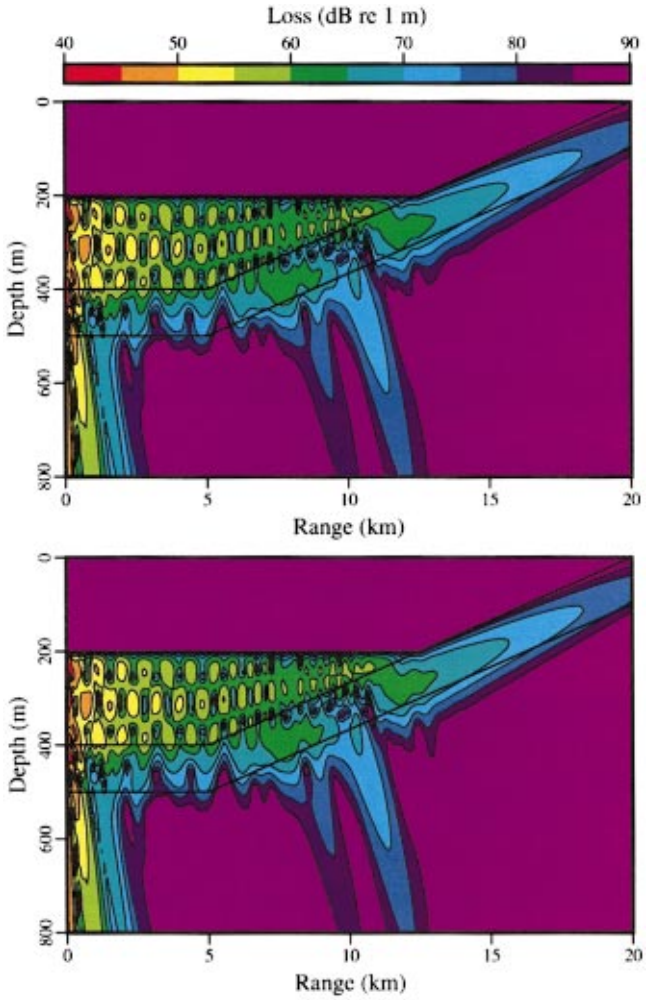

FIG. 7. Transmission loss for example F, which involves a 25-Hz source, variable topography, a sediment layer, and a basement. The mapping solution (top), which was obtained by applying a translation that flattens the ocean surface, is in agreement with the reference solution (bottom).

proach, there is no need for boundary conditions in Eq. (9) and the decomposition only has to be performed once at each range.

Example F involves a 25-Hz source at $z=112$ m in an ocean that is 200-m deep for $r<5$ km and linearly sloping to a beach at $r=12.5$ km. Beyond the beach, the topography increases with the same slope as the ocean bottom to 200 m above sea level at $r=20$ km. The ocean bottom consists of a 100-m-thick layer that parallels the ocean bottom in which the sound speed is 1704.5 m/s, the density is 1.15 g/cm^3, and the attenuation is 0.1 dB/λ. In the basement half space, the sound speed is 1850 m/s, the density is 1.5 g/cm^3, and the attenuation is 0.25 dB/λ. Results for example F appear in Fig. 7. The mapping solution is in agreement with the reference solution, which was obtained using the approach described in Ref. 19.

V. CONCLUSION

A mapping approach has been developed for solving problems involving sloping interfaces. At each range, the medium is mapped vertically so that a sloping interface becomes horizontal. Additional terms that arise in the wave equation are neglected to simplify the approach. A leading-order correction can be applied to approximately account for the effects of these terms. Since the mapping conserves energy, the correction term only affects the phase. The accuracy of the mapping solution was demonstrated for problems involving fluid sediments. The approach was also applied to problems involving elastic sediments and to a problem involving variable topography.

ACKNOWLEDGMENT

This work was supported by the Office of Naval Research.

[1] F. B. Jensen, W. A. Kuperman, M. B. Porter, and H. Schmidt, *Computational Ocean Acoustics* (American Institute of Physics, New York, 1994), pp. 343–412.
[2] A. Bamberger, B. Engquist, L. Halpern, and P. Joly, ''Higher order paraxial wave equation approximations in heterogeneous media,'' SIAM (Soc. Ind. Appl. Math.) J. Appl. Math. **48**, 129–154 (1988).
[3] M. D. Collins, ''Applications and time-domain solution of higher-order parabolic equations in underwater acoustics,'' J. Acoust. Soc. Am. **86**, 1097–1102 (1989).
[4] M. B. Porter, F. B. Jensen, and C. M. Ferla, ''The problem of energy conservation in one-way models,'' J. Acoust. Soc. Am. **89**, 1058–1067 (1991).
[5] M. D. Collins and E. K. Westwood, ''A higher-order energy-conserving parabolic equation for range-dependent ocean depth, sound speed, and density,'' J. Acoust. Soc. Am. **89**, 1068–1075 (1991).
[6] M. D. Collins, ''A self-starter for the parabolic equation method,'' J. Acoust. Soc. Am. **92**, 2069–2074 (1992).
[7] M. D. Collins, ''The stabilized self-starter,'' J. Acoust. Soc. Am. **106**, 1724–1726 (1999).
[8] M. D. Collins, ''A split-step Padé solution for the parabolic equation method,'' J. Acoust. Soc. Am. **93**, 1736–1742 (1993).
[9] R. R. Greene, ''A high-angle one-way wave equation for seismic wave propagation along rough and sloping interfaces,'' J. Acoust. Soc. Am. **77**, 1991–1998 (1985).
[10] M. D. Collins, ''A higher-order parabolic equation for wave propagation in an ocean overlying an elastic bottom,'' J. Acoust. Soc. Am. **86**, 1459–1464 (1989).
[11] B. T. R. Wetton and G. H. Brooke, ''One-way wave equations for seismoacoustic propagation in elastic waveguides,'' J. Acoust. Soc. Am. **87**, 624–632 (1990).
[12] M. D. Collins, ''Higher-order parabolic approximations for accurate and stable elastic parabolic equations with application to interface wave propagation,'' J. Acoust. Soc. Am. **89**, 1050–1057 (1991).
[13] M. D. Collins, ''An energy-conserving parabolic equation for elastic media,'' J. Acoust. Soc. Am. **94**, 975–982 (1993).
[14] M. D. Collins and W. L. Siegmann, ''A complete energy-conservation correction for the elastic parabolic equation,'' J. Acoust. Soc. Am. **95**, 2907 (A) (1994).
[15] L. B. Dozier, ''PERUSE: A numerical treatment of rough surface scattering for the parabolic equation,'' J. Acoust. Soc. Am. **75**, 1415–1432 (1984).
[16] G. V. Norton, J. C. Novarini, and R. S. Keiffer, ''Coupling scattering from the sea surface to a one-way marching propagation model via conformal mapping: Validation,'' J. Acoust. Soc. Am. **97**, 2173–2180 (1995).
[17] R. B. Evans, ''The flattened surface parabolic equation,'' J. Acoust. Soc. Am. **104**, 2167–2173 (1998).
[18] J. S. Perkins and R. N. Baer, ''An approximation to the three-dimensional parabolic-equation method for acoustic propagation,'' J. Acoust. Soc. Am. **72**, 515–522 (1982).
[19] M. D. Collins, R. A. Coury, and W. L. Siegmann, ''Beach acoustics,'' J. Acoust. Soc. Am. **97**, 2767–2770 (1995).
[20] A. D. Pierce, ''Extension of the method of normal modes to sound propagation in an almost-stratified medium,'' J. Acoust. Soc. Am. **37**, 19–27 (1965).
[21] F. B. Jensen and W. A. Kuperman, ''Sound propagation in a wedge-shaped ocean with a penetrable bottom,'' J. Acoust. Soc. Am. **67**, 1564–1566 (1980).

[22] A. T. Abawi, W. A. Kuperman, and M. D. Collins, ''The coupled mode parabolic equation,'' J. Acoust. Soc. Am. **102**, 233–238 (1997).
[23] W. H. Munk, ''Sound channel in an exponentially stratified ocean with applications to SOFAR,'' J. Acoust. Soc. Am. **55**, 220–226 (1974).
[24] M. D. Collins, ''The rotated parabolic equation and sloping interfaces,'' J. Acoust. Soc. Am. **87**, 1035–1037 (1990).
[25] M. D. Collins and S. A. Chin-Bing, ''A three-dimensional parabolic equation model that includes the effects of rough boundaries,'' J. Acoust. Soc. Am. **87**, 1104–1109 (1990).
[26] D. Lee, G. Botseas, and W. L. Siegmann, ''Examination of three-dimensional effects using a propagation model with azimuth-coupling capability (FOR3D),'' J. Acoust. Soc. Am. **91**, 3192–3202 (1992).

Environmentally adaptive wedge modes

Peter C. Mignerey
Acoustics Division 7120, Naval Research Laboratory, Washington, D.C. 20375-5350

(Received 2 September 1998; revised 9 December 1999; accepted 22 December 1999)

The notion of environmentally adaptive, curvilinear, uncoupled normal modes is developed by writing the Helmholtz equation in curvilinear coordinates. The depth-dependent vertical scaling function provides some coordinate freedom missing from the Cartesian formulation. This freedom permits adaptation of the normal mode approach to variable depth and variable sound-speed problems for environments that change slowly in range. A W.K.B. approximation to the eigenfunctions shows modal decoupling can be realized when the vertical scaling function is chosen equal to the reciprocal of the depth-dependent vertical wave number of the lowest mode. Numerical simulations demonstrate that a requirement for constant inter-modal ratios of the vertical wave number is valid throughout several wedges with different bottom boundary conditions. The horizontal refraction of such modes agrees closely with analytic solutions. For a wide-angle wedge, the acoustic field agrees qualitatively well with the benchmark solution of Dean and Buckingham [J. Acoust. Soc. Am. **93**, 1319–1328 (1993)]. [S0001-4966(00)02804-6]

PACS numbers: 43.30.Bp [SAC-B]

INTRODUCTION

The development of efficient three-dimensional acoustic-propagation models suitable for the accurate computation of acoustic fields throughout large regions of realistic ocean environments remains elusive. Such environments with nontrivial bottom topography and complicated sound-speed profiles exhibit three-dimensional effects which are poorly described by either sophisticated two-dimensional models or idealized three-dimensional models. One well known approach to three-dimensional propagation is through the use of independently propagating normal modes (adiabatic modes) as an expansion basis for the acoustic field. In the current paper a geometric approach is used to advance adiabatic mode theory by formulating the mode coupling equations in environmentally adaptive curvilinear coordinates.

The notion that acoustic energy may be effectively described by a superposition of normal modes was first explored in detail by Pekeris.[1] Williams and Lewis[2] then extended the Pekeris solutions to the case of slowly varying water depth. By interpreting ray invariants with respect to normal modes, Weston[3] concluded that nondegenerate modes conserve energy in slowly changing, stratified environments. Pierce[4] derived mode-coupling equations by separating the horizontal coordinates from the vertical. Eby *et al.*[5] did a tank experiment that verified the Pekeris model. When the bottom slope was varied the modes were found to adapt to the changing water depth.

Graves *et al.*[6] explored the approximations necessary for mode separation in environments with gradual, range-dependant boundaries. Rutherford and Hawker[7,8] demonstrated that nonhorizontal interfaces induce nonconservation of energy in coupled mode theory. Fawcett[9] determined the contribution of sloped-interface boundary terms to the mode-coupling equations. Godin[10] derived the mode-coupling equations for sloping interfaces based on the reciprocity principle.

Weston[3,11] demonstrated that normal modes propagate with a phase velocity varying as a function of horizontal position. Pierce[4] and Weinberg and Burridge[12] derived ray equations for the horizontal refraction of normal modes. Doolittle *et al.*[13] presented data showing slope-induced horizontal refraction on the continental slope of Australia. Hall and Irving[14] applied adiabatic normal modes to the analysis of horizontal refraction of acoustic energy propagating through an ocean eddy.

As demonstrated by Pierce,[4] adiabatic modes ignore the continuous spectrum and therefore cannot model the cutoff region. Jensen and Kuperman[15] used a PE model to show how modes propagating up-slope past the cutoff depth transfer energy into the continuous spectrum via beams that turn downward into the bottom. Pierce[16] described this process analytically using Airy's functions. These results were subsequently verified by several other investigators.[17–21]

For the same reason adiabatic modes cannot model mode capturing. Tindle and Deane[22] showed how the continuous spectrum contributes to the acoustic field propagating down-slope by leaking energy into higher order modes. Using a PE model, Jensen and Tindle[23] observed down-slope mode capturing for cases where there were no trapped modes at the source. From a ray-theoretic perspective, Westwood[24] determined that mode capturing is caused by rays that are partially reflected within the evanescent-wave region where high-order source modes are nonpropagating.

For isovelocity linear wedge problems, modes with cylindrical wavefronts centered on the wedge apex arise naturally from physical interactions with the bottom. Using a PE model, Jensen and Tindle[23] demonstrated that wedge modes propagate adiabatically both up-slope and down-slope while local Cartesian modes showed clear evidence of coupling. Tindle *et al.*[25,26] did a down-slope tank experiment in which curved modes centered on the wedge apex were found to

propagate without coupling. Hobaek and Westwood[27] did an up-slope experiment in a penetrable wedge using a point source. Even though the source excited a spherical wavefront centered on the source location, the field at the receiver was found to be consistent with wedge modes centered on the wedge apex.

Cylindrical coordinates were used in the image solution of Bradley[28] and modal solutions of Buckingham.[29–31] However, coupling between wedge modes was found to be significant for realistic sound-speed profiles in the cylindrical wedge-mode model developed by Primack and Gilbert.[32] Harrison[33] generalized the notion of wedge modes by using conformal mapping to obtain curvilinear coordinate systems that follow the bottom. Separable solutions were then found in the curvilinear system. Solutions of this form are valid when the radius of curvature of the bottom is large compared to the water depth. More recently, Galanenko[34] employed two-dimensional orthogonal curvilinear coordinates in a coupled mode solution to the problem of elastic propagation in a slowly varying layered waveguide.

Unfortunately, conformal mapping does not extend to three dimensions where only a few well-known orthogonal coordinate systems exist. Thus it is necessary to find a nearly orthogonal coordinate system that separates an approximate Helmholtz equation for realistic propagation problems. Desaubies and Dysthe[35] demonstrated the existence of such coordinate systems by establishing a geometric equivalence between the phase of an intrinsic mode with phase deviations induced by coordinate curvature.

Extensive effort has gone into the development of three-dimensional isovelocity linear wedge models by Buckingham,[29,31] Dean and Buckingham,[36] and Westwood[24] for the purposes of physical understanding and providing benchmarks.[37] Kuperman *et al.*[38] developed their WRAP model using adiabatic normal modes with forward coupling. Horizontal refraction was ignored by assuming an Nx2D approximation. Three-dimensional parabolic equation models developed by Collins[39] and Lee[40] include horizontal refraction.

In this paper the coupled mode theory of Pierce[4] is revisited in a curvilinear coordinate system. The acoustic wavelength is assumed to be commensurate with the water depth but short compared to the horizontal extent of the problem. Under these conditions, vertical modes are expected to propagate independently along characteristic curves in the horizontal plane. For environments that do not vary too rapidly in the horizontal direction, the coupling of energy between modes can be minimized with the proper choice of a curvilinear coordinate system. Nearly orthogonal coordinate systems are obtained from the vertical wave number of a reference mode such that coordinate surfaces are conformal to physical interfaces. The lowest mode is chosen as the reference because it propagates where the higher modes are evanescent. The horizontal-refraction problem is solved using Gaussian-beam ray-tracing[41–43] to obtain solutions valid across caustics and inside evanescent-wave regions. No attempt is made to model the deposition of energy into the bottom as modes pass the critical depth and downslope mode capturing is also ignored.

The remainder of this paper is organized as follows. Section I covers the mathematical basis of curvilinear adiabatic normal modes. The Helmholtz equation is written in curvilinear coordinates and the vertical scale factor is seen to provide an extra degree of freedom missing from the Cartesian formulation. An eigenvalue problem is posed in curvilinear coordinates and mode coupling shown to vanish when horizontal derivatives of the eigenfunctions can be ignored. A W.K.B. approximation to the eigenfunctions shows this can be realized when the vertical scale factor is chosen equal to the reciprocal of the vertical wave number. Section II briefly covers some aspects of the computer algorithms used in the simulations. Section III contains a discussion of numerical benchmarks that includes a validation of using reciprocal vertical wave numbers for the scale factors. The slope-induced horizontal refraction of modal ray paths is compared to analytic solutions for modal caustics. Plots of the modal amplitude demonstrate some defects in both cell methods and Gaussian beams for the slope problem. The total acoustic field is then compared to a secondary benchmark. Section IV summarizes some of the important findings and concludes by reviewing the strengths and weaknesses of both the theory and numerical implementation.

I. CURVILINEAR ADIABATIC NORMAL MODES

Here it is shown how an adiabatic normal mode solution to the Helmholtz equation may be expressed in curvilinear coordinates. A coordinate system is found in which the modes have adiabatic properties for environments which change slowly enough. The construction of this coordinate system is based on the phase of a reference eigenfunction. The resulting coordinate scale factors are then seen to provide the extra degree of freedom needed to support decoupling of the modes.

A normal mode expansion is used to show that mode coupling is related to horizontal derivatives of the eigenfunctions in the curvilinear coordinate system. Coordinate scale factors are then found using a W.K.B. approximation such that the horizontal derivatives of a reference eigenfunction vanish. The horizontal derivatives of a W.K.B. approximation for all other modes depend on a ratio of wave numbers with the reference mode. The nearly constant horizontal behavior of this ratio provides a justification for adiabatic propagation of the other modes.

A. Curvilinear Helmholtz equation

Let $\mathbf{x}$ be a Cartesian coordinate system and let $\mathbf{u}=(\eta,\xi,\zeta)$ be a curvilinear coordinate system. $\mathbf{u}(x,y,z)$ is assumed to be invertible so that $\mathbf{x}(\eta,\xi,\zeta)$ exists and is well defined. The local wave number $k(\mathbf{x})$ depends on position within the ocean. Once the curvilinear coordinate system is constructed, a change of variables may be done to find $k(\mathbf{u})$. A solution is then found for the acoustic field $\Phi(\mathbf{u})$ induced by a point source of strength Q_s located at $\mathbf{u}_s$ in the curvilinear system. Any frequency dependence of Φ, k and Q_s is implicit. The Helmholtz equation is expressed in general curvilinear coordinates,

$$\frac{1}{h_1h_2h_3}\sum_{i=1}^{3}\left[\frac{\partial}{\partial u_i}\left(\frac{h_1h_2h_3}{h_i^2}\frac{\partial\Phi}{\partial u_i}\right)\right]+k^2(\mathbf{u})\Phi$$

$$=-Q_s\frac{\delta_{\mathbf{u}}(\mathbf{u}-\mathbf{u}_s)}{h_1h_2h_3}, \tag{1}$$

where $\delta_{\mathbf{u}}(\mathbf{u}-\mathbf{u}_s)$ is the Dirac delta function describing the point source. The horizontal and vertical scale lengths may be very different, but there is no preferred directionality to the horizontal scaling. Furthermore, the precise choice of horizontal scaling turns out to be unimportant. Without loss of generality the horizontal scaling will be chosen as unity,

$$h_1=h_2=1, \tag{2}$$

$$h_3=h(\eta,\xi;\zeta). \tag{3}$$

The notation emphasizes that the scale factor h is assumed to vary slowly as a function of the horizontal coordinates. The separation of variables sought is between the horizontal and vertical coordinates. The determination of h will be deferred to a later section where it will be associated with the reciprocal of the vertical wave number of a reference mode. Surfaces of constant ζ will be chosen as surfaces of constant vertical wave number for the eigenfunction of a reference normal mode. In particular, surfaces defined by the bottom bathymetry and thermocline interfaces are approximate ζ surfaces. With this assumed form for the scale factors, the Helmholtz equation becomes

$$\frac{\partial^2\Phi}{\partial\eta^2}+\frac{1}{h}\frac{\partial h}{\partial\eta}\frac{\partial\Phi}{\partial\eta}+\frac{\partial^2\Phi}{\partial\xi^2}+\frac{1}{h}\frac{\partial h}{\partial\xi}\frac{\partial\Phi}{\partial\xi}+\frac{1}{h}\frac{\partial}{\partial\zeta}\left(\frac{1}{h}\frac{\partial\Phi}{\partial\zeta}\right)$$

$$+k^2(\eta,\xi;\zeta)\Phi=-\frac{Q_s}{h}\delta_{\mathbf{u}}(\mathbf{u}-\mathbf{u}_s). \tag{4}$$

The problem is simplified by transforming the Helmholtz equation to be a square with respect to the $\partial/\partial\eta$ and $\partial/\partial\xi$ operators. In cylindrical coordinates the well-known change of variables[44] needed to achieve this condition is $\Phi=\rho^{-1/2}\tilde{\Phi}$. For curvilinear coordinates the appropriate change of variables is $\Phi=\tilde{f}\tilde{\Phi}$ where $\tilde{f}\equiv h^{-1/2}$. The transformed Helmholtz equation is then a square with respect to both the $\partial/\partial\eta$ and $\partial/\partial\xi$ operators,

$$\frac{\partial^2\tilde{\Phi}}{\partial\eta^2}+\frac{\partial^2\tilde{\Phi}}{\partial\xi^2}+\frac{1}{\tilde{f}h}\frac{\partial}{\partial\zeta}\left(\frac{1}{h}\frac{\partial\tilde{f}\tilde{\Phi}}{\partial\zeta}\right)+\tilde{K}^2(\eta,\xi;\zeta)\tilde{\Phi}$$

$$=\frac{-Q_s}{\tilde{f}h}\delta_{\mathbf{u}}(\mathbf{u}-\mathbf{u}_s), \tag{5}$$

where

$$\tilde{K}^2(\eta,\xi;\zeta)\equiv k^2(\eta,\xi;\zeta)+\frac{1}{\tilde{f}}\left[\frac{\partial^2\tilde{f}}{\partial\eta^2}+\frac{\partial^2\tilde{f}}{\partial\xi^2}\right]$$

$$-\frac{2}{\tilde{f}^2}\left[\left(\frac{\partial\tilde{f}}{\partial\eta}\right)^2+\left(\frac{\partial\tilde{f}}{\partial\xi}\right)^2\right] \tag{6}$$

is a modified wave number with corrections induced by the curved wavefront of the intrinsic wedge mode.

B. Eigenvalue problem

Following Pierce[16] the acoustic field is expressed as a superposition of normal modes. However, here the modes are curvilinear,

$$\tilde{\Phi}(\eta,\xi;\zeta)\equiv\sum_m A_m(\eta,\xi)\tilde{\Psi}_m(\eta,\xi;\zeta), \tag{7}$$

where the A_m are complex mode amplitudes and the $\tilde{\Psi}_m$ are the normalized eigenfunctions of

$$\frac{1}{\tilde{f}h}\frac{\partial}{\partial\zeta}\left(\frac{1}{h}\frac{\partial\tilde{f}\tilde{\Psi}_m}{\partial\zeta}\right)+\tilde{K}^2(\eta,\xi;\zeta)\tilde{\Psi}_m\equiv k_m^2(\eta,\xi)\tilde{\Psi}_m. \tag{8}$$

Orthogonality conditions are determined by writing the eigenfunction equation in self adjoint form (Arfken, Ref. 45, p. 498). Letting $\Psi_m\equiv\tilde{f}\tilde{\Psi}_m$, Eq. (8) becomes

$$\frac{\partial}{\partial\zeta}\left(\frac{1}{h}\frac{\partial\Psi_m}{\partial\zeta}\right)+\tilde{K}^2h\Psi_m-k_m^2h\Psi_m=0. \tag{9}$$

In this form the scale factor, h, is seen to be the weight function. It is well known from Sturm–Liouville theory that the eigenfunctions of the self adjoint form satisfy the following orthogonality condition (Arfken, Ref. 45, pp. 510–511):

$$\int_0^\infty\Psi_m\Psi_n h\,d\zeta=\delta_{mn}, \tag{10}$$

where δ_{mn} is the Kronecker delta. The homogeneous boundary conditions chosen for this problem are

$$\Psi_m(\eta,\xi;0)=0\quad\text{and}\quad\Psi_m(\eta,\xi;\infty)=0. \tag{11}$$

These conditions are sufficient to make the boundary conditions for the total acoustic field Φ homogeneous also.

C. Mode coupling

Mode coupling is established by substituting Eq. (7) into (5), using Eq. (8) and expanding the Dirac delta function,

$$\sum_m\left[\frac{\partial^2A_m\tilde{\Psi}_m}{\partial\eta^2}+\frac{\partial^2A_m\tilde{\Psi}_m}{\partial\xi^2}+k_m^2A_m\tilde{\Psi}_m\right]$$

$$=\frac{-Q_s}{\tilde{f}h}\delta(\eta-\eta_s)\delta(\xi-\xi_s)\delta(\zeta-\zeta_s). \tag{12}$$

Next expand the derivatives, multiply by $\tilde{\Psi}_n$, integrate with respect to ζ, and apply the orthogonality conditions while recalling that $h=\tilde{f}^{-2}$ and $\Psi_n=\tilde{\Psi}_n/\tilde{f}h$. The mode coupling equations in curvilinear coordinates result:

$$\sum_m\left[2\frac{\partial A_m}{\partial\eta}\int_0^\infty\frac{\partial\tilde{\Psi}_m}{\partial\eta}\tilde{\Psi}_n\,d\zeta+2\frac{\partial A_m}{\partial\xi}\int_0^\infty\frac{\partial\tilde{\Psi}_m}{\partial\xi}\tilde{\Psi}_n\,d\zeta\right.$$

$$\left.+A_m\int_0^\infty\frac{\partial^2\tilde{\Psi}_m}{\partial\eta^2}\tilde{\Psi}_n\,d\zeta+A_m\int_0^\infty\frac{\partial^2\tilde{\Psi}_m}{\partial\xi^2}\tilde{\Psi}_n\,d\zeta\right]+\frac{\partial^2A_n}{\partial\eta^2}$$

$$+\frac{\partial^2A_n}{\partial\xi^2}+k_n^2A_n=-Q_s\Psi_{ns}\delta(\eta-\eta_s)\delta(\xi-\xi_s), \tag{13}$$

where the notation Ψ_{ns} emphasizes evaluation of the physical eigenfunction at the source position (η_s, ξ_s, ζ_s). The integrals represent mode coupling and for the propagation to be adiabatic it is sufficient that

$$\frac{\partial \tilde{\Psi}_m}{\partial \eta} = 0 \quad \text{and} \quad \frac{\partial \tilde{\Psi}_m}{\partial \xi} = 0, \quad \text{for all} \quad \eta, \xi; m. \tag{14}$$

In the next section, the scale factors of a coordinate system are found in which conditions (14) are approximately true. Note that the horizontal derivatives are with respect to curvilinear coordinate surfaces that must follow the contours of any interfaces in the medium.

Under conditions of decoupling, a separation of variables is obtained with a two-dimensional Helmholtz equation describing the independent, horizontal propagation of normal mode amplitudes:

$$\frac{\partial^2 A_n}{\partial \eta^2} + \frac{\partial^2 A_n}{\partial \xi^2} + k_n^2 A_n = -Q_s \Psi_{ns} \delta(\eta - \eta_s)\delta(\xi - \xi_s). \tag{15}$$

This equation is solved on the surface of the ocean where the curvilinear coordinates are chosen such that, $\eta = x$ and $\xi = y$ and are thus orthogonal. A Gaussian-beam ray-trace algorithm is used for solving this equation.

The ray-trace solution requires initial conditions at the source location. These are provided by a solution to the Helmholtz equation that has constant coefficients within an infinitesimal volume enclosing a point source. Unfortunately the solution behaves logarithmically near the source and ray-trace solutions are far-field approximations which cannot properly describe such behavior. However, ray-trace solutions can describe the far-field behavior of a point source. Thus it is necessary to replace the source with an effective source that has the same far-field solution but is better behaved at the origin. The effective source is obtained from a far-field approximation to the constant coefficient Helmholtz equation. The well behaved effective-source solution is then evaluated at the source location to obtain the required initial conditions. The required far-field solution is

$$A_m(\eta, \xi) \approx Q_s \Psi_{ms} \sqrt{\frac{1}{8\pi k_{ms} \rho}} \exp i(k_{ms}\rho + \pi/4), \tag{16}$$

where $k_{ms} \equiv k_m(\eta_s, \xi_s)$, $\Psi_{ms} \equiv \Psi_m(\eta_s, \xi_s; \zeta_s)$ and

$$\rho(\eta, \xi) \equiv |(\eta - \eta_s)^2 + (\xi - \xi_s)^2|^{1/2}. \tag{17}$$

Equation (16) provides the initial conditions for the amplitude and phase required by the ray-trace discussed in the next section.

D. Scale factor

In this section, a W.K.B. approximation for a reference mode, $m = 0$, is shown to provide a solution for the scale factors h. Although the existence of suitable coordinate systems is demonstrated, the actual construction is circular requiring an iteration with no guarantee of convergence. It is important to note that a W.K.B. approximation is *not* made for the solution to the Helmholtz equation. Rather, the W.K.B. approximation is used only to obtain scale factors and demonstrate certain properties which hold within that approximation.

In essence, a curvilinear coordinate system is defined such that surfaces of constant depth coincide with surfaces of constant phase of the reference eigenfunction. Thus for example, any particular zero of an eigenfunction lies on a constant-depth surface in the curvilinear system.

Let κ_m be the modified vertical wave number of mode m,

$$\kappa_m(\eta, \xi; \zeta) \equiv [\tilde{K}^2(\eta, \xi; \zeta) - k_m^2(\eta, \xi)]^{1/2}. \tag{18}$$

Define $\overline{\kappa_m}$ as a reference vertical wave number of each mode,

$$\overline{\kappa_m} \equiv \max_{\eta, \xi, \zeta}(\kappa_m(\eta, \xi; \zeta)). \tag{19}$$

Also let $n_m(\eta, \xi; \zeta)$ be an index of refraction such that

$$\kappa_m(\eta, \xi; \zeta) = \overline{\kappa_m} n_m(\eta, \xi; \zeta), \quad |n_m| \leqslant 1. \tag{20}$$

Now assume a W.K.B. approximation in the curvilinear coordinate system for each eigenfunction,

$$\tilde{\Psi}_m(\eta, \xi; \zeta) \equiv B_m(\eta, \xi; \zeta) e^{i\overline{\kappa_m}\tau_m(\eta, \xi; \zeta)}. \tag{21}$$

A solution for $\tau_m(\eta, \xi; \zeta)$ is obtained beginning with Eq. (8) and is provided by the $O(\overline{\kappa_m^2})$ terms,

$$\frac{\partial \tau_m}{\partial \zeta} = n_m h. \tag{22}$$

Thus the W.K.B. approximation is related to the integral of the modified vertical wave number,

$$\tilde{\Psi}_m(\eta, \xi; \zeta) = B_m(\eta, \xi; \zeta) e^{i\int_0^\zeta \kappa_m(\eta, \xi; \zeta') h(\eta, \xi; \zeta') d\zeta'}. \tag{23}$$

The vertical derivatives of B_m are negligible because they are of order $O(\overline{\kappa_m})$. Because the B_m represent the amplitudes of eigenfunctions normalized by Eq. (10) it is reasonable to assume the horizontal derivatives of B_m are also small. Thus derivatives of B_m may be ignored in comparison with derivatives of the exponential.

Returning to the question of adiabatic propagation as expressed by Eqs. (13) and (14), the partial derivatives of $\tilde{\Psi}_m$ along surfaces of constant ζ behave like

$$\frac{\partial \tilde{\Psi}_m}{\partial \eta} = iB_m e^{i\int_0^\zeta \kappa_m h : d\zeta'} \int_0^\zeta \frac{\partial \kappa_m h}{\partial \eta} d\zeta'. \tag{24}$$

Thus, the horizontal derivatives of the eigenfunctions, and hence mode coupling, vanish within the W.K.B. approximation when

$$\frac{\partial \kappa_m h}{\partial \eta} = 0 \quad \text{for all} \quad \eta, \xi; m. \tag{25}$$

The curvilinear coordinate system is chosen such that this condition is true for one reference mode, $m = 0$, by arbitrarily setting $\kappa_0 h = 1$ so that

$$\frac{\partial \kappa_0 h}{\partial \eta} = 0, \tag{26}$$

TABLE I. Wide-angle wedge parameters.

Slope angle	21 deg
Frequency	25 Hz
C_w	1500 m/s
ρ_w	1.0 g/cm^3
Down-slope range	1 km
Cross-slope scale	6 km
Max water depth	384 m
Depth at source	200 m
Source range	0.52 km
Source depth	100 m

and

$$h(\eta,\xi;\zeta)=\kappa_0^{-1}(\eta,\xi;\zeta). \tag{27}$$

The horizontal derivatives of the other eigenfunctions are

$$\frac{\partial \kappa_m h}{\partial \eta}=\frac{\partial \kappa_m \kappa_0^{-1}}{\partial \eta}. \tag{28}$$

But ratios of the modified vertical wave numbers are insensitive to changes in horizontal position *in the chosen curvilinear coordinate system*,

$$\kappa_m(\eta,\xi;\zeta)\propto\kappa_n(\eta,\xi;\zeta), \quad m\neq n. \tag{29}$$

This is because orthogonality of the modes constrains the vertical wave numbers to specific ratios relative to the reference mode; that is, the modes compress and expand in unison with changing depth.

For example, in the isovelocity linear wedge with free surface and either a hard or free bottom, ratios of the vertical wave numbers are rational fractions because the eigenfunctions are sine functions with integer arguments. In this case the ratios are constant everywhere within the wedge.

More generally, bottom penetration and sound-speed variability cause nonrational ratios. But orthogonality of the modes constrains those ratios. Consider the highest mode, Ψ_M. The zeros of this mode define surfaces of constant ζ. Now consider the next lower mode, Ψ_{M-1}. It is well known that in the absence of degenerate eigenvalues, the zeros of Ψ_{M-1} lie between the zeros of Ψ_M (Coddington and Levinson, Ref. 46, p. 208). This same relationship is also true for all other pairs of adjacent modes. Now let the frequency go to infinity. Here surfaces formed by zeros of the eigenfunctions become arbitrarily close together; yet they cannot intersect. Because the zeros of the various modes interleave, the wave number ratios change in unison with changing depth. It appears that bottom impedance is the dominant determinant of the wave number ratios. Thus penetrable bottoms can be accommodated so long as the bottom impedance remains constant as a function of horizontal position.

At finite frequencies there is nothing special in the above argument specific to the particular phase angle associated with the zeros of an eigenfunction. Similar relationships must hold for any fixed phase angle. Thus all of the surfaces of constant phase angle in the eigenfunction are nonintersecting. These constant phase surfaces define constant ζ in the curvilinear coordinate system. But in the W.K.B. approximation, the vertical wave number is related to the vertical scale factor defined by these surfaces. Thus the vertical wave number also follows those surfaces and is therefore insensitive to horizontal position,

$$\frac{\partial \kappa_m \kappa_0^{-1}}{\partial \eta}\approx 0 \quad \text{and} \quad \frac{\partial \kappa_m \kappa_0^{-1}}{\partial \xi}\approx 0, \quad \text{for all} \quad m. \tag{30}$$

Consequently, a curvilinear coordinate system has been found in which the modes are very nearly adiabatic. To the extent that the local modified vertical wave numbers satisfy conditions (30) the propagation will be adiabatic. When these conditions are violated, as occurs with degenerate eigenvalues or large horizontal gradients in the bottom impedance, the propagation will not be adiabatic within this theory. The validity of this proposition will be explored below in the numerical benchmarks section for propagation in an isovelocity wedge.

TABLE II. Wide-angle, soft bottom, $C_b=1700$ m/s, $\rho_b=1.5$ g/cm^3.

	κ_2/κ_1	κ_3/κ_1
Mean	2.000 41	3.001 77
Std. Dev.	0.004 24	0.009 19

TABLE III. Wide-angle, hard bottom, $C_b=\infty$, $\rho_b=\infty$.

	κ_2/κ_1	κ_3/κ_1
Mean	2.897 23	4.814 84
Std. Dev.	0.000 97	0.001 65

II. CURVILINEAR EIGENVALUE ALGORITHMS

The above sections demonstrate the existence of adiabatic modes under reasonable conditions. However, the actual curvilinear coordinate system in which such propagation occurs remains undetermined. Although the theory is formulated in a curvilinear coordinate system, that system need not be constructed. Instead, computations are done in a coordinate system, similar to σ-coordinates, that approximates the curvilinear system such that geometric effects appear within a modified wave number.

A computational coordinate system closely related to the desired curvilinear system is constructed using Cartesian local modes. This allows coordinate transformations which permit the eigenvalue problem to be solved using an ordinary depth variable, z', rather than the curvilinear depth ζ. A set of Jacobi matrices describing these coordinate transformations must be maintained throughout the computations. An

TABLE IV. Narrow-angle wedge parameters.

Slope angle	5 deg
Frequency	100 Hz
C_w	1500 m/s
ρ_w	1.0 g/cm^3
Down-slope range	5 km
Cross-slope scale	15 km
Max water depth	437 m
Depth at source	100 m
Source range	1.143 km
Source depth	25 m

TABLE V. Narrow-angle, silty clay, $C_b = 1520$ m/s, $\rho_b = 1.4$ g/cm^3.

	κ_2/κ_1	κ_3/κ_1	κ_4/κ_1	κ_5/κ_1	κ_6/κ_1	κ_7/κ_1
Mean	2.001 87	3.003 47	4.003 82	5.006 64	6.005 50	7.006 23
Std. Dev.	0.002 38	0.004 81	0.010 16	0.005 58	0.010 26	0.007 49

iterative procedure is then used in the computational system to determine simultaneously the eigenvalues, scale factors and coordinate transformation matrices of the curvilinear problem. A shooting method is used in conjunction with bisection and Newton–Raphson algorithms to obtain all of the eigenvalues in parallel.

Ray paths are determined using an n^2-linear cell method discussed by Jensen *et al.*[43] The computational region is gridded into half-wavelength squares with diagonals forming right triangles. Analytic solutions within each cell are used to project the ray paths and phase from one cell to another. Following Červený[41] an auxiliary set of coupled first order equations is integrated to obtain the Gaussian-beam parameters.

III. NUMERICAL BENCHMARKS

Benchmarking of the model proceeded in steps from the basic checking of eigenvalues to the well characterized field of the ASA wide-angle benchmark wedge presented by Dean and Buckingham.[36] The properties of this wedge are shown in Table I. Eigenvalues for both hard and soft bottoms were checked against those from the KRAKEN program developed by Porter.[47]

Solutions for both the modal amplitude given by Eq. (15) and the total acoustic field given by Eq. (7) were computed for a constant-depth, hard-bottom environment. This problem has a well known solution discussed, among other sources, by Jensen *et al.*[43] The computational region was a 0.9 km square with a water depth of 200 m which corresponds to the water depth at the source of the wide-angle wedge (Table I). Three modes were found to propagate at the 25 Hz source frequency. For both the modal amplitudes and total fields, the magnitude of the numerical solutions was found to be correct within 1 dB, except around the edges of the square. The phase of the numerical solutions was also correct within 0.1 rad, again excepting the edges.

The problem around the perimeter of the computational region occurs where Gaussian beams terminate at the edge. Because the beams have finite width and strike the edge at an angle, their contribution to the interior field is prematurely truncated. To avoid termination errors around the edges, the computational region can be enlarged by placing a guard band around the perimeter. Such guard bands were placed around the wedges for the results presented below. Following these preliminaries, the constancy of vertical wave number ratios, the horizontal refraction of modes, and a nontrivial acoustic field were checked for accuracy.

TABLE VI. Narrow-angle, coarse sand, $C_b = 1800$ m/s, $\rho_b = 2.0$ g/cm^3.

	κ_2/κ_1	κ_3/κ_1	κ_4/κ_1	κ_5/κ_1	κ_6/κ_1	κ_7/κ_1
Mean	1.999 80	2.999 84	4.000 15	5.000 79	6.001 83	7.003 31
Std. Dev.	0.013 95	0.022 27	0.027 76	0.031 65	0.034 47	0.036 50

TABLE VII. Narrow-angle, hard bottom, $C_b = \infty$, $\rho_b = \infty$.

	κ_2/κ_1	κ_3/κ_1	κ_4/κ_1	κ_5/κ_1	κ_6/κ_1	κ_7/κ_1
Mean	2.992 99	4.988 79	6.984 05	8.979 33	10.974 74	12.970 08
Std. Dev.	0.000 21	0.000 39	0.000 41	0.000 53	0.000 27	0.000 32

A. Scale factor validity

One necessary requirement for the existence of curvilinear adiabatic normal modes is the constancy of the ratio of the vertical wave number of each mode to that of a reference mode as expressed by Eq. (30). Simulations were run in a sloping environment for both a soft and hard bottom to check this proposition. Propagation parameters were taken from the wide-angle wedge (Table I). These parameters were chosen to support the benchmarking of the ray paths and field amplitude discussed below.

Shown in Tables II and III, for the soft and hard bottoms, respectively, are the mean value and standard deviation of the vertical wave number ratio $\kappa_m \kappa_1^{-1}$, $m = (2,3)$, obtained by averaging over the entire wedge domain where both modes in the ratio are propagating. The lowest mode, $m = 1$, is used as the reference. In all cases the standard deviation is less than 1% of the mean ratio indicating that curvilinear adiabatic normal modes provide a valid basis for computing the field of the ASA wide-angle benchmark wedge.

To explore this proposition further, additional simulations were run in an environment having more modes. For these examples propagation parameters were taken from the narrow-angle wedge discussed by Westwood[24] with realistic bottom impedances published by Hamilton.[48] Parameters for the narrow-angle wedge are given in Table IV.

Shown in Tables V–VII, for three different realistic bottoms, are the mean value and standard deviation of the vertical wave number ratios. Again the standard deviations are small compared to the mean ratio with the worst case having a 4% error for the highest mode propagating above a coarse sand bottom. Also note that except for an infinitely hard bottom, the mean ratio changes slowly with the bottom parameters and is within the 4% error of each individual wedge.

From these results it may be concluded that, except for environments spanning both soft and anomalously hard bottoms, curvilinear coordinate systems can be constructed such that the normal modes decouple for those environmental conditions most commonly found in shallow water shelf regions.

Another interesting observation concerning the soft bottom results of Tables II, V, VI, is that the wave number ratios are nearly equal to the integer ratios of 2,3,4 . . . that should exist for a pressure release bottom. That is because the normal modes are multiples of a half-wavelength for the case of pressure release boundary conditions both above and below. For an infinitely hard bottom the modes are a multiple of one and a half wavelengths giving rise to wave number

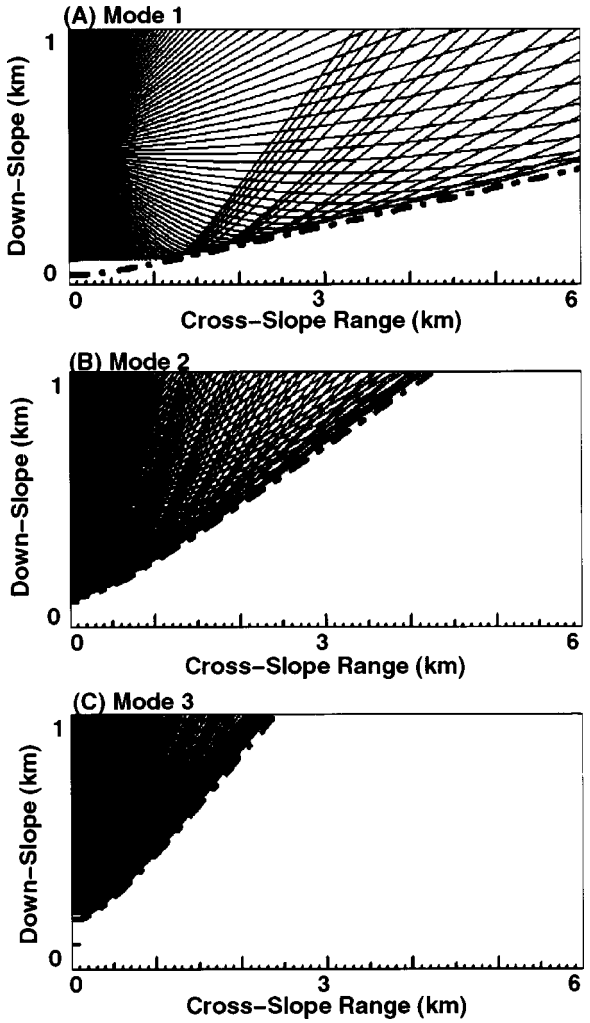

FIG. 1. Ray paths (solid lines) of modes 1–3 (A)–(C) for the wide-angle, hard-bottom wedge in comparison with exact caustic hyperbolas (dotted lines) due to Harrison. The wedge apex lies along the bottom edge. See Tables I–VII for the wedge parameters.

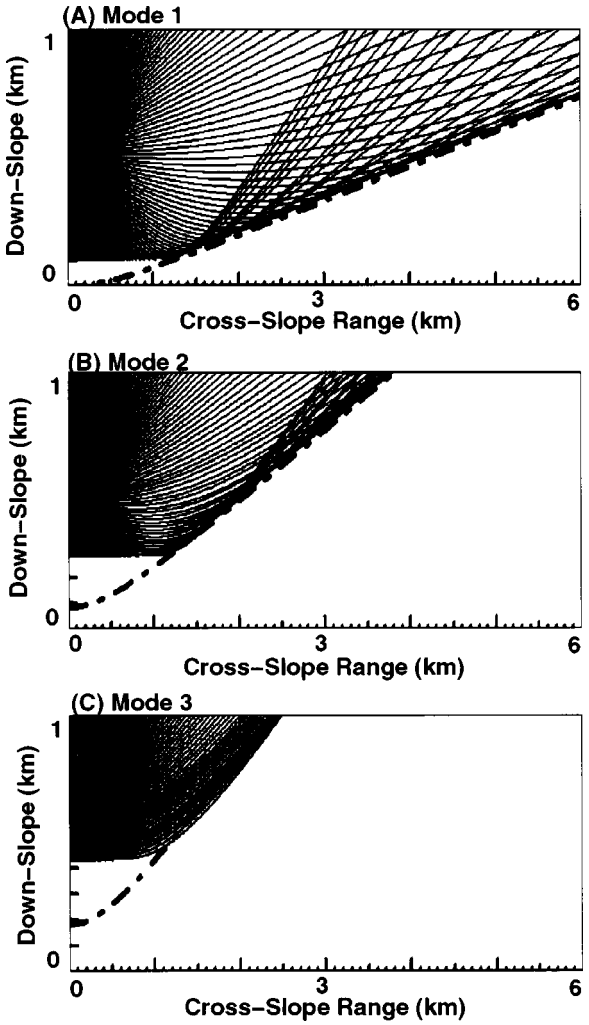

FIG. 2. Ray paths (solid lines) of modes 1–3 (A)–(C) for the wide-angle soft-bottom wedge in comparison with approximate caustic hyperbolas (dotted lines) due to Buckingham. The wedge apex lies along the bottom edge. See Tables I–VII for the wedge parameters.

ratios of 3,5,7, . . . Fairly close approximations to these ratios are observed in Table VII for the narrow-angle, hard-bottom wedge. However, the results in Table III for the wide-angle wedge are less than satisfactory. The reason for this discrepancy has not yet been determined.

B. Horizontal refraction

The accuracy of slope induced horizontal refraction produced by the computer model was studied using the wide-angle wedge (Table I) with both a hard bottom and a soft bottom. Exact solutions for the horizontal refraction of modal rays propagating above a hard bottom and governed by Eq. (15) have been obtained by Harrison.[49,50] In particular Harrison gives exact equations for the hyperbolas that describe modal caustics. These are shown by dotted lines for modes 1–3 in Fig. 1(a)–(c) in comparison with the caustics produced by the computer model as the rays, solid lines, fold over on themselves. For all three modes the agreement is quite good. The apparent discrepancy for the first mode at a range of 0.1 km merely results from not computing the rays for that mode so close to the wedge apex. The cell method used to compute the ray paths in the model under discussion must stop at a finite distance from the apex.

Approximate solutions for the horizontal refraction of modal rays propagating above a soft bottom have been obtained by Buckingham[30] using an approximate penetrable wedge theory. Dean and Buckingham[36] also present the equations for the resulting caustics with their data. These approximate caustics are shown by dotted lines for modes 1–3 in Fig. 2(a)–(c) in comparison with the caustics produced by the computer model. Again agreement is good except for the second and third modes up near the apex. Here the rays are being prematurely cutoff because of the finite width of the cells used to compute the ray trajectories. The problem occurs where caustic edges lie entirely within cells that span the mode cutoff line. Rays entering such cells must be terminated because finite difference estimates of the eigenvalue gradients cannot be computed. All computations done in this paper used a half-wavelength grid spacing. The use of a finer quarter-wavelength grid might help. Unfortunately the model, written in Fortran 90, requires a prohibitive amount of memory for the finer grid.

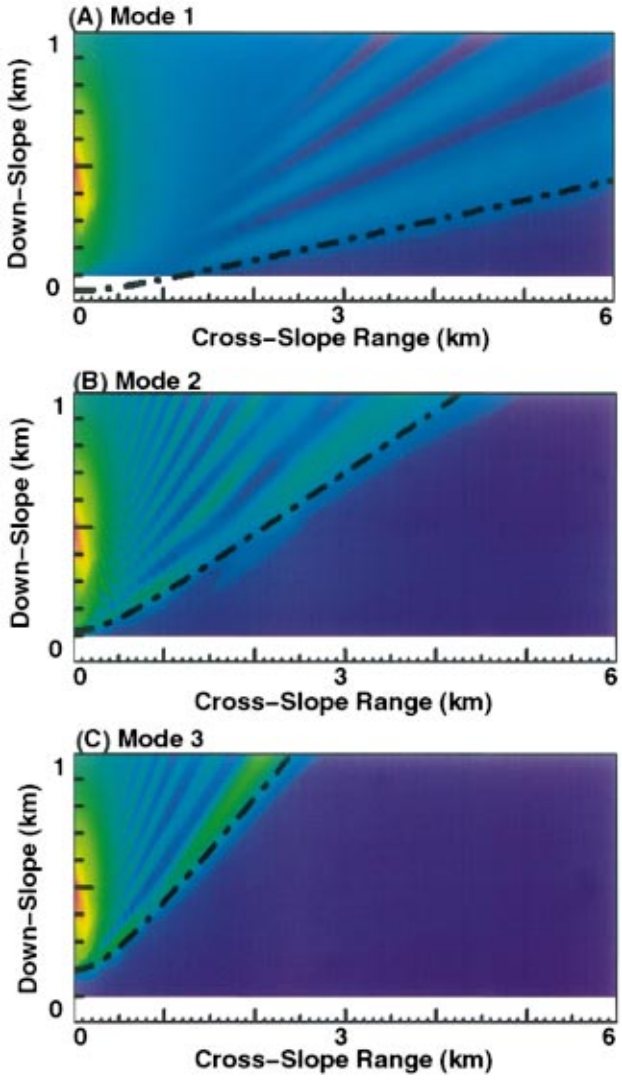

FIG. 3. Normal mode amplitude for modes 1–3 (A)–(C) of the wide-angle, hard-bottom wedge. The dynamic range is −52 to −22 dB. Red is high. Blue is low. The wedge apex lies along the bottom edge. See Tables I–VII for the wedge parameters.

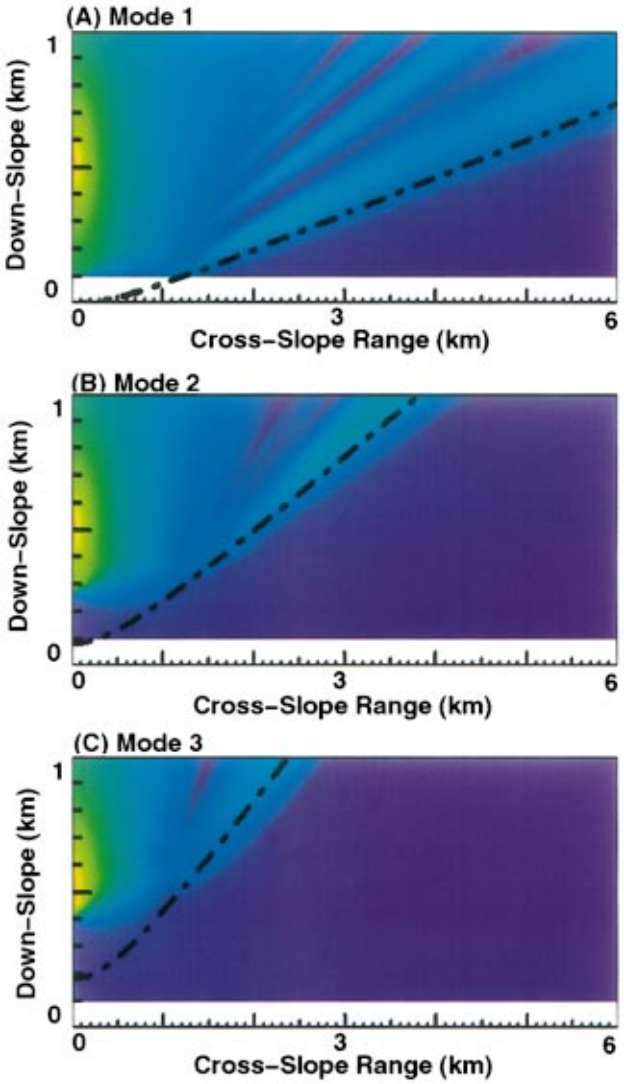

FIG. 4. Normal mode amplitude for modes 1–3 (A)–(C) of the wide-angle, soft-bottom wedge. The dynamic range is −49 to −19 dB. Red is high. Blue is low. The wedge apex lies along the bottom edge. See Tables I–VII for the wedge parameters.

C. Modal and field amplitudes

The modal amplitudes produced by Eq. (15) are obtained by summing up the Gaussian beams associated with each ray. A 300 m wide guard band was placed around the wedge to provide a buffer against edge effects from Gaussian-beam termination. The resulting modal amplitudes for the hard bottom are shown in Fig. 3(a)–(c) and soft bottom in Fig. 4(a)–(c). Note the way the Gaussian beam-width causes energy to spill past the caustics and over into the shadow zone.

Of interest in the modal amplitude figures is the comparative smoothness of the soft-bottom amplitudes with respect to the hard-bottom amplitudes. This phenomenon which is apparent for the second and third modes does not occur for the first mode. The reason for the smoothness of the higher modes is the above-mentioned premature cutoff of the rays due to nonpropagating cells along the caustic. Such cutoff makes the acoustic field presented below too smooth as well.

The complete acoustic field for the wide-angle wedge is shown in Fig. 5. This figure is directly comparable to the secondary benchmark solution shown in Fig. 7 of Ref. 36. Qualitatively, the environmentally adaptive, curvilinear normal mode results are good. The overall field amplitude is correct while modal cutoff and deep nulls occur in the correct locations. Proper location of the deep nulls is particularly significant because they imply the contributions being summed into the total field from all of the modes must have the correct amplitude and phase for the null to form.

In detail though, the adaptive mode solution has some problems. It is too smooth because of premature ray termination and the lack of the continuous spectrum near the source. These two problems are most pronounced up-slope in the vicinity of the wedge apex where the field amplitude is too low.

IV. CONCLUSION

Normal mode solutions to the Helmholtz equation were derived in curvilinear coordinates. Within this formulation,

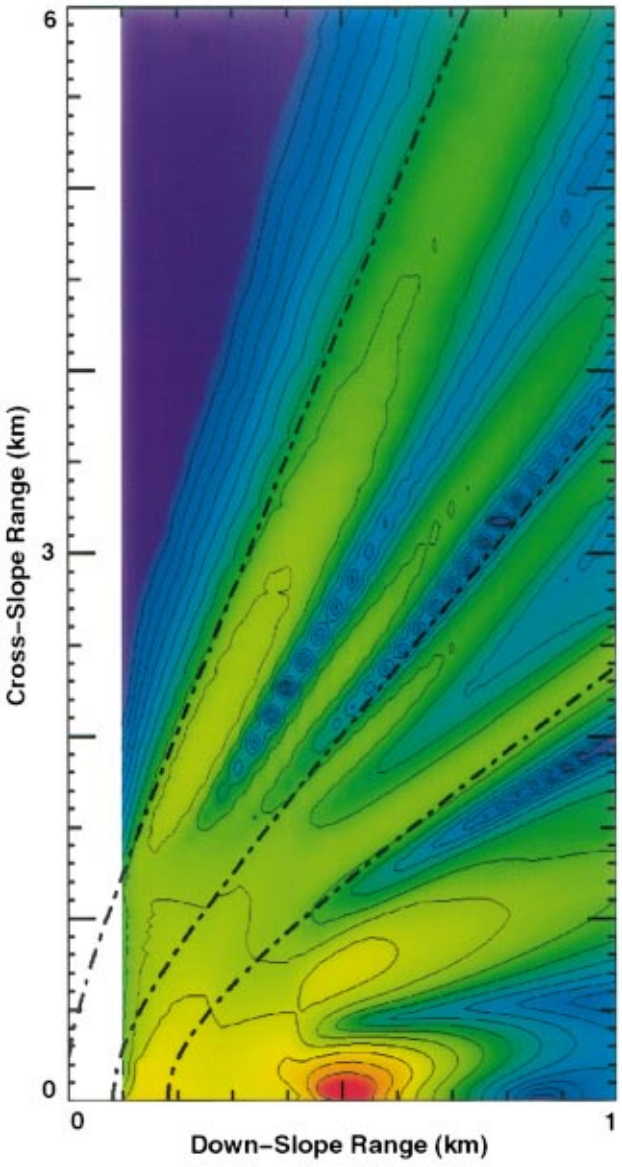

FIG. 5. Total acoustic field amplitude for the wide-angle, soft-bottom wedge with approximate caustic hyperbolas (black) of modes 1–3. The dynamic range is −80 to −38 dB with 3 dB contours. Red is high. Blue is low. The wedge apex lies along the left-hand edge. See Tables I–VII for the wedge parameters.

the vertical wave number was found to be modified by curvature terms. Mode coupling was shown to depend on the horizontal derivatives of eigenfunctions in the curvilinear coordinate system. A W.K.B. analysis of the eigenfunctions demonstrated that the vertical scale factor may be chosen such that a reference mode decouples. Decoupling of the other modes was shown to depend on a ratio of wave numbers with the reference mode. The nearly constant horizontal behavior of this ratio provides a justification for adiabatic propagation of all modes.

Numerical simulations demonstrated that the fundamental requirement for constant vertical wave number ratios is valid throughout several wedges with different bottom boundary conditions. These results do provide a basis for decoupling modes in nontrivial environments. The horizontal refraction of such modes agrees closely with the theories of Harrison[49,50] and Buckingham.[30] For the wide-angle wedge the acoustic field agrees qualitatively well with the benchmark solution of Dean and Buckingham,[36] but the details are smoothed out because of premature ray cutoff problems with the Gaussian-beam cell method used to compute the simulations shown in this work.

Environmentally adaptive modes provide a geometric basis for the decoupling of acoustic modes in environments which vary slowly in range. Thus they extend the applicability uncoupled modes to environments with nontrivial bathymetry and sound-speed profiles. As such, they provide a clear description of how energy, trapped in normal modes, propagates along unique paths which refract in the horizontal plane. This viewpoint can provide useful insight into the physical properties of an acoustic field propagating in sloping shallow-water regions.

Unfortunately the underlying assumptions of environmentally adaptive modes break down for rapidly varying environments such as those produced by internal waves. Other important physics is also left out including the continuous spectrum near the source, modal beams entering the bottom at mode cutoff and mode capturing down-slope from the source.

ACKNOWLEDGMENTS

This work was supported by the Office of Naval Research. Computations were supported in part by a grant of HPC time from the DoD HPC Center at NRL (TMC CM-500e and SGI Origin 2000).

[1] C. L. Pekeris, ''Theory of propagation of explosive sound in shallow water,'' in *The Geological Society of America Memoir 27: Propagation of Sound in the Ocean*, edited by M. Ewing, J. L. Worzel, and C. L. Pekeris (Geological Society of America, New York, NY, 1948), pp. 1–117,
[2] A. O. Williams, Jr. and M. N. Lewis, ''Approximate normal-mode methods of calculation for sound propagation in shallow water,'' Technical Report 56-1, Brown University, Providence, RI (1956).
[3] D. E. Weston, ''Guided propagation in a slowly varying medium,'' Proc. Phys. Soc. London **73**, 365–384 (1959).
[4] A. D. Pierce, ''Extension of the method of normal modes to sound propagation in an almost-stratified medium,'' J. Acoust. Soc. Am. **37**, 19–27 (1965).
[5] R. K. Eby, A. O. Williams, Jr., R. P. Ryan, and P. Tamarkin, ''Study of acoustic propagation in a two-layered model,'' J. Acoust. Soc. Am. **32**, 88–99 (1960).
[6] R. D. Graves, A. Nagl, H. Überall, and G. L. Zarur, ''Range-dependent normal modes in underwater sound propagation: Application to the wedge-shaped ocean,'' J. Acoust. Soc. Am. **58**, 1171–1177 (1975).
[7] S. R. Rutherford and K. E. Hawker, ''An examination of the influence of the range dependence of the ocean bottom on the adiabatic approximation,'' J. Acoust. Soc. Am. **66**, 1145–1151 (1979).
[8] S. R. Rutherford and K. E. Hawker, ''Consistent coupled mode theory of sound propagation for a class of nonseparable problems,'' J. Acoust. Soc. Am. **70**, 554–564 (1981).
[9] J. A. Fawcett, ''A derivation of the differential equations of coupled-mode propagation,'' J. Acoust. Soc. Am. **92**, 290–295 (1992).
[10] O. A. Godin, ''A note on differential equations of coupled-mode propagation in fluids,'' J. Acoust. Soc. Am. **103**, 159–168 (1998).
[11] D. E. Weston, ''Horizontal refraction in a three-dimensional medium of variable stratification,'' Proc. Phys. Soc. London **78**, 46–52 (1961).
[12] H. Weinberg and R. Burridge, ''Horizontal ray theory for ocean acoustics,'' J. Acoust. Soc. Am. **55**, 63 (1974).
[13] R. Doolittle, A. Tolstoy, and M. J. Buckingham, ''Experimental confirmation of horizontal refraction of cw acoustic radiation from a point source in a wedge-shaped ocean environment,'' J. Acoust. Soc. Am. **83**, 2117–2125 (1988).

[14] M. V. Hall and M. A. Irving, ''Application of adiabatic mode theory to the calculation of horizontal refraction through a mesoscale ocean eddy,'' J. Acoust. Soc. Am. **86**, 1465–1477 (1989).
[15] F. B. Jensen and W. A. Kuperman, ''Sound propagation in a wedge shaped ocean with a penetrable bottom,'' J. Acoust. Soc. Am. **67**, 1564–1566 (1980).
[16] A. D. Pierce, ''Guided mode disappearance during up-slope propagation in variable depth shallow water overlying a fluid bottom,'' J. Acoust. Soc. Am. **72**, 523–531 (1982).
[17] R. B. Evans, ''A coupled mode solution for acoustic propagation in a waveguide with stepwise depth variations of a penetrable bottom,'' J. Acoust. Soc. Am. **74**, 188–195 (1983).
[18] A. Kamel and L. B. Felsen, ''Spectral theory of sound propagation in an ocean channel with weakly sloping bottom,'' J. Acoust. Soc. Am. **73**, 1120–1130 (1983).
[19] E. Topuz and L. B. Felsen, ''Intrinsic modes: Numerical implementation in a wedge-shaped ocean,'' J. Acoust. Soc. Am. **78**, 1735–1745 (1985).
[20] G. B. Deane and C. T. Tindle, ''A three-dimensional analysis of acoustic propagation in a penetrable wedge slice,'' J. Acoust. Soc. Am. **92**, 1583–1592 (1992).
[21] E. K. Westwood, ''Ray methods for flat and sloping shallow-water waveguides,'' J. Acoust. Soc. Am. **85**, 1885–1894 (1989).
[22] C. T. Tindle and G. B. Deane, ''Sound propagation over a sloping bottom using rays with beam displacement,'' J. Acoust. Soc. Am. **78**, 1366–1374 (1985).
[23] F. B. Jensen and C. T. Tindle, ''Numerical modeling results for mode propagation in a wedge,'' J. Acoust. Soc. Am. **82**, 211–216 (1987).
[24] E. K. Westwood, ''Broadband modeling of the three-dimensional penetrable wedge,'' J. Acoust. Soc. Am. **92**, 2212–2222 (1992).
[25] C. T. Tindle, H. Hobaek, and T. G. Muir, ''Downslope propagation of normal modes in a shallow water wedge,'' J. Acoust. Soc. Am. **81**, 275–286 (1987).
[26] C. T. Tindle, H. Hobaek, and T. G. Muir, ''Normal mode filtering for down slope propagation in a shallow water wedge,'' J. Acoust. Soc. Am. **81**, 287–294 (1987).
[27] H. Hobaek and E. K. Westwood, ''Measurements of upslope wave-front curvature in a sand-bottom wedge,'' J. Acoust. Soc. Am. **84**, 1787–1790 (1988).
[28] D. L. Bradley and A. A. Hudimac, ''The propagation of sound in a wedge shaped shallow water duct,'' Tech. Rep. NOLTR 70-325, Naval Ordinance Laboratory, Silver Spring, MD (1970).
[29] M. J. Buckingham, ''Acoustic propagation in a wedge-shaped ocean with perfectly reflecting boundaries,'' NRL Report 8793, Naval Research Laboratory, Washington, DC (1984).
[30] M. J. Buckingham, ''Theory of three-dimensional acoustic propagation in a wedgelike ocean with a penetrable bottom,'' J. Acoust. Soc. Am. **82**, 198–210 (1987).
[31] M. J. Buckingham, ''Theory of acoustic radiation in corners with homogeneous and mixed perfectly reflecting boundaries,'' J. Acoust. Soc. Am. **86**, 2273–2291 (1989).
[32] H. Primack and K. E. Gilbert, ''A two-dimensional downslope propagation model based on coupled wedge modes,'' J. Acoust. Soc. Am. **90**, 3254–3262 (1991).
[33] C. H. Harrison, ''Wave solutions in three-dimensional ocean environments,'' J. Acoust. Soc. Am. **93**, 1826–1840 (1993).
[34] V. B. Galanenko, ''On coupled modes theory of two-dimensional wave motion in elastic waveguides with slowly varying parameters in curvilinear orthogonal coordinates,'' J. Acoust. Soc. Am. **103**, 1752–1762 (1998).
[35] Y. Desaubies and K. Dysthe, ''Normal-mode propagation in slowly varying ocean waveguides,'' J. Acoust. Soc. Am. **97**, 933–946 (1995).
[36] G. B. Deane and M. J. Buckingham, ''An analysis of the three-dimensional sound field in a penetrable wedge with a stratified fluid or elastic basement,'' J. Acoust. Soc. Am. **93**, 1319–1328 (1993).
[37] L. B. Felsen, ''Benchmarks: An option for quality assessment,'' J. Acoust. Soc. Am. **87**, 1497–1498 (1990).
[38] W. A. Kuperman, M. B. Porter, J. S. Perkins, and R. B. Evans, ''Rapid computation of acoustic fields in three-dimensional ocean environments,'' J. Acoust. Soc. Am. **89**, 125–133 (1991).
[39] M. D. Collins and S. A. Chin-Bing, ''A three-dimensional parabolic equation model that includes the effects of rough boundaries,'' J. Acoust. Soc. Am. **87**, 1104–1109 (1990).
[40] D. Lee and M. H. Schultz, *Numerical Ocean Acoustic Propagation in Three Dimensions* (World Scientific, Singapore, 1995).
[41] V. Červený, ''Ray tracing algorithms in three-dimensional laterally varying layered structures,'' in *Seismic Tomography*, edited by G. Nolet (Reidel Publishing, Dordrecht, Holland, 1987), pp. 99–133.
[42] M. B. Porter and H. P. Bucker, ''Gaussian beam tracing for computing ocean acoustic fields,'' J. Acoust. Soc. Am. **82**, 1349–1359 (1987).
[43] F. B. Jensen, W. A. Kuperman, M. B. Porter, and H. Schmidt, *Computational Ocean Acoustics* (American Institute of Physics Press, Woodbury, NY, 1993).
[44] M. D. Collins, ''The adiabatic mode parabolic equation,'' J. Acoust. Soc. Am. **94**, 2269–2278 (1993).
[45] G. Arfken, *Mathematical Methods for Physicists*, 3rd ed. (Academic, Orlando, FL, 1985).
[46] E. A. Coddington and N. Levinson, *Theory of Ordinary Differential Equations* (Robert E. Krieger, Malabar, FL, 1984).
[47] M. B. Porter, ''The KRAKEN normal mode program,'' SACLANTCEN Memorandum SM-245, SACLANT Undersea Research Centre, La Spezia, Italy (1991).
[48] E. L. Hamilton, ''Elastic properties of marine sediments,'' J. Geophys. Res. **76**, 579–604 (1971).
[49] C. H. Harrison, ''Three-dimensional ray paths in basins, troughs, and near seamounts by use of ray invariants,'' J. Acoust. Soc. Am. **62**, 1382–1388 (1977).
[50] C. H. Harrison, ''Acoustic shadow zones in the horizontal plane,'' J. Acoust. Soc. Am. **65**, 56–61 (1979).

Three-dimensional density spectra of sandy sediments

Dajun Tang
Applied Physics Laboratory, University of Washington, Seattle, Washington 98105

Thomas H. Orsi
Planning Systems, Inc., Slidell, Louisiana 70458

(Received 29 June 1999; revised 7 December 1999; accepted 17 December 1999)

Power spectra of density variability for sandy sediments offshore Panama City, Florida, are estimated and modeled using digital x-ray computed tomography images of sediment structure. Spectral analysis reveals that while shell pieces and mud mixtures are the main contributors to density variability at large scales, intrinsic density variability associated with sand grain contacts dominates at small scales. The power spectrum of sandy sediments is modeled by an analytic form that consists of two power-law components, one associated with the shell and mud contributions and the other with the intrinsic density variability of sand. The dominant term has a much higher power-law exponent than previously reported. Implications for the scattering of high-frequency sound in sandy sediments are discussed. © *2000 Acoustical Society of America.*
[S0001-4966(00)00304-0]

PACS numbers: 43.30.Ft, 43.30.Gv, 43.30.Ma [DLB]

INTRODUCTION

Owing to the interaction of various geological, physical, and biological processes in the ocean, sediment structure is inherently heterogeneous. Quantification and understanding such heterogeneity has a multitude of benefits to diverse ocean sciences ranging from geology (diagenesis) to biology (bio-mixing of sediments) and from ecology (sediment remediation) to engineering (sediment strength). In this paper, we will concentrate on the importance of sediment heterogeneity to ocean acoustics, more specifically, to sound scattering by sediment volume heterogeneity. Sediment heterogeneity is important in underwater acoustics for two reasons: values of sediment heterogeneity are inputs to acoustic scattering models; and acoustics may provide a powerful remote sensing tool for measuring sediment heterogeneity in large areas once the relationship between heterogeneity and the scattered sound is established.

In recent years, acoustic research has confirmed that volume heterogeneity is one of the major causes of bottom scattering.[1–7] To properly predict such scattering, models require as inputs the spectra of the sediment heterogeneity. Therefore, measuring and properly modeling sediment heterogeneity are crucial to predicting bottom scattering. While sediment heterogeneity is a general term describing a large variety of natural spatial variations in sediment physical properties that can cause acoustic scattering, in this paper we will concentrate on the density spectra of sandy sediments. Scatterers such as rocks and gas bubbles are not considered.

Because of the complexity of sediment heterogeneity, and hence the complexity of the acoustic fields scattered from such heterogeneity, a stochastic approach is usually taken in which the sediment is modeled as a random medium and its statistical properties are related to those of the scattered acoustic fields. Since in most cases sediment volume heterogeneities are small deviations from their mean values, a first-order perturbation method is adequate for addressing the scattering problem. In such a case, the only statistical quantities required by models to predict the volume scattering coefficients are the three-dimensional spatial auto- and cross-correlation functions, or equivalently, their companion spectra of all the random quantities (sound speed, density, etc.).[1] Therefore, measuring the spectra of real sediments is of great importance in understanding and predicting sound scattering in and from sediments.

A power spectrum can be properly obtained by taking the ensemble average of three-dimensional spectral estimates from multiple data sets of sediment volume heterogeneity. However, obtaining such spectra is difficult because (1) measurements of sediment physical properties without disturbance are difficult to make, (2) the spatial dimensions of each measurement need to cover several orders of magnitude to ensure that the spectral estimates are accurate, and (3) to form proper ensemble averages, multiple data sets from statistically homogeneous regions are required. When sediment heterogeneities are assumed to be isotropic, one-dimensional data sets from sediment collected with cores have been used to extract power spectra.[1] In that approach, since density is measured by weighing samples of small volume, spatial resolution is limited to about 1 cm, so spectral behavior at large wave numbers cannot be obtained. Acoustic tomography is an approach that has been used to estimate sediment sound speed spectra. This technique can provide two-dimensional data,[6,7] but it is difficult to obtain multiple sets of measurements in one statistically homogeneous area. Another shortcoming of the tomographic approach is that high spatial resolution has yet to be achieved. Recently, Briggs *et al.*[8] and Jackson *et al.*[9] have reported using x-radiography and resistivity methods to quantify sediment variabilities. In short, measuring sediment power spectra is gaining increased attention because of its importance to predicting acoustic scattering, but the number of measurements and the techniques developed to obtain such measurements are still limited and need to be expanded. This paper is an effort toward that goal. Sediment density spectra will be estimated from

digital data obtained by x-ray computed tomography (CT) scans. These data sets have a submillimeter spatial resolution and satisfy the ensemble average requirement. The data are calibrated so that they are quantitatively related to sediment density. Section I defines the power spectra and sound scattering cross section. Section II describes the sediment samples and CT-scan procedures. In Sec. III, it will be detailed how the density data sets are prepared for spectral analysis. The probability density functions of the density variations are estimated using the median absolute deviation (MAD) method. Some preliminary conclusions as to the nature of density variability in the sediments are also made. Section IV describes the procedure used to estimate the density power spectra from the CT data. Also provided in that section is a theoretical model of the spectrum that is consistent with the spectra obtained from the data, and discussions on the origins of heterogeneities and their impact on the power spectra of sandy sediments are presented. In Sec. V, the high-frequency sound scattering cross section resulting from the density power spectra will be discussed. Also in that section, three-dimensional Monte Carlo realizations of density variation based on the theoretical power spectrum will be given. A comparison between the simulation and the CT images will be presented. A final discussion is given in Sec. VI, where the results of this paper are summarized.

I. CROSS SECTION AND POWER SPECTRUM

For the purpose of modeling propagation and scattering of high-frequency sound in sandy sediments, the sediment is assumed to be a fluid medium with varying sound speed and density; elasticity effects have been shown to be unimportant.[10] In such a medium, spatial fluctuations of two parameters are the primary mechanisms for scattering of sound waves: the sediment sound speed c and density ρ. We use density ρ and sediment compressibility κ as independent variables, and sound speed c is related to ρ and κ through.[4,11]

$$c=(\kappa\cdot\rho)^{-0.5}. \tag{1}$$

Treating ρ and κ as random processes in space, we can express them as mean values plus respective fluctuating parts

$$\rho=\langle\rho(\mathbf{r})\rangle+\delta\rho(\mathbf{R}),\quad \kappa=\langle\kappa(\mathbf{R})\rangle+\delta\kappa(\mathbf{R}), \tag{2}$$

where $\langle ...\rangle$ represents an ensemble average. These random processes are often assumed to be locally stationary. If we define the following two zero-mean random quantities,

$$\epsilon_\rho(\mathbf{R})=\frac{\delta\rho}{\langle\rho\rangle},\quad \epsilon_\kappa(\mathbf{R})=\frac{\delta\kappa}{\langle\kappa\rangle}, \tag{3}$$

then, the wave equation governing the acoustic field P with monochromatic frequency f in the random medium has the following form:

$$(\nabla^2+k^2)P=-\hat{Q}(\mathbf{R})P, \tag{4}$$

where k is the acoustic wave number. In general, k is a complex number; its real part is $2\pi f/\langle c\rangle$ and its imaginary part is a small, frequency-dependent quantity related to the sediment attenuation coefficient.[1] The inhomogeneous operator $\hat{Q}(\mathbf{R})$ is given by

$$\hat{Q}(\mathbf{R})=-k^2\cdot(\epsilon_\kappa+\epsilon_\rho)+\nabla\epsilon_\rho\cdot\nabla. \tag{5}$$

Such an equation can be solved iteratively. If the random variables ϵ_ρ and ϵ_κ have a stationary Gaussian distribution, all orders of scattering can be determined from three spectra: the density spectrum W_ρ, the compressibility spectrum W_κ, and the cross spectrum between ρ and κ, $W_{\rho\kappa}$. If the random quantities are small, first-order perturbation suffices to account for the scattered field. In this situation, even if the random processes are not Gaussian, the first-order scattered field is fully determined by these three spectra. Explicitly, if the random processes are isotropic, the differential scattering cross section $[\sigma(\theta)]$ under first-order perturbation can be easily derived (see, e.g., Ref. 12),

$$\sigma(\theta)=\frac{|k|^4}{(4\pi)^2}\cdot[W_\kappa(\alpha)+\cos^2\theta W_\rho(\alpha)+2\cdot\cos\theta W_{\rho\kappa}(\alpha)], \tag{6}$$

which is the scattered intensity per unit solid angle per unit volume at unit distance owing to an incident plane wave with unit intensity. The scattering cross section has systeme International (SI) units of m^{-1}. The power spectra are defined by their respective two-point correlation functions. For example, the density spectrum is related to its correlation function $N(\mathbf{r})=\langle\epsilon_\rho(\mathbf{r}+\mathbf{r}')\cdot\epsilon_\rho(\mathbf{r}')\rangle$ by

$$W_\rho(\alpha)=\frac{1}{(2\pi)^3}\int_{-\infty}^{\infty}d^3rN(\mathbf{r})e^{-i\boldsymbol{\alpha}\cdot\mathbf{r}}, \tag{7}$$

where $\boldsymbol{\alpha}$ is the wave vector and α its magnitude. Consequently, W_ρ is normalized to the density variance σ_ρ^2 by

$$\sigma_\rho^2=\int_{-\infty}^{\infty}W_\rho d^3\alpha. \tag{8}$$

The angle θ is the scattering angle relative to the incident wave direction and is related to α by

$$\alpha=2\,\mathrm{Re}(k)\sin\frac{\theta}{2}. \tag{9}$$

For forward scattering, $\theta=0$; for backscattering, $\theta=\pi$. According to the definition (7), the three-dimensional spectra have SI units of m^3. If we further assume that density and compressibility are linearly dependent on each other, as has been suggested,[1,4,11]

$$\epsilon_\kappa=\mu\cdot\epsilon_\rho, \tag{10}$$

we then have

$$\sigma(\theta)=\frac{|k|^4}{(4\pi)^2}\cdot(\mu^2+\cos^2\theta+2\mu\cos\theta)\cdot W_\rho(\alpha). \tag{11}$$

When the assumption given by (10) is made, it is clear from the above expression that the power spectrum $W_\rho(\alpha)$ determines the scattering cross section under the first-order perturbation approximation. In deriving Eq. (11), it is not necessary to make any assumption about the statistical distribution of density variation; in particular, the distribution need not be Gaussian. It is important to note that in obtaining the cross section above, we have assumed that the random processes are locally stationary. In the more general

and complicated case of nonstationary processes, spectra are needed which are functions of spatial position. Nevertheless, even in that case, the scattering cross section is still related to the power spectra.

As defined in Eq. (7), the density power spectrum depends on measurements of density in all three spatial dimensions. However, such data are difficult to obtain. Efforts have been made to estimate such spectra using one-dimensional core data[1] or two-dimensional data inverted from acoustic tomography.[6,7] As indicated previously, estimating sediment power spectra at different spatial scales is still at its early stages of development and improved measurement techniques and data processing methods with better resolution and signal-to-noise ratio are in high demand. In the present paper, we estimate spectra using three-dimensional, high spatial resolution data. The results are applicable to sound scattering models in the frequency range 10–500 kHz.

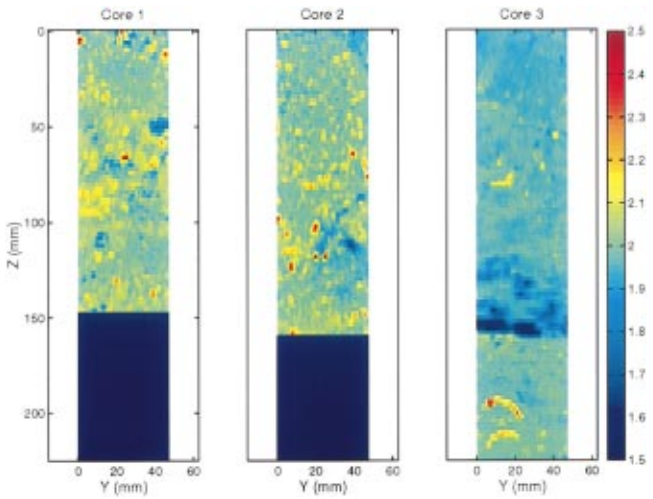

FIG. 1. Slices of density data from the three studied cores. The units on the colorbar are in g/cm^3.

II. CORE DATA DESCRIPTION

The three data sets used in this study were derived from sediments collected in August 1993 from the northeastern Gulf of Mexico as part of the Office of Naval Research's Coastal Benthic Boundary Layer (CBBL) Project. The first two data sets, CBBL Cores 413-2-PC-DC and 413-3-PC-DC, were collected from the same site (water depth: 29–30 m), and therefore were similar both in composition and physical characteristics. We call the data sets core 1 and core 2 throughout the paper. The sediments were a coarse to very coarse-grained quartz sand with numerous shell fragments and coralline algae. The third set of data, CBBL 490-PC-DC (or core 3), were also collected from a water depth between 29 and 30 m. Sediments at this site were fine sands with only a few scattered shell fragments. However, notable volume inhomogeneities include one large mollusk shell and a thin zone of muddy inclusions. Details of the study area and relevant sediment properties can be found in Richardson and Bryant.[13] Each sediment sample was collected by a diver and handled with care to minimize sample disturbance during retrieval and subsequent transport to the laboratory.

The unopened cores were scanned using a Technicare 2060 CT scanner, located at the Texaco E&P Technology Department in Houston, Texas. The Technicare 2060 CT scanner is a 4th generation machine, operated at 120 kV/75 mA. Let's designate the dimension along the depth of core samples by the z axis, and the cross-sectional dimensions by the x and y axes. The scanner has a resolution of $dx=dy=0.25$ mm, and $dz=2$ mm, resulting in a volume element of 0.125 mm^3 (i.e., $0.25\times0.25\times2$ mm). The digital value for each volume element is the average of the element. These numerical values, called CT numbers, were then converted to sediment density values using the calibration approach discussed in Refs. 14–16. In summary, strong linearity and an essentially perfect correlation (correlation coefficient $r=1.00$) in the scanner's response to density were first demonstrated during controlled experiments using artificial sediments of pure silica powder and seawater. Clean Ottawa sand, saturated with seawater, and a fused quartz disk were also scanned to extend the relationship to bulk densities of almost 2.2 g/cm^3. Thereafter, an empirical expression was developed using a least-squares regression technique by matching sediment volumes taken from cores for laboratory density determinations with their corresponding CT volume. The analysis incorporated a variety of marine sediments including high-porosity muds from Eckernforde Bay (western Baltic Sea), coarse sands from the Louisiana continental shelf, and the fine to medium quartz sand used in this study. The resulting correlation was strong, with a correlation coefficient $r=0.98$. In the calibration process, the total number of samples used is 137. Variations about the mean for the calibration result mainly from the difficulties and inaccuracy involved in fine-scale laboratory sampling and then in matching the physical property volumes with the CT volumes.[14]

To facilitate later Fourier statistical analysis, we selected from each of the three-dimensional data sets a subset of data that form a three-dimensional matrix. For all three data sets, both the x and y directions have $N_x=N_y=190$ points, but the z direction for each core has fewer sampled points. Specifically, $N_z=74$ for core 1, $N_z=80$ for core 2, and $N_z=112$ for core 3. Therefore, the number of elements in each of the three matrices is $190^2\times74=2\,671\,400$ for core 1; $190^2\times80=2\,888\,000$ for core 2; and $190^2\times112=4\,043\,200$ for core 3, respectively. Since the top 8 mm of sediment for all three cores was damaged, we have excluded that portion of the data. Hence, $z=0$ corresponds to sediments 8 mm below the water/sediment interface.

It is worth noting that when the CT numbers are converted to density, an empirical linear relation between density and the CT numbers established in Refs. 14 and 15 was used. Since the error statistics associated with the conversion are not available, we assume that such errors are negligible. Therefore, the final conclusions made in the paper should be understood as being contingent on this assumption being correct.

Figure 1 shows a typical vertical slice of density data selected from each core. Since the three cores have different lengths, to show all three cores on the same scale, we padded the shorter cores 1 and 2 to have the same length as core 3 with a constant, hence the dark regions in the figure signify areas void of real data. The heterogeneity in density in each

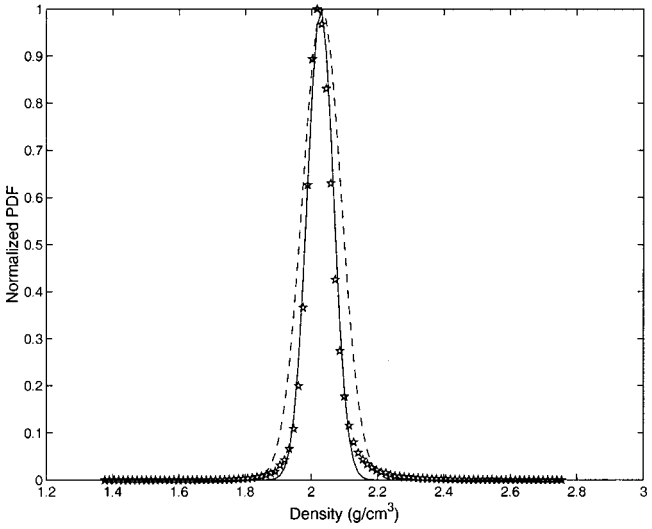

FIG. 2. Probability density functions for core 1. The stars are data points, the dashed curve is the Gaussian fit using the mean and standard deviation of the data, and the solid curve is the Gaussian fit obtained using the MAD method.

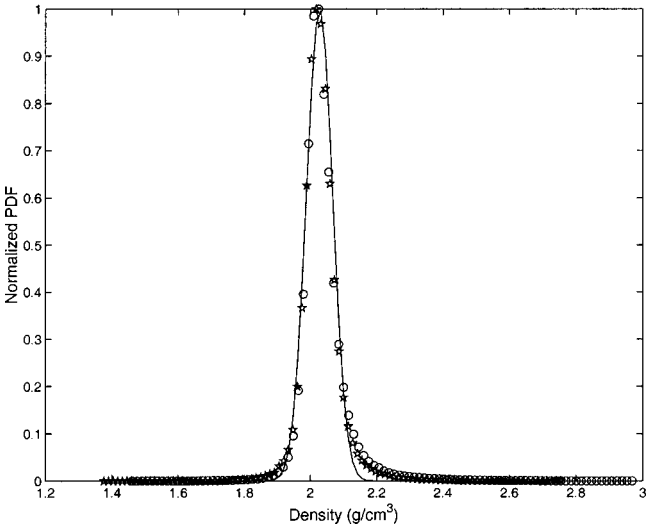

FIG. 3. Probability density functions. The stars are data from core 1, the circles are data from core 2, and the solid curve is the Gaussian fit for core 1 using the MAD method.

core is apparent. Note the distribution of high-density regions with values above 2.2 g/cm^3 and low-density areas with values below 1.6 g/cm^3. High-density values are from shell fragments and the low-density values are from mud mixtures; both were identified when the cores were extruded and visually inspected. A large feature can be seen in core 3, where at the 150-mm depth there is a low-density region that corresponds to a mud intrusion which exceeds 1 cm in extent. All the raw data cannot be shown due to space limitations, but the features shown in Fig. 1 are consistently seen throughout all slices of the cores. From the above observations, we point out that heterogeneities in these cores consist of (1) shells, (2) mud intrusions, and (3) intrinsic density variations associated with the sand matrix. Since the mud intrusions in core 3 introduce inhomogeneous features with sizes on the same order of magnitude of the core size, care is needed in estimating the power spectrum of that data set.

III. PRELIMINARY ANALYSIS

First we estimate the probability density function (PDF) for sediment density. Figure 2 gives the normalized histogram of density variability from data of core 1. For this case the statistical mean is $\langle\rho\rangle = 2.0312\ \mathrm{g/cm^3}$ and the standard deviation is $\sigma_\rho = 0.0585\ \mathrm{g/cm^3}$. If we fit the histogram with a normalized Gaussian distribution PDF,

$$p(x) = \exp\left(-\frac{(x-x_m)^2}{2\sigma_x^2}\right), \tag{12}$$

using $x_m = \langle\rho\rangle$ and $\sigma_x = \sigma_\rho$, we find the fitting poor (shown by the dashed curve in the figure). This poor fit is understandable, since the very large and very small density values are from shells and muds with variability governed by different random processes than for the density variation associated with the sand matrix alone.

To minimize the influence of extreme values in order to estimate the PDF of the density variation for the sand matrix alone, we employ the median absolute deviation (MAD) method.[17] In this approach, the mean value x_m is approximated by the median value $M(x_i) = 2.0271$ for this core, where $M(x_i)$ is the median for the sample set $\{x_i\}$. The standard deviation σ_x is estimated according to

$$\sigma_{\mathrm{MAD}} = \frac{M(|x_i - M(x_i)|)}{0.6745} = 0.0398, \tag{13}$$

where x_i are data points. The idea of the MAD method is to deemphasize the extreme data values. The Gaussian PDF estimated by the MAD method is also shown in Fig. 2 (solid curve). Note that data and the MAD model coincide in almost all regions of density; it is evident that the MAD fit is a superior approach to the one using the data mean and variance, indicating that the intrinsic variation of sand is probably Gaussian distributed.

If the PDF estimated using the MAD method indeed describes the intrinsic variation in sand, it should be the same for cores with the same statistics. To test this, we calculated the histogram for core 2. (Core 3 is not suitable for a consistency check owing to the presence of large regions of mud intrusion that would greatly influence its PDF.) The histograms of both cores along with the MAD PDF are given in Fig. 3. Since the median value of core 2 is slightly different from that of core 1, a shift of 0.02 of x_m for core 2 has been applied in the figure. Such a difference can result from the presence of a few more large shell pieces in one of the cores. As stated, shells will not change the PDFs of the intrinsic density variability. The fact that the same MAD PDF fits data from both core samples suggests that the intrinsic heterogeneity of sandy sediments in the studied region has a Gaussian distribution. Such intrinsic heterogeneity should be the result of random distribution of sand particles and random packing. Expressed in terms of a spectrum, the intrinsic heterogeneity should dictate the high-wave number portion of the spectra. In the future, this hypothesis can be tested when cores from sandy sediments without shells and muds become available.

IV. POWER SPECTRA ESTIMATION

In this section, we estimate the three-dimensional density spectrum and then obtain the two-and one-dimensional marginal spectra. A model will then be given for these spectra. Since statistical averaging is required to estimate a power spectrum, large sets of data from a statistically homogeneous pool are needed. Because of our limited data set, one might argue that our results are suspect. However, it will be shown that since the data do not show strong anisotropy, we assume the spectrum is isotropic. Therefore, estimating the one-dimensional marginal spectrum is sufficient to determine the three-dimensional spectrum. Because many parts of the three-dimensional spectrum are statistically independent, when reducing the three-dimensional spectrum to a one-dimensional spectrum, we effectively smoothed the estimate of the spectrum through averaging.

The three-dimensional power spectrum can be estimated from the data according to[18]

$$W(\mathbf{k}) = \lim_{L_x, L_y, L_z \to \infty} \frac{1}{(2\pi)^3 L_x L_y L_z} \times \left\langle \left| \int_0^{L_x} \int_0^{L_y} \int_0^{L_z} \hat{W}(\mathbf{R}) \cdot \epsilon(\mathbf{R}) \cdot e^{-i\boldsymbol{\kappa}\cdot\mathbf{R}} d^3 r \right|^2 \right\rangle, \tag{14}$$

where L_x, L_y, and L_z are the sampled physical dimensions of the cores and $\hat{W}(\mathbf{R})$ is a window function to help reduce spectral leakage. Throughout this paper we use meters as the length unit for all spectra, so the three-dimensional power spectrum has units of m^3. Numerically, let x, y, and z take on the discrete values as given by

$$\begin{aligned} &L_x = N_x \cdot \Delta x, \quad x = l\Delta x, \quad l = 0,1,2,...,(N_x - 1), \\ &L_y = N_y \cdot \Delta y, \quad y = m\Delta y, \quad m = 0,1,2,...,(N_y - 1), \\ &L_z = N_z \cdot \Delta z, \quad z = n\Delta z, \quad n = 0,1,2,...,(N_z - 1). \end{aligned} \tag{15}$$

As given earlier, $\Delta x = \Delta y = 0.25$ mm, $\Delta z = 2$ mm, $N_x = N_y = 190$, and N_z varies for each core. Accordingly, the three-dimensional wave number is defined as follows:

$$\begin{aligned} &\Delta k_x = 2\pi/(N_x \cdot \Delta x), \quad k_x = u\Delta k_x, \\ &u = -N_x/2,...,(N_x/2 - 1), \\ &\Delta k_y = 2\pi/(N_y \cdot \Delta y), \quad k_y = v\Delta k_y, \\ &v = -N_y/2,...,(N_y/2 - 1), \\ &\Delta k_z = 2\pi/(N_z \cdot \Delta z), \quad k_z = 2\Delta k_z, \\ &w = -N_z/2,...,(N_z/2 - 1). \end{aligned} \tag{16}$$

Then the numerical version of Eq. (14) can be written as

$$W_{u,v,w} = \frac{\Delta x \Delta y \Delta z}{(2\pi)^3 N_x N_y N_z} \times \left\langle \left| \sum_{l,m,n=0}^{N_x-1, N_y-1, N_z-1} \hat{W}_{l,m,n} \cdot \epsilon_{l,m,n} \cdot e^{-i2\pi[lu/N_x + mv/N_y + nw/N_z]} \right|^2 \right\rangle. \tag{17}$$

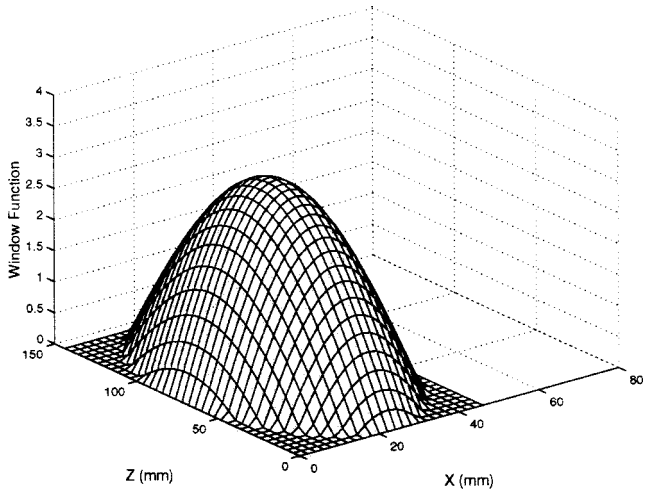

FIG. 4. A slice of the three-dimensional window $\hat{W}(x, y = L_y/2, z)$ applied to core 1.

Here we have chosen $\hat{W}$ to be a three-dimensional spheroidal window function. Since in our case $L_x = L_y < L_z$, the window is given by a prolate spheroid,

$$\hat{W}(x,y,z) = N^2 \cdot \frac{1}{2} \cdot \left[\cos\left(\frac{\pi}{L_x} \cdot P \right) + \left| \cos\left(\frac{\pi}{L_x} \cdot P \right) \right| \right], \tag{18}$$

where P is a scaled radius

$$P^2 = (x - L_x/2)^2 + (y - L_x/2)^2 + (z - L_z/2)^2 \cdot \left(\frac{L_x}{L_z} \right)^2, \tag{19}$$

and N is a normalization factor such that

$$\frac{1}{L_x \cdot L_y \cdot L_z} \int \int \int \hat{W}^2(x,y,z) dx dy dz = 1. \tag{20}$$

The absolute value employed in Eq. (18) guarantees that when $P > L_x/2$, $\hat{W} = 0$. In other words, data points lying outside the outermost layer of the spheroid are set to zero. Figure 4 shows a slice of the window so defined and applied to core 1.

For each core data set, a single realization of Eq. (17) is calculated and one three-dimensional estimate of the density power spectrum obtained. Figures 5 and 6 show three different two-dimensional slices of the three-dimensional spectrum for core 1. Figure 5 shows the $k_x - k_y$ view while holding k_z constant. The upper panel of Fig. 6 is the $k_y - k_z$ view when k_x is constant, and the lower panel shows the $k_x - k_z$ view when k_y is constant. The different length of the wave number axes results from different sampling rates; the different resolution between Figs. 5 and 6 is due to the difference in size between the horizontal (x and y) and the vertical (z) dimensions. Note also the horizontal and vertical axes have the same scales.

It is clear that the spectrum does not show appreciable anisotropy in the x-y plane for this core. There is a slight anisotropy between the horizontal and vertical axes. These are further evidenced by calculating the two-dimensional marginal spectra,

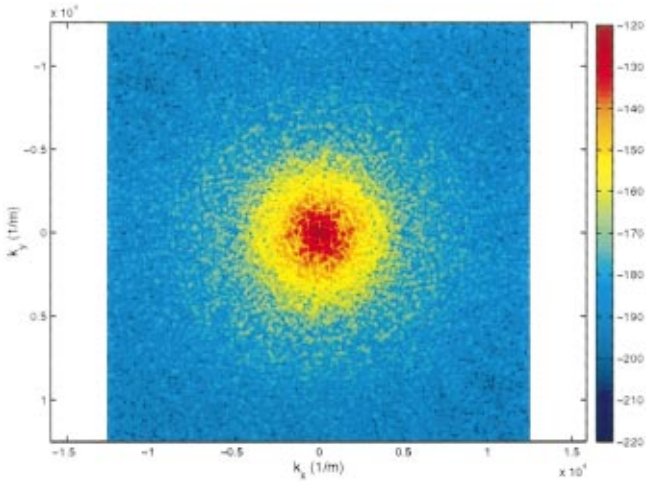

FIG. 5. A slice of the three-dimensional spectrum, $W(k_x, k_y, k_z = 0)$. Units are dB *re* 1 m^3.

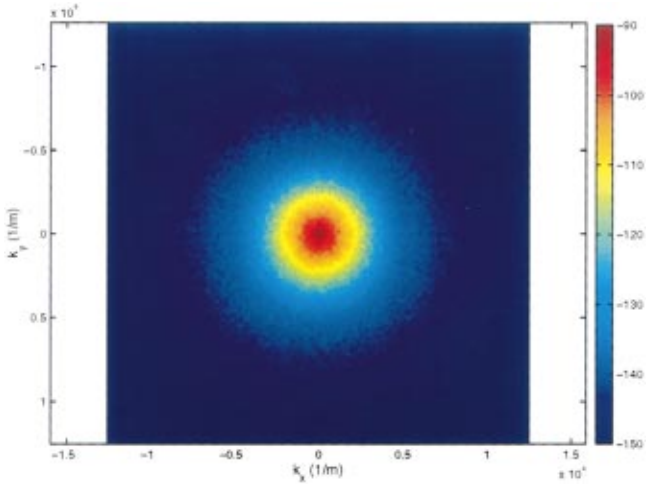

FIG. 7. Two-dimensional marginal spectrum $W(k_x, k_y)$. Units are dB *re* 1 m^2.

$$W_{u,v} = \Delta k_z \cdot \sum_{w=0}^{N_z - 1} W_{u,v,w},$$

$$W_{v,w} = \Delta k_x \cdot \sum_{u=0}^{N_x - 1} W_{u,v,w}, \tag{21}$$

$$W_{u,w} = \Delta k_y \cdot \sum_{v=0}^{N_y - 1} W_{u,v,w}.$$

These results are given in Figs. 7 and 8.

After collapsing the data to two dimensions, we find that the spectra are more smooth than the three-dimensional spectra, a result of averaging. The earlier observations on the spectral isotropy are unchanged. If we collapse the spectra further to one dimension according to

$$W_u = \Delta k_y \cdot \sum_{v=0}^{N_y - 1} W_{u,v},$$

$$W_v = \Delta k_x \cdot \sum_{u=0}^{N_x - 1} W_{u,v}, \tag{22}$$

$$W_w = \Delta k_y \cdot \sum_{v=0}^{N_y - 1} W_{u,w},$$

we arrive at the three one-dimensional marginal spectra plotted in Fig. 9. The circles and the solid curve are W_u and W_v, respectively, and the dots are W_w. Since W_u and W_v essentially coincide, it is clear that the random process is isotropic in the horizontal plane. There is a slight difference between W_w and the other spectra, but it is not significant. Also notice that there are few fluctuations in these curves, reflecting the fact that we have smoothed the spectra by reducing the three-dimensional spectrum to one dimension. We conclude that, for core 1, the density power spectrum is isotropic in the horizontal dimensions and slightly anisotropic between horizontal and vertical dimensions.

Since the anisotropy is not strong, we assume the spectrum can be represented by an isotropic spectrum. Therefore,

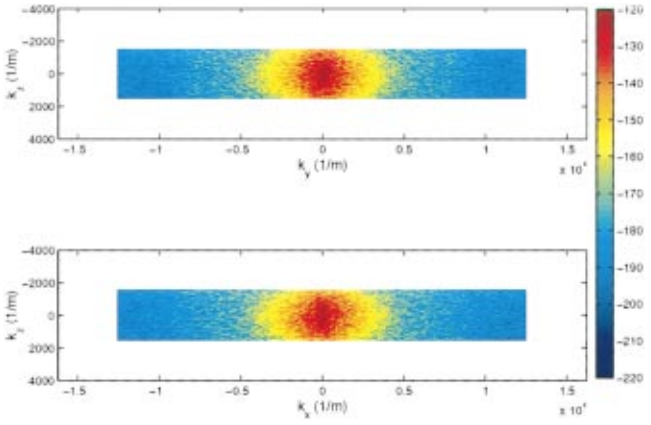

FIG. 6. A slice of the three-dimensional spectrum $W(k_x = 0, k_y, k_z)$ (top) and a perpendicular slice $W(k_x, k_y = 0, k_z)$ (bottom). Units are in dB *re* 1 m^3.

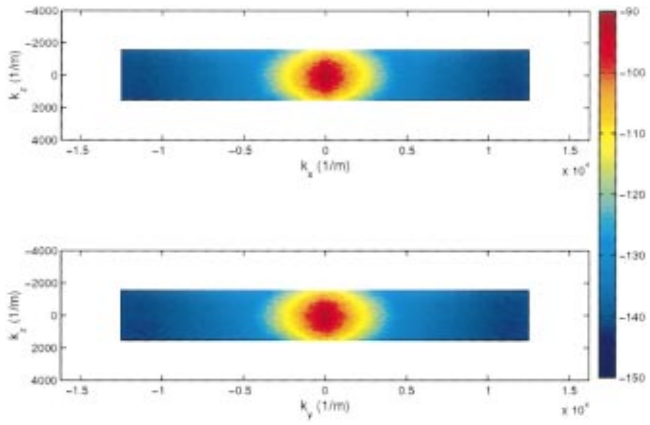

FIG. 8. Two-dimensional marginal spectra $W(k_x, k_z)$ (top) and $W(k_y, k_z)$ (bottom). Units are dB *re* 1 m^2.

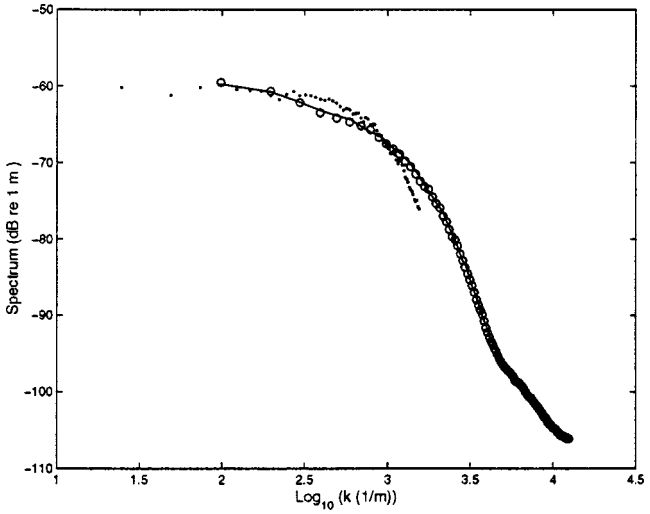

FIG. 9. One-dimensional spectra $W(k)$. Units are dB *re* 1 m. The circles and solid curve are one-dimensional marginal spectra W_x, W_y, and the dots are W_z.

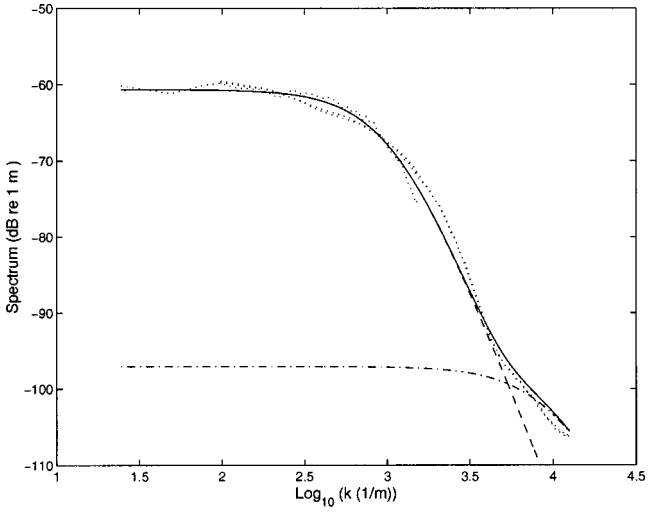

FIG. 10. One-dimensional spectrum. Units are dB *re* 1 m. The dots are the one-dimensional marginal spectra W_x, W_y, and W_z, the dashed curve is the first term in the model spectrum, the dash-dot curve is the second term, and the solid curve is the entire model spectrum.

a one-dimensional spectrum can represent the isotropic three-dimensional spectrum. Now we fit the one-dimensional spectra by an analytic form. Notice that there are two distinct trends in the spectra estimated from data. The approximate turning point dividing the two is given by $\log_{10} k = 3.5$. We fit the entire spectrum by two modified power-law terms,

$$W_{\text{model}-1\text{D}}(k) = \frac{a_1}{[1+(l_1 k)^2]^{\gamma_1}} + \frac{a_2}{[1+(l_2 k)^2]^{\gamma_2}}, \qquad (23)$$

where a_1, a_2, l_1, l_2, γ_1, and γ_2 are constants to be determined. An iterative optimization procedure was employed to determine these parameters from the three one-dimensional spectra for core 1. In this procedure, the parameters determining the spectral slopes, γ_1 and γ_2, were found first by comparing the model in Eq. (23) with data at large and small wave numbers. Then l_1 and l_2, which determine the outer scales of the two power-law terms in Eq. (23), were adjusted to fit the data. Finally, a_1 and a_2 were chosen to scale the model spectrum to fit the data in a least-square sense. The results were: $a_1 = 8.593 \times 10^{-7}$ m, $a_2 = 1.964 \times 10^{-10}$ m, $l_1 = 0.9$ mm, $l_2 = 0.1$ mm, $\gamma_1 = 2.8$, and $\gamma_2 = 2.1$. To make it easy to compare the modeled spectrum and those estimated from data, we have plotted $W_{\text{model}-1\text{D}}(k)$ along with the data in Fig. 10. All three one-dimensional marginal spectra from the data are shown by the dots. The first term of $W_{\text{model}-1\text{D}}(k)$ is shown by the dashed curve, the second term by the dash-dot curve, and the total model spectrum is given by the solid curve.

To test the universality of the spectrum modeled by Eq. (23), we processed data from core 2 following the same procedure applied to core 1. The resultant one-dimensional marginal spectra are plotted in Fig. 11 against the modeled spectrum for core 1. Without any adjustments of the model parameters, the fit of the model spectrum to the new data set is remarkable. The match indicates that the modeled spectrum is a fair abstraction of the random processes for both cores. Stated differently, we can conclude that fluctuations in cores 1 and 2 are due to the same random process.

Before considering core 3, which contains a mud intrusion, we propose mechanisms that control the power spectrum. We assume that the small wave number portion of the spectrum is dominated by large-scale fluctuations, in our case, the shell pieces and muds, whereas the large wave number portion is determined by the intrinsic variations of sand. To test this assumption, we visually selected portions of data from cores 1 and 2, where shells were not apparent, as our shell-free data sets. We then directly calculated the one-dimensional spectra of these data subsets; those spectra are statistically the same as the one-dimensional marginal spectra. If our assumption is correct, the spectra for the shell-free data should agree with the spectrum modeled by Eq. (23) at large wave numbers and diverge from the model at small wave numbers. In Fig. 12, the shell-free spectra for each of the two cores are plotted along with the model spectrum. Indeed, the shell-free spectra behave consistently with our assumption.

Now we turn our attention to core 3, which contained a

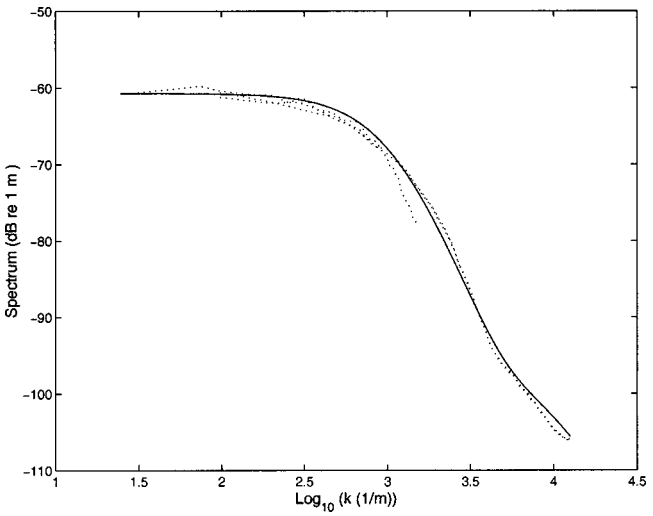

FIG. 11. Same as Fig. 10, but for core 2.

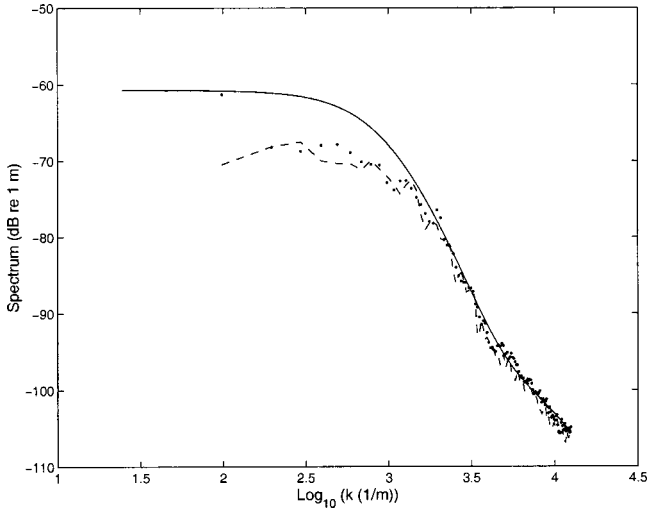

FIG. 12. Comparison of shell-free spectra with the modeled spectrum. Dots are for core 1 data, dashes are for core 2 data, and the solid curve is for the model from Eq. (23).

substantial mud intrusion. The one-dimensional marginal spectra are again calculated and shown in Fig. 13. Note that (1) the marginal spectra show that core 3 is again approximately isotropic, and (2) the modeled spectrum without the mud intrusion no longer fits the data. At high wave numbers, however, although the fits are not good, the spectral decay rate (the slope) is still close to that of the model; at low wave numbers, the model underpredicts the spectrum, an easily understandable result because the mud intrusion introduces additional fluctuations at large spatial scales. Since the size of our cores is smaller than the size of the mud intrusion, we are effectively facing a nonstationary process. Therefore it will not be possible to estimate the spectrum including the mud effects; larger cores are needed for that purpose. But again, since the high-wave number decay rate matches the model, which is derived from data with no mud intrusion, the results for core 3 support our conclusion based on analysis on cores 1 and 2, namely, that the high-wave number portion

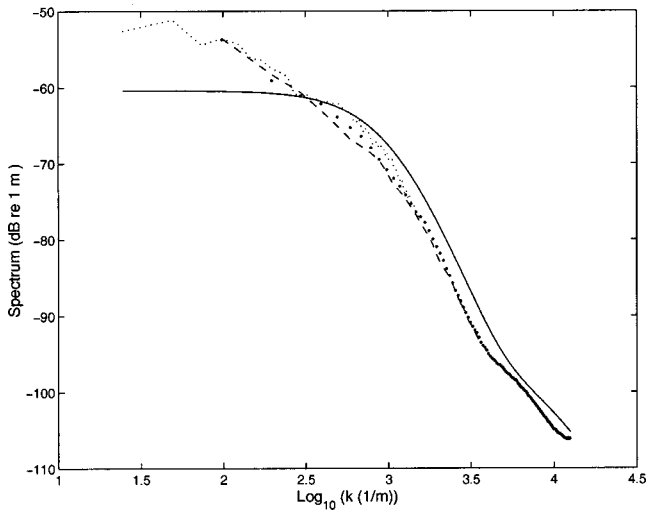

FIG. 13. Same as Fig. 10, but for core 3. The dark dots are for W_u, the dashes are for W_v, and the light dots are for W_w. Again, the solid curve is the model.

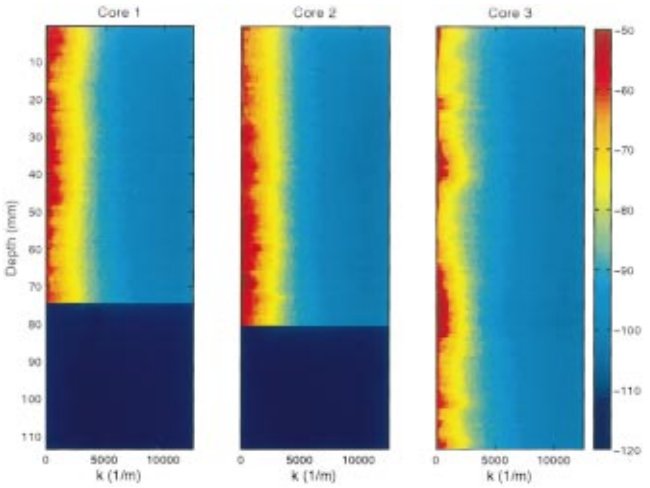

FIG. 14. Depth dependence of 1D spectra for cores 1, 2, and 3. Units are dB *re* 1 m.

of the spectrum depends on intrinsic fluctuations of sand.

Before concluding this section, we investigate the depth-dependence of the one-dimensional spectra of each core. At each depth z, we calculated the one-dimensional marginal spectrum using the two-dimensional data, and the results are presented in Fig. 14. The results for cores 1 and 2 have a weak depth dependence, whereas for core 3, the depth dependence is much stronger.

We end this section with the following conclusions:

(1) When mud intrusions are absent, the modeled spectrum given in Eq. (23) describes well the fluctuations due to two distinct factors, shell pieces and mud mixtures, and the intrinsic variations associated with sand; the former influences the lower portion of the spectrum, and the latter the higher portion.

(2) When mud intrusions are present, the modeled spectrum based on cores without mud intrusions no longer agrees with the data. Larger sized cores are needed to estimate the spectrum including mud intrusion effects. However, the similarity of the spectra at high wave number hints that even when a mud intrusion is present, the spectrum at high wave number is still dominated by the intrinsic variations of sand.

(3) An exponential correlation function has often been applied to sediment density variations for the acoustic backscattering model at the 10–50 kHz range.[1,3,6] Therefore, it is interesting to compare the exponential correlation function to the one corresponding to that given by Eq. (23). At this frequency range, the comparable portion of the modeled spectrum is the first term of Eq. (23). Note that for an exponential correlation function, the spectral slope is $2\gamma_1 = 4$. However, the value we have found is $2\gamma_1 = 5.6$, much higher than the exponential case, implying that there is a lack of scatterers at small scales compared to common assumption. It will be interesting to extend the spectral estimation to even higher wave numbers so that intergrain heterogeneities can be revealed.

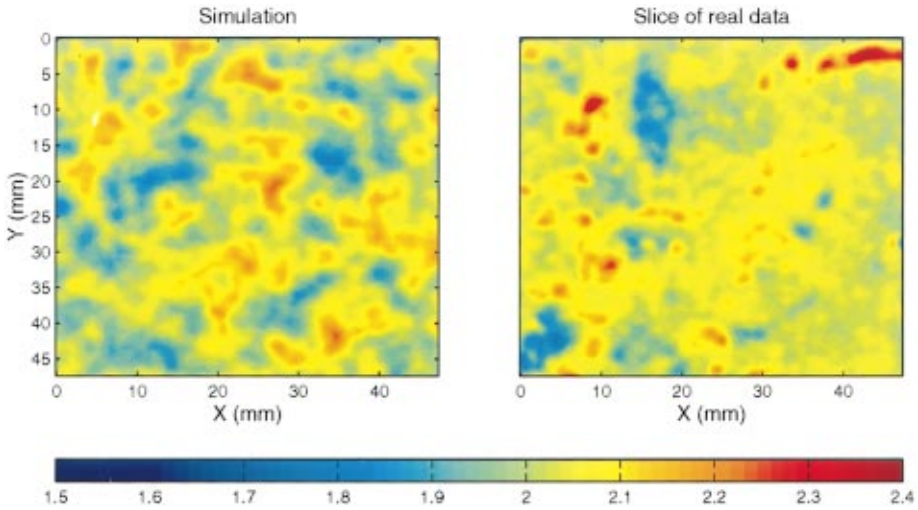

FIG. 15. A slice of a three-dimensional Monte Carlo simulation of density based on the model spectrum in Eq. (25) is on the left. On the right is a slice of data from core 1. Units are g/cm^3.

V. IMPLICATIONS FOR THE SCATTERING CROSS SECTION

We have modeled the density variation as an isotropic process with a one-dimensional power spectrum given by Eq. (23). For an isotropic process, its three-dimensional power spectrum can be conveniently expressed through its one-dimensional spectrum by[19]

$$W_{3D}(k) = -\frac{1}{2\pi k}\frac{dW_{1D}}{dk}. \tag{24}$$

Therefore, the model for the three-dimensional power spectrum can be easily found to be

$$W_{\text{model}-3D}(k) = \frac{l_1^2\gamma_1}{\pi}\cdot\frac{a_1}{[1+(l_1k)^2]^{\gamma_1+1}} + \frac{l_2^2\gamma_2}{\pi}\cdot\frac{a_2}{[1+(l_2k)^2]^{\gamma_2+1}}. \tag{25}$$

Now, Monte Carlo realizations of density variations can be obtained from[18]

$$f_{lmn} = \frac{1}{L_xL_yL_z}\sum_{u=-N_x/2}^{N_x/2-1}\sum_{v=-N_y/2}^{N_y/2-1}\sum_{w=-N_z/2}^{N_z/2-1} F_{uvw}\cdot e^{-i2\pi[lu/N_x+mv/N_y+nw/N_z]}, \tag{26}$$

where

$$F_{uvw} = \sqrt{(2\pi)^3L_xL_yL_zW_{uvw}}\cdot R_{uvw} \tag{27}$$

and R_{uvw} is a three-dimensional Gaussian random vector with zero-mean and unit variance and satisfies

$$R^*_{-u-v-w} = R_{uvw}. \tag{28}$$

So we have

$$R_{uvw} = \frac{N(0,1)+iN(0,1)}{\sqrt{2}} \quad u,v,w \neq N/2,0,$$
$$R_{uvw} = N(0,1) \quad u,v,w = N/2,0, \tag{29}$$

where $N(0,1)$ are independent, zero-mean, and unit variance Gaussian random variables. When f_{lmn} is calculated, a density realization is given by

$$\rho_{lmn} = \langle\rho\rangle(1+f_{lmn}). \tag{30}$$

The left panel of Fig. 15 shows a slice of the three-dimensional realization based on the model spectrum given by Eq. (25). On the right is a slice of data from core 1 for comparison. The color scales are the same for both panels and are the same as in Fig. 1. While the overall patchiness and the fluctuation amplitude in the realization are captured by the simulation, the highlights due to shell pieces are not as well represented in the simulation. The simulated realization has been constructed to produce a Gaussian random process that obeys the prescribed power spectrum; thus, any non-Gaussian features will be missed. As indicated before, the shell pieces and muds contribute a non-Gaussian component in addition to the Gaussian PDF due to intrinsic density variations of sand alone. If first-order perturbation theory is valid, the spectrum is sufficient to model the scattered sound field. However, if multiple scattering has to be considered, higher-order statistics of the random process have to be properly incorporated.

Recalling Eqs. (11) and (9), we can apply the modeled power spectrum in Eq. (25) to study the frequency dependence of the acoustic scattering cross section. For the special case of backscatter the frequency dependence of the cross section is

$$\sigma(f,\theta=\pi) = \frac{|k|^4}{(4\pi)^2}\cdot(\mu^2+1-2\mu)\cdot W_\rho(2|k|). \tag{31}$$

In Fig. 16 we plot the modeled three-dimensional power spectrum from Eq. (25) versus wave number. Superimposed on the figure are the corresponding frequencies for backscatter. Based on our earlier argument, we find that shell pieces and mud mixtures dominate the backscattering in the frequency range of 10–100 kHz. Only at the very high frequencies ($f > 400$ kHz) will intrinsic heterogeneity dominate backscatter.

Figure 17 shows the backscattering cross section as a function of frequency. Two values of μ, $\mu = -1$ and $\mu = -2.44$,[1] are shown since they have been cited in previous publications. Note that the backscattering cross section peaks at around 140 kHz. At lower frequencies, the factor of k^4 in Eq. (31) results in a scattering cross section similar to that of

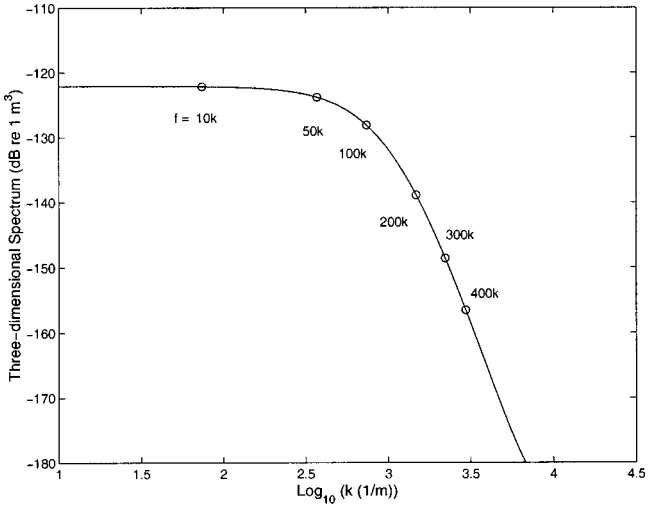

FIG. 16. Modeled three-dimensional power spectrum in dB *re* 1 m^3. The circles are the corresponding acoustic frequencies for backscattering when sound speed is set to be 1700 m/s. The frequency unit k denotes kHz.

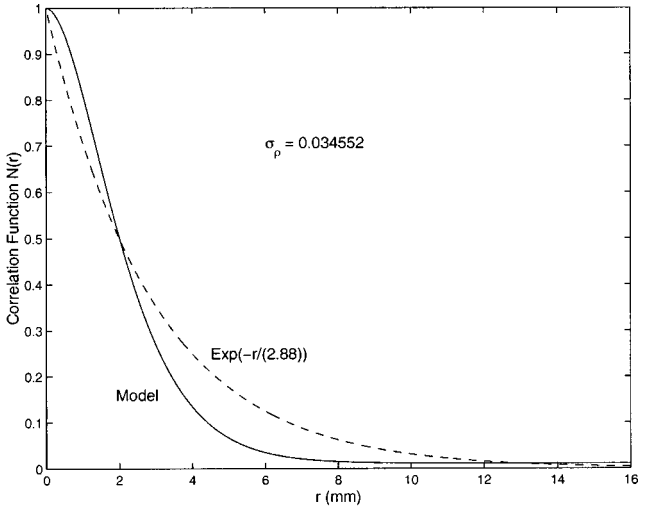

FIG. 18. Correlation function comparison. The solid curve is for the model based on Eq. (32) normalized by σ_ρ^2. Dashed curve is for an exponential correlation function with a correlation length of 2.88 mm.

Rayleigh scattering due to small particles. The reduction in the scattering cross section at higher frequencies is the result of the rapid falloff of the spectrum for large k (large γ_1). Also note that the choice of μ can have a profound influence on the level of the scattering cross section. This highlights the need to measure μ directly and reliably to complete the model of bottom volume scattering.

Before ending this section, we discuss a companion quantity of the power spectrum, i.e., the spatial correlation function. According to the definition in Eq. (7), the correlation function $N(r)$ is related to the power spectrum through an inverse Fourier transform. Since the spectrum we have modeled is isotropic, $N(r)$ can be conveniently determined by the one-dimensional transform of $W_{\text{model}-1\text{D}}$ in Eq. (23),

$$N(r)=\int_{-\infty}^{\infty} W_{\text{model}-1\text{D}}(k)e^{ikr}dk. \tag{32}$$

It is found from numerical integration based on Eq. (32) that $\sigma_\rho^2=N(0)=0.0012$, or $\sigma_\rho=0.0346$, or 3.46%. Since the exponential correlation function has often been assumed,[1,3] we will make a comparison between it and the results from Eq. (32). The exponential correlation function has the form

$$N(r)=\sigma_\rho^2 e^{-r/l}, \tag{33}$$

and its corresponding one- and three-dimensional spectra are

$$W_1(k)=\frac{\sigma_\rho^2}{\pi}\frac{l}{[1+(kl)^2]},$$
$$W_3(k)=\frac{\sigma_\rho^2}{\pi^2}\frac{l^3}{[1+(kl)^2]^2}. \tag{34}$$

Compared to spectra in Eq. (34), the spectra predicted by Eqs. (23) and (25) decay much faster at large wave numbers than the spectra for an exponential correlation function. This can also be seen in a comparison of the correlation functions. Figure 18 plots the correlation function normalized by σ_ρ^2. The solid curve is for the model, and the dashed curve is for an exponential correlation function with a correlation length of $l=2.88$. This correlation length was chosen so that the exponential correlation function and the modeled correlation function would be equal at their 50% levels. It is evident that the correlation function of the model is significantly different from the exponential correlation function.

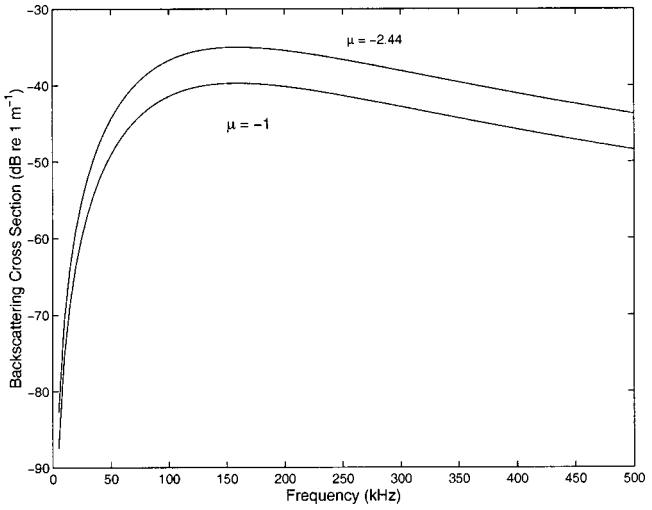

FIG. 17. Backscattering cross section versus frequency.

VI. SUMMARY

In this paper we have estimated sediment density power spectra based on cores subjected to x-ray CT scans. As is well known, sandy cores are difficult to retrieve without disturbance. Our analysis relied on cores which, although handled with care, were not in pristine condition. Therefore, the following conclusions should be considered preliminary and tentative. In the future, core data need to be compared with *in situ* data to assess the effect of disturbance. Another improvement would be to increase the size of the cores to extend the spectral estimation to lower wave numbers. Since the data sets have a high spatial resolution and are three

dimensional, the estimated spectra cover about three orders of magnitude in wave number. We can conclude the following:

(1) There are three mechanisms causing variability in the sandy sediments off Panama City: shell pieces, mud mixtures, and the intrinsic variability of the sand matrix. All three demonstrate isotropy in the horizontal plane and approximate isotropy in the vertical direction relative to the horizontal plane.
(2) The intrinsic variability is consistent with a Gaussian distribution.
(3) Shells and mud mixtures dominate the low-wave number portion of the spectrum, whereas intrinsic variability dominates the high-wave number portion.
(4) An analytical model with two power-law terms describes well the inferred spectrum. The exponent of the first power-law term in the spectrum is much higher than previously believed. This has direct implications to acoustic backscattering at 10–50 kHz.
(5) Variability due to mud intrusions and its implications for the power spectrum cannot be properly addressed given the insufficient size of the cores used here. However, there are indications that the high-wave number portion of the spectrum is still dominated by intrinsic variability of the sand.
(6) Monte Carlo simulations of sediment density variation based on the inferred spectrum suggest that while the overall patchiness and the fluctuation amplitude in the realizations are captured by the simulation, highlights due to shell pieces and mud patches are not well represented. An investigation into the probability distribution of shells, including their sizes, spatial distribution and, possibly, their orientations, would be informative.
(7) In the case of backscatter, the relationship between the power spectrum and the acoustic frequency shows that between 10–100 kHz, backscatter will be strongly influenced by the presence of shell pieces and mud mixtures. Intrinsic variability influences backscatter at frequencies above 400 kHz. In addition, when the frequency is lower than 70 kHz, the backscattering cross section behaves like that of a Rayleigh scatterer.

ACKNOWLEDGMENTS

We thank Mike Richardson and Kevin Briggs, who provided the cores for this study. We are grateful to Don Percival for his help on the MAD estimates and other useful discussions on statistics. We feel especially indebted to Eric Thorsos, who made critical suggestions and careful editing which improved the quality of this paper. Thanks also to Program Managers Jeff Simmen and Joe Kravitz, Office of Naval Research, for their support of this study.

[1] D. R. Jackson, K. B. Briggs, K. L. Williams, and M. D. Richardson, ''Tests of models for high-frequency seafloor backscatter,'' IEEE J. Ocean Eng. **21**, 458–470 (1996).
[2] A. N. Ivakin and Yu. P. Lysanov, ''Theory of underwater sound scattering by random inhomogeneities of the bottom,'' Sov. Phys. Acoust. **27**, 61–64 (1981).
[3] P. C. Hines, ''Theoretical model of acoustic backscatter from a smooth seabed,'' J. Acoust. Soc. Am. **88**, 324–334 (1990).
[4] A. P. Lyons, A. L. Anderson, and F. S. Dwan, ''Acoustic scattering from the seafloor: Modeling and data comparison,'' J. Acoust. Soc. Am. **95**, 2441–2451 (1994).
[5] D. Tang, G. V. Frisk, C. J. Sellers, and D. Li, ''Low-frequency acoustic backscattering by volume inhomogeneities in deep-ocean sediments,'' J. Acoust. Soc. Am. **98**, 508–516 (1995).
[6] T. Yamamoto, ''Velocity variabilities and other physical properties of marine sediments measured by crosswell acoustic tomography,'' J. Acoust. Soc. Am. **98**, 2235–2248 (1995).
[7] T. Yamamoto, ''Acoustic scattering in the ocean from velocity and density fluctuations in the sediments,'' J. Acoust. Soc. Am. **99**, 866–879 (1996).
[8] K. B. Briggs, P. D. Jackson, R. J. Holyer, R. C. Flint, J. C. Sandidge, and D. K. Young, ''Two-dimensional variability in porosity, density, and electrical resistivity of Echernfoerde Bay sediment,'' Cont. Shelf Res. **18**, 1939–1964 (1998).
[9] P. D. Jackson, K. B. Briggs, and R. C. Flint, ''Evaluation of sediment heterogeneity using microresistivity imaging and x-radiography,'' Geomarine Lett. **16**, 219–225 (1996).
[10] A. N. Ivakin and D. R. Jackson, ''Effect of shear elasticity on seabed scattering, numerical examples,'' J. Acoust. Soc. Am. **103**, 346–354 (1998).
[11] D. R. Jackson, ''Models for scattering from the sea bed,'' Proc. Inst. Acoust. **16**, 161–169 (1994).
[12] L. A. Chernov, *Wave Propagation in a Random Medium* (McGraw-Hill, New York, 1960), translated from Russian by R. A. Silverman.
[13] M. D. Richardson and W. R. Bryant, ''Benthic boundary layer processes in coastal environments: An introduction,'' Geomarine Lett. **16**, 133–139 (1996).
[14] T. H. Orsi, ''Computed tomography of macrostructure and physical property variability of seafloor sediments,'' Ph.D. dissertation, Texas A&M University, College Station, Texas, 1994.
[15] T. H. Orsi and A. L. Anderson, ''Bulk density calibration for X-ray tomographic analyses of marine sediments,'' Geo-Marine Lett. **19**, 270–274 (1999).
[16] A. P. Lyons and T. H. Orsi, ''The effect of a layer of varying density on high-frequency reflection, forward loss, and backscatter,'' IEEE J. Ocean Eng. **23**, 411–422 (1998).
[17] R. V. Hogg, ''An introduction to robust estimation,'' in *Robustness in Statistics*, edited by R. L. Launer and G. N. Wilkinson (Academic, New York, 1979).
[18] M. B. Priestly, *Spectral Analysis and Time Series* (Academic, New York, 1981).
[19] A. Ishimaru, *Wave Propagation and Scattering in Random Media* (IEEE, New York 1997), p. 509.

An energy-conserving spectral solution

Michael D. Collins[a)]
Naval Research Laboratory, Washington, D.C. 20375

Henrik Schmidt
Massachusetts Institute of Technology, Cambridge, Massachusetts 02139

William L. Siegmann
Rensselaer Polytechnic Institute, Troy, New York 12180

(Received 10 June 1999; accepted for publication 15 December 1999)

An energy-conserving spectral solution is derived and tested. A range-dependent medium is approximated by a sequence of range-independent regions. In each region, the acoustic field is represented in terms of the horizontal wave-number spectrum. A condition corresponding to energy conservation is derived for the vertical interfaces between regions. The accuracy of the approach is demonstrated for problems involving sloping ocean bottoms. The energy-conserving spectral solution is less efficient than the energy-conserving parabolic equation solution, but might be suitable for generalization to problems involving elastic bottoms. © *2000 Acoustical Society of America.* [S0001-4966(00)00704-9]

PACS numbers: 43.30.Bp, 43.30.Dr, 43.30.Gv [SAC-B]

INTRODUCTION

Several approaches have been developed for solving range-dependent propagation problems in ocean acoustics. Range-dependent normal-mode[1] and spectral[2] solutions are based on a local separation of variables. It is important to continue to develop these approaches despite the fact that the parabolic equation method[3] usually provides greater efficiency by avoiding the field decomposition. All three of these approaches are based on the approximation of a range-dependent medium by a sequence of range-independent regions. Accurate solutions can be obtained for many problems by applying single-scattering[4] or energy-conservation[5,6] conditions at the vertical interfaces between regions. Although some progress has been made for problems involving elastic sediments,[7–11] no existing approach provides the level of accuracy and efficiency that has been achieved for problems involving fluid sediments. In this paper, we derive an energy-conserving spectral solution for problems involving fluid sediments. It might be possible to extend this approach to the elastic case. An interface condition for conserving energy is described in Sec. I. The derivation of the energy-conserving spectral solution is presented in Sec. II. Examples are presented in Sec. III.

I. ENERGY CONSERVATION

In this section, we discuss background material and derive the complete energy-conservation correction,[8] which is accurate for problems involving gradual range dependence and a wide spectrum of horizontal wave numbers. We work in the frequency domain and consider the case of a line source in plane geometry, where the range x is the horizontal distance from the source and z is the depth below the ocean surface. Minor modifications are required for the more realistic case of a point source in cylindrical geometry.[12] A range-dependent medium is approximated by a sequence of range-independent regions. In each region, the acoustic pressure p satisfies the wave equation,

$$\frac{\partial^2 p}{\partial x^2} + Lp = 2\,\delta(x)\,\delta(z - z_0), \tag{1}$$

$$L = \rho \frac{\partial}{\partial z} \frac{1}{\rho} \frac{\partial}{\partial z} + k^2, \tag{2}$$

where ρ is the density, k is the wave number, and z_0 is the source depth. Away from the source, we factor the operator in Eq. (1) into a product of outgoing and incoming operators to obtain

$$\left(\frac{\partial}{\partial x} + iL^{1/2} \right) \left(\frac{\partial}{\partial x} - iL^{1/2} \right) p = 0. \tag{3}$$

Assuming that outgoing energy dominates incoming energy, we obtain the parabolic equation,

$$\frac{\partial p}{\partial x} = iL^{1/2} p. \tag{4}$$

To completely define the solution, it is necessary to specify conditions at the vertical interfaces between regions. Since the parabolic equation contains only one range derivative, it is not possible to conserve both pressure and particle velocity across the vertical interfaces. Accurate solutions can be obtained for many problems by conserving the energy flux,

$$E = \mathrm{Im} \int \rho^{-1} p^* \frac{\partial p}{\partial x}\, dz. \tag{5}$$

The direct application of Eq. (5) would lead to a nonlinear interface condition. To obtain a linear condition, we apply the modal representation,[13]

a)Electronic mail: collins@noddy.nrl.navy.mil

$$p(x,z)=\sum_n a_n\phi_n(z)\exp(ik_nx), \tag{6}$$

in each range-independent region, where the a_n are constants and the nth mode $\phi_n(z)$ and eigenvalue k_n^2 satisfy the equations,

$$L\phi_n=k_n^2\phi_n, \tag{7}$$

$$\int \rho^{-1}\phi_m\phi_n\,dz=\delta_{mn}. \tag{8}$$

Substituting the normal-mode representation into Eq. (5) and using the properties of the modes, we obtain

$$E=\mathrm{Re}\int \rho^{-1}p^*L^{1/2}p\,dz=\int |\rho^{-1/2}L^{1/4}p|^2dz, \tag{9}$$

and conclude that the energy flux can be conserved by conserving $\rho^{-1/2}L^{1/4}p$ across the vertical interfaces.

II. THE SPECTRAL SOLUTION

In this section, we describe the energy-conserving spectral solution. The subscript j is used to denote evaluation in the jth range-independent region, which corresponds to $x_j<x<x_{j+1}$. We express the acoustic pressure in terms of the wave-number representation,[14]

$$p_j(x,z)=\frac{1}{2\pi}\int_{-\infty}^{\infty}\hat{p}_j(h,z)\exp(ih(x-x_j))dh, \tag{10}$$

where $\hat{p}_j$ is the wave-number spectrum. In the first region, the spectrum satisfies

$$(L_1-h^2)\hat{p}_1=2\delta(z-z_0). \tag{11}$$

We define the fields $F_j(x,z)$ and $G_{j+1}(x,z)$ by the equations,

$$F_j(x,z)=L_j^{1/4}p_j$$
$$=\frac{1}{2\pi}\int_{-\infty}^{\infty}h^{1/2}\hat{p}_j(h,z)\exp(ih(x-x_j))dh, \tag{12}$$

$$\frac{\partial^2G_{j+1}}{\partial x^2}+L_{j+1}G_{j+1}=2\delta(x-x_{j+1})F_j(x_{j+1},z). \tag{13}$$

The spectral solution of Eq. (13) is

$$G_{j+1}(x,z)=\frac{1}{2\pi}\int_{-\infty}^{\infty}\hat{G}_{j+1}(h,z)\exp(ih(x-x_{j+1}))dh, \tag{14}$$

$$(L_{j+1}-h^2)\hat{G}_{j+1}=2F_j(x_{j+1},z). \tag{15}$$

Integrating Eq. (13) over an arbitrarily small interval about $x=x_{j+1}$, we obtain

$$\frac{\partial G_{j+1}}{\partial x}(x_{j+1},z)=F_j(x_{j+1},z). \tag{16}$$

From Eq. (14), we obtain

$$\frac{\partial G_{j+1}}{\partial x}=\frac{i}{2\pi}\int_{-\infty}^{\infty}h\hat{G}_{j+1}(h,z)\exp(ih(x-x_{j+1}))dh. \tag{17}$$

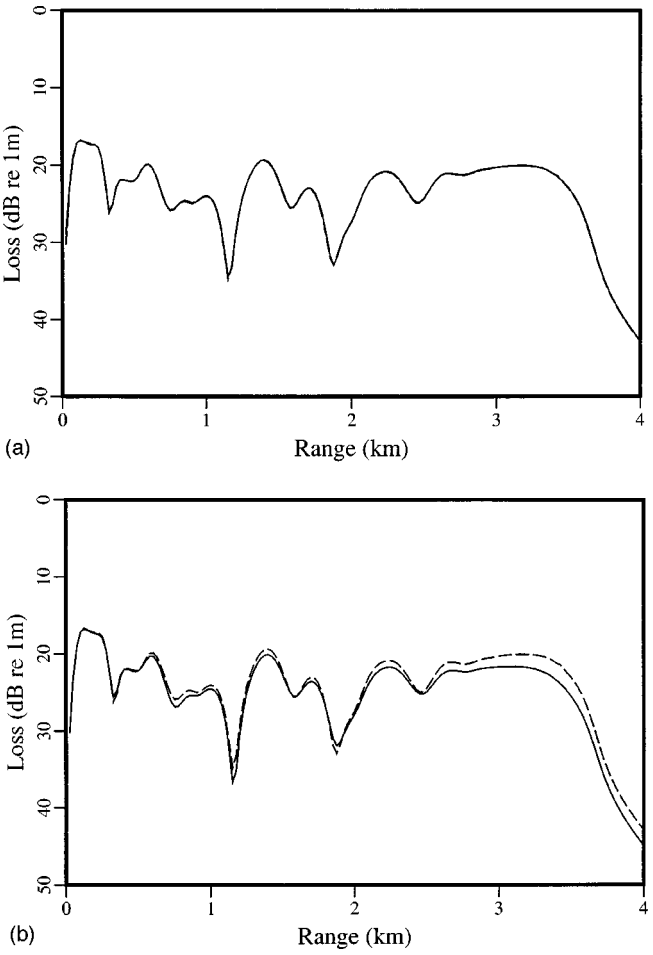

FIG. 1. Transmission loss for example *A*, which involves a 25-Hz source in a water column that decreases in depth with range. The dashed curves correspond to a reference solution that was generated using the energy-conserving parabolic equation. (a) The energy-conserving spectral solution (solid curve) is in agreement with the reference solution. (b) The pressure-conserving solution (solid curve) contains a negative amplitude error.

Setting $\rho_{j+1}^{-1/2}F_{j+1}(x_{j+1},z)=\rho_j^{-1/2}F_j(x_{j+1},z)$ and applying Eqs. (12), (16), and (17), we obtain

$$i\rho_j^{-1/2}h\hat{G}_{j+1}=\rho_{j+1}^{-1/2}h^{1/2}\hat{p}_{j+1}. \tag{18}$$

From Eqs. (15) and (18), we obtain

$$\hat{p}_{j+1}=2i\rho_{j+1}^{1/2}\rho_j^{-1/2}h^{1/2}(L_{j+1}-h^2)^{-1}F_j(x_{j+1},z). \tag{19}$$

The energy-conserving solution is generated using Eqs. (12) and (19).

III. IMPLEMENTATION AND EXAMPLES

To obtain a stable solution, it is necessary to choose the integration contour carefully. We have obtained good results using an integration contour that consists of five linear segments. The endpoints of the segments are $h=i\epsilon$, $h=0$, $h=h_a$, $h=h_a-i\delta$, $h=h_b-i\delta$, and $h=h_b+i\epsilon$. The wave numbers h_a and h_b are selected so that the sharp peaks in the spectrum lie between these values. The small parameters ϵ and δ are selected so that the integrand is negligible for $\mathrm{Im}(h)>\epsilon$ and to avoid the peaks in the spectrum in the region $h_a<\mathrm{Re}(h)<h_b$. For the examples, we use values of h_a and h_b that correspond to horizontal phase speeds of 1400 m/s

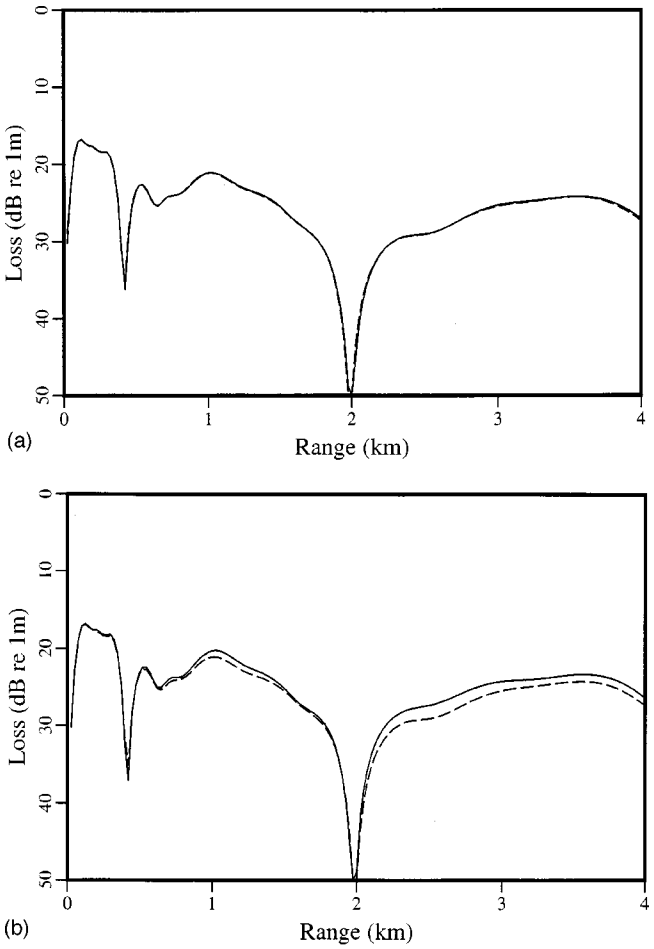

FIG. 2. Transmission loss for example *B*, which involves a 25-Hz source in a water column that increases in depth with range. The dashed curves correspond to a reference solution that was generated using the energy-conserving parabolic equation. (a) The energy-conserving spectral solution (solid curve) is in agreement with the reference solution. (b) The pressure-conserving solution (solid curve) contains a positive amplitude error.

and 1800 m/s. Reference solutions were generated using a parabolic equation implemented with the complete energy-conservation correction.

Example *A* is identical to the wedge benchmark problem[15] with the exception that we consider a line source in plane geometry. This problem involves a 25-Hz source at $z=100$ m in a water column in which $c=1500$ m/s. The ocean depth decreases linearly from 200 m at the source location to zero at $x=4$ km. In the sediment, $c=1700$ m/s, $\rho=1.5$ g/cm^3, and the attenuation is 0.5 dB/λ. Transmission loss for example *A* appears in Fig. 1. The energy-conserving spectral solution is in agreement with the reference solution. The pressure-conserving solution contains a negative amplitude error. Example *B* is identical to example *A*, with the exception that the ocean depth increases linearly to 400 m at $x=4$ km. Transmission loss for example *B* appears in Fig. 2. The energy-conserving spectral solution is in agreement with the reference solution. The pressure-conserving solution contains a positive amplitude error.

IV. CONCLUSION

An energy-conserving spectral solution has been derived and tested. The complete energy-conservation correction is applied at vertical interfaces in two steps. A quantity that is related to the pressure by the fourth root of the depth operator is first computed using a spectral integral. The forcing function for the spectrum in the next range-independent region is composed of this quantity plus factors of the square roots of density and horizontal wave number. The accuracy of the energy-conserving spectral solution was demonstrated for problems involving sloping ocean bottoms. Although this approach is not as efficient as the energy-conserving parabolic equation, it might be easier to generalize to the elastic case, which is an important unresolved problem.

ACKNOWLEDGMENT

This work was supported by the Office of Naval Research.

[1] R. B. Evans, ''A coupled mode solution for acoustic propagation in a waveguide with stepwise depth variations of a penetrable bottom,'' J. Acoust. Soc. Am. **74**, 188–195 (1983).
[2] K. E. Gilbert and R. B. Evans, ''A Green's function method for one-way wave propagation in a range-dependent ocean environment,'' in *Ocean Seismo-Acoustics*, edited by T. Akal and J. M. Berkson (Plenum, New York, 1986).
[3] F. B. Jensen, W. A. Kuperman, M. B. Porter, and H. Schmidt, *Computational Ocean Acoustics* (American Institute of Physics, New York, 1994), pp. 343–412.
[4] M. D. Collins and R. B. Evans, ''A two-way parabolic equation for acoustic backscattering in the ocean,'' J. Acoust. Soc. Am. **91**, 1357–1368 (1992).
[5] M. B. Porter, F. B. Jensen, and C. M. Ferla, ''The problem of energy conservation in one-way models,'' J. Acoust. Soc. Am. **89**, 1058–1067 (1991).
[6] M. D. Collins and E. K. Westwood, ''A higher-order energy-conserving parabolic equation for range-dependent ocean depth, sound speed, and density,'' J. Acoust. Soc. Am. **89**, 1068–1075 (1991).
[7] M. D. Collins, ''A two-way parabolic equation for elastic media,'' J. Acoust. Soc. Am. **93**, 1815–1825 (1993).
[8] M. D. Collins, ''An energy-conserving parabolic equation for elastic media,'' J. Acoust. Soc. Am. **94**, 975–982 (1993).
[9] H. Schmidt, W. Seong, and J. T. Goh, ''Spectral super-element approach to range-dependent ocean acoustic modeling,'' J. Acoust. Soc. Am. **98**, 465–472 (1995).
[10] J. T. Goh and H. Schmidt, ''A hybrid coupled wave-number integration approach to range-dependent seismoacoustic modeling,'' J. Acoust. Soc. Am. **100**, 1409–1420 (1996).
[11] M. D. Collins and W. L. Siegmann, ''A complete energy conservation correction for the elastic parabolic equation,'' J. Acoust. Soc. Am. **105**, 687–692 (1999).
[12] Reference 3, pp. 272–277.
[13] Reference 3, pp. 271–341.
[14] Reference 3, pp. 203–269.
[15] F. B. Jensen and C. M. Ferla, ''Numerical solutions of range-dependent benchmark problems,'' J. Acoust. Soc. Am. **87**, 1499–1510 (1990).

Hybrid geoacoustic inversion of broadband Mediterranean Sea data

Mark R. Fallat[a)]
School of Earth and Ocean Sciences, University of Victoria, Victoria, British Columbia V8W 3P6, Canada

Peter L. Nielsen
SACLANT Undersea Research Centre, Viale S. Bartolomeo, 400 19138 La Spezia, Italy

Stan E. Dosso
School of Earth and Ocean Sciences, University of Victoria, Victoria, British Columbia V8W 3P6, Canada

(Received 7 June 1999; revised 18 November 1999; accepted 3 December 1999)

This paper describes an acoustic experiment (PROSIM'97) carried out to investigate inversion for seabed properties at a site off the west coast of Italy where previous acoustic and geophysical studies have been performed. Acoustic fields were measured at a vertical hydrophone array due to a swept-frequency source towed over weakly range-dependent bathymetry. Based on the known geology, the seabed is modeled as a sediment layer overlying a semi-infinite basement with unknown model parameters consisting of the sediment thickness, sediment and basement sound speeds, source range and depth, water depth at the source and array, and array tilt. A hybrid inversion algorithm is applied to determine the model values that minimize the mismatch with the measured acoustic fields. Multiple data sets are analyzed to examine the consistency of the inversion results. It is found that the low sound speed of the sediment layer, together with a large uncertainty in bathymetry, leads to strong correlations between the water depths and sediment thickness. This precludes reliable estimation of these parameters individually; however, the total depth to the basement can be estimated reliably. In addition, the basement speed and geometric parameters are estimated consistently, and all parameters compare favorably with the geophysical ground-truth information and with previous inversion results. © *2000 Acoustical Society of America.* [S0001-4966(00)00104-1]

PACS numbers: 43.30.Pc, 43.60.Pt [DLB]

INTRODUCTION

In May 1997, SACLANT Undersea Research Centre performed a shallow-water acoustic experiment, known as PROSIM'97, in the Mediterranean Sea off the west coast of Italy near Elba Island.[1] Acoustic fields were recorded on a 48-sensor vertical array due to a swept-frequency source (300–850 Hz) towed over a track with weakly range-dependent bathymetry. Environmental parameters such as ocean sound speed and current velocity were recorded throughout the experiment; notably, however, the bathymetry measurements along the source track were subject to relatively large uncertainties due to experimental difficulties.

The purpose of the experiment was to study matched-field inversion for seabed geoacoustic properties. In matched-field inversion, model parameters (representing environmental properties and/or experiment geometry) are determined by minimizing the mismatch between the measured acoustic fields and replica fields computed using a numerical propagation model. Since the parameter search space can be of high dimension and include many local minima, global inversion methods, such as simulated annealing[2–5] (SA) and genetic algorithms,[6–8] are typically employed. Global inversion methods widely search the parameter space without becoming trapped in local minima; however, as they neglect local gradient information, they can be inefficient, particularly when correlations exist between model parameters.[5] In this paper, matched-field geoacoustic inversion is applied to the PROSIM'97 acoustic data using a hybrid inversion algorithm, simplex simulated annealing[9,10] (SSA), which combines the local downhill simplex method[11,12] with a fast simulated annealing (FSA) global search.[13,14] The algorithm has previously been applied to synthetic geoacoustic data, and has proven to be an efficient and effective inversion scheme.[9,10]

The PROSIM'97 experiment was conducted in the same region as the earlier Yellow Shark experiments (1994, 1995), which made use of both ocean acoustic and geophysical measurements to determine seabed geoacoustic properties.[8,15,16] Hence, the Yellow Shark results provide a relevant baseline for comparison with the results derived in this paper. The geophysical studies included analysis of sediment core samples, high-resolution seismic surveys, and inversion of reflection coefficient versus angle data. The geoacoustic model for the region determined from these studies consisted of a thin, low-speed sediment layer overlaying a higher-speed basement of consolidated sediments. Two different approaches were applied to the inversion of Yellow Shark acoustic data. Hermand and Gerstoft[8] inverted continuous wave (CW) data (seven tones at frequencies of 200–800 Hz) using genetic algorithms with the normal-mode model SNAP.[17] The unknown parameters consisted of geo-

[a)]Currently at MacDonald Dettwiler and Associates, Richmond, British Columbia V6V 2J3, Canada.

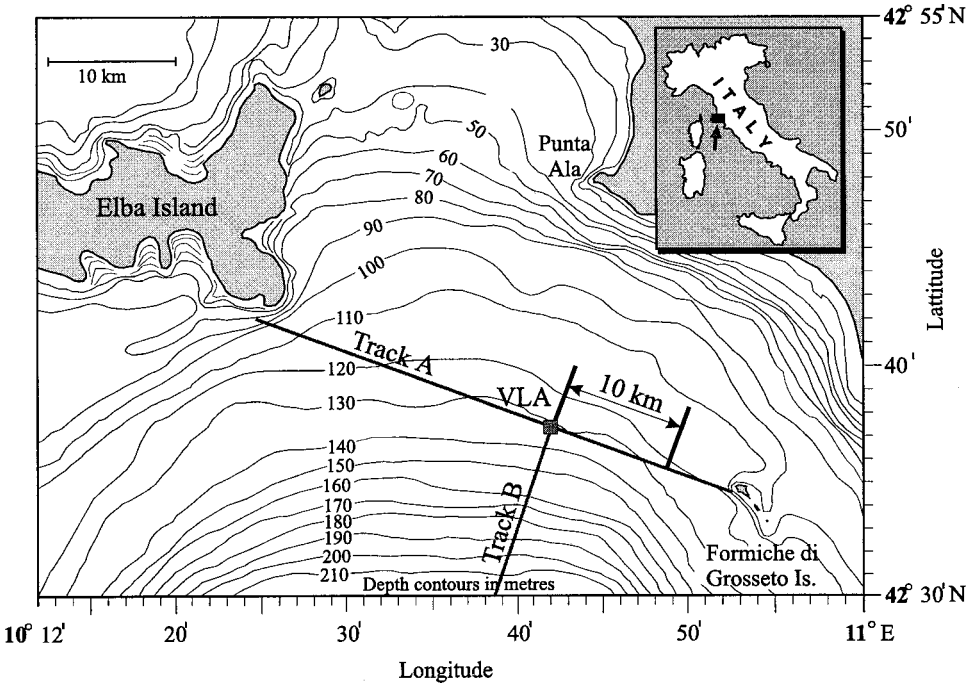

FIG. 1. The PROSIM'97 experiment site, including ship tracks and the 10-km section used for the inversions in this paper. VLA indicates the site of the vertical line array.

metric and (range-independent) geoacoustic properties and included a compressional-speed gradient in the sediment layer. Siderius and Hermand[15] inverted broadband (200–800 Hz) transmission-loss data from five ranges at a sparse array of four sensors. A range-dependent geoacoustic model was compiled by performing separate range-independent inversions for each of the five range segments, with the sediment and basement compressional speeds and the sediment thickness as unknowns. The inversions consisted of systematically varying these three parameters to obtain the best match to the measured data using the parabolic-equation model RAM.[18]

In this paper, independent SSA inversions are carried out for acoustic-field measurements at 17 ranges from 0.7–10 km in the PROSIM'97 experiment. The unknown model consists of seabed properties including the sediment thickness and sediment and basement compressional speeds, and geometric parameters including the source range and depth, array tilt, and water depth at the source and array. The adiabatic normal-mode propagation model PROSIM[19] is used to accommodate the range-dependent bathymetry. Multiple data sets are analyzed to examine the consistency of the inversion results, and the model parameters are compared with available ground-truth information and with previous inversion results.

This paper is organized as follows. Section I provides a description of the experiment and the measured acoustic and environmental data. Section II briefly describes the SSA inversion algorithm, and Sec. III presents a synthetic inversion study simulating the experiment. Section IV presents the inversion results for the PROSIM'97 data, and Sec. V summarizes this work.

I. PROSIM'97 EXPERIMENT

The PROSIM'97 experiment[1] was conducted between 15–23 May 1997, in the region southeast of Elba Island in the Mediterranean Sea off the western coast of Italy (Fig. 1). Environmental data, including water-temperature profiles, current velocity, sea-surface wave height, and weather conditions, were recorded during the experiment. Sound-speed profiles were measured throughout the experiment area using a CTD (conductivity, temperature, depth) chain towed by the source ship. Bathymetric data were measured along the source track using a swath multibeam echosounder. Swath data can be accurate to within approximately 0.5%. Unfortunately, in this case the system had not been calibrated properly and the water depth measurements, although accurate in a relative sense, have an absolute uncertainty of approximately 10%. As a result, the bathymetry must be treated as an unknown, rather than a known parameter in the geoacoustic inversions formulated in Secs. III and IV.

The acoustic data were recorded at a vertical line array (VLA) of 48 hydrophones which spanned from 26–120-m depth with a 2-m spacing between sensors (data from one hydrophone were omitted from the analysis because of low gain). The water depth at the array site was approximately 130 m. Both a piezoelectric (flextensional) transducer and explosive charges (0.8-kg signal, underwater sound or SUS) were used as acoustic sources. The transducer produced both linear frequency modulated (LFM) sweeps and CW signals. The experiment involved three parts consisting of: (i) towing the transducer and deploying charges over a region of weakly range-dependent bathymetry, (ii) deploying charges over a region of strongly range-dependent bathymetry, and (iii) transmitting continuously from a moored transducer to study time-dependent propagation along a fixed path. In total, the PROSIM'97 experiment provided a very large suite of data, including source frequencies from 50 Hz to 7.5 kHz.

In this paper, only a portion of the acoustic data are considered. These data were recorded on May 18 along a 10-km track to the east of the VLA site, as shown in Fig. 1.

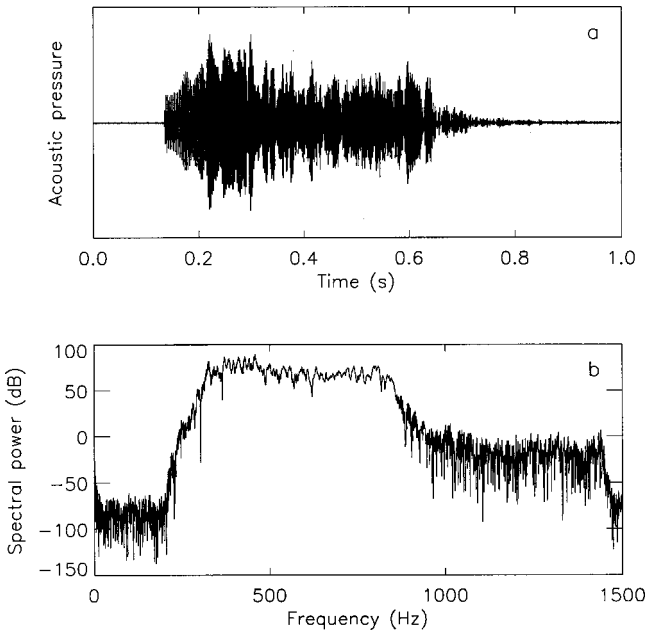

FIG. 2. The acoustic signal recorded at the closest point of approach (~700 m) on a mid-water column hydrophone. (a) Shows the time series (arbitrary pressure units); (b) shows the corresponding power spectrum.

These data were selected because the bathymetry along this portion of the track is only weakly range-dependent with less small-scale variation than to the west of the VLA (near Elba Island).[1] The source was towed at a depth of about 12 m, passing within approximately 700 m of the array. The acoustic signal consisted of a LFM sweep from 300–850 Hz. The acoustic pressure at each hydrophone of the VLA was sampled at 3 kHz and recorded on optical disc. Figure 2(a) shows an example of the acoustic signal recorded on a mid-water column sensor due to the source at its closest point of approach. The acoustic time series were transformed using the fast Fourier transform (FFT) to produce a frequency-domain signal with a sampling of 5 Hz. Figure 2(b) shows an example of the signal power spectrum. The Doppler shift due to the motion of the towed source was assumed to be negligible since the ship speed of approximately 2 m/s leads to a frequency shift of only about 0.1%.

II. INVERSION ALGORITHM

In this paper, geoacoustic inversions are carried out using a matched-field technique. Matched-field methods attempt to determine the set of model-parameter values that minimizes a measure of the mismatch between the measured acoustic fields and modeled replica fields computed using a numerical propagation model. The measure of the mismatch adopted here is based on the (normalized) Bartlett correlator for a broadband signal,

$$E(\mathbf{m}) = 1 - \frac{1}{F}\sum_{i=1}^{F} \frac{|\mathbf{p}(f_i)\cdot\mathbf{p}^*(\mathbf{m},f_i)|^2}{|\mathbf{p}(f_i)|^2|\mathbf{p}(\mathbf{m},f_i)|^2}. \quad (1)$$

In (1), $\mathbf{p}(f_i)$ is a vector of acoustic pressures measured at the VLA at a frequency f_i, $\mathbf{p}(\mathbf{m},f_i)$ is a vector of replica pressures computed for a model $\mathbf{m}$, and F is the number of frequencies. The mismatch has a value $E \in [0,1]$, with zero indicating a perfect match. In (1), the acoustic pressures are summed coherently in depth and incoherently in frequency (the relative merit of coherent and incoherent processing in frequency is currently under debate; however, based on the study of Taroudakis and Markaki,[20] frequency-incoherent processing is applied here). The replica acoustic fields are generated using PROSIM,[19] which is a (weakly) range-dependent version of the normal-mode acoustic propagation model ORCA.[21] Range dependence is built into the model using the adiabatic approximation,[22,23]

$$p(r,z) = \frac{\exp(i\pi/4)}{\rho(z_s)\sqrt{8\pi r}} \sum_{m=1}^{M} \phi_m(r,z)\,\phi_m(0,z_s) \times \frac{\exp(i\int_0^r k_m(u)\,du)}{\sqrt{k_m(r)}}, \quad (2)$$

where $p(r,z)$ is the acoustic pressure at range r and depth z due to a source at zero range and depth z_s, $\phi_m(r,z)$ and $k_m(r)$ represent the mth mode function and wave number computed for the local environment at range r, M is the minimum number of propagating modes supported between source and receiver, and ρ is the density. In practice, the modal wave numbers are computed for a finite number of realizations of the environment between source and receiver, and are assumed to change in a piecewise linear manner with range.

The geoacoustic inversions performed in this paper were carried out using SSA, a hybrid inversion algorithm that incorporates the local downhill simplex (DHS) method into a FSA global search. The SSA algorithm is only briefly outlined here; a complete description is given elsewhere.[9,10] The DHS method[11,12] operates on a simplex of $N+1$ models, where N is the number of unknown model parameters. The method is based on a simple set of geometric transformations for moving downhill in mismatch E, and does not require computing partial derivatives or solving systems of equations. This provides an efficient approach to moving downhill, but is prone to becoming trapped in local minima.

SA[2–5] consists of a series of iterations involving random perturbations of the model parameters. After each iteration, a control parameter (temperature T) is decreased slightly. Perturbations that decrease the mismatch E are always accepted; perturbations that increase E are accepted with a probability drawn from a temperature-dependent Boltzmann distribution. Accepting some perturbations that increase E allows SA to avoid becoming trapped in local minima. However, as T is decreased, accepting increases in E becomes increasingly improbable, and the algorithm eventually converges to a solution. The convergence can be accelerated by reducing the perturbation size as the inversion progresses. FSA[13,14] is based on drawing parameter perturbations from a Cauchy distribution and decreasing the distribution width with T. Global inversion methods widely search the parameter space. However, as no gradient information is used, they can be inefficient, particularly near convergence and in cases where correlated parameters produce narrow valleys in the parameter space that are not aligned with the parameter axes.[5]

The goal of hybrid inversions is to combine local and global methods in a way that retains the advantages of each

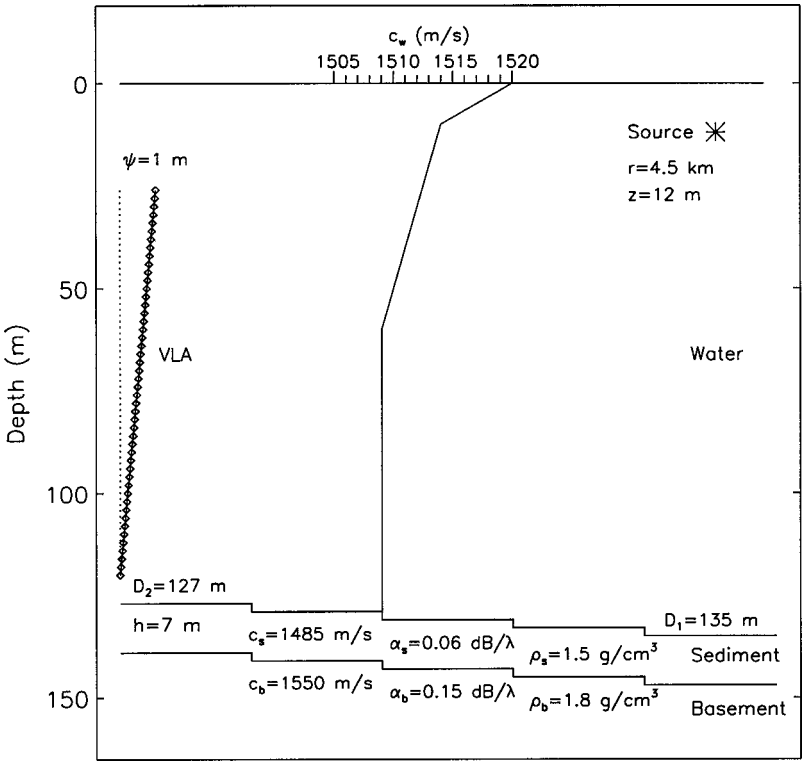

FIG. 3. Schematic diagram of the ocean environment used in the synthetic test case inversions.

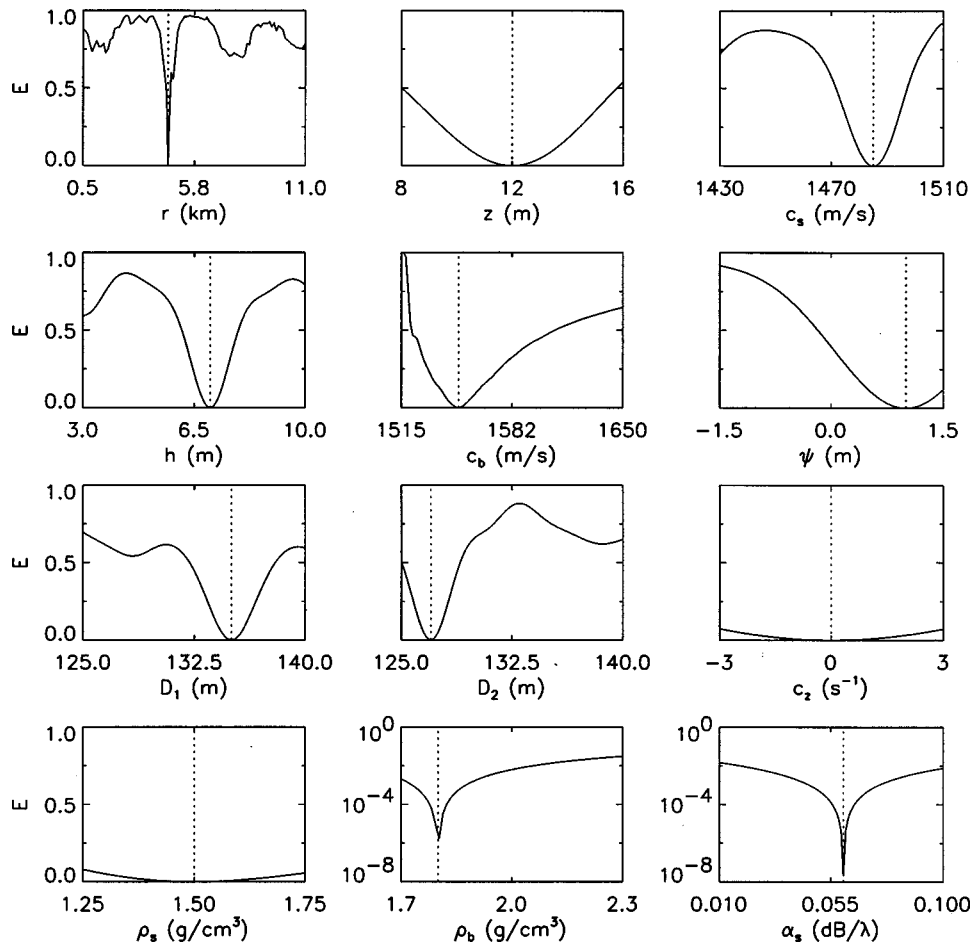

FIG. 4. 1D cross sections of the parameter space for the synthetic test case. The dotted lines represent the true parameter values. Results for basement attenuation α_b are very similar to α_s and are not shown.

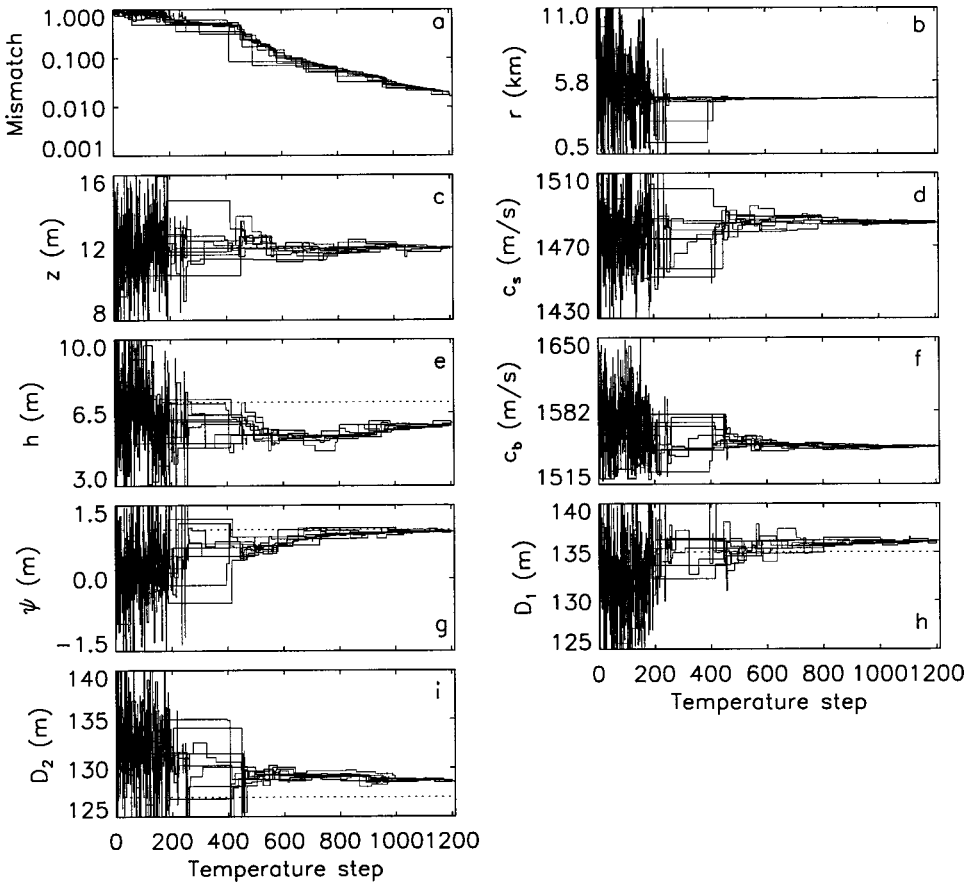

FIG. 5. Inversion results for the synthetic test case including the mismatch E and all model parameters. The dotted lines indicate the true parameter values, and the range of ordinate values indicate the search intervals for each parameter.

(i.e., to move effectively downhill, yet avoid becoming trapped in local minima). SSA is based on adding a Cauchy-distributed random component to the geometric transformations of the DHS algorithm, and employing these in the place of purely random parameter perturbations in a FSA algorithm. The relative importance of the random component is reduced with temperature, so gradient information becomes increasingly important as the inversion proceeds. The SSA algorithm has been found to effectively navigate complicated parameter spaces (including correlated parameters) in synthetic geoacoustic inversion examples[9,10,24] and in other challenging inverse problems.[25]

III. SYNTHETIC STUDY

To investigate geoacoustic inversion for the PROSIM'97 experiment, a synthetic inversion study was carried out to simulate the acoustic experiment as closely as possible. Previous geophysical and geoacoustic studies in the region[6,8,15,16] indicated that the seabed is characterized by a sediment layer 5–9-m thick, consisting of clays and silty clays with a compressional speed of 1460–1490 m/s (slightly lower than the water sound speed of approximately 1510 m/s), a density of 1.3–1.5 g/cm^3, and an attenuation 0.06 dB/λ (where λ is the acoustic wavelength). Underlying this layer is a basement of consolidated sediments (silt) with a compressional speed of approximately 1540–1550 m/s, a density of 1.8 g/cm^3, and an attenuation of 0.15 dB/λ. The environmental properties of the synthetic test case were chosen in accordance with the above values, and are shown in Fig. 3. In particular, the seabed is represented as a single uniform sediment layer overlying a semi-infinite basement. The water depth varies from 127–135 m over a 4.5-km range, representative of the bottom slope in the PROSIM'97 experiment. To apply the adiabatic normal-mode approximation (2), wave numbers were computed for water depths at five intermediate points (previous studies[10,26] indicated this was adequate to accurately model the slope). The ocean sound-speed profile in Fig. 3 represents a compilation of the sound-speed measurements obtained during the experiment with the towed CTD chain. Forward-modeling indicated that the range dependence of the measured sound speed is an order of magnitude less important (in terms of mismatch) than that of the water depth. Hence, range dependence of the bathymetry, but not of the sound speed, is included in the synthetic test case.

To investigate the relative importance of the geoacoustic properties, a sensitivity study was carried out. Figure 4 shows the mismatch E, computed using PROSIM for frequencies 300–850 Hz in 5-Hz increments, as a function of various geoacoustic and geometric parameters [i.e., one-dimensional (1D) cross sections of the parameter space]. In each case, the parameters that are not varied are held at their true value. This figure indicates that the sensitivity of the acoustic fields to the various parameters varies over a number of orders of magnitude. For instance, large mismatches of $E>0.5$ occur when varying properties such as source range and depth r and z, sediment thickness h, sediment and basement sound speed c_s and c_b, water depth at the source and at the VLA D_1 and D_2, and array tilt ψ (measured as a horizontal displacement of the top hydrophone with the bot-

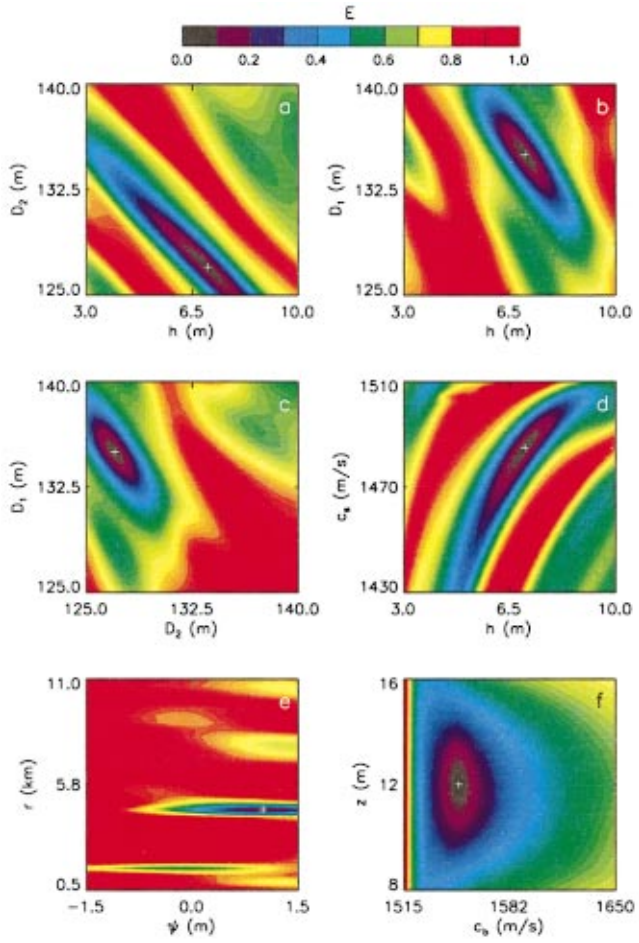

FIG. 6. Selected 2D cross sections of the parameter space for the synthetic test case. The crosses indicate the true parameter values.

tom hydrophone fixed). Therefore, these properties are important acoustically, and are included as unknown parameters in the geoacoustic model. However, small mismatches $E<0.1$ occur for properties such as the sediment sound-speed gradient c_z, and the densities and attenuations of the sediment and basement ρ_s, ρ_b, α_s, and α_b. These properties represent relatively insensitive parameters in applying matched-field inversion based on the Bartlett processor in this environment (particularly for measured field data which contain noise and other sources of mismatch). Holding these parameters fixed will not have a large effect on the Bartlett mismatch; conversely, it is unlikely matched-field inversion of noisy data will provide meaningful estimates for these parameters. Hence, they are not included in the model as unknown parameters, but are held fixed (at their true values) in the synthetic test case. In analyzing the Yellow Shark experiment, Siderius and Hermand[15] carried out a similar synthetic sensitivity study and came to the same conclusions: the sensitive geoacoustic parameters are the sediment thickness and sediment and basement sound speed. Their inversion involved only these parameters.

The test case consisted of inverting (noise-free) synthetic data for the seabed/geometric parameters included in the geoacoustic model, as described above. Figure 5 shows the results of SSA inversion of the synthetic data. Search bounds for each parameter were chosen to represent a reasonable range of values, given the *a priori* information available from the geophysical and geoacoustic studies described above. These bounds are indicated in Fig. 5 by the range of ordinate values on the plot for each parameter. Figure 5 shows the mismatch and the model parameters as a function of temperature step (iteration), including the results for all models in the simplex. Figure 5(a) shows that the mismatch E decreases steadily from an initial value of approximately 1 to a final value of $E=0.015$, at which point the mismatches of all models have essentially converged to a single value. The convergence of the model parameters are shown in Fig. 5(b)–(i), with the dotted lines indicating the true parameter values. Excellent inversion results are obtained for all parameters except water depths D_1 and D_2 and sediment thickness h (discussed below). The source range r is clearly the most sensitive parameter as it converges at a very early stage in the inversion; the basement sound speed c_b appears to be the second most sensitive parameter. The inversion involved approximately 10 000 forward models, and required about 3 h of CPU time on a 500-MHz DEC Alpha workstation.

Although relatively poor inversion results are obtained for D_1, D_2, and h in Fig. 5, Fig. 4 shows that these are sensitive parameters with well-defined minima. The poor results appear to be due to interparameter correlations. Figure 6 illustrates these correlations in terms of selected two-dimensional (2D) cross sections of the parameter space. For instance, while sharp minima in E occur as 1D functions of h and of D_2 (Fig. 4), Fig. 6(a) shows that the 2D dependence of E on both h and D_2 exhibits an elongated narrow valley not aligned with the parameters axes, indicative of correlated parameters. A similar correlation between h and D_1 is illustrated in Fig. 6(b). In each case, a negative correlation is indicated, with D_1 or D_2 decreasing as h increases. Correlated parameters cause difficulty in determining the minimum-mismatch model, even for SSA, as different parameter combinations within the valley all produce very similar (low) mismatch values. Physically, these correlations seem to be related to the low sound speed and density of the sediment layer, which appears acoustically similar to the water. Although the water/sediment interface is not well defined acoustically, the sediment/basement interface is, which means that the total depth to the basement is the acoustically important quantity. The fact that the same depth to basement can be obtained by increasing h while decreasing D_1 or D_2 (and vice versa) leads to the observed correlations. A somewhat weaker (negative) correlation between D_1 and D_2 is illustrated in Fig. 6(c). This correlation likely results from the fact that the average water depth along the track is more important acoustically than the water depth at either the source or receiver, and a similar average depth can be obtained by increasing D_1 while decreasing D_2 (and vice versa). Finally, Fig. 6(d) indicates a (positive) correlation between c_s and h, although this correlation does not seem to degrade the inversion results for c_s in Fig. 5. No other significant parameter correlations were found for this test case. Figure 6(e) and (f) show examples of parameter combinations that are uncorrelated.

To further investigate the effect of correlations between D_1, D_2, and h, the synthetic inversion was repeated with

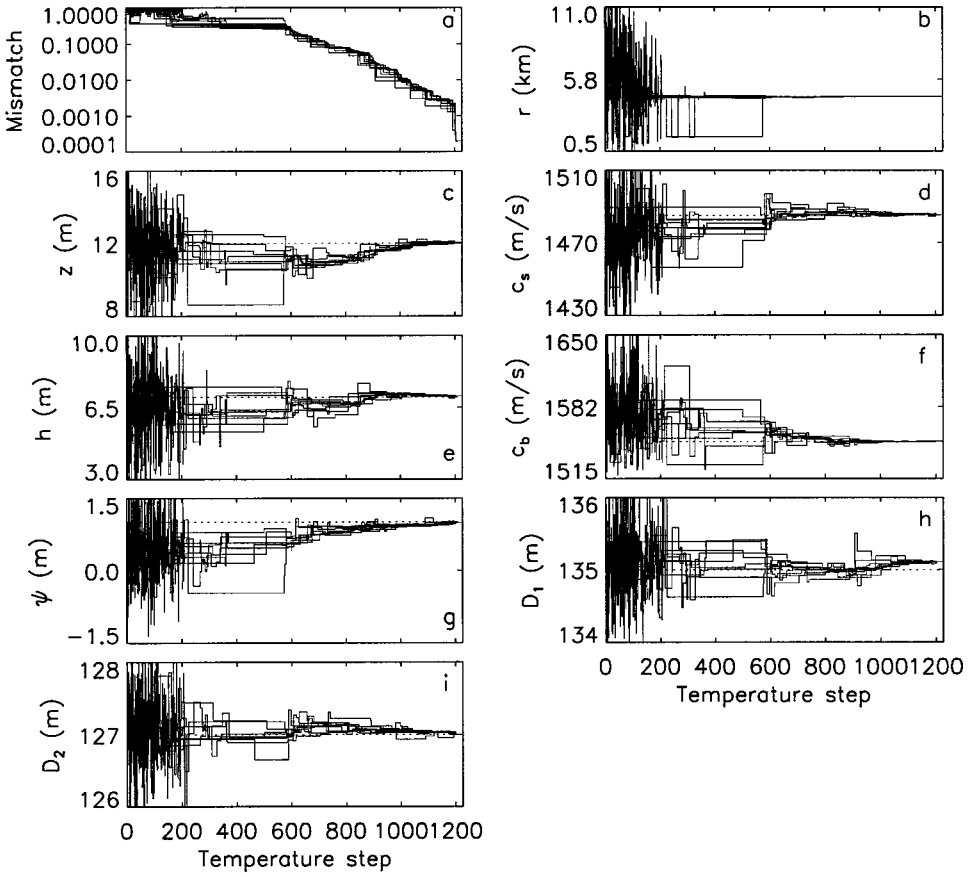

FIG. 7. Inversion results for the synthetic test case with the search interval for water depths D_1 and D_2 reduced to ± 1 m about the true values. The dotted lines indicate the true parameter values, and the range of ordinate values indicate the search intervals for each parameter.

smaller search bounds for D_1 and D_2 of ± 1 m about the true values (representative of the accuracy of calibrated swath bathymetry). The results, given in Fig. 7, show that all parameters, including h, are now accurately determined.

IV. PROSIM'97 INVERSION RESULTS

This section describes the inversion of the acoustic data recorded during the PROSIM'97 experiment described in Sec. I. The inversion is carried out using the SSA algorithm described in Sec. II, and the geoacoustic model parameters are the same as those used for the synthetic test case in Sec. III. Acoustic data for 17 ranges from 0.7–10 km along the source track were selected for inversion, as shown in Fig. 8. The goal of inverting data from multiple ranges is not to determine a range-dependent geoacoustic model, but rather to consider a large enough number of independent measurements to provide an indication of the consistency of the inversion results for the various model parameters. Several independent SSA inversions were carried out for the acoustic data at each range, for a total of 52 inversions (each inversion involved approximately 10 000 forward models and required about 3 h of CPU time). Figure 9 shows the model parameters determined in all inversions plotted as a function of the source longitude (Fig. 8), with the inversion results that produced the lowest mismatch at each range connected by a solid line.

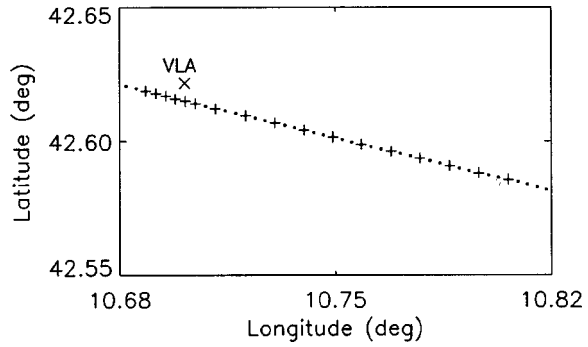

FIG. 8. Ship track: the small crosses represent points used in the inversions while the dots represent all points where the source was transmitted.

The SSA inversion results for the source range r are shown in Fig. 9(a), with the dotted line representing the ranges calculated using differential global positioning system (DGPS) measurements of the ship and VLA positions. The lowest-mismatch results closely track the DGPS range, and the variation between inversion results at each range is small (i.e., the results are highly consistent from inversion to inversion). Figure 9(b) shows the inversion results for the source depth z. The dotted line at 12 m indicates the nominal source depth (i.e., the depth at which the source was supposed to be towed). With a small number of exceptions, the inversion results are within approximately 1 m of the nominal depth, and exhibit a moderate amount of variation.

Figure 9(c)–(e) show the results for the seabed properties: sediment sound speed c_s, sediment thickness h, and basement sound speed c_b. The PROSIM'97 results are compared to the results obtained for the two Yellow Shark experiments carried out in the same region. The dashed lines represent the results of Hermand and Gerstoft's[8] inversion of broadband acoustic-field data (the line for c_s represents the

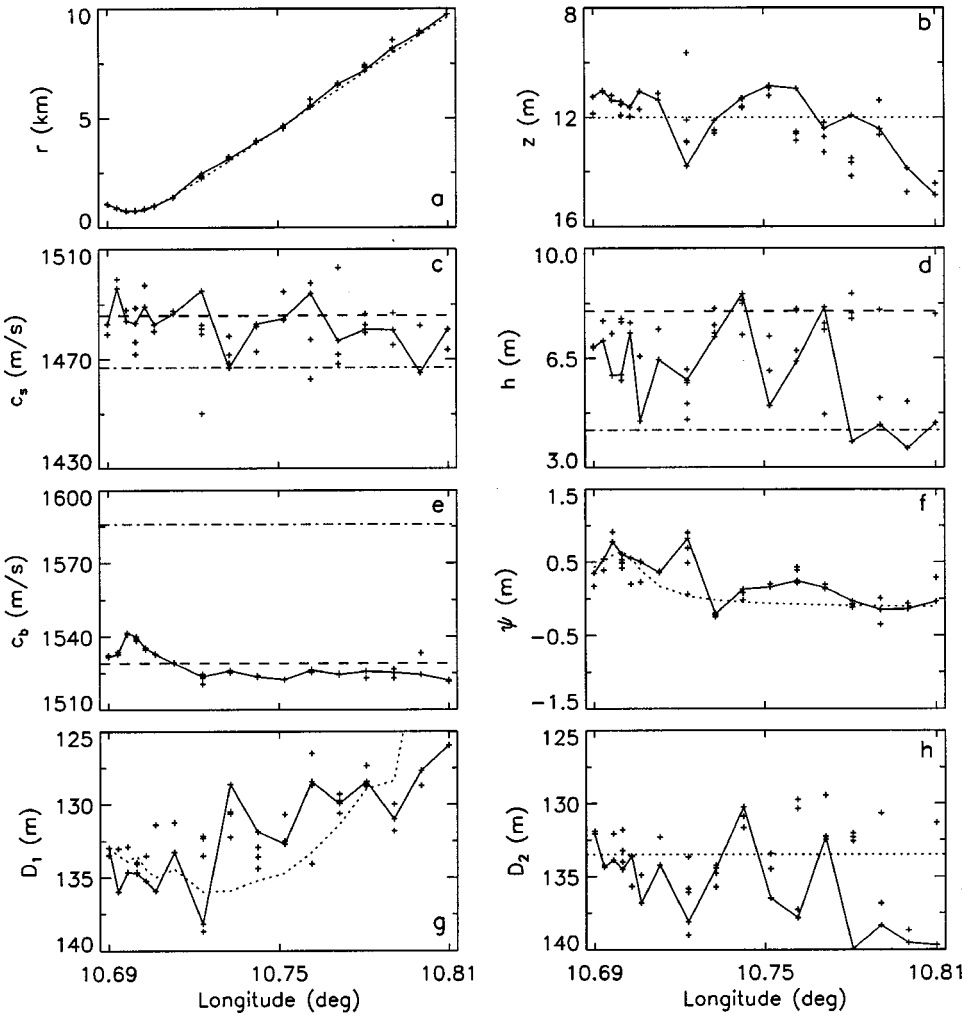

FIG. 9. Summary of the inversion results for the PROSIM'97 data. The crosses represent all inversion results, with the solid line connecting the lowest-mismatch results. The dotted lines represent independent estimates of the true values (when information was available). The dashed and dash-dotted lines represent the Yellow Shark inversion results of Hermand and Gerstoft (Ref. 8) and Siderius and Hermand (Ref. 15), respectively.

average value from their model which included a gradient in sediment sound speed). The dash-dotted lines represent the results of Siderius and Hermand's[15] inversion for the range-independent segment that was closest to the PROSIM'97 experiment site. Figure 9(c) shows that the PROSIM'97 results for c_s are in reasonably good agreement with the Yellow Shark results, generally falling between the two lines, and exhibit a moderate amount of variation from inversion to inversion. The PROSIM'97 results for h [Fig. 9(d)] also fall between the two Yellow Shark results, but with a somewhat greater amount of variation. The PROSIM'97 results for c_b [Fig. 9(e)] are in excellent agreement with the results of Hermand and Gerstoft,[8] and are highly consistent from inversion to inversion.

Figure 9(f) shows the inversion results for the array tilt ψ. The dotted line represents the estimated tilt, calculated by projecting the measured current vector onto the radial vector between the source and the VLA. The current was essentially constant in direction and magnitude over the duration of the acoustic measurements; however, the projection changes with the source position for a moving source. Since the actual array tilt produced by a given current is not known, the projection provides only a relative estimate of the tilt as a function of source position. In Fig. 9(f), this estimate has been arbitrarily scaled to produce the best agreement with the inversion results. This figure shows that, with the exception of a few points, the inversion results are highly consistent and are in excellent agreement with the estimated (relative) tilt.

Figure 9(g) shows the inversion results for the water depth at the source D_1. The dotted line represents the water depth estimates from the swath data. As the swath system was not calibrated properly (see Sec. I), the swath measurements represent only relative water depth. For the purpose of comparison, the absolute depth is fixed in Fig. 9(g) by assigning the depth at the VLA (measured by echo-sounding) to the source water depth at the point of closest approach (700-m range, the fourth inversion result from the left). Figure 9(g) shows that the general features of the inversion results for D_1 are in reasonably good agreement with the swath data. Figure 9(h) shows the inversion results for the water depth at the VLA D_2 with the dotted line indicating the echo-sounder depth measurement. The inversion results are in reasonable agreement for the first 8–10 points, but are in poorer agreement beyond. The results for both water depths D_1 and D_2 show a substantial amount of variation from inversion to inversion.

The SSA inversion results shown in Fig. 9 were obtained by minimizing the Bartlett mismatch E between measured and modeled acoustic fields. The mismatches obtained by the SSA inversions are shown in Fig. 10. The mismatches range from 0.15–0.5, with an average value of 0.3. Figure 11

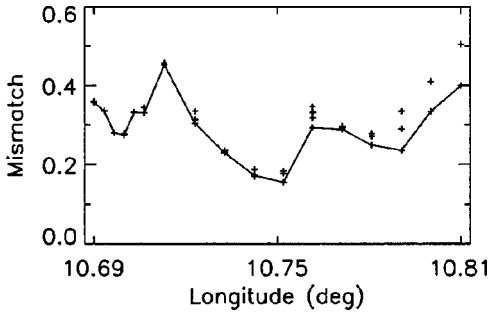

FIG. 10. Mismatches of the SSA inversions of the PROSIM'97 data shown in Fig. 9.

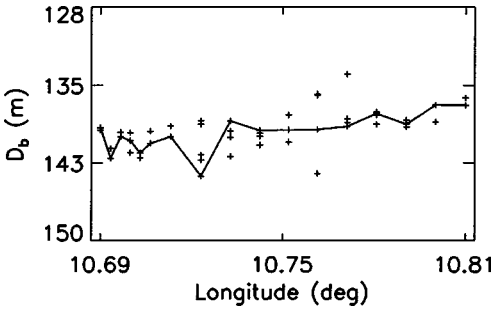

FIG. 12. PROSIM'97 inversion results expressed as the approximate depth to the basement layer $D_b=(D_1+D_2)/2+h$, with the solid line connecting the lowest-mismatch results.

illustrates the agreement between the measured and modeled fields. This figure shows the magnitude of the acoustic fields as a function of depth and frequency for short- and mid-range sources at the 0.88- and 4.55-km ranges, respectively. The mid-range fields are in excellent agreement ($E=0.15$), with all of the major features and some of the small-scale structure of the measured fields reproduced in the modeled results. At short range, the measured fields contain a great deal of fine structure due to the near-field interference of evanescent (leaky) modes. This is not modeled by the propagation model PROSIM, which considers only the trapped (propagating) modes. Hence, while the modeled fields ($E=0.3$) reproduce the major features of the measured fields reasonably well, they do not reproduce the fine structure.

In the inversion results of Fig. 9, the parameters that show the greatest consistency are the source range r, basement sound speed c_b, and array tilt ψ. The first two correspond to the parameters that were determined to highest precision in the synthetic study in Sec. III. The parameters that show the most variability in Fig. 9 are the water depths D_1 and D_2 and the sediment thickness h, which correspond to the most poorly determined parameters in the synthetic study. The synthetic study indicated that correlations between these parameters lead to the ambiguous inversion results. As the sediment layer appears acoustically similar to the water column, the water depth and sediment thickness are difficult to determine individually. Rather, it is their sum, the depth to the basement, that is well determined. This is illustrated in Fig. 12, which shows the inversion results for D_1, D_2, and h combined to produce an approximate depth-to-basement defined as $D_b=(D_1+D_2)/2+h$. It is apparent that the scatter of D_b in Fig. 12 (particularly for the lowest-mismatch results) is considerably less than that of D_1, D_2, and h in Fig. 9(d), (g), and (h). Note also that D_b decreases

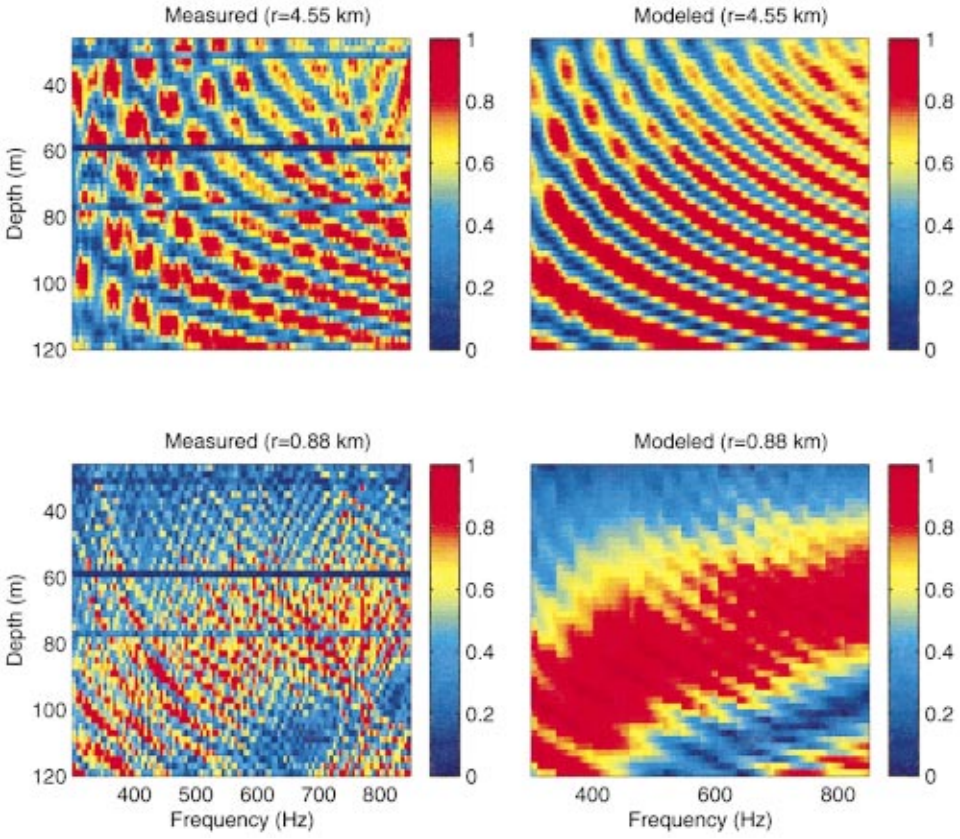

FIG. 11. Measured and modeled acoustic pressure fields for two of the PROSIM'97 inversions, normalized in 5-Hz bands.

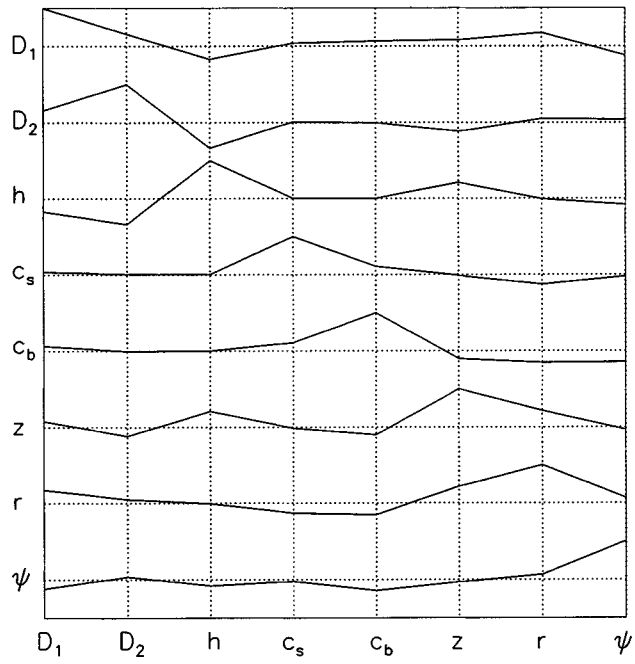

FIG. 13. Correlation matrix computed from the PROSIM'97 inversion results shown in Fig. 9.

slightly with longitude, as expected for a source moving into shallower water.

The correlation between model parameters can be considered further for the PROSIM'97 results by computing the correlation matrix **C**. Specifically, the correlation between parameters m_i and m_j is defined to be

$$C_{ij}=\frac{\langle (m_i-\langle m_i\rangle)(m_j-\langle m_j\rangle)\rangle}{\sqrt{\langle (m_i-\langle m_i\rangle)^2\rangle\langle (m_j-\langle m_j\rangle)^2\rangle}}, \tag{3}$$

where $\langle\cdot\rangle$ indicates the expected value or ensemble average computed from a population of samples. Values of C_{ij} vary from -1 to 1, with -1 $(+1)$ indicating a perfect negative (positive) correlation between parameters, and zero indicating completely uncorrelated parameters. The main diagonal of **C** contains the parameter autocorrelations which are, by definition, unity. Figure 13 shows the correlation matrix computed using the SSA inversion results shown in Fig. 9. For the range-independent parameters (D_2, h, c_s, c_b, and z), the expected values can be computed from all 52 inversion results, providing a reasonable, if small, sample size. For the range-dependent parameters (D_1, r and ψ), $\langle m_k\rangle$ must be computed at each range independently; this results in very small sample sizes, and the correlations obtained for these parameters may not be meaningful. In addition, since the inversions for the PROSIM'97 data do not obtain as low mismatches as the synthetic inversions of Sec. III, correlations evident in the synthetic study may not be observable for the measured data. Nonetheless, the major feature of Fig. 13 is a strong negative correlation between sediment thickness h and VLA water depth D_2. A somewhat weaker negative correlation between h and the source water depth D_1 is also evident. These observations agree with the correlation results for the synthetic test case shown in Fig. 6(a) and (b), and help explain the inconsistent inversion results for sediment thickness and water depth. The other parameter correlations indicated by the synthetic study are not evident in Fig. 13.

V. SUMMARY AND DISCUSSION

This paper describes and analyzes a geoacoustic inversion experiment, PROSIM'97, carried out off the west coast of Italy at a shallow-water site where previous acoustic and geophysical studies have been performed. Acoustic fields were measured at a vertical array of 48 hydrophones due to a LFM source (300–850 Hz) towed along a 10-km track over weakly range-dependent bathymetry. Guided by a synthetic sensitivity study, the geoacoustic model parameters were taken to consist of the sediment thickness h, sediment and basement sound speeds c_s and c_b, source range and depth r and z, water depth at the source and array D_1 and D_2, and array tilt ψ. Broadband matched-field inversion for these parameters was carried out using a hybrid algorithm, simplex simulated annealing, that combines the local downhill simplex method and a fast simulated annealing global search. A total of 52 independent inversions were performed for data from 17 different ranges to investigate the consistency of the results for the various parameters. It was found that for r, c_b, and ψ, the inversion results were highly consistent and in excellent agreement with independent estimates. The results for the remaining parameters were in reasonably good agreement with independent estimates, but showed greater variation from inversion to inversion, particularly for D_1, D_2, and h.

A synthetic study carried out to simulate the experiment indicated the difficulty in determining D_1, D_2, and h was likely due to strong interparameter correlations that arise because the low-speed sediment layer appears similar acoustically to the water column. The correlation matrix derived from the PROSIM'97 inversion results supported this observation. These correlations preclude reliable estimation of the parameters individually. However, a combination of parameters that can be interpreted as the approximate depth to the basement can be estimated more reliably. The synthetic study indicated that in cases when the bathymetry is well known, the sediment thickness can be determined accurately. Note also that if the goal of the inversion is to determine an effective environment for accurate propagation modeling, errors in the seabed properties due to interparameter correlations may not pose a serious problem.

Sources of potential error for this inversion study include the choice of model parameterization (which included only two layers and neglected sound-speed gradients, density, and attenuation), range dependence of the geoacoustic properties, and three-dimensional (3D) propagation effects. However, the PROSIM'97 inversion results can be validated in a number of ways. The geometric parameters obtained are in good agreement with independent estimates, and the sediment and basement sound speeds agree well with the results of previous geophysical and geoacoustic experiments in the region. In addition, low mismatch values were obtained for most source ranges, and consistent values were obtained for the geometric parameters, basement sound speed, and (to a lesser extent) sediment sound speed over a large number of

independent inversions. These lines of evidence provide confidence that matched-field methods can provide meaningful estimates of environmental properties.

ACKNOWLEDGMENTS

The first author would like to thank SACLANT Undersea Research Centre for the Summer Research Assistant position that made this work possible, and to thank Martin Siderius for helpful discussions. A portion of this work was supported by the National Science and Engineering Research Council (NSERC) and the Department of National Defense (DND) through an NSERC research grant and the NSERC/DND Ocean Acoustics Chair Program at the University of Victoria.

[1] P. L. Nielsen, F. Bini-Verona, and F. B. Jensen, ''Environmental and acoustic data collected south of the island of Elba during the PROSIM'97 experiment,'' SACLANT Undersea Research Centre, La Spezia, Italy, SACLANTCEN document SM-357, 1999.

[2] M. D. Collins, W. A. Kuperman, and H. Schmidt, ''Nonlinear inversion for ocean-bottom properties,'' J. Acoust. Soc. Am. **92**, 2770–2783 (1992).

[3] S. E. Dosso, M. L. Yeremy, J. M. Ozard, and N. R. Chapman, ''Estimation of ocean-bottom properties by matched-field inversion of acoustic field data,'' IEEE J. Ocean Eng. **18**, 232–239 (1993).

[4] M. R. Fallat and S. E. Dosso, ''Geoacoustic inversion for the Workshop '97 benchmark test cases using simulated annealing,'' J. Comput. Acoust. **6**, 29–44 (1998).

[5] M. D. Collins and L. Fishman, ''Efficient navigation of parameter landscapes,'' J. Acoust. Soc. Am. **98**, 1637–1644 (1995).

[6] P. Gerstoft, ''Inversion of acoustic data using a combination of genetic algorithms and the Gauss-Newton approach,'' J. Acoust. Soc. Am. **97**, 2181–2190 (1995).

[7] P. Gerstoft, ''Inversion of seismoacoustic data using genetic algorithms and *a posteriori* probability distributions,'' J. Acoust. Soc. Am. **95**, 770–782 (1994).

[8] J.-P. Hermand and P. Gerstoft, ''Inversion of broad-band multitone acoustic data from the YELLOW SHARK summer experiments,'' IEEE J. Ocean Eng. **21**, 324–346 (1996).

[9] M. R. Fallat and S. E. Dosso, ''Geoacoustic inversion via local, global and hybrid algorithms,'' J. Acoust. Soc. Am. **105**, 3219–3230 (1999).

[10] M. R. Fallat, ''Simplex simulated annealing, a hybrid approach to geoacoustic inversion with application to Mediterranean Sea acoustic data,'' M.Sc. thesis, University of Victoria, Victoria, British Columbia, Canada, 1999.

[11] J. A. Nelder and R. Mead, ''A simplex method for function minimization,'' Comput. J. (UK) **7**, 308–313 (1965).

[12] W. H. Press, S. A. Teukolsky, W. T. Vetterling, and B. P. Flannery, *Numerical Recipes in FORTRAN*, 2nd ed. (Cambridge University Press, Cambridge, 1992), Ch. 10.

[13] H. Szu and R. Hartley, ''Fast simulated annealing,'' Phys. Lett. A **122**, 157–162 (1987).

[14] P. Liu, S. Hartzell, and W. Stephenson, ''Non-linear multiparameter inversion using a hybrid global search algorithm: Applications in reflection seismology,'' Geophys. J. Int. **122**, 991–1000 (1995).

[15] M. Siderius and J.-P. Hermand, ''Yellow Shark Spring 95: Inversion results from sparse broad-band acoustic measurements over a highly range dependent soft clay layer,'' J. Acoust. Soc. Am. **106**, 637–651 (1999).

[16] J.-P. Hermand, ''Broad-band geoacoustic inversion in shallow water from waveguide impulse response measurements on a single hydrophone: Theory and experimental results,'' IEEE J. Ocean Eng. **24**, 41–66 (1999).

[17] F. B. Jensen and M. C. Ferla, ''SNAP—The SACLANTCEN normal mode acoustic propagation model,'' SACLANT Document SM-121, SACLANT Undersea Research Centre, La Spezia, Italy, 1979.

[18] M. D. Collins and E. K. Westwood, ''A higher-order energy conserving parabolic equation for range-dependent ocean depth, sound speed, and density,'' J. Acoust. Soc. Am. **89**, 1068–1075 (1991).

[19] F. Bini-Verona, P. L. Nielsen, and F. B. Jensen, ''PROSIM broadband normal-mode model: A user's guide,'' SACLANT Undersea Research Centre, La Spezia, Italy, SACLANT CEN document SM-358, 1999.

[20] M. I. Taroudakis and M. G. Markaki, ''Geoacoustic inversion by broadband matched-field processing,'' J. Comput. Acoust. **6**, 167–184 (1998).

[21] E. K. Westwood, C. T. Tindle, and N. R. Chapman, ''A normal mode model for acoustoelastic ocean environments,'' J. Acoust. Soc. Am. **100**, 3631–3645 (1996).

[22] A. D. Pierce, ''Extension of the method of normal modes to sound propagation in an almost-stratified medium,'' J. Acoust. Soc. Am. **37**, 19–27 (1965).

[23] F. B. Jensen, W. A. Kuperman, M. B. Porter, and H. Schmidt, *Computational Ocean Acoustics* (AIP, New York, 1994), pp. 320–323.

[24] S. E. Dosso, R. T. Kessel, and M. R. Fallat, ''Hybrid matched-field inversion for geoacoustic properties and uncertainties,'' *Proceedings of the Fourth European Conference on Underwater Acoustics*, edited by A. Alippi and G. B. Cannelli (Italian National Research Council, Rome, Italy, 1998), pp. 313–318.

[25] S. E. Dosso and B. J. Sotirin, ''Optimal array element localization,'' J. Acoust. Soc. Am. **106**, 3445–3459 (1999).

[26] M. R. Fallat, P. L. Nielsen, and F. B. Jensen, ''Geoacoustic inversion of the PROSIM'97 experimental data using simplex simulated annealing,'' SACLANT Undersea Research Centre, La Spezia, Italy, 1999.

Estimation of coherent detection performance for spread scattering in reverberation-noise mixtures

D. W. Ricker and A. J. Cutezo
Applied Research Laboratory, The Pennsylvania State University, P.O. Box 30, State College, Pennsylvania 16804

(Received 1 February 1999; revised 13 December 1999; accepted 17 December 1999)

Narrow-band matched filter processing gain is estimated for medium- and high-frequency active sonars for which the random backscattering processes are assumed to be wide sense stationary in time frequency and uncorrelated in delay-Doppler wide sense stationary and uncorrelated scattering [WSSUS conditions]. Echo and reverberation processes that are WSSUS are described by two-dimensional scattering functions defined in the delay-Doppler plane. The average receiver responses are estimated from the convolution of the appropriate scattering function with the waveform ambiguity function. Estimates of matched filter processing gain are derived for continuous wave (CW) linear frequency modulation (LFM), and discrete frequency shift keyed (FSK) (hop code) waveforms reflected from point and uniform delay spread scatterers masked by reverberation. These bound matched filter performance for a particular waveform and interference distribution since most delay spread scattering falls somewhere between these extremes. The scattering and ambiguity functions are modeled by bounded constant amplitude functions in delay-Doppler that permit the convolutions to be approximated by overlapping area calculations. The results are presented in tabular form as simple formulas that are functions of the reverberation, noise, and waveform parameters. The estimates are shown to be consistent with processing gain measurements made from multiple realizations of synthesized and in-water data. © *2000 Acoustical Society of America.* [S0001-4966(00)00604-4]

PACS numbers: 43.30.Vh, 43.60.Gk [DLB]

LIST OF SYMBOLS

AF	ambiguity function
B_r	reverberation SF bandwidth (Hz)
$E_x = P_x T$	transmitted signal energy (Joules)
E_s	received signal energy (Joules)
E_r	received reverberation energy (Joules)
E_{rsl}	reverberation contribution of an FSK sidelobe when Doppler is not zero (Joules)
E_{fs}	MF signal response (Joules)
E_{fr}	MF reverberation response (Joules)
$E\{\ \}$	expectation operator
fonts	random quantities are denoted by sans serif fonts, i.e., s, S
f_s	sampling frequency, effective system noise bandwidth (Hz)
$G_p = \mathrm{SIR}_{\mathrm{out}}/\mathrm{SIR}_{\mathrm{in}}$	processing gain
M	number of chips or subpulses in the FSK code
MF	matched filter
N_0	noise power spectral density (Watts/Hz, Joules)
ϕ	Doppler frequency (Hz)
P_x	transmitted power (Watts)
P_s, P_r	received signal and reverberation power (Watts)
$P_n = N_0 f_s$	noise power at the receiver (Watts)
ROC	receiver operating characteristic, plot of detection $\wp_d$ vs $\wp_f$
$r_n = P_r/P_n$	reverberation to noise power ratio
$\mathcal{R}_r$	reverberation SF level per unit time-frequency (no dim.)
$\mathcal{R}_{sp}$	point scatter SF level (no dim.)
$\mathcal{R}_{sl}$	line scatter SF level (1/sec)
SF	scattering function
$\mathrm{SIR}_{\mathrm{in}}, \mathrm{SIR}_{\mathrm{out}}$	input and output signal to interference ratios
T	waveform duration (sec.)
$T_p = T/M$	FSK subpulse duration (sec.)
τ	range delay parameter (sec.)
τ_t	range delay extent of the linescatterer (sec.)
W	waveform design bandwidth ($f_{\max} - f_{\min}$) (Hz)
WSSUS	wide sense stationary and uncorrelated scattering

INTRODUCTION

The estimation of active sonar detection performance is a multistep process involving the modeling of two-way propagation, the scattering or reflection process, interference, and the system parameters including projector and receiver array, waveform, processing methodology, and receiver echo and interference response. In a benign environment where there is no channel-induced signal spreading, the scattering is pointlike, and the interference is white Gaussian noise (WGN) with power density N_0, scattering is described by a single parameter, the backscatter strength. The signal response of the optimum coherent matched filter receiver de-

 0001-4966/2000/107(4)/1978/9/$17.00

pends only upon the signal energy E_s and the output performance is proportional to the SNR E_s/N_0. In the presence of reverberation and non-point-like (delay and/or Doppler spread) scattering, the waveform modulation becomes an important factor. For both cases, performance is characterized by the processing gain defined as the ratio of output to input signal to interference ratio $\mathrm{SIR}_{\mathrm{out}}/\mathrm{SIR}_{\mathrm{in}}$.

The design of signals and receivers to maximize reverberation performance and the problem of performance estimation have occupied researchers in the field for many years and much has been published on the subject.[1–8] Much of this work has been related to performance analysis for point scattering or to the design of signals and mismatched receivers to maximize SIR. Receivers such as whitening filters that are optimized for, or adapt to, particular reverberation characteristics can be sensitive to the prior information and the lack of stationarity in the input time series; therefore the conventional matched filter is often used in practice. When used alone it is simply called a matched filter but it can also serve as a component of a combiner or diversity receiver that incoherently (energy) combines the outputs of multiple matched filters and is often used for detection in fading channels.[9] Matched filtering is the optimal maximum likelihood detector only for point scattering in WGN, but it is widely used under conditions where it is suboptimal because of its simplicity and ease of implementation. It can be made to perform nearly as well as an optimum mismatched receiver with proper signal design.[6]

This paper provides a method for the estimation of matched filter (MF) reverberation and noise performance based upon the assumption that random scattering and reverberation arise from wide sense stationary (WSS) stochastic processes. The WSS condition is a consequence of the assumption that scattering is uncorrelated in delay and Doppler[3,6] and applies most generally to sonars operating in the medium to high-frequency ranges. The combined conditions are called the WSSUS conditions for WSS and uncorrelated scattering (US).[10] Backscatter is described by a *scattering function* (SF) that represents backscatter strength as a function of delay τ and Doppler frequency ϕ. The beauty of this approach is that the expected MF output is the convolution of the scattering and waveform *ambiguity functions* (AF) and the simple graphical approach of Van Trees[6] can be adopted to predict reverberation and echo responses. The convolutions are merely calculations of overlapping areas if constant amplitude AF and SF models are used.

Estimates of both scatter and reverberation MF response are made for continuous wave (CW), linear frequency modulation (LFM), and frequency shift keyed (FSK) waveforms. Point and uniform spreading models are used because they bound the elongation and multipath induced delay spreading often encountered at zero Doppler. The results are provided in a series of tables-containing formulas relating SIR and processing gain to the parameters of the waveform and the reverberation. Only the narrow-band MF receiver that hypothesizes delay and Doppler frequency is considered because reverberation limited conditions at zero Doppler are assumed and it is not necessary to invoke the more complex wide-band-time dilation model.[11,12] The waveform bandwidth is assumed to be limited to that for which frequency-dependent scattering and absorption effects are negligible.

I. SCATTERING AND AMBIGUITY FUNCTIONS

The scattering function (SF) is a particularly useful description of both reverberation and combined scatterer and propagation channel induced random spreading. It is based upon the assumption that the transmitted signal $\sqrt{E_x}f(t)$ is passed through a random time varying linear filter such that the received signal $s(t)$ is related to the waveform by

$$\mathsf{s}(t)=\sqrt{E_x}\int_{-\infty}^{\infty}\int_{-\infty}^{\infty}\mathsf{S}(\tau,\phi)f(t-\tau)\exp(j2\pi\phi t)\,d\phi\,d\tau. \tag{1}$$

The parameters $(\tau,\ \phi)$ are the range delay and Doppler frequency, respectively, E_x is the transmitted signal energy, and $\mathsf{S}(\tau,\phi)$ is the *spreading function*. It is a random-complex function describing the combined effects of channel and scatter spreading upon the transmit waveform. This is a narrow-band model because Doppler is expressed in terms of a frequency. The random echo $\mathsf{s}(t)$ is the aggregate contribution of delayed and Doppler-shifted replications of the transmit function $f(t-\tau)\exp(j2\pi\phi t)$ weighted by $\mathsf{S}(\tau,\phi)$. If the scattering and propagation processes are only range spread, the spreading function becomes $\mathsf{S}(\tau)\delta(\phi)$ and

$$\mathsf{s}(t)=\sqrt{E_x}\int_{-\infty}^{\infty}\mathsf{S}(\tau)f(t-\tau)\,d\tau,$$

where $\delta(x)$ represents the Dirac delta function in the variable x. Range (delay) spreading occurs because of scatterer range extent and multipath or a combination of both. Reverberation, on the other hand, is an example of a doubly spread process described by (1) that is inherently range (delay) spread and Doppler spread because of wave and sonar motion, internal waves, or scattering from fish schools. The analogous wide-band or wavelet representation expresses Doppler as a time dilation and is applicable for situations involving high scatterer velocities and large time-bandwidth (TW) waveforms. If the ratio of twice the scatterer to propagation velocity, called the dilation parameter $2v/c$, is small with respect to the inverse of the waveform TW product, the narrow-band model is sufficient for the prediction of low Doppler reverberation performance.[12]

The SF is

$$\mathcal{R}_s(\tau,\phi)=E\{|\mathsf{S}(\tau,\phi)|^2\}$$

under WSSUS conditions and the convolution

$$E_{fs}(\hat{\tau},\hat{\phi})=\int_{-\infty}^{\infty}\int_{-\infty}^{\infty}\mathcal{R}_s(\tau,\phi)\Phi_{ff}(\Delta\tau,\Delta\phi)\,d\phi\,d\tau \tag{2}$$

is the expected response of a matched filter receiver to the signal (1) at the hypothesized delay $(\hat{\tau})$ and Doppler $(\hat{\phi})$.

$$\Phi_{ff}(\Delta\tau,\Delta\phi)=\left|\int_{-\infty}^{\infty}f(t)f^*(t-\Delta\tau)\exp-j2\pi\Delta\phi t\,dt\right|^2$$

is the waveform AF with $\Delta\tau=\tau-\hat{\tau},\Delta\phi=\phi-\hat{\phi}$.

The convolution (2) is often written in the shorthand notation

$$E_{fs}=E_x(\mathcal{R}_s{**}\Phi_{ff}), \tag{3}$$

indicating that the average filter response is a double convolution of the scattering and ambiguity functions in the delay Doppler plane. Reverberation is also a backscatter process represented by the SF $\mathcal{R}_r(\tau,\phi)$ and the average receiver reverberation response is

$$E_{fr}=E_x(\mathcal{R}_r{**}\Phi_{ff}). \tag{4}$$

The total received signal and reverberation energies E_s, E_r are

$$\begin{aligned} E_s&=E_x\int_{-\infty}^{\infty}\int_{-\infty}^{\infty}\mathcal{R}_s(\tau,\phi)\,d\phi\,d\tau\leqslant E_x,\\ E_r&=E_x\int_{-\infty}^{\infty}\int_{-\infty}^{\infty}\mathcal{R}_r(\tau,\phi)\,d\phi\,d\tau\leqslant E_x, \end{aligned} \tag{5}$$

and bounded from above by the transmitted energy E_x. The expected MF output signal and reverberation energies depend upon the hypotheses $\hat{\tau},\hat{\beta}$ and are bounded by

$$E_{fs}\leqslant E_s\leqslant E_x, \quad E_{fr}\leqslant E_r\leqslant E_x.$$

The average realized signal-only output of a matched filter will always be less than the available energy unless the scattering is pointlike. Then, the total signal energy can be realized at the correct delay-Doppler hypothesis and $E_{fs}=E_s$.

Matched filter processing gain is defined as

$$G_p=\frac{\mathrm{SIR}_{\mathrm{out}}}{\mathrm{SIR}_{\mathrm{in}}}, \tag{6}$$

and relates sonar equation related parameters that determine $\mathrm{SIR}_{\mathrm{in}}$ such as target strength, propagation loss, source level, directivity index, etc. to those that determine $\mathrm{SIR}_{\mathrm{out}}$ and relate to MF signal processing. The calculation of receiver operating characteristics for individual receiver realizations is then a simple calculation for Gaussian statistics given $\mathrm{SIR}_{\mathrm{out}}$.[6] It is

$$\mathrm{SIR}_{\mathrm{out}}=\frac{E_{fs}}{E_{fr}+N_0}, \tag{7}$$

and in addition to the reverberation energy, includes ambient, electronic, and other noise sources that in the aggregate are described by the white noise power spectral density (psd)N_0 (Joules). The input SIR is

$$\mathrm{SIR}_{\mathrm{in}}=\frac{P_s}{P_n+P_r}, \tag{8}$$

where $P_s=E_s/T$ is the signal power, $P_n=N_0 f_s$ is the input noise power, and f_s is the system bandwidth (sampling frequency). It is assumed to exceed the maximum frequency excursion $f_{\max}-f_{\min}$ of the waveform which is its design bandwidth W. P_r is the reverberation power at the range at which the MF performance is to be estimated.

II. SCATTERING MODELS

A. The signal component

Point scattering is the simplest model and corresponds to a specular reflection in a homogeneous environment with no boundary interactions. Its SF is the delta function $\mathcal{R}_{sp}\delta(\tau)\delta(\phi)$ and the received echo power and energy (5) are related to the transmitted energy by

$$P_s=E_s/T, \quad E_s=E_x\mathcal{R}_{sp}. \tag{9}$$

The continuous line scatterer with no Doppler spread is modeled by a SF that is confined to the τ axis and

$$E_s=E_x\int_{-\infty}^{\infty}\mathcal{R}_s(\tau)\,d\tau. \tag{10}$$

$\mathcal{R}_s(\tau)$ represents the incremental backscatter strength per unit time delay at the range delay (τ). It has units of (1/sec) or Hz and is the only one under consideration with dimension. Objects that are pointlike or doubly spread in delay-Doppler are characterized by SF's that represent scattering per unit time-frequency and hence are dimensionless.

Uniform scattering on a delay interval τ_t about a nominal delay τ_0 is represented by

$$\mathcal{R}_s(\tau)=\mathcal{R}_{sl}, \quad \tau\in[\tau_0-\tau_t/2,\tau_0+\tau_t/2]. \tag{11}$$

The corresponding signal power is

$$P_s=\begin{cases} P_x\mathcal{R}_{sl}\tau_t, & \text{when } \tau_t\leqslant T\\ P_x\mathcal{R}_{sl}T, & \text{when } \tau_t>T. \end{cases} \tag{12}$$

While most echoes do not emanate from uniformly dense scattering mechanisms, point and uniform scattering represent the delay spreading extremes that can be encountered in practice. Matched filters are optimum for point scattering but their performance is degraded in the presence of delay spreading. Uniform scattering is the worst case and serves to bound the performance.

B. The reverberation component

The reverberation SF is assumed to extend in delay beyond the pulse length and scatterer duration and has a uniform distribution $\mathcal{R}_r$ over the Doppler spread B_r and duration T. It represents backscatter strength per unit time-frequency and hence has no dimension. Reverberation varies with range but it is assumed that the variation is small over time intervals commensurate with the scatterer and pulse duration.[6] B_r is determined by inherent motion in the medium such as surface, internal waves, and fish schools, and platform-induced effects such sonar velocity, look angle, and beamwidth. It is not the reverberation bandwidth observed at the receiver input. That bandwidth is determined from the convolution of the inherent scattering spectrum with that of the waveform.[6,10,13] The assumption that the reverberation is uniformly distributed over B_r does not introduce significant error as long as the marginal Doppler condition of low, but not zero Doppler is avoided. The conditions considered in this paper assume that the scatterer is either at zero Doppler or at sufficiently high Doppler so that there is no ambiguity main lobe interaction with the reverberation SF. The received reverberation energy and power (5) are

$$\begin{aligned} E_r&=E_x\int_{-T/2}^{T/2}\int_{-B_r/2}^{B_r/2}\mathcal{R}_r\,d\phi\,d\tau=E_x\mathcal{R}_rB_rT\\ P_r&=E_r/T, \end{aligned} \tag{13}$$

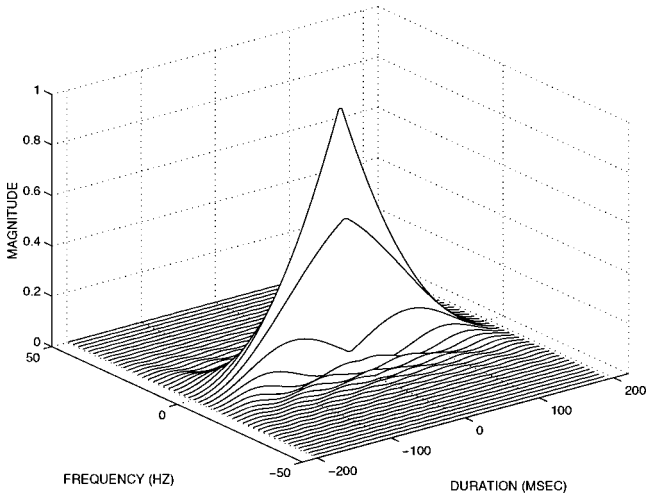

FIG. 1. CW ambiguity function, $T=200$ msec.

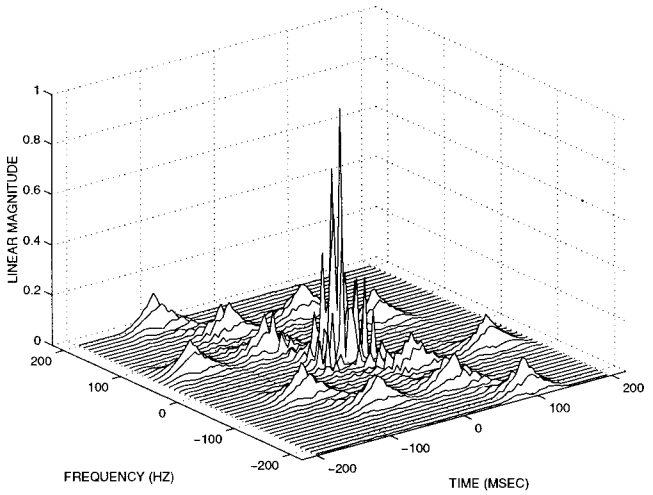

FIG. 3. FSK (Costas code) ambiguity function, $M=4$, $T=200$ msec, $W=200$ Hz.

and $P_i=P_r+P_n$ is the total input interference power.

$\mathrm{SIR}_{\mathrm{in}}$ expressions for the three scattering situations being considered are obtained from (8), (9), (12), and (13), where

$$\mathrm{SIR}_{\mathrm{in}}=\frac{P_x\mathcal{R}_{sp}}{P_i}(\text{point scattering})$$

$$=\frac{P_x\mathcal{R}_{sl}\tau_t}{P_i}(\text{line scattering}),\quad \tau_t\leqslant T$$

$$=\frac{P_x\mathcal{R}_{sl}T}{P_i}(\text{line scattering}),\quad \tau_t>T$$

$$P_i=E_x\mathcal{R}_rB_r+N_0f_s. \tag{14}$$

III. MATCHED FILTER RECEIVER OUTPUTS AND PROCESSING GAINS

Closed form estimates of MF output are computed from the convolutions (3), (4) and unit height approximations to CW, LFM, and FSK waveform ambiguity functions, examples of which are shown in Figs. 1–3. The volume and origin magnitude of a narrow-band AF are unity, and since the volume of CW and LFM waveform AF's is concentrated in the main lobe, the unit height approximations shown in Fig. 4 are used. This approximation facilitates the derivation of the closed form expressions sought and is analogous to the approximation of a bandpass filter characteristic by a constant amplitude ''boxcar'' characteristic with a width equivalent to its 3-dB width. The approximation is about 1.8 dB high for the worst case situation of the line scatterer convolved with a CW AF over its full duration T.

The FSK waveforms consist of M contiguous CW pulses spaced in frequency over the band W(Hz) such that the ambiguity sidelobes are distinct and of uniform amplitude. This requires that $M^2<TW$ for uniformly separated pulses. These codes include QC[14] and Costas codes[15] and are called ''single hit'' codes since each sidelobe represents the overlap of one subpulse pair. This property guarantees that the sidelobes will be of uniform amplitude. They have $1/M$ of their ambiguity volume in the main lobe and the remainder is apportioned equally among the $M(M-1)$ sidelobes. The main lobe support region is that of a CW with duration T/M and consequently the main lobe has a grating or ''hairbrush'' structure as shown in Fig. 3 and is modeled as in Fig. 4. The illustrated FSK waveform AF of Fig. 3 is a Costas code with $M=4$ subpulses, $TW=40$, and has distinct uniform amplitude sidelobes.

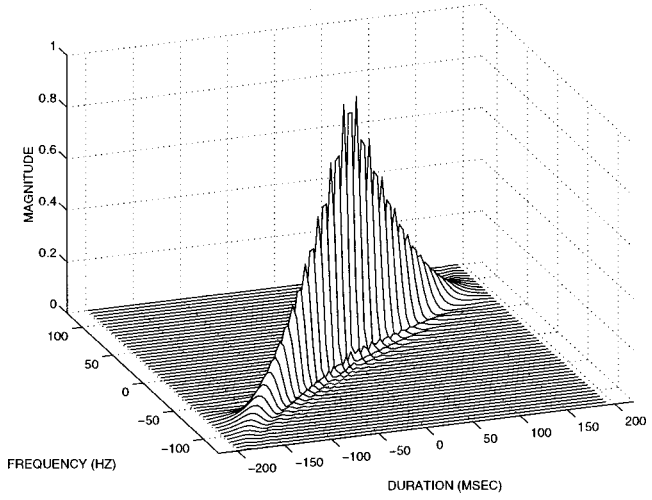

FIG. 2. LFM ambiguity function, $T=200$ msec, $W=100$ Hz.

The receiver response and output are evaluated for zero Doppler conditions and it is assumed that the filter delay and Doppler match those of the echo. Then, point scattering occurs at the origin and the line scatterer lies along the τ axis as shown in Fig. 5. It is then a simple matter to obtain the expected maximum output responses by calculating the overlap area or intersection of the SF and AF by using this simple geometry and the constant amplitude AF and SF models. The expected MF responses are

$$E_{fs}=E_x\mathcal{R}_{sp}\ (\text{point scatterer})$$

$$=E_x\mathcal{R}_{sl}\tau_i\ (\text{line scatter})$$

$$=E_x\mathcal{R}_rA_r\ (\text{reverberation}). \tag{15}$$

A_r is the overlap area between the reverberation SF and the

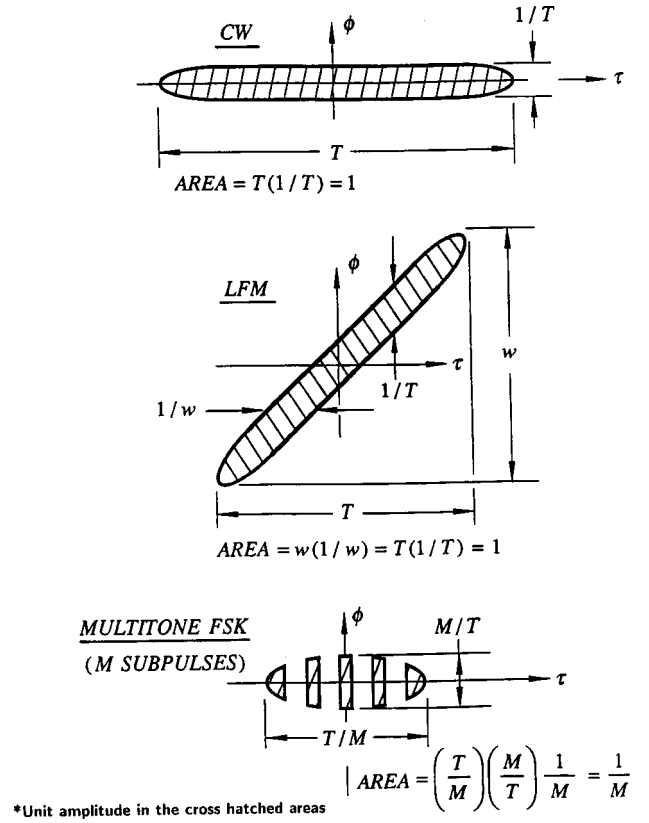

FIG. 4. Unit height ambiguity function approximations.

AF and τ_i is the intersection of the line scatterer SF and the AF main lobe as in Fig. 5. For example, consider the response for a CW waveform of duration T reflected from a line scatterer of length $\tau_t \leqslant T$. The intersection is $\tau_i = \tau_t$ and $E_{fs} = E_x \mathcal{R}_{sl} \tau_t$. If $\tau_t > T$, $\tau_i = T$ and $E_{fs} = E_s \mathcal{R}_{sl} T$. The FSK responses are somewhat more complex as the main lobe area A_r and support τ_i are reduced by the factor $1/M$ and

$$\tau_i = \begin{cases} \tau_t/M, & \text{when } \tau_t \leqslant T_p \\ T_p/M, & \text{when } \tau_t > T_p, \end{cases}$$

where $T_p = T/M$. The FSK line scatter responses are

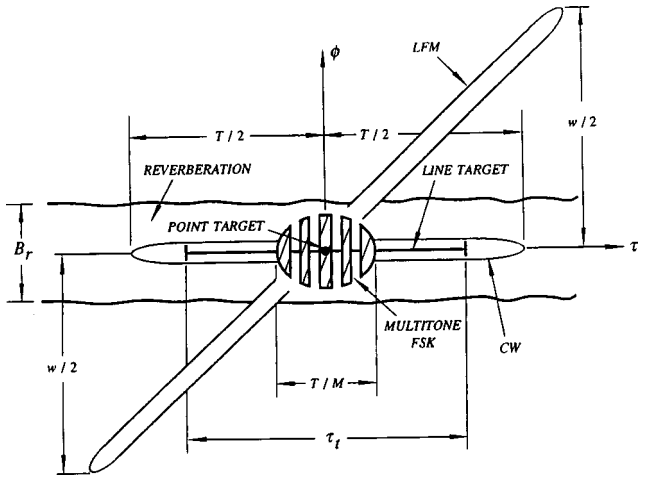

FIG. 5. Zero Doppler ambiguity and scattering function convolution regions.

TABLE I. Matched filter scatterer response expressions.

Scatterer	CW response	Scatterer	LFM response	Scatterer	FSK response
Point	$E_x \mathcal{R}_{sp}$	Point	$E_x \mathcal{R}_{sp}$	Point	$E_x \mathcal{R}_{sp}$
Line $\tau_t \leqslant T$	$E_x \mathcal{R}_{sl} \tau_t$	Line $\tau_t \leqslant 1/W$	$E_x \mathcal{R}_{sl} \tau_t$	Line $\tau_t \leqslant T_p$	$E_x \mathcal{R}_{sl} \tau_t / M$
Line $\tau_t > T$	$E_x \mathcal{R}_{sl} T$	Line $\tau_t > 1/W$	$E_x \mathcal{R}_{sl} / W$	Line $\tau_t > T_p$	$E_x \mathcal{R}_{sl} T_p / M$

$$E_{fs} = \begin{cases} E_x R_{sl} \tau_t / M, & \text{if } \tau_t < T_p \\ E_x R_{sl} T / M^2, & \text{if } \tau_t > T_p. \end{cases}$$

The scatterer response expressions for all scatterers and waveforms under consideration are summarized in Table I. The reverberation responses are likewise summarized in Table II. The processing gains are summarized in Table III–V and are computed from (6),(7),(8) using the input expressions (14) and the output expressions (15). They are parameterized by the reverberation to noise input power ratio

$$r_n = \frac{P_r}{P_n},$$

where noise and reverberation limited conditions correspond to $r_n = 0, \infty$, respectively.

IV. HIGH DOPPLER SCATTERING

The relationships given in the tables are based upon the assumption that the scatterer is at zero Doppler with respect to the reverberation, or in other words, the ambiguity main lobe is centered in the reverberation SF. Reverberation is the dominant zero Doppler interference at short range but as range increases and reverberation dies out to the ambient level, $r_n \to 0$ and the signal becomes noise limited even though it is still at zero Doppler. On the other hand, when the scatterer has a down range velocity component and has Doppler sufficient to move the ambiguity main lobe from the reverberation, G_p must be modified to reflect the fact that while the input SIR is unchanged, the output is noise limited and

$$\mathrm{SIR}_{\mathrm{out}} = \frac{E_{fs}}{N_0}.$$

The CW and FSK processing gain relationships are affected but not those of the LFM unless Doppler exceeds the LFM bandwidth, an unlikely situation in most cases. The high Doppler processing gain relationship for the CW waveform is

$$G_p(\mathrm{CW}) = f_s T (1 + r_n) \qquad \text{(High Dopp. point and line scatt.).} \quad (16)$$

An FSK waveform has ambiguity sidelobe structure that can affect the processing gain calculations when Doppler is not zero. The reverberation SF has width B_r around the zero Doppler frequency, and if the scatterer Doppler is sufficient to remove the FSK main lobe from the reverberation region yet insufficient to move one of the sidelobes into it, the re-

TABLE II. Matched filter reverberation response expressions.

Rev. bandwidth	CW response	Rev. bandwidth	LFM response	Rev. bandwidth	FSK response
$B_r \leqslant 1/T$	$E_x \mathcal{R}_r B_r T$	$B_r < W$	$E_x \mathcal{R}_r B_r / W$	$B_r \leqslant 1/T_p$	$E_x \mathcal{R}_r B_r T_p / M$
$B_r > 1/T$	$E_x \mathcal{R}_r$	$B_r > W$	$E_x \mathcal{R}_r$	$B_r > 1/T_p$	$E_x \mathcal{R}_r / M$

verberation contributes minimally and the FSK matched filter is noise limited with interference output N_0. If a sidelobe is moved into the reverberation band, its contribution denoted by E_{rsl} is equivalent to that of a CW waveform of duration T_p but attenuated by the sidelobe volume which is $1/M^2$ for single hit codes. For example, let $B_r \leqslant 1/T_p$ so that the reverberation sidelobe response from the first column of Table V is $E_{rsl} = E_x \mathcal{R}_r B_r T_p / M^2$. The total MF interference is then $E_{rsl} + N_0$.

Assuming no sidelobe reverberation contribution, the high Doppler FSK processing gain depends upon scatterer extent in relation to the AF main lobe support and is

$$G_p(\mathrm{FSK}) = \begin{cases} f_s T(1+r_n), & \text{(High Dopp. point scattering)} \\ f_s T(1+r_n)/M, & \text{(High Dopp. line scattering } \tau_t \leqslant T_p\text{)} \\ f_s T^2(1+r_n)/(M^2 \tau_t), & \text{(High Dopp. line scattering } T_p < \tau_t \leqslant T\text{)} \\ f_s T(1+r_n)/M^2, & \text{(High Dopp. line scattering } T < \tau_t\text{)}. \end{cases} \tag{17}$$

The reverberation SF bandwidth B_r is not a factor in these relationships.

V. EXPERIMENTAL RESULTS

A. Synthetic point and line scattering

The accuracy of the processing gain estimation formulas was investigated by comparing the estimates to processing gains obtained by matched filtering synthesized LFM and in-water high frequency FSK echo data. The real FSK reverberation data were obtained in a shallow-water (300 ft), sandy bottom, open ocean environment with a downward refracting sound velocity profile. The directional projector and receiver were co-located on a moving platform at mid-depth and each interrogation provided about 3 sec of reverberation. Ray path analysis revealed no significant surface but considerable bottom interaction so that the reverberation was dominated by bottom backscatter. Most of the data were of reverberation but a few echoes were obtained from a zero Doppler scatterer that could be compared to the estimate bounds. In all cases the reverberation dominated and $r_n \to \infty$. The synthesized LFM reverberation was generated with environmental conditions duplicating those of the in-water FSK database.

The deviation from the predicted average processing gains given in the tables was assessed by generating histograms of G_p from synthesized zero Doppler random point and line scatterers embedded in the in-water FSK and synthesized LFM reverberation. The input SIR of each realization was set at a level sufficient to provide a measurable MF scatterer output response for the processing gain calculation. $\mathrm{SIR}_{\mathrm{out}}$ was calculated by computing the ratio of the MF peak output to the average background level and subtracting unity. Dividing this by $\mathrm{SIR}_{\mathrm{in}}$ yielded the processing gain realization.

The FSK waveform consisted of $M=6$ subpulses with duration such that the measured in-water reverberation Doppler width was $B_r > 1/T_p$. The synthesized line scatterer had delay extent $T_p < \tau_t \leqslant T$ and the G_p estimates

$$G_p(\mathrm{FSK}) = \begin{cases} B_r M T (18.8\,\mathrm{dB}), & \text{(point scatterer)} \\ B_r T^2 / M \tau_t (10.8\,\mathrm{dB}), & \text{(line scatterer)} \end{cases}$$

were calculated from the point and line scattering relationships given in Table V with $r_n \to \infty$. Histograms resulting from 1000 interrogations of the FSK point and line scatterer in real reverberation are shown in Figs. 6 and 7 along with the predicted values.

The LFM estimates were made with the same point and line scatterers with $1/W < \tau_t \leqslant T$. The estimates

$$G_p(\mathrm{LEM}) = \begin{cases} TW(28.1\,\mathrm{dB}), & \text{(point scattering)} \\ T/\tau_t (8.8\,\mathrm{dB}), & \text{(line scatterer)} \end{cases}$$

TABLE III. CW zero Doppler processing gain for all scatterers.

Rev. bandwidth	G_p
$B_r \leqslant 1/T$	$\dfrac{f_s T(1+r_n)}{1+f_s T r_n}$
$B_r > 1/T$	$\dfrac{f_s T(1+r_n)}{1+(f_s r_n / B_r)}$

TABLE IV. LFM zero Doppler processing gains for $B_r \leqslant W$.

Point scatt.	Line scatt. $0 < \tau_t \leqslant 1/W$	line scatt. $1/W < \tau_t \leqslant T$	Line scatt. $T < \tau_t$
$\dfrac{f_s T(1+r_n)}{1+(f_s r_n / W)}$	$\dfrac{f_s T(1+r_n)}{1+(f_s r_n / W)}$	$\dfrac{f_s T(1+r_n)}{\tau_t (W + f_s r_n)}$	$\dfrac{1+r_n}{r_n + (W/f_s)}$

TABLE V. FSK zero Doppler processing gains for codes with ($M^2 < TW$).

Rev. bandwidth	Point scatt.	Line scatt. $\tau_t \leq T_p$	Line scatt. $T_p < \tau_t \leq T$	Line scatt. $T < \tau_t$
$B_r \leq 1/T_p$	$\frac{f_s T(1+r_n)}{1+(f_s T r_n/M^2)}$	$\frac{f_s T(1+r_n)}{M+(f_s T r_n/M)}$	$\frac{f_s T^2(1+r_n)}{\tau_t(M^2+f_s T r_n)}$	$\frac{f_s T(1+r_n)}{M^2+f_s T r_n}$
$B_r > 1/T_p$	$\frac{f_s T(1+r_n)}{1+(f_s r_n/MB_r)}$	$\frac{f_s T(1+r_n)}{M+(f_s r_n/B_r)}$	$\frac{f_s T^2(1+r_n)/\tau_t}{M^2+(M f_s r_n/B_r)}$	$\frac{f_s T(1+r_n)}{M^2+(M f_s r_n/B_r)}$

were obtained from Table V with $r_n \to \infty$. LFM processing gain histograms were generated using synthesized LFM reverberation and are shown as Figs. 8 and 9 for point and line scattering, respectively. As for the FSK data, the predicted processing gain is very close to the average of the ensemble but deviations of as much as 3–4 dB can be expected to occur for individual realizations.

B. In-water scatterer echoes

Point and line scattering represent extreme situations and in-water echoes from real delay spread scattering mechanisms may be expected to exhibit behavior that falls somewhere between them. This was illustrated experimentally by computing processing gains for seven of the in-water FSK scatterer echoes that were strong enough to permit the calculation of the input SIR's directly from the received time series envelope. Typical MF input and output realizations are shown in Fig. 10. The measured processing gains were G_p =(10.4,12.4,12.7,13.4,13.6,14,15.2) dB and the linear average converted to dB is 13.3. The average and all but one of the measured values fell within the estimated point-line scatter bounds of 10.8–18.8 dB established for the in-water environmental conditions.

VI. DISCUSSION

The area convolution approach to MF performance estimation is not meant to take the place of direct simulations of entire interrogation cycles using sophisticated propagation and scatter models. It is rather a means for the estimation of medium- and high-frequency sonar performance bounds for nominal environmental conditions that may exist locally at particular ranges. There are many more waveforms and detection methods used in sonar signal processing than were discussed. However, CW, LFM, and FSK or Hop code waveforms and matched filter processing are widely used in mid- to high-frequency sonars and often serve as benchmarks against which other processors are compared.

Processing gain is a particularly useful quantity because it connects simple sonar equation estimates of $\mathrm{SIR}_{\mathrm{in}}$ to a probabilistic measure of performance. The receiver operating characteristics (ROC's) relating detection and false alarm probabilities for matched filters in Gaussian interference are computed from

$$\log \wp_d = (1 + \mathrm{SIR}_{\mathrm{out}}) \log \wp_f,$$

assuming the scatterer is the slowly fluctuating Gaussian model of Van Trees.[6] Consequently, it is possible to assess MF detection performance at the fundamental ROC level by starting with the sonar equation, using estimates of the processing gain to obtain $\mathrm{SIR}_{\mathrm{out}}$, and computing the ROC's.

Matched filter performance estimates can be extended to the assessment of detection processes that incoherently combine the outputs of several coherent matched filters. These are the so-called diversity combiners that are often used when communicating or interrogating over fading channels.[9,16] FSK waveforms are often used but each CW component is individually filtered rather than the waveform

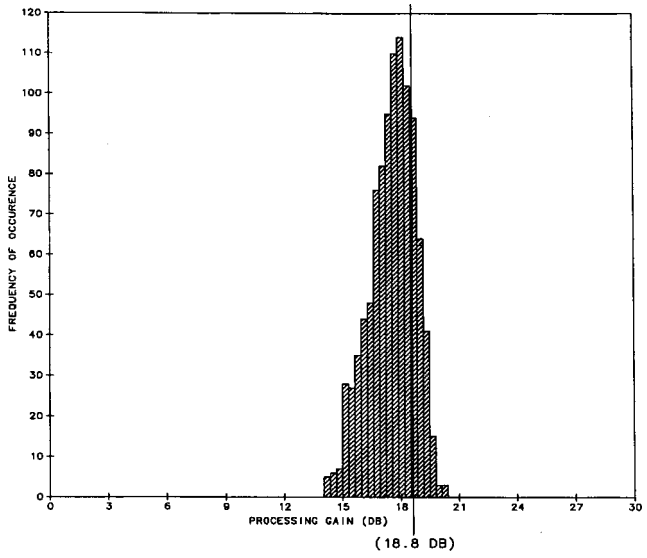

FIG. 6. 1000 sample histogram of measured point scatter G_p for the FSK waveform in real reverberation. Predicted value= 18.8 dB.

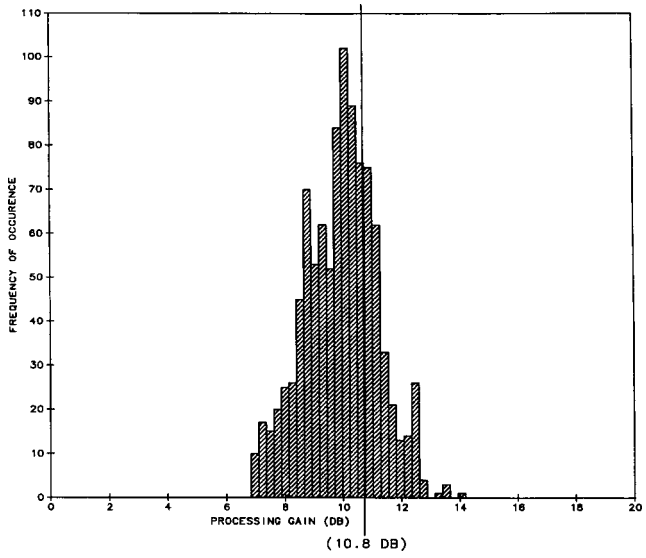

FIG. 7. 1000 sample histogram of measured line scatter G_p for the FSK waveform in real reverberation. Predicted value= 10.8 dB.

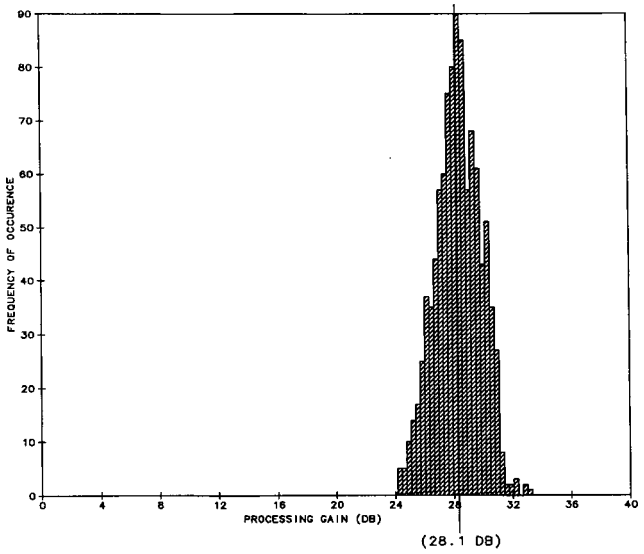

FIG. 8. Histogram of measured point scatterer G_p for the LFM waveform in synthetic reverberation. Predicted value=28.1 dB.

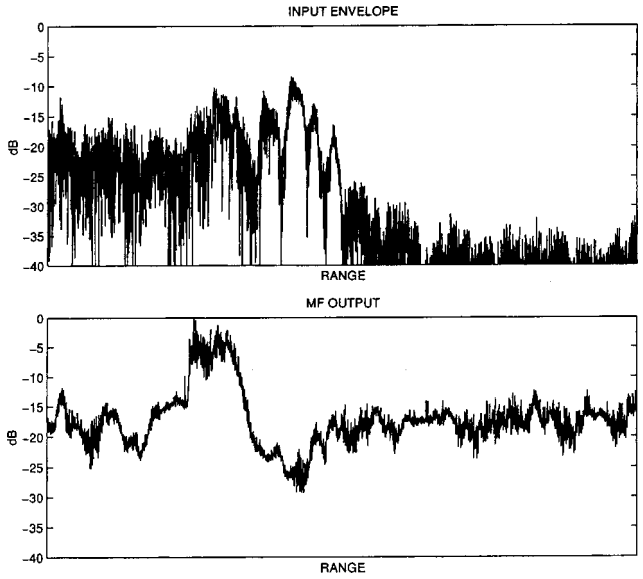

FIG. 10. Six-tone FSK input and matched filtered output time series of a real delay spread scatterer in an ocean environment.

as a whole. The ROC performance of the combiner depends upon the average SIR of each subpulse filter that in turn is estimated by the techniques discussed in this paper.

Reverberation is a nonstationary process with varying amplitude and spectrum and the simple estimate model is only applicable over short-range increments where the conditions can be assumed to be constant and not changing within the duration of the interrogating signal. The technique can be extended to include Doppler as well as delay spreading for simple ambiguity functions when only the delay-Doppler region near the origin loosely defined as the main lobe region is involved. Ambiguity functions of finite duration waveforms have unbounded Doppler support and delay support over an interval of $2T$. While most of the volume of CW or LFM waveforms is contained in the main lobe, more complex waveforms often have a significant amount of ambiguity volume distributed in the sidelobe regions. This contributes to receiver response if the scattering function extends to, or the echo is Doppler shifted into the sidelobe region.

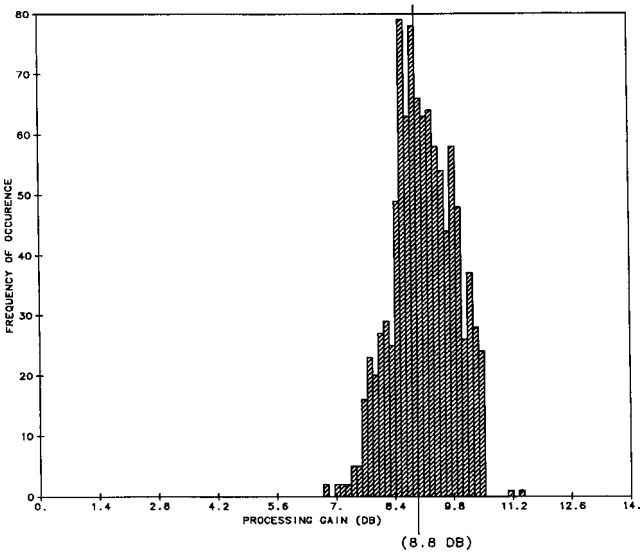

FIG. 9. Histogram of measured line scatterer G_p for the LFM waveform in synthetic reverberation. Predicted value=8.8 dB.

For example, Costas codes for which $TW \gg M^2$ have $2M(M-1)$ distinct sidelobes each of volume $1/M^2$ and Doppler spacing of $W(M-1)$. The area calculations used to construct the tables were done assuming that $B_r \ll W(M-1)$, but if the echo or reverberation Doppler spread approaches the sidelobe spacing, the volume contributed by one or more sidelobes will contribute to the scattering/ambiguity convolution.

The formulas given in the tables are meant only to bound the processing gain under quasistationary conditions that may exist locally for a particular reverberation to noise ratio, reverberation Doppler spread, and scatterer strength. Estimates of processor performance under very specific conditions of a particular scatterer as a function of range when the reverberation varies significantly must be done with more sophisticated time series models that simulate a whole ping cycle. No attempt has been made to separate spreading effects such as inherent scatterer extent from that generated by propagation (multipath). The time series as observed at the receiver reflects both effects and cannot separate them. The processing gain bounds of point versus line scattering serve to bound matched filter performance under these best and worst possible echo spreading conditions.

ACKNOWLEDGMENT

This work was supported by ONR code 333.

[1] E. C. Stewart and E. C. Westerfield, ''A theory of active sonar detection,'' Proc. IRE **47**, 872–881 (1959).
[2] E. C. Westerfield, R. H. Prager, and J. L. Stewart, ''Processing gains against reyerberation (clutter) using matched filters,'' IRE Trans. Inf. Theory **6**(3), 342–348 (1960).
[3] L. J. Ziomek and L. H. Sibul, ''Maximization of the signal to interference ratio for a doubly spread target: Problems in nonlinear programming'' Signal Process. **5**, 355–368 (1983).
[4] R. A. Altes, ''Radar/sonar signal design for bounded Doppler shifts,'' IEEE Trans. Aerosp. Electron. Syst. **18(4)**, 369–380 (1982).

[5] D. M. Drumheller and D. W. Ricker, ''Receiver optimization for detection in doubly spread channels,'' J. Acoust. Soc. Am. **89**, 1714–1723 (1991).
[6] H. L. Van Trees, *Detection, Estimation, and Modulation Theory, Part III* (Wiley, New York, 1971).
[7] T. J. Kincaid, ''On optimum waveforms for correlation detection in the sonar environment: Reverberation limited conditions,'' J. Acoust. Soc. Am. **44**(3), 787–796 (1968).
[8] S. V. Marić, J. R. Bellegarda, and E. L. Titlebaum, ''Signal design for clutter suppression in radar and sonar systems,'' Proc. CISS-91, Johns Hopkins University, 962–967 (1991).
[9] J. V. DiFranco and W. L. Rubin, *Radar Detection* (Artech House, Dedham, MA, 1980).
[10] L. J. Ziomek, ''A scattering function approach to underwater acoustic detection and signal design,'' Ph.D. thesis, Penn State University, November 1981, ARL TR 81–144.
[11] D. W. Ricker, ''The Doppler sensitivity of large TW phase modulated waveforms,'' IEEE Trans. Signal Process. **40**, 2406–2413 (1992).
[12] L. G. Weiss, ''Wavelets and wideband correlation processing,'' IEEE Signal Process. Mag. **11**(1), 13–32 (1994).
[13] R. Laval, ''Time-frequency-space generalized coherence and scattering functions,'' in *Aspects of Signal Processing, Part 1*, edited by G. Tacconi (Reidel, Dordrecht, 1977).
[14] E. L. Titlebaum and L. H. Sibul, ''Time-frequency hop signals part II: Coding based upon the theory of quadratic congruences,'' IEEE Trans. Aerosp. Electron. Syst. **17(4)**, 494–499 (1981).
[15] J. Costas, ''A study of a class of detection waveforms having nearly ideal range-doppler ambiguity properties,'' Proc. IEEE **72**, 996–1009 (1984).
[16] D. Barton, *Radars—Frequency agility and diversity* (Artech House, Dedham, MA, 1977).

Measurements of nanometer scale interface diffusion between tungsten and niobium thin films using high frequency laser based ultrasound

C. J. K. Richardson, M. J. Ehrlich, and J. W. Wagner[a)]
Department of Materials Science and Engineering, Johns Hopkins University, Baltimore, Maryland 21218

(Received 15 July 1999; accepted for publication 6 January 2000)

This article presents the use of a quantitative analysis technique to describe time-resolved acoustic spectroscopy (high frequency laser based ultrasound) measurements of atomic diffusion on nanometer length scales occurring at the interface between sputter-deposited tungsten and niobium films. The extent of diffusion at the tungsten-niobium interface is determined by comparing experimental, simulated, and theoretical transfer functions between acoustic arrivals. The experimental and simulated transfer functions use the spectral content of successive reflected acoustic waves and the theoretical transfer function is based on the transfer matrix of an equivalent stratified interface region. This combination of theoretical, simulated, and experimental analyses makes it possible to separate signals with distinct differences between the as-deposited interface and those interfaces diffused to an experimentally determined 0.8-nm and 1.4-nm extent. Comparison of predicted and measured diffusion depths for this diffusion couple indicates that bulk diffusivities are not appropriate for describing nanometer scale interface diffusion. © *2000 Acoustical Society of America.* [S0001-4966(00)01904-4]

PACS numbers: 43.35.Ns, 68.35.Gy, 68.35.Ct, 68.35.Fx [HEB]

INTRODUCTION

The miniaturization of thin film structures for use in mechanical, chemical, and electrical applications increases the effect of interface regions in device function and performance.[1] Most often, destructive techniques are employed to determine mechanical interface structure[2,3] or to correlate electronic performance with structure.[4] However, the difficulty in preparing samples for transmission electron microscopy and the inability of such destructive techniques to examine samples both before and after testing makes correlation of the properties difficult. In contrast to destructive techniques, methods based on ultra-high frequency thermoelastic laser ultrasonics provide a means to determine noninvasively the interface composition on a nanometer scale.[5,6] While there are a number of less complicated techniques that are capable of measuring film properties,[7–9] only those techniques that generate GHz longitudinal waves which propagate through the film like bulk waves allow material properties to be determined independently from each other.

The examination of films thinner than 1 μm with longitudinal acoustic waves requires systems with bandwidth in excess of 1 GHz. This requirement results from the necessity of the acoustic wavelengths to be the same approximate size or smaller than the subject of interest. To achieve this bandwidth a sub-picosecond laser pulse is used for generation and detection. For films of this thickness the acoustic time-of-flight are sufficiently short that the cooling of the near surface region which follows heating caused by the generation laser pulse and the acoustic arrivals are superimposed. The observation of thermal and acoustic behavior allows one to examine simultaneously the thermal and acoustic behavior of the thin film structure. In this paper, the thermal contribution of the observed signal is removed in order to focus on the acoustic information of the measured signal.

Pump–probe spectroscopy is a correlation technique that has been used to measure picosecond duration thermal and acoustic transients. When applied to thermal and acoustic transients, pump–probe spectroscopy is often referred to as time-resolved thermal[10] and acoustic[11] spectroscopies. The term time-resolved spectroscopy is used to indicate that a pulsed laser is used for both the generation (pump) and detection (probe) of the transients of interest. The pulsed probe acts like a strobe, to which a variable time delay is imparted with respect to the pump pulse. This arrangement is a form of gated detection with a variable window position. A single experiment shifts the window through all delays of interest during a repetitive transient in order to observe the complete picosecond duration event.[12]

Typically, these ultrashort duration transients are detected by monitoring perturbations of the optical reflectivity of the sample. The application of reflectivity-sensitive pump–probe spectroscopy for the inspection of thin films began in the mid 1980's and has been applied to numerous materials.[5,6,10–15] The experiments presented here use a modified self-stabilized Michelson interferometer to detect ultrafast thermal and acoustic transients.[16,17]

Even though thermoelastic generation of ultrasound in the picosecond time domain has received considerable attention it is common for theoretical descriptions to focus on only the thermal or the acoustic contribution to the observed signal.[5,10–15,18–20] Here, computer simulations of the complete observed signal are accomplished through the use of a partially coupled thermoelastic description for the case of a

[a)]Current affiliation: Department of Materials Science and Engineering, Case Western Reserve University, Cleveland, OH 44106-7220.

 0001-4966/2000/107(4)/1987/7/$17.00

film in perfect contact with a semi-infinite substrate.[21,22] The results of these computer simulations are used to elicit information regarding the thin film.

The analysis of the acoustic signature to determine interface extent is accomplished by comparing the frequency components of consecutive free surface arrivals through the use of a transfer function. The shape of the transfer function between the first $(L2)$ and second $(L4)$ longitudinal acoustic arrivals is used to predict quantitatively the interface profile. The broadband frequency content of the ultrafast laser generated ultrasound provides a large frequency range in which direct comparison of the experimental, simulated, and theoretical transfer function is possible. Analyzing both the simulated and experimental results in the frequency domain is done to identify artifacts that are introduced through the analysis technique.

I. THEORY

A. Ideal thermoelastic material behavior

The thermal and acoustic response of the thin film to an ultrafast optical pulse is described with the one-dimensional time-dependent classical partially coupled thermoelastic differential equations for homogeneous nondispersive materials:[23]

$$\kappa \frac{\partial^2 T}{\partial x^2} + W = \rho C_v \frac{\partial T}{\partial t}, \quad c \frac{\partial^2 u}{\partial x^2} - B \frac{\partial T}{\partial x} = \rho \frac{\partial^2 u}{\partial t^2}, \tag{1}$$

where ρ is the density, T is the temperature field, κ is the thermal conductivity tensor, C_v is the specific heat, c is the effective stiffness tensor, B is the thermal-stress tensor, and u is the displacement vector. The multidimensional heating function, W, is selected to describe the temporal shape of the laser pulse and the spatial extent of the heated region, which according to classical thermoelasticity is defined by the absorption volume. The spatially one-dimensional description is applicable in this situation because the laser spot size is large ($\sim$10 μm) compared to the film thickness ($\sim$300 nm). The material properties as determined from anisotropy or polycrystallinity are used as constants in this homogeneous one-dimensional description. It is important to note that these governing equations are based on the continuum model for linear elasticity, which assumes small displacements and a linear acoustic dispersion relationship. This continuum model neglects the microscopic atomic structure of solids that become important on small length scales, but is still usable for frequencies approaching several THz. Complete numerical solutions of the thermal and displacement differential equations have been obtained through transform techniques for a system initially at rest and a film in perfect contact with a semi-infinite substrate (continuity of displacements, temperature, heat flow, and tractions).[17]

The experiments reported here use interferometric detection to measure ultrafast thermal and acoustic transients. In addition to displacements between the reference and signal mirrors, interferometers are sensitive to changes in the index of refraction of either mirror. Changes in the index of refraction of the signal mirror manifest themselves as changes in the magnitude and phase of the reflected light, both of which alter the measured interferometric signal. By itself, reflectivity-sensitive measurements of temperature (thermoreflectivity) and strain (piezoreflectivity) variations have been used extensively in the measurement of ultrashort acoustic and thermal transients. The effects of changes in index of refraction cannot be removed from the observed interferometric signal. The interferometric representation that considers changes in path length from near-surface displacements, δ, changes in optical reflectivity, $\Delta R/R$, and changes in the phase of the reflected light, $\Delta\theta$, for a stabilization point of $\Phi_0 \sim \pi/2$ is[17]

$$I_d = (I_1 + I_2) - 4\sqrt{I_1 I_2} K_0 \delta - 2\sqrt{I_1 I_2}\Delta\theta + \frac{\Delta R}{R} I_1, \tag{2}$$

where I_d is the measured intensity, I_1 is the intensity in the signal beam, I_2 is the intensity in the reference beam, and K_0 is the optical wave number. The first term in Eq. (2) is constant and thus can be neglected. The second term denotes changes resulting from near-surface displacements. The last two terms represent changes in the optical signal from perturbations in the complex index of refraction, manifesting in changes of phase of the reflected light (third term) and changes in the optical reflectivity (fourth term).

B. Frequency-dependent acoustic reflectivity

In many cases computer simulations based on the model described above are sufficient. The results from this theory can be used to analyze quantitatively the experimental results regarding the thickness, elastic, and thermal properties of the film. The most easily questionable assumption in the derivation of these theoretical results is the conjecture that the film and substrate are in perfect contact. In such a case, the interface region has no effect on the acoustic and thermal behavior of the film/substrate system, i.e., the system behavior is described using the dissimilarity of the two materials, accordingly the acoustic reflectivity is often written as[24]

$$R = \frac{z_1 - z_2}{z_1 + z_2}, \tag{3}$$

where $z_i = \rho_i c_i$ $(i = 1,2)$, ρ_i is the density, and c_i is the acoustic velocity.

A thorough analysis method that describes the experimental acoustic observations must consider the medium through which the pulse propagates and the interfaces from which it reflects. In a one-dimensional homogeneous film on a homogeneous substrate variations in acoustic impedance near the interface are of particular interest. Such variation could be caused by intermixing of the two materials (changes in the acoustic velocity), a variation in density of either materials, or a combination of both.

Interfaces that are rough or composed of intermixing atomic species give the interface region a finite physical extent. In the one-dimensional models used here, the physical extent and the variation in acoustic impedance perpendicular to the interface are the parameters of importance. Therefore, the one-dimensional analysis cannot distinguish between the two since the statistical average of acoustic impedance, and therefore composition is measured in only the surface normal

direction. To distinguish between roughness and atomic intermixing a two-dimensional imaging technique must be used.

The analysis of film/substrate systems with interfaces of finite width is completed using the method of resultant waves, also known as the transfer matrix method.[25] The method of resulting waves is a numerical technique that separates the interface region into a multilayer stack of homogeneous layers. In such a stratified region the incident wave is partially reflected off the interface between the film material and the topmost interfacial layer. The transmitted energy propagates through the next layer and is again partially reflected from the next interface. The transmitted energy propagates to the next interface while the reflected energy propagates back to the first interface. Energy is reflected at each interface and therefore energy is incident at the multilayer interfaces from the forward and backward directions. It is the combined effect of all of these reflections and the phase changes caused by propagation through the layers that gives the stratified system its reflectivity. In general, the reflectivity has a complex frequency dependence, representing the amplitude and phase of the reflected harmonic waves. The analysis relies on the linear acoustic dispersion relationship and acoustic boundary conditions at the interfaces of the stratified interface region.

It is convenient to represent the incident acoustic pulse in terms of its equivalent Fourier representation. This representation allows the Fourier domain components, $\Phi(\omega)$, to be considered independently. The harmonic component in the mth layer traveling in the positive $(+)$ or negative $(-)$ x-direction is described as

$$\Phi_m^{\pm} = A_m^{\pm} \exp[\, i(\pm k_m x - \omega t + \varphi_m)], \tag{4}$$

where A_m is the amplitude, ω the angular frequency, k_m the wave number, and φ_m is a phase factor. To determine the acoustic reflectivity of the stratified interface region appropriate acoustic boundary conditions must be maintained between each of the homogeneous layers for waves that are propagating in both the forward and backward directions. Consider the mth and $(m+1)$th layers, where continuity of the normal displacements and continuity of the normal stresses are written as

$$[\Phi_m^+ + \Phi_m^-]_{x=d_m} = [\Phi_{m+1}^+ + \Phi_{m+1}^-]_{x=d_m}, \tag{5}$$

$$z_m[\Phi_m^+ + \Phi_m^-]_{x=d_m} = z_{m+1}[\Phi_{m+1}^+ + \Phi_{m+1}^-]_{x=d_m}. \tag{6}$$

These two results can be combined and written in matrix form yielding a transfer matrix between the positive and negative traveling waves. A recursive expression is readily obtained for the complex acoustic reflectivity of the $m-1$ layer[25]

$$R_{m-1} e^{i\Delta_{m-1}} = \frac{r_{m-1} + R_m e^{i\Delta_m} e^{-2i\delta_{m-1}}}{1 + r_{m-1} R_m e^{i\Delta_m} e^{-2i\delta_{m-1}}}, \tag{7}$$

where R_m is the magnitude and Δ is the phase change of the reflected signal, while δ is the phase delay caused by traversing the mth film, and r_m is the reflectivity between the r_m and r_{m-1} layers. This operation is applied successively to lower layer indices until the first layer has been incorporated. At this point R_0 and Δ_0 represent one Fourier component of the entire stratified region, which in turn models the continuously varying region. The experimentally pertinent frequency dependent reflectivity of the interface is obtained through calculating the magnitude of the complex reflectivity for each frequency component:

$$R(\omega_1, \omega_2, \omega_3, \ldots \omega_n) = [R_0(\omega_1), R_0(\omega_2), R_0(\omega_3), \ldots R_0(\omega_n)]. \tag{8}$$

This computationally demanding technique is beneficial because it allows arbitrary variations to be modeled, such that theoretical predictions of the reflectivity of extended interfaces can be modeled in addition to any combination of thin interfacial alternative phase layers. For example, through this analysis the acoustic reflectivity of a Grube type diffusion interface can be determined. This type of interface occurs when two distinct materials are brought into contact such that interdiffusion of atoms occurs without forming an alternate phase. Such an interface is mathematically described as[26]

$$C = C_1 + \frac{C_2 - C_1}{2}\left[1 + \operatorname{erf}\left(\frac{x}{\sqrt{4Dt}}\right)\right], \tag{9}$$

where D is the atomic diffusivity, t is time during which interdiffusion occurs, x is distance from the original interface, and C_i are the initial material concentrations on each side of the original interface. Using this form for the interface, the frequency-dependant acoustic reflectivity has been calculated.

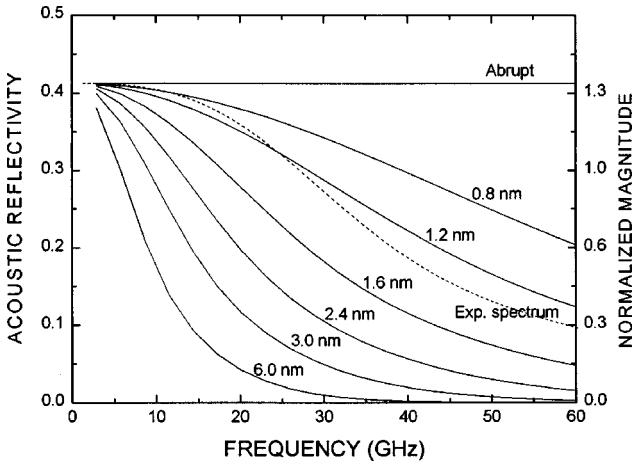

FIG. 1. Theoretical acoustic reflectivity for tungsten-niobium diffusion interfaces that have undergone various amounts of diffusion (Abrupt, 0.8 nm, 1.2 nm, 1.6 nm, 2.4 nm, 3.0 nm, and 6.0 nm), and the experimentally determined spectrum of an acoustic pulse generated from a 100-fs laser pulse in a 300-nm-thick as-deposited tungsten film on niobium. Interfaces of larger extent have a smaller bandwidth transfer function. Those that have a similar reflectivity bandwidth as the acoustic pulse offer the greatest region of sensitivity.

Figure 1 shows the results of the calculated magnitude of the acoustic reflectivity for a tungsten film on a niobium substrate for an abrupt interface (straight line) interfaces of various extents (solid curved lines) and the acoustic spectrum calculated from experimental measurements of an as-deposited tungsten-niobium sample (dashed line). The inter-

TABLE I. Heat treatment schedule for the tungsten-niobium-tungsten samples.

Schedule	Heating ramp	Hold temperature	Hold time	Cool ramp
I	~7 °C/min	875 °C	~15 min	Free cool
II	4 °C/min	900 °C	1 min	4 °C/min
III	4 °C/min	900 °C	1 h	4 °C/min

face extent is defined as the distance where 99% of the composition changes. High frequencies (small wavelengths when compared to the interface region) experience a slowly varying change in acoustic impedance, while low frequencies (large wavelengths when compared to the interface region) still encounter an abrupt interface. This relative extent is the basis of the frequency dependent acoustic reflectivity. It is apparent in Fig. 1 that the ultrasonic spectrum of an ultrafast laser generated acoustic pulse is similar to the reflectivity spectra of interfaces with a physical extent of approximately 1–2 nanometers. This physical extent parameter is the most interesting to work with, since those interfaces of much higher reflectivity bandwidth do not sufficiently alter the acoustic pulse and those of much lower reflectivity bandwidth reflect too little energy to be detected. Therefore, the system should be most sensitive to interfaces with a physical extent of approximately 1–2 nanometers.

II. EXPERIMENT

Tungsten and niobium were selected for this experimental work because they are completely miscible,[27] nearly isotropic and exhibit different elastic impedances. Complete miscibility of the materials provides an interface free of additional phases, isotropy eliminates orientation dependent effects, and different elastic impedances result in a strong acoustic reflection, $R=41\%$. A series of thin film samples were deposited onto tungsten disks that were metallurgically polished with 0.3-μm diamond suspension. Two layers were deposited in a single sputtering run under a 5-mT atmosphere of argon. A 4-μm-thick niobium layer was dc magnetron sputtered at approximately 1 nm/s and was capped with a 300-nm-thick layer of tungsten that was rf magnetron sputtered at a rate of 0.6 nm/s, producing an oxide free tungsten-niobium interface between the two films. The niobium layer is thick enough that it can be modeled as an infinite layer for the time-resolved experiments.

To verify consistency in the fabrication process, four identical samples were fabricated and tested with Rutherford backscattering and time-resolved acoustic spectroscopy. As described in Table I, three of these samples were then heat treated to promote interfacial diffusion in a sealed retort furnace under an argon-5% hydrogen environment. Normal incidence optical reflectivity measurements at 633 nm were conducted on the pre- and post-treated samples to verify that no significant oxide growth occurred. In all cases, there was no statistically distinguishable change in optical reflectivity. Each of these samples was then re-examined using time-resolved thermal and acoustic spectroscopy.

Time-resolved thermal and acoustic spectroscopy experiments were conducted using a mode-locked Ti:sapphire laser operating at 800 nm and producing 10-nJ, 100-fs duration pulses at a repetition rate of 82 MHz. The signals were detected using the rotated-Michelson interferometer scheme shown in Fig. 2 where the plane of amplitude division is perpendicular to the propagation direction of the probe beam. Refraction at the cube faces cause the two beams exiting the beam splitter cube to be nearly parallel, thus creating two beams that may be focused at different locations on the sample surface. The two focal points on the sample surface make up the reference and signal locations. The pump pulse train is focused on top of the signal point while the reference point is only a few millimeters distant. The reference and signal beams are combined as they pass through the beamsplitter a second time, thus allowing measurement of the relative phase and amplitude. Because both the reference and signal legs of the interferometer reflect off the sample, this interferometer is self-stabilized to reasonably high frequencies.

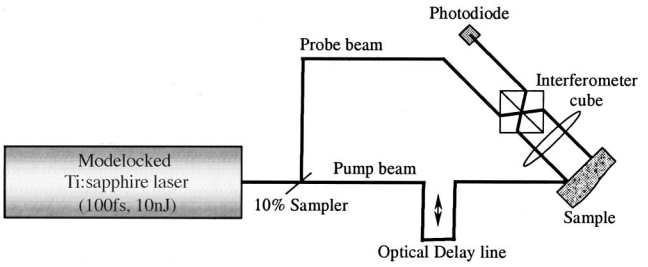

FIG. 2. Schematic of the interferometric pump–probe spectroscopic experimental setup. The signal leg of the interferometer and the pump beam are co-located on the sample surface.

III. ANALYSIS

Figure 3(a) shows a typical measured interferometric signal of the tungsten-niobium samples. The abrupt change at time equals zero is attributed to heating caused by absorption of the pump pulse. The slow recovery is thermal relaxation and the small negative going spikes are acoustic arrivals. This experimental result is compared to a simulated signal using the thermoelastic model for a film in perfect contact with the substrate using the values shown in Table II.

At this point, the sample properties can be assessed. The values in Table II match those found in the literature for bulk values except for those that lead to a thermal diffusivity that is lower than the bulk values by approximately an order of magnitude. This result has been reported elsewhere and is attributed to increased disorder produced by the limiting geometry of a thin film.[28] Despite this analysis, the presumption of a film in perfect contact with the substrate has not been sufficiently addressed. To resolve this issue a more stringent analysis of the acoustic information is required.

Analysis of the acoustic information is facilitated by isolating it from the thermal contribution. The quick rise and subsequent decaying thermal relaxation is removed by discarding the first 20 picoseconds of data and curve fitting a sixth order polynomial to the remaining thermal relaxation. This polynomial is then subtracted from the thermal/acoustic signal. The result of these operations is shown in Fig. 3(b) where it is evident that the acoustic information dominates

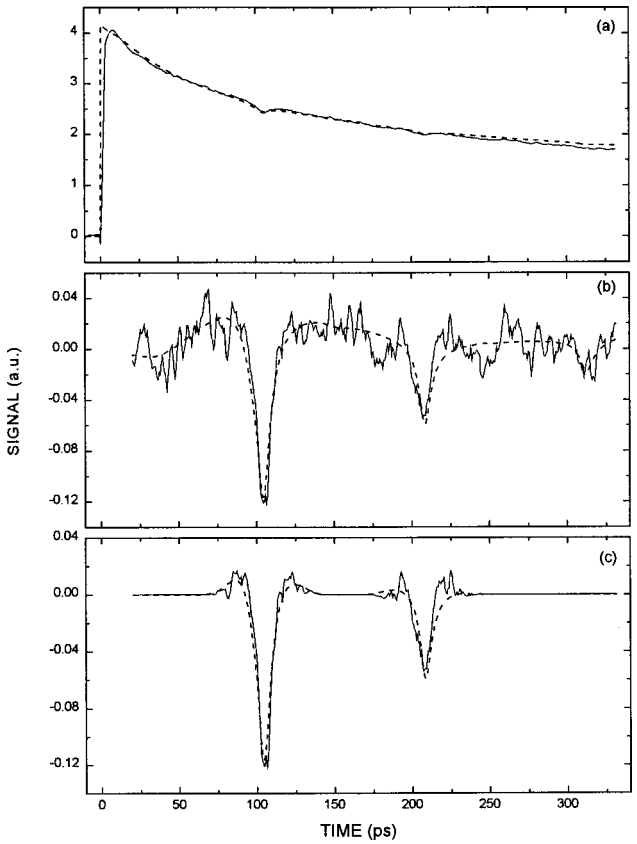

FIG. 3. Raw signal as measured (a), acoustic arrivals obtained by subtracting the thermal relaxation (b), and isolated acoustic arrivals obtained by windowing (c). Each figure shows the measured interferometric (solid) and simulated (dashed) curves. The thermal artifact results from the shoulders in the windowed arrivals resulting from the subtraction of the thermal relaxation.

the remaining signal. To maintain consistency and to determine the effects of the analysis routines, both the simulated results and the experimental results from Fig. 3(a) are analyzed using identical procedures. Despite these efforts to isolate completely the acoustic portion of the data, the polynomial fit and subtraction operation leaves a slight ripple to the baseline signal.

The next step in the analysis is to isolate each acoustic pulse. The acoustic arrivals are separated by individually windowing each arrival with a Hamming window that is approximately three to five times wider than the arrivals, and is centered on the arrival peaks. Figure 3(c) shows the acoustic data of the windowed arrivals. The shoulders of each arrival are a result of the slight ripple that is left over from the subtraction of the thermal relaxation.

TABLE II. Physical parameters used in the classical thermoelastic model to simulate experimental results.

Parameter	Film	Substrate
Material	Tungsten	Niobium
Thickness (nm)	272.3[a]	∞
Density (kg/m^3)	19 300	8570
Specific heat (J/kg K)	210[a]	268
Thermal conductivity (W/mK)	20[a]	538
Young modulus (GPa)	411	105
Poisson ratio	0.28	0.397
Coefficient of thermal expansion (1/K)$\times 10^6$	4.5	7.2
Real part of index of refraction	3.54	$\cdots$
Absorption coefficient	2.76	$\cdots$
Thermoreflectivity sensitivity	$5e$-5	$\cdots$

[a]Experimentally determined value.

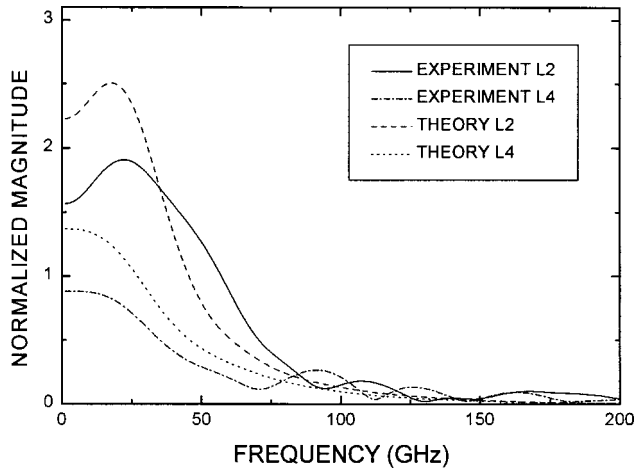

FIG. 4. Frequency content of the windowed arrivals as determined through fast Fourier transforms. The decreased low frequency components of the spectra are the results of the thermal artifact.

Figure 4 shows the frequency contents of the windowed arrivals that are determined with a fast Fourier transform algorithm. It is evident from these Fourier representations of the individual arrivals that there is a low frequency suppression resulting from the shoulders. Comparisons of the relative shoulder heights between the four arrivals pictured in Fig. 3(c) shows a correlation between shoulder height and low frequency suppression. Because this decrease is observed in both the simulated and the experimental signals, it is evident that it is an artifact of removing the thermal contribution and not necessarily physically pertinent, it is from here forward referred to as the thermal artifact. It is also clearly evident that this artifact will remain in all subsequent analyses and must be considered while drawing quantitative conclusions.

Two analysis methods are used on the reduced experimental data. The first method compares the energy centroid calculated from the first moment of the transformed signals of the individual arrivals

$$M = \frac{\int f A(f) df}{\int A(f) df}, \tag{10}$$

where f is frequency, $A(f)$ is the fourier transform, and M is the frequency centroid. Comparison of the energy centroids is shown in Fig. 5. This method of analysis allows a quick determination of the heat-treated samples to determine the changes that are occurring; that is, the energy centroid is a relative measure of the interface extent. The thermal artifact and the high frequency noise in the experimental signals affect the average values of the centroids when comparing the arrivals against each other. However, comparing the changes of each arrival only against itself shows a clear decrease that is more significant for both experimental arrivals than the simulated arrivals. The centroid analysis of the simulated arrivals provides a baseline for determining the influence of

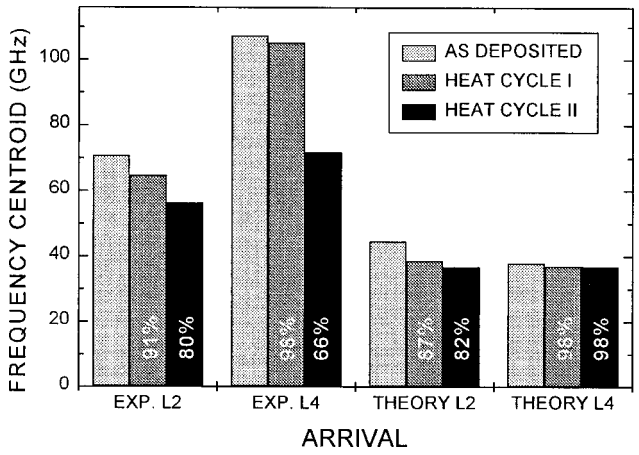

FIG. 5. Frequency centroid for experimental and theoretical acoustic arrivals. The larger percentage decrease in the experimental signals (compared to the simulated signals) illustrates a decrease in frequency centroid that indicates an expanding interface region and not the effect of an artifact.

the thermal artifact. The observations of larger percent changes in the experimental signals show that the heat treatments are changing the spectral content of the reflected arrivals more than the artifact can explain.

The second method allows the interface extent to be completely characterized by using the magnitude of the transfer function between successive acoustic arrivals, i.e., the ratio of each frequency component of the $L2$ and $L4$ Fourier magnitudes. This transfer function describes the effects of propagation on the acoustic pulse. Frequency-dependent attenuation or reflectivity will reduce the area under the transfer function in addition to changing its shape, while material dispersion will only rearrange the acoustic energy, thus changing the shape of the transfer function but not the area under the curve.[5] The experimentally determined transfer function can be compared directly to the theoretical frequency-dependent reflectivity of an extended interface calculated from Eq. (8) in order to select the shape and extent of the interface. Figure 6 shows these comparisons. Figure 6(a) compares the theoretical reflectivity of an abrupt interface (horizontal line), with the transfer functions calculated from the experimental signal (with error bars) and simulated signal (dashed-dot). The shallow long period ripple in the transfer functions from both the experimental and simulated signals is a result of the thermal artifact. The error bars associated with the experimentally determined transfer function are obtained from estimating a uniform noise floor and calculating the error associated with each frequency component of the transfer function. The error bars are displayed periodically for readability of the figures.

Figure 6(b) and (c) clearly show a decrease in the high frequency components that cannot be accounted for by the noise floor, nor the long period ripple of the thermal artifact. This lowering of the reflectivity of the high frequency component follows the theory described in Sec. II B. As the interface region increases through atomic diffusion, the reflection of the acoustic pulse becomes increasingly frequency dependent. Figure 6(b) illustrates reasonable agreement between the experimental transfer function from the schedule I sample and the frequency-dependent reflectivity of an interface with an extent of 0.8 nm. However, confidence is reduced because of the presence of the thermal artifact. On the other hand, Fig. 6(c) illustrates excellent agreement between the experimental transfer function of the schedule II sample and the calculated reflectivity of an interface of 1.4-nm extent. While a better agreement in Fig. 6(b) would be desirable, the agreement in Fig. 6(c) is so convincing that it is clear that this amount of atomic intermixing has occurred.

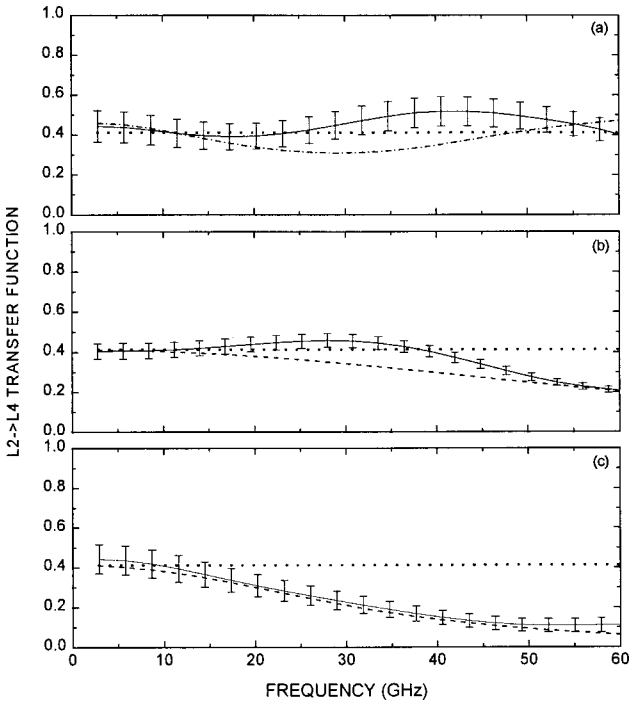

FIG. 6. Comparison of the experimental, simulated and theoretical transfer functions indicating a distinct difference between the as-deposited (a), heat schedule I (b), and heat schedule II (c) samples. Solid lines with error bars indicate experimental curves, dashed lines represent theoretical curves for a 0.8-nm (b) and 1.4-nm (c) interface, while dotted lines show the ideal frequency independent reflectivity for an abrupt interface. The dash-dot line in (a) shows an analyzed simulated signal to illustrate the effects of the thermal artifact, which does not account for the decrease in higher frequency associated with (b) and (c).

It is not surprising that the best agreement is reached with an interface extent between 1 and 2 nm since this was the region that has a large effect on the observed acoustic signal. The comparisons shown in Fig. 6 compare the as-deposited sample with only two of the three treated samples. This is done because the acoustic signals are undetectable in the sample that underwent heat treatments according to schedule III. The lack of acoustic arrivals indicates that interface restructuring is occurring at the niobium-tungsten interface and not the free surface. If surface roughening occurred at the free surface a single arrival would be observed. This arrival would travel through the film, reflect off the tungsten-niobium interface, and get scattered from the free surface as it was observed. The absence of an acoustic arrival indicates that no detectable acoustic energy is reflected to the free surface from a subsurface structure. These undetectable signals are the result of low acoustic reflectivity caused by an interface region that is large compared to the acoustic frequencies, which is consistent to theoretical predictions.[5]

The observation associated with the schedule II sample allows analysis of the dynamics associated with atomic in-

termixing at the tungsten-niobium interface. The diffusion regions measured through this technique are much larger than what would be calculated given bulk values for tungsten diffusing into niobium, with an activation energy, $Q=0.5\times10^{-3}$ cal/atom, and diffusivity, $D_0=91.7$ cm^2/s,[29] According to these values it would take approximately 18 h to increase the diffusion region to 1.4 nm at 900 °C, which is in contrast to the measurements made on the heat schedule II sample. This discrepancy is most likely caused by disorder at the interface, thus requiring the need for effective physical parameters that are different than those used for bulk diffusion.

IV. CONCLUSION

The analyses described show that the nanometer scale extent of an interface can be quantitatively determined through frequency domain analysis of broadband high frequency acoustic waveforms produced through thermoelastic generation from an ultrafast laser pulse. The extent of diffusion for the low heat treatments conducted here indicates that this technique can be used to monitor the nanometer scale dynamics of diffusing species at the interface between two materials. For the case of sputter-deposited tungsten and niobium, it was found that the bulk diffusivities underestimate diffusion on the nanometer length scale.

ACKNOWLEDGMENTS

The authors would like to thank Michael Reiss for fabricating the samples, and Dr. Dereck Demaree for the Rutherford backscattering measurements. This work was supported through the Army Research Laboratory–Johns Hopkins University Advanced Materials Characterization program.

[1] M. Ohring, *The Materials Science of Thin Films* (Academic, London, 1992).
[2] J. Valli, J. Vac. Sci. Technol. A **4**, 3007 (1986).
[3] P. A. Steinmann and H. E. Hintermann, J. Vac. Sci. Technol. A **7**, 2267 (1989).
[4] K. A. Jones, M. W. Cole, W. Y. Han, D. W. Echart, K. P. Hilton, M. A. Crouch, and B. H. Hughes, J. Appl. Phys. **82**, 1723 (1997).
[5] C. J. K. Richardson, M. J. Ehrlich, and J. W. Wagner, J. Appl. Phys. **85**, 861 (1999).
[6] G. Tas, R. J. Stoner, H. J. Maris, G. W. Rubloff, G. S. Oehrlein, and J.-M. Halbout, Appl. Phys. Lett. **61**, 1787 (1992).
[7] H. Cho, S. Ogawa, K. Yamanaka, and M. Takemoto, JSME Int. J., Ser. A **41**, 439 (1998).
[8] A. R. Duggal, J. A. Rogers, and K. A. Nelson, J. Appl. Phys. **72**, 2823 (1992).
[9] T. W. Murray, S. Krishnaswamy, and J. D. Achenbach, Appl. Phys. Lett. **74**, 3561 (1999).
[10] C. A. Paddock and G. L. Eesley, Opt. Lett. **11**, 273 (1986).
[11] H. T. Grahn, H. J. Maris, J. Tauc, and K. S. Hatton, Appl. Phys. Lett. **53**, 2281 (1988).
[12] T. Q. Qiu, T. Juhasz, C. Suarez, W. E. Bron, and C. L. Tien, Int. J. Heat Mass Transf. **37**, 2799 (1994).
[13] H.-N. Lin, R. J. Stoner, and H. J. Maris, J. Nondestruct. Eval. **9**, 239 (1990).
[14] H. T. Grahn, H. J. Maris, J. Tauc, and B. Abeles, Phys. Rev. B **38**, 6066 (1988).
[15] C. J. Morath, H. J. Maris, J. J. Cuomo, D. L. Pappas, A. G. Vishnubhai, V. Patel, J. P. Doyle, and K. L. Saenger, J. Appl. Phys. **76**, 2636 (1994).
[16] C. J. Fiedler and J. W. Wagner, Rev. Prog. Quant. Nondestr. Eval. **16**, 1579 (1997).
[17] C. J. K. Richardson, M. J. Ehrlich, and J. W. Wagner, J. Opt. Soc. Am. B **16**, 1007 (1999).
[18] T. Q. Qiu and C. L. Tien, Int. J. Heat Mass Transf. **35**, 719–726 (1992).
[19] O. B. Wright, Phys. Rev. B **49**, 9985–9988 (1994).
[20] O. B. Wright and V. E. Gusev, IEEE Trans. Ultrason. Ferroelectr. Freq. Control **42**, 331–338 (1995).
[21] A. Miklos and A. Lorincz, J. Appl. Phys. **63**, 2391–2395 (1988).
[22] A. Miklos, Z. Bozoki, and A. Lorincz, J. Appl. Phys. **66**, 2968–2972 (1989).
[23] W. Nowacki, *Dynamic Problems in Thermoelasticity* (Polish Scientific Press, Warsawa, 1975).
[24] J. D. Achenbach, *Wave Propagation in Elastic Solids* (North Holland, New York, 1984).
[25] O. S. Heavens, *Optical Properties of Thin Solid Films* (Dover, New York, 1991).
[26] R. E. Reed-Hill and R. Abbaschian, *Physical Metallurgy Principles*, 3rd ed. (PWS Publishing, Boston, 1994).
[27] H. Baker, Ed., *ASM Handbook V3 Phase Diagrams* (ASM International, Materials Park, OH, 1992).
[28] A. Paddock and G. L. Eesley, J. Appl. Phys. **60**, 285–290 (1986).
[29] F. H. Wohlbeir, Ed., Diffusion Data **5**, 51 (1971) [taken from G. B. Federov, F. I. Zhomar, and E. A. Smienov, Met. Metalloved Chist. Metal **8**, 145–153 (1969)].

Rigid piston approximation for computing the transfer function and angular response of a fiber-optic hydrophone

Jochen F. Krücker, Alexander Eisenberg, Martin Krix, Ralf Lötsch, Martin Pessel, and Hans-Georg Trier

Professur für experimentelle Ultraschalldiagnostik, Medizinische Einrichtungen der Universität Bonn, Sigmund-Freud-Str. 25, D-53105 Bonn, Germany

(Received 19 May 1998; accepted for publication 28 December 1999)

The transfer function of a fiber-optic hydrophone (FOH) is computed for various fiber core radii. The hydrophone is modeled as a rigid disk, with plane waves impinging at normal or oblique incidence. The total sound field is written as the sum of the incident field and the field diffracted from the hydrophone. The diffracted field is approximated by the field generated by a vibrating planar piston in an infinite rigid baffle. For normal incidence and a pointlike fiber core, an analytical solution is presented. For finite fiber core radii, and for oblique incidence, the transfer functions are computed numerically. The calculated transfer functions exhibit an oscillatory frequency dependency that is most pronounced for small fiber cores. The solution for a core radius of 2.5 μm can be very well approximated by the analytical solution for a pointlike core at frequencies of up to 30 MHz. The results for normal incidence can be directly employed to deconvolute ultrasonic pressure signals measured with an FOH. From the transfer functions for oblique incidence, the angular response of the hydrophone is calculated. The angular response obtained here differs significantly from the model commonly used for piezoelectric hydrophones. The effective hydrophone radius derived from the angular response shows a strong frequency dependency. For low frequencies, it is found to be larger than the outer fiber radius, whereas it generally lies between the outer radius and the fiber core radius for frequencies above 10 MHz. © *2000 Acoustical Society of America.* [S0001-4966(00)01504-6]

PACS numbers: 43.38.Zp, 43.35.Bf, 43.35.Yb [SLE]

INTRODUCTION

Regarding the current development of medical ultrasound devices and of its related international standards, the measurement of ultrasound field parameters is certainly a point of major interest. Besides the quantitative determination of physical parameters like ultrasonic power, spatial peak-temporal average intensity, etc., parameters leading to a qualitative description of the acoustic output of medical ultrasound devices also need to be measured. Here, for example, the shape of the sound field of a transducer gives valuable insight in the performance of an ultrasound machine, both in quality control and in the development of new ultrasonic systems. The national and international guidelines[1,2] for declaration of sound field parameters of diagnostic ultrasound equipment require accurate acoustical measurements. More recently, the possibility of undesired bioeffects of diagnostic ultrasound have become a concern. To investigate the relationship between sound field parameters and bioeffects, and to establish safe levels for these parameters in the full range of diagnostic and therapeutic ultrasound machines, accurate acoustical sensors are required.

The principal physical quantity measured in most ultrasonic measurements is the acoustic pressure p. Essential for accurate measurements are sensors with high bandwidth, spatial resolution, sensitivity, linearity, and low noise, capable of transforming ultrasonic pressure into electrical voltage.

By far the most commonly used sensors are piezoelectric hydrophones, which exploit the piezoelectric effect to directly convert ultrasonic pressure into voltage.[3–5] These hydrophones come in two types, membrane hydrophones and needle (probe) hydrophones. Membrane hydrophones are generally made of a thin sheet of a polymer, usually PVDF (polyvinylidine fluoride), which is polarized at a small spot in the center. The active area of needle hydrophones usually consists of either PVDF, or a piezoelectric ceramic like PZT (lead zirconate titanate).

The spatial resolution of these hydrophones is determined by the size of the polarized area and ranges from about 1.5 mm to 0.1 mm for commercially available hydrophones. The bandwidth of piezoelectric hydrophones is systematically limited by acoustical resonance in the PVDF foil itself, and is therefore determined by the thickness of the PVDF. Bandwidths up to 100 MHz and more are possible but the usable bandwidth is usually limited to much lower frequencies due to amplifier electronics. Even if this problem is solved by taking special care in designing the electronic circuit,[6] the lack of accurate and easy to implement calibration methods above about 20 MHz still makes quantitative piezoelectric hydrophone measurements difficult in the high frequency range.

Current medical diagnostic ultrasound systems usually employ center frequencies ranging from ~2 MHz to 20 MHz. Already, some commercially available devices used, for example, in ophthalmology or dermatology tend to exceed this frequency range. For high spatial resolution imaging, higher frequencies are used, and the development of new

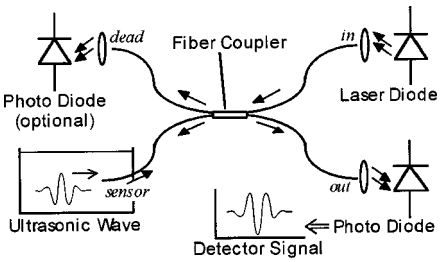

FIG. 1. Sketch of the functional principle of the fiber-optic hydrophone.

transducers allows special applications with center frequencies of 50 MHz to 100 MHz and beyond, exceeding the range where commercial piezoelectric hydrophones can be used. Thus a need for the development and testing of new sensors is obvious.

In 1988, Eisenmenger and Staudenraus[7] proposed a new type of hydrophone based on the piezo-optic effect. The so-called fiber-optic hydrophone (FOH) surpasses conventional hydrophones in spatial resolution, acoustical bandwidth, and mechanical stability but has a considerably lower signal-to-noise ratio. So far, this limitation has prevented its routine use for measuring diagnostic ultrasound fields. Yet, the FOH has already proven to be a valuable tool in measuring high-pressure shock waves.[8] As recent studies show,[9] it also has the potential for further improvements in SNR, making it a promising, and, in several aspects, superior alternative to piezoelectric hydrophones.

To fully exploit the capabilities of the FOH as an ultrasound sensor, its impulse response or, in frequency domain, its transfer function must be known. Measurements using the FOH have shown the detected, uncorrected signal to be distorted, which can be explained by a strongly varying transfer function. Deconvolution of the measured signal with its calculated impulse response is expected to greatly reduce these distortions.

In this work, a semi-analytical approach is presented to compute the transfer function of the FOH. Under certain simplifying assumptions, a completely analytical solution was found. The more general case including angular dependency of the transfer function involved substantial numerical calculations.

I. FUNCTIONAL PRINCIPLE OF THE FIBER-OPTIC HYDROPHONE

The fiber-optic hydrophone is based on either a 3 dB *X*- or *Y*-single mode or multimode fiber coupler (Fig. 1). Laser light is coupled into one end (*in*) of the coupler. In an ideal 3-dB coupler, the optical power is equally distributed to the two opposite arms of the coupler, so that half of the power reaches the *sensor* end and is partially reflected back into the fiber. The reflected power is again distributed to the two opposite ends and ideally 50% of it reaches the *output* end where it is detected by a fast photodiode. The signal is then amplified and can be further processed and displayed. If an *X*-fiber coupler is employed, the *dead* end of the coupler is not essential for the hydrophone, but may be used to monitor the power coupled into the fiber or to apply a noise suppression technique.[10]

The pressure variations of an acoustic wave impinging on the sensor fiber change the indexes of refraction of the fluid and the fiber due to the piezo-optic effect.[11,12] To a very good approximation, the change in refractive index is linearly dependent on the applied pressure in the pressure range of interest (approximately 10^{-2} MPa to 10^{2} MPa). Therefore, one can define the piezo-optic constant $\Xi = \partial n/\partial p$. For water, theoretical and experimental values for the piezo-optic constant range from $\Xi_{\text{water}} = 1.32 \times 10^{-4}$/MPa to 1.66×10^{-4}/MPa. In this study, an average value of $\Xi_{\text{water}} = 1.5 \times 10^{-4}$/MPa is assumed.

The piezo-optic constant of the fiber material is typically two orders of magnitude smaller than Ξ_{water} (e.g., $\Xi_{\text{silica}} = 5 \times 10^{-6}$/MPa). Since no optical interferometry but merely a power detection is employed here, the change of index of refraction of the fiber core due to the ultrasonic wave can then be neglected at the fiber end as well as in the fiber body.

Ideally, the *sensor* end of the coupler has a plane front face perpendicular to the fiber axis so that the optical power reflected back into the fiber can be well approximated by the Fresnel formula for normal incidence. (For typical single mode and multimode fibers, the angles of incidence of the guided modes are small so that polarization effects can be neglected and the error made by assuming normal incidence is negligible.) The Fresnel formula holds as long as the index of refraction of the water in the sensitive volume, given by the fiber core area and approximately extending one optical wavelength in front of the sensor fiber, is constant. One optical wavelength is approximately the distance from a reflecting surface up to which the adjacent medium can affect the reflection by modifying the evanescent wave.

For normal incidence, this condition is well fulfilled for acoustical frequencies up into the GHz range. In the ultrasonic MHz range, the sensitive volume can therefore be approximated by a sensitive area. Geometrically, this area is given by the fiber core area at the sensor fiber front face, but as discussed in Sec. III, the apparent sensitive area of the FOH can vary due to diffraction effects.

The change of index of refraction in the sensitive area leads to a change in the reflected optical power, which can be detected, amplified, and displayed. For typical optical wavelengths in the near infrared, the relative signal amplitude is approximately $\Delta I_r / I_{r,0} = -2.50 \times 10^{-3}\, \Delta p/\text{MPa}$, where ΔI_r is the change in reflected optical power, $I_{r,0}$ is the average reflected optical power at normal pressure, and Δp is the mean pressure change in the sensitive area. Assuming a laser output power of 30 mW, a coupling of 30% into the fiber, and an ideal 3-dB fiber coupler, the sensitivity is 11.4 nW/MPa. These values are based on equations found in the abovementioned publications by Staudenraus and Eisenmenger.

II. CALCULATION OF THE TRANSFER FUNCTION

A. Model

The insertion of a hydrophone into a sonic field causes reflection and diffraction of the sound waves at the sensor. Therefore, the pressure measured by the hydrophone differs

from the free-field pressure, defined as the sound pressure at the same position in the absence of the sensor. In the case of the fiber-optic hydrophone, the finite size of the aperture and the sharp circular edge of the sensor fiber can cause strong diffraction effects. In order to approximate the measured pressure signal three simplifying assumptions are made: (1) The pressure in the sensitive area can be described by diffraction at the circular fiber front face alone, independent of diffraction effects at the cylindrical fiber body. (2) The diffracted wave can be approximated using the model of a planar piston in an infinite rigid baffle. (3) The fiber front face acts rigid to the incoming wave.

All three assumptions are commonly used in modeling the angular response of membrane and needle-type hydrophones, as, for example, in the AIUM standard.[13] The rigid fiber assumption is based on the large characteristic impedance of the fiber [13.1×10^6 kg/(m^2 s) for silica] compared to the characteristic impedance of water [1.48×10^6 kg/(m^2 s)], leading to an amplitude reflection coefficient of $R=0.80$ at normal incidence. Penetration of sound into the fiber is ignored, and possible consequences of this simplification are discussed in Sec. III C.

The signal detected by the FOH is the mean optical power reflected back into the fiber at the sensor fiber end. The change of reflected optical power is in very good approximation directly proportional to the change of acoustic pressure at the fiber end. Therefore, the total acoustic pressure created by an ultrasonic wave impinging on a circular, acoustically rigid reflector was calculated and averaged over the fiber core area.

The most convenient way to find the transfer function is to choose a plane wave as the incoming waveform. Assuming superposition, the transfer function can then directly be derived from the calculated detected signal. Using complex notation, a plane wave traveling in the $+z$ direction can be written as

$$p(z,t)=\Re\{\hat{p}(z,t)\}=\Re\{\hat{p}_{pk}e^{i(kz-\omega t)}\}, \tag{1}$$

where p is sound pressure, the hat $\hat{}$ indicates a complex variable, $\Re$ denotes the real part of a complex variable, and $|\hat{p}_{pk}|$ is the peak sound pressure.

The boundary conditions require that the component of the total sound velocity perpendicular to the rigid reflector must vanish on the reflector surface:

$$\nu^{\perp}_{\text{total}}(\mathbf{r}_F,t)=0, \tag{2}$$

where $\boldsymbol{\nu}_{\text{total}}$ is the particle velocity of the total field, $\perp$ denotes the component normal to the reflector plane, and $\mathbf{r}_F$ is a planar vector in the reflector surface.

The boundary condition Eq. (2) can be fulfilled by rewriting the total sound velocity as the superposition of the incoming wave with velocity $\boldsymbol{\nu}_1$ and an outgoing wave with velocity $\boldsymbol{\nu}_2$, so that

$$\boldsymbol{\nu}_1+\boldsymbol{\nu}_2=\boldsymbol{\nu}_{\text{total}}, \quad \nu^{\perp}_2(\mathbf{r}_F,t)=-\nu^{\perp}_1(\mathbf{r}_F,t). \tag{3}$$

The fiber can now be considered an image source, generating a second wave with velocity distribution $\nu^{\perp}_2(\mathbf{r}_F,t)$ at the fiber front face. This reduces the problem to calculating the sound field radiated by a planar circular piston, which has

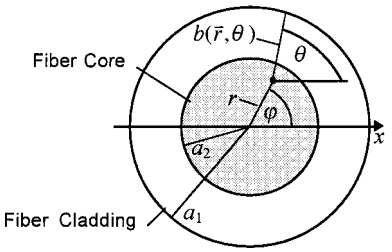

FIG. 2. Sketch of the fiber front face and variables used for calculation of the total sound pressure at normal incidence.

earlier been solved by various authors.[14–16] Using the model of a piston in an infinite rigid baffle, the most straightforward solutions employ the Rayleigh surface integral

$$\hat{\phi}_2(\mathbf{r},t)=\int\int_A \frac{\hat{\nu}^{\perp}_2(\mathbf{r}',t-s/c)}{2\pi s}\,r'\,dr'\,d\varphi', \qquad s=|\mathbf{r}-\mathbf{r}'|, \tag{4}$$

which relates the sound velocity potential $\hat{\phi}_2$ at position $\mathbf{r}$, time t, to the piston velocity normal to the source plane, $\hat{\nu}^{\perp}_2$, where A is the area of the source (fiber front face), s is the distance between $\mathbf{r}$ and point of integration $\mathbf{r}'$, and c denotes the speed of sound.

The case of plane waves at normal incidence to the fiber is studied in Sec. II B, and oblique incidence is studied and the angular response of the fiber hydrophone derived in Sec. II C.

B. Normal incidence

For plane waves with a wave vector perpendicular to the fiber front face, the amplitude and phase of $\hat{\nu}^{\perp}_2(\mathbf{r},t)$ are uniform over the sensor area. For points whose projection onto the $z=0$ plane lies inside the sensor area, Eq. (4) simplifies to

$$\hat{\phi}_2(\mathbf{r},t)=\frac{\hat{\nu}^{\perp}_{2,pk}\cdot e^{-i\omega t}}{ik}\left(e^{-ikz}-\frac{1}{2\pi}\int_0^{2\pi}e^{-ikb(\mathbf{r},\theta)}\,d\theta\right), \tag{5}$$

where $k=\omega/c$ is the magnitude of the wave vector of the incoming wave, and $b(\mathbf{r},\theta)$ is the distance between the point of observation and the fiber edge at angle θ, as illustrated in Fig. 2. Equation (5), called the Schoch solution, can be interpreted as a superposition of a plane reflected wave and a phase-inverted, diffraction, or edge wave (Fig. 3). Thus the total sound field can be written as the sum of the incoming plane wave, the reflected plane wave, and the edge wave:

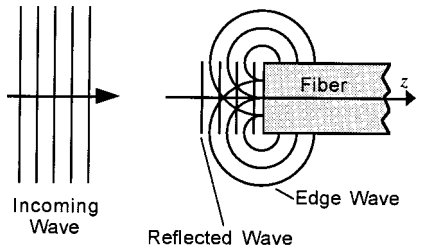

FIG. 3. Schematic sketch of the diffraction effects at the fiber.

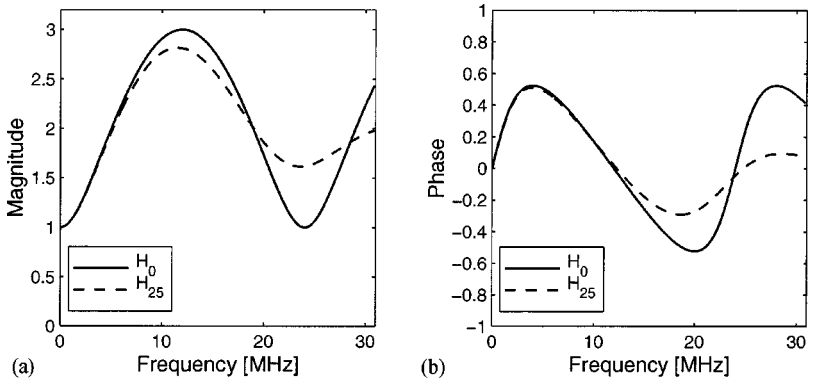

FIG. 4. Magnitude (a) and phase (b) of the transfer functions of the FOH for a pointlike fiber core (H_0) and for a fiber core radius of $a_2=25\,\mu$m (H_{25}). In both cases, the outer fiber radius was $a_1=62.5\,\mu$m. For a fiber core radius of $a_2=2.5\,\mu$m, the transfer function differed by less than 0.8% from H_0 and looked identical.

$$\hat{\phi}_{\text{total}}(\mathbf{r},t)=\hat{\phi}_1(\mathbf{r},t)+\hat{\phi}_2(\mathbf{r},t)$$
$$=\frac{\hat{v}_{1,pk}e^{-i\omega t}}{ik}\left(e^{ikz}+e^{-ikz}-\frac{1}{2\pi}\int_0^{2\pi}e^{-ikb(\mathbf{r},\theta)}\,d\theta\right). \tag{6}$$

Using the general relationship between sound pressure p, velocity potential $\hat{\phi}$, and density of the medium ρ_0,

$$p(\mathbf{r},t)=\Re\left\{\rho_0\frac{\partial\hat{\phi}(\mathbf{r},t)}{\partial t}\right\}, \tag{7}$$

the expression for the total sound pressure averaged over the fiber core at $z=0$ becomes

$$\langle p\rangle_{a_2}(k,t)=\Re\left\{\hat{p}_{1,pk}e^{-i\omega t}\left(2-\frac{1}{\pi a_2^2}\times\int_0^{2\pi}\int_0^{a_2}e^{-ikb(r,\theta)}r\,dr\,d\theta\right)\right\},$$
$$b(r,\theta)=\sqrt{r^2\cos^2\theta+(a_1^2-r^2)}-r\cos\theta, \tag{8}$$

where a_1 is the outer fiber radius, a_2 is the radius of the fiber core, $\langle\ldots\rangle_a$ indicates spatial averaging over a circular area with radius a at the origin of the $z=0$ plane, and $|\hat{p}_{1,pk}|$ is the pressure magnitude of the incoming wave.

Note that in Eq. (8) the optical power in the fiber is assumed to be uniformly distributed over the core area with an abrupt cutoff at the core/cladding interface. Real power distributions are continuous at $r=a_2$ and can extend significantly into the fiber cladding, depending on fiber parameters and optical wavelength. However, the error made using this simplification is generally very small. Calculations for some special cases using Gaussian and parabolic power distributions across the fiber are discussed in the Appendix.

Equation (8) also holds for a superposition of incoming plane waves and can therefore be generalized for wave packages

$$p(t)=\int_{-\infty}^{\infty}\hat{P}(\omega)e^{-i\omega t}\,d\omega. \tag{9}$$

Substituting $\hat{P}(\omega)$, the component of the pressure wave at frequency ω, for $\hat{p}_{1,pk}$ in Eq. (8), and integrating over all frequencies yields

$$\langle p\rangle_{a_2}(t)=\int_{-\infty}^{\infty}\hat{P}(\omega)\left(2-\frac{1}{\pi a_2^2}\times\int_0^{2\pi}\int_0^{a_2}e^{-i\omega b(r,\theta)/c}r\,dr\,d\theta\right)e^{-i\omega t}\,d\omega, \tag{10}$$

which is the inverse Fourier transform of $\hat{P}(\omega)\cdot\hat{H}(\omega)$, where $\hat{H}$ is the transfer function of the FOH:

$$\hat{H}_{a_2}(\omega)=2-\frac{1}{\pi a_2^2}\int_0^{2\pi}\int_0^{a_2}e^{-i\omega b(r,\theta)/c}r\,dr\,d\theta. \tag{11}$$

$\hat{H}_{a_2}(\omega)$ was computed numerically for two different fiber core diameters and for a frequency range from 0 to 30 MHz [Fig. 4(a),(b)].

If a single mode fiber is used as a sensor, the core diameter is usually much smaller than the acoustical wavelength of the detected wave. For $ka_2\ll 1$ (pointlike fiber core) the transfer function in Eq. (11) simplifies to

$$\hat{H}_0(\omega)=2-e^{-i\omega a_1/c}, \tag{12}$$

which is also plotted in Fig. 4(a),(b).

In time-domain, the detected pressure $p_{\text{FOH}}(t)$ can then be written as a convolution of the free-field pressure p_1 with the impulse response $h(t)$ which is the inverse Fourier transform of the transfer function

$$p_{\text{FOH}}(t)=p_1(t)\otimes h(t). \tag{13}$$

Yet, the free-field pressure is more easily derived in frequency-domain using

$$p_1(t)=\mathcal{F}^{-1}\left(\frac{\mathcal{F}(p_{\text{FOH}}(t))}{\hat{H}(\omega)}\right), \tag{14}$$

where $\mathcal{F}$ denotes the Fourier transformation.

C. Oblique incidence and angular response

The most commonly used model for the angular response of hydrophones is that of a circular piston in a rigid, infinite baffle, which exhibits a sensitivity

$$s(k,\vartheta)=s_0\cdot M(k,\vartheta),$$
$$M(k,\vartheta)=\frac{2J_1(ka\sin\vartheta)}{ka\sin\vartheta} \tag{15}$$

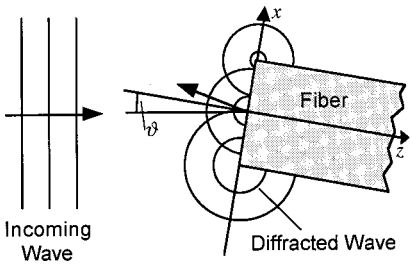

FIG. 5. Schematic sketch of the diffraction effects at the fiber end for oblique incidence of a plane wave.

for plane waves with wave vector magnitude k, where s_0 is the on-axis response, J_1 is a Bessel function of first degree, first order, a is the radius of the active sensor area, and ϑ is the angle of incidence of the ultrasound wave. This result can also be understood in a time-domain model: If a plane wave impinges on a circular area at angle ϑ, the pressure amplitude, averaged over this area, varies like $M(k,\vartheta)$.

Equation (15) is also the basis of the AIUM and IEEE guidelines for hydrophones used in medical ultrasonics.[13,17] Yet, experiments have shown that the angular response of hydrophones rarely follows Eq. (15) exactly.[18]

In general, the angular response depends on a number of factors that are difficult to quantify. Among the most important factors are the size, shape, and sensitivity distribution of the active area that determines averaging and diffraction effects. For simple geometries, these effects can be calculated using various mathematical models. However, hydrophone design and material can also play an important role and affect the angular response so that current models are inappropriate in many cases.[19]

For the FOH, no supporting structure is needed in the immediate proximity of the sensitive area except the fiber itself, the fiber front face can be very well approximated by a circular disk, and the fiber material can be considered homogeneous. This allows an approximate calculation of the angular response of the FOH including diffraction effects. Moreover, for single mode FOHs, the actual sensitive area is small compared to the acoustical wavelength up to very high frequencies. This enables experimental verification of the theoretically derived diffraction effects without spatial averaging during the detection process.

The model used and approximations made for the following calculation are the same as in Sec. II A. Assuming a plane wave impinging on the fiber end with a wave vector at angle ϑ to the fiber axis in the xz-plane (Fig. 5), the pressure across the fiber front face depends on the x-coordinate according to

$$\hat{p}_1(x) = \hat{p}_{1,pk} \cdot e^{-ikx \sin \vartheta}. \tag{16}$$

Here and in the following, the time dependency $e^{-i\omega t}$ has been omitted for simplicity. The component of the wave velocity perpendicular to the fiber end is then given by

$$\hat{v}_1^{\perp}(x) = \frac{\hat{p}_{1,pk}}{\rho_0 c} \cdot \cos \vartheta \cdot e^{-ikx \sin \vartheta}. \tag{17}$$

Using the surface integral Eq. (4), and adding primary and secondary pressure, the total sound pressure on the sensor surface evaluates to

$$\hat{p}_{\text{total}}(\mathbf{r}_f, \vartheta) = \hat{p}_{1,pk} \cdot \left(e^{-ikx \sin \vartheta} + ik \cos \vartheta \times \int\int_F \frac{e^{-ikx' \sin \vartheta} e^{-iks}}{2\pi s} r'\, dr'\, d\varphi' \right), \tag{18}$$

where F is the area of the fiber end, $s = \sqrt{r^2 + r'^2 - 2rr' \cos(\varphi' - \varphi)}$ is the distance between the point of observation $\mathbf{r}_f$ and point of integration $\mathbf{r}'$, and x and x' are the x-coordinates of $\mathbf{r}_f$ and $\mathbf{r}'$, respectively.

Averaging over the fiber core area yields the pressure detected by the FOH

$$\langle p \rangle_{a_2}(\vartheta) = \Re\left\{ \hat{p}_{1,pk} \cdot \left(\frac{2}{\pi a_2^2} \int_{-a_2}^{a_2} \sqrt{a_2^2 - x^2} e^{-ikx \sin \vartheta}\, dx + \frac{ik \cos \vartheta}{\pi a_2^2} \int_A \int_F \frac{e^{-ikx' \sin \vartheta} e^{-iks}}{2\pi s} dF'\, dA \right) \right\}, \tag{19}$$

where A and a_2, respectively, are the area and the radius of the fiber core. The first term in this expression evaluates to the commonly used Eq. (15) and represents the angular dependent averaging over phases of the incoming wave intersected by the sensor surface. The second term represents the diffracted and reflected wave and was computed numerically. To simplify computation for small fiber cores ($ka_2 \ll 1$), Eq. (19) can be approximated by

$$\begin{aligned} \langle p \rangle_0(\vartheta) &= \Re\left\{ \hat{p}_{1,pk} \cdot \left(1 + \frac{ik \cos \vartheta}{2\pi} \times \int_0^{2\pi} \int_0^{a_1} e^{-ikr'(1 + \cos \varphi' \sin \vartheta)}\, dr'\, d\varphi' \right) \right\} \\ &= \Re\left\{ \hat{p}_{1,pk} \cdot \left(1 + \frac{\cos \vartheta}{2\pi} \times \int_0^{2\pi} \frac{1 - e^{-ika_1(1 + \cos \varphi' \sin \vartheta)}}{(1 + \cos \varphi' \sin \vartheta)} d\varphi' \right) \right\}, \end{aligned} \tag{20}$$

which is the total pressure at the center of the sensor.

In complete analogy to the reasoning in Sec. II B, the expressions in parentheses in Eqs. (19) and (20) represent the transfer functions of the FOH for oblique incidence. The transfer functions $\hat{H}_{\vartheta}(\omega)$ were computed numerically for five angles of incidence from 0° to 80°, an outer fiber radius of $a_1 = 62.5\,\mu$m, and three fiber core radii of $a_2 = 25\,\mu$m, $a_2 = 2.5\,\mu$m [both using Eq. (19)], and $a_2 = 0\,\mu$m [pointlike, using Eq. (20)]. The results for $a_2 = 2.5\,\mu$m and $a_2 = 0\,\mu$m looked virtually identical and only the latter is plotted in Fig. 6(a) (magnitude) and 6(b) (phase). The result for $a_2 = 25\,\mu$m is shown in Fig. 7(a) and (b).

Of more practical interest than the angular dependent transfer function is the directivity or angular response

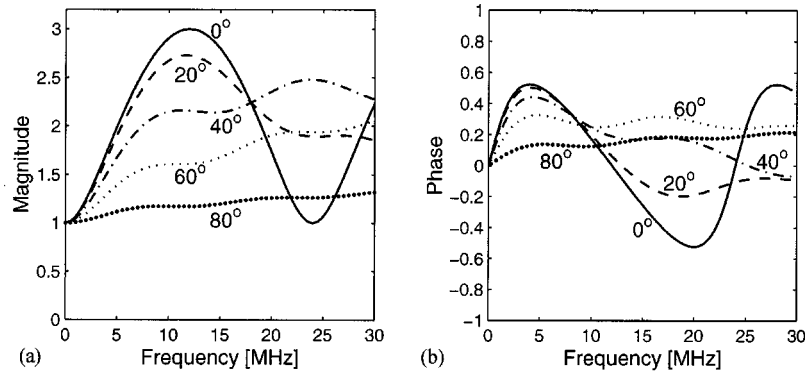

FIG. 6. Magnitude (a) and phase (b) of the calculated angular-dependent transfer function of the FOH with pointlike fiber core.

$M_\omega(\vartheta)$, which is the relative sensitivity at a specific frequency as a function of angle of incidence. $M_\omega(\vartheta)$ was calculated for an outer fiber radius of $a_1 = 62.5\ \mu$m and frequencies from 5 MHz to 30 MHz, using fiber core radii of $a_2 = 2.5\ \mu$m [Fig. 8(a)] and $a_2 = 25\ \mu$m [Fig. 8(b)].

III. RESULTS AND DISCUSSION

A. Normal incidence

The calculated transfer functions of the FOH for normal incidence are strongly oscillatory. The oscillatory behavior originates from the interference of the edge wave with the incoming wave in the sensitive area and is most pronounced for small fiber cores where averaging effects are negligible. It should be noted that a decrease of fiber core area does not necessarily result in a decrease in overall sensitivity, since basically the same optical power can be coupled into a smaller fiber core, and the sensitivity of the FOH is directly proportional to the optical power in the sensor fiber. Therefore, the sensitivity of an experimental setup employing a single mode fiber should be sufficient to observe the oscillatory behavior of the transfer function.

For larger fiber cores, considerable averaging of the edge wave over the core area occurs. For high frequencies, this results in washing out the contribution of the edge wave to the detected signal. In the high-frequency limit, the positive and negative phases of the edge wave will average out completely across the fiber core area. The transfer function then approaches a constant value of 2.0, due to the superposition of the incoming and the rigidly reflected wave.

The transfer functions of the fiber with a pointlike core and of the fiber with a core radius of 2.5 μm are virtually identical in magnitude and phase up to frequencies of 30 MHz, and even for higher frequencies the differences are very subtle. This result was expected since the wavelength at 30 MHz ($\approx$51 μm) is still large compared to the assumed fiber core diameter. However, for the 25-μm fiber core radius, typical for a multimode fiber, the transfer function differs markedly from the other two for frequencies above $\approx$10 MHz, where the wavelength approaches the diameter of the fiber core.

The transfer functions calculated in this work differ quantitatively, but not qualitatively from measured or modeled transfer functions of piezoelectric hydrophones. In the limit $a_2 = a_1$, which would correspond to a needle-type hydrophone with uniform sensitivity across its circular front face, the transfer function (Fig. 9) approaches a shape well-known in literature: For very low frequencies the hydrophone response goes toward 1.0 because the wavelength is very large compared to the diameter of the hydrophone, so that the diffracted edge wave fully cancels out the reflected wave component. In the high-frequency limit, the transfer function approaches 2.0 because the positive and negative phases of the edge wave average out across the sensitive area and the sum of the incoming and rigidly reflected wave is detected. This result agrees particularly well with the geometrical model used by Fay *et al.* in Ref. 20.

Discrepancies between this model and experimental results for needle-type hydrophones are partly due to the layered structure of piezoelectric hydrophones and to hydrophone geometries differing from an ideal cylinder shape. The edges of needle-type hydrophones, for example, are usually less clear cut than those of an optical fiber. The resulting diffraction wave will then be ''blurred'' and have lower amplitude, making its impact on the detected signal weaker.

For the FOH, however, the simple design and geometry

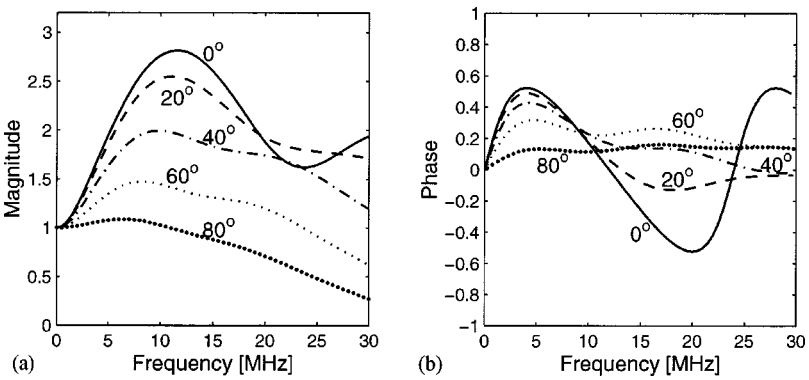

FIG. 7. Magnitude (a) and phase (b) of the calculated angular-dependent transfer function of the FOH with fiber core radius of 25 μm.

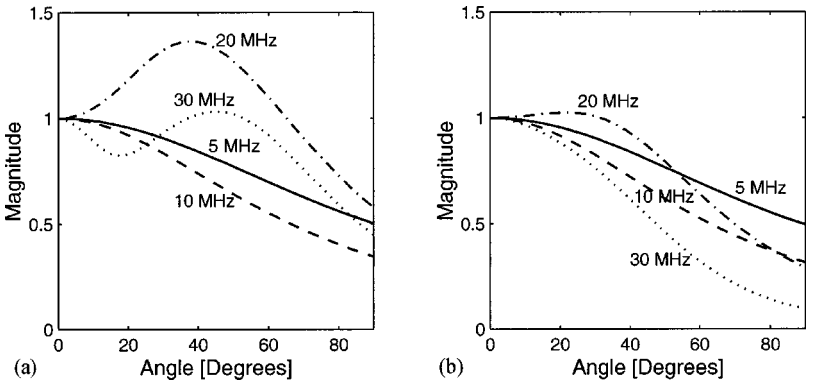

FIG. 8. Calculated angular response of the FOH with fiber core radii of 2.5 μm (a) and 25 μm (b).

of the sensor tip agree very well with the theoretical model. This gives confidence in the assumption that the calculated transfer functions can be verified experimentally. Experimental work regarding the transfer function of a single mode FOH is currently being carried out at the University of Bonn.

The apparent disadvantage of a nonconstant transfer function for the FOH can be compensated in two ways, experimentally or computationally. Experimentally, the sensor fiber end would have to be prepared to diminish the diffraction effects. This can be achieved by either rounding off the fiber end by means of coating or etching, or by mounting the fiber end into a larger, rigid reflector with a central drilling, and polishing its surface so that no distortion of the reflected wave at the boundary between the fiber cladding and the mount occurs. The mount itself would have to have rounded-off edges to minimize diffraction effects, which will be easier to manufacture than a preparation of the fiber end itself. However, by any of these techniques the FOH loses one of its major advantages over piezoelectric hydrophones, that is, the easy and cheap replacement of the sensor tip by simply cutting it again once it got damaged.

To circumvent this drawback, the detected signal can be corrected computationally using the transfer functions calculated above. Using fast Fourier transforms, the deconvolution can be implemented very time efficiently once the signal has been digitized.

B. Oblique incidence

The angular dependency of the transfer function was calculated for frequencies up to 30 MHz. In this range, the calculated transfer functions of the fiber with pointlike core and of the fiber with a core radius of 2.5 μm were indistinguishable for all angles considered (0°, 20°, 40°, 60°, and 80°) because the acoustical wavelengths were large compared to the fiber core diameter.

The angular dependency of the transfer function is governed by two effects: the decrease of amplitude of the diffracted wave with $\cos\vartheta$, and the increase of averaging of the incident and diffracted waves with a_2 and $\cos\vartheta$. The first effect leads to a decrease of oscillations in the transfer function with increasing angle of incidence both in the pointlike fiber core model, and for the larger fiber core. The second effect is similar to the one considered in current models which lead to Eq. (15), but instead of averaging only the incoming wave, our model includes the averaging of the diffracted wave across the fiber core area.

The angular response [Fig. 8(a) and (b)] reveals a shape quite different from that obtained using Eq. (15), particularly for very small a_2. The curve is no longer monotonically decreasing to its first zero crossing. Instead, it can have local minima and maxima and the angle of the overall maximum response may differ from $\vartheta=0°$. For a pointlike fiber core, for example, the maximum response at an acoustic frequency of 30 MHz is reached at $\vartheta\approx 45°$.

It is also instructive to compare the angular response computed here to the current model of angular dependency, Eq. (15), and to compute an effective radius for the FOH.

The comparison was performed for fiber core radii of $a_2=2.5\,\mu$m and $a_2=25\,\mu$m, an outer fiber radius $a_1=62.5\,\mu$m, and for various frequencies from 0.5 MHz to 30 MHz. For each frequency, the classical angular response given by Eq. (15) was least squares fitted to the calculated angular response, using the radius a as fitting variable. The results are displayed in Table I. The classical equivalent hydrophone radius a_c that best fits the FOH angular response generally decreases with frequency. For low frequencies, a_c can even be larger than the outer fiber radius, but the somewhat surprising result at 0.5 MHz is put into perspective by the fact that for both fiber core radii, the FOH still exhibits an almost ideal angular response with less than 2% decrease in sensitivity at 90° angle of incidence. For frequencies larger than 10 MHz, a_c is generally smaller than the outer

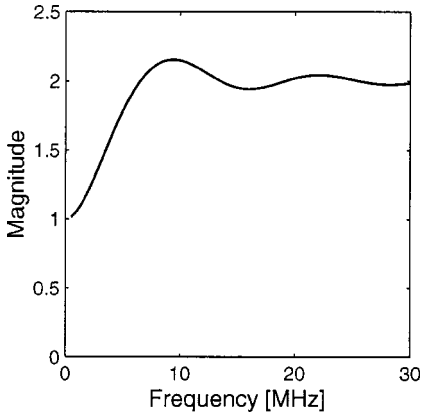

FIG. 9. Magnitude of the calculated transfer function for a hydrophone with $a_1=a_2=62.5\,\mu$m.

TABLE I. Equivalent radii a_c of hydrophones whose angular response, according to the classical directivity model, best fits the calculated angular response of the FOH ($a_1 = 62.5\ \mu$m) for a given frequency and core radius.

	Equivalent radius a_c [μm] at frequency				
Core radius a_2 [μm]	0.5 MHz	5 MHz	10 MHz	20 MHz	30 MHz
2.5	164.4	94.7	58.7	5.6	12.6
25	164.1	95.8	60.7	26.5	25.2

fiber radius and can even approach the radius of the fiber core.

The effective radius of the FOH was then calculated according to the IEC 1102 and AIUM standards,[1,13] which define the average effective radius of a hydrophone based on the measured 3-dB and 6-dB half-angles of the angular response at two different frequencies. For the FOH, the calculated instead of measured half-angles were used, at frequencies of 15 MHz and 30 MHz. For fiber core radii of 2.5 μm and 25 μm, this calculation yielded effective radii of $a_e = 25.9\ \mu$m and 32.0 μm, respectively, in good qualitative agreement with the comparison above.

The fact that comparison to the classical angular response can lead to effective radii larger than the outer fiber radius suggests that this model is not appropriate for hydrophones such as the FOH, with strong diffraction effects and sensitive areas small compared to the diffracting aperture. To characterize these hydrophones other models might have to be applied, based on calculated angular responses like the ones presented in this study.

C. Limitations of the model and future work

The calculation of the diffracted wave was based on the model of a planar piston in an infinite, rigid baffle. Strictly, this approximation is valid only for point sources on the fiber end that lie at least one wavelength inside the fiber boundary. This implies wavelengths of less than 62.5 μm, i.e., acoustic frequencies of more than 20 MHz. For very low frequencies, the field radiated by the fiber can be more accurately described by a vibrating disk in free space, which would reduce the sound pressure of the secondary wave by a factor of 2.[21] In the intermediate frequency range, the secondary sound pressure is expected to lie between the results of the baffled piston and the freely suspended disk. A more quantitative evaluation of the effects of baffling, e.g., by numerically solving the wave equation in the proximity of the fiber end, goes beyond the scope of this study. The validation of the model used here will therefore be left for experimental investigations.

The rigid fiber assumption neglects all elastic properties of the fiber including penetration of sound into the fiber, excitation of transverse waves in and surface waves on the fiber, and resonances at discrete angles and frequencies. Analytic solutions for the elastic fiber, modeled as an elastic, half-infinite cylinder, do no exist. To estimate the errors made in our approximation we can compare the reflection at an infinite, planar boundary for rigid and elastic boundary conditions. In general, the acoustic amplitude reflection coefficient for transitions from nonviscous media to solids exhibits a complex angular dependency. The phase of the coefficient varies particularly strongly close to the critical angles where new types of waves are excited in the solid. Between these critical angles, the coefficient is approximately real and unity, and the boundary can be well approximated as rigid.[22] For the fiber, similar effects can be expected. At discrete angle-dependent resonance frequencies, new types of waves can be excited in the fiber, leading to strong penetration of sound into the fiber and significant discrepancies between the measured sound pressure and the pressure predicted using the rigid fiber model. In between these resonant frequencies the pressure is likely to be close to the envelope given by the rigid fiber model.

The image source method employed here cannot easily be extended to take penetration of sound into the fiber into account. In future work, a more accurate description of the sound field at the fiber including the abovementioned effects could be obtained analytically using integral transform methods, or numerically using three-dimensional boundary element calculations.

IV. SUMMARY AND CONCLUSIONS

To summarize, the transfer function of the fiber-optic hydrophone was computed for normal and oblique incidence using the model of a planar piston in a rigid baffle. The transfer functions exhibit an oscillatory frequency dependency caused by alternating constructive and destructive interference of the incoming and the diffracted wave in the sensor area. In the limit of very large fiber core radii, the results presented here agree well with the calculation of the geometry-dependent transfer function of needle hydrophones published earlier.

For all angles considered, the transfer function of a fiber with core radius $a_2 = 2.5\ \mu$m could be very well approximated using the model of a pointlike fiber core. Therefore, the signal measured with single mode fiber-optic hydrophones can be deconvoluted using the much simpler analytical approximation Eq. (12).

The angular response of the FOH was derived from the transfer function at oblique incidence and therefore included diffraction effects. This leads to a more complex directivity pattern than can be explained using the standard model for hydrophones, which only considers phase averaging effects. Comparison between the standard model of directivity and the directivity calculated in this work suggest that the effective radius of the FOH is frequency dependent and can be larger than the outer fiber diameter for very low frequencies, but generally lies between the fiber core diameter and the outer fiber diameter for higher frequencies. Hence, the sensitive area is not identical with the fiber core area, even if this is the only area where the conversion from sound pressure to reflected optical power physically takes place. This holds true for the angular response as well as for spatial averaging effects in sound fields with spatially strongly varying peak pressure amplitudes. Without a deconvolution of the detected signal, the effective sensor area can not be reduced far below the outer fiber diameter, even if single mode fibers are employed.

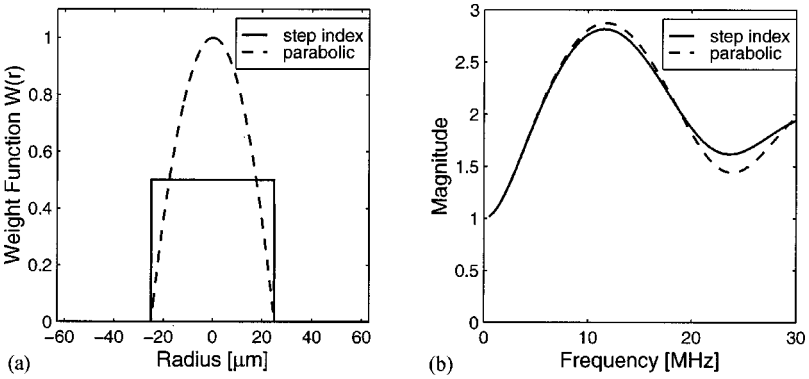

FIG. A1. (a) Weight functions used for comparing the transfer functions of step index and parabolic graded index multimode fibers. (b) Magnitude of the resulting transfer functions for normal incidence.

To validate the model used in this study and to verify the theoretical results presented here, experimental measurements with a fiber-optic hydrophone must be performed. The angular response has to be determined for various frequencies. Different ultrasonic waveforms must be detected with the FOH, deconvoluted using the calculated transfer function, and compared to waveforms acquired using a standard measurement technique, e.g., piezoelectric hydrophones. These measurements may reveal limitations of the rigid fiber model used here, and may thus motivate future theoretical work on the transfer function of the FOH. Experimental work regarding these questions is now being carried out at the University of Bonn.

ACKNOWLEDGMENT

This work was supported by the European Commission Contract SMT4-CT96-2124, and by TIMUG e.V., Scientific Assoc., Bonn.

APPENDIX: NONUNIFORM DISTRIBUTION OF OPTICAL POWER IN THE SENSOR FIBER

In single mode fibers, the power distribution across the fiber can be well-approximated by a Gaussian if only the LP_{01} mode is present. The power distribution determines the sensitivity distribution of the sensor fiber and can be modeled by introducing a weight function $W(r)$ in Eq. (8), yielding

$$\langle p\rangle_{a_2}(k,t)=\Re\left\{\hat{p}_{1,pk}e^{-i\omega t}\left(2-\frac{1}{N}\times\int_0^{2\pi}\int_0^{a_1}W(r)e^{-ikb(r,\theta)}r\,dr\,d\theta\right)\right\},$$

$$N=2\pi\int_0^{a_1}W(r)r\,dr,$$

$$W(r)=\exp\left[-2\left(\frac{r}{w_0}\right)^2\right], \tag{A1}$$

where w_0, the mode spot radius, is usually close to or slightly larger than the fiber core radius.[23] The transfer function of the single mode fiber was re-calculated for normal incidence in the frequency range from 0 to 30 MHz using Eq. (A1) with w_0 ranging from $1.0\,a_2$ to $1.4\,a_2$. The largest differences to the previously computed transfer functions occurred for $w_0=1.4\,a_2$, where only about 64% of the total optical power are carried in the fiber core. For this case, the result differed by 0.15% on average (0.76% max) from the transfer function obtained without the weight function, and by 0.29% on average (1.52% max) from the transfer function for the pointlike fiber core. Thus the approximation of the single mode fiber core as pointlike is still valid.

In multimode fibers, the distribution of optical power closely matches the distribution of the refractive index, given that all modes are excited equally.[24] The calculations using Eq. (8) without weight function are therefore a good approximation for step index fibers. Many multimode fibers, however, are graded index fibers that have a nonuniform (typically parabolic) core refractive index. The transfer function of the multimode fiber was re-calculated for normal incidence using Eq. (A1) with the parabolic weight function

$$W(r)=\begin{cases}1-r^2/a_2^2 & \text{for } 0\leqslant r\leqslant a_2\\ 0 & \text{for } a_2<r\leqslant a_1\end{cases}. \tag{A2}$$

In Fig. A1, this parabolic weight function is displayed together with the step index function used before. Figure A1(b) shows the transfer functions for normal incidence obtained using these two weight functions. The results differ by 3.1% on average (11.1% max) in the frequency range from 0 to 30 MHz. The higher concentration of optical power close to the fiber center reduces the effective radius of the sensor area and leads to stronger oscillations in the transfer function for the parabolic profile. The results imply that the parabolic weight function can slightly improve the accuracy of the transfer function for graded index fibers. However, the difference to the step index profile is likely to be small compared to the potential errors incurred by the simple model used in this study.

[1] IEC 61102 (1991-11). ''Measurement and characterization of ultrasonic fields using hydrophones in the frequency range 0.5 MHz to 15 MHz,'' IEC, 1991.
[2] IEC 61157 (1992-08). ''Requirements for the declaration of the acoustic output of medical diagnostic ultrasonic equipment,'' IEC, 1992.
[3] D. R. Bacon, ''Characteristics of a PVDF membrane hydrophone for use in the range 1–100 MHz,'' IEEE Trans. Sonics Ultrason. **SU-29**, 18–25 (1982).
[4] P. A. Lewin, ''Miniature piezoelectric polymer ultrasonic hydrophone probes,'' Ultrasonics **19**, 213–216 (1981).
[5] D. G. Shombert and G. R. Harris, ''Use of miniature hydrophones to determine peak intensities typical of medical ultrasound devices,'' IEEE Trans. Ultrason. Ferroelectr. Freq. Control **UFFC-33**, 287–294 (1986).
[6] P. Lum, M. Greenstein, C. Grossman, and T. L. Szabo, ''High-frequency

membrane hydrophone,'' IEEE Trans. Ultrason. Ferroelectr. Freq. Control **UFFC-43**, 536–544 (1996).
[7] J. Staudenraus and W. Eisenmenger, ''Optisches Sondenhydrophon,'' Fortschritte der Akustik—DAGA '88, pp. 467–470 (1988).
[8] J. Staudenraus, M. Köhler, and W. Eisenmenger, ''Charakterisierung verschiedener Hydrophone unter Stoßwellenbedingungen,'' Fortschritte der Akustik—DAGA '91, pp. 221–224 (1991).
[9] C. Koch, ''Coated fiber-optic hydrophone for ultrasonic measurement,'' Ultrasonics **34**, 687–689 (1996).
[10] J. Staudenraus and W. Eisenmenger, ''Fiber-optic probe hydrophone for ultrasonic and shock-wave measurements in water,'' Ultrasonics **31**, 267–272 (1993).
[11] W. A. Riley and W. R. Klein, ''Piezo-optic coefficients of liquids,'' J. Acoust. Soc. Am. **42**, 1258–1261 (1967).
[12] H. Yadav, D. S. Murty, S. N. Verma, K. H. C. Sinha, B. M. Gupta, and D. Chand, ''Measurement of refractive index of water under high dynamic pressures,'' J. Appl. Phys. **44**, 2197–2200 (1973).
[13] AIUM, ''Acoustic output measurement standard for diagnostic ultrasound equipment,'' American Institute for Ultrasound in Medicine, Laurel, MD (1998).
[14] G. R. Harris, ''Review of transient field theory for a baffled planar piston,'' J. Acoust. Soc. Am. **70**, 10–20 (1981).
[15] G. R. Harris, ''Transient field of a baffled planar piston having an arbitrary vibration amplitude distribution,'' J. Acoust. Soc. Am. **70**, 186–2044 (1981).
[16] P. R. Stephanishen, ''Acoustic transients from planar axisymmetric vibrators using the impulse response approach,'' J. Acoust. Soc. Am. **70**, 1176–1181 (1981).
[17] IEEE, ''IEEE Guide for Medical Ultrasound Field Parameter Measurements,'' IEEE Std 790-1989 (1990).
[18] M. Platte, ''A polyvinylidene fluoride needle hydrophone for ultrasonic applications,'' Ultrasonics **23**, 113–116 (1985).
[19] D. G. Shombert, S. W. Smith, and G. R. Harris, ''Angular response of miniature ultrasonic hydrophones,'' Med. Phys. **9**, 484–492 (1982).
[20] B. Fay, G. Ludwig, C. Lankjaer, and P. A. Lewin, ''Frequency response of PVDF needle-type hydrophones,'' Ultrasound Med. Biol. **20**, 361–366 (1994).
[21] P. M. Morse and K. U. Ingard, *Theoretical Acoustics* (Princeton University Press, Princeton, 1986), p. 375.
[22] A. Schoch, ''Schallreflexion, Schallbrechung und Schallbeugung,'' Ergeb. Exakten. Naturwiss. **23**, 127–234 (1950).
[23] L. B. Jeunhomme, *Single-Mode Fiber Optics* (Marcel Dekker, New York, 1983), pp. 8–26.
[24] G. Mahlke and P. Gössing, *Fiber Optic Cables* (Siemens Aktiengesellschaft, Berlin, 1993), pp. 43, 69.

A perturbation technique for the prediction of the displacement of a line-driven plate with discontinuities

Daniel T. DiPerna and David Feit[a)]
Signatures Directorate, Naval Surface Warfare Center, Carderock Division, 9500 MacArthur Boulevard, West Bethesda, Maryland 20817

(Received 16 August 1999; revised 18 January 2000; accepted 21 January 2000)

A novel technique is presented for obtaining approximate analytic expressions for an inhomogeneous line-driven plate. The equation of motion for the inhomogeneous plate is transformed, and the transform of the total displacement is written as a sum of the solution for a homogeneous line-driven plate plus a term due to the inhomogeneity. The result is an integral equation for the transform of the inhomogeneous contribution. This expression may in general be solved numerically. However, by introducing a small parameter into the problem, it may be solved approximately using perturbation techniques. This series may not be convergent, but its convergence may be improved using Padé approximation. Results are presented for the case of a single mass discontinuity, and a distribution of mass discontinuities. [S0001-4966(00)05304-2]

PACS numbers: 43.40.Dx, 43.40.Fz [CBB]

INTRODUCTION

Exact solutions for wave propagation and scattering from elastic structures are only feasible for a few types of canonical problems. These include a spherical shell, an infinite cylindrical shell, and an infinite plate, where separation of variables can be used to turn a partial differential equation into several ordinary differential equations.[1] The solutions for these problems have been known and analyzed extensively in the literature[2–4] and provide insight into the underlying wave phenomena responsible for the observed radiated or scattered fields.[5] As mentioned above, the class of problems that can be solved exactly is very small, and the methods used cannot be easily extended to more complicated problems, such as when the radiating surface does not conform to a separable coordinate system,[6] or when there are inhomogeneities on the radiating or scattering surface.

In order to solve these more complicated problems, recourse is often made to numerical solutions.[7–9] While numerical results may be generated, the underlying wave physics may be obscured. To gain further insight into the problem of the inhomogeneous structure, we present a new approach applied to the problem of a line-driven infinite plate with inhomogeneities. The solution is given as a sum of the solution for the homogeneous plate plus a term which is due solely to the presence of the inhomogeneity. The second term is given in terms of an integral equation, which may in general be solved numerically, but which may also be solved approximately in terms of a perturbation series. The first term in this perturbation series is equivalent to the Born approximation. Unfortunately, when higher-order terms are included, this series will diverge when the ratio of the impedance of the discontinuity to the impedance of the homogeneous plate is larger than one, and will be slowly convergent when the ratio is near one. However, the series may be summed by using Padé approximation, which approximates a power series by a rational function.[10] Using Padé approximation enables us to obtain approximate analytic solutions for more complicated problems, enabling us to more easily identify the underlying wave physics causing the observed wave field. In this paper we introduce this method and apply it to the problem of an *in vacuo* plate with line discontinuities, although the method should also be applicable to a fluid-loaded plate. Additionally, the case of a distributed discontinuity, such as when a spatially limited section of the plate has a different mass, may also be treated by considering the continuous inhomogeneity to consist of closely spaced discrete inhomogeneities.

I. THEORY

Consider the equation of motion for the transverse plate displacement $u(x)$ for an inhomogeneous line-driven plate assuming time harmonic excitation of the form $\delta(x-x_0)e^{-i\omega t}$:

$$Du'''' - m\omega^2 u + f(x)u = \delta(x-x_0), \tag{1}$$

where ω is the angular frequency, $D=Eh^3/(12(1-\nu^2))$ is the bending stiffness of the plate, E is the Young's modulus, h is the plate thickness, m is the mass per unit length of the plate, and $f(x)$ is the inhomogeneity distribution. Taking the Fourier transform yields

$$(Dk_x^4 - m\omega^2)\tilde{u}(k_x) + \frac{1}{2\pi}\int_{-\infty}^{\infty}\tilde{f}(k_x-\tau)\tilde{u}(\tau)\,d\tau = e^{-ik_x x_0}. \tag{2}$$

We will now assume a solution for $\tilde{u}(k_x)$ in the following form:

$$\tilde{u}(k_x) = \frac{e^{-ik_x x_0}(1+\tilde{A}(k_x))}{(Dk_x^4 - m\omega^2)}. \tag{3}$$

This form is chosen because the first term in the parentheses represents the response of the plate in the absence of the

a)Electronic mail: feitd@nswccd.navy.mil

inhomogeneity, and the second term represents the response due to the inhomogeneity. Inserting this expression into Eq. (2), we arrive at the following equation for $\tilde{A}(k_x)$:

$$\tilde{A}(k_x) = -e^{ik_x x_0}\frac{1}{2\pi}\int_{-\infty}^{\infty}\tilde{f}(k_x-\tau)\frac{e^{-i\tau x_0}(1+\tilde{A}(\tau))}{(D\tau^4-m\omega^2)}d\tau. \tag{4}$$

This equation is an inhomogeneous Fredholm integral of the second kind, which can in general be solved numerically.[11] For certain inhomogeneity profiles this equation can be solved analytically. For more complicated profiles, approximate analytic solutions can be obtained by using a perturbation technique in conjunction with Padé approximation.

To get an approximate solution using a perturbation technique, we introduce the small parameter ϵ as follows:

$$f(x)=\epsilon f(x), \quad \tilde{f}(k_x)=\epsilon\tilde{f}(k_x). \tag{5}$$

The solution for the original equation can be recovered by taking the limit as $\epsilon\to 1$. Inserting this into Eq. (4), we obtain

$$\tilde{A}(k_x) = -\epsilon e^{ik_x x_0}\frac{1}{2\pi}\int_{-\infty}^{\infty}\tilde{f}(k_x-\tau)\frac{e^{-i\tau x_0}(1+\tilde{A}(\tau))}{(D\tau^4-m\omega^2)}d\tau. \tag{6}$$

Expanding $\tilde{A}(k_x)$ in a power series in ϵ yields

$$\tilde{A}(k_x)=\sum_{n=1}^{\infty}\epsilon^n\tilde{A}_n(k_x). \tag{7}$$

Inserting this into Eq. (6) and equating coefficients of ϵ^n yields the following conditions for $\tilde{A}_1(k_x)$ and $\tilde{A}_{n+1}(k_x)$:

$$\begin{aligned}\tilde{A}_1(k_x) &= -e^{ik_x x_0}\frac{1}{2\pi}\int_{-\infty}^{\infty}\tilde{f}(k_x-\tau)\frac{e^{-i\tau x_0}}{(D\tau^4-m\omega^2)}d\tau,\\ \tilde{A}_{n+1}(k_n) &= -e^{ik_x x_0}\frac{1}{2\pi}\int_{-\infty}^{\infty}\tilde{f}(k_x-\tau)\frac{e^{-i\tau x_0}\tilde{A}_n(\tau)}{(D\tau^4-m\omega^2)}d\tau.\end{aligned} \tag{8}$$

The power series in Eq. (7) may not converge for all values of ϵ. The radius of convergence of the power series is determined by the distance to the nearest pole of the function considered as a function of ϵ. For the problem considered here, the location of this pole is determined by the ratio of the impedance of the discontinuity to the impedance of the plate. Therefore, an alternate representation in terms of a rational function is more appropriate since it can represent this singularity. This rational function may be obtained from the power series using Padé approximation.[12] This representation will converge for larger values of ϵ. The Padé approximation is as follows:

$$\sum_{n=0}^{N+M} a_n z^n \simeq \frac{\Sigma_{n=0}^{N} C_n z^n}{1+\Sigma_{n=1}^{M} D_n z^n}. \tag{9}$$

By multiplying both sides by the denominator of the right side and equating powers of z, a linear system of equations is found to solve for C_n and D_n in terms of the power series coefficients a_n. In the following we will only be concerned with two cases, that of $M=1$, $N=0$ (i.e., two perturbation terms), and $M=2$, $N=1$ (four perturbation terms). For the case of two perturbation terms, we obtain the following coefficients in the Padé approximation: $C_0=a_0$ and $D_1=-a_1/a_0$. For the case of four perturbation terms, the coefficients are $C_0=a_0$, $C_1=(a_1^3-2a_0a_1a_2+a_0^2a_3)/(a_1^2-a_0a_2)$, $D_1=(-a_1a_2+a_0a_3)/(a_1^2-a_0a_2)$, and $D_2=(a_2^2-a_1a_3)/(a_1^2-a_0a_2)$.

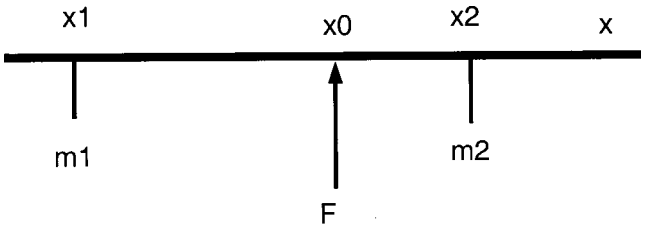

FIG. 1. Geometry for an infinite plate with two mass attachments.

In the following sections we will use the two-term approximation to obtain analytic solutions for several inhomogeneity profiles. Numerical results will also be presented for the four-term approximation, although the detailed expressions for the four-term approximations will be omitted.

A. Plate response with a single line discontinuity

The case where there is a single line discontinuity is one in which the original integral equation may be solved exactly. We will solve both the integral equation, and derive the approximate solution.

1. Exact solution

Consider the case where there is a line discontinuity located at $x=x_1$. We assume that the discontinuity is a mass attachment, giving

$$f(x)=R\delta(x-x_1), \quad \tilde{f}(k_x)=Re^{-ik_x x_1}, \tag{10}$$

where $R=-m_1\omega^2$ and m_1 is the mass of the attachment. Putting this form for $\tilde{f}(k_x)$ into Eq. (6) gives

$$\tilde{A}(k_x) = -Re^{ik_x(x_1-x_0)}\frac{1}{2\pi}\int_{-\infty}^{\infty}e^{i\tau x_1}\frac{e^{-i\tau x_0}(1+\tilde{A}(\tau))}{(D\tau^4-m\omega^2)}d\tau. \tag{11}$$

The value of this integral is not a function of k_x, which we will temporarily denote as S,

$$\begin{aligned}S &= \frac{1}{2\pi}\int_{-\infty}^{\infty}e^{i\tau x_1}\frac{e^{-i\tau x_0}(1+\tilde{A}(\tau))}{(D\tau^4-m\omega^2)}d\tau,\\ \tilde{A}(k_x) &= -RSe^{-ik_x(x_1-x_0)}.\end{aligned} \tag{12}$$

Integrating gives

$$S=G(x_1|x_0)-RSG(x_1|x_1), \tag{13}$$

where the integrals are recognized as being the Green's functions for the homogeneous plate. Solving for S and inserting into the expression for $\tilde{A}(k_x)$ gives

$$\tilde{A}(k_x) = -\frac{RG(x_1|x_0)}{1+RG(x_1|x_1)}e^{-ik_x x_1-x_0)}. \tag{14}$$

Using this result we find $\tilde{u}(k_x)$ to be

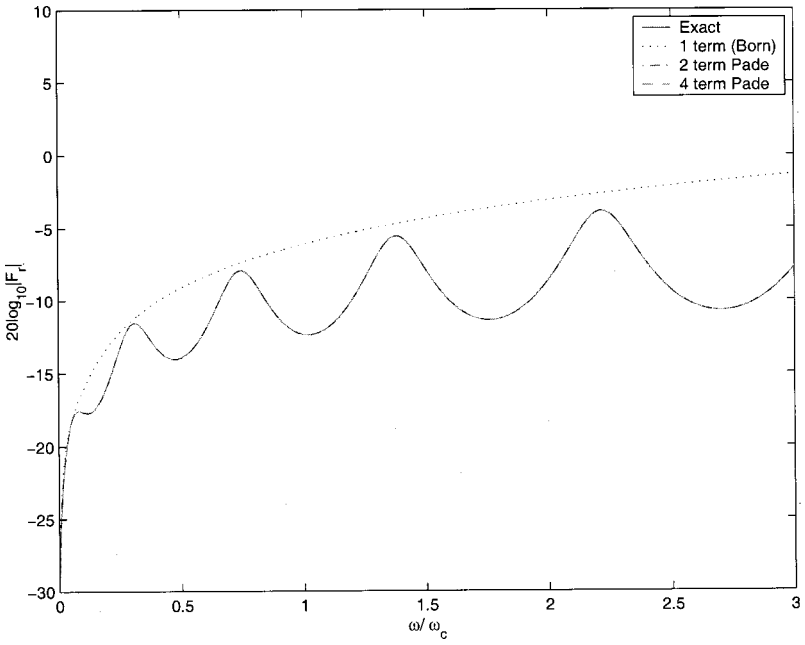

FIG. 2. Equivalent source at $x=-10h$ for a plate with two discontinuites of equal mass at $x=\pm 10h$ due to a line source located at $x=0$. The exact solution is plotted along with the first term in the perturbation series, the two-term Padé approximation, and the four-term Padé approximation.

$$\tilde{u}(k_x)=\frac{e^{-ik_x x_0}}{(Dk_x^4-m\omega^2)}-\frac{RG(x_1|x_0)}{1+RG(x_1|x_1)}\frac{e^{-ik_x x_1}}{(Dk_x^4-m\omega^2)}, \tag{15}$$

which agrees with the expression given by Junger and Feit.[13] Note that the first term is simply the transformed response of the homogeneous plate displacement to the externally applied line force located at $x=x_0$, while the second term is the reaction to the internal force applied by the mass discontinuity on the plate at $x=x_1$, the location of the line discontinuity. The amplitude of this internal force depends on the mass of the discontinuity and its distance from the applied force.

2. Perturbation solution

In order to apply a perturbation method to obtain an approximate solution, we introduce a parameter ϵ into the problem as follows:

$$f(x)=\epsilon R\,\delta(x-x_1), \quad \tilde{f}(k_x)=\epsilon\, Re^{-ik_x x_1}. \tag{16}$$

The first two terms in this series are easily found to be

$$\begin{aligned}\tilde{A}_1(k_x)&=-Re^{ik_x(x_1-x_0)}G(x_1|x_0),\\ \tilde{A}_2(k_x)&=R^2e^{ik_x(x_1-x_0)}G(x_1|x_0)G(x_1|x_1).\end{aligned} \tag{17}$$

We now have the following expression for $\tilde{A}(k_x)$:

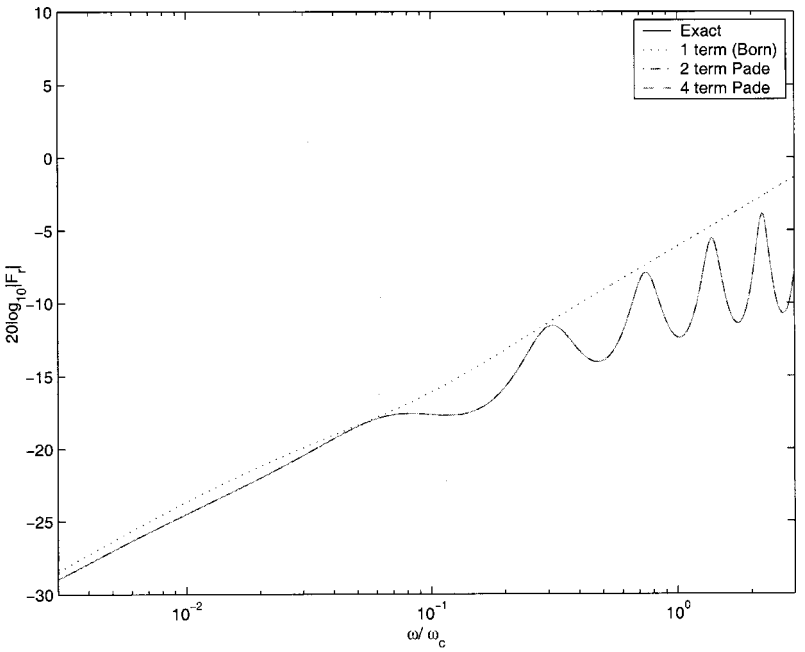

FIG. 3. Same as Fig. 2 except plotted on a logarithmic scale to show the fact that the Born approximation is restricted to very low values of frequency.

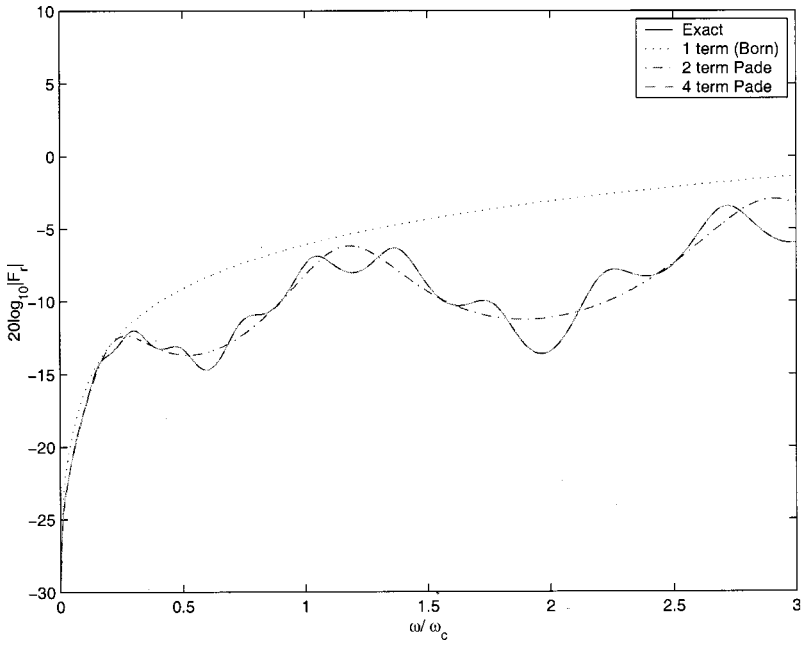

FIG. 4. Equivalent source at $x=-10h$ for a plate with two discontinuities of equal mass at $x=\pm 10h$ due to a line source located at $x=5h$. The exact solution is plotted along with the first term in the perturbation series, the two-term Padé approximation, and the four-term Padé approximation.

$$\tilde{A}(k_x)=-\epsilon R e^{ik_x(x_1-x_0)}G(x_1|x_0)[1-\epsilon RG(x_1|x_1)+\cdots]. \tag{18}$$

Using the Padé approximation for two perturbation terms allows us to rewrite the series in brackets as the following rational function:

$$\tilde{A}(k_x)=\frac{-\epsilon RG(x_1|x_0)}{1+\epsilon RG(x_1|x_1)}e^{-ik_x(x_1-x_0)}. \tag{19}$$

By allowing $\epsilon=1$, we recover the exact solution from the perturbation series.

B. Arbitrary set of line impedances

We will now consider the case where there is an arbitrary set of line discontinuities. This can be used as an approximation to a spatially limited discontinuity such as a rectangular function with a different mass than the plate. The inhomogeneity profile becomes

$$\tilde{f}(k_x)=\epsilon\sum_n R_n e^{ik_x x_n}, \tag{20}$$

where R_n and x_n are the size and location of the nth line discontinuities, respectively. It is straightforward to calculate the first four terms to be

$$\tilde{A}_1(k_x)=\sum_n R_n e^{ik_x(x_0-x_n)}H_1(x_n|x_0),$$

$$\tilde{A}_j(k_x)=\sum_n R_n e^{ik_x(x_0-x_n)}H_j(x_n|x_0),$$

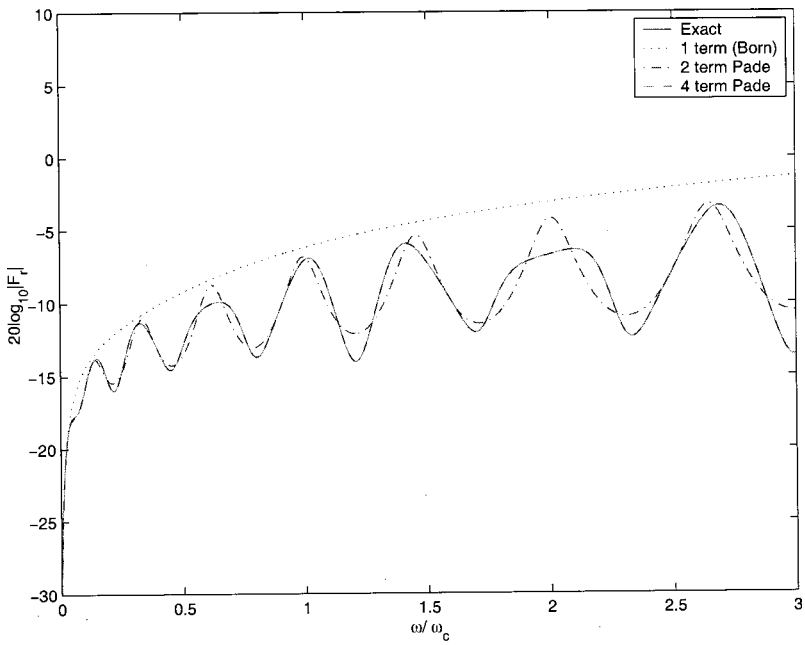

FIG. 5. Equivalent source at $x=10h$ for a plate with two discontinuities of equal mass at $x=\pm 10h$ due to a line source located at $x=5h$. The exact solution is plotted along with the first term in the perturbation series, the two-term Padé approximation, and the four-term Padé approximation.

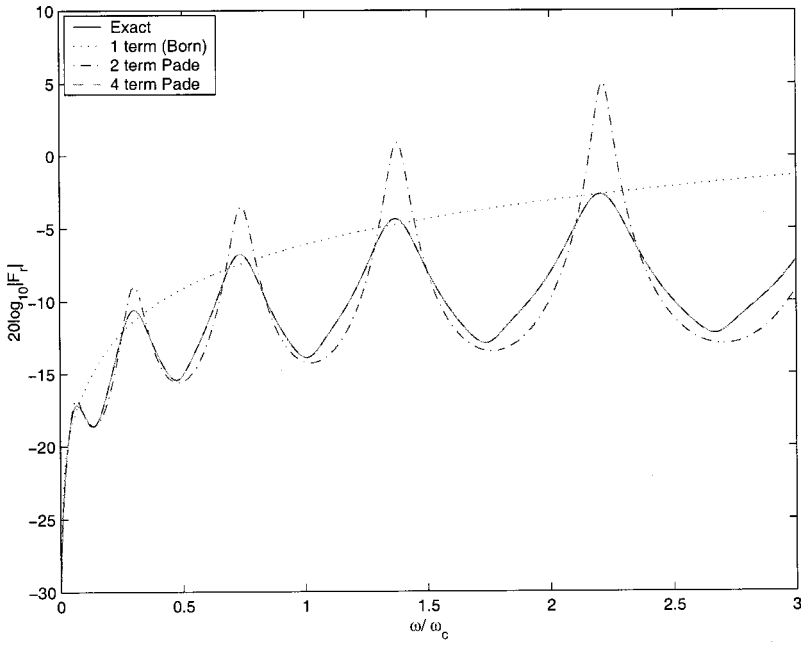

FIG. 6. Equivalent source at $x=-10h$ for a plate with two discontinuities of unequal mass at $x=\pm 10h$ due to a line source located at $x=0$. The exact solution is plotted along with the first term in the perturbation series, the two-term Padé approximation, and the four-term Padé approximation.

where

$$H_1(x_n|x_0)=-G(x_n|x_0),$$
$$H_{j+1}(x_n|x_0)=-\sum_m R_m G(x_n|x_m)H_j(x_m|x_0). \tag{21}$$

The sequence of terms represented in Eq. (21) can be given a physical interpretation. The term $H_1(x_n|x_0)$ is the displacement response at the observation point x_n due to the external force applied at x_0, while $H_2(x_n|x_0)$ again represents the response at x_0, but includes the effects of the internal forces generated at the line discontinuities by a single interaction with the incident field. Higher orders of H_n represent multiple interactions between the line discontinuities.

Using the Padé approximation for the first two terms in the perturbation series for $\tilde{A}(k_x)$ and allowing $\epsilon\rightarrow 1$ yields

$$\tilde{A}(k_x)\simeq -\sum_n e^{ik_x(x_0-x_n)}\left\{\frac{R_n H_1(x_n|x_0)}{1-H_2(x_n|x_0)/H_1(x_n|x_0)}\right\}, \tag{22}$$

and, substituting into Eq. (3), we obtain for the transform of the displacement

$$\tilde{u}(k_x)=\frac{e^{-ik_x x_0}}{(Dk_x^4-m\omega^2)} -\sum_n \frac{e^{-ik_x x_n}}{(Dk_x^4-m\omega^2)}\left\{\frac{R_n H_1(x_n|x_0)}{1-H_2(x_n|x_0)/H_1(x_n|x_0)}\right\}. \tag{23}$$

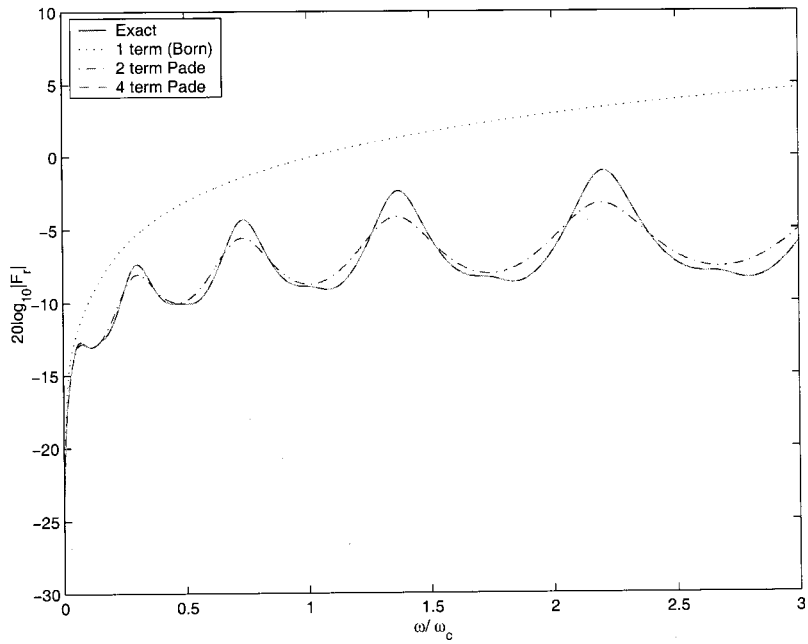

FIG. 7. Equivalent source at $x=10h$ for a plate with two discontinuities of unequal mass at $x=\pm 10h$ for due to a line source located at $x=0$. The exact solution is plotted along with the first term in the perturbation series, the two-term Padé approximation, and the four-term Padé approximation.

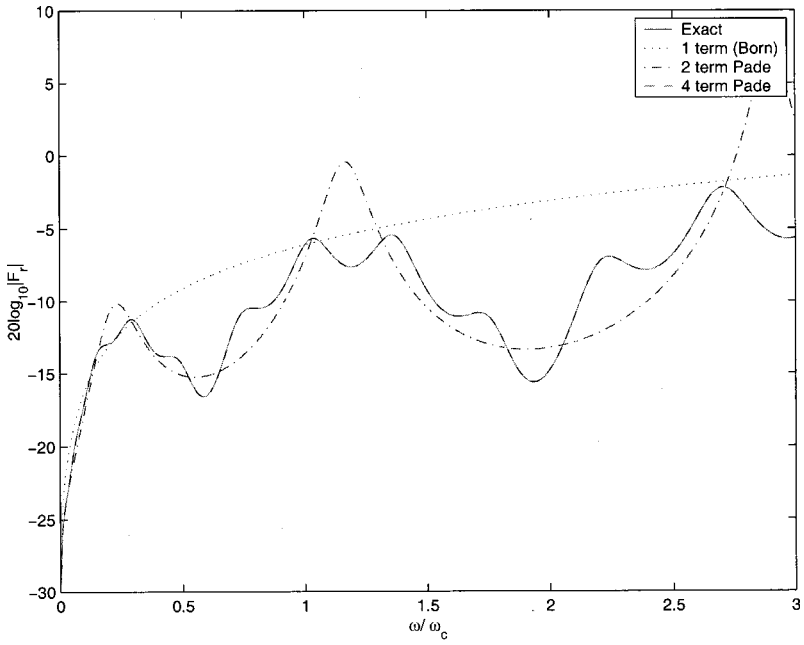

FIG. 8. Equivalent source at $x=-10h$ for a plate with two discontinuities of unequal mass at $x=\pm 10h$ due to a line source located at $x=5h$. The exact solution is plotted along with the first term in the perturbation series, the two-term Padé approximation, and the four-term Padé approximation.

The first term is the displacement of the unperturbed plate due to a unit amplitude line force applied at $x=x_0$. The second term is the response of the plate due to the inhomogeneities. For the case of isolated mass discontinuities, the term in brackets can be interpreted as the amplitude of a reaction force at each mass location x_n.

II. RESULTS

As previously discussed, for the case of a single mass discontinuity, the approximate solution is equal to the exact solution, and therefore no results will be presented. We will show results for the case of two masses, each with mass $m_1=m_2=2h^2$, located at $x=\pm 10h$, as is shown in Fig. 1. Figure 2 shows the magnitude of the reaction force F_r at the discontinuity located at $x=-10h$ due to a unit amplitude line force located at $x_0=0$. The solid curve is simply the first term in the perturbation series, which is equivalent to the Born approximation. The Padé approximations from the two- and four-term perturbation solutions exactly overlay the exact solution. Figure 3 shows the same plot shown on a logarithmic axis. The fact that the Born approximation is only good at very low values of frequency can be seen clearly. Figure 4 shows the magnitude of the reaction force at $x=-10h$ due to a unit amplitude line force located at $x=5h$. Here the two-term Padé approximation matches the general trend of the exact solution, but misses the more rapidly varying components. The four-term Padé approximation lies directly on top of the exact solution. Presumably, the higher frequency oscillations seen in the exact solution are due to multiple interactions between the mass discontinuities

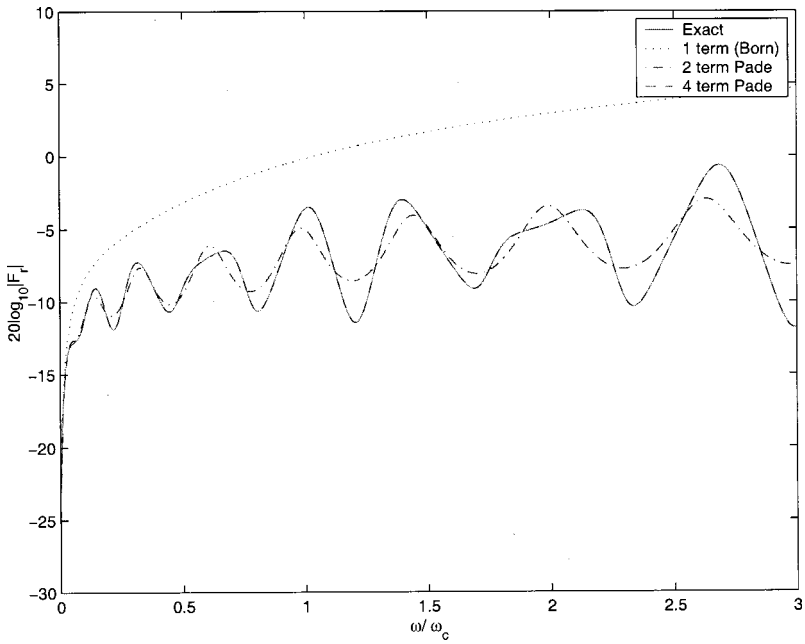

FIG. 9. Equivalent source at $x=10h$ for a plate with two discontinuities of unequal mass at $x=\pm 10h$ due to a line source located at $x=5h$. The exact solution is plotted along with the first term in the perturbation series, the two-term Padé approximation, and the four-term Padé approximation.

and drive point, and are accounted for in higher-order terms in the perturbation series. Figure 5 shows the magnitude of the reaction force at the mass discontinuity located at $x = 10h$. Again, the Padé approximation based on the two-term perturbation is far superior to the Born approximation, but misses some details of the exact curve, while the Padé approximation based on four terms lies directly on top of the exact solution.

Figures 6–9 show results for the case where the discontinuity located at $x_1 = -10h$ has mass $m_1 = 2h^2$ and the mass at $x_2 = 10h$ has mass $m_2 = 4h^2$, for the drive at $x_0 = 0$ and $x = 5h$. In all of these cases, the Padé approximation based on two terms does not precisely match the exact solution, but it is superior to the Born approximation, whereas the Padé approximation based on four terms is indistinguishable from the exact solution.

III. CONCLUSIONS

We have presented a novel technique for obtaining an approximate solution for the vibration of a line-driven infinite plate with discontinuities. The solution is expressed as the solution of the homogeneous plate plus a term due to the discontinuity. The term due to the discontinuity is obtained analytically in terms of the Green's function of the homogeneous plate. For the case of a single isolated mass discontinuity, the approximate solution has been shown to be equal to the exact solution. For the case of multiple line discontinuities, the approximate solution based on two terms of the perturbation series has been shown to have a far larger range of validity than the Born approximation. Numerical results for the approximate solution based on four perturbation terms are indistinguishable from the exact solution.

[1] M. C. Junger, ''Radiation and scattering by submerged elastic structures,'' J. Acoust. Soc. Am. **57**, 1318–1326 (1975).
[2] J. J. Bowman, T. B. A. Senior, and P. L. E. Uslenghi, *Electromagnetic and Acoustic Scattering by Simple Shapes* (Hemisphere, New York, 1987).
[3] M. C. Junger, ''Sound scattering by thin elastic shells,'' J. Acoust. Soc. Am. **24**, 366–373 (1952).
[4] J. J. Faran, Jr., ''Sound scattering by solid cylinders and spheres,'' J. Acoust. Soc. Am. **23**, 405–418 (1951).
[5] L. B. Felsen and N. Marcuvitz, *Radiation and Scattering of Waves* (IEEE, New York, 1994).
[6] D. T. DiPerna and T. K. Stanton, ''Sound scattering by cylinders of noncircular cross section: A conformal mapping approach,'' J. Acoust. Soc. Am. **96**, 3064–3079 (1994).
[7] J. M. Cuschieri and D. Feit, ''A hybrid numerical and analytical solution for the green's function of a fluid-loaded elastic plate,'' J. Acoust. Soc. Am. **95**, 1998–2005 (1994).
[8] D. Feit and J. M. Cuschieri, ''Scattering of sound by a fluid-loaded plate with a distributed mass inhomogeneity,'' J. Acoust. Soc. Am. **99**, 2686–2700 (1996).
[9] D. Feit and J. M. Cuschieri, ''Fluid-loaded plate coupled to a distributed inhomogeneity—review,'' J. Acoust. Soc. Am. **99**, 2585–2603 (1996).
[10] G. A. Baker, Jr. and P. Graves-Morris, *Padé Approximants*, 2nd ed. (Cambridge U.P., Cambridge, 1996).
[11] W. H. Press, W. T. Vetterling, S. A. Teukolsky, and B. P. Flannery, *Numerical Recipes in C*, 2nd ed. (Cambridge U. P., Cambridge, 1992).
[12] C. M. Bender and S. A. Orszag, *Advanced Mathematical Methods for Scientists and Engineers*, 1st ed. (McGraw–Hill, New York, 1978).
[13] M. Junger and D. Feit, *Sound, Structures, and their Interaction*, 2nd ed. (American Institute of Physics, New York, 1993).

Estimation of fuzzy structure parameters for continuous junctions

Christian Soize and Karina Bjaoui
Structural Dynamics and Coupled Systems Department, ONERA, BP 72, 92322 Chatillon Cedex, France

(Received 25 May 1999; accepted for publication 9 December 1999)

The fuzzy structure theory introduced 15 years ago is designed to predict the frequency response functions of structures and structural acoustic systems with structural complexity, in the low- and medium-frequency ranges. This paper constitutes a first validation of the fuzzy structure theory for continuous junctions between the master structure and the fuzzy substructures. In addition, a method to estimate the fuzzy structure parameters introduced in the fuzzy structure theory is presented and it is validated for the case of continuous junctions. This validation obtained by numerical simulations opens the field of experimental identifications. © *2000 Acoustical Society of America.* [S0001-4966(00)04103-5]

PACS numbers: 43.40.Dx, 43.40.Hb [CBB]

INTRODUCTION

The fuzzy structure theory was introduced by Soize[1] in order to model structural complexity in the medium frequency range. This structural complexity plays a fundamental role in the response of a master structure coupled with complex substructures in the context of structural-acoustic systems. In 1993, a second fuzzy impedance law was proposed[2] to model the case of fuzzy substructures attached to the master structure through a continuous junction. Since 1993, much research has been published concerning the problem of a master structure coupled with a large number of simple linear oscillators[3–18] and a few concerning continuous cases.[19–22] Two main problems had to be solved to be able to apply the fuzzy structure theory (described in detail in Ref. 23) to the case of continuous junctions. The first problem was related to the construction of a procedure for identifying the fuzzy structure parameters in order to solve complex problems and to allow experimental identifications to be performed. The second one, which requires solving the first, is related to validation of the fuzzy structure theory for continuous junctions. A general procedure has been developed[24] to solve the first problem. In this paper, we present a first validation of the fuzzy structure theory for continuous junctions between the master structure and the fuzzy substructures. We introduce a new cost function replacing the cost function previously introduced.[24] It allows an efficient estimation of the fuzzy structure parameters using a procedure based on the statistical energy approach. In Sec. I we introduce the reference complex structure, its model, and the numerical simulation of its response. All the validations are performed with respect to this reference. Section II deals with modeling of the reference complex structure using the fuzzy structure theory. In Sec. III we present the procedure for estimating the fuzzy structure mean parameters. Finally, the last section is devoted to validation by comparison with reference results.

I. REFERENCE COMPLEX STRUCTURE MODEL AND NUMERICAL SIMULATION OF ITS RESPONSE

The complex structure consists of a master structure coupled with four complex substructures (see Fig. 1). The master structure is constituted of two rectangular homogeneous isotropic thin plates denoted as (1) and (2), in bending mode and simply supported. Plate (1) is coupled to plate (2) along their common edge; the rotation around this edge is continuous. The complex substructures are denoted as (*a*), (*b*), (*c*), and (*d*) and are constituted of a rectangular homogeneous isotropic thin plate on which many simple linear oscillators are attached. The plate of each complex substructure is in bending mode, simply supported and coupled to a plate of the master structure along their common edge; the rotation around this edge is continuous. Consequently, there is a continuous junction between each complex substructure and the master structure. Two plates belonging to different complex substructures are not coupled along their common edge (there is coupling only between each complex substructure and the master structure). The method used to construct the model of the reference complex structure consists in constructing the generalized impedance matrix of an isolated plate belonging to the master structure and an isolated complex substructure. Then the isolated subsystems constituting the reference complex structure are coupled using a Lagrange multiplier technique in order to express the continuity of the rotation on the junctions.

A. Generalized impedance matrix of an isolated plate belonging to the master structure

Each rectangular thin plate (r) (with r equal to 1 or 2) of the master structure is referenced to an (x,y) local coordinate system and is located in plane Oxy. This plate has a constant thickness, a length L_{r1}, a width L_{r2}, surface-mass density ρ_r (mass per unit area), a constant damping rate ξ_r and a constant flexural rigidity D_r. The domain of this plate (middle surface) is defined by $\Omega_r =]0,L_{r1}[\times]0,L_{r2}[$. We consider linear vibrations of this plate formulated in the frequency domain ω. The transverse displacement of plate (r) in a point (x,y) is denoted as $u_r(\omega,x,y)$. The external forces applied to the plate are represented by a complex-valued function $f_r(\omega,x,y)$. The bending moment around the edges of plate (r) is denoted as $\mathcal{M}_{\mathbf{n}_r}$ in which $\mathbf{n}_r$ is the outward unit normal to the boundary $\partial\Omega_r$ of domain Ω_r. The boundary value problem is written as

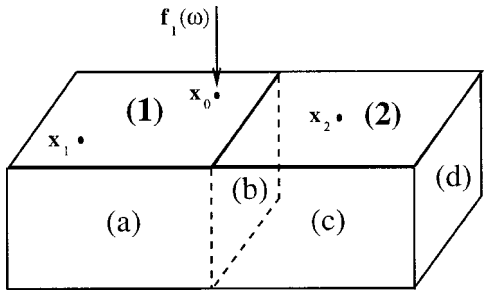

FIG. 1. Reference complex structure.

$$
\begin{aligned}
&-\omega^2\rho_r u_r - 2i\omega\xi_r\{\rho_r D_r\}^{1/2}\,\boldsymbol{\nabla}^2 u_r + D_r\,\boldsymbol{\nabla}^4 u_r \\
&\quad = f_r \quad \text{in } \Omega_r, \\
&u_r = 0 \quad \text{on } \partial\Omega_r, \\
&\mathcal{M}_{\mathbf{n}_r} = 0 \quad \text{on } \partial\Omega_r.
\end{aligned} \tag{1}
$$

The boundary value problem defined by Eq. (1) is solved using the Ritz–Galerkin method for which the complete family of independent functions in the admissible function space is constituted of the normal modes related to the simply supported plate. We then introduce the normal modes[25]

$$
\varphi_{r\beta}(x,y) = \frac{2}{\sqrt{L_{r1}L_{r2}}}\sin\left(\frac{\beta_1\pi x}{L_{r1}}\right)\sin\left(\frac{\beta_2\pi y}{L_{r2}}\right), \tag{2}
$$

and the corresponding eigenfrequencies

$$
\omega_{r\beta} = \sqrt{\frac{D_r}{\rho_r}}\left\{\left(\frac{\beta_1\pi}{L_{r1}}\right)^2 + \left(\frac{\beta_2\pi}{L_{r2}}\right)^2\right\}, \tag{3}
$$

in which $\boldsymbol{\beta}=(\beta_1,\beta_2)$ where β_1 and β_2 are positive integers. The finite dimension approximation of field u_r is written as $\tilde{u}_r(\omega,x,y)=\Sigma_{\boldsymbol{\beta}\in\mathcal{B}^r} q_{r\boldsymbol{\beta}}(\omega)\varphi_{r\boldsymbol{\beta}}(x,y)$ in which $\mathcal{B}^r$ is the set of all the pairs of integers (β_1,β_2) such that $\tilde{u}_r(\omega,x,y)$ approaches $u_r(\omega,x,y)$. Let $\mathbf{q}_r(\omega)$ and $\mathbf{f}_r(\omega)$ be the vectors of generalized coordinates and generalized forces such that

$$
\mathbf{q}_r(\omega)=\{q_{r\boldsymbol{\beta}}(\omega)\}_{\boldsymbol{\beta}\in\mathcal{B}_r}, \quad \mathbf{f}_r(\omega)=\{f_{r\boldsymbol{\beta}}(\omega)\}_{\boldsymbol{\beta}\in\mathcal{B}_r}, \tag{4}
$$

in which $f_{r\beta}(\omega)=\int_0^{L_{r1}}\int_0^{L_{r2}} f_r(\omega,x,y)\varphi_{r\beta}(x,y)dx\,dy$. Consequently, for all real ω, vector $\mathbf{q}_r(\omega)$ is the solution of the complex matrix equation $i\omega[Z_r(\omega)]\mathbf{q}_r(\omega)=\mathbf{f}_r(\omega)$ in which $[Z_r(\omega)]$ is the generalized impedance complex diagonal matrix such that

$$
i\omega[Z_r(\omega)]_{\boldsymbol{\beta}\boldsymbol{\beta}'} = \rho_r\{-\omega^2 + 2i\omega\xi_r\omega_{r\boldsymbol{\beta}} + \omega_{r\boldsymbol{\beta}}^2\}\delta_{\boldsymbol{\beta}\boldsymbol{\beta}'}, \tag{5}
$$

with $\delta_{\boldsymbol{\beta}\boldsymbol{\beta}'}=1$ if $\boldsymbol{\beta}=\boldsymbol{\beta}'$ and $=0$ otherwise.

B. Generalized impedance matrix of an isolated complex substructure

Each complex substructure (s) (with s equal to a, b, c or d) is constituted of a rectangular thin plate (s) on which K_s simple linear oscillators are attached. Plate (s) is referenced to an (x,y) local coordinate system and is located in plane Oxy. This plate has a constant thickness, a length L_{s1}, a width L_{s2}, a surface-mass density ρ_s (mass per unit area), a constant damping rate ξ_s and a constant flexural rigidity D_s. The domain of this plate (middle surface) is defined by $\Omega_s=]0,L_{s1}[\times]0,L_{s2}[$. We consider linear vibrations of this complex substructure formulated in the frequency domain ω. The transverse displacement of the plate (s) in a point (x,y) is denoted as $u_s(\omega,x,y)$. The external forces applied to the plate are represented by a complex-valued function $f_s(\omega,x,y)$. The bending moment around the edges of plate (s) is denoted as $\mathcal{M}_{\mathbf{n}_s}$ in which $\mathbf{n}_s$ is the outward unit normal to the boundary $\partial\Omega_s$ of domain Ω_s. The mass, damping rate and stiffness of the κth simple linear oscillator ($\kappa=1,\ldots,K_s$) attached to plate (s) are constant and denoted as m_s^κ, ξ_s^κ, and $m_s^\kappa(\omega_s^\kappa)^2$, respectively ($\omega_s^\kappa$ is the eigenfrequency of the undamped oscillator with a fixed support). Oscillator κ is located in point (x^κ,y^κ). The area of the plate of the complex substructure is divided into $\sqrt{K_s}$ subelements (rectangular subelement) and $\sqrt{K_s}$ oscillators are uniformly distributed in space inside each subelement and in frequency inside the frequency band of analysis. The boundary value problem is written as

$$
\begin{aligned}
&-\omega^2\rho_s u_s - 2i\omega\xi_s(\rho_s D_s)^{1/2}\,\boldsymbol{\nabla}^2 u_s + D_s\,\boldsymbol{\nabla}^4 u_s \\
&\quad = f_s - \sum_{\kappa=1}^{K_s} g_s^\kappa \quad \text{in } \Omega_s, \\
&u_s = 0 \quad \text{on } \partial\Omega_s, \\
&\mathcal{M}_{\mathbf{n}_s} = 0 \quad \text{on } \partial\Omega_s.
\end{aligned} \tag{6}
$$

Force $g_s^\kappa(\omega)$ induced by oscillator κ is such that

$$
g_s^\kappa(\omega) = i\omega z_s^\kappa(\omega) u_s(\omega,x^\kappa,y^\kappa), \tag{7}
$$

in which z_s^κ is such that

$$
\begin{aligned}
i\omega z_s^\kappa(\omega) = &-\omega^2\left(\frac{m_s^\kappa(\omega_s^\kappa/\omega)^2((\omega_s^\kappa/\omega)^2 - 1 + 4(\xi_s^\kappa)^2)}{((\omega_s^\kappa/\omega)^2-1)^2 + 4(\omega_s^\kappa/\omega)^2(\xi_s^\kappa)^2}\right) \\
&+ i\omega\left(\frac{2m_s^\kappa\omega\xi_s^\kappa(\omega_s^\kappa/\omega)}{((\omega_s^\kappa/\omega)^2-1)^2 + 4(\omega_s^\kappa/\omega)^2(\xi_s^\kappa)^2}\right).
\end{aligned} \tag{8}
$$

The boundary value problem defined by Eq. (6) is solved similarly to Eq. (1), introducing the normal modes,

$$
\varphi_{s\beta}(x,y) = \frac{2}{\sqrt{L_{s1}L_{s2}}}\sin\left(\frac{\beta_1\pi x}{L_{s1}}\right)\sin\left(\frac{\beta_2\pi y}{L_{s2}}\right), \tag{9}
$$

and the corresponding eigenfrequencies,

$$
\omega_{s\beta} = \sqrt{\frac{D_s}{\rho_s}}\left\{\left(\frac{\beta_1\pi}{L_{s1}}\right)^2 + \left(\frac{\beta_2\pi}{L_{s2}}\right)^2\right\}, \tag{10}
$$

in which $\boldsymbol{\beta}=(\beta_1,\beta_2)$ where β_1 and β_2 are positive integers. The finite dimension approximation of field u_s is written as $\tilde{u}_s(\omega,x,y)=\Sigma_{\boldsymbol{\beta}\in\mathcal{B}^s} q_{s\boldsymbol{\beta}}(\omega)\varphi_{s\boldsymbol{\beta}}(x,y)$ in which $\mathcal{B}^s$ is the set of all the pairs of integers (β_1,β_2) such that $\tilde{u}_s(\omega,x,y)$ approaches $u_s(\omega,x,y)$. As in Sec. I A, we introduce vectors $\mathbf{q}_s(\omega)$ and $\mathbf{f}_s(\omega)$ such that

$$
\mathbf{q}_s(\omega)=\{q_{s\boldsymbol{\beta}}(\omega)\}_{\boldsymbol{\beta}\in\mathcal{B}_s}, \quad \mathbf{f}_s(\omega)=\{f_{s\boldsymbol{\beta}}(\omega)\}_{\boldsymbol{\beta}\in\mathcal{B}_s}, \tag{11}
$$

in which $f_{s\boldsymbol{\beta}}(\omega)=\int_0^{L_{s1}}\int_0^{L_{s2}} f_s(\omega,x,y)\varphi_{s\boldsymbol{\beta}}(x,y)dx\,dy$ and for all real ω, vector $\mathbf{q}_s(\omega)$ is the solution of the complex matrix equation $i\omega[Z_s(\omega)]\mathbf{q}_s(\omega)=\mathbf{f}_s(\omega)$ in which $[Z_s(\omega)]$ is the

generalized impedance complex dense matrix such that

$$i\omega[Z_s(\omega)]_{\beta\beta'} = \rho_s\{-\omega^2 + 2i\omega\xi_s\omega_{s\beta} + \omega_{s\beta}^2\}\delta_{\beta\beta'} + z_s^{\kappa}(\omega)\varphi_{s\beta}(x^{\kappa},y^{\kappa})\varphi_{s\beta'}(x^{\kappa},y^{\kappa}). \quad (12)$$

C. Generalized impedance matrix of the reference complex structure

The coupling between two plates of the master structure or between the master structure and a complex substructure is obtained by writing the continuity of rotations along the junctions (it should be noted that the continuity of the displacement field is satisfied). These resulting linear constraint equations are then taken into account using Lagrange multipliers. Using the generalized impedance matrices introduced in Secs. I A and I B yields

$$\begin{bmatrix} i\omega[Z_{\text{mast}}(\omega)] & 0 & [B_{\text{mast}}]^T & [B_{\text{mast-sub}}]^T \\ 0 & i\omega[Z_{\text{sub}}(\omega)] & 0 & [B_{\text{sub-mast}}]^T \\ [B_{\text{mast}}] & 0 & 0 & 0 \\ [B_{\text{mast-sub}}] & [B_{\text{sub-mast}}] & 0 & 0 \end{bmatrix} \times \begin{bmatrix} \mathbf{q}_{\text{mast}}(\omega) \\ \mathbf{q}_{\text{sub}}(\omega) \\ \mathbf{p}_{\text{mast}}(\omega) \\ \mathbf{p}_{\text{sub}}(\omega) \end{bmatrix} = \begin{bmatrix} \mathbf{f}_{\text{mast}}(\omega) \\ 0 \\ 0 \\ 0 \end{bmatrix} \quad (13)$$

in which $\mathbf{q}_{\text{mast}}(\omega) = (\mathbf{q}_1(\omega), \mathbf{q}_2(\omega))$ and $\mathbf{q}_{\text{sub}}(\omega) = (\mathbf{q}_a(\omega), \mathbf{q}_b(\omega), \mathbf{q}_c(\omega), \mathbf{q}_d(\omega))$ are the vectors of the generalized coordinates of the master structure and the complex substructures, respectively, and $\mathbf{p}_{\text{mast}}(\omega)$ and $\mathbf{p}_{\text{sub}}(\omega) = (\mathbf{p}_{1a}(\omega), \mathbf{p}_{1b}(\omega), \mathbf{p}_{2c}(\omega), \mathbf{p}_{2d}(\omega))$ are the vectors of the generalized coordinates of the Lagrange multipliers related to the coupling between the plates of the master structure and between the plates of the master structure and the complex substructures respectively. Finally, $\mathbf{f}_{\text{mast}}(\omega) = (\mathbf{f}_1(\omega), \mathbf{f}_2(\omega))$ is the vector of the generalized forces applied to the master structure. Impedance matrices $[Z_{\text{mast}}(\omega)]$ and $[Z_{\text{sub}}(\omega)]$ are written as

$$[Z_{\text{mast}}(\omega)] = \begin{bmatrix} [Z_1(\omega)] & 0 \\ 0 & [Z_2(\omega)] \end{bmatrix}, \quad (14)$$

in which $[Z_1(\omega)]$ and $[Z_1(\omega)]$ are defined by Eq. (5) and

$$[Z_{\text{sub}}(\omega)] = \begin{bmatrix} [Z_a(\omega)] & 0 & 0 & 0 \\ 0 & [Z_b(\omega)] & 0 & 0 \\ 0 & 0 & [Z_c(\omega)] & 0 \\ 0 & 0 & 0 & [Z_d(\omega)] \end{bmatrix}, \quad (15)$$

in which $[Z_a(\omega)]$, $[Z_b(\omega)]$, $[Z_c(\omega)]$, and $[Z_d(\omega)]$ are defined by Eq. (12). Finally, matrices $[B_{\text{mast}}]$, $[B_{\text{mast-sub}}]$ and $[B_{\text{sub-mast}}]$ are deduced[26] from the linear constraint equations introduced by the Lagrange multipliers. Equation (13) can be rewritten as

$$\begin{bmatrix} i\omega[Z(\omega)] & [B]^T \\ [B] & 0 \end{bmatrix} \begin{bmatrix} \mathbf{q}(\omega) \\ \mathbf{p}(\omega) \end{bmatrix} = \begin{bmatrix} \mathbf{f}(\omega) \\ 0 \end{bmatrix}. \quad (16)$$

In general, and in particular for the reference complex structure under consideration, the matrix of Eq. (16) is not invertible due to redundant linear constraint equations induced by multiple connectivities. In order to circumvent this difficulty, we use a method[26] based on the use of the singular value decomposition of matrix $[B]$. This method allows the redundant equations to be automatically eliminated and Eq. (16) to be solved. Its solution $\mathbf{q}(\omega)$ is written as

$$\mathbf{q}(\omega) = [T(\omega)]\mathbf{f}(\omega). \quad (17)$$

D. Dynamical response of the reference complex structure

The response of the reference complex structure is obtained on the frequency band of analysis [0,1000] Hz. The plates of the master structure are identical. Each plate is homogeneous and isotropic with length $L_{r1} = 1$ m, width $L_{r2} = 0.5$ m, constant thickness 0.003 m, surface-mass density $\rho_r = 23.46\ \text{kg/m}^2$, Young's modulus $= 2.1 \times 10^{11}\ \text{N/m}^2$, Poisson's ratio 0.3, and constant damping rate $\xi_r = 0.003$. Each plate of the complex substructures is homogeneous and isotropic with constant thickness 0.002 m, surface-mass density $\rho_r = 15.64\ \text{kg/m}^2$, Young's modulus $= 2.1 \times 10^{11}\ \text{N/m}^2$, Poisson's ratio 0.3 and constant damping rate $\xi_r = 0.003$. The length and width of the plates of complex substructures (*a*) and (*c*) are equal to $L_{s1} = 1$ m and $L_{s2} = 0.5$ m, respectively. The plates of complex substructures (*b*) and (*d*) are square and their length is equal to 0.5 m. In each complex substructure, there are 2401 oscillators having a total mass of 1 kg. The damping rate of each oscillator is equal to 0.003. The eigenfrequencies of the oscillators are uniformly distributed over frequency band [0,1000] Hz. The excitation force is applied to plate (1) at point located in $\mathbf{x}_0 = (0.707, 0.316)$, with a constant modulus equal to 1 N over the frequency band. The responses are calculated at point $\mathbf{x}_1 = (0.33, 0.166)$ in plate (1) and point $\mathbf{x}_2 = (0.48, 0.23)$ in plate (2). Figures 2–4 show the modulus (in dB) of frequency response function for the acceleration at points $\mathbf{x}_0$, $\mathbf{x}_1$, and $\mathbf{x}_2$ of the master structure; the thin solid lines and the thick solid lines represent the response of the master structure uncoupled with the complex substructures and coupled with the complex substructures, respectively. It should be noted that

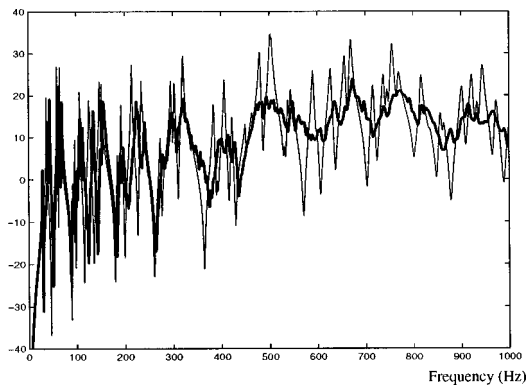

FIG. 2. Modulus (in dB) of the frequency response function for the acceleration at point $\mathbf{x}_0$ of the master structure: master structure not coupled with the complex substructures (thin solid line); master structure coupled with the complex substructures (thick solid line).

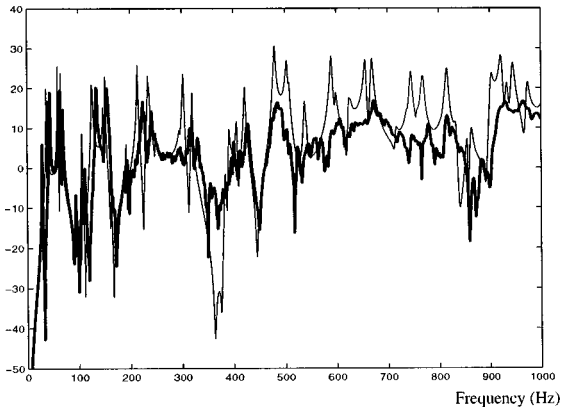

FIG. 3. Modulus (in dB) of the frequency response function for the acceleration at point $\mathbf{x}_1$ of the master structure: master structure not coupled with the complex substructures (thin solid line); master structure coupled with the complex substructures (thick solid line).

frequency band [0,300] Hz corresponds to the low-frequency range for which complex substructures do not significantly affect the responses of the master structure. In medium-frequency band [300,1000] Hz, the complex substructures play an important role in the response of the master structure, inducing an apparent strong damping in the master structure due to the power flow from the master structure to the structural complexity.

II. MODELING THE REFERENCE COMPLEX STRUCTURE USING THE FUZZY STRUCTURE THEORY

The fuzzy structure theory[1,2,23,24] is used to model the reference complex structure. The junctions between plate (1) of the master structure and its two attached fuzzy substructures (*a*) and (*b*) are denoted as $\Gamma^1_{1,\mathrm{fuz}}$ and $\Gamma^2_{1,\mathrm{fuz}}$ respectively. The junctions between plate (2) of the master structure and its two attached fuzzy substructures (*c*) and (*d*) are denoted as $\Gamma^1_{2,\mathrm{fuz}}$ and $\Gamma^2_{2,\mathrm{fuz}}$, respectively (see Fig. 5).

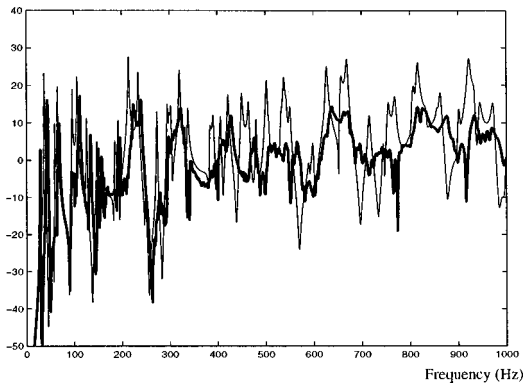

FIG. 4. Modulus (in dB) of the frequency response function for the acceleration at point $\mathbf{x}_2$ of the master structure: master structure not coupled with the complex substructures (thin solid line); master structure coupled with the complex substructures (thick solid line).

A. Generalized impedance matrix of a master-structure plate coupled with its fuzzy substructures

Using the same notation as in Sec. I A and denoting random displacement u_r as U_r, the boundary value problem related to plate (r) of the master structure coupled with its attached fuzzy substructures is written as

$$
\begin{aligned}
&-\omega^2\rho_r U_r - 2i\omega\xi_r(\rho_r D_r)^{1/2}\,\boldsymbol{\nabla}^2 U_r + D_r\,\boldsymbol{\nabla}^4 U_r \\
&\quad = f_r \quad \text{in } \Omega_r, \\
&U_r = 0 \quad \text{on } \partial\Omega_r, \\
&\mathcal{M}_{\mathbf{n}_r} = \mathcal{M}^1_{r,\mathrm{fuz}} \quad \text{on } \Gamma^1_{r,\mathrm{fuz}}, \\
&\mathcal{M}_{\mathbf{n}_r} = \mathcal{M}^2_{r,\mathrm{fuz}} \quad \text{on } \Gamma^2_{r,\mathrm{fuz}}, \\
&\mathcal{M}_{\mathbf{n}_r} = 0 \quad \text{on } \partial\Omega_r \backslash \{\Gamma^1_{r,\mathrm{fuz}} \cup \Gamma^2_{r,\mathrm{fuz}}\},
\end{aligned}
\tag{18}
$$

in which $\mathcal{M}^1_{r,\mathrm{fuz}}$ and $\mathcal{M}^2_{r,\mathrm{fuz}}$ are the moments induced by the two attached fuzzy substructures on plate (r) of the master structure. The fuzzy structure theory gives the expression of these moments $\mathcal{M}^l_{r,\mathrm{fuz}}$ for $l=1$ or 2,

$$
\mathcal{M}^l_{r,\mathrm{fuz}}(\omega;s) = \int_{\Gamma^l_{r,\mathrm{fuz}}} i\omega Z^l_{r,\mathrm{fuz}}(\omega;s,s')\,\frac{\partial U_r(\omega;s')}{\partial \mathbf{n}_r}\,ds', \tag{19}
$$

in which random variable $Z^l_{r,\mathrm{fuz}}(\omega;s,s')$ is written as

$$
\begin{aligned}
i\omega Z^l_{r,\mathrm{fuz}}(\omega;s,s') = \{&-\omega^2 S^l_{r,\mathrm{fuz}}(\omega) \\
&+ i\omega D^l_{r,\mathrm{fuz}}(\omega)\}\,\delta_{\Gamma^l_{r,\mathrm{fuz}}}(s'-s),
\end{aligned}
\tag{20}
$$

where $\delta_{\Gamma^l_{r,\mathrm{fuz}}}$ is the Dirac function and where $\mathbb{Z}^l_{r,\mathrm{fuz}}(\omega) = -\omega^2 S^l_{r,\mathrm{fuz}}(\omega) + i\omega D^l_{r,\mathrm{fuz}}(\omega)$ is the homogeneous fuzzy impedance law of fuzzy substructure l such that

$$
S^l_{r,\mathrm{fuz}}(\omega) = S^l_{r,\mathrm{mean}}(\omega) + \sum_{j=1}^{4} X^l_{r,j} S^l_{r,j,\mathrm{rand}}(\omega), \tag{21}
$$

$$
D^l_{r,\mathrm{fuz}}(\omega) = D^l_{r,\mathrm{mean}}(\omega) + \sum_{j=1}^{4} X^l_{r,j} D^l_{r,j,\mathrm{rand}}(\omega). \tag{22}
$$

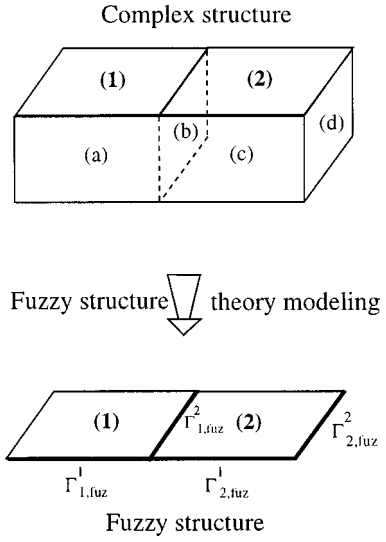

FIG. 5. Model of the reference complex structure by fuzzy structure theory.

In Eqs. (21) and (22), $\{X^l_{r,1}, X^l_{r,2}, X^l_{r,3}, X^l_{r,4}\}$ are mutually independent second-order normalized random variables (centered and with a variance of 1) with a uniform probability distribution over $[-\sqrt{3},\sqrt{3}]$ and

$$S^l_{r,\mathrm{mean}}(\omega) = \omega \underline{\mu}^l_r \underline{n}^l_r \rho^R(\omega;\boldsymbol{\lambda}^l_r), \tag{23}$$

$$S^l_{r,1,\mathrm{rand}}(\omega) = \omega \underline{\mu}^l_r \underline{n}^l_r \frac{\lambda^l_{r,1}}{\sqrt{3}} \rho^R(\omega;\boldsymbol{\lambda}^l_r), \tag{24}$$

$$S^l_{r,2,\mathrm{rand}}(\omega) = \omega \underline{\mu}^l_r \underline{n}^l_r \frac{\sqrt{3}}{\lambda^l_{r,2}} \underline{\alpha}^l_r \underline{J}_5(\omega;\boldsymbol{\lambda}^l_r), \tag{25}$$

$$S^l_{r,3,\mathrm{rand}}(\omega) = \omega \underline{\mu}^l_r \underline{n}^l_r \frac{\sqrt{3}}{\lambda^l_{r,3}} \underline{\alpha}^l_r \underline{J}_4(\omega;\boldsymbol{\lambda}^l_r), \tag{26}$$

$$S^l_{r,4,\mathrm{rand}}(\omega) = \omega \underline{\mu}^l_r \underline{n}^l_r \frac{\lambda^l_{r,4}}{\sqrt{3}} \underline{\alpha}^l_r (\kappa_0(\omega) + \underline{J}_3(\omega;\boldsymbol{\lambda}^l_r)), \tag{27}$$

in which $\boldsymbol{\lambda}^l_r = (\lambda^l_{r,1}, \lambda^l_{r,2}, \lambda^l_{r,3}, \lambda^l_{r,4})$ and

$$D^l_{r,\mathrm{mean}}(\omega) = \frac{\pi}{2} \omega^2 \underline{\mu}^l_r \underline{n}^l_r \rho^I(\omega;\boldsymbol{\lambda}^l_r), \tag{28}$$

$$D^l_{r,1,\mathrm{rand}}(\omega) = \frac{\pi}{2} \omega^2 \underline{\mu}^l_r \underline{n}^l_r \frac{\lambda^l_{r,1}}{\sqrt{3}} \rho^I(\omega;\boldsymbol{\lambda}^l_r), \tag{29}$$

$$D^l_{r,2,\mathrm{rand}}(\omega) = \frac{\pi}{2} \omega^2 \underline{\mu}^l_r \underline{n}^l_r \frac{\sqrt{3}}{\lambda^l_{r,2}} \times \left[\kappa_1(\omega) \frac{{\lambda^l_{r,2}}^2}{3} (1 - \underline{\alpha}^l_r) + \underline{\alpha}^l_r \underline{J}_2(\omega;\boldsymbol{\lambda}^l_r) \right], \tag{30}$$

$$D^l_{r,3,\mathrm{rand}}(\omega) = \frac{\pi}{2} \omega^2 \underline{\mu}^l_r \underline{n}^l_r \frac{\sqrt{3}}{\lambda^l_{r,3}} \underline{\alpha}^l_r \underline{J}_1(\omega;\boldsymbol{\lambda}^l_r), \tag{31}$$

$$D^l_{r,4,\mathrm{rand}}(\omega) = \frac{\pi}{2} \omega^2 \underline{\mu}^l_r \underline{n}^l_r \frac{\lambda^l_{r,4}}{\sqrt{3}} \underline{\alpha}^l_r (\underline{J}_0(\omega;\boldsymbol{\lambda}^l_r) - \kappa_1(\omega)). \tag{32}$$

In Eqs. (23)–(32), functions ρ^R, ρ^I, κ_0, κ_1, $\underline{J}_0$, $\underline{J}_1$, $\underline{J}_2$, $\underline{J}_3$, $\underline{J}_4$, and $\underline{J}_5$ are explicitly defined in Appendix (Ref. 23, pp. 368 to 370). The functions defined by Eqs. (23) to (32) depend on mean coefficients (or mean parameters) which are the mean coefficients of the participating inertial moment $\underline{\mu}^l_r(\omega)$, the mean rate of internal damping $\underline{\xi}^l_r(\omega)$, the mean modal density $\underline{n}^l_r(\omega)$ and the mean equivalent coupling factor $\underline{\alpha}^l_r(\omega)$ and their associated deviation coefficients $\lambda^l_{r,1}(\omega)$, $\lambda^l_{r,2}(\omega)$, $\lambda^l_{r,3}(\omega)$, and $\lambda^l_{r,4}(\omega)$, respectively. Mean coefficient $\underline{\mu}^l_r(\omega)$ is described by the dimensionless mean coefficient $\underline{\nu}^l_r(\omega)$ which is such that

$$\underline{\mu}^l_r(\omega) = \underline{\nu}^l_r(\omega) \frac{\mathcal{I}^l_r}{|\Gamma^l_{r,\mathrm{fuz}}|}, \tag{33}$$

in which $\mathcal{I}^l_r$ is an arbitrary reference inertial moment and $|\Gamma^l_{r,\mathrm{fuz}}|$ is the measure of $\Gamma^l_{r,\mathrm{fuz}}$ (equal to L_{r1} or L_{r2}). It is assumed that a direct estimation of mean coefficients $\underline{\xi}^l_r(\omega)$ and $\underline{n}^l_r(\omega)$ can be obtained. Since the junction between plate (r) of the master structure and fuzzy substructure l is continuous, the fuzzy structure theory yields $\underline{\alpha}^l_r \ll 1$. In order to construct the generalized impedance matrix of plate (r) of the master structure coupled with its fuzzy substructures, we use the Ritz–Galerkin method introduced in Sec. I A. The boundary value problem defined by Eq. (18) is then solved by introducing normal modes defined by Eq. (2) and their corresponding eigenfrequencies defined by Eq. (3). The finite dimension approximation of field U_r is again denoted as U_r and is written as

$$U_r(\omega,x,y) = \sum_{\boldsymbol{\beta} \in \mathcal{B}^r} Q_{r\boldsymbol{\beta}}(\omega) \varphi_{r\boldsymbol{\beta}}(x,y). \tag{34}$$

As in Sec. I A, we introduce the vector $\mathbf{Q}_r(\omega)$ such that

$$\mathbf{Q}_r(\omega) = \{Q_{r\boldsymbol{\beta}}(\omega)\}_{\boldsymbol{\beta} \in \mathcal{B}_r}, \tag{35}$$

and for all real ω, vector $\mathbf{Q}_r(\omega)$ is the solution of the complex matrix equation $i\omega([Z_r(\omega)] + [Z_{r,\mathrm{fuz}}(\omega)])\mathbf{Q}_r(\omega) = \mathbf{f}_r(\omega)$ in which $[Z_r(\omega)]$ is given by Eq. (5) and $[Z_{r,\mathrm{fuz}}(\omega)]$ is the generalized impedance complex dense matrix such that

$$[Z_{r,\mathrm{fuz}}(\omega)]_{\boldsymbol{\beta}\boldsymbol{\beta}'} = [Z_{r,\mathrm{mean}}(\omega)]_{\boldsymbol{\beta}\boldsymbol{\beta}'} + [Z_{r,\mathrm{rand}}(\omega)]_{\boldsymbol{\beta}\boldsymbol{\beta}'}, \tag{36}$$

in which

$$i\omega[Z_{r,\mathrm{mean}}(\omega)]_{\boldsymbol{\beta}\boldsymbol{\beta}'} = \sum_{l=1}^{2} \{-\omega^2 S^l_{r,\mathrm{mean}}(\omega) + i\omega D^l_{r,\mathrm{mean}}(\omega)\} \times \int_{\Gamma^l_{r,\mathrm{fuz}}} \frac{\partial \varphi_{r\boldsymbol{\beta}'}}{\partial \mathbf{n}_r}(s) \frac{\partial \varphi_{r\boldsymbol{\beta}}}{\partial \mathbf{n}_r}(s)\, ds \tag{37}$$

and

$$i\omega[Z_{r,\mathrm{rand}}(\omega)]_{\boldsymbol{\beta}\boldsymbol{\beta}'} = \sum_{l=1}^{2} \sum_{j=1}^{4} X^l_{r,j} \{-\omega^2 S^l_{r,j,\mathrm{rand}}(\omega) + i\omega D^l_{r,j,\mathrm{rand}}(\omega)\} \times \int_{\Gamma^l_{r,\mathrm{fuz}}} \frac{\partial \varphi_{r\boldsymbol{\beta}'}}{\partial \mathbf{n}_r}(s) \frac{\partial \varphi_{r\boldsymbol{\beta}}}{\partial \mathbf{n}_r}(s)\, ds. \tag{38}$$

B. Method for constructing the random response of the fuzzy structure

The coupling between the two plates of the master structure is written using Lagrange multipliers as in Sec. I C. The generalized impedance matrix of the fuzzy structure is then written as

$$\begin{bmatrix} i\omega([Z_{\mathrm{mast}}(\omega)] + [Z_{\mathrm{mean}}(\omega)] + [Z_{\mathrm{rand}}(\omega)]) & [B_{\mathrm{mast}}]^T \\ [B_{\mathrm{mast}}] & 0 \end{bmatrix} \times \begin{bmatrix} \mathbf{Q}_{\mathrm{mast}}(\omega) \\ \mathbf{P}_{\mathrm{mast}}(\omega) \end{bmatrix} = \begin{bmatrix} \mathbf{f}_{\mathrm{mast}}(\omega) \\ 0 \end{bmatrix}, \tag{39}$$

in which $[Z_{\mathrm{mast}}(\omega)]$ is defined by Eq. (14), vector $\mathbf{Q}_{\mathrm{mast}}(\omega)$ is such that

$$\mathbf{Q}_{\mathrm{mast}}(\omega) = (\mathbf{Q}_1(\omega), \mathbf{Q}_2(\omega)), \tag{40}$$

in which $\mathbf{Q}_r(\omega)$ is defined by Eq. (35), $\mathbf{P}_{\mathrm{mast}}(\omega)$ is the vector of the generalized coordinates of the Lagrange multipliers related to the coupling between the two plates of the master structure and where

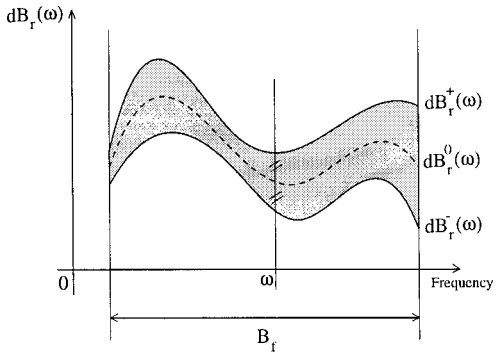

FIG. 6. Confidence region defined by the upper and lower envelopes of the frequency-response-function modulus corresponding to a given probability level.

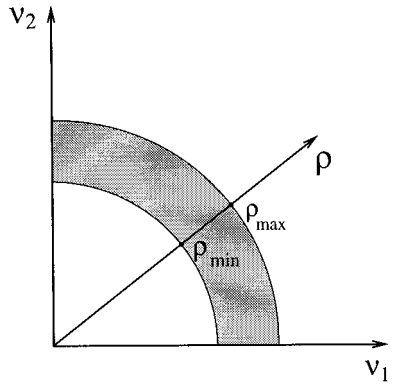

FIG. 7. Geometrical shape of the domain in which the solution of the optimization problem belongs.

$$[Z_{\text{mean}}(\omega)]=\begin{bmatrix}[Z_{1,\text{mean}}(\omega)] & 0\\ 0 & [Z_{2,\text{mean}}(\omega)]\end{bmatrix}, \tag{41}$$

$$[Z_{\text{rand}}(\omega)]=\begin{bmatrix}[Z_{1,\text{rand}}(\omega)] & 0\\ 0 & [Z_{2,\text{rand}}(\omega)]\end{bmatrix}, \tag{42}$$

in which $[Z_{r,\text{mean}}(\omega)]$ and $[Z_{r,\text{rand}}(\omega)]$ are defined by Eqs. (37) and (38), respectively. Equation (39) can be rewritten as

$$\begin{bmatrix} i\omega[Z_{\text{det}}(\omega)]+i\omega[Z_{\text{rand}}(\omega)] & [B_{\text{mast}}]^T\\ [B_{\text{mast}}] & 0\end{bmatrix}\begin{bmatrix}\mathbf{Q}_{\text{mast}}(\omega)\\ \mathbf{P}_{\text{mast}}(\omega)\end{bmatrix} =\begin{bmatrix}\mathbf{f}_{\text{mast}}(\omega)\\ 0\end{bmatrix}, \tag{43}$$

in which $[Z_{\text{det}}(\omega)]=[Z_{\text{mast}}(\omega)]+[Z_{\text{mean}}(\omega)]$ is a deterministic impedance matrix. The method used to solve Eq. (43) is based on the use of the Neumann series expansion. Consequently, we rewrite Eq. (43) as

$$\begin{bmatrix} i\omega[Z_{\text{det}}(\omega)] & [B_{\text{mast}}]^T\\ [B_{\text{mast}}] & 0\end{bmatrix}\begin{bmatrix}\mathbf{Q}_{\text{mast}}(\omega)\\ \mathbf{P}_{\text{mast}}(\omega)\end{bmatrix} =\begin{bmatrix}\mathbf{f}_{\text{mast}}(\omega)-i\omega[Z_{\text{rand}}(\omega)]\mathbf{Q}_{\text{mast}}(\omega)\\ 0\end{bmatrix}, \tag{44}$$

and the inverse matrix of the matrix appearing on the left-hand side of Eq. (44) is denoted as $[T_{\text{det}}(\omega)]$ (if this matrix is not invertible due to redundant equations induced by multiple connectivities in the master structure, then the method presented in Sec. I C should be used to construct $[T_{\text{det}}(\omega)]$; for the present reference complex structure, since the master structure has only two plates, the matrix is invertible). We obtain the solution $\mathbf{Q}_{\text{mast}}(\omega)$ such that

$$\mathbf{Q}_{\text{mast}}(\omega)=[T_{\text{det}}(\omega)](\mathbf{f}_{\text{mast}}(\omega) -i\omega[Z_{\text{rand}}(\omega)]\mathbf{Q}_{\text{mast}}(\omega)). \tag{45}$$

Equation (45) is rewritten as $([I_d]+i\omega[T_{\text{det}}(\omega)]\times[Z_{\text{rand}}(\omega)])\mathbf{Q}_{\text{mast}}(\omega)=[T_{\text{det}}(\omega)]\mathbf{f}_{\text{mast}}(\omega)$ in which $[I_d]$ is the identity matrix. An approximation of the inverse of matrix $([I_d]+i\omega[T_{\text{det}}(\omega)][Z_{\text{rand}}(\omega)])$ is calculated using Neumann's series expansion limited to order 2 and yields $([I_d]+i\omega[T_{\text{det}}(\omega)][Z_{\text{rand}}(\omega)])^{-1}\simeq[I_d]+\Sigma_{k=1}^{2}(-i\omega[T_{\text{det}}(\omega)]\times[Z_{\text{rand}}(\omega)])^k$. Solution $\mathbf{Q}_{\text{mast}}(\omega)$ can be written as

$$\mathbf{Q}_{\text{mast}}(\omega)=\mathbf{Q}_{\text{det}}(\omega)+\mathbf{Q}_{\text{rand}}(\omega), \tag{46}$$

in which

$$\mathbf{Q}_{\text{det}}(\omega)=[T_{\text{det}}(\omega)]\mathbf{f}_{\text{mast}}(\omega), \tag{47}$$

$$\mathbf{Q}_{\text{rand}}(\omega)=\mathbf{Q}^{(1)}_{\text{rand}}(\omega)+\mathbf{Q}^{(2)}_{\text{rand}}(\omega), \tag{48}$$

with

$$\mathbf{Q}^{(1)}_{\text{rand}}(\omega)=-i\omega[T_{\text{det}}(\omega)][Z_{\text{rand}}(\omega)]\mathbf{Q}_{\text{det}}(\omega), \tag{49}$$

$$\mathbf{Q}^{(2)}_{\text{rand}}(\omega)=-i\omega[T_{\text{det}}(\omega)][Z_{\text{rand}}(\omega)]\mathbf{Q}^{(1)}_{\text{rand}}(\omega). \tag{50}$$

From Eqs. (34), (35), (40), (46)–(50), we deduce that in a point (x,y) of plate (r) of the master structure, the random response can be written as

$$U_r(\omega,x,y)=U_{r,\text{det}}(\omega,x,y)+U_{r,\text{rand}}(\omega,x,y), \tag{51}$$

$$U_{r,\text{rand}}(\omega,x,y)=\sum_{l=1}^{16}U^{(1)}_{r,l,\text{rand}}(\omega,x,y)X_l +\sum_{l=1}^{16}\sum_{l'=1}^{16}U^{(2)}_{r,ll',\text{rand}}(\omega,x,y)X_lX_{l'}, \tag{52}$$

in which X_l is the lth coordinate of vector $(X^1_{1,1},\ldots,X^1_{1,4},\ldots,X^2_{2,4})$. The mean value and the variance of $U_r(\omega,x,y)$ are denoted as $E\{U_r(\omega,x,y)\}$ and $V_{U_r}(\omega,x,y)$, respectively, and are defined by

$$E\{U_r(\omega,x,y)\}=U_{r,\text{det}}(\omega,x,y)+E\{U_{r,\text{rand}}(\omega,x,y)\}, \tag{53}$$

and

$$V_{U_r}(\omega,x,y)=E\{|U_r(\omega,x,y)-E\{U_r(\omega,x,y)\}|^2\}. \tag{54}$$

In order to get more information about the random response level $dB_r(\omega,x,y)=20\log_{10}(|U_r(\omega,x,y)|)$ of plate (r) expressed in dB, we construct the envelope of this random response in dB introducing the mean response level in dB:

$$dB^0_r(\omega,x,y)=20\log_{10}(|E\{U_r(\omega,x,y)\}|). \tag{55}$$

The upper envelope $dB^+_r(\omega,x,y)$ is then defined by

$$\mathcal{P}(dB^-_r(\omega,x,y)<dB_r(\omega,x,y)\leqslant dB^+_r(\omega,x,y))=P_c, \tag{56}$$

in which the lower envelope is such that

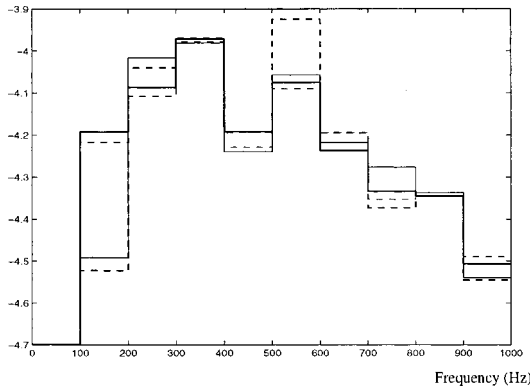

FIG. 8. Dimensionless mean coefficients $\underline{\boldsymbol{\nu}}$ in $\log_{10}$: mean coefficient $\underline{\nu}_1^1$ (thin solid line); mean coefficient $\underline{\nu}_1^2$ (thin dashed line); mean coefficient $\underline{\nu}_2^1$ (thick solid line); mean coefficient $\underline{\nu}_2^2$ (thick dashed line).

$$dB_r^-(\omega,x,y)=2\,dB_r^0(\omega,x,y)-dB_r^+(\omega,x,y). \tag{57}$$

In Fig. 6, the gray region represents the confidence region defined by the upper and lower envelopes of the frequency-response-function modulus corresponding to a given probability level P_c. We construct the upper envelope using Chebychev's inequality which can be written as

$$\mathcal{P}(|U_r(\omega,x,y)-E\{U_r(\omega,x,y)\}|\geqslant a_r(\omega,x,y)) \leqslant \frac{V_{U_r}(\omega,x,y)}{a_r(\omega,x,y)^2}, \tag{58}$$

in which $V_{U_r}(\omega,x,y)$ is given by Eq. (54). Inequality (58) yields

$$\mathcal{P}(dB_r^-(\omega,x,y)<dB_r(\omega,x,y)<dB_r^+(\omega,x,y))\geqslant P_c, \tag{59}$$

in which $dB_r^-(\omega,x,y)$ is defined by Eq. (57) and

$$dB_r^+(\omega,x,y)=20\log_{10}(|E\{U_r(\omega,x,y)\}|+a_r(\omega,x,y)), \tag{60}$$

in which $a_r(\omega,x,y)$ is such that

$$P_c=1-\frac{V_{U_r}(\omega,x,y)}{a_r(\omega,x,y)^2}. \tag{61}$$

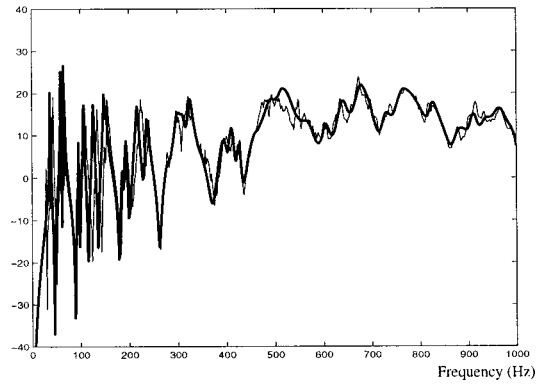

FIG. 9. Modulus (in dB) of the frequency response function for the acceleration at point $\mathbf{x}_0$ of the master structure: response of the reference complex structure (thin solid line); mean response of the fuzzy structure (thick solid line).

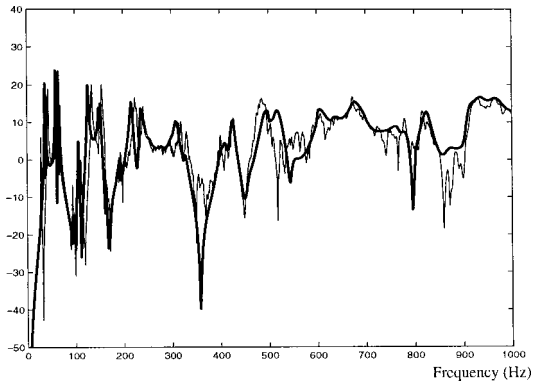

FIG. 10. Modulus (in dB) of the frequency response function for the acceleration at point $\mathbf{x}_1$ of the master structure: response of the reference complex structure (thin solid line); mean response of the fuzzy structure (thick solid line).

The confidence region calculated using the envelope defined by Eq. (59) is overestimated by comparison with a calculation made using Eq. (56), but the calculation is faster due to the use of an explicit numerical calculation of $E\{U_r(\omega,x,y)\}$ and $V_{U_r}(\omega,x,y)$.

III. ESTIMATION OF FUZZY STRUCTURE MEAN PARAMETERS

The fuzzy impedance law mean parameters $\underline{\alpha}_r^l$ and $\underline{\nu}_r^l$ of the fuzzy substructures introduced in Sec. II A have to be estimated. Concerning mean parameter $\underline{\alpha}_r^l$, we know that $\underline{\alpha}_r^l \ll 1$ due to the continuous junctions. A sensitivity analysis with respect to this mean parameter was performed[27] and showed that the frequency-independent values

$$\underline{\alpha}_1^1=\underline{\alpha}_1^2=\underline{\alpha}_2^1=\underline{\alpha}_2^2=0.005, \tag{62}$$

were a good approximation. Concerning mean parameter $\underline{\nu}_r^l$, we use the statistical energy approach introduced in Ref. 24 but using the following cost function[27]

$$J(\underline{\boldsymbol{\nu}})=\sum_{r=1}^{2}(\langle\Pi_{r,\mathrm{diss}}(t;\underline{\boldsymbol{\nu}};0)\rangle-\langle\Pi_{r,\mathrm{diss}}^{\mathrm{MSE}}(t)\rangle)^2, \tag{63}$$

in which $\underline{\boldsymbol{\nu}}=(\underline{\nu}_1^1,\underline{\nu}_1^2,\underline{\nu}_2^1,\underline{\nu}_2^2)$; $\langle\Pi_{r,\mathrm{diss}}(t;\underline{\boldsymbol{\nu}};0)\rangle$ is the mean power dissipation in plate (r) of the master structure of the

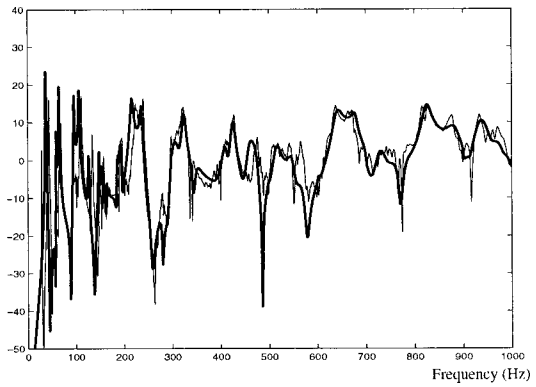

FIG. 11. Modulus (in dB) of the frequency response function for the acceleration at point $\mathbf{x}_2$ of the master structure: response of the reference complex structure (thin solid line); mean response of the fuzzy structure (thick solid line).

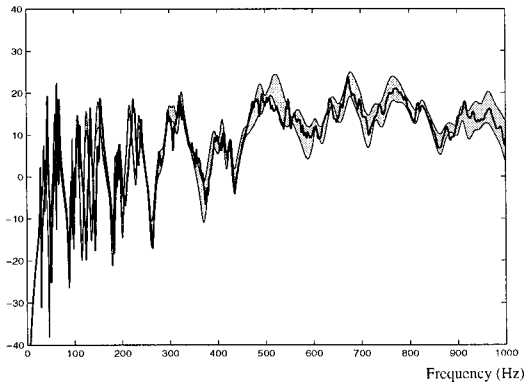

FIG. 12. Modulus (in dB) of the frequency response function for the acceleration at point $\mathbf{x}_0$ of the master structure: response of the reference complex structure (thick solid line); confidence region defined by the upper and lower envelopes predicted by the fuzzy structure theory and corresponding to a probability level equal to 0.95.

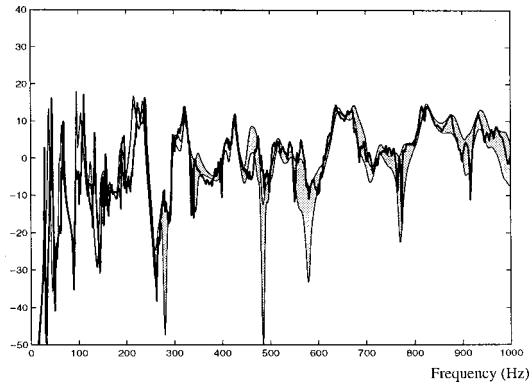

FIG. 14. Modulus (in dB) of the frequency response function for the acceleration at point $\mathbf{x}_2$ of the master structure: response of the reference complex structure (thick solid line); confidence region defined by the upper and lower envelopes predicted by the fuzzy structure theory and corresponding to a probability level equal to 0.95.

fuzzy structure, calculated using the fuzzy structure model; $\langle \Pi^{\mathrm{MSE}}_{r,\mathrm{diss}}(t) \rangle$ is the mean power dissipation in plate (r) of the master structure of the reference complex structure, estimated using statistical energy analysis applied to the reference complex structure. These mean power dissipations are calculated for a limited band time-stationary stochastic excitation force applied to the master structure.[23,24] Consequently, the estimation $\underline{\boldsymbol{\nu}}^*$ of $\underline{\boldsymbol{\nu}}$ is given by solving the following optimization problem:[24]

$$J(\underline{\boldsymbol{\nu}}^*) = \min_{\underline{\boldsymbol{\nu}} \geqslant 0} J(\underline{\boldsymbol{\nu}}), \tag{64}$$

in which $\underline{\boldsymbol{\nu}} \geqslant 0$ means $\underline{\nu}_1^1 \geqslant 0$, $\underline{\nu}_1^2 \geqslant 0$, $\underline{\nu}_2^1 \geqslant 0$, and $\underline{\nu}_2^2 \geqslant 0$. The optimization problem defined by Eq. (64) is not easy to solve because cost function J is not convex and each evaluation of $J(\underline{\boldsymbol{\nu}})$ needs an evaluation of $\langle \Pi_{r,\mathrm{diss}}(t;\underline{\boldsymbol{\nu}};0) \rangle$. Consequently, we developed[27] an algorithm with two main steps. In the first step, a neighborhood $\mathcal{D}$ containing solution $\underline{\boldsymbol{\nu}}^*$ is constructed using a random search algorithm. Domain $\mathcal{D}$ is described by the polar coordinates $(\rho, \boldsymbol{\theta})$ such that

$$\underline{\boldsymbol{\nu}} = \rho \frac{\boldsymbol{\theta}}{\|\boldsymbol{\theta}\|_2}, \tag{65}$$

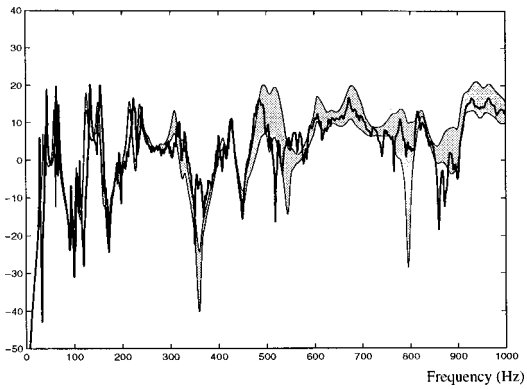

FIG. 13. Modulus (in dB) of the frequency response function for the acceleration at point $\mathbf{x}_1$ of the master structure: response of the reference complex structure (thick solid line); confidence region defined by the upper and lower envelopes predicted by the fuzzy structure theory and corresponding to a probability level equal to 0.95.

and is defined by

$$\mathcal{D} = \{ \rho \in]\rho_{\min}, \rho_{\max}[, \boldsymbol{\theta} \in [0,1]^4 \}. \tag{66}$$

The random search method is performed using a logarithmic scale for variable ρ. In Fig. 7, the gray region illustrates the $\mathcal{D}$ region dimension 2. In the second step, the optimization problem defined by Eq. (64) is rewritten as

$$J(\underline{\boldsymbol{\nu}}^*) = \min_{\underline{\boldsymbol{\nu}} \in \mathcal{D}} J(\underline{\boldsymbol{\nu}}), \tag{67}$$

and is solved using sequential quadratic programming[28] (SQP).

IV. VALIDATION

A. Description of the fuzzy structure modeling the reference complex structure

The frequency band of analysis is $B = [0,1000]$ Hz. Band B is written as the union of 10 frequency sub-bands with a bandwidth of 100 Hz. Since the plate damping rate and the oscillator damping rates of each complex substructure are equal to 0.003, the mean rate of internal damping of each fuzzy substructure is taken equal to 0.003 over band B. The mean modal densities of the fuzzy substructures are equal to the mean modal densities of the systems constituted of the plates coupled with their attached oscillators. They are taken as constant over each frequency sub-band and are such that $\underline{n}_1^1 = \underline{n}_2^1 = 0.393$ s/rad and $\underline{n}_1^2 = \underline{n}_2^2 = 0.388$ s/rad. The mean equivalent coupling factors of the fuzzy substructures are such that $\underline{\alpha}_1^1 = \underline{\alpha}_1^2 = \underline{\alpha}_2^1 = \underline{\alpha}_2^2 = 0.005$ and are constant over band B. The arbitrary reference inertial moments of the fuzzy substructures are such that $\mathcal{I}_1^1 = \mathcal{I}_2^1 = 8.85\,\mathrm{kg}\times\mathrm{m}^2$ and $\mathcal{I}_1^2 = \mathcal{I}_2^2 = 4.925\,\mathrm{kg}\times\mathrm{m}^2$. Each mean coefficient of the participating inertial moment of a fuzzy substructure is taken as constant over each frequency sub-band. These mean coefficients are estimated using the method presented in Sec. III. The values obtained for $\underline{\nu}_1^1 \geqslant 0$, $\underline{\nu}_1^2 \geqslant 0$, $\underline{\nu}_2^1 \geqslant 0$, and $\underline{\nu}_2^2 \geqslant 0$, expressed in $\log_{10}$, are presented in Fig. 8 as a function of the frequency.

B. Mean response

We consider the mean response of the fuzzy structure with zero deviation coefficients. Figures 9–11 show the modulus (in dB) of the frequency response function for the acceleration at points $\mathbf{x}_0$, $\mathbf{x}_1$, and $\mathbf{x}_2$ of the master structure; the thin solid lines represent the response of the reference complex structure and the thick solid lines represent the mean response of the fuzzy structure. It can be seen that the fuzzy structure's mean response with zero deviation coefficients gives a good representation of the reference complex structure response.

C. Envelopes

We consider the envelopes of the fuzzy structure response with nonzero deviation coefficients. The deviation coefficients associated with the participating inertial moments and the modal densities are nonzero and are taken as $\lambda^1_{1,1}=\lambda^2_{1,1}=\lambda^1_{2,1}=\lambda^2_{2,1}=\lambda^1_{1,3}=\lambda^2_{1,3}=\lambda^1_{2,3}=\lambda^2_{2,3}=0.3$ whereas those associated with internal damping rates and equivalent coupling factors are taken equal to zero $\lambda^1_{1,2}=\lambda^2_{1,2}=\lambda^1_{2,2}=\lambda^2_{2,2}=\lambda^1_{1,4}=\lambda^2_{1,4}=\lambda^1_{2,4}=\lambda^2_{2,4}=0$. Figures 12–14 show the modulus (in dB) of the frequency response function for the acceleration at points $\mathbf{x}_0$, $\mathbf{x}_1$, and $\mathbf{x}_2$ of the master structure; the thick solid lines represent the response of the reference complex structure and the gray region represents the confidence region defined by the upper and lower envelopes predicted by the fuzzy structure theory and corresponding to a probability level equal to 0.95. It can be seen that the responses of the reference complex structure belong to this confidence region. Consequently, the prediction is satisfactory and this example validates the fuzzy structure theory for continuous junctions (line couplings).

V. CONCLUSION

This paper constitutes a first validation of the fuzzy structure theory for continuous junctions (line couplings) between the master structure and the fuzzy substructures. In particular, the capability of this theory to model fuzzy substructures constituted of local modes and equipment should be noted. The mean response function calculated by the fuzzy structure theory with zero deviation coefficients gives a good representation of the reference complex structure response and calculation of the envelopes with nonzero deviation coefficients based on the use of a second-order Neumann series expansion and Chebychev's inequality is very efficient. In addition, we have introduced a new cost function allowing estimation of the fuzzy structure parameters and we have proved that the statistical energy approach proposed in this procedure is very efficient. This procedure for estimating the fuzzy structure parameters, validated by numerical simulation, opens the field to experimental identifications.

APPENDIX: DEFINITIONS FOR THE FUNCTIONS IN EQS. (23)–(32)

Function $\rho^R(\omega;\boldsymbol{\lambda}^l_r)$ is defined by

$$\rho^R(\omega;\boldsymbol{\lambda}^l_r)=(\underline{\alpha}^l_r-1)\,\kappa_0(\omega;\boldsymbol{\lambda}^l_r)+\underline{\alpha}^l_r\underline{J}_3(\omega;\boldsymbol{\lambda}^l_r),$$

$\kappa_0(\omega;\boldsymbol{\lambda}^l_r)$ is given by

$$\kappa_0(\omega;\boldsymbol{\lambda}^l_r)=[\omega\underline{n}^l_r]^{-1}+[12\omega^3\{\underline{n}^l_r\}^3(1-\{\lambda^l_{r,3}\}^2)]^{-1},$$

function $\rho^I(\omega;\boldsymbol{\lambda}^l_r)$ is defined by

$$\rho^I(\omega;\boldsymbol{\lambda}^l_r)=(1-\underline{\alpha}^l_r)\kappa_1(\omega;\boldsymbol{\lambda}^l_r)+\underline{\alpha}^l_r\underline{J}_0(\omega;\boldsymbol{\lambda}^l_r),$$

$\kappa_1(\omega;\boldsymbol{\lambda}^l_r)$ is given by

$$\kappa_1(\omega;\boldsymbol{\lambda}^l_r)=4\xi^l_r[\pi\omega\underline{n}^l_r]^{-1}.$$

For $\kappa\in\{0,1,2,3,4,5\}$, functions $\underline{J}_\kappa(\omega;\boldsymbol{\lambda}^l_r)$ are defined by

$$\underline{J}_\kappa(\omega;\boldsymbol{\lambda}^l_r)=\frac{1}{4}\int_{-1}^{1}dy_2\int_{-1}^{1}dy_3\,J_\kappa(\omega;\xi^l_r(1+\lambda^l_{r,2}y_2),\lambda^l_{r,3}y_3),$$

with

$$J_0(\omega;x,y)=(1+y)[\pi\sqrt{1-x^2}]^{-1}\times[\arctan Y_+(\omega;x,y)-\arctan Y_-(\omega;x,y)],$$

$$J_1(\omega;x,y)=yJ_0(\omega;x,y),$$

$$J_2(\omega;x,y)=(\xi^l_r)^{-1}(x-\xi^l_r)J_0(\omega;x,y),$$

$$J_3(\omega;x,y)=[\omega\underline{n}^l_r]^{-1}-(1+y)\times[4\sqrt{1-x^2}]^{-1}\ln[N(\omega;x,y)/D(\omega;x,y)],$$

$$J_4(\omega;x,y)=yJ_3(\omega;x,y),$$

$$J_5(\omega;x,y)=(\xi^l_r)^{-1}(x-\xi^l_r)J_3(\omega;x,y).$$

Function $Y_\pm(\omega;x,y)$ is defined by

$$Y_\pm(\omega;x,y)=(\theta_\pm(\omega;y)+x^2)[x\sqrt{1-x^2}]^{-1},$$

in which

$$\theta_\pm(\omega;y)=[(1\pm\tau(\omega;y))^2-1]/2,$$

with

$$\tau(\omega;y)=[2\omega\underline{n}^l_r(1+y)]^{-1}.$$

Functions $N(\omega;x,y)$ and $D(\omega;x,y)$ are defined by

$$N(\omega;x,y)=[U_+(\omega;y)+W_+(\omega;x,y)]\times[U_-(\omega;y)-W_-(\omega;x,y)],$$

$$D(\omega;x,y)=[U_+(\omega;y)-W_+(\omega;x,y)]\times[U_-(\omega;y)+W_-(\omega;x,y)],$$

in which

$$U_\pm(\omega;y)=2(\theta_\pm(\omega;y)+1),$$

$$W_\pm(\omega;x,y)=2\sqrt{1-x^2}[1\pm\tau(\omega;y)].$$

[1] C. Soize, ''Probabilistic structural modeling in linear dynamic analysis of complex mechanical systems. I. Theoretical elements,'' Rech. Aerosp. **5**, 23–48 (1986). (English edition).

[2] C. Soize, ''A model and numerical method in the medium frequency range for vibroacoustic predictions using the theory of structural fuzzy,'' J. Acoust. Soc. Am. **94**, 849–865 (1993).

[3] V. W. Sparrow, D. A. Russel, and J. L. Rochat, ''Implementation of discrete fuzzy structure models in mathematica,'' Int. J. Numer. Methods Eng. **37**, 3005–3014 (1994).

[4] D. Trentin and J. L. Guyader, ''Vibration of a master plate with attached masses using modal sampling method,'' J. Acoust. Soc. Am. **96**, 235–245 (1994).
[5] G. Maidanik, ''Power dissipation in a sprung mass attached to a master structure,'' J. Acoust. Soc. Am. **98**, 3527–3533 (1995).
[6] A. D. Pierce, V. W. Sparrow, and D. A. Russel, ''Fundamental structural-acoustic idealizations for structures with fuzzy internal,'' J. Vib. Acoust. **117**, 339–348 (1995).
[7] D. A. Russel, ''The Theory of Fuzzy Structures and its Application to Waves in Plates and Shells,'' Ph.D. dissertation at Pennsylvania State University, Graduate Program in Acoustics, State College, PA, 1995.
[8] D. A. Russel and V. W. Sparrow, ''Backscattering from a baffled finite plate strip with fuzzy attachments,'' J. Acoust. Soc. Am. **98**, 1527–1533 (1995).
[9] G. Maidanik and J. Dickey, ''Design criteria for the damping effectiveness of structural fuzzies,'' J. Acoust. Soc. Am. **100**, 2029–2033 (1996).
[10] M. Strasberg and D. Feit, ''Vibration damping of large structures induced by attached small resonant structures,'' J. Acoust. Soc. Am. **99**, 335–344 (1996).
[11] R. L. Weaver, ''The effect of an undamped finite degree of freedom ''fuzzy'' substructure: Numerical solutions and theoretical discussion,'' J. Acoust. Soc. Am. **100**, 3159–3164 (1996).
[12] Y. K. Lin, ''On the standard deviation of change-in-impedance due to fuzzy subsystems,'' J. Acoust. Soc. Am. **101**, 616–618 (1997).
[13] D. M. Photiadis, J. A. Bucaro, and B. H. Houston, ''The effect of internal oscillators on the acoustic response of a submerged shell,'' J. Acoust. Soc. Am. **101**, 895–899 (1997).
[14] A. D. Pierce, ''Resonant-frequency-distribution of internal mass inferred from mechanical impedance matrices, with application to fuzzy structure theory,'' ASME Paper 93-WA/NCA-17, 1993, also published in J. Vib. Sound **119**, 324–333 (1997).
[15] R. L. Weaver, ''Mean and mean-square responses of a prototypical master/fuzzy structure,'' J. Acoust. Soc. Am. **101**, 1441–1449 (1997).
[16] A. Cherukuri and P. E. Barbone, ''High modal density approximations for equipment in the time domain,'' J. Acoust. Soc. Am. **104**, 2048–2053 (1998).
[17] G. Maidanik and K. J. Becker, ''Various loss factors of a master harmonic oscillator coupled to a number of satellite harmonic oscillators,'' J. Acoust. Soc. Am. **103**, 3184–3195 (1998).
[18] N. J. Tarp-Johansen, O. Ditlevsen, and Y. K. Lin, ''Secondary systems modeled as fuzzy substructures,'' in *Structural Safety and Reliability*, edited by Shiraishi, Shinozuka, and Wen (Balkema, Rotterdam, 1998), pp. 803–810.
[19] G. Maidanik and J. Dickey, ''An impulse response function for a fuzzy structure,'' J. Acoust. Soc. Am. **97**, 1460–1476 (1995).
[20] J. Garrelick, ''The modeling of a continuous structure as a fuzzy,'' J. Acoust. Soc. Am. **101**, 613–615 (1997).
[21] J. J. MacCoy and B. Z. Steinberg, ''Addressing complexity in structural acoustics-fuzzy structure and effective impedance theories,'' Comput. Struct. **65**, 403–421 (1997).
[22] R. S. Langley and P. Bremmer, ''A hybrid method for the vibration analysis of complex structural-acoustic systems,'' J. Acoust. Soc. Am. **105**, 1657–1672 (1999).
[23] R. Ohayon and C. Soize, *Structural Acoustics and Vibration* (Academic, San Diego, 1998).
[24] C. Soize, ''Estimation of the fuzzy substructure model parameters using the mean power flow equation of the fuzzy structure,'' Proceeding of the ASME Noise Control and Acoustics Divisions, Vol. 1, ASME/WAM, 28–30, NCA-Vol. 22, 23–30 (1996), also published in Journal of Vibration and Acoustic **120**, 279–286 (1998).
[25] A. Leissa, *Vibration of Plates and Vibration of Shells* (Acoust. Soc. Am. Publications on Acoustics, Woodbury, 1993). Originally published by NASA, 1973.
[26] R. Ohayon, R. Sampaio, and C. Soize, ''Dynamic substructuring of damped structures using singular value decomposition,'' J. Appl. Mech. **64**, 292–298 (1997).
[27] K. Bjaoui, *Estimation des paramètres d'une structure floue pour des jonctions continues* (Thèse du Conservatoire National des Arts et Métiers, Paris, 1999).
[28] R. Fletcher, *Practical Methods of Optimization, Vol. 2, Constrained Optimization* (Wiley, New York, 1980).

On acoustic and structural modal cross-couplings in plate-cavity systems

K. S. Sum and J. Pan
Department of Mechanical and Materials Engineering, The University of Western Australia, Nedlands, Western Australia 6907, Australia

(Received 18 August 1998; revised 8 December 1999; accepted 10 December 1999)

Modal cross-couplings are sometimes neglected in the prediction of sound field and structural responses of vibroacoustic systems where an enclosed sound field is coupled to a vibrating boundary structure. In such systems, there are two types of modal cross-couplings and they are commonly referred to as acoustic modal cross-coupling (ACC) and structural modal cross-coupling (SCC). The prediction errors generated from neglecting either of these cross-couplings are dependent not only on the modal properties of the vibroacoustic system (e.g., modal densities, dampings, etc.), but also on whether the sound field or the structure is directly driven. However, the physical mechanisms and characteristics of both cross-couplings are not well understood and, consequently, the conditions when ACC or SCC has a significant contribution to the system responses become unknown. This paper presents a mathematical description which allows the two types of modal cross-couplings to be studied independently. This description is then used to obtain the physical mechanisms and features of both cross-couplings. The effects of each type of cross-couplings on the system responses are then investigated and the general conditions under which these modal cross-couplings may be ignored are underlined. [S0001-4966(00)04603-8]

PACS numbers: 43.40.Dx, 43.40.Rj [CBB]

INTRODUCTION

Modal analysis has been widely used to study the response of vibroacoustic systems and sound radiation from structures. In the analysis, cross-coupling between acoustic modes (ACC) (i.e., inter-modal coupling between acoustic modes) and/or cross-coupling between structural modes (SCC) (i.e., inter-modal coupling between structural modes) usually occur. In systems where a structure is radiating sound to a free space, only SCC occurs, and it is induced by the mutual interactions between acoustic fields generated by different structural modes. The structural modes are cross-coupled to each other through their impedance terms, and, thus, the response of each structural mode is dependent on the responses of all the other structural modes. For such systems, the role and significance of SCC in the prediction of structural sound radiation have been widely studied,[1–6] and SCC is sometimes neglected in the prediction of sound transmission through structures.[7] In vibroacoustic systems which consist of an enclosure with locally reactive boundaries, only ACC occurs, and it is induced by the finite impedances of the boundaries. Acoustic modes are cross-coupled to each other through impedance terms of the boundaries which describe acoustic modal dampings. Thus, the response of each acoustic mode is dependent on the responses of all the other acoustic modes. For such vibroacoustic systems, effects of ACC on the enclosed sound field response have also been well-studied and general criteria related to the negligence of ACC in the prediction of the sound field response are well-established.[8–12]

In vibroacoustic systems which consist of an enclosure with modally reactive boundaries, for example, a flexible vibrating structure backed by an enclosure, both ACC and SCC occur. Acoustic modes of the enclosed sound field are cross-coupled to each other through their couplings with structural modes, and the structural modes are cross-coupled to each other through their couplings with the acoustic modes. Thus, the predictions of both the structural and sound field responses become complicated as couplings between various structural and acoustic modes have to be considered. To circumvent the lengthy numerical solutions and complicated phenomena in the coupled system responses, SCC is sometimes neglected in the modal coupling analysis.[13–17] This cross-coupling is also neglected in the development of high frequency methods such as the asymptotic modal analysis.[18] Significance of SCC to the structural response of the coupled system has been studied and Guyader *et al.*[19] show that the negligence of SCC in the prediction of structural acoustic radiation is well-adapted for the case of light fluid coupling. Pretlove[20] investigates the first few structural modes and he shows that the effect of SCC on the modal response of the structural modes is insignificance except when the structure is very thin and the backing enclosure is very shallow. However, the roles of both ACC and SCC are hidden in the complicated details of the modal coupling analysis and therefore, characteristics of the cross-couplings are not well understood. Consequently, the negligence of either ACC or SCC in the prediction of the structural and sound field responses of such coupled system has not been clearly justified. Even the negligence of modal cross-couplings in the early development of statistical energy analysis (SEA) has to rely on various assumptions including the weak coupling assumption (for example, see Refs. 21 and 22).

The aim of this paper is to obtain a physical insight into the mechanisms involved in both ACC and SCC in vibroacoustic systems which consist of an enclosure with modally

reactive boundaries. Air-structural coupling is considered, and a mathematical description which allows the two types of modal cross-couplings to be studied independently is presented. Physical features of ACC and SCC are then obtained and effects of the cross-couplings on the sound field and structural responses of the system at steady-state are investigated. Although a significant and comparable reduction of computational effort in the prediction of the system responses can be achieved when either ACC or SCC is neglected,[23] it is shown in this paper that the negligence of ACC incurs different prediction errors to that of the negligence of SCC. The characteristics of the errors under different system modal properties are studied and general criteria related to the negligence of ACC and SCC in the prediction of the system responses are then established. Some physical aspects related to the cross-couplings, such as the phenomenon of redistributions of resonance frequencies and modal dampings of structural and acoustic modes, are also discussed.

I. MODAL COUPLING ANALYSIS

A. Mathematical descriptions of cross-couplings in the modal response of acoustic and structural modes

The vibroacoustic system considered here consists of an enclosed sound field which couples with a flexible vibrating plate-type structure. The system response is described by the sound pressure, p, and the structural velocity, v. In a modal coupling analysis, they are expressed in terms of the normal modes of the sound field and the structure as

$$p=\sum_{i=1}^{N} P_i\Phi_{ai}, \tag{1}$$

$$v=\sum_{j=1}^{M} V_j\Phi_{sj}, \tag{2}$$

where P_i and V_j are, respectively, the complex pressure and velocity modal amplitudes of the ith acoustic mode and jth structural mode. Φ_{ai} and Φ_{sj} are acoustic and structural mode shape functions. By introducing the modal coupling analysis into the system equations of motion, a set of system modal equations can be obtained where the steady-state P_i and V_j can be solved.[24] They can be decomposed into two parts such that $P_i=P_i^D+P_i^C$ and $V_j=V_j^D+V_j^C$. The contributions from the excitation source and/or acoustic-structural modal couplings to each modal amplitude are described by P_i^D and V_j^D. The contributions from acoustic–acoustic (ACC) or structural–structural (SCC) modal couplings are described by P_i^C and V_j^C. These contributions depend on whether the sound field or the structure is directly excited.

1. Direct sound field excitation

If the sound field is directly excited by a distributed steady-state sound source and the structure is driven through coupling with the sound field, the vibroacoustic system modal equations obtained from the modal coupling analysis are[23]

$$P_i=H_{ai}\int_{V_0} q\Phi_{ai}\,dV-H_{ai}A_s\sum_{j=1}^{M} V_jB_{j,i}, \tag{3}$$

$$V_j=H_{sj}\sum_{k=1}^{N} P_kB_{j,k}, \tag{4}$$

where

$$H_{ai}=j\omega(\rho_0c_0)^2/M_{ai}(\omega_{ai}^2-\omega^2+j\eta_{ai}\omega_{ai}^2), \tag{5}$$

$$H_{sj}=j\omega A_s/M_{sj}(\omega_{sj}^2-\omega^2+j\eta_{sj}\omega_{sj}^2), \tag{6}$$

$$M_{ai}=\rho_0\int_{V_0}\Phi_{ai}^2\,dV, \tag{7}$$

$$M_{sj}=\rho_sh\int_{A_s}\Phi_{sj}^2\,dA, \tag{8}$$

$$B_{j,i}=\frac{1}{A_s}\int_{A_s}\Phi_{sj}\Phi_{ai}\,dA. \tag{9}$$

η_{ai}, η_{sj}, ω_{ai}, ω_{sj} are acoustic and structural modal loss factors and resonance frequencies. $B_{j,i}$ is the modal coupling coefficient between the ith acoustic mode and jth structural mode, V_0 is the volume of the enclosure, q is the volume velocity of the sound source per unit volume of the enclosure, ρ_0 is air density, c_0 is speed of sound in air, and A_s, h, and ρ_s are, respectively, surface area, thickness, and density of the structure. By substituting Eq. (4) into (3) and then splitting ACC terms, it can be shown that the corresponding P_i^C and P_i^D are

$$P_i^C|_{\mathrm{ACC}}=-\frac{A_s\Sigma_{k\neq1}^{N}P_k\Sigma_{j=1}^{M}H_{sj}B_{j,i}B_{j,k}}{(1/H_{ai})+A_s\Sigma_{j=1}^{M}H_{sj}B_{j,i}^2}, \tag{10}$$

$$P_i^D|_{\mathrm{ACC}}=\int_{V_0} q\Phi_{ai}\,dV\Big/\left(\frac{1}{H_{ai}}+A_s\sum_{j=1}^{M}H_{sj}B_{j,i}^2\right). \tag{11}$$

$P_i^D|_{\mathrm{ACC}}$ accounts for direct excitation of the ith acoustic mode by the sound source [i.e., the numerator in Eq. (11)]. The participation of structural modes in $P_i^D|_{\mathrm{ACC}}$ [i.e., second term of the denominator in Eq. (11)] provides shift in resonance frequency and damping to the acoustic mode. These will be discussed in details in Sec. II. $P_i^C|_{\mathrm{ACC}}$ accounts for indirect excitation of the ith acoustic mode by other acoustic modes (ACC) [i.e., through P_k where $k\neq i$ in Eq. (10)]. The main role of the structural modes in $P_i^C|_{\mathrm{ACC}}$ is to act as a bridge to cross-couple the ith acoustic mode to other acoustic modes [see the numerator in Eq. (10)]. Therefore, the total ACC contribution to the mode described by $P_i^C|_{\mathrm{ACC}}$, relative to $P_i^D|_{\mathrm{ACC}}$ (i.e., ratio of $P_i^C|_{\mathrm{ACC}}$ to $P_i^D|_{\mathrm{ACC}}$), is significantly controlled by the structural modal properties described by H_{sj}, as well as the degree of spatial couplings between the acoustic and structural modes described by $B_{j,i}$ and $B_{j,k}$. Thus, $P_i^C|_{\mathrm{ACC}}$ at resonance of the ith acoustic mode is only significant when this mode is well coupled in terms of resonance frequency proximity (well coupled condition[25,26]) to the structural modes. However, the well coupled condition does not have to be satisfied for low order acoustic or structural modes which have strong spatial couplings, i.e., large $B_{j,i}$ and/or $B_{j,k}$.

V_j^D and V_j^C associated with ACC can be obtained by substituting P_k in Eq. (4) with $P_i^D|_{\mathrm{ACC}}$ and $P_i^C|_{\mathrm{ACC}}$:

$$V_j^D|_{\mathrm{ACC}} = H_{sj} \sum_{i=1}^{N} \frac{B_{j,i} \int_{V_0} q \Phi_{ai}\, dV}{1/H_{ai} + A_s \Sigma_{l=1}^{M} H_{sl} B_{l,i}^2}, \tag{12}$$

$$V_j^C|_{\mathrm{ACC}} = -H_{sj} \sum_{i=1}^{N} \frac{B_{j,i} A_s \Sigma_{k\neq i}^{N} P_k \Sigma_{l=1}^{M} H_{sl} B_{l,i} B_{l,k}}{1/H_{ai} + A_s \Sigma_{l=1}^{M} H_{sl} B_{l,i}^2}. \tag{13}$$

$V_j^D|_{\mathrm{ACC}}$ describes the excitation of the jth structural mode by all directly excited acoustic modes. The main role of the acoustic modes in $V_j^D|_{\mathrm{ACC}}$ is to couple the structural mode to the sound source [see Eq. (12)]. $V_j^C|_{\mathrm{ACC}}$ describes the excitation of the jth structural mode by all indirectly excited acoustic modes. The total ACC contribution to the response of this structural mode is accounted for, by the participation of acoustic modes in $V_j^C|_{\mathrm{ACC}}$ [i.e., through P_k where $k \neq i$ in Eq. (13)]. Since structural modes play a main role in the acoustic–acoustic modal couplings (ACC) as described before, the contribution of $V_j^C|_{\mathrm{ACC}}$ relative to $V_j^D|_{\mathrm{ACC}}$ (i.e., ratio of $V_j^C|_{\mathrm{ACC}}$ to $V_j^D|_{\mathrm{ACC}}$) is still greatly controlled by the structural modal properties described by H_{sl}, apart from $B_{j,i}$, $B_{l,i}$, and $B_{l,k}$ [see the numerator in Eq. (13)].

As $P_i^C|_{\mathrm{ACC}}$ and $V_j^C|_{\mathrm{ACC}}$ have been expressed in terms of the total ACC contribution, they can be, respectively, used to evaluate the effect of ACC on P_i and V_j. Mathematically, the modal amplitudes, P_i and V_j, can also be expressed in terms of structural–structural modal couplings (SCC). By substituting Eq. (3) into (4) and then splitting SCC terms, it can be shown that the corresponding V_j^C and V_j^D are

$$V_j^C|_{\mathrm{SCC}} = -\frac{A_s \Sigma_{k\neq j}^{M} V_k \Sigma_{i=1}^{N} H_{ai} B_{j,i} B_{k,i}}{(1/H_{sj}) + A_s \Sigma_{i=1}^{N} H_{ai} B_{j,i}^2}, \tag{14}$$

$$V_j^D|_{\mathrm{SCC}} = \sum_{i=1}^{N} B_{j,i} H_{ai} \int_{V_0} q \Phi_{ai}\, dV \Bigg/ \left(\frac{1}{H_{sj}} + A_s \sum_{i=1}^{N} H_{ai} B_{j,i}^2 \right). \tag{15}$$

$V_j^D|_{\mathrm{SCC}}$ accounts for direct excitation of the jth structural mode by acoustic modes. The main roles of the acoustic modes in $V_j^D|_{\mathrm{SCC}}$ are to couple the structural mode to the sound source and to provide shift in resonance frequency and damping to the mode. These are, respectively, accounted for, in the numerator and denominator in Eq. (15). Thus $V_j^D|_{\mathrm{SCC}}$ in Eq. (15) has a different physical meaning to $V_j^D|_{\mathrm{ACC}}$ in Eq. (12). $V_j^C|_{\mathrm{SCC}}$ accounts for indirect excitation of the jth structural mode by other structural modes (SCC) [i.e., through V_k where $k \neq j$ in Eq. (14)]. The main role of the acoustic modes in $V_j^C|_{\mathrm{SCC}}$ is to act as a bridge to cross-couple the jth structural mode to other structural modes [see the numerator in Eq. (14)]. Therefore, the total SCC contribution to the mode described by $V_j^C|_{\mathrm{SCC}}$, relative to $V_j^D|_{\mathrm{SCC}}$ (i.e., ratio of $V_j^C|_{\mathrm{SCC}}$ to $V_j^D|_{\mathrm{SCC}}$), is significantly controlled by the acoustic modal properties described by H_{ai}, as well as the degree of spatial couplings between the acoustic and structural modes described by $B_{j,i}$ and $B_{k,i}$. Thus, $V_j^C|_{\mathrm{SCC}}$ at resonance of the jth structural mode is only significant when this mode is well coupled to the acoustic modes. Again, the well coupled condition does not have to be satisfied for low order acoustic or structural modes which have strong spatial couplings, i.e., large $B_{j,i}$ and/or $B_{j,k}$.

P_i^D and P_i^C expressed in terms of SCC are obtained by substituting V_j in Eq. (3) with $V_j^D|_{\mathrm{SCC}}$ and $V_j^C|_{\mathrm{SCC}}$:

$$P_i^D|_{\mathrm{SCC}} = H_{ai} \int_{V_0} q \Phi_{ai}\, dV - H_{ai} \sum_{j=1}^{M} \frac{B_{j,i} A_s \Sigma_{k=1}^{N} B_{j,k} H_{ak} \int_{V_0} q \Phi_{ak}\, dV}{1/H_{sj} + A_s \Sigma_{k=1}^{N} H_{ak} B_{j,k}^2}, \tag{16}$$

$$P_i^C|_{\mathrm{SCC}} = H_{ai} \sum_{j=1}^{M} \frac{B_{j,i} A_s^2 \Sigma_{k\neq j}^{M} V_k \Sigma_{l=1}^{N} H_{al} B_{j,l} B_{k,l}}{1/H_{sj} + A_s \Sigma_{k=1}^{N} H_{ak} B_{j,k}^2}. \tag{17}$$

$P_i^D|_{\mathrm{SCC}}$ describes the excitation of the ith acoustic mode by the sound source and all directly excited structural modes. $P_i^C|_{\mathrm{SCC}}$ describes the excitation of the ith acoustic mode by all indirectly excited structural modes. The total SCC contribution to the response of this acoustic mode is accounted for, by the participation of structural modes in $P_i^C|_{\mathrm{SCC}}$ [i.e., through V_k where $k \neq j$ in Eq. (17)]. Since acoustic modes play a main role in the structural–structural modal couplings (SCC) as described before, the contribution of $P_i^C|_{\mathrm{SCC}}$ relative to $P_i^D|_{\mathrm{SCC}}$ (i.e., ratio of $P_i^C|_{\mathrm{SCC}}$ to $P_i^D|_{\mathrm{SCC}}$) is still significantly controlled by the acoustic modal properties described by H_{al}, apart from $B_{j,i}$, $B_{j,l}$, and $B_{k,l}$ [see the numerator in Eq. (17)]. $P_i^C|_{\mathrm{SCC}}$ and $V_j^C|_{\mathrm{SCC}}$ in the above can be, respectively, used to evaluate the effect of SCC on P_i and V_j as they have been expressed in terms of the total SCC contribution.

2. Direct structural excitation

If the structure is now directly driven by some mechanical forces and/or an external pressure field and the enclosed sound field is driven by the vibrating structure only, the modal equations for the vibroacoustic system become

$$P_i = -H_{ai} A_s \sum_{j=1}^{M} V_j B_{j,i}, \tag{18}$$

$$V_j = H_{sj} \sum_{k=1}^{N} P_k B_{j,k} - \frac{H_{sj}}{A_s} \int_{A_s} p_{\mathrm{ext}} \Phi_{sj}\, dA. \tag{19}$$

p_{ext} is the distributed sound pressure on the external surface of the boundary structure. By substituting Eq. (19) into (18) and then splitting ACC terms, it can be shown that

$$P_i^D|_{\mathrm{ACC}} = \sum_{j=1}^{M} B_{j,i} H_{sj} \int_{A_s} p_{\mathrm{ext}} \Phi_{sj} dA \Bigg/ \left(\frac{1}{H_{ai}} + A_s \sum_{j=1}^{M} H_{sj} B_{j,i}^2 \right), \tag{20}$$

and $P_i^C|_{\mathrm{ACC}}$ is given in Eq. (10). Substituting P_k in Eq. (19) with Eqs. (20) and (10) gives

$$V_j^D|_{\mathrm{ACC}} = -\frac{H_{sj}}{A_s} \int_{A_s} p_{\mathrm{ext}} \Phi_{sj}\, dA + H_{sj} \sum_{i=1}^{N} \frac{B_{j,i} \Sigma_{k=1}^{M} B_{k,i} H_{sk} \int_{A_s} p_{\mathrm{ext}} \Phi_{sk}\, dA}{1/H_{ai} + A_s \Sigma_{k=1}^{M} H_{sk} B_{k,i}^2}, \tag{21}$$

and $V_j^C|_{\mathrm{ACC}}$ is given in Eq. (13). However if Eq. (18) is now substituted into (19) and then the SCC terms are split, it can be shown that V_j^D and V_j^C associated with SCC are

$$V_j^D|_{\mathrm{SCC}} = -\frac{1}{A_s}\int_{A_s} p_{\mathrm{ext}}\Phi_{sj}\,dA \Big/ \left(\frac{1}{H_{sj}} + A_s\sum_{i=1}^{N} H_{ai}B_{j,i}^2\right), \tag{22}$$

and $V_j^C|_{\mathrm{SCC}}$ is given in Eq. (14). Substituting V_j in Eq. (18) with Eqs. (22) and (14) yields

$$P_i^D|_{\mathrm{SCC}} = H_{ai}\sum_{j=1}^{M} \frac{B_{j,i}\int_{A_s} p_{\mathrm{ext}}\Phi_{sj}\,dA}{1/H_{sj} + A_s\sum_{k=1}^{N} H_{ak}B_{j,k}^2}, \tag{23}$$

and $P_i^C|_{\mathrm{SCC}}$ is given in Eq. (17). The physical meanings of $P_i^D|_{\mathrm{ACC}}$, $V_j^D|_{\mathrm{ACC}}$, $V_j^D|_{\mathrm{SCC}}$, and $P_i^D|_{\mathrm{SCC}}$ in Eqs. (20) to (23) are analogous to that for the case of direct sound field excitation in the preceding section. In summary, for direct structural excitation, the effect of ACC and SCC on the modal response of acoustic and structural modes can also be examined using the same expressions given in Eqs. (10), (13), (14), and (17). However, the components corresponding to the direct coupling/excitation are different to that for direct sound field excitation because in this case, the excitation is directly on the structure.

B. Mathematical descriptions of cross-couplings in the sound field and structural responses

Regardless of whether the sound field or the structure is directly excited, as P_i and V_j have been previously expressed in terms of either the total ACC or SCC contribution, both the sound field and structural responses can now be decomposed into the direct coupling/excitation part as well as the cross-couplings (either ACC or SCC) part. These can be obtained by first substituting P_i^D and P_i^C into Eq. (1), and V_j^D and V_j^C into Eq. (2):

$$p = \sum_{i=1}^{N} P_i^D\Phi_{ai} + \sum_{i=1}^{N} P_i^C\Phi_{ai}, \tag{24}$$

$$v = \sum_{j=1}^{M} V_j^D\Phi_{sj} + \sum_{j=1}^{M} V_j^C\Phi_{sj}. \tag{25}$$

Then, the time-averaged mean-square sound pressure and velocity are obtained as

$$\overline{p^2} = \tfrac{1}{2}pp^* = \tfrac{1}{2}(I_D + I_C), \tag{26}$$

$$\overline{v^2} = \tfrac{1}{2}vv^* = \tfrac{1}{2}(J_D + J_C), \tag{27}$$

where

$$I_D = \left(\sum_{i=1}^{N} P_i^D\Phi_{ai}\right)\left(\sum_{i=1}^{N} P_i^D\Phi_{ai}\right)^*, \tag{28}$$

$$I_C = \left(\sum_{i=1}^{N} P_i^C\Phi_{ai}\right)\left(\sum_{i=1}^{N} P_i^C\Phi_{ai}\right)^* + \left(\sum_{i=1}^{N} P_i^C\Phi_{ai}\right) \times \left(\sum_{i=1}^{N} P_i^D\Phi_{ai}\right)^* + \left(\sum_{i=1}^{N} P_i^C\Phi_{ai}\right)^*\left(\sum_{i=1}^{N} P_i^D\Phi_{ai}\right), \tag{29}$$

$$J_D = \left(\sum_{j=1}^{M} V_j^D\Phi_{sj}\right)\left(\sum_{j=1}^{M} V_j^D\Phi_{sj}\right)^*, \tag{30}$$

$$J_C = \left(\sum_{j=1}^{M} V_j^C\Phi_{sj}\right)\left(\sum_{j=1}^{M} V_j^C\Phi_{sj}\right)^* + \left(\sum_{j=1}^{M} V_j^C\Phi_{sj}\right) \times \left(\sum_{j=1}^{M} V_j^D\Phi_{s_i}\right)^* + \left(\sum_{j=1}^{M} V_j^C\Phi_{sj}\right)^*\left(\sum_{j=1}^{M} V_j^D\Phi_{sj}\right). \tag{31}$$

The asterisk denotes a complex conjugate. I_D and J_D are the parts which describe the contributions of the direct coupling/excitation. I_C and J_C are the parts which describe the contributions of the cross-couplings. The last two terms, respectively, in I_C and J_C, describe the correlation between the direct coupling/excitation and the cross-couplings because the terms contain phase relations between the direct coupling/excitation and the cross-couplings. Therefore, in contrast to I_D and J_D, I_C and J_C are not positive definite. It can be seen that the cross-couplings contribution to either the sound field or structural response depends on the superposition of various acoustic or structural modes. If acoustic modes superimpose in such a way that the magnitude of I_C is equal or greater than half of the magnitude of I_D, then the cross-couplings have pronounced effect on the sound field response. Similarly, if structural modes superimpose in such a way that the magnitude of J_C is equal or greater than half of the magnitude of J_D, then the cross-couplings have pronounced effect on the structural response. It has been obvious from the preceding section that even though $P_i = P_i^D|_{\mathrm{ACC}} + P_i^C|_{\mathrm{ACC}} = P_i^D|_{\mathrm{SCC}} + P_i^C|_{\mathrm{SCC}}$ and $V_j = V_j^D|_{\mathrm{ACC}} + V_j^C|_{\mathrm{ACC}} = V_j^D|_{\mathrm{SCC}} + V_j^C|_{\mathrm{SCC}}$, the ACC contribution to both the sound field and structural responses, as well as the errors due to the negligence of ACC in the prediction of those responses, are different from that for the case of SCC. This is because $P_i^D|_{\mathrm{ACC}} \neq P_i^D|_{\mathrm{SCC}}$, $P_i^C|_{\mathrm{ACC}} \neq P_i^C|_{\mathrm{SCC}}$, $V_j^D|_{\mathrm{ACC}} \neq V_j^D|_{\mathrm{SCC}}$, and $V_j^C|_{\mathrm{ACC}} \neq V_j^C|_{\mathrm{SCC}}$. Hence, $I_D|_{\mathrm{ACC}} \neq I_D|_{\mathrm{SCC}}$, $I_C|_{\mathrm{ACC}} \neq I_C|_{\mathrm{SCC}}$, $J_D|_{\mathrm{ACC}} \neq J_D|_{\mathrm{SCC}}$, and $J_C|_{\mathrm{ACC}} \neq J_C|_{\mathrm{SCC}}$, even though $I_D|_{\mathrm{ACC}} + I_C|_{\mathrm{ACC}} = I_D|_{\mathrm{SCC}} + I_C|_{\mathrm{SCC}}$ and $J_D|_{\mathrm{ACC}} + J_C|_{\mathrm{ACC}} = J_D|_{\mathrm{SCC}} + J_C|_{\mathrm{SCC}}$.

II. APPARENT RESONANCE FREQUENCIES AND APPARENT MODAL LOSS FACTORS

From the modal coupling analysis, it can be seen from Eqs. (3)–(6), (18), and (19) that the coupled response of each acoustic mode (i.e., P_i) and each structural mode (i.e., V_j), is not only dependent on the uncoupled acoustic and structural resonance frequencies (ω_{ai} and ω_{sj}), and uncoupled modal loss factors (η_{ai} and η_{sj}), but also on the couplings between acoustic and structural modes. Therefore, these quantities are related to each other, and thus both P_i and V_j can actually be interpreted, respectively, as the response for the coupled/apparent resonance frequency and coupled/apparent loss factor of the ith acoustic mode and the jth structural mode. The coupled/apparent resonance frequency and coupled/apparent loss factor, are the redistributed versions of the uncoupled resonance frequency and uncoupled loss factor of the mode, and they are functions of acoustic-structural couplings. The subsequent section shows that the apparent resonance fre-

quency and apparent loss factor of each mode can be mathematically separated into two parts; one part corresponds to the uncoupled resonance frequency or uncoupled loss factor, and the other part corresponds to acoustic-structural couplings. The couplings part can be further expressed in terms of either ACC or SCC because it also depends on cross-couplings. Since both ACC and SCC have different physical mechanisms, their contributions to the apparent resonance frequency and apparent loss factor of each coupled mode, are also different.

A. Mathematical descriptions in terms of acoustic cross-couplings (ACC)

$P_i^D|_{\mathrm{ACC}}$ and $P_i^C|_{\mathrm{ACC}}$ derived in Sec. I A can be rewritten as

$$P_i^D|_{\mathrm{ACC}}=F_{ai}\Big/\left(\frac{1}{H_{ai}}+\frac{G_{ai}^D}{P_i}\right), \tag{32}$$

$$P_i^C|_{\mathrm{ACC}}=-G_{ai}^C\Big/\left(\frac{1}{H_{ai}}+\frac{G_{ai}^D}{P_i}\right). \tag{33}$$

G_{ai}^D contains direct coupling terms and G_{ai}^C contains the ACC terms, and they are given by

$$G_{ai}^D=P_iA_s\sum_{j=1}^{M}H_{sj}B_{j,i}^2, \tag{34}$$

$$G_{ai}^C=A_s\sum_{k\neq a}^{N}P_k\sum_{j=1}^{M}H_{sj}B_{j,i}B_{j,k}. \tag{35}$$

The forcing function of the ith acoustic mode, F_{ai}, is given by

$$F_{ai}=\begin{cases}\displaystyle\int_{V_0}q\Phi_{ai}\,dV & \text{for direct sound field excitation,} \quad (36a)\\ \displaystyle\sum_{j=1}^{M}B_{j,i}H_{sj}\int_{A_s}p_{\mathrm{ext}}\Phi_{sj}\,dA & \\ \quad\text{for direct structural excitation.} & (36b)\end{cases}$$

By adding Eqs. (32) and (33), it can be shown that

$$\frac{P_i}{H_{ai}}+G_{ai}^D+G_{ai}^C=F_{ai}. \tag{37}$$

By substituting Eq. (5) for H_{ai} into Eq. (37) and with some algebraic manipulation, it can be shown that

$$P_i\{M_{ai}[(\omega_{ai}^c)^2-\omega^2+j\,\eta_{ai}^c\omega_{ai}^2]\}=j\omega(\rho_0c_0)^2F_{ai}, \tag{38}$$

where

$$(\omega_{ai}^c)^2=\omega_{ai}^2+\mathrm{Re}[j\omega(\rho_0c_0)^2(G_{ai}^D+G_{ai}^C)/P_iM_{ai}], \tag{39}$$

$$\eta_{ai}^c=\eta_{ai}+\mathrm{Im}[j\omega(\rho_0c_0)^2(G_{ai}^D+G_{ai}^C)/P_iM_{ai}\omega_{ai}^2]. \tag{40}$$

Re[ ] and Im[ ], respectively, denotes the real and imaginary parts of the complex quantity. From Eq. (38), the coupled acoustic mode is at resonance when $\omega=\omega_{ai}^c$, and under this condition, ω_{ai}^c in Eq. (39) is the coupled/apparent resonance frequency and η_{ai}^c in Eq. (40) is the coupled/apparent loss factor of the mode in free vibration. It can be seen from Eqs. (39) and (40) that both ω_{ai}^c and η_{ai}^c are, respectively, related to ω_{ai} and η_{ai}, as well as to acoustic-structural couplings. Since the couplings part depends on P_i, the solutions to ω_{ai}^c and η_{ai}^c require either the solution to P_i or an iterative method. It is obvious from Eqs. (39) and (40) that the parts which describe the couplings, redistribute ω_{ai} and η_{ai} to ω_{ai}^c and η_{ai}^c, and the redistributions are controlled by G_{ai}^D and G_{ai}^C. Thus, as far as Eq. (39) is concerned, negligence of ACC (i.e., G_{ai}^C) means a different redistribution of ω_{ai}. This effect is shown as either an increase or a drop in ω_{ai}^c, depending on G_{ai}^D, G_{ai}^C, and P_i. As far as Eq. (40) is concerned, negligence of ACC also means a different redistribution of η_{ai} and this effect is shown as either an increased or a decreased η_{ai}^c, depending also on G_{ai}^D, G_{ai}^C, and P_i. However, if G_{ai}^C is neglected, then P_i will varnish if Eq. (34) is substituted into (40), and thereafter, the imaginary term in Eq. (40) can be shown to be positive definite after Eq. (6) has been substituted for H_{sj}. Thus, negligence of ACC always causes the coupling to provide added damping to uncoupled acoustic modes (i.e., $\eta_{ai}^c>\eta_{ai}$).

For the structural response, the previously obtained $V_j^D|_{\mathrm{ACC}}$ and $V_j^C|_{\mathrm{ACC}}$ can be written as

$$V_j^D|_{\mathrm{ACC}}=H_{sj}\left(F_{sj}+\sum_{i=1}^{N}B_{j,i}P_i^D|_{\mathrm{ACC}}\right), \tag{41}$$

$$V_j^C|_{\mathrm{ACC}}=H_{sj}\sum_{i=1}^{N}B_{j,i}P_i^C|_{\mathrm{ACC}}, \tag{42}$$

where the forcing function of the jth structural mode is

$$F_{sj}=\begin{cases}0 \quad \text{for direct sound field excitation,} & (43a)\\ \displaystyle-\frac{1}{A_s}\int_{A_s}p_{\mathrm{ext}}\Phi_{sj}\,dA & \\ \quad\text{for direct structural excitation.} & (43b)\end{cases}$$

By adding Eqs. (41) and (42), it can be shown that

$$V_j\left(\frac{1}{H_{sj}}-\frac{1}{V_j}\sum_{i=1}^{N}B_{j,i}P_i^C|_{\mathrm{ACC}}\right)=F_{sj}+\sum_{i=1}^{N}B_{j,i}P_i^D|_{\mathrm{ACC}}. \tag{44}$$

By substituting Eq. (6) for H_{sj} into Eq. (44) and with some algebraic manipulation, Eq. (44) becomes

$$V_j\{M_{sj}[(\omega_{sj}^c)^2-\omega^2+j\,\eta_{sj}^c\omega_{sj}^2]\}=j\omega A_s\left[F_{sj}+\sum_{i=1}^{N}B_{j,i}P_i^D|_{\mathrm{ACC}}\right], \tag{45}$$

where

$$(\omega_{sj}^c)^2=\omega_{sj}^2-\mathrm{Re}\left[j\omega A_s\sum_{i=1}^{N}B_{j,i}P_i^C|_{\mathrm{ACC}}/V_jM_{sj}\right], \tag{46}$$

$$\eta_{sj}^c=\eta_{sj}-\mathrm{Im}\left[j\omega A_s\sum_{i=1}^{N}B_{j,i}P_i^C|_{\mathrm{ACC}}/V_jM_{sj}\omega_{sj}^2\right]. \tag{47}$$

From Eq. (45), the coupled structural mode is at resonance when $\omega=\omega_{sj}^c$. Under this condition, ω_{sj}^c in Eq. (46) is the

coupled/apparent resonance frequency and η_{sj}^c in Eq. (47) is the coupled/apparent loss factor of the mode in free vibration. It is obvious from Eqs. (46) and (47) that acoustic-structural couplings redistribute ω_{sj} and η_{sj} to ω_{sj}^c and η_{sj}^c, and the redistributions are controlled by ACC. Therefore, when ACC is ignored (i.e., $P_i^C|_{\mathrm{ACC}}=0$), it is evident that ω_{sj}^c becomes the uncoupled resonance frequency and η_{sj}^c becomes the uncoupled loss factor of the mode. Thus, in contrast to the case for acoustic modes, neglecting ACC in the prediction of the response of structural modes means that ω_{sj} and η_{sj} are not redistributed at all. Note that the forcing function is also redistributed due to couplings but the redistribution is not controlled by cross-couplings [see Eq. (45)].

B. Mathematical descriptions in terms of structural cross-couplings (SCC)

Mathematical expressions for the apparent resonance frequencies and apparent loss factors of the ith acoustic mode and jth structural mode which are associated with SCC, are of similar forms to that associated with ACC above. Thus, a summary of expressions is given here without any lengthy descriptions. For the case of the structural response, $V_j^D|_{\mathrm{SCC}}$ and $V_j^C|_{\mathrm{SCC}}$ can be rewritten as

$$V_j^D|_{\mathrm{SCC}}=F_{sj}\Big/\left(\frac{1}{H_{sj}}+\frac{G_{sj}^D}{V_j}\right), \tag{48}$$

$$V_j^C|_{\mathrm{SCC}}=-G_{sj}^C\Big/\left(\frac{1}{H_{sj}}+\frac{G_{sj}^D}{V_j}\right), \tag{49}$$

where

$$G_{sj}^D=V_jA_s\sum_{i=1}^{N}H_{ai}B_{j,i}^2, \tag{50}$$

$$G_{sj}^C=A_s\sum_{k\neq j}^{M}V_k\sum_{i=1}^{N}H_{ai}B_{j,i}B_{k,i}. \tag{51}$$

In the above, G_{sj}^D contains the direct coupling term and G_{sj}^C contains the SCC term. For the case of direct structural excitation, F_{sj}, is given by Eq. (43b). For the case of direct sound field excitation, it is

$$F_{sj}=\sum_{i=1}^{N}B_{j,i}H_{ai}\int_{V_0}q\Phi_{ai}\,dV. \tag{52}$$

By adding Eqs. (48) and (49), using Eq. (6) for H_{sj}, and with some algebraic manipulation, it can be shown that V_j is related to ω_{sj}^c and η_{sj}^c as

$$V_j\{M_{sj}[(\omega_{sj}^c)^2-\omega^2+j\,\eta_{sj}^c\omega_{sj}^2]\}=j\,\omega A_sF_{sj}, \tag{53}$$

where

$$(\omega_{sj}^c)^2=\omega_{sj}^2+\mathrm{Re}[j\,\omega A_s(G_{sj}^D+G_{sj}^C)/V_jM_{sj}], \tag{54}$$

$$\eta_{sj}^c=\eta_{sj}+\mathrm{Im}[j\,\omega A_s(G_{sj}^D+G_{sj}^C)/V_jM_{sj}\omega_{sj}^2]. \tag{55}$$

As far as Eq. (54) is concerned, negligence of SCC (i.e., G_{sj}^C) means a different redistribution of ω_{sj} and this effect is shown as either an increase or a drop in ω_{sj}^c, depending on G_{sj}^D, G_{sj}^C, and V_j. As far as Eq. (55) is concerned, negligence of SCC also means a different redistribution of η_{sj}. This effect is shown as either an increased or a decreased η_{sj}^c, depending also on G_{sj}^D, G_{sj}^C, and V_j. However, if G_{sj}^C is neglected, then V_j will varnish if Eq. (50) is substituted into (55). Thereafter, the imaginary term in Eq. (55) can be shown to be positive definite after Eq. (5) has been substituted for H_{ai}. Thus, negligence of SCC always causes the coupling to provide added damping to uncoupled structural modes (i.e., $\eta_{sj}^c>\eta_{sj}$).

P_i^D and P_i^C associated with SCC as derived in Sec. I A can be rewritten as

$$P_i^D|_{\mathrm{SCC}}=H_{ai}\left(F_{ai}-A_s\sum_{j=1}^{M}B_{j,i}V_j^D|_{\mathrm{SCC}}\right), \tag{56}$$

$$P_i^C|_{\mathrm{SCC}}=-H_{ai}A_s\sum_{j=1}^{M}B_{j,i}V_j^C|_{\mathrm{SCC}}. \tag{57}$$

For the case of direct sound field excitation, F_{ai}, is given in Eq. (36a). For the case of direct structural excitation, $F_{ai}=0$. By adding Eqs. (56) and (57), and then using Eq. (5) for H_{ai}, it can be shown that

$$P_i\{M_{ai}[(\omega_{ai}^c)^2-\omega^2+j\,\eta_{ai}^c\omega_{ai}^2]\}=j\,\omega(\rho_0c_0)^2\left[F_{ai}-A_s\sum_{j=1}^{M}B_{j,i}V_j^D|_{\mathrm{SCC}}\right], \tag{58}$$

where

$$(\omega_{ai}^c)^2=\omega_{ai}^2+\mathrm{Re}\left[j\,\omega(\rho_0c_0)^2A_s\sum_{j=1}^{M}B_{j,i}V_j^C|_{\mathrm{SCC}}/P_iM_{ai}\right], \tag{59}$$

$$\eta_{ai}^c=\eta_{ai}+\mathrm{Im}\left[j\,\omega(\rho_0c_0)^2A_s\sum_{j=1}^{M}B_{j,i}V_j^C|_{\mathrm{SCC}}/P_iM_{ai}\omega_{ai}^2\right]. \tag{60}$$

It can be seen from Eqs. (59) and (60) that acoustic-structural couplings redistribute ω_{ai} and η_{ai} to ω_{ai}^c and η_{ai}^c, and the redistributions are controlled by SCC. Therefore, when SCC is ignored (i.e., $V_j^C|_{\mathrm{SCC}}=0$), it is evident that ω_{ai}^c becomes the uncoupled resonance frequency and η_{ai}^c becomes the uncoupled loss factor of the mode. Thus, in contrast to the case for structural modes, neglecting SCC in the prediction of the response of acoustic modes means that ω_{ai} and η_{ai} are not redistributed at all. Note that the forcing function is also redistributed due to couplings but the redistribution is not controlled by cross-couplings [see Eq. (58)].

III. COMPUTATIONAL EXAMPLES

A. Physical features of ACC and SCC

Mathematical descriptions obtained in the preceding sections are used to investigate characteristics of ACC and SCC in this section. A rectangular cavity of dimensions (0.868, 1.150, 1.000) m which couples with a $0.868\times1.150\,\mathrm{m}^2$ rectangular simply supported aluminum plate located at $z=1.000$ m is used. The characteristics are studied and compared for the cases of direct acoustic excitation in the cavity and direct mechanical excitation on the plate.

1. Direct sound field excitation

For the case of direct acoustic excitation, a monopole source located at a cavity corner $[(x,y,z)=(0,0,0)\,\mathrm{m}]$ is used in this section. Effect of excitation positions on the characteristics of ACC and SCC will be explained in Sec. III A 3. For the convenience of calculations, all acoustic modes are assumed to have the same decay time and this is also applicable to all plate modes. Although this choice of equal decay times may affect the contributions of both ACC and SCC to the sound field and plate responses, it does not affect the corresponding physical features of the cross-couplings because the mechanisms in both cross-couplings do not change.

Figure 1 shows $|P_i^C|$ and $|P_i^D|$ of acoustic mode (2,3,1) (resonance frequency, $f_{(2,3,1)}=622.9\,\mathrm{Hz}$), associated with ACC and SCC (i.e., $|P^C_{(2,3,1)}|_{\mathrm{ACC}}|$, $|P^D_{(2,3,1)}|_{\mathrm{ACC}}|$, $|P^C_{(2,3,1)}|_{\mathrm{SCC}}|$, and $|P^D_{(2,3,1)}|_{\mathrm{SCC}}|$), for the case of the corner excitation in the frequency range of 550–750 Hz. Plate thickness of 2 mm (modal density, $n_p=0.168\,\mathrm{Hz}^{-1}$), and some combinations of acoustic and plate modal decay times (T_a and T_p) shown are used. A peak at $f_{(2,3,1)}$, respectively, in $|P^D_{(2,3,1)}|_{\mathrm{ACC}}|$ and $|P^D_{(2,3,1)}|_{\mathrm{SCC}}|$, indicates the sound source contribution to the response of mode (2,3,1) at resonance. On the other hand, the peaks in $|P^C_{(2,3,1)}|_{\mathrm{ACC}}|$ and $|P^C_{(2,3,1)}|_{\mathrm{SCC}}|$ indicate cross-coupling contributions to the mode from plate modes and other acoustic modes. Guided by Table I which shows details of acoustic and plate modes that couple with mode (2,3,1) in the frequency range of interest, Fig. 1 shows that the peaks in $|P^C_{(2,3,1)}|_{\mathrm{ACC}}|$ and $|P^C_{(2,3,1)}|_{\mathrm{SCC}}|$ appear at $f_{(2,3,1)}$ and at the resonance frequencies of those modes listed in Table I. The peaks due to the acoustic and plate modes are, respectively, labeled ''*a*'' and ''*p*'' in the figure. There can be more than one mode at a single peak where an overlapping of modes occurs. Since $|P^D_{(2,3,1)}|_{\mathrm{ACC}}|$ and $|P^D_{(2,3,1)}|_{\mathrm{SCC}}|$ due to the sound source, mainly account for the response of mode (2,3,1) at resonance, $f_{(2,3,1)}$, it is obvious that $|P^C_{(2,3,1)}|_{\mathrm{ACC}}|$ and $|P^C_{(2,3,1)}|_{\mathrm{SCC}}|$ contain much details of the couplings between the mode and the plate modes, and details of the cross-couplings between the mode and other acoustic modes. Therefore, the so-called plate-controlled peaks and cavity-controlled peaks[27] at resonance or off-resonance of mode (2,3,1) may either disappear or have different response if either $|P^C_{(2,3,1)}|_{\mathrm{ACC}}|$ or $|P^C_{(2,3,1)}|_{\mathrm{SCC}}|$ is not included the prediction of the sound field response, but both are, respectively, comparable in magnitude to $|P^D_{(2,3,1)}|_{\mathrm{ACC}}|$ and $|P^D_{(2,3,1)}|_{\mathrm{SCC}}|$. However, the response at $f_{(2,3,1)}$ is most important because mode (2,3,1) has the largest response there. Since the mechanism of SCC at $f_{(2,3,1)}$ involves cross-couplings between plate modes through mode (2,3,1), the contribution of $|P^C_{(2,3,1)}|_{\mathrm{SCC}}|$ relative to $|P^D_{(2,3,1)}|_{\mathrm{SCC}}|$ at resonance is mainly controlled by the properties of this mode. Because this mode is at resonance, it can be seen from Fig. 1 that $|P^C_{(2,3,1)}|_{\mathrm{SCC}}|$ at $f_{(2,3,1)}$ is relatively large compared to $|P^D_{(2,3,1)}|_{\mathrm{SCC}}|$. In the case of ACC, the mechanism at $f_{(2,3,1)}$ involves cross-couplings between mode (2,3,1) and other acoustic modes through the plate modes. Therefore, the properties of the plate modes mainly control the contribution of $|P^C_{(2,3,1)}|_{\mathrm{ACC}}|$ relative to $|P^D_{(2,3,1)}|_{\mathrm{ACC}}|$. Since there are no plate modes that well-couple in terms of resonance frequency proximity to mode (2,3,1), $|P^C_{(2,3,1)}|_{\mathrm{ACC}}|$ is much smaller than $|P^D_{(2,3,1)}|_{\mathrm{ACC}}|$ as shown in the figure. It can also be seen that regardless of ACC or SCC, changing T_p only affects the responses at the plate resonance frequencies while changing T_a only affects the responses at the cavity resonance frequencies. If the acoustic and plate modes have very close or same resonance frequencies, then changing either T_p or T_a will affect the responses at both the plate and cavity resonance frequencies. Reducing T_a and T_p means the resistance of the acoustic and plate modes in acquiring energy has in-

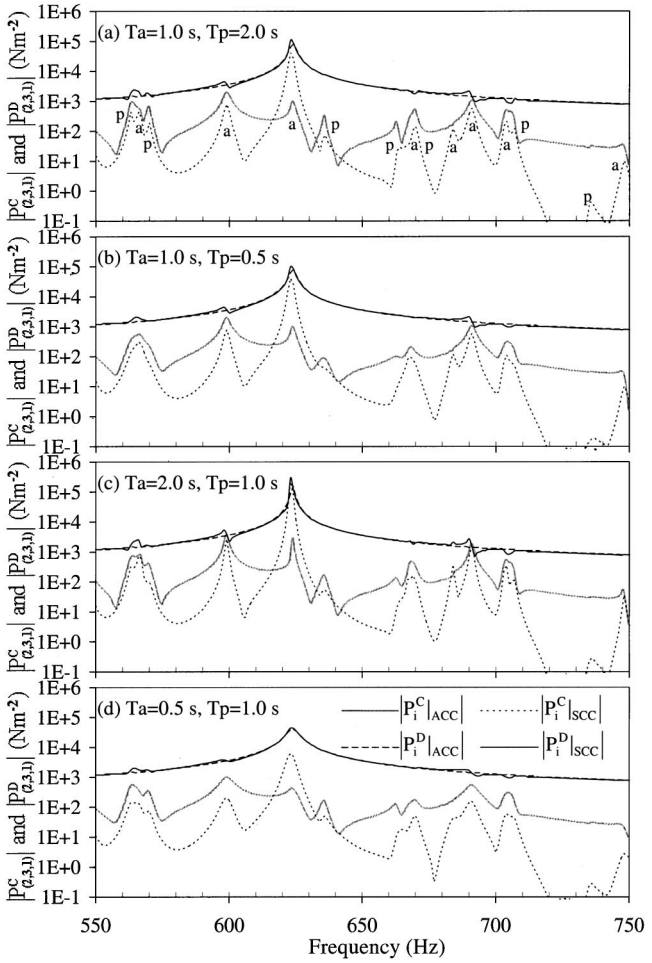

FIG. 1. $|P_i^C|$ and $|P_i^D|$ of mode (2,3,1), for $h=2$ mm and direct sound field excitation at (0.0, 0.0, 0.0) m. ''*a*'' denotes cavity-controlled peaks and ''*p*'' denotes plate-controlled peaks.

TABLE I. Acoustic and plate modes which couple with acoustic mode (2,3,1) in frequency range 550–750 Hz, for the plate-cavity system of dimensions (0.868, 1.150, 1.000) m and $h=2$ mm.

Acoustic modes and their resonance frequencies (Hz)		Panel modes and their resonance frequencies (Hz)	
(0,3,2)	565.4	(9,4)	564.2
(2,3,0)	598.7	(3,12)	570.0
(2,1,3)	667.6	(9,6)	635.6
(0,3,3)	683.8	(7,10)	663.5
(2,3,2)	690.5	(5,12)	670.2
(0,1,4)	704.1	(1,14)	705.4
(0,5,0)	747.8	(9,8)	735.4

creased. Thus, the contribution of ACC or SCC is reduced if the decay times are reduced. Observing the response at $f_{(2,3,1)}$ again, due to the mechanism of SCC described above, the contribution of $|P^C_{(2,3,1)}|_{\mathrm{SCC}}|$ relative to $|P^D_{(2,3,1)}|_{\mathrm{SCC}}|$ is shown in Fig. 1 to be significantly changed when T_a is adjusted while adjusting T_p gives only little or no difference. Also, due to the mechanism of ACC, it can be seen that adjusting T_p also gives little difference at $f_{(2,3,1)}$ since none of the plates modes are located in the vicinity of mode (2,3,1). When T_a is adjusted, not much difference is also observed in the relative contribution since both $|P^C_{(2,3,1)}|_{\mathrm{ACC}}|$ and $|P^D_{(2,3,1)}|_{\mathrm{ACC}}|$ are changed by almost the same amount.

When the plate thickness is changed to $h=1.96$ mm, the peak due to plate mode (9,6) at 636 Hz in Fig. 1 is shifted to around 623 Hz (see Fig. 2) because of the change in resonance frequency of the mode. As far as the mechanism of ACC at $f_{(2,3,1)}$ is concerned, it can be seen from Fig. 2 that the contribution of $|P^C_{(2,3,1)}|_{\mathrm{ACC}}|$ relative to $|P^D_{(2,3,1)}|_{\mathrm{ACC}}|$ is significantly changed when T_p is adjusted because the plate mode is now well-coupled to mode (2,3,1). Similar result can also be seen when T_a is adjusted because the well-coupled plate mode (9,6) and acoustic mode (2,3,1) now have more pronounced effect on each other. Due to this same reason and as far as SCC is concerned, the contribution of $|P^C_{(2,3,1)}|_{\mathrm{SCC}}|$ relative to $|P^D_{(2,3,1)}|_{\mathrm{SCC}}|$ has a more distinguished change than before when T_p is adjusted. On the other hand, the mechanism of SCC implies that adjusting T_a still significantly changes this relative contribution. All these observations at around $f_{(2,3,1)}$ are evident in Fig. 2.

2. Direct structural excitation

For the case of direct structural excitation, the acoustic source in the sound field is replaced by a mechanical point force excitation on the plate. All acoustic modes are now driven only through couplings with plate modes. A random location of the excitation force is used and in this case, at (0.152, 0.448) m. For this excitation, Fig. 3 shows

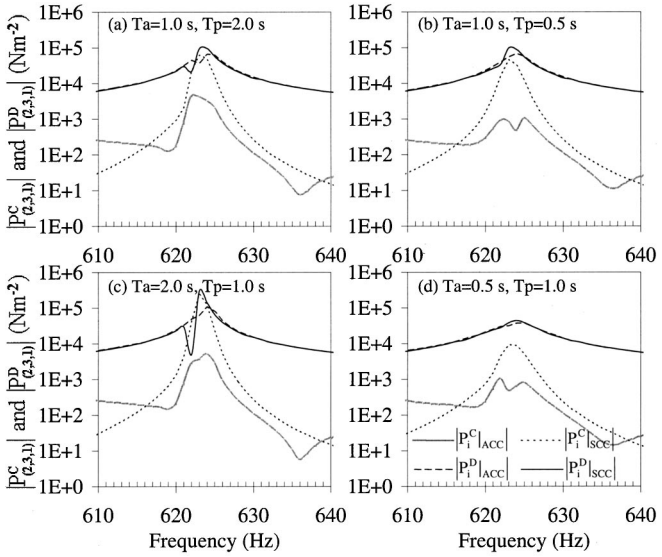

FIG. 2. $|P^C_i|$ and $|P^D_i|$ of mode (2,3,1), for $h=1.96$ mm and direct sound field excitation at (0.0, 0.0, 0.0) m.

$|P^C_{(2,3,1)}|_{\mathrm{ACC}}|$, $|P^D_{(2,3,1)}|_{\mathrm{ACC}}|$, $|P^C_{(2,3,1)}|_{\mathrm{SCC}}|$, and $|P^D_{(2,3,1)}|_{\mathrm{SCC}}|$ for $h=2$ mm and the same combinations of T_a and T_p as used in Fig. 1. Similar to the results in Fig. 1, the peaks in $|P^C_{(2,3,1)}|_{\mathrm{ACC}}|$ and $|P^C_{(2,3,1)}|_{\mathrm{SCC}}|$ in Fig. 3 also indicate cross-coupling contributions to mode (2,3,1) from plate modes and other acoustic modes, whose details are shown in Table I. $|P^D_{(2,3,1)}|_{\mathrm{ACC}}|$ and $|P^D_{(2,3,1)}|_{\mathrm{SCC}}|$ have a peak at $f_{(2,3,1)}$ which accounts for the response of mode (2,3,1) at resonance. They also have peaks at the resonance frequencies of the plate modes which account for direct acoustic-structural coupling contributions to mode (2,3,1) from the plate modes. Since the plate is directly excited, the plate modes contain most of the system's energy. Thus, at those peaks of the plate modes, $|P^C_{(2,3,1)}|_{\mathrm{ACC}}|$ and $|P^C_{(2,3,1)}|_{\mathrm{SCC}}|$, respectively, has a comparatively large response to $|P^D_{(2,3,1)}|_{\mathrm{ACC}}|$ and $|P^D_{(2,3,1)}|_{\mathrm{SCC}}|$. Hence, compared to the case of direct sound field excitation, the cross-couplings (both ACC and SCC) for the case of direct structural excitation may contribute more to the responses of the plate-controlled peaks. At resonance of mode (2,3,1), $f_{(2,3,1)}$, it can be seen from Fig. 3 that the contributions of $|P^C_{(2,3,1)}|_{\mathrm{ACC}}|$ relative to $|P^D_{(2,3,1)}|_{\mathrm{ACC}}|$, and $|P^C_{(2,3,1)}|_{\mathrm{SCC}}|$ relative to $|P^D_{(2,3,1)}|_{\mathrm{SCC}}|$, are slightly larger than that in Fig. 1 because of increased dominations of the plate modes which have most of the system's energy. However,

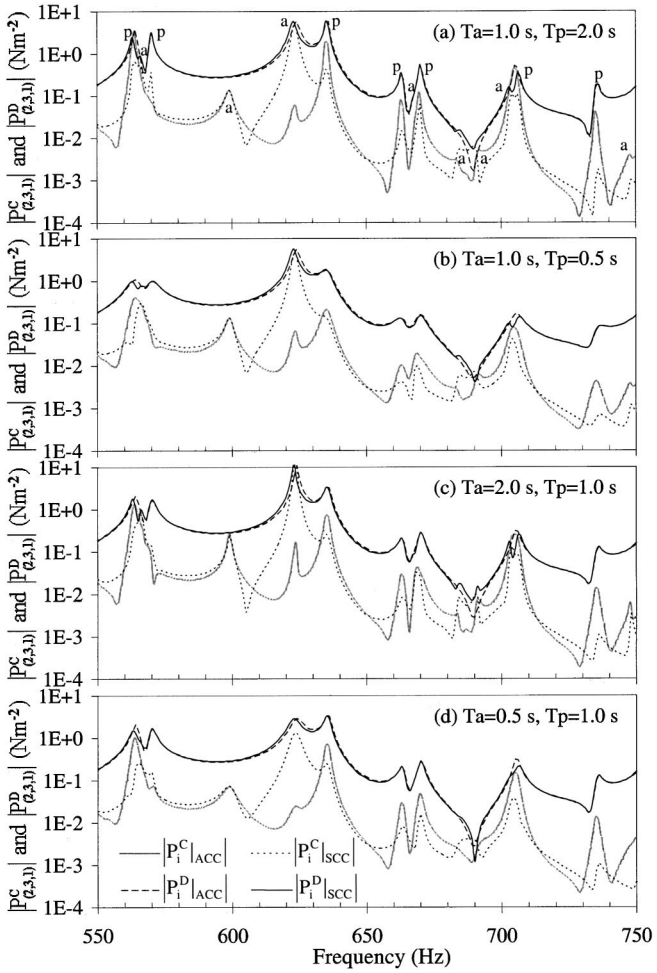

FIG. 3. $|P^C_i|$ and $|P^D_i|$ of mode (2,3,1), for $h=2$ mm and direct plate excitation at (0.152, 0.448) m. ''*a*'' denotes cavity-controlled peaks and ''*p*'' denotes plate-controlled peaks.

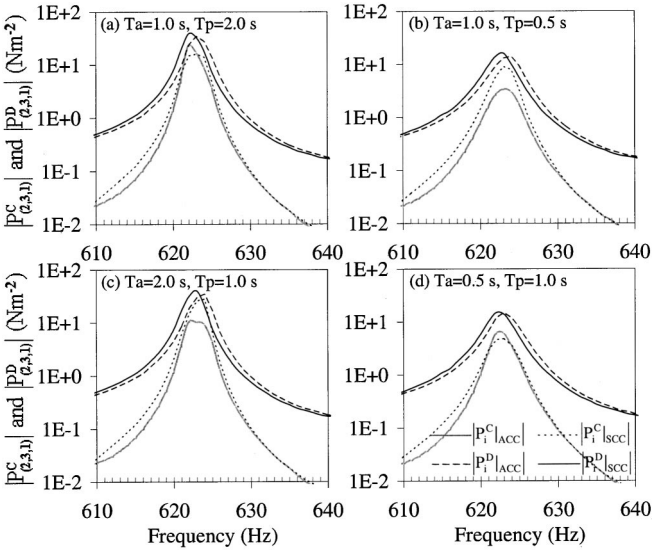

FIG. 4. $|P_i^C|$ and $|P_i^D|$ of mode (2,3,1), for $h=1.96$ mm and direct plate excitation at (0.152, 0.448) m.

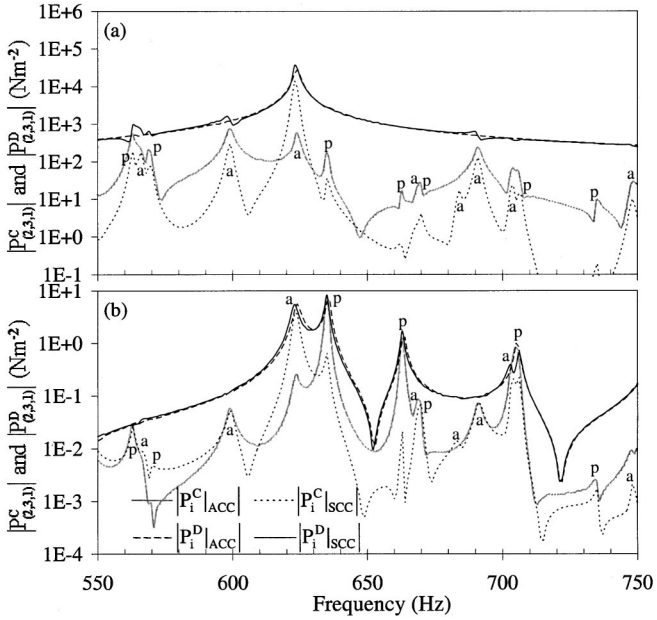

FIG. 5. $|P_i^C|$ and $|P_i^D|$ of mode (2,3,1), for $T_a=1.0$ s, $T_p=2.0$ s, and $h=2$ mm, for (a) direct sound field excitation at (0.152, 0.448, 0.152) m, and (b) direct plate excitation at (0.434, 0.2875) m. ''*a*'' denotes cavity-controlled peaks and ''*p*'' denotes plate-controlled peaks.

the trends of these relative contributions with respect to the change in either T_a or T_p, can be seen to be still the same as before even though the plate is now directly excited. This is because the mechanisms of ACC and SCC have not changed (note in Sec. I A that both cases of direct sound field excitation and direct structural excitation share the common $P_i^C|_{\mathrm{ACC}}$ and $P_i^C|_{\mathrm{SCC}}$). Figure 4 shows results for $h=1.96$ mm where mode (2,3,1) is well-coupled to plate mode (9,6) and now, adjusting either T_a or T_p provides a more distinguished change in the relative contributions of both ACC and SCC.

3. Effect of excitation position on characteristics of ACC and SCC

In the case of power flow between coupled oscillators, modal cross-couplings have been shown mathematically to depend on the location of the excitation source.[28] Similarly, regardless of whether the sound field or the structure is directly excited, it has been noted in the mathematical developments in Sec. I A that both P_i^D and V_j^D are functions of the distribution of the excitation source. Therefore, these direct components are dependent on the location of the excitation (defined in the acoustic or structural mode shape function), and the choice of excitation position will have influence on P_i and V_j, and hence P_i^C and V_j^C, since these quantities are related to each other. The excitation position actually controls the extent of each acoustic or structural mode being directly driven by the excitation source.

For the case of direct sound field excitation, Fig. 1 has shown results where all acoustic modes are directly excited to maximum since for the corner excitation, the modes are directly driven at their antinodal points. If the acoustic modes are not directly driven to maximum, for example at an off-antinodal point of (0.152, 0.448, 0.152) m, the features of $|P^C_{(2,3,1)}|_{\mathrm{ACC}}|$, $|P^C_{(2,3,1)}|_{\mathrm{SCC}}|$, $|P^D_{(2,3,1)}|_{\mathrm{ACC}}|$, and $|P^D_{(2,3,1)}|_{\mathrm{SCC}}|$ as observed before can still be seen in Fig. 5(a). However, each individual peak there has lower response than before because all the acoustic modes are not directly driven to maximum, and thus, less energy is injected into the system by the sound source. Since the cross-couplings do not change proportionately with the contribution of the sound source when the excitation position is changed, the contributions of $|P^C_{(2,3,1)}|_{\mathrm{ACC}}|$ relative to $|P^D_{(2,3,1)}|_{\mathrm{ACC}}|$ and $|P^C_{(2,3,1)}|_{\mathrm{SCC}}|$, relative to $|P^D_{(2,3,1)}|_{\mathrm{SCC}}|$, either at resonance or off-resonance of mode (2,3,1), will be different for different excitation positions [for example, compare Fig. 5(a) to Fig. 1(a)]. However, at the resonance of the mode, $f_{(2,3,1)}$, it can be shown that these relative contributions with respect to the change in either T_a or T_p still have the similar trends as before because the mechanisms of ACC and SCC have not changed. These results are also applicable to other excitation positions. However, there are a few excitation positions (e.g., the middle of a cavity edge) where mode (2,3,1) is excited at its nodal point and is not directly driven at all. In such a case, the sound source will not directly contribute to mode (2,3,1) in the case of ACC (i.e., $P^D_{(2,3,1)}|_{\mathrm{ACC}}=0$) as $P_i^D|_{\mathrm{ACC}}$ is greatly dependent on the excitation position [see Eq. (11)]. This leaves only $P^C_{(2,3,1)}|_{\mathrm{ACC}}$ to contribute to the response of the mode since other acoustic modes are still directly excited by the sound source and then, cross-couple with the mode. In the case of SCC, $P^D_{(2,3,1)}|_{\mathrm{SCC}}$ shows a less dependence on the excitation position than $P^D_{(2,3,1)}|_{\mathrm{ACC}}$ because it is contributed by direct acoustic-structural couplings when the mode is directly driven at its nodal point by the sound source [see Eq. (16)]. In this case, $P^D_{(2,3,1)}|_{\mathrm{SCC}}$ may still contribute to the response of the mode in addition to $P^C_{(2,3,1)}|_{\mathrm{SCC}}$.

Figure 5(b) shows results for direct plate excitation at (0.434, 0.2875) m. At this excitation position, some plate modes which couple with mode (2,3,1) are directly excited to maximum since they are directly driven at their antinodal points. However, at the same excitation position, other plate modes which also couple with mode (2,3,1) are not directly

TABLE II. Absolute error in SPL (dB) at 623 Hz at (0.868,1.150,0.000) m in the cavity.

Directly excited subsystem	$T_a=1.0$ s, $T_p=2.0$ s		$T_a=1.0$ s, $T_p=0.5$ s		$T_a=2.0$ s, $T_p=1.0$ s		$T_a=0.5$ s, $T_p=1.0$ s	
	Neglect		Neglect		Neglect		Neglect	
	ACC	SCC	ACC	SCC	ACC	SCC	ACC	SCC
				$h=2$ mm				
Sound field	0.2	3.1	0.2	3.0	0.2	11.7	0.2	0.5
Plate	0.0	5.5	0.3	5.5	0.6	13.1	0.1	1.6
				$h=1.96$ mm				
Sound field	2.8	10.5	0.3	6.0	1.6	23.4	0.2	1.2
Plate	2.9	2.9	0.0	3.7	1.9	5.0	0.5	1.1

driven at all because they are directly excited at their nodal points. Thus, some peaks due to the plate modes, in $P^D_{(2,3,1)}|_{\mathrm{ACC}}$ and $P^D_{(2,3,1)}|_{\mathrm{SCC}}$ as observed in Fig. 3 are no longer seen in Fig. 5(b). The responses at the remaining peaks are slightly larger than before because more energy is injected into the system by the driving force now as the corresponding plate modes are directly excited at their antinodal points. By comparing Fig. 5(b) to Fig. 3(a) it can be seen that the contributions of $|P^C_{(2,3,1)}|_{\mathrm{ACC}}|$ relative to $|P^D_{(2,3,1)}|_{\mathrm{ACC}}|$, and $|P^C_{(2,3,1)}|_{\mathrm{SCC}}|$ relative to $|P^D_{(2,3,1)}|_{\mathrm{SCC}}|$, either at resonance or off-resonance of mode (2,3,1), are different for different excitation positions because the cross-couplings do not change proportionately with the contribution of the driving force when the excitation position is changed. However, as the mechanisms of ACC and SCC at $f_{(2,3,1)}$ have not changed, it can be shown that these relative contributions with respect to the change in either T_a or T_p still have the similar trends as before. At some special excitation positions (e.g., middle of the plate), all plate modes which couple with mode (2,3,1) are directly excited at their nodal points. In such a case, direct acoustic-structural couplings in both cases of ACC and SCC will not contribute to mode (2,3,1) at all (i.e., $P^D_{(2,3,1)}|_{\mathrm{ACC}}=P^D_{(2,3,1)}|_{\mathrm{SCC}}=0$) as both $P^D_i|_{\mathrm{ACC}}$ and $P^D_i|_{\mathrm{SCC}}$ are greatly dependent on the excitation position [see Eqs. (20) and (23)]. Because the corresponding plate modes are not excited, all other acoustic mode which cross-couple with mode (2,3,1) are also not excited at all, and thus, there are also no cross-couplings (i.e., $P^C_{(2,3,1)}|_{\mathrm{ACC}}=P^C_{(2,3,1)}|_{\mathrm{SCC}}=0$). Hence, mode (2,3,1) has no response.

Although examples in Figs. 1–5 have been shown only for acoustic mode (2,3,1), other acoustic modes as well as the plate modes, also exhibit the similar physical features of ACC and SCC as shown by this mode. The only difference between the features in the acoustic modes and those in the plate modes, is the trends of $|V^C_j|_{\mathrm{ACC}}|$ relative to $|V^D_j|_{\mathrm{ACC}}|$, and $|V^C_j|_{\mathrm{SCC}}|$ relative to $|V^D_j|_{\mathrm{SCC}}|$, with respect to the change in either T_a or T_p. In the case of SCC, the mechanism at resonance of a plate mode under consideration involves cross-couplings between the mode and other plate modes through acoustic modes. Thus, at the resonance, the properties of the acoustic modes mainly control the contribution of $|V^C_j|_{\mathrm{SCC}}|$ relative to $|V^D_j|_{\mathrm{SCC}}|$ and adjusting T_a will not significantly change the relative contribution if none of the acoustic modes are well-coupled to the plate mode. Similarly, adjusting T_p will also give little or no difference if the well-coupled condition is not satisfied. In the case of ACC, the mechanism at resonance of the plate mode involves cross-couplings between acoustic modes through the plate mode. Thus, the properties of this plate mode mainly control the contribution of $|V^C_j|_{\mathrm{ACC}}|$ relative to $|V^D_j|_{\mathrm{ACC}}|$ at the resonance of the mode, and adjusting T_p will significantly change the relative contribution regardless of whether the well-coupled condition is satisfied or not. On the other hand, adjusting T_a will only produce a pronounced effect if the well-coupled condition is satisfied.

B. Effects of ACC and SCC on the sound field and plate responses

The effects of ACC and SCC on the sound field and plate responses can be realized in terms of errors in the prediction of those responses when either of these cross-couplings is neglected. In this section, the characteristics of the errors and their trends with the physical properties of the plate-cavity system are obtained. The characteristics will then be related to the physical features of ACC and SCC as discussed in the preceding section.

1. Characteristics of errors in the plate-cavity system responses

Table II shows the absolute errors in SPL in dB at a cavity corner $[(x,y,z)=(0.868,1.150,0.000)\ \mathrm{m}]$, generated from ignoring ACC and SCC, respectively, under the same conditions used in Figs. 1–4. The excitation frequency is 623 Hz where acoustic modes (2,3,1) and (0,4,1) are dominant. The errors shown are dependent on the contribution of $|P^C_i|$ relative to $|P^D_i|$ of the dominant acoustic modes. As described in Sec. III A, the contribution of $|P^C_{(2,3,1)}|_{\mathrm{SCC}}|$ relative to $|P^D_{(2,3,1)}|_{\mathrm{SCC}}|$ in the case of SCC, is larger than the contribution of $|P^C_{(2,3,1)}|_{\mathrm{ACC}}|$ relative to $|P^D_{(2,3,1)}|_{\mathrm{ACC}}|$ in the case of ACC, and this is also similar for mode (0,4,1). Thus, the SPL errors due to neglecting SCC are generally larger than that due to neglecting ACC as evident in Table II regardless of whichever subsystem is excited or whether mode (2,3,1) is well coupled to mode (9,6) or not. When $h=2$ mm, Table II shows that changing either T_a or T_p has no significant effect on the SPL errors generated from ignoring ACC while the SPL errors generated from ignoring SCC are only significantly affected by changing T_a. When $h=1.96$ mm, the errors due to neglecting either ACC or SCC is larger than that

TABLE III. Absolute error in velocity level (dB) at 609 Hz at (0.609, 0.881) m on the plate, for $h=2$ mm.

Directly excited subsystem	$T_a=1.0$ s, $T_p=2.0$ s		$T_a=1.0$ s, $T_p=0.5$ s		$T_a=2.0$ s, $T_p=1.0$ s		$T_a=0.5$ s, $T_p=1.0$ s	
	Neglect		Neglect		Neglect		Neglect	
	ACC	SCC	ACC	SCC	ACC	SCC	ACC	SCC
				$L_z=1.000$ m				
Sound field	3.5	1.8	1.3	0.6	2.2	1.2	2.3	0.7
Plate	0.9	0.7	0.0	0.5	0.0	0.6	0.1	0.5
				$L_z=0.975$ m				
Sound field	9.2	3.9	5.5	4.2	9.7	9.7	5.2	1.1
Plate	3.5	0.1	0.2	0.0	1.1	0.2	0.8	0.1

for $h=2$ mm because acoustic mode (2,3,1) is well-coupled to plate mode (9,6). These errors are also now significantly affected by the change in either T_a or T_p as can be seen from Table II. These observations show that the characteristics of errors in the sound field response are similar to the aforementioned behaviors of the contributions of $|P_i^C|$ relative to $|P_i^D|$ of dominant acoustic modes.

Table III shows the absolute errors (dB) in the plate velocity level at (0.609, 0.881) m when either ACC or SCC is ignored in the prediction of the plate response. The same conditions used in Table II are used here. The excitation frequency is 609 Hz where plate mode (1,13) is dominant ($f_{(1,13)}=609.1$ Hz). When $L_z=1.000$ m, regardless of whether the sound field or the plate is directly excited, Table III shows that changing either T_a or T_p only has small effects on the velocity errors generated from ignoring SCC because no acoustic modes are well-coupled to the dominant plate mode. The errors generated from ignoring ACC are only greatly affected by changing T_p. When $L_z=0.975$ m, the errors incurred when either ACC or SCC is ignored are significantly affected by the change in either T_a or T_p as evident in Table III because mode (1,13) is now well-coupled to acoustic mode (2,2,2) ($f_{(2,2,2)}=609.1$ Hz). These results show that the characteristics of errors in the plate response are similar to the behaviors of the contributions of $|V_j^C|$ relative to $|V_j^D|$ of dominant plate modes as described in the preceding section. Thus, the characteristics of the errors can actually be obtained from the understanding of the aforementioned physical mechanisms of ACC and SCC.

2. Effects of excitation and observation positions on errors in the plate-cavity system responses

As described in Sec. III A 3, the choice of excitation position will have influence on P_i and V_j. This choice eventually affects the errors due to the negligence of ACC or SCC in the prediction of the plate-cavity system responses. In addition, the errors are also dependent on the observation position. This is because the choice of observation position controls how the various acoustic modes superimpose with each other in the case of the sound field response and it also controls the superposition of various plate modes in the case of the plate response. For each of the responses, the observation position is, respectively, defined in the acoustic and structural mode shape functions, and the relationships between the mode shape functions and the system responses have been mathematically described in Sec. I B. Table IV shows the SPL errors at 623 Hz for some combinations of excitation and observation positions. For the case of direct sound field excitation, the combinations include locations at some randomly selected positions [e.g., (0.152, 0.448, 0.152) m, (0.464, 0.423, 0.315) m, (0.268, 0.319, 0.626) m], corners [e.g. (0.0, 0.0, 0.0) m, (0.868, 1.15, 0.0) m], middle of cavity edges [e.g., (0.0, 0.0, 0.5) m, (0.0, 1.15, 0.5) m], the middle of a cavity boundary surface [e.g., (0.434, 0.575, 0.0) m] and

TABLE IV. Absolute error in SPL (dB) at 623 Hz, for $T_a=2.0$ s, $T_p=1.0$ s, and $h=2$ mm.

Excitation positions	Observation positions: (0.868, 1.15, 0.0) m		(0.268, 0.319, 0.626) m		(0.0, 1.15, 0.5) m		(0.434, 0.575, 0.5) m	
	Neglect		Neglect		Neglect		Neglect	
	ACC	SCC	ACC	SCC	ACC	SCC	ACC	SCC
				Direct and field excitation				
(0.0, 0.0, 0.0) m	0.2	11.7	1.6	17.7	0.2	0.5	4.1	9.6
(0.152, 0.448, 0.152) m	0.0	10.0	0.4	8.7	19.2	5.7	1.8	2.4
(0.464, 0.423, 0.315) m	0.4	11.4	0.4	8.8	27.3	5.5	0.2	0.4
(0.0, 0.0, 0.5) m	11.3	14.4	2.0	2.8	0.2	0.0	0.1	0.1
(0.434, 0.575, 0.0) m	0.1	11.1	0.8	9.2	4.2	9.5	3.2	5.9
				Direct plate excitation				
(0.152, 0.448) m	0.6	13.1	0.4	1.6	1.6	2.7	2.6	2.9
(0.464, 0.423) m	0.2	0.3	0.5	10.9	4.5	3.6	15.7	8.8
(0.434, 0.2875) m	0.1	4.1	0.9	3.6	4.8	2.9	1.9	3.2
(0.434, 0.575) m	0.0	3.7	0.9	3.6	2.9	0.7	2.2	0.1

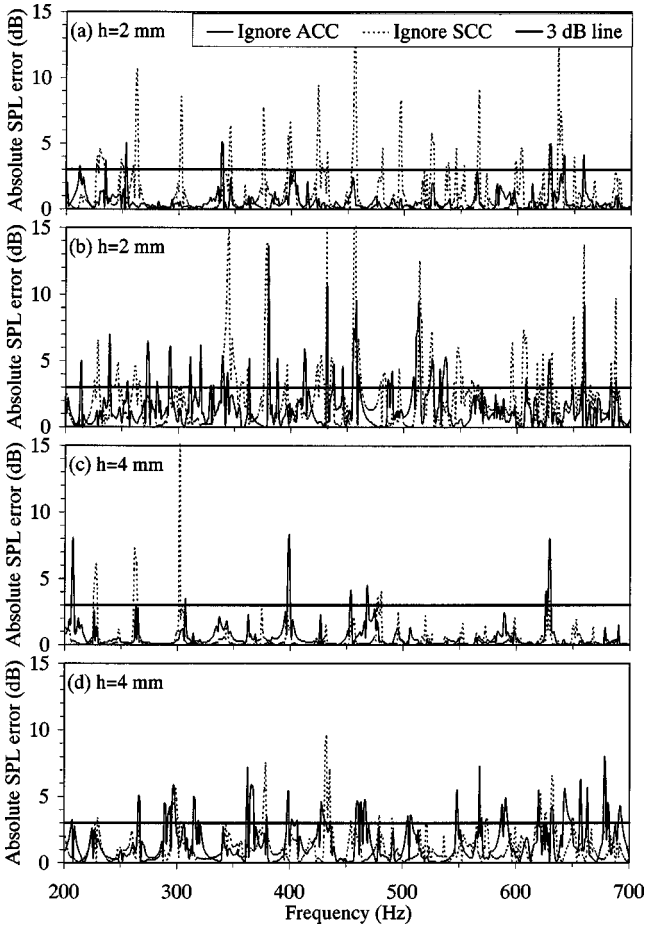

FIG. 6. Absolute SPL error at (0.868,1.150, 0.000) m in the cavity for $T_a = 1.0$ s and $T_p = 1.0$ s, for direct sound field excitation [(a) and (c)], and direct plate excitation [(b) and (d)].

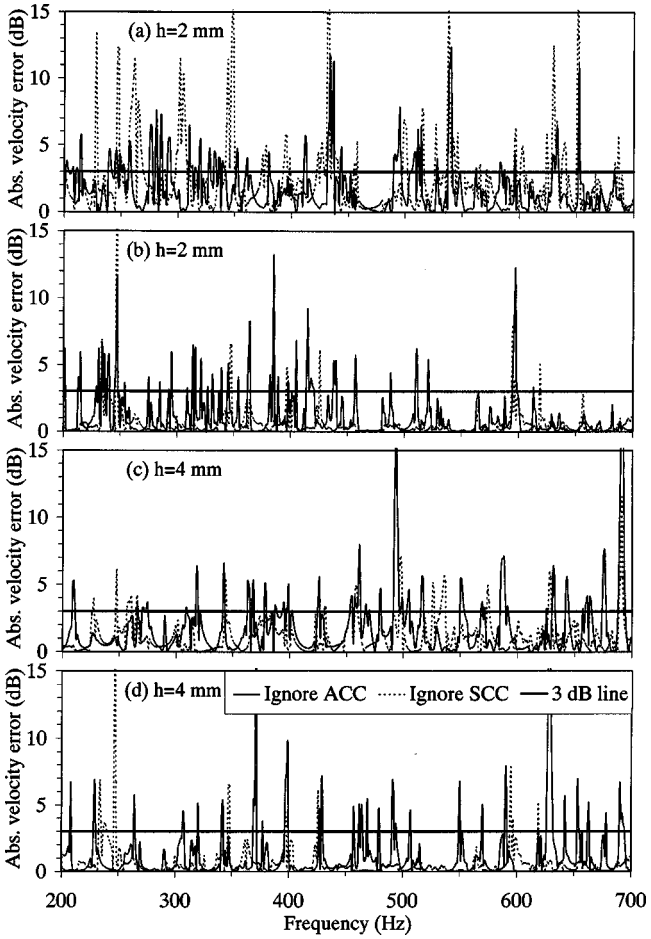

FIG. 7. Absolute error in velocity level at (0.609, 0.881) m on the plate for $T_a = 1.0$ s and $T_p = 1.0$ s, for direct sound field excitation [(a) and (c)], and direct plate excitation [(b) and (d)].

the middle of the cavity [i.e., (0.434, 0.575, 0.5) m]. For the case of direct plate excitation, excitations at some random positions [e.g., (0.152, 0.448) m, (0.464, 0.423) m], as well as at some distinct positions such as the middle of the plate [i.e., (0.434, 0.575) m] and at the nodal lines of some plate modes [e.g., (0.434, 0.2875) m], are used in conjunction with the few selected observation positions. It can be seen that the SPL errors are different for different excitation and/or observation positions. When the direct sound field excitation is at the corner or the random positions, and the SPL response is observed at another corner or random position, the errors are of about the same order of magnitude although individual results vary. At distinct excitation and/or observation positions like the middle of the cavity, boundary surfaces or edges, larger variations in the error are observed. At such excitation positions, the excitation source and direct coupling component of dominant acoustic modes may slightly or not contribute to the SPL response as have been described in Sec. III A 3, while at those distinct observation positions, the response of the dominant modes may or may not be observable. Thus, a considerable variation in the SPL error is observed when the excitation and/or observation position is changed from one distinct location to the other. The same explanation is also applicable for the case of direct plate excitation when the excitation and observation are at distinct positions. The behavior of velocity errors with repect to excitation and observation positions in the case of the plate response is also similar to the behavior of the SPL errors obtained from Table IV, and will not be shown here.

3. Distributions of errors in the plate-cavity system responses

In this section, distributions of the errors are investigated for broader frequency ranges. Figure 6 shows the SPL errors at the same cavity corner for the same corner excitation as used in Table II, for the frequency range 200–700 Hz. In Fig. 6(a) and (b), $h = 2$ mm while in Fig. 6(c) and (d), $h = 4$ mm (low modal density, $n_p = 0.084\,\mathrm{Hz}^{-1}$). When $h = 2$ mm, it can be seen that negligence of SCC generates larger localized errors than negligence of ACC due to the reasons which have been explained in the previous sections. The errors due to negligence of ACC is slightly larger than that due to negligence of SCC at some frequencies where plate modes are well coupled to dominant acoustic modes. When $h = 4$ mm, the number of well coupled acoustic and plate modes is small. In this case, the errors due to negligence of either ACC or SCC are smaller than that for $h = 2$ mm, regardless of whichever subsystem is directly excited. By comparing the case of direct sound field excitation to the case of direct plate excitation (for both $h = 2$ mm and $h = 4$ mm), it is evident from Fig. 6 that negligence of either

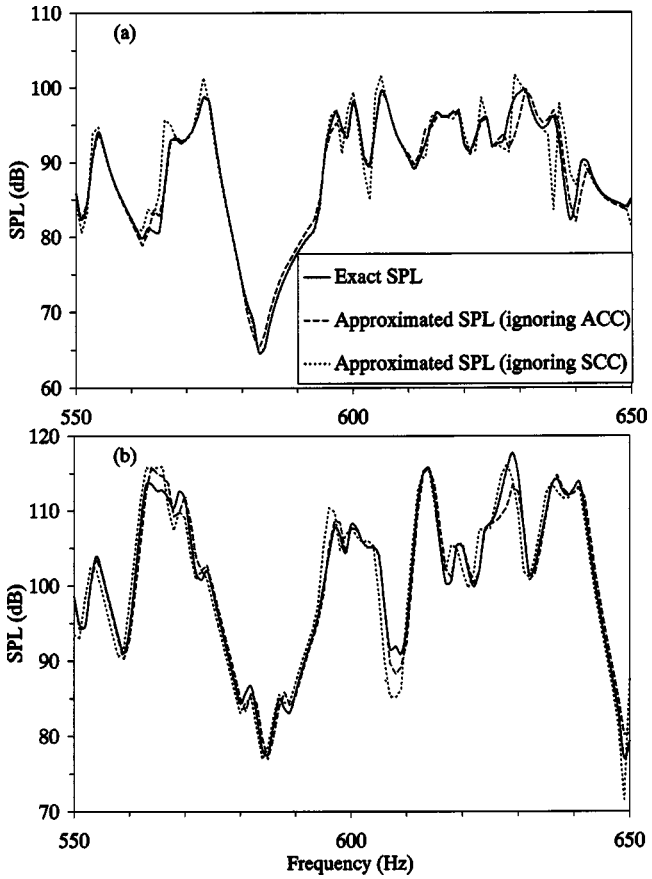

FIG. 8. Approximated SPLs when ACC or SCC is ignored and exact SPL, at (0.868, 1.150, 0.000) m in the cavity for $T_a=1.0$ s, $T_p=1.0$ s, and $h=2$ mm, for (a) direct sound field excitation, and (b) direct plate excitation.

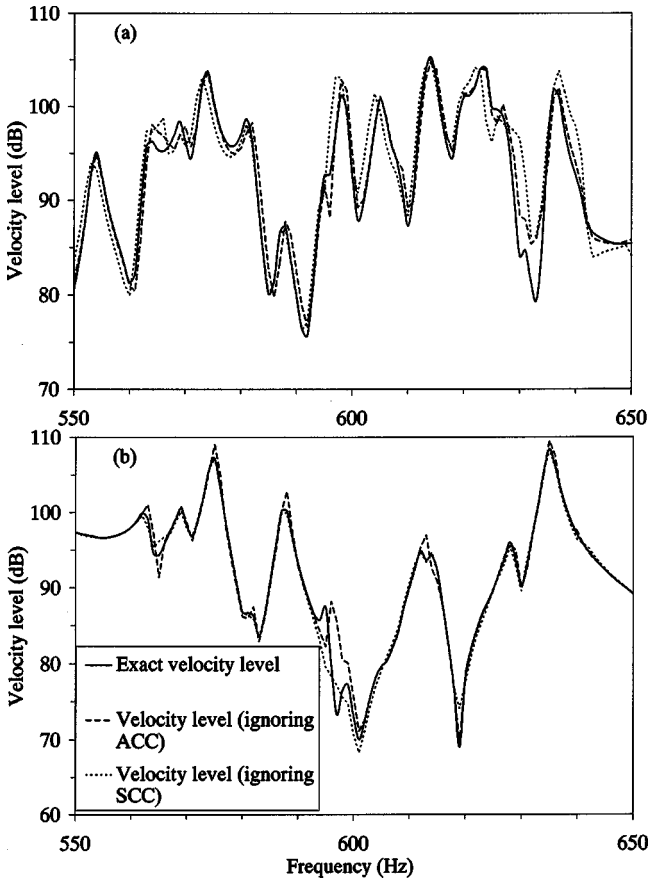

FIG. 9. Approximated velocity levels when ACC or SCC is ignored and exact velocity level, at (0.609, 0.881) m on the plate for $T_a=1.0$ s, $T_p=1.0$ s, and $h=2$ mm, for (a) direct sound field excitation, and (b) direct plate excitation.

ACC or SCC in the latter generally generates larger errors than the previous. This is because in the latter case, the plate modes contain most of the system's energy which increases their dominations to both ACC and SCC.

Figure 7 shows the errors in the plate velocity level for the same excitation and observation positions as used in Table III. In contrast to the SPL errors, it can be seen that the velocity errors in the case of direct sound field excitation are generally larger than that in the case of direct plate excitation because directly driven acoustic modes now contain most of the system's energy which increases their dominations to both ACC and SCC. Also, the negligence of ACC generates larger localized errors than the negligence of SCC. This is because the mechanism of ACC at resonance of various plate modes involves cross-couplings between acoustic modes through the plate modes, and therefore, ACC is mainly controlled by the properties of the plate modes as have been described in Sec. III A. Thus, the contribution of ACC to the plate response is large when it significantly depends on the responses of the plate modes which are large at their resonances. It can also be seen from Fig. 7 that the errors for $h=4$ mm are smaller than that for $h=2$ mm because of the small number of plate modes which are well-coupled with acoustic modes. However, while the errors are reduced at certain frequencies, they are increased at some other frequencies especially higher frequencies. This is because lower order plate modes are shifted to higher frequencies when the plate thickness is changed from 2 to 4 mm. These lower order plate modes have stronger spatial couplings with acoustic modes, and therefore, larger errors are generated at some higher frequencies when either ACC or SCC is ignored.

The corresponding exact and approximated SPLs which give rise to the errors shown in Fig. 6(a) and (b) are presented in Fig. 8 for frequency range 550–650 Hz. According to Sec. II, both ACC and SCC have effects on the apparent resonance frequencies and apparent modal loss factors of acoustic modes, regardless of whether the sound field or the plate is directly excited. Thus, the SPL errors generated from the negligence of either ACC or SCC can also be interpreted as the difference between the exact SPL where acoustical apparent resonance frequencies as well as loss factors of exact distributions are employed, and the approximated SPL where acoustical apparent resonance frequencies as well as loss factors of different distributions are employed. This difference is observed either as shifts in the locations of resonance peaks (due to a different distribution of apparent resonance frequencies), or higher or lower response of the peaks (due to a different distribution of apparent modal loss factors), or a combination of both. These are revealed in Fig. 8 by comparing the response magnitude at the peaks as well as the location of these peaks in the exact and approximate SPLs. The same phenomena can also be observed in the plate

TABLE V. 95% confidence limit for the population of absolute errors in SPL (dB), for frequency range 1–1000 Hz, $h=2$ mm and various combinations of excitation and observation positions in 40 plate-cavity systems of different dimensions.

		Neglect		Neglect		Neglect		Neglect		Neglect	
		ACC	SCC	ACC	SCC	ACC	SCC	ACC	SCC	ACC	SCC
(a) Direct sound field excitation											
T_p	100.0	**1.0**	*0.1*	**1.6**	*0.3*	**4.4**	*3.2*	**8.4**	*16.4*	**10.7**	*25.4*
	10.0	**1.0**	*0.1*	**1.5**	*0.2*	**3.4**	*3.1*	**6.4**	*15.8*	**8.2**	*24.6*
	1.0	**0.5**	*0.1*	**0.9**	*0.1*	**2.1**	*2.6*	**3.8**	*15.1*	**4.6**	*22.9*
	0.1	**0.1**	*0.1*	**0.6**	*0.1*	**1.2**	*1.9*	**2.4**	*14.7*	**3.0**	*20.4*
	0.01	**0.1**	*0.0*	**0.5**	*0.1*	**1.0**	*1.6*	**2.0**	*13.4*	**2.3**	*19.0*
		0.01		0.1		1.0		10.0		100.0	
		T_a									
(b) Direct plate excitation											
T_p	100.0	**8.4**	*0.6*	**8.8**	*1.3*	**10.8**	*4.9*	**13.2**	*13.4*	**14.3**	*18.6*
	10.0	**6.6**	*0.6*	**7.2**	*1.2*	**8.8**	*4.8*	**11.1**	*12.5*	**11.9**	*17.1*
	1.0	**2.7**	*0.5*	**3.0**	*1.1*	**4.0**	*4.3*	**4.7**	*10.5*	**5.0**	*14.5*
	0.1	**0.6**	*0.5*	**0.9**	*1.0*	**1.4**	*3.3*	**1.8**	*9.1*	**2.0**	*12.9*
	0.01	**0.2**	*0.1*	**0.8**	*0.6*	**1.5**	*2.9*	**1.8**	*8.2*	**1.9**	*12.0*
		0.01		0.1		1.0		10.0		100.0	
		T_a									

velocity level. These are revealed in Fig. 9 which shows the exact and approximated velocity levels that give rise to the errors in Fig. 7(a) and (b) for frequency range 550–650 Hz.

4. Effects of plate-cavity system properties on errors in the system responses

In the previous sections, physical features of ACC and SCC, and the effects of both cross-couplings on the sound field and plate responses have been shown for a plate-cavity system of fixed dimensions. For a plate-cavity system of different dimensions, the features of ACC and SCC, as well as the characteristics of errors due to the negligence of either cross-couplings, are still the same as before because the physical mechanisms which govern both cross-couplings have not changed. While the characteristics of both ACC and SCC do not change, the relative contributions of the cross-couplings to the system responses are different for each individual plate-cavity system of different dimensions. Thus, it is also desired to investigate the influence of dimensions of the plate-cavity system on the errors in the system responses when either ACC or SCC is neglected. However, since there are no scaling factors involved in the relative contributions of the cross-couplings with respect to any physical properties of the system including dampings, the trends and overall effects of ACC and SCC on the sound field and plate responses will be obtained. It is also not the aim of this paper to evaluate both cross-couplings for each particular application and therefore, all results are made more general in this section and are averaged/statistical quantities.

Absolute SPL errors (dB) at each discrete frequency of 1 Hz spacing in the frequency range 1–1000 Hz, are evaluated for various combinations of T_a and T_p extending over 4 decades from 0.01 to 100.0 s, and for 40 plate-cavity systems, each of different dimensions. Various combinations of excitation and observation positions are used for both cases of

TABLE VI. 95% confidence limit for the population of absolute errors in velocity level (dB), for frequency range 1–1000 Hz, $h=2$ mm and various combinations of excitation and observation positions in 40 plate-cavity systems of different dimensions.

		Neglect		Neglect		Neglect		Neglect		Neglect	
		ACC	SCC	ACC	SCC	ACC	SCC	ACC	SCC	ACC	SCC
(a) Direct sound field excitation											
T_p	100.0	**10.6**	*0.6*	**12.2**	*1.5*	**13.8**	*6.4*	**17.2**	*17.3*	**19.3**	*24.8*
	10.0	**8.2**	*0.6*	**9.1**	*1.4*	**10.5**	*6.2*	**12.7**	*16.4*	**13.7**	*23.6*
	1.0	**3.0**	*0.6*	**3.2**	*1.2*	**4.0**	*5.6*	**4.4**	*14.5*	**4.5**	*21.0*
	0.1	**0.6**	*0.4*	**0.5**	*1.0*	**0.6**	*5.2*	**0.8**	*13.0*	**0.9**	*19.3*
	0.01	**0.2**	*0.1*	**0.2**	*0.6*	**0.3**	*4.1*	**0.5**	*12.2*	**0.5**	*18.4*
		0.01		0.1		1.0		10.0		100.0	
		T_a									
(b) Direct plate excitation											
T_p	100.0	**18.2**	*0.7*	**20.7**	*1.5*	**23.1**	*4.3*	**24.8**	*10.5*	**25.7**	*13.7*
	10.0	**13.0**	*0.7*	**15.4**	*1.4*	**16.8**	*3.8*	**17.6**	*8.8*	**18.0**	*11.8*
	1.0	**2.2**	*0.4*	**2.6**	*0.8*	**3.1**	*2.1*	**3.6**	*4.8*	**3.7**	*6.8*
	0.1	**0.0**	*0.2*	**0.1**	*0.4*	**0.1**	*0.9*	**0.2**	*2.1*	**0.1**	*2.9*
	0.01	**0.0**	*0.3*	**0.1**	*0.6*	**0.2**	*1.2*	**0.2**	*2.4*	**0.2**	*3.8*
		0.01		0.1		1.0		10.0		100.0	
		T_a									

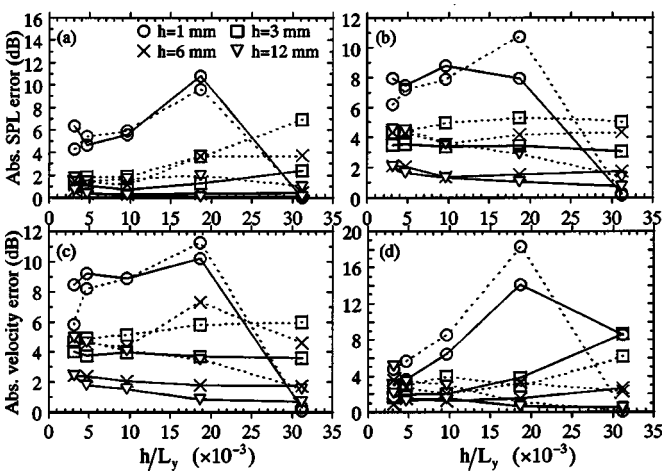

FIG. 10. 95% confidence limits for the population of absolute SPL errors and the population of absolute errors in velocity level, as a function of the plate slenderness ratio, for frequency range 1–1000 Hz, $T_a = T_p = 1.0$ s, $L_x = 1.302$ m, $L_z = 1.0$ m, and various combinations of excitation and observation positions (dotted lines—negligence of ACC, solid lines—negligence of SCC).

direct sound field and direct plate excitations, and all results are gathered to obtain a large population of SPL errors for each combination of T_a and T_p. The 95% confidence limit for the population is then obtained for each combination, and it is defined as the bound within which 95% of the error populations lie. The results are shown in Table V for the case of direct sound field excitation and the case of direct plate excitation, for some selected 25 combinations of T_a and T_p. It is evident that the SPL error associated with the negligence of ACC changes significantly with T_p as the relative contribution of ACC is mainly controlled by the properties of plate modes, whereas the SPL error associated with the negligence of SCC changes significantly with T_a as the relative contribution of SCC is mainly controlled by the properties of acoustic modes. This result is consistent with the mechanisms of ACC and SCC described earlier on, and further

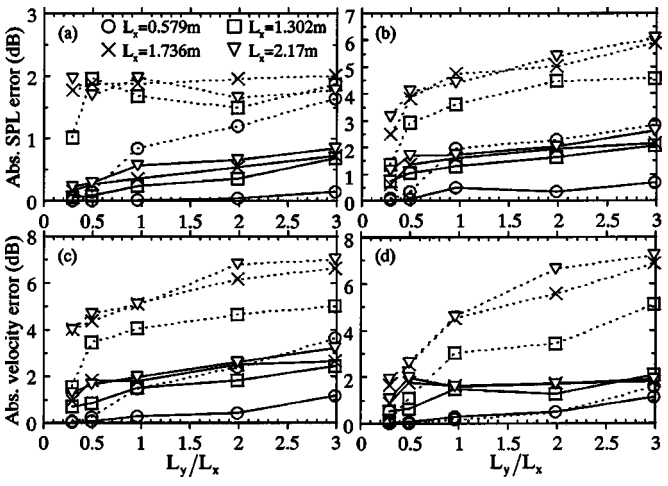

FIG. 11. 95% confidence limits for the population of absolute SPL errors and the population of absolute errors in velocity level, as a function of the cavity aspect ratio, for frequency range 1–1000 Hz, $T_a = T_p = 1.0$ s, $h = 12$ mm, $L_z = 1.0$ m, and various combinations of excitation and observation positions (dotted lines—negligence of ACC, solid lines—negligence of SCC).

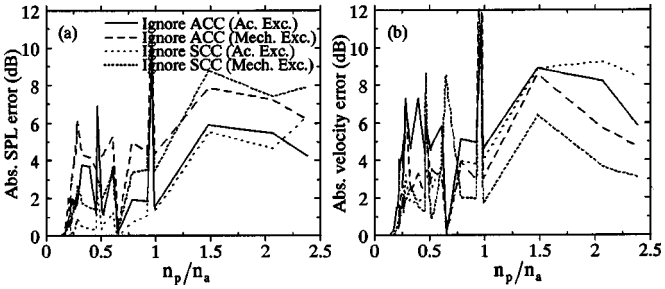

FIG. 12. 95% confidence limits for the population of absolute SPL errors and the population of absolute errors in velocity level, as a function of the ratio of modal densities of the plate and the cavity, for frequency range 1–1000 Hz, $T_a = T_p = 1.0$ s, $L_z = 1.0$ m, and various combinations of excitation and observation positions.

justifies the characteristics of errors obtained in the previous sections. It can also be seen from Table V that the SPL errors generated from ignoring either ACC or SCC are unacceptably large (i.e., >3 dB) when either T_a or T_p is in the order of 1.0 s or more. All observations for the SPL errors are also similar for the plate response whose 95% confidence limits for the populations of absolute errors in the velocity level (dB) are shown in Table VI. In general, negligence of ACC in the prediction of the sound field and plate responses is more favorable than negligence of SCC if $T_a \gg T_p$ and vice versa. It should be noted that there are no consistent trends of the characteristics of the errors with the ratio of decay times (i.e., either T_p/T_a or T_a/T_p) because the errors are dependent on individual decay times. In addition, some combinations of different T_a and T_p can give the same ratio of decay times (e.g., $T_a = T_p = 100.0$ s gives the same ratio as $T_a = T_p = 0.01$ s).

It is also of great interest to investigate the characteristics of the errors for some widely used dimensionless parameters such as the slenderness ratio of the plate (i.e., h/L_y) and the aspect ratio of the cavity (i.e., L_y/L_x). Absolute SPL and velocity errors are also evaluated for the frequency range 1–1000 Hz and the 95% confidence limits for the populations of errors are obtained. The results for some selected 20 combinations of h and L_y are shown in Fig. 10 for the case of the slenderness ratio of the plate. For the case of the aspect ratio of the cavity, the results for some selected 20 combinations of L_x and L_y are shown in Fig. 11. Similar excitation and observation conditions used in Tables V and VI are used. Other conditions used are shown in the captions of the figures. Figure 10 shows that the errors in both the sound field and plate responses slowly vary with the slenderness ratio except for the case of a thin plate (e.g., $h = 1$ mm). The trends of the errors with the ratio are not obvious but it can be seen that larger errors are generated for thinner plates. The trends of the errors in Fig. 11 are evidently increasing with the aspect ratio and larger errors are generated for larger dimensions of L_x. However, similar to the case of modal decay times, it can be seen from Figs. 10 and 11 that the errors in both the sound field and plate responses are largely differed for different combinations of h, L_x, and L_y even though the combinations give the same slenderness ratio, or the same aspect ratio. Thus, there are no obvious indications of the order of magnitude of the errors for a given slender-

ness ratio or aspect ratio. The results in Figs. 10 and 11 have been rearranged in terms of the modal densities of the sound field (n_a) and the plate which are functions of the dimensions of the system. These are shown in Fig. 12. It can be seen that the trends of the errors are increasing with n_p/n_a although individual results vary. The errors are unacceptably and consistently large for large n_p/n_a (i.e., either a large n_p or a small n_a or both), regardless of whether ACC or SCC is ignored, or whether the sound field or the plate is directly excited. This is because when n_p is large (e.g., thin or large plate), there are a large number of plate modes which are well-coupled to acoustic modes, and when n_a is small (e.g., small or shallow cavity), low order acoustic modes are distributed towards the medium and high frequency ranges. The sudden increase in errors at around the unity ratio is an example of the latter case for a very shallow cavity. These observations are consistent with the conclusions obtained by Pretlove[20] earlier on.

Effects of the ratio of wavelength to cavity depth (i.e., λ/L_z where $\lambda=2\pi c_0/\omega$) on the characteristics of errors are also investigated. Figure 13 shows the averaged errors in the SPL and the velocity level in frequency bands of 40 Hz bandwidth, for the frequency range 1–1000 Hz and four different cavity depths. The conditions of excitation and observation are the same as those used in Tables V and VI. It is evident that in the low frequency range where $\lambda/L_z \gg 1$, the errors are much larger than that in the medium and high frequency ranges because of the presence of low order mode couplings. Due to the same reason also, larger errors are observed for a shallower cavity (e.g., $L_z=0.3$ m).

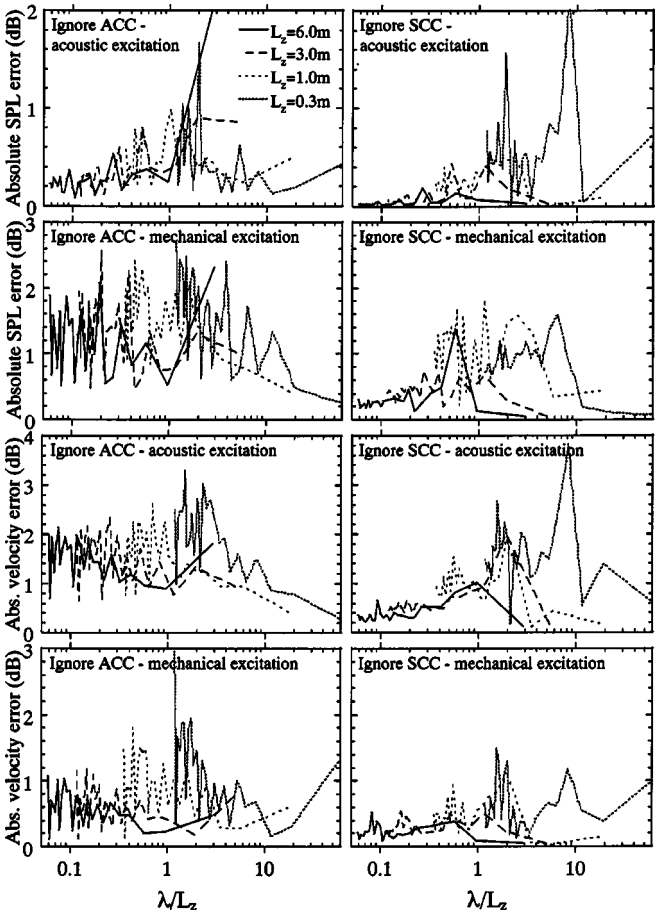

FIG. 13. Absolute SPL errors and absolute errors in velocity level, averaged in 40 Hz frequency bands, as a function of the ratio of wavelength to the cavity depth, for frequency range 1–1000 Hz, $T_a=T_p=1.0$ s, $h=4$ mm, $L_x=0.868$ m, $L_y=1.15$ m, and various combinations of excitation and observation positions.

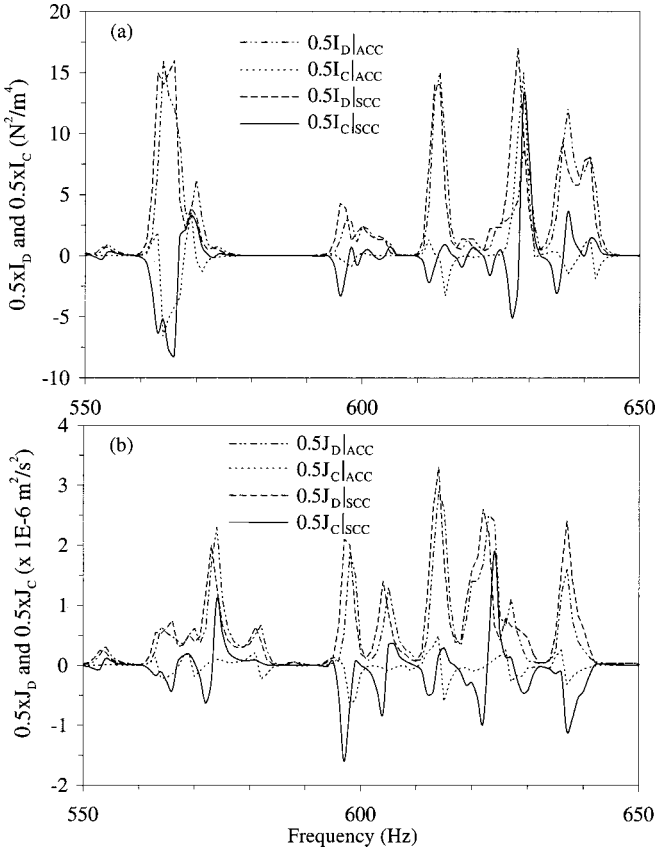

FIG. 14. (a) $0.5I_D$ and $0.5I_C$ at (0.868, 1.150, 0.000) m in the cavity for direct plate excitation at (0.152, 0.448) m, and (b) $0.5J_D$ and $0.5J_C$ at (0.609, 0.881) m on the plate for direct sound field excitation at (0.0, 0.0, 0.0) m, for $T_a=1.0$ s, $T_p=1.0$ s, and $h=2$ mm.

C. Effect of frequency and/or space averaging

Frequency band-limited sound pressure and velocity have some practical importance when the sound field or the plate in the plate-cavity system is directly excited by a band of noise. Therefore, effect of frequency averaging on the cross-coupling contribution (either ACC or SCC) to the system responses is studied. Figure 14(a) shows the direct coupling/excitation components ($0.5I_D|_{\mathrm{ACC}}$ and $0.5I_D|_{\mathrm{SCC}}$) and the cross-coupling components ($0.5I_C|_{\mathrm{ACC}}$ and $0.5I_C|_{\mathrm{SCC}}$) of the sound field response. The case of direct plate excitation is illustrated here for the same conditions used in Fig. 6(b). These components have been derived and explained in Sec. I B. Each peak or trough in the figure corresponds to one system mode (either an acoustic or a plate mode). The peaks or troughs may overlap if the resonance frequencies of the system modes are close to each other. It can be seen that the direct coupling/excitation components are always positive while the cross-coupling components can be either positive or negative. Thus, when the sound pressure is averaged over a frequency band $\Delta\omega$ which contains sev-

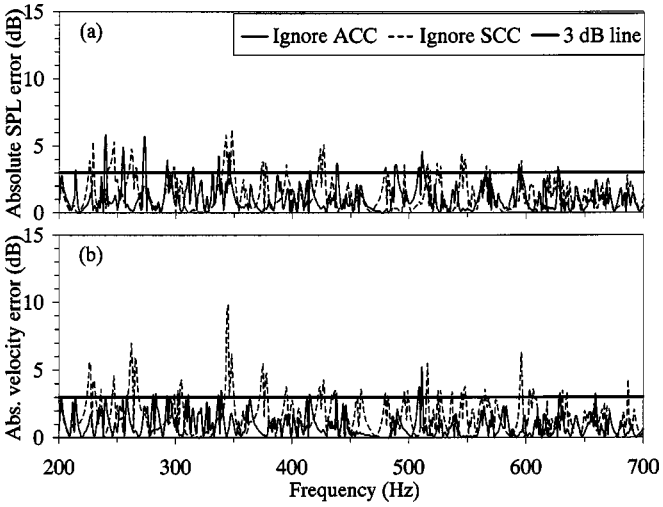

FIG. 15. Absolute error in (a) space-averaged SPL in the cavity [direct plate excitation at (0.152, 0.448) m], and (b) space-averaged velocity level of the plate [direct sound field excitation at (0.0, 0.0, 0.0) m], for $T_a = 1.0$ s, $T_p = 1.0$ s, and $h = 2$ mm.

eral system modes, the positive and negative contributions from individual modes in $0.5I_C|_{\mathrm{ACC}}$ and $0.5I_C|_{\mathrm{SCC}}$ may destructively superimpose. The similar features are also shown in the plate response where the cross-coupling components ($0.5J_C|_{\mathrm{ACC}}$ and $0.5J_C|_{\mathrm{SCC}}$) can be either positive or negative [see Fig. 14(b)—the case of direct sound field excitation is shown here for the same conditions used in Fig. 7(a)]. These positive and negative contributions may also destructively superimpose if the contributions are averaged over a frequency band. Thus, large localized errors such as that for pure tone excitations are reduced for band-limited excitations. Hence, the errors generated from ignoring either ACC or SCC in the prediction of the band-limited sound field and plate responses are generally smaller [for example, compare the results in Figs. 6(c) and (d), as well as 7(c) and (d), to the results in Fig. 13].

In practice, averaged quantities such as space-averaged sound pressure and space-averaged velocity are also important because they are, respectively, related to the acoustic energy of the sound field and vibration energy of the plate. Similar to the case of band-limited responses in the above, $0.5I_C|_{\mathrm{ACC}}$ and $0.5I_C|_{\mathrm{SCC}}$, and, $0.5J_C|_{\mathrm{ACC}}$ and $0.5J_C|_{\mathrm{SCC}}$, respectively, can also be either positive or negative at different locations in the sound field and on the plate. Thus, when the sound pressure is space-averaged over V_0 and the velocity is space-averaged over A_s, the errors incurred when either ACC or SCC is ignored, are generally reduced. For example, the reduction in errors is evident when comparing Fig. 15(a) which shows the errors in the space-averaged SPL (direct plate excitation) to Fig. 6(b), and Fig. 15(b) which shows the errors in the space-averaged velocity level (direct sound field excitation) to Fig. 7(a), under the same conditions.

IV. CONCLUSIONS

This paper has described two different types of modal cross-couplings in plate-cavity systems, namely acoustic modal cross-coupling (ACC) and structural modal cross-coupling (SCC). Negligence of ACC can be interpreted as different redistributions (i.e., drift away from the exact redistributions) of uncoupled resonance frequencies and uncoupled modal decay times of acoustic modes. Whereas in the case of the structure, it means that uncoupled resonance frequencies and uncoupled modal decay times of structural modes are not redistributed at all. On the other hand, negligence of SCC means that there are no redistributions for the acoustic modes but different redistributions for the structural modes. The mechanisms and physical features of both cross-couplings have been investigated. The effects of ACC and SCC on the sound field and plate responses of the system can be realized in terms of the errors in the responses when either of the cross-couplings is neglected in the prediction of those responses. The characteristics of the errors under different physical properties of the system can be obtained from the understanding of the physical mechanisms and behaviors of ACC and SCC. The errors due to the negligence of ACC significantly changes with the plate modal decay time as the relative contribution of ACC is mainly controlled by the properties of plate modes, whereas the errors due to the negligence of SCC significantly changes with the acoustic modal decay time as the relative contribution of SCC is mainly controlled by the properties of acoustic modes. The errors are generally increased with the increase in the modal decay times. When acoustic and plate modes are well-coupled in terms of proximity of resonance frequencies, the errors are generally larger than that in the case where the well-coupled condition is not satisfied. However, it is not necessary for low order acoustic or plate modes to satisfy this condition because these modes have larger spatial coupling factors. Therefore, the errors in the low frequency range where the ratio of wavelength to cavity depth is much greater than unity, are much larger than that in the medium and high frequency ranges. Some general criteria have been obtained since there are no scaling factors involved in the errors with respect to the physical properties of the system. For a point excitation, regardless of whether the excitation is pure tone or a band of noise, and regardless of whether the sound field or the plate is directly excited, the errors incurred when either ACC or SCC is neglected, are generally acceptable (i.e., generally <3 dB) when the acoustic and plate modal decay times are in the order of 1.0 s or less, and the ratio of plate to sound field modal densities is much less than unity. If the acoustic modal decay time is much greater than the plate modal decay time, then negligence of ACC is generally more favorable than negligence of SCC in the prediction of both the sound field and plate responses (either direct sound field or direct plate excitation). However, if the plate modal decay time is much larger than the acoustic modal decay time, then negligence of SCC is more favorable. Prediction errors in the system responses which are associated with the negligence of the cross-couplings are generally reduced when the sound field response is averaged over the cavity volume and the plate response is averaged over the plate surface area, and/or when the responses are averaged over a frequency bandwidth for a band excitation. This study will hopefully improve understanding into the mechanisms and the behaviors of cross-couplings in vibroacoustic systems with air-structural coupling and be useful to the field of structural-acoustics.

[1] H. G. Davies, ''Low frequency random excitation of water-loaded rectangular plates,'' J. Sound Vib. **15**, 107–126 (1971).
[2] R. A. Mkhitarov, ''Interaction of the vibrational modes of a thin bounded plate in a liquid,'' Sov. Phys. Acoust. **18**, 123–126 (1972).
[3] L. D. Pope and R. C. Leibowitz, ''Intermodal coupling coefficient for a fluid-loaded rectangular plate,'' J. Acoust. Soc. Am. **56**, 408–415 (1974).
[4] R. F. Keltie and H. Peng, ''The effects of modal coupling on the acoustic power radiation from panels,'' J. Vib. Acoust. Stress Rel. Design **109**, 48–54 (1987).
[5] K. A. Cunefare, ''Effect of modal interaction on sound radiation from vibrating structures,'' AIAA J. **30**, 2819–2828 (1992).
[6] J. E. Farstad, M. R. Lee, and R. Singh, ''Analysis of structure-borne and radiated sound using component modal bases,'' Appl. Acoust. **43**, 217–246 (1994).
[7] Y. A. Gurovich, ''Low-frequency acoustic reduction of a rectangular panel,'' Sov. Phys. Acoust. **24**, 289–292 (1979).
[8] E. H. Dowell, ''Reverberation time, absorption, and impedance,'' J. Acoust. Soc. Am. **64**, 181–191 (1978).
[9] Y. Kubota and E. H. Dowell, ''Asymptotic modal analysis for sound fields of a reverberant chamber,'' J. Acoust. Soc. Am. **92**, 1106–1112 (1992).
[10] L. P. Franzoni and E. H. Dowell, ''On the accuracy of modal analysis in reverberant acoustical systems with damping,'' J. Acoust. Soc. Am. **97**, 687–690 (1995).
[11] J. Pan, ''A second note on the prediction of sound intensity,'' J. Acoust. Soc. Am. **97**, 691–694 (1995).
[12] L. P. Franzoni and D. B. Bliss, ''A discussion of modal uncoupling and an approximate closed-form solution for weakly-coupled systems with application to acoustics,'' J. Acoust. Soc. Am. **103**, 1923–1932 (1998).
[13] L. D. Pope, ''On the transmission of sound through finite closed shells: statistical energy analysis, modal coupling, and nonresonant transmission,'' J. Acoust. Soc. Am. **50**, 1004–1018 (1971).
[14] R. W. Guy and M. C. Bhattacharya, ''The transmission of sound through a cavity-backed finite plate,'' J. Sound Vib. **27**, 207–223 (1973).
[15] E. H. Dowell, G. F. Gorman, and D. A. Smith, ''Acoustoelasticity: general theory, acoustic natural modes and forced response to sinusoidal excitation, including comparisons with experiment,'' J. Sound Vib. **52**, 519–542 (1977).
[16] L. D. Pope and J. F. Wilby, ''Band-limited power flow into enclosures,'' J. Acoust. Soc. Am. **62**, 906–911 (1977).
[17] W. B. McDonald, R. Vaicaitis, and M. K. Myers, ''Noise transmission through plates into an enclosure,'' NASA Tech. Paper No. 1173, NASA (1978).
[18] Y. Kubota, H. D. Dionne, and E. H. Dowell, ''Asymptotic modal analysis and statistical energy analysis of an acoustic cavity,'' J. Vib. Acoust. Stress Rel. Design, **110**, 371–376 (1988).
[19] J. L. Guyader and B. Laulagnet, ''Structural acoustic radiation prediction: expanding the vibratory response on a functional basis,'' Appl. Acoust. **43**, 247–269 (1994).
[20] A. J. Pretlove, ''Free vibrations of a rectangular panel backed by a closed rectangular cavity,'' J. Sound Vib. **2**, 197–209 (1965).
[21] D. E. Newland, ''Calculation of power flow between coupled oscillators,'' J. Sound Vib. **3**, 262–276 (1966).
[22] D. E. Newland, ''Power flow between a class of coupled oscillators,'' J. Acoust. Soc. Am. **43**, 553–559 (1968).
[23] K. S. Sum and J. Pan, ''An analytical model for band-limited response of acoustic-structural coupled systems. I. Direct sound field excitation,'' J. Acoust. Soc. Am. **103**, 911–923 (1998).
[24] J. Pan, ''The forced response of an acoustic-structural coupled system,'' J. Acoust. Soc. Am. **91**, 949–956 (1992).
[25] F. J. Fahy, ''Vibration of containing structures by sound in the contained fluid,'' J. Sound Vib. **10**, 490–512 (1969).
[26] F. J. Fahy, ''Response of a cylinder to random sound in the contained fluid,'' J. Sound Vib. **13**, 171–194 (1970).
[27] J. Pan and D. A. Bies, ''The effect of fluid-structural coupling on sound waves in an enclosure—Theoretical part,'' J. Acoust. Soc. Am. **87**, 691–707 (1990).
[28] F. J. Fahy, ''Energy flow between oscillators: special case of point excitation,'' J. Sound Vib. **11**, 481–483 (1970).

Experimental results for multichannel feedforward ANC with noninvasive system identification

William C. Nowlin,[a] Gary S. Guthart, and Gregory K. Toth
SRI International, 333 Ravenswood Avenue, Menlo Park, California 94025

(Received 23 April 1997; accepted for publication 3 December 1999)

This paper presents experimental validation of a class of algorithms designed to enable active noise control (ANC) to function in environments when transfer functions change significantly over time. The experimental results presented are for broadband, local quieting in a diffuse field using a multichannel ANC system. The reverberant enclosure is an ordinary room, measuring approximately $1.4\times2.4\times2.4\,m^3$ and containing a seated occupant, with six microphones defining the quiet zone near the occupant's ears. The control system uses a single reference signal and two error channels to drive four secondary sources. Using an ideal reference sensor, reduction in sound pressure level is obtained at the quiet-zone microphones averaged over the frequency range 50 to 1000 Hz with an occupant seated in the room. Two main results are presented: first for an adaptive cancelling algorithm that uses static system models, and second for the same algorithm joined with a noninvasive real-time system identification algorithm. In the first case better than 23 dB of performance is obtained if the occupant remains still through calibration and testing. In the second case, approximately 18 dB is obtained at the error microphones regardless of the motion of the occupant. © *2000 Acoustical Society of America.* [S0001-4966(00)00404-5]

PACS numbers: 43.40.Vn [PJR]

INTRODUCTION

Active control of sound in a reverberant space such as the cabin of a vehicle has long been an area of research.[1–5] The engineering problems that must be overcome to build a realistic active noise control (ANC) system, however, are daunting. Of particular interest is the challenge of varying system dynamics and transfer functions in a broadband system, such as an occupant of a vehicle cabin opening a window or changing position.

Research concerning active noise control in enclosures has proceeded along two paths. The first avenue of research has been the study of harmonic noise sources. Much progress has been reported in controlling noise in enclosures that is produced by sources generating tones or a small set of harmonics.[4,6–8] Applications of this research include quieting of repetitive engine noise in automobiles.[2] The second path is the control of random, broadband noise in an enclosure. Achievements in the control of random noise in reverberant enclosures have been fewer because of the increased difficulty in controlling random noise. Theoretical aspects of noise control in enclosures have been analyzed by several authors.[3,4,9–11] Laugesen and Elliott demonstrated success in global control of noise throughout a small room using an adaptive infinite impulse response (IIR) filter for frequencies up to approximately 200 Hz. Local control of noise in an enclosure using an H_∞ control objective has been shown for a single monitor sensor by Yang *et al.*[12] Multiple channel control using an adaptive algorithm for noise control in a small duct up to 400 Hz has been shown by Melton and Greiner.[13] In both cases (harmonic and broadband noise), an accurate model of mode shapes and responses or transfer functions is required.

The objective of this work is to investigate experimentally the feasibility of creating a locally quiet region across a broad band of frequencies in a reverberant enclosure that is large enough to contain a person. The control system is intended to produce a quiet zone of sufficient size to enclose a person's ears for a limited range of head motion over a frequency range of practical interest. Further, we wish to design and test a system that calibrates its internal model of system transfer functions automatically and continually, so that system performance accommodates changing environmental conditions robustly without manual recalibration. Applications include quieting the driver's position of a vehicle or quieting an operator's workspace near a machine.

Measurements of actual noise in vehicle cabins and in the presence of machines show that the frequency range of unwanted noise extends to at least 1 kHz. In an enclosure big enough to surround a person, these sources are capable of exciting hundreds of room modes. The presence of so many excited modes makes the global control of these frequencies infeasible when the secondary sources are not coincident with the unwanted noise source. However, targeting a particular location of the enclosure to quiet enables the operating frequency of a control system to be increased significantly given a fixed number of control speakers and quiet-zone microphones. Of course, in some regions of the enclosure outside the quiet zone, the noise will be enhanced by the control system. Since the control objective is that of *local* control in the quiet zone, enhancement elsewhere in the enclosure is not penalized. Applications of this kind of local control include single-operator environments, such as truck cabins, where an operator in a known location is exposed to high levels of noise over long periods of time. In this work, we demonstrate the feasibility of active noise control in re-

[a]Current address: Intuitive Surgical, Inc., 1340 W. Middlefield Rd., Mountain View, CA 94043.

verberant enclosures by creating a quiet zone that attenuates random noise in the frequency range from 50 Hz to 1 kHz.

The experimental results we present in this paper are divided into two parts. The first provides a baseline performance of a statically calibrated multichannel adaptive ANC system. The novel contribution in this work is the experimental demonstration of active noise control in a reverberant room large enough to contain an operator when the unwanted noise is random and the controller attenuates noise to 1 kHz. The combination of a moderately sized room and a high-frequency range forces us to control a rich dynamical system in which hundreds of room modes are present. We use proven control algorithms and custom hardware designed specifically for real-time active control to demonstrate the feasibility of active noise control for rooms and frequency ranges of practical interest.

The second experimental result validates a new class of algorithms, introduced in our companion paper,[14] that add noninvasive system identification to the first system. These algorithms extend the work of Sommerfeldt[5,15] and are closely related to those developed by Montazeri and Duhamel[16,17] and others summarized by Morgan and Kratzer.[18] By experimentally validating these algorithms, we can demonstrate the ability to overcome identification errors that might otherwise result in poor performance, enhancement, or instability in statically calibrated systems. The experimental setup is identical to that of the previous paragraph, and we believe represents a first demonstration of real-time, multi-input, multi-output, noninvasive broadband system identification combined with control.

In both experiments, we address the feedforward control problem: the reference signal used by the controller is chosen to be uncoupled from the output of the control drivers. We chose a feedforward control arrangement for the simplicity with which we can vary the propagation path from the reference signal to the quiet zone. Further, acoustically uncoupled reference signals may be found in applications. For example, accelerometers or engine tachometers are reference signals that are often uncoupled from the control drivers. Control of ANC systems having nonzero coupling has been achieved here and elsewhere using *Q*-parametrized controllers (otherwise known as neutralized-feedforward control or Youla parametrization[19]). The use of *Q*-parametrization enables the formation of a natural link between feedforward systems and feedback systems, as the parametrization of the latter makes it formally appear as the former. It is thus possible to ask whether the algorithms tested here are applicable in the feedback case as well.

I. SYSTEM DESIGN

The experiments take place in an ordinary rectangular room measuring 1.4 m wide by 2.4 m long by 2.4 m high. The room is finished with textured gypsum drywall, low-nap floor carpeting, and has exposed pipes and ducts in the ceiling. Figure 1 shows a schematic of the experimental apparatus and mirrors the block diagram structure of the control system shown in Fig. 2. The room contains a seated operator surrounded by six error microphones that are arrayed about the operator's head at roughly ear-level. The three microphones on either side of the operator's head are electrically summed into two error channels, one corresponding to each ear, to improve the signal-to-noise ratio (SNR). Also surrounding the operator are four control drivers (loudspeakers). At the rear of the room is a fifth speaker, the unwanted noise source.

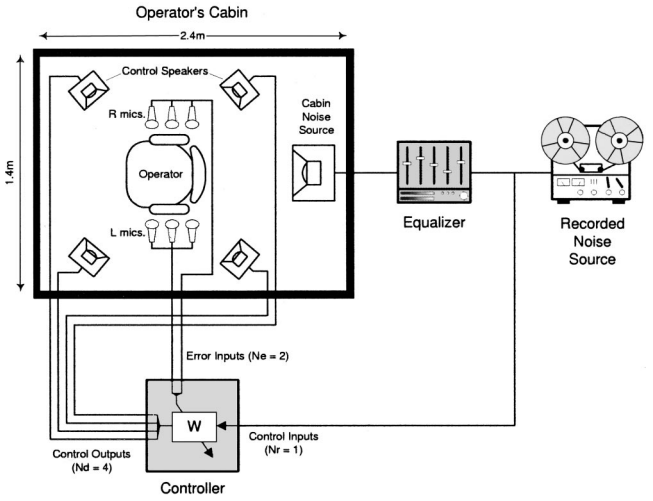

FIG. 1. System schematic. The position of the ''operator,'' or room occupant, defines the zone where sound pressure should be reduced.

Unwanted noise is provided by a digital tape recorder playing nonstationary engine noise recorded inside a vehicle cabin. The output of the digital tape recorder is split into a reference signal that is sent to the controller and a source signal that is passed to a graphic equalizer. The output of the equalizer is then sent to the source speaker in the room. We use the equalizer in the source path after the reference signal so that we can simulate changes in the propagation path of the source signal relative to the reference signal. For example, if the reference signal is obtained by measuring noise inside an engine compartment, the equalizer may be used to simulate the transfer function resulting from transmission loss through an open or closed door and into an operator cabin. The control hardware used for the experiment is an extension of the real-time, multichannel digital signal processor (DSP) developed by Weeks *et al.*[20,21]

The choice of control drivers, error channels, and microphones is motivated as follows. We chose two error channels because of computational constraints in our real-time controller. Each error channel is composed of three quiet-zone microphones arrayed on each side of the operator's head and summed into a single channel; one for the right side of the

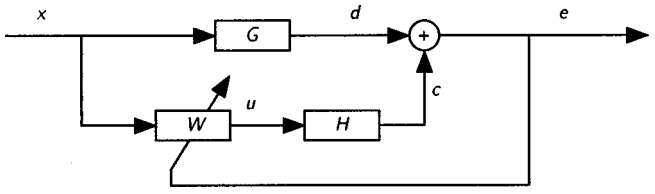

FIG. 2. Common representation of adaptive feedforward control system. The exogenous input is *x*, the error quantity is *e*, and *u* is the controller output. The signal *d* is what we desire to cancel, and *c* is the cancelling signal. The open-loop transfer function is *G*, and the actuator transfer function is *H*. The controller is *W*.

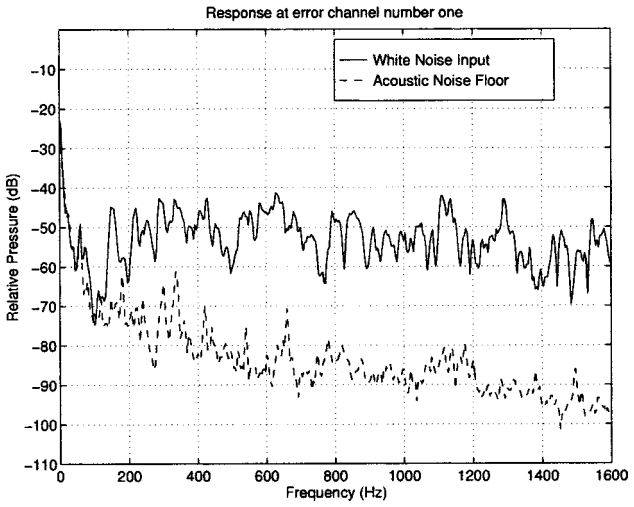

FIG. 3. Response at a quiet-zone microphone to white noise output from the source speaker. Also shown is the noise floor for the combination of the room acoustics and the measurement electronics.

operator's head (labeled ''A'') and one for the left (''B''). Three microphones were summed into each error channel to increase the signal-to-noise ratio and to shape the quiet zone at frequencies at the high end of the control band, near 1 kHz. For frequencies near the low end of the control band, the summed microphones form a nearly omni-directional array.

At first glance, the use of four control drivers appears to make the solution for the controller underdetermined. However, unlike the case of single frequency control (control of harmonics), the solution for the optimal control weights given known transfer functions is well conditioned in the case of broadband control. This can be motivated by two observations. First, each control driver has nulls at the error channels as a function of frequency, so that at a given frequency, some drivers have better access to a given error channel than others. Second, the constraint of causality of the controller weights links the optimal control weights across frequencies. As a check, the condition of the inverse problem for solving for optimal control weights given known transfer functions can be evaluated numerically, and demonstrates that the formulation for the broadband control weights given four control drivers and two error channels is well conditioned and that the condition improves as more control drivers are added. A detailed analysis of the condition number of the inverse problem for the control weights is possible but is beyond the scope of the present work. Lastly, the use of a Tikhanov factor in the solution for the weights, described in the companion paper, penalizes rms energy in the control weights, further improving the condition of the inverse problem.

As a test of the room dynamics, white noise is sent to the source speaker and is recorded at one of the quiet-zone microphones. The resulting power spectral density for the microphone signal is shown in Fig. 3. Notice that there are few room resonances below 200 Hz and that the density of resonances increases dramatically as frequency increases towards 1 kHz. For completeness, Fig. 3 also shows the power spectral density for one of the quiet-zone microphones when no input is given to any of the drivers, thus establishing the noise floor for the room acoustics and measurement electronics.

Figure 2 shows a block diagram of the control system. Output from the two quiet-zone error channels is sampled by the controller along with the reference signal from the tape recorder output. The controller generates a vector of voltages to drive the four control drivers at each clock cycle. Our controller uses finite-impulse-response (FIR) representations of both the speaker-to-quiet-zone transfer functions and the control weights.

The control algorithm used in both experiments is a multichannel filtered-X least-mean squares (FXLMS) adaptive algorithm for identification of the control weights. We choose this control algorithm for its relative simplicity in implementation, recognizing that other algorithms may be appropriate for various applications (e.g., normalization when the statistics of the reference signal are unknown). The FXLMS algorithm developed by Widrow *et al.*[22] and applied to active-noise control by Burgess[23] has been studied by several authors. The multichannel form of the algorithm is described by Douglas and Olkin.[24] We refer the reader to their work for a detailed description of the multichannel FXLMS algorithm, its convergence properties, and computational complexity. We make use of the block-update algorithm described in the companion paper (and summarized here in Table I) for identification of the transfer functions from the reference input to the quiet-zone microphones and identification of the transfer functions from the control drivers to the quiet-zone microphones. We explicitly vary the propagation path from the reference input signal to the quiet-zone error channels. Other than initial convergence, we do not explicitly vary the transfer functions from the control drivers to the quiet-zone microphones.

If we now adopt the same notation as in the companion paper, ρ indexes reference sensors, of which there is one in this experiment. Likewise, δ indexes drivers, of which there are four. Finally, ϵ indexes error sensors, of which there are two. (The subscripts are chosen to be spelled with the same first letter as the objects they index: ''rho'' and ''reference sensor,'' ''delta'' and ''driver,'' and ''epsilon'' and ''error sensor.'') The plant transfer functions, measuring the dynamics from each of the secondary drivers to each of the two error microphones, are represented as FIRs written as $h_{\epsilon,\delta}$. Because the plant has multiple inputs and outputs, we find it convenient to represent it as a matrix transfer function, with one scalar transfer function for every input–output pair: $\mathbf{H}=\{h_{\epsilon,\delta}\}_{\forall\epsilon,\delta}$. Each scalar FIR in $\mathbf{H}$ is of length L_h.

Plant transfer function models are obtained in our experiments by one of two methods: calibration using numerical deconvolution, or on-line system identification. To calibrate the plant model directly, the sequences $h_{\epsilon,\delta}$ are experimentally determined by driving the δth driver with a known pseudorandom sequence from the controller and measuring the response at the ϵth error channel of the controller with all other drivers still. By using the controller to drive the sequence and measure the error output, we identify the combined electrical and acoustical transfer path from the controller voltage output to the controller error input. We

TABLE I. Summary of important variables developed in Ref. 14 and used in the text. Scalars are set in italics. Lowercase bold Roman letters represent vectors as a function of time. Uppercase bold Roman letters represent matrix transfer functions, matrices of multivariable histories, and block collections of histories and transfer functions.

Variable	Dimensions	Definition
		Vector signals of time
$\mathbf{x}$	$N_r \times \langle time \rangle$	Input source signal of infinite duration
$\mathbf{u}$	$N_d \times \langle time \rangle$	Controller output: $u_\delta(k) = \Sigma_{\rho=1}^{N_r} (\mathbf{X}_\rho^k)^T (w_{\delta,\rho}^k)$
$\mathbf{d}$	$N_e \times \langle time \rangle$	Desired signal to cancel: $\mathbf{d}(k) = (\mathbf{x}*)\mathbf{G})(k)$
$\mathbf{c}$	$N_e \times \langle time \rangle$	Cancelling signals: $c_\epsilon(k) = \Sigma_{\delta=1}^{N_d} (\mathbf{U}_\delta^k)^T (h_{\epsilon,\delta})$
$\mathbf{e}$	$N_e \times \langle time \rangle$	Cancellation error: $\mathbf{e}(k) = (\mathbf{c}(k) + \tilde{\mathbf{d}}(k)$
$\hat{\mathbf{e}}$	$N_e \times \langle time \rangle$	Internal model error: $\hat{\mathbf{e}}(k) = [\mathbf{\Theta}^k]^T \boldsymbol{\phi}^k$
$\tilde{\mathbf{e}}$	$N_e \times \langle time \rangle$	Model prediction error: $\tilde{\mathbf{e}}(k) = \mathbf{e}(k) - [\mathbf{\Theta}^k]^T \boldsymbol{\phi}^k$
$\tilde{\mathbf{d}}$	$N_e \times \langle time \rangle$	Desired signal: $\tilde{\mathbf{d}}(k) = \mathbf{e}(k)$
		Matrix transfer functions
$\mathbf{W}^k$	$N_d \times N_r \times L_w$	Control FIR: $w_{\delta,\rho}^{k+1} = w_{\delta,\rho}^k - \mu \mathbf{V}_{\delta,\rho}^k e(k)$
$\mathbf{G}$	$N_e \times N_r \times L_g$	Transfer functions from disturbances to error sensors
$\hat{\mathbf{G}}$	$N_e \times N_r \times L_g$	Internal model of $\mathbf{G}$
$\mathbf{H}$	$N_e \times N_d \times L_h$	Transfer functions from drivers to error sensors
$\hat{\mathbf{H}}$	$N_e \times N_d \times L_h$	Internal model of $\mathbf{H}$
		Histories
$\mathbf{X}^k$	$L_w \times N_r$	$\mathbf{X}^k = [\mathbf{X}_1^k \quad \cdots \quad \mathbf{X}_{N_d}^k]$
$\mathbf{U}^k$	$L_w \times N_r$	$\mathbf{U}^k = [\mathbf{U}_1^k \quad \cdots \quad \mathbf{U}_{N_d}^k]$
		Block collections
$\boldsymbol{\phi}^k$	$(N_d L_h + N_r L_g) \times 1$	$\boldsymbol{\phi}^k = [(\mathbf{U}^k)^T \mid (\mathbf{X}^k)^T]^T$
$\mathbf{\Theta}$	$(N_d L_h + N_r L_g) \times N_e$	$\mathbf{\Theta} = [(\hat{\mathbf{H}})^T \mid (\hat{\mathbf{G}})^T]^T$
$\mathbf{\Phi}^k$	$(N_d L_h + N_r L_g) \times N_b$	$\mathbf{\Phi}^k = [\boldsymbol{\phi}^k \quad \boldsymbol{\phi}^{k-1} \quad \cdots \quad \boldsymbol{\phi}^{k-N_b+1}]$
$\tilde{\mathbf{D}}$	$N_b \times N_e$	$\tilde{\mathbf{D}}^k = [\tilde{\mathbf{d}}(k) \quad \tilde{\mathbf{d}}(k-1) \quad \cdots \quad \tilde{\mathbf{d}}(k-N_b+1)]^T$
$\tilde{\mathbf{E}}$	$N_b \times N_e$	$\tilde{\mathbf{E}}^k = [\tilde{\mathbf{e}}(k) \quad \tilde{\mathbf{e}}(k-1) \quad \cdots \quad \tilde{\mathbf{e}}(k-N_b+1)]^T$

identify $h_{\epsilon,\delta}$ by numerical deconvolution. The process is repeated for all combinations of drivers and error channels.

The control weights are computed and stored by the controller as FIR sequences as well. The sequences $\omega_{\delta,\rho=1}^k(n)$ are indexed by the number of drivers ($\delta \in \{1,\ldots,4\}$) and single reference sensor ($\rho=1$), with n indexing the filter taps ($n \in \{1,\ldots,L_w\}$) and k indexing the weights' adaption in time. At each cycle k, the controller computes the voltages $u_\delta(k)$ and new control weights $w_{\delta,1}^{k+1}(n)$ for all δ and n. The details of this computation are given in the companion paper.

For the case where the on-line system identification is used, data are moved from the real-time DSP hardware to a general-purpose BriteLite IPX Sparc computer (also used to control the DSP hardware), where the system identification update is computed. The updated system transfer functions, also stored as FIRs, are then downloaded to the DSP hardware. This system identification takes place asynchronously, so that the DSP continues to generate a cancelling waveform, using the most recent representation of the system dynamics that it has available.

II. SYSTEM PERFORMANCE

The objective of the controller is to minimize the cost function,

$$\arg\min_{\mathbf{W}^k} \|\mathbf{e}(k;f)\|, \tag{1}$$

where $\|\mathbf{e}(k;f)\|$ is the H_2 norm of the vector error signal $\mathbf{e}$ weighted over a set of frequencies, f. The performance band in frequency is set by prefiltering both the reference signal and the error channels with bandpass filters that also serve to prevent aliasing due to controller sampling. These filters are implicit in the error channels, $\mathbf{e}(k)$, and in the reference signal, $\mathbf{x}(k)$. Performance at the low end of the band is limited by driver rolloff as frequency approaches zero. We also have implemented a one-tap adaptive high-pass filter on $\mathbf{e}$ when updating the control law in order to minimize dc biasing problems.

Since the system is designed to cancel random noise, we design the delay in the $h_{\epsilon,\delta}$ filters to be smaller than the propagation delay in the transfer function from the reference input to the quiet-zone microphones. Simply stated, the system is designed such that the control drivers are sufficiently close to the quiet zone to enable causal control of the quiet zone given computational and propagation delays for any reference signal. By this design the control system is able to cancel broadband, random noise sources. The performance of the system is described below.

A. Experimental verification of statically calibrated control system

For the experiment presented here, the controller sampling rate is 4162 Hz. All inputs to the controller are low-pass filtered with the corner frequency at 1200 Hz to prevent

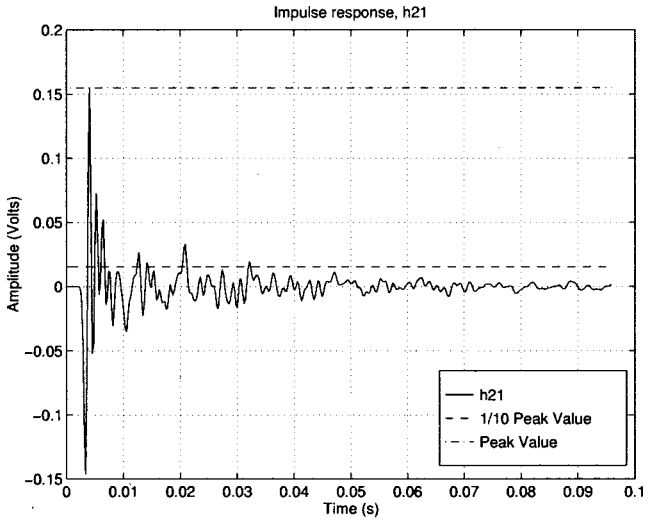

FIG. 4. The FIR representation of the speaker to quiet-zone transfer function, $h_{2,1}$.

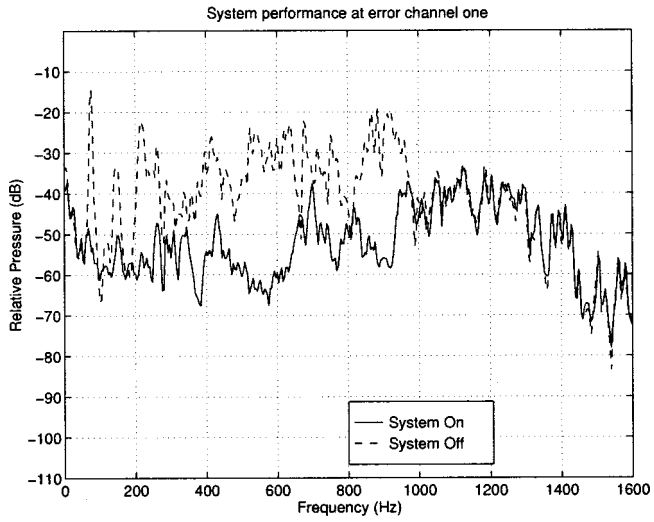

FIG. 6. System performance at one of the error channels with the controller on and off. The performance band is 50 Hz to 1 kHz.

aliasing. The lengths of the propagation filters and the weight filters are $L_h = 400$ taps and $L_w = 512$ taps, respectively, the longest filters the real-time controller can compute at this sample rate with static $h_{\epsilon,\delta}$ filters. The $h_{\epsilon,\delta}$ filters are calibrated off-line with an operator seated in the room using numerical deconvolution of a pseudo-random noise source. A representative filter, $h_{2,1}$, is shown in Fig. 4. Recalling that the filter is a FIR representation of the impulse response from a speaker to the quiet zone, one can detect the initial propagation delay of 3.5 ms, indicating the propagation delay from the controller output to the error channel input. The reverberation time of the room is also evident from Fig. 4, where the impulse response rings down below $\frac{1}{10}$ of its peak value after approximately 33 ms.

We evaluate the performance of the system as follows. With the equalizer switched out of the source path, we input recorded engine noise directly to the source speaker in the rear of the room. The spectrum of the recorded engine noise (not yet transmitted to the room) is shown in Fig. 5. The noise has been recorded inside a vehicle cabin while the engine idles. Note that there is significant response as high as 1 kHz. The control system is activated and allowed to converge to a solution (approximately 1 min from startup). Noise attenuation is measured at each error channel. Both error channels exhibit similar behavior, achieving reduction as shown in Fig. 6. The figure shows the unattenuated (system off) and attenuated (system on) noise at the first error channel as a function of frequency with pressure measured in decibels. Recalling that the performance band has been set to be 50 to 1000 Hz, we measure performance as the average attenuation across the band.

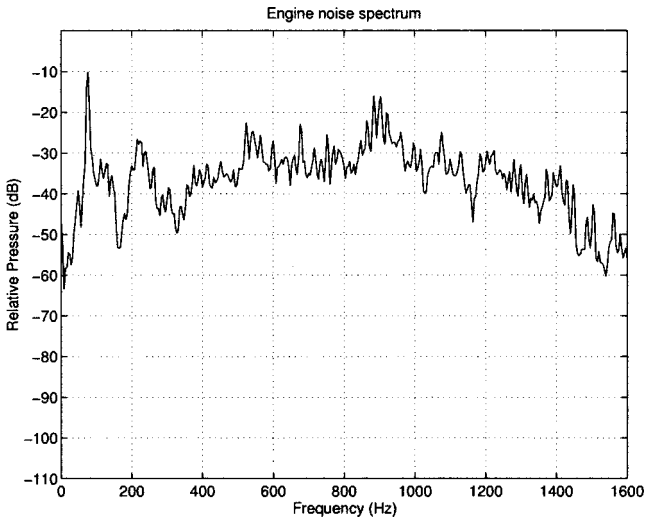

FIG. 5. Spectrum of engine noise recorded before transmission into the room.

The performance metric is

$$P = 10 \log_{10} \left[\frac{\Sigma_{f=50}^{1000} \mathcal{E}_{\text{off}}^2(f)}{\Sigma_{f=50}^{1000} \mathcal{E}_{\text{on}}^2(f)} \right],$$

where $\mathcal{E}$ is the Fourier transform of the voltage at the error microphone, as a function of frequency, f. The data are collected using an HP 35670A dynamic signal analyzer sampling at 4096 Hz (giving a 1600-Hz measurement bandwidth), with 32 time averages to average out nonstationarity of the source. In the case of Fig. 6, we achieve 23-dB noise attenuation after allowing the system to converge for 2 min.

After allowing the system to converge to a solution, as above, we switch the equalizer into the source path while the control system is running. Insertion of the equalizer changes the transfer path from the reference signal to the quiet zone, forcing the control system to adapt its weights in compensation. The particular equalizer setting that has been used is shown in Fig. 7. The equalizer is set to approximate transmission through 0.64-cm (0.25 in.) Plexiglas so that the change in the transfer function from the source to the quiet zone is similar to that resulting from an operator closing a window. After the equalizer is switched into the transfer path, we allow the system to converge to a new solution (approximately 30 s) and then measure performance again. The performance at the first error channel for the new source path is shown in Fig. 8. Again, pressure for the unattenuated

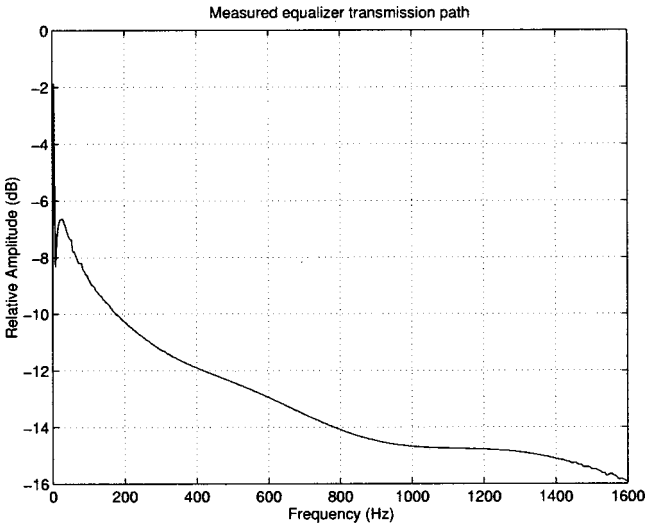

FIG. 7. Equalizer transfer function approximating transmission through 0.64-cm Plexiglas.

(system off) and attenuated (system on) responses is shown as a function of frequency. Average performance in the 50 to 1000 Hz range is again 23 dB.

B. Experimental verification of control system with on-line system identification algorithm

We first describe the implementation of the block-update scheme in hardware. To do so, we rely on definitions and notation from the companion paper. The most important definitions from that paper are summarized in Table I. Subsequent to the successful numerical simulation of the block projection algorithm in single- and multiple-channel cases, the DSP hardware was configured to upload data records, $\boldsymbol{\phi}$ and $\tilde{\mathbf{E}}$, when called for by the BriteLite host computer. (Recall that $\boldsymbol{\phi}$ is the collection of system input/output pairs and $\tilde{\mathbf{E}}$ is a corresponding collection of error signals.) Code was written for implementing the multichannel algorithm on the BriteLite, and diagnostic software was included to record the progress of the algorithm and provide a real-time interface to

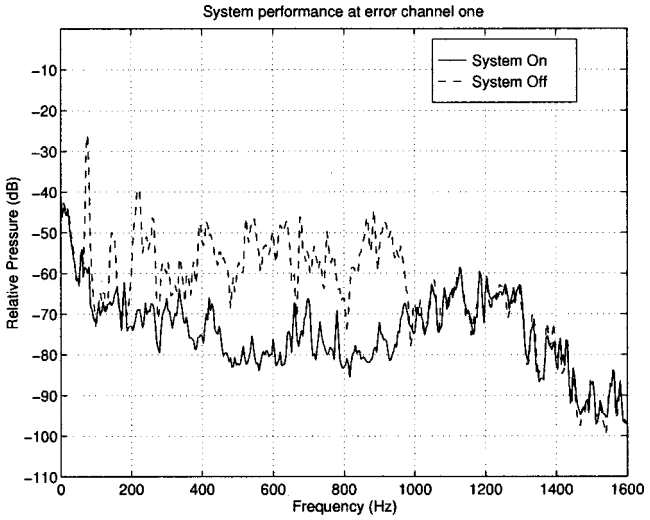

FIG. 8. System performance after the equalizer is impulsively switched into the source path and the controller is allowed to adjust.

MATLAB, where transfer functions were plotted. Additionally, code was implemented that enabled the adaptation gain, μ, to be adjusted while the system was operating.

The information in the matrix $\boldsymbol{\phi}$ is highly redundant, and many fewer than $(N_d L_h + N_r L_g) N_b$ variables need to be transferred from the control hardware to the general-purpose computer. Examination reveals that $\boldsymbol{\phi}^k$ differs from $\boldsymbol{\phi}^{k-1}$ exactly in the deletion of $N_d + N_r$ scalars and the addition of $N_d + N_r$ new scalars. The total number of data points required to construct $\boldsymbol{\phi}$ is thus $N_d(L_h + N_b - 1) + N_r(L_g + N_b - 1)$. The data are all obtained from time histories of $\{x_m\}_{m=1}^{N_s}$ and $\{u_j\}_{j=1}^{N_d}$. Each x_m source input history must be $L_g + N_b - 1$ samples long. Likewise, each u_j driver output history must be $L_h + N_b - 1$ samples long. Data of this form are sufficient to compute $\boldsymbol{\phi}$ immediately. Furthermore, recall that $\tilde{\mathbf{D}}$ is a time history of the external errors. The update requires a history of errors equal to the block size N_b, with each time sample containing all N_e errors. Thus the data required are $N_b N_e$ scalars. The old parameter estimate is still in the general-purpose computer from the previous iteration, so it need not be transferred. The total number of scalars needed is thus $N_d(L_h + N_b - 1) + N_r(L_g + N_b - 1) + N_b N_e$.

Some computation tasks were also optimized to remove redundancy and exploit structure. The expense of the formation of the matrix $\boldsymbol{\Phi}^T \boldsymbol{\Phi}$ was greatly reduced by taking advantage of the structure of $\boldsymbol{\phi}$, a Toeplitz matrix. If $L = (N_d L_h + N_r L_g)$, the number of free parameters being solved for, then the number of multiplications when computing $\boldsymbol{\Phi}^T \boldsymbol{\Phi}$ may be reduced from $N_b^2 L$ to $(N_b/2)(N_b + 2L - 1)$. For large L, the savings is proportional to the block size.

Writing the new plant estimate to the DSP hardware in the current implementation requires a transfer of $\hat{h}_{\epsilon,\delta}$ to each of the feedforward crosspoints (a crosspoint is the controller associated with an input–output pair). Note that $\hat{g}_{\epsilon,\rho}$ does not need to be transferred, since it is not used directly by the controller. As a result, the total number of scalars downloaded per block update is $N_r N_d N_e L_h$. If one ignores these implementation-specific details, the minimum number of scalars needed to represent all $N_d N_e$ transfer functions $\hat{h}_{\epsilon,\delta}$ is $N_d N_e L_h$.

The algorithm is implemented using the *C* programming language and calls a standard matrix equation solver in FORTRAN. Because uploading the data to the BriteLite takes approximately 0.1 s, it was expected that large block sizes (dozens to hundreds of time samples) would be most efficient. The matrix $\boldsymbol{\Phi}^T \boldsymbol{\Phi}$ is symmetric, positive definite, and a product of two Toeplitz matrices. As such, its associated matrix equation can be solved using a generalized Levinson recursion algorithm, as noted by Montazeri and Duhamel. Because transfer times dominate here, we use the more pedestrian Gaussian elimination with back-substitution.

Convergence of the block algorithm is exponential, but the rate is difficult to quantify and depends on the statistical properties of the driving signal as well as the noise. Ideally, the rate of convergence (per update) for various block sizes should be experimentally determined. This figure could then the combined with the known update rate (per second),

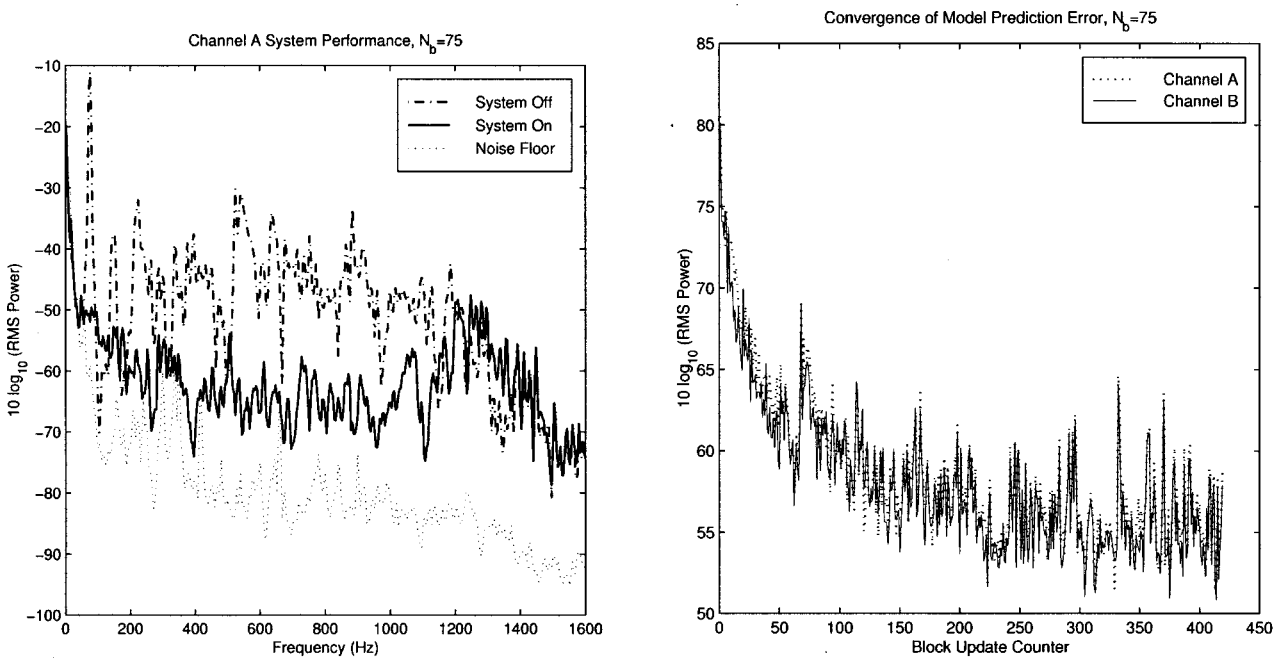

FIG. 9. Left: system performance for channel A (approximately 27 dB of signal reduction between 50 and 1000 Hz); right: convergence of model prediction error as a function of update number (updates occur approximately once per second). Note that no ''operator'' is in the test room for this experiment, so performance is better than in Fig. 6.

which depends on the algorithm complexity and hardware capability, to produce a rate of convergence (per second) as a function of block size. This has not been done, and block sizes are instead set for each application by trial and error. Intuitively, we expect convergence rate to be a unimodal function of block size. The shape of this curve would depend primarily on the problem size and the statistics of the input signal and noise.

For the system identification experiment, the ANC system again comprises one reference sensor, four secondary actuators, and two error channels each consisting of three ganged microphones. The exogenous input is a loudspeaker in the reverberant room against one wall, and is driven by recorded engine noise. The input is measured by splitting the signal to the loudspeaker and feeding it directly to the DSP hardware. The filter tap lengths are $L_g = L_h = 250$, and $L_w = 512$, and the sampling rate is 4162 Hz. As before, L_h and L_w were set to the maximum the controller can compute at this sample rate. However, hardware overhead imposed by the periodic data transfer of new $h_{\epsilon,\delta}$ filters to the real-time controller forced the reduction of the filter lengths from those used in the static plant experiments. The block size is $N_b = 75$ and scaling was unity (because of balancing the output signal levels of the microphone preamplifiers by adjusting gains, which performs the same function). For our experiments, we use a snr model for $\tilde{\mathbf{E}}$ of 100, or 40 dB, to determine the noise variance, $\sigma_{\tilde{\mathbf{E}}}^2$. The prior variance, $\sigma_{\Delta\Theta}^2$, is a few percent of the expected magnitude of the largest tap weight. The ratio of the two variances is added to the diagonal matrix $\mathbf{\Phi}^T\mathbf{\Phi}$, effectively a Tikhanov regularization for the computation of the plant transfer functions.

Initialization of the system is as follows. The host computer's internal transfer functions, $\hat{g}_{\epsilon,\rho}$ and $\hat{h}_{\epsilon,\delta}$, are all initialized to zero, while $w_{\delta,\rho}$ is initialized with random noise and the adaptation gain, μ, is set to zero. The system is then started and the block projection algorithm given time to start converging, thus avoiding startup transients or instability and subsequent speaker damage. After a suitable period, approximately 60 s, the weight adaptation is activated by switching μ to be nonzero.

Figure 9 shows, on the left, system performance for channel A (first error microphone) across the band of interest and, on the right, convergence of the model prediction error as a function of the number of updates. The performance metric is still

$$P = 10 \log_{10} \left[\frac{\sum_{f=50}^{1000} \mathcal{E}_{\text{off}}^2(f)}{\sum_{f=50}^{1000} \mathcal{E}_{\text{on}}^2(f)} \right],$$

where $\mathcal{E}$ is the Fourier transform of the voltage at the error microphone, as a function of frequency, f. Performance for this case, as compared to that of Sec. II A, is summarized in Table II. The performance for channel A is measured at 26.8 dB, while channel B yields 27.9 dB of attenuation. In understanding these results, it is important to know that no human was present in the reverberant room during the measurements, as opposed to the case presented above, where per-

TABLE II. Summary of experimental cancellation performance with and without the ''operator'' present in reverberant room. Note that in both cases the cancellation performance is essentially unchanged when using the equalizer to modify the propagation path.

Setup	Static calibration (dB)	On-line estimate (dB)
Room empty	33	27
Operator present	23	18

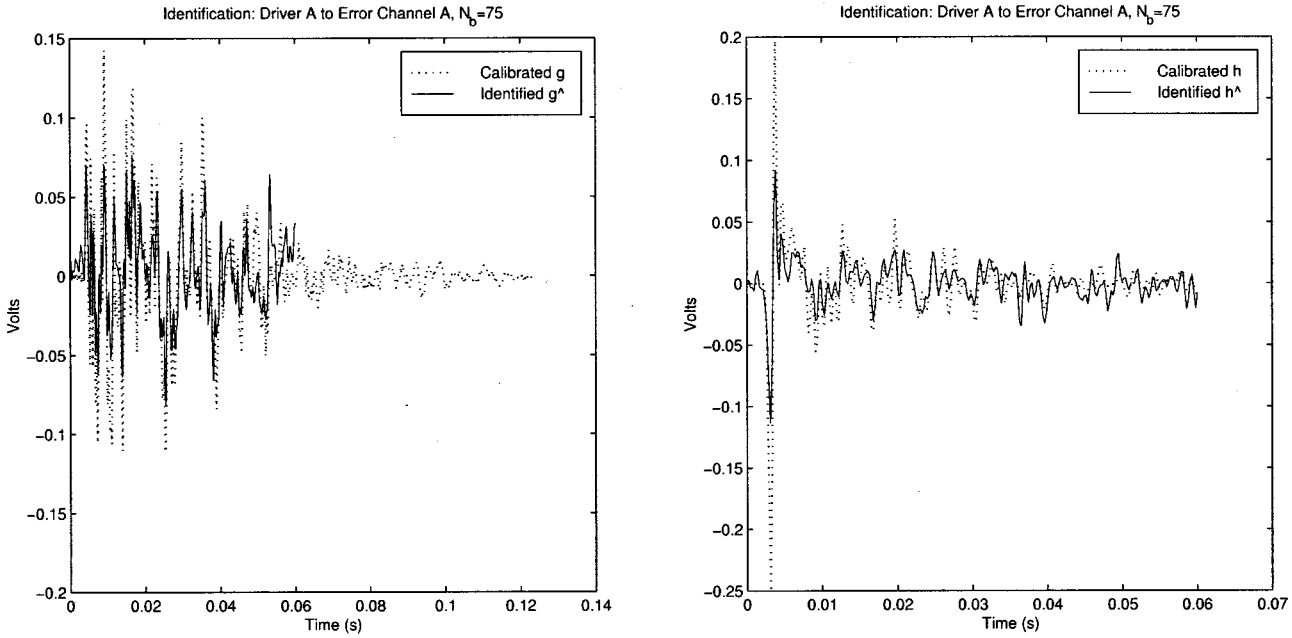

FIG. 10. Representative estimates of transfer functions using block projection algorithm. Results are for 420 iterations with a block size of 75 and 2500 free parameters.

formance of 23 dB is reported. If on-line system identification is replaced by static calibration and no one is in the room, we achieve better than 30 dB, averaged over the band. Conversely, if on-line system identification is used and a human is present in the room, performance in the neighborhood of 18 dB is achieved. It is also important to note that, for these experiments, an ideal reference sensor consisting of an electrical signal direct from the source recording is used as the system input. This type of measurement enables simulation of a situation with no coupling, but also gives outstanding coherence between the noise source and the reference input sensor.

Convergence of the model prediction error, shown on the right of Fig. 9, is shown as a function of block-update number. Updates happen asynchronously, according to the vagaries of the BriteLite operating system, but the period was approximately 1 s for this setup. A distinct anomaly in the convergence curve is visible at around update 60; this is the instant that the weight adaptation gain, μ, is made nonzero. A nonzero μ enables $w_{\delta,\rho}^{k}$ to change and forces $(\hat{\mathbf{G}},\hat{\mathbf{H}})$ into a new subspace of solutions.[14]

Representative estimates, $\hat{g}_{1,1}$ and $\hat{h}_{1,1}$, are shown in Fig. 10. Recall that the tap-for-tap accuracy of these transfer functions is a misleading indicator of system performance. Figure 11 shows the comparison of the same estimated and calibrated transfer functions in magnitude and phase. The figures show reasonable match in magnitude for both transfer functions in the control band. The difference in angle between the estimate and calibration, important to guarantee stability, also matches well in band. The poorest performance in phase is seen near nulls in the magnitude response and should therefore have little impact on stability margin or overall cancellation performance. Note that the estimate for $\hat{h}_{1,1}$ is marginally better than that for $\hat{g}_{1,1}$, especially in phase. Remember that for our purposes, the $\hat{h}_{1,1}$ transfer function is more important than $\hat{g}_{1,1}$ as it is directly used in the control path to update the weight estimates.

III. CONCLUSIONS

The purpose of this work is to demonstrate the viability of real-time, multichannel active noise control in a reverberant environment when the control objective is local quieting of a random noise source. While the control algorithm used in this study is well known, we are unaware of an experimental application of this algorithm to a multichannel ANC system controlling noise spanning 1 kHz in frequency in a room large enough to contain a person, as shown here. The performance measurements shown here of 23-dB attenuation in the quiet-zone demonstrate the feasibility of attenuating random noise over a wide frequency band. In addition, we believe the multichannel implementation of broadband noninvasive system identification is novel. The next step is to demonstrate a fully adaptive active noise control system for realistically varying environments without coupling between the control drivers and the reference input.

Open issues in the implementation of the control system remain. First, the spatial extent of the quiet zone created by the control system is known to decrease as temporal frequency increases. Therefore, while performance in the quiet zone may be strong, the operator may move out of the quiet zone. In part, our system identification algorithm addresses this if the error microphones move with the operator's head. Other techniques to increase the size of the quiet zone may prove beneficial, such as the energy density metric which measures a combination of pressure and velocity. Second, the use of a reference signal that is uncoupled from the control drivers simplifies the control design, yielding a feedforward controller. We and others have addressed the problem of nonzero coupling between the reference sensors and the control drivers by devising *Q*-parametrized controllers. Real-

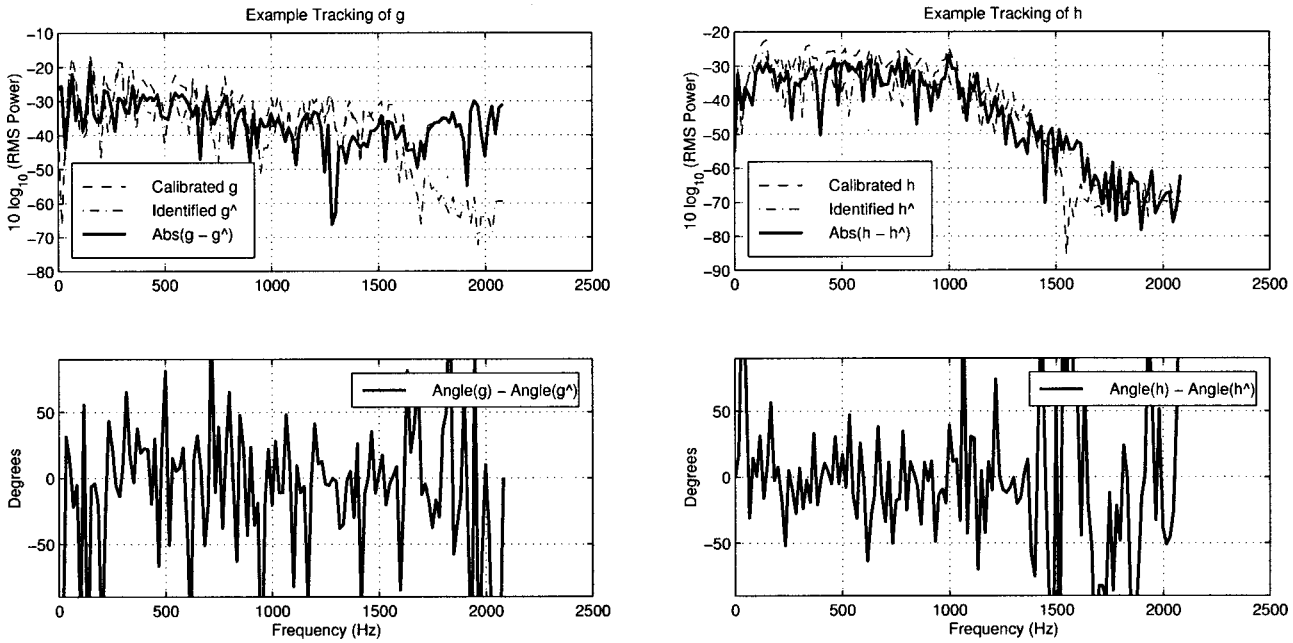

FIG. 11. Representative estimates of transfer functions using block projection algorithm. The top figures show the magnitude comparison and the lower figures show the phase error between the calibrated and identified functions for $\hat{g}_{1,1}$ and $\hat{h}_{1,1}$.

time control using *Q*-parametrized controllers has been demonstrated for an active noise control application by Peterson *et al.*[25] Lastly, optimal placement of drivers and optimal selection of reference sensors remains an important problem.

The fully adaptive system with on-line system identification has also been tested in an anechoic chamber, providing similar results for a one-input, four-output, two-error configuration. In this case, an acoustic sensor was used to measure the output of a loudspeaker, and a neutralization filter was calibrated off-line to cancel the coupling path from secondary loudspeakers to the input sensor, thus implementing the *Q*-parametrization in hardware. The implementation in the comparatively expansive anechoic chamber enabled the error microphones to be moved about, providing a ''mobile quiet zone.'' Successful application of a mobile quiet zone in a reverberant environment has not yet been achieved. In summary, moving the quiet zone in the reverberant room results in poor performance in the mid to high end of the performance band in frequency. We believe this lack of performance is due to the relatively slow update rate of the system identification compared to the rate at which the transfer functions change in a reverberant environment.

ACKNOWLEDGMENTS

The authors gratefully acknowledge the efforts of Dr. J. Raúl Martínez of the System Technology Division at SRI International in supporting this work. The authors also thank the anonymous reviewers, whose comments were insightful and appreciated.

[1] S. J. Elliott, P. Joseph, A. J. Bullmore, and P. A. Nelson, ''Active cancellation at a point in a pure tone diffuse sound field,'' J. Sound Vib. **120**(1), 183–189 (1988).

[2] S. J. Elliott, I. M. Strothers, P. A. Nelson, A. M. McDonald, D. C. Quinn, and T. Saunders, ''The active control of engine noise inside cars,'' in *Proc. Inter-noise 88,* pp. 987–990.

[3] P. M. Joplin and P. A. Nelson, ''Active control of low-frequency random sound in enclosures,'' J. Acoust. Soc. Am. **87**, 2396–2404 (1990).

[4] P. A. Nelson, A. R. D. Curtis, S. J. Elliott, and A. J. Bullmore, ''The active minimization of harmonic enclosed sound fields, Part I: Theory,'' J. Sound Vib. **117**, 1–13 (1987).

[5] S. D. Sommerfeldt and J. Tichy, ''Adaptive control of a two-stage vibration isolation mount,'' J. Acoust. Soc. Am. **88**, 938–944 (1990).

[6] A. J. Bullmore, P. A. Nelson, A. R. D. Curtis, and S. J. Elliott, ''The active minimization of harmonic enclosed sound fields, Part II: A computer simulation,'' J. Sound Vib. **117**(1), 15–33 (1987).

[7] S. J. Elliott, A. R. D. Curtis, A. J. Bullmore, and P. A. Nelson, ''The active minimization of harmonic enclosed sound fields, Part III: Experimental verification,'' J. Sound Vib. **117**(1), 35–58 (1987).

[8] P. J. Nashif and S. D. Sommerfeldt, ''An active control strategy for minimizing the energy density in enclosures,'' in *Proc. Inter-noise 92*, Toronto, Ontario, July 1992, pp. 357–362.

[9] D. Guicking and M. Bronzel, ''Multichannel broadband active noise control in small enclosures,'' in *Proc. Inter-Noise 90*, pp. 1255–1258.

[10] S. Laugesen and S. J. Elliott, ''Multichannel active control of random noise in a small reverberant room,'' IEEE Trans. Speech Audio Process. **1**(2), 241–249 (1993).

[11] D. R. Morgan and D. A. Quinlan, ''Local silencing of room acoustic noise using broad-band active noise control,'' in *IEEE Workshop on Applications of Signal Processing to Audio and Acoustics*, 1993.

[12] X. H. Yang, J. Van Niekerk, K. S. Parwani, A. Packard, and B. Tongue, ''Attenuation of structurally generated interior noise through active control,'' in *Proc. 1993 Am. Control Conference*.

[13] D. E. Melton and R. A. Greiner, ''Adaptive feedforward multiple-input, multiple-output active noise control,'' in *Proc. ICASSP 1992*, pp. 229–232.

[14] W. C. Nowlin, G. S. Guthart, and G. K. Toth, ''Noninvasive system identification for multichannel broadband active noise control,'' J. Acoust. Soc. Am. **107**, 2049–2060 (2000).

[15] S. D. Sommerfeldt, ''Multi-channel adaptive control of structural vibration,'' Noise Cont. Eng. **37**(2), 77–89 (1991).

[16] M. Montazeri and P. Duhamel, ''A set of algorithms linking NLMS and block RLS algorithms,'' in *Proc. IEEE Intern. Conf. Acoust. Speech, Signal Processing*, Minneapolis, MN, April 1993, pp. 412–415.

[17] M. Montazeri and P. Duhamel, ''A set of algorithms linking NLMS and block RLS algorithms,'' IEEE Trans. Signal Process. **43**(2), 444–453 (1995).

[18] D. R. Morgan and S. G. Kratzer, ''On a class of computationally efficient, rapidly converging, generalized NLMS algorithms,'' IEEE Signal Process.Lett. **3**(8), 245–247 (1996).
[19] J. M. Maciejowski, *Multivariable Feedback Design* (Addison–Wesley, Reading, MA, 1989).
[20] W. A. Weeks, C. T. Chittenden, and P. M. Heilman, ''Hardware control of a real-time multichannel digital signal processing system,'' in *Proc. 25th Asilomar Conference on Signals, Systems and Computers*, 1991, pp. 423–428.
[21] W. A. Weeks and B. L. Curless, ''A real-time, multichannel system with parallel digital signal processors,'' in *Proc. ICASSP 90*, pp. 1787–1790.
[22] B. Widrow, D. Shur, and S. Schaffer, ''On adaptive inverse control,'' in *Proc. 15th Asilomar Conference on Circuits, Systems and Computers*, 1981, pp. 185–189.
[23] J. C. Burgess, ''Active adaptive sound control in a duct: A computer simulation,'' J. Acoust. Soc. Am. **70**, 715–726 (1981).
[24] S. C. Douglas and J. A. Olkin, ''Multiple-input, multiple-output, multiple-error adaptive feedforward control using the filtered-*x* normalized LMS algorithm,'' in *Second Conference on Recent Advances in Active Control of Sound and Vibration*, 1993, pp. 743–755.
[25] D. K. Peterson, W. A. Weeks, and W. C. Nowlin, ''Active control of complex noise problems using a broadband, multichannel controller,'' in *Proc. Noise-Con 1994*, pp. 315–320.

Noninvasive system identification for multichannel broadband active noise control

William C. Nowlin,[a] Gary S. Guthart, and Gregory K. Toth
SRI International, 333 Ravenswood Avenue, Menlo Park, California 94025

(Received 23 April 1999; accepted for publication 3 December 1999)

Many real-world applications of active noise control are characterized by transfer functions that vary significantly and unpredictably. The controller's transfer-function models must adapt to these variations. Presented here is a class of adaptive filters that accomplish quasiperiodic system identification updates for feedforward control by using blocks of input–output histories. The algorithms form a one-dimensional family linking normalized least-mean squares (LMS) adaptive filters and block recursive least-squares, termed ''block projection'' algorithms, and generalize the noninvasive system identification studied by Sommerfeldt and Tichy. The system identification proceeds noninvasively, producing nonparametric impulse responses. Simulations show that the algorithm's convergence is faster than that of normalized LMS, even after the additional overhead of computing the update is taken into account. Both the multichannel generalization and application of these algorithms to system identification are novel. Simulations of the algorithms' performance using measured data are presented here, while experimental results of an implemented algorithm are contained in the companion paper.
[S0001-4966(00)01004-3]

PACS numbers: 43.40.Vn [PJR]

INTRODUCTION

A pressing problem preventing active noise and vibration control technology from achieving broad applicability is the inability of controllers to ensure performance and stability in all operating conditions that they might face. All controllers, feedforward and feedback, make use of a model of these system transfer functions (which if nothing else contain modeled actuator dynamics); the accuracy of this ''plant model'' is crucial to their success, since inaccurate models lead to poor performance and possible instability. Although a static (nonadaptive) feedforward controller can never become unstable, it can augment, rather than reduce, the signal it attempts to cancel. If a feedforward controller is adaptive, in the sense that the control law depends on past performance, then instability is also possible.

In many control systems, including many active noise-control (ANC) systems, the plant is measured explicitly in a calibration step.[1–4] Subsequent plant variation is unavoidable. To ensure system performance as the plant changes, one usually employs notions of robustness and/or adaptivity.[5–8] These techniques, while differing significantly in their approach, share the assumption that the controller's internal plant model remains fixed.

However, if the true plant varies beyond the bounds used to design a static control law, then enhancement will result for that control law. Analogously, instability may result for any adaptive filter based on a static plant model. In these situations, a control system must determine the change in the plant model and change its control law accordingly.

With this mandate in mind, systems have been developed that continually or periodically update the system model. In this paper we present such an approach that is multichannel, noninvasive, and broadband, and runs efficiently on blocks of data to thereby execute on real-world hardware.

The design builds on a technique for nonparametric on-line system identification that is itself an adaptation of the filtered-X LMS (FXLMS) adaptive algorithm wrapped around the plant and controller. This scheme, which does not inject test signals into the operational system or require additional transducers, was first proposed and tested for tonal ANC by Sommerfeldt and Tichy. Other nonparametric approaches to on-line system identification may inject a low-level random signal into the secondary source signal to track the changing plant,[9,10] and may purposefully add delay to the control filter to decrease correlation in the plant inputs.[11]

Here, we generalize Sommerfeldt and Tichy's approach[12,13] by extending the algorithm to the broadband multichannel case. In addition, the FXLMS variant is further extended to update asynchronously, using a block of data for each update. The block-update concept is not new to FXLMS, having been discovered a number of times in related fields and summarized succinctly by Morgan and Kratzer.[14] The contribution herein is one of extension of the block-update concept to the multichannel case and application of the extension to FXLMS in the context of on-line system identification. The latter results in considerations unique to the application of system identification. In particular, this paper contributes the selection of proper scaling to ensure identification of all plant models, and develops a Bayesian formulation for ''regularizing'' the matrix update equations.

The resulting approach is an identification algorithm that updates a multiple-input, multiple-output (MIMO) system

[a]Current address: Intuitive Surgical, Inc., 1340 W. Middlefield Rd., Mountain View, CA 94043.

model based on blocks of past input–output data. The model is broadband and is updated continually while the controller is adapting. The size of the data block may range from 1 (corresponding to standard least-mean squares, or LMS) to a block size equaling the number of free parameters in the plant model (corresponding to block recursive least squares). Simulations show that for single-channel problems, the block algorithm converges faster than normalized LMS, when the block algorithm is implemented on slow general-purpose hardware and normalized LMS is implemented on special-purpose digital signal-processor (DSP) boards. In addition, the block structure is well matched to the hardware implementation because of its relatively small requirements on sample-by-sample communications. In our companion paper,[15] we implement a multichannel evaluation of the algorithm. We believe the resulting approach to nonparametric system identification is broadly applicable to feedforward control and adaptive signal processing.

I. REVERBERANT ENCLOSURE PROBLEM AS MOTIVATION

The ANC application that motivates this work is localized control of noise in a reverberant enclosure. Active control of sound in a structurally rich environment such as the cabin of a vehicle has long been an area of research.[16–18,11,4,13] The engineering problems that must be overcome to build a realistic ANC system, however, are daunting. In particular, for broadband control the ''plant'' to be identified is the MIMO broadband matrix transfer function from control actuators to error sensors.

For applications we envision (small, highly reverberant environments), system drift may be rapid and wide-ranging, resulting in instability, enhancement, or limited performance if on-line system identification is not employed. For example, opening a window in the cabin of a vehicle will cause severe distortion of the system transfer function matrix. Other effects are less pronounced, but still important, such as deterioration of components over time, environmental changes, and operator motion.

For real-world reverberant environments, the number of modes in a control band may be quite large. Typical approaches have treated a few modes.[4,18–21] Transducers that couple effectively into a mode are used to control it. Hence, this technique is effective if only a few resonances need to be controlled to reduce the sound-pressure level acceptably. This in turn limits the bandwidth to which these systems can be successfully applied.

True multichannel broadband control has been reported in the literature relatively recently, most notably by Laugesen and Elliott.[2] This work demonstrates real-time attenuation using a fully interconnected multichannel system for broadband signals up to approximately 200 Hz. Melton and Greiner[3] achieve similar results for a small duct, controlling noise up to 400 Hz. In Chapter 9 of Kuo,[11] the author reports broadband results up to 250 Hz for a $1\times2\times2$ system as implemented by Finn, Luan, and Ji. In all cases, static plant models were used.

This paper explores a nonparametric system identification, where the dynamics of the plant are represented as finite-impulse responses (FIR) of a given duration. The benefits include the ability to use fast convolution-based hardware and LMS-style algorithms for control, in addition to representing the plant transfer functions in a vector space directly related to the measured data. This closeness to the data implies both speed and accuracy of system identification, at the expense of a noncompact transfer function representation. Using this computational structure, complex plants with many thousands of free parameters have been successfully quieted.[22,23] The technique is especially efficient if the plant in question has a large number of damped modes, so that the impulse response is rich, yet of short duration, as may be the case for a vehicle cabin.

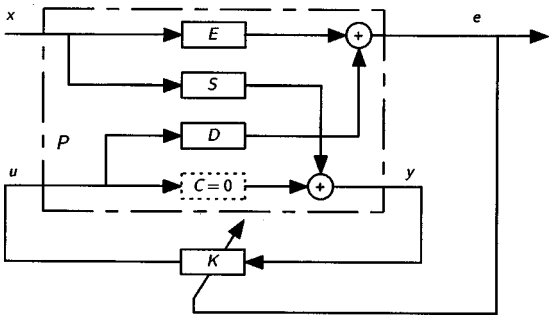

FIG. 1. MIMO plant, *P*, with adaptive feedback control system. The exogenous input is *x*, and the controller output is *u*. The error quantity sensed, *e*, may or may not be the same as the quantity sensed for control, *y*. The transfer matrices are *E* (exogenous, or uncontrolled), *S* (sensor), *D* (driver), and *C* (coupling). The controller is *K*. If $C=0$, the system is equivalent to a feedforward one.

The subsequent system has been implemented both in simulations and in hardware, and shown to be effective. The experimental verification, which is described in a companion paper, has the following attributes:

(i) Identifies a MIMO matrix of FIR transfer functions.
(ii) Runs in real time, asynchronously on the same computer that controls the ANC hardware.
(iii) Identifies a broadband system.
(iv) Identifies thousands of free parameters in a few seconds.

This verification, we believe, represents an advance in the accomplishment of multichannel adaptive ANC using on-line system identification.

II. SYSTEM REQUIREMENTS

The control system we seek to describe has multiple disturbance sensors and multiple secondary sources. Figure 1 shows a familiar system representation for feedback control (see, for example, Boyd and Barratt[24]). This block diagram is general, and shows the exogenous transfer function (the one existing as distinct from the controller), as well as the sensor, driver, and coupling transfer functions. (Each line in the diagram is multichannel.) An important distinction we make throughout this work is that we assume the *coupling* transfer function from secondary sources to disturbance sensors is negligible. In the figure we have illustrated this assumption by using a dashed box to represent the *C* transfer function. In MIMO feedback control theory, the collection of system

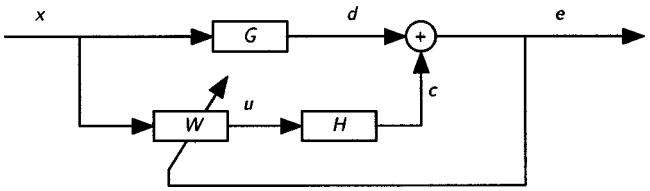

FIG. 2. Common representation of adaptive feedforward control system. The exogenous input is *x*, the error quantity is, *e*, and *u* is the controller output. The signal *d* is what we desire to cancel, and *c* is the cancelling signal. The open-loop transfer function is *G*, and the actuator transfer function is *H*. The controller (now feedforward) is *W*.

transfer functions is generally called the plant. In feedforward control, and especially in adaptive filtering, however, one often hears the matrix *D* described as the plant. These different views, while confusing, are not irreconcilable. That is, note that when $C=0$, the block diagram can be unwound to form two parallel paths. If we further formally convolve *E* with S^{-1}, defining *G* as the result, and rename *D* as *H*, we obtain the standard representation of a feedforward control system as seen in the adaptive filter literature[8] and in Fig. 2. Adaptive filterers may define the ''plant'' as *H* because the proper modeling of *H* (and not *G*) is required for convergence of adaptive filters (*viz.*, filtered-X). Thus, when $C=0$, the block diagram of Fig. 1 is formally equivalent to that of Fig. 2.

In this experiment, we address the feedforward control problem. The reference signal used by the controller is chosen to be uncoupled from the output of the control speakers (which we call drivers). We choose a feedforward control arrangement for the simplicity with which we can vary the propagation path from the reference signal to the quiet zone. Further, acoustically uncoupled reference signals may be found in applications. For example, accelerometers or engine tachometers are reference signals that are often uncoupled from the control drivers. Control of ANC systems having nonzero coupling has been achieved here and elsewhere using *Q*-parametrized controllers (otherwise known as neutralized feedforward control or Youla parametrization[7]).

The control algorithm mated with our system identification is a multichannel FXLMS adaptive algorithm. We choose this control algorithm for its relative simplicity in implementation, recognizing that other algorithms may be appropriate for various applications (e.g., normalization when the statistics of the reference signal are unknown). The FXLMS algorithm developed by Widrow *et al.*[25] and applied to ANC by Burgess[26] has been studied by many authors. We employ a multichannel form of the algorithm described by Douglas and Olkin,[27] and refer the reader to their work for a detailed description of the algorithm, its convergence properties, and computational complexity. The adaptive algorithm enables control in the presence of large changes in the propagation path from the reference input signal to the quiet-zone error channels. The control hardware used for the experiment is a real-time, multichannel digital signal processor developed by Weeks *et al.*[23,28]

The hardware that implements the ANC system is a combination of (1) a special-purpose digital signal processor, called the advanced signal processor (ASP),[28] designed to implement a multichannel FIR control law in real time, and (2) a general-purpose BriteLite IPX Sparc computer that is the master system controller. The former has been modified to implement the FXLMS algorithm but lacks the necessary interprocessor communication bandwidth and connectivity to run simultaneously a MIMO system identification algorithm.

System identification is implemented on the general-purpose computer, which can upload and download data from the ASP using interrupt-driven protocols. Modifications to the ASP control software enable this data transfer to occur on demand from the Sparc, without interrupting ANC system operation. This design modification was undertaken specifically to enable a block-update system identification algorithm to run on the Sparc. Since each data transfer has an associated fixed overhead, block-update algorithms that reduce the frequency of data transfer while increasing the effectiveness of each update are especially attractive. However, although the batch-processing scheme is suited for the computational hardware on which it was developed, the resulting approach to nonparametric system identification is efficiently implementable on custom multiprocessor DSP boards with higher interprocessor communication bandwidths. The approach relaxes the requirements on interprocessor communication to fewer, larger transfers that can take greater advantage of background direct memory access (DMA) controllers. Additionally, computational loading among different processors can be optimized more easily by untying the block rate from the control-loop sample rate.

III. THEORETICAL APPROACH

In this section we give a discussion of the theoretical approach to the system equations for the on-line system identification as well as the FXLMS controller, both given for the multi-input, multioutput, multierror generalization. The section is broken down into the following parts. Subsection A introduces the definitions and notation required to write the subsequent equations in a compact and recognizable form. Subsection B provides a brief review of multichannel FXLMS for cancellation, following Douglas and Olkin.[27] During this discussion, the plant model is assumed known. Subsection C provides a brief review of the method for constructing the model prediction error signal that drives the system identification and extends this concept to the multichannel case. Finally, Subsection D writes the matrix equations that update the system models to reduce the model prediction error, used with blocks of data and extended to the multichannel case, and Subsection E briefly discusses its convergence properties.

A. Definitions

Let *k* be an integer time index, and let the vector valued signal $\mathbf{x}$ at time *k* be denoted by $\mathbf{x}(k)$. If ϵ and ρ are integer indices, then the ρth scalar component of $\mathbf{x}$ at time *k* is written $x_\rho(k)$. Matrix transfer functions have one scalar transfer function for every input–output pair: $\mathbf{G}=\{g_{\epsilon,\rho}\}_{\forall\epsilon,\rho}$. The value of the convolution of a signal and a transfer function, $g_{\epsilon,\rho}*x_\rho$ at time *k*, is written $(g_{\epsilon,\rho}*x_\rho)(k)$. Vector-valued versions of convolutions are written in the obvious way: $(\mathbf{G}*\mathbf{x})(k)$.

TABLE I. Summary of important variables from the text. Scalars are set in italics. Lowercase bold roman letters represent vectors as a function of time. Uppercase bold roman letters represent matrix transfer functions, matrices of multivariable histories, and block collections of histories and transfer functions.

Var	Dimensions	Eq. #	Definition
		Vector signals of time	
$\mathbf{x}$	$N_r \times \langle time \rangle$		Input signal of infinite duration
$\mathbf{u}$	$N_d \times \langle time \rangle$	(3)	$\mathbf{u}=[u_1 \ \cdots \ u_{N_d}]^T$; $u_\delta(k)=\Sigma_{\rho=1}^{N_r}(\mathbf{X}_\rho^k)^T(w_{\delta,\rho}^k)$
$\mathbf{d}$	$N_e \times \langle time \rangle$		$\mathbf{d}(k)=(\mathbf{x}*\mathbf{G})(k)$
$\mathbf{c}$	$N_e \times \langle time \rangle$	(5)	$\mathbf{c}=[c_1 \ \cdots \ c_{N_e}]^T$; $c_\epsilon(k)=\Sigma_{\delta=1}^{N_d}(\mathbf{U}_\delta^k)^T(h_{\epsilon,\delta})$
$\mathbf{e}$	$N_e \times \langle time \rangle$	(6)	$\mathbf{e}(k)=\mathbf{c}(k)+\mathbf{d}(k))$
$\mathbf{v}_{\delta,\rho}$	$N_e \times \langle time \rangle$	(9)	$\mathbf{v}_{\delta,\rho}=[v_{1;\delta,\rho}\cdots v_{N_e\delta,\rho}]^T$; $v_{\epsilon;\delta,\rho}(k)=(x_\rho * h_{\epsilon,\delta})(k)$
$\hat{\mathbf{e}}$	$N_e \times \langle time \rangle$	(14)	$\hat{\mathbf{e}}(k)=[\mathbf{\Theta}^k]^T\boldsymbol{\phi}^k$
$\tilde{\mathbf{e}}$	$N_e \times \langle time \rangle$	(15)	$\hat{\mathbf{e}}(k)=\mathbf{e}(k)-[\mathbf{\Theta}^k]^T\boldsymbol{\phi}^k$
$\tilde{\mathbf{d}}$	$N_e \times \langle time \rangle$	(16)	$\tilde{\mathbf{d}}(k)=\mathbf{e}(k)$
		Matrix transfer functions	
$\mathbf{W}^k$	$N_d \times N_r \times L_w$	(11)	Control FIR: $w_{\delta,\rho}^{k+1}=w_{\delta,\rho}^k-\mu\mathbf{V}_{\delta,\rho}^k\mathbf{e}(k)$
$\mathbf{G}$	$N_e \times N_r \times L_g$		Transfer functions from disturbances to error sensors
$\hat{\mathbf{G}}$	$N_e \times N_r \times L_g$		Internal model of $\mathbf{G}$
$\mathbf{H}$	$N_e \times N_d \times L_h$		Transfer functions from drivers to error sensors
$\hat{\mathbf{H}}$	$N_e \times N_d \times L_h$		Internal model of $\mathbf{H}$
		Histories	
$\mathbf{X}^k$	$L_w \times N_r$	(1)	$\mathbf{X}^k=[\mathbf{X}_1^k \ \cdots \ \mathbf{X}_{N_r}^k]$
$\mathbf{U}^k$	$L_w \times N_r$	(4)	$\mathbf{U}^k=[\mathbf{U}_1^k \ \cdots \ \mathbf{U}_{N_d}^k]$
$\mathbf{V}_{\delta,\rho}^k$	$L_w \times N_e$	(10)	$\mathbf{V}_{\delta,\rho}^k=[\mathbf{v}_{\delta,\rho}(k) \ \cdots \ \mathbf{v}_{\delta,\rho}(k-L_w+1)]^T$
		Block collections	
$\boldsymbol{\phi}^k$	$(N_dL_h+N_rL_g)\times 1$	(12)	$\boldsymbol{\phi}^k=[(\mathbf{U}^k)^T \mid (\mathbf{X}^k)^T]^T$
$\mathbf{\Theta}$	$(N_dL_h+N_rL_g)\times N_e$	(12)	$\mathbf{\Theta}=[(\hat{\mathbf{H}})^T \mid (\hat{\mathbf{G}})^T]^T$
$\mathbf{\Phi}^k$	$(N_dL_h+N_rL_g)\times N_b$	(17)	$\mathbf{\Phi}^k=[\boldsymbol{\phi}^k \ \boldsymbol{\phi}^{k-1} \ \cdots \ \boldsymbol{\phi}^{k-N_b+1}]$
$\tilde{\mathbf{D}}$	$N_b \times N_e$	(18)	$\tilde{\mathbf{D}}^k=[\tilde{\mathbf{d}}(k) \ \tilde{\mathbf{d}}(k-1) \ \cdots \ \tilde{\mathbf{d}}(k-N_b+1)]^T$
$\tilde{\mathbf{E}}$	$N_b \times N_e$	(19)	$\tilde{\mathbf{E}}^k=[\tilde{\mathbf{e}}(k) \ \tilde{\mathbf{e}}(k-1) \ \cdots \ \tilde{\mathbf{e}}(k-N_b+1)]^T$

Referring now to Fig. 2, we first define the vector signals and matrix transfer functions that make up this system. All transfer functions that follow will be written as finite-impulse responses (FIRs). All multi-input, multioutput transfer functions will be represented by matrices of FIRs.

Define N_r to be the number of reference sensors, N_e to be the number of error sensors, and N_d to be the number of control drivers. Let $\mathbf{x}$ be the vector of reference sensor signals of dimension $N_r \times \langle time \rangle$, with $\mathbf{x}(k)$ being the vector of measurements at time k. Now, let x_ρ be the ρth reference sensor signal. Similarly, define d_ϵ and $\mathbf{d}$ as the ϵth signal at the error sensor without cancellation and its associated vector signal (the signal we ''desire'' to replicate and cancel). Similarly, define u_δ and $\mathbf{u}$ as the input signal to the δth driver and its associated vector. Likewise, one may define c_ϵ, $\mathbf{c}$, e_ϵ and $\mathbf{e}$. In our notation, the subscript ρ always indexes a reference sensor, subscript ϵ always indexes an error sensor, and subscript δ always indexes a driver. That is, $\rho \in \{1, \ldots, N_r\}$, $\epsilon \in \{1, \ldots, N_e\}$, and $\delta \in \{1, \ldots, N_d\}$. The choices of ρ for reference sensor, ϵ for error sensor, and δ for driver is meant to offer a mnemonic aid for the subscripts.

Let $g_{\epsilon,\rho}$ be the transfer function between the ρth reference sensor and the ϵth error sensor. Likewise, let $h_{\epsilon,\delta}$ be the transfer function between the δth driver and the ϵth error sensor. The control transfer function between the ρth reference sensor and the δth driver is $w_{\delta,\rho}$. Since the control function is adapting over time, we will write $w_{\delta,\rho}^k$ to indicate the kth iteration. The superscript k always indexes a processor clock.

To simplify notation, we define $\mathbf{G}$ to be the matrix of transfer functions whose (ϵ,ρ)th element is $g_{\epsilon,\rho}$. $\mathbf{H}$ and $\mathbf{W}^k$ are defined analogously. Thus, $\mathbf{G}$ is a matrix of transfer functions with dimensions $N_e \times N_r$, $\mathbf{H}$ has dimensions $N_e \times N_d$, and $\mathbf{W}^k$ has dimensions $N_d \times N_r$. The length (that is, the number of FIR taps) of any transfer function $g_{\epsilon,\rho}$ is L_g, while the length of each $h_{\epsilon,\delta}$ is L_h. Finally, the length of the control filter is L_w. A summary is given in Table I.

B. Review of multichannel FXLMS

For implementation of the cancellation filter, we choose an adaptive filtering algorithm (FXLMS) that is capable of attenuating sound in the presence of large variations in the propagation path from the reference signal to the quiet zone. For an example of a varying propagation path, consider the path between a piece of machinery and its operator, when the two are in relative motion. This section reviews a multichannel extension to the FXLMS control algorithm used for our system. The review is provided partially as a method for introducing notation that is relied on for the exposition of the block system identification algorithm later, and for providing a seamless connection between the two algorithms. For more

detailed derivations of the algorithm and the hardware architecture, see work by Douglas and Olkin[27] and Weeks *et al.*,[28] respectively.

FXLMS relies on an internal model of the driver-to-error-sensor transfer matrix, **H**. The transfer function from each control driver to each error channel, $h_{\epsilon,\delta}$, is stored by the controller as an FIR sequence of length L_h. The algorithm may make use of a model measured ahead of time (''off-line calibration''), or the model may be improved during use (''on-line identification''), or some combination may be employed. Regardless, the information extracted is fundamentally the same and assumed available to the FXLMS controller.

Once a model of **H** is available to the controller, we may iteratively adjust the control filter weights. We start by defining the data structures used by the controller. The controller stores a time history of the ρth sampled reference signal, x_ρ, as a vector of length L_w.

$$\mathbf{X}_\rho^k=[x_\rho(k) \quad \cdots \quad x_\rho(k-L_w+1)]^T, \tag{1}$$

where k indexes controller cycles and $[\cdot]^T$ denotes vector transpose. (Here, bold roman notation, $\mathbf{X}_\rho^k$, represents a segment of time series stored in computer memory. These segments are updated every iteration.) The convolution of x_ρ and $w_{\delta,\rho}^k$ is thus

$$(x_\rho * w_{\delta,\rho}^k)(k)=(\mathbf{X}_\rho^k)^T(w_{\delta,\rho}^k). \tag{2}$$

The control signal for the δth driver will be a linear combination of responses due to all reference sensors

$$u_\delta(k)=\sum_{\rho=1}^{N_r}(\mathbf{X}_\rho^k)^T(w_{\delta,\rho}^k). \tag{3}$$

In a similar fashion to the formation of $\mathbf{X}_\rho^k$, the computer also stores the last L_h values of u_δ in $\mathbf{U}_\delta^k$,

$$\mathbf{U}_\delta^k=[u_\delta(k) \quad \cdots \quad u_\delta(k-L_h+1)]^T. \tag{4}$$

The contribution of the N_d control drivers to the measurement at the ϵth error channel is given by another linear combination of convolutions

$$c_\epsilon(k)=\sum_{\delta=1}^{N_d}(\mathbf{U}_\delta^k)^T(h_{\epsilon,\delta}), \tag{5}$$

and the total measurement at the ϵth error channel is given by

$$e_\epsilon(k)=d_\epsilon(k)+c_\epsilon(k), \tag{6}$$

where $d_\epsilon(k)=\Sigma_{\rho=1}^{N_r}(x_\rho * g_{\epsilon,\rho})(k)$ is the contribution of the open-loop (uncontrolled) signal at time k to the ϵth error-channel measurement.

In the FXLMS algorithm, the FIR taps for each control filter are updated using an instantaneous estimate of the gradient of the expected mean-square error. This update for the jth tap is formally given by

$$w_{\delta,\rho}^{k+1}(j)=w_{\delta,\rho}^k(j)-\mu\frac{1}{2}\frac{\partial}{\partial w_{\delta,\rho}^k(j)}\mathbf{e}^T(k)\mathbf{e}(k), \tag{7}$$

where μ is the familiar LMS step size. The correction term can be computed as

$$\begin{aligned}\frac{\mu}{2}\frac{\partial}{\partial w_{\delta,\rho}^k(j)}\mathbf{e}^T(k)\mathbf{e}(k)&=\mu\frac{\partial\mathbf{e}^T(k)}{\partial w_{\delta,\rho}^k(j)}\mathbf{e}(k)\\&=\mu\frac{\partial\mathbf{c}^T(k)}{\partial w_{\delta,\rho}^k(j)}\mathbf{e}(k),\end{aligned} \tag{8}$$

where the first equality follows from $(\partial/\partial x)(\mathbf{a}^T\mathbf{a})=\mathbf{a}^T(\partial\mathbf{a}/\partial x)+(\partial\mathbf{a}^T/\partial x)\mathbf{a}$, and the last equality follows from $\mathbf{e}(k)=\mathbf{c}(k)+\mathbf{d}(k)$, with $\mathbf{d}(k)$ being uncontrolled and hence independent of $w_{\delta,\rho}^k$. Following standard single-channel derivations, we write $v_{\epsilon;\delta,\rho}(k)$ as the ϵth component of $\mathbf{v}_{\delta,\rho}(k)$, which is x_ρ filtered by the transfer function from the δth driver to the ϵth error sensor

$$v_{\epsilon;\delta,\rho}(k)=(x_\rho * h_{\epsilon,\delta})(k). \tag{9}$$

If we make the standard approximation also needed for single-channel FXLMS, namely that the filter weights change slowly, so that $w_{\delta,\rho}^{\hat{k}}(j)\approx w_{\delta,\rho}^k(j)$ for $k-L_h<\hat{k}\leqslant k$, then an elementary calculation yields the approximation

$$\frac{\partial\mathbf{c}^T(k)}{\partial w_{\delta,\rho}^k(j)}\approx\mathbf{v}_{\delta,\rho}^T(k-j+1).$$

With the help of the final definition (a history of the filtered-X signal of size $L_w\times N_e$),

$$\mathbf{V}_{\delta,\rho}^k=[\mathbf{v}_{\delta,\rho}(k) \quad \mathbf{v}_{\delta,\rho}(k-1) \quad \cdots \quad \mathbf{v}_{\delta,\rho}(k-L_w+1)]^T, \tag{10}$$

we are able to write the MIMO FXLMS update for each reference-sensor/driver pair

$$w_{\delta,\rho}^{k+1}=w_{\delta,\rho}^k-\mu\mathbf{V}_{\delta,\rho}^k\mathbf{e}(k). \tag{11}$$

There are $N_r\times N_d$ such equations being updated simultaneously in our implementation. Of course these equations, while resembling the single-channel case, actually contain all the ''cross-coupling'' information needed for a fully interconnected solution.

C. Computation of model prediction error signal

We now turn to the noninvasive identification of the system models, which is needed to update the system models used by FXLMS. In this section we present some definitions that enable us to form the model prediction error signal, which is the difference between what the error microphones measure and what the internal models predict they should measure. We next write an update that modifies the internal models in a way that drives the model prediction error signal to a minimum. This material is a summary and MIMO extension to published approaches,[11,12] and defines the components needed to write the multichannel block-update result that follows.

Here, we require the notational differentiation between a true transfer function and the controller's internal model of that transfer function. We employ the standard convention wherein the true and estimated quantities are represented by the absence and presence of a carat, as in $h_{\epsilon,\delta}$ and $\hat{h}_{\epsilon,\delta}$. Additionally, because updates for the block algorithm happen less frequently than updates for $\mathbf{W}^k$, we will avoid tying

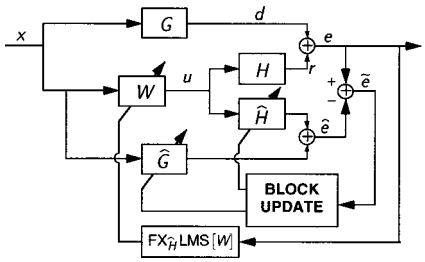

FIG. 3. Formation of model prediction error signal for noninvasive on-line system identification.

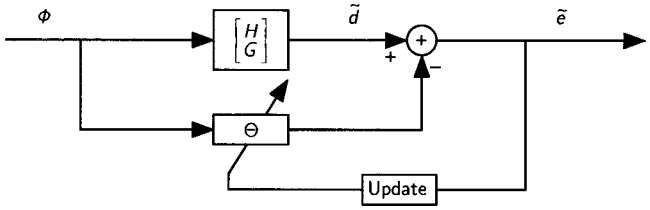

FIG. 4. LMS update of internal model, Θ, using model prediction error signal. Note that Θ plays the role of the adapting parameters and ϕ is the system input. The desired signal is $\tilde{d}$, and $\tilde{e}=\tilde{d}-\boldsymbol{\phi}^T\Theta$.

the rates together. If a block update occurs at time k, then the next block update is written to occur at some time greater than k.

The adaptive system identification algorithm is driven by a model prediction error signal. This signal, which is the key to a noninvasive system identification, is the difference between the true (measured) error at an error sensor and what one predicts the error should be based on the internal models, $\hat{\mathbf{G}}$ and $\hat{\mathbf{H}}$. In forming this signal, the true error, $\mathbf{e}$, and the predicted error, $\hat{\mathbf{e}}$, are computed in parallel and subtracted (Fig. 3).

To compute these signals in the multichannel case, we define the following compact notation. We denote by $\boldsymbol{\phi}$ a collection of time histories of system input and controller output. To do this, we define a history of inputs, $\mathbf{X}_\rho^k$, and controller outputs, $\mathbf{U}_\delta^k$, as before. Here, the length of the column vector $\mathbf{X}_\rho^k$ is L_g (which may be different than L_w), while the length of $\mathbf{U}_\delta^k$ is L_h as in Section B. We can then write

$$(x_\rho * \hat{g}_{\epsilon,\rho})(k)=(\mathbf{X}_\rho^k)^T\hat{g}_{\epsilon,\rho}$$

$$(u_\delta * \hat{h}_{\epsilon,\delta})(k)=(\mathbf{U}_\delta^k)^T\hat{h}_{\epsilon,\delta}.$$

Next, we define the collection of histories and the collection of transfer functions, both stacked head-to-tail, as

$$\boldsymbol{\phi}^k \triangleq \begin{bmatrix} \mathbf{U}_1^k \\ \mathbf{U}_2^k \\ \vdots \\ \mathbf{U}_{N_d}^k \\ \hline \mathbf{X}_1^k \\ \mathbf{X}_2^k \\ \vdots \\ \mathbf{X}_{N_r}^k \end{bmatrix}; \quad \boldsymbol{\Theta}^k \triangleq \left[\begin{array}{cccc} \hat{h}_{1,1} & \hat{h}_{1,2} & \cdots & \hat{h}_{1,N_e} \\ \hat{h}_{2,1} & \hat{h}_{2,2} & \cdots & \hat{h}_{2,N_e} \\ \vdots & \vdots & \ddots & \vdots \\ \hat{h}_{N_d,1} & \hat{h}_{N_d,2} & \cdots & \hat{h}_{N_d,N_e} \\ \hline \hat{g}_{1,1} & \hat{g}_{1,2} & \cdots & \hat{g}_{1,N_e} \\ \hat{g}_{2,1} & \hat{g}_{2,2} & \cdots & \hat{g}_{2,N_e} \\ \vdots & \vdots & \ddots & \vdots \\ \hat{g}_{N_r,1} & \hat{g}_{N_r,2} & \cdots & \hat{g}_{N_r,N_e} \end{array}\right]. \quad (12)$$

(The horizontal lines in the $\boldsymbol{\phi}^k$ and $\boldsymbol{\Theta}^k$ matrices are drawn only to show the distinction in the different groupings of elements.) For convenience, we have not explicitly shown that both $\hat{h}_{\epsilon,\delta}$ and $\hat{g}_{\epsilon,\rho}$ depend on time, although they are updated inside the control computer quasiperiodically. The vector $\boldsymbol{\phi}^k$ is an $N_dL_h+N_rL_g$ column vector, and the matrix $\boldsymbol{\Theta}^k$ has dimensions $(N_dL_h+N_rL_g)\times N_e$ (since each ''element'' is really a vector).

The output of the error sensors at time k is written

$$\mathbf{e}(k)\triangleq[e_1(k)\ \ e_2(k)\ \ \cdots\ \ e_{N_e}(k)]^T \quad (13)$$

(a column vector of length N_e). The error predicted by the internal models, on the other hand, is given by

$$\hat{\mathbf{e}}(k)=[\hat{e}_1(k)\ \ \hat{e}_2(k)\ \ \cdots\ \ \hat{e}_{N_e}(k)]^T=[\boldsymbol{\Theta}^k]^T\boldsymbol{\phi}^k. \quad (14)$$

The *model prediction error signal* is thus defined to be

$$\tilde{\mathbf{e}}(k)\triangleq\mathbf{e}(k)-[\boldsymbol{\Theta}^k]^T\boldsymbol{\phi}^k. \quad (15)$$

Note that $\mathbf{e}(k)$ may be recognized as the *desired signal* in a simple LMS-style block diagram (as in Fig. 4). Hence, it may be convenient to also write

$$\tilde{\mathbf{d}}(k)\triangleq\mathbf{e}(k). \quad (16)$$

D. Multiple constraints for system identification

Having defined the model prediction error signal, we are prepared to derive the update that reduces it. The block-update approach enables us to gather data over a period of time and take a large step toward the optimal estimate for the system transfer functions. This paper addresses only some of the tradeoffs among block size, step complexity, and update frequency. See Montazeri and Duhamel[29] for discussion of convergence for a closely related single-channel algorithm, and Morgan and Kratzer[14] for a discussion of related single-channel algorithms.

The block-update algorithm proposed is an extension of the normalized LMS adaptive algorithm, also called the projection algorithm. Recall that at each update the projection algorithm solves the following problem: Given a current $\boldsymbol{\phi}^k$, $\boldsymbol{\Theta}^k$, and a desired signal, $\tilde{\mathbf{d}}(k)$, find the new $\boldsymbol{\Theta}^{\hat{k}}$ that is *closest* to $\boldsymbol{\Theta}^k$ (using an appropriate norm) and that satisfies the constraint, $\tilde{\mathbf{d}}(k)-[\boldsymbol{\Theta}^{\hat{k}}]^T\boldsymbol{\phi}^k=0$. The application of a single vector constraint is natural when the projection algorithm is updating $\boldsymbol{\Theta}^k$ every clock cycle, because the error from the previous cycle generates the constraint.

The extension uses N_b vector constraints instead of a single vector constraint. Here, N_b is called the *block size*. It, too, is natural when $\boldsymbol{\Theta}^k$ is being updated less often than every clock cycle, because errors from previous cycles can be grouped together. The additional constraints are obtained by recording the input and error signals for N_b consecutive samples, or more generally for any N_b samples.

This subsection reviews standard projection-algorithm techniques on the way to writing the multichannel block update of Eq. (22). Recall that $[\boldsymbol{\Theta}^k]^T\boldsymbol{\phi}^k$ predicts $\tilde{\mathbf{d}}(k)$. Likewise, note that $[\boldsymbol{\Theta}^k]^T\boldsymbol{\phi}^{k-1}$ predicts $\tilde{\mathbf{d}}(k-1)$, if we assume

that the true plant is varying slowly. We construct a matrix of different histories of inputs in the following manner;

$$\mathbf{\Phi}^k \triangleq [\boldsymbol{\phi}^k \quad \boldsymbol{\phi}^{k-1} \quad \cdots \quad \boldsymbol{\phi}^{k-N_b+1}]. \tag{17}$$

In this way, $\mathbf{\Phi}^k$ is an $(N_d L_h + N_r L_g) \times N_b$ matrix. Similarly, we collect a history of desired signals

$$\tilde{\mathbf{D}}^k \triangleq [\tilde{\mathbf{d}}(k) \quad \tilde{\mathbf{d}}(k-1) \quad \cdots \quad \tilde{\mathbf{d}}(k-N_b+1)]^T. \tag{18}$$

The model prediction error history is then given by

$$\tilde{\mathbf{E}}^k \triangleq [\tilde{\mathbf{e}}(k) \quad \tilde{\mathbf{e}}(k-1) \quad \cdots \quad \tilde{\mathbf{e}}(k-N_b+1)]^T. \tag{19}$$

The model prediction error and the desired signal are thus related by the important equation

$$\tilde{\mathbf{E}}^k = \tilde{\mathbf{D}}^k - [\mathbf{\Phi}^k]^T \mathbf{\Theta}^k. \tag{20}$$

As in standard FXLMS, the $N_b \times N_e$ scalar constraints are obtained by setting the right side of Eq. (20) to zero, with $\mathbf{\Theta}^k$ replaced by $\mathbf{\Theta}^{k+1}$: $0 = \tilde{\mathbf{D}}^k - [\mathbf{\Phi}^k]^T \mathbf{\Theta}^{k+1}$.

To write the cost function, we append the constraints to a minimum-norm cost function by means of a Lagrange multiplier, $\mathbf{\Lambda}$, of size $N_e \times N_b$. Use of the trace function enables us to write the result compactly. We drop the superscript-k notation, writing $\mathbf{\Theta}$ for the current $\mathbf{\Theta}^k$, and $\mathbf{\Theta} + \Delta\mathbf{\Theta}$ for $\mathbf{\Theta}^{k+1}$. The cost function is

$$J = \tfrac{1}{2} \mathrm{tr}[(\Delta\mathbf{\Theta})^T (\Delta\mathbf{\Theta})] + \mathrm{tr}\{\mathbf{\Lambda}^T [\tilde{\mathbf{D}} - \mathbf{\Phi}^T (\mathbf{\Theta} + \Delta\mathbf{\Theta})]\}. \tag{21}$$

We make use of the identities $(\partial/\partial\mathbf{X})\mathrm{tr}[\mathbf{AX}] = \mathbf{A}^T$ and $(\partial/\partial\mathbf{X})\mathrm{tr}[\mathbf{X}^T\mathbf{A}] = \mathbf{A}$ (see Ref. 30) to write normal equations which are readily solved to yield the optimal update

$$\Delta\mathbf{\Theta} = \mathbf{\Phi}(\mathbf{\Phi}^T\mathbf{\Phi})^{-1}(\tilde{\mathbf{D}} - \mathbf{\Phi}^T\mathbf{\Theta}) = \mathbf{\Phi}(\mathbf{\Phi}^T\mathbf{\Phi})^{-1}\tilde{\mathbf{E}}. \tag{22}$$

Many will recognize (22) as the minimum norm estimate for the parameters $\Delta\mathbf{\Theta}$ given the data $\tilde{\mathbf{E}}$, *in the absence of noise*. In Sec. IV B we modify this expression using a Bayesian approach based on specific noise assumptions. Additionally, in Sec. IV A we address the need to impose a norm which is balanced in $\mathbf{H}$ and $\mathbf{G}$. Both modifications to the algorithm make it more robust and faster converging in practice. However, the convergence of the block-update system identification algorithm may not be readily apparent. Therefore, we next address a simple analysis of the algorithm's convergence properties.

E. Convergence

The analysis proceeds under the assumption that the cancellation filter is able to converge in concert with the system identification filter. In addition, we assume that the system is noiseless; a straightforward extension is available when system error levels converge to nonzero limits.

Consider the initial situation where the system identification algorithm has converged completely, so that the model prediction error is zero in the noiseless limit. Recalling Fig. 3, this results in the constraint subspace relating $\hat{\mathbf{H}}$ and $\hat{\mathbf{G}}$

$$\mathbf{G} + \mathbf{W}^{(1)} * \mathbf{H} - (\hat{\mathbf{G}}^{(1)} + \mathbf{W}^{(1)} * \hat{\mathbf{H}}^{(1)}) = 0, \tag{23}$$

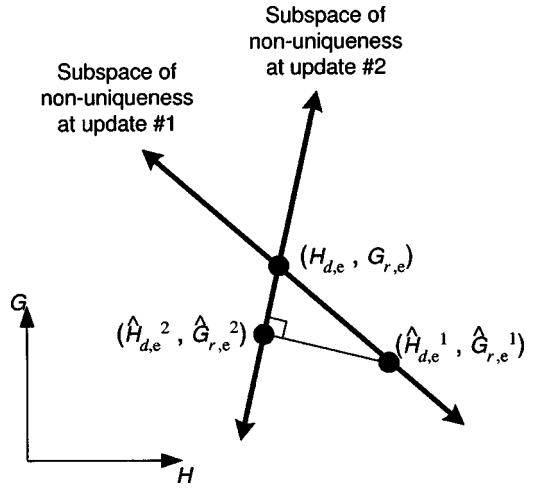

FIG. 5. Representation of successive updates of the system-identification algorithm, assuming that the cancellation adaptation is running concurrently.

where the superscript notation ''(1)'' refers to the first update. Figure 5 shows a cartoon of such a subspace, labeled as ''update #1.'' Any system model in that subspace has the same model prediction error, and therefore the system cannot differentiate these systems and pick the correct one.

Consider next the evolving situation where the cancellation filter has changed because it was still converging after the first update. The system identification procedure is now ready to make its second update. Again, the update will lie in another subspace containing the true plant. However, because the cancellation filter is allowed to change, the new solution will be closer to the true solution, to wit.

If, in computing the result of the second update, we write $\hat{\mathbf{H}}^{(2)} = \mathbf{H} + \Delta\mathbf{H}^{(2)}$ and $\hat{\mathbf{G}}^{(2)} = \mathbf{G} + \Delta\mathbf{G}^{(2)}$, then by analogy to (23), the subspace of nonuniqueness that the second update must lie in may be written

$$\Delta\mathbf{G}^{(2)} = -\mathbf{W}^{(2)} * \Delta\mathbf{H}^{(2)}.$$

Thus, any vector lying in that subspace may always be written as

$$\begin{bmatrix} \hat{\mathbf{H}}^{(2)} \\ \hat{\mathbf{G}}^{(2)} \end{bmatrix} = \begin{bmatrix} \mathbf{H} \\ \mathbf{G} \end{bmatrix} + \begin{bmatrix} \Delta\mathbf{H}^{(2)} \\ -\mathbf{W}^{(2)} * \Delta\mathbf{H}^{(2)} \end{bmatrix}.$$

Finally, recall that the update given by Eq. (22) is a projection algorithm, so that the incremental update will be perpendicular to this subspace. That is, the update has a direction vector given by

$$\Delta\mathbf{\Theta}^{(2)} = \begin{bmatrix} \mathbf{W}^{(2)} * \mathbf{x} \\ \mathbf{x} \end{bmatrix}$$

for each history in the block. The inner product $\langle \Delta\mathbf{\Theta}^{(2)}, [\Delta\mathbf{H}^{(2)}, -\mathbf{W}^{(2)} * \Delta\mathbf{H}^{(2)}]^T \rangle$ is indeed zero. Thus, after updating we see that the solution has been projected onto a new subspace, along a path perpendicular to that subspace. Using the induced norm $\|(\mathbf{H},\mathbf{G})\| = (\|\mathbf{H}\|^2 + \|\mathbf{G}\|^2)^{1/2}$, the second update is seen to be closer to the true plant than the first.

This argument suggests that the concurrent actions of adapting the cancellation filter and adapting the system model are sufficient to avoid getting the system identification model stuck far from the true solution. The fundamental

problem is one of being unable to tell the difference between components in **H** and **G**, because they are mixed in the measurement of the error signal. However, adjusting **W** breaks the symmetry, since changes in **W** will affect the signal through **H** and not the signal through **G**. Therefore, the changing **W** gives the identification algorithm the extra information it needs to converge.

As a corollary, we conclude that if the cancellation adaptation is not permitted to accompany the system identification, then the reduction of the model prediction error signal is not sufficient to argue that the system identification is good. Conversely, concurrent convergence of both the model prediction error and the cancellation error is sufficient to indicate a well-identified system.

Kuo and Morgan[11] argue that deliberately setting and holding **W** to a unit delay achieves the desired result as well. This is because the delay acts to decorrelate the excitation of **H** and that of **G**. It may be worth noting that broadband cancellation systems usually will have such a delay built into their processors. That is, secondary sources must be closer to the error sensors than are the primary sources, typically by slightly more than the minimum required for causality. The extra delay must be provided by the processor.

A second manner in which the system identification algorithm may appear not to converge, and indeed where any noninvasive system identification algorithm will not converge, results when insufficient signal-to-noise ratio (SNR) is available at certain frequencies in the error signal. In this case, which can be caused by insufficient power in the input signal or nulls in the system transfer functions due to nodes, the components are unobservable by the adapting algorithm or uncorrelated with what it is adapting, or both. The implications to system performance are minimal, however, as is discussed further in Sec. V.

IV. WELL-CONDITIONED SYSTEM IDENTIFICATION

This section discusses two practical considerations that arise during use of the system-identification algorithm with real hardware under realistic situations. Both affect the speed with which the algorithm converges. First, we discuss how arbitrary gains in the sensor and driver amplifiers result in arbitrary scalings of the transfer matrices $\hat{\mathbf{G}}$ and $\hat{\mathbf{H}}$. This scaling preferentially weights the data from one or the other, resulting in slow convergence. Second, we discuss how correlated input signals and noise in the error and sensor measurements result in a poorly conditioned matrix, $\mathbf{\Phi}^T\mathbf{\Phi}$. Simple approaches to improve both situations without overly complicating (and hence slowing) the algorithms are presented.

A. Scaling

The pseudoinverse solution of Eq. (22) returns a $\Delta\mathbf{\Theta}$ that solves $\mathbf{\Phi}^T\Delta\mathbf{\Theta}=\tilde{\mathbf{E}}$ and has minimum norm. However, when $\|\mathbf{x}\|$ and $\|\mathbf{u}\|$ are unbalanced, $\hat{\mathbf{G}}$ and $\hat{\mathbf{H}}$ are also unbalanced, so that the minimum $\|\Delta\mathbf{\Theta}\|$ is computed in a transformed (scaled) space, thus penalizing updates in the larger function more heavily than updates in the smaller. Therefore, iterations will progress slowly toward the larger of the two transfer functions, causing slow convergence. Limits of convergence for the smaller function are also reduced, as it is closer to the overall noise threshold.

The solution to the problem of internal scaling is straightforward. We take advantage of the knowledge that our system is used to *cancel* a signal at the error microphone. Therefore, we assume, *a priori*, that the acoustic transfer functions **H** and **G** should be of the same order. Clearly, a solution is to rescale $\hat{\mathbf{H}}$ and $\hat{\mathbf{G}}$ to be of the same order of magnitude. We accomplish the rescaling by normalizing **u** with respect to **x**, since the true values of **H** and **G** are not known to the algorithm. The multiple-channel case is also susceptible to poor performance because of unbalanced scales within a single channel or between channels, but the solution is again straightforward. By scaling all of the inputs and control outputs to a reference scale, we can ensure consistency among the channels as well as within a channel, leading to improved performance over the uncompensated case.

Simulations and experiments show the improved performance of the block-update algorithm with the scaling correction in place. It is important, however, to note that this scaling can be achieved in other ways. In the laboratory, where the dynamic range of processors and analog components constricts the computation accuracy, it is beneficial to maximize SNR by adjusting the various amplifiers so that measured signals are large in the processors' representation, without causing overflow. This constraint, when implemented carefully, is identical in spirit to the automatic approach discussed. As a result, our laboratory scaling factors were often essentially unity. Nevertheless, in systems where manual *a priori* scaling cannot be ensured, such as adaptive systems in the field, automatic scaling correction such as that we have proposed will likely be necessary.

B. Well-conditioned inverse

The abstraction of Eq. (22) represents the application of N_bN_e distinct constraints, which ideally uniquely identify an N_bN_e-dimensional subspace of the $(N_rL_g+N_dL_h)N_e$ free parameters in $\mathbf{\Theta}$. In actuality, such a system operates in the presence of noise. This noise will result in nonphysical solutions if the matrix $\mathbf{\Phi}^T\mathbf{\Phi}$ is poorly conditioned.[31]

In practice, we have observed condition numbers, given by $\sigma_{\max}(\mathbf{\Phi}^T\mathbf{\Phi})/\sigma_{\min}(\mathbf{\Phi}^T\mathbf{\Phi})$, on the order of ten to a few hundred. For such a condition number to be meaningful, it must be compared with the level of noise in the measurements, $\tilde{\mathbf{E}}$, in a consistent manner. One approach, reviewed in Ref. 32, assumes that the noise is independent, identically distributed (IID), and additive. Under such assumptions, one can show that computed updates become meaningless as the ratio of the SNR to the condition number drops below unity, in which case components of random noise and components of the solution reach equal magnitude.

A well-known and attractive method for stabilizing the inverse, to make the update meaningful in the presence of noise, is to use a Bayesian strategy to precondition the space of admissible solution vectors. We postulate that both the solution $\Delta\mathbf{\Theta}$ and the noise process are random variables.

Accordingly, our knowledge of the solution $\Delta\boldsymbol{\Theta}$ given a measurement $\tilde{\mathbf{E}}$ is described by the conditional density function $p(\Delta\boldsymbol{\Theta}|\tilde{\mathbf{E}})$. If we have a model for the noisy measurements, $p(\tilde{\mathbf{E}}|\Delta\boldsymbol{\Theta})$, and an *a priori* model for the solution vector, $p(\Delta\boldsymbol{\Theta})$, then the maximum *a posteriori* estimator, $\widehat{\Delta\hat{\boldsymbol{\Theta}}}$, for the solution (the maximum likelihood estimator for the conditional density function) is given by

$$\widehat{\Delta\boldsymbol{\Theta}} = \underset{\Delta\boldsymbol{\Theta}}{\operatorname{argmax}}\, p(\tilde{\mathbf{E}}|\Delta\boldsymbol{\Theta}) p(\Delta\boldsymbol{\Theta}),$$

where $\tilde{\mathbf{E}}$ is known data.

For simplicity here, we model both the prior for $\Delta\boldsymbol{\Theta}$ and the statistics of the noise added to $\hat{\mathbf{E}}$ as IID normal processes with differing variances. Certain improvements to these statistical assumptions are apparent, however, since it is likely that the prior for $\Delta\boldsymbol{\Theta}$ should reflect a correlation between neighboring taps. As is straightforward to show, the maximum *a posteriori* estimator is given by

$$\widehat{\Delta\boldsymbol{\Theta}} = \boldsymbol{\Phi}\left(\boldsymbol{\Phi}^T\boldsymbol{\Phi} + \frac{\sigma_{\Delta\boldsymbol{\Theta}}{}^2}{\sigma_{\tilde{E}}^2} I\right)^{-1} \tilde{\mathbf{E}}. \tag{24}$$

Recall that Eq. (22) is the minimum norm estimate for $\Delta\boldsymbol{\Theta}$, given $\tilde{\mathbf{E}}$, in the absence of noise. We have replaced this equation in the block-update scheme with Eq. (24), which is the maximum *a posteriori* estimate for $\Delta\boldsymbol{\Theta}$, given $\tilde{\mathbf{E}}$, and is optimal under the assumption of IID normal distributions. Although much more detailed distributions may be easily incorporated into the formulation, our simplistic, preliminary assumptions offer the comfort of reducing the Bayesian estimate to the familiar Tikhanov regularized solution. Morgan and Kratzer review several other related assumptions that lead to the same regularization term and motivate its occurrence differently.

V. SIMULATION AND DISCUSSION

The on-line system identification algorithm presented in this paper was simulated on a digital computer and subsequently implemented in hardware for experimental verification. The simulation results are for a much smaller system than that finally implemented.

All simulations reported here are single channel, although multiple-channel simulations have been completed. We report only single-channel simulations because excessive simulation time is required to complete multichannel ones, and all the essential behavior of the system is found in the single-channel cases. A multichannel experiment is presented in our companion paper.

The algorithm embodied in Eq. (22) and modified in Eq. (24) was tested using transfer functions measured in an anechoic chamber. To obtain the ''true'' transfer functions, **H** and **G**, the measured transfer functions are low-pass filtered and decimated from the original 4-kHz sampling rate by a factor of 12, thus further reducing simulation times. Both **H** and **G** are represented by a 32-tap FIR, while the control filter, **W**, is represented by a 64-tap FIR, and is adapted using standard FXLMS. The adaptation gain, μ, is set according to the formula

$$\mu = \frac{2}{9\|\mathbf{H}\|_2^2 (L_w + L_{\text{delay}})}, \tag{25}$$

where L_{delay} is the delay in samples from the actuator to the error microphone.

All varying transfer functions, $\hat{\mathbf{H}}$, $\hat{\mathbf{G}}$, and **W**, are initialized to zero at the beginning of each simulation, and white noise is used to drive the system. Additionally, uncorrelated white noise is injected into the system to simulate measurement errors at two points: where **x** is measured prior to convolution with **W**, and where **e** is measured prior to computation of the FXLMS update and $\hat{\mathbf{E}}$. The SNR in both cases is 100.

Updates are computed only once every BLOCK_WAIT samples, where

$$\text{BLOCK\_WAIT} = \frac{F_3}{10} + \frac{N_b^3}{100^3}\frac{F_s}{2}, \tag{26}$$

and $F_s = 333$ Hz is the sampling rate modeled by the simulation. This quantity is the overhead time, in samples, associated with computing the inverse, and includes a constant 0.1-s polling, interrupt, and transfer time, and a matrix inverse time that grows as the cube of the block size, calibrated so that an inverse for a block size of 100 takes 0.5 s.

Figure 6 shows representative convergence for a system with block size $N_b = 20$, and illustrates an important point. The way to interpret the plots is as follows. The true transfer function is the top (dashed) line on either graph. The first iteration, a horizontal line of all zeros, is shown at the bottom of each plot, at time $t = 0$ on the abscissa. Subsequent iterations are plotted next to the time of their recording. The final iteration is the next-to-top line on each plot, and occurs at about $t = 9$ s. The lines are more closely spaced at the bottom of each plot because nonuniform, logarithmic spacing was used to determine the 42 time slices at which $\hat{\mathbf{G}}$ and $\hat{\mathbf{H}}$ were recorded.

It is important to note that the iterations are visibly dissimilar from the true transfer functions, despite an adequate SNR. This is a direct limitation of noninvasive system identification, and not a reflection on the particular algorithm. In fact, we now show under certain mild assumptions that there is an equivalence class of transfer functions, $\{\hat{\mathbf{G}}, \hat{\mathbf{H}}\}$, for which $\tilde{\mathbf{E}}$ is minimized, and it is impossible for the algorithm to distinguish members of this class. However, *performance* of the ANC system is invariant for this class; thus, we conclude that plots such as Fig. 6 can appear overly conservative, as explained below.

Consider a stationary input, **x**, that is the output of an idealized low-pass filter. Above some f_c, its power spectral density is zero. Noisy measurements of **e** cause $\hat{\mathbf{G}}$ to have a nonzero frequency response above f_c; however, this high-frequency estimate would be based entirely on noise. The true high-frequency response is unknowable, because there is no power in the probing signal at that frequency. Let $\hat{\mathbf{G}}_h$ be the high-frequency component of the estimate, $\hat{\mathbf{G}}$, and let $\hat{\mathbf{G}}_l$ be the complementary low-frequency component. Similarly, define $\mathbf{G}_h$ and $\mathbf{G}_l$. The response of **G** to its input is

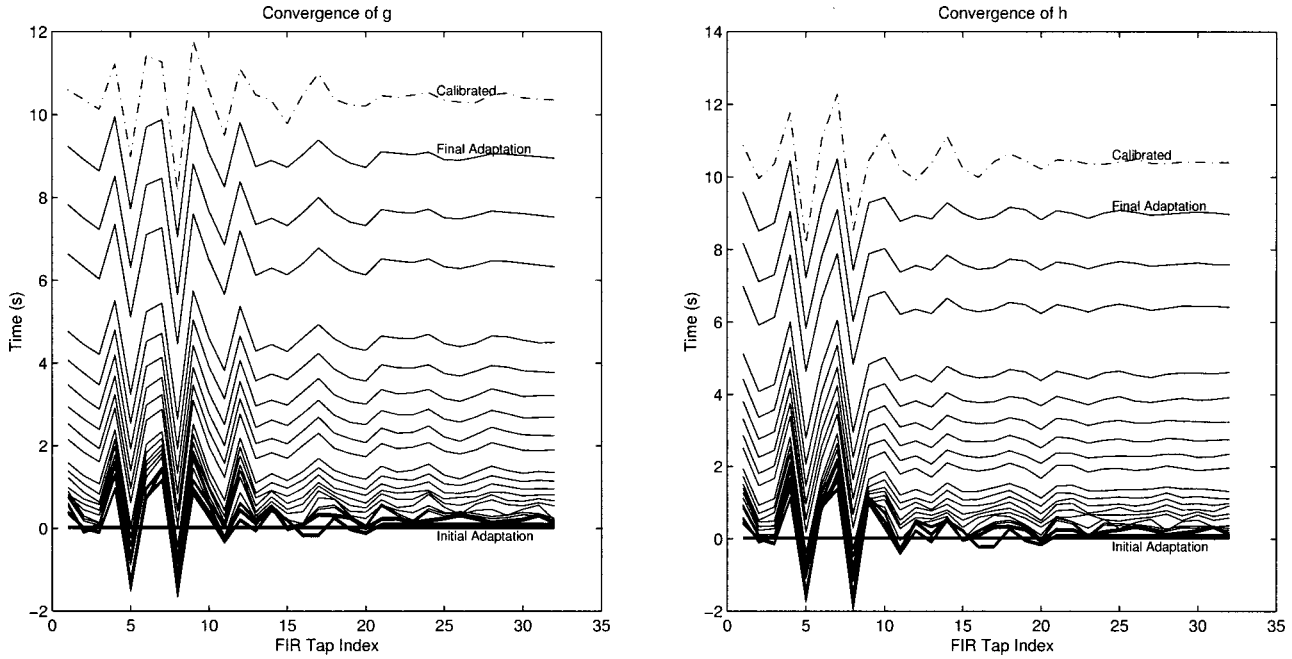

FIG. 6. Iterative convergence of the algorithm to the true transfer functions, G^e and H^e. The first iteration is at the bottom of the plot, and subsequent iterations are plotted moving up the time axis. The final (dashed) curve is the true transfer function.

$$\mathbf{x}*\mathbf{G}=\mathbf{x}*\mathbf{G}_l\,.$$

Similarly, the internally predicted response is

$$\mathbf{x}*\hat{\mathbf{G}}=\mathbf{x}*\hat{\mathbf{G}}_l\,.$$

Thus, the contribution to the model prediction error from $\mathbf{G}$ and $\hat{\mathbf{G}}$ is independent of $\mathbf{G}_h-\hat{\mathbf{G}}_h$. Analogous definitions for $\mathbf{H}_h$, $\mathbf{H}_l$, $\hat{\mathbf{H}}_h$, and $\hat{\mathbf{H}}_l$ show that the model prediction error is independent of $\mathbf{H}_h-\hat{\mathbf{H}}_h$, as well.

We have defined an equivalence class, $\{\hat{\mathbf{G}},\hat{\mathbf{H}}\}$, where elements of the class cannot be resolved by the model prediction error. Members of the class differ exactly at frequencies where the power of the input signal is zero (e.g., nodal frequencies at particular points in a reverberant room). This class contains the true plant, $\{\mathbf{G},\mathbf{H}\}$, and performance is identical for all models in the class.

In reality, there will always be some power in $\mathbf{x}$ at all frequencies. The engineering generalization of the above discussion is that frequencies with lower power in the input signal are identified more slowly and tend to have larger errors. It is important to note that, although these components are identified more slowly, the same masking mechanism that slows convergence also ensures that the resulting misidentification does not hinder performance. Convergence can be sped if the statistics of $\mathbf{x}$ change, so that the noiseless signal, $\mathbf{e}$, has improved SNR at troublesome frequencies. When this happens, the shape of the error function changes and the convergence rate increases. In addition, one may bandpass filter $\mathbf{e}$ and $\hat{\mathbf{e}}$ before comparing them, to avoid attempting to identify noise, if the additional delay is tolerable.

An example of the inability to identify the system at nodal frequencies is shown in the frequency domain plot of Fig. 7. These plots are analogous to those of Fig. 6, and show comparison in frequency for amplitude and phase for the same simulation. The plots clearly indicate that identification has proceeded well except for frequencies near where the SNR is particularly low.

Instead of trusting direct comparison of internal and external transfer functions, we turn to the convergence of the model prediction error as a measure of system identification performance. Recall that when the system cancellation filter is allowed to adapt, the model prediction error is a good measure of system identification performance. Figure 8 shows convergence of this quantity for a number of different block sizes. Further recall that the block-update period varies as a constant 0.1 s plus a term proportional to the cube of the block size. For N_b taken from the set {5,20,40,75}, the corresponding update periods in samples are {34,35,45,104}. The constant transfer time penalty is approximately 33 samples.

Also plotted in Fig. 8 is the convergence of the model prediction error signal for system identification using standard normalized LMS (NLMS) as implemented in the manner of Sommerfeldt. Note that this curve is obtained by updating the estimates every sample, and is not a viable option for implementation in large MIMO systems because of extreme interprocessor communication requirements due to the large overhead of many small data transfers.

Figure 8 shows that as block size increases, the block projection algorithm's performance matches that of NLMS. This is true despite the fact that the block algorithm is updating at only a fraction of the frequency of NLMS. It is important to note that the block algorithm is actually using less data than NLMS, because of the imposed delay for each update consisting of transfer delay and computation delay is longer than the time required to collect a block of data. For a block size of 5, the constant overhead of data transfer overly penalizes the block algorithm, but for $N_b=20$, the algorithm

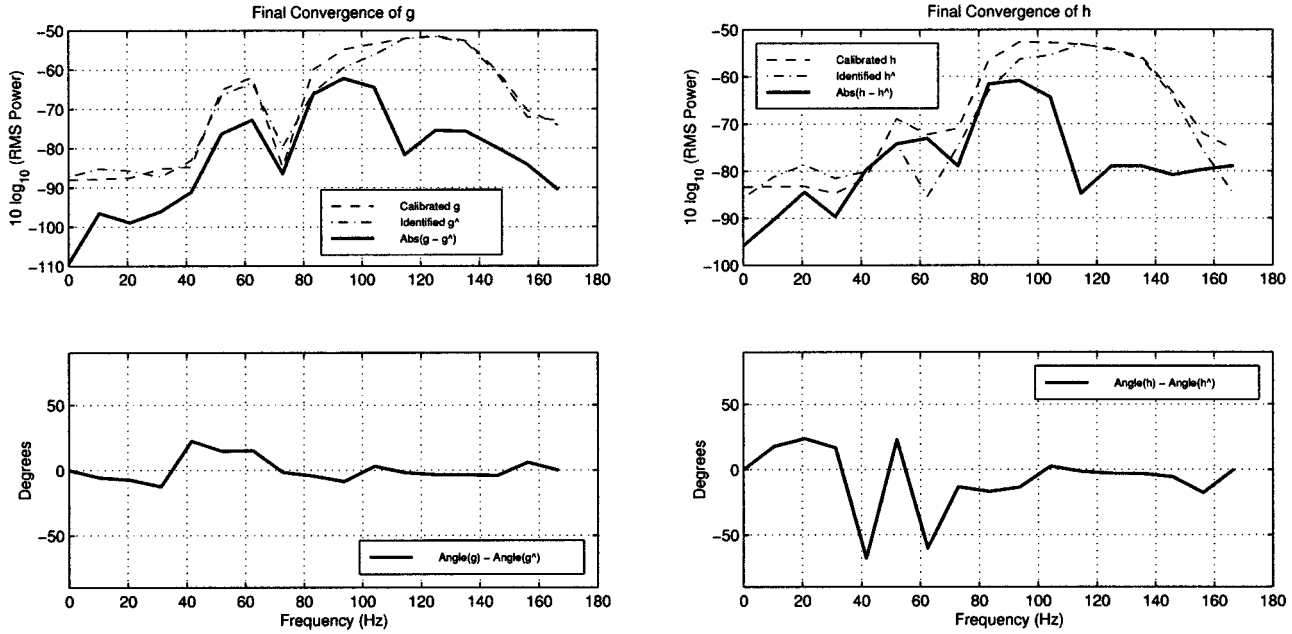

FIG. 7. Comparison of identified and deconvolved system transfer functions in the frequency domain. The top plot of each pair compares magnitude of the complex filter weights, and the bottom plot compares phase. Note in particular the poor performance around 60 Hz for both functions.

is able to make up the difference and achieve results similar to NLMS. Finally, the $N_b = 75$ case represents an overdetermined update, with more measurements than unknowns. The algorithm continues to provide good performance in this case as well. The plot also shows that the block algorithm is slower than standard NLMS to begin achieving reduction of model prediction error. We believe that this is caused by the delay associated with waiting to group a large block of data together. In general, smaller blocks track fast changes in system dynamics more readily, while larger blocks do better at achieving a lower final model prediction error if the system is static.

There are significant structures in the formation of the matrix $\mathbf{\Phi}^T\mathbf{\Phi}$ which enable the efficient computation of its inverse. These have not been detailed here; many are covered by Montazeri and Duhamel.[33,29] However, their discussion is restricted to the single-channel case where a single transfer function is being identified. Of particular distinction, therefore, is the block structure of $\mathbf{\Phi}$. Within each block is the identical structure of a Toeplitz matrix, but there is no structure in the arrangement of the blocks themselves. It is possible to take advantage of the block structure in computing the inverse; however, we have not done so here. Instead, we have formed $\mathbf{\Phi}$ rapidly and computed the inverse using general techniques.

VI. CONCLUSIONS

We have presented a novel algorithm for noninvasively identifying the FIR transfer functions of a broadband multichannel feedforward adaptive ANC problem. The algorithm is robust to certain types of noise and adapts to changes in scale of $\mathbf{x}$ compared to $\mathbf{u}$, thus speeding convergence. The algorithm was simulated using measured data and found to converge in times comparable to or faster than NLMS. We have argued that the model prediction error is the most appropriate measure of estimating system-identification performance, under the assumption that the cancellation adaptation and system-identification adaptation take place concurrently.

This algorithm has been tested as part of a broadband, real-time multichannel ANC system for a reverberant environment, and the test and its results are described in the companion paper. Performance in excess of 20 dB, as measured at the error microphones, was achieved over a band from 50 to 1000 Hz. The system has also been tested in an anechoic chamber, providing similar results for a 1-input, 4-output, 2-error configuration, and for a 2-input, 4-output, 2-error configuration. In this case, sensors were used to measure the output of loudspeakers, and a neutralization filter was calibrated off-line to cancel the coupling path from sec-

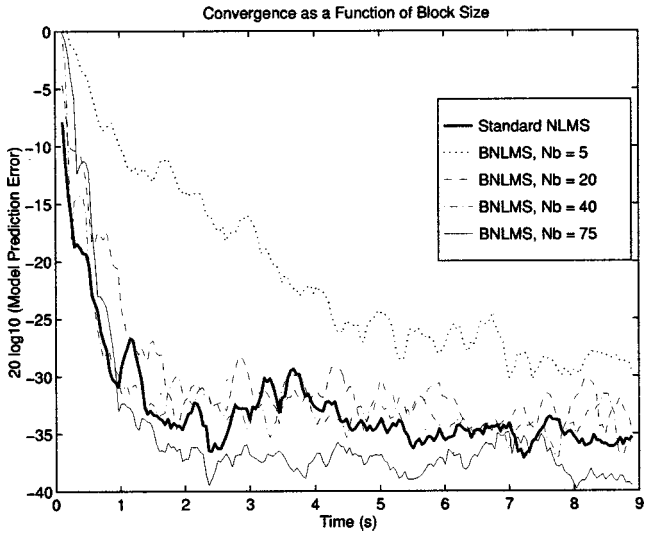

FIG. 8. Convergence of the block projection algorithm as function of block size. Also shown is the convergence of standard NLMS updating every cycle. The data have been smoothed for plotting purposes by application of a 75-point moving rms filter.

ondary loudspeakers to the input sensors (the *Q*- or Youla parameterization[7]). The implementation in the comparatively expansive anechoic chamber enabled the error microphones to be moved about, providing a ''mobile quiet zone.''

This technique is motivated by certain computational limitations of the signal-processing hardware used. However, if transfer times are reduced or the block update is implemented in hardware, then the block projection algorithm will outperform NLMS, because each update uses a multitude of measurements rather than a single measurement. As such, we believe its applicability to be broad.

This paper focuses on system identification issues at the expense of ANC system design or performance issues. Hence, the problems of quiet-zone size and related issues have not been fully addressed; performance numbers that are effective measures of the system identification algorithm are less illuminating concerning overall efficacy of the ANC system. The informed tradeoff of performance vs quiet-zone size and other issues remains an unsolved problem. Finally, there are additional open issues for feedback control. Most importantly, we are aware of no technique for noninvasively determining the coupling transfer functions while such a system is running.

ACKNOWLEDGMENTS

The authors gratefully acknowledge the efforts of Dr. J. Raúl Martínez of the System Technology Division at SRI International in supporting this work. The authors also thanks the anonymous reviewers, whose comments were insightful and appreciated.

[1] K. Fukumizu, H. Kitagawa, and M. Yoneyama, ''Active noise control with indoor positioning system,'' in *Proc. Second International Congress on Recent Developments in Air- and Structure-Borne Sound and Vibration*, March 1992, pp. 329–336.
[2] S. Laugesen and S. J. Elliott, ''Multichannel active noise control of random noise in a small reverberant room,'' IEEE Trans. Speech Audio Process. **1(2)**, 241–249 (1993).
[3] D. E. Melton and R. A. Greiner, ''Adaptive feedforward multiple-input, multiple-output active noise control,'' in *Proc. IEEE Intern. Conference on Acoustics, Speech, Signal Processing*, Vol. II, San Francisco, CA, 1992, pp. 229–232.
[4] P. A. Nelson, A. R. D. Curtis, S. J. Elliott, and A. J. Bullmore, ''The active minimization of harmonic enclosed sound fields. Theory'' J. Sound Vib. **117(1)**, 1–13 (1987).
[5] K. J. Åström, ''Theory and application of adaptive control—a survey,'' Automatica **19**, 471–486 (1983).
[6] K. J. Åström and B. Wittenmark, *Adaptive Control* (Addison-Wesley, Reading, MA, 1989).
[7] J. M. Maciejowski, *Multivariable Feedback Design* (Addison-Wesley, Wokingham, England, 1989).
[8] B. Widrow and S. D. Sterns, *Adaptive Signal Processing* (Prentice-Hall, Englewood Cliffs, NJ, 1985).
[9] L. J. Eriksson, ''Development of the filtered-U algorithm for active noise control,'' J. Acoust. Soc. Am. **89**, 257–265 (1991).
[10] D. R. Morgan and D. A. Quinlan, ''Local silencing of room acoustic noise using broadband active noise cancellation,'' in *Final Program and Paper Summaries*, IEEE Workshop on Applications of Signal Processing to Audio and Acoustics, 1993.
[11] S. M. Kuo and D. R. Morgan, *Active Noise Control Systems: Algorithms and DSP Implementations* (Wiley, New York, 1996).
[12] S. D. Sommerfeldt, ''Multi-channel adaptive control of structural vibration,'' Noise Control Eng. J. **37**(2), 77–89 (1991).
[13] S. D. Sommerfeldt and J. Tichy, ''Adaptive control of a two-stage vibration isolation mount,'' J. Acoust. Soc. Am. **88**, 938–944 (1990).
[14] D. R. Morgan and S. G. Kratzer, ''On a class of computationally efficient, rapidly converging, generalized NLMS algorithms.'' IEEE Signal Process. Lett. **3**(8), 245–247 (1996).
[15] W. C. Nowlin, G. S. Guthart, and G. K. Toth, ''Experimental results for multichannel feedforward ANC with noninvasive system identification,'' J. Acoust. Soc. Am. **107**, 2039–2048 (2000).
[16] S. J. Elliott, P. Joseph, A. J. Bullmore, and P. A. Nelson, ''Active cancellation at a point in a pure tone diffuse sound field,'' J. Sound Vib. **120**(1), 183–189 (1988).
[17] S. J. Elliott, I. M. Strothers, P. A. Nelson, A. M. McDonald, D. C. Quinn, and T. Saunders, ''The active control of engine noise inside cars,'' in *Proc. Inter-noise 88*, pp. 987–990.
[18] P. M. Joplin and P. A. Nelson, ''Active control of low-frequency random sound in enclosures,'' J. Acoust. Soc. Am. **87**, 2396–2404 (1990).
[19] A. J. Bullmore, P. A. Nelson, A. R. D. Curtis, and S. J. Elliott. ''The active minimization of harmonic enclosed sound fields. A computer simulation,'' J. Sound Vib. **117**(1), 15–33 (1987).
[20] S. J. Elliott, A. R. D. Curtis, A. J. Bullmore, and P. A. Nelson. ''The active minimization of harmonic enclosed sound fields. Experimental verification,'' J. Sound Vib. **117**(1), 35–58 (1987).
[21] P. J. Nashif and S. D. Sommerfeldt, ''An active control strategy for minimizing the energy density in enclosures,'' in *Proc. Inter-noise 92*, Toronto, Ontario, pp. 357–362.
[22] P. J. Titterton, Jr., ''Practical multi-constraint H-infinity controller synthesis from time-domain data,'' Int. J. Robust Nonlinear Control **6**, 415–420 (1996).
[23] W. A. Weeks, C. T. Chittenden, and P. M. Heilman, ''Hardware control of a real-time multichannel digital signal processing system,'' in *Proc. 25th Asilomar Conference on Signals, Systems, and Computers*, 1991, pp. 423–428.
[24] S. P. Boyd and C. H. Barratt, *Linear Controller Design: Limits of Performance* (Prentice-Hall, Princeton, NJ, 1991).
[25] B. Widrow, D. Shur, and S. Schaffer, ''On adaptive inverse control,'' in *Proc. 15th Asilomar Conference on Circuits, Systems and Computers*, 1981, pp. 185–189.
[26] J. C. Burgess, ''Active adaptive sound control in a duct: A computer simulation,'' J. Acoust. Soc. Am. **70**, 715–726 (1981).
[27] S. C. Douglas and J. A. Olkin, ''Multiple-input, multiple-output, multiple-error adaptive feedforward control using the filtered-X normalized LMS algorithm,'' in *Second Conference on Recent Advances in Active Control of Sound and Vibration*, 1993, pp. 743–755.
[28] W. A. Weeks and B. L. Curless, ''A real-time, multichannel system with parallel digital signal processors,'' in *Proc. of ICASSP 90*, pp. 1787–1790.
[29] M. Montazeri and P. Duhamel, ''A set of algorithms linking NLMS and block RLS algorithms,'' IEEE Trans. Signal Process. **43**(2), 444–453 (1995).
[30] M. Athans and F. C. Schweppe, ''Gradient matrices and matrix calculations,'' Technical Report, Massachusetts Institute of Technology Lincoln Laboratory, Lincoln, MA, 1965.
[31] G. H. Golub and C. F. Van Loan, *Matrix Computations*, 2nd ed. (The Johns Hopkins University Press, Baltimore, 1989).
[32] W. C. Nowlin, ''Tactile Sensing with Compliant Manipulators,'' Ph.D. thesis, Harvard University, 1991.
[33] M. Montazeri and P. Duhamel, ''A set of algorithms linking NLMS and block RLS algorithms,'' in *Proc. IEEE International Conference on Acoustics, Speech, Signal Processing*, Minneapolis, MN, April 1993, pp. 412–415.

Modal control of beam flexural vibration

Nicolas Rizet, Michel Brissaud, and Paul Gonnard
Laboratoire de Génie Electrique et Ferroélectricité, I.N.S.A. Lyon, Bât 504, 20 Av. A. Einstein, F69621 Villeurbanne Cedex, France

Jean-Christophe Béra and Michel Sunyach
Centre Acoustique, Ecole Centrale de Lyon, F69131 Ecully Cedex, France

(Received 25 August 1998; accepted for publication 27 December 1999)

An active control system was developed to control the flexural vibrations of a beam with a modal filtering with only one secondary actuator. Segmented piezoelectric actuators and sensors were used for driving and sensing the bending beam vibrations. The primary actuator was fed by a broadband random disturbance signal in order to excite the first five modes of the structure. However, only the second to fifth modes were controlled. The control algorithm was implemented on a DSP board and the input and output signals were filtered using high order low pass filters. These filters, implemented on the DSP board avoid the degrading effect on the control performances of the higher order modes and which are not controlled. The modal filtering was achieved by computing. To this end, it is based on a previous identification procedure. This latter models, in one step, the dynamics of the structure and also the transfer function of the electronic circuits of the controller. The identified filtered modes were then used to compute the gain matrix using a LQR technique (linear quadratic regulator). Simulations of the active control were carried out and practical implementation of the control algorithms was performed. Experimental and simulation results were then compared and discussed. © *2000 Acoustical Society of America.* [S0001-4966(00)03804-2]

PACS numbers: 43.40.Vn [PJR]

INTRODUCTION

Active control is nowadays an efficient tool for attenuating low frequency sounds and vibrations. The basic ideas of Lueg[1] and Olson and May[2] have been developed by numerous authors and applied to control lumped and distributed parameter structures.[3–7] The theory of this technique is now well established, and industrial and space applications become possible because fast advanced DSP chips become available. Active control is very effective for simple cases, but its application to more complicated structures like distributed parameter structure[4] is not so easy. Several authors stated the theoretical bases of the control of such systems. Among them, Meirovitch *et al.*[3] adapted the independent modal space control theory to these particular structures and proposed an experimental procedure for implementing this method in a controller.[6] To this end, he introduced the modal filtering concept. The displacements, at different points of the structure, were measured using a sensor array. The sensor signal is proportional to the amplitude of each mode at the measuring point. That is, it is a linear combination of the different mode amplitudes at that point. They have shown that, if no optimizing techniques are used, the actuator number must be equal to the controlled modes. Lindberg[8] showed that the actuator number can be reduced using an optimization method. As a result, spill over is also reduced. As summarized by Fuller,[9] modal filtering can be achieved either by computing or by an appropriate sensor shape. Bailey *et al.*[10] proposed a distributed piezoelectric polymer for control the vibration of a cantilever beam. Lee *et al.*[11] stated the charge equations deliver by laminated piezoelectric plates used as sensors and actuators.

The purpose of this paper is the modal control implementation in order to attenuate the global bending vibrations of simple supported beam. Piezoceramic sensors and actuators were used. Contrary to Meirovitch or Lindberg approaches, only one secondary actuator was used for controlling the flexural vibrations of the beam. A LQR technique[12,13] was performed for optimizing the controller functioning. As it will be shown, the secondary actuator placement is not obvious for actuating these modes. The primary piezoceramic is fed with a broadband disturbance signal in order to excite the first five modes of the structure. This paper focuses on the experimental procedure for implementing an efficient active control of the beam vibrations.

I. MODAL FILTERING PROCEDURE

The control equations of a system are generally written in the space state on the form:[6]

$$\dot{\mathbf{x}}(\mathbf{t}) = \mathbf{A}\mathbf{x}(\mathbf{t}) + \mathbf{B}\mathbf{u}(\mathbf{t}), \quad \mathbf{y}(\mathbf{t}) = \mathbf{C}\mathbf{x}(\mathbf{t}) + \mathbf{D}\mathbf{u}(\mathbf{t}), \tag{1}$$

where $\mathbf{x}(\mathbf{t})$, $\mathbf{u}(\mathbf{t})$, and $\mathbf{y}(\mathbf{t})$ are the state vector, the perturbation vector and the system output. The components of matrices *A, B, C, D* are generally constant. If the system outputs do not explicitly depend on the inputs then, matrix *D* is equal to zero.

Distributed parameter structures like beams exhibit resonance modes.[14] Displacements associated to the modes constitute the modal basis if and only if the losses associated to these modes are small. Hence, control modes can be independently controlled in terms of stiffness and damping.[9,15] Using the modal state vector $\mathbf{z}(\mathbf{t})$, the state equations (1) can be then be rewritten as follows:

$$\dot{\mathbf{z}}(\mathbf{t}) = \mathbf{A}'\mathbf{z}(\mathbf{t}) + \mathbf{B}'\mathbf{u}(\mathbf{t}), \quad \mathbf{y}(\mathbf{t}) = \mathbf{C}'\mathbf{z}(\mathbf{t}). \tag{2}$$

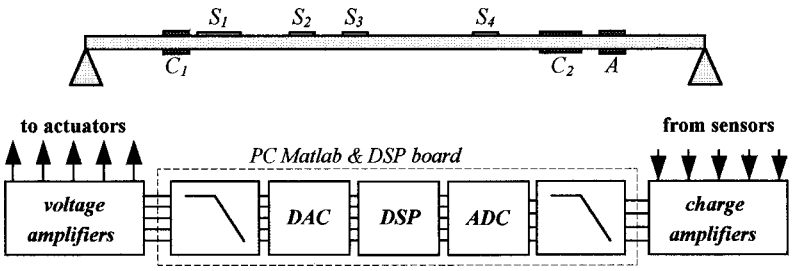

FIG. 1. Experimental setup.

The state vector $\mathbf{z}(\mathbf{t})$ is constituted by the modal coordinate and velocity vectors $[\eta(t), \dot{\eta}(t)]$, respectively. Participation C' matrix coefficients are the mode amplitudes W_{ij} at the sensor position. It should be noted that practical measurements do not directly give the components of the $\mathbf{z}(\mathbf{t})$ vector; they have to be obtained using modal filtering.

Modal filtering is the key point of this method. It leads to the modal state vector from the outputs of the system. Denoting V_i the vector formed by the sensor patch outputs. It is the image of modal displacement W_j filtered by the modal participation matrix *Mij*:

$$V_i = M_{ij} W_j . \tag{3}$$

The dimension of the matrix M coefficients is V/m. Modal participation matrix M_{ij} is related to both the sensor patch transfer function and the amplitudes of the modes at the sensor location when a broadband excitation of the beam is considered. The different components of matrix C are determined in the specific procedure as follows. The displacement reference sensor is successively located at the maximum of vibration of each mode and constitutes the reference signal for each mode. Sensor responses are then normalized according to this reference. When the matrix components have been determined, the modal coordinates can be calculated by inverting M_{ij} matrix:

$$K_{ij} = M^{-1}. \tag{4}$$

The dimension of the matrix K coefficients is m/V. They are the coefficients to be applied to the sensor i for the calculation of the modal coordinate j. Matrix K is then computed and implemented on the DSP board.

II. EXPERIMENTAL SETUP

The experimental setup is depicted in Fig. 1. A steel beam is used and its dimensions are $600 \times 41 \times 2.7\ \mathrm{m}^3$. The simply supported boundary conditions are achieved using heavy rollers. The control algorithm is implemented on a DSP board developed at the Center Acoustique of the Ecole Centrale de Lyon. This board is based on the Analog Devices ADSP2101 processor and presents 4 inputs/5 outputs with parallel sampling. The PZT sensor patch outputs are connected to some charge amplifiers developed in our laboratory. Four channels with adjustable gains are available. The output signals from the charge amplifiers are passed through anti-aliasing filters so as to present a bandwidth limited to the modes of interest, namely below 450 Hz. Two Trek 50/750 amplifiers are used to provide the required voltages to the PZT actuator patches.

A. Actuator patches

As illustrated in Fig. 2, the piezoceramic patches used for actuating have the same size and are co-located on the beam. They are bonded with inverted polarization directions in order to produce opposite displacement when driving with the same voltage V. In this case, when the upper patch is extending the lower patch contracting which induces pure bending of the beam. The patch dimensions are $20 \times 10 \times 1\ \mathrm{mm}^3$.

B. Sensor patches

Piezoceramic patches are also used as motion sensors (Fig. 3). They have the same dimensions as the actuator patches and are also bonded on the beam. Lee[11] developed the governing equations for such distributed piezoelectric sensor. Denoting $q(t)$ the charges deliver by the piezoelectric sensor they are related to the beam displacement by

$$q(t) = -\frac{(h_b + h_p)}{2} \int_{S_p} e_{31} \frac{\partial^2 w(x,t)}{\partial x^2} dx\, dy, \tag{5}$$

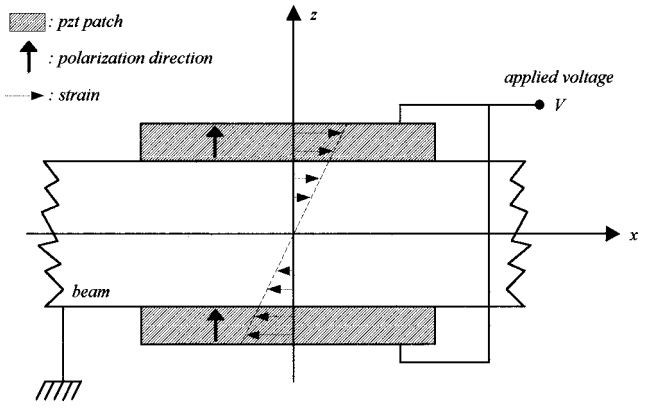

FIG. 2. Actuator patches and strain distribution along the z direction.

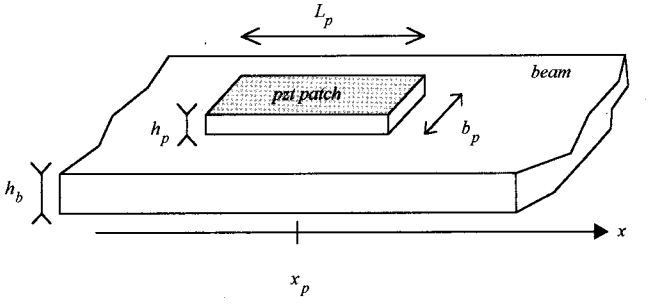

FIG. 3. Sensor patch configuration.

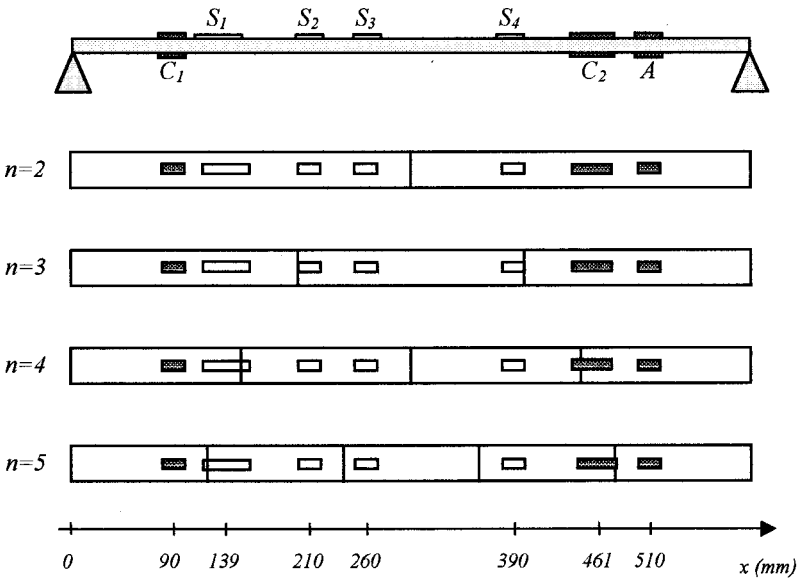

FIG. 4. Piezoelectric patch locations.

where S_p is the area covered by the sensor patch, e_{31} is the piezoelectric stress/charge constant, and h_b and h_p are the beam and the patch thickness, respectively. In the considered case, the generated charge can be written

$$q(t)=\sum_{n=1}^{\infty} q_n(t) \tag{6}$$

with

$$q_n(t)=A\sin(\gamma_n x_p)W_n\eta_n(t) \tag{7}$$

and

$$A=n^2\pi^2 b_p\frac{(h_b+h_p)}{2L_p}e_{31}, \tag{8}$$

where n is the modal index, W_n is the nth modal maximum amplitude, $\gamma_n=n\pi/L$ is the nth eigenvalue, L is the beam length (x direction), and η_n is the nth modal coordinate.

Equation (7) shows that the charge is proportional to the displacement for a given mode. For a number of excited modes limited to N, the charge can be approximated by

$$q(t)=\sum_{n=1}^{N} q_n(t). \tag{9}$$

The sensor output is then the sum of the weighted contributions of modal displacements. In the case of low frequency structural vibrations as in this paper, the assumption of slightly damped and well-separated modes is justified. Consequently, the modal responses can be extracted by combining the outputs of a sensor array. Modal control is based on this property and it is used in this paper.

C. Patch locations

Three actuators (A, C1, and C2) and four sensors (S1 to S4) have been implemented on the beam. Figure 4 presents the patch locations and their positions relative to the nodal lines (found from the analytical modeling of the beam). The locations have been chosen in such a way to avoid the nodal lines appearing for the low frequency bending modes.[14] Consequently, the patches are likely to sense or to excite (according to the affected function) the four modes of interest.

Several configurations of disturbance and control actuators have been tested. This paper only presents one configuration, with A as primary actuator (perturbation) and C2 as secondary actuator (control).

D. Broadband disturbance signal

The disturbance actuator is driven by a pseudo-random band-limited signal so as to excite four bending modes of the structure. The average frequency spectrum of the disturbance signal is plotted in Fig. 5. The first flexural mode has not been considered because of the difficulties to sense efficiently the corresponding displacement in the frequency range below 30 Hz.

III. CONTROL DESIGN SIMULATION

A. Matrix *K* calculation

As it was mentioned in Sec. I, the *Kij* matrix-using equation were computed by inverting matrix *M* and implemented

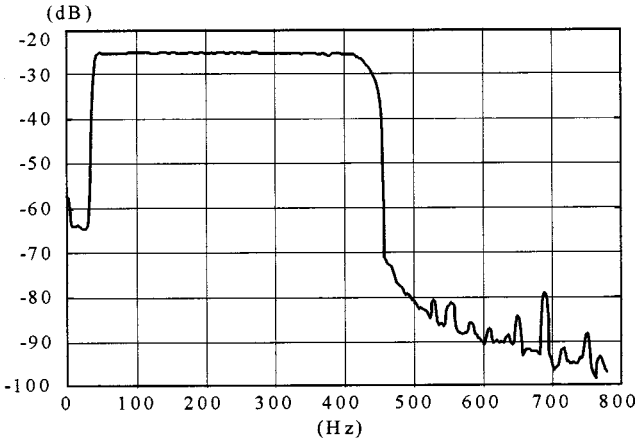

FIG. 5. Frequency spectrum of the disturbance signal.

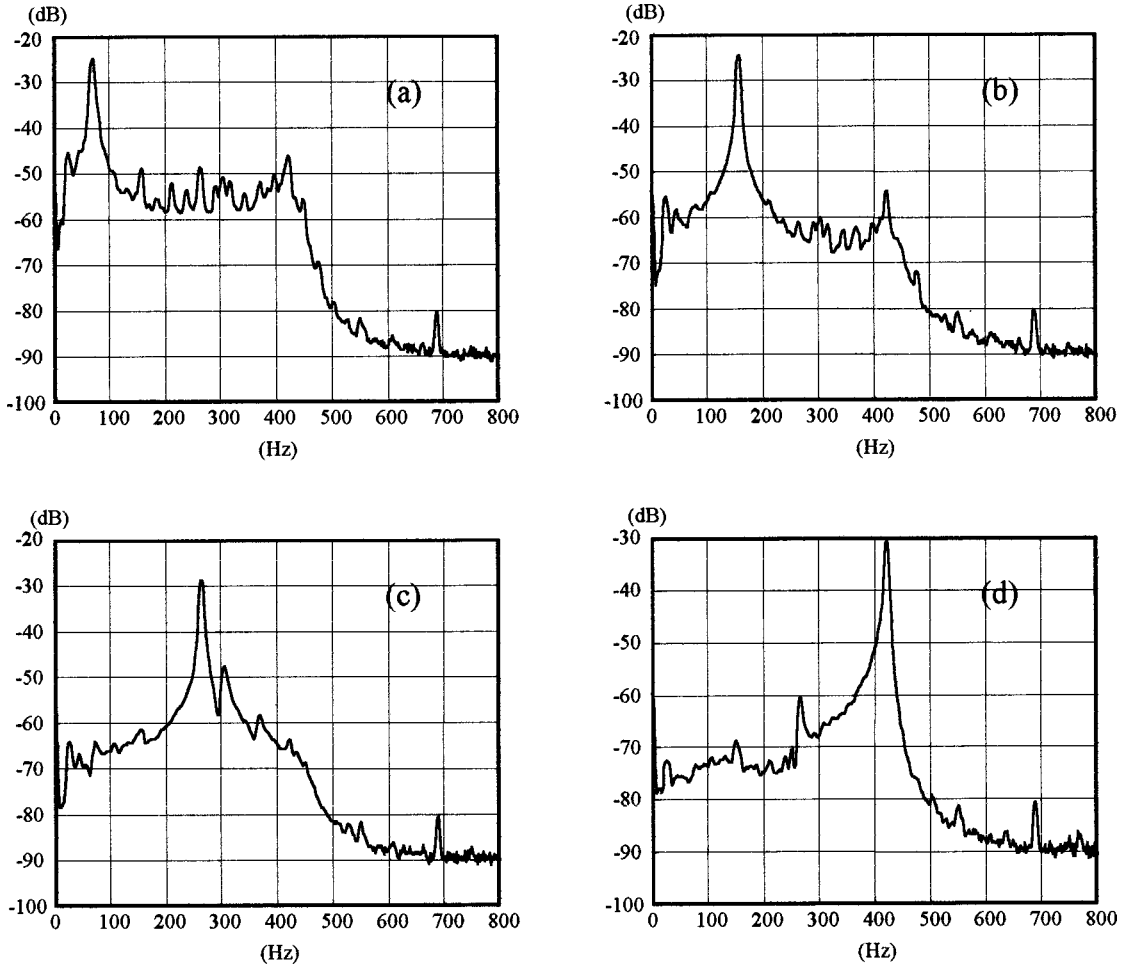

FIG. 6. Filtered modes: mode II (a), mode III (b), mode IV (c), and mode V (d).

on the DSP board to extract the modal coordinates from the sensor outputs. White noise excitation signal span is 30–450 Hz in order to excite four mode of the structure. The resulted spectra of the four filtered modes are given in Fig. 6. The modes are well-separated and the maximum amplitudes are nearly the same. The minimum noise, in the white noise range is within 55 dB to 75 dB.

B. Electronic FRFs

The phase lags and time delays of the anti-aliasing and reconstruction filters, the samplers, the amplifier, and the actuators are identified. Figure 7 shows the measured and the modeled FRF of the system DSP card/amplifier. It is the transfer function between DSP card input and voltage amplifier output.

As both input and output filters are of sixth order filters, the identified model is a simple polynomial of degree 12 coupled to a delay term that represents the sampling time.

C. Numerical simulations for control system design

To calculate the control gain matrix, the FRFs between control patches and modal filter outputs are identified in a parametric identification program which returns the eigenvalues (Figs. 8 and 9). The modal input matrix, which characterizes the modal response of the structure for the excitation of the control actuator, is also measured [matrix B in the space-state model; see Eq. (8)]. Hence, a state-space model is constructed in the modal domain.

To illustrate the identification results, Fig. 10 shows the modeled and experimental FRF modules placed between actuator patch C1 and sensor S4 for the frequency range (0–700 Hz).

The LQ control is first simulated with Matlab using the actual dimensions of our structure. The four modes of interest are modeled with the assumption of proportional damping, justified by the small measured damping factors, as indicated by Meirovitch.[7] The experimental FRFs previously identified are used. The modal displacements are supposed to be perfectly known.

Given the discrete-time state-space system,

$$x_{n+1}=Ax_n+Bu_n, \quad y_n=Cy_n+Du_n. \tag{10}$$

LQR control gives the optimal control matrix K such that:

$$u_n=-Kx_n \tag{11}$$

minimizes the cost function J given by,

$$J=\sum y'Qy+u'Ru, \tag{12}$$

where Q and R weight the outputs and the control inputs, respectively. Different simulations have been investigated to

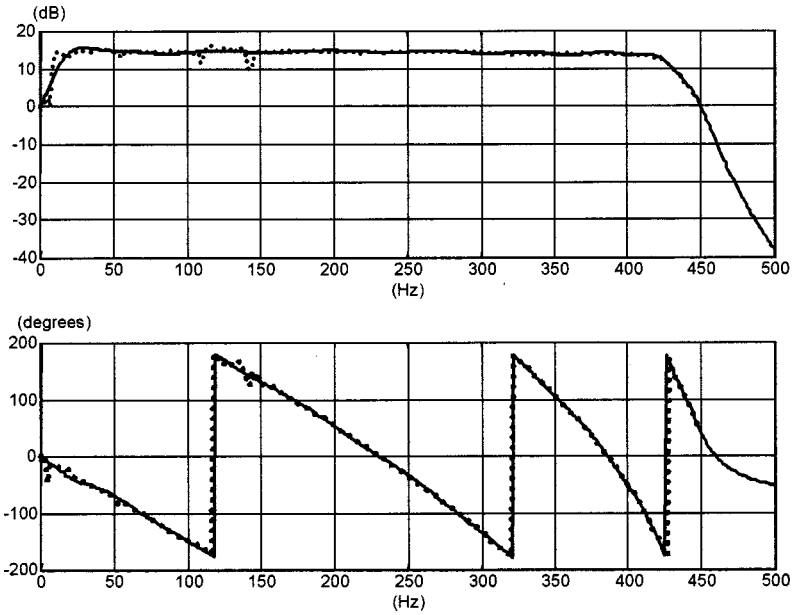

FIG. 7. Measured (dotted line) and modeled (solid line) DSP card/amplifier FRF.

adjust the values of Q and R that permit the best experimental control. The simulated frequency responses of S1, S2, S3, and S4 are shown in Fig. 9 for the uncontrolled and the controlled beam. These numerical results are produced to be compared with the experimental control performed in the next section.

D. Flexural vibration modeling

In order to determine the resonance frequencies of the simply supported beam, two approaches were used. First, an analytical method based on classic propagation was developed.[14,15] Due to the presence of a number of sensors and actuators cemented on the beam, this simple model was not very accurate. The second modeling carried out the finite element method[16] (FEM). It gives the exact resonance frequencies of the beam structure and also the coupling coefficients related to each flexural mode. Comparison between FEM calculations and measurements shows that experimental simple supported boundary limit conditions are not exactly verified. The major difference concerns the first two resonance frequencies. They are lower than the experimental one.[15] This discrepancy is not important because an identification procedure is used for determining the experimental parameters of the transfer functions used for controlling the beam vibrations.

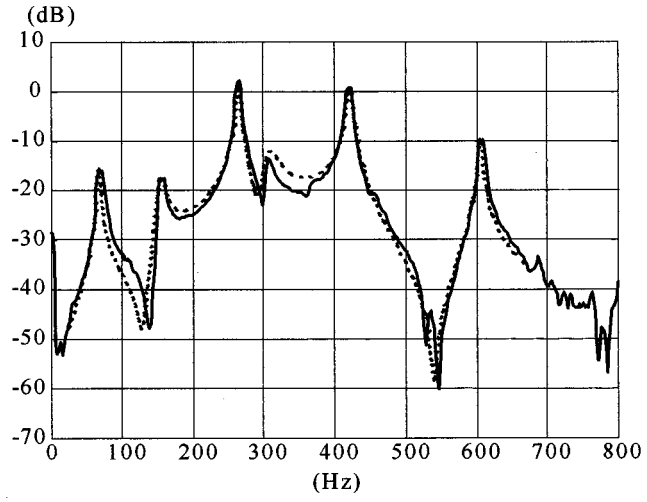

FIG. 8. FRF identification: modeled (dotted line) and measured (solid line) FRF amplitudes.

IV. EXPERIMENTAL RESULTS

It has to be mentioned that in the practical system, the ideal states—modal displacements and velocities—are not directly available but observable through low pass filters and A/D converters. The velocities are estimated through a simple differentiation.

Actually, the experimental control is given by

$$u_e = -K_e x_e, \tag{13}$$

where K_e is the control matrix to be implement and

$$\mathbf{x}_e = E\mathbf{x}, \tag{14}$$

where x is the experimental state vector and E is the electronic FRF identified in the previous section. Then, the control matrix K_e is such that

$$K_e x_e = Kx \tag{15}$$

with the constrain that K_e must be real to be computed. Inserting Eq. (14) into Eq. (15) leads to

$$\hat{K}_e = E^{-1}K, \tag{16}$$

which is a complex matrix, thus a transformation is needed. If the assumption of slightly damped and well-separated modes and if xe is assumed to be harmonic, it can then be written:

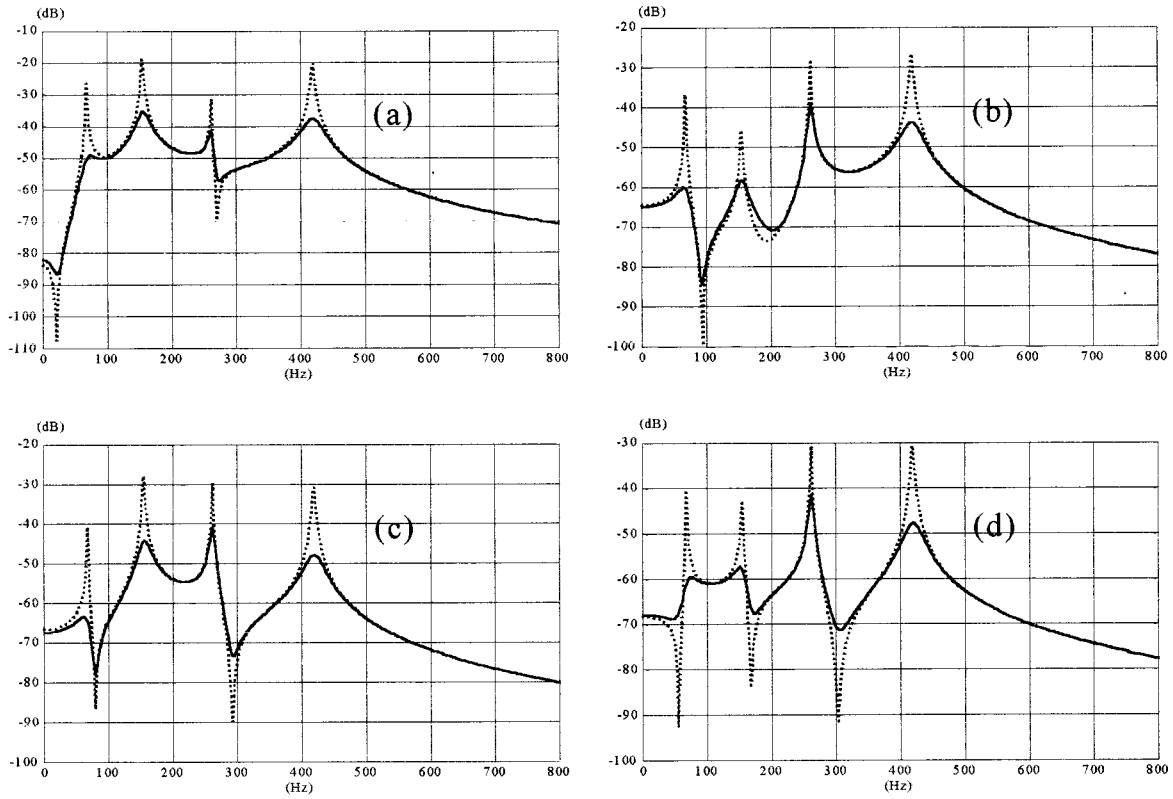

FIG. 9. Simulated frequency responses of the sensor patches S1 (a), S2 (b), S3 (c), and S4 (d) for uncontrolled beam (dotted lines) and controlled beam (solid lines).

$$x_e = \begin{bmatrix} W_1 \\ \vdots \\ W_n \\ j\omega_1 W_1 \\ \vdots \\ j\omega W_n \end{bmatrix}. \tag{17}$$

Finally, K_e is given by

$$K_e = \begin{bmatrix} \mathrm{Re}(\hat{K}_e(1)) - \mathrm{Im}(\hat{K}_e(n+1)) x \omega_1 \\ \vdots \\ \mathrm{Re}(\hat{K}_e(n)) - \mathrm{Im}(\hat{K}_e(2n)) x \omega_1 \vdots \\ \mathrm{Re}(\hat{K}_e(n+1)) - \mathrm{Im}(\hat{K}_e(1)) x \omega_1^{-1} \\ \vdots \\ \mathrm{Re}(\hat{K}_e(2n)) - \mathrm{Im}(\hat{K}_e(n)) x \omega_n^{-1} \end{bmatrix}, \tag{18}$$

where ω_n is the nth modal frequency and $\mathrm{Re}(X)$ and $\mathrm{Im}(X)$ mean the real and the imaginary part of the X variable.

The controller schematic is given in Fig. 10. Five parts form it. The heart of the controller is formed by the matrix computation modules denoted $[-K]$ and $[M]^{-1}$, respectively. On the board the analog and digital converters and the input and output filters were also implemented.[15] Measured frequency responses of patches S1, S2, S3, and S4 are plotted in Fig. 11 for the uncontrolled and the controlled beam.

The control provides similar results for the four sensor patches. The obtained attenuation of the four mode peaks is about 10, 20, 12, and 12 dB, respectively. These results are comparable to those obtained with the model, except for the mode at 70 Hz which shows a smaller attenuation. This is explained by the poor quality of its filtering (see Fig. 6) whereas in the simulation, the modes are perfectly known. The 600 Hz peaks for the uncontrolled and the controlled beam illustrate the absence of spillover and hence the efficiency of the anti-aliasing filters. Actually, the only in-

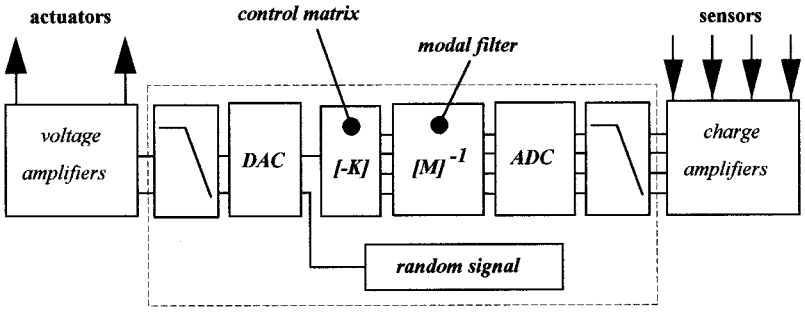

FIG. 10. Control implementation schematic.

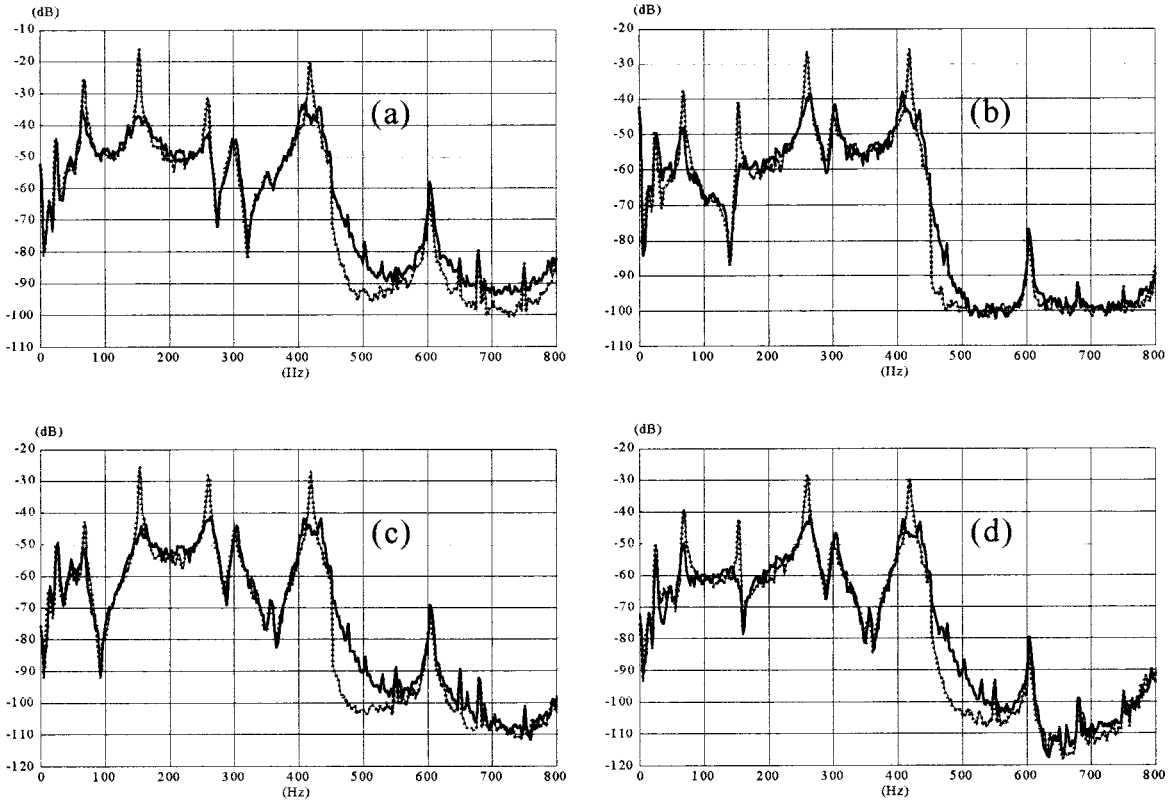

FIG. 11. Measured frequency responses of the sensor patches S1 (a), S2 (b), S3 (c), and S4 (d) for uncontrolled beam (dotted lines) and controlled beam (solid lines).

creased band is the frequency range around 500 Hz but it concerns very low vibration levels.

V. CONCLUSIONS

Modal control of beam flexural vibration has been modeled and practically implemented successfully. A good agreement between modeled and experimental data is obtained. The attenuation of the beam resonance modes is at least 10 dB. Some attenuation is up to 20 dB. This work presents an approach for implementing modal control of proportionally damped systems. The method carried out is very attractive and spillover is avoided. The procedure needs identification steps for determining carefully the transfer functions of the physical system as well as the electronic controller. This identification step is very important because it will allow the determination of the control gain matrix with LQ control design. The control is simulated and allows setting the control parameters and the modal weights in order to get the best results. The obtained control matrix is then changed in the appropriate form to be computed in the controller. Finally, the experimental control is conducted and shows good results with only one control actuator.

[1] P. Lueg, ''Process of silencing sound oscillations,'' US Patent 2 043 416, 1936, 06-6.
[2] H. F. Olson and E. G. Lay, ''Electronic absorber,'' J. Acoust. Soc. Am. **25**, 1130–1136 (1953).
[3] L. Meirovitch, *Computational Methods in Structural Dynamics* (Sijthoff & Noordhoff, The Netherlands, 1980).
[4] L. Meirovitch and H. Baruh, ''Control of self-adjoin distributed parameters systems,'' J. Guidance **15**, 60–66 (1982).
[5] E. F. Crawley and J. de Luis, ''Use of piezoelectric actuators as elements of intelligent structures,'' AIAA J. **25**, 1373–1385 (1987).
[6] L. Meirovitch, *Dynamics and Control of Structures* (Wiley, New York, 1990).
[7] R. L. Clark, C. R. Fuller, and Al. Wicks, ''Characterization of multiple piezoelectric actuators for structural excitation,'' J. Acoust. Soc. Am. **90**, 346–357 (1991).
[8] R. E. Lindberg and R. W. Longman, ''On the number and placement of actuators for independent modal shape control,'' J. Guid. Control. Dyn. **2**, 215–221 (1984).
[9] C. R. Fuller, S. J. Elliott, and P. A. Nelson, *Active Control of Vibration* (Academic, London, 1996).
[10] T. Bailey and J. E. Hubbard, Jr., ''Distributed piezoelectric-polymer active vibration control of a cantilever beam,'' AIAAJ. Guidance **8**, 605–611 (1985).
[11] C. K. Lee, ''Theory of laminated piezoelectric plates for the design of distributed sensors/actuators. Part I: Governing equations and reciprocal relationships,'' J. Acoust. Soc. Am. **87**, 1144–1158 (1990).
[12] S. P. Rubenstein, W. R. Saunders, and G. K. Ellis, ''Demonstration of LQG vibration controller for a simply-supported plate,'' Proc. Conf. Recent advances in active control of sound and vibration, Blacksburg, Virginia, Technomic Press, pp. 618–630, 1991.
[13] N. Rizet, M. Brissaud, P. Gonnard, J. C. Béra, and M. Sunyach, ''Active control of beam flexural vibration excited by broadband disturbance using piezoceramic devices,'' Proc. Active'97, Budapest, 21–23 August 1997.
[14] A. Leissa, ''Vibration of plates'' (originally issued by NASA, 1973, reprint by Acoust. Soc. Am., 1993).
[15] N. Rizet, ''Contrôle actif de vibrations utilisant des matériaux piézoélectriques,'' Thesis dissertation, ISAL 0001, 1999.
[16] ATILA. Finite Element Code for piezoelectric and magnetostrictive transducers modeling. User's manual, ISEN 1991.

Broad spectrum diffusion model for room acoustics ray-tracing algorithms

J. J. Embrechts[a)]
University of Liège, Sart-Tilman B28, B-4000 Liège, Belgium

(Received 15 June 1999; revised 25 November 1999; accepted 12 December 1999)

Geometrical acoustics methods have already been transformed to account for diffusely reflecting boundaries. In randomized ray-tracing algorithms, the sound rays are either specularly reflected or scattered, according to the value of a random number which is compared with the diffusion factor. However, this method becomes inefficient if this factor depends on frequency, since the process must then be repeated for each frequency band. A method is proposed in this paper to compute all frequency components simultaneously in a single pass. The diffuse reflection model is based on the definition of a new concept: the ''splitting coefficient,'' which can differ from the diffusion factor. First, the randomized ray-tracing method is described and the diffusion model is applied to a single diffusing surface in free field. It is shown that the results computed by the program are in accordance with theoretical results. Then, the method is shown to work properly when it is applied to more realistic enclosures: This is proved in theory and illustrated by some examples. A particular problem is the increase of the statistical error which has been solved by an appropriate control of the splitting coefficient. © *2000 Acoustical Society of America.* [S0001-4966(00)04503-3]

PACS numbers: 43.55.Ka, 43.55.Br [JDQ]

INTRODUCTION

It is presently admitted that accounting for the scattering (or diffusion) of sound by surfaces generally improves room acoustics predictions. The investigations carried out by (among others) Kuttruff,[1] Hodgson,[2,3] or Lam[4] have shown that room acoustics calculations based on specular reflections only overestimate reverberation times in situations where diffusion is significant. Also, the predicted sound propagation decays (i.e., the sound pressure level as a function of the distance to the source) are less steep than those measured in real enclosures, particularly in disproportionate rooms. On the other hand, the simulation of sound diffusion by surfaces results in lower reverberation times (and more linear reverberation decays) and in sound propagation decays which are closer to measurements performed in real rooms. Dalenbäck[5] and Stephenson[6] also pointed out that the quality of auralization can be improved by the introduction of some diffuse reflections.

Therefore, geometrical acoustics methods have been transformed and developed to account for sound diffusion. Concerning randomized ray tracing, Kuttruff[7] suggested that each ray hitting a diffusing surface can be reflected in a random direction given by the generation of two random angles, in such a way that the whole process creates a Lambert cosine distribution of the reflected intensity. Moreover, a third random number can be generated for partially diffusing walls: These are walls for which a given fraction of the reflected energy is diffused (this fraction is called the diffusion factor or diffusion coefficient or again diffuse-reflection coefficient), the remainder being specular. The random number is comprised between 0 and 1: If it is less than the diffusion factor, then the reflection of the ray is diffuse. Otherwise, it is specular.

This method has been applied by several authors,[3,4,7,8] and also by the author of this paper. Two main drawbacks of these fully randomized ray-tracing models are that they require a great number of rays (typically 100 000) to calculate detailed echograms,[5] and that the process must be repeated for each frequency band,[4,5,9] since the scattering of rays depends on the value of the diffusion factor, which itself depends on frequency. Li and Hodgson[10] have also considered this problem for the scattering by fittings in industrial workrooms. The frequency dependence of sound diffusion will be addressed in the following. On the other hand, fully randomized ray tracing is easy to implement, it does not require elaborate corrections such as approximate cone or beam-tracing methods,[5,6] and it is able to handle all orders of mixed (specular and diffuse) reflections.

This paper describes an implementation of the randomized ray-tracing model which computes all frequency components simultaneously, avoiding the repetition of the algorithm for each different value of the diffusion factor. This method will be applied on a specific algorithm developed some years ago,[11] but it is not restricted to this algorithm. In fact, it could be used in any process based on the same general principles of the randomized ray tracing. The conclusions which will be drawn are also quite general, and particularly the effect of the method on the statistical accuracy of the computations.

Before going on further, it must be mentioned that this method is not the only one able to compute all frequency components simultaneously. For example, Dalenbäck[5] proposed a technique in which partially diffusing surfaces are subdivided into patches. A first pass gives the specular contributions at the receivers and at the patches. Then, in a second pass, these patches act as secondary sources which give

a)Electronic mail: jjembrechts@ulg.ac.be

contributions of the type S^k-D-S^j (this notation introduced by Dalenbäck *et al.*[12] means: k specular reflections followed by a single diffusion, and again j specular reflections). The process is repeated to account for more than one order of diffusion, but it has been essentially limited to two passes. Another method has been suggested by Kuttruff[13,14] and applied by Lam:[4] Once a ray hits a (partially) diffusing surface, the diffuse contribution is computed at the receivers assuming an exponential time decay. Then, the sound ray is reflected in the specular direction. The accuracy of this method depends of course on the assumption of the exponential decay, and in particular on the determination of the decay constant.

The original features of the method described in this paper are that it is easy to implement, it does not require any particular assumption on the time decay, and it can account for any combination of specular and diffuse reflections. However, the accuracy of the calculated room acoustics parameters must be carefully analyzed, since the efficiency of the method will be significantly affected by the way the statistical errors are taken into account.

I. DESCRIPTION OF THE SOUND RAY MODEL

This model has already been described in a previous publication.[11] The method is based on a randomized ray-tracing algorithm in which sound rays are emitted by an isotropic point source. The detectors are small rectangular surfaces centered on the receiving points. The usual way of defining these detectors is to divide an audience surface into several patches, each patch being specified as a surface detector. This obviously leads to a spatial distribution of the room acoustics parameters on the audience. The choice between surface and volume detectors will not be discussed here, since it does not have any fundamental consequence on further developments and conclusions.

Hereafter are recalled some results of Ref. 11 which will be used this paper. The squared rms sound pressure averaged on the surface receiver ΔS is given by

$$p^2(\Delta S)=\frac{\rho_0 c}{\Delta S}\int_0^{2\pi} d\phi \int_0^{\pi} \nu(\theta,\phi)\sin\theta\, d\theta,$$
$$\nu(\theta,\phi)=\left(\sum_{k=0}^{\infty}\frac{a_k(\theta,\phi)\,\delta_k(\theta,\phi)}{|\cos\hat{i}_k(\theta,\phi)|}\right) I(\theta,\phi). \tag{1}$$

In this expression, the angles (θ,ϕ) define any direction of sound emission in a spherical coordinate system attached to the point source: θ is comprised between 0 and π, and ϕ is comprised between 0 and 2π, as usual. $\nu(\theta,\phi)$ expresses the contribution of the sound energy emitted in the solid angle $d\Omega=\sin\theta d\,\theta d\phi$ to the detector: it is the sum of all orders of reflection, from $k=0$ being the direct sound to (theoretically) $k=\infty$. The contribution of the kth order includes the following.

(1) $I(\theta,\phi)$, the intensity expressed as the power emitted per unit solid angle, in watts per steradian.

(2) This intensity is attenuated by the factor $a_k(\theta,\phi)$, which includes the exponential decay due to air absorption and the reflection factors of all walls hit by the sound energy beam $d\Omega$.

(3) A factor $\delta_k(\theta,\phi)$ accounting for the possible contribution of the beam $d\Omega$ at the detector, at the kth reflection: $\delta=1$ if the beam crosses ΔS at the kth reflection, otherwise $\delta=0$.

The denominator of Eq. (1) is the cosine of $\hat{i}_k$, the angle of incidence of the beam on the surface receiver ΔS at the kth reflection. This factor is not fundamental, since it is closely linked to the shape of the detector. Finally, $\rho_0 c$ is the characteristic impedance of the medium ($\mathrm{kg\,m^{-2}\,s^{-1}}$).

One may wonder where the $1/r^2$ law is hidden in this expression (r being the distance traveled by the sound energy). In fact, it is taken into account by the constant area of the receiver ΔS, which subtends a solid angle decreasing proportionally to $1/r^2$ as the distance to the source increases.

Equation (1) has only been established for specular reflections, and it will be extended later for diffuse reflections. It will now be expressed for the particular case of a fully randomized ray tracing algorithm: If N rays (θ_i,ϕ_i) are emitted from the source in random directions with a probability density function (pdf) $(1/4\pi)\sin\theta$, their energy and local angle of incidence can be recorded each time they cross a detector surface. This leads to the evaluation of $\nu(\theta_i,\phi_i)=\nu_i$, which includes as in Eq. (1) the initial intensity of the sound ray attenuated by the absorption of the walls and the medium. The following expression is an unbiased (meaning that the expectation or statistical mean of the estimate is the squared rms pressure) estimate of the squared rms pressure:

$$\hat{p}^2(\Delta S)=\frac{4\pi\rho_0 c}{N\Delta S}\sum_{i=1}^{N}\nu_i. \tag{2}$$

It is interesting to mention that it is possible to estimate the accuracy of the sound pressure calculations in randomized ray-tracing algorithms. This important point is seldom addressed in the literature, but it is a fact that room acoustics algorithms generally introduce calculation errors which are never estimated. Each method has its own errors. In the case of randomized ray tracing, statistical errors are introduced and can be evaluated by the variance of expression (2). This variance is estimated by[11]

$$\mathrm{Var}(\hat{p}^2)\approx\frac{1}{N}\left[\left(\frac{4\pi\rho_0 c}{\Delta S}\right)^2\left(\frac{1}{N}\sum_{i=1}^{N}\nu_i^2\right)-(\hat{p}^2(\Delta S))^2\right], \tag{3}$$

which illustrates the well-known dependence of the statistical error [the square root of Eq. (3) or standard deviation] in $N^{-1/2}$.

The calculation of Eq. (2) at each detector surface by the sound ray algorithm gives the distribution of the sound pressure levels in the room. If this calculation is restricted to the contributions of the rays longer than ct, then the sound pressure at time t of the time decay is obtained, and this leads to reverberation time computations. Finally, the echogram is derived from the calculation of Eq. (2) in prescribed (small) time intervals.

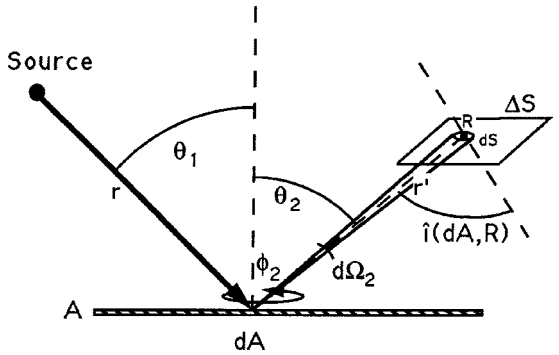

FIG. 1. The diffusing surface A is ''illuminated'' by the sound source and reflects the sound wave to the receiving surface ΔS. The local angle of incidence on surface element dA is θ_1 and the scattering angles are θ_2 and ϕ_2 (ϕ_2 is in the plane of the diffusing surface). The surface element dS centered on R subtends a solid angle $d\Omega_2$ at dA, and $\hat{i}$ is the local angle of incidence of the reflected ray on that element.

II. THE SOUND SCATTERING MODEL

A. Totally diffusing surface, single frequency band

Figure 1 illustrates the very simple case of a single diffusing surface A in free field. The local angle of incidence on the surface element dA is θ_1 and the scattering direction is defined by the angles θ_2 and ϕ_2. It is assumed that the absorption factor α_A and the diffusion properties are constant along the surface. If $I_{\text{rel}}(\theta_1,\theta_2,\phi_2)$ is the relative distribution of the scattered power per unit solid angle, such that

$$\int_0^{2\pi} d\phi_2 \int_0^{\pi/2} I_{\text{rel}}(\theta_1,\theta_2,\phi_2)\sin\theta_2\, d\theta_2 = 1, \tag{4}$$

then the scattered rms pressure p_{sc} at point R is given by

$$p_{\text{sc}}^2(R) = \rho_0 c(1-\alpha_A) \int\int_A W_r(dA) I_{\text{rel}}(\theta_{1A},\theta_{2AR},\phi_{2AR}) \times \frac{A_{\text{air}}(r')}{(r')^2}, \tag{5}$$

$$W_r(dA) = \frac{W_S}{4\pi} A_{\text{air}}(r)\Omega(dA).$$

In this expression, $W_r(dA)$ is the power received by the surface element dA, while W_S is the power emitted by the isotropic sound source. $\Omega(dA)$ is the solid angle subtended by dA at the point source, θ_{1A} is the angle of incidence of the spherical sound wave on dA, and $(\theta_{2AR},\phi_{2AR})$ are the angles associated with the scattering direction (dAR). The last factor contains A_{air}, which is the attenuation of the medium depending on the length r' of the scattered ray.

The squared rms pressure can be averaged on the surface receiver ΔS, which gives

$$p_{\text{sc}}^2(\Delta S) = \frac{1}{\Delta S}\int\int_{\Delta S} p_{\text{sc}}^2(R)\,dS = \rho_0 c(1-\alpha_A)\frac{W_s}{4\pi\Delta S}\int\int_A \Omega(dA) \times \int\int_{\Omega(dA,\Delta S)} I_{\text{rel}}(\theta_{1A},\theta_{2AR},\phi_{2AR}) \times A_{\text{air}}(r+r')\frac{d\Omega_2}{|\cos\hat{i}(dA,R)|}, \tag{6}$$

where $\Omega(dA,\Delta S)$ is the solid angle subtended by ΔS at dA (see also Fig. 1 for the definition of other symbols). In this expression, an exponential law has been assumed to account for the attenuation of the medium.

Expression (6) can be formulated as Eq. (1), performing the substitution of the angles (θ,ϕ) attached to the sound source for dA. The domain of integration is extended to the whole solid angle (4π), provided that the integrand is multiplied by a function $\delta_A(\theta,\phi)$ [$\delta=1$ if the sound ray (θ,ϕ) reaches A, otherwise $\delta=0$]:

$$p_{\text{sc}}^2(\Delta S) = \frac{\rho_0 c}{\Delta S}\int_0^{2\pi} d\phi \int_0^{\pi} \sin\theta\, d\theta \int_0^{2\pi} d\phi_{2AR} \times \int_0^{\pi/2} I_{\text{rel}}(\theta_{1A},\theta_{2AR},\phi_{2AR}) \times \nu(\theta,\phi,\theta_{2AR},\phi_{2AR})\sin\theta_{2AR}\, d\theta_{2AR},$$
$$\nu(\theta,\phi,\theta_{2AR},\phi_{2AR}) = \frac{(1-\alpha_A)W_s A_{\text{air}}(r+r')}{4\pi|\cos\hat{i}(dA,R)|} \times \delta_A(\theta,\phi)\,\delta_{\Delta S}(\theta_{2AR},\phi_{2AR}). \tag{7}$$

This theoretical expression of the scattered sound pressure will now be evaluated by a sound ray algorithm. If N rays (θ_i,ϕ_i) are emitted from the source in random directions with a pdf $(1/4\pi)\sin\theta$, only some of them will reach the diffusing surface A and then be scattered: Of course, this is not an efficient algorithm for a single scattering surface since most of the rays will miss the target, but it must be remembered that this is only a special application of a more general algorithm designed for closed rooms, where all rays are (*a priori*) almost equally important.

For these sound rays reaching A, a random scattering direction (θ_2,ϕ_2) is determined with a pdf $I_{\text{rel}}(\theta_1,\theta_2,\phi_2)\sin\theta_2$. Their energy is then decreased by a factor $(1-\alpha_A)$. Again, most reflected rays will be lost, but those which are reaching the detector ΔS are recorded (with their energy and local angle of incidence), giving the evaluation of $\nu(\theta_i,\phi_i,\theta_2,\phi_2)=\nu_i$. It will be shown that the following expression is an unbiased estimate of the squared rms pressure:

$$\hat{p}_{\text{sc}}^2(\Delta S) = \frac{4\pi\rho_0 c}{N\Delta S}\sum_{i=1}^{N}\nu_i. \tag{8}$$

This is exactly the same expression as Eq. (2), which was established for specular reflections. In both expressions, ν_i is

TABLE I. Comparison of some sound pressure levels computed at the receiver R by Eqs. (5) and (8), in the situation illustrated in Fig. 2. The squared rms pressure values computed by the sound ray algorithm (last column) are averaged on an horizontal square surface (0.25 m^2) centered on R.

Surface area (m^2)	Source: (x_S, z_S)	Receiver: (x_R, z_R)	$p_{sc}^2(R)$ dB	$\hat{p}_{sc}^2(\Delta S)$ dB
100	(−6.0,3.0)	(6.0,3.0)	80.11	79.8±0.6
100	(−7.49,14.5)	(7.25,10.0)	72.88	72.4±1.1
100	(0.0,14.5)	(7.25,10.0)	74.50	74.7±0.4
100	(0.0,14.5)	(0.0,3.0)	82.78	82.8±0.3
4	(−6.0,3.0)	(6.0,3.0)	67.04	67.1±1.3

not evaluated if the sound ray does not reach the detector ($\nu_i = 0$).

The proof is as follows: $\hat{p}_{sc}^2(\Delta S)$ is a random variable, since it is a function of the random variables $(\theta_i, \phi_i, \theta_2, \phi_2)$. Each random variable ν_i has the same expectation $\langle \nu \rangle$, since the same random process is applied for all rays. To evaluate this expectation, one has to consider that each variable ν (the index ''i'' can be omitted as a consequence of the previous statement) has two possible realizations:

(1) $\nu \neq 0$ if the direction (θ,ϕ) leads to the diffusing surface A [i.e., belongs to the solid angle $\Omega(A)$];
(2) $\nu = 0$ if this direction does not belong to $\Omega(A)$.

Only the first one must be considered to compute $\langle \nu \rangle$ since the second realization gives a null contribution. For a direction (θ,ϕ) leading to the surface A, the random function ν depends on the four random variables $(\theta, \phi, \theta_2, \phi_2)$. Their pdf $f(\theta, \phi, \theta_2, \phi_2)$ is expressed in Eq. (9) by the product of the pdf of (θ,ϕ) and the conditional probability of (θ_2, ϕ_2) if (θ,ϕ) has been chosen. Therefore, the expectation of $\hat{p}_{sc}^2$ is given by

$$\begin{aligned}\langle \hat{p}_{sc}^2 \rangle &= \frac{4\pi\rho_0 c}{\Delta S}\langle \nu \rangle \\ &= \frac{4\pi\rho_0 c}{\Delta S}\int\int_{\Omega(A)} d\theta\, d\phi \int_0^{2\pi} d\phi_2 \\ &\quad \times \int_0^{\pi/2} \nu(\theta,\phi,\theta_2,\phi_2) f(\theta,\phi,\theta_2,\phi_2) d\theta_2, \\ f(\theta,\phi,\theta_2,\phi_2) &= \frac{1}{4\pi}\sin\theta I_{rel}(\theta_1,\theta_2,\phi_2)\sin\theta_2 .\end{aligned} \tag{9}$$

Finally, $\langle \hat{p}_{sc}^2 \rangle$ in Eq. (9) is found to be exactly the same as $p_{sc}^2(\Delta S)$ in Eq. (7), confirming the correct implementation of the scattering model. This will be illustrated by the following simple example.

A square diffusing surface (Fig. 2) is scattering the sound emitted by an isotropic point source to the receiving point R. The acoustical power of the source is 120 dB, the absorption factor of the surface is $\alpha_A = 0.5$, and the scattering distribution follows the Lambert law ($I_{rel} = (1/\pi)\cos\theta_2$). Air absorption is neglected. Numerical integration of Eq. (5) gives $p_{sc}^2(R)$, which is compared in Table I with the results of the sound ray algorithm.

The numerical calculation of Eq. (5) is carried out with an error less than 0.01 dB, whereas the statistical error inherent to the sound ray algorithm is mentioned in the last column of Table I. This statistical error is computed as the 95% confidence interval, through the evaluation of the variance by Eq. (3). The error depends of course on the number of rays used in the calculations and (roughly) on the probability for a ray to reach the surface detector, which explains the different values of the errors mentioned in Table I. However, the results of the ray-tracing algorithm completed by their statistical errors are consistent with the corresponding ''theoretical'' values of the squared rms pressure.

B. Partially diffusing surface, single frequency band

In the more general case of a partially diffusing surface, a random number Z is first generated between 0 and 1 (uniform pdf) for each sound ray reaching the surface A. If $Z \leqslant d_A$ (the diffusion factor), a random direction (θ_2, ϕ_2) is determined with pdf $I_{rel}(\theta_1, \theta_2, \phi_2)\sin\theta_2$. Otherwise ($Z > d_A$), the sound ray is reflected in the specular direction. In both cases, the sound ray energy is decreased by a factor $(1-\alpha_A)$.

It can again be shown that Eq. (8) is an unbiased estimate of the scattered squared rms pressure. Indeed, the expectation $\langle \nu \rangle$ in Eq. (9) is now evaluated as follows: Each variable ν has three possible realizations, depending on whether the direction (θ,ϕ):

(a) leads to the diffusing surface A and $Z \leqslant d_A$,
(b) leads to the surface A and $Z > d_A$,
(c) or does not lead to the surface A ($\nu = 0$).

The first contribution to the expectation $\langle \hat{p}_{sc}^2 \rangle$ is given by

$$\begin{aligned}\overline{P_{dif}^2} &= \frac{4\pi\rho_0 c}{\Delta S}\int\int_{\Omega(A)} d\theta\, d\phi \int_0^{d_A} dZ \int_0^{2\pi} d\phi_2 \\ &\quad \times \int_0^{\pi/2} \nu(\theta,\phi,\theta_2,\phi_2) f(\theta,\phi,Z,\theta_2,\phi_2) d\theta_2, \\ f(\theta,\phi,Z,\theta_2,\phi_2) &= \frac{1}{4\pi}\sin\theta I_{rel}(\theta_1,\theta_2,\phi_2)\sin\theta_2 .\end{aligned} \tag{10}$$

The five random variables are now: $(\theta, \phi, Z, \theta_2, \phi_2)$. Their pdf ($f$) does not depend on Z, since the conditional probability of Z if (θ,ϕ) has been chosen is simply dZ. Neither does the function ν defined in Eq. (7). Therefore, expression (10) is reduced to the product of the diffusion factor d_A and the squared rms pressure at the detector $p_{dif}^2(\Delta S)$ obtained for a totally diffusing surface (9).

The second contribution to the expectation $\langle \hat{p}_{sc}^2 \rangle$ can be derived in the same way, giving the product of $(1-d_A)$ and $p_{spec}^2(\Delta S)$, the squared rms pressure at the detector ΔS ob-

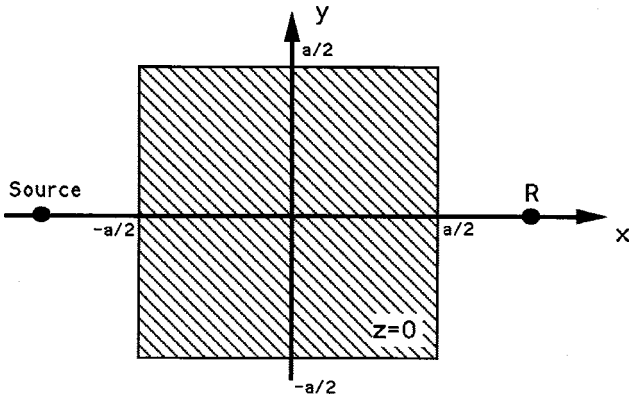

FIG. 2. The square (hatched) scattering surface (side$=a$) lies in the horizontal plane $z=0$. The point source is in $(x_S,0,z_S)$ and the receiving point in $(x_R,0,z_R)$.

tained for a totally specular surface. Finally, considering that the third contribution vanishes (since $\nu=0$), the expectation of Eq. (8) is

$$\langle \hat{p}^2_{\rm sc} \rangle = d_A p^2_{\rm dif}(\Delta S) + (1-d_A) p^2_{\rm spec}(\Delta S). \tag{11}$$

This is exactly the value of the squared rms pressure that can be expected at the detector, considering the definition of the diffusion factor.

The situation illustrated in Fig. 2 has been simulated by the sound ray algorithm, with several values of the diffusion factor d_A. The results (which are not reported here) were consistent with the theoretical evaluations of $p^2(R)$.

C. Partially diffusing surface, several frequency bands

The problem of the possible variation of the diffusion factor with frequency must now be addressed. The idea of this research is to propose a method to compute all the SPL spectrum in a single pass, without altering the general framework of the randomized ray-tracing algorithm. First of all, a ''splitting coefficient'' β_A is defined for the surface A. The value of this coefficient is unique (it does not depend on frequency) and it can be chosen independently of the diffusion factor. It will also be shown further that the coefficient β_A can possibly change from one reflection order to another, in order to optimize the sound ray algorithm.

Once the splitting coefficient has been defined, the process can be initiated: A random number Z is generated for each ray hitting the diffusing surface. If $Z \leqslant \beta_A$, the reflection is diffuse, otherwise it is specular. However, if d_A is replaced by β_A in Eq. (11), the calculated sound pressure level is no longer correct. To compensate for this effect, the energy of the sound ray must be corrected (at all frequencies f) by a factor $d_A(f)/\beta_A$ if the reflection is diffuse and by a factor $(1-d_A(f))/(1-\beta_A)$ if it is specular.

This energy compensation is valid in theory, and this allows one to calculate all frequency components of the spectrum simultaneously. However, it will raise other problems which are addressed in See. III. For example, if $d_A(f) > \beta_A$, the energy of a sound ray in that particular frequency band is artificially amplified at each diffuse reflection. What is the consequence of this amplification on the sound ray process? The answer can be related to the value attributed to β_A. If $\beta_A=0.5$, then the previous effect of artificial amplification or attenuation is limited to a factor 2, whatever the value of the diffusion factor. However, if the diffusion factor does not depend on frequency ($d_A(f)=d_A\neq 0.5$), $\beta_A=d_A$ would be a better choice than $\beta_A=0.5$, in order to avoid any amplification or excessive attenuation. A compromise could be found in attributing the average value of the diffusion factor (for all frequencies) to the splitting coefficient: This would limit artificial energy manipulations while reducing to $\beta_A=d_A$ for a constant diffusion factor.

Before going into more detail, it will now be shown that the method works properly. This could be easily proved by extending the mathematical developments of Sec. II B, but rather the proof will be illustrated in the following by an example.

The single diffusing surface (Fig. 2) is again simulated, but with a diffusion factor depending on frequency. Table II shows the results of three executions of the sound ray program.

(1) All frequency bands one by one (method B): This requires five passes, since the results are the same at 500 Hz and 1 kHz (no air absorption, surface absorption and diffusion identical).
(2) All frequency bands simultaneously with $\beta_A=$mean $\{d_A(f)\}=0.5$ (method C).
(3) All frequency bands simultaneously with $\beta_A=\max\{d_A(f)\}=0.75$ (method D).

Interesting conclusions can be drawn from these results. First of all, it can be seen that the method works properly, since the sound pressure levels computed by methods B, C,

TABLE II. SPL (dB) computed at the receiver R in six octave bands, using different algorithms: (A) numerical integration of Eq. (5) and addition of the theoretical specular component; (B) sound ray program, $N=5\times10^6$ rays, one pass per different diffusion factor value (five passes); (C) sound ray program, $N=5\times10^6$ rays, single pass with $\beta_A=0.5$; (D) sound ray program, $N=5\times10^6$ rays, single pass with $\beta_A=0.75$. The size of the diffusing surface is 7 m×7 m, the source is in $(x_S=-6,z_S=3)$ and the receiving position R in $(x_R=6,z_R=3)$. The distance between the source and the receiver is 12 m.

Calculation method	125 Hz	250 Hz	500 Hz	1 kHz	2 kHz	4 kHz
A	82.63	81.98	81.49	81.49	80.93	79.94
B	82.8±0.6	82.3±0.6	81.8±0.7	81.8±0.7	81.5±0.7	79.7±0.9
C	83.1±0.7	82.3±0.7	81.8±0.7	81.8±0.7	81.1±0.7	79.8±0.8
D	82.9±1.0	82.2±1.0	81.6±0.9	81.6±0.9	81.0±0.9	79.7±0.9
Diffusion factor	0.25	0.4	0.5	0.5	0.6	0.75

and D are consistent with the theoretical values of method A. Second, method B (five passes) requires 663 s (computing time), while methods C and D (one single pass) only require 133 s on the same computer (Pentium 233 MMX personal computer) and with the same number of rays.

The third conclusion is that the drastic gain in computing time has been obtained at the expense of an increasing statistical error. This effect is restricted to some tenths of decibel in this simple situation, but it could introduce a limitation to the method. Indeed, to compensate this increase of the statistical error, a greater number of rays is needed and this in turn requires a greater computing time, reducing the benefit of the single pass. This limitation is particularly significant in the case $\beta_A = \max\{d_A(f)\}$: At 125 Hz, the relative statistical error is 23% (about 1.0 dB) for the ''single pass'' process, instead of 14% (about 0.6 dB) for the ''five passes.'' To obtain the same statistical error with a single pass, the number of rays should be increased by a factor 2.7 [remember the law in $\sqrt{N}$ expressed in Eq. (3)].

This increase of the statistical error will be addressed in the next sections. An explanation will be found in Sec. III for the simple case of a single reflection on a diffusing surface, and the analysis will be further carried out for more general situations including several diffuse and/or specular reflections (Sec. IV B).

The last conclusion that can be drawn from Table II is that the statistical errors are greater with method D ($\beta_A = \max\{d_A(f)\}$) than with method C ($\beta_A = \text{mean}\{d_A(f)\}$). This must be related to the effect of amplification or excessive attenuation mentioned earlier, but this assumption must still be confirmed.

III. THE INCREASE OF THE STATISTICAL ERROR

An explanation must be found for the increase of the statistical error by the methods using a splitting coefficient β_A different from the diffusion factor. In this respect, the variance of the following estimate must be evaluated [see Eq. (8)]:

$$\hat{p}^2_{\text{sc}}(\Delta S) = \frac{4\pi\rho_0 c}{N\Delta S}\sum_{i=1}^{N}\mu_i = \frac{\xi}{N}\sum_{i=1}^{N}\mu_i,$$

$$\mu_i = \frac{d_A}{\beta_A}\nu_i \quad \text{if } Z_i \leqslant \beta_A \tag{12}$$

and

$$\mu_i = \frac{1-d_A}{1-\beta_A}\nu_i \quad \text{if } Z_i > \beta_A.$$

The expectation of this random variable is $\xi\langle\mu\rangle$, which does not depend on the splitting coefficient, as explained in Sec. II C. Now, the variance of Eq. (12) is given by

$$\sigma_p^2 = \frac{\xi^2}{N}\text{var}(\mu) = \frac{\xi^2}{N}(\langle\mu^2\rangle - \langle\mu\rangle^2). \tag{13}$$

It is implicitly assumed in Eq. (13) that all rays are emitted from the source in an independent way, such that the random variables μ_i are statistically independent. Referring to the development of $\langle\hat{p}^2_{\text{sc}}\rangle$ in Sec. II B, the expectation $\langle\mu^2\rangle$ can be formulated as the sum of two components, one diffuse (index d) and the other specular (index s):

$$\begin{aligned}\langle\mu^2\rangle &= \beta_A\langle\mu_d^2\rangle + (1-\beta_A)\langle\mu_s^2\rangle \\ &= \beta_A\frac{d_A^2}{\beta_A^2}\langle\nu_d^2\rangle + (1-\beta_A)\frac{(1-d_A)^2}{(1-\beta_A)^2}\langle\nu_s^2\rangle.\end{aligned} \tag{14}$$

The expectation $\langle\nu_d^2\rangle$ is closely related to the variance of the squared rms pressure created by a totally diffusing surface ($d_A = 1$), since

$$\text{var}(\hat{p}_d^2(\Delta S)) = \frac{\xi^2}{N}(\langle\nu_d^2\rangle - \langle\nu_d\rangle^2), \tag{15}$$

where the index d has been appended to distinguish from the specular component. In most situations where the statistical error is significant, $\langle\nu_d^2\rangle$ is the main contribution to the variance. Similarly, $\langle\nu_s^2\rangle$ is generally the most significant contribution to the variance of the specular squared rms pressure. Finally, after some manipulations, expressions (13) and (14) lead to

$$\begin{aligned}\sigma_p^2 &= \sigma_{p,0}^2 + \frac{\xi^2}{N}\frac{(d_A-\beta_A)^2}{(1-\beta_A)\beta_A} \\ &\quad\times\left[\langle\nu_d^2\rangle - \frac{\beta_A(1-d_A)(\langle\nu_s^2\rangle - \langle\nu_d^2\rangle)}{d_A-\beta_A}\right], \\ \sigma_{p,0}^2 &= \frac{\xi^2}{N}(d_A\langle\nu_d^2\rangle + (1-d_A)\langle\nu_s^2\rangle - \langle\mu\rangle^2),\end{aligned} \tag{16}$$

where $\sigma_{p,0}^2$ is the variance obtained when the splitting coefficient coincides with the diffusion factor. Equation (16) clearly shows the difference between the variances computed in the cases $\beta_A = d_A$ and $\beta_A \neq d_A$. If $\langle\nu_d^2\rangle \approx \langle\nu_s^2\rangle$, the variance of the estimate $\langle\hat{p}^2_{\text{sc}}\rangle$ (and thus the statistical error) increases with the absolute difference between the diffusion factor and the splitting coefficient. Limiting this effect can be realized by the following techniques:

(1) reducing the absolute difference between β_A and d_A, for example, by choosing β_A as the average value of the spectrum $d_A(f)$;
(2) avoiding the values $\beta_A = 0$ and $\beta_A = 1$ (denominator = 0). In fact, the denominator is maximum (minimizing the variance) for $\beta_A = 0.5$.

If $\langle\nu_d^2\rangle \neq \langle\nu_s^2\rangle$, a second term comes forth in the expression of the variance, and this term can be either positive or negative. Therefore, reductions of the statistical error can be observed for suitable values of β_A: This is the case for method C at 4 kHz in Table II. But these are very limited cases which cannot help in finding general rules for the choice of β_A.

The theoretical analysis of the variance has thus confirmed the results of the last example described in Sec. II C namely that the choice of the splitting coefficient β_A has an influence on the statistical error. The algorithm of the splitting coefficient generally increases the statistical error: This has been proved for a single reflection on a single diffusing surface but, as will be seen later, more complex effects are created when several reflections are considered.

IV. TESTING THE SOUND SCATTERING MODEL IN AN ENCLOSURE

A. Test in a single frequency band

The algorithms presented in Secs. II B and II C must now be tested in a more real situation where several diffusing surfaces are present. First, it can be shown in theory that these methods used in randomized ray-tracing algorithms lead to a valid evaluation (an unbiased estimate) of the sound pressure level at the detector. This has already been established by Embrechts[10] for specular enclosures, and this proof is extended to partially specular/diffuse reflections in the Appendix.

Next, the algorithms will be tested in some particular room acoustics' applications. The rooms which will be used are two enclosures described by Hodgson[2,3] in his famous studies about the evidence of diffusion, and also used by Lam[4] in his tests.

The first room (called in the following. ''room 1'' or ''cubic room'') is a cubic room with side 27.5 m. The geometry is described by a system of three Cartesian coordinates (X,Y,Z), with X and Y in the horizontal plane (the floor) and Z measuring the height above the floor. The point source is located at midheight, near the wall $(Y=0)$: Its coordinates are $X_S=13.75\,\mathrm{m}$, $Y_S=4.0\,\mathrm{m}$, $Z_S=13.75\,\mathrm{m}$. Its acoustical power has been arbitrarily set to $L_W=120\,\mathrm{dB}$. Four receiving positions have been defined at several distances from the source (from 5 to 20 m): They are also situated at midheight, along an horizontal line parallel to the Y axis. To collect the sound rays, small vertical surfaces ΔS are centered on these four receiving positions, at right angles to the horizontal line joining the source and the receiving points.

All room surfaces are identical with respect to their absorption and diffusion properties, as in Hodgson and Lam's papers. However, the absorption factors used by these authors have not been explicitly mentioned in their works and they will be recovered from the published reverberation times (RT). In Lam's paper,[4] the following values are found: RT (Eyring)=8.8 s for room 1 and RT=5.0 s for room 2 (which will be described later). With these two values, and applying Eyring's formula, the absorption factor of the walls is found to be $\alpha=0.068$ and the absorption coefficient of the medium $m=0.344\,\mathrm{dB/100\,m}$. The diffusion factor is a variable in this problem.

The results of the simulations in a single frequency band are listed in Table III. As can be expected, the two values of the diffusion factor ($d=0$ and $d=1$) do not lead to significant differences in this cubic room. The statistical errors on the sound pressure levels are about 0.2 dB in both cases. The reverberation times computed at the three receiving positions R2, R3, and R4 are averaged, which gives 8.95 s for $d=0$ and 8.80 s for $d=1$. The sound decays used to compute these reverberation times are quite linear.

These results show that the scattering algorithm works properly, at least when it is applied in a single frequency band with the splitting coefficient set to the diffusion factor. There are of course some small differences with the results published by Lam[4] for three other algorithms, but these deviations remain acceptable and they can be explained by the different methods used, their different ways of computing the reverberation time, and their accuracy (which are not published for the other algorithms).

TABLE III. Comparison of the sound pressure levels (L_P in dB) measured in room 1 at the four receiving positions R1–R4, and the corresponding SPL computed by the sound ray algorithm with ($d=1$) or without diffusion ($d=0$). The results are computed in a single frequency band ($\beta=d$).

Receiver	Source-receiver distance (m)	L_P-L_W (dB) measured[a]	L_P-L_W (dB) computed ($d=0$)	L_P-L_W (dB) computed ($d=1$)
R1	5.0	−19.6	−19.1	−18.9
R2	10.0	−20.2	−19.9	−19.9
R3	15.0	−20.7	−20.2	−20.2
R4	20.0	−21.0	−20.3	−20.4

[a]Estimated from Fig. 3 of Ref. 2.

The influence of the diffusion factor will be more noticeable in the next enclosure, which is a ''disproportionate long room'' called room 2. The dimensions are 55 m along OX, 110 m along OY, and 5.5 m along OZ. The absorption factors are the same as in room 1. The source is again at midheight ($X_S=27.5$, $Y_S=10.0$, $Z_S=2.75$), and the receiving positions are located on a horizontal line parallel to the Y axis ($X_R=27.5$, $Z_R=27.5$, $Y_R=15,20,...,100$).

The reverberation times (averages of the values computed at six receiving positions) are the following: 14.6 s ($d=0$), 5.97 s ($d=0.25$), and 4.94 s ($d=1$). These results are consistent with those published by Lam[4] for the same enclosure. Unlike the cubic room, the disproportionate long room is characterized by decay curves which are clearly nonlinear in the totally specular case ($d=0$), and this implies that the method used to interpolate the decays can have an influence on the reverberation time values.[15] In the diffuse case ($d=1$), the decay curves are quite linear and the computed reverberation time approaches the Eyring's value (5.0 s).

The computed sound propagation decays are illustrated in Fig. 3. The associated statistical errors are comprised between 0.2 and 0.4 dB. These results confirm the findings of Hodgson and Lam, namely that in disproportionate long rooms, the decay is steeper for totally diffusing walls. There is nothing new in this conclusion, but these consistent results again indicate that the algorithm is working properly. Note that the decays illustrated in Fig. 3 are closer to the results of Hodgson (Fig. 5 of Ref. 3) than those of Lam (Fig. 1 of Ref. 4).

B. Tests in several frequency bands

Now that the diffusion algorithm can be trusted, the procedure proposed in Sec. II C for the simultaneous treatment of several frequency bands will be tested. The acoustical data (source power and absorption factors) are identical in all octave bands (from 62.5 to 8000 Hz), except the diffusion factor which is the same for all surfaces but depends on frequency. The splitting coefficient performing the separation between specular and diffuse reflections is set to the average value of the diffusion factor (about 0.5).

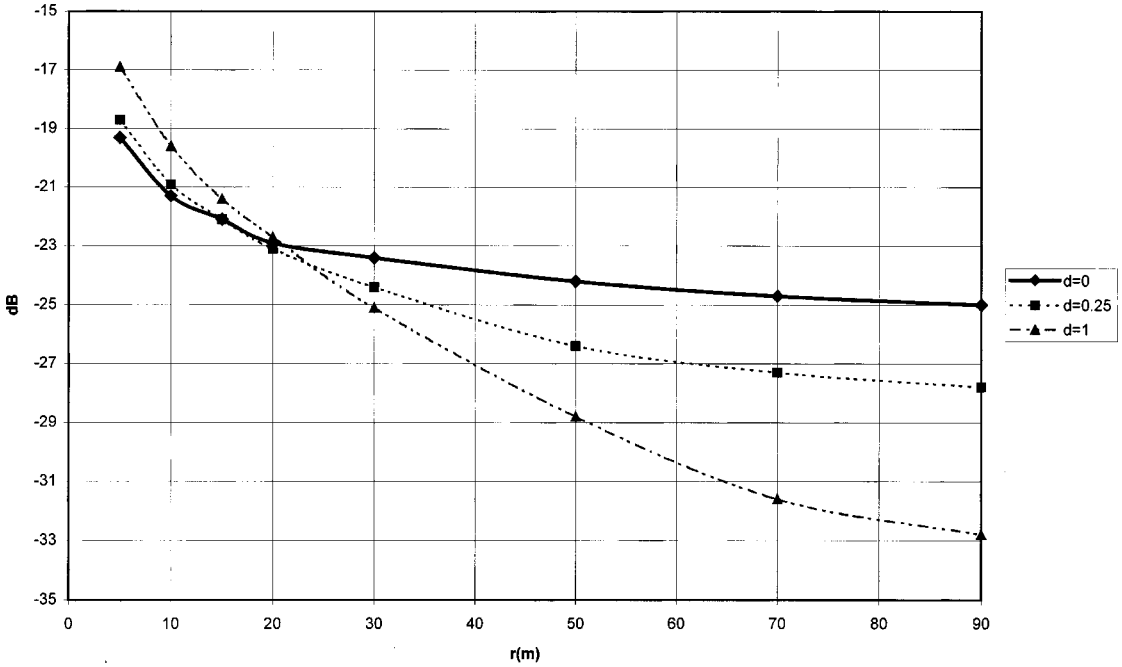

FIG. 3. Difference between the sound pressure levels (decibels) computed at several distances (r) from the point source in the disproportionate long room and the power level of this source (also in decibels). These results are computed in single frequency bands with the splitting coefficient set to the diffusion factor (d).

The first results were disappointing and are not reported here. It appeared that the statistical errors on the computed sound pressure levels were significantly increased when passing from a single frequency band to the broad spectrum model (the number of rays being quite the same in both situations). This effect was rather limited at frequencies where the diffusion factor was close to the splitting coefficient (0.5), but the statistical errors at $d=0$ and $d=1$ were unacceptable. Of course, this increase could be compensated by a greater number of rays but the gain obtained by a simultaneous treatment of all frequency bands would be lost.

This important effect has already been discussed in Sec. III. Though it was still acceptable for a single diffusing surface, the influence on the statistical errors is here so amplified that the algorithm becomes effectively useless. Fortunately, a solution will be found in the following through an adequate control of the splitting coefficient.

The increase of the statistical error is explained as follows: If all surfaces of the enclosure are identical, the amplification of the sound ray's intensity after n reflections is given by

$$A_n(f)=\left(\frac{1-d(f)}{1-\beta}\right)^{n_s}\left(\frac{d(f)}{\beta}\right)^{n_d}, \tag{17}$$

where n_s and $n_d(=n-n_s)$ are the number of specular and diffuse reflections, respectively. All sound rays following the same sequence of specular and diffuse reflections are equally amplified. Their number is (on average) $N_n=N(1-\beta)^{n_s}(\beta)^{n_d}$. Therefore, the product $N_nA_n(f)$ does not depend on the splitting coefficient, and this is true for any sequence defined by n_s and n_d. The effect of the splitting coefficient is thus to amplify or attenuate the intensity of the sound rays belonging to that given sequence, while respectively reducing or increasing the number of rays in comparison with the case $\beta=d(f)$. This situation leads to ill-conditioned ray-tracing algorithms, since most of the computing time and efforts are dedicated to the less important contributions.

Consider for example the case $d=0$ (or $d=1$). With $\beta=0.5$, only an eighth of the total number of rays are still active after three reflections (the other rays are completely attenuated). After n reflections, this number is reduced by 2^n and this can explain why the statistical errors arise.

The problem is also illustrated by the sound decay curves obtained with several values of the diffusion factor (see Fig. 4). The splitting coefficient for all these curves is $\beta=0.5$. As the diffusion factor deviates from the splitting coefficient, the decays are more and more disturbed by the reduction of the active number of rays. It is not surprising that the computed reverberation times will be affected by these significant statistical errors.

The solution to this problem is to adapt the splitting coefficient to the past history of the sound ray at each order of reflection, in order to limit its amplification at all frequencies. With this process, any sound ray will be naturally dedicated to the particular frequency bands where it gives the most significant contribution after n reflections. This constant modification of the splitting coefficient is theoretically correct (it will not change the estimate of the sound pressure level), provided that all rays belonging to the same sequence of reflections and diffusions are submitted to the same sequence of splitting coefficients (see the Appendix).

The sequence of the splitting coefficients is obtained by limiting the amplification of the sound ray's intensity at each reflection. Given the amplification $A_n(f)$ at the nth reflection, its value at the $(n+1)$th reflection will be one of the following:

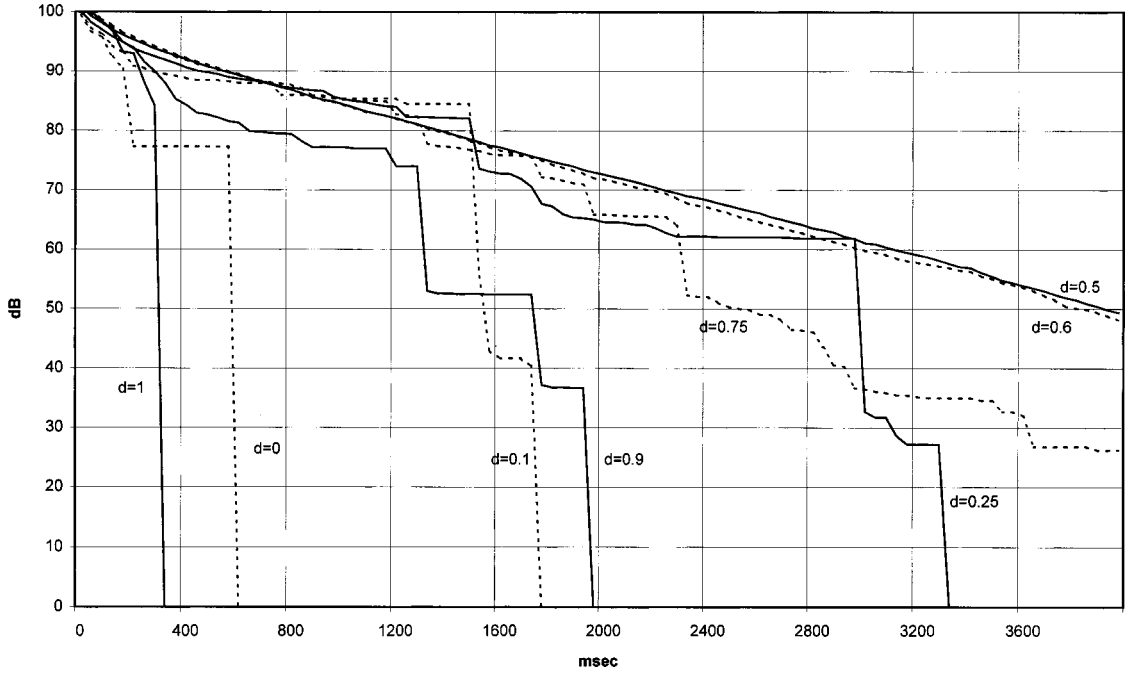

FIG. 4. Reverberation time decays obtained with the same splitting coefficient ($\beta=0.5$) at all orders of reflection. The results are computed at 5 m from the source, in the disproportionate long room. The eight values of the diffusion factor (d) identify the results computed in the eight octave bands (wall's and medium's absorption factors do not depend on frequency).

$$A_{n+1}(f)=A_n(f)\frac{1-d(f)}{1-\beta_{n+1}} \quad \text{if } Z_{n+1}>\beta_{n+1},$$

or (18)

$$A_{n+1}(f)=A_n(f)\frac{d(f)}{\beta_{n+1}} \quad \text{if } Z_{n+1}\leqslant\beta_{n+1}.$$

The optimum value of the splitting coefficient is the one which minimizes the maximum of $A_{n+1}(f)$ in both situations:

$$\beta_{n+1}=\frac{\max_f\{A_n(f)d(f)\}}{\max_f\{A_n(f)d(f)\}+\max_f\{A_n(f)(1-d(f))\}}. \quad (19)$$

Therefore, a new value of the splitting coefficient will be computed at each reflection of the sound ray according to Eq. (19). This procedure ensures that all rays belonging to the same sequence of reflections and diffusions are submitted to the same sequence of splitting coefficients.

Room 2 is again used as a test enclosure, with the same absorption factors as in Sec. IV A. The diffusion factor is given in eight octave bands ($d=0.0,0.1,0.25,0.5,0.6,0.75,0.9,1.0$). The results of the new algorithm (β var.) are compared in Table IV with the results obtained in Sec. IV A for a single octave band ($d=\beta$).

The results of the new algorithm are shown to be consistent with their corresponding values computed with $d=\beta$. As could be expected, the statistical deviations increase though the number of rays is the same. For example, the average increase of the statistical error is about 1.9 for $d=0$: therefore, the number of rays should be multiplied by $(1.9)^2=3.6$ to obtain the same accuracy. For $d=0.25$, only $2.8N$ rays would be required, and $4.2N$ rays for $d=1$. In all cases, the simultaneous computation in all frequency bands is faster, even in the less favorable situations.

It has also been observed that the amplification of the sound ray's intensity $A_n(f)$ is generally less than $(n+1)$

TABLE IV. Comparison of the sound pressure levels (dB) computed at several distances r (m) from the point source in room 2. The three executions ($d=\beta$) are carried out in single frequency bands with the splitting coefficient set to the diffusion factor, while the results noted (β var) are obtained with a single execution of the new algorithm. The number of rays is the same for all executions ($N=1.6\times10^6$).

r (m)	$d=\beta=0$	$d=0$, β var[a]	$d=\beta=0.25$	$d=0.25$, β var	$d=\beta=1$	$d=1$, β var
5	100.7±0.2	100.6±0.4	101.3±0.2	101.4±0.3	103.1±0.2	103.1±0.4
10	98.7±0.2	98.7±0.4	99.1±0.2	99.1±0.3	100.3±0.2	100.3±0.3
15	97.9±0.2	98.0±0.4	97.9±0.2	98.0±0.3	98.6±0.2	98.7±0.5
20	97.1±0.2	96.8±0.4	96.9±0.2	96.9±0.4	97.3±0.2	96.9±0.4
30	96.6±0.2	96.7±0.4	95.5±0.2	95.6±0.4	94.9±0.3	95.1±0.5
50	95.8±0.2	95.9±0.4	93.7±0.2	94.0±0.5	91.2±0.3	91.0±0.6
70	95.3±0.2	95.1±0.4	92.7±0.3	92.5±0.5	88.4±0.4	89.0±1.0
90	95.0±0.2	94.8±0.4	92.2±0.3	92.2±0.5	87.2±0.4	86.1±1.0

[a]β given by Eq. (19) at each reflection.

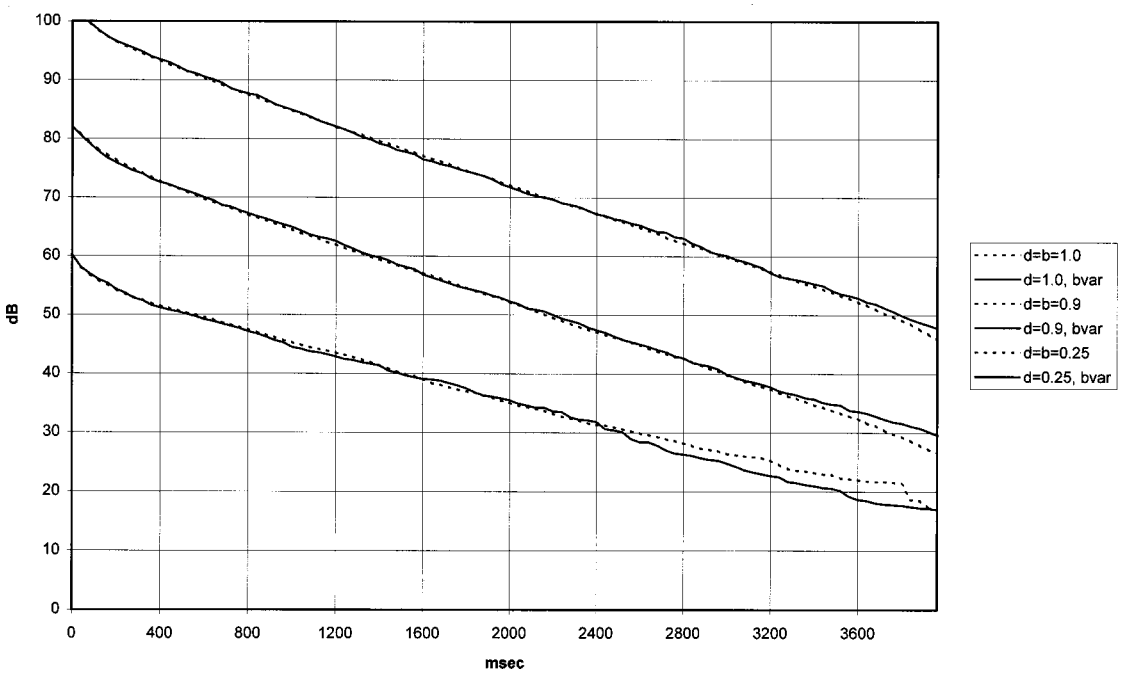

FIG. 5. Reverberation time decays obtained with a variable splitting coefficient (b_{var}), compared with the corresponding decays computed in single frequency bands with $\beta = d$ (dotted curves). The curves ($d = 0.9$) and ($d = 0.25$) have been shifted downwards (respectively, 20 and 40 dB below their computed values). The receiver is situated at 5 m from the source, in the disproportionate long room.

with this procedure, which indicates a linear increase as a function of the order of reflection. As the natural attenuation (due to sound's absorption) is rather exponential, this ensures that the sound ray will not travel indefinitely in the enclosure.

Figures 5 and 6 show some reverberation decays obtained by the new algorithm, compared with the corresponding decays computed with $\beta = d$ (the number of rays is quite the same). The receiver position is at 5 m from the source in Fig. 5, and at 15 m from the source in Fig. 6. In these figures, the curves ($d = 0.9$) and ($d = 0.25$) have been shifted downwards (respectively 20 and 40 dB, respectively, below their computed values) to allow an easier observation.

A drastic improvement has been obtained by the new algorithm, in comparison with the poor results shown in Fig. 4. This improvement is confirmed by the values of the computed reverberation times in Table V, which are clearly consistent with the values delivered by the program in a single frequency band. Note that the slightly higher value found for $d = 1.0$ (in comparison with $d = 0.9$) is not really significant,

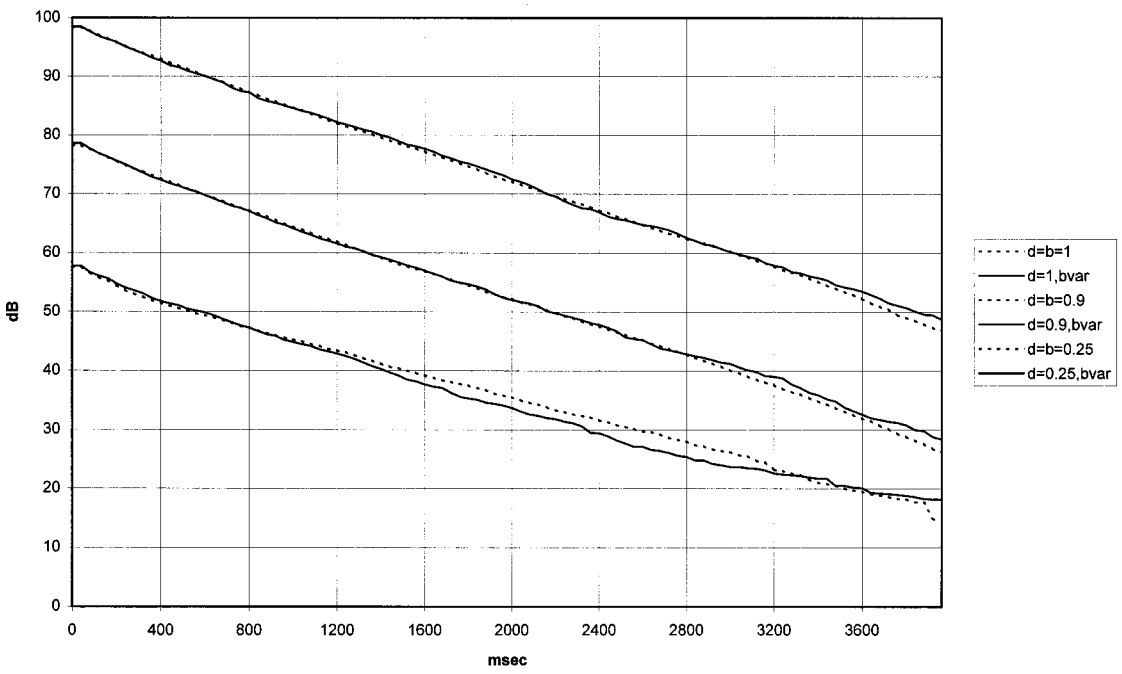

FIG. 6. Same as Fig. 5, but at 15 m from the source.

TABLE V. Comparison of the reverberation time T_{30} (s) computed by the sound ray algorithm in each octave band separately and in all octave bands simultaneously. The values are the averages of the reverberation times computed at six receiving positions comprised between 10 and 70 m from the source.

Diffusion factor d	T_{30} (s) computed in a single octave band ($\beta=d$)	T_{30} (s) computed in eight octave bands (β variable)
0.25	5.97	5.79
0.9	4.90	4.79
1.0	4.94	4.83

since it must be due to the statistical errors affecting the sound decay curves.

The last application will illustrate the influence of the wall's absorption properties on the efficiency of the new algorithm. The previous example was quite unfavorable in this respect, since a low absorption (or a high reverberation) creates a great number of long rays which still have a significant contribution at the detectors after several diffusions or specular reflections. The contribution of these long rays is clearly the most affected by the choice of the splitting coefficient: This is evident from the decays shown in Fig. 4, but appears also (to a lesser extent) in Figs. 5 and 6.

Therefore, it seems that more favorable cases are obtained as wall's absorption increases. To show this, the same disproportionate long room is again simulated with $\alpha=0.2$ instead of 0.068. It is found that the sound pressure levels computed in eight octave bands simultaneously are still consistent with those computed in single octave bands separately. Other results are found in Table VI.

Table VI shows that the reverberation times computed by both methods are still very close. What is more interesting here is the ratio σ/σ_0 showing the increase of the statistical error when passing from a single octave band to the simultaneous treatment of all octave bands. This increase of the statistical error would be compensated by a greater number of rays: $2.8N$ (for $d=0$), $2.3N$ ($d=0.25$), and $2.5N$ ($d=1$). If these numbers are compared with those obtained for $\alpha=0.068$ (respectively, $3.6N$, $2.8N$ and $4.2N$), it can be concluded that the efficiency of the method increases with the (mean) absorption factor.

C. Still further improvements

A still more efficient algorithm could take advantage of the differences observed in the reverberation times (as a function of frequency) and also in the statistical errors.

TABLE VI. Comparison of some results obtained by the sound ray algorithm in a single octave band ($\beta=d$, statistical error σ_0, number of rays N) and by a simultaneous treatment of eight octave bands (β var, statistical error σ). The values of the reverberation times are the averages computed for six receiving positions comprised between 10 and 70 m from the source.

Diffusion factor	σ/σ_0 (average)	T_{30} (s), $\beta=d$	T_{30} (s), β var.	N
$d=0$	1.68	6.63	6.70	2×10^6
$d=0.25$	1.50	3.09	3.15	5×10^6
$d=1$	1.59	1.75	1.76	16×10^6

Consider again the results presented in Table VI. It seems evident that the very long rays are only useful in the octave band where the reverberation time is longer ($d=0$). The adaptation process of the splitting coefficient could take this into account, e.g., by removing from Eq. (19) the frequency bands where the sound ray's intensity has fallen below a given threshold.

The analysis of Table VI leads to another suggestion: The number of rays N mentioned in the last column leads approximately to the same statistical errors in each single frequency band. Now, if 16×10^6 rays are used in the simultaneous treatment of all bands, the required accuracy is already obtained in the band where $d=0$ after 2×10^6 rays. Therefore, it does not make sense to spend more computing efforts for this particular frequency band, and the modification of the splitting coefficient could be used to progressively concentrate these efforts in the frequency bands requiring more rays. This would of course necessitate a periodic evaluation of the statistical errors in all bands.

V. CONCLUSION

Randomized ray-tracing algorithms can be adapted to simulate diffusely reflecting boundaries. However, a major problem of this adaptation is the dependence of the diffusion factor on frequency, which implies that the execution of the program must be repeated for each frequency band. A solution could be found in the method proposed in this paper: It is based on a particular coefficient called the ''splitting coefficient,'' which controls the sequences of consecutive diffuse and specular reflections without any influence of frequency.

Theoretical developments and examples have shown the adequacy of this method. They also indicated that the statistical errors on the computed results tend to increase (for the same number of sound rays). Therefore, an appropriate control of the splitting coefficient is necessary, in order to preserve the efficiency of the algorithm. The best efficiency is of course obtained when the diffusion factor is nearly constant as a function of frequency. As stronger differences occur in the diffusion spectrum, the method becomes less efficient. The reverberation time is also a significant factor in this respect, since less reverberant enclosures lead to more efficient executions of the program.

Still further improvements are possible, but the method as it stands can already be applied in any randomized ray-tracing algorithm, since the developments and conclusions are not restricted to a particular algorithm.

APPENDIX

It will be proved that Eq. (2), which was established in the case of specular reflections, can be extended to the more general case of an enclosure bounded by partially diffusing surfaces.

First of all, the squared rms sound pressure will be averaged on the surface receiver ΔS to find an expression similar to Eq. (1). The multiple contributions at a receiving point R belonging to ΔS are[11]

(1) contributions S^n-R: sound intensity reaching R after ''n'' specular reflections, $n=0$ being the direct sound;
(2) contributions $S^k-D-S^\kappa-R$: ''k'' specular reflections followed by a diffusion and again ''κ'' specular reflections ($n\geqslant 1$, $k=0,...,n-1$ and $\kappa=n-k-1$);
(3) contributions $S^k-D-S^l-D-S^\lambda-R$: contributions with two diffusions;
(4) contributions with more than two diffusions.

This analysis is restricted to the first and second orders of diffusion, but the procedure (which becomes more and more complex) can be extended to any order of diffusion.

The first contributions (S^n-R) involve ''n'' specular reflections. The expression of the squared rms pressure is therefore similar to Eq. (1), but restricted to these nth order reflections:

$$p^2(\Delta S)=\frac{\rho_0 c}{\Delta S}\int_0^{2\pi} d\phi \int_0^{\pi} \nu_n(\theta,\phi)\sin\theta\, d\theta,$$
$$\nu_n(\theta,\phi)=\frac{a_n(\theta,\phi)\,\delta_n(\theta,\phi)}{|\cos i_n(\theta,\phi)|} I(\theta,\phi). \tag{A1}$$

However, there is a significant difference from Eq. (1), more precisely in the expression of the attenuation $a_n(\theta,\phi)$ which now includes the factors $(1-d_i)$ of the (partially) diffusing surfaces hit by the sound ray.

The second contribution to the squared rms pressure involves a single diffusion: $S^k-D-S^\kappa-R$. An equivalent situation can here be defined by considering a single diffusing surface, a single image source and a single image detector. The image source is any kth order image Q_{ki} of the real source, while the image detector is any κth order image $R_{\kappa j}$ (belonging to $\Delta S_{\kappa j}$) of the real detector, taking into account the last κ specular reflections. Expression (7) can be used for this equivalent situation:

$$p_{\mathrm{sc}}^2(\Delta S_{\kappa j})=\frac{\rho_0 c}{\Delta S_{\kappa j}}\int_0^{2\pi} d\phi \int_0^{\pi} \sin\theta\, d\theta \int_0^{2\pi} d\phi_2 \int_0^{\pi/2} I_{\mathrm{rel}}(\theta_1,\theta_2,\phi_2)\,\nu_{kn}(\theta,\phi,\theta_2,\phi_2)\sin\theta_2\, d\theta_2,$$
$$\nu_{kn}=\frac{d_{k+1}(1-\alpha_{k+1})(\Pi_{k+1\neq l=1}^{n}(1-\alpha_l)(1-d_l))A_{\mathrm{air},n}(\theta,\phi,\theta_2,\phi_2)I(\theta,\phi)}{|\cos\hat{i}(dA,R_{\kappa j})|}\,\delta_{ki}(\theta,\phi)\,\delta_{\Delta S_{kj}}(\theta_2,\phi_2). \tag{A2}$$

In this expression, the angles θ and ϕ are attached to the image source Q_{ki}. The effective angular extent of this source is limited by the factor $\delta_{ki}(\theta,\phi)$ [$\delta=1$ if the sound ray emitted by the image source in the direction (θ,ϕ) effectively hits the diffusing surface at the element dA]. The angles (θ_2,ϕ_2) defining the direction of scattering are attached to dA. The notation has been here simplified: It is clear that these angles (as well as I_{rel}) depend on dA, and therefore on (θ,ϕ). The effective angular extent of the secondary source dA is limited by the factor $\delta_{\Delta S_{\kappa j}}(\theta_2,\phi_2)$. ν_{kn} includes the contributions of the absorption (α_l) and diffusion (d_l) factors which depend on $(\theta,\phi,\theta_2,\varphi_2)$.

To obtain the total contribution $S^k-D-S^\kappa-R$, the next step is to sum for all kth order image sources and for all κth order image detectors. This can be done by the following procedure: The local spherical coordinates (θ,ϕ) of each image source are first transformed into the corresponding coordinates attached to the real source. Each kth order image source defines an effective solid angle (corresponding to $\delta_{ki}\neq 0$) on the unit sphere surrounding the real source. These solid angles do not overlap each other, since the ''k'' specular reflections of any sound ray (θ,ϕ) can only be realized by a single image source. Therefore, the first double integral in Eq. (A2) includes the contributions of all kth order image sources, provided that one changes the signification of θ and ϕ and that δ_{ki} is replaced by δ_k ($=1$ if the ray hits the diffusing surface of the enclosure after k specular reflections).

The same development can be done for the image detectors: All of them subtend solid angles at the diffusing element dA, which do not overlap each other. Therefore, $\delta_{\Delta S_{kj}}$ can be simply replaced by δ_κ in Eq. (A2), which finally leads to

$$p_{\mathrm{sc}}^2(\Delta S)=\frac{\rho_0 c}{\Delta S}\int_0^{2\pi} d\phi \int_0^{\pi} \sin\theta\, d\theta \int_0^{2\pi} d\phi_2 \int_0^{\pi/2} I_{\mathrm{rel}}(\theta_1,\theta_2,\phi_2)\,\nu_{kn}(\theta,\phi,\theta_2,\phi_2)\sin\theta_2\, d\theta_2,$$
$$\nu_{kn}=\frac{d_{k+1}(1-\alpha_{k+1})(\Pi_{k+1\neq l=1}^{n}(1-\alpha_l)(1-d_l))A_{\mathrm{air},n}(\theta,\phi,\theta_2,\phi_2)I(\theta,\phi)}{|\cos i_n(\theta,\phi,\theta_2,\phi_2)|}\,\delta_k(\theta,\phi)\,\delta_\kappa(\theta_2,\phi_2). \tag{A3}$$

The third contribution to the squared rms pressure involves two diffuse reflections: $S^k-D-S^l-D-S^\lambda-R$. An equivalent situation can here be defined by considering a diffuse reflection on the surface element dA, after ''k'' specular reflections. Element dA is then considered as a sound source, emitting in a hemisphere with the relative intensity distribution $I_{\mathrm{rel}}(\theta',\epsilon,\eta)$, where θ_1' is the angle of incidence on dA. The total contribution of the source dA to the squared rms pressure at the receiver (from the type $S^l-D-S^\lambda-R$) can be deduced from Eq. (A3):

$$p_{\mathrm{sc}}^2(dA,\Delta S)=\frac{\rho_0 C}{\Delta S}\int_0^{2\pi} d\eta\int_0^{\pi/2}\sin\epsilon\, d\epsilon\int_0^{2\pi} d\phi_2 \times\int_0^{\pi/2} I_{\mathrm{rel}}(\theta_1,\theta_2,\phi_2)\,\nu_{l\lambda}(\epsilon,\eta,\theta_2,\phi_2) \times\sin\theta_2\, d\theta_2. \tag{A4}$$

$\nu_{l\lambda}$ is taken from ν_{kn} in Eq. (A3), with l and λ instead of k and κ, respectively, and the angles (ϵ,η) instead of (θ,ϕ). It contains $I_{dA}(\epsilon,\eta)$, the power emitted by dA per unit solid angle in the direction (ϵ,η):

$$I_{dA}(\epsilon,\eta)=d_{k+1}(1-\alpha_{k+1})W_r(Q_{ki},dA)I_{\mathrm{rel}}(\theta_1',\epsilon,\eta), \tag{A5}$$

$$W_r(Q_{ki},dA)=I(\theta,\phi)\left(\prod_{j=1}^{k}(1-d_j)(1-\alpha_j)\right)\times A_{\mathrm{air}}(Q_{ki},dA)\,d\Omega(Q_{ki},dA)\,\delta_{ki}(\theta,\phi).$$

The notation has been again simplified. For example, the indices ''$k+1$'' or ''j'' in the absorption and diffusion factors indicate their values at the $k+1$ th or the jth reflection for the particular ray (θ,ϕ), the $k+1$ th reflection being the diffuse reflection on dA. $W_r(Q_{ki},dA)$ is the power received by dA from the image source Q_{ki}, dA subtending a solid angle $d\Omega(Q_{ki},dA)$ at Q_{ki}. Finally, the angles θ and ϕ are attached to the image source.

Integrating for all diffusing elements dA can be realized by integrating for all angles (θ,ϕ): Remember that $d\Omega(Q_{ki},dA)=\sin\theta\, d\theta d\phi$. Summing for all kth order image sources can be done with the method used to derive Eqs. (A3) from (A2), which gives

$$p_{\mathrm{sc}}^2(\Delta S)=\frac{\rho_0 C}{\Delta S}\int_0^{2\pi} d\phi\int_0^{\pi}\sin\theta\, d\theta\int_0^{2\pi} d\eta\int_0^{\pi/2} I_{\mathrm{rel}}(\theta_l',\epsilon,\eta)\sin\epsilon d\epsilon\int_0^{2\pi} d\phi_2\int_0^{\pi/2} I_{\mathrm{rel}}(\theta_1,\theta_2,\phi_2) \times\nu_{k\,\ln}(\theta,\phi,\epsilon,\eta,\theta_2,\phi_2)\sin\theta_2 d\theta_2,$$

$$\nu_{k\,\ln}=\frac{d_{k+1}(1-\alpha_{k+1})d_{k+l+2}(1-\alpha_{k+l+2})\left(\Pi_{\substack{m=1\\ m\neq k+1,k+l+2}}^{n}(1-\alpha_m)(1-d_m)\right)A_{\mathrm{air},n}(\theta,\phi,\epsilon,\eta,\theta_2,\phi_2)I(\theta,\phi)}{\left|\cos\hat{i}_n(\theta,\phi,\epsilon,\eta,\theta_2,\phi_2)\right|} \times\delta_k(\theta,\phi)\,\delta_l(\epsilon,\eta)\,\delta_\lambda(\theta_2,\phi_2). \tag{A6}$$

The total contribution to the squared rms pressure at the receiving surface ΔS is therefore given by the sum of the expressions (A1), for all n, (A3) for all k,n, (A6) for all k,l,n and all next orders of diffusions.

Now, it will be shown that the following expression (computed by the tracing of N rays) is an unbiased estimate of this total contribution:

$$\hat{p}^2(\Delta S)=\frac{4\pi\rho_0 C}{N\Delta S}\sum_{i=1}^{N}\mu(\theta_i,\phi_i) =\frac{4\pi\rho_0 C}{N\Delta S}\sum_{i=1}^{N}\mu_0(\theta_i,\phi_i) +\mu_1(\theta_i,\phi_i,Z_{i1},\epsilon_{i1},\eta_{i1}) +\mu_2(\theta_i,\phi_i,Z_{i1},\epsilon_{i1},\eta_{i1},Z_{i2},\epsilon_{i2},\eta_{i2})+\cdots. \tag{A7}$$

The function μ has already been defined in Eq. (12) for first-order diffusions. To obtain μ, the function ν [expressed in Eq. (A1), (A3) or (A6)] must be divided by the product of all ''splitting coefficients'' β_{ik} (if diffusion occurs at the kth order reflection) or $(1-\beta_{ik})$ (if specular reflection occurs). In Eq. (A7), μ_0 is the direct sound (depending only on the angles characterizing the direction of emission from the source), μ_1 symbolizes the first-order reflections (depending, besides θ_i and ϕ_i, on the random variables Z_{i1} separating the diffuse and specular components, and on the angles of scattering ϵ_{i1} and η_{i1} if necessary), μ_2 symbolizes the second-order reflections, and so on.

The expectation of Eq. (A7) is simply the sum of the expectations of all contributions corresponding to the different orders of reflection. Consider the nth contribution $\mu_n(\theta_i,\phi_i,Z_{i1},\epsilon_{i1},\eta_{i1},\ldots,Z_{in},\epsilon_{in},\eta_{in})$ which has several possible realizations:

(1) only specular reflections $(Z_{ik}>\beta_{ik},\forall k)$: μ_n is reduced to $\mu_n(\theta_i,\phi_i,Z_{i1},\ldots,Z_{in})$;
(2) only one particular value $Z_{ij}\leqslant\beta_{ij}$ (this corresponds to a single diffusion): μ_n is reduced to $\mu_n(\theta_i,\phi_i,Z_{i1},\ldots,Z_{ij},\epsilon_{ij},\eta_{ij},Z_{i,j+1},\ldots,Z_{in})$;
(3) two particular values $Z_{ij}\leqslant\beta_{ij}$ and $Z_{ik}\leqslant\beta_{ik}$, corresponding to two diffusions and $(n-2)$ specular reflections;
(4) more than two diffuse reflections.

The expectation of the nth order contribution μ_n is the sum of the expectations corresponding to all these possible realizations. The first one, for example, gives

$$\langle \mu_n \rangle = \int_0^{2\pi} d\phi \int_0^{\pi} \frac{\sin\theta}{4\pi} d\theta \times \int_{\beta_1}^{1} dZ_1 \cdots \int_{\beta_n}^{1} \mu_n(\theta,\phi,Z_1,\ldots,Z_n) dZ_n . \quad \text{(A8)}$$

In this expression, it has been considered that all random variables $(\theta,\phi,Z_1,\ldots,Z_n)$ are independent: Therefore, their joint probability density function is simply $\sin\theta/4\pi$ (since the uniform pdf of any Z_k is 1). It has also been considered that the splitting coefficients β_k could be different at each order of reflection of the sound ray, not only because the surface hit by the ray is itself different, but also to introduce the possibility that the splitting coefficient could be changed at each reflection for the same surface. This is a more general concept which is used in the definition of an algorithm in Sec. IV: In Eq. (A8), β_k generally depends on the past history of the sound ray.

As μ_n does not depend explicitly on Z_n, the rightmost integral in Eq. (A8) can be solved, giving $(1-\beta_n)\mu_n$. Furthermore, the new integrand does not depend explicitly on Z_{n-1} since the denominator of μ_n contains the factor $(1-\beta_n)$. The consecutive integrals are then likewise solved, giving

$$\langle \mu_n \rangle = \int_0^{2\pi} d\phi \int_0^{\pi} \nu_n(\theta,\phi) \frac{\sin\theta}{4\pi} d\theta, \quad \text{(A9)}$$

which leads exactly to the same expression as Eq. (A1) if the constant factor $4\pi\rho_0 c/\Delta S$ of Eq. (A7) is reintroduced.

The second realization of the random variable μ_n corresponds to a single diffusion. Its expectation is

$$\langle \mu_n \rangle = \int_0^{2\pi} d\phi \int_0^{\pi} \frac{\sin\theta}{4\pi} d\theta \int_{\beta_1}^{1} dZ_1 \cdots \int_0^{\beta_j} dZ_j \times \int_0^{2\pi} d\eta_j \int_0^{\pi/2} I_{\mathrm{rel}}(\theta_1,\epsilon_j,\eta_j)\sin\epsilon_j d\epsilon_j \cdots \int_{\beta_n}^{1} \mu_n(\theta,\phi,Z_1,\ldots,Z_j,\epsilon_j,\eta_j,\ldots,Z_n) dZ_n . \quad \text{(A10)}$$

The joint pdf of all random variables has here been completed by the conditional probability of (ϵ_j,η_j) if $(\theta,\phi,Z_1,\ldots,Z_j)$ have been realized, which is $I_{\mathrm{rel}}(\theta_1,\epsilon_j,\eta_j)\sin\epsilon_j$ (see Sec. II A). Proceeding as before, the rightmost $(n-j)$ integrals can be solved consecutively. Then, the integral on Z_j is solved, considering that the integrand does not depend explicitly on Z_j. This gives a factor β_j, which simplifies with the same factor in the denominator of μ_n. Finally,

$$\langle \mu_n \rangle = \int_0^{2\pi} d\phi \int_0^{\pi} \frac{\sin\theta}{4\pi} d\theta \int_0^{2\pi} d\eta_j \times \int_0^{\pi/2} \nu_{jn}(\theta,\phi,\epsilon_j,\eta_j) I_{\mathrm{rel}}(\theta_1,\epsilon_j,\eta_j)\sin\epsilon_j d\epsilon_j . \quad \text{(A11)}$$

Reintroducing the factor $4\pi\rho_0 c/\Delta S$, the contributions $S^j - D - S^{n+1} - R$ in Eq. (A3) are retrieved.

The same procedure can be used to retrieve Eq. (A6) from the expectation of the μ_n's third realization (two diffusions): The extension is straightforward. And this finally proves that expression (A7) computed by a sound ray algorithm can be used as an unbiased estimate of the squared rms pressure at the receiving surface ΔS.

[1] H. Kuttruff, *Room Acoustics*, 3rd ed. (Elsevier, Barking, England, 1991), p. 84.
[2] M. R. Hodgson, ''On the prediction of sound fields in large empty rooms,'' J. Acoust. Soc. Am. **84**, 253–261 (1988).
[3] M. R. Hodgson, ''Evidence of diffuse surface reflection in rooms,'' J. Acoust. Soc. Am. **89**, 765–771 (1991).
[4] Y. W. Lam, ''A comparison of three difuse reflection modeling methods used in room acoustics computer models,'' J. Acoust. Soc. Am. **100**, 2181–2192 (1996).
[5] B.-I. L. Dalenbäck, ''Room acoustic prediction based on a unified treatment of diffuse and specular reflection,'' J. Acoust. Soc. Am. **100**, 899–909 (1996).
[6] U. M. Stephenson, ''Quantized pyramidal beam tracing—a new algorithm for room acoustics and noise immission prognosis,'' Acust. Acta Acust. **82**, 517–525 (1996).
[7] H. Kuttruff, ''Simulierte nachhallkurven in rechteckräumen mit diffusem schallfeld,'' Acustica **25**, 333–342 (1971).
[8] D. Gen-Hua, ''Estimation of the influence of diffusion on reverberation using ray-tracing simulation,'' Acustica **54**, 43–45 (1983).
[9] M. Vorländer, ''Simulation of the transient and steady-state sound propagation in rooms using a new combined ray-tracing/image-source algorithm,'' J. Acoust. Soc. Am. **86**, 172–178 (1989).
[10] K. Li and M. Hodgson, ''Improved methods for estimating fitting density in industrial workrooms,'' J. Sound Vib. **218**, 463–479 (1998).
[11] J. J. Embrechts, ''Sound field distribution using randomly traced sound ray techniques,'' Acustica **51**, 288–295 (1982).
[12] B.-I. Dalenbäck, M. Kleiner, and P. Svensson, ''A macroscopic view of diffuse reflection,'' J. Audio Eng. Soc. **42**, 793–806 (1994).
[13] H. Kuttruff, ''A simple iteration scheme for the computation of decay constants in enclosures with diffusely reflecting boundaries,'' J. Acoust. Soc. Am. **98**, 288–293 (1995).
[14] H. Kuttruff, ''Energetic sound propagation in rooms,'' Acust. Acta Acust. **83**, 622–628 (1997).
[15] J. J. Embrechts, ''A safe method of truncating an echogram calculated by a sound ray technique,'' J. Acoust. Soc. Am. **103**, 2788 (A) (1998).

Acoustic load on the ear caused by headphones

Michael Vorländer[a)]
Institute of Technical Acoustics, Technical University Aachen (RWTH Aachen), D-52056 Aachen, Germany

(Received 22 June 1999; revised 4 January 2000; accepted 10 January 2000)

The standardized method for measurement of complex impedances according to ISO 10534 Part 2 is applied to the acoustic impedance of the ear with an ''open-pinna'' condition and with different types of headphones. The method is based on measurement of the transfer function of two microphone locations in an impedance tube and subsequent signal processing of the complex signal spectra. The termination of the tube is interpreted as ear canal entrance, while the measurement direction is, apparently, from ''inside'' the head towards outside. A tube which was specifically designed for this purpose works well, even though extremely small impedances must be measured. The impedances of the free pinna are similar to the ''soft'' end condition in the open tube, approximately following the radiation impedance of a piston into free space. The headphone impedances can be separated according to the type of headphone. In addition, the absolute impedances as the differences to the open ear compared with a number of headphones are interesting and may be starting point for further investigations. One possibility is, of course, quality control of headphones. The results are also expected to be useful for psychoacoustic research, for better understanding of sound perception, and for use in development of audio equipment. © *2000 Acoustical Society of America.* [S0001-4966(00)02504-2]

PACS numbers: 43.58.Bh, 43.66.Yw, 43.38.Si [SLE]

INTRODUCTION

The acoustic load on the human ear caused by headphones or earphones is among the essential parameters for a realistic impression of reproduced sound. Several studies identified the ''open ear'' as a necessary condition for listening tests, particularly for tests on source localization, source distance, and externalization.[1–3] The predominant construction of open-type headphones is the consequent choice for commercial audio applications as well as for scientific studies on sound perception. In the latter applications, commercial headphones are often modified to be more ''open.'' Of course, this is only possible for applications with sufficient sound insulation against background noise.

Although there is common agreement that ear occlusion causes disturbing effects of internalization, in-head localization, or even loudness differences (''missing 6 dB'' [4–6]), there is no evidence for these effects in a quantitative determination of the relation between ear occlusion and psychoacoustic effects. This work is motivated by the fact that the ear is not simply a passive system with linear and time-invariant features, but an active transducer of sound pressure into spike rates. And, it is well-known that the cochlea actively emits sound energy (otoacoustic emissions) which is an important function of normal hearing. The hypothesis might be posed that the eardrum as a source might be sensitive to ear occlusion which introduces unnatural feedback. Another point is that the auditory part of multidimensional sensations can hardly be separated from other inputs like tactile excitation of the skin around the ear and in the ear canal. These suppositions, however, are to be investigated in additional future studies.

This study is focused on the development of a measurement technique for the impedance, $\underline{Z}_{\mathrm{HP}}$, of headphones, earphones, or any other transducer-like hearing aid applied to the human ear. The aim is to quantify the acoustic load in terms of the complex impedance and by comparison with the impedance ''seen'' from inside the open ear. The results are expected to be useful in headphones design and in psychoacoustic tests focused on the questions mentioned above.

Figure 1 illustrates the impedance conditions of a headphone fitted to the ear. $\underline{Z}_{\mathrm{HP}}$ is the impedance to be measured, $\underline{Z}_{\mathrm{ec}}$ the impedance of the ear canal, and $\underline{Z}_{\mathrm{tym}}$ the impedance at the eardrum. The dashed line marks the reference plane for the impedance determination.

I. EXPERIMENTAL ARRANGEMENT

The well-known approach of the two-microphone impedance tube and digital frequency analysis[7] is applied. The method includes measurement of the acoustic transfer function of the two microphone signals and the determination of the complex impedance at the termination of the tube (see below). The construction, however, must be modified to match the geometrical conditions of the ear canal, pinna, and headphone, for instance, as represented in standard dummy heads. Thus, the dimensions of the tube are not typical. The measurement is (apparently) performed from the inside to the outside of the ear canal. Accordingly, the impedance tube is constructed in such a way that the loudspeaker is considered inside the head with the measurement direction to the sample toward the outside, the termination of the tube being the ear reference point near *cavum conchae* and pinna simulators (see below).

A. Impedance tube specifications

The tube is made of brass and has the following dimensions: $d=10\,\mathrm{mm}$, $s_1=7\,\mathrm{mm}$, $s_2=40\,\mathrm{mm}$, $l=25\,\mathrm{mm}$, w

[a)]Electronic mail: mvo@akustik.rwth-aachen.de

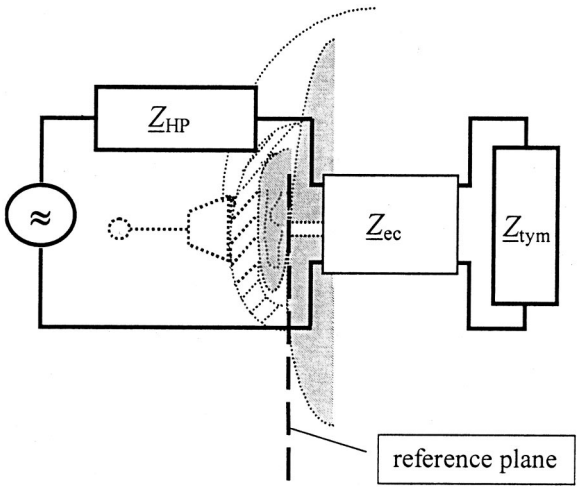

FIG. 1. Equivalent circuit of a headphone fitted to the ear.

$=4$ mm, and a total length of 320 mm (Fig. 2). With these conditions, the tube is intended to be used in a nominal frequency range between 200 Hz and 15 kHz. The choice of three microphone positions allows a wide frequency range. Condenser microphones (Sennheiser KE4) are used. Furthermore, it was found necessary to add porous material near the loudspeaker to avoid reflections and tube modes. This should theoretically not cause any problem, but sufficiently accurate compensation of strong modal effects in amplitude and phase is hardly possible in the practical realization.[8]

The calculation of the reflection factor and the impedance complies with the method described in the ISO standard.[7] In formulation in the frequency domain, with the spectra $\underline{S}_{M1}$ and $\underline{S}_{M2}$

$$\underline{S}_{M1}=e^{jkl}\underline{S}_{d}+e^{-jkl}\underline{S}_{r}, \tag{1}$$

$$\underline{S}_{M2}=e^{jkl}e^{jks}\underline{S}_{d}+e^{-jkl}e^{-jks}\underline{S}_{r}, \tag{2}$$

measured at the microphone positions 1 and 2, respectively, the wave field in the tube can be expanded into one primary (direct) wave and one reflected wave

$$\underline{S}_{d}=e^{-jkl}\frac{\underline{S}_{M2}-e^{-jks}\underline{S}_{M1}}{e^{jks}-e^{-jks}}, \tag{3}$$

$$\underline{S}_{r}=e^{jkl}\frac{e^{jks}\underline{S}_{M1}-\underline{S}_{M2}}{e^{jks}-e^{-jks}}, \tag{4}$$

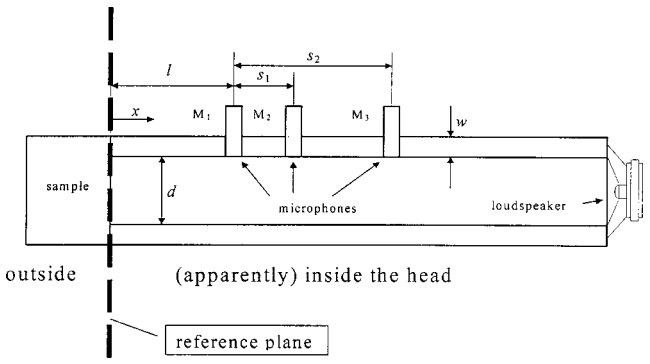

FIG. 2. Sketch of the impedance tube with three microphone positions.

and, finally, it is well-known that the reflection factor $\underline{R}$ is

$$\underline{R}=\frac{\underline{S}_{r}}{\underline{S}_{d}}=e^{j2kl}\frac{e^{jks}\underline{S}_{M1}-\underline{S}_{M2}}{\underline{S}_{M2}-e^{-jks}\underline{S}_{M1}}, \tag{5}$$

or in another formulation

$$\underline{R}=e^{j2kl}\frac{e^{jks}-\underline{H}_{12}}{\underline{H}_{12}-e^{-jks}} \quad \text{with} \quad \underline{H}_{12}=\frac{\underline{S}_{M2}}{\underline{S}_{M1}}. \tag{6}$$

As usual, the impedance, $\underline{Z}$, or normalized impedance, $\underline{\zeta}$, is derived from the reflection factor

$$\underline{Z}=\rho_0 c\,\frac{1+\underline{R}}{1-\underline{R}} \quad \text{and} \quad \underline{\zeta}=\frac{1+\underline{R}}{1-\underline{R}}. \tag{7}$$

B. Signal processing

According to the above-mentioned theoretical basis, there remains the task of measuring the transfer function $\underline{H}_{12}(\omega)$. To achieve best possible reproducibility and noise immunity, methods with deterministic signals like 2-channel fast Fourier transform (FFT) technique (signals like noise, chirps, or any broadband signal with suitable FFT length) or MLS technique (binary sequences of length 2^n-1) may be used. The efficiencies of these methods are similar and differ only in the specific method of signal processing. With broadband white signals, both formulations in time or frequency domain are indeed identical. In this study, PC-based MLS technique (ITADDA and software MF by ITA RWTH Aachen) is used with sequences of order 13. With a sampling rate of 44.1 kHz. the time response length is 186 ms and the frequency line spacing is 5.4 Hz. Time aliasing is avoided since the decay time (0 to -60 dB) of the system is below 80 ms.

The calculation method described in the ISO standard was extended to ensure a smooth transition of the microphone signals in the overlap region between the microphone spacings. The broadband reflection factor is calculated from the reflection factors for small (M1M2) and large (M1M3) spacing according to a weighting function[9]

$$\underline{R}=\frac{\sin^2(ks_1)\cdot\underline{R}_{M1M2}+\sin^2(ks_2)\cdot\underline{R}_{M1M3}}{\sin^2(ks_1)+\sin^2(ks_2)}. \tag{8}$$

Hence, the critical frequencies where the wavelength equals twice the microphone distances are completely excluded from the evaluation.

II. VERIFICATION OF THE MEASUREMENT METHOD

At first, results are to be discussed regarding the efficiency and accuracy of the complete arrangement. This is important due to the very small geometrical conditions and corresponding sources of errors. A rigid termination and the open tube are used as reference samples.

A. Rigid termination

Results for the rigid termination are shown in Fig. 3. The measured reflection factor can be interpreted well up to 12 kHz. Problems above this frequency limit are caused mainly by insufficient output of the loudspeaker. Nevertheless, it is interesting to note how accurate the results are

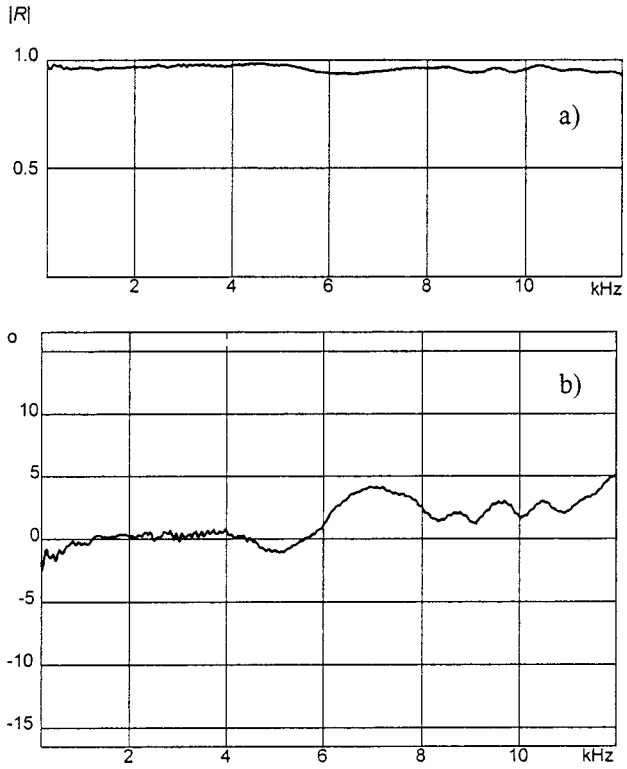

FIG. 3. (a) Magnitude and (b) phase of reflection factor ''rigid.''

between 200 Hz and 12 kHz. The deviation from the theoretical result phase ''0'' and magnitude ''1'' is only 5° and 0.0329, respectively, which corresponds to a minimum measurable absorption coefficient of 0.064.

B. Open-ended tube

Another, even more important test involves a ''soft'' termination, i.e., measurement of a very small impedance and a reflection factor near -1. This is achieved by using the open end of the tube. Here, it is expected that the impedance can be compared with the radiation impedance, $\underline{Z}_{\mathrm{rad}}$, of a circular piston at the end of a tube[10] (see below, Fig. 5). The agreement of the imaginary part is very good, whereas the real part shows some losses other than the those due to radiation. This may be caused by the air flow around the edges of the tube's end and by friction near the microphone supports and along the perimeter U and the cross section S of the tube. The latter effect is estimated [see Ref. 7, Eq. (A.18)] by the imaginary part of the wave number and the corresponding attenuation per distance unit of

$$m_{\mathrm{tube}} \approx 1.5 \cdot 10^{-5} \sqrt{f/\mathrm{Hz}}\, \frac{U}{S}, \tag{9}$$

which introduces over the double distance between the microphones and the termination ($2l = 50\,\mathrm{mm}$) an apparent absorption of

$$\alpha_{\mathrm{tube}} = 1 - e^{-2 m_{\mathrm{tube}} l}. \tag{10}$$

In a rough estimation, this energy loss is concentrated in a transmission line with a serial real resistance of w to be added to the complex radiation impedance $\underline{Z}_{\mathrm{rad}}$. This yields

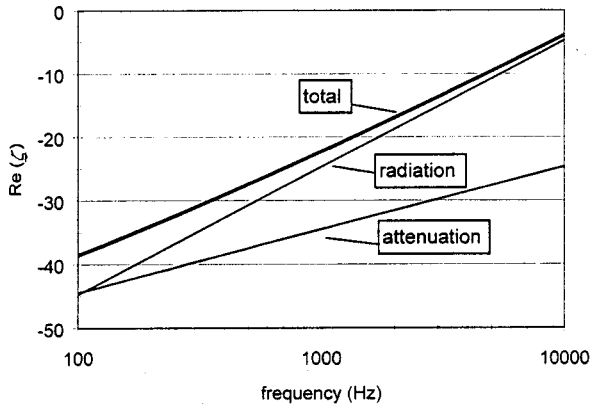

FIG. 4. Real part of open-end impedance with components ''radiation'' and ''tube attenuation.''

$$w = \frac{1 - \sqrt{1 - \alpha_{\mathrm{tube}}}}{1 + \sqrt{1 - \alpha_{\mathrm{tube}}}}. \tag{11}$$

The validity of the estimation is supported by the fact that all distances are small compared with the wavelength, at least for frequencies up to 3 kHz. The magnitudes of w (attenuation) and $\mathrm{Re}(\underline{Z}_{\mathrm{rad}})$ (radiation) are illustrated in Fig. 4. The thick broken line in Fig. 5 shows the real part, including both losses. Taking into account the losses in the narrow tube in this way, the agreement of the real part is as good as for the imaginary part. This or a more elaborate, modified correction of the tube losses similar to Eq. (11) can even be used for correction of measured absolute impedances, if they are as small as in the example of the open tube.

The deviations from the ideal rigid or open conditions are not as small as for precision measurements with standard tube dimensions like 3- or 10-cm diameter. However, they are not too serious.

C. Open ear

For the purpose mentioned above, the headphone measurements, the results will be related to the results of the open ear. Therefore, the open pinna as the termination is chosen as the reference impedance for the evaluation of headphones. The pinna used is taken from the head and torso

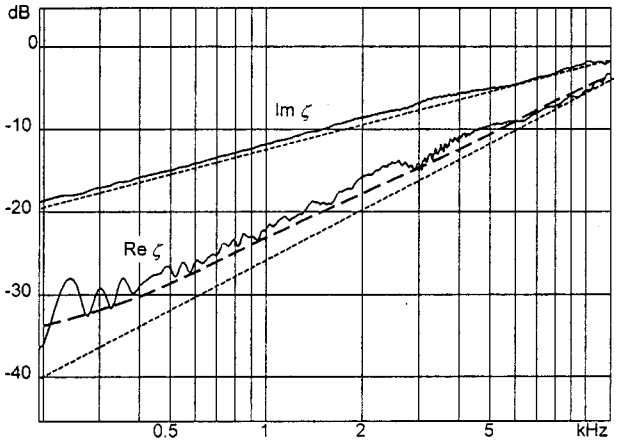

FIG. 5. Real and imaginary part of the impedance of the open-ended tube.

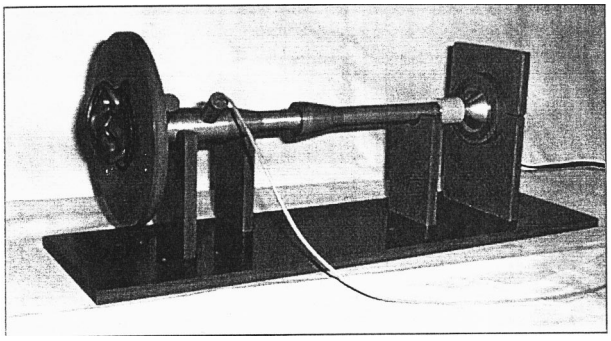

FIG. 6. Impedance tube with ''pinna'' termination.

simulator (ITA head).[11] It is mounted in the middle of a circular plate (15-cm diameter) (see Fig. 6). The results shown in Fig. 7 are used to obtain the reference for the open-ear impedance. They are basically similar to the result of the open tube, but the magnitude impedance curve is slightly shifted due to changes in shape and cross section along the ear canal between the tube, tragus, and *cavum conchae*.

For the interpretation of impedances of headphones, the set of curves is shown in linear scale. Furthermore, the plots show results from repeated measurements over several days. The complete setup was dismantled and reassembled. Thus, these variations allows for judgment of the variances and the overall accuracy. The standard deviation of reproducibility was thus determined to be less than 10% over the whole frequency range. Accordingly, impedance variations smaller than 10% cannot be regarded as significant effects. Furthermore, to check relevance of room reflections or diffraction at surfaces near the end of the tube, the same experiment was repeated in an anechoic environment instead of a laboratory room. In another experiment, the tube was mounted straight through a dummy head to achieve a situation with the pinna located in a head. All these tests did not produce any significant changes, so it can be concluded that mounting the pinna in the center of a circular plate of 15-cm diameter and measurement in an ordinary laboratory room is sufficient.

Of course, any other pinna like the KEMAR type (IEC TR 959) or the geometrically described HEAD acoustics

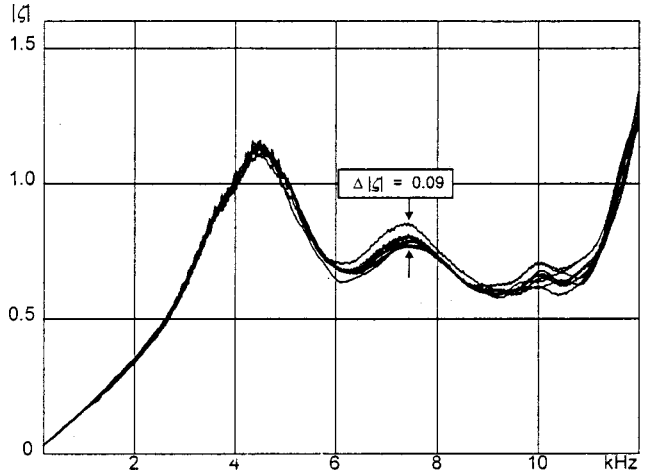

FIG. 7. Magnitude of open-ear impedance from ten independent measurements.

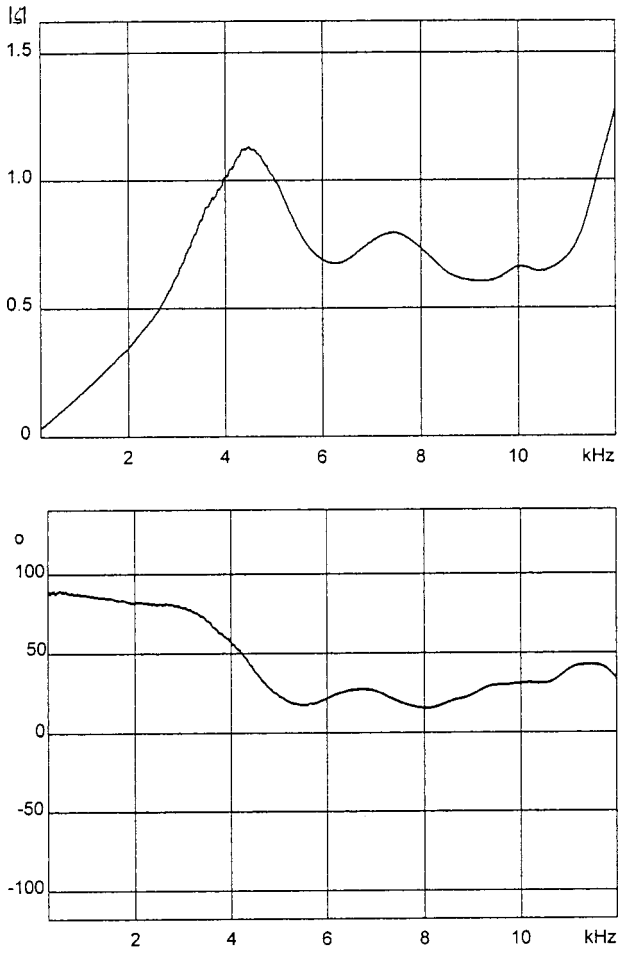

FIG. 8. Magnitude and phase of open-ear reference impedance.

type (HMS II) can be used as well. It was observed that the differences of the open-ear impedances are quite small and hardly significant. Around 4.5 kHz the HMS pinna has a slightly lower impedance than the ITA pinna, particularly due to a lesser convergence of the cross section.

Finally, Fig. 8 shows the reference impedance in linear scale for the open ear (arbitrarily chosen as ITA pinna with mounting plate) used for the subsequent investigations.

III. HEADPHONE IMPEDANCES

Now, the measurement of headphone impedances is straightforward. The headphone is adjusted to the pinna and the mounting plate according to usual wearing conditions. Then, the acoustic impedance of the termination is measured in the same way as described before. It should be noted that the headphone types chosen are an arbitrary ensemble that was available for first experiments. The choice is not related to any investigation of the audio quality of headphones.

A. Open headphones

As an open headphone, the classical headphone for laboratory listening tests, STAX SR λ Professional, was used as an example. For the experiment, ten headphones of the same type were available (denoted by OK_i, $i=0$ to 9). Figure 9 shows the results which indicate the general magnitude of this headphone type and the deviation between different

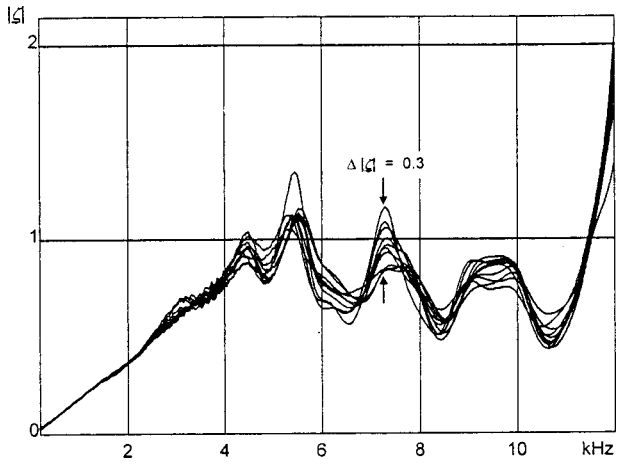

FIG. 9. Magnitude of the impedance of STAX SR λ Professional measured on the reference pinna.

specimen. The deviations are mostly significant: thus, the production spread of the headphones is larger than the deviations caused by measurement uncertainties. For comparison, this headphone type will be included in some of the following figures.

B. Semiopen headphones

Four different Sennheiser headphones (denoted by HK_1: HD 540 Reference, HK_2: HD 560 Ovation, HK_3: HD 560 Ovation II, HK_4: HD 480) are measured. The magnitudes of the impedances are compared in Fig. 10. Larger differences than for the open headphones are noticeable. This also applies to the differences between the headphone types and in comparison to the open ear.

Figure 11 shows the impedance ζ_{HP} that is obtained after subtraction of the open-ear impedance from the measured impedance

$$\underline{\zeta}_{\mathrm{HP}}=\frac{\underline{Z}_{\mathrm{HP}}-\underline{Z}_{\mathrm{pinna}}}{\rho_0 c}. \tag{12}$$

The remaining difference can be interpreted as the acoustic load caused by the headphone. Three headphones are presented as examples: HK_4 (supra-aural, semiopen), HK_3 (circumaural, semiopen), and OK_0 (circumaural, open).

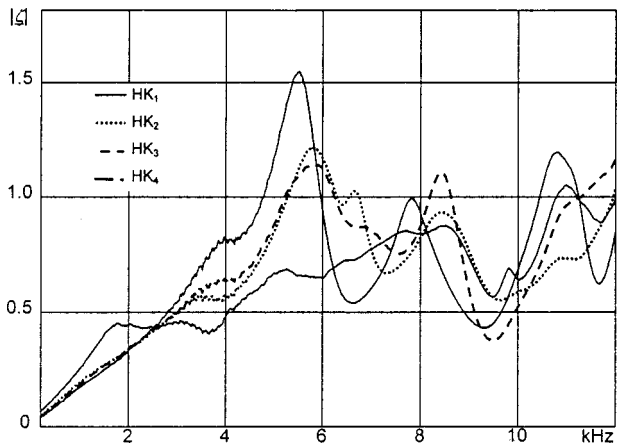

FIG. 10. Magnitude of the impedance of four semiopen headphones (Sennheiser) measured on the reference pinna.

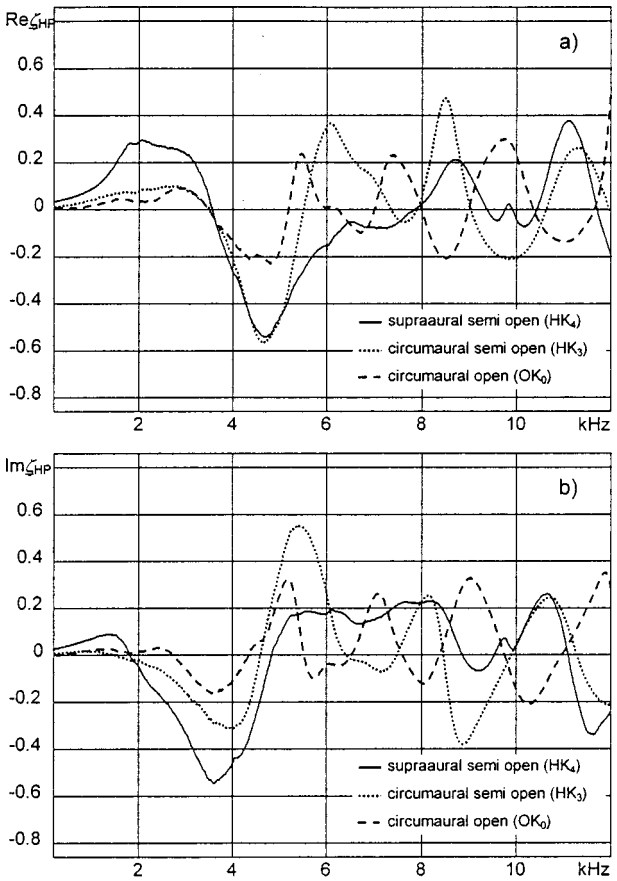

FIG. 11. Acoustic load by headphones ζ_{HP} of three headphones types (open and semiopen).

C. Closed headphones

Two different closed headphones (GK_1: Beyerdymanic DT 770, GK_2: Sennheiser HD 224) were measured. The magnitudes of the impedances are compared in Fig. 12. Much larger differences than for the open and semiopen headphones are noticeable. Figure 13 shows an example of the influence of the application force on the closed headphone.

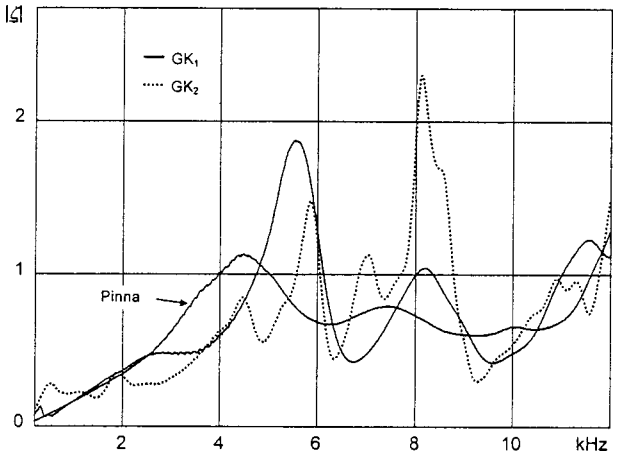

FIG. 12. Magnitude of the impedance of two closed headphones measured on the reference pinna.

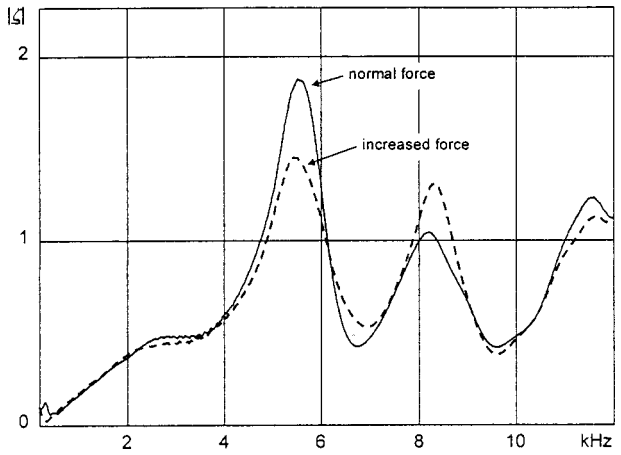

FIG. 13. Magnitude of the impedance of a closed headphone (GK_2) measured on the reference pinna with normal and with increased application force.

Figure 14 shows, similarly to Fig. 11, the impedance ζ_{HP} that is obtained after subtraction of the open-ear impedance from the measured impedance. Again, the remaining difference can be interpreted as the acoustic load caused by the headphone. Three headphones are presented as examples: GK_1 (circumaural, close), HK_2 (circumaural, semiopen) and OK_0 (circumaural, open). It is evident that the type of headphone can be related quantitatively to the acoustic load. And, it is interesting that the acoustic load differs from the open ear only above roughly 2 kHz, which applies to open and semiopen headphones, and partly to closed headphones, but not to the next example, the insert earphone.

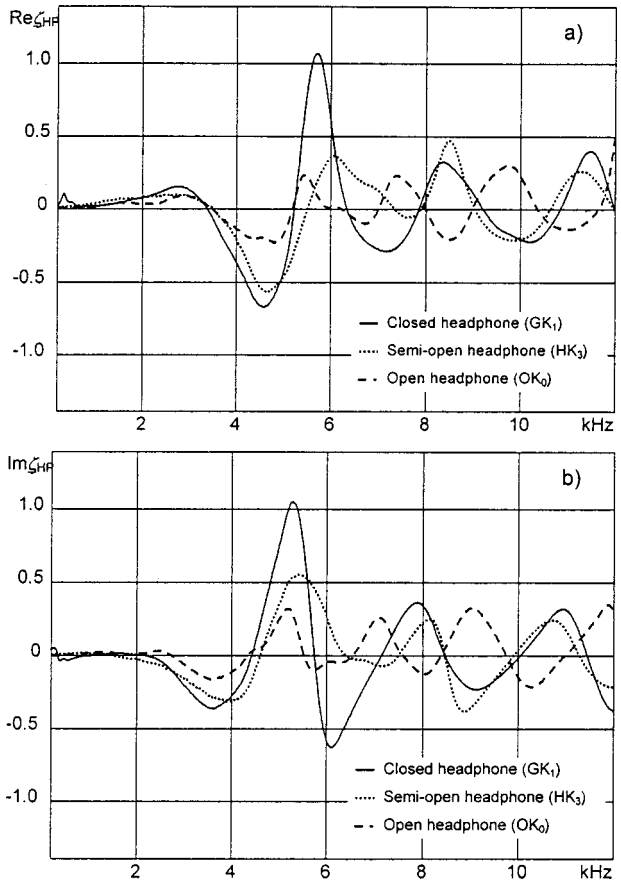

FIG. 14. Acoustic load by headphones ζ_{HP} of two closed and one open headphones.

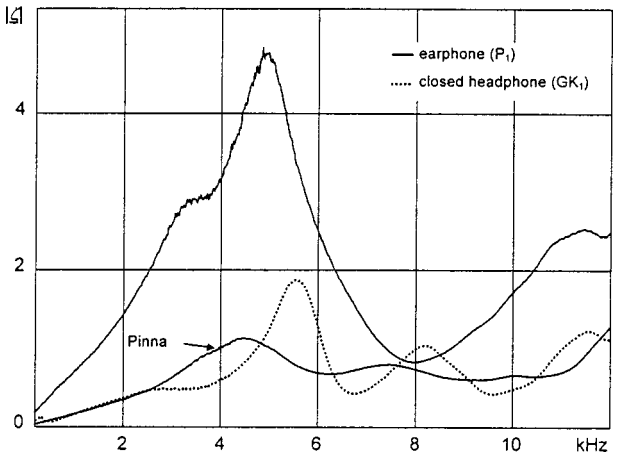

FIG. 15. Magnitude of the impedance of a ''Walkman-type'' earphone in comparison with the impedance of a closed headphone and the open pinna.

D. Insert earphones

The final example is a small ''Walkman'' earphone (P_1: Sony MDR 11). It has the maximum occlusion of the ear, which is clearly visible in the magnitude of the impedance (Fig. 15).

IV. CONCLUSIONS

A standardized method for measurement of complex impedances is applied to the acoustic impedance of the ear with an ''open-pinna'' condition and with different types of headphones. The impedance tube designed for this purpose works well, even though extremely small impedances must be measured. The attenuation effects due to unfavorable tube dimensions having a large ratio of perimeter to cross section must be taken into account, but they can be corrected.

The results of comparing the impedances of the free pinna with a number of headphones are interesting and may be starting points for further investigations. One idea is, of course, the possibility of quality control of headphones.

Another task is seen in subjective tests with several headphone types on problems of localization and externalization. It should be possible to obtain a correlation between the headphone impedance (as opposed to the open-ear impedance) and certain psychoacoustic criteria. This type of project is in preparation and will hopefully begin soon. The results are expected to be useful for psychoacoustic research, for better understanding of sound perception, and for use in development of audio equipment. In the distant future there may be closed headphone types with high sound insulation but with impedances of the open ear. The same will also be useful for insert earphones or hearing aids.

ACKNOWLEDGMENTS

Christian Schüring is acknowledged for the construction and testing of the impedance tube in his diploma thesis. The Institute of Communication Engineering (IENT) of RWTH Aachen is thanked for loaning STAX headphones.

[1] J. Blauert, *Spatial Hearing* (MIT Press, Cambridge, MA, 1997).
[2] W. M. Hartmann and A. Wittenberg, ''On the externalization of sound images,'' J. Acoust. Soc. Am. **99**, 3678–3688 (1996).
[3] A. Kulkarni and S. Colburn, ''Role of spectral detail in sound-source localization,'' Nature (London) **396**, 747–749 (1998).
[4] W. A. Munson and F. M. Wiener, ''In search of the missing 6 dB,'' J. Acoust. Soc. Am. **24**, 498–501 (1952).
[5] W. Rudmose, ''The case of the missing 6 dB,'' J. Acoust. Soc. Am. **71**, 650–659 (1982).
[6] H. Fastl, W. Schmid, G. Theile, and E. Zwicker, ''Schallpegel im Gehörgang für gleichlaute Schalle aus Kopfhörem oder Lautsprechern,'' Fortschritte der Akustik—DAGA 85, Stuttgart, 471–474 (1985).
[7] ISO 10534-2: 1996, Determination of sound absorption coefficient and impedance in impedance tubes—Part 2: Transfer-function method.
[8] C. Schüring, ''Development and testing of a method for determination of the acoustic field impedance at the ear entrance'' (in German), Diploma thesis ITA RWTH Aachen (1999).
[9] I. Deißmann, ''Extension of a method for measurement of the acoustic impedance and application to electroacoustic transducers'' (in German), Diploma thesis ITA RWTH Aachen (1996).
[10] H. F. Olsen, *Elements of Acoustical Engineering* (Van Nostrand, Princeton, 1957), Chap. 5.
[11] A. Schmitz, ''A new digital dummy-head measuring system'' (in German, ''Ein neues digitales Kunstkopfmeßsystem''), Acustica **81**, 416–420 (1995).

Beam profile measurements and simulations for ultrasonic transducers operating in air

Graham Benny and Gordon Hayward
Centre for Ultrasonic Engineering, Department of Electronic and Electrical Engineering, University of Strathclyde, Glasgow G1 1XW, United Kingdom

Roy Chapman
Signal Processing Division, Department of Electronic and Electrical Engineering, University of Strathclyde, Glasgow G1 1XW, United Kingdom

(Received 12 April 1999; accepted for publication 7 December 1999)

This paper outlines a method that has been implemented to predict and measure the acoustic radiation generated by ultrasonic transducers operating into air in continuous wave mode. Commencing with both arbitrary surface displacement data and radiating aperture, the transmitted pressure beam profile is obtained and includes simulation of propagation channel attenuation and where necessary, the directional response of any ultrasonic receiver. The surface displacement data may be derived directly, from laser measurement of the vibrating surface, or indirectly, from finite element modeling of the transducer configuration. To validate the approach and to provide experimental measurement of transducer beam profiles, a vibration-free, draft-proof scanning system that has been installed within an environmentally controlled laboratory is described. A comparison of experimental and simulated results for piezoelectric composite, piezoelectric polymer, and electrostatic transducers is then presented to demonstrate some quite different airborne ultrasonic beam-profile characteristics. Good agreement between theory and experiment is obtained. The results are compared with those expected from a classical aperture diffraction approach and the reasons for any significant differences are explained. [S0001-4966(00)03103-9]

PACS numbers: 43.58.Vb, 43.35.Yb [SLE]

INTRODUCTION

There is increasing interest in the use of noncontact, gas-coupled ultrasound for a variety of applications, mainly in the fields of nondestructive evaluation (NDE) and industrial process control, spanning the frequency range 100 kHz–5 MHz. The significant advantages in terms of simplicity and cost offered by the removal of the usual fluid coupling requirements are well recognized and several practical instruments have been reported.[1–4] Such developments have been led by improvements in transducer technology, mainly to reduce the influence of mechanical mismatch between the transducer and gas load medium. Most recent gas-coupled ultrasonics research has been based on employing either electrostatic, piezoelectric composite, or piezoelectric polymer based transducers[5–9] for airborne ultrasound generation and detection, that are intended to achieve better performance than more conventional homogeneous piezoelectric ceramic counterparts. Important data have been produced on transducer bandwidth and sensitivity as functions of the various design parameters and much of the actual transduction behavior is now well documented for all three types of device. The influence of the gas propagation channel has also been recognized and acoustic attenuation has been quantified with regard to operating frequency and ambient conditions such as temperature, pressure, and humidity.[10,11]

However, the nature of the radiating pressure field has received less attention, which is somewhat surprising, given its importance for many NDE applications such as Lamb wave and through-transmission scanning.[2,12,13] Measurements are more difficult to perform than in the more conventional water environment, due to the shorter wavelengths in air, instability of the propagation medium, and the finite dimensions and sensitivity of the ultrasonic detector, which is generally not well matched to the gas medium. Moreover, for operation in air at frequencies above 1 MHz, phase uniformity across the radiating surface can be critical, especially for those field regions close to the transducer, in which many measurements are constrained to take place. The requirement for both phase and amplitude uniformity in turn places a premium on transducer manufacture, and this is perhaps best illustrated by the improved performance achieved through micromachining methods. In a relatively recent publication, Bashford *et al.*[14] described the ultrasonic field characteristics of micromachined electrostatic transducers and good agreement was obtained between experiment and rudimentary theory that included the influence of frequency dependent attenuation in the air propagation channel. In terms of field structure, the results were excellent, confirming the uniformity achieved through the manufacturing process.

The present work is intended to complement that described in Ref. 14 and describes a methodology for evaluation of the radiating pressure fields from different ultrasonic transducers when operating in the air environment. Specifically, the fields from piezoelectric composite, polyvinylidene fluoride (PVDF), and electrostatic transducers are measured at different frequencies using a precision scanning system, and the results compared with those achieved using two

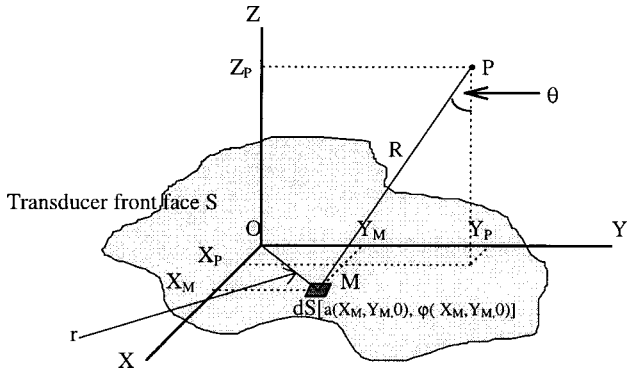

FIG. 1. Geometry and notation used for acoustic field calculation [*dS* is the elemental area of side dimensions *dX*, *dY*, situated at $M(X_M, Y_M, 0)$ on the surface *S*, radiating with amplitude $a(X_M, Y_M)$ and phase $\varphi(X_M, Y_M)$].

other methods. First, the surface of each transducer is scanned by a laser interferometer and the surface displacement magnitude and phase used as the input to a radiation field model that also incorporates the influence of the air channel. The field simulation method is based upon the approach described by Lerch[15] and uses a discrete version of the Rayleigh integral that is directly compatible with the surface displacement data. Following the approach indicated in Ref. 15, this technique can accommodate the variation in attenuation coefficient with frequency, temperature, pressure, and relative humidity, as described in the ANSI Standard,[16] the work of Bass *et al.*,[10,11] and by Bond *et al.*[17] Details of the exact attenuation model are provided in the Appendix. Where possible, the second approach involves finite element modeling (FEM) via the ANSYS code[18] to derive surface displacement data, and then uses the same theoretical approach to obtain the pressure field profile. Since the finite element model can be constructed to assume perfection in terms of manufacture, differences with practical devices may be readily ascertained. Moreover, the influence of radiating surface uniformity may be determined, along with limitations inherent in the measurement system. With regard to the latter, the measurement device was a small piezoelectric ceramic disc ''pinducer,'' [19] which was chosen in preference to an alternative PVDF membrane ultrasonic detector[20] on the basis of sensitivity and improved directional response. Although membrane devices have been shown to provide accurate calibration data in air, the presence of Lamb waves in the membrane can distort off-axis beam profile measurements.[20] However, the larger dimensions of the pinducer necessitate inclusion of the ultrasonic detector directional response within the theoretical model. For completeness, this has been done and provided that theoretical data are in good agreement with that derived experimentally, the true radiation field structure may be interpolated by removal of the ultrasonic detector spatial field response from the measured or simulated data.

I. THEORY

In a homogeneous medium, the acoustic pressure field generated by a planar transducer surface *S*, in an infinite rigid planar baffle can be calculated from the Rayleigh integral. Figure 1 depicts the geometry and notation used.

$$p(R,t) = \frac{\rho}{2\pi}\frac{\partial}{\partial t}\int_S \frac{v(R,t-R/c)}{R}\,dS, \tag{1}$$

where ρ is the medium density, c is the sound velocity in the medium, R is the distance between the field point P and the elementary area dS at point M on the radiating surface, and v is the velocity function, assumed non-uniform across the surface S.

If the transducer operates in a lossy environment in continuous wave mode at an angular frequency ω, the surface velocity function will undergo the frequency dependent influence of the attenuating medium. That is,

$$v(R,t) = a(r)e^{-\alpha R + j\omega t},$$

where $a(r)$ is the complex velocity strength at dS ($r = |r(X_M, Y_M)|$) and α is the frequency dependent medium attenuation coefficient.

Hence, $a(r)e^{-\alpha R}$ represents the velocity function amplitude at distance R from the elementary area dS.

The pressure distribution $p(R,t)$ can then be calculated

$$p(R,t) = \frac{\rho}{2\pi} j\omega e^{j\omega t}\int_S \frac{a(r)e^{-\beta R}}{R}\,dS, \tag{2}$$

where $\beta = \alpha + jk$ and $k = \omega/c = 2\pi/\lambda$.

To allow comparison between computed and measured pressure beam profiles, the ultrasonic detector directional response $L(\omega,\theta)$ must be considered. Since the excitation velocity function is harmonic, we can express Eq. (2) in the frequency domain

$$p(R,\omega) = \frac{\rho}{2\pi} j\omega \int_S \frac{a(r)e^{-\beta R}}{R}\,dS\cdot L(\omega). \tag{3}$$

For a small circular ultrasonic detector in an infinite baffle the directional response may be approximated by[21]

$$L(\omega,\theta) = \frac{2J_1\left(\left(\frac{\pi D}{2\lambda}\right)\sin\theta\right)}{\left(\frac{\pi D}{2\lambda}\right)\sin\theta},$$

where D is the ultrasonic detector diameter, λ is the wavelength at angular frequency ω, θ is the wavefront incident angle on the ultrasonic detector from the elemental area dS, and J_1 is the first-order Bessel function.

If Eq. (3) is discretized for computational purposes and the ultrasonic detector directional response is incorporated, the complete, discrete, expression for pressure at any point in the field is

$$p_\omega(X_P, Y_P, Z_P) = \frac{\rho\omega}{2\pi}\sum_{M=1}^{N}\frac{a(X_M, Y_M)e^{(j\varphi(X_M,Y_M)-\beta R)}dX\,dY}{R} \times \frac{2J_1\left(\left(\frac{\pi D}{2\lambda}\right)\sin\theta\right)}{\left(\frac{\pi D}{2\lambda}\right)\sin\theta}, \tag{4}$$

where $R = \sqrt{(X_P - X_M)^2 + (Y_P - Y_M)^2 + Z_P^2}$,

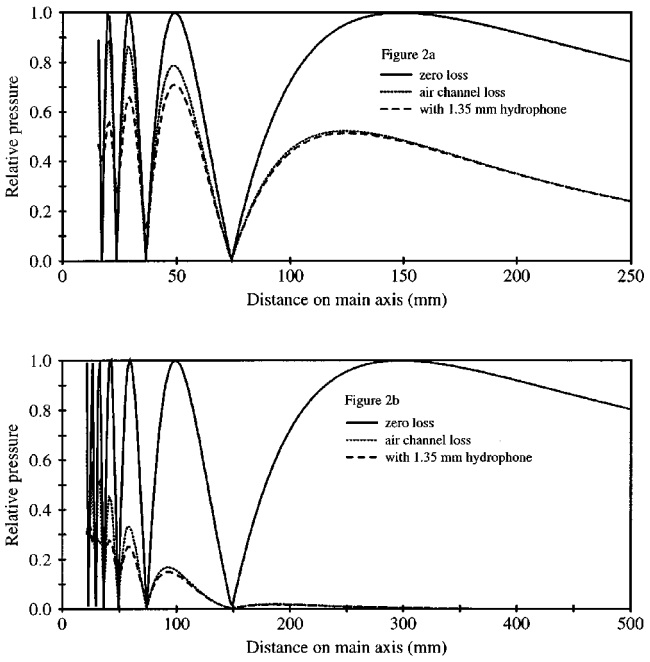

FIG. 2. Axial field profiles of a 20 mm disk transducer operating (a) in air at 500 kHz and (b) at 1 MHz. Three different situations are shown, corresponding to zero loss and an ideal ultrasonic detector (——); air channel loss and an ideal ultrasonic detector (···); air channel loss and an ultrasonic detector of 1.35 mm diameter (– – –).

$$\theta = \arctan\left(\sqrt{(X_P - X_M)^2 + (Y_P - Y_M)^2}/Z_P\right),$$

N is the number of nodes used to discretize the radiating surface S, each of them acting as a virtual point source of side dimensions dX, dY according to Huygen's principle, and $\varphi(X_M, Y_M)$ is the phase related to the amplitude $a(X_M, Y_M)$.

It is useful at this stage to assess the influence of channel attenuation and the finite measurement device on the data to be presented in Sec. III. Figure 2(a) and (b) depict the theoretical axial pressure field structure as a function of distance from an ideal, planar, 20 mm disk transducer, contained in an infinite rigid baffle and operating in the continuous wave mode at 500 kHz [Fig. 2(a)] and at 1 MHz [Fig. 2(b)]. Three examples are considered in each figure, the first two corresponding to zero channel attenuation and the attenuation set for air as defined in the Appendix, both assuming the ultrasonic detector to be ideal, with an omnidirectional field of view. The third case incorporates the directional characteristics of a 1.35 mm diameter disk receiver and with the channel attenuation set for air in the theoretical model, as encountered in the experimental arrangement described in Sec. II. For the sake of clarity, the field structure of the region close to the transducer surface (< 15 mm) has been omitted from the figures. Considering the first case, it is possible to observe a classical field structure for a disk transducer operating in continuous wave (cw) mode, with the near/far-field boundaries at the anticipated positions for both frequencies. The second examples indicate that channel attenuation has more influence at the higher frequency, as expected, and that the main consequence is to reduce the extent of near-field fluctuation (as indicated by the imperfect interference pattern) and to produce more rapid decay in the far-field response. The position of the last axial maximum (corresponding to the near/far-field boundary) is brought closer to the radiating aperture, to the extent that the feasibility of operation in the true far-field at frequencies above 1 MHz is questionable. Otherwise, the field structure is close to that predicted by classical diffraction theory. The influence of the finite ultrasonic detector aperture is most profound in the near-field region, where the inability of the device to detect the diffracted waves from the boundary of the transducer aperture is evidenced from the incomplete near-field interference pattern. However, in the far field, the ultrasonic detector is expected to provide an accurate reproduction of the axial field structure.

These results serve to highlight a difficulty in making accurate field measurements in air with the conventional ultrasonic detector approach. Ideally, the reception device should be omnidirectional with respect to the propagating field and exert zero influence on that field structure. Since the wavelength in air at 1 MHz is 0.34 mm, an ultrasonic detector diameter of approximately 0.04 mm would be required to provide an accurate representation of the field. This is difficult to achieve from a manufacturing viewpoint and moreover, the reduced sensitivity in air would render meaningful signal extraction almost impossible. To some extent the same situation arises in water at higher frequencies, although the sensitivity problem is much reduced. As a result of experiments conducted within the laboratory using different piezoelectric ceramic and PVDF ultrasonic detectors, it was decided to adopt the approach stated in the Introduction and employ the more sensitive pinducer device, despite its clear inability to provide an exact reconstruction of the radiated pressure field.

II. THE EXPERIMENTAL CONFIGURATION

It is important to be able to measure the subtleties of the transducer response as accurately as possible to allow validation of the simulation output. The necessary measurements were carried out in a facility which comprised a three-axis precision positioning system, installed in a controlled environment room and mounted within an enclosure to provide still air conditions, along with computer controlled driving and measuring equipment. Two types of analyses are supported: (1) interrogation of the transducer front face by a laser vibrometer to provide surface displacement information, and (2) scanning of the ultrasonic field with an ultrasonic detector to determine the pressure distribution.

The configuration for the facility as used for surface displacement profiling is shown in Fig. 3. For beamplotting, a receiver (ultrasonic detector and amplifier assembly) is substituted in place of the laser vibrometer head and controller/decoder.

The three-axis manipulator can be controlled to a step resolution of 1 μm over a range of 300 mm in both the X (horizontal) and Y (vertical) directions and to 24 μm over a range of 1000 mm in the Z (longitudinal) direction. The laser vibrometer operates over a frequency range of 50 kHz to 20 MHz with displacement resolution typically better than 2 nm with a noise-limited figure of 0.25 nm for an ideal reflector. The focused spot size, and hence the maximum spatial resolution, is 20 μm. The measurement range is ± 75 nm. The

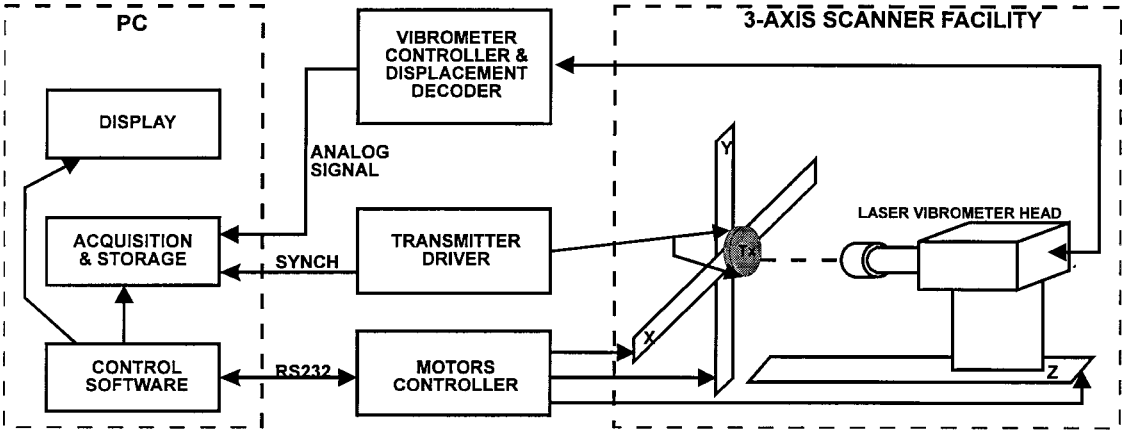

FIG. 3. Surface displacement profiling configuration using the laser vibrometer to measure the transducer front face motion.

most successful ultrasonic detector employed to date has been a pinducer with an active circular aperture 1.35 mm in diameter and frequency response from dc to 10 MHz. Its open-circuit voltage response has been measured as −223 dB *re* 1 V/μPa by the substitution method with a calibrated membrane ultrasonic detector.[19] The associated amplifier has a gain of 66 dB and a frequency bandwidth of 2 MHz, selected to maintain workable intrinsic noise levels. The excitation voltage was derived from an HP 33120A function generator and used a 20 cycle, gated sinusoid at the desired frequency of operation. The voltage amplitude was typically in the region of 10 V pk-pk. In the case of the PVDF transmitter a Kalmus 155LCR rf power amplifier was also employed to provide an excitation voltage amplitude in the region of 100 V pk-pk.

III. COMPARISON BETWEEN THEORETICAL PREDICTIONS AND EXPERIMENTAL MEASUREMENTS

Three transducer technologies, which have been proposed as effective for through-air generation of ultrasound, were examined. The range comprised a ceramic–epoxy 1–3 piezoelectric composite device, a commercially available PVDF immersion transducer, and an electrostatic design based around a conventional backing plate and radiating membrane. For each technology the complex surface displacement was measured, using the laser vibrometer, and the data obtained were used as an input to the model. The corresponding sound fields were measured, with the field extent, step resolution, environmental data, and the characteristics of the measuring device also used as inputs to the model. In addition, the surface displacement profile for the piezoelectric composite device was predicated using a finite element model and the resultant data were used as input to the beam profile model for comparison with the measured output and the output predicted from the measured surface displacement data.

A. 1–3 piezoelectric composite transducer

1–3 piezoelectric composite transducers[22] comprise a regular mesh of piezoelectric ceramic pillars embedded in a passive supporting medium such as polymer resin. The introduction of the polymer phase lowers the characteristic impedance, reducing the impedance mismatch between the device and the transmission medium and hence enhancing energy transfer into the sound field. The device chosen for this investigation was an 18 mm square, 40% volume fraction, 1–3 piezoelectric composite manufactured from PZT5H piezoelectric ceramic material and Ciba–Geigy CY1301/HY1300 two-part, hard-set epoxy filler. The device was mounted, unbacked, in a 30 mm diameter holder, fitted with a quarter-wavelength, hard-set epoxy matching layer (not optimized for air) and excited by a tone burst at an electrical resonance frequency of 425 kHz. A schematic diagram of the device structure is presented in Fig. 4(a).

As can be seen from the measured surface displacement amplitude and phase plots of Fig. 4(b) and (c), the ceramic and polymer phases do not vibrate equally or uniformly when subject to air loading. In Fig. 4(b) it is evident that the displacement amplitude at the center of the composite is greater (shown in white) than amplitudes towards the edges where there is reduced pillar support and increased damping due to the epoxy support medium. It is also clear that the ceramic pillars are vibrating with much greater amplitude than the polymer filler throughout the device surface. By comparison with Fig. 4(c) it becomes clear that the polymer structure vibrates out of phase by approximately $\lambda/3$ with respect to the ceramic and, since the polymer's measured phase is greater (shown in white) than that of the ceramic, the polymer motion lags in time.

A prediction of the expected surface displacement was obtained from a full 3-D model implemented in the ANSYS code.[23] The entire transducer structure, excluding the nylon holder (since it was considered that due to damping exerted by the polymer support medium, the holder would not contribute significantly to the overall response), was included in the simulation and the data generated for surface displacement amplitude and phase are shown in Fig. 4(d) and (e). By comparison with the measured equivalents in Fig. 4(b) and (c) discrepancies from ideal behavior introduced by manufacturing tolerances can be appreciated. Although a very good correspondence between measured and predicted surface displacement characteristics is apparent, two other features are of special note. First, the reduced displacement of the outer pillars is also predicted by the model arising

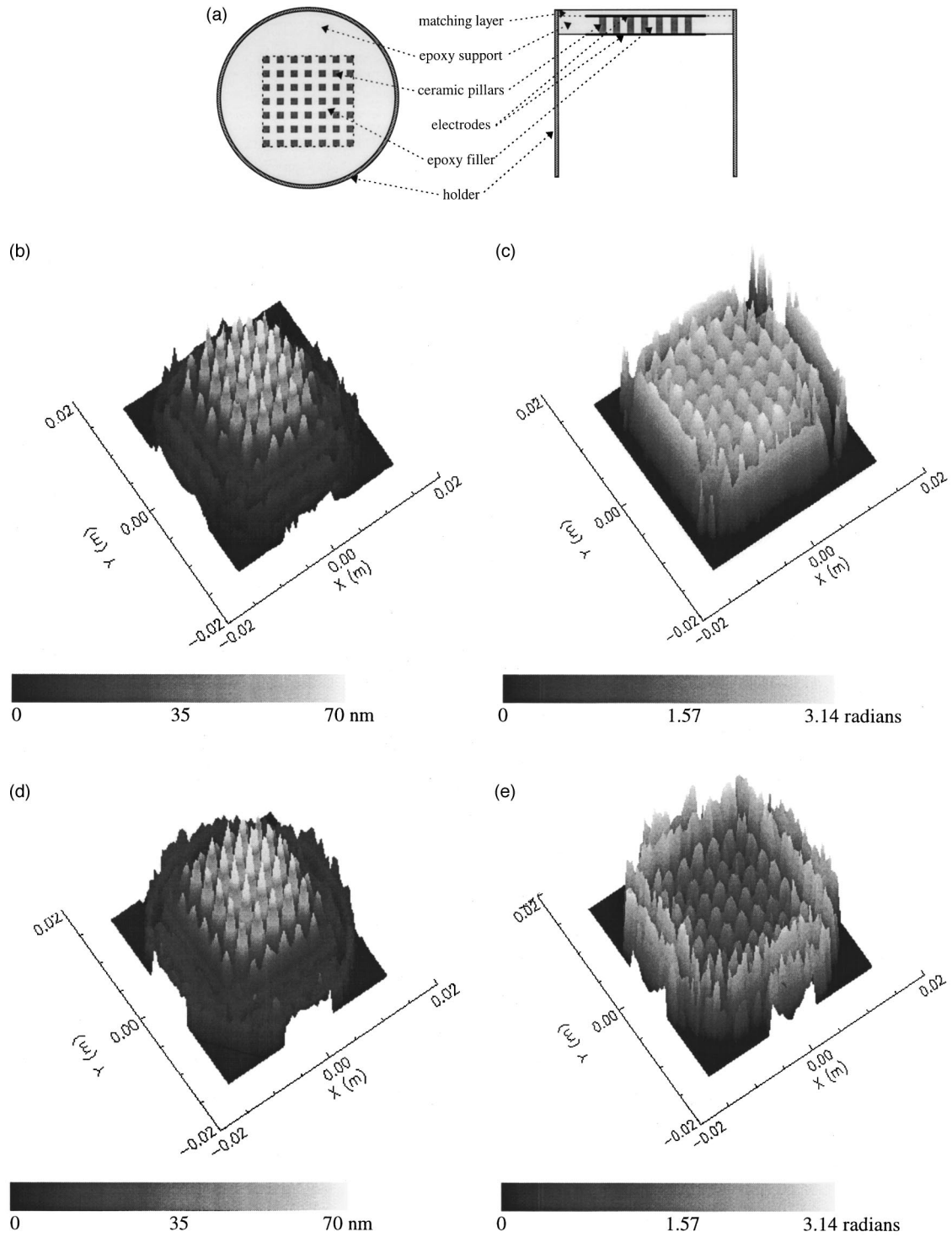

FIG. 4. (a) Structure of 18 mm square composite transducer mounted in a circular holder fitted with a matching layer designed for use in water (not to scale). (b), (c) Amplitude and phase plots of surface displacement of 18 mm square composite transducer mounted in a circular holder fitted with a front face layer, and excited at 425 kHz. (d), (e) FEM generated amplitude and phase plots of surface displacement of the composite transducer. (f) Predicted sound field in air (normalized pressure) using measured surface displacement data. (g) Measured sound field in air (normalized pressure). (h) Predicted sound field in air (normalized pressure) using FEM generated surface displacement data. (i) Comparison of normalized pressure profiles on main transducer axis of measured sound field (Exp), predicted sound field from measured surface displacement data (Surf), and predicted sound field from FEM generated surface displacement data (FEM).

from the lack of piezoelectric ceramic support at the outer edges. This phenomenon is to be observed in most piezoelectric composite transducer configurations, which of necessity have finite pillar regions. Second, there is considerable displacement within the polymer support region and this is also predicted well by the ANSYS data. Although in this example the holder does indeed exert little influence on the device response, this may not be true for other transducer configurations, where the holder may be positioned close to the transducer boundaries.

The normalized sound fields in the $x-z$ plane, over a range of ± 20 mm in the x direction and from 5 to 300 mm in

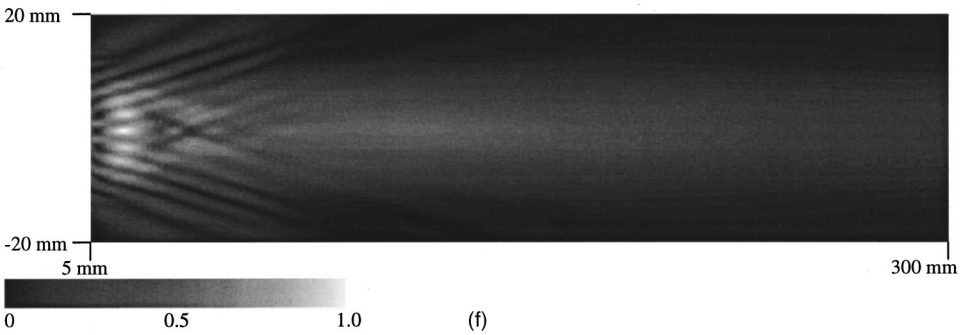

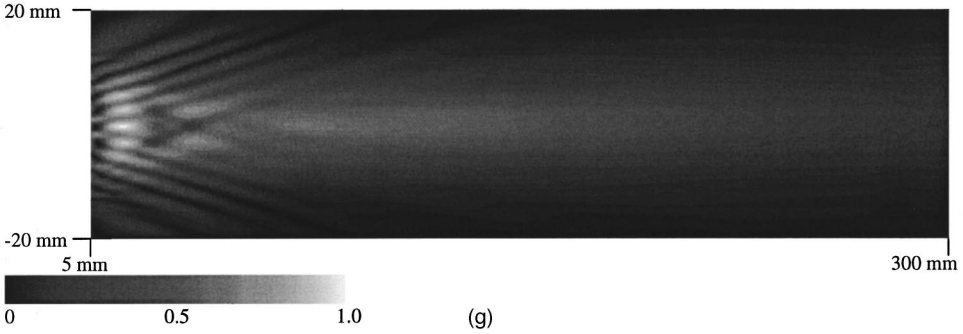

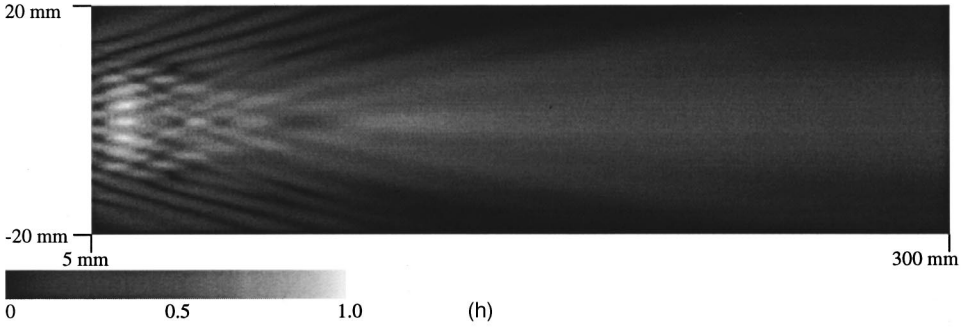

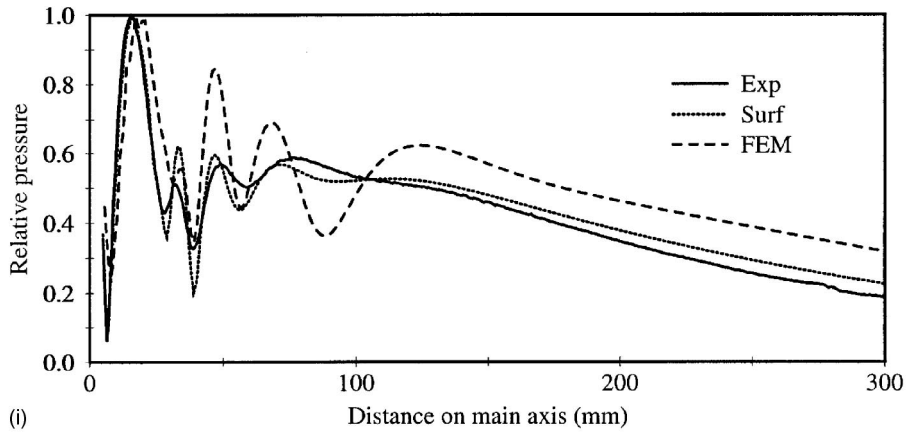

FIG. 4. (*Continued.*)

the *z* direction, as predicted from the model using the laser vibrometer surface displacement data, as measured experimentally and as predicted from the model using the FEM generated surface displacement data, are shown in Fig. 4(f), (g), and (h), respectively. Close correspondence is obvious, especially between Fig. 4(f) and (g), and it is only on inspection of the near field of Fig. 4(h) that any significant discrepancies can be discerned.

To appreciate these differences more clearly, the pressure profiles along the central transducer axis for both the predicted and the measured sound fields are presented in Fig. 4(c). These small differences between the measured pressure profile (Exp) and that generated from the measured surface displacement data (Surf) are presumed to arise from registration inaccuracies in experimental measurements of the surface displacement, for input to the prediction model, and of

the measured field. The origin of the 3-D measurement space is normally taken as the center of the transducer output face, assuming a regularly shaped device. For surface displacement measurements, this origin can be ascertained to within ± 0.5 mm. For the pinducer ultrasonic detector, an uncertainty of less than ± 0.3 mm can be achieved. Hence, in comparisons on the main transducer axis, a registration discrepancy of ± 0.8 mm may occur. In addition, the receiver directivity characteristics $L(\omega, \theta)$ incorporated in Eq. (3) are idealized and assume a simple disk receiver mounted in an infinite rigid baffle, whereas the practical mounting arrangements will inevitably deviate from this fixed disk model. Sample measurements of the directional response of the pinducer used, at a single frequency, revealed that the support medium for the receiver disk damped the motion of the disk edges such that the nulls predicted by the Bessel function in $L(\omega, \theta)$ were not achieved. Moreover, the measured beamwidth corresponded to that of a device with an effective diameter approximately 20% greater than that predicted by theory. Eventually discrete, measured values of $L(\omega, \theta)$ will be included in the model rather than the idealized Bessel function relationship.

Nevertheless, the close agreement between the measured pressure profile and that generated from measured surface displacement data is very encouraging and reveals that the ultrasonic detector scanning system is operating as expected at this particular frequency. The reduced near-field activity in these examples is a direct consequence of the lower vibration at the extremities of the transducer aperture, in addition to the lack of aperture symmetry arising through manufacturing deficiencies. This latter point is confirmed in the finite element data shown in Fig. 4(i). The differences between the pressure profiles generated from FEM derived surface displacement data (FEM) and the measured equivalent (Surf) arise from the regularity of the idealized response compared to that generated by the device with nonregularities imposed by manufacturing techniques. This regularity tends to produce more intense constructive and destructive interference in the near-field as is evident from the finite element data.

There may also be errors introduced by the device driving characteristics. Whereas the theory describes continuous wave excitation, it is impractical to drive devices in this manner and measure the resultant field, as reflected pressure waves from the front surface of the ultrasonic detector interfere with transducer surface motion. This problem is obviated by exciting transducers with a gated tone burst of typically 20 cycles of the fundamental drive frequency. Any tendency for interference by reflected waves is confined to measurements within a short range from the transducer surface, whose distance is governed by the length of the tone burst. In the results presented in this paper, this range is never more than 5 mm. However, the gating waveform may introduce additional drive frequencies other than the fundamental frequency which may lead to discrepancies between the predicted and measured sound fields. For a resonant device such as the composite transducer presented here this is not considered to be a significant problem.

B. PVDF transducer

The PVDF transducer investigated was a commercially available, 18 mm diameter device, designed originally for off-resonance operation into a water load medium This type of transducer is characterized by a relatively wideband frequency response and as assumed in Ref. 24 should possess a field structure that approximates closely an ideal, planar aperture when radiating into water. Since the exact structural configuration was unknown, it was not possible to perform finite element modeling. Instead, the classical approach, assuming an ideal, planar aperture in an infinite rigid baffle as described in Sec. I, was used to obtain the axial pressure distribution, including both air attenuation and the influence of ultrasonic detector directivity. Data at two well-separated frequencies, 400 and 700 kHz, were collected with the following results.

The measured surface displacement plots shown in Fig. 5(a) and (b) at 400 kHz, and in Fig. 6(a) and (b) at 700 kHz, reveal the presence of unexpected modes at both frequencies, instead of displaying uniform, piston-like displacement as expected. The origin of these modes is unclear without more detailed knowledge of the transducer fabrication process. However, at both frequencies, there is evidence of radial mode activity, possibly as a result of interaction between the transducer and the cylindrical metallic holder. The sound fields obtained by experiment and from extrapolation from the measured surface displacement data were in good agreement, but without any distinguishing features and are not reproduced in the present context. However, a more detailed examination of the pressure profile on the main axis was chosen for presentation in Figs. 5(c) and 6(c) at 400 and 700 kHz, respectively, using the same symbolism as in the piezoelectric composite example. In both figures it can be seen that the positions of the diffraction induced maxima and minima are predicted accurately by extrapolation of the measured surface-displacement data. However, results obtained from the classical aperture diffraction theory are quite different, providing further confirmation that the real aperture displacement function is non-uniform. Closer inspection of the data shown in Figs. 5 and 6 indicates that at the lower frequency the vibration pattern appears as a series of concentric rings, in both amplitude and phase. However, at 700 kHz such a pattern is more difficult to discern and the more random surface displacement may be due to factors other than the generation of radial mode activity. The usual method for manufacturing such a transducer is to cement the PVDF film directly onto the surface of a suitable backing block, before mounting within the holder. It may be that the cement bond is imperfect or non-uniform, giving rise to the more random surface displacement pattern. A final point of interest is that the surface displacement at the aperture boundary is relatively small at both frequencies. This phenomenon has been observed in other PVDF designs[24] and could be due to edge clamping by the holder. This of course will reduce the extent of any edge-diffracted interference in the field pattern and help to explain the differences in the positions of the maxima and minima when compared with the classical field theory. From measurement of Figs. 5(a) and 6(a), it would appear that the true radiating aperture is 14 mm in diameter, as

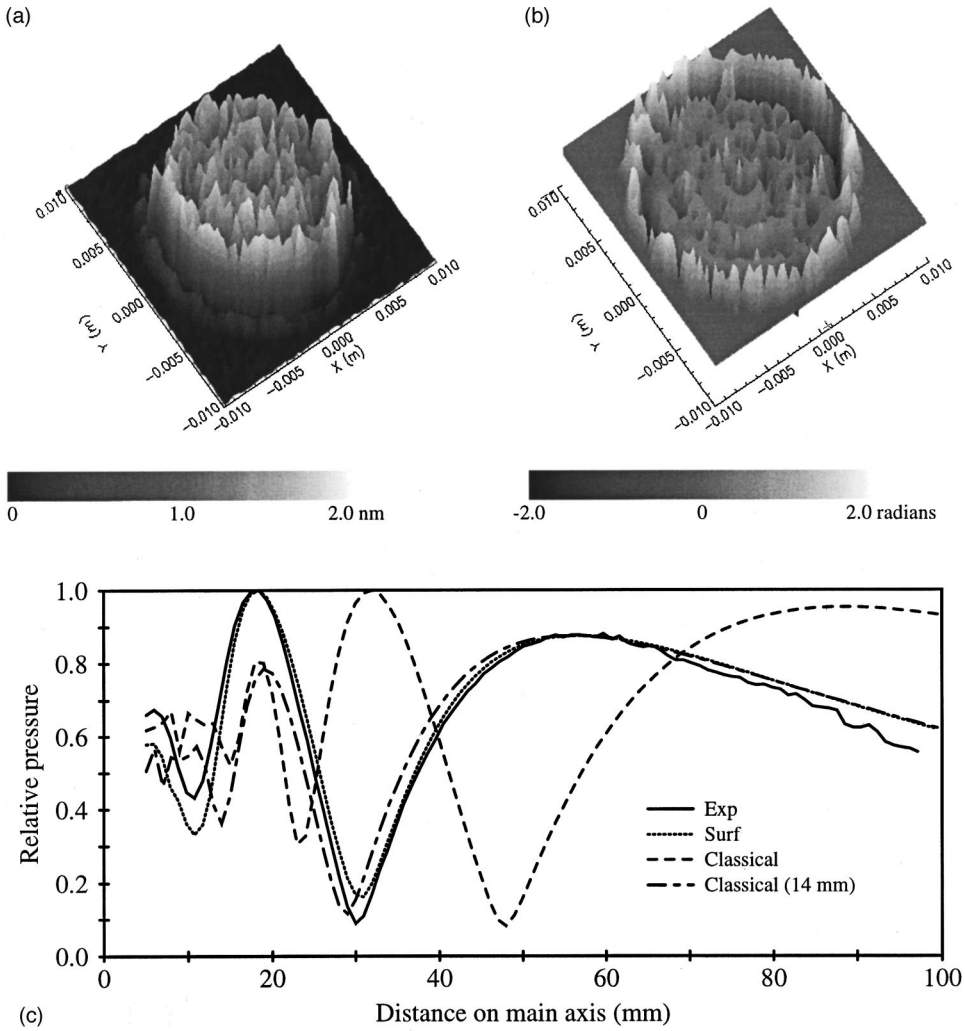

FIG. 5. (a), (b) Measured surface displacement amplitude and phase of 18 mm PVDF transducer excited at 400 kHz. (c) Predicted and measured pressure profiles on main axis of 18 mm PVDF transducer excited at 400 kHz.

opposed to the actual device dimension of 18 mm. Inserting the reduced aperture dimension into the classical field theory produces an axial field profile that is much closer to that observed experimentally. For completeness, this is also shown in Figs. 5(c) and 6(c).

C. Electrostatic transducer

One design of electrostatic transducer comprises a metallized polymer film (Mylar), which is brought into close proximity with a conducting backing block by the application of a dc bias voltage, typically of the order of 200 V. Numerous small regions of trapped air between the film and the backing block form small, individual, varied-size sources which are excited by an applied sinusoidal signal. Several designs are possible,[5,25,26] with the main design aim being the control of source numbers, size, and position using different machining regimes for the face of the backing block. The device shown in Fig. 7, utilizing 3.5 μm thick Mylar film, was used to produce the results shown in Fig. 8(a)–(f) and utilized a grooved backing plate. These horizontal, semicylindrical grooves, at a pitch of 0.25 mm and a width and depth of 0.1 mm, can be seen in the high-resolution surface-displacement amplitude scan in Fig. 8(a). Electrostatic devices exhibit relatively wide bandwidth characteristics and, as noted previously, will respond to other frequencies inherent in the tone burst gating waveform. To minimize this influence on what is an extremely complex surface-amplitude distribution, a Hanning amplitude window was applied to the driving tone burst at the measured center frequency of 300 kHz.

As can be seen from the surface displacement scans in Fig. 8(a) and (b) the radiating aperture appears as a semirandom distribution of individual sources. The distribution is influenced by the machining regime of the backing block, but it is clear that the displacement amplitude of the sources is more random and spans a wide range of values. Interestingly, the phase data display relatively uniform values (within the range $\pm 0.2\pi$, allowing for the phase wraparound inherent in the measurement process at the $\pm\pi$ boundary) regardless of source amplitude. The ''bulk'' distribution of the sources towards one side of the device surface is presumed to be due to uneven tensioning of the Mylar film, a major drawback with this form of design. The surface displacement data are presented in this case as two-dimensional plots rather than the previous three-dimensional style, since the random nature of the distribution and amplitude of the sources made visualization of the data difficult. It can be seen from Fig. 8(a) that the individual sources are very small; hence, the surface displacement data must be measured at sufficiently high resolution. When these higher

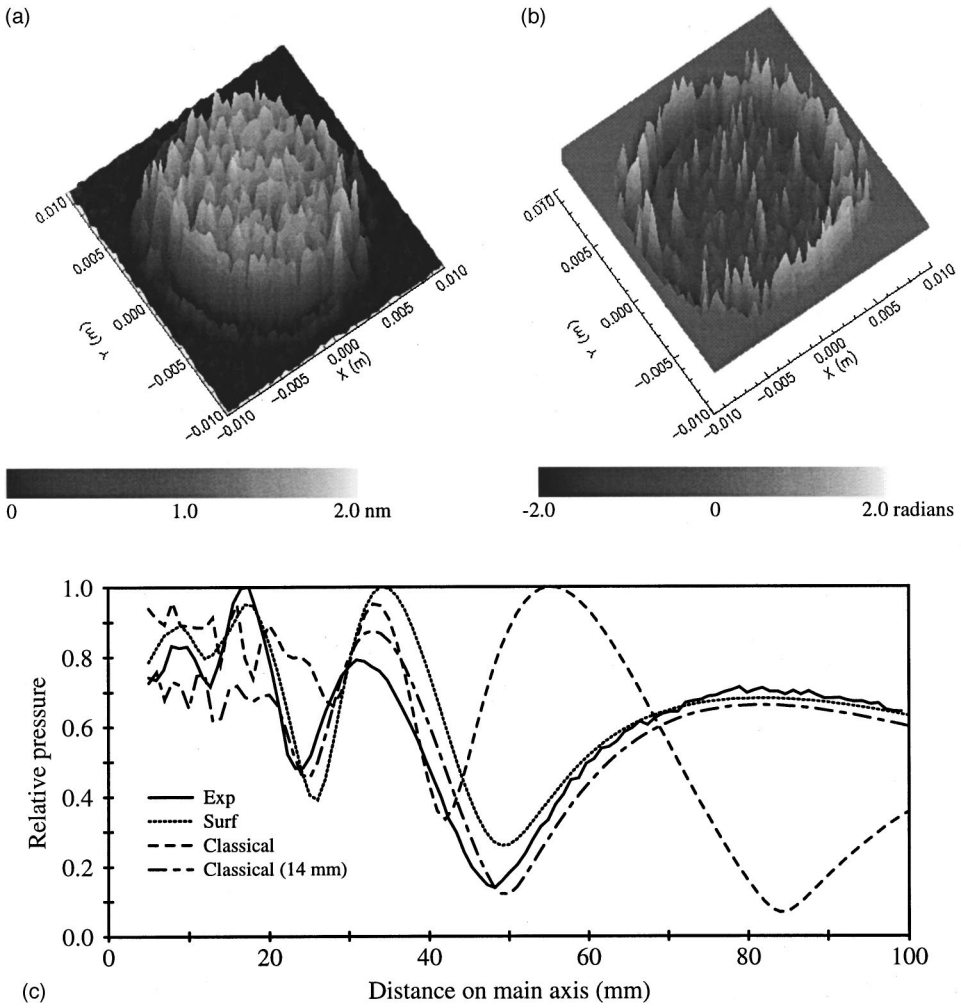

FIG. 6. (a), (b) Measured surface displacement amplitude and phase of 18 mm PVDF transducer excited at 700 kHz. (c) Predicted and measured pressure profiles on main axis of 18 mm PVDF transducer excited at 700 kHz.

resolution (0.05 mm step size) data are used as the input to the model, the extrapolated field as shown in Fig. 8(d) exhibits good correlation with the measured beam profile of Fig. 8(c). However, the beam pattern appears extremely uneven, with, at first sight, no natural aperture focus or near/far-field regions. Since the phase distribution is reasonably uniform, this is assumed to arise from the amplitude distribution of the various sources within the transducer aperture. This hypothesis is supported by Fig. 8(e), which shows the extrapolated field structure using the amplitude data of Fig. 8(a), but setting the phase data to zero. That is, each point on the radiating aperture is now assumed to possess uniform phase. A non-uniform pressure field is still evident, with no significant differences with the actual measured data. In all three cases, the influence of the uneven Mylar tensioning is evident from the enhanced intensity in the upper portions of each of Fig. 8(c), (d), and (e).

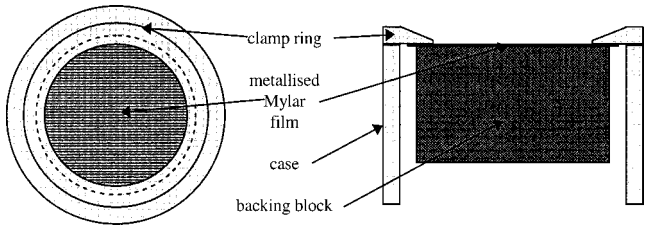

FIG. 7. Structure of 28 mm active diameter electrostatic transducer (not to scale).

Again, to provide a better basis for comparison, normalized pressure profiles along the central axis are provided in Fig. 8(f). For completeness, the corresponding data for zero surface displacement phase and those obtained from classical aperture diffraction theory (including channel loss and ultrasonic detector directivity) are also shown. Setting the phase of the surface displacement to zero produces significant differences only in the field region close to the transducer surface, as expected from the previous discussion. However, these differences are sufficient to merit further study of the effect of surface-displacement phase variation on the output field, and the present model is believed to be an ideal tool for this work. Reasonable correlation exists between the measured and extrapolated data sets. Interestingly, the classical field theory provides a good approximation to the actual axial field profile, despite the non-uniformity of the aperture. However, such correspondence does not exist with other planes (e.g., transverse profiles) of the field and the result should not be interpreted as indicative of a true, ideal radiating piston.

IV. CONCLUDING REMARKS

This work has described the ultrasonic pressure fields in air for three very different transducer technologies. Even at

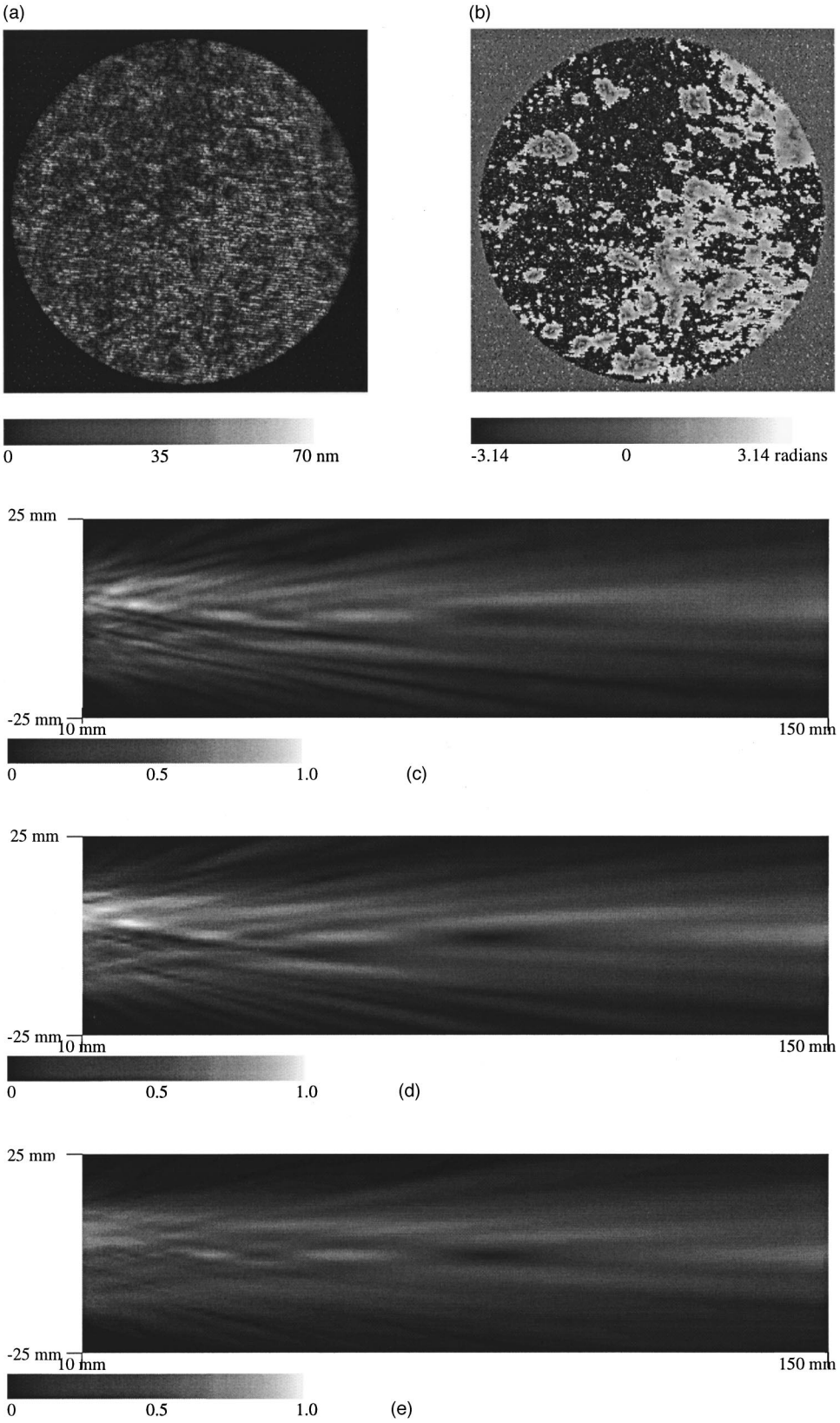

FIG. 8. (a), (b) Normalized amplitude and phase plots of surface displacement of 28 mm diameter electrostatic transducer excited at 300 kHz measured at a resolution 0.05 mm. (For improved visualization of the nature and size of the source regions, the data are presented as a 2-D image.) (c) Measured sound field of 28 mm diameter electrostatic transducer excited at 300 kHz. (d) Predicted sound field of 28 mm diameter electrostatic transducer excited at 300 kHz using high-resolution input data. (e) Predicted sound field of 28 mm diameter electrostatic transducer excited at 300 kHz using high-resolution input data with phase set to zero. (f) Comparison of classical, measured, predicted from surface-displacement data, and predicted with phase set to zero pressure profiles on main axis of 28 mm diameter electrostatic transducer excited at 300 kHz.

the relatively low operating frequencies (i.e., less than 1 MHz) considered in the present context, no device produced a field structure that could be predicted using simple, closed-form classical techniques. Indeed, it has been shown in Sec. I that conventional fluid field prediction theory is inappropriate at frequencies above 1 MHz due to the high attenuation characteristics inherent in a gaseous environment, and that the accepted concept of a well-defined near/far-field boundary is no longer applicable. For this reason, in addition to ease of measurement and the fact that many air-coupled ultrasonic applications are centered in the frequency range 250–750 kHz, the present work was confined to that regime.

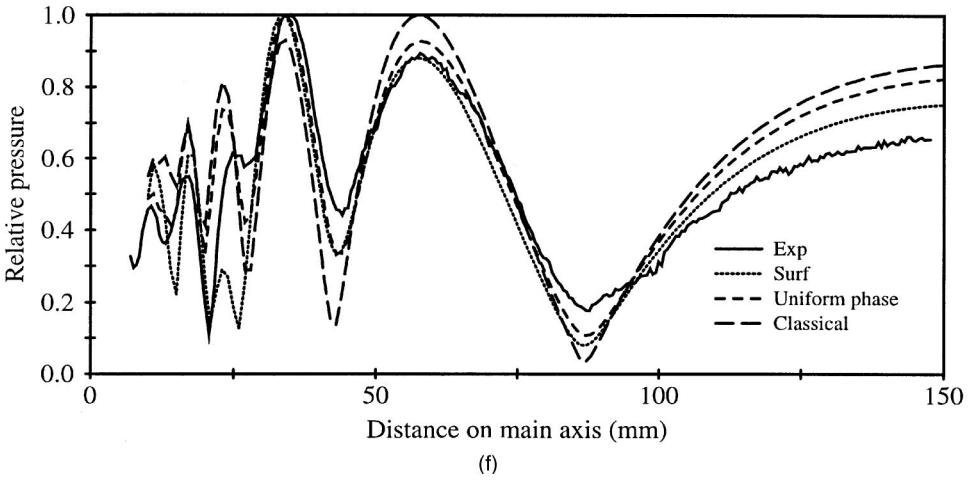

FIG. 8. (*Continued.*)

Given that the individual transducer configurations are essentially straightforward, the findings serve to highlight extremely complex behavior and the consequent requirement for sophisticated measurement and simulation tools. In each case, the radiated field profiles were dominated by behavioral characteristics introduced through the manufacturing procedures. Moreover, it is apparent that the most accurate prediction of the field will be obtained if the highest resolution input data are used. For the piezoelectric composite transducer examined in Sec. III A, the resolution was determined by applying Nyquist's sampling criterion so that at least two points were interrogated within the smallest internal structure of the transducer. Applying a typical resolution of 0.25 mm for this technology proved to be inadequate for the electrostatic device, where a spatial sampling period of 0.05 mm was required. Clearly, to avoid significant trial and error, some *a priori* knowledge is required in relation to the surface displacement features.

A similar problem exists with the use of finite element analysis, which has considerable potential for investigation of complex transducer configurations. However, the method requires high-quality input data, which is only feasible if accurate knowledge of manufacturing procedures and constituent materials parameters is available. The piezoelectric composite transducer used in the present work was manufactured in the laboratories at Strathclyde under very strictly controlled conditions and parameters of all the constituent materials were measured prior to insertion in the ANSYS code.

Nevertheless, the methodology described is believed to constitute a solid platform for evaluation and measurement of the field structures of air ultrasonic transducers and, indeed, may be extended readily for devices operating into other fluid media. Some future uses for the technique will be to assess how channel parameters such as temperature, pressure, or relative humidity influence the beam profile for a given transducer. Variations in device performance as a consequence of manufacturing tolerances and design deficiencies may also be evaluated, provided that the finite element model is sufficiently accurate. This will be reported at a later date.

ACKNOWLEDGMENTS

The authors wish to record their gratitude for assistance received from past and present colleagues within CUE. In particular thanks to Christian Pasquier for coding the early field model and to Robbie Banks and Jamie Hyslop for the FEM contributions to the analysis of the piezoelectric composite device.

APPENDIX: DETERMINATION OF THE MEDIUM CHARACTERISTICS

The velocity c and attenuation coefficient α vary with the physical properties of air such as temperature, pressure and relative humidity, therefore they have to be determined before equation (4) can be used.

Within normal atmospheric pressure and temperature ranges, the velocity c is simply defined by[27]

$$c = c_0 \sqrt{T/T_{01}} \tag{A1}$$

where the triple point of water, $T_{01} = 273.16\,\mathrm{K}$; the velocity at T_{01}, $c_0 = 331.31\,\mathrm{m/s}$, and T is temperature in Kelvin.

Attenuation coefficient α is a complex quantity containing loss elements generated by ''classical,'' thermal, and viscous losses, rotational molecular energy conversion, and molecular energy interchanges between the gaseous components of air. These losses are denoted by α_{cr}. In addition, molecular dipole resonances in oxygen and nitrogen give rise to vibrational losses $\alpha_{\mathrm{vib,O}}$ and $\alpha_{\mathrm{vib,N}}$. These losses combine to give

$$\alpha = \alpha_{\mathrm{cr}} + \alpha_{\mathrm{vib,O}} + \alpha_{\mathrm{vib,N}}. \tag{A2}$$

Given the constant parameters of standard pressure and temperature $P_0 = 1$ bar and $T_0 = 293.15\,\mathrm{K}$, respectively, the triple point of water, $T_{01} = 273.16\,\mathrm{K}$ and the methodology derived from the ANSI Standard[16] and work by Bass *et al.*[10,11] and by Bond *et al.*,[17] the following four calculation steps lead to the determination of the attenuation coefficient α:

(1) Saturation pressure ratio P_{sat}/P_0 is calculated from the expression

$$\log_{10}\left(\frac{P_{\text{sat}}}{P_0}\right) = 10.795\,86\left(1-\left(\frac{T_{01}}{T}\right)\right) + 1.504\,74\times 10^{-4} \times (1-10^{-8.296\,92(T/T_{01}-1)}) + 0.428\,73 \times 10^{-3}(10^{4.769\,55(1-T_{01}/T)}-1) - 2.219\,598\,3. \quad \text{(A3)}$$

(2) Water mole fraction, h (%) is derived from the relative humidity h_r and relevant pressure ratios as follows:

$$h = h_r(P_{\text{sat}}/P_0)/(P/P_0). \quad \text{(A4)}$$

(3) Oxygen and nitrogen relaxation frequencies $f_{r,\text{O}}$ and $f_{r,\text{N}}$(Hz), respectively, are calculated from

$$f_{r,\text{O}} = \left(\frac{P}{P_0}\right)\left(24+\left(4.04\times 10^4 h\left(\frac{0.02+h}{0.391+h}\right)\right)\right), \quad \text{(A5)}$$

$$f_{r,\text{N}} = \left(\frac{P}{P_0}\right)\sqrt{\frac{T_0}{T}}\left(9+\left(280h\,e^{-4.17((T_0/T)^{-1/3}-1)}\right)\right). \quad \text{(A6)}$$

(4) The individual attenuation components may now be calculated from the following relationships:

classical+rotational attenuation coefficient α_{Cr} from

$$\alpha_{\text{cr}} = 1.84\times 10^{-11} f^2\left(\frac{P}{P_0}\right)\sqrt{\frac{T}{T_{01}}}; \quad \text{(A7)}$$

vibrational, oxygen $\alpha_{\text{vib,O}}$ attenuation coefficient from

$$\alpha_{\text{vib,O}} = f^2\left(\frac{T_0}{T}\right)^{5/2}\left(1.278\times 10^{-2}\frac{e^{-2239.1/T}}{f_{r,\text{O}}+\frac{f^2}{f_{r,\text{O}}}}\right); \quad \text{(A8)}$$

vibrational, nitrogen $\alpha_{\text{vib,N}}$ attenuation coefficient from

$$\alpha_{\text{vib,N}} = f^2\left(\frac{T_0}{T}\right)^{5/2}\left(1.068\times 10^{-1}\frac{e^{-3352/T}}{f_{r,\text{N}}+\frac{f^2}{f_{r,\text{N}}}}\right). \quad \text{(A9)}$$

The resultant values may now be substituted in Eq. (A2) to give the overall attenuation coefficient α in $\text{N}_\text{p}\cdot\text{m}^{-1}$.

[1] W. A. Grandia and C. M. Fortunko, ''NDE applications of air-coupled ultrasonic transducers,'' Proceedings of the 1985 IEEE Ultrasonic. Symposium, pp. 697–709 (unpublished).

[2] S. P. Kelly, G. Hayward, and R. Farlow, ''Applications of through-air ultrasound for rapid scanning in the aerospace industry,'' IEEE Trans. Ultrason. Ferroelectr. Freq. Control **43**(4), 581–591 (1996).

[3] D. A. Hutchins and D. W. Schindel, ''Advances in non-contact and air-coupled transducers,'' Proceedings of the 1994 IEEE Ultrasonic. Symposium, pp. 1245–1254 (unpublished).

[4] V. Dahlmann and R. Hickling, ''Focused ultrasound to inspect locking keys in engine valves,'' Sensors, J. Mach. Percep. **7**, 27–38 (1990).

[5] M. Rafiq and C. Wykes, ''The performance of capacitive ultrasonic transducers using v-grooved backplates,'' Meas. Sci. Technol. **2**, 168–174 (1991).

[6] G. Hayward and A. Gachagan, ''An evaluation of 1–3 connectivity composite transducers for air-coupled applications,'' J. Acoust. Soc. Am. **99**, 2148–2157 (1996).

[7] M. I. Haller and B. T. Khuri-Yakub, ''Micromachined 1–3 composites for ultrasonic air transducers,'' Rev. Sci. Instrum. **65**(6), 2095–2098 (1994).

[8] D. A. Hutchins, A. G. Bashford, W. M. D. Wright, and D. W. Schindel, ''Advances in wide-bandwidth air-coupled capacitance transducers,'' Proceedings of the 1985 IEEE Ultrasonic. Symposium, pp. 981–984 (unpublished).

[9] W. Manthey, N. Kroemer, and V. Magori, ''Ultrasonic transducers and transducer arrays for operation in air,'' Meas. Sci. Technol. **3**(3), 249–261 (1992).

[10] H. E. Bass, L. C. Sutherland, and L. Evans, ''Atmospheric absorption of sound: Theoretical predictions,'' J. Acoust. Soc. Am. **51**, 1565–1572 (1972).

[11] H. E. Bass, L. C. Sutherland, J. Piercy, and L. Evans, ''Absorption of sound by the atmosphere,'' in *Physical Acoustics*, edited by W. P. Mason and R. N. Thurston (Academic, London, 1984), Vol. XVII.

[12] D. W. Schindel and D. A. Hutchins, ''Applications of micromachined capacitive transducers in air-coupled ultrasonics and nondestructive evaluation,'' IEEE Trans. Ultrason. Ferroelectr. Freq. Control **42**(1), 51–58 (1995).

[13] I. Ladabaum, X. C. Jin, and B. T. Khuri-Yakub, ''Air-coupled through transmission of aluminum and other recent results using MUTs,'' Proceedings of the 1997 IEEE Ultrasonics Symposium, pp. 983–986 (unpublished).

[14] A. G. Bashford, D. W. Schindel, D. A. Hutchins, and W. M. D. Wright, ''Field characterization of an air-coupled micromachined ultrasonic capacitance transducer,'' J. Acoust. Soc. Am. **101**, 315–323 (1997).

[15] R. Lerch and W. Friedrich, ''Field patterns of ultrasonic transducers in attenuating media,'' Proceedings of the 1985 IEEE Ultrasonics Symposium, pp. 677–682 (unpublished).

[16] ANSI (1995). ANSI S1.26-1995, ''Method for the calculation of the absorption of sound by the atmosphere'' (American National Standards Institute, New York).

[17] L. J. Bond, C. Chiang, and C. M. Fortunko, ''Absorption of ultrasonic waves in air at high frequencies (10–20 MHz),'' J. Acoust. Soc. Am. **92**, 2006–2015 (1992).

[18] ANSYS Swanson Analysis Systems, Inc., ANSYS *User's Manual for Revision 5.4*, Houston, Texas, 1998.

[19] Valpey–Fisher Corporation, 75 South Street, Hopkinson, MA 01748.

[20] W. Galbraith and G. Hayward, ''Development of a PVDF membrane hydrophone for use in air-coupled ultrasonic transducer calibration,'' IEEE Trans. Ultrason. Ferroelectr. Freq. Control **45**(6), 1549–1558 (1998).

[21] L. E. Kinsler and A. R. Frey, *Fundamentals of Acoustics*, 2nd ed. (Wiley, New York, 1962), Chap. 8.

[22] T. R. Gururaja, W. A. Schulze, L. E. Cross, R. E. Newnham, B. A. Auld, and Y. J. Wang, ''Piezoelectric composite-materials for ultrasonic transducer applications. I Resonant modes of vibration of PZT rod polymer composites,'' IEEE Trans. Sonics Ultrason. **32**(4), 481–498 (1985).

[23] P. Reynolds, ''Analysis and design of piezocomposite ultrasonic transducers using finite element technique and surface displacement profiles,'' Ph.D. thesis, University of Strathclyde, Glasgow, U.K. (1998).

[24] D. A. Hutchins and G. Hayward, ''The radiated field of ultrasonic transducers,'' in *Physical Acoustics*, edited by R. N. Thurston and A. D. Pierce (Academic, New York, 1990), Vol. XIX.

[25] M. I. Haller and B. T. Khuri-Yakub, ''A surface micromachined electrostatic ultrasonic air transducer,'' Proceedings of the 1994 Ultrasonics Symposium, pp. 1241–1243.

[26] D. W. Schindel, D. A. Hutchins, L. Zou, and M. Sayer, ''The design and characterisation of micromachined air-coupled capacitance transducers,'' IEEE Trans. Ultrason. Ferroelectr. Freq. Control **42**(1), 42–50 (1995).

[27] R. Hickling and S. P. Marin, ''The use of ultrasonics for gauging and proximity sensing in air,'' J. Acoust. Soc. Am. **79**, 1151–1160 (1986).

On array design for matched-field processing

Stacy L. Tantum and Loren W. Nolte
Department of Electrical and Computer Engineering, Box 90291, Duke University, Durham, North Carolina 27708-0291

(Received 1 December 1998; revised 30 November 1999; accepted 22 December 1999)

Conventional plane-wave beamforming array design guidelines are motivated by the desire to obtain particular beampattern characteristics, such as main lobe width and side lobe levels. These design guidelines are appropriate for arrays employed for beamforming, where a plane-wave signal model is utilized to derive both the array design parameters and the beamforming algorithm. However, matched-field processing utilizes full-field acoustic propagation models to exploit the complexities of ocean acoustic propagation. As a result, there may be more appropriate design guidelines for arrays employed for matched-field processing. In this paper, general guidelines for matched-field processing array design utilizing a normal mode propagation model are proposed. Various line array configurations are evaluated with respect to source localization performance, and the results suggest that arrays designed for matched-field processing should provide a unique representation of each propagating mode along the extent of the array. Further, the empirical analyses support the guidelines suggested by the theoretical analyses and show that arrays which are far from meeting conventional beamforming array design requirements may be more than sufficient for matched-field processing. [S0001-4966(00)00904-8]

PACS numbers: 43.60.Gk, 43.30.Yj, 43.30.Wi [SAC-B]

INTRODUCTION

Conventional beamforming array design guidelines are based on a plane-wave signal model and the assumption of plane-wave propagation. As such, they have been developed with the goal of resolving plane-wave arrival angles, which is accomplished by resolving spatial frequencies. Consequently, the design requirements for array length and shading functions are motivated by the desire to achieve particular beampattern characteristics, such as main lobe width and side lobe levels. Furthermore, conventional beamforming array design dictates maximum element spacing of a half wavelength in order to avoid the presence of grating lobes. The maximum frequency for which this condition is satisfied is often referred to as the design frequency. These design guidelines are appropriate for arrays employed for beamforming, where a plane-wave signal model is utilized to derive both the array design parameters and the beamforming algorithm. However, matched-field processing utilizes full-field acoustic propagation models to exploit the complexities of ocean acoustic propagation, such as coherent multipath propagation.[1] As a result, there may be more appropriate array design guidelines for arrays employed for matched-field processing. When the array design is based on knowledge of the full-field acoustic propagation, the resulting guidelines are different from those utilized for conventional plane-wave beamforming. In this paper, general guidelines for matched-field processing array design utilizing a normal mode acoustic propagation model are proposed. Results are presented as functions of the array parameters, such as array length and number of sensors, and various horizontal and vertical line array configurations are evaluated with respect to source localization performance. The results support the guidelines suggested by the theoretical analyses and show that arrays which are far from meeting conventional beamforming design requirements, such as the design frequency, are more than sufficient for matched-field processing.

The normal mode acoustic propagation model is first presented in Sec. I. Then conventional plane-wave beamforming and matched-field processing array design considerations are discussed in Secs. II and III. Section IV contains the results of applying the general matched-field processing array design considerations presented in Sec. III to obtain array design guidelines specific to horizontal and vertical line arrays. Empirical analyses of the effects of line array configuration on matched-field source localization performance are presented in Sec. V. Finally, arbitrary array configurations for matched-field processing are considered in Sec. VI, and Sec. VII concludes with a discussion of the results.

I. ACOUSTIC PROPAGATION MODEL

Acoustic propagation models are an integral component of matched-field processing due to the forward modeling required to compute the replica fields. There are several models available,[2] and the choice of the model depends on the purpose for which the model will be used. Normal mode methods provide an accurate and computationally efficient propagation model for matched-field processing applications. Normal mode theory expresses the acoustic pressure field in terms of a normal mode expansion and then solves for the eigenfunctions and eigenvalues which are solutions to the wave equation and satisfy the boundary conditions. The total acoustic pressure field is then the weighted sum of the contributions from each mode. Once the geoacoustic parameters are defined, a single evaluation of the propagation model determines the mode shape functions (eigenfunctions) and horizontal wave numbers (eigenvalues). From this information, all the replica fields may be computed. Other methods

may require evaluating the propagation model more than once to compute all the replica fields. Further, normal mode methods are easily automated, which provides another level of efficiency when the model must be evaluated many times for different geoacoustic environments, as is the case for statistical approaches to matched-field processing, and for evaluating statistical measures of performance.

Applying separation of variables to solve the acoustic wave equation for an isotropic point source with a harmonic time dependence $s(t)=e^{-j\omega_0 t}$ results in a Sturm-Liouville eigenvalue problem. As such, it has an infinite number of solutions, each characterized by an eigenfunction and eigenvalue. The eigenfunction $\Phi_m(z)$ describes the shape of the mth mode, and the eigenvalue k_m^2 is its associated horizontal propagation constant. As solutions to the Sturm–Liouville eigenvalue problem, the modes form an orthonormal basis,

$$\int_0^D \frac{\Phi_m(z)\Phi_n(z)}{\rho(z)}\,dz=\begin{cases}0 & m\neq n\\ 1 & m=n,\end{cases} \tag{1}$$

where D is the depth of the waveguide. They also form a complete set, allowing the total acoustic pressure field to be expressed as a sum of the modes. Therefore, the acoustic pressure field at a range r and depth z due to a source at a depth z_s can be calculated from

$$p(r,z)=\frac{j}{4\rho(z_s)}\sum_{m=1}^{\infty}\Phi_m(z_s)\Phi_m(z)H_0^{(1)}(k_m r), \tag{2}$$

where the Hankel function of the first kind is chosen to satisfy the condition of outward radiating energy as $r\to\infty$. This exact solution to the wave equation is the weighted sum of the contributions from each mode, where the weighting of the mth mode is proportional to the amplitude of that mode at the source depth. When $k_m r\gg 1$, the Hankel function may be replaced by its asymptotic approximation, and the pressure equation reduce to

$$p(r,z)\approx\frac{j}{\rho(z_s)\sqrt{8\pi r}}e^{-j\pi/4}\sum_{m=1}^{\infty}\Phi_m(z_s)\Phi_m(z)\frac{e^{jk_m r}}{\sqrt{k_m}}. \tag{3}$$

Thus, given the amplitudes of the mode shape functions at the source and receiver depths and the corresponding horizontal wavenumbers, the pressure field observed across the receiving array due to a source at an arbitrary range may be calculated.

The normal mode program KRAKEN[3,4] efficiently and accurately calculates the mode shape functions and horizontal wavenumbers for an ocean acoustic waveguide. Given a description of the source and the acoustic environment, KRAKEN numerically evaluates the mode shape functions and horizontal wavenumbers, from which the acoustic pressure field can be calculated using either the exact representation [Eq. (2)] or the far-field approximation [Eq. (3)].

II. CONVENTIONAL PLANE-WAVE BEAMFORMING ARRAY DESIGN CONSIDERATIONS

Conventional plane-wave beamforming may be viewed as spatial filtering, where plane-wave signals arriving from a particular direction are selected and signals arriving from other directions are rejected. This interpretation is directly analogous to narrow-band frequency filtering, where signals at a particular frequency are selected and signals at other frequencies are rejected. The analogy between spatial filtering of plane-wave signals and frequency filtering of time-domain (sinusoidal) signals is prevalent throughout beamforming. As a result, many of the concepts pertaining to frequency-domain filter design and sampling theory for time-domain signals have been directly applied to plane-wave beamforming to obtain guidelines for array design.[5–7]

Frequency filters are often characterized by their transfer functions, which describe the response of the filter as a function of frequency. The Fourier transform of a sampled time-domain window function is a sampled, periodic version of the Fourier transform of the window function. Generally, the length of the window function determines the bandwidth of the filter, where a broader window implies smaller bandwidth. The sampling period determines the periodicity of the Fourier transform, where a smaller sampling period implies longer periodicity in the transfer function. A windowing function other than simple uniform weighting may be applied to reduce the side lobe levels at the expense of increasing the bandwidth. The corresponding characterization for beamforming is the beampattern, which describes the response of the beamformer as a function of the plane-wave arrival angle. The beampattern is essentially the Fourier transform of the array shading function, where the aperture length determines the width of the main lobe and the element spacing determines the presence of grating lobes.

Just as the design of frequency-domain filters is motivated by the need to obtain a desired transfer function, array design for plane-wave beamforming is motivated by the need to obtain a desired beampattern. The array length, L, determines the main lobe width, which is a measure of angular resolution, or selectivity. For an array with uniform shading, the rectangular array shading function transforms to a sinc function, and the main lobe width is measured by its first zero crossing, w,

$$w=\frac{1}{L}=\frac{\sin\theta}{\lambda}, \tag{4}$$

where θ is the arrival angle measured from broadside and λ is the wavelength. Hence, the angular resolution may be expressed as

$$\theta=\arcsin\left(\frac{\lambda}{L}\right). \tag{5}$$

From this relationship, it is clear that angular resolution improves as the array length increases, or the wavelength of the plane-wave signal decreases. Since the array elements are in effect spatially sampling the plane-wave signal, the element spacing, D, determines the periodicity of the beam pattern, and the main lobe is repeated at intervals of $2\pi/D$. Consequently, grating lobes, which are the result of spatial frequency aliasing, appear in the beampattern if the element spacing exceeds half a wavelength. This leads to the notion of a design frequency, f_d, which is the highest frequency for which the maximum element spacing requirement is met. In

terms of the sound speed, c, the element spacing requirement may be expressed as

$$D \leqslant \frac{\lambda}{2} = \frac{c}{2 f_d}. \tag{6}$$

As with frequency filter design, the side lobe levels may be decreased by choosing an appropriate array shading function other than simple uniform shading. However, improved side lobes are achieved at the expense of increased main lobe width.

III. MATCHED-FIELD PROCESSING ARRAY DESIGN CONSIDERATIONS

Matched-field processing typically involves correlating the received field with replica fields calculated using a full-field propagation model. The signal processing is not based on resolving plane-wave arrival angles, or spatial frequencies, as with conventional plane-wave beamforming, but rather on extracting information from the received field concerning the nature of the acoustic propagation. Consequently, the receiving array should be designed based on knowledge of full-field propagation, since that is precisely what is exploited by matched-field processing techniques to achieve improved performance.

When a normal mode propagation model is employed, knowledge of the modal structure of the acoustic field may be utilized to guide the design of the receiving array. Since the replica fields can be expressed as the weighted sum of normal modes, the correlation between the observed field and the replica field may be decomposed into the weighted sum of the correlations between the observed field and each of the modes. In order to obtain an accurate measure of the degree of correlation between the observed and replica fields, the array must sample the modal structure such that each of the modes has a unique representation along the extent of the receiving array. The correlation among modes across the receiving array may be measured by examining the structure of the modal cross-correlation matrix, $\mathbf{R}_\Phi$, which is an $M \times M$ matrix, where M is the number of modes. The cross-correlation between the mth and nth modes is defined by

$$\mathbf{R}_{\Phi_{m,n}} = \frac{\sum_{a=1}^{A} \Phi_{m,a} e^{jk_m r_a} \Phi_{n,a} e^{-jk_n r_a}}{\sqrt{\sum_{a=1}^{A} \Phi_{m,a} e^{jk_m r_a}} \sqrt{\sum_{a=1}^{A} \Phi_{n,a} e^{jk_n r_a}}}, \tag{7}$$

where the number of array elements is denoted by A, $\Phi_{m,a}$ is the amplitude function of the mth mode at array element a, k_m is the horizontal wavenumber associated with the mth mode, and r_a is the horizontal range of array element a relative to the middle array element. Essentially, this is the inner product of the mode functions across the receiving array normalized by the energy in each of the modes. When the modes are sampled such that their representations are unique, the rank of the modal cross-correlation matrix is equal to the number of modes. As will be shown subsequently, it is necessary only to obtain unique representations of the propagating modes, meaning those modes without significant imaginary components in their horizontal wavenumbers.

IV. LINE ARRAYS FOR MATCHED-FIELD PROCESSING

A common receiving array configuration follows a linear geometry with uniformly spaced sensors. Most often, line arrays are assumed to be either vertical or horizontal. The physical parameters defining a line array for matched-field processing are its length, the number of elements, and for horizontal line arrays, its depth. The element spacing, or density, is implicitly determined once the array length and number of elements are defined. This is in contrast to arrays designed for conventional plane-wave beamforming, where the number of elements is implicitly determined once the array length and element spacing are defined. The design guidelines for each of these parameters are developed independently.

A. Array length

It is necessary for the modes to be uncorrelated over the extent of the receiving array in order to obtain an accurate measure of the correlation between the received field and the replica fields. For a continuous array, the correlation between the mth and nth modes is given by[8]

$$\mathbf{R}_{\Phi_{m,n}} = \int_{-L/2}^{L/2} \Phi_m(z(l)) e^{jk_m r(l)} \Phi_n(z(l)) e^{-jk_n r(l)} dl. \tag{8}$$

This is a general expression that is valid for any continuous array, where the range, $r(l)$, and depth, $z(l)$, are functions of the distance, l, along the array.

The length of a horizontal line array, assuming a bearing of 90°, or endfire, may be determined directly from the preceding expression. The minimum array length necessary to resolve the modes is[8]

$$L \geqslant \frac{2\pi}{\min \Delta k}, \tag{9}$$

where Δk is the difference in horizontal wavenumbers between modes. Using the absolute minimum Δk will provide the ability to distinguish all the modes. However, as will be shown later, it is not necessary to be able to resolve all the modes, only to be able to represent each of them uniquely, and an array which is long enough to accomplish this task is sufficient.

For a continuous vertical line array, the range parameter in the exponential term is 0 and the correlation reduces to

$$\mathbf{R}_{\Phi_{m,n}} = \int_{-L/2}^{L/2} \Phi_m(z(l)) \Phi_n(z(l)) dl, \tag{10}$$

which is the correlation between the normal mode shape functions. Since the normal modes are by definition orthogonal over the depth of the water column [Eq. (1)], the array length for vertical line arrays is naturally defined. A fully spanning aperture is necessary in order to adequately sample the pressure field and provide a unique representation of each mode. It should be noted that when there are soft sediments, rather than a rigid bottom, this integral must be extended into the sediment layer to achieve orthogonality between the modes.[2,9] In addition, it has been previously suggested that vertical arrays which span only a fraction of the water col-

umn are subject to performance degradation due to inadequate sampling of some of the acoustic modes.[10–13]

B. Number of elements

The number of sensors is the second parameter that defines an array for matched-field processing. Once the array satisfies the minimum length requirement, the performance is largely determined by the number of array elements. The rank of the modal cross-correlation matrix is equal to the number of linearly independent pieces of information, and in this case is equal to the number of modes with unique representations. The rank is the minimum of the number of sensors, or the number of modes. Since it is necessary to obtain a unique representation of each of the propagating modes, the number of sensors should be at least equal to the number of propagating modes.

The number of propagating modes increases with the source frequency as well as the channel depth. Therefore, it may not be possible to include enough sensors in the array to satisfy this requirement if the number of propagating modes becomes prohibitively large. However, it has been shown that accurate source localization is possible with a small number of modes,[14] which indicates this requirement may be relaxed without sacrificing source localization performance.

C. Array depth

Due to the depth dependence of the modal amplitude functions, the performance achieved by a horizontal array is dependent upon the depth at which the array is located. If the array depth coincides with a zero crossing in a mode amplitude function, then that particular mode does not contribute to the received pressure field along the array, and the information it contains regarding the source position is lost. Ideally, the array should be located at a depth where none of the mode amplitude functions is equal to zero. While it is important to remember that performance is a function of the horizontal line array depth and to consider its impact on the performance attained by matched-field processing techniques, the issues of evaluating the effects of array depth and optimizing this parameter with respect to performance are left for future research.

V. EMPIRICAL ANALYSIS OF THE EFFECTS OF LINE ARRAY CONFIGURATION ON MATCHED-FIELD SOURCE LOCALIZATION PERFORMANCE

The effects of line array configuration on source localization performance are investigated by examining the modal cross-correlation matrices and the ambiguity surfaces as well as by evaluating the probability of correctly localizing a source as a function of signal-to-noise ratio (SNR) when the matched-field processor (MFP) (Sec. V A 3) is implemented. These analyses provide qualitative as well as quantitative measures of performance for various array configurations, and validate the guidelines for array parameters suggested by the theoretical analysis. The source localization performance, as measured by probability of correct localization (P_{CL}),[15] is compared as a function of the total SNR across the array, not the sensor level SNR. This enables the fair comparison of arrays of different configurations in that changes in performance cannot be attributed solely to changes in the total available SNR due to variations in the number of sensors. If the noise is spatially uncorrelated across the array, the total SNR ($\mathrm{SNR}_{\mathrm{TOT}}$) is related to the average sensor level SNR ($\overline{\mathrm{SNR}}_{\mathrm{SEN}}$) by

$$\mathrm{SNR}_{\mathrm{TOT}}=\overline{\mathrm{SNR}}_{\mathrm{SEN}}+10\log_{10}(KA), \tag{11}$$

where K is the number of observations, or snapshots, A is the number of array elements, and the SNR is measured in dB.

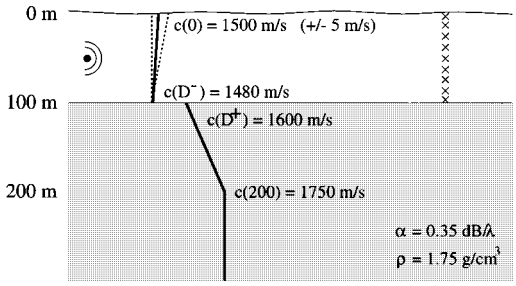

FIG. 1. NRL Workshop ocean model.

A. Simulation description

The geoacoustic ocean model utilized for the following simulations is the NRL Workshop ocean described in Sec. V A 1. Generally, environmental uncertainty is a concern, and must be addressed when implementing matched-field processing algorithms.[16,17] However, for this analysis, the parameters defining the geoacoustic environment are assumed to be known. This assumption enables the various array configurations to be compared with respect to source localization performance without incurring performance degradation due to environmental mismatch or uncertainty. The source is narrow-band at a frequency of 250 Hz and is located somewhere in the water channel at a range of 5 to 10 km from the receiving array. The source range is defined as the horizontal distance from the source to the middle array element, and for the horizontal arrays, the signal is assumed to arrive endfire, or a bearing of 90°. If the source is at some other bearing, then the array is effectively shorter and the elements are more closely spaced. The relationship between the actual array length and sensor positions and the effective array length and sensor positions is a function of the source range and may be determined through trigonometric relationships. The depth of the horizontal line arrays evaluated in the simulations is 30 m.

1. Geoacoustic ocean model

The geoacoustic ocean model is also an important element of any matched-field processing algorithm. The ocean model must be defined before the acoustic propagation can be modeled and the replica fields computed. The geoacoustic model implemented for computer simulations is a canonical shallow-water model introduced for the May 1993 NRL Workshop on Acoustic Models in Signal Processing.[18] It is an idealized range-independent shallow-water channel, 100 m in depth, illustrated in Fig. 1. The sound speed in the water is modeled as a downward refracting linear profile. The

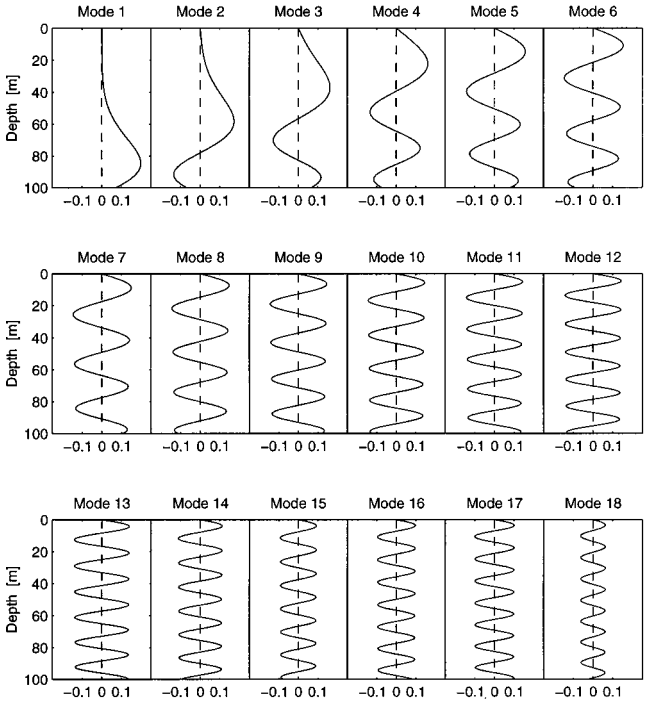

FIG. 2. First 18 modes supported by the NRL Workshop ocean for a 250-Hz source.

sound speed at the ocean surface has a value between 1495 and 1505 m/s, and at the bottom of the channel it is 1480 m/s. The ocean bottom is modeled as two layers which meet at a depth of 200 m. The sound speed in the upper sediment layer increases linearly from 1600 to 1750 m/s between 100 and 200 m in depth, at which point it becomes constant at 1750 m/s in the lower half-space. The bottom attenuation, α, is 0.35 dB/λ, and the bottom density, ρ, is 1.75 g/cm^3.

For a 250-Hz source, this ocean supports 26 modes, the first 18 of which are illustrated in Fig. 2. The real and imaginary components of the corresponding horizontal wavenumbers are shown in Fig. 3. The imaginary component of the wavenumber corresponds to attenuation. The greater the magnitude of the imaginary component, the more quickly the mode is attenuated. As this figure illustrates, the degree of attenuation increases with mode number and is a significant factor beginning with mode 14. This implies that at a distance from the source, only the first 13 modes contribute to the acoustic pressure field.

2. Signal and noise models for Bayesian matched-field processing

The signal emitted by the source is assumed to be a narrow-band sinusoid with a known frequency, f_0 [Hz], and

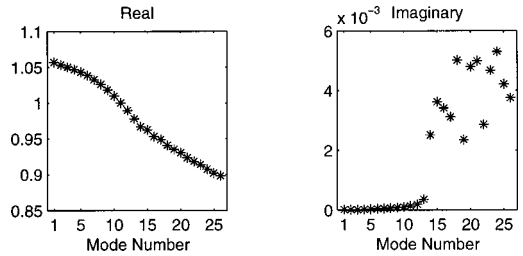

FIG. 3. Real and imaginary components of the horizontal wave numbers for modes supported by the NRL Workshop ocean for a 250-Hz source.

the observed time-domain signal across the receiving array, $\mathbf{r}(\mathbf{S},\boldsymbol{\Psi},\boldsymbol{\Phi},t)$, is assumed to consist of the received source signal, $\mathbf{s}(\mathbf{S},\boldsymbol{\Psi},\boldsymbol{\Phi},t)$, plus additive noise, $\mathbf{n}$,

$$\mathbf{r}(\mathbf{S},\boldsymbol{\Psi},\boldsymbol{\Phi},t)=\mathbf{s}(\mathbf{S},\boldsymbol{\Psi},\boldsymbol{\Phi},t)+\mathbf{n}. \tag{12}$$

The received signal at each array element is a function of the source position relative to the array element, $\mathbf{S}$, the propagation parameters associated with the ocean acoustic waveguide, $\boldsymbol{\Psi}$, and the amplitude and phase parameters of the source, $\boldsymbol{\Phi}$.

The frequency transform of the received signal is of the form

$$\mathbf{P}(\mathbf{r})=A\mathbf{H}(\mathbf{S},\boldsymbol{\Psi})+\mathbf{N}, \tag{13}$$

where A is a complex Gaussian random variable with variance σ_A^2 associated with the source parameters $\boldsymbol{\Phi}$, and $\mathbf{H}(\mathbf{S},\boldsymbol{\Psi})$ is the acoustic transfer function, or replica field in matched-field terminology, for the narrow-band source located at the position $\mathbf{S}$ in the ocean $\boldsymbol{\Psi}$. The observation $\mathbf{P}(\mathbf{r})$ is assumed to contain additive zero-mean complex Gaussian noise $\mathbf{N}$ with a known spatial covariance matrix $\mathbf{Q}$. For this work, the noise is assumed to be isotropic, consequently $\mathbf{Q}=\sigma_N^2\mathbf{I}$.

Given the assumptions regarding the source amplitude A, the probability density function of the observation given the source position and the environmental parameters is[17]

$$p(\mathbf{r}|\mathbf{S},\boldsymbol{\Psi})=\frac{1}{E(\mathbf{S},\boldsymbol{\Psi})+1}\exp\left(\frac{|R(\mathbf{r},\mathbf{S},\boldsymbol{\Psi})|^2}{E(\mathbf{S},\boldsymbol{\Psi})+1}\right), \tag{14}$$

where $E(\mathbf{S},\boldsymbol{\Psi})$ is related to the energy in the replica field, and $R(\mathbf{r},\mathbf{S},\boldsymbol{\Psi})$ is related to the correlation between the replica field and the observed field. The quantities $E(\mathbf{S},\boldsymbol{\Psi})$ and $R(\mathbf{r},\mathbf{S},\boldsymbol{\Psi})$ are defined by

$$\begin{aligned}E(\mathbf{S},\boldsymbol{\Psi})&=\sigma_A^2\mathbf{H}^\dagger(\mathbf{S},\boldsymbol{\Psi})\mathbf{Q}^{-1}\mathbf{H}(\mathbf{S},\boldsymbol{\Psi})\\&=\frac{\sigma_A^2}{\sigma_N^2}\mathbf{H}^\dagger(\mathbf{S},\boldsymbol{\Psi})\mathbf{H}(\mathbf{S},\boldsymbol{\Psi})\end{aligned} \tag{15}$$

and

$$R(\mathbf{r},\mathbf{S},\boldsymbol{\Psi})=\sigma_A^2\mathbf{H}^\dagger(\mathbf{S},\boldsymbol{\Psi})\mathbf{Q}^{-1}\mathbf{P}(\mathbf{r})=\frac{\sigma_A^2}{\sigma_N^2}\mathbf{H}^\dagger(\mathbf{S},\boldsymbol{\Psi})\mathbf{P}(\mathbf{r}). \tag{16}$$

The observed signal-to-noise ratio (SNR) is measured at the receivers and is defined by

$$\begin{aligned}\mathrm{SNR}&=\mathcal{E}\{E(\mathbf{S},\overline{\boldsymbol{\Psi}})\}\\&=\sigma_A^2\mathcal{E}\{\mathbf{H}^\dagger(\mathbf{S},\overline{\boldsymbol{\Psi}})\mathbf{Q}^{-1}\mathbf{H}(\mathbf{S},\overline{\boldsymbol{\Psi}})\}\\&=\frac{\sigma_A^2}{\sigma_N^2}\mathcal{E}\{\mathbf{H}^\dagger(\mathbf{S},\overline{\boldsymbol{\Psi}})\mathbf{H}(\mathbf{S},\overline{\boldsymbol{\Psi}})\},\end{aligned} \tag{17}$$

where $\mathbf{S}$ is the source position, $\overline{\boldsymbol{\Psi}}$ is the mean ocean environment, and $\mathcal{E}\{\cdot\}$ is the expectation operator.

3. Bayesian matched-field source localization

Bayesian *a posteriori* probability approaches to matched-field processing systematically and directly incorporate the uncertainties associated with the parameters defin-

ing the physical models into the processor when it is derived by applying optimal signal detection and parameter estimation philosophies to matched-field processing. The optimum uncertain field processor (OUFP)[17] is a Bayesian method used for parameter estimation in an uncertain ocean environment which calculates the *a posteriori* probability of the parameter(s) to be estimated given the received signal. By incorporating the uncertainties concerning the source and array parameters as well as the inherent variability in the geoacoustic environment, the OUFP is robust with respect to these parameters. Its narrow-band and wide-band source localization performance and robustness to environmental uncertainty has been investigated at short ranges in a highly uncertain shallow-water environment[15,19] and at long ranges in a deep ocean environment with internal waves.[20,21]

When the goal is source localization, the OUFP calculates $p(\mathbf{S}|\mathbf{r})$, the *a posteriori* probability density function of the source location $\mathbf{S}$ given the received signal $\mathbf{r}$. The OUFP is a robust source localization technique with respect to environmental variability because it does not assume a particular propagation environment. Instead, it assumes a range of probable propagation environments and then integrates over the environmental uncertainty to calculate the *a posteriori* probability density function

$$p(\mathbf{S}|\mathbf{r}) = \frac{\int_{\Psi} p(\mathbf{r}|\mathbf{S},\boldsymbol{\Psi}) p(\mathbf{S}|\boldsymbol{\Psi}) p(\boldsymbol{\Psi}) d\boldsymbol{\Psi}}{p(\mathbf{r})}. \tag{18}$$

Given the assumptions regarding the signal model, the conditional probability density function, or ambiguity surface, $p(\mathbf{S}|\mathbf{r})$, can be expressed as

$$p(\mathbf{S}|\mathbf{r}) = C(\mathbf{r}) p(\mathbf{S}) \int_{\boldsymbol{\Psi}} \frac{1}{E(\mathbf{S},\boldsymbol{\Psi})+1} \times \exp\left(\frac{|R(\mathbf{r},\mathbf{S},\boldsymbol{\Psi})|^2}{E(\mathbf{S},\boldsymbol{\Psi})+1} \right) p(\boldsymbol{\Psi}|\mathbf{S}) d\boldsymbol{\Psi}, \tag{19}$$

where $C(\mathbf{r})$ is a normalization constant chosen to make $p(\mathbf{S}|\mathbf{r})$ a proper probability density function; $\int_{\mathbf{S}} p(\mathbf{S}|\mathbf{r}) d\mathbf{S} = 1$. Typically, the ambiguity surface is examined and the maximum *a posteriori* (MAP) estimate, defined as the source position $\mathbf{S}$ for which $p(\mathbf{S}|\mathbf{r})$ is maximum, is chosen as the source location estimate,

$$\hat{\mathbf{S}} = \max_{\mathbf{S}} p(\mathbf{S}|\mathbf{r}). \tag{20}$$

When $\boldsymbol{\Psi}$ contains a small number of environmental parameters, a brute force numerical integration may be performed to evaluate the integral. However, when $\boldsymbol{\Psi}$ contains many uncertain parameters, brute force integration is computationally prohibitive. In this case, the integral can be evaluated efficiently using Monte Carlo integration.[15,22]

When the acoustic environment is known exactly, the environmental integration performed by the OUFP [Eq. (19)] is not necessary, and the matched-field processor (MFP) is used to calculate the ambiguity surface,

$$p(\mathbf{S}|\mathbf{r}) = C(\mathbf{r}) p(\mathbf{S}) \frac{1}{E(\mathbf{S},\boldsymbol{\Psi})+1} \exp\left(\frac{|R(\mathbf{r},\mathbf{S},\boldsymbol{\Psi})|^2}{E(\mathbf{S},\boldsymbol{\Psi})+1} \right). \tag{21}$$

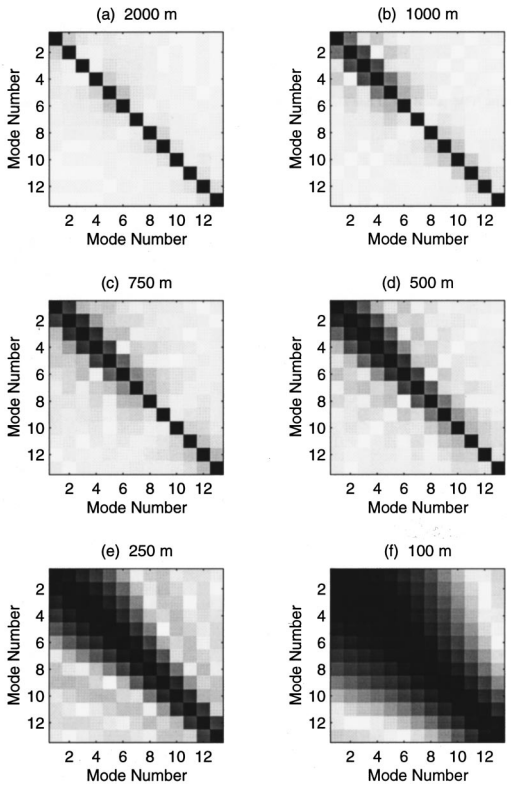

FIG. 4. Model cross-correlation matrices for horizontal line array lengths of (a) 2000, (b) 1000, (c) 750, (d) 500, (e) 250, and (f) 100 m.

Although this scenario is an artificial experiment and can be realized only in computer simulations, it provides an upper bound on the performance which can be achieved. It also provides a benchmark against which the more realistic scenario where the environment is not exactly known can be compared, and with which the performance degradation due to environmental uncertainty can be quantified.

B. Performance evaluation

The performance of various line array configurations is evaluated with respect to source localization performance as a function of SNR. The probability of correct localization (P_{CL}) is the probability the maximum *a posteriori* estimate of the source location computed by the MFP is within ± 4 m in depth and ± 100 m in range of the actual source location. The probabilities were calculated from 500 independent Monte Carlo realizations of the environment and source position. First, the length of horizontal arrays is investigated in Sec. V B 1. Then the effect of the number of sensors for both vertical and horizontal arrays is investigated in Sec. V B 2.

1. Array length

The notion of array length is relevant only for horizontal line arrays since vertical line arrays typically span the entire water column. The effect of horizontal line array length on matched-field source localization performance is evaluated by implementing arrays of various lengths with 1-m interelement spacing. The magnitude of the modal cross-correlations for the propagating modes for arrays of several lengths ranging from 100 to 2000 m are shown in Fig. 4, and the rank of each of these matrices is listed in Table I. The modal cross-

TABLE I. Ranks of the model cross-correlation matrices displayed in Fig. 4 for several horizontal line array lengths.

Array length (m)	Rank of $\mathbf{R}_\Phi$
2000	13
1000	13
750	13
500	13
250	11
100	9

correlation matrices and their corresponding ranks indicate the propagating modes may be uniquely represented utilizing arrays as short as 500 m.

Representative ambiguity surfaces for each of these arrays are presented in Fig. 5. Each of these surfaces displays the natural log of the *a posteriori* probability of the source position given the received data and a known ocean environment [Eq. (21)]. The intensity of the image is proportional to the probability associated with the source position; areas of high probability are dark and areas of low probability are light. The ambiguity surfaces are calculated by the MFP for a source located at 7.5 km in range and 50 m in depth at an SNR of 30 dB. The replica fields are computed from 1 to 99 m in depth, at 2-m intervals, and from 5 to 10 km in range, at 50-m intervals. The maximum *a posteriori* source location estimate for each of these array configurations is listed in Table II. The maximum in the ambiguity surfaces is located at the correct location for array lengths as short as 500 m.

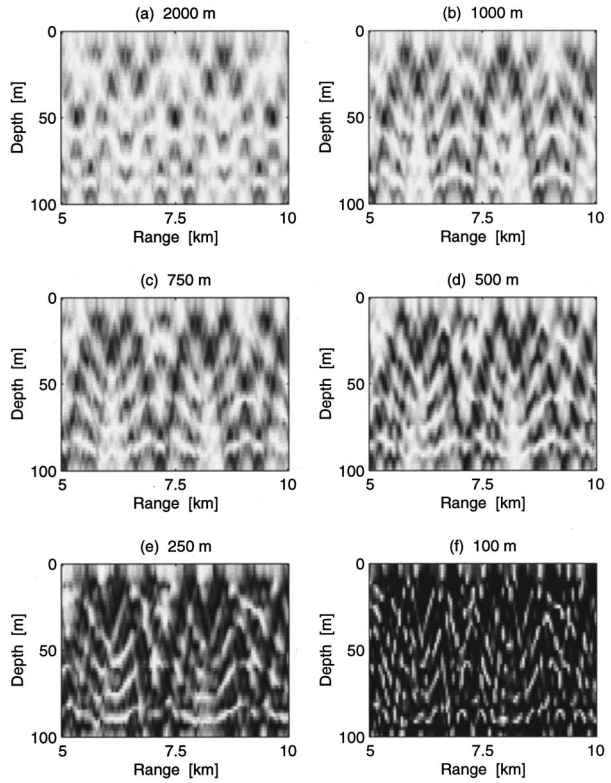

FIG. 5. Representative ambiguity surfaces computed by the MFP at an SNR of 30 dB for horizontal line array lengths of (a) 2000, (b) 1000, (c) 750, (d) 500, (e) 250, and (f) 100 m. The actual source location is 7.5 km in range and 50 m in depth.

TABLE II. Maximum *a posteriori* source location estimates from the representative ambiguity surfaces displayed in Fig. 5 for several horizontal line array lengths. The actual source location is 7.5 km in range and 50 m in depth.

Array length (m)	Range estimate (km)	Depth estimate (m)
2000	7.50	51
1000	7.50	51
750	7.50	49
500	7.50	51
250	9.55	13
100	9.50	67

However, below this length, one can visually detect deterioration in the quality of the ambiguity surfaces, and the source is no longer correctly localized.

The analyses completed thus far concerning array length have been qualitative in nature. A quantitative measure of matched-field source localization performance, probability of correct localization (P_{CL}), for each of the array configurations is presented in Fig. 6. Due to computational constraints, the arrays implemented to evaluate the probability of correct localization have 5-m interelement spacing rather than the 1-m spacing utilized to compute the previous results. This change in the array configuration does not affect the P_{CL} values calculated since the minimum number of sensors, which is 13 for this particular environment, is still exceeded in each of the array configurations and the probabilities are evaluated as a function of the total available SNR. The performance attained by the horizontal line array, as measured by probability of correct localization, does not begin to degrade until the array reaches 500 m in length. After this point, there is noticeable performance degradation. This result is consistent with the previous analysis of the modal cross-correlation matrices and representative ambiguity surfaces.

The theory discussed in the previous section indicates the minimum desirable array length [Eq. (9)] for this environmental scenario is approximately 2000 m. This is calculated by evaluating Δk for all possible mode combinations and choosing the minimum value, from which the array

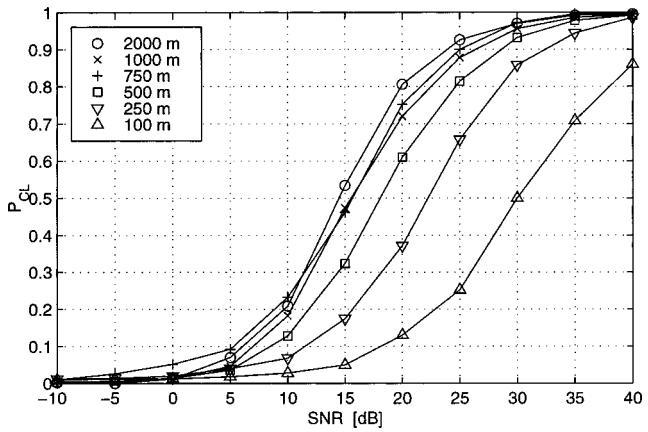

FIG. 6. Probability of correct localization P_{CL} curves quantifying MFP source localization performance as a function of SNR for horizontal line array lengths of 2000, 1000, 750, 500, 250, and 100 m.

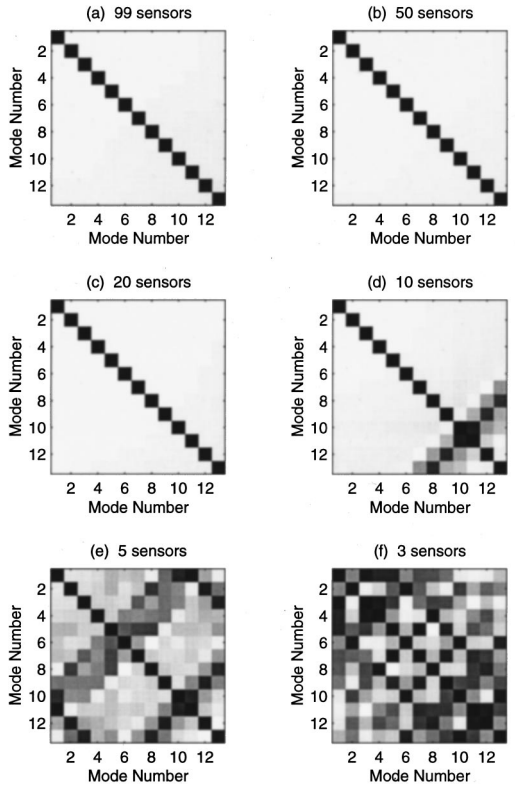

FIG. 7. Modal cross-correlation matrices for a vertical line array with (a) 99, (b) 50, (c) 20, (d) 10, (e) 5, and (f) 3 sensors.

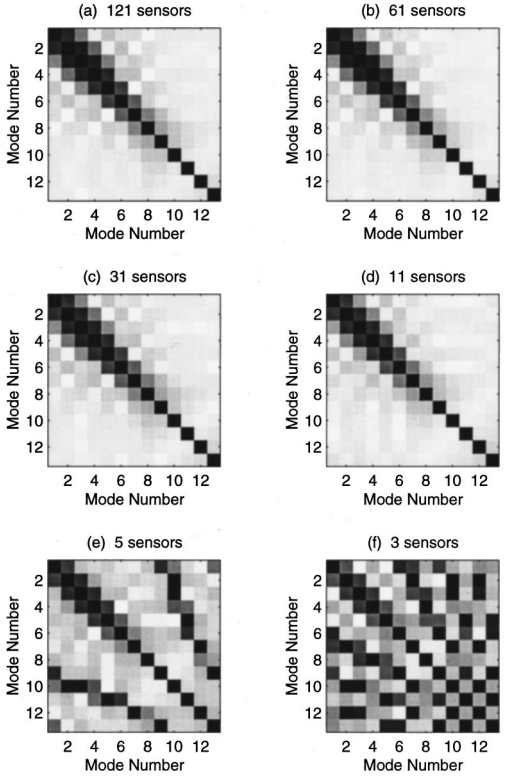

FIG. 8. Modal cross-correlation matrices for a 600-m horizontal line array with (a) 121, (b) 61, (c) 31, (d) 11, (e) 5, and (f) 3 sensors.

length may be computed using Eq. (9). However, as the results illustrate, the performance degrades only slightly as the array length decreases below this minimum desirable array length. It is not until the array reaches 500 m in length that there is significant performance loss. This array length coincides with the minimum cycle distance for this geoacoustic environment. The minimum cycle distance, or loop length, L_m, is defined as[2]

$$L_m = \frac{-2\pi}{dk_{rm}/dm} \approx \frac{2\pi}{k_{rm} - k_{r(m+1)}}. \tag{22}$$

Physically, the cycle distance corresponds to the horizontal distance over which the ray associated with a mode completes a full up and down cycle.

Although in theory the minimum desirable array length is designed to be capable of resolving all the modes and is determined by the minimum difference in the horizontal wavenumbers, the simulation results suggest that in practice it is only necessary to be able to represent each of the modes uniquely and this may be accomplished with an array whose length is at least as great as the minimum cycle distance; $L \geqslant L_m$. This expression is similar to the theoretical minimum desirable array length derived to ensure all the modes are uncorrelated along the array [Eq. (9)]. The difference is in the definition of the difference in the wavenumbers in the denominator. For the modes to be uncorrelated along the array, the denominator is set equal to the minimum difference in the wavenumbers, which yields an array length of approximately 2000 m. However, the minimum cycle distance is determined by setting the denominator equal to the maximum in the derivative of the horizontal wavenumber with respect to mode number.[2] The minimum horizontal array length using the minimum cycle distance criteria is approximately 550 m, which is consistent with the simulation results presented here. Further studies are necessary in order to fully quantify the relationship between the minimum array length required in practice and its physical basis.

2. Number of elements

Array length is typically relevant only for horizontal line arrays; however, the number of sensors is a parameter which applies to both horizontal and vertical line arrays. The effect of the number of array elements on matched-field source localization performance is evaluated by implementing arrays with various numbers of elements which meet the minimum array length requirement [Eq. (22)]. This analysis parallels that presented for the horizontal line array length requirement. Based on the preceding results regarding line

TABLE III. Ranks of the modal cross-correlation matrices displayed in Fig. 7 for a vertical line array with various numbers of sensors.

Number of sensors	Rank of $\mathbf{R}_\Phi$
99	13
50	13
20	13
10	10
5	5
3	3

TABLE IV. Ranks of the modal cross-correlation matrices displayed in Fig. 8 for a 600-m horizontal line array with various numbers of sensors.

Number of sensors	Rank of $\mathbf{R}_\Phi$
121	13
61	13
31	13
11	11
5	5
3	3

array length, the length of the horizontal line arrays is chosen to be 600 m and the vertical arrays are assumed to be fully spanning.

The modal cross-correlation matrices for those modes which do not experience appreciable attenuation are shown in Figs. 7 and 8 for vertical and horizontal line arrays with various numbers of sensors, respectively, and the rank of each of the modal cross-correlation matrices is listed in Tables III and IV. The modal cross-correlation matrices and their ranks indicate the modes are uniquely represented as long as the number of sensors is at least as great as the number of propagating modes.

Representative ambiguity surfaces for each of the vertical and horizontal line array configurations are shown in Figs. 9 and 10, respectively. These ambiguity surfaces have been calculated under the same conditions as for the analysis of array length. The actual source location is 7.5 km in range and 50 m in depth, and the SNR is 30 dB. The corresponding maximum *a posteriori* source location estimates for each of the array configurations are listed in Tables V and VI. The ambiguity surfaces exhibit deterioration once the number of sensors is less than the number of propagating modes. However, for this particular example, the source is correctly localized with the vertical array using as few as three elements, and with the horizontal array using as few as five elements.

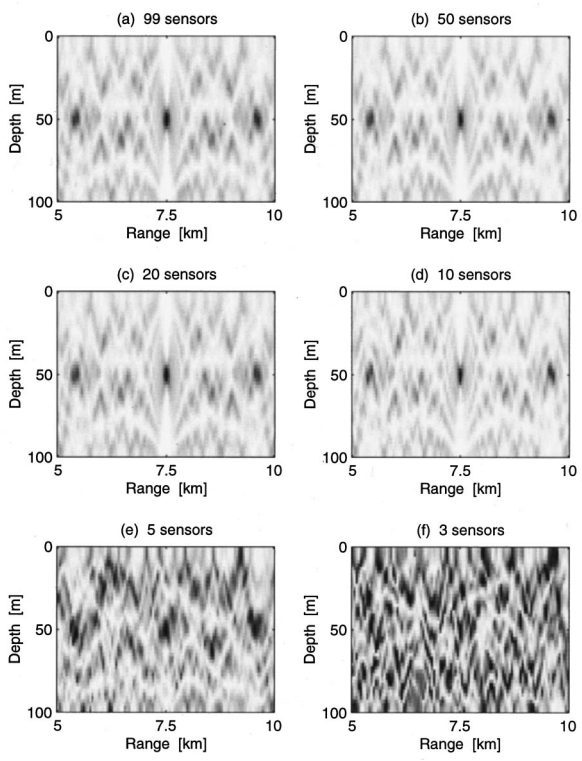

FIG. 9. Representative ambiguity surfaces computed by the MFP at an SNR of 30 dB for a vertical line array with (a) 99, (b) 50, (c) 20, (d) 10, (e) 5, and (f) 3 sensors. The source location is 7.5 km in range and 50 m in depth.

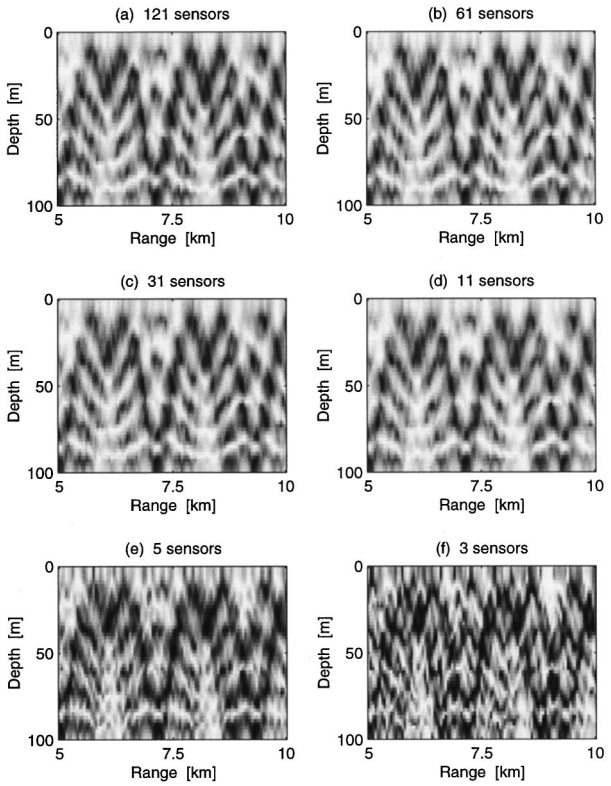

FIG. 10. Representative ambiguity surfaces computed by the MFP at an SNR of 30 dB for a 600-m horizontal line array with (a) 121, (b) 61, (c) 31, (d) 11, (e) 5, and (f) 3 sensors. The source location is 7.5 km in range and 50 m in depth.

In order to evaluate the performance of these array configurations as a function of the number of sensors utilized, it is necessary to compute the probability of correctly localizing the source over a range of SNRs. These measures of performance are presented for the vertical and horizontal arrays in Figs. 11 and 12, respectively. The P_{CL} curves indicate that performance suffers when the number of sensors decreases below the number of propagating modes used for localization, and support the notion that it is necessary to construct an array with at least as many sensors as propagat-

TABLE V. Maximum *a posteriori* source location estimates from the representative ambiguity surfaces displayed in Fig. 9 for a vertical line array with various numbers of sensors. The actual source location is 7.5 km in range and 50 m in depth.

Number of sensors	Range estimate (km)	Depth estimate (m)
99	7.50	51
50	7.50	49
20	7.50	49
10	7.50	51
5	7.50	49
3	7.50	49

TABLE VI. Maximum *a posteriori* source location estimates from the representative ambiguity surfaces displayed in Fig. 10 for a 600-m horizontal line array with various numbers of sensors. The actual source location is 7.5 km in range and 50 m in depth.

Number of sensors	Range estimate (km)	Depth estimate (m)
121	7.50	49
61	7.50	49
31	7.50	49
11	7.50	49
5	7.50	51
3	6.85	47

ing modes used for localization so that the modal cross-correlation matrix is full rank.

VI. ARBITRARY ARRAY CONFIGURATIONS FOR MATCHED-FIELD PROCESSING

Although a line array may be one of the more obvious choices for an array configuration, in practice, array configurations are not limited to linear geometry with uniformly spaced sensors. It is possible to construct arrays with arbitrary geometries and element positions, as well as in two or three dimensions. The critical factor is to ensure the array samples the modal structure such that each of the modes possesses a unique representation. The ability of a potential array design to meet this criterion may be evaluated by examining the modal cross-correlation matrix. As long as $\mathbf{R}_\Phi$ calculated for the propagating modes, meaning those modes without significant imaginary components in their horizontal wave numbers, is full rank, the modes are sampled such that their representations are unique. If the array is unable to provide a unique representation of each of the modes, then matched-field processing techniques employed using that array will experience performance degradation when compared to the performance attained using arrays which are capable of providing a sufficient representation of the modes.

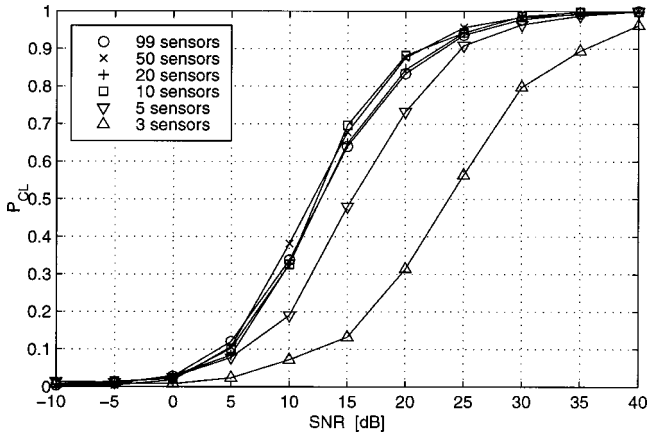

FIG. 11. Probability of correct localization P_{CL} curves quantifying MFP source localization performance as a function of SNR for a vertical line array with 99, 50, 20, 10, 5, and 3 sensors.

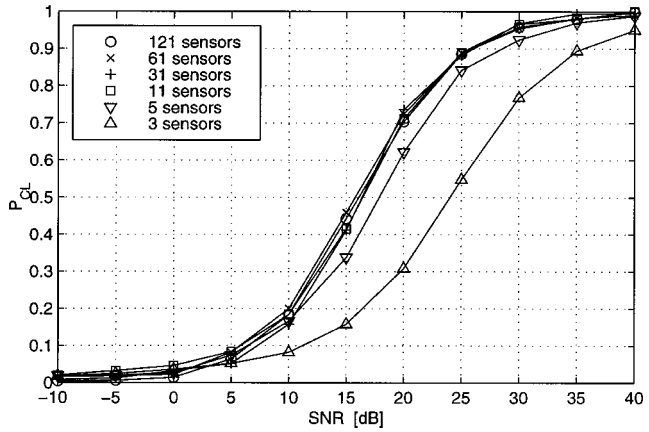

FIG. 12. Probability of correct localization P_{CL} curves quantifying MFP source localization performance as a function of SNR for a 600-m horizontal line array with 121, 61, 31, 11, 5, and 3 sensors.

VII. CONCLUSIONS

The proposed matched-field processing array design guidelines have been derived assuming a normal mode propagation model, and are quite different from those commonly employed for conventional plane-wave beamforming. Arrays designed for matched-field processing should provide a unique representation of each propagating mode along the extent of the array. The ability of an array to accomplish this may be determined by examining its associated modal cross-correlation matrix for the propagating modes. If the modal cross-correlation matrix is full rank, then each mode possesses a unique representation along the array.

The results obtained utilizing a horizontal line array assume the source is located at endfire, or a bearing of 90°. For some bearing other than endfire, the bearing angle is smaller and the array is effectively shorter with more closely spaced sensors. When this is viewed in context of the probability of correct localization (P_{CL}) summary performance curves, it implies that as long as the effective array length remains greater than the minimum array length, the performance will not be significantly affected by the source bearing. This is true since performance is determined by the number of sensors, not the element spacing, as long as the array satisfies the minimum length requirement. Alternatively, this suggests a possible array geometry for which performance is not a function of the source bearing. It may be possible to construct an array composed of two horizontal line arrays in a cross configuration so that the smallest bearing angle with respect to either of the sub-arrays is 45°. Further, the P_{CL} summary performance results are presented not as a function of the sensor level SNR but as a function of the total available SNR, which is determined by the number of array elements and the number of snapshots, as well as the sensor level SNR [Eq. (11)]. The desired performance level, as paramaterized by the total available SNR, may be attained even with low sensor level SNR by increasing the number of sensors beyond the minimum requirement, or by increasing the number of snapshots.

ACKNOWLEDGMENTS

The authors would like to thank Dr. Leslie Collins for helpful discussions, and the anonymous reviewers for valuable comments. Support for this work has been provided by the Office of Naval Research.

[1] H. P. Bucker, ''Use of calculated sound fields and matched-field detection to locate sound sources in shallow water,'' J. Acoust. Soc. Am. **59**, 368–373 (1976).
[2] F. B. Jensen, W. A. Kuperman, M. B. Porter, and H. Schmidt, *Computational Ocean Acoustics* (American Institute of Physics, Woodbury, NY, 1994).
[3] M. B. Porter and E. L. Reiss, ''A numerical method for ocean acoustic normal modes,'' J. Acoust. Soc. Am. **76**, 244–252 (1984).
[4] M. Porter, The KRAKEN normal mode program, Rep. SM-245 (SACLANT Undersea Research Centre, La Spezia, Italy, 1991).
[5] W. S. Burdic, *Underwater Acoustic System Analysis*, 2nd ed. (Prentice-Hall, Englewood Cliffs, NJ, 1991).
[6] L. J. Ziomek, *Underwater Acoustics: A Linear Systems Theory Approach* (Academic, San Diego, 1985).
[7] D. E. Dudgeon and R. M. Mersereau, *Multidimensional Digital Signal Processing* (Prentice-Hall, Englewood Cliffs, NJ, 1984).
[8] V. Premus, ''Modal scintillation index: A physics-based statistic for acoustic source depth discrimination,'' J. Acoust. Soc. Am. **105**, 2170–2180 (1999).
[9] M. J. Buckingham, ''A theoretical model of ambient noise in a low-loss, shallow water channel,'' J. Acoust. Soc. Am. **67**, 1186–1192 (1980).
[10] S. Li, Localization of Remote Sources Using Multipath Propagation, Ph.D. thesis (Yale University, 1991).
[11] S. Li and P. M. Schultheiss, ''Depth measurement of remote sources using multipath propagation,'' IEEE J. Ocean Eng. **18**, 379–387 (1993).
[12] S. Narasimhan and J. L. Krolik, ''Fundamental limits on acoustic source range estimation performance in uncertain ocean channels,'' J. Acoust. Soc. Am. **97**, 215–226 (1995).
[13] S. Narasimhan and J. L. Krolik. ''Source range estimation performance bounds in a random shallow water channel,'' Proceedings of the 15th International Congress on Acoustics, Trondheim, Norway, June 1995, pp. 293–296.
[14] G. R. Wilson, R. A. Koch, and P. J. Vidmar, ''Matched mode localization,'' J. Acoust. Soc. Am. **84**, 310–320 (1998).
[15] J. A. Shorey, L. W. Nolte, and J. L. Krolik, ''Computationally efficient Monte Carlo estimation algorithms for matched field processing in uncertain ocean environments,'' J. Comput. Acoust. **2**, 285–314 (1994).
[16] A. Tolstoy, ''Sensitivity of matched field processing to sound-speed profile mismatch for vertical arrays in a deep water Pacific environment,'' J. Acoust. Soc. Am. **85**, 2394–2404 (1989).
[17] A. M. Richardson and L. W. Nolte, ''*A posteriori* probability source localization in an uncertain sound speed, deep ocean environment,'' J. Acoust. Soc. Am. **89**, 2280–2284 (1991).
[18] M. B. Porter and A. Tolstoy, ''The matched field processing benchmark problems,'' J. Comput. Acoust. **2**, 161–185 (1994).
[19] J. A. Shorey and L. W. Nolte, ''Wideband optimal *a posteriori* probability source localization in an uncertain shallow water environment,'' J. Acoust. Soc. Am. **103**, 355–361 (1998).
[20] P. J. Book and L. W. Nolte, ''Narrow-band source localization in the presence of internal waves for 1000-km range and 25-Hz acoustic frequency,'' J. Acoust. Soc. Am. **101**, 1336–1346 (1997).
[21] P. J. Book and L. W. Nolte, ''Wide-band source localization in the presence of internal waves,'' J. Acoust. Soc. Am. **102**, 2597–2506 (1997).
[22] M. A. Tanner, *Tools for Statistical Inference: Methods for the Exploration of Posterior Distributions and Likelihood Functions*, 2nd ed. (Springer-Verlag, New York, NY, 1993).

Modeling the temporal behavior of distortion product otoacoustic emissions

Arnold Tubis
Department of Physics, Purdue University, West Lafayette, Indiana 47907

Carrick L. Talmadge
National Center for Physical Acoustics, University of Mississippi, University, Mississippi 38677

Christopher Tong
Department of Physics, Purdue University, West Lafayette, Indiana 47907

(Received 3 September 1999; revised 29 November 1999; accepted 6 December 1999)

The temporal behavior of the $2f_1-f_2$ distortion product otoacoustic emission is theoretically investigated for the case in which the lower frequency (f_1) primary tone is on continuously, and the higher frequency (f_2) one is pulsed on and off [e.g., Talmadge *et al.*, J. Acoust. Soc. Am. **105**, 275–292 (1999)]. On physical grounds, this behavior is expected to be characterized by various group delays associated with the propagation of (1) the f_2 cochlear primary wave between the cochlear base and the primary distortion product generation region around $\hat{x}_2$ (the f_2 tonotopic place), and (2) the $2f_1-f_2$ cochlear distortion product (DP) waves between the cochlear base, the primary generation region of the distortion product, and the region around the $2f_1-f_2$ tonotopic place where the generated apical moving DP wave is reflected toward the cochlear base [e.g., Talmadge *et al.*, J. Acoust. Soc. Am. **104**, 1517–1543 (1998)]. An approximate analytic expression is obtained for this behavior from the analysis of the Fourier integral representation of the auditory peripheral response to the primary stimuli. This expression also approximately describes the transient build-up of the components of different latencies in terms of the damping properties of the cochlear partition. It is shown that considerable caution must be applied in attempting to relate phase derivatives of the distortion product otoacoustic emissions for steady state stimuli and the physical time delays which are associated with the temporal behavior of a distortion product emission in the case of a pulsed primary. [S0001-4966(00)03503-7]

PACS numbers: 43.64.Bt, 43.64.Ha, 43.64.Jb [BLM]

INTRODUCTION

If a stimulus consisting of tones of two or more frequencies is presented to the ear, nonlinear signal processing in the cochlea results in the production of intermodulation distortion products (DPs). These may be detected psychoacoustically or as objective acoustic signals in the ear canal (distortion product otoacoustic emissions or DPOAEs) (reviewed in Talmadge *et al.*, 1998, 1999). In the case of a two-tone stimulus of frequencies f_1 and f_2 ($>f_1$), the DPOAE with frequency $2f_1-f_2$ is the largest under many experimental conditions. The amplitude and phase of this DPOAE can be extracted from the ear canal recording by signal processing. Changes in the level and phase of the DPOAE with changes in the levels and frequencies of the two external tones (primaries) provide us with insight into the mechanisms responsible for the generation of this distortion product and its transmission back to the ear canal.

It is generally understood that the generation region of the DPs in the cochlea is near the maximal overlap of the cochlear waves evoked by the external tones (e.g., Hall, 1974; Kemp and Brown, 1983). There has been some disagreement, however, over whether the DPOAE (which is the DP signal as measured in the ear canal) is entirely comprised of a signal component originating at the generator region (for example, He and Schmiedt, 1993, 1996, 1997; Sun *et al.*, 1994a,b) or whether it is a combination of two components (the so-called ''two-source'' model), one originating around the generator region and the other originating near the DP tonotopic location (reviewed in Talmadge *et al.*, 1998). Investigators who have assumed that the generator region is the sole source of the DPOAE have used the steady state DPOAE phase characteristics in an attempt to estimate the time it takes for the two primary tone signals to travel to the overlap region and the generated DPOAE signal to reach the external ear (e.g., Kimberley *et al.*, 1993; O'Mahoney and Kemp, 1995; Moulin and Kemp, 1996a, b; Bowman *et al.*, 1997, 1998; Schneider *et al.*, 1999). (See Sec. IV of this paper for some potential pitfalls associated with this procedure.)

The results of recent investigations, both experimental (e.g., Kummer *et al.*, 1995; Brown *et al.*, 1996; Gaskill and Brown, 1996; Stover *et al.*, 1996; Talmadge *et al.*, 1999) and theoretical (reviewed in Talmadge *et al.*, 1998), have given strong support for the following underlying physical picture: The $2f_1-f_2$ DPOAE is initially produced in a region (usually called the *generation* or *overlap region*) where, as just mentioned, the activity patterns for the primary cochlear waves overlap maximally (near the tonotopic site for the f_2 primary). DP waves emerge and propagate both basally and apically from the generation region. A fraction of the basal moving wave is transmitted through the base of the cochlea and into the middle ear and ear canal, where it contributes to the DPOAE signal. If the cochlea had no inhomogeneities,

the apically moving DP wave would simply damp out after passing its tonotopic site. However, if the cochlear response gives rise to a tall/broad activity pattern, then a small level of inhomogeneity of the cochlear properties may produce a significant reflection of the apically moving DP wave around its tonotopic site. This reflection mechanism was first suggested by Zweig and Shera (Shera and Zweig, 1993; Zweig and Shera, 1995; see also Talmadge and Tubis, 1993; Talmadge *et al.*, 1997, 1998, 1999). This reflected DP wave would also be partially transmitted through the cochlea and into the ear canal, where it would combine with the signal from the initial basally moving DP wave to produce a characteristic interference behavior (local maxima and minima of the DPOAE amplitude as the primary frequencies are varied). In addition to the ear canal signals from the initially generated DP waves, there would also be a series of other signal contributions in the ear canal from the partial transmission through the cochlear base of basally moving DP waves that originate from multiple reflections from the cochlear base and from around the DP tonotopic site. These additional contributions to the DPOAE signal would, of course, also produce interference effects. [For a detailed discussion of these additional interference terms see, e.g., Shera and Zweig (1992), Zweig and Shera (1995), and Talmadge *et al.* (1998).]

Formal expressions for the DPOAE amplitude and phase, including the effects of multiple internal reflections of the DP waves in the cochlea, have been derived by Talmadge *et al.* (1997, 1998, 1999) for the case of steady state primary tones. As was shown by Talmadge *et al.* (1999), it is instructive to also study the temporal behavior of DPOAEs when one of the primaries is on steady state but the other is pulsed on and off. [This paradigm is to be distinguished from the one in which both primaries are pulsed on and off (e.g., Martin *et al.*, 1998), which is harder to interpret theoretically.] It is especially easy to interpret data obtained near a minimum in the DPOAE fine structure where the two components are almost 180 degrees out of phase. In this instance, as was demonstrated by Talmadge *et al.* (1999), the appearance of a null in the DPOAE amplitude following the turn on of the pulsed primary clearly indicates that the contribution to the DPOAE from the reflection around the DP tonotopic site is the dominant one. Conversely, the appearance of a null in the DPOAE amplitude following the turn off of the pulsed primary indicates that the contribution to the DPOAE from the generation region is the dominant one.

If the effect of cochlear nonlinearity is taken into account only to the lowest nonvanishing order, the connection between the steady state DPOAE signal and the signal in a pulsed primary paradigm is, in principle, straightforward. The latter can be simply represented by a Fourier integral whose integrand involves the complex steady state signal.[1] In this paper, the temporal behavior of the $2f_1-f_2$ DPOAE in a pulsed (f_2) primary paradigm (with the f_1 primary on steady state) is studied theoretically. In order to obtain a physically transparent result, the integrand of the Fourier expression for this temporal behavior is approximated so that the integral may be evaluated analytically using the calculus of residues (e.g., Arfken and Weber, 1995, pp. 414–432). The result is then expressed in terms of the basal and apical cochlear reflectances, the various relevant latencies (those for the propagation of the primary f_2 wave from the cochlear base to the f_2 tonotopic site, the propagation of the DP wave from the f_2 tonotopic site to the DP tonotopic site, and the propagation of the DP wave from the f_2 tonotopic site to the cochlear base), and the cochlear damping parameters which characterize the approach of the DPOAE behavior to steady state conditions after the turn on of the pulsed primary tone. The appearance of latencies in their true role as time delays (rather than as phase derivatives of steady state signals) will hopefully make their physical origin and significance clear, and help researchers to avoid the dangers of always interpreting the phase derivatives of the steady state DPOAE behaviors as physical time delays. This point will be discussed in Sec. IV.

The relevant formal expressions for the $2f_1-f_2$ DPOAE under steady state and pulsed (f_2) primary conditions are given in Sec. I. Approximations of the integrand of the Fourier integral for the pulsed primary case, which allow the integral to be evaluated analytically using the calculus of residues, are introduced in Sec. I C. The analytic expression is obtained in Sec. II, and its implications are explored in Secs. III and IV.

I. THE $2f_1-f_2$ DPOAE

A. Steady state primaries

The basic formulas for various types of otoacoustic emissions, and details on the underlying model and approximations used to obtain them, have been extensively discussed in Talmadge *et al.* (1998), to which the reader is directed for the precise definitions and meanings of the symbols used in this paper. The model used was a one-dimensional macromechanical model with a time-delayed stiffness component in the basilar membrane mechanics of the form suggested by Zweig (1991). The model also includes simplified models of the middle and outer cars. A low level of spatial inhomogeneity of cochlear properties (Shera and Zweig, 1993; Zweig and Shera, 1995) is assumed. In conjunction with the tall/broad activity pattern which is given by the Zweig form of the cochlear partition impedance, the inhomogeneities give rise to cochlear wave reflections. A simple third-order nonlinearity in the cochlear damping function is introduced to account for the generation of DPOAEs, as well as to stabilize SOAEs. For reasons discussed in Talmadge *et al.* (1998), the essential features of the results obtained with the model are expected to be valid for more elaborate and realistic models of the auditory periphery.

For a steady state ''calibrated'' driving pressure, $P_{dr}^{ss}(t)$, given by

$$P_{dr}^{ss}(t)=A_1e^{i\omega_1 t}+A_2e^{i\omega_2 t}+\text{complex conjugate}, \qquad (1)$$

where A_1 and A_2 are complex constants, the complex $2f_1-f_2$ DPOAE pressure signal amplitude in the ear canal, $P_{dp}^{ss}(\omega_1,\omega_2,\omega_{dp})$, $(\omega_{dp}=2\omega_1-\omega_2)$, is given by Eq. (162) of Talmadge *et al.* (1998),

$$P_{dp}^{ss}(\omega_1,\omega_2,\omega_{dp})$$

$$= -T_{pd}(\omega_{dp})\frac{k_{ow}(\omega_{dp})}{k_r(0,\omega_{dp})+k_l(0,\omega_{dp})} \times\frac{\rho_0(\omega_1,\omega_2)}{\Delta_{sm}(0,\omega_{dp})}\frac{1+R_a(\omega_{dp})\mathcal{R}_d(\omega_1,\omega_2)}{1-R_a(\omega_{dp})R_b(\omega_{dp})} \times I_r(\infty,\omega_1,\omega_2), \quad (2)$$

$$\equiv \frac{P_l(\omega_1,\omega_2,\omega_{dp})+R_a(\omega_{dp})P_r(\omega_1,\omega_2,\omega_{dp})}{1-R_a(\omega_{dp})R_b(\omega_{dp})}. \quad (3)$$

Some of the relevant expressions for the various terms in Eq. (2) are

$$I_{r,l}(x,\omega_1,\omega_2)=\int_0^x dx'\,\omega_0(x')\chi_r^2(x',\omega_1)\chi_r^*(x',\omega_2) \times\chi_{r,l}(x',\omega_{dp}), \quad (4)$$

$$\rho_0(\omega_1,\omega_2)=\frac{i\sigma_{bm}k_0^2\epsilon_\gamma(2\omega_1-\omega_2)^3b_r^2(0,\omega_1)b_r^*(0,\omega_2)}{b_{nl}^2}, \quad (5)$$

$$\omega_0(x)=\omega_{0c}e^{-k_\omega x}+\omega_{1c}, \quad (6)$$

$$\mathcal{R}_d(\omega_1,\omega_2)=\frac{I_l(\infty,\omega_1,\omega_2)}{I_r(\infty,\omega_1,\omega_2)}=\frac{P_r(\omega_1,\omega_2,\omega_{dp})}{P_l(\omega_1,\omega_2,\omega_{dp})}, \quad (7)$$

$$b_r(0,\omega)=\frac{-G_{me}(\omega)k_{ow}(\omega)P_{dr}(\omega)}{\sigma_{bm}\Delta_{sm}(0,\omega)(k_r(0,\omega)+k_{ow}(\omega))}, \quad (8)$$

$$P_{dr}(\omega_{1,2})=A_{1,2}, \quad (9)$$

$$\psi_r(x,\omega)\cong\sqrt{\frac{k(0,\omega)}{k(x,\omega)}}\exp\left\{-i\int_0^x k(x',\omega)dx'\right\}, \quad (10)$$

$$\psi_l(x,\omega)\cong\sqrt{\frac{k(0,\omega)}{k(x,\omega)}}\exp\left\{+i\int_0^x k(x',\omega)dx'\right\}, \quad (11)$$

$$k(x,\omega)=\frac{k_0\omega}{\sqrt{\Delta_{sm}(x,\omega)}}, \quad (12)$$

$$\Delta_{sm}(x,\omega)=\omega_0^2(x)-\omega^2+i\omega\gamma_0(x)+\rho_f\omega_0(x)^2 \times e^{-i\psi_f\omega/\omega_0(x)}+\rho_s\omega_0(x)^2e^{-i\psi_s\omega/\omega_0(x)}, \quad (13)$$

$$\chi_{r,l}(x,\omega)=\frac{\Delta_{sm}(0,\omega)}{\Delta_{sm}(x,\omega)}\psi_{r,l}(x,\omega), \quad (14)$$

and

$$R_a(\omega)\approx-\frac{2r_0k_0^2\omega^2}{W_0(\omega)\Delta_{sm}^2(0,\omega)}\int_0^\infty dx\,\omega_0^2(x)\chi_r^2(x,\omega)\tilde{r}(x). \quad (15)$$

Here $\tilde{r}(x)$ is a function that gives a pseudo-random Gaussian number with $\langle\tilde{r}^2(x)\rangle=1$, $W_0(\omega)=\psi_r(x,\omega)\psi_l'(x,\omega)-\psi_r'(x,\omega)\psi_l(x,\omega)$ is the Wronskian and is independent of x, and r_0 characterizes the magnitude of the roughness.

For simplicity, it is assumed that

$$R_b(\omega)=R_be^{-i\omega\tau_b}, \quad (16)$$

where R_b is a constant, and that apical reflections of the primary f_1, f_2 cochlear waves can be ignored. If significant apical reflections of the primaries were present, Eq. (8) would have to be modified according to Eqs. (53) and (97) of Talmadge *et al.* (1998), since internal reflection of the primaries would lead to an additional modulation of the DP generator due to the variation in the activity patterns of the primaries with frequency.

The WKB approximation (e.g., Mathews and Walker, 1964; Zweig *et al.*, 1976) has been used for the transpartition pressure basis functions [Eqs. (10)–(13)]. The explicit phase behaviors given by this approximation will be useful in deriving approximate expressions for various time delays in terms of spatial integrals of $\partial k(x,\omega)/\partial\omega$.

B. Pulsed f_2 primary

If, instead of the steady state driving pressure given by Eq. (1), only the f_1 primary is on steady state, and the f_2 primary is turned on at $t=0$, Eq. (1) would be replaced by

$$P_{dr}^{\rm on}(t)=A_1e^{i\omega_1t}+\Theta(t)A_2e^{i\omega_2t}+\text{complex conjugate},$$

$$=A_1e^{i\omega_1t}+\frac{A_2}{2\pi i}\int_{-\infty}^{\infty}d\omega_2'\frac{e^{i\omega_2't}}{\omega_2'-\omega_2-i\epsilon} +\text{complex conjugate}, \quad (17)$$

where ϵ is a positive infinitesimal, and $\Theta(t)$ is the Heaviside theta function given by

$$\Theta(t)\equiv\begin{cases}0, & t<0,\\ 1/2, & t=0,\\ 1, & t>0.\end{cases} \quad (18)$$

The correctness of the integral representation of $\Theta(t)A_2e^{i\omega_2t}$ may be established by noting that the ω_2' integral may be converted into a closed contour integral by adding an integration around an infinite semicircle in the lower-half complex ω_2' plane for $t<0$, and the upper-half complex ω_2' plane for $t>0$. By Jordan's lemma (e.g., Arfken and Weber, 1995, p. 425), the contributions from the semicircular paths vanish. Since the integrand has a simple pole in the upper-half complex ω_2' plane, the application of the calculus of residues (e.g., Arfken and Weber, 1995, pp. 414–432) then shows that the integral vanishes for $t<0$, and is equal to $A_2e^{i\omega_2t}$ for $t>0$. If both primaries are on steady state up to $t=0$, and the f_2 primary is turned off at $t=0$, then $P_{dr}(t)$ would be represented as

$$P_{dr}^{\rm off}(t)=A_1e^{i\omega_1t}+A_2e^{i\omega_2t}(1-\Theta(t))+\text{complex conjugate},$$

$$=A_1e^{i\omega_1t}-\frac{A_2}{2\pi i}\int_{-\infty}^{\infty}d\omega_2'\frac{e^{i\omega_2't}}{\omega_2'-\omega_2+i\epsilon} +\text{complex conjugate}, \quad (19)$$

where ϵ is again a positive infinitesimal.

To lowest nonvanishing order in the cochlear nonlinearity, using Eq. (17), the Fourier expansion of the DP ear canal signal after signal turn on corresponding to the steady state frequency $2f_1-f_2$ is

$$P_{dp}^{\rm on}(t)=-\frac{e^{2i\omega_1 t}}{2\pi i}\int_{-\infty}^{\infty}d\omega_2'\,\frac{e^{-i\omega_2' t}}{\omega_2'-\omega_2+i\epsilon}\times P_{dp}^{ss}(\omega_1,\omega_2',2\omega_1-\omega_2')+\text{complex conjugate},\tag{20}$$

where $P_{dp}^{ss}(\omega_1,\omega_2,2\omega_1-\omega_2)$ is given by Eq. (2), and where we have used $\omega_{dp}=2\omega_1-\omega_2'$. (The reader who finds it difficult to understand the procedure used here is referred to Appendix B of this paper, where the same methodology is illustrated in the context of DP generation for a simple driven nonlinear oscillator with a single degree of freedom.) $P_{dp}^{\rm off}(t)$ is obtained from Eq. (20), with ϵ replaced by $-\epsilon$, and with an overall minus sign, and describes how the steady state DP response decays after the turn off of the f_2 primary at $t=0$.

Because of the rather complicated functional dependence of the integrand of Eq. (20) on ω_2', the evaluation of $P_{dp}^{\rm on}(t)$ is a very formidable task. In the next section, a number of simplifying approximations will be applied to the integrand so as to permit the analytic evaluation of the relevant part of $P_{dp}^{\rm on}(t)$ via contour integration and the calculus of residues.

C. Approximate representation of $P_{dp}^{\rm on}(t)$

The experimental temporal measurement of the $2f_1-f_2$ DPOAE under pulsed f_2 primary conditions (Talmadge *et al.*, 1998) essentially entails the detection of the steady state $2f_1-f_2$ DPOAE component, and the components with frequencies in close proximity to $2f_1-f_2$ and decaying amplitudes (which determine the transient behavior). This suggests a procedure in which the ω_2' dependence of $P_{dp}^{ss}(\omega_1,\omega_2',2\omega_1-\omega_2')$ in Eq. (20) is approximated so as to emphasize this dependence in the neighborhood of $\omega_2'=\omega_2$ (especially the pole behavior). Furthermore, the integrand of Eq. (20) is sharply peaked near $\omega_2'=\omega_2$, which means that quantities that slowly vary over the region where this integrand is large may either be assumed constant, and for other sufficiently slowly varying quantities, only the leading order contribution to the variation of the quantity with respect to $\omega_2-\omega_2'$ will need to be considered.

The following approximations will therefore be made:

(i) It is assumed that the effect of the middle ear on the DPOAE amplitude and phase is a slowly varying function of ω_2, so that

$$F(\omega_1,\omega_2',2\omega_1-\omega_2')\equiv\frac{-T_{pd}(2\omega_1-\omega_2')k_{ow}(2\omega_1-\omega_2')}{k_r(0,2\omega_1-\omega_2')+k_l(0,2\omega_1-\omega_2')}\times\frac{\rho_0(\omega_1,\omega_2')}{\Delta(0,2\omega_1-\omega_2')}\approx F(\omega_1,\omega_2,2\omega_1-\omega_2),\tag{21}$$

where $F(\omega_1,\omega_2,2\omega_1-\omega_2)$ characterizes the effects of forward and reverse transmission through the middle ear.

(ii) The level of the $2\omega_1-\omega_2$ DP wave is assumed to slowly vary near ω_2, so that

$$\chi_r(x,\omega_2')\approx\chi_r(x,\omega_2)\frac{\Delta_{sm}(x,\omega_2)}{\Delta_{sm}(x,\omega_2')}e^{-i\hat{\tau}_2(x)(\omega_2'-\omega_2)},\tag{22}$$

$$\chi_r(x,2\omega_1-\omega_2')\approx\chi_r(x,2\omega_1-\omega_2)\frac{\Delta_{sm}(x,2\omega_1-\omega_2)}{\Delta_{sm}(x,2\omega_1-\omega_2')}\times e^{-i\tau(x,\omega_{dp})(\omega_2-\omega_2')},\tag{23}$$

$$\chi_l(x,2\omega_1-\omega_2')\approx\chi_l(x,2\omega_1-\omega_2)\frac{\Delta_{sm}(x,2\omega_1-\omega_2)}{\Delta_{sm}(x,2\omega_1-\omega_2')}\times e^{i\tau(x,\omega_{dp})(\omega_2-\omega_2')},\tag{24}$$

$$\hat{\tau}_2(x)=\int_0^x dx'\,\frac{\partial k(x',\omega_2')}{\partial\omega_2'}\bigg|_{\omega_2'=\omega_2},\tag{25}$$

$$\tau(x,\omega_{dp})=\int_0^x dx'\,\frac{\partial k(x',\omega_{dp})}{\partial\omega_{dp}}\bigg|_{\omega_{dp}=2\omega_1-\omega_2}.\tag{26}$$

Note also that the phase variations of $\chi_r(x,\omega_2')$, $\chi_r(x,2\omega_1-\omega_2')$, and $\chi_l(x,2\omega_1-\omega_2')$ have been approximated by their first-order expansions in $\omega_2-\omega_2'$. The coefficients of these expansions are the group delays, $\hat{\tau}_2(x)$ and $\tau(x,\omega_{dp})$, which are those for the propagation of narrow-band cochlear wave packets of center frequencies ω_2 and ω_{dp}, respectively, between locations $x\approx\hat{x}(\omega_2)$ and 0. Note that an equivalent assumption is that the group delays of $\hat{\tau}_2(x)$ and $\tau(x,\omega_{dp})$ are slowly varying over the region where the integrand in Eq. (20) is nonnegligible.

(iii) The level and phase of the coefficient multiplying the integral expression for the reflectance $R_a(\omega)$ in Eq. (15) is assumed to be slowly varying, so that

$$f(\omega_{dp}')|_{\omega_{dp}'=2\omega_1-\omega_2'}\equiv\frac{2r_0k_0^2(\omega_{dp}')^2}{W_0(\omega_{dp}')\Delta_{sm}^2(0,\omega_{dp}')}\bigg|_{\omega_{dp}'=2\omega_1-\omega_2'}\approx\frac{2r_0k_0^2(2\omega_1-\omega_2)^2}{W_0(2\omega_1-\omega_2)\Delta_{sm}^2(0,2\omega_1-\omega_2)}.\tag{27}$$

(iv) The group delay $\hat{\tau}_{dp}(x)$, which is that for a narrow-band cochlear wave packet of center frequency ω_{dp}, which is propagating between the positions, $x=0$ and $x=\hat{x}(\omega_{dp})$, will be assumed to slowly vary over the region where the integrand of Eq. (20) is nonnegligible, so that

$$\hat{\tau}_{dp}(x)=\int_0^x dx'\,\frac{\partial k}{\partial\omega_{dp}}(x',\omega_{dp})\bigg|_{\omega_{dp}=2\omega_1-\omega_2}.\tag{28}$$

(v) Finally, the branch cuts associated with the ω_2' dependence in Eqs. (10) through (12) will be neglected. This is equivalent to assuming that the branch points and their associated branch cuts lie outside the region where the integrand of Eq. (20) has its maximum. In this case, only the variation of the functions containing branch cuts [such as $\sqrt{\Delta_{sm}(0,\omega)}$] within the region where this integrand is maximum need be considered.

With all of these approximations introduced, Eq. (20) becomes

$$P_{dp}^{\mathrm{on}}(t)=-\frac{e^{2i\omega_1 t}}{2\pi i}F(\omega_1,\omega_2,2\omega_1-\omega_2)\int_{-\infty}^{\infty}d\omega_2'\frac{e^{-i\omega_2' t}}{\omega_2'-\omega_2+i\epsilon}\left\{\left[\int_0^{\infty}dx'\,\omega_0(x')\chi_r^2(x',\omega_1)\chi_r^*(x',\omega_2)\chi_r(x',2\omega_1-\omega_2)\right.\right.$$
$$\times\frac{\Delta_{sm}^*(x',\omega_2)}{\Delta_{sm}^*(x',\omega_2')}\frac{\Delta_{sm}(x',2\omega_1-\omega_2)}{\Delta_{sm}(x',2\omega_1-\omega_2')}e^{i[\hat{\tau}_2(x')+\tau(x',\omega_{dp})](\omega_2'-\omega_2)}\Big]+\Big[f(2\omega_1-\omega_2)\int_0^{\infty}dx'\,\omega_0^2(x')\chi_r^2(x',2\omega_1-\omega_2)$$
$$\times\tilde{r}(x')\frac{\Delta_{sm}^2(x',2\omega_1-\omega_2)}{\Delta_{sm}^2(x',2\omega_1-\omega_2')}\,e^{-2i\hat{\tau}_{dp}(x')(\omega_2-\omega_2')}\int_0^{\infty}dx''\,\omega_0(x'')\chi_r^2(x'',\omega_1)\chi_r^*(x'',\omega_2)\chi_l(x'',2\omega_1-\omega_2)$$
$$\left.\left.\times\frac{\Delta_{sm}^*(x'',\omega_2)}{\Delta_{sm}^*(x'',\omega_2')}\frac{\Delta_{sm}(x'',2\omega_1-\omega_2)}{\Delta_{sm}(x'',2\omega_1-\omega_2')}e^{i[\hat{\tau}_2(x'')-\tau(x'',\omega_{dp})](\omega_2'-\omega_2)}\Big]\right\}\left\{1-f(2\omega_1-\omega_2)R_b e^{-i\tau_b(2\omega_1-\omega_2)}\int_0^{\infty}dx'\,\omega_0^2(x')\right.$$
$$\left.\times\chi_r^2(x',2\omega_1-\omega_2)\tilde{r}(x')\frac{\Delta_{sm}^2(x',2\omega_1-\omega_2)}{\Delta_{sm}^2(x',2\omega_1-\omega_2')}e^{i[\tau_b+2\hat{\tau}_{dp}(x')](\omega_2'-\omega_2)}\right\}^{-1}+\text{complex conjugate}. \tag{29}$$

In the following sections, it will be shown that this expression can be approximately represented as

$$P_{dp}^{\mathrm{on}}(t)\approx P_{dp}^{\mathrm{gen}}(t)+P_{dp}^{\mathrm{refl}}(t)+\cdots. \tag{30}$$

Here the superscript ''gen'' denotes the component of $P_{dp}^{\mathrm{on}}(t)$ from the generator region, and the superscript ''refl'' denotes the component from the reflection site. The time-dependent DP components $P_{dp}^{\mathrm{gen}}(t)$ and $P_{dp}^{\mathrm{refl}}(t)$ have the steady state analogues $P_l^{ss}(\omega_1,\omega_2,\omega_{dp})$ and $R_a(\omega_{dp})P_r^{ss}(\omega_1,\omega_2,\omega_{dp})$ in Eq. (3). In the next section, it will be shown that the time constants, $\hat{\tau}_2(x)$ and $\tau(x,\omega_{dp})$, may be approximately set equal to their values at $x=\hat{x}_2=\hat{x}(\omega_2)$, and the time constant $\hat{\tau}_{dp}(x)$ set equal to its value at $x=\hat{x}(2\omega_1-\omega_2)$. Then,

$$\overline{\tau}_{\mathrm{gen}}\equiv-\frac{\partial}{\partial\omega_{dp}}\arg[P_l(x,\omega_1,\omega_2,\omega_{dp})]\cong\hat{\tau}_2+\tau(\hat{x}_2,\omega_{dp}), \tag{31}$$

$$\overline{\tau}_{\mathrm{refl}}\equiv-\frac{\partial}{\partial\omega_{dp}}\arg[R_a(\omega_{dp})P_r(x,\omega_1,\omega_2,\omega_{dp})]$$
$$\cong\hat{\tau}_2+2\hat{\tau}_{dp}-\tau(\hat{x}_2,\omega_{dp}), \tag{32}$$

where

$$\hat{\tau}_2=\hat{\tau}_2(\hat{x}_2),\quad \hat{\tau}_{dp}=\hat{\tau}_{dp}(\hat{x}_2), \tag{33}$$

are, respectively, the latency of the DPOAE component from the generation region and the latency of the component which results from the initial reflection of the generated DP wave around the DP tonotopic site. Note that $\overline{\tau}_{\mathrm{gen}}$ and $\overline{\tau}_{\mathrm{refl}}$ characterize, respectively, the rate of change of the phase from the initial contribution from the generation region and from the DPOAE reflection site.

Section II of this paper is devoted to the extraction of the various DPOAE temporal components from Eq. (29). The latencies of these components are concisely summarized in Sec. II A.

II. EVALUATION OF THE DPOAE SIGNAL IN THE CASE OF A PULSED f_2 PRIMARY

A. Component latencies

On physical grounds, the pulsing on of the f_2 primary is expected to result in a series of $2f_1-f_2$ components of increasing latency. The first, corresponding to the initially generated component, will have a latency around $\overline{\tau}_{\mathrm{gen}}$, given by Eq. (31). The next will correspond to the signal in the ear canal which results from the reflection of the initial apical moving generated wave from around the DP tonotopic site, whose latency will be approximately given by $\overline{\tau}_{\mathrm{refl}}$ in Eq. (32). This will be followed by the signal in the ear canal which results from successive reflections of the initially generated basal-moving wave, from the base of the cochlea and from around the DP tonotopic site. The latency of this component will be given approximately by $\overline{\tau}_{\mathrm{gen}}+2\hat{\tau}_{dp}+\tau_b$, where $\hat{\tau}_{dp}$ and τ_b are defined by Eqs. (33) and (16), respectively. The next signal component will have latency, $\overline{\tau}_{\mathrm{refl}}+2\hat{\tau}_{dp}+\tau_b$, and so on. In summary, the latencies of the various components will be approximately given by

$$\overline{\tau}_{\mathrm{gen},n}=\overline{\tau}_{\mathrm{gen}}+n(2\hat{\tau}_{dp}+\tau_b);\quad n=0,1,2,3,\ldots, \tag{34}$$

and

$$\overline{\tau}_{\mathrm{refl},n}=\overline{\tau}_{\mathrm{refl}}+n(2\hat{\tau}_{dp}+\tau_b);\quad n=0,1,2,3,\ldots. \tag{35}$$

B. The $\overline{\tau}_{\mathrm{gen}}$ latency component

The $\overline{\tau}_{\mathrm{gen}}$ latency component is obtained from the first term of Eq. (29), with the $\{\ldots\}^{-1}$ factor set equal to one. In order to evaluate this component, it is convenient to first perform the integration over ω_2',

$$-\frac{e^{2i\omega_1 t}}{2\pi i}\int_{-\infty}^{\infty}d\omega_2'\frac{e^{-i\omega_2' t}}{\omega_2'-\omega_2+i\epsilon}\frac{\Delta_{sm}^*(x,\omega_2)}{\Delta_{sm}^*(x,\omega_2')}$$
$$\times\frac{\Delta_{sm}(x,2\omega_1-\omega_2)}{\Delta_{sm}(x,2\omega_1-\omega_2')}e^{i[\overline{\tau}_2(x)+\tau(x,\omega_{dp})](\omega_2'-\omega_2)}, \tag{36}$$

where for simplicity, analytic structures not containing ω_2' are not shown.

The time-delayed stiffness terms in $\Delta_{sm}(x,\omega_2')$ [Eq. (13)] greatly complicate the evaluation of the integral. Therefore, for the purpose of obtaining a simple result for the transient build up of the signal, which should at least have qualitative validity, these terms will be neglected.[2] Then

$$\frac{\Delta_{sm}^*(x,\omega_2)}{\Delta_{sm}^*(x,\omega_2')}\frac{\Delta_{sm}(x,2\omega_1-\omega_2)}{\Delta_{sm}(x,2\omega_1-\omega_2')}\approx\frac{\Delta_{sm}^*(x,\omega_2)\Delta_{sm}(x,2\omega_1-\omega_2)}{(\omega_0^2(x)-\omega_2'^2-i\omega_2'\gamma_0(x))(\omega_0^2(x)-(2\omega_1-\omega_2')^2+i(2\omega_1-\omega_2')\gamma_0(x))}$$

$$=\frac{\Delta_{sm}^*(x,\omega_2)}{(\omega_2'-\bar{\omega}_0(x)+i\gamma_0(x)/2)(\omega_2'+\bar{\omega}_0(x)+i\gamma_0(x)/2)}$$

$$\times\frac{\Delta_{sm}(x,2\omega_1-\omega_2)}{(2\omega_1-\omega_2'-\bar{\omega}_0(x)-i\gamma_0(x)/2)(2\omega_1-\omega_2'+\bar{\omega}_0(x)-i\gamma_0(x)/2)}, \tag{37}$$

where

$$\bar{\omega}_0(x)=\sqrt{\omega_0^2(x)-\frac{\gamma_0^2(x)}{4}}, \tag{38}$$

and thus the integral in Eq. (36) may be evaluated using the calculus of residues to yield

$$\Theta(t-\hat{\tau}_2(x)-\tau(x,\omega_{dp}))\Bigg[e^{i(2\omega_1-\omega_2)t}-e^{2i\omega_1 t}e^{-i(\omega_0(x)-i\gamma_0(x)/2)t}e^{i[\omega_0(x)-\omega_2-i\gamma_0(x)/2](\hat{\tau}_2(x)+\tau(x,\omega_{dp}))}$$

$$\times\frac{\Delta_{sm}^*(x,\omega_2)\Delta_{sm}(x,2\omega_1-\omega_2)}{(\bar{\omega}_0(x)-\omega_2-i\gamma_0(x)/2)(2\bar{\omega}_0(x))\Delta_{sm}(x,2\omega_1-\bar{\omega}_0(x)+i\gamma_0(x)/2)}\Bigg], \tag{39}$$

plus terms that have the temporal behaviors,

$$\Theta(t-\hat{\tau}_2(x)-\tau(x,\omega_{dp}))e^{i(2\omega_1+\bar{\omega}_0(x)+i\gamma_0(x)/2)t} \tag{40}$$

and

$$\Theta(t-\hat{\tau}_2(x)-\tau(x,\omega_{dp}))e^{i(\pm\bar{\omega}_0(x)+i\gamma_0(x)/2)t}. \tag{41}$$

In order to obtain analytic results for the DPOAE, a final series of approximations is required in the integration over x. The approximations are based on the facts that $\gamma_0(x)\ll\bar{\omega}_0(x)$ and that the magnitude of the integrand of the x integration is peaked about $x=\hat{x}_2$, where $\bar{\omega}_0(\hat{x}_2)\approx\omega_0(\hat{x}_2)\approx\omega_2$. Accordingly, x in Eqs. (39), (40), and (41) is set equal to $\hat{x}_2$, and $\bar{\omega}_0(x)-i\gamma_0(x)/2$ in $\Delta_{sm}(x,2\omega_1-\bar{\omega}_0(x)+i\gamma_0(x)/2)$ is replaced by ω_2. Also,

$$\lim_{x\to\hat{x}_2}\frac{\Delta_{sm}^*(x,\omega_2)e^{i[\bar{\omega}_0(x)-\omega_2-i\gamma_0(x)/2][\hat{\tau}_2(x)+\tau(x,\omega_{dp})]}}{(\bar{\omega}_0(x)-\omega_2-i\gamma_0(x)/2)(2\bar{\omega}_0(x))}$$

$$=e^{\gamma_0(\hat{x}_2)\bar{\tau}_{\rm gen}/2}. \tag{42}$$

The contributions with temporal behaviors described by Eqs. (40) and (41) need not be considered since they can be experimentally distinguished from the (amplitude varying) $2\omega_1-\omega_2$ DPOAE signal.

The final expression for the $\bar{\tau}_{\rm gen}$ latency component is

$$P_{dp}^{\rm gen}(t)=\Theta(t-\bar{\tau}_{\rm gen})e^{i(2\omega_1-\omega_2)t}(1-e^{-\gamma_0(\hat{x}_2)(t-\bar{\tau}_{\rm gen})/2})$$

$$\times P_l(\omega_1,\omega_2,2\omega_1-\omega_2)+\text{complex conjugate}, \tag{43}$$

where

$$P_l(\omega_1,\omega_2,2\omega_1-\omega_2)$$

$$=F(\omega_1,\omega_2,2\omega_1-\omega_2)\int_0^\infty dx\,\omega_0(x)\chi_r^2(x,\omega_1)\chi_r^*(x,\omega_2)$$

$$\times\chi_r(x,2\omega_1-\omega_2). \tag{44}$$

The superscript ''gen'' in $P_{dp}^{\rm gen}(t)$ is used in order to denote that this component is the direct (shortest latency) contribution to $P_{dp}^{\rm on}(t)$ from the generator region.

C. The $\bar{\tau}_{\rm refl}$ latency component

From Eq. (29), the $\bar{\tau}_{\rm refl}$ latency component is

$$P_{dp}^{\rm refl}(t)=F(\omega_1,\omega_2,2\omega_1-\omega_2)f(2\omega_1-\omega_2)$$

$$\times\int_0^\infty dx'\int_0^\infty dx\,\omega_0^2(x')\chi_r^2(x',2\omega_1-\omega_2)\tilde{r}(x')$$

$$\times\omega_0(x)\chi_r^2(x,\omega_1)\chi_r^*(x,\omega_2)\chi_l(x,2\omega_1-\omega_2)$$

$$\times I_{dp}^{\rm refl}(x,x',\omega_1,\omega_2,t)+\text{complex conjugate}, \tag{45}$$

where

$$I_{dp}^{\mathrm{refl}}(x,x',\omega_1,\omega_2,t)=-\frac{e^{i2\omega_1 t}}{2\pi i}\int_{-\infty}^{\infty}d\omega_2'\frac{e^{-i\omega_2'(t-\overline{\tau}_{\mathrm{refl}}(x,x'))}e^{-i\omega_2\overline{\tau}_{\mathrm{refl}}(x,x')}}{\omega_2'-\omega_2+i\epsilon}\,\frac{\Delta_{sm}^2(x',2\omega_1-\omega_2)}{\Delta_{sm}^2(x',2\omega_1-\omega_2')}\,\frac{\Delta_{sm}^*(x,\omega_2)}{\Delta_{sm}(x,\omega_2')}\,\frac{\Delta_{sm}(x,2\omega_1-\omega_2)}{\Delta_{sm}(x,2\omega_1-\omega_2')},\tag{46}$$

and

$$\overline{\tau}_{\mathrm{refl}}(x,x')=\hat{\tau}_2(x)+2\hat{\tau}_{dp}(x')-\tau(x,\omega_{dp}).\tag{47}$$

From the discussion of the previous section, it is seen that $\Delta_{sm}(x,2\omega_1-\omega_2)/\Delta_{sm}(x,2\omega_1-\omega_2')$ may be approximated by unity if only the transient signal with $\omega_2'=2\omega_1-\omega_2$ is being tracked. Also, since the magnitudes of the integrands of the x and x' integrations are peaked about $\hat{x}(\omega_2)$ and $\hat{x}(2\omega_1-\omega_2)$, respectively, the approximation of setting x,x' to these values in Eq. (46) will be used. Finally, the time-delayed stiffness terms in $\Delta(x,\omega_2')$ will again be dropped and γ_0 will be assumed to be independent of x. Then:

$$\begin{aligned}
&I_{dp}^{\mathrm{refl}}(x=\hat{x}(\omega_2),x'=\hat{x}(2\omega_1-\omega_2),\omega_1,\omega_2,t)\\
&\quad=-\frac{e^{i2\omega_1 t}}{2\pi i}\int_{-\infty}^{\infty}d\omega_2'\frac{e^{-i\omega_2'(t-\overline{\tau}_{\mathrm{refl}})}e^{-i\omega_2\overline{\tau}_{\mathrm{refl}}}}{\omega_2'-\omega_2+i\epsilon}\,\frac{\Delta_{sm}^2(\hat{x}(2\omega_1-\omega_2),2\omega_1-\omega_2)}{\Delta_{sm}^2(\hat{x}(2\omega_1-\omega_2),2\omega_1-\omega_2')}\,\frac{\Delta_{sm}^*(\hat{x}(\omega_2),\omega_2)}{\Delta_{sm}^*(\hat{x}(\omega_2),\omega_2')}\\
&\quad\approx-\frac{e^{i2\omega_1 t}}{2\pi i}\int_{-\infty}^{\infty}d\omega_2'\frac{e^{-i\omega_2'(t-\overline{\tau}_{\mathrm{refl}})}e^{-i\omega_2\overline{\tau}_{\mathrm{refl}}}}{\omega_2'-\omega_2+i\epsilon}\left(\frac{i(2\omega_1-\omega_2)\gamma_0}{-(2\omega_1-\omega_2')^2+(2\omega_1-\omega_2)^2+i(2\omega_1-\omega_2')\gamma_0}\right)^2\frac{(-i\omega_2\gamma_0)}{-\omega_2'^2+\omega_2^2-i\omega_2'\gamma_0}.
\end{aligned}\tag{48}$$

In Eq. (48), only the residue contributions from poles at $\omega_2'=\omega_2-i\epsilon$, $\omega_2-i\gamma_0/2$, and $4\omega_1-\omega_2-i\gamma_0/2$, which give components of frequency $2\omega_1-\omega_2$, with time varying amplitudes in the latter two cases, will be retained. Also, terms containing powers of the dimensionless factors γ_0/ω_2, $\gamma_0/(2\omega_1-\omega_2)$,..., will be neglected. (These terms include the residue contribution from $\omega_2'=4\omega_1-\omega_2-i\gamma_0/2$.) Then Eq. (48) has the approximate form,

$$\begin{aligned}
&I_{dp}^{\mathrm{refl}}(x=\hat{x}(\omega_2),x'=\hat{x}(2\omega_1-\omega_2),\omega_1,\omega_2,t)\\
&\quad\approx-\frac{e^{i2\omega_1 t}}{2\pi i}\int_{-\infty}^{\infty}d\omega_2' e^{-i\omega_2'(t-\overline{\tau}_{\mathrm{refl}})}\\
&\qquad\times e^{-i\omega_2\overline{\tau}_{\mathrm{refl}}}\frac{(i\gamma_0/2)^3}{(\omega_2'-\omega_2+i\epsilon)(\omega_2'-\omega_2+i\gamma_0/2)^3}\\
&\quad=\Theta(t-\overline{\tau}_{\mathrm{refl}})e^{i2\omega_1 t}\left[e^{-i\omega_2 t}+e^{-i\omega_2\overline{\tau}_{\mathrm{refl}}}\left(i\frac{\gamma_0}{2}\right)^3\right.\\
&\qquad\left.\times\frac{1}{2}\frac{d^2}{d\omega_2'^2}\left\{\frac{e^{-i\omega_2'(t-\overline{\tau}_{\mathrm{refl}})}}{\omega_2'-\omega_2+i\epsilon}\right\}\Bigg|_{\omega_2'=\omega_2-i\gamma_0/2}\right]\\
&\quad=\Theta(t-\overline{\tau}_{\mathrm{refl}})e^{i(2\omega_1-\omega_2)t}\left[1-e^{-\gamma_0\overline{t}/2}\right.\\
&\qquad\left.\times\left(1+\frac{\gamma_0\overline{t}}{2}+\frac{\gamma_0^2\overline{t^2}}{8}\right)\right]\Bigg|_{\overline{t}=t-\overline{\tau}_{\mathrm{refl}}}.
\end{aligned}\tag{49}$$

Substitution of the result in Eq. (49) into Eq. (45) gives the final form of the $\overline{\tau}_{\mathrm{refl}}$ latency component,

$$\begin{aligned}
P_{dp}^{\mathrm{refl}}(t)&=R_a(2\omega_1-\omega_2)P_r(\omega_1,\omega_2,2\omega_1-\omega_2)\\
&\quad\times\Theta(t-\overline{\tau}_{\mathrm{refl}})e^{i(2\omega_1-\omega_2)t}\left[1-e^{-\gamma_0\overline{t}/2}\right.\\
&\quad\left.\times\left(1+\frac{\gamma_0\overline{t}}{2}+\frac{\gamma_0^2\overline{t^2}}{8}\right)\right]\Bigg|_{\overline{t}=t-\overline{\tau}_{\mathrm{refl}}},
\end{aligned}\tag{50}$$

where

$$\begin{aligned}
P_r(\omega_1,\omega_2,2\omega_1-\omega_2)&=F(\omega_1,\omega_2,2\omega_1-\omega_2)\\
&\quad\times\int_0^{\infty}dx\,\omega_0(x)\chi_r^2(x,\omega_1)\chi_r^*(x_1,\omega_2)\\
&\quad\times\chi_l(x,2\omega_1-\omega_2).
\end{aligned}\tag{51}$$

D. Components with latencies, $\overline{\tau}_{\mathrm{gen},n}$ and $\overline{\tau}_{\mathrm{refl},n}$, $n\geqslant 1$, and final form of $P_{dp}^{\mathrm{on}}(t)$

The expansion of the factor

$$\{1-R_a(\omega_{dp})R_b(\omega_{dp})\}^{-1},\tag{52}$$

where

$$\begin{aligned}
R_a(\omega_{dp})R_b(\omega_{dp})&=f(2\omega_1-\omega_2)R_b e^{-i\tau_b(2\omega_1-\omega_2)}\\
&\quad\times\int_0^{\infty}dx\,\omega_0^2(x)\chi_r^2(x,2\omega_1-\omega_2)\tilde{r}(x)\\
&\quad\times\frac{\Delta_{sm}^2(x,2\omega_1-\omega_2)}{\Delta_{sm}^2(x,2\omega_1-\omega_2')}\\
&\quad\times e^{i[\tau_b+2\hat{\tau}_{dp}(x)(\omega_2'-\omega_2)]},
\end{aligned}\tag{53}$$

in Eq. (29) in a geometric series in R_aR_b, gives the contributions to the DPOAE with latencies $\overline{\tau}_{\mathrm{gen}}$ or $\overline{\tau}_{\mathrm{refl}}$ plus multiples of $2\hat{\tau}_{dp}+\tau_b$.

With the same approximations as those used in the three proceeding sections, the contributions with these latencies, along with the $\overline{\tau}_{\rm gen}$ and $\overline{\tau}_{\rm refl}$ latency ones, may be written in the concise form:

$$P_{dp}^{\rm on}(t)=e^{i\omega_{dp}t}\Bigg\{P_l(\omega_1,\omega_2,\omega_{dp})\sum_{n=0}^{\infty}R_a^n(\omega_{dp})R_b^n(\omega_{dp})\times\mathcal{F}_{2n}\left(\frac{\gamma_0\overline{t}_{{\rm gen},n}}{2}\right)+R_a(\omega_{dp})P_r(\omega_1,\omega_2,\omega_{dp})\times\sum_{n=0}^{\infty}R_a^n(\omega_{dp})R_b^n(\omega_{dp})\mathcal{F}_{2n+2}\left(\frac{\gamma_0\overline{t}_{{\rm refl},n}}{2}\right)\Bigg\}+\text{complex conjugate},\tag{54}$$

where

$$\overline{t}_{{\rm gen},n}=t-\overline{\tau}_{{\rm gen},n},\tag{55}$$

$$\overline{t}_{{\rm refl},n}=t-\overline{\tau}_{{\rm refl},n},\tag{56}$$

$$\mathcal{F}_n(\xi)\equiv\Theta(\xi)[1-e_n(\xi)e^{-\xi}],\quad e_n(\xi)\equiv\sum_{s=0}^{n}\frac{1}{s!}\xi^s,\tag{57}$$

and terms of order $(\gamma_0/\omega_2)^n$, $n=1,2,...$, are neglected.

E. The DPOAE signal after the turning off of the f_2 primary

If both primaries are on for a long time preceding $t=0$ and the f_2 primary is turned off at $t=0$, the representation of $P_{dr}^{\rm off}(t)$ is given by Eq. (19), which gives

$$P_{dr}^{\rm off}(t)=A_1e^{i\omega_1t}+(1-\Theta(t))A_2e^{i\omega_2t}+\text{complex conjugate}.\tag{58}$$

The corresponding Fourier expansion of the $2f_1-f_2$ DP ear canal signal is

$$P_{dp}^{\rm off}(t)=\frac{e^{2i\omega_1t}}{2\pi i}\int_{-\infty}^{\infty}d\omega_2'\frac{e^{-i\omega_2't}}{\omega_2'-\omega_2-i\epsilon}P_{dp}^{ss}(2\omega_1-\omega_2')+\text{complex conjugate}.\tag{59}$$

Equation (59) can be written in a more convenient form if the identity

$$\frac{1}{2\pi i}\left(\frac{e^{i\omega_2't}}{\omega_2'-\omega_2-i\epsilon}\right)=\frac{1}{2\pi i}\left(\frac{e^{i\omega_2't}}{\omega_2'-\omega_2+i\epsilon}\right)+e^{i\omega_2't}\delta(\omega_2'-\omega_2),\tag{60}$$

where $\delta(\omega_2'-\omega_2)$ is the Dirac delta function, is used.[3] As a result,

$$P_{dp}^{\rm off}(t)=P_{dp}^{ss}(2\omega_1-\omega_2)e^{i(2\omega_1-\omega_2))t}-P_{dp}^{\rm on}(t)+\text{complex conjugate},\tag{61}$$

where $P_{dp}^{\rm on}(t)$ is given by Eq. (29) and in approximate form by Eq. (54). Thus the decay of the DPOAE from its steady state value is obtained formally by subtracting from the steady state value the originally evolving DPOAE from the build-up stage. As is expected, the various components of the DPOAE decay away in the order of their increase in latency during the build-up phase.

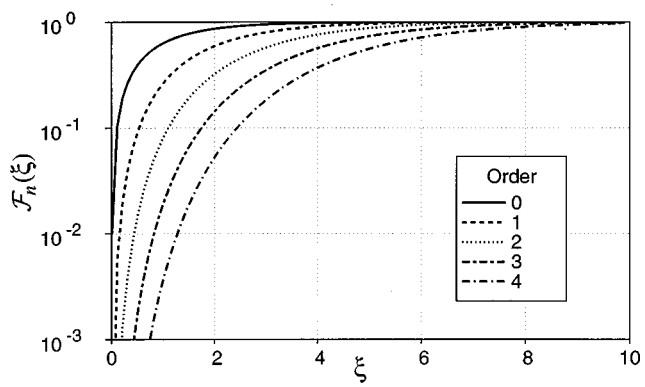

FIG. 1. Comparison of various orders of $\mathcal{F}_n(\xi)$ to $\mathcal{F}_0(\xi)=1-e^{-\xi}$.

F. The DPOAE signal with a pulsed-f_2 primary

Given the previously derived results, it is now a simple matter to write down the equations describing the transient behavior of the DPOAE ear canal signal for a pulsed-f_2 primary. Assuming the f_2 signal turn on is at $T_{\rm on}$, the turn off is at $T_{\rm off}$, and that $T_{\rm off}-T_{\rm on}$ is sufficiently long to allow $P_{dp}^{\rm pulsed}(T_{\rm off}-\epsilon)\rightarrow P_{dp}^{ss}(T_{\rm off})$ (where ϵ a positive infinitesimal), gives

$$P_{dp}^{\rm pulsed}(t)=e^{i\omega_{dp}t}\Bigg\{P_l(\omega_1,\omega_2,\omega_{dp})\sum_{n=0}^{\infty}R_a^n(\omega_{dp})R_b^n(\omega_{dp})\times\mathcal{E}_{2n}(\overline{t}_{{\rm gen},n},T_{\rm on},T_{\rm off})+R_a(\omega_{dp})P_r(\omega_1,\omega_2,\omega_{dp})\times\sum_{n=0}^{\infty}R_a^n(\omega_{dp})R_b^n(\omega_{dp})\mathcal{E}_{2n+2}(\overline{t}_{{\rm refl},n},T_{\rm on},T_{\rm off})\Bigg\}+\text{complex conjugate},\tag{62}$$

where $\mathcal{E}_n(t,T_{\rm on},T_{\rm off})$ is the envelope function given by

$$\mathcal{E}_n(t,T_{\rm on},T_{\rm off})=\begin{cases}t<T_{\rm on}, & 0,\\ T_{\rm on}\leqslant t<T_{\rm off}, & \mathcal{F}_n[\gamma_0(t-T_{\rm on})/2],\\ T_{\rm off}\leqslant t, & 1-\mathcal{F}_n[\gamma_0(t-T_{\rm off})/2].\end{cases}\tag{63}$$

III. PHENOMENOLOGY OF PULSED DPOAEs

It should be noted that the form of Eq. (62) is very similar to what one might naively expect based on the behavior of simple damped harmonic oscillators [hereafter referred to as the harmonic oscillator model, e.g., Talmadge *et al.* (1999)], but with the modification $e^{-x}\rightarrow e_n(x)e^{-x}$. To illustrate the differences in the behavior of the envelope $\mathcal{E}_n(t,T_{\rm on},T_{\rm off})$ from the harmonic oscillator model, the first five orders of $\mathcal{F}_n(\xi)$ are plotted in Fig. 1. Since $\mathcal{F}_0(\xi)=1-e^{-\xi}$ is the purely exponentially varying form expected, the deviation of $\mathcal{F}_n(\xi)$ from this gives the difference between the results of this more detailed analysis from those for the harmonic oscillator model. From Fig. 1, this deviation can be seen to be quite significant even for $\mathcal{F}_2(\xi)$, which is the envelope term present in the $\overline{\tau}_{\rm refl}$ latency component of the DPOAE ear canal signal.

TABLE I. Least-squares fit (LSF) of $P_{dp}^{\text{pulsed}}(t)$, where the model was based on Eq. (62), and was fit to the harmonic oscillator model [i.e., Eq. (62) with $e_n(\xi)\rightarrow 1$]. Shown are the LSF parameter values for γ_0, $\overline{\tau}_{\text{gen},n}$ and $\overline{\tau}_{\text{refl},n}$ versus order of the DPOAE component, for $f_1=2194$ Hz, $f_2=2688$ Hz, and $f_{dp}=1700$ Hz. The LSF values of these parameters are denoted by primes (e.g., $\overline{\tau}'_{\text{gen},n}$ and $\overline{\tau}'_{\text{refl},n}$), and the LSF value of γ_0 is given separately for the $\overline{\tau}_{\text{gen},n}$ ($\gamma'_{0,\text{gen}}$) and for the $\overline{\tau}_{\text{refl},n}$ ($\gamma'_{0,\text{refl}}$) components. The input value of γ_0 was 200 s^{-1} throughout.

Order	$\gamma'_{0,\text{gen}}$ [s^{-1}]	$\overline{\tau}_{\text{gen},n}$ [ms]	$\overline{\tau}'_{\text{gen},n}$ [ms]	$\gamma'_{0,\text{refl}}$ [s^{-1}]	$\overline{\tau}_{\text{refl},n}$ [ms]	$\overline{\tau}'_{\text{refl},n}$ [ms]
0	200	4.5	4.5	70	11.9	17.7
1	70	15.5	21.3	38	22.9	34.7
2	38	26.5	38.3	25	33.9	51.8
3	25	37.5	55.4	18	44.9	67.0
4	18	48.5	72.6	13	55.9	86.2

It is also interesting to note that the family of curves given by $\mathcal{F}_n(\xi)$ can be approximately represented by the function, $1-e^{-\alpha(\xi-\xi_0)}$, and correspondingly, $1-\mathcal{F}_n(\xi)$ can be approximated by $e^{-\alpha(\xi-\xi_0)}$. If one were to use the harmonic oscillator model to fit the DPOAE temporal variation resulting from Eq. (62), one would get a good qualitative fit, though the higher order DPOAE components would have artificially longer delays, and smaller effective damping factors. This point is quantified in Table I, where the agreement between fitted and input parameters for the higher order DPOAE components are seen to get exponentially worse with increasing order. Even at lowest order, $\overline{\tau}_{\text{refl},0}$ is 50% too large, while the fitted damping factor γ_0 is merely 30% of the input value.

In the ensuing discussion, it will be assumed that $|R_b|<|P_r/P_l|$,[4] so that the dominant DPOAE components will be the two components with the shortest latencies. Then,

$$P_{dp}^{\text{pulsed}}(t)\approx e^{i\omega_{dp}t}[P_l(\omega_1,\omega_2,\omega_{dp})\mathcal{E}_0(\overline{t}_{\text{gen},n},T_{\text{on}},T_{\text{off}}) + R_a(\omega_{dp})P_r(\omega_1,\omega_2,\omega_{dp}) \times\mathcal{E}_2(\overline{t}_{\text{refl},n},T_{\text{on}},T_{\text{off}})]+\text{complex conjugate}. \tag{64}$$

Letting

$$L_{\text{gen}}=|P_l|,\quad \Phi_{\text{gen}}=\arg(P_l), \tag{65}$$

$$L_{\text{refl}}=|R_aP_r|,\quad \Phi_{\text{refl}}=\arg(P_r), \tag{66}$$

then it can be seen that the overall behavior of Eq. (64) will be governed by whether or not L_{gen} is greater or less than L_{refl} and whether $\Phi_{\text{gen}}-\Phi_{\text{refl}}$ is approximately an even or an odd multiple of π. As was discussed in Talmadge *et al.* (1999), the experimental measurement in a region where the phases are an odd multiple of π corresponds to a minimum of the DPOAE level fine structure $L_{dp}^{ss}=|P_{dp}^{ss}|$, but also corresponds to a condition under which a null will be observed in level of the DPOAE car canal signal $L_{dp}^{\text{pulsed}}=|P_{dp}^{\text{pulsed}}(t)|$. If $L_{\text{gen}}>L_{\text{refl},}$ then the null will occur after $t=T_{\text{off}}$, and if $L_{\text{gen}}<L_{\text{refl}}$ then the null will occur shortly after $t=T_{\text{on}}$ [see Talmadge *et al.* (1999) for a detailed discussion of this point].

When higher order DPOAE components are included, then in addition, the phase of R_aR_b can further influence the behavior of $L_{dp}^{\text{pulsed}}(t)$. In particular if $\arg(R_aR_b)\cong 2n\pi$, then the higher order internal reflections will arrive in the ear canal approximately in phase with the initial pulses, whereas if $\arg(R_aR_b)\cong(2n+1)\pi$, they will arrive out of phase and therefore produce corresponding interference nulls.

These observations are illustrated in Fig. 2, using a variety of conditions. The conditions are shown (see caption and figure annotations) in which $L_{\text{gen}}>L_{\text{refl}}$ or $L_{\text{gen}}<L_{\text{refl}}$; $\arg(R_aR_b)\approx 2n\pi$ or $\arg(R_aR_b)\approx(2n+1)\pi$; and $\Phi_l\approx\Phi_r+2n\pi$ or $\Phi_l\approx\Phi_r+(2n+1)\pi$. As expected from the above discussion, switching from the case $L_{\text{gen}}>L_{\text{refl}}$ to $L_{\text{gen}}<L_{\text{refl}}$ moves the initial interference null from shortly after the f_2 primary turn off (at $t=T_{\text{off}}=0.150$ s) to shortly after the f_2 primary turn on (at $t=T_{\text{on}}=0.050$ s). Further, this first null will only be seen if the initial two components are approximately out of phase with each other. The phenomenology of the train of higher order pulses, as expected, gives rise to a smoothly varying tail of $L_{dp}^{\text{pulsed}}(t)$ if $\arg(R_aR_b)\cong 2n\pi$, but gives rise to a train of additional nulls if $\arg(R_aR_b)\cong(2n+1)\pi$.

An important element of the behavior of the pulsed DPOAE is the phase behavior of the DPOAE in the region of an interference null. Since the null is the result of the cancellation of the DPOAE due to nearly equal level components with opposite phase, the DPOAE phase will be discontinuous at t_{null}, with the phase jumping from that of the component dominant at times $<t_{\text{null}}$, to the phase of the component which is dominant after t_{null}.

IV. INTERPRETATION OF DPOAE LATENCIES

From the discussion in Talmadge *et al.* (1998, 1999), and in the first three sections of the present paper, it should be clear that the validity of the two-source model in describing both steady state and temporal DPOAE data highlights the danger of interpreting a phase derivative of the steady state DPOAE in terms of a single physical group delay. The complex representation of the steady state DPOAE signal may be decomposed into an infinite series of terms involving increasing powers of the reflectances, R_a and R_b. Each term has a phase behavior which corresponds in the temporal evolution of the pulsed DPOAE to one of the latencies,

$$\overline{\tau}_{\text{gen},n}=\overline{\tau}_{\text{gen}}+n(2\hat{\tau}_{dp}+\tau_b),\quad \overline{\tau}_{\text{refl},n}=\overline{\tau}_{\text{refl}}+n(2\hat{\tau}_{dp}+\tau_b),\quad n=0,1,2,\ldots. \tag{67}$$

In the steady state behavior, the fine structure which has been extensively discussed in Talmadge *et al.* (1998, 1999) is mainly due to the interference of the generator and first reflected cochlear wave components, which correspond in the pulsed DPOAE case to component latencies with $n=0$ in Eq. (67).

As was just mentioned in the Introduction, it has been tacitly assumed by many investigators that the physical group delays or latencies for the production of DPOAEs may be inferred from appropriate phase derivatives of the steady state DPOAEs. For recent reviews of this approach, which include many references to earlier work see, e.g., Bowman *et al.* (1997, 1998). However, as will now be demonstrated, great care must be exercised in attempts to infer physical

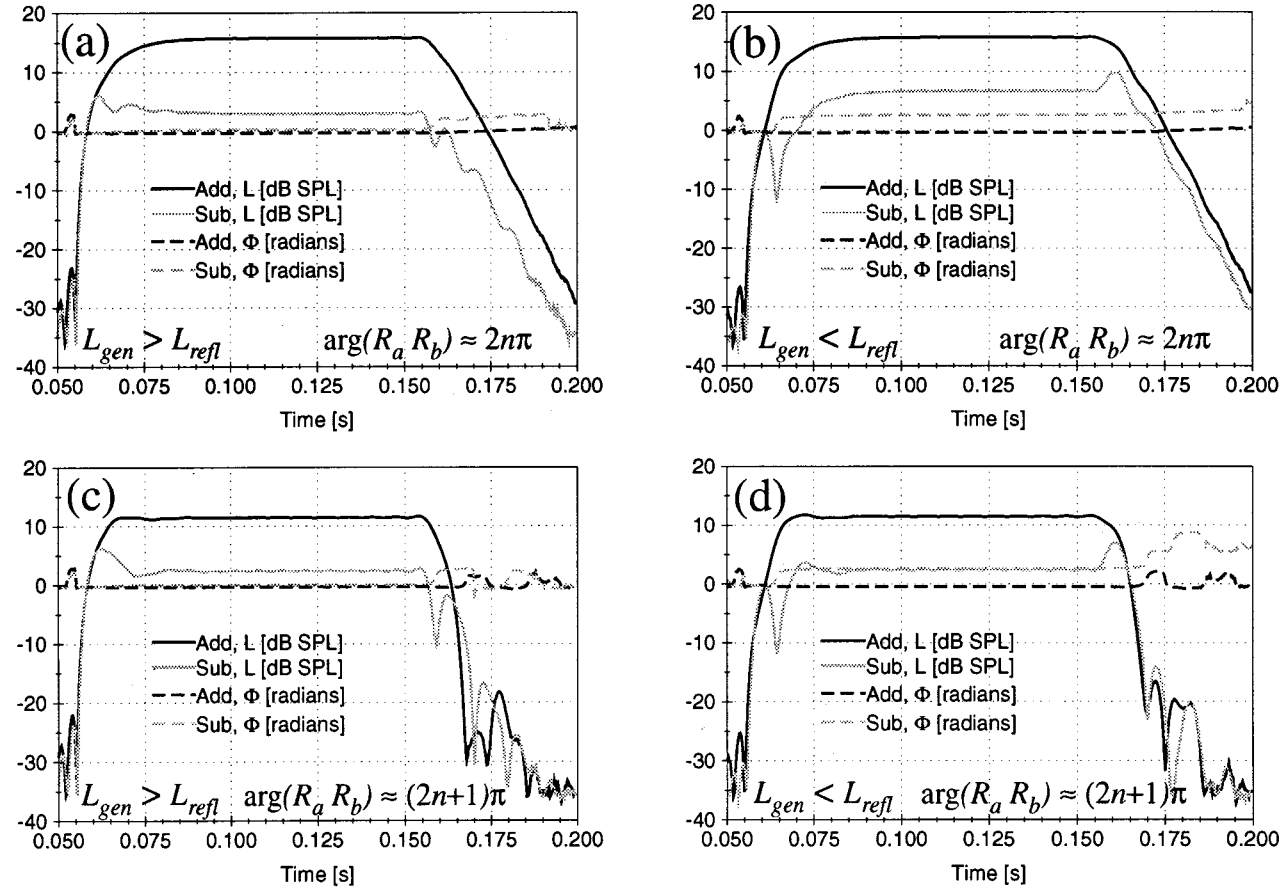

FIG. 2. Model calculations showing the main behaviors that are predicted using Eq. (54). In these figures, the f_2 primary is assumed to be pulsed from 50 ms to 150 ms, with $f_1=2194$ Hz, $f_2=2688$ Hz, and $f_{dp}=1700$ Hz. For each panel, the conditions are shown both where P_l and R_aP_r ''add'' (dark lines; e.g., they *constructively* interfere) and ''subtract'' (gray lines; e.g., they *destructively* interfere).

group delays from phase derivatives of the steady state responses, even in the case of $R_a=0$, for which there is only a single generation region.

The integral expression for the *physical* group delay $\bar{\tau}_{\rm gen}$, obtained from Eqs. (25), (26), (31), and (33), is

$$\bar{\tau}_{\rm gen}=\int_0^{\hat{x}(\omega_2)} dx\,\frac{\partial k(x,\omega_2)}{\partial \omega_2}+\int_0^{\hat{x}(\omega_2)} dx\,\frac{\partial k(x,\omega_{dp})}{\partial(\omega_{dp})}, \quad (68)$$

where the first term is the group delay for the cochlear wave travel from the cochlear base to the generation region, and the second is the group delay for the DP cochlear wave travel from the generation region back to the cochlear base. The integrations of Eq. (68) may be performed by assuming approximate scale invariance (e.g., Zweig and Shera, 1995; Talmadge *et al.*, 1998, 1999) in the form

$$k(x,\omega_2')=k(\omega_2'/\hat{\omega}(x)), \quad (69)$$

where

$$\hat{\omega}(x)\approx\omega_{0c}e^{-k_\omega x}, \quad (70)$$

which gives

$$\frac{\partial k(x,\omega_2')}{\partial \omega_2'}=\frac{1}{k_\omega \omega_2'}\,\frac{\partial k(x,\omega_2')}{\partial x}. \quad (71)$$

Then

$$\begin{aligned}\bar{\tau}_{\rm gen}&\approx\frac{1}{k_\omega\omega_2}(k(\hat{x}(\omega_2),\omega_2)-k(0,\omega_2))\\&\quad+\frac{1}{k_\omega(\omega_{dp})}(k(\hat{x}(\omega_2),\omega_{dp})-k(0,\omega_{dp}))\\&\approx\frac{\hat{k}}{k_\omega\omega_2}+\frac{k(\hat{x}(\omega_2),\omega_{dp})}{k_\omega(\omega_{dp})},\end{aligned} \quad (72)$$

where $\hat{k}$ is the wave number in the peak activity region (Talmadge *et al.*, 1998; Zweig and Shera, 1995), and it has been assumed that

$$k(0,\omega_2)\ll k(\hat{x}_2(\omega_2),\omega_2), \quad (73)$$

$$k(0,\omega_{dp})\ll k(\hat{x}_2(\omega_2),\omega_{dp}). \quad (74)$$

Equation (72) can be further simplified if it is assumed that $\hat{x}(\omega_2)$ corresponds to the long-wavelength region for frequency ω_{dp}. Then

$$k(\hat{x}(\omega_2),\omega_{dp})\approx k_0\frac{\omega_{dp}}{\omega_2}, \quad (75)$$

where k_0 is a constant defined in Eq. (12). In summary,

$$\bar{\tau}_{\rm gen}\approx\frac{\hat{k}+k_0}{k_\omega\omega_2}. \quad (76)$$

Latencies for the $2f_1-f_2$ DPOAE have been associated with the so-called f_1- and f_2-sweep phase derivatives (e.g., Kimberley *et al.*, 1993; O'Mahoney and Kemp, 1995; Moulin and Kemp, 1996a, b; Bowman *et al.*, 1997, 1998; Schneider *et al.*, 1999)

$$\overline{\tau}_{f_2-\text{sweep}} \equiv -\left(\frac{\partial}{\partial \omega_{dp}}\varphi_{\text{gen}}(\omega_1,\omega_2,\omega_{dp})\right)_{\omega_1} = \left(\frac{\partial}{\partial \omega_2}\varphi_{\text{gen}}(\omega_1,\omega_2,\omega_{dp})\right)_{\omega_1} \tag{77}$$

and

$$\overline{\tau}_{f_1-\text{sweep}} \equiv -\left(\frac{\partial}{\partial \omega_{dp}}\varphi_{\text{gen}}(\omega_1,\omega_2,\omega_{dp})\right)_{\omega_2} = -\frac{1}{2}\left(\frac{\partial}{\partial \omega_1}\varphi_{\text{gen}}(\omega_1,\omega_2,\omega_{dp})\right)_{\omega_2}, \tag{78}$$

where $\varphi_{\text{gen}}(\omega_1,\omega_2,\omega_{dp})$ is the approximate phase of the generator-site component of the steady state DPOAE.

The phase derivative $\overline{\tau}_{f_2-\text{sweep}}$ is usually associated with the shortest latency $2f_1-f_2$ DPOAE component for the experimental conditions (steady state f_1 primary, pulsed-f_2 primary) assumed in this paper. The phase derivative $\overline{\tau}_{f_1-\text{sweep}}$ is associated with the case in which the roles of f_1 and f_2 are interchanged.

If the approximate expression,

$$\varphi_{\text{gen}}(\omega_1,\omega_2,\omega_{dp}) = -\int_0^{\hat{x}(\omega_2)} dx[2k(x,\omega_1) - k(x,\omega_2)+k(x,\omega_{dp})], \tag{79}$$

obtained from Eqs. (2) through (14), is used for the steady state DPOAE phase when $R_a=0$, it follows that

$$\overline{\tau}_{f_2-\text{sweep}} = \left[\frac{\partial}{\partial \omega_2}\varphi_{\text{gen}}(\omega_1,\omega_2,\omega_{dp})\right]_{\omega_1} \approx \frac{2}{k_\omega \omega_2}k(\hat{x}(\omega_2),\omega_1)+\frac{2\omega_1 k(\hat{x}(\omega_2),\omega_{dp})}{k_\omega \omega_2 \omega_{dp}} \approx \frac{4\omega_1 k_0}{k_\omega \omega_2^2}, \tag{80}$$

and

$$\overline{\tau}_{f_1-\text{sweep}} = -\frac{1}{2}\left[\frac{\partial}{\partial \omega_1}\varphi_{\text{gen}}(\omega_1,\omega_2,\omega_{dp})\right]_{\omega_2} \approx \frac{2k_0}{k_\omega \omega_2} \tag{81}$$

from an analysis based on the assumption of approximate scale invariance which largely parallels the calculations described by Eqs. (68)–(76). It is thus seen that $\overline{\tau}_{f_2-\text{sweep}}$ [see Eq. (80)] is substantially different from the physical time delay, $\overline{\tau}_{nl}$ [see Eq. (76)], even though both delays do have the property of decreasing with increasing ω_2 (for fixed ω_1).

It is interesting to note that the approximate expressions obtained for $\overline{\tau}_{f_1-\text{sweep}}$ and $\overline{\tau}_{f_2-\text{sweep}}$ imply that

$$\frac{\overline{\tau}_{f_2-\text{sweep}}}{\overline{\tau}_{f_1-\text{sweep}}} \approx \frac{2\omega_1}{\omega_2}, \tag{82}$$

a result that may be useful in interpreting the experimental finding (e.g., Kimberley *et al.*, 1993; O'Mahoney and Kemp, 1995; Moulin and Kemp, 1996a, b; Bowman *et al.*, 1997, 1998; Schneider *et al.*, 1999); and references cited therein) that f_2-sweep group delays tend to be larger than f_1-sweep delays. It should be stressed that in obtaining this result, the contribution to the phase from $\Delta_{sm}(x,\omega_2)$ in Eq. (4) has been neglected.[5] This contribution is connected with the so-called ''filter build-up time,'' which Bowman *et al.* (1998) associate with the *entire* difference between $\overline{\tau}_{f_2-\text{sweep}}$ and $\overline{\tau}_{f_1-\text{sweep}}$. The various issues concerning the phase derivatives in relation to the filter build-up time and the physical time delays in pulsed DPOAEs, and comparisons of relations such as Eq. (82) with results derived from experimental data, will be addressed more carefully and extensively in another paper.

It is also instructive to compare the latencies from Eqs. (80) and (81) to the latency associated with the travel time of a wave packet of frequency ω_2 from the base to its tonotopic position, $\hat{x}_2$. The travel time of a traveling wave of frequency ω from the base to $\hat{x}(\omega)$ can be evaluated using the assumption of scale invariance [see, e.g., Talmadge *et al.* (1998)],

$$\hat{\tau}(\omega) = \int_0^{\hat{x}(\omega)} dx' \frac{\partial k(x',\omega)}{\partial \omega} \cong \frac{1}{k_\omega \omega}\int_0^{\hat{x}(\omega)} dx' \frac{\partial k(x',\omega)}{\partial x'} = \frac{\hat{k}}{k_\omega \omega}, \tag{83}$$

so that $\hat{\tau}_2=\hat{k}/k_\omega\omega_2$. From swept$-f_1$ measurements [Talmadge *et al.* (1998)], $\hat{k}\approx 3.6k_0$, which gives

$$\overline{\tau}_{f_1-\text{sweep}} \approx 0.6\hat{\tau}_2, \quad \overline{\tau}_{f_2-\text{sweep}} \approx 1.1\frac{\omega_1}{\omega_2}\hat{\tau}_2, \quad \overline{\tau}_{\text{fixed-ratio}} \approx 0, \quad \overline{\tau}_{\text{gen}} \approx 1.3\hat{\tau}_2, \tag{84}$$

where the group delay for sweeping $2f_1-f_2$ while fixing the ratio f_2/f_1 (i.e., the ''fixed-ratio'' paradigm) has also been included for comparison. None of the conventional delays correspond to $\hat{\tau}_2$, although $\overline{\tau}_{f_2-\text{sweep}} \approx \hat{\tau}_2$ for $\omega_2/\omega_1 \cong 1.2$. An important implication of this result is that the measured $\overline{\tau}_{f_2-\text{sweep}}$ group delay should be a function of ω_2/ω_1.

An even larger problem is encountered in attempting to associate the group delay with $\hat{\tau}_2$ when the DPOAE reflection site component is either comparable or dominant. As was discussed in Talmadge *et al.* (1999), the presence of two DPOAE components with different phase dependencies on the frequencies involved implies that there will be a group delay fine structure, which will in general either strongly correlate with or anti-correlate with the level fine structure. When significant group delay fine structure is present, in

terms of group delays for wave packet travel between the cochlear base and the DP generation region is clearly problematic.

The ''worst case'' scenario is when the reflection site component is dominant. For this case, the equivalent group delays can be computed using the phase equation corresponding to Eq. (79):

$$\varphi_{\text{refl}}(\omega_1,\omega_2,\omega_{dp}) = -\int_0^{\hat{x}(\omega_2)} dx[2k(x,\omega_1) - k(x,\omega_2) - k(x,\omega_{dp})] - \frac{2\hat{k}}{k_\omega}\log\left(\frac{\omega_{dp}}{\omega_{0c}}\right), \quad (85)$$

where $\varphi_{\text{refl}}(\omega_1,\omega_2,\omega_{dp})$ is the approximate phase of the reflection-site component of the steady state DPOAE and the $(2\hat{k}/k_\omega)\log(\omega_{dp}/\omega_{0c})$ term is the approximate phase shift due to the reflection of the DPOAE from its best place (e.g., Shera and Zweig, 1993; Zweig and Shera, 1995; see also Talmadge and Tubis, 1993; Talmadge *et al.*, 1998). The group delays associated with Eq. (85) are

$$\overline{\tau}[\text{refl}]_{f_1-\text{sweep}} = \overline{\tau}[\text{refl}]_{f_2-\text{sweep}} = \overline{\tau}[\text{refl}]_{\text{fixed-ratio}} = \frac{2\hat{k}}{k_\omega \omega_{dp}} = 2\hat{\tau}_{dp}, \quad (86)$$

where Eq. (83) has been used in obtaining this result.

Finally, if $\hat{\tau}_2$ can be measured via some other means (such as TEOAE measurements), then, since $\hat{k}$ is known from measurements of the spacing of fine structure, the remaining uncertain parameter k_0 can be determined:

$$k_0 \approx \left(\frac{\overline{\tau}_{\text{gen}}}{\hat{\tau}_2} - 1\right)\hat{k}. \quad (87)$$

The inter-relationship given between the various parameters of the cochlear model, which result from comparing different OAE fine structures and different DPOAE paradigms, may provide an important test of the theoretical framework given in Talmadge *et al.* (1998) as utilized here, as the cochlear models and theoretical formalism continue to be refined and as the experimental data continue to improve.

V. SUMMARY AND CONCLUSIONS

Approximate expressions [Eqs. (54) and (61)] have been derived for the explicit time dependence of the $2f_1-f_2$ DPOAE under conditions of a steady state f_1 primary and an f_2 primary which is turned on and off. The approximations made were sufficient to allow the evaluation of the Fourier integral for the time dependence by use of the calculus of residues. Major simplifications were introduced by the neglect of the complications from (1) branch cuts associated with the ω_2' dependence in Eqs. (10)–(12), (2) time-delayed stiffness terms in the determination of the complex ω_2' zeroes of $\Delta_{sm}(x,\omega_2')$, and (3) the continuous character (x dependencies) of the latencies of the various group delay terms (see Sec. II B).

On the basis of some general notions about group velocity and group delay (e.g., Lighthill, 1978), most of the temporal details of the simplified expressions could, of course, have been written down intuitively. The fact that the characteristic time for the transient build-up (or decay) of the DPOAE components of various latencies is $2/\gamma_0$ is also expected on the basis of the well-known dynamic properties of simple damped harmonic oscillators. However, the behavior of the envelope of the DPOAE transient, as determined by this analysis, differs in important ways from that expected from the harmonic oscillator model, as is illustrated by Fig. 1 and by Table I. As shown in this table, even the lowest order (shortest latency) reflected DPOAE component differs significantly from that expected on the basis of the harmonic oscillator model.

Most of the transient DPOAE phenomenology illustrated by Fig. 2 have been experimentally observed and reported on in Talmadge *et al.* (1999). Included in that paper are measurements in which the reflected components are modified by the placement of an external suppressing tone near in frequency to the DPOAE. In this way, the relative levels of the DPOAEs can be modified. When this is done, the pulsed DPOAE level and phase vary in a manner which is qualitatively consistent with the theory presented in this paper.

A future direction of research will be to fit Eq. (64) directly to experimental measurement. If the level of approximation given by this paper is sufficient, this method could yield direct measurements of the values of R_aR_b, P_l, and R_aP_r as a function of level, DPOAE frequency, and primary frequency ratio, as well the effective damping factor $\gamma_0/2$ and the various latencies, $\overline{\tau}_{\text{gen},n}$ and $\overline{\tau}_{\text{refl},n}$. Because the measurements are based on measurements at a single DPOAE frequency, the analysis of this class of data may be more robust than methods based on measurement of the steady state DPOAE behavior across frequency.

The exercise of determining the approximations that are needed to to obtain these results is also useful in its own right. In particular, it should prompt further investigations of the extent to which the simple behaviors in Eqs. (54) and (61) describe actual experimental data and/or the results of time-domain cochlear model simulations. Some of the experimental implications of the results have already been explored in Talmadge *et al.* (1999). It would also be interesting to apply the formalism to more realistic two- and three-dimensional cochlear models.

ACKNOWLEDGMENTS

We wish to thank Professor Glenis R. Long, Sumit Dhar, and Lauren A. Shaffer for many useful discussions on the topies of this paper. We would also like to acknowledge the careful reviews by Chris Shera and an anonymous reviewer. This research was supported in part by NIH/NICD Grants No. R01 DC00307 and No. R29 DC03094.

APPENDIX A. FREQUENTLY USED SYMBOLS AND THEIR MEANING

Mathematical symbols frequently used in this study and their meaning are summarized below. For additional notational definitions, see also Talmadge *et al.* (1998). In cases for which the symbol has a defining equation, its corresponding equation number is also included.

Operators

$\arg(z)$	phase of z
$\lvert z\rvert$	magnitude of z
$\hat{A}$	denotes a quantity evaluated at the activity pattern maximum
$\tilde{A}$	denotes that the quantity A contains a random component
$\overline{A}$	denotes an effective value, usually as the result of combining several more fundamental quantities

Independent variables and physical quantities

f	frequency with units of inverse length.
P	pressure
t	time
x	position along basilar membrane ($x=0$ corresponds to base)
λ	wavelength
ω	angular frequency ($2\pi\times f$)
φ	phase
Φ	total or ''unwrapped'' phase
ξ	linear displacement, also dimensionless variable
ϵ	a positive infinitesimal

Constants

$A_{1,2}$	steady state amplitudes of lower, higher frequency primaries
ϵ_γ	nonlinear damping strength
$f_{1,2}$	frequencies of lower, higher frequency primaries
f_{dp}	$2f_1-1f_2$; frequency of DP under consideration
k	wave number ($2\pi/\lambda$), also used to signify quantities
k_0	geometrical wave number constant [see Talmadge *et al.* (1998)]
k_ω	exponential constant for frequency map
$\hat{k}$	real part of wave number at activity pattern maximum
T_{on}	time of f_2 primary signal turn on
T_{off}	time of f_2 primary signal turn off
$\omega_{0c,1c}$	exponential coefficient and offset of frequency map

Functions

$\Theta(x)$	Heaviside Theta function [Eq. (18)]
$e_n(\xi)$	truncated exponential series [Eq. (57)]
$\mathcal{F}_n(\xi)$	DPOAE transient function for a f_2 primary turned on at $t=0$ [Eq. (57)]
$\mathcal{E}_n(t,T_{\text{on}},T_{\text{off}})$	envelope function for a pulsed-f_2 primary [Eq. (63)]
$W_0(\omega)$	the Wronskian of $\psi_{r,l}(x,\omega)$ [$W_0(\omega)=\psi_r(x,\omega)\psi_l'(x,\omega)-\psi_r'(x,\omega)\psi_l(x,\omega)$]

Pressure

$P_{dr}^{ss}(t)$	steady state ''calibrated'' driving pressure [Eq. (1)]
$P_{dr}^{\text{on}}(t)$	a driving pressure that is turned on at $t=0$ [Eq. (17)]
$P_{dr}^{\text{off}}(t)$	a driving pressure that is turned off at $t=0$ [Eq. (19)]
$P_{dp}^{ss}(\omega_1,\omega_2,\omega_{dp})$	steady state DPOAE ear canal amplitude [Eq. (2)]
$P_{dp}^{\text{on}}(t)$	ear canal DPOAE level associated with a turn on of the f_2 primary at $t=0$ [Eq. (20)]
$P_{dp}^{\text{off}}(t)$	ear canal DPOAE level associated with a turn off of the f_2 primary at $t=0$ [Eq. (59)]
$P_{dp}^{\text{gen}}(t)$	ear canal DPOAE level associated with a turn on of the f_2 primary at $t=0$, for the initial basally moving component that was directly transmitted to the ear canal [Eq. (43)]
$P_{dp}^{\text{refl}}(t)$	ear canal DPOAE level associated with a turn on of the f_2 primary at $t=0$, for the initial apically moving component that was reflected at its best place, and then transmitted to the ear canal [Eq. (45)]
$P_l(\omega_1,\omega_2,\omega_{dp})$	ear canal DPOAE amplitude due to an initially generated basally moving DP component [Eq. (3)]
$R_a(\omega_{dp})\times P_r(\omega_1,\omega_2,\omega_{dp})$	ear canal DPOAE amplitude due to an initially generated apically moving DP component [Eq. (3)]

Latencies

$\tau(x,\omega)$	travel time of a wave packet of central frequency ω from the base to position x [Eq. (26)]
$\hat{\tau}_2(x)$	travel time of a wave packet of central frequency ω_2 from the base to position x [Eq. (25)]
$\hat{\tau}_2$	travel time of a wave packet of central frequency ω_2 from the base to its tonotopic location [Eq. (33)]
$\hat{\tau}_{dp}(x)$	travel time of a wave packet of central frequency ω_{dp} from the base to position x [Eq. (28)]
$\hat{\tau}_{dp}$	travel time of an ω_{dp} wave packet of central frequency from the base to its tonotopic location [Eq. (33)]

$\overline{\tau}_{\text{gen}}$ latency of the DPOAE transient response associated with a change in the f_2 signal component, for the DPOAE component initially produced at the generator site [Eq. (31)]

$\overline{\tau}_{\text{refl}}$ latency of the DPOAE transient response associated with a change in the f_2 signal component, for the initial apically moving DP component, which is transmitted to the ear canal after being reflected from the region of the DP best place [Eq. (32)]

$\overline{\tau}_{\text{gen},n}$ latency of the DPOAE transient response associated with a change in the f_2 signal component, for the initial basally moving DP component, which is transmitted to the ear canal after being multiply internally reflected n times [Eq. (34)]

$\overline{\tau}_{\text{refl},n}$ latency of the DPOAE transient response associated with a change in the f_2 signal component, for the initial apically moving DP component, which is transmitted to the ear canal after being multiply internally reflected n times [Eq. (35)]

APPENDIX B. A PERTURBATIVE CALCULATION OF THE $2f_1-f_2$ DISTORTION PRODUCT UNDER STEADY STATE AND PULSED PRIMARY CONDITIONS IN A SIMPLE OSCILLATOR MODEL

Consider a simple driven nonlinear oscillator described by

$$\ddot{x}+\omega_{0c}^2 x+R_0\dot{x}+R_2x^3=f(t). \tag{B1}$$

In the case of a steady state forcing function,

$$f(t)=\frac{A_1}{2}e^{i\omega_1 t}+\frac{A_2}{2}e^{i\omega_2 t}+\text{complex conjugate}, \tag{B2}$$

the steady state response, to first order in R_2, is (e.g., Nayfeh and Mook, 1979),

$$\begin{aligned} x_{\text{steady state}}(t)=&\frac{A_1}{2}\frac{e^{i\omega_1 t}}{-\omega_1^2+\omega_{0c}^2+i\omega_1 R_0}\\ &+\frac{A_2}{2}\frac{e^{i\omega_2 t}}{-\omega_2^2+\omega_{0c}^2+i\omega_2 R_0}\\ &+A_{dp}(\omega_1,\omega_2)e^{i(2\omega_1-\omega_2)t}\\ &+\text{complex conjugate}, \end{aligned} \tag{B3}$$

where

$$A_{dp}(\omega_1,\omega_2)=-\frac{3}{8}A_1^2A_2^*R_2\frac{1}{(-\omega_1^2+\omega_{0c}^2+i\omega_1R_0)^2(-\omega_2^2+\omega_{0c}^2+i\omega_2R_0)^*}\,\frac{1}{(-(2\omega_1-\omega_2)^2+\omega_{0c}^2+iR(2\omega_1-\omega_2))}, \tag{B4}$$

the nonlinear contributions to the ω_1 and ω_2 components are neglected, and where only the ω_1, ω_2, and $2\omega_1-\omega_2$ components of the response are indicated.

Now consider the response to a force with a steady state ω_1 component and a pulsed ω_2 one,

$$\begin{aligned} f(t)=&\frac{A_1}{2}e^{i\omega_1 t}+\Theta(t)\frac{A_2}{2}e^{i\omega_1 t}+\text{complex conjugate}\\ =&\frac{A_1}{2}e^{i\omega_1 t}+\frac{A_2}{2}\frac{1}{2\pi i}\int_{-\infty}^{\infty}d\omega_2'\frac{e^{i\omega_2' t}}{\omega_2'-\omega_2-i\epsilon}\\ &+\text{complex conjugate}. \end{aligned} \tag{B5}$$

The perturbative response, to first order in R_2, is now given by

$$\begin{aligned} x(t)=&\frac{A_1}{2}\frac{e^{i\omega_1 t}}{(-\omega_1^2+\omega_{0c}^2+i\omega_1R_0)}+\frac{A_2}{2}\frac{1}{2\pi i}\\ &\times\int_{-\infty}^{\infty}d\omega_2'\frac{e^{i\omega_2' t}}{i(\omega_2'-\omega_2-i\epsilon)(-\omega_2'^2+\omega_{0c}^2+i\omega_2'R_0)}\\ &+\text{complex conjugate}+x_{dp}(t)+\ldots, \end{aligned} \tag{B6}$$

where

$$\begin{aligned} x_{dp}(t)=&-\frac{1}{2\pi i}\int_{-\infty}^{\infty}d\omega_2'\frac{e^{i(2\omega_1-\omega_2')t}A_{dp}(\omega_1,\omega_2')}{(\omega_2'-\omega_2-i\epsilon)^*}\\ &+\ldots+\text{complex conjugate}. \end{aligned} \tag{B7}$$

Equation (B7) is the correspondent of Eq. (20) in the case of the auditory periphery. The simple analytic structure of $A_{dp}(\omega_1,\omega_2)$ allows an exact evaluation of the integral of Eq. (B7) by use of the calculus of residues. The evaluation gives 0 for $t<0$ and the steady state response, $A_{dp}(\omega_1,\omega_2)e^{i(2\omega_1-\omega_2)t}+\text{complex conjugate}$, plus transient terms for $t>0$.

[1]If the stimulation level is sufficiently low, the effects of nonlinearity can be self-consistently expanded in a perturbative fashion, as was done by Talmadge *et al.* (1998) to first order in the perturbative expansion. This procedure linearizes the system of equations and in particular allows the direct application of the Fourier method employed in this paper, for the effect of a pulsed-f_2 primary on the $2f_1-f_2$ DPOAE. As higher order nonlinear effects are included, the relationship between the levels of the primaries and the resulting level of the distortion product now depends on contributions from other frequency components of the cochlear response, (such as $3\omega_1, 3\omega_2, \ldots$), which can no longer be neglected. In this case, the Fourier method is in general still applicable, although its application becomes increasingly more complex with increasing order of the perturbative expansion. At sufficiently high stimulation levels, the perturbative solution fails to converge, and another approach, such as that utilized by Kanis and de Boer (e.g., Kanis and de Boer, 1997) must be employed in order to relate

the primary pressure levels to the resulting DPOAE pressure. In this limit, the Fourier method utilized in this paper is no longer applicable.

[2]In practice, it is necessary to digitally filter the ear canal signal in order to extract the DPOAE waveform. Typically this filter has a width no larger than 300 Hz, which imposes a temporal smearing of the DPOAE waveform on the order of 3 ms. Even at moderately low frequencies (e.g., $f=1000\,\mathrm{Hz}$), the delay associated with the slow stiffness feedback $\sim 1.75/1000\,\mathrm{Hz}=1.75$ ms. Consequently, except at low frequencies, direct effects of the stiffness feedback may be safely neglected, and the only effect of the stiffness feedback term is to shift the place-frequency map and to modify the effective value of γ_0.

[3]This identity can be derived by comparing Eqs. (17) and (19), which gives

$$\frac{1}{2\pi i}\int_{-\infty}^{\infty} d\omega_2'\left(\frac{e^{i\omega_2' t}}{\omega_2'-\omega_2-i\epsilon}-\frac{e^{i\omega_2' t}}{\omega_2'-\omega_2+i\epsilon}\right)=e^{i\omega_2 t}[\Theta(t)+1-\Theta(t)]=e^{i\omega_2 t}.$$

Comparison of the left- and right-hand sides of this equation gives

$$\frac{1}{2\pi i}\int_{\infty}^{-\infty} d\omega_2'\left(\frac{e^{i\omega_2' t}}{\omega_2'-\omega_2-i\epsilon}-\frac{e^{i\omega_2' t}}{\omega_2'-\omega_2+i\epsilon}\right)=\int_{-\infty}^{\infty} d\omega_2' e^{i\omega_2' t}\delta(\omega_2'-\omega_2).$$

An alternative way of proving this result is to note that

$$\lim_{\epsilon\to 0_+}\frac{1}{2\pi i}\left(\frac{1}{\omega_2'-\omega_2-i\epsilon}-\frac{1}{\omega_2'-\omega_2+i\epsilon}\right)=\frac{1}{\pi}\lim_{\epsilon\to 0_+}\left[\frac{\epsilon}{\epsilon^2+(\omega_2'-\omega_2)^2}\right]$$

is a well known representation of $\delta(\omega_2'-\omega_2)$ (e.g., Arfken and Weber, 1995, p. 83).

[4]To understand this caveat, consider the leading terms in the expansion of Eq. (3) under the assumption that $|R_a|\ll 1$:

$$P_{dp}^{ss}=P_l\left[1+\left(\frac{P_r}{P_l}-R_b\right)R_a+\ldots\right].$$

This expansion follows from the fact that $|R_b|\leqslant 1$, and the frequency dependence of the various terms has been ignored for brevity. In this expansion. P_{dp}^{ss} will be dominated by the P_l and R_aP_r terms if $|R_b|<|P_r/P_l|$. The effect of $|R_b|>|P_r/P_l|$ will be explored in a future paper.

[5]It might be suggested that neglect of the ''filter build-up time'' can be justified only in a scale-invariant cochlear model. However, even in cochlear models with a significant scale-invariance violations (e.g., one which has the Q of the activity pattern maximum varying from 15 at the base to 5 at the apex), it turns out that the corresponding variations in $\Delta_{sm}(x,\omega)$ are still very small over the region of the activity pattern maximum, and can be safely neglected.

Arfken, G. B., and Weber, H. J. (**1995**). *Mathematical Methods for Physicists*, 4th ed. (Academic, San Diego).

Bowman, D. M., Brown, D. K., Eggermont, J. J., and Kimberley, B. P. (**1997**). ''The effect of sound intensity on f_1-sweep and f_2-sweep distortion product otoacoustic emissions phase delay estimates in human adults,'' J. Acoust. Soc. Am. **101**, 1550–1559.

Bowman, D. M., Eggermont, J. J., Brown, D. K., and Kimberly, B. P. (**1998**). ''Estimating cochlear filter response properties from distortion product otoacoustic emission (DPOAE) phase delay measurements in normal hearing human adults,'' Hear. Res. **119**, 14–26.

Brown, A. M., Gaskill, S. A., and Williams, D. M. (**1992**). ''Mechanical filtering of sound in the inner ear,'' Proc. R. Soc. London, Ser. B **250**, 29–34.

Brown, A. M., Harris, F. P., and Beveridge, H. A. (**1996**). ''Two sources of acoustic distortion products from the human cochlea,'' J. Acoust. Soc. Am. **100**, 3260–3267.

Brown, A. M., Gaskill, S. A., Carlyon, R. P., and Williams, D. M. (**1993**). ''Acoustic distortion as a measure of frequency selectivity: relation to psychophysical equivalent rectangular bandwidth,'' J. Acoust. Soc. Am. **93**, 3291–3297.

Gaskill, S. A., and Brown, A. M. (**1996**). ''Suppression of human acoustic distortion product: Dual origin of $2f_1-f_2$,'' J. Acoust. Soc. Am. **100**, 3268–3274.

Hall, J. L. (**1974**). ''Two-tone distortion products in a nonlinear model of the basilar membrane,'' J. Acoust. Soc. Am. **56**, 1818–1828.

He, N.-J., and Schmiedt, R. A. (**1993**). ''Fine structure of the $2f_1-f_2$ acoustic distortion product: Changes with primary level,'' J. Acoust. Soc. Am. **94**, 2659–2669.

He, N.-J., and Schmiedt, R. A. (**1996**). ''Effects of aging on the fine structure of the $2f_{(1)}-f_{(2)}$ acoustic distortion product,'' J. Acoust. Soc. Am. **99**, 1012–1015.

He, N.-J., and Schmiedt, R. A. (**1997**). ''Fine structure of the $2f_1-f_2$ acoustic distortion product: Effects on primary level and frequency ration,'' J. Acoust. Soc. Am. **101**, 3554–3565.

Kanis, L. J., and de Boer, E. (**1997**). ''Frequency dependence of acoustic distortion products in a locally active model of the cochlea,'' J. Acoust. Soc. Am. **101**, 1527–1531.

Kemp, D. T., and Brown, A. M. (**1983**). ''An integrated view of the cochlear mechanical nonlinearities observable in the ear canal,'' in *Mechanics of Hearing*, edited by E. de Boer and M. A. Viergever (Martinus Nijhoff, The Hague, The Netherlands), pp. 75–82.

Kimberley, B. P., Brown, D. K., and Eggermont, J. J. (**1993**). ''Measuring human cochlear traveling wave delay using distortion product emission phase responses,'' J. Acoust. Soc. Am. **94**, 1343–1350.

Kummer, P., Janssen, T., and Arnold, W. (**1995**). ''Suppression tuning characteristics of the $2f_1-f_2$ distortion product otoacoustic emission in humans,'' J. Acoust. Soc. Am. **98**, 197–210.

Lighthill, J. (**1978**). *Waves in Fluids* (Cambridge University Press, Cambridge), pp. 237–244.

Martin, G. K., Jassir, D., Stagner, B. B., Whitehead, M. L., and Lonsbury-Martin, B. L. (**1998**). ''Locus of generation for the $2f1-f2$ vs $2f2-f1$ distortion-product otoacoustic emissions in normal-hearing humans revealed by suppression tuning, onset latencies, and amplitude correlations,'' J. Acoust. Soc. Am. **103**, 1957–1971.

Mathews, J., and Walker, R. (**1964**). *Mathematical Methods of Physics* (Benjamin, New York).

Mills, D. M. (**1997**). ''Interpretation of distortion product otoacoustic emission measurements: I. Two stimulus tones,'' J. Acoust. Soc. Am. **102**, 413–429.

Moulin, A., and Kemp, D. T. (**1996a**). ''Multicomponent acoustic distortion product otoacoustic emission phase in humans. I. General characteristics,'' J. Acoust. Soc. Am. **100**, 1617–1639.

Moulin, A., and Kemp, D. T. (**1996b**). ''Multicomponent acoustic distortion product otoacoustic emission phase in humans. II. Implications for distortion product generation,'' J. Acoust. Soc. Am. **100**, 1640–1666.

Nayfeh, A. T., and Mook, D. T. (**1979**). *Nonlinear Oscillations* (Wiley, New York), Chap. 4.

O'Mahoney, C. F., and Kemp, D. (**1995**). ''Distortion product otoacoustic emission delay measurement in humans,'' J. Acoust. Soc. Am. **97**, 3721–3735.

Schneider, S., Prijs, V. F., and Schoonhoven, R. (**1999**). ''Group delays of distortion product otoacoustic emissions in the guinea pig,'' J. Acoust. Soc. Am. **105**, 2722–2730.

Shera, C. A., and Zweig, G. (**1992**). ''Analyzing reverse middle-ear transmission: Noninvasive *gedankenexperiments*,'' J. Acoust. Soc. Am. **92**, 1371–1381.

Shera, C. A., and Zweig, G. (**1993**). ''Order from chaos: resolving the paradox of periodicity in evoked otoacoustic emission,'' in *Biophysics of Hair Cell Sensory Systems*, edited by H. Duifhuis, J. W. Horst, P. van Dijk, and S. M. van Netten (World Scientific, Singapore), pp. 54–63.

Stover, L. J., Neely, S. T., and Gorga, M. P. (**1996**). ''Latency and multiple sources of distortion product emissions,'' J. Acoust. Soc. Am. **99**, 1016–1024.

Sun, X. M., Schmiedt, R. A., He, N.-J., and Lam, C. F. (**1994a**). ''Modeling the fine structure of the $2f_{(1)}-f_{(2)}$ acoustic distortion product. 1. Model development,'' J. Acoust. Soc. Am. **96**, 2166–2174.

Sun, X. M., Schmiedt, R. A., He, N.-J., and Lam, C. F. (**1994b**). ''Modeling the fine structure of the $2f_{(1)}-f_{(2)}$ acoustic distortion product. 2. Model evaluation,'' J. Acoust. Soc. Am. **96**, 2175–2183.

Talmadge, C., and Tubis, A. (**1993**). ''On modeling the connection between spontaneous and evoked otoacoustic emissions,'' in *Biophysics of Hair Cell Sensory Systems*, edited by H. Duifhuis, J. W. Horst, P. van Dijk, and S. M. van Netten (World Scientific, Singapore), pp. 25–32.

Talmadge, C., Tubis, A., Piskorski, P., and Long, G. R. (**1997**). ''Modeling otoacoustic emission fine structure,'' in *Diversity in Auditory Mechanics*, edited by E. Lewis, G. Long, R. Lyon, P. Narins, and C. Steele (World Scientific, Singapore), pp. 462–471.

Talmadge, C. L., Long, G. R., Tubis, A., and Dhar, S. (**1999**). ''Experimental confirmation of the two-source interference model for the fine structure of distortion product otoacoustic emissions,'' J. Acoust. Soc. Am. **105**, 275–292.

Talmadge, C. L., Tubis, A., Long, G. R., and Piskorski, P. (**1998**). ''Modeling otoacoustic emission and hearing threshold fine structures,'' J. Acoust. Soc. Am. **104**, 1517–1543.
Zweig, G. (**1991**). ''Finding the impedance of the organ of Corti,'' J. Acoust. Soc. Am. **89**, 1229–1254.
Zweig, G., Lipes, R., and Pierce, J. R. (**1976**). ''The cochlear compromise,'' J. Acoust. Soc. Am. **59**, 975–982.
Zweig, G., and Shera, C. A. (**1995**). ''The origins of periodicity in the spectrum of evoked otoacoustic emissions,'' J. Acoust. Soc. Am. **98**, 2018–2047.

Distortion product otoacoustic emission test performance when both $2f_1-f_2$ and $2f_2-f_1$ are used to predict auditory status

Michael P. Gorga,[a] Kimberly Nelson, Thomas Davis, Patricia A. Dorn, and Stephen T. Neely
Boys Town National Research Hospital, Omaha, Nebraska 68131

(Received 12 October 1999; revised 11 January 2000; accepted 12 January 2000)

The objective of this study was to determine whether distortion product otoacoustic emission (DPOAE) test performance, defined as its ability to distinguish normal-hearing ears from those with hearing loss, can be improved by examining response and noise amplitudes at $2f_1-f_2$ and $2f_2-f_1$ simultaneously. In addition, there was interest in knowing whether measurements at both DPs and for several primary frequency pairs can be used in a multivariate analysis to further optimize test performance. DPOAE and noise amplitudes were measured at $2f_1-f_2$ and $2f_2-f_1$ for 12 primary levels (L_2 from 10 to 65 dB SPL in 5-dB steps) and 9 pairs of primary frequencies (0.5 to 8 kHz in 1/2-octave steps). All data were collected in a sound-treated room from 70 subjects with normal hearing and 80 subjects with hearing loss. Subjects had normal middle-ear function at the time of the DPOAE test, based on standard tympanometric measurements. Measurement-based stopping rules were used such that the test terminated when the noise floor around the $2f_1-f_2$ DP was $\leqslant -30$ dB SPL or after 32 s of artifact-free averaging, whichever occurred first. Data were analyzed using clinical decision theory in which relative operating characteristics (ROC) curves were constructed and areas under the ROC curves were estimated. In addition, test performance was assessed by selecting the criterion value that resulted in a sensitivity of 90% and determining the specificity at that criterion value. Data were analyzed using traditional univariate comparisons, in which predictions about auditory status were based only on data obtained when f_2=audiometric frequency. In addition, multivariate analysis techniques were used to determine whether test performance can be optimized by using many variables to predict auditory status. As expected, DPOAEs were larger for $2f_1-f_2$ compared to $2f_2-f_1$ in subjects with normal hearing. However, noise amplitudes were smaller for $2f_2-f_1$, but this effect was restricted to the lowest f_2 frequencies. A comparison of signal-to-noise ratios (SNR) within normal-hearing ears showed that the $2f_1-f_2$ DP was more frequently characterized by larger SNRs compared to $2f_2-f_1$. However, there were several subjects in whom $2f_2-f_1$ produced a larger SNR. ROC curve areas and specificities for a fixed sensitivity increased only slightly when data from both DPs were used to predict auditory status. Multivariate analyses, in which the inputs included both DPs for several primary frequency pairs surrounding each audiometric frequency, produced the highest areas and specificities. Thus, DPOAE test performance was improved slightly by examining data at two DP frequencies simultaneously. This improvement was achieved at no additional cost in terms of test time. When measurements at both DPs were combined with data obtained for several primary frequency pairs and then analyzed in a multivariate context, the best test performance was achieved. Excellent test performance (ROC) curve areas $>0.95\%$ and specificities $>92\%$ at all frequencies, including 500 Hz, were achieved for these conditions. Although the results described should be validated on an independent set of data, they suggest that the accuracy with which DPOAE measurements identify auditory status can be improved with multivariate analyses and measurements at multiple DPs. [S0001-4966(00)04204-1]

PACS numbers: 43.64.Jb [BLM]

INTRODUCTION

Distortion product otoacoustic emissions (DPOAEs) are produced when two tones slightly different in frequency are presented to ''normally functioning'' ears. In humans, the most prominent DPOAE occurs at the $2f_1-f_2$ cubic distortion product. This distortion product occurs at a frequency that is about 1/2 octave lower than the higher frequency (f_2) of the primary frequency pair. It generally is accepted that this distortion product is produced at a place close to where f_2 is represented (e.g., Brown and Kemp, 1984; Harris *et al.*, 1992; Kummer *et al.*, 1995; Gaskill and Brown, 1996). Thus, it is response amplitude at the $2f_1-f_2$ frequency that typically is measured when DPOAEs are used to assess cochlear function for the f_2 place. This means that cochlear status at f_2 is predicted from response amplitudes at a lower frequency, $2f_1-f_2$. DPOAEs must be resolved in a background of acoustic noise, whose energy increases as frequency decreases (see, for example, Gorga *et al.*, 1993a). For some lower frequencies, especially f_2 frequencies $\leqslant$1 kHz, it

[a]Electronic mail: gorga@boystown.org

is difficult to measure a response under routine conditions. One reason for this occurrence is the increased noise levels that typically are observed when DPOAEs are measured at lower f_2 frequencies (e.g., Gorga *et al.*, 1993a). Difficulties in measuring DPOAEs for lower f_2's may be less a consequence of differences in the amount of distortion produced by the cochlea as frequency decreases. This higher noise level and its influence on measurement reliability is, no doubt, an important factor that contributes to the poorer DPOAE test performance for lower frequency f_2's (e.g., Martin *et al.*, 1990; Gorga *et al.*, 1993a, 1993b, 1996, 1997; Kim *et al.*, 1996; Stover *et al.*, 1996; Dorn *et al.*, 1999).

There are, however, several other distortion products (DP) generated when two primary tones are presented to the ear (e.g., Brown and Kemp, 1985; Kemp and Brown, 1986; Lonsbury-Martin *et al.*, 1987). In terms of absolute amplitude, the component occurring at $2f_1-f_2$ is the largest, followed by the component at $2f_2-f_1$. The $2f_2-f_1$ DP, although smaller in amplitude compared to the $2f_1-f_2$ DP, occurs at a frequency that is approximately 1/2 octave above f_1. Thus, it occurs at a higher frequency where the noise levels may be more favorable. Since this distortion product is also generated at the same time as the $2f_1-f_2$ DP no additional time or measurements would be necessary to evaluate both DPs simultaneously. It is possible, therefore, to examine response amplitudes and/or signal-to-noise ratios (SNR) at both DPs simultaneously to determine auditory status. Potentially, such an approach may improve test performance for lower frequencies, where noise levels make it difficult to measure DPOAEs at $2f_1-f_2$.

The actual generator site for $2f_2-f_1$, however, does not appear to be the same as the site at which the $2f_1-f_2$ DP is generated. As a general rule, distortion products are generated at two places: (1) at the place where the primaries interact, near the characteristic place (CP) of f_2, and (2) at the CP of each DP. Typically, one of these two places will dominate in its contribution to the DPOAE. Recent data suggest that these two distortion products ($2f_1-f_2$ and $2f_2-f_1$) may differ as to which place provides the dominant contribution to the DPOAE (e.g., Brown and Kemp, 1985; Whitehead *et al.*, 1996; Moulin and Kemp, 1996; Martin *et al.*, 1998; Schneider *et al.*, 1999). For example, Martin *et al.* (1998), using a suppression paradigm, provided data to suggest that $2f_1-f_2$ is primarily generated at a place that is on the apical side but still very near the f_2 place, while $2f_2-f_1$ is primarily generated at a place that is basal relative to the f_2 place. These observations complicate the interpretation of simultaneous measurements of both DPs relative to predictions about outer hair-cell integrity (and, therefore, auditory status) for different places along the cochlea. They suggest that measurement of both DPs for a fixed set of primaries may result in descriptions of cochlear function for slightly different places.

On the other hand, DPOAEs and auditory status (dichotomously classified as either normal hearing or hearing impaired) are related over wide frequency ranges (Dorn *et al.*, 1999) that exceed the spacing between the ''generator'' sites that are implicit in the work of Martin *et al.* (1998). If DPOAE measurements from distant regions have predictive accuracy for a given audiometric frequency (Dorn *et al.*, 1999), one would expect that even though $2f_2-f_1$ and $2f_1-f_2$ are not generated at exactly the same place, the two DPs would retain predictive value because their generators still occur in close proximity to the f_2 place. Phenomenologically, information from both DPs might be used to predict auditory status, recognizing that they may be generated from slightly different places within the cochlea. There are several reasons why this might be the case, including (1) alterations in forward and reverse energy transmission through damaged regions of the cochlea basal to f_2, (2) distributed generation sites when two primary tones are presented to the ear, and/or (3) correlations of auditory status across frequency (Dorn *et al.*, 1999). While it may not be possible in humans to determine which, if any, of these hypotheses account for interactions across frequency, it still may be possible to exploit these interactions in order to improve upon the accuracy with which auditory status is predicted.

The purpose of this study was to determine if simultaneous measurements of $2f_1-f_2$ and $2f_2-f_1$ could be used to improve the accuracy with which DPOAEs predict auditory status. To this end, DPOAEs were measured in a group of normal-hearing and hearing-impaired subjects. These measurements were made over a wide range of levels in order to determine if information at several levels and for two DPs could be combined to improve upon how well auditory status (normal hearing or hearing loss) is identified. Additionally, the inclusion of two DPs was examined within the context of univariate and multivariate analyses. This enabled us to assess test performance when both DPs were considered for the same primary frequency pair and across different primary pairs.

I. METHODS

A. Subjects

DPOAE data were collected on 70 adult subjects with normal hearing and 80 adult subjects with hearing loss. Special emphasis was placed on including hearing-impaired subjects with at least low-frequency losses, given the hypothesis that measurements at the $2f_2-f_1$ DP would potentially improve test performance more for low frequencies, compared to high frequencies, where noise levels are already reduced. For the purposes of subject selection, normal hearing was defined as pure-tone audiometric thresholds of 10 dB HL or better (ANSI, 1996) for octave and interoctave frequencies from 250 Hz to 8 kHz. This stringent criterion for normal hearing was selected in the hope that this would increase the likelihood of observing responses at $2f_2-f_1$. This hypothesis was based on the view that the DP at $2f_2-f_1$ was of small amplitude, even among normal ears, and would be difficult to resolve from the noise among ears if more ''traditional'' definitions of normal hearing (such as 20 dB HL) were used. In addition, all subjects had normal middle-ear function on the day of the DPOAE tests, as determined by standard tympanometric measurements.

B. Stimuli

DPOAEs were elicited by pairs of primary tones (f_1 and f_2), with $f_2/f_1=1.22$. F_2 varied from 500 Hz to 8 kHz in 1/2-octave steps, thus providing data at nine f_2 frequencies. Data were collected in the form of DPOAE input/output (I/O) functions. The level of f_2 (L_2) was varied from 10 to 65 dB SPL in 5-dB steps. The level of L_1 was adjusted in order to maximize response amplitudes for normal-hearing subjects, following the work of Whitehead *et al.* (1995), Janssen *et al.* (1998), and Kummer *et al.* (1998). Specifically, there were no level differences for the highest levels of stimulation. However, L_2 decreased more rapidly than L_1, resulting in larger dB-differences between the two primaries as level decreased.

C. DPOAE measurements

Custom-designed software (EMAV, Neely and Liu, 1993) was used that is capable of simultaneously measuring both $2f_1-f_2$ and $2f_2-f_1$. Noise was estimated as the average level in the three frequency bins above and the three frequency bins below each distortion product, meaning that noise estimates were specific to each DP. Measurement-based stopping rules were used such that data collection terminated if the noise floor around $2f_1-f_2$ was $\leqslant -30$ dB SPL, or after 32 s of artifact-free averaging, whichever occurred first. This rule was chosen to assure that none of the present measurements was contaminated by system distortion. All DPOAE data were obtained while the subject was comfortably seated in a sound-treated booth.

D. Data analyses

Clinical decision theory was used to evaluate DPOAE test performance (Swets, 1988; Swets and Pickett, 1982). Relative operating characteristic (ROC) curves were constructed and areas under these curves were estimated. ROC curves are plots of hit rate (sensitivity) as a function of the false-alarm rate (1 minus specificity). They can be used to describe the relation between these two variables for all values of a criterion measure (such as DPOAE amplitude or SNR). As a result, they provide complete descriptions of how well a diagnostic test distinguishes between normal and impaired systems. Area under the ROC curve provides a single number summarizing diagnostic test performance. It ranges from 0.5 (chance) to 1.0 (perfect performance).

Test performance was also evaluated by examining specificity for a fixed sensitivity. Specificity is the proportion of the time that ears with normal hearing were correctly identified. Sensitivity is the proportion of time that ears with hearing loss were correctly identified. For the purposes of these analyses, sensitivity was fixed at 90% and specificity was evaluated. For the present study, 90% was chosen because of the small number of hearing-impaired subjects (80) and the reduced confidence in estimates from the tails of underlying distributions. Using 90%, data from eight subjects defined the ''tail'' of the distribution of responses from impaired ears. Higher sensitivities, such as 95%, were not used because the fewer number of subjects (four) would result in a less reliable estimate.

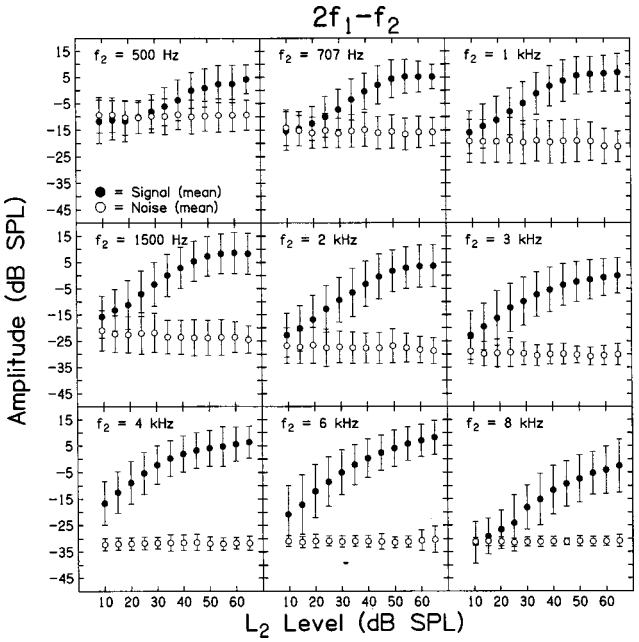

FIG. 1. DPOAE and noise amplitudes (in dB SPL) for the $2f_1-f_2$ distortion product as a function of L_2 (in dB SPL). For each L_2, L_1 was chosen in order to optimize the amplitude of the $2f_1-f_2$ distortion product (Whitehead *et al.*, 1995; Janssen *et al.*, 1998; Kummer *et al.*, 1998). Filled circles represent mean DPOAE amplitude, and open circles represent mean noise amplitudes. Error bars represent ± 1 standard deviation. Data for a different f_2 frequency are shown in each panel. These data were obtained in 70 subjects with normal hearing.

ROC curve areas and specificities for fixed sensitivities also were evaluated using multivariate analysis techniques in order to determine if the information from several primary frequency pairs, at several primary levels, and for both DPs can be combined in an optimal fashion to improve test performance. For the purposes of this study, test performance was defined as the test's ability to accurately identify auditory status. Auditory status was classified dichotomously as normal or impaired, based on audiometric threshold.

II. RESULTS

A. Cumulative distributions of SNR for normal-hearing subjects

Figure 1 shows DPOAE and noise amplitudes at $2f_1-f_2$ as a function of L_2 for the 70 normal-hearing subjects. Each panel shows data for a different f_2 frequency. Error bars represent ± 1 standard deviation (s.d.) around the mean. A number of observations may be made from the data summarized in this figure. DPOAE amplitudes were slightly lower for lower f_2's, compared to f_2's>1 kHz. In contrast, noise amplitudes were lower for higher f_2 frequencies. In fact, noise levels between -20 and -35 dB SPL were achieved once f_2 was greater than 1.5 or 2.0 kHz.

Figure 2 shows similar DPOAE and noise amplitudes at the $2f_2-f_1$ frequency. On average, the response amplitudes were less at this DP, compared to the amplitudes observed at $2f_1-f_2$. In addition, noise amplitudes were less for f_2's at and below 1 kHz, compared to the results for $2f_1-f_2$. Examining mean data only, however, one might conclude that there is no advantage in considering both DPs because, in

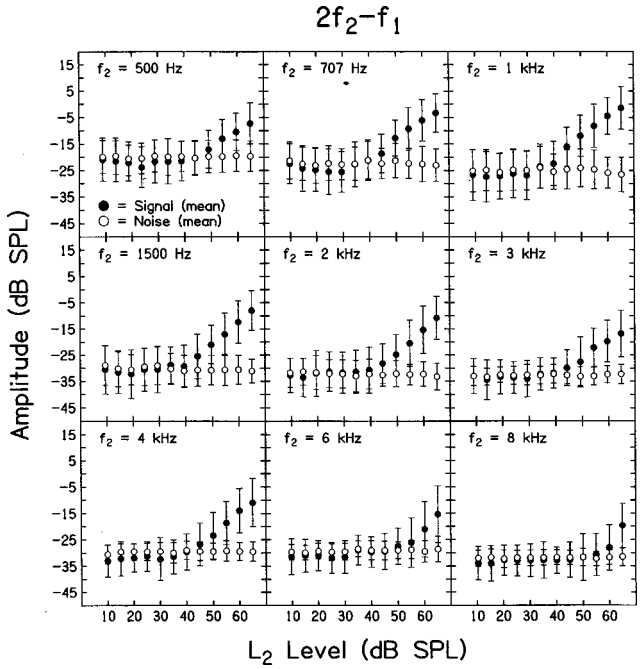

FIG. 2. DPOAE and noise amplitudes (in dB SPL) as a function of L_2 (in dB SPL) for the $2f_2-f_1$ distortion product, following the same convention used in Fig. 1.

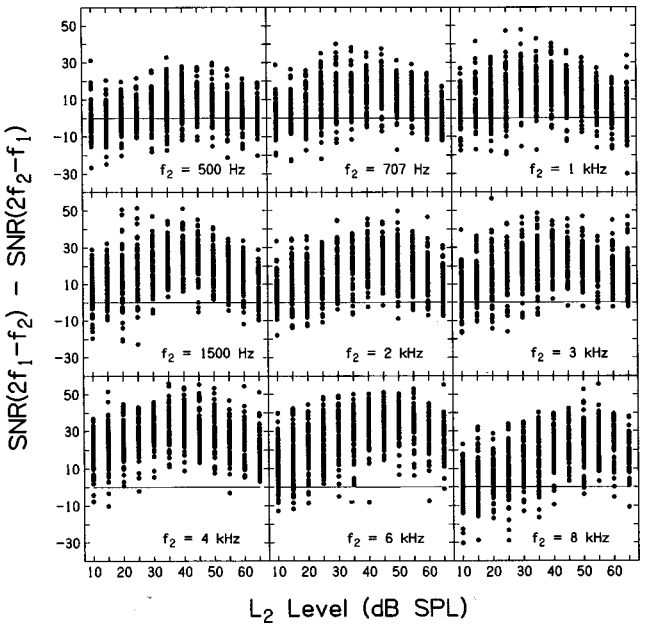

FIG. 3. SNR ($2f_1-f_2$) minus the SNR ($2f_2-f_1$) in dB as a function of L_2 (in dB SPL). These dB differences were estimated for each of the 70 normal-hearing subjects individually. The horizontal line at 0 dB is drawn to provide a reference. Points above the line signify that the SNR at $2f_1-f_2$ was larger, while points below the line indicate that the SNR was larger at $2f_2-f_1$. Data for a different f_2 frequency are shown in each panel.

spite of the reduced noise levels, the lower mean response amplitudes result in small mean response-to-noise differences (SNRs) at the $2f_2-f_1$ DP. However, averaging data cross all 70 normal-hearing subjects potentially could obscure individual cases in which the SNR was larger at $2f_2-f_1$.

B. Differences in SNR across primary levels

Figure 3 shows the difference (in dB) between the SNR at $2f_1-f_2$ and at $2f_2-f_1$ as a function of primary level in the 70 normal-hearing subjects. Each data point represents the difference for an individual subject. Data for a different f_2 is shown in each panel. A line is drawn at 0 dB to provide a point of reference. Data points above this line indicate that the SNR was larger at $2f_1-f_2$. Data points below it signify that the SNR was larger for $2f_2-f_1$. While the majority of data points falls above the line, there are points below the line at every frequency. There are more points for which the SNR was larger at $2f_2-f_1$ for lower f_2's and (at some frequencies) for lower primary levels. This suggests that, if there is any advantage to examining data at these two DPs, that advantage will be restricted to lower f_2's.

C. Area under the ROC curve

While the data reviewed thus far indicate that there may be some advantage in examining DP and noise amplitudes at $2f_1-f_2$ and $2f_2-f_1$ simultaneously, a direct test of the clinical value of such a paradigm requires an examination of data from both normal-hearing and hearing-impaired ears. In the remainder of this paper, therefore, test performance is explored by comparing responses from both normal and impaired ears. Test performance is described by the test's ability to classify auditory status, and auditory status is defined dichotomously as normal or impaired, based upon audiometric threshold. In the first analysis, DPOAE test performance was evaluated when $2f_1-f_2$ and/or $2f_2-f_1$ were used to determine auditory status in the sample of 70 normal-hearing and 80 hearing-impaired subjects. While data were available for a wide range of intensities, the best performance (either largest areas under the ROC curves or highest specificities for fixed sensitivities) were achieved when L_2 was set to a moderate level (55 dB SPL). This finding is consistent with previous observations indicating that moderate-level primaries more accurately identify auditory status, compared to either higher or lower primary levels (Stover *et al.*, 1996; Whitehead *et al.*, 1995). The primary-level effect held regardless of which DP was used to predict auditory status or whether univariate or multivariate analyses were used. Thus, the data summarized below are restricted to the condition when $L_2=55$ dB SPL.

Figure 4 shows areas under the ROC curves (A_{roc}) as a function of f_2. The results for univariate analyses are shown in the left panel, while the results from multivariate analyses (logistic regressions) are shown in the right panel. In the left panel, areas were calculated using either DP separately (squares for $2f_1-f_2$; circles for $2f_2-f_1$), or when the DP having the largest SNR (triangles) was used to determine auditory status. However, the analyses included DP data restricted to the condition when f_2 frequency=audiometric frequency.

For these analyses, normal hearing was defined as a threshold of 20 dB HL or better (ANSI, 1996). Although our initial normal-hearing group was defined based on a more stringent criterion (10 dB HL or better for the DPOAE data summarized in Figs. 1, 2, and 3), a more traditional criterion of 20 dB HL was used for test performance analyses. There

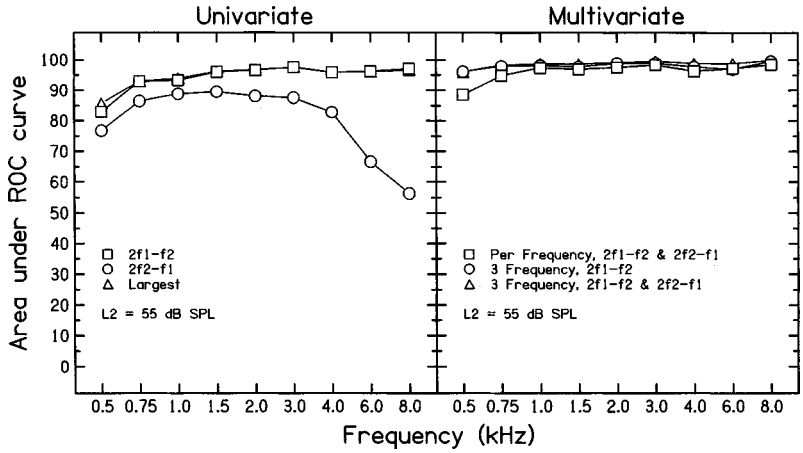

FIG. 4. Area under the ROC curve as a function of audiometric frequency (in kHz). For the purposes of these analyses, normal hearing was defined as thresholds of 20 dB HL or less. Data are shown only for the case when L_2=55 dB SPL. Left panel: results for univariate analyses in which predictions of auditory status were based only on data obtained when f_2 frequency=audiometric frequency. Squares, circles, and triangles represent the cases when the SNR at $2f_1-f_2$, $2f_2-f_1$, or the DP with the largest SNR were used to predict auditory status. Right panel: results from multivariate analyses in which logistic regressions were used to optimize predictions about auditory status. Squares represent the case when the inputs to the analyses were signal and noise at both $2f_1-f_2$ and $2f_2-f_1$ when f_2=audiometric frequency. Circles show the results when $2f_1-f_2$ data in response to three f_2 frequencies were used to make the prediction. Triangles show the results when signal and noise at both DP frequencies and for three f_2 frequencies were used to predict auditory status.

were hearing-impaired subjects with thresholds >10 dB HL but ≤20 dB HL at some frequencies who also had thresholds >20 dB HL at other frequencies. Their data were included in the ''normal'' group at those frequencies for which their thresholds were ≤20 dB HL.

Without exception, larger A_{roc} values were observed when the experimental measure was restricted to the SNR at $2f_1-f_2$, compared to when decisions about auditory status were based solely on data at $2f_2-f_1$. However, there were cases when larger A_{roc} values were observed when the decision about auditory status was based on the largest SNR, whether measured at $2f_1-f_2$ or $2f_2-f_1$. These increases in A_{roc} were no more than 2% and were restricted to low f_2's (500 Hz and perhaps 1 kHz). There was no increase in A_{roc} for f_2's at and above 1.5 kHz. This means that for higher f_2 frequencies, there was no improvement in test performance when data from both DPs were considered simultaneously.

These data were analyzed next using multivariate statistical techniques. Inputs to the multivariate analyses (see below) were expressed in terms of dB SPL (DPOAE and noise amplitudes). Several approaches were followed when multivariate analyses (logistic regressions) were performed (right panel, Fig. 4). In the first, DP data at both $2f_1-f_2$ and $2f_2-f_1$ were provided to the analyses for optimization; however, data were provided only for the case when f_2 frequency=audiometric frequency (squares). A second multivariate analysis was performed, in which DP data were provided for three f_2 frequencies but only for the $2f_1-f_2$ DP. With the exception of 500 Hz and 8 kHz, these f_2 frequencies were selected such that one was equal to audiometric frequency, and one each was from the 1/2 octave above and below the audiometric frequency about which predictions were being made. At 500 Hz, $2f_1-f_2$ DP data were included for f_2 frequencies of 500, 707, and 1000 Hz, while at 8 kHz, $2f_1-f_2$ DP data were included at 4, 6, and 8 kHz. The selection of three ''adjacent'' frequencies was based on the assumption that frequencies close to an individual audiometric frequency would hold the greatest value for predicting auditory status at that frequency. In the final multivariate analyses, the above two conditions were combined such that data were included for both DPs ($2f_1-f_2$ and $2f_2-f_1$) and three f_2 frequencies.

Logistic regressions resulted in larger increases in ROC curve areas, compared to the results achieved by univariate analyses. This result is consistent with previous observations in which multivariate analyses were applied to DPOAE data (Dorn *et al.*, 1999; Gorga *et al.*, 1999). Recall that these multivariate analyses are designed to optimize the separation in ''response properties'' between normal and impaired ears. This is accomplished by applying nonuniform weightings to response and noise amplitudes. Improvements were evident even when the inputs to these analyses included DPOAE data (at both $2f_1-f_2$ and $2f_2-f_1$) that were restricted to the single frequency about which predictions of auditory status were being made (''per frequency'' in Fig. 4). If data were included from several frequencies but at only one DP ($2f_1-f_2$), further improvements were achieved. Including data from several f_2 frequencies and both DPs ($2f_1-f_2$ and $2f_2-f_1$) provided small additional increases in ROC curve areas (note the tips of triangles extending slightly above the circles in the right panel of Fig. 4). For this latter condition, A_{roc} ranges from a low of about 0.96 (500 Hz) to a high of 0.99 (e.g., 3 kHz).

D. Sensitivity and specificity

Figure 5 plots specificity (100%–false-alarm rate) as a function of frequency when sensitivity (hit rate) was fixed at 90%. Results for univariate analyses are shown in the left panel, and results for multivariate analyses are shown in the right panel. The convention followed in Fig. 4 is also followed in this figure. As expected from the univariate results summarized in Fig. 4, specificities were highest for $2f_1-f_2$ compared to $2f_2-f_1$ (left panel, Fig. 5). However, at some

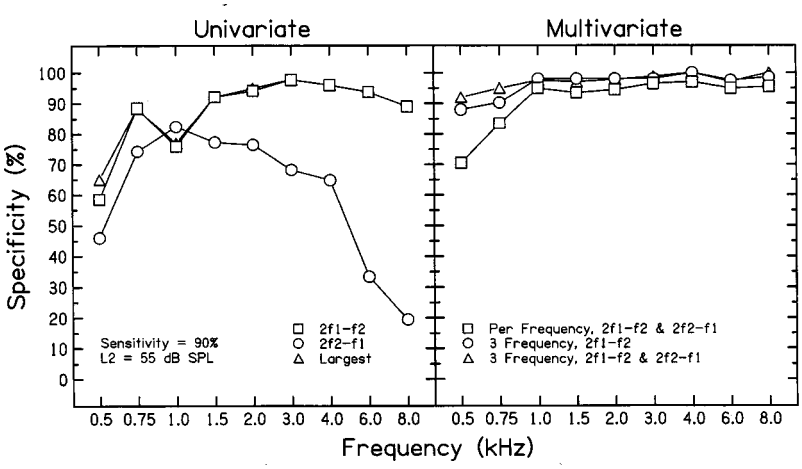

FIG. 5. Specificity (%) as a function of audiometric frequency (kHz) when sensitivity was held constant at 90%. In all other respects, the conventions used in Fig. 4 apply here.

frequencies, there was a slight increase in specificity when the largest SNR or the SNR at $2f_2-f_1$ was used to determine auditory status. This effect was restricted to lower f_2's. There was no difference between test performance (in this case, as defined by test specificity) for the largest SNR and the SNR at $2f_1-f_2$ once f_2 exceeded 1 kHz.

As expected from the results summarized in Fig. 4, multivariate analyses (right panel) resulted in higher specificities compared to the univariate approach. This was evident for all three multivariate analyses. The best performance was achieved when the analyses included DPs at both $2f_1-f_2$ and $2f_2-f_1$ for three frequencies close to the frequency about which auditory status was being predicted. Specificities exceeded 90% for all frequencies, including 500 Hz, a frequency at which univariate analyses typically result in poor performance (e.g., Gorga *et al.*, 1993a, 1993b; Stover *et al.*, 1996).

III. DISCUSSION

At all f_2 frequencies, DPOAE amplitude was larger for $2f_1-f_2$ (Fig. 1) compared to $2f_2-f_1$ (Fig. 2). This is not an unexpected finding, and is consistent with previous observations (Knight and Kemp, 1999; Schneider *et al.*, 1999). Noise levels, however, were lower for $2f_2-f_1$ compared to $2f_1-f_2$. This effect depended on f_2, in that lower noise levels were observed at 500, 707, and perhaps 1000 Hz, but not at higher frequencies. The reduced noise levels at lower frequencies are a consequence of the fact that noise was estimated around a DP that occurred above f_2, in contrast to the case for $2f_1-f_2$, where noise is estimated around a DP that is below f_1. Noise in DPOAE measurements is produced primarily by the subject as a result of movement and breathing. These noise sources tend to produce more low-frequency energy. Thus, the observation that noise levels increase as frequency decreases is expected.

The above comparisons between DPOAE and noise amplitudes for both DPs were based on average data among subjects with normal hearing. While these data suggest that there may be some small advantage in evaluating two DPOAEs simultaneously, they may also mask the value of such an approach for individual patients in whom more favorable SNRs might occur at the $2f_2-f_1$ DP. For individual patients, we were interested in knowing whether simultaneous measurements at $2f_1-f_2$ and $2f_2-f_1$ result in more accurate predictions of auditory status. The results summarized in Fig. 3 are more pertinent to this issue. In this analysis, the SNRs for $2f_1-f_2$ and $2f_2-f_1$ were compared for each normal-hearing subject. While the vast majority of comparisons revealed larger SNRs for $2f_1-f_2$, there were several cases in which larger SNRs were observed for $2f_2-f_1$. This latter observation was more evident at lower f_2 frequencies, compared to higher f_2's, where larger SNRs at $2f_2-f_1$ were uncommon. This occurs because any advantage in measuring responses at the higher DP would be expected for the lower frequencies, where noise levels are greater. At higher frequencies, noise levels are already low. At some f_2's, noise levels less than -30 dB SPL were observed (4, 6, and 8 kHz, Fig. 1). For these higher f_2's, shifting the measurement of response to a frequency slightly higher than f_2 does not result in lower noise estimates.

In summary, SNRs sometimes were larger at $2f_2-f_1$ compared to $2f_1-f_2$, but mainly for f_2's at and below 1 kHz. For higher f_2's, the SNR was greater at $2f_1-f_2$. Thus, measurements at the higher DP ($2f_2-f_1$) had a favorable influence on SNR because of the reduced levels of noise, but only for lower frequencies. The concomitant reduction in $2f_2-f_1$ DP amplitude for higher f_2's exceeded the reduction in noise at these frequencies, resulting in poorer SNRs for f_2's above 1 kHz.

The frequency effect suggests that there might be some limited value in considering data for the $2f_1-f_2$ and the $2f_2-f_1$ DPs in efforts to improve measurement reliability for lower frequencies. This, in turn, might be expected to have a positive influence on test performance, presumably by reducing the false positive rate. Under typical conditions, it is difficult to measure DPs at low frequencies. ''Absence'' of a response in normal ears might be a result of high noise levels. Thus, an ear with normal hearing would be classified as ''impaired,'' not necessarily because the ear did not produce a response, but because the response it produced could not be measured because of high levels of background noise. The fact that specificity increased slightly at lower frequencies when both $2f_2-f_1$ and $2f_1-f_2$ were evaluated simultaneously supports this view. The observation of ROC curve

areas that increased by small amounts at lower frequencies also would be consistent with this view. Unfortunately, the improvements in test performance were small (on the order of 2% or less), and were restricted to f_2's below 1 kHz. Thus, only slight test performance benefit was accrued by examining two DPs. On the other hand, these improvements come at no cost. That is, DPOAE measurements were taken simultaneously at both $2f_2-f_1$ and $2f_1-f_2$. No additional test time was required to obtain data at an additional DP. Algorithms could be designed in which both DPs are evaluated simultaneously, and the one with the largest SNR is used in the determination of auditory status.

The most compelling improvements in test performance occurred when multivariate analyses were used to optimize the prediction of normal or impaired auditory status. Both area under the ROC curve and specificity for fixed sensitivities increased when data from multiple primary pairs were used to predict auditory status at individual audiometric frequencies (right panel, Figs. 4 and 5). This result is consistent with our previous observations when either DPOAEs (Dorn *et al.* 1999; Gorga *et al.*, 1999) or transient-evoked otoacoustic emissions (TEOAEs) (Hussain *et al.*, 1998) were used to predict auditory status. This finding suggests that there is an inter-relation among either DP measurements across frequency or audiometric threshold across frequency. In either case, these data suggest that logistic regressions were able to exploit the inter-relation, whatever the source, to improve test performance.

Having demonstrated that simultaneous measurements at $2f_1-f_2$ and $2f_2-f_1$ can provide small improvements in test performance at low frequencies with no cost, and that test performance can be improved to a greater extent by using multivariate analysis techniques, an important caveat must be stated. Multivariate analysis techniques are designed to optimize the separation between normal and impaired ears on a dimensionless variable. This optimization is derived from the data provided as input to the analyses, and thus, could be idiosynchratic to this specific data set. The optimization may not be ideal for an independent set of data. Any conclusion about the success of the logistic regression must be tempered until the results are validated for an independent data set. It is important to note, however, that the advantages of multivariate analyses of OAE data have now been demonstrated in several papers (Hussain *et al.*, 1998; Dorn *et al.*, 1999; Gorga *et al.*, 1999), although one paper reports little advantage from such techniques (Kimberley *et al.*, 1994).

There are two other considerations that may limit the value of the present data set. Although data are reported for 70 normal-hearing and 80 hearing-impaired subjects (a relatively large sample by most standards), one must be cautious when interpreting these results. For example, specificities were evaluated when sensitivity was held constant at 90%. By definition, the criterion that resulted in a sensitivity of 90% was failed by 90% of the subjects with hearing loss. That also means that 10% (or eight) of the subjects with hearing loss passed this criterion. While 90% sensitivity might seem low under some clinical conditions, the small *N* and the increased variability on the ''tails'' of distributions makes the use of higher sensitivities less reliable. Even so, the specificities reported in Fig. 5 were based on a criterion that was derived from a relatively small number of subjects. We would have greater confidence in the conclusions from this study if data were available from larger samples.

Additionally, the data reported in this paper were obtained under laboratory conditions in cooperative adult subjects. Most clinical OAE measurements are not made under such controlled conditions. We expect that a proportion of the patients seen clinically for OAE measurements are likely to be less cooperative than the subjects participating in the present study. Validation under clinical conditions in a more diverse patient population would be useful.

Finally, in order to obtain measurements at two DPs simultaneously, only one test paradigm could be used. The paradigm used here (such as f_2/f_1 and primary level differences) optimized the $2f_1-f_2$ DP, not the $2f_2-f_1$ DP. Larger $2f_2-f_1$ DPs would be expected for different $2f_2/f_1$ or primary levels (Knight and Kemp, 1999). However, we sought to enhance predictive accuracy by maintaining optimum conditions for the $2f_1-f_2$ DP, as this DP is generally the largest in humans and its measurement is in common clinical use.

ACKNOWLEDGMENTS

This work was supported by a grant from the NIH (NIDCD R01 002251). We would like to thank Beth O'Connor for her help in preparation of the figures. We also would like to thank two anonymous reviewers for their helpful suggestions on an earlier version of this manuscript.

ANSI (**1996**). ANSI 53, 6-1996, ''Specifications for audiometers'' (American National Standards Institute, New York).

Brown, A. M., and Kemp, D. T. (**1984**). ''Suppressibility of the $2f_1-f_2$ stimulated acoustic emissions in gerbil and man,'' Hear. Res. **13**, 29–37.

Brown, A. M., and Kemp, D. T. (**1985**). ''Intermodulation distortion in the cochlea: Could basal vibration be the major cause of round window CM distortion?,'' Hear. Res. **19**, 191–198.

Dorn, P. A., Piskorski, P., Gorga, M. P., Neely, S. T., and Keefe, D. H. (**1999**). ''Predicting audiometric status from distortion product otoacoustic emissions using multivariate analyses,'' Ear Hear. **20**, 149–163.

Gaskill, S. A., and Brown, A. M. (**1996**). ''Suppression of human acoustic distortion product: Dual origin of $2f_1-f_2$,'' J. Acoust. Soc. Am. **100**, 3260–3274.

Gorga, M. P., Neely, S. T., Bergman, B., Beauchaine, K. L., Kaminski, J. R., Peters, J., and Jesteadt, W. (**1993a**). ''Otoacoustic emissions from normal-hearing and hearing-impaired subjects: Distortion product responses,'' J. Acoust. Soc. Am. **93**, 2050–2060.

Gorga, M. P., Neely, S. T., Bergman, B., Beauchaine, K. L., Kaminski, J. R., Peters, J., Schulte, L., and Jesteadt, W. (**1993b**). ''A comparison of transient-evoked and distortion-product otoacoustic emissions in normal-hearing and hearing-impaired subjects,'' J. Acoust. Soc. Am. **94**, 2639–2648.

Gorga, M. P., Neely, S. T., and Dorn, P. A. (**1999**). ''Distortion product otoacoustic emission test performance for *a priori* criteria and for multi-frequency audiometric standards,'' Ear Hear. **20**, 345–362.

Gorga, M. P., Stover, L., Neely, S. T., and Montoya, D. (**1996**). ''The use of cumulative distributions to determine critical values and levels of confidence for clinical distortion product otoacoustic emission measurements,'' J. Acoust. Soc. Am. **100**, 968–977.

Gorga, M. P., Neely, S. T., Ohlrich, B., Hoover, B., Redner, J., and Peters, J. (**1997**). ''From laboratory to clinic: A large scale study of distortion product otoacoustic emissions in ears with normal hearing and ears with hearing loss,'' Ear Hear. **18**, 440–455.

Harris, F. P., Probst, R., and Xu, L. (**1992**). ''Suppression of the $2f_1-f_2$ otoacoustic emission in humans,'' Hear. Res. **64**, 133–141.

Hussain, D. M., Gorga, M. P., Neely, S. T., Keefe, D. H., and Peters, J. (**1998**). ''Characteristics of transient evoked otoacoustic emissions in normal-hearing and hearing-impaired children,'' Ear Hear. **20**, 75–86.

Janssen, T., Kummer, P., and Arnold, W. (**1998**). ''Growth behavior of the $2f_1-f_2$ distortion product otoacoustic emission in tinnitus,'' J. Acoust. Soc. Am. **103**, 3418–3430.

Kemp, D. T., and Brown, A. M. (**1986**). ''Wideband analysis of otoacoustic intermodulation,'' in *Peripheral Auditory Mechanisms*, edited by J. B. Allen, J. L. Hall, A. Hubbard, S. T. Neely, and A. Tubis (Springer, New York), pp. 306–313.

Kim, D. O., Paparello, J., Jung, M. D., Smurzynski, J., and Sun, X. (**1996**). ''Distortion product otoacoustic emission test of sensorineural hearing loss: Performance regarding sensitivity, specificity, and receiver operating characteristics,'' Acta Oto-Laryngol. **116**, 3–11.

Kimberley, B. P., Hernadi, I., Lee, A. M., and Brown, D. K. (**1994**). ''Predicting pure-tone thresholds in normal and hearing-impaired ears with distortion product emissions and age,'' Ear Hear. **15**, 199–209.

Knight, R. D., and Kemp, D. T. (**1999**). ''Relationships between DPOAE and TEOAE amplitude and phase characteristics,'' J. Acoust. Soc. Am. **106**, 1420–1435.

Kummer, P., Janssen, T., and Arnold, W. (**1995**). ''Suppression tuning characteristics of the $2f_1-f_2$ distortion-product emissions in humans,'' J. Acoust. Soc. Am. **98**, 197–210.

Kummer, P., Janssen, T., and Arnold, W. (**1998**). ''The level and growth behavior of the $2f_1-f_2$ distortion product otoacoustic emission and its relationship to auditory sensitivity in normal hearing and cochlear hearing loss,'' J. Acoust. Soc. Am. **103**, 3431–3444.

Lonsbury-Martin, B. L., Martin, G. K., Probst, R., and Coats, A. C. (**1987**). ''Acoustic distortion products in rabbit ear canal. I. Basic features and physiological vulnerability,'' Hear. Res. **28**, 173–189.

Martin, G. K., Jassir, D., Stagner, B. B., Whitehead, M. L., and Lonsbury-Martin, B. L. (**1998**). ''Locus of generation for the $2f_1-f_2$ vs $2f_2-f_1$ distortion product otoacoustic emissions in normal-hearing humans revealed by suppression tuning, onset latencies, and amplitude correlations,'' J. Acoust. Soc. Am. **103**, 1957–1971.

Martin, G. K., Ohlms, L. A., Franklin, D. J., Harris, F. P., and Losnbury-Martin, B. L. (**1990**). ''Distortion product emissions in humans: III. Influence of sensorineural hearing loss,'' Ann. Otol. Rhinol. Laryngol. **99**, 30–42.

Moulin, A., and Kemp, D. T. (**1996**). ''Multicomponent acoustic distortion product otoacoustic emission phase in humans. II. Implications for distortion product otoacoustic emissions generation,'' J. Acoust. Soc. Am. **100**, 1640–1662.

Neely, S. T., and Liu, Z. (**1993**). ''EMAV: Otoacoustic emission averager,'' Technical Memorandum Number 17, Boys Town National Research Hospital, Omaha, NE.

Schneider, S., Prijs, V., and Schoonhoven, R. (**1999**). ''Group delays of distortion product otoacoustic emissions in the guinea pig,'' J. Acoust. Soc. Am. **105**, 2722–2730.

Stover, L., Gorga, M. P., Neely, S. T., and Montoya, D. (**1996**). ''Towards optimizing the clinical utility of distortion product otoacoustic emission measurements,'' J. Acoust. Soc. Am. **100**, 956–967.

Swets, J. A. (**1988**). ''Measuring the accuracy of diagnostic systems,'' Science **240**, 1285–1293.

Swets, J. A., and Pickett, R. M. (**1982**). *Evaluation of Diagnostic Systems: Methods from Signal Detection* (Academic, New York).

Whitehead, M. L., Stagner, B. B., Lonsbury-Martin, B. L., and Martin, G. K. (**1995**). ''Dependence of distortion-product otoacoustic emissions on primary levels in normal and impaired ears: II. Asymmetry in L_1,L_2 space,'' J. Acoust. Soc. Am. **97**, 2359–2377.

Whitehead, M. L., Stagner, B. B., Martin, G. K., and Lonsbury-Martin, B. L. (**1996**). ''Visualization of the onset of distortion-product otoacoustic emissions, and measurements of their latency,'' J. Acoust. Soc. Am. **100**, 1663–1679.

Excitotoxic effect of kainic acid on chicken otoacoustic emissions and cochlear potentials

H. Sun,[a] R. J. Salvi,[b] D.-L. Ding, E. Hashino, M. Shero, and X.-Y. Zheng
Center for Hearing and Deafness, SUNY State University at Buffalo, Buffalo, New York 14214

(Received 23 December 1998; revised 22 December 1999; accepted 6 January 2000)

Kainic acid (KA) is a potent glutamate analog that can temporarily or permanently damage glutamatergic neurons. The purpose of the present study was to determine the short- and long-term effects of KA on chicken otoacoustic emissions and cochlear potentials. A chronic electrode was used to record the compound action potential (CAP), cochlear microphonic (CM), and the slow, positive neural potential (SPNP), a predominantly dc response. The CM, CAP, SPNP, and distortion product otoacoustic emissions (DPOAEs) were recorded before and after infusing 10 μl of a low dose (KA-L, 0.3 mM) or high dose (KA-H, 5 mM) of KA into scala tympani. KA caused a rapid and large reduction in CAP and SPNP amplitude in both the KA-H and KA-L groups; however, the CM and DPOAEs were largely unchanged. The amplitude of the CAP and SPNP in the KA-L group began to recover around 1 week post-KA, but was approximately 50% below normal at 4 weeks post-KA. In contrast, the CAP and SPNP showed no signs of recovery in the KA-H group. The results suggest that KA has no effect on the CM and DPOAEs generated by the hair cells, but selectively damages the CAP generated by the cochlear ganglion neurons. The reduction in the avian SPNP suggests that the response originates in the cochlear afferent neurons, unlike the summating potential (SP) in mammals that is generated in hair cells. [S0001-4966(00)02704-1]

PACS numbers: 43.64.Nf, 43.64.Jb, 43.64.Pg [RDF]

INTRODUCTION

Excess glutamate or glutamate analogs, such as kainic acid (KA) and alpha-amino-3-hydroxy-5-methyl-isoxazol-propionic acid (AMPA), can induce transient or permanent excitotoxic damage to glutamatergic neurons in the peripheral and central nervous system (Choi and Rothman, 1990). In the mammalian ear, the type I afferent dendrites that synapse on inner hair cells (IHCs) are selectively damaged by excess glutamate, KA, and AMPA (Puel *et al.*, 1991, 1994; Pujol *et al.*, 1985). Although KA and AMPA cause massive swelling of the type I afferent dendrites, little or no damage is observed on IHCs, outer hair cells (OHCs), or the efferent and afferent neurons beneath OHCs (Gil-Loyzaga and Pujol, 1990; Pujol *et al.*, 1985; Zheng *et al.*, 1997b). Similar pathological features were observed in the afferent dendrites in the organ of Corti after ischemia and acoustic trauma (Bohne, 1976; Pujol *et al.*, 1990; Spoendlin, 1976).

Acute application of KA or AMPA to the mammalian cochlea caused a significant decrease or complete loss of the compound action potential (CAP) and the auditory brainstem response (ABR). However, the cochlear microphonic (CM) potential, endolymphatic potentials (EP), summating potential (SP), crossed olivocochlear potential (COCP), and distortion product otoacoustic emissions (DPOAEs) were essentially unchanged (Bledsoe *et al.*, 1981; Dolan *et al.*, 1990; Puel *et al.*, 1991, 1994; Zheng *et al.*, 1997b, 1996). Interestingly, KA caused an increase in SP amplitude at high intensities whereas destruction of IHCs caused a significant reduction in SP amplitude (Durrant *et al.*, 1998; Zheng *et al.*, 1997a).

An acute exposure to KA has been shown to cause significant loss (34%) of type I afferent neurons in young rats (Juiz *et al.*, 1989). However, the amount of damage did not increase significantly when the dose was increased from 5 to 40 mM. More recent studies suggest that KA- and AMPA-induced excitotoxicity is reversible. The CAP and ABR completely recovered following treatment with AMPA or KA; however, the brainstem response recovered more rapidly than the CAP (d'Aldin *et al.*, 1997; Puel *et al.*, 1995; Pujol *et al.*, 1996; Zheng *et al.*, 1997b, 1998). Immediately after KA and AMPA treatment, the afferent dendrites were severely swollen and devoid of cytoplasmic content, but within 1–2 days regenerated afferent dendrites were present on IHCs. Approximately 5–10 days later, the afferent dendrites were almost normal (Puel *et al.*, 1997; Pujol *et al.*, 1996; Zheng *et al.*, 1997b, 1998). These results indicate that mammalian type I afferent neurons can rapidly recover from excitotoxic damage and regenerate by sprouting dendrites that elongate and form functional synapses on IHCs.

Over the past decade, considerable interest has focused on the ability of avian hair cells to regenerate following cochlear damage (Corwin and Cotanche, 1988; Ryals and Rubel, 1988). However, in order for hearing to recover, the cochlear ganglion neurons must survive the ototraumatic insult and form new synapses on the regenerated sensory cells (Duckert and Rubel, 1990; Rubel, 1992). Surprisingly, even though most hair cells regenerate following acoustic overstimulation, a significant number of cochlear ganglion neurons degenerate 30–90 days following overstimulation (Ryals *et al.*, 1989). Degeneration could occur because of excitotoxic damage to the neurons or loss of neurotrophic

[a]Current address: Hunan Medical University, PO Box 424, Changsha, Hunan 410078, People's Republic of China.
[b]Author to whom correspondence should be addressed. Electronic mail: salvi@acsu.buffalo.edu

factors from the hair cells (Ernfors *et al.*, 1995; Lefebvre *et al.*, 1994).

Recently, we examined the acute excitotoxic effects of KA treatment on the avian inner ear and found a highly selective pattern of neuronal damage in the apical 70% of the basilar papilla (Shero *et al.*, 1998). KA treatment caused massive swelling and loss of cytoplasmic content in the afferent terminals beneath the tall hair cells located near the neural edge of the papilla. No damage was seen in the neuropil beneath the short hair cells that lie along the abneural edge of the papilla. Hair-cell morphology was remarkably normal except for some distortion of the basal pole of the tall hair cells caused by the swollen afferent dendrites. These acute morphological changes were similar to those seen in mammals and suggested that avian cochlear afferent neurons might regenerate and become functional. The purpose of the present study was twofold. First, we wanted to determine how selective KA damage affects the cochlear potentials and otoacoustic emissions of the chicken's inner ear. A major difference found in this study was that the avian dc potential originates postsynaptically, unlike the dc summating potential in mammals that originates in the hair cells. We refer to the avian dc response as the slow positive neural potential (SPNP). Second, we wanted to determine if the physiological changes were reversible, as reported in some physiological studies with mammals (d'Aldin *et al.*, 1997; Puel *et al.*, 1997; Zheng *et al.*, 1997b), or permanent, as suggested by anatomical studies (Juiz *et al.*, 1989; Ryals *et al.*, 1989).

I. METHODS

A. Subjects

Fourteen, female, white Leghorn chickens (*Gallus domesticus*), 5–6 months old and weighing between 1.0–1.5 kg were used as subjects. The animals were anesthetized with ketamine (100 mg/kg, i.m.) and xylazine (2 mg/kg, i.m.). With the aid of an operating microscope, the left middle-ear space was opened from a posterolateral direction to expose the basal end of the cochlea and the round window membrane (Salvi *et al.*, 1994). A ball-tip electrode made of Teflon-coated silver wire was implanted in the upper bony margin of the round window. The electrode wire was cemented to the surface of the skull with dental cement. Afterwards, the anesthetized animal was moved to the test booth where the CAP, SPNP, and CM were recorded to obtain baseline amplitudes. After the measurements were completed, KA was infused into the cochlea. This was accomplished by making a tiny hole ($<$0.2 mm) in the posterolateral wall of scala tympani. KA was infused into the cochlea using a 34-gauge needle (World Precision Instruments, Microfil MF34G) coupled by tubing to a syringe pump (SAGE Instruments, model 341 B) set to a flow rate of 0.17 μL/s and a total volume of 10 μL. Immediately after the infusion, the opening was sealed with bone wax, the hole in the middle ear sealed with dental cement, and the wound closed. Six chickens were perfused with a high dose of KA (KA-H) consisting of 5 mM KA in Hank's balanced salt solution (HBSS) (GIBCO). Four chickens were perfused with a low dose of KA (KA-L) consisting of 0.3 mM KA in HBSS. Four control animals received the identical procedures, but were perfused only with HBSS. Afterward, the CAP, SP, CM, and DPOAE were recorded at 0.5–1 h, 2 h, 1 day, and 1, 2, and 4 weeks post-KA treatment in the KA-H group and the control group. Because the DPOAE and CM were unaffected by the high dose of KA, only the CAP was recorded from the KA-L group in order to determine the degree of neural recovery.

B. CM, SPNP, CAP, and DPOAE

Prior to each recording session, the animals were anesthetized with ketamine and xylazine as described above. Supplemental doses were administered as needed. The CAP, SPNP, and CM were measured in a double-walled sound booth (Industrial Acoustics Company, Inc.). Acoustic stimuli were generated digitally using a D/A converter (16 bits, 50 kHz) on a signal-processing board (Spectrum Signal Processing, TMS320C25) in a personal computer. The output of the D/A converter was low-pass filtered (TDK HFL 0030, 90-dB rolloff between 20 and 24 kHz) and then led to a computer-controlled attenuator (127.5 dB, 0.5-dB step size), current amplifier, and loudspeaker (Realistic 401197). The speaker was located approximately 25 cm directly in front of the entrance of the ear canal.

Tone bursts (1-ms rise/fall, 2-ms duration, cosine gating, alternating phase, 20/s, 0–80 dB SPL in 5-dB steps, 250, 500, 1000, 2000, and 4000 Hz) were used to elicit the CAP. The output of the round window electrode was amplified (10 000$\times$), filtered (100–3000 Hz), and then delivered to an A/D converter on a signal-processing board (Spectrum Signal Processing, TMS320C25) in a computer. The response was sampled at 50 kHz over a 10-ms interval and the response was averaged to 200 stimulus presentations. The CAP amplitude was measured from peak to peak (N1 to P1) (Chen *et al.*, 1993).

Tone bursts (3-ms rise/fall, 15-ms duration, cosine gating, alternating phase, 20/s, 20–85 dB SPL in 5-dB steps, 20/s, 250, 500, 1000, 2000, and 4000 Hz) were used to elicit the SPNP. The output of the electrode was amplified (5000$\times$), filtered (1–300 Hz), and then delivered to the A/D converter. The response was sampled at 50 kHz for 40 ms and the average response was determined to 150 stimulus presentations. The SPNP amplitude was measured as the largest positive voltage 10–20 ms following stimulus onset relative to the prestimulus baseline.

The CM was evoked by a 1000-ms continuous tone (0 to 90 dB SPL in 5-dB steps, 250, 500, 1000, 2000, and 4000 Hz). The output of the electrode was amplified (2000$\times$), bandpass filtered (100–30 000 Hz), low-pass filtered (TDK HFL 0030, 90-dB rolloff from 20–24 kHz), and delivered to the 16-bit A/D converter on the signal-processing board in the computer. The data were sampled at 70 kHz for 1000 ms beginning 20 ms after stimulus onset. A discrete Fourier transform was performed on the data to determine the CM amplitude at the stimulus frequency (Blackman windowing function, 1-Hz nominal spectral bandwidth) (Powers *et al.*, 1995; Trautwein *et al.*, 1996a).

The procedures for measuring DPOAEs have been described previously (Froymovich *et al.*, 1995; Trautwein

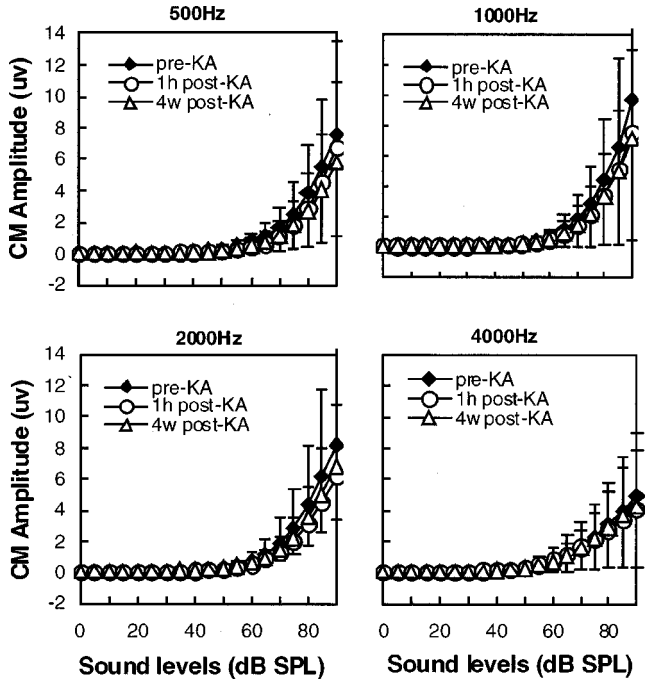

FIG. 1. Mean ($n=6$) cochlear microphonic (CM) I/O functions at 500, 1000, 2000, and 4000 Hz in the kainic acid, high-dose (KA-H) group. Measurements obtained pre-KA, 1-h post-KA and 4 weeks post-KA as indicated in inset. Upward vertical bars (pre-KA and 4 weeks post-KA) and downward vertical bars (1 h post-KA) represent one standard deviation above or below the mean values, respectively.

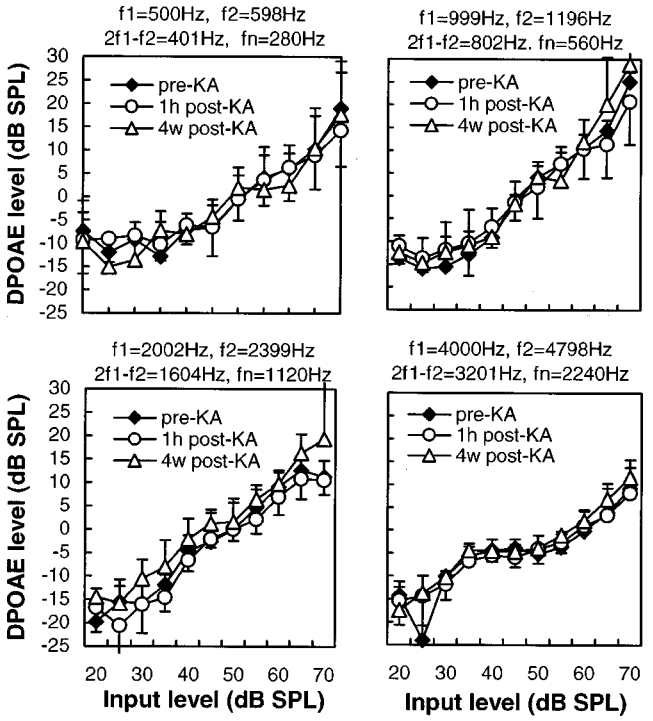

FIG. 2. Mean ($n=6$) distortion product otoacoustic emission (DPOAE) I/O functions at 500, 1000, 2000, and 4000 Hz in the KA-H group. Measurements obtained pre-KA, 1 h post-KA and 4 weeks post-KA as indicated in inset ($f2/f1=1.2$, $L1=L2$). Upward vertical bars (pre-KA and 4 weeks post-KA) and downward vertical bars (1 h post-KA) represent one standard deviation above or below the mean values, respectively.

et al., 1996b). Briefly, stimuli were presented through a closed acoustic system. The primary tones, $f1$ and $f2$, were set at a $f2/f1$ ratio of 1.2. DPOAE input/output functions were measured at $f1$ values of 500, 999, 2002, and 4000 Hz. The levels of the primary tones, L1 and L2, were equal and varied in 5-dB steps from 20 to 70 dB SPL. Stimuli were generated by D/A converters (16 bits, 100 kHz) on two separate signal-processing boards in a personal computer. The output of each channel was low-pass filtered (rolloff 90 dB, 20–24 kHz) and then sent to a computer-controlled attenuator, current amplifier, and sound source (Etymotic ER-2) that was coupled through a narrow tube to the mouth of a low-noise microphone (Etymotic ER10B). The output of the microphone was low-pass filtered (14 kHz) and led to an A/D converter (16 bits, 31-kHz sampling rate) on a separate signal-processing board in the computer. The microphone output was sampled for 500 ms and a discrete Fourier analysis (nominal spectral bandwidth 2 Hz) was computed for frequencies, $f1$, $f2$, $2f1-f2$, and fn, where $fn=0.7\times(2f1-f2)$. Data samples containing measurement artifacts were rejected if the noise level at fn was 10 dB SPL or greater.

The University Institutional Animal Care and Use Committee approved all of the procedures involving the care and use of animals.

II. RESULTS

A. CM and DPOAEs

Figure 1 shows mean ($n=6$) CM input–output (I/O) functions at 500, 1000, 2000, and 4000 Hz in the KA-H group. Measurements were obtained pre-KA, approximately 1 h post-KA and 4 weeks post-KA. The post-KA I/O functions were nearly identical to pre-KA I/O functions. Figure 2 shows the mean ($n=6$) DPOAE I/O functions at $f1$ frequencies of 500, 999, 2002, and 4000 Hz for the KA-H group. Measurements were obtained pre- and post-KA. The pre-KA DPOAE I/O functions were comparable to those for normal chickens (Froymovich *et al.*, 1995; Trautwein *et al.*, 1996b). After the KA-H treatment, there was no reduction in DPOAE amplitude and post-KA I/O functions were nearly identical to the pre-KA functions. Since the CM and DPOAE I/O functions were unchanged after the KA-H treatment, the CM and DPOAE were not measured after the KA-I dose.

B. CAP and SPNP

Figure 3(A) shows a sample of CAP waveforms collected at different intensities. Amplitude was measured from the first large negative peak (N1) to the first large positive peak (P1). Figure 3(B) shows a series of SPNP waveforms collected at different intensities. SPNP amplitude was measured from the baseline to the largest positive peak between 20–30 ms. Figures 4 and 5 show CAP I/O functions at 500, 1000, 2000, and 4000 Hz for the KA-H and KA-L group, respectively. Measurements were obtained pre-KA, 30 min post-KA, and 4 weeks post-KA. The CAP was almost completely abolished in the KA-H group 30 min post-KA except for a small response at high stimulus levels. At 4 weeks post-KA, the CAP amplitude was nearly the same as that measured immediately after KA treatment, indicating no long-term recovery. The amplitude of the CAP was signifi-

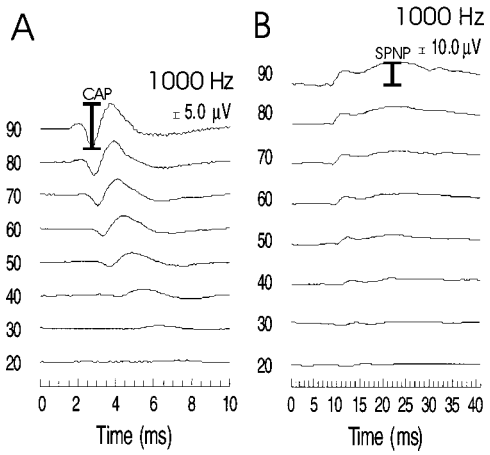

FIG. 3. (A) Example of compound action potential (CAP) waveforms measured at different intensities. Amplitude measured from first large negative peak to first large positive peak. (B) Example of slow positive negative potential (SPNP) waveform measured at different intensities. Amplitude measured from baseline to largest positive peak between 20–30 ms.

cantly reduced 30 min after the KA-L treatment. The amplitude reduction after KA-L was almost as great as that seen after KA-H. However, the CAP amplitude in the KA-L group recovered substantially between 30 min and 4 weeks post-KA. At 4 weeks post-KA, the maximum CAP amplitudes were approximately 50% to 70% of the pre-KA amplitudes.

Figure 6 shows the mean amplitude of the CAP (average of 500, 1000, 2000, and 4000 Hz at 70 dB SPL) as a function of time after applying KA-L, KA-H, or the carrier solution,

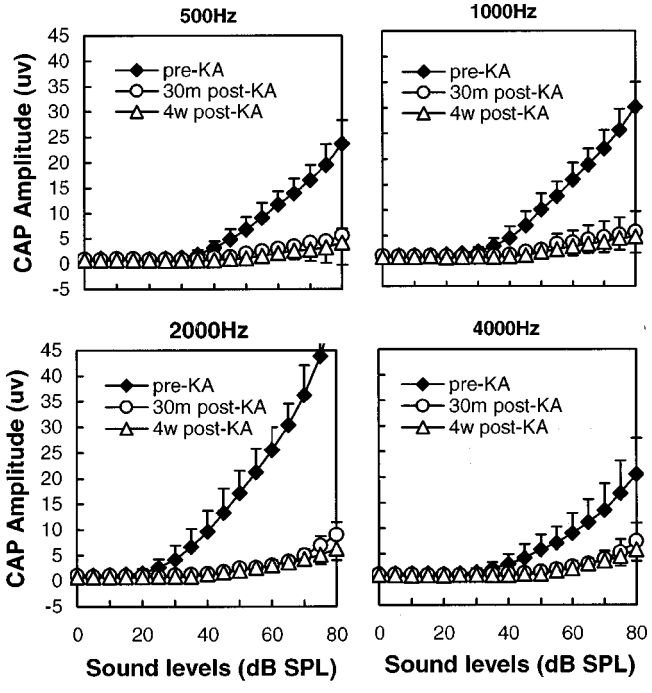

FIG. 4. Mean ($n=6$) compound action potential (CAP) I/O functions at 500, 1000, 2000, and 4000 Hz in the KA-H group. Measurements obtained pre-KA, 30 min post-KA and 4 weeks post-KA as indicated in inset. Upward vertical bars (pre-KA and 4 weeks post-KA) and downward vertical bars (1 h post-KA) represent one standard deviation above or below the mean values, respectively.

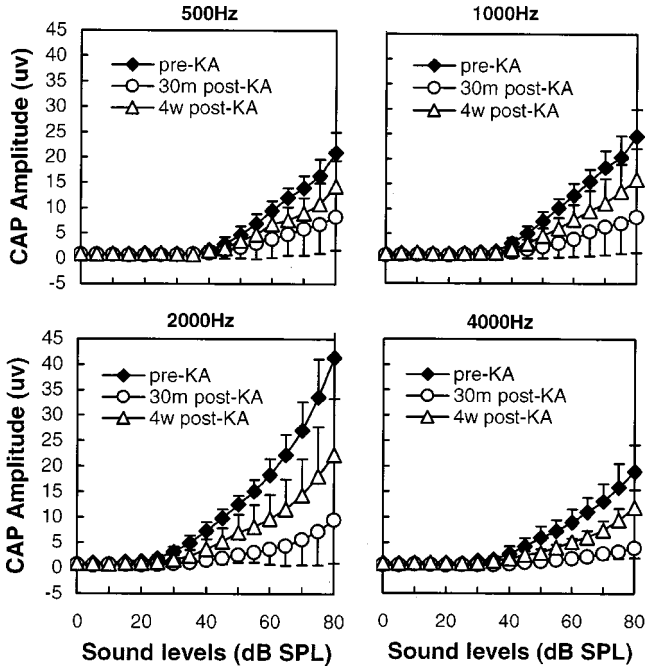

FIG. 5. Mean ($n=4$)CAP I/O functions at 500, 1000, 2000, and 4000 Hz in the kainic acid-low dose (KA-L) group. Measurements obtained pre-KA, 30 min post-KA and 4 weeks post-KA as indicated in inset. Upward vertical bars (pre-KA and 4 weeks post-KA) and downward vertical bars (1 h post-KA) represent one standard deviation above or below the mean values, respectively.

HBSS. The amplitude of the CAP decreased significantly in both the KA-H ($n=6$) and KA-L ($n=4$) groups at 30 min post-KA, whereas the CAP amplitude in the HBSS group ($n=4$) showed only a minor decrease. The CAP amplitude in the KA-H group remained depressed out to 4 weeks post-KA. To determine if there was any further recovery in the KA-H group, one animal (E2) was tested at 8 weeks and 20 weeks post-KA. CAP amplitude in this animal was still depressed at 20 weeks post-KA. The mean ($n=4$) CAP amplitude in the KA-L group remained depressed out to 1 week post-KA, but recovered to slightly more than 50% of pre-KA values between 2 and 4 weeks post-KA. One animal (E8) was allowed to survive for 8 weeks post-KA to determine if there was any further recovery in the KA-L group; however, no further recovery was observed.

Figure 7 shows the mean ($n=6$) SPNP I/O functions at

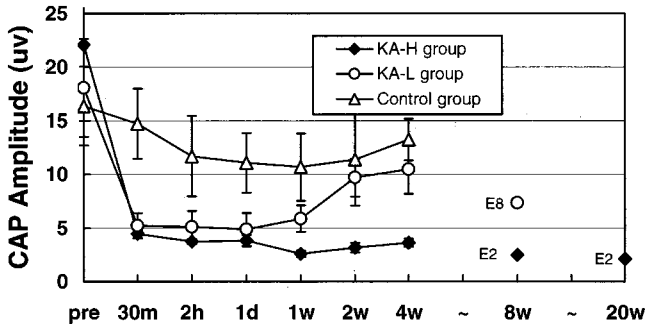

FIG. 6. Mean CAP amplitude (500, 1000, 2000, and 4000 Hz, 70 dB SPL) as a function of time following treatment with KA-H ($n=6$), KA-L ($n=4$), and Hanks balance salt solution (HBSS) ($n=4$). Vertical bars represent±one standard deviation around the pre-KA mean values.

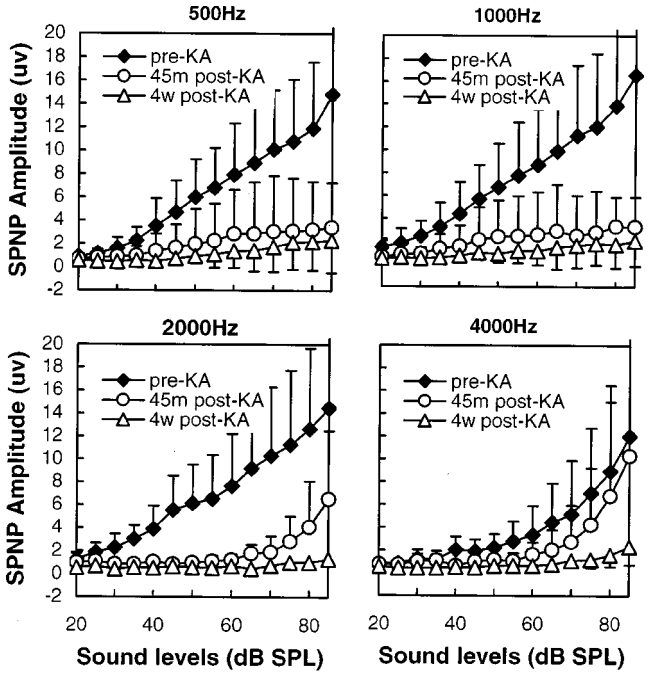

FIG. 7. Mean ($n=6$) SPNP I/O functions at 500, 1000, 2000, and 4000 Hz in the KA-H group. Measurements obtained pre-KA, 45-min post-KA and 4 weeks post-KA as indicated in inset. Upward vertical bars (pre-KA and 4 weeks post-KA) and downward vertical bars (1 h post-KA) represent one standard deviation above or below the mean values, respectively.

500, 1000, 2000, and 4000 Hz in the KA-H group. Like the CAP, the SPNP was also severely depressed at 45 min post-KA. At 4 weeks post-KA, the SPNP amplitude was lower than that recorded 45 min post-KA, particularly at 2000 and 4000 Hz. Figure 8 shows the mean amplitude of the SPNP ($n=6$, average of 500, 1000, 2000, and 4000 Hz at 70 dB SPL) as a function of time after applying KA-H, KA-L, or HBSS. The SPNP in the control group remained almost normal after the HBSS infusion. By contrast, the SPNP in the KA-H group was almost abolished and showed no recovery after 8 weeks ($n=1$) and 20 weeks ($n=1$) of recovery. The SPNP showed a substantial decrease after the KA-L treatment followed by a slow recovery. In the ear allowed to recover up to 8 weeks post-KA, the SPNP amplitude showed only partial recovery.

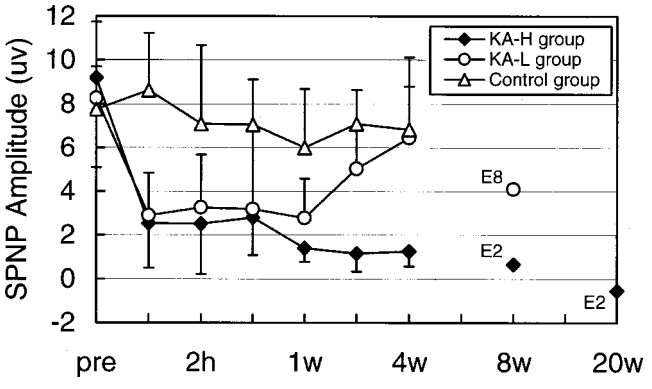

FIG. 8. Mean SPNP amplitude (500, 1000, 2000, and 4000 Hz 70 dB SPL) as a function of time following treatment with KA-H ($n=6$), KA-L ($n=4$), and HBSS ($n=4$). Vertical bars represent±one standard deviation around the pre-KA mean values.

III. DISCUSSIONS

Our results show that KA abolishes the CAP response originating in the cochlear ganglion, but it has little or no effect on the CM and DPOAE that originate in the hair cells. Thus, our physiological results suggest that KA damage is postsynaptic to the hair cell. This interpretation is consistent with our recent anatomical results from KA-treated chickens that show that anatomical damage is restricted to postsynaptic structures (Shero *et al.*, 1998). Our CM, CAP, and DPOAE data are similar to those reported for mammals. That is, the CM and DPOAE showed little or no change after KA treatment, whereas the CAP was abolished or significantly reduced in amplitude (Bledsoe *et al.*, 1981; Zheng *et al.*, 1996).

A major difference between birds and mammals is that KA abolished the avian SPNP, the slow, positive dc response. By contrast, KA had no effect on the mammalian SP at low intensities (Zheng *et al.*, 1997b). In fact, KA damage enhanced the mammalian SP at high intensities. Recent lesion studies in mammals suggest that the SP is generated predominantly by the IHCs with the OHCs making a smaller contribution (Durrant *et al.*, 1998; Zheng *et al.*, 1997b). In contrast, the avian SPNP appears to be generated postsynaptically (Patuzzi and Bull, 1991), most likely in the afferent dendrites. This interpretation is abased on the fact that the SPNP is abolished by tetrodotoxin and has a latency longer than the CM. Our previous anatomical data (Shero *et al.*, 1998) from KA-treated chickens plus the current results indicate that the avian SPNP is generated in the afferent dendrites. Thus, the avian SPNP does not behave like the mammalian SP, which is clearly generated by the hair cells.

An unexpected finding of the present study was the lack of recovery of the CAP and SPNP following KA-H treatment and the extremely prolonged and partial recovery in the KA-L group. These results contrast markedly with the near complete recovery of the mammalian CAP and evoked response from the inferior colliculus (Puel *et al.*, 1995; Pujol *et al.*, 1996; Zheng *et al.*, 1997b, 1998). In addition, the mammalian, type I afferent dendrites beneath the IHCs recovered rapidly after KA and AMPA treatment.

The incomplete recovery of the CAP in the KA-H and KA-L groups could be due to the degeneration of cochlear ganglion neurons or the inability of surviving neurons to form viable synaptic contacts with the hair cells. Excess KA presumably leads to the influx of cations through voltage-gated ion channels and the passive influx of Cl^- and water that causes massive swelling of the dendrites and cell death if these effects are severe or prolonged (Olney, 1986; Rothman, 1985). Several different KA doses were utilized in our preliminary studies to find ones that would abolish the CAP. Since no recovery was seen after the KA-H dose, we suspect that the cochlear ganglion neurons may have degenerated. This hypothesis is currently under evaluation in our lab. The KA-L dose used in the present study was just high enough to abolish the CAP immediately after KA treatment; therefore, we expected that the CAP would be transiently reduced and then gradually recover. However, recovery from the KA-L dose was slow and incomplete unlike the rapid and largely

reversible recovery seen in mammals (Puel *et al.*, 1997; Pujol *et al.*, 1996; Zheng *et al.*, 1997b).

The lack of recovery of the chicken CAP is somewhat puzzling because avian, cochlear afferent dendrites reestablish synaptic contact with regenerated hair cells after acoustic trauma and aminoglycoside ototoxicity (Corwin and Cotanche, 1988; Duckert and Rubel, 1993; Rubel, 1992; Ryals and Rubel, 1988; Ryals *et al.*, 1992). Moreover, evoked potential amplitudes and behavioral thresholds show significant or complete recovery (Adler *et al.*, 1993; Chen *et al.*, 1993; McFadden and Saunders, 1989; Saunders *et al.*, 1995). One interpretation of these results is that acoustic trauma and aminoglycoside ototoxicity cause little or no permanent damage to the cochlear ganglion neurons. However, this interpretation conflicts with anatomical studies showing that a significant number of cochlear ganglion neurons degenerate several months after acoustic overstimulation despite the fact that most hair cells regenerate (Ryals *et al.*, 1989). The loss of cochlear ganglion neurons could conceivably account for the partial recovery of CAP amplitude seen many months following aminoglycoside treatment (Chen *et al.*, 1993). However, small to moderate loss of cochlear ganglion neurons is likely to have little effect on threshold (Schuknecht and Woellner, 1953; Wang *et al.*, 1997).

Recent *in situ* hybridization studies in mammals have provided clues regarding the molecular mechanisms involved in regeneration of type-I afferent dendrites. Auditory neurons contain mRNAs coding for the GluR2 and GluR3 subunits of the AMPA/kainate receptors, the NMDAR1 subunit coding for NMDA receptors and the nGluR1 subunit coding for the metabotropic receptor (Puel *et al.*, 1995). AMPA-induced damage to spiral ganglion neurons resulted in increased expression of mRNA coding for NMDAR1 and mGluR1, whereas no change was observed for mRNA coding for GluR2 and GluR3. The up-regulation of NMDAR1 and mGluR1 reached a maximum 1 day post-treatment and returned to baseline 3 days post-AMPA. These results are consistent with earlier studies and suggest that NMDAR1 and mGluR1 play an important role in synaptogenesis, neural plasticity, and repair of excitotoxic damage (Burgoyne *et al.*, 1993; Chen *et al.*, 1988; Cline, 1991; Hori *et al.*, 1991; Kalb *et al.*, 1992; Komuro and Rakic, 1993; Mayat *et al.*, 1994a, 1994b; Seren *et al.*, 1989). The delayed and incomplete recovery observed in the avian ear may reflect fundamental differences in glutamate receptor subtypes or the level of expression following excitotoxic damage. Future studies aimed at elucidating the type of glutamate receptors present in avian cochlear ganglion neurons could provide a more complete understanding of the neural regeneration process in the avian ear.

ACKNOWLEDGMENTS

This work was supported by a grant from NIDCD (No. R01-DC01685).

Adler, H. J., Poje, C. P., and Saunders, J. C. (**1993**). ''Recovery of auditory function and structure in the chick after two intense pure-tone exposures,'' Hearing Res. **71**, 214–224.

Bledsoe, Jr., S. C., Bobbin, R. P., and Chihal, D. M. (**1981**). ''Kainic acid: An evaluation of its action on cochlear potentials,'' Hearing Res. **4**, 109–120.

Bohne, B. (**1976**). ''Mechanisms of noise damage in the inner ear,'' in *Effects of Noise on Hearing*, edited by D. Henderson, R. P. Hamernik, D. S. Dosanjh, and J. H. Mills (Raven, New York), pp. 41–68.

Burgoyne, R. D., Graham, M. E., and Cambray-Deakin, M. (**1993**). ''Neurotrophic effects of NMDA receptor activation on developing cerebellar granule cells,'' J. Neurocytol. **22**, 689–695.

Chen, C. K., Silverstein, F. S., Fisher, S. K., Statman, D., and Johnston, M. V. (**1988**). ''Perinatal hypoxic-ischemic brain injury enhances quisqualic acid-stimulated phosphoinositide turnover,'' J. Neurochem. **51**, 353–359.

Chen, L., Salvi, R. J., and Hashino, E. (**1993**). ''Recovery of CAP threshold and amplitude in chickens following kanamycin ototoxicity,'' Hearing Res. **69**, 15–24.

Choi, D. W., and Rothman, S. M. (**1990**). ''The role of glutamate neurotoxicity in hypoxic-ischemic neuronal death,'' Annu. Rev. Neurosci. **13**, 171–182.

Cline, H. T. (**1991**). ''Activity-dependent plasticity in the visual systems of frogs and fish,'' Trends Neurosci. **14**, 104–111.

Corwin, J. T., and Cotanche, D. A. (**1988**). ''Regeneration of sensory hair cells after acoustic trauma,'' Science **240**, 1772–1774.

d'Aldin, C. G., Ruel, J., Assie, R., Pujol, R., and Puel, J. L. (**1997**). ''Implication of NMDA type glutamate receptors in neural regeneration and neoformation of synapses after excitotoxic injury in the guinea pig cochlea,'' Int. J. Dev. Neurosci. **15**, 619–629.

Dolan, D. F., Nuttall, A. L., and Avinash, G. (**1990**). ''Asynchronous neural activity recorded from the round window,'' J. Acoust. Soc. Am. **87**, 2621–2627.

Duckert, L. G., and Rubel, E. W. (**1990**). ''Ultrastructural observations on regenerating hair cells in the chick basilar papilla,'' Hearing Res. **48**, 161–182.

Duckert, L. G., and Rubel, E. W. (**1993**). ''Current concepts in hair cell regeneration,'' Otolaryngol. Clin. North Am. **26**, 873–901.

Durrant, J. D., Wang, J., Ding, D. L., and Salvi, R. J. (**1998**). ''Are inner or outer hair cells the source of summating potentials recorded from the round window?,'' J. Acoust. Soc. Am. **104**, 370–377.

Ernfors, P., Van De Water, T., Loring, J., and Jaenisch, R. (**1995**). ''Complementary roles of BDNF and NT-3 in vestibular and auditory development,'' Neuron **14**, 1153–1164.

Froymovich, O., Rebala, V., Salvi, R. J., and Rassael, H. (**1995**). ''Long-term effect of acoustic trauma on distortion product otoacoustic emissions in chickens,'' J. Acoust. Soc. Am. **97**, 3021–3029.

Gil-Loyzaga, P., and Pujol, R. (**1990**). ''Neurotoxicity of kainic acid in the rat cochlea during early developmental stages,'' Eur. Arch. Oto-Rhino-Laryngol. **248**, 40–48.

Hori, N., Doi, N., Miyahara, S., Shinoda, Y., and Carpenter, D. O. (**1991**). ''Appearance of NMDA receptors triggered by anoxia independent of voltage *in vivo* and *in vitro*,'' Exp. Neurol. **112**, 304–311.

Juiz, J. M., Rueda, J., Merchan, J. A., and Sala, M. L. (**1989**). ''The effects of kainic acid on the cochlear ganglion of the rat,'' Hearing Res. **40**, 65–74.

Kalb, R. G., Lidow, M. S., Halsted, M. J., and Hockfield, S. (**1992**). ''N-methyl-D-aspartate receptors are transiently expressed in the developing spinal cord ventral horn,'' Proc. Natl. Acad. Sci. USA **89**, 8502–8506.

Komuro, H., and Rakic, P. (**1993**). ''Modulation of neuronal migration by NMDA receptors,'' Science **260**, 95–97.

Lefebvre, P. P., Malgrange, B., Staecker, H., Moghadass, M., Van de Water, T. R., and Moonen, G. (**1994**). ''Neurotrophins affect survival and neuritogenesis by adult injured auditory neurons *in vitro*,'' NeuroReport **5**, 865–868.

Mayat, E., Lebrun, F., Sassetti, I., and Recasens, M. (**1994a**). ''Ontogenesis of quisqualate-associated phosphoinositide metabolism in various regions of the rat nervous system,'' Int. J. Dev. Neurosci. **12**, 1–17.

Mayat, E., Larner-Natoli, M., Rondouin, G., Lebrun, F., Sassetti, I., and Reasens, M. (**1994b**). ''Kainate-induced status epilepticus leads to a delayed increase in various specific glutamate metabotropic receptor responses in the hippocampus,'' Brain Res. **645**, 186–200.

McFadden, E. A., and Saunders, J. C. (**1989**). ''Recovery of auditory function following intense sound exposure in the neonatal chick,'' Hearing Res. **41**, 205–216.

Olney, J. W. (**1986**). ''Inciting excitotoxic cytocide among central neurons,'' Adv. Exp. Med. Biol. **203**, 631–645.

Patuzzi, R. B., and Bull, C. L. (**1991**). ''Electrical responses from the chicken basilar papilla,'' Hearing Res. **53**, 57–77.
Powers, N. L., Salvi, R. J., Wang, J., Spongr, V., and Qiu, C. X. (**1995**). ''Elevation of auditory thresholds by spontaneous cochlear oscillations,'' Nature (London) **375**, 585–587.
Puel, J. L., d'Aldin, C., Ruel, J., Ladrech, S., and Pujol, R. (**1997**). ''Synaptic repair mechanisms responsible for functional recovery in various cochlear pathologies,'' Acta Oto-Laryngol. **117**, 214–218.
Puel, J. L., Pujol, R., Ladrech, S., and Eybalin, M. (**1991**). ''Alpha-amino-3-hydroxy-5-methyl-4-isoxazole propionic acid electrophysiological and neurotoxic effects in the guinea-pig cochlea,'' Neuroscience (NY) **45**, 63–72.
Puel, J. L., Pujol, R., Tribillac, F., Ladrech, S., and Eybalin, M. (**1994**). ''Excitatory amino acid antagonists protect cochlear auditory neurons from excitotoxicity,'' J. Comp. Neurol. **341**, 241–256.
Puel, J. L., Saffiedine, S., Gervais d'Aldin, C., Eybalin, M., and Pujol, R. (**1995**). ''Synaptic regeneration and functional recovery after excitotoxic injury in the guinea pig cochlea,'' Comptes Rendus de I Academic des Sciences—Serie Iii, Sciences de la Vie 318, pp. 67–75.
Pujol, R., D'Aldin, G., Saffiedine, S., and Eybalin, M. (**1996**). ''Repair of inner hair cell-auditory nerve synapses and recovery of function after an excitotoxic injury,'' in *Auditory Plasticity and Regeneration*, edited by R. J. Salvi, D. Henderson, F. Fiorino, and V. Colletti (Thieme Medical, New York), pp. 100–107.
Pujol, R., Lenoir, M., Robertson, D., Eybalin, M., and Johnstone, B. M. (**1985**). ''Kainic acid selectively alters auditory dendrites connected with cochlear inner hair cells,'' Hearing Res. **18**, 145–151.
Pujol, R., Rebillard, G., Puel, J. L., Lenoir, M., Eybalin, M., and Recasens, M. (**1990**). ''Glutamate neurotoxicity in the cochlea: a possible consequence of ischaemic or anoxic conditions occurring in ageing,'' Acta Oto-Laryngol. Suppl. **476**, 32–36.
Rothman, S. M. (**1985**). ''The neurotoxicity of excitatory amino acids is produced by passive chloride influx,'' J. Neurosci. **5**, 1483–1489.
Rubel, E. W. (**1992**). ''Regeneration of hair cells in the avian inner ear,'' in *Noise Induced Hearing Loss*, edited by A. Dancer, D. Henderson, R. J. Salvi, and R. P. Hamernik (Mosby Year Book, St. Louis), pp. 204–227.
Ryals, B. M., and Rubel, E. W. (**1988**). ''Hair cell regeneration after acoustic trauma in adult Coturnix quail,'' Science **240**, 1774–1776.
Ryals, B. M., Ten Eyck, B., and Westbrook, E. W. (**1989**). ''Ganglion cell loss continues during hair cell regeneration,'' Hearing Res. **43**, 81–90.
Ryals, B. M., Westbrook, E. W., Stoots, S., and Spencer, R. F. (**1992**). ''Changes in the acoustic nerve after hair cell regeneration,'' Exp. Neurol. **115**, 18–22.
Salvi, R. J., Saunders, S. S., Hashino, E., and Chen, L. (**1994**). ''Discharge patterns of chicken cochlear ganglion neurons following kanamycin-induced hearing loss and regeneration,'' J. Comp. Physiol. A **174**, 351–369.
Saunders, S. S., Salvi, R. J., and Miller, K. M. (**1995**). ''Recovery of thresholds and temporal integration in adult chickens after high-level 525-Hz pure-tone exposure,'' J. Acoust. Soc. Am. **97**, 1150–1164.
Schuknecht, H. F., and Woellner, R. C. (**1953**). ''Hearing losses following partial section of the cochlear nerve,'' Laryngoscope **63**, 441–465.
Seren, M. S., Aldinio, C., Zanoni, R., Leon, A., and Nicoletti, F. (**1989**). ''Stimulation of inositol phospholipid hydrolysis by excitatory amino acids is enhanced in brain slices from vulnerable regions after transient global ischemia,'' J. Neurochem. **53**, 1700–1705.
Shero, M., Salvi, R. J., Chen, L., and Hashino, E. (**1998**). ''Excitotoxic effect of kainic acid on chicken cochlear afferent neurons,'' Neurosci. Lett. **257**, 81–84.
Spoendlin, H. (**1976**). ''Anatomical changes following various noise exposures,'' in *Effects of Noise on Hearing*, edited by D. Henderson, R. P. Hamernik, J. Mills, and D. Dosanjh (Raven, New York), pp. 69–89.
Trautwein, P., Hofstetter, P., Wang, J., Salvi, R., and Nostrant, A. (**1996a**). ''Selective inner hair cell loss does not alter distortion product otoacoustic emissions,'' Hearing Res. **96**, 71–82.
Trautwein, P., Salvi, R. J., Miller, K., Shero, M., and Hashino, E. (**1996b**). ''Incomplete recovery of chicken distortion product otoacoustic emissions following acoustic overstimulation,'' Audiol. Neuro-Otol. **1**, 86–103.
Wang, J., Powers, N. L., Hofstetter, P., Trautwein, P., Ding, D., and Salvi, R. (**1997**). ''Effects of selective inner hair cell loss on auditory nerve fiber threshold, tuning and spontaneous and driven discharge rate,'' Hearing Res. **107**, 67–82.
Zheng, X. Y., Ding, D. L., McFadden, S. L., and Henderson, D. (**1997a**). ''Evidence that inner hair cells are the major source of cochlear summating potentials,'' Hearing Res. **113**, 76–88.
Zheng, X. Y., Henderson, D., Hu, B. H., and McFadden, S. L. (**1997b**). ''Recovery of structure and function of inner ear afferent synapses following kainic acid excitotoxicity,'' Hearing Res. **105**, 65–76.
Zheng, X. Y., McFadden, S. L., and Henderson, D. (**1998**). ''Faster recovery in central than in peripheral auditory system following a reversible cochlear deafferentation,'' Neuroscience (NY) **85**, 579–586.
Zheng, X. Y., Wang, J., Salvi, R. J., and Henderson, D. (**1996**). ''Effects of kainic acid on the cochlear potentials and distortion product otoacoustic emissions in chinchilla,'' Hearing Res. **95**, 161–167.

Rate-intensity functions in the emu auditory nerve

Graeme K. Yates[a)]
The Auditory Laboratory, Department of Physiology, The University of Western Australia Nedlands, 6009, Australia

Geoffrey A. Manley and Christine Köppl
Institut für Zoologie der Technischen Universität München, Lichtenbergstrasse, 4, 85747 Garching, Germany

(Received 18 March 1999; revised 6 December 1999; accepted 13 December 1999)

Rate-versus-intensity functions recorded from mammalian auditory-nerve fibers have been shown to form a continuum of shapes, ranging from saturating to straight and correlating well with spontaneous rate and sensitivity. These variations are believed to be a consequence of the interaction between the sensitivity of the hair-cell afferent synapse and the nonlinear, compressive growth of the cochlear amplifier that enhances mechanical vibrations on the basilar membrane. Little is known, however, about the cochlear amplifier in other vertebrate species. Rate-intensity functions were recorded from auditory-nerve fibers in chicks of the emu, a member of the Ratites, a primitive group of flightless birds that have poorly differentiated short and tall hair cells. Recorded data were found to be well fitted by analytical functions which have previously been shown to represent well the shapes of rate-intensity functions in guinea pigs. At the fibers' most sensitive frequencies, rate-intensity functions were almost exclusively of the sloping (80.9%) or straight (18.6%) type. Flat-saturating functions, the most common type in the mammal, represented only about 0.5% of the total in the emu. Below the best frequency of each fiber, the rate-intensity functions tended more towards the flat-saturating type, as is the case in mammals; a similar but weaker trend was seen above best frequency in most fibers, with only a small proportion (18%) showing the reverse trend. The emu rate-intensity functions were accepted as supporting previous evidence for the existence of a cochlear amplifier in birds, the conclusion was drawn further that the nonlinearity observed is probably due to saturation of the hair-cell transduction mechanism. [S0001-4966(00)05903-8]

PACS numbers: 43.64.Pg, 43.64.Ri [RDF]

INTRODUCTION

Winter *et al.* (1990) described three types of rate-intensity (RI) function in the auditory nerve of the guinea pig: flat-saturating, sloping-saturating and straight. These three shapes were strongly related to the threshold at the fiber's characteristic frequency (CF) and to its spontaneous rate. Although these types actually represent a continuum, it is convenient to deal with them as different types of RI function, in which the flat-saturating fibers have the lowest thresholds and the highest spontaneous rates. Straight fibers have the highest thresholds and the lowest spontaneous rates, while sloping-saturating fibers are intermediate in both respects. Based on these findings, Yates *et al.* (1990) expanded on a model previously proposed by Sachs and Abbas (1974), in which the known nonlinear characteristics of basilar-membrane (BM) motion in the guinea pig explains the variety and the specific shapes of these RI function types both qualitatively and quantitatively. Depending on their threshold, each fiber is influenced by a different region of the basilar-membrane level-dependent nonlinearity. Thus, whereas the flat-saturating type of fiber reaches discharge saturation before the basilar membrane reaches the break-point in its slope, the straight fibers do not begin to raise their discharge above the spontaneous level until this break-point has been surpassed. In the intermediate case of sloping-saturating fibers, the basilar-membrane break-point lies somewhere within the range of sound-pressure levels (SPLs) which causes an increase in the firing rate, and the RI function of the fiber thus shows a clear inflection at the level where the basilar-membrane break-point is reached.

The mammalian system is characterized by a separation of the amplification function performed by the outer hair cells (OHCs), and the purely sensory function of the inner hair cells (IHCs). This independence means that the sensitivity of either cell type may be varied to alter the overall behavior of the system. Of importance to the present paper, however, is the global nature of the mechanical amplification in mammals, whereby OHCs act cooperatively to increase the vibrations detected by the IHCs. It implies that all IHCs—and their associated afferents—of a given CF in a given animal should reflect some part of the same mechanical input–output function. Differences in sensitivity of individual OHCs should change the sensitivity of all IHC responses, whereas changes in IHC sensitivity or of the afferent synapse will affect the segment of the BM input–output function transduced by the unit between its threshold and saturation. In birds, however, there is no evidence for such a clear differentiation of function between amplification and sensory transduction, and we might not necessarily expect the same characteristics of neural RI functions in birds as we find in mammals.

a)Electronic mail: gyates@cyllene.uwa.edu.au

As yet, the evolutionary selection pressures that led to differentiation of hair-cell form and innervation pattern in the cochlea are not well understood, although such differentiation presumably plays a key role in the hearing process (Manley, 1995; Manley and Köppl, 1998). Compared with our knowledge of the mechanics of the mammalian organ of Corti, the hearing organ of birds is poorly understood. It is, however, known that birds have also developed specialized hair-cell populations arranged across the width of the sensory epithelium, which show similarities to those of mammals (Manley, 1990; Manley *et al.*, 1988, 1989). It would therefore be very interesting to know to what extent similar phenomena occur in the excitatory micromechanical processes that lie between the motion of the hair-cell epithelium and the afferent fiber discharge. In particular, one major question in the physiology of hearing is whether an active process similar to that seen in mammals has been developed in other groups and whether there are physiological indicators for particular specializations of hair-cell populations. Is a division of labor of the kind seen in mammals typical of auditory papillae that show more than one type of hair cell across their width? In such papillae, one hair-cell population may, as in mammals, be specialized as reverse transducers (Manley *et al.*, 1989).

In the pigeon, the basilar membrane has been shown to support a traveling wave, but there are significant differences from its mammalian homologue. Unlike in mammals, the tuning of the mechanical response of the basilar membrane (BM) is much broader than in the neural frequency-threshold curves (FTCs), suggesting the presence of an additional filtering mechanism between the BM and the neuron. Also, the input–output function of the pigeon BM appears to be linear (Gummer *et al.*, 1987), again in sharp contrast with mammals. Another interesting difference between birds and mammals with respect to physiological correlates of cochlear mechanics is that, in birds, the most heavily afferently innervated and most sensitive hair cells are often situated not over the free basilar membrane but over the cartilagenous neural limbus (Gleich, 1989; Smolders *et al.*, 1995). This suggests that the stimulus for these bird hair cells is derived through motion of the tectorial membrane, which may not be closely linked to basilar-membrane motion (Manley, 1995), so that there may be significant differences in micromechanics between mammals and birds. Indeed, there is evidence that in lizards, the mechanics of the BM play no significant role in the frequency selectivity of sensitive neural tuning (Manley, 1990).

There is evidence for an active process in birds: The barn owl shows spontaneous otoacoustic emissions (SOAE; Manley and Taschenberger, 1993; Taschenberger and Manley, 1997), and SOAE are commonly regarded as resulting from hair-cell motility, a likely basis of the cochlear amplifier (Köppl, 1995). Barn-owl SOAE have also been shown to have the statistical properties associated with sinusoidal generators (van Dijk *et al.*, 1996). If the active process performs the same function in birds as it does in mammals, i.e., increases the sensitivity of the hair-cell system by increasing the mechanical stimulus to their stereocilia, then it must do so by a mechanism not directly involving the basilar membrane itself. One might speculate that this could involve amplifying the vibration of the tectorial membrane (Manley, 1995) without a concomitant increase in basilar-membrane vibration. In that case, the basilar membrane would simply couple the initial stimulus to the hair cells, as is apparently the case in lizards (Manley, 1990). The characteristics of such a cochlear amplifier may well be quite different from those in mammals and might manifest themselves in different behavior of the auditory-nerve recordings.

In order to further our understanding of these processes, we have continued anatomical and physiological studies of a series of bird species by looking at the emu, a representative of a primitive group of flightless birds, the Ratites. The Ratites are a monophyletic group of closely related species (Cracraft, 1974, 1981; Hennig, 1983; Sibley and Ahlquist, 1981) whose anatomy shows a number of primitive and/or neotenic features. The morphology of the inner ear of the emu is more primitive than that of any bird so far investigated (Fischer, 1994, 1998; Köppl *et al.*, 1998). In particular, an unusually large percentage of the hair cells belongs to the putatively primitive, tall type, and only a small percentage at the abneural edge in the basal area shows the morphology of typical short hair cells. Thus, it might be expected that any physiological features attributable to specializations of short hair cells would be weak or absent in this species. We have previously reported the general physiological characteristics of primary auditory-nerve fibers recorded in the cochlear ganglion of emu chicks (Manley *et al.*, 1997).

In this paper, we analyze the characteristics of rate-intensity (RI) functions of emu single auditory afferents at different stimulus frequencies and compare them with the different RI types described in mammalian systems. We ask whether there are different types of RI shape characteristics in the emu chick, and whether there are resemblances to functions in other species that might permit some speculation on avian micromechanics. It is now widely accepted that nonlinear saturation of the mammalian cochlear amplifier mechanism manifests itself in the form of a compressive input–output function on the BM (Rhode, 1971; Sellick *et al.*, 1982; Robles *et al.*, 1986; Cooper and Rhode, 1992). This, in turn, is reflected in mammalian neural RI functions (Sachs and Abbas, 1974; Winter *et al.*, 1990; Yates *et al.*, 1990; Yates, 1990; Schoonhoven *et al.*, 1997). Since the involvement of the BM as the link between the active process in the OHCs and the sensory transduction stage in the IHCs apparently does not have a parallel in the avian cochlea, saturation of the cochlear amplifier in birds could occur without concomitant nonlinearity involving the basilar membrane.

I. METHODS

A. Subjects and surgical procedures

Experimental methods of data gathering have been described in detail elsewhere (Manley *et al.*, 1997) and will therefore not be repeated in detail here. In summary, data were collected from emu chicks (*Dromaius novaehollandiae*) ranging in age from 1 to 14 days post-hatching, after anesthesia with pentobarbital (Nembutal, 30 mg/kg, i.m.) and

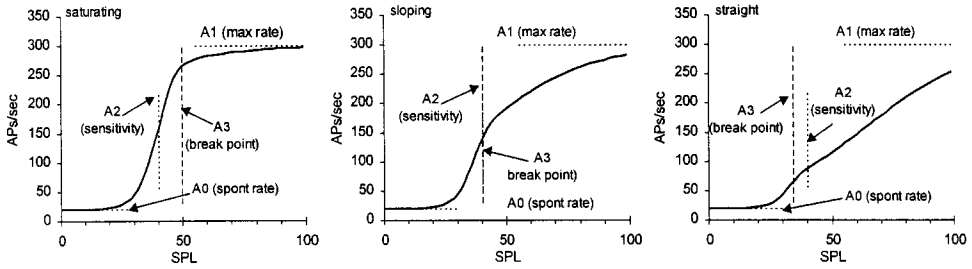

FIG. 1. Illustration of the definitions of four of the five parameters used in fitting Eqs. (1) and (2) to the observed rate-intensity data. The three panels show the shapes of the fitted function for three different ratios of $A3/A2$, representing (left) a flat-saturating fiber ($A3/A2>3$, or 9.5 dB), (middle) sloping saturating (0.5, or -6 dB$<A3/A2<3$ or 9.5 dB), and (right) straight ($A3/A2<0.5$ or -6 dB). Values of $A3/A2$ less than 0.4 can produce rate-intensity functions that are actually concave upwards. The fifth parameter, not added here, controls the slope of the curve above the break-point.

chloral hydrate (Chlorthesin, 100–170 mg/kg, i.m.). Maintenance doses of 20–28 mg/kg pentobarbital and 60–120 mg/kg Chlorthesin per hour were given according to individual need. The birds were artificially ventilated and held at a rectal temperature of 38.5 ± 0.5 °C using a heating pad with thermostatic control. The cochlear ganglion was exposed using a dorsolateral approach, permitting access to the entire length of the ganglion in some cases.

B. Stimulation and recording procedure

Recordings of nerve action potentials were made via glass microelectrodes advanced using a custom-made motor drive. Noise bursts were used as a search stimulus. All recordings were made in a sound-attenuating booth. Stimuli for data collection were tone bursts generated by a frequency synthesizer (HP3325A) and a custom-built tone gate and attenuator. Control over the experiments was by desktop computer using custom software. In the majority of neurons, an initial frequency-threshold curve (FTC) was recorded using a threshold-hunting technique (Winter *et al.*, 1990). In all cases, tone bursts were then presented, pseudo-randomly selected from a rectangular matrix of frequency and intensity combinations that included the characteristic frequency (CF) and threshold sound intensity of the fiber. Each frequency-intensity combination was presented a total of either ten times for a small number of frequencies (typically three), or three times for a larger number of frequencies (typically 15–30). The action potentials were counted during the duration of each stimulus (50 ms, repeated 3/s for ten-repeat data, and 5/s for three-repeat data), and counts from repeated presentations were averaged. Complete sets of ten repeats were collected from 51 units and sets of three repeats from 157 units. The sound pressure was calibrated individually in all animals and normalized to dB *re* 20 μPa (dB SPL).

Approval for the experiments was obtained from the University of Western Australia's Animal Experimentation Ethics Committee, approval numbers 64/93/93 and 180/94/94. The protocols also followed the guidelines of the Australian National Health and Medical Research Council.

C. Data analysis

For analysis, each file containing data on the responses of a cell to one set of frequencies and SPLs was read into a spreadsheet program (Microsoft EXCEL) and analyzed semi-automatically using scripts written in the spreadsheet macro language. The data were fitted with the following function using a least-squares criterion, which has previously been shown to represent well the RI functions of auditory-nerve afferent fibers in guinea pig (Yates, 1990), in the pigeon (Richter *et al.*, 1995), and the barn owl (Köppl and Yates, 1999):

$$d=\left[\frac{A_3^{(1/A_4-1)}\cdot p^{1/A_4}}{A_3^{(1/A_4-1)}+p^{(1/A_4-1)}}\right]^{A_4}, \tag{1}$$

$$R=A_0+\frac{(A_1-A_0)\cdot d^2}{A_2^2+d^2}, \tag{2}$$

where R=mean firing rate in spikes/s, p=sound pressure (in Pascals), A_0=spontaneous firing rate, A_1=maximum firing rate, A_2=value of d which produces half-maximum increase in firing rate; also the sound pressure which produces half maximum increase in firing rate in a flat-saturating fiber, A_3=sound-pressure break-point at which sloping saturation begins, and A_4=exponent of the power-law slope of the sloping-saturating region.

In the case of the guinea pig, d was understood to represent the basilar-membrane displacement in response to sound pressure, but in the avian case its interpretation is still open. Figure 1 shows the definition of parameters A_0 to A_3 in diagrammatic form.

In previous studies, each RI curve for a given frequency was fitted independently of the other frequencies, with fresh estimates of all five parameters being obtained for each. This leads to a minimum sum-of-squared residuals for each set of RI data but also to significant variability of the parameters across frequencies. In the present work we implemented a different strategy in which we made the reasonable assumption that the spontaneous rates for all frequencies and the maximum firing rates for frequencies above the cycle-by-cycle phase-locking limit will be the same in any one fiber. The latter assumption was tested in several cases by comparing fits with and without the assumption: the mean difference across a single set of data was always close to zero. Even where saturation is not evident in the experimental data, an estimate of the saturation rate is inherent in Eqs. (1) and (2). We also assumed that the parameter A_4 (the compression slope) is the same for any one fiber, an assumption without justification other than that it produces convincing fits. Ac-

cordingly, each collection of RI data for a single fiber, representing the RI functions for different frequencies, was processed as a single set sharing the values for A_0, A_1, and A_4.

For frequencies above the range of phase locking (600 Hz), only the parameters A_2 and A_3 were free to vary between frequencies. RI curves for low-frequency stimuli, i.e., below 600 Hz, appeared to saturate at a rate which varied with stimulus frequency and which was usually, but not always, less than that for higher frequencies, an effect we attribute to phase locking at these lower frequencies. It was for this reason that we permitted the maximum firing rate parameter, A_1, to vary for frequencies at or below 600 Hz.

Since the A_2 parameter represents the sensitivity of the fiber, it may be used as a surrogate for threshold. In fact, the threshold that would be estimated by our FTC program may be determined from the A_0, A_1, and A_2 parameters according to the equation

$$p_t = A_2 \sqrt{\frac{R - A_0}{A_1 - R}}, \tag{3}$$

where R is the criterion rate. This equation holds true to within 1 dB for all but the most extreme of the straight functions. For our FTC program, where the criterion threshold rate increase was approximately 20 spikes/s, Eq. (3) implies that the FTC threshold is typically between 6 and 13 dB below A_2, depending on spontaneous and maximum rates. During the fitting procedure, a plot of A_2 and A_3 against stimulus frequency was maintained for comparison with the FTC that had been determined separately for a subset of neurons during the course of data collection.

For some fibers, RI functions were collected twice, once with ten repetitions for a small number of frequencies (typically three), and once with three repetitions for a larger number of frequencies. For statistical analysis, however, each fiber is represented only once. If the data set with the ten repetitions included the most sensitive frequency (as defined by the set with three repetitions and many frequencies), then CF results were used from that set. If not, then the CF data from the set with three repetitions were used. In the final analysis, 188 sets of data were included.

D. Definition of RI types

It is important at this stage to clarify the definitions of the various classifications of cell RI functions. We use a criterion based solely on the quantitative analysis of each set of data according to which a flat-saturating fiber is defined not by the presence of a high-intensity rate saturation, but rather by the absence of a break-point in the RI function before saturation. In other words, both flat-saturating and sloping-saturating fibers may approach a constant firing rate at high intensities (Sachs and Abbas, 1974, introduced the terms ''flat-saturating'' and ''sloping-saturating'' fibers). This classification in mammals may be related back to the supposed origin of the break-point, namely the nonlinearity of the cochlear amplifier. If the response range of the fiber includes this nonlinear break-point, then it is classified as sloping saturating even if it does subsequently saturate, because it will clearly show a break-point in the discharge-vs-intensity behavior, i.e., it will show sloping-saturation behavior. All fibers correctly classified as flat saturating will have the same shape of the RI function and dynamic range, i.e., 19.1 dB for 10%–90% of driven firing rate. This is a mathematical consequence of Eq. (2) (see later). Thus, if a fiber has a dynamic range greater than this, its best fit will also show a break-point in the slope and the fiber will not be classified as flat saturating.

Quantitatively, we define a sloping-saturating fiber as one in which the ratio A_3/A_2 is less than 3, which is equivalent to 9.5 dB [example shown in Fig. 1(B)]. For such curves, the nonlinear break-point occurs in the region between threshold and saturation and is a distinct feature of the response. Straight fibers are an extreme case of sloping saturation [$A_3/A_2 < 0.5$, example in Fig. 1(C)]. Such classifications are, of course, arbitrary, since the RI shapes form a continuum. However, a careful visual comparison of the fits with all experimental data indicated that they provided a good description of the data. The purpose of the curve-fitting procedures was twofold: first, to compare the data with descriptions of rate-intensity functions which have previously been shown to provide a good description of similar data in the guinea pig (Yates *et al.*, 1990) and second, to provide objective estimates of the various parameters of interest in this study.

II. RESULTS

The analysis in this paper was carried out on a subset of the auditory afferent fibers whose general properties were previously described (Manley *et al.*, 1997). The distribution of the selected data in terms of the age of the animals and the distribution of the CF thresholds and $Q10$ dB tuning selectivity coefficients was very similar to the ranges of these parameters in the whole data set. The only systematic bias in the present data sample was a deliberate attempt to collect sufficient RI data from high-frequency fibers. Thus, in the data set of Manley *et al.* (1997), fibers of CF below 1 kHz made up almost two-thirds of the sample, whereas in the present data sample such fibers made up only one-third of the sample.

A. Fitted RI functions

The functions (1) and (2) were found to be an excellent description of the RI data from the emu chick. The quality of the fit was similar for frequencies below, at, and above CF, and for fibers with RI functions of all types. In a few cases, the fit was less than perfect around threshold, with the spontaneous rate appearing slightly depressed before threshold and the rate rising slightly faster than predicted by the curve of best fit. For most sets of data, however, this effect was either absent or small and is presumed to be the phenomenon of single-tone, or primary, suppression previously documented in birds (e.g., Hill *et al.*, 1989a).

Figure 2 shows six representative sets of data and their corresponding fitted RI functions, covering the frequency range from phase-locking frequencies up to a CF of 3.2 kHz. In Fig. 2(a) all stimulus frequencies are in the phase-locking range and consequently the maximum discharge rate was

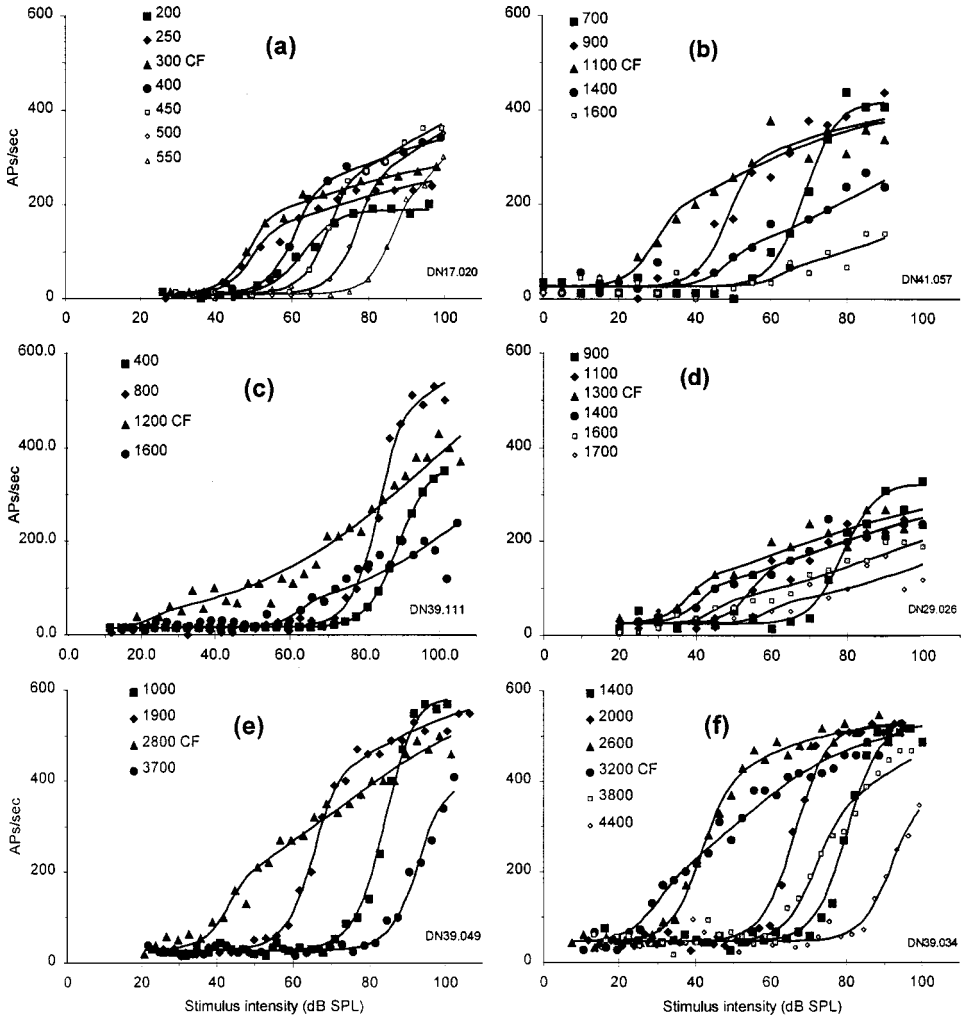

FIG. 2. Rate-vs-intensity functions recorded in six auditory-nerve fibers in four emu chicks. Symbols show the discharge rates as recorded; lines indicate the respective best fit. CF is indicated in each legend.

free to vary for all RI functions in this set. At 200 Hz, below CF, the RI function is clearly flat saturating while all other RI functions for this set are sloping saturating. The response with the greatest degree of sloping saturation (the smallest ratio of A_3/A_2) is the CF response, while either side the functions return closer to, but never become, flat saturating. Figure 2(b) is from a fiber with a higher CF and, with increasing frequency, shows a continuous progression of RI type from flat saturating to almost straight, typical of the mammalian pattern (Sachs and Abbas, 1974) but found in only 18% of the emu fibers. The functions shown in Fig. 2(c) are an extreme example of the sloping-saturating form for a fiber with a CF of 1200 Hz. In this case, A_3 was only 0.24 times A_2 at CF, resulting in a RI curve that is actually concave upwards. Even the above-CF curve, at 1600 Hz is of the same form, although less extreme. Only a few fibers of this extreme shape were found. This concave-upwards form was also seen occasionally in the guinea pig (Winter *et al.*, 1990) and is predicted by Eqs. (1) and (2) to occur whenever A_3 is less than approximately 0.4 times A_2. Figure 2(d) shows another example of a continuous progression of RI type, from flat saturating to almost straight. Figure 2(e) and (f) are the more usual types, with flat-saturating functions well below CF, gradually assuming a more sloping-saturating form approaching CF and then tending back towards, but not reaching, the flat-saturating type.

Figure 3 shows three more examples, each showing significant saturation at least at one stimulus frequency. During the curve-fitting procedure, these frequencies provide excellent estimates for the saturation rate for all frequencies in the set. In other cases, where no clear saturation is evident at any frequency (the majority of fibers), estimates of the saturation rate are still inherent in the equations and their match to the available data. For flat-saturating fibers and for sloping-saturating functions below the sloping-saturation breakpoint, the functions scale directly with driven rate (maximum–spontaneous, A_1-A_0), so estimates of the maximum rate are available from all data points above the spontaneous rate.

Figure 4 shows a histogram of numbers of units grouped by shape of RI curve (A_3/A_2). Of a total of 188 fibers analyzed, 1 (0.5%) was flat saturating at CF ($A_3/A_2 >= 9.5$ dB), 152 (80.9%) were sloping saturating ($9.5 > A_3/A_2 >= -6$ dB) and 35 (18.6%) were straight or concave upwards ($A_3/A_2 < -6$ dB).

As for the sloping-saturating and straight classifications, we found no significant differences between them in spontaneous rate, maximum rate, threshold, frequency selectivity defined as the $Q_{10\,\mathrm{dB}}$, CF, or dynamic range (Mann-Whitney U-tests, $p > 0.05$).

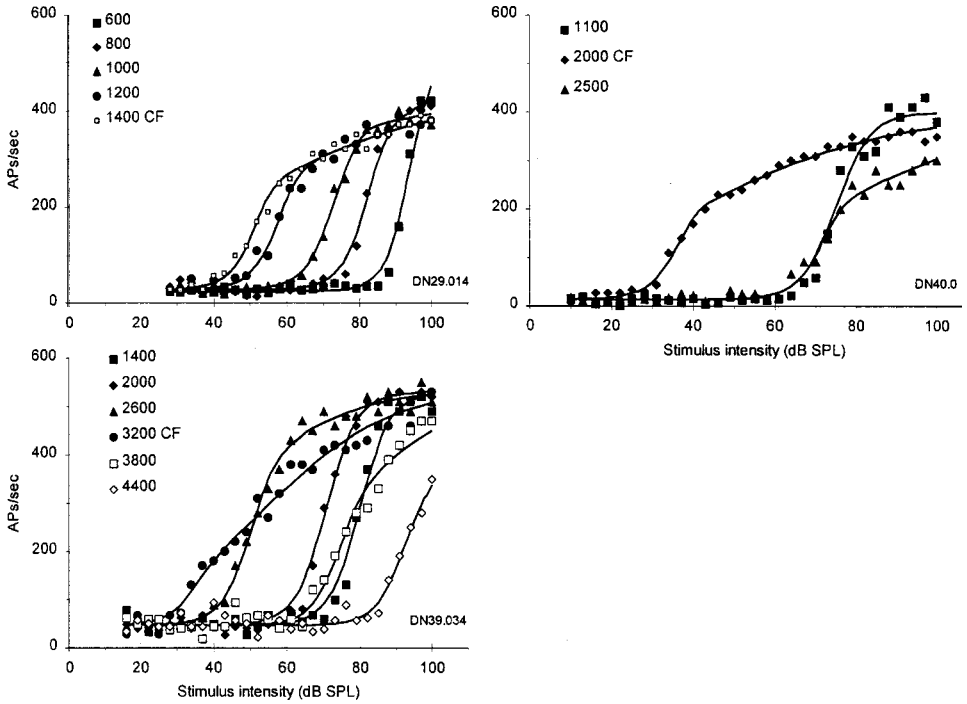

FIG. 3. Rate-versus-intensity functions for three fibers from the emu auditory nerve. These examples illustrate that the assumption that all RI functions from the same fiber converge at a common saturation discharge rate is valid and does not distort the individual fits. Note that this assumption was only made for frequencies above 600 Hz; below that, the effect of phase locking on discharge rate appeared considerable (see the text).

B. Effectiveness of collective fitting of parameters

Since our technique of simultaneously fitting all data from a single RI data matrix is new, some comment on its effectiveness is necessary. Fitting single frequencies independently (Yates, 1990) allows the maximum number of degrees of freedom but takes no account of known redundancies in the parameters. Collective fitting, although reducing the number of degrees of freedom, actually reduces the variability in fitted parameters, as demonstrated in Fig. 5. The top panel of Fig. 5 shows values of A_2 and A_3 estimated from independent fitting of data for each frequency, plotted against the corresponding frequency. Although clearly displaying the general shape of a frequency-threshold curve (compare with the threshold curve measured by the FTC program), there is a good deal of scatter. This may be compared with the lower panel, where parameters obtained under constrained fitting are similarly plotted. The frequency-response characteristics are much smoother, demonstrating that the constrained fitting procedure is effective. Since there is nothing in the data or the fitting procedure to influence the fitted parameters across frequencies (apart from the common values of A_0, A_1, and A_4), we interpret the smoothing of the frequency responses to be an indication that a better fit is resulting.

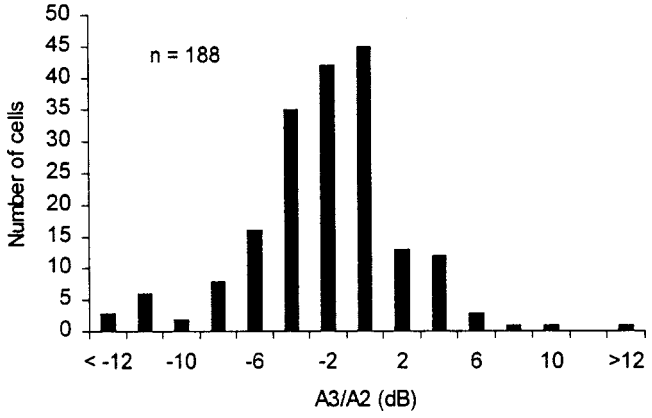

FIG. 4. Histogram showing number of cells in each range of the ratio A_3/A_2 (at CF). Bins are 2 units wide, except for the extreme end bins. Straight or concave-upwards cells are to the left, sloping saturating in the middle, and flat saturating to the right. For comparison, the curves shown in Fig. 1 are for A_3/A_2 values of +9.5, 0, and −6 dB, respectively.

C. Relationship between threshold and break-point

The tendency for all RI functions to be sloping saturating should be evident as a strong correlation between the A_2 and A_3 parameters when other factors are maintained constant. To examine this, we plotted values of A_3 against A_2 for small groups of fibers of similar CF within individual animals. Figure 6 shows sensitivity and break-point values obtained from sets of RI functions and grouped according to CF in four emu chicks. The relationship between A_3 and A_2 is nearly linear, with a slope close to unity. The grouping according to CF was arbitrary, being chosen simply to provide a useful number of points in each set. The choice of frequency ranges seemed to be irrelevant to the correlation since each of the sets individually indicated the same trend.

The pooled data from all emu chicks are even more convincing (Fig. 7). Here, all 188 fibers from 16 chicks are represented, without regard to their CF or threshold. Points cluster tightly around a line of slope 1.096, with a correlation coefficient of 0.946 ($p<0.1\%$, $n=188$). Figure 6 also illustrates that, as previously shown by Manley *et al.* (1997), threshold improves somewhat during development, since the points from the older chicks are grouped closer to the low-threshold region of the graph.

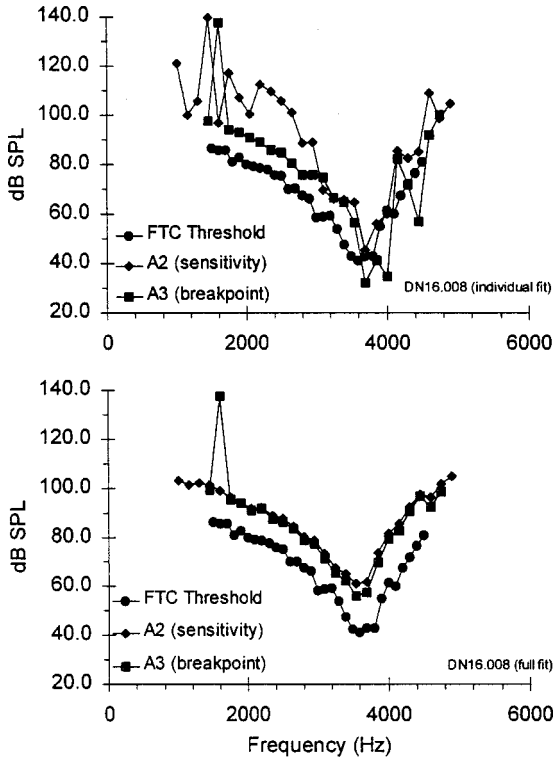

FIG. 5. Comparison of fitted parameters plotted against stimulus frequency for independent fits (top panel) and fits in which the spontaneous rate, maximum firing rate, and compression slope were held constant for all RI functions in the data set (bottom). Also shown is the threshold curve as determined independently by our FTC program. For clarity, we have used a linear frequency scale in this plot.

D. Tuning curves

Since A_2 may be taken as a surrogate for neural threshold, plots of A_2 against frequency should be directly comparable with frequency-threshold curves obtained from the threshold-tracking program. Furthermore, given the parameters of the fitted curves, it is possible to calculate the SPL that produced any given spike rate. In those data sets in which we collected only three passes over each RI function, we were able to acquire data for sufficient frequencies to generate an A_2-vs-frequency curve. Although the number of passes was small, there were sufficient frequencies in each file, and hence a sufficient number of data points overall, to produce good estimates for all the parameters when collectively fitted.

We verified the A_2 tuning curves by direct comparison with the independently measured frequency-threshold curves (Manley *et al.*, 1997). Also shown in Fig. 5, along with A_2 and A_3, are the actual FTC data determined experimentally for the same fiber. The agreement is excellent over most of the frequency range, with the A_2 curve approximately 12 dB above the threshold data, as expected (see Sec. I C).

The A_3 curve closely follows the A_2 curve in the vicinity of the CF region, reflecting the fact that the shape of the RI function varies little over that range. At the extremes, however, A_3 rises above A_2 as the curves are closer to flat saturating on the low-frequency tail and, usually, above CF. It is also instructive to plot the ratio A_3/A_2, which is another indicator of RI shape. More importantly, however, this ratio might be interpreted as the influence of the cochlear amplifier, for if the gain of the amplifier were increased it would appear in the RI functions as an extension of the low-intensity region with a lesser effect on the higher SPL region, thus lowering the value of A_3 (Yates, 1990). It is clear from Fig. 8 that the A_3/A_2 ratio is tuned, with its minimum value centered approximately at the CF. This was a general finding, but not universal. In almost every case A_3/A_2 fell as frequency approached CF from above or below, but in some fibers the sharp dip near CF and the subsequent rise was missing.

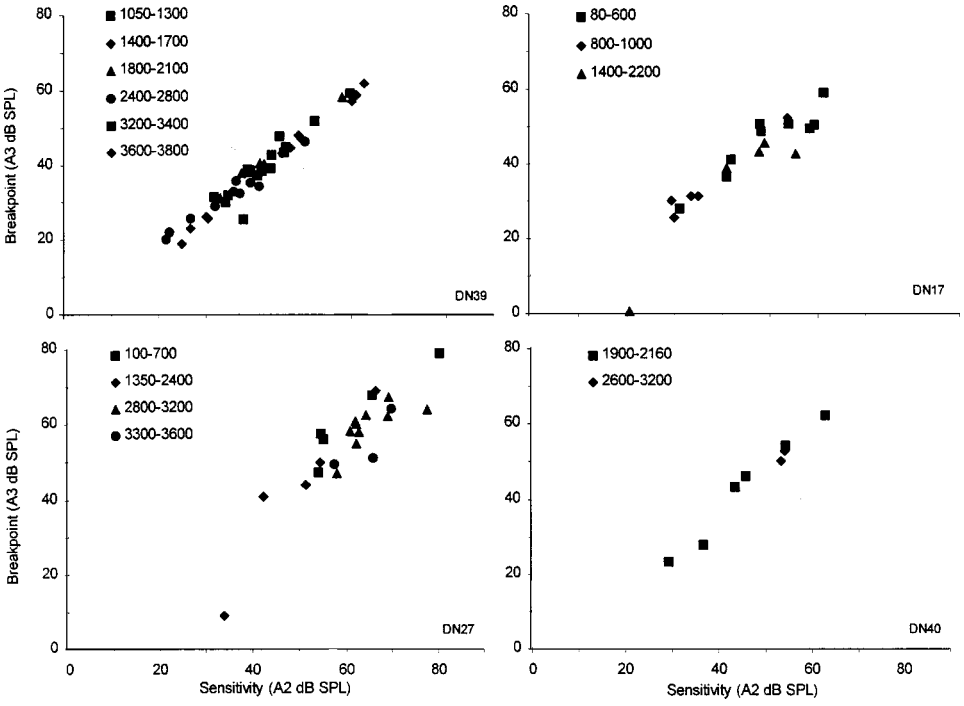

FIG. 6. Four plots illustrating the similarity among CF rate-intensity shapes for a range of fibers in a single emu chick. Each A_3, the SPL at which the sloping-saturation break occurs, is plotted against A_2, a measure of neural sensitivity (both at CF). If the shapes of the rate-intensity functions were all the same and did not change with sensitivity, then all points would lie on a straight line. The data are divided into CF ranges as shown in the legends.

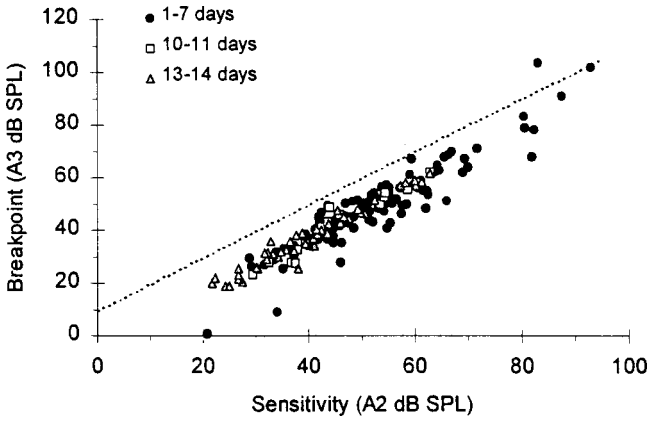

FIG. 7. Plot of $A3$ as a function of $A2$ for 188 CF rate-intensity functions analyzed from 16 emu chicks. Data are divided into three age groups. The dashed line marks the division between flat-saturating and sloping-saturating fibers. Only one point falls above this line and therefore represents a flat-saturating fiber.

E. Dynamic range

One of the more interesting features of sloping-saturating and straight RI functions is that they are capable of coding stimulus intensity over a much wider dynamic range than are flat-saturating fibers. Since virtually all of the fibers encountered in emu chicks were of this form, it is of interest to investigate the spread of dynamic ranges at CF. Dynamic range may be defined in several ways, but we chose the difference between the SPLs required to produce spikes rates of 10% and 90% of driven rate, i.e., maximum rate minus spontaneous rate (A_1-A_0). Thus, we chose spike rates of $A_0+0\cdot1(A_1-A_0)$ and $A_0+0\cdot9(A_1-A_0)$ and calculated the SPLs which produced these. This definition depends only on the difference between maximum and minimum firing rates and not on their particular values, and so should be more easily comparable across studies. As the fits were excellent descriptions of the data, we calculated the dynamic ranges this way rather than estimate them directly from the raw responses.

For flat-saturating fibers only, Eq. (2) may be inverted analytically to find the SPL in terms of spike rate. This reveals a point that is often neglected in the interpretation of RI-function fitting, that for all flat-saturating fibers, regardless of the parameters, the dynamic range is the same and is numerically equal to 19.1 dB for the 10%–90% range (see also Eatock *et al.*, 1991). For sloping-saturating data, however, the 90%-rate SPL must be estimated by interpolation, since Eq. (2) is not easily inverted. For each of the 188 fibers analyzed, the dynamic ranges were calculated by interpolation (Fig. 9).

The numbers range from 19.1 dB for the flat-saturating fiber up to very large values that occur because this method of calculation extrapolates to stimulus intensities above the actual observations. All our measurements terminated at approximately 100 dB SPL and in many cases the responses were far from approaching asymptote, so that extrapolation to the values estimated by the fitted curves results in estimates for the upper limit to the dynamic range beyond our maximum stimulus level. Restricting our calculation of dynamic range to the difference between the 10% SPL and the maximum-applied stimulus SPL would lead to values which are experimentally demonstrable, but which would certainly underestimate many of the dynamic ranges.

Figure 9 shows dynamic range estimates for all fibers, as calculated from the 10% SPL to the lesser of the calculated 90%-rate SPL and the maximum-applied SPL. Many points scatter around and below a straight line with a negative slope. Such a line is simply another demonstration that most CF RI functions have very similar shapes, regardless of threshold. As a consequence, many of them have the maximum-applied SPL as their upper limit, while their lower limit is the fiber's threshold.

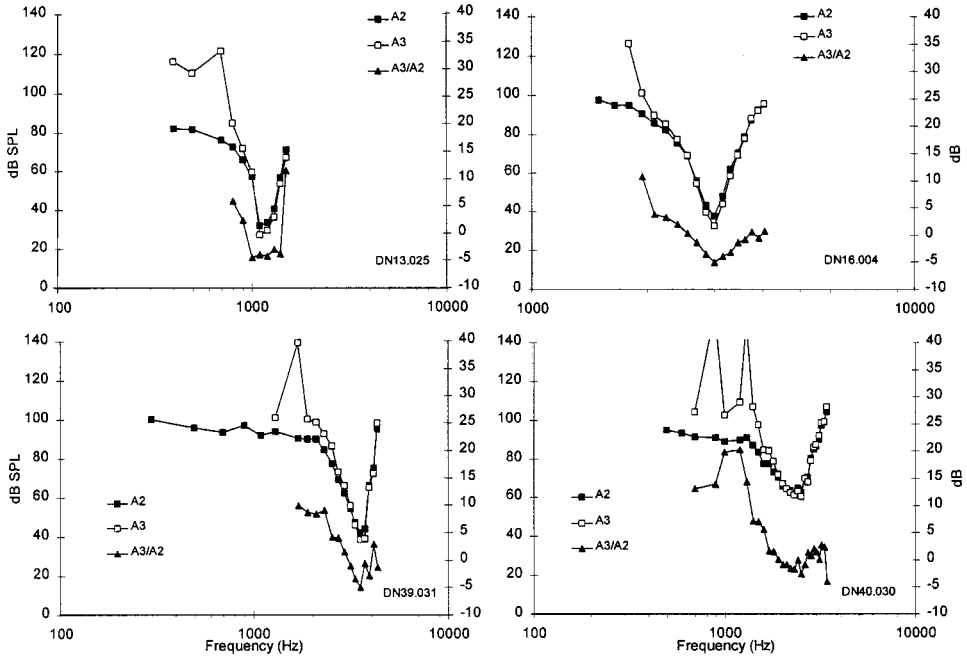

FIG. 8. Frequency response curves for A_2, A_3, and A_3/A_2 for four different fibers. All show the general shape of the frequency-threshold curves, although the ratio A_3/A_2 is less sharply tuned. Data for $A3$ have been omitted when the estimated RI functions were classified as flat saturating. The scale for the A_3/A_2 ratio is on the right of each panel and is expanded relative to the scale for A_2, A_3, which is on the left.

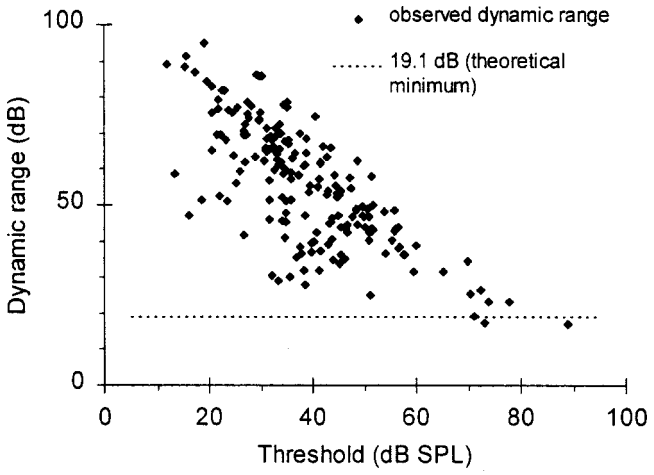

FIG. 9. Scatter plot of dynamic range as a function of FTC threshold for 188 fibers at CF. Symbols show the range actually observed during data collection as defined in the text.

III. DISCUSSION

A. The significance of the RI shape

It has been shown previously that RI functions in the guinea pig auditory nerve may be described well by Eqs. (1) and (2), regardless of threshold or stimulus frequency (Yates, 1990). The particular form of these equations was originally chosen somewhat arbitrarily, although there were guiding principles. Equation (1) describes the spike rate of a fiber as a function of the presumed input to its inner hair cell (IHC) stereocilia. It describes a simple hyperbolic saturation in the relationship between the square of stimulus intensity and the spike rate, with the parameter A_2 setting the intensity at which the rate is reduced by 50% due to (presumed synaptic) saturation. The square-law relationship between displacement and rate of action-potential generation presumably reflects the square-law growth in the hair-cell dc receptor potential as a function of SPL, as shown in mammals (Goodman *et al.*, 1982; Patuzzi and Sellick, 1983), supported in the alligator lizard (Eatock *et al.*, 1991) and expected from theory. Equation (2) assumes a relationship between stimulus intensity and mechanical input to the IHCs (which in mammals would correspond to the basilar-membrane vibration amplitude) which is initially linear for low intensities and which then changes to a power-law growth at some intensity defined by A_3. The transition is believed to be due to partial saturation of the cochlear amplifier mechanism, in mammals probably at the site of the outer hair cell (OHC) transduction of mechanical vibration to electrical current. Thus, above this break-point the amplifier gain is progressively reduced as the stimulus strength increases, resulting in a nonlinear region in the input–output function. Such a break-point is a hallmark of the current concept of the cochlear amplifier (Yates, 1990).

In mammals, the cochlear amplifier is believed to act through the basilar membrane (Rhode, 1971; Robles *et al.*, 1986; Sachs and Abbas, 1974; Sellick *et al.*, 1982; Winter *et al.*, 1990), which in turn drives the IHCs. Mammalian flat-saturating fibers are believed to be more sensitive to basilar-membrane vibration: they are driven over their full response range by basilar-membrane displacements that are below the saturation threshold of the cochlear amplifier. Sloping-saturating fibers, in contrast, have sensitivities that span the onset of basilar-membrane nonlinearity (Winter *et al.*, 1990; Yates, 1990).

It is important to understand, however, that the sloping-saturating form of RI function is not necessarily dependent upon a nonlinear basilar-membrane response. It is simply a consequence of saturation of a nonlinear element within a positive feedback loop driving the sensory hair cells (Zwicker, 1979; Mountain *et al.*, 1983; Yates, 1990) and other forms of cochlear amplifier should lead to similar RI functions. Thus, it should not be surprising if species that show a different development of the basilar-membrane–hair-cell complex should show sloping-saturating growth of auditory-nerve discharge rate without nonlinear basilar-membrane motion. It might indicate that they have evolved some other form of sensitivity-enhancing cochlear amplifier process which does not include the basilar membrane. There is considerable evidence that the most significant nonlinear element in the mammalian cochlear amplifier is the (outer) hair cell forward transduction channel (Patuzzi *et al.*, 1989; Geisler *et al.*, 1990). This channel is a feature common to all hair cells, and it is reasonable to expect that it may also be the nonlinear element in other species' hearing organs. Thus, the typical form of the RI functions might indicate that the common nonlinearity in the active process is the forward transduction stage of the hair cell (Hudspeth, 1997).

There is evidence for the existence of a cochlear amplifier mechanism in birds (e.g., Manley, 1995), but the form it takes is unknown. In the avian cochlea, the hair cells are less clearly differentiated into two types as compared with a mammal. Instead, there is a continuous variation between a short form that occurs abneurally and has little or no afferent innervation, and a tall form that occurs neurally and always has an afferent innervation (e.g., Fischer, 1994). There may well be a corresponding differentiation of role, as is the case for the inner and outer hair cells of mammals, with the short hair cells being specialized for electrical-to-mechanical transduction (Manley, 1995), but there is no evidence for this. There is, however, no alternative to the mechanical-to-electrical transduction, which still appears to be situated in the stereocilia at the tops of hair cells. Thus, we expect this transduction stage to play as important a role in the nonlinearity of the cochlear amplifier in birds as it does in mammals.

B. Alternative explanations

We propose saturation of the cochlear amplifier as being responsible for the sloping-saturating form of auditory-nerve RI functions. There appear to us to be few alternatives. One possibility might be the saturation of hair-cell dc receptor potential, which might cause an abrupt change in the slope of the RI curve. We reject this because (a) published evidence shows that the receptor potential does not saturate until well after the RI function break-point (Patuzzi and Sellick, 1983; Goodman *et al.*, 1982; Eatock *et al.*, 1991), and (b) such saturation would not be expected to be frequency dependent and so would not influence RI functions only near CF. A

global mechanism, such as a single effect operating on all cells (e.g., an inherent mechanical nonlinearity not associated with the cochlear amplifier) must also be ruled out, since that would imply that all RI functions should show a break-point at the same stimulus intensity instead of the very wide range shown in the present data.

C. Tuned cochlear amplifier

In the majority of fibers examined, we found the shape of the RI function, quantified as the ratio A_3/A_2, to follow a bandpass characteristic, usually but not always centered on the CF of the fiber. In general, we could say that the ratio A_3/A_2 was tuned approximately to the CF, but with a shallower tip region. The significance of such tuning is not clear, but since the shape of the RI function indicates the presence of a cochlear amplifier, it might be inferred that the A_3/A_2 tuning represents a frequency selectivity in the underlying positive feedback loop (Yates, 1990). Two observations support this view. First, tuning of the positive feedback is essential if the cochlear amplifier is to enhance the frequency selectivity of the response. Second, the shape of the presumed feedback tuning is clearly appropriate, in most cases, to producing an enhancement at the CF since it would provide greatest amplifier gain at that frequency. Further theoretical work would be needed to confirm this.

D. Comparison with other birds

There are two further detailed studies of RI responses in the avian auditory nerve, which used the same basic methods of analysis employed in the present paper, on the pigeon (Richter *et al.*, 1995) and on the barn owl (Köppl and Yates, 1999). Both agree with the important conclusions (1) that avian RI data are well described by the mammalian model, and (2) that there is a fundamental and tight correlation between the sensitivity and the break-point in the individual fibers' RI function at CF. This important feature, with the implications discussed below, is thus typical for birds. In the barn owl, a clear variation of RI shape at frequencies off the CF, similar to that shown here for the emu, was also documented. This further supports the conclusion that the underlying nonlinearity is restricted to frequencies around CF and thus is present in the mechanical input to the hair cell, as discussed in Sec. B above. Richter *et al.* (1995) reported lower maximum discharge rates below CF but no differences in shape of the RI function for different stimulus frequencies. The maximum CF they recorded, however, was 1414 Hz, so in fact the CFs of most fibers and most below-CF responses would have been in the range where phase locking occurs in the pigeon (Hill *et al.*, 1989b). In the emu also, maximum discharge rates for stimuli below approximately 600 Hz were dependent upon the stimulus frequency [example in Fig. 2(a); Manley *et al.*, 1997, their Fig. 10). In addition, low-CF fibers ($<$1–2 kHz) in the guinea pig also typically show little variation in the shape of RI function across their response range (Cooper and Yates, 1994). We thus suggest that there may be no fundamental discrepancy between the bird species, but that a sample of RI functions from the pigeon at higher frequencies might reveal the variation of RI shape across frequency typically seen in emu and barn owl fibers.

A difference in detail between emu and barn owl is seen in the frequency of occurrence of the different RI types. While in both species the great majority of fibers (81% and 86%, respectively) showed responses of the sloping-saturating type at CF, the remainder was typically of the straight type in the emu, but of the flat-saturating type in the owl. Interestingly, all the fibers with a flat-saturating response in the owl were beyond the CF range of the emu ($>$4.7 kHz). A comparison with the pigeon is difficult, unfortunately, because of the different criteria used for classification. Richter *et al.* (1995) found 37% of fibers ''reached saturation'' and were classified as ''saturating'', but they further state that dynamic ranges of such fibers ranged from 11 to 40 dB. Many RI functions of the sloping-saturating type do in fact reach saturation but, as we stated earlier, the defining characteristic of flat saturation is the absence of a clear change in slope somewhere above threshold and below saturation, not the mere presence of ultimate saturation. Furthermore, their definition of dynamic range was the difference between the SPL for a 25% increase in rate above the spontaneous rate and the SPL to drive the cell to 80% of maximum. Without knowledge of spontaneous and maximum rates for individual fibers, this cannot be compared with the fibers we classified as flat saturating (which, according to our criterion, always had a dynamic range of 19.1 dB). Although the exact proportions are thus not comparable, sloping saturation was still the most frequent type in the pigeon, found in 50% of the fibers. Plontke *et al.* (1999) assessed changes in some RI function characteristics occurring after hair-cell damage and regeneration in young chickens. Although they described the same three types of RI function, in this case also their subjective classification does not permit a comparison of the proportions of RI types with the present data.

E. Comparison with mammals

When comparing the emu RI functions with the mammalian, clear similarities and differences are seen. First, for both cases the RI functions are flat saturating for stimulus frequencies well below CF and sloping saturating only for near-CF and above. Second, the emu RI functions at CF, and, indeed, those of other bird species investigated (Richter *et al.*, 1995; Köppl and Yates, 1999), are mostly sloping saturating, whereas in cat and guinea pig most are flat saturating (Liberman, 1978; Winter *et al.*, 1990). The type of RI function shows no correlation with the fibers' sensitivity in birds, whereas in mammals, flat saturation is correlated with lower thresholds and sloping saturation with higher thresholds. Hence, there is a clear distinction between birds and mammals in the relationship between threshold and RI shape.

Another difference exists in the relationship between threshold and the SPL at which the nonlinear break-point occurs. In mammals, the break-point is the same for all fibers of similar CF in any given animal (Müller and Robertson, 1991), apparently because all IHCs at a particular site are driven by the same BM vibration amplitude. In emu chicks, in the pigeon (Richter *et al.*, 1995), and in the barn owl (Kö-

ppl and Yates, 1999), however, the break-point varied almost directly with threshold and therefore varied over a wide range of SPLs at a given CF. We interpret this as indicating that, in birds, the cochlear amplifier is far more localized to a single hair cell or a small group of hair cells.

There is clear anatomical evidence in the cat that the distinctions between fiber RI types are correlated with the different locations of synapses on the inner hair cells (Liberman, 1982), of the cell bodies in the spiral ganglion (Kawase and Liberman, 1992), and with their different central projections (Liberman, 1991, 1993). Similar distinctions have recently been reported in the guinea pig (Tsuji and Liberman, 1997). If spontaneous activity is simply a sustained response of sensitive synapses to standing currents in IHCs, then the correlation between spontaneous rate and shape of the RI function seen in mammals may simply indicate that the mechanical sensitivity is fixed and thus reflects the correlation between synaptic sensitivity and shape of the RI function (Yates, 1990, 1991). In birds, the two hair-cell types are not clearly differentiated and the large range of sensitivities is likely to derive from fibers connected to different hair cells within the same frequency range (Gleich, 1989; Smolders *et al.*, 1995). This may be a consequence of localized efficacy of the cochlear amplifier rather than having anything to do with the synapses. If so, any correlation between spontaneous rate and shape of the RI function would not be expected, and, indeed, was not found for any of the birds (Richter *et al.*, 1995; Köppl and Yates, 1999; this study).

IV. CONCLUSIONS

Sloping saturation in mammalian auditory-nerve fibers has been taken as evidence of nonlinearity in the cochlear amplifier that enhances the vibration amplitude of the basilar membrane. We have found that most fibers recorded in the emu auditory nerve are of the sloping-saturating type and we suggest that this is evidence that a cochlear amplifier is operating in the emu cochlea and that it is nonlinear is much the same way as in the mammal. The major differences between the mammal and the emu may relate to the lack of differentiation in the emu hair cells, whereby the separation between amplification and detection is blurred. The cochlear amplifier feed back loop does not seem to include the basilar membrane in avian species, since the basilar membrane is more broadly tuned than the nerve responses and appears to be linear. It is more likely that amplified tuning in the bird is related to micromechanical properties and that both the tuning and the nonlinearity are more local to individual hair cells than in the mammal. The uniting property, however, is that the cochlear amplifier operates in the same way in both to expand the dynamic range of hearing.

ACKNOWLEDGMENTS

This work was supported by a Visiting International Exchange Fellowship from the Australian Research Council to G. A. M., by the Australian National Health and Medical Research Council (G. K. Y.), and by the Deutsche Forschungsgemeinschaft within the program of the SFB 204 ''Gehör'' (G. A. M. and C. K.) and through a Habilitation Fellowship to C. K.

Cooper, N. P., and Rhode, W. S. (**1992**). ''Basilar membrane mechanics in the hook region of cat and guinea-pig cochleae—sharp tuning and nonlinearity in the absence of baseline position shifts,'' Hearing Res. **63**, 163–190.

Cooper, N. P., and Yates, G. K. (**1994**). ''Nonlinear input–output functions derived from the responses of guinea-pig cochlear nerve fibers: Variations with characteristic frequency'' Hearing Res. **78**, 221–234.

Cracraft, J. (**1974**). ''Phylogeny and evolution of the ratite birds.'' Ibis **116**, 494–521.

Cracraft, J. (**1981**). ''Towards a phylogenetic classification of recent birds of the world (class Aves),'' Auk **98**, 681–714.

Eatock, R. A., Weiss, T. F., and Otto, K. L. (**1991**). ''Dependence of discharge rate on sound pressure level in cochlear nerve fibers of the alligator lizard—implications for cochlear mechanisms,'' J. Neurophysiol. **65**, 1580–1597.

Fischer, F. P. (**1994**). ''General pattern and morphological specializations of the avian cochlea,'' Scan. Electr. Micros. **8**, 351–364.

Fischer, F. P. (**1998**). ''Hair-cell morphology and innervation in the basilar papilla of the emu (*Dromaius novaehollandiae*),'' Hearing Res. **121**, 112–124.

Geisler, C. D., Yates, G. K., Patuzzi, R. B., and Johnstone, B. M. (**1990**). ''Saturation of outer hair cell receptor current causes two-tone suppression,'' Hearing Res. **44**, 241–256.

Gleich, O. (**1989**). ''Auditory primary afferents in the starling: Correlation of function and morphology,'' Hearing Res. **37**, 255–267.

Goodman, D. A., Smith, R. L., and Chamberlain, S. C. (**1982**). ''Intracellular and extracellular responses in the organ of Corti of the gerbil,'' Hearing Res. **7**, 161–179.

Gummer, A. W., Smolders, J. W. T., and Klinke, R. (**1987**). ''Basilar membrane motion in the pigeon measured with the Mössbauer technique,'' Hearing Res. **29**, 63–92.

Hennig, W. (**1983**). *Stammesgeschichte der Chordaten* (Paul Parey, Hamburg).

Hill, K. G., Mo, J., and Stange, G. (**1989a**). ''Excitation and suppression of primary auditory fibers in the pigeon,'' Hearing Res. **39**, 37–48.

Hill, K. G., Stange, G., and Jianwu, M. (**1989b**). ''Temporal synchronization in the primary auditory nerve in the pigeon,'' Hearing Res. **39**, 63–74.

Hudspeth, A. J. (**1997**). ''Mechanical amplification of stimuli by hair cells,'' Curr. Opin. Neurobiol. **7**, 480–486.

Kawase, T., and Liberman, M. C. (**1992**). ''Spatial organization of the auditory nerve according to spontaneous discharge rate,'' J. Comp. Neurol. **319**, 312–318.

Köppl, C. (**1995**). ''Otoacoustic emissions as indicators of active cochlear mechanics: A primitive property of vertebrate auditory organs,'' In *Advances in Hearing Research*, edited by G. A. Manley, G. M. Klump, C. Köppl, H. Fastl, and H. Oeckinghaus (World Scientific, Singapore), pp. 200–209.

Köppl, C., Gleich, O., Schwabedissen, G., Siegl, E., and Manley, G. A. (**1998**). ''Fine structure of the basilar papilla of the emu: Implications for the evolution of avian hair-cell types,'' Hearing Res. **126**, 99–112.

Köppl, C., and Yates, G. K. (**1999**). ''Coding of sound pressure level in the barn owl's auditory nerve,'' J. Neurosci. **19**, 9674–9686.

Liberman, M. C. (**1978**). ''Auditory nerve responses from cats raised in a low-noise chamber,'' J. Acoust. Soc. Am. **63**, 442–455.

Liberman, M. C. (**1982**). ''Single-neuron labeling in the cat auditory nerve,'' Science **216**, 1239–1241.

Liberman, M. C. (**1991**). ''Central projections of auditory nerve fibers of differing spontaneous rate. I Anterventral cochlear nucleus,'' J. Comp. Physiol. **313**, 240–258.

Liberman, M. C. (**1993**). ''Central projections of auditory nerve fibers of differing spontaneous rate. II. Postero-ventral and dorsal cochlear nucleus,'' J. Comp. Physiol. **327**, 17–36.

Manley, G. A. (**1990**). *Peripheral Hearing Mechanisms in Reptiles and Birds* (Springer, Heidelberg).

Manley, G. A. (**1995**). ''The avian hearing organ: a status report,'' in *Advances in Hearing Research*, edited by G. A. Manley, G. M. Klump, C. Köppl, H. Fastl, and H. Oeckinghaus (World Scientific, Singapore), pp. 219–229.

Manley, G. A., and Köppl, C. (**1998**). ''Phylogenetic development of the cochlea and its innervation,'' Curr. Opin. Neurobiol. **8**, 468–474.
Manley, G. A., Gleich, O., Brix, J., and Kaiser, A. (**1988**). ''Functional parallels between hair-cell populations of birds and mammals,'' in *Basic Issues in Hearing*, edited by H. Duifhuis, J W. Horst, and H. P. Wit (Academic, London) pp. 64–71.
Manley, G. A., Gleich, O., Kaiser, A., and Brix, J. (**1989**). ''Functional differentiation of sensory cells in the avian auditory periphery,'' J. Comp. Physiol. A **164**, 289–296.
Manley, G. A., Köppl, C., and Yates, G. K. (**1997**). ''Activity of primary auditory neurons in the cochlear ganglion of the emu *Dromaius novaehollandiae*: Spontaneous discharge, frequency tuning and phase locking,'' J. Acoust. Soc. Am. **101**, 1560–1573.
Manley, G. A., and Taschenberger G. (**1993**). ''Spontaneous otoacoustic emissions from a bird: a preliminary report,'' in *Biophysics of Hair-Cell Sensory Systems*, edited by H. Duifhuis, J. W. Horst, P. Van Dijk, and S. van Netten (World Scientific, London), pp 33–39.
Mountain, D. C., Hubbard, A. E., and McMullen, T. A. (**1983**). ''Electromechanical processes in the cochlea,'' in *Mechanics of Hearing*, edited by E. de Boer and M. A. Viergever (Delft University Press, The Hague), pp. 119–126.
Müller, M., and Robertson, D. (**1991**). ''Shapes of rate-versus-level functions of primary auditory nerve fibers: Test of the basilar membrane mechanical hypothesis,'' Hearing Res. **57**, 71–78.
Patuzzi, R., and Sellick, P. M. (**1983**). ''A comparison between basilar membrane and inner hair cell receptor potential input–output functions in the guinea pig cochlea,'' J. Acoust. Soc. Am. **74**, 1734–1741.
Patuzzi, R., Yates, G. K., and Johnstone, B. M. (**1989**). ''Changes in cochlear microphonic and neural sensitivity produced by acoustic trauma,'' Hearing Res. **39**, 189–202.
Plontke, S. K.-R., Lifshitz, J., and Saunders, J. C. (**1999**). ''Distribution of rate-intensity function types in chick cochlear nerve after exposure to intense sound,'' Brain Res. **842**, 262–274.
Rhode, W. S. (**1971**). ''Observations of the vibration of the basilar membrane using the Mössbauer technique,'' J. Acoust. Soc. Am. **49**, 1218–1231.
Richter, C.-P., Heynert, S., and Klinke, R. (**1995**). ''RI functions of pigeon auditory primary afferents,'' Hearing Res. **83**, 19–25.
Robles, L., Ruggero, M. A., and Rich, N. C. (**1986**). ''Basilar membrane mechanics at the base of the chinchilla cochlea. I. Input–output functions, tuning curves, and phase responses,'' J. Acoust. Soc. Am. **80**, 1364–1374.
Sachs, M. B., and Abbas, P. J. (**1974**). ''Rate versus level functions for auditory-nerve fibers in cats: Tone-burst stimuli,'' J. Acoust. Soc. Am. **56**, 1835–1847.
Schoonhoven, R., Prijs, V. F., and Frijns, H. M. (**1997**). ''Transmitter release in inner hair cell synapses: A model analysis of spontaneous and driven rate properties of cochlear nerve fibers,'' Hearing Res. **113**, 247–260.
Sellick, P. M., Patuzzi, R., and Johnstone, B. M. (**1982**). ''Measurement of basilar membrane motion in the guinea pig using the Mössbauer technique,'' J. Acoust. Soc. Am. **72**, 131–141.
Sibley, C. G., and Ahlquist, J. E. (**1981**). ''The phylogeny and relationships of the ratite birds as indicated by DNA–DNA hybridization,'' in *Evolution Today*, edited by G. Scudder and J. Reveal. Proceedings of the 2nd International Congress of Systematic and Evol. Biology (Carnegie Mellon University Press, Pittsburgh), pp. 305–335.
Smolders, J. W. T., Ding-Pfennigdorff, D., and Klinke, R. (**1995**). ''A functional map of the pigeon basilar papilla: Correlation of the properties of single auditory nerve fibers and their peripheral origin,'' Hearing Res. **92**, 151–169.
Taschenberger, G., and Manley, G. A. (**1997**) ''Spontaneous otoacoustic emissions in the barn owl,'' Hearing Res. **110**, 61–76.
Tsuji, T., and Liberman, M. C. (**1997**). ''Intracellular labeling of auditory nerve fibers in guinea pig: central and peripheral projections,'' J. Comp. Neurol. **381**, 188–202.
van Dijk, P., Manley, G. A., Gallo, L., Pavusa, A., and Taschenberger, G. (**1996**). ''Statistical properties of spontaneous otoacoustic emissions in one bird and three lizard species,'' J. Acoust. Soc. Am. **100**, 2220–2227.
Winter, I. M., Robertson, D., and Yates, G. K. (**1990**). ''Diversity of characteristic frequency RI functions in guinea pig auditory nerve fibers,'' Hearing Res. **45**, 191–202.
Yates, G. K. (**1990**). ''Basilar membrane nonlinearity and its influence on auditory nerve RI functions,'' Hearing Res. **50**, 145–162.
Yates, G. K. (**1991**). ''Auditory-nerve spontaneous rates vary predictably with threshold,'' Hearing Res. **57**, 57–62.
Yates, G. K., Winter, I. M., and Robertson, D. (**1990**). ''Basilar membrane nonlinearity determines auditory nerve RI functions and cochlear dynamic range,'' Hearing Res. **45**, 203–220.
Zwicker, E. (**1979**). ''A model describing nonlinearities in hearing by active processes with saturation at 40 dB,'' Biol. Cybern. **35**, 243–250.

Cortical, auditory, evoked potentials in response to changes of spectrum and amplitude[a)]

Brett A. Martin
Program in Speech and Hearing Sciences, Graduate Center, City University of New York, 33 West 42 Street, New York, New York 10036 and Department of Speech-Language-Hearing Sciences, Hofstra University, 106 Davison Hall, Hempstead, New York 11550

Arthur Boothroyd
Program in Speech and Hearing Sciences, Graduate Center, City University of New York, 33 West 42 Street, New York, New York 10036

(Received 28 April 1999; revised 4 October 1999; accepted 28 December 1999)

The acoustic change complex (ACC) is a scalp-recorded negative–positive voltage swing elicited by a change during an otherwise steady-state sound. The ACC was obtained from eight adults in response to changes of amplitude and/or spectral envelope at the temporal center of a three-formant synthetic vowel lasting 800 ms. In the absence of spectral change, the group mean waveforms showed a clear ACC to amplitude increments of 2 dB or more and decrements of 3 dB or more. In the presence of a change of second formant frequency (from perceived /u/ to perceived /i/), amplitude increments increased the magnitude of the ACC but amplitude decrements had little or no effect. The fact that the just detectable amplitude change is close to the psychoacoustic limits of the auditory system augurs well for the clinical application of the ACC. The failure to find a condition under which the spectrally elicited ACC is diminished by a small change of amplitude supports the conclusion that the observed ACC to a change of spectral envelope reflects some aspect of cortical frequency coding. Taken together, these findings support the potential value of the ACC as an objective index of auditory discrimination capacity. [S0001-4966(00)01704-5]

PACS numbers: 43.64.Qh, 43.64.Ri [RDF]

INTRODUCTION AND PURPOSE

The study reported here is one of a series in which a specific electrophysiological response is being explored in terms of its ability to demonstrate peripheral discrimination capacity. This response is a negative–positive complex that is elicited by a change that occurs during an ongoing acoustic stimulus. This complex has been named the acoustic change complex (ACC) (Martin and Boothroyd, 1999).

In appearance and timing, the ACC is very similar to the well-known negative–positive ($N1-P2$) complex that occurs in response to stimulus onset (Hillyard and Picton, 1978; Näätänen, 1992; Näätänen and Picton, 1987; Onishi and Davis, 1968; Pantev *et al.*, 1996). It has been demonstrated that both amplitude and frequency modulation during an ongoing sound can evoke an $N1-P2$ complex (Clynes, 1969; Jerger and Jerger, 1970; Näätänen and Picton, 1987; Kohn *et al.*, 1978, 1980; McCandless and Rose, 1970; Spoor *et al.*, 1969; Yingling and Nethercut, 1983), as can an acoustic change during a sustained speech sound (Kaukoranta *et al.*, 1987).

In the first study of the present series, the ACC was demonstrated in response to the transition from fricative to vowel in a naturally produced syllable (Ostroff *et al.*, 1998). The transition, however, included at least three kinds of change: intensity, periodicity, and spectral envelope. In subsequent studies, it was shown that the ACC can be elicited by a change of spectral envelope alone or by a change of periodicity alone (Martin and Boothroyd, 1999) when rms amplitude is held constant. These findings raise the possibility that this response can be used as an index of the capacity for perceiving the kinds of acoustic cues that are important in differentiating speech sounds.

If the acoustic change complex is to be useful as an index of peripheral spectral resolution, and therefore of the potential for development of speech perception skills, it is important to establish that the observed response to a spectral change is, indeed, attributable to spectral change and not simply to a difference in the magnitude of excitation. In an earlier study rms amplitude remained constant for the duration of the stimuli. There is no guarantee, however, that the rms level of the external stimulus is the sole determinant of the amount of internal excitation. The amount of synchronous neural excitation may depend on some property of the acoustic waveform other than its rms amplitude (for example, peak-to-peak amplitude). It is possible that the spectral change is accompanied by a change in the magnitude of excitation and that this, alone, is responsible for the observed response.

The present study had three goals. The first was to confirm that the ACC is elicited by amplitude change alone—in the absence of changes of spectral envelope or periodicity. It will be recalled that the ACC was observed in response to a

[a)]Portions of this paper were presented at the Twenty-Second Midwinter Research Meeting of the Association for Research in Otolaryngology, St. Petersburg Beach, FL, February 13, 1999, and at the Biennial Meeting of the International Evoked Response Audiometry Study Group, Tromso, Norway, May 31, 1999.

fricative-vowel transition, which involved simultaneous changes of spectral envelope, periodicity, and amplitude. It has already been established that the changes of the first two parameters alone can elicit the complex. Although there was every reason to expect that a change of amplitude alone would also be effective as a stimulus, it was appropriate to confirm this prediction.

The second goal of the present study was to determine the sensitivity of the ACC to changes of rms amplitude. There were two reasons for seeking this information. First, a finding that sensitivity is close to that reported in the psychoacoustic literature would support the possibility of electrophysiological measures replacing behavioral measures in the clinical evaluation of auditory capacity in young children. Second, data on amplitude sensitivity can help establish the likelihood that an ACC in response to spectral change is actually produced by a change in some measure of amplitude.

The third goal was to measure the effect of simultaneous amplitude change on the magnitude of the ACC elicited by a change of spectral envelope. If the response to spectral change is, in fact, a response to some aspect of waveform amplitude then it should be possible to offset the effect by an opposing change of rms amplitude. In other words, there should be some value of amplitude change for which the spectrally elicited ACC is weakened or even eliminated. The absence of such a finding would lend support to the conclusion that the ACC in response to a change of spectral envelope, in the absence of a change of rms amplitude, is not confounded by a change in some other aspect of waveform amplitude.

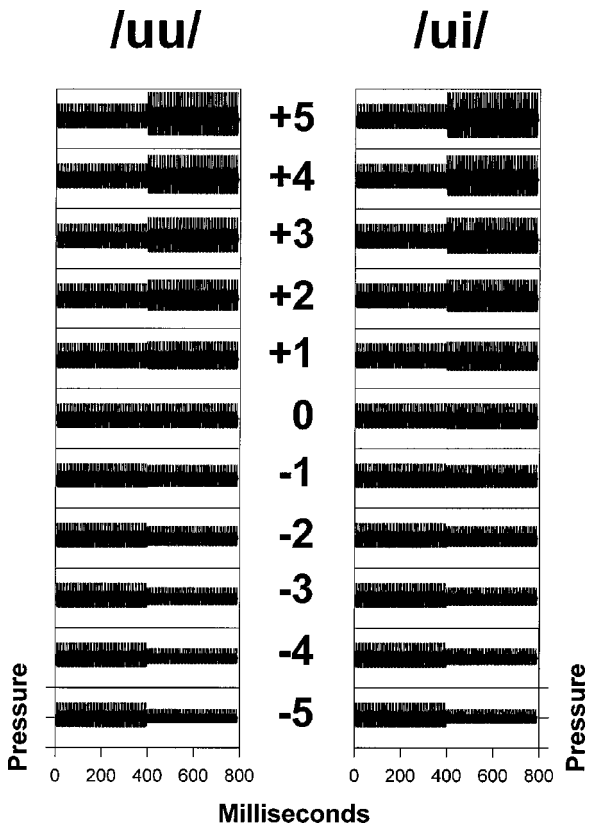

FIG. 1. The acoustic waveforms for the /uu/ and /ui/ stimuli are shown for all amplitude change conditions. In the 0-dB amplitude change condition, the /uu/ stimulus contains no acoustic change, while the /ui/ stimulus contains a change of spectrum alone. For the remaining amplitude change conditions, /uu/ contains a change of amplitude alone, while /ui/ contains changes of spectrum and amplitude.

I. METHOD

A. Subjects

Three men and five women, aged 26 to 35 years (mean=29 years), participated. All subjects had normal hearing sensitivity (thresholds≤25 dB HL from 250 through 8000 Hz bilaterally) and no history of neurological disorder.

B. Stimuli

The acoustic change used in this study was a transition from /u/ to /i/ in synthesized vowels. The vowels were synthesized with a constant fundamental frequency of 150 Hz. Each vowel lasted for 400 ms and included three formants. The first and third formants were fixed at 300 and 3000 Hz, respectively, for the two vowels. The second formants for the /u/ and /i/ were 900 and 2400 Hz, respectively. Onsets and offsets of the two vowels were shaped with raised cosine functions lasting for one cycle. The stimulus containing the acoustic change was created by concatenating the /u/ and the /i/ with one cycle of overlap. The overlap was introduced to minimize spectral splatter at the transition. This stimulus will be referred to as /ui/. A reference stimulus without spectral change was also created by concatenating two samples of /u/. This stimulus will be referred to as /uu/. The amplitude of the first half of both stimuli (/ui/, /uu/) was 70 dB SPL. Eleven versions of each stimulus were created in which the rms amplitude changed at the midpoint by an amount ranging from −5 dB to +5 dB in 1-dB steps. The waveforms of the resulting stimuli are shown in Fig. 1. All stimuli were digitized at 12 bits and 22 050 samples per second, and were presented to subjects via a Neuroscan STIM system.

Note that when no amplitude change is introduced at stimulus midpoint (the 0-dB change condition), the /uu/ stimulus contains no acoustic change, and the /ui/ stimulus contains only a change of spectrum. The /uu/ stimuli across the remaining amplitude change conditions contain only a change of amplitude, while the /ui/ stimuli in the remaining amplitude change conditions contain a change of both spectrum and amplitude.

C. EEG recordings

Using a Neuroscan SCAN system and Grass amplifiers, seven EEG channels were recorded from surface electrodes placed at Fz, Cz, Pz, T3, T4, A1, and A2. The EEG channels were referenced to an electrode at the tip of the nose (Vaughan and Ritter, 1970). An eighth channel to monitor vertical eye movements and eye blinks (EOG) was recorded from electrodes placed above and below the right eye. An electrode at Fpz served as ground. Electrode impedances were maintained below 5000 Ohms.

During acquisition, the EEG channels were amplified using a gain of 20 000 (except for the EOG channel where

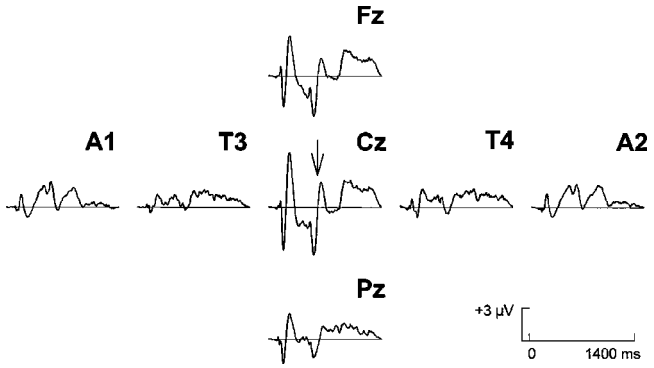

FIG. 2. The scalp distribution of the response is shown for the /ui/ stimulus in the +5-dB amplitude change condition. The acoustic change complex (indicated by the arrow) is clearly present. It is largest in amplitude at electrode site Cz, is smaller at the other electrode sites, and inverts in polarity at the earlobe sites (A1, A2).

the gain was 5000), and band-pass filtered with a roll-off of 6 dB/octave below 0.1 Hz and above 100 Hz.

D. Procedure

Stimuli were presented via a loudspeaker placed 70 cm from the subject at a 0 degree azimuth. They were presented in homogeneous blocks of 125 stimuli, using an onset-to-onset interval of 3 s. Two replications were obtained for each condition. Thus each stimulus was heard 250 times. Stimulus presentation was randomized across conditions and subjects. Subjects watched a silent, captioned video during testing and were instructed to ignore the stimuli.

The amplified EEG signals were digitized using the Neuroscan SCAN system at 341 Hz over a 1501-ms (512 point) window, beginning 100 ms before stimulus onset. After acquisition, single trials were rejected from averaging when activity in any channel (except the EOG channel) exceeded ± 100 μV. Single trials were baseline corrected (across the entire sweep duration) and an ocular artifact reduction algorithm was applied (Semlich *et al.*, 1986). Additional band-pass filtering was applied with a roll-off of 12 dB/octave below 0.1 Hz and above 30 Hz. Responses to each of the 22 stimuli were averaged separately for each subject. Each averaged waveform was then baseline corrected for the prestimulus period (0–100 ms). Finally, individual averaged waveforms were combined to generate 22 group waveforms.

II. RESULTS

A. Scalp distribution of the ACC

Figure 2 shows the scalp distribution of the group mean waveforms in response to the /ui/ stimulus containing a +5-dB amplitude change. Results are shown for electrode sites Fz, Cz, Pz, T3, T4, A1, and A2. Clear $P1-N1-P2$ potentials are seen in response to the onset of stimulation, followed by a sustained potential that continues for the duration of the stimulus, and a return to baseline in response to the offset of stimulation. There is an additional $P1-N1-P2$ complex seen in response to the change of both spectrum and amplitude at stimulus midpoint. This is the acoustic change complex (ACC), and it is largest in amplitude at the vertex.[1]

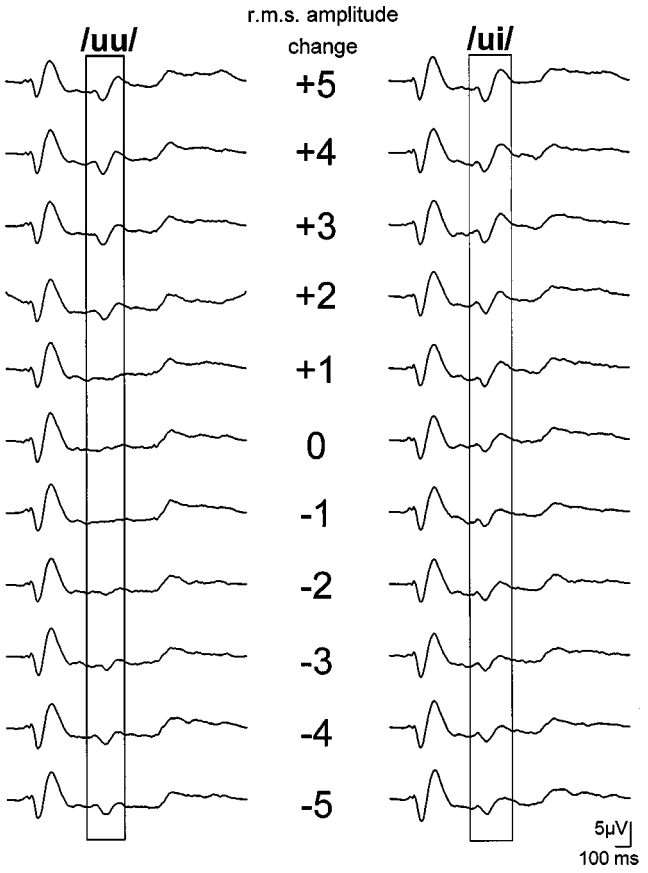

FIG. 3. The group mean waveforms are displayed for the 2 stimuli (/uu/, /ui/) and the 11 amplitude change conditions. There is a clear $N1-P2$ obtained to the onset of stimulation in all conditions. For amplitude change alone, the acoustic change complex (shown in the boxes) is clearly present for changes of 2–3 dB or more. For spectrum plus amplitude change, the acoustic change complex is clearly present for all conditions.

The rms amplitude of the ACC is reduced by approximately 21% at Fz, 57% at Pz, and 73% at temporal electrode sites (T3, T4). In addition, the response inverts in polarity at the earlobes (A1, A2).

B. Group mean waveforms

The group mean waveforms obtained for each acoustic change at Cz (the electrode site giving the largest amplitude) are displayed in Fig. 3. The waveforms on the right show results for spectral and amplitude change (i.e., the /ui/ stimulus). There is a clearly observable ACC for each level of rms amplitude change when combined with a spectral change. The waveforms on the left show results for amplitude change alone (i.e., the /uu/ stimulus). In this case, the ACC is only clearly observable only for amplitude changes of 2–3 dB or more. It can also be seen that, for both stimuli, the amplitude of the ACC is higher for amplitude increments than for amplitude decrements.

C. Waveforms for individual subjects

The waveforms obtained to the /ui/ stimulus in the +5-dB amplitude change condition are shown for each individual subject in Fig. 4. Responses are shown at electrode site Cz (the electrode site giving the largest amplitude in the

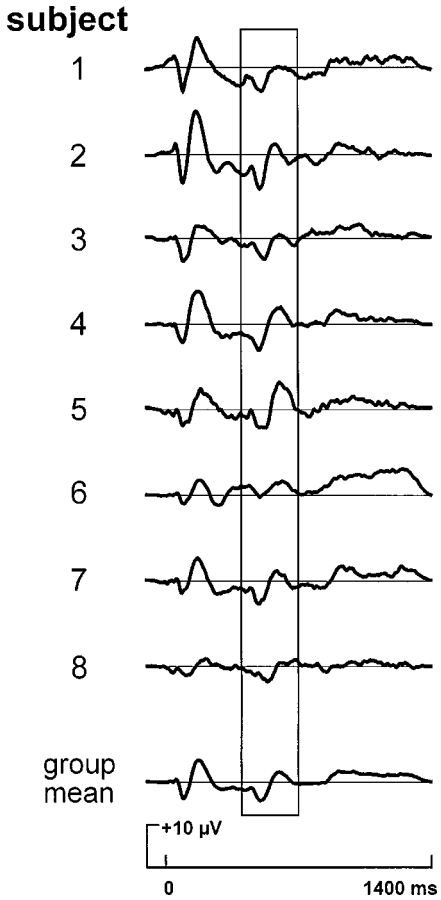

FIG. 4. The waveforms from each individual subject are displayed for the /ui/ stimulus in the +5-dB amplitude change condition. In addition, the group mean waveform is also shown. The acoustic change complex (shown in the box) is clearly present in all subjects in response to the change of spectrum and amplitude.

group mean waveforms). There is a clearly observable ACC for each subject in response to the change of spectrum and amplitude.

D. Quantification of ACC amplitude

For purposes of analysis, the root mean square (rms) amplitude of the ACC was calculated for each subject and each of the 22 stimuli. The steps involved in this process were as follows:

(1) The latencies of the *N*1 and *P*2 maxima in the group mean waveforms were obtained for conditions with a clearly present response (±3 to 5 dB).
(2) A ''response window'' was defined beginning 50 ms before the average *N*1 minimum and ending 50 ms after the average *P*2 maximum. The resulting window extended from 454 to 645 ms *re*: stimulus onset (i.e., 61 to 252 ms after the onset of acoustic change).
(3) The standard deviations of the waveforms for each stimulus and each subject within this window were calculated. The result, which is the rms amplitude of the waveform within the response window, excluding any dc offset, was used as a measure of the amplitude of the complex.[2]

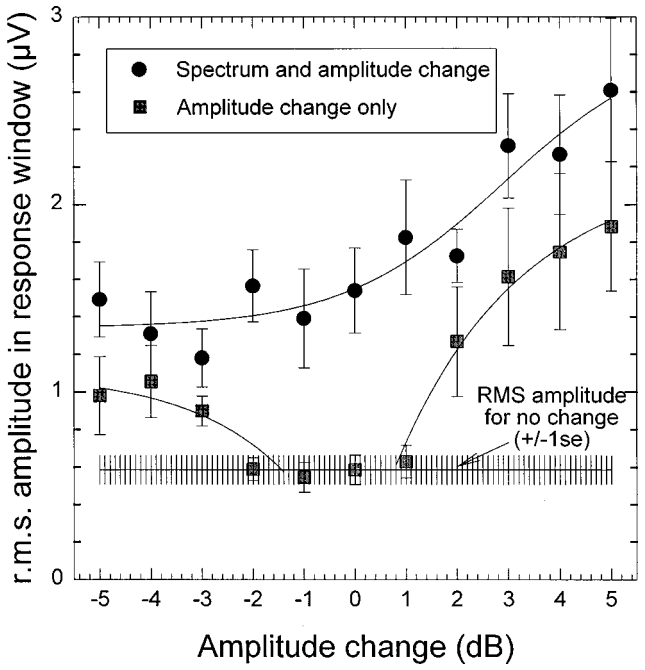

FIG. 5. Group mean rms amplitude of the acoustic change complex (±1 s.e.) is shown as a function of amplitude change, with and without a simultaneous spectral change. Lines show least squares fits to hypothetical functions.

(4) Group means and standard errors of the rms amplitudes were then calculated for each of the stimuli.

Figure 5 shows group mean response amplitude, ±1 ''between-subject'' standard error, as a function of stimulus amplitude change, for the /uu/ and /ui/ stimuli. The lines in Fig. 5 show the result of curve fitting procedures described below.

E. ACC to amplitude change only

The data for amplitude change only were fit with exponential growth functions of the form:

$$y = a(1 - e^{-x/b}), \tag{1}$$

where y is the rms amplitude of ACC in μV; a is the asymptote in μV; e is the base of natural logarithms; x is the amplitude change in dB; and b is a constant, in dB, providing an inverse measure of rate of growth of ACC amplitude with increasing amplitude change.[3]

A least-squares fitting procedure produced the following parameter values: $a = 2.2\,\mu$V and $b = 2.5$ dB for amplitude increments and $a = 1.1\,\mu$V and $b = -1.9$ dB for amplitude decrements. The fitting procedure was limited to those conditions in which the ACC amplitude was clearly above the noise floor, as defined by the rms amplitude of the ACC for the /uu/ stimulus with 0-dB amplitude change (i.e., no change of either spectrum or amplitude).

Several observations can be made from the amplitude change data illustrated in Fig. 5. First, the ACC amplitude is greater for amplitude increments than for amplitude decre-

ments. Second, for the stimuli and protocols used in this study, an amplitude change of at least +2 or −3 dB is required in order to produce an ACC that is clearly above the noise floor. Third, the standard errors (a measure of intersubject variability) are small within the noise floor but increase with increasing ACC amplitude.

F. ACC to spectrum change plus amplitude change

The data for spectrum plus amplitude change were fit with a sigmoid transition function of the form:

$$y = a + (b - a)/(1 + e^{-(x-c)/d}), \tag{2}$$

where y = rms amplitude of ACC in μV; a = lower asymptote in μV; b = upper asymptote in μV; e = base of natural logarithms; x = amplitude change in dB; c = mid-point of transition in dB; and d = a constant in dB providing an inverse measure of rate of change of ACC amplitude in the transition region.

A least-squares fitting procedure produced the following parameter values: $a = 1.3\,\mu$V, $b = 2.9\,\mu$V, $c = 2.9$ dB, and $d = 1.6$ dB. Several observations can be made from the spectrum-plus-amplitude change data illustrated in Fig. 5. First, the amplitude of the ACC is well above the noise floor when there is no change of amplitude (group mean rms amplitude = 1.5 μV). Second, the addition of an amplitude increment has the effect of increasing amplitude of the ACC. Third, for amplitude increments, the ACC amplitude continues to increase as the amplitude change increases. Fourth, for amplitude decrements, there is no evidence to show that the ACC amplitude continues to increase with increasing amplitude change. Fifth, and most important, there is no evidence from these data that a small amplitude change can cancel the ACC produced by the change of spectrum.

G. Statistical tests

Statistical tests were used to explore the generalizability of these findings to the means of the population represented by this sample of subjects. A two-factor repeated-measures analysis of the variance in the ACC amplitudes was performed. The two factors were spectrum change at 2 levels (present or absent) and amplitude change at 11 levels. The main effect of spectrum change was highly significant [$F(1,7) = 44.90$; $p < 0.001$] as was the main effect of amplitude change [$F(10,70) = 11.26$; $p < 0.001$]. There was also a significant interaction between the two [$F(10,70) = 1.97$; $p = 0.049$]. Post hoc testing, using the least significant difference test, confirmed the presence of a significant effect ($p \leqslant 0.05$) of spectrum change for most amplitude changes, with the exception of amplitude changes of −3 dB ($p = 0.192$) and −4 dB ($p < 0.240$). When the data for spectrum plus amplitude increment were examined separately, there was a significant main effect of amplitude change [$F(1,5) = 5.05$; $p = 0.001$]. In the data for spectrum change plus amplitude decrement, however, the main effect of amplitude change did not reach the 5% level of significance [$F(1,5) = 1.75$; $p = 0.15$].

III. DISCUSSION

The ACC was detectable in the group mean waveforms to amplitude changes of +2 and −3 dB. These thresholds compare favorably with those obtained from psychoacoustic studies, which range from 0.2 to 0.5 dB, depending on experimental paradigm, frequency, and sensation level (Gelfand, 1990). Moreover, it may be possible to increase the sensitivity of the ACC by a change of protocol to increase signal-to-noise ratio.

The finding of stronger responses to amplitude increments than to amplitude decrements is in keeping with those of studies using amplitude modulated stimuli (Arlinger and Jervall, 1979; Clynes, 1969; McCandless and Rose, 1970). This finding can be explained if it is assumed that stimulus amplitude determines the total amount of synchronous cortical excitation. Amplitude increments would then be expected to produce an *onset* response from previously unexcited neural elements whereas decrements would produce *offset* responses from previously excited elements. The different amplitudes of the ACC waveform are in keeping with the known differences between the onset and offset $N1-P2$ response (Hillyard and Picton, 1978).

There is some evidence, however, that amplitude is coded, at least partially, by locus of cortical excitation. In a classic study, Pantev *et al.* (1989) measured neuromagnetic responses to 1-kHz tones presented at six amplitudes. The amplitude change produced both vertical and horizontal shifts in the hypothetical dipole generators of the $M100$ wave (equivalent to the $N100$, or $N1$ response in electrical recordings). Amplitopic organization would not explain why stimulus amplitude increments produce a larger ACC response than equivalent amplitude decrements, but it is possible that amplitopic effects are accompanied by changes in total amount of synchronous excitation.

The demonstration of an ACC in response to spectral change, in the absence of a change of rms amplitude, is in keeping with the established tonotopic organization of the auditory cortex. The spectral change used in the present study involved an amplitude decrement at one frequency and a simultaneous amplitude increment at another frequency. The resulting ACC may, therefore, be assumed to reflect a combination of an onset response from one cortical region and an offset response from another. The alternative explanation—that the ACC in response to spectral change simply reflects a change of overall synchronous excitation—is not supported by the findings of the present study. There was no condition under which a small amplitude increment or decrement eliminated, or even reduced, the amplitude of the ACC response to spectral change. The present findings provide strong evidence for dissociation of cortical responses to changes of spectrum and overall amplitudes. In other words, the ACC elicited by spectral change in this and earlier studies can be assumed to reflect the effects of spectral change rather than an incidental change in the total amount of synchronous excitation.

Amplitude increments enhanced the effects of spectral change, whereas amplitude decrements had little or no effect. This asymmetry has been observed previously. Mäkelä *et al.* (1987) found evidence for different processing of amplitude

and frequency modulations up to the level of the supratemporal auditory cortex. Moreover, the order of presentation of the two types of modulation had an effect on response magnitude. The asymmetry observed in the present study can also be explained in terms of the amplitopic effects discussed earlier. Differences in locus and orientation of generators in response to amplitude increments and decrements could easily affect the results of vector summation.

The foregoing attempts to explain the amplitude findings are clearly an oversimplification. It is well known that cortical encoding of amplitude modulated stimuli is complex (Pickles, 1988), and it is likely that multiple mechanisms at different cortical generator areas are at work. Further, surface-recorded data, particularly using a small number of electrode sites, cannot equal the specificity of intracranial recordings for determining what is happening at the single-cell level of the auditory cortex.

The findings of this study are encouraging in terms of the potential clinical use of the ACC as an index of spectral resolution in the impaired auditory system. The high amplitude of the ACC, and the fact that it is elicited by spectral changes of the type encountered in speech, are particularly important. Further, it has been shown in subsequent studies that the ACC can be demonstrated in response to small changes of second formant frequency—of the magnitude involved in vowel distinctions (Ostroff, 1999). Further research will be required, however, to establish adequate reliability and sensitivity in individual waveforms as opposed to group waveforms. Approaches to improving sensitivity must address such issues as rate of spectral change (Onishi and Davis, 1968; Ruhm, 1970), frequency region of spectral change (Arlinger *et al.*, 1976; Kohn *et al.*, 1978), and the duration of stimulus on-time before the spectral change is introduced (Budd and Michie, 1994; Hillyard and Picton, 1978).

Application to persons with sensorineural hearing loss must also take account of the frequency-dependence of threshold and loudness, together with the effects of cochlear damage on the relationship between amplitude and loudness. In the present study, it was demonstrated that maintaining constant rms amplitude served to dissociate frequency and amplitude effects. In hearing-impaired subjects, it may be necessary to measure the effects of spectral change when accompanied by amplitude increments and decrements—as in the present study.

IV. CONCLUSIONS

(1) The acoustic change complex was evoked by amplitude change alone, in the absence of changes of spectral envelope or periodicity.
(2) The amplitude change required to elicit an observable ACC in the group waveforms was 2–3 dB. This threshold is not far above those reported in the behavioral literature on amplitude discrimination.
(3) The acoustic change complex was evoked by a change of second formant frequency during a sustained synthetic vowel, regardless of the simultaneous presence of rms amplitude increments or decrements. The findings support the conclusion that the ACC produced in response to a change of spectrum, in a signal with unchanging rms amplitude, reflects the auditory systems's response to spectrum and not to accompanying changes of perceived magnitude.

ACKNOWLEDGMENT

This work was supported by NIH-NIDCD Grant No. 5P50DC00178.

[1]The amplitude of *P*1 was quite small in some individual subjects. Data for *P*1 are not, therefore, analyzed in this paper.
[2]The rms amplitude was used in preference to the more traditional peak-to-peak measure in order to take full advantage of all data in the response window.
[3]Note that *b* is the equivalent of ''time constant'' when the independent variable is time. It takes approximately three time constants for the dependent variable to come within 95% of the asymptote.

Arlinger, S. D., and Jerlvall, L. B. (**1979**). ''Results of psychoacoustic and cortical evoked potential experiments using frequency and amplitude modulated stimuli,'' in *Models of the Auditory System and Related Signal Processing Techniques, Scandinavian Audiology Supplement 9*, edited by M. Hoke and E. de Boer (Nordic Audiology Society), pp. 229–239.

Arlinger, S. D., Jerlvall, L. B., Ahren, T., and Holmgren, E. C. (**1976**). ''Slow evoked cortical responses to linear frequency ramps of a continuous pure tone,'' Acta Physiol. Scand. **98**, 412–424.

Budd, T. W., and Michie, P. T. (**1994**). ''Facilitation of the *N*1 peak of the auditory ERP at short stimulus intervals,'' Neuroreport **5**, 2513–2516.

Clynes, M. (**1969**). ''Dynamics of vertex evoked potentials: The R-M brain function,'' in *Average Evoked Potentials: Methods, Results, and Evaluations* (NASA SP-191), edited by E. Donchin and D. B. Lindsley (Washington: U.S. Government Printing Office), pp. 363–374.

Gelfand, S. (**1990**). *Hearing: An Introduction to Psychological and Physiological Acoustics* (Marcel Decker, New York), pp. 335–341.

Hillyard, S. A., and Picton, T. W. (**1978**). ''ON and OFF components in the auditory evoked potential,'' Percept. Psychophys. **24**, 391–398.

Jerger, J., and Jerger, S. (**1970**). ''Evoked responses to intensity and frequency change,'' Arch. Otolaryngol. **91**, 433–436.

Kaukoranta, E., Hari, R., and Lounasmaa, O. V. (**1987**). ''Responses of the human auditory cortex to vowel onset after fricative consonants,'' Exp. Brain Res. **69**, 19–23.

Kohn, M., Lifshitz, K., and Litchfield, D. (**1980**). ''Average evoked potentials and amplitude modulation,'' Electroencephalogr. Clin. Neurophysiol. **50**, 134–140.

Kohn, M., Lifshitz, K., and Litchfield, D. (**1978**). ''Average evoked potentials and frequency modulation,'' Electroencephalogr. Clin. Neurophysiol. **45**, 236–243.

Mäkelä, J. P., Hari, R., and Linnankivi, A. (**1987**). ''Different analysis of frequency and amplitude modulations of a continuous tone in the human auditory cortex: A neuromagnetic study,'' Hear. Res. **27**, 257–264.

Martin, B. A., and Boothroyd, A. (**1999**). ''Cortical, auditory, event-related potentials in response to periodic and aperiodic stimuli with the same spectral envelope,'' Ear Hear. **20**, 33–44.

McCandless, G. A., and Rose, D. E. (**1970**). ''Evoked cortical responses to stimulus change,'' J. Speech Hear. Res. **13**, 624–634.

Näätänen, R. (**1992**). *Attention and Brain Function* (Lawrence Erlbaum, New Jersey).

Näätänen, R., and Picton, T. W. (**1987**). ''The N1 wave of the human electric and magnetic response to sound: A review and an analysis of the component structure,'' Psychophysiology **24**, 375–425.

Onishi, S., and Davis, H. (**1968**). ''Effects of duration and rise time of tone bursts on evoked V potentials,'' J. Acoust. Soc. Am. **44**, 582–591.

Ostroff, J. M. (**1999**). ''Parametric study of the acoustic change complex to synthetic vowel stimuli as a measure of peripheral auditory discrimination capacity,'' Unpublished doctoral dissertation, Graduate Center of the City University of New York.

Ostroff, J. M., Martin, B. A., and Boothroyd, A. (**1998**). ''Cortical evoked response to acoustic change within a syllable,'' Ear Hear. **19**, 290–297.

Pantev, C., Eulitz, C., Hampton, S., Ross, B., and Roberts, L. E. (**1996**). ''The auditory evoked ''off'' response: Sources and comparison with the ''on'' and the ''sustained'' responses,'' Ear Hear. **17**, 255–265.

Pantev, C., Hoke, M., Lehnertz, K., and Lütkenhöner, B. (**1989**). ''Neuromagnetic evidence of an amplitopic organization of the human auditory cortex,'' Electroencephalogr. Clin. Neurophysiol. **71**, 225–231.
Pickles, J. O. (**1988**). *An Introduction to the Physiology of Hearing* (Academic, London), pp. 205–234.
Ruhm, H. B. (**1970**). ''Rate of frequency change and the acoustically evoked response,'' Journal of Auditory Research **10**, 29–34.
Semlitch, H. V., Anderer, P., Schuster, P., and Presslich, O. (**1986**). ''A solution for reliable and valid reduction of ocular artifacts applied to the P300 ERP,'' Psychophysiology **23**, 695–703.
Spoor, A., Timmer, F., and Odenthal, D. W. (**1969**). ''The evoked auditory response (EAR) to intensity modulated and frequency modulated tones and tone bursts,'' International Audiology **8**, 410–415.
Vaughan, H. G., and Ritter, W. (**1970**). ''The sources of auditory evoked responses recorded from the human scalp,'' Electroencephalogr. Clin. Neurophysiol. **28**, 360–367.
Yingling, C. D., and Nethercut, G. E. (**1983**). ''Evoked responses to frequency shifted tones: Tonotopic and contextual determinants,'' Int. J. Neurosci. **22**, 107–118.

Conditioning-induced protection from impulse noise in female and male chinchillas

Sandra L. McFadden, Xiang-Yang Zheng, and Da-Lian Ding
Center for Hearing and Deafness, 215 Parker Hall, University at Buffalo, Buffalo, New York 14214

(Received 27 July 1999; revised 30 December 1999; accepted 8 January 2000)

Sound conditioning (pre-exposure to a moderate-level acoustic stimulus) can induce resistance to hearing loss from a subsequent traumatic exposure. Most sound conditioning experiments have utilized long-duration tones and noise at levels below 110 dB SPL as traumatic stimuli. It is important to know if sound conditioning can also provide protection from brief, high-level stimuli such as impulses produced by gunfire, and whether there are differences between females and males in the response of the ear to noise. In the present study, chinchillas were exposed to 95 dB SPL octave band noise centered at 0.5 kHz for 6 h/day for 5 days. After 5 days of recovery, they were exposed to simulated M16 rifle fire at a level of 150 dB peak SPL. Animals that were sound conditioned showed less hearing loss and smaller hair cell lesions than controls. Females showed significantly less hearing loss than males at low frequencies, but more hearing loss at 16 kHz. Cochleograms showed slightly less hair cell loss in females than in males. The results show that significant protection from impulse noise can be achieved with a 5-day conditioning regimen, and that there are consistent differences between female and male chinchillas in the response of the cochlea to impulse noise. © *2000 Acoustical Society of America.* [S0001-4966(00)03404-4]

PACS numbers: 43.64.Wn, 43.64.Ri, 43.64.Tk [RDF]

INTRODUCTION

Pre-exposure to a moderate-level acoustic stimulus (''sound conditioning'') can induce resistance to noise-induced hearing loss (NIHL). The protective effects of sound conditioning were reported first by Canlon *et al.* (1988), who found that guinea pigs that had been exposed to a 1-kHz tone at 81-dB sound pressure level (SPL *re*: 20 μPa) for 24 days incurred less permanent threshold shift (PTS) from a subsequent exposure to the tone at 105 dB SPL for 72 h than animals that had not been similarly ''trained'' or ''conditioned.'' Since then, numerous studies have shown that sound conditioning can provide protection from NIHL in a wide variety of species and across a wide range of conditioning parameters. However, nearly all sound conditioning experiments have used long-duration tones or noise at levels below 110 dB SPL as their high-level stimuli. In four recent experiments, for example, high-level exposures consisted of an octave band noise (OBN) centered at 0.5 kHz at a level of 106 dB SPL for 48 h (McFadden *et al.*, 1997), an OBN centered at 1.4 kHz at 105 dBA for 3 days (Skellett *et al.*, 1998), an OBN centered at 2 kHz at 107 dBA for 48 h (White *et al.*, 1998), and a 6.3-kHz tone at 100 dB SPL for 24 h (Canlon and Fransson, 1998). These long-duration stimuli may induce cochlear damage by disrupting normal metabolic processes. In contrast, brief stimuli (impacts and impulses) at levels above 120 dB damage the cochlea by a combination of metabolic and mechanical processes (Hamernik *et al.*, 1984; Luz and Hodge, 1971). Many individuals develop NIHL as a result of exposure to impact noises in industrial settings and impulse noises produced by gunfire and explosions, particularly in the military. Therefore, it is important to know if sound conditioning can provide protection from brief, high-level noises as well as from continuous tones and noise.

Protection from impulse noise was reported by Henselman *et al.* (1994), who pre-exposed chinchillas to an OBN centered at 0.5 kHz at a level of 95 dB SPL for 6 h/day for 10 days. The animals were allowed to recover for 5 days, then they were exposed to impulse noise simulating M16 rifle fire at a level of 150-dB peak SPL. When assessed 30 days later, conditioned chinchillas had significantly less PTS and smaller hair cell lesions than control animals exposed to the impulse noise alone.

The present experiment has two primary aims. The first aim is to determine if significant protection from impulse noise can be achieved with a shorter conditioning regimen than that used by Henselman *et al.* (1994). The second aim is to determine if there are differences between female and male chinchillas in their response to impulse noise, or in their ability to develop resistance to NIHL through sound conditioning. This is an important issue to address in light of previous studies showing gender differences in susceptibility to NIHL in humans (Berger *et al.*, 1978; Gallo and Glorig, 1964; Ward, 1966) and sex differences in PTS in chinchillas exposed to impulse noise (McFadden *et al.*, 1999). In the latter study, female and male chinchillas were exposed to impulse noise at 150-dB peak SPL and PTS was assessed 30 days later. Female chinchillas developed approximately 10 dB more high-frequency hearing loss, but approximately 5 dB less low-frequency hearing loss than male chinchillas. On average, cochleas from females had 18% less inner hair cell (IHC) loss and 15% less outer hair cell (OHC) loss than males. The results suggested that there are sex/gender differences in the response of the cochlea to acoustic overstimulation that cannot be attributed to prior noise exposure history or other confounding factors.

I. METHODS

A. Subjects and surgery

Subjects were seven female and seven male adult chinchillas obtained from a commercial breeder (Jarr Chinchilla).

Each subject was anesthetized with an intramuscular injection of ketamine hydrochloride (54 mg/kg) and acepromazine (0.64 mg/kg). A midline incision was made through the skin overlying the skull, and a small hole was made in the dorsal cranium overlying each inferior colliculus (IC). A recording electrode was advanced through the IC to a depth that produced a clear, large-amplitude response to an 80 dB SPL click, and cemented to the skull with cyanoacrylic adhesive and dental cement. A short tungsten electrode was implanted in the rostral cranium to serve as the common lead for evoked potential (IC-EVP) recording. Animals were allowed to recover for at least 10 days before testing. All procedures were reviewed and approved by the University of Buffalo Animal Care and Use Committee, and conformed to federal guidelines for the humane treatment of laboratory animals.

B. Evoked potential test procedures

The awake chinchilla was placed in a restraining device (Snyder and Salvi, 1994) in a foam-lined sound attenuating booth. Stimuli were digitally generated tones (2-ms rise/fall, 10-ms duration, 20/s rate) converted to analog signals by a 16-bit D/A converter on a digital signal processing (DSP) board in a personal computer. Stimuli were routed through a computer-controlled attenuator and impedance matching transformer to a loudspeaker (Realistic 401197) in the test booth. The speaker was located on the side of the animal's test ear, approximately 9 cm from the animal's pinna. The nontest ear was plugged with a foam insert earplug. Stimuli were presented in ascending order of frequency (in octave steps from 0.5 kHz to 16 kHz) and intensity (in 5-dB steps). Responses (electrical activity from the recording electrode in the IC contralateral to the test ear) were amplified (20 000×) and filtered (10–3000 Hz) by a Grass P511 bioamplifier and converted to digital signals by an A/D converter on a separate DSP board in the computer. Responses were computer averaged for 100 stimulus presentations. Threshold was defined as the mid-point between the level at which there was a clear deflection in the waveform and the next lower level at which there was none.

IC-EVPs were recorded (a) prior to noise exposure in order to establish pre-exposure baselines, (b) during the conditioning exposure in order to monitor temporary TS, (c) 5 days after conditioning to document TS recovery, (d) 15 min, 24 h, and 5 days after impulse noise exposure in order to monitor temporary TS, and (e) after 20 days recovery from high-level exposure to determine PTS. Pre-exposure and PTS measures for each animal represent the average of three tests performed on separate days. Threshold shifts were calculated by subtracting mean pre-exposure IC-EVP thresholds from post-exposure thresholds.

C. Noises and noise exposures

Animals were exposed to 0.5-kHz OBN for 5 days (6 h/day) at a level of 95 dB SPL, followed 5 days later by impulse noise simulating M16 rifle fire (Danielson *et al.*, 1991; Henselman *et al.*, 1994; McFadden *et al.*, 1999). The 0.5-kHz OBN was digitally generated, low-pass filtered (TDK HAF0030 active filter set at 20 kHz), manually attenuated (Hewlett Packard 350D), amplified (NAD 2200), and delivered to a compression driver (JBL 2446J) fitted to a bi-radial exponential horn (JBL 2360H). The driver/horn assembly was suspended from the ceiling of a sound booth. Animals were housed in separate cages (approximately 27 cm×21 cm×22 cm) placed beneath the loudspeaker, and provided free access to food and water during noise exposure. For acoustic calibration, sound pressure levels were measured with a calibrated Type I precision sound level meter (Larson-Davis 800B) and a 1/2-in. condenser microphone positioned at a height corresponding to the level of the ear canal of a standing chinchilla. SPL measurements were averaged across five positions within each cage (geometric center and each corner). Attenuator settings and cage positions were adjusted so that the average SPL in each cage was within 1 dB of the specified SPL. Animals were rotated to different cages each day to minimize any effects of slight differences in SPL between cages.

The impulse noise was generated digitally, converted to an analog signal by a 16-bit D/A converter on a DSP board, attenuated (Hewlett-Packard 350D), amplified (NAD 2200) and routed in parallel to two compression drivers (JBL 2446) in a sound booth. Each driver was fitted with a sound delivery tube (5 cm diameter×20 cm) with its end angled at 45° to broaden its range of resonance (Danielson *et al.*, 1991). Analysis of the impulse noise was performed with a Stanford Research Systems SR785 dynamic signal analyzer. The duration of the waveform was 29 μs, and the spectrum approximated a low-pass function with a half-power point at 400 Hz, rolling off at approximately 4 dB/octave between 400 Hz and 25.6 kHz.

The ends of the sound delivery tubes were separated by 10 cm. The animal in a restraining tube was placed between the drivers with the tubes directed at the animals' ears. Each animal was exposed to 50 pairs of impulses, with 50 ms between the two impulses of each pair and a 1000-ms interval between the onset of each pair. The total exposure time was 50 s. The impulse noise was calibrated using a 1/8-in. microphone (Bruel & Kjaer 4138) and voltmeter to a level corresponding to 150-dB peak SPL.

D. Cochlear analyses

After the completion of testing, chinchillas were deeply anesthetized with sodium pentobarbital (Somlethal, 400 mg/kg i.p.) and decapitated. The cochleas were quickly removed and perfused through the oval window with a succinate dehydrogenase (SDH) staining solution consisting of 2.5 ml of 0.2-M sodium succinate, 2.5 ml of 0.2-M phosphate buffer (pH 7.6), and 5 ml of 0.1% tetranitro blue tetrazolium. Cochleas were incubated in the SDH staining solution for 45 min at 37 °C, post-fixed with 10% formalin, and stored in fixative for at least 24 h. Stained cochleas were dissected from the apex to the base, mounted in sections in glycerin on microscope slides, coverslipped, and examined using light microscopy (400× magnification). The numbers of missing OHCs and IHCs were determined for successive segments of the organ of Corti. Individual cochleograms were constructed to show the percentage of hair cells missing

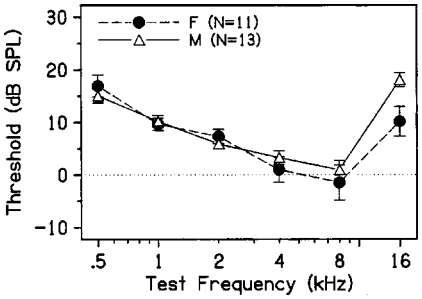

FIG. 1. Mean thresholds of female (solid circles) and male chinchillas (open triangles) before noise exposure. Bars in this and subsequent figures represent standard errors of the means (SEM).

as a function of distance from the apex of the cochlea. Percent hair cells missing was referenced to our lab standards based on normal chinchillas. Percent distance from the apex was converted to frequency using the frequency-place map of Greenwood (1990).

E. Data analysis

One male and two female chinchillas lost one or both IC recording electrodes during the experiment. Data from these ears were excluded from analysis. The final sample consisted of data from 11 ears of females and 13 ears of males. Data were analyzed using Statistical Package for the Social Sciences software (SPSS; version 8.0). An alpha level of 0.05 was adopted as the criterion level of significance for all statistical tests. Analyses of variance (ANOVAs) were used to assess differences between means, with IC-EVP thresholds and threshold shifts as dependent variables. Independent variables were Sex (a between-subjects factor), Frequency, and Time (within-subjects factors). Significant main effects and interactions involving Sex were analyzed further using independent Student *t*-tests. Changes as a function of time were assessed using paired *t*-tests. In order to determine if sound conditioning produced significant protection from impulse noise, data obtained from animals in this experiment were compared to data obtained from a control group of nine female and nine male chinchillas exposed to impulse noise alone under identical conditions, described in a previous publication (McFadden *et al.*, 1999). Comparisons between groups were made using separate two-way Group×Sex ANOVAs for mean low-frequency PTS (average of PTS values at 0.5, 1, and 2 kHz) and high-frequency PTS (average of PTS values at 4, 8, and 16 kHz).

II. RESULTS

A. Pre-exposure thresholds

Prior to exposure, females had lower threshold at 16 kHz than males (Fig. 1). A two-way (Sex×Frequency) mixed ANOVA showed a significant Sex×Frequency interaction, $F(5,110)=2.62$, $p=0.028$. The interaction occurred because females had similar or slightly higher thresholds than males at low frequencies, but consistently lower thresholds at high frequencies. The difference between females and males at 16 kHz was statistically significant [Student *t*-test, $t(22)=2.68$, $p=0.014$], with females having significantly lower thresholds than males. Pre-exposure thresholds were similar to those of control animals in our previous study (McFadden *et al.*, 1999). Control females also had significantly lower threshold at 16 kHz compared to control males, with no other significant differences between groups (Student *t*-tests).

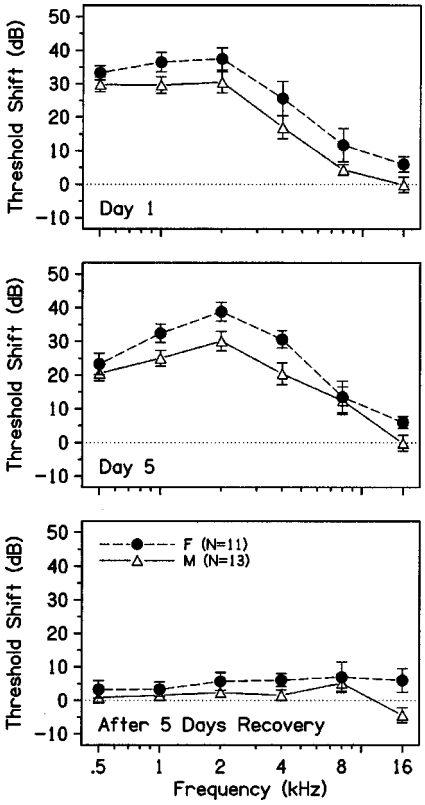

FIG. 2. Mean threshold shifts (±SEM) during and after sound conditioning. Top panel: threshold shifts after the first day (6 h) of sound conditioning. Middle panel: threshold shifts after the last day of conditioning. Bottom panel: threshold shifts 5 days after the last conditioning exposure and before exposure to impulse noise.

B. Threshold shifts from conditioning noise

After the first day of sound conditioning, thresholds were elevated by approximately 30–40 dB SPL at low frequencies, and by 0–25 dB at high frequencies (Fig. 2). Thresholds were significantly elevated at all frequencies for females and at all frequencies except 16 kHz for males (paired *t*-tests; all *p* values <0.04). Two-way (Sex×Time) mixed ANOVAs for TS at each frequency yielded significant main effects of Sex at 1, 2, 4, and 16 kHz [$F(1,22)=5.17$, 6.64, 7.02, and 8.35, respectively; all *p* values <0.04] and main effects of Time at all frequencies except 16 kHz (all *p* values <0.02). The main effect of Sex arose because females consistently showed more TS than males during and after the conditioning exposure.

TS decreased significantly at 0.5 kHz between Day 1 and Day 5 of conditioning for both males, $t(12)=2.84$, $p=0.015$, and females, $t(10)=2.97$, $p=0.014$. The decreases in TS that occurred between the last day of conditioning and the end of the 5-day recovery period were significant at frequencies below 16 kHz (all *p* values <0.04). After 5 days of

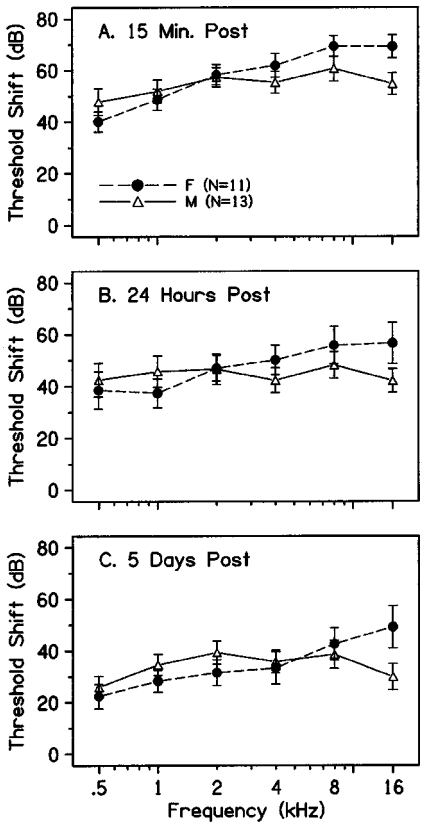

FIG. 3. Mean threshold shifts (±SEM) at three times after impulse noise exposure. Top panel: threshold shifts 15 min after impulse noise exposure. Middle panel: threshold shifts 1 day after impulse noise exposure. Bottom panel: threshold shifts 5 days after impulse noise exposure.

recovery from conditioning, thresholds were within approximately 5 dB of pre-exposure values at all frequencies (Fig. 2, bottom panel).

C. Threshold shifts after impulse noise

Mean TS values are shown in Fig. 3. Two-way (Sex×Time) mixed ANOVAs for TS at each frequency showed significant Sex×Time interactions at 2 and 4 kHz [$F(3,66)=5.36$ and 3.14, respectively, p values <0.04], and significant main effects of Time at all frequencies (all p values <0.001). The interactions occurred because females showed more recovery (approximately 10 dB) at 2 and 4 kHz

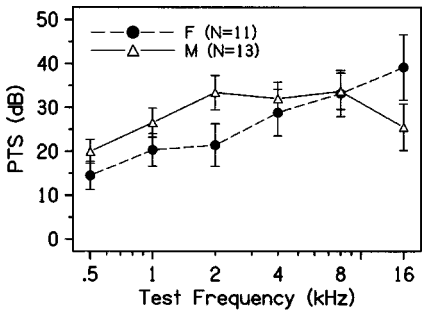

FIG. 4. Permanent threshold shifts (PTS) measured 20 days after impulse noise exposure for females (solid circles) and males (open triangles). Bars show SEMs.

over time than males. Between 15 min and 5 days post-exposure, TS decreased by approximately 20 dB for males, and 30 dB for females.

Impulse noise produced significant PTS at all frequencies (Fig. 4) for both males and females (paired t-tests; all p values ≤ 0.01). A two-way (Sex×Frequency) ANOVA on PTS showed a significant Sex×Frequency interaction, $F(5,110)=4.20$, $p=0.002$. The interaction occurred because of the reversal of sex differences at 2 kHz and 16 kHz. Males developed approximately 12 dB more PTS than females at 2 kHz, but approximately 15 dB less PTS than females at 16 kHz. Absolute thresholds of females and males at 16 kHz differed by less than 6 dB at 20 days post-exposure; this difference was not statistically significant.

To summarize the IC-EVP test results, females had a significantly lower mean threshold at 16 kHz than males prior to exposure (Fig. 1). During conditioning, females consistently showed greater TS than males, but thresholds of both sexes were essentially normal within 5 days after conditioning (Fig. 2). Subsequent exposure to M16 rifle fire produced more TS at low frequencies for males, and more TS at high frequencies for females (Fig. 3). When PTS was assessed 20 days after exposure to M16 rifle fire, females showed 6–12 dB less PTS than males at 0.5, 1, and 2 kHz, but approximately 15 dB more PTS than males at 16 kHz (Fig. 4).

D. Noise-induced hair cell losses

Hair cell lesions were slightly smaller in cochleas from females (Fig. 5). Average OHC losses in the apical half of

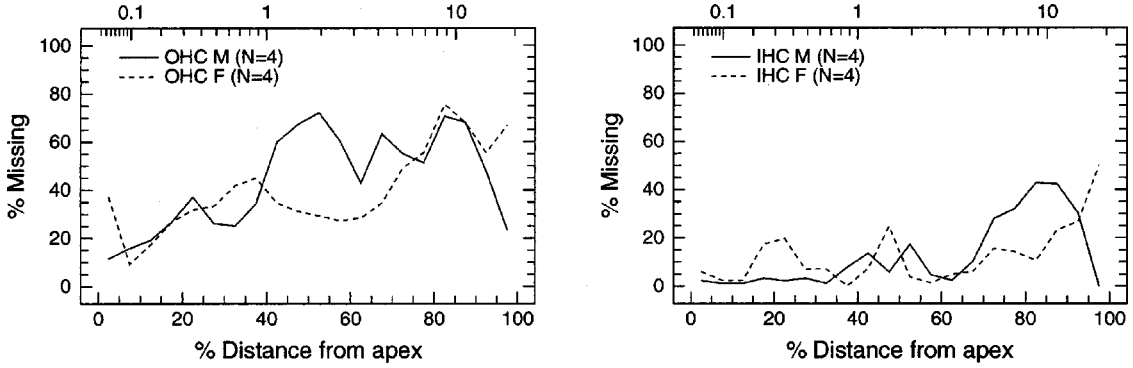

FIG. 5. Cochleograms showing hair cell loss after impulse noise exposure. Left panel: outer hair cell (OHC) losses for males (solid lines) and females (dashed lines). Right panel: inner hair cell (IHC) losses for males (solid lines) and females (dashed lines).

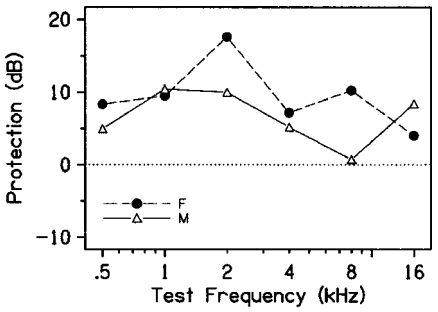

FIG. 6. Protection from permanent noise-induced hearing loss afforded by sound conditioning in females (solid circles) and males (open triangles). Protection is the difference in permanent threshold shift (PTS) between control animals exposed to the impulse noise alone and animals conditioned with 0.5-kHz octave band noise at 95 dB SPL for 5 days (6 h/day).

the cochlea were approximately 30% for females and 40% for males. Average OHC losses in the basal half were approximately 50% for females and 60% for males. The most striking difference was seen in the 2-kHz region of the cochlea, where males showed approximately 30% more OHC loss than females. Mean IHC losses were not remarkably different between females and males. Averaged across the entire cochlea, females had 11% IHC loss and 38% OHC loss, whereas males had 14% IHC loss and 47% OHC loss.

E. Protection from M16 rifle fire

One purpose of exposing animals to the 5-day conditioning regimen was to provide protection from subsequent exposure to M16 rifle fire. A perspective on the success of this approach is provided by Fig. 6, which shows differences in PTS between conditioned animals in the present study and control animals exposed only to the impulse noise (McFadden *et al.*, 1999). Sound conditioning provided up to 18-dB protection for females and up to 10-dB protection for males at individual frequencies. Collapsed across sex, the protective effect was 5–12 dB across frequencies, with greater protection at low frequencies than at high frequencies.

Figure 7 compares average low-frequency PTS and high-frequency PTS for conditioned and control animals. The pattern of PTS was similar for conditioned animals and controls. For both groups, females showed less low-frequency PTS but more high-frequency PTS than males. Conditioned females and males both showed less PTS than their same-sex controls. Two-way (Group×Sex) ANOVAs showed significant main effects of Group, $F(1,51)=6.70$, $p=0.012$, and Sex, $F(1,51)=4.70$, $p=0.035$, for low-frequency PTS. Thus conditioned animals showed significantly less low-frequency PTS than controls, and females showed significantly less low-frequency PTS than males. Despite the consistent trends for high-frequency PTS, neither differences between males and females nor differences between conditioned animals and controls were statistically significant.

Hair cell lesions were smaller in the conditioned animals compared to controls. Conditioned males had approximately 20% less IHC loss and 24% less OHC loss than control males. Conditioned females had approximately 5% less IHC loss and 18% less OHC than control females. Collapsed

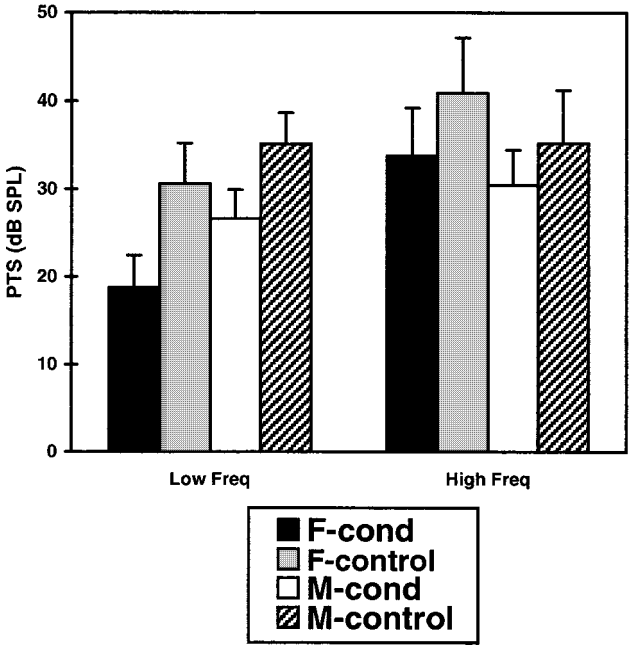

FIG. 7. Mean permanent threshold shifts (PTS) at low frequencies (average of 0.5, 1, and 2 kHz) and high frequencies (average of 4, 8, and 16 kHz) for conditioned females and males and their same-sex controls. Bars show SEMs.

across sex, sound conditioning resulted in approximately 12% less IHC loss and 21% less OHC loss compared to controls.

III. DISCUSSION

A. Protective effects of sound conditioning

The results show that sound conditioning provides protection from PTS and hair cell loss caused by impulse noise exposure. Chinchillas conditioned with a 0.5-kHz OBN at 95 dB SPL for 6 h/day for 5 days developed approximately 5–12 dB less PTS across frequencies, and 13%–21% less hair cell loss than chinchillas exposed to the impulse noise alone. As shown in Fig. 7, protection was apparent at high frequencies (approximately 6 dB overall) as well as low frequencies (approximately 10 dB overall). However, only the protection at low frequencies reached statistical significance.

The present results confirm and extend the results of an earlier study by Henselman *et al.* (1994) by showing that a 5-day conditioning regimen can protect the ear from impulse noise. A comparison between the two studies also shows a ''dose effect'' related to the duration of the conditioning exposure. In the Henselman experiment, a 10-day conditioning regimen produced approximately 7–23 dB of protection across frequencies, with the greatest protection (20–23 dB) at 2 and 4 kHz. Averaged across frequencies, the protective effect of a 10-day conditioning regimen was approximately 16 dB SPL. The 5-day conditioning regimen used in the present study also provided significant protection from PTS. However, the magnitude of protection was approximately 6–10 dB less than that provided by the longer conditioning exposure. Differences related to the duration of the conditioning exposure are also apparent in hair cell losses. The pattern of hair cell loss we observed in the present study was

similar to the pattern seen by Henselman *et al.* (1994). However, the magnitude of hair cell protection was considerably greater for the 10-day conditioning regimen. Animals conditioned for 5 days (present study) had approximately 40% OHC loss across the entire cochlea, whereas animals conditioned for 10 days (Henselman *et al.*, 1994) had less than 20% OHC loss. The dose effect of conditioning is interesting because it indicates that the magnitude of protection can be increased by extending the ''training'' period.

The mechanisms by which sound conditioning increase resistance to NIHL are not known, but they are clearly not ''all or none'' phenomena. Previous studies have indicated dose effects of sound conditioning related to exposure duration (Canlon and Fransson, 1998; Subramaniam *et al.*, 1993) and rest period between conditioning and high level exposure (McFadden *et al.*, 1997; Subramaniam *et al.*, 1992). In the experiment by Subramaniam *et al.* (1993), chinchillas were exposed to 0.5-kHz OBN at 95 dB SPL for 20 days, 10 days, or 2 times with 9 days between exposures. All three conditioning exposures provided protection from PTS, but the 10-day exposure provided the most protection overall. It is worth noting that similar protection was afforded by the 20-day conditioning exposure which resulted in residual TS and the two-time exposure that did not. The optimal ''dosing'' parameters for sound conditioning are difficult to determine, because the phenomenon depends on a complex interplay between species and stimulus variables (see McFadden and Henderson, 1999). Nevertheless, it is clear that exposure duration is an important dosing parameter to consider.

It is interesting that sound conditioning can protect the cochlea from impulse noise, which can damage the cochlea by causing direct mechanical failure as well as through metabolic disruption. Whether sound conditioning actually increases resistance to mechanical damage, or whether it only attenuates damage brought about by metabolic changes is not clear. However, there is some evidence that the structural components of the ear may be altered by sound conditioning in a way that could afford protection from mechanical damage (Hu and Henderson, 1997; Pack *et al.*, 1999).

B. Differences between female and male chinchillas

The results show significant differences between female and male chinchillas in their response to noise. During sound conditioning, females consistently showed greater TS than males. After impulse noise exposure, females developed approximately 10 dB less PTS at low frequencies, but approximately 5 dB more PTS at high frequencies than males. The difference in low-frequency PTS between females and males was statistically significant and is uncomplicated by preexisting threshold differences. The pattern of PTS in sound conditioned animals was very similar to that reported previously for animals exposed to impulse noise alone (McFadden *et al.*, 1999). In both cases, females had less TS at low frequencies and greater TS at high frequencies than males. Sound conditioning provided significant protection for both females and males, with little difference in the magnitude of protection.

The reasons for the sex differences cannot be determined from this study. However, since the differences were observed in chinchillas, extraneous factors such as differences in noise exposure history, recreational activities, and dietary factors can be ruled out. One possibility is that sex/gender differences in susceptibility to NIHL arise from acoustical properties of the outer and middle ears, as has been demonstrated for humans (Hellstrom, 1995). A second possibility is that sex/gender differences arise from basic physiological differences between female and male cochleas. Interestingly, Mills *et al.* (1999) recently reported that male rats are more susceptible to kanamycin ototoxicity than female rats, a difference that clearly cannot be attributed to acoustical properties of the ear. McFadden *et al.* (1998) observed changes in otoacoustic emissions in a human male treated with estrogen, indicating that sex hormones can influence outer hair cell function. Because the outer hair cell system is a likely candidate as a site for conditioning-induced changes (Canlon, 1996; Canlon and Fransson, 1995; Hu and Henderson, 1997), observations such as this may be important for understanding the sex differences we have observed in chinchillas. Future studies using the chinchilla may help determine the relative importance of anatomical and physiological factors in sex/gender differences in sound conditioning and susceptibility to NIHL.

ACKNOWLEDGMENTS

This research was supported by Grant No. DAMD 17-96-1-6330 to SLM. The authors are grateful to Marty Howard for her assistance in data collection and noise exposures.

Berger, E. H., Royster, L. H., and Thomas, W. G. (**1978**). ''Presumed noise-induced permanent threshold shift resulting from exposure to an A-weighted Leq of 89 dB,'' J. Acoust. Soc. Am. **64**, 192–197.

Canlon, B. (**1996**). ''The effects of sound conditioning on the cochlea,'' in *Auditory System Plasticity and Regeneration*, edited by D. H. RJ Salvi, F. Fiorino, and V. Colletti (Thieme Medical, New York), pp. 128–142.

Canlon, B., Borg, E., and Flock, A. (**1988**). ''Protection against noise trauma by pre-exposure to a low level acoustic stimulus,'' Hear. Res. **34**, 197–200.

Canlon, B., and Fransson, A. (**1995**). ''Morphological and functional preservation of the outer hair cells from noise trauma by sound conditioning,'' Hear. Res. **84**, 112–124.

Canlon, B., and Fransson, A. (**1998**). ''Reducing noise damage by using a mid-frequency sound conditioning stimulus,'' NeuroReport **9**, 269–274.

Danielson, R., Henderson, D., Gratton, M. A., Bianchi, L., and Salvi, R. (**1991**). ''The importance of ''temporal pattern'' in traumatic impulse noise exposures,'' J. Acoust. Soc. Am. **90**, 209–218.

Gallo, R., and Glorig, A. (**1964**). ''Permanent threshold shift changes produced by noise exposure and aging,'' J. Ind. Hygiene **25**, 237–245.

Greenwood, D. D. (**1990**). ''A cochlear frequency-position function for several species—29 years later,'' J. Acoust. Soc. Am. **87**, 2592–2605.

Hamernik, R. P., Turrentine, G., Roberto, M., Salvi, R., and Henderson, D. (**1984**). ''Anatomical correlates of impulse noise-induced mechanical damage in the cochlea,'' Hear. Res. **13**, 229–247.

Hellstrom, P.-A. (**1995**). ''Individual differences in peripheral sound transfer function: Relation to NIHL,'' in *Scientific Basis of Noise-Induced Hearing Loss*, edited by A. Axelsson, H. M. Borchgrevink, R. J. Hamernik, P.-A. Hellstrom, D. Henderson, and R. J. Salvi (Thieme Medical, New York), pp. 110–116.

Henselman, L. W., Henderson, D., Subramaniam, M., and Sallustio, V. (**1994**). ''The effect of 'conditioning' exposures on hearing loss from impulse noise,'' Hear. Res. **78**, 1–10.

Hu, B. H., and Henderson, D. (**1997**). ''Changes in *F*-actin labeling in the outer hair cell and the Deiters cell in the chinchilla cochlea following noise exposure,'' Hear. Res. **110**, 209–218.

Luz, G. A., and Hodge, D. C. (**1971**). ''Recovery from impulse-noise induced TTS in monkeys and men: A descriptive model,'' J. Acoust. Soc. Am. **49**, 1770–1777.
McFadden, D., Pasanen, E. G., and Callaway, N. L. (**1998**). ''Changes in otoacoustic emissions in a transsexual male during treatment with estrogen,'' J. Acoust. Soc. Am. **104**, 1555–1558.
McFadden, S. L., and Henderson, D. (**1999**). ''Recent advances in understanding and preventing noise-induced hearing loss,'' Current Opinion Otolaryngol. **7**, 266–273.
McFadden, S. L., Henderson, D., and Shen, Y. H. (**1997**). ''Low-frequency 'conditioning' provides long-term protection from noise-induced threshold shifts in chinchillas,'' Hear. Res. **103**, 142–150.
McFadden, S. L., Henselman, L. W., and Zheng, X. Y. (**1999**). ''Sex differences in auditory sensitivity of chinchillas before and after exposure to impulse noise,'' Ear Hear. **20**, 164–174.
Mills, C. D., Loos, B. M., and Henley, C. M. (**1999**). ''Increased susceptibility of male rats to kanamycin-induced cochleotoxicity,'' Hear. Res. **128**, 75–79.
Pack, A., Relkin, E., and Slepecky, N. (**1999**). ''Changes in distribution of tubulin isoforms in the organ of Corti following a sound exposure that causes protection from loud noise,'' Assoc. Res. Otolaryngol. Abstr. **591**, 150.
Skellett, R. A., Cullen, Jr., J. K., Fallon, M., and Bobbin, R. P. (**1998**). ''Conditioning the auditory system with continuous vs. interrupted noise of equal acoustic energy: Is either exposure more protective?'' Hear. Res. **116**, 21–32.
Snyder, D., and Salvi, R. (**1994**). ''A novel chinchilla restraint device,'' Lab. An. **23**, 42–44.
Subramaniam, M., Henderson, D., Campo, P., and Spongr, V. (**1992**). ''The effect of 'conditioning' on hearing loss from a high frequency traumatic exposure,'' Hear. Res. **58**, 57–62.
Subramaniam, M., Henderson, D., and Spongr, V. P. (**1993**). ''Protection from noise induced hearing loss: is prolonged 'conditioning' necessary?'' Hear. Res. **65**, 234–239.
Ward, D. (**1996**). ''Temporary threshold shift in males and females,'' J. Acoust. Soc. Am. **40**, 478–485.
White, D. R., Boettcher, F. A., Miles, L. R., and Gratton, M. A. (**1998**). ''Effectiveness of intermittent and continuous acoustic stimulation in preventing noise-induced hearing and hair cell loss,'' J. Acoust. Soc. Am. **103**, 1566–1572.

Enhancement of the edges of temporal masking functions by complex patterns of overshoot and undershoot

C. Formby and L. P. Sherlock
Division of Otolaryngology—HNS, Department of Surgery, University of Maryland School of Medicine, 16 South Eutaw Street, Suite 500, Baltimore, Maryland 21201

S. H. Ferguson
Department of Speech and Hearing Sciences, Indiana University, Bloomington, Indiana 47405-7002

(Received 25 June 1999; revised 5 October 1999; accepted 11 January 2000)

The purpose of this report is to present new data that provide a novel perspective on temporal masking, different from that found in the classical auditory literature on this topic. Specifically, measurement conditions are presented that minimize rather than maximize temporal spread of masking for a gated (200-ms) narrow-band (405-Hz-wide) noise masker logarithmically centered at 2500 Hz. Masked detection thresholds were measured for brief sinusoids in a two-interval, forced-choice (2IFC) task. Detection was measured at each of 43 temporal positions within the signal observation interval for the sinusoidal signal presented either preceding, during, or following the gating of the masker, which was centered temporally within each 500-ms observation interval. Results are presented for three listeners; first, for detection of a 1900-Hz signal across a range of masker component levels (0–70 dB SPL) and, second, for masked detection as a function of signal frequency ($fs = 500-5000$ Hz) for a fixed masker component level (40 dB SPL). For signals presented off-frequency from the masker, and at low-to-moderate masker levels, the resulting temporal masking functions are characterized by sharp temporal edges. The sharpness of the edges is accentuated by complex patterns of temporal overshoot and undershoot, corresponding with diminished and enhanced detection, respectively, at both masker onset and offset. This information about the onset and offset timing of the gated masker is faithfully represented in the temporal masking functions over the full decade range of signal frequencies (except for $fs = 2500$ Hz presented at the center frequency of the masker). The precise representation of the timing information is remarkable considering that the temporal envelope characteristics of the gated masker are evident in the remote masking response at least two octaves below the frequencies of the masker at a cochlear place where little or no masker activity would be expected. This general enhancement of the temporal edges of the masking response is reminiscent of spectral edge enhancement by lateral suppression/inhibition. [S0001-4966(00)03504-9]

PACS numbers: 43.66.Ba, 43.66.Dc, 43.66.Fe, 43.66.Mk [RVS]

INTRODUCTION

A traditional textbook depiction of temporal masking from Zwicker and Fastl (1990) is shown in Fig. 1. This idealized temporal masking function represents increased detection thresholds for a brief signal measured at selected times preceding, during, and following the presentation of a gated masker. Temporal spread of masking, in this idealized example, extends backward in time before masker onset (i.e., backward masking) and forward in time after masker offset (i.e., forward masking). The temporal spread of masking is usually more prolonged at masker offset than at masker onset. The extent of the temporal spread of masking is dependent on a number of factors, especially the relative frequencies of the signal and masker and the masker presentation level (see Soderquist *et al.*, 1981; Moore, 1989). In general, classical patterns of temporal masking like that depicted in Fig. 1 are reported for spectrally matched or spectrally similar signal and masker conditions for masker sensation levels >40 dB (Moore, 1989).

In this report, we present temporal masking functions that are very different from the classical pattern depicted in Fig. 1. Of interest in this study are measurement conditions that restrict and minimize, rather than accentuate, temporal spread of masking. In experiment 1, we evaluated the effect of masker level, including sensation levels <40 dB, on the temporal masking response measured for a brief signal presented off-frequency from the frequencies of the masker. In experiment 2, we systematically evaluated the effect of signal frequency on the temporal masking response. We sampled detection over a 5000-Hz range of signals presented off-frequency from the frequencies of the masker, both below and above the masker spectral components. An increment signal presented at the logarithmic center frequency of the masker band was also evaluated and provided an on-frequency signal/masker measurement of the temporal masking response. In experiment 3, we performed additional experiments to elucidate the nature of the temporal masking response at signal frequencies very distant from the masker frequencies.

In each of the three experiments, we carefully sampled detection of a brief probe signal at selected times before the onset of a masker, during the gated masker, and after masker offset, with detailed sampling around masker onset and off-

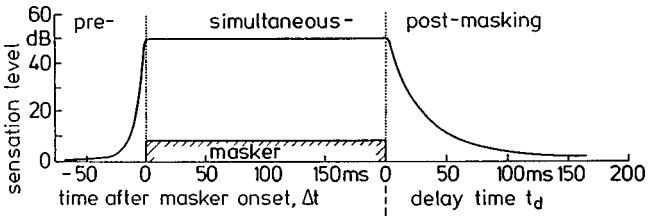

FIG. 1. Schematic representation of the three components of the temporal masking function: (1) pre- (backward) masking—diminished detection for a probe that precedes the masker onset; (2) perstimulatory or simultaneous masking—diminished detection for a brief probe presented during the on-time of a longer masker; and (3) post- (forward) masking—diminished detection for a probe that follows the masker offset. Note that post-masking uses a different time origin than pre-masking and simultaneous masking (from Zwicker and Fastl, 1990).

set to assess temporal edge effects. Our motivation for probing the masker response carefully in time, under conditions of reduced temporal spread of masking, is considered below in terms of the underlying peripheral adaptation response expected to the masker. The temporal masking results described here reveal an auditory temporal microstructure characterized by complex patterns of diminished and enhanced masked signal detection coinciding with the gated masker's temporal onset and offset. These complex detection patterns appear to accentuate and sharpen the perceptual representation of the temporal edges of the masker in a manner not previously described.

I. BACKGROUND AND RATIONALE

The temporal masking experiments described in this report were motivated by a pair of features that characterize peripheral neutral adaptation for low-threshold, high-spontaneous rate, primary auditory afferent fibers. These features are highlighted in Fig. 2. This figure from Eggermont (1985) models the adapting single-unit discharge rate in response to a toneburst. The first feature of interest is the large peak in the neural firing pattern at stimulus onset. The firing rate then decays exponentially over time, despite continued stimulation. Ultimately, the firing rate is reduced by about half and a steady state response is achieved. This reduction in the discharge rate between the unadapted and the adapted neural responses corresponds to a change of about 3–5 dB (Smith and Zwislocki, 1975). The second feature of interest is that the single-unit spontaneous discharge activity is momentarily suppressed immediately following stimulus offset. The spontaneous firing rate then recovers with an exponential time course somewhat longer than the response decay at stimulus onset (Smith, 1977; Harris and Dallas, 1979).

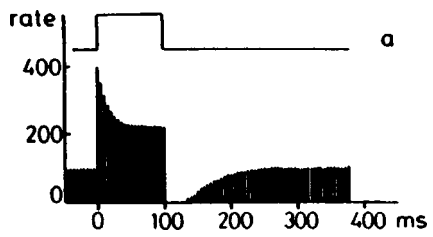

FIG. 2. Simulation of perstimulatory adaptation and recovery of spontaneous rate for an auditory nerve fiber in response to toneburst stimulation represented by step waveform a (from Eggermont, 1985).

Adaptation processes underlying the neural response decay in onset firing rate are widely believed to contribute to auditory masking (see Bacon and Smith, 1991; Green, 1969; McFadden and Champlin, 1990; Smith, 1979). The basis of this belief is the fact that detection thresholds are elevated more in simultaneous masking tasks for brief signals presented at or near the temporal onset of a gated masker than for signals presented at later times within the gated masker. This exaggerated masking effect, which has been studied extensively, is termed ''temporal overshoot'' (e.g., Bacon and Smith, 1991; Bacon and Viemeister, 1985a; Carlyon and White, 1992; Elliott, 1965; Green, 1969; Zwicker, 1965). An overshoot pattern near masker offset has also been documented and is sometimes referred to as a ''bounce'' (Bacon and Moore, 1986; Bacon and Viemeister, 1985b; Bacon *et al.*, 1989; Elliott, 1969; Leshowitz and Cudahy, 1972; Soderquist *et al.*, 1981; Wright, 1991). This offset overshoot, which is usually smaller in amplitude than onset overshoot, has received relatively much less attention in the literature than temporal overshoot at masker onset. The origin of the ''bounce'' is not known, but it is generally believed to be mediated by central auditory processes (Bacon and Moore, 1986; Bacon and Viemeister, 1985b; Elliott, 1965). This belief is attributable largely to the fact that there is no corresponding increase in neural firing rate at stimulus offset to explain the bounce (see Fig. 2). Neither temporal overshoot at masker onset nor masker offset are represented in the traditional textbook depiction of temporal masking shown in Fig. 1.

If temporal overshoot is due in part to the adapting neural discharge rate at masker onset, then it is perplexing that there is not some psychophysical evidence for a transient reduction in masker effectiveness, or unmasking, associated with the suppression of spontaneous neural activity immediately following masker offset (see Fig. 2). Perhaps this is because traditional forward-masking protocols have routinely used spectrally matched signals and masker stimuli or signals sharing frequencies in common with those of the masker to evaluate the listener's response to the masker (see Moore, 1989). Such stimuli would not appear to be conducive to probing transient reductions in masker effectiveness over time because a set of neural fibers in a refractory state at masker offset would be unresponsive and temporarily unable to respond either to the masker or probe signal activating the same fibers. It is this refractory process and the subsequent recovery from short-term peripheral adaptation that have, until recently, been assumed to explain forward masking (see Relkin and Turner, 1988; Shannon, 1990; Turner *et al.*, 1994). At issue in this study is the nature of the temporal masking response measured for signals presented off-frequency from the masker frequencies. These are stimulus conditions for which the signal and masker are probably not subjected to simultaneous refractory and adaptation processes and, therefore, conditions for which it appeared feasible to probe transient reductions in masker effectiveness.

There is very little good evidence for temporal unmasking in the traditional auditory literature. The most widely

cited reports described facilitation or sensitization processes (Moore and Welsh, 1970; Rubin, 1960; Zwislocki *et al.*, 1959). The basic concepts assume that residual auditory excitation produced by a conditioning stimulus reduces the detection threshold for a signal that precedes or follows the conditioning stimulus. These enhancement processes both suppose much longer time intervals between the masker and the signal than is represented in Fig. 2 by the temporal course of recovery from suppression of spontaneous activity due to peripheral adaptation. In this report we will present new evidence of temporal unmasking at masker offset. We have successfully modeled this unmasking pattern and it appears to be the inverse counterpart to the temporal overshoot pattern measured at masker onset (Formby *et al.*, 1998b, 1999). Accordingly, we will refer to this phenomenon as temporal undershoot. Other evidence of temporal undershoot near masker onset will also be presented. Whatever the explanation for this onset undershoot, it appears to be more complex than one might predict from knowledge of peripheral adaptation at the level of single units.

II. GENERAL METHOD

A. Subjects

Three adult listeners ages 25 (JS), 43 (BS), and 45 (CF) years participated as subjects in this series of experiments. Each subject had audiometrically normal hearing sensitivity. Listeners JS and BS were paid for their participation. Listener CF was the senior author. Each subject had previous experience as a listener in our laboratory and was well practiced on the temporal masked detection task prior to formal data collection.

The experiments were performed over roughly a two-year period, during which time each listener contributed a total of about 180–190 h to this project. This effort for listeners CF and JS was distributed relatively uniformly over the two years, whereas the listening schedule for BS was arranged around out-of-town work assignments. His availability typically alternated on and off in two or three month blocks, requiring him to complete three to four sessions a week when available.

B. Apparatus and stimuli

All stimuli were produced using Tucker-Davis Technology (TDT) hardware. The signal and masker were generated digitally by programming an array processor (TDT, model AP2) to implement an inverse Fast Fourier Transform (FFT) procedure. The narrow-band noise masker was produced in the frequency domain by specifying equal magnitude and random phase for each sinusoidal component (frequency bin-width of 9.7 Hz) within the masker passband. The inverse FFT procedure provided a 102.4-ms temporal waveform that was repeated and windowed to produce a 200-ms masker with the desired rise/fall ramps. For the off-frequency signal conditions, each tone-pip signal was generated in an identical manner as that described for the masker (i.e., with random phase), but using only a single frequency component. The masker and signal were added to produce the masker and signal stimulus waveform. For the on-frequency signal condition, the signal was created by setting the magnitude of the center frequency component ($fs = 2500$ Hz) of the masker to the desired level within the duration of the signal and specifying the desired rise/fall ramps. The signal component and the corresponding 2500-Hz component of the masker therefore had identical phase in this condition for all signal locations (i.e., before, within, or after the masker).

The masker and signal were played via a digital-to-analog converter (DAC) (TDT, model DA1) with 16-bit precision and a sampling period of 25 μs. The DAC output was low-pass filtered (TDT, model FT5-9) below 7500 Hz to prevent aliasing, then attenuated (TDT, model PA4 and model SM3) and routed (TDT, model HB5) to an earphone (Telephonics, model TDH-39) for presentation to the right ear of each subject. The subject was seated in front of a monitor and keyboard in a sound-attenuating double-wall room for these experiments.

The masker stimulus in all experiments was approximately a critical-band noise logarithmically centered at 2500 Hz. The nominal masker bandwidth extended from 2367 to 2767 Hz; the measured masker bandwidth was about 405 Hz. The attenuation of the energy outside of the nominal masker bandwidth was very steep and was at least 150 dB per octave. The masker duration was 200 ms, exclusive of 2-ms linear rise/fall ramps. The sinusoidal signal frequency (*fs*) was gated with 2-ms linear rise/fall ramps and had a 5-ms plateau.

C. Procedure

The listener's task in these experiments was to detect the signal, which was presented with equal likelihood in one of two visually cued 500-ms observation intervals of each trial. The narrow-band noise masker was presented in both observation intervals of each trial. Within each observation interval, the masker was gated fully on at 150 ms and fully off at 350 ms. Each stimulus had a different set of random phases chosen for each interval of every trial. At the conclusion of the second observation interval of each trial (500-ms interstimulus interval) the listener entered his response (via computer keyboard), indicating the observation interval that he perceived to contain the signal. Visual feedback for the correct observation interval was then provided on the computer monitor.

A computer algorithm controlled the level of the signal, which the listener tracked adaptively across a block of 40 two-interval, forced-choice (2IFC) trials to estimate a 70.7% correct detection threshold. The adaptive algorithm decreased the signal level after two consecutive correct responses and increased the level after an incorrect response (Levitt, 1971). The level of the signal was decreased (or increased) from the starting value with steps of 5 dB for the first three response reversals. Thereafter, the signal level was increased or decreased with 2-dB steps. The estimate of the threshold level for a given block of trials was based on the arithmetic mean of the signal level at the last even number of reversals (typically 8–12) for the small adaptive steps. For the on-frequency condition, masked detection threshold was calculated as the level of an uncorrelated signal that when

TABLE I. Signal temporal positions presented in experiments 1, 2, and 3. All values shown are referenced to the onset of the 500-ms signal observation interval. Each value is presented in ms and corresponds to the temporal center of the signal. The values in parentheses are the 13 additional signal temporal positions presented only in experiment 3.

50	100	120	130	140	141	142	144	(145)	146	148	150	151	152	154	155
156	158	160	165	170	(175)	180	190	200	(220)	(240)	250	(260)	(280)	300	(310)
(320)	325	(330)	(335)	340	341	342	344	(345)	346	348	350	351	352	354	355
356	358	(359)	360	370	380	(400)	450								

added to the masker would have produced the measured threshold level of the incremented signal component.

It is customary in our laboratory to base a listener's average detection threshold for a given condition on three consistent estimates obtained from three blocks of trials, all yielding threshold values within 5 dB of one another. We used this criterion to obtain a masked detection threshold at each of 43 signal temporal positions within the 500-ms observation interval. Temporal masking functions were constructed from these data. For some signal temporal positions, this strict performance criterion required the listener to produce as many as 10 or 11 threshold estimates to achieve three consistent values. Usually, however, estimates from about four or five blocks of trials were sufficient to achieve three consistent estimates for averaging. The very low reliability at certain signal temporal positions within the observation interval is curious and, ultimately, motivated us to conduct an analysis that is considered later in this report.

Shown in Table I is a list of the 43 signal temporal positions that we used in experiments 1 and 2. Thirteen additional signal temporal positions were evaluated in experiment 3 and these are also presented in Table I. The temporal positions reported are referenced to the onset of the 500-ms signal observation interval and correspond to the temporal center of the signal. The order of presentation of the 43 signal temporal positions depended on a randomly selected order of 7 grouping sequences. Each grouping sequence consisted of a fixed set of five to seven signal temporal positions that were always presented in the same order. The signal temporal positions within a given set either corresponded closely in time or sampled a common portion of the observation interval (e.g., the signal was presented in one set prior to masker onset, in another set following masker offset, and in other sets within the duration of the masker; sets of signal temporal positions also sampled detection immediately around the temporal onset or offset of the masker to assess temporal edge effects).

Within a given listening session, usually lasting about 1.5–2.0 hr for listeners CF and BS, from five to seven of the grouping sequences were randomly selected for presentation to these listeners. Listener JS typically listened in sessions lasting about 0.5 to 1.0 h (over a lunch break) in which he was randomly presented three or four of the grouping sequences within a session. On average, to construct the temporal masking function for a given signal condition, each listener required about 11 h to achieve 3 consistent thresholds for all of the 43 signal temporal positions.

III. EXPERIMENT 1: EFFECT OF MASKER LEVEL

A. Overview

In experiment 1, our purpose was to measure the effect of masker level on temporal masking of an off-frequency signal (Formby *et al.*, 1997). The signal used in this experiment was presented at $fs = 1900$ Hz. We measured temporal masking functions as a function of masker component level (0 to 70 dB SPL in 10-dB increments), as well as in quiet. The corresponding equivalent masker spectrum levels ranged from $N_0 = -10$ to 60 dB SPL and the corresponding overall rms levels ranged from about 16 to 86 dB SPL.

B. Results

Shown in separate panels of Fig. 3 are the individual temporal masking functions for each of the three listeners for each masker component level. Each column represents one listener and each row shows a different value of masker component level. The shaded region in each panel indicates the temporal extent and the level of the components of the noise masker. Onset and offset effects can be seen emerging in the temporal masking functions for each listener at masker levels of 10 and 20 dB, and are clearly evident at both the onset and offset of the masker for CF for masker levels of 30 and 40 dB. These onset and offset effects are also evident, but to a lesser extent, for JS. Listener BS exhibits evidence of undershoot, but not overshoot, at masker onset for a masker level of 30 dB, and only overshoot at 40 dB. These complex patterns of temporal undershoot and overshoot persist to varying degrees for all three listeners for the masker presented at 50, 60, and 70 dB SPL. The latter set of temporal masking functions is, in general, characterized by steep skirts at masker onset and offset, especially for masker levels 50 and 60 dB. These steep skirts provide very sharp definition of the temporal edges of the masker. Backward spread of masking was evident at masker onset for all three listeners for the masker presented at 70 dB and for CF for the 60-dB masker component level. Notably, as overshoot and backward and forward masking became more prominent for these high-level masker conditions, undershoot was either obscured or became less obvious in the temporal masking functions, especially at masker onset.

To summarize trends in the onset and offset dynamics and steady state properties of the temporal masking functions in Fig. 3, we performed some simple quantitative analyses. These analyses used the points identified for listener CF in the panel displaying his results for the 40-dB masker component level. These points included the maximum (max) and minimum (min) masked detection thresholds measured at

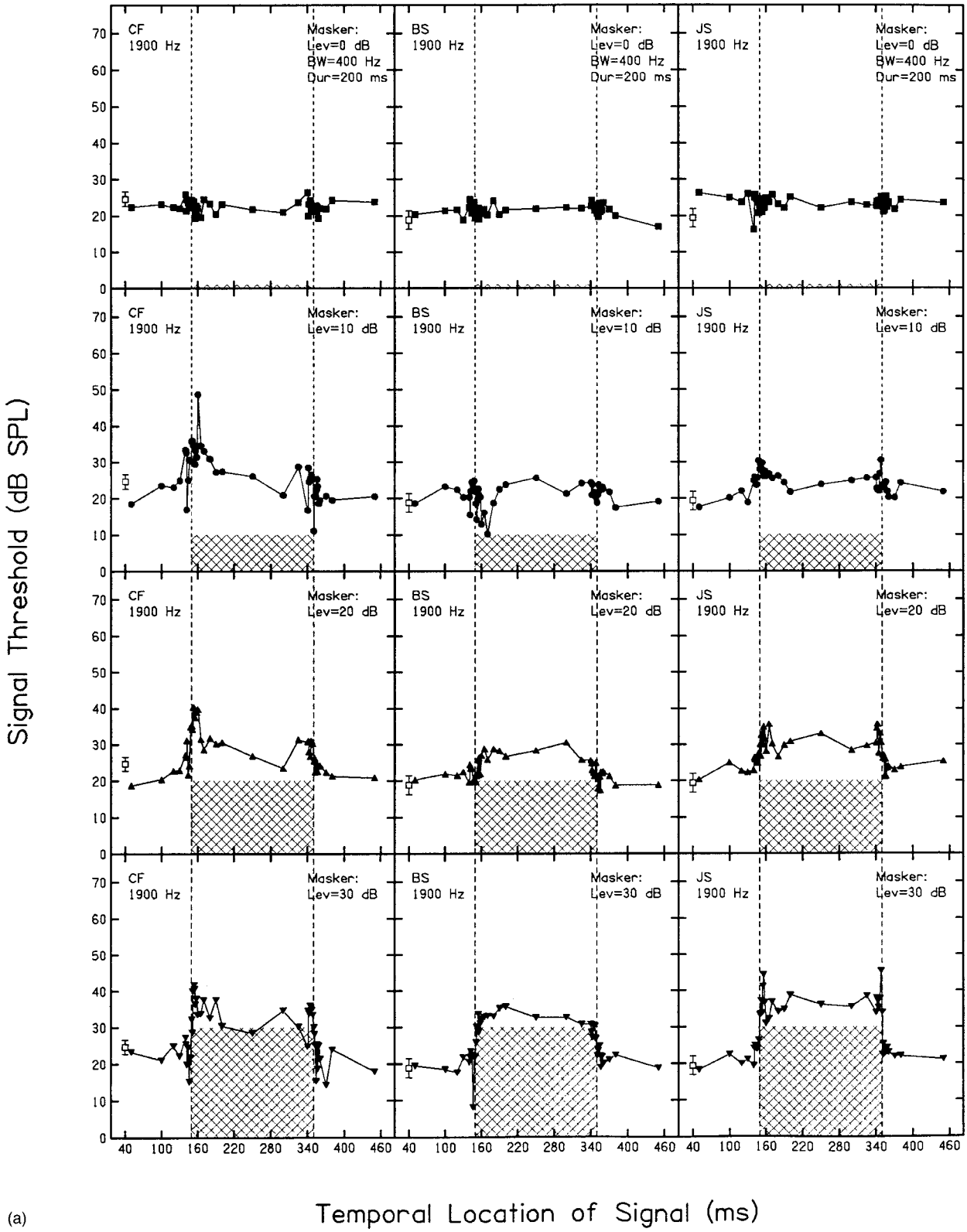

(a)

FIG. 3. Temporal masking functions for a brief sinusoidal probe presented at $fs = 1900$ Hz masked by a critical-band noise centered at 2500 Hz. Results for one masker level are displayed in each row, with masker component level increasing systematically downward within each column. In each column, results are presented separately for an individual listener (identified by initials within each panel). In each panel, a single point on the temporal masking function represents the arithmetic mean of three consistent masked detection threshold estimates. A mean (across each of the 43 signal temporal positions) quiet threshold (± 1 standard deviation bars) for each listener is shown by the open symbol in the lower left corner of each panel in the series. Dashed vertical lines at 150 and 350 ms indicate the nominal temporal onset and offset of the masker. The shaded region in each panel represents the masker level for the corresponding measurement condition. The identified data points denoted in the panel containing the temporal masking function measured for listener CF for the 40-dB masker component level correspond to the maximum (max) and minimum (min) masked detection threshold values measured near masker onset and offset. The mid-point threshold value (measured at 250 ms in the signal observation interval) corresponds to steady state masked detection. These specific points will be used in subsequent analyses.

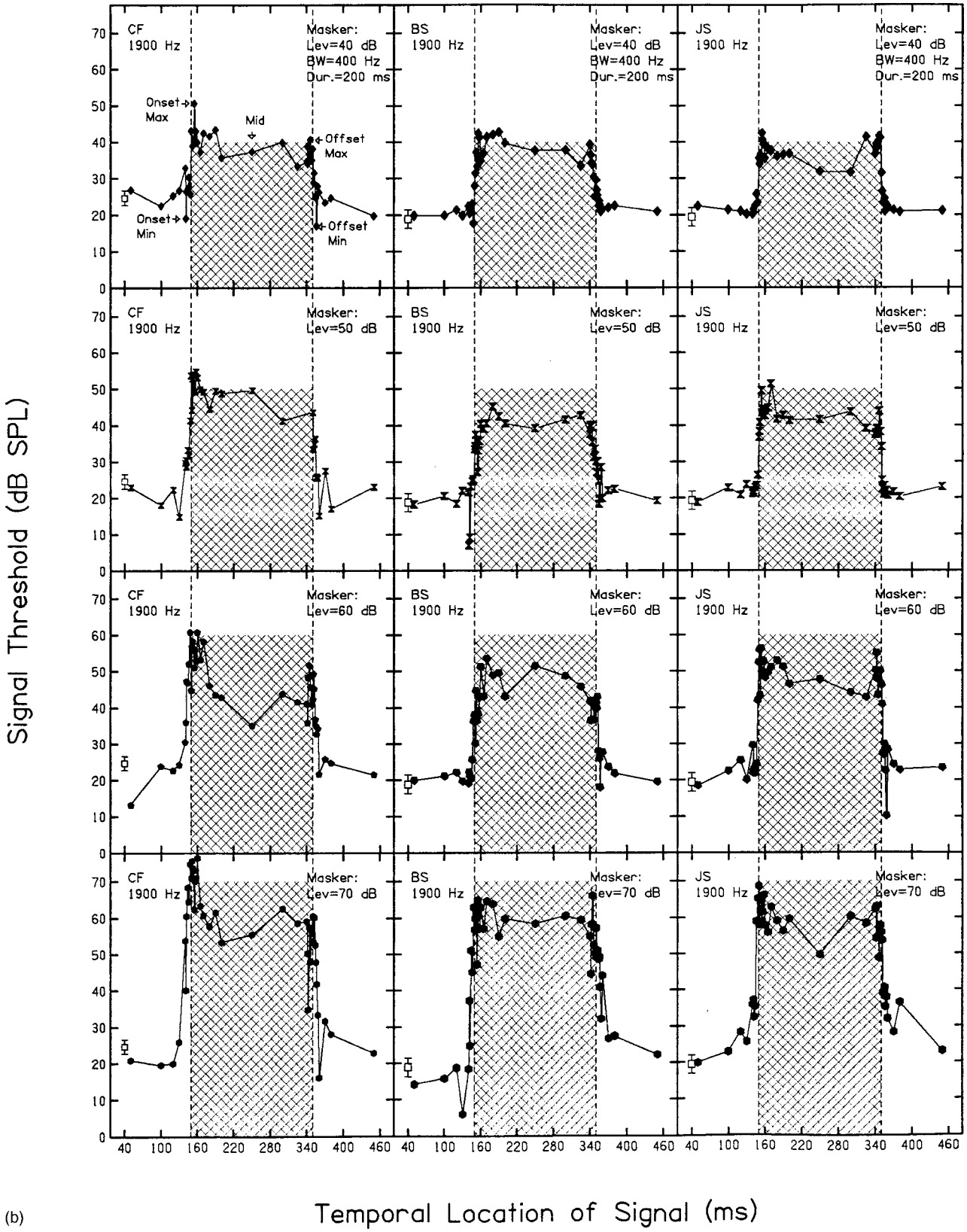

FIG. 3. (*Continued.*)

masker onset and offset for each of the temporal masking functions shown in Fig. 3. We also evaluated the masked detection thresholds measured at the temporal center (mid, 250 ms) of the observation interval (and of the masker). These mid-point thresholds provide reasonable estimates of the steady state response to the masker. Our analyses were based on masked detection data normalized for each listener relative to his individual quiet detection threshold measured at each of the 43 signal temporal positions. The normalized max and min values at masker onset and offset and the mid-

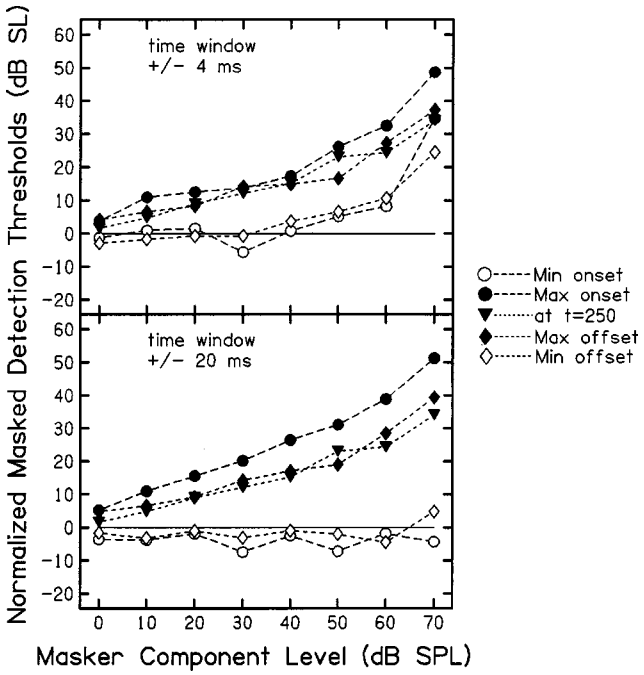

FIG. 4. Group average minima (min) and maxima (max) masked detection threshold values measured at masker onset and offset are shown as a function of masker component level for ±4-ms (top panel) and ±20-ms (bottom panel) temporal windows centered symmetrically in time around the onset or offset of the masker. Mid-point masked detection thresholds, corresponding to steady state values measured at the 250-ms signal temporal position, are also shown for the group. All min, max, and mid-point values were normalized relative to each listener's quiet threshold for the corresponding temporal location of the probe signal prior to calculating each group mean value.

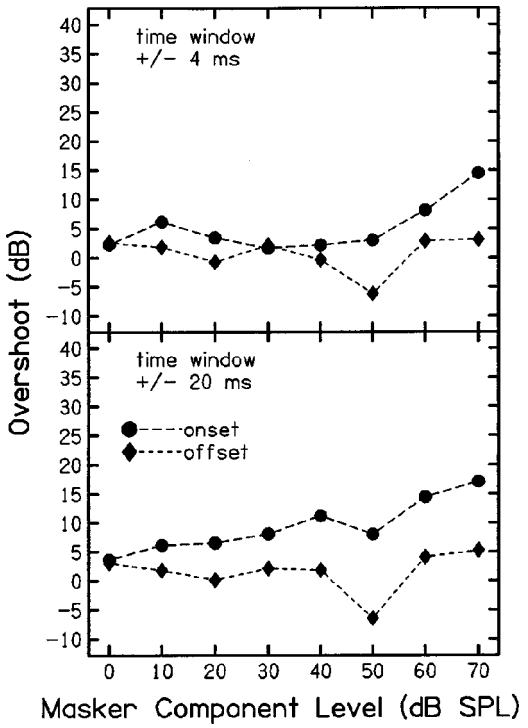

FIG. 5. Group average estimates of temporal overshoot at masker onset and offset are shown as a function of masker component level for the ±4-ms (top panel) and ±20-ms (bottom panel) temporal windows.

point values were calculated separately for each listener. Values for each index were then averaged across the listeners to obtain the group results that are displayed in Fig. 4 as a function of masker component level.

Two different time windows are represented and identified in the two panels of Fig. 4. Each window provides a different perspective on the auditory processing. The one in the top panel assumes that our listeners centered a small (±4-ms) rectangular temporal window symmetrically in time around the onset (at 150 ms in the observation interval) and offset (at 350 ms in the observation interval) of the masker. This window is typical of estimates of the equivalent rectangular duration for the human auditory temporal window (Plack and Moore, 1990) and is consistent with the nominal signal duration (~9 ms) used throughout this study. The window considered in the lower panel assumes that our listeners set a larger (±20-ms) rectangular temporal window around masker onset and offset to establish the max and min values. Past estimates of the ''skirts'' of the auditory temporal window at 2000 Hz suggest that our listeners likely had access to temporal information about the masker onset and offset dynamics over at least this range of times (see Moore *et al.*, 1988).

In Fig. 4 onset minima are shown by unfilled circles and offset minima by unfilled diamonds. For comparison, the onset and offset maxima are shown by the respective filled symbols and the temporal mid-point thresholds are shown by filled inverted triangles. Consider initially the min threshold values, corresponding to undershoot conditions. Two patterns are of interest. First, within a given temporal window, the onset and offset minima were similar in magnitude. Second, for the ±4-ms time window, the minima thresholds differed most from the mid-point thresholds at moderate masker levels. At the extreme low and high masker levels, the minima and mid-point thresholds converged. In contrast, minima for the ±20-ms time window were virtually uniform across masker level; most values fell below 0 dB SL. On average, these minima values were about 3–6 dB below the quiet threshold.

The onset and offset threshold maxima, corresponding to overshoot conditions, behaved very differently than the threshold minima. These maxima increased systematically as a function of masker level in both panels. Onset maxima were consistently greater than offset maxima and spanned a range of about 45 dB across the 70-dB range of masker levels. The offset maxima thresholds were generally similar to the mid-point thresholds and spanned a range of about 30 dB across masker component level in each panel. Thus, on average, there was very little evidence of an ''offset bounce'' in these group results despite evidence to the contrary among the individual data in Fig. 3.

Estimates of temporal overshoot in each temporal window are shown in Fig. 5 as a function of masker component level. These results represent the dB difference between the respective maxima masked detection thresholds measured at masker onset (filled circles) or offset (filled diamonds) and the corresponding mid-point (inverted triangles) masked detection thresholds from Fig. 4 for each masker component level. The amount of temporal overshoot at masker onset was usually ≤10 dB in both time windows, except at the

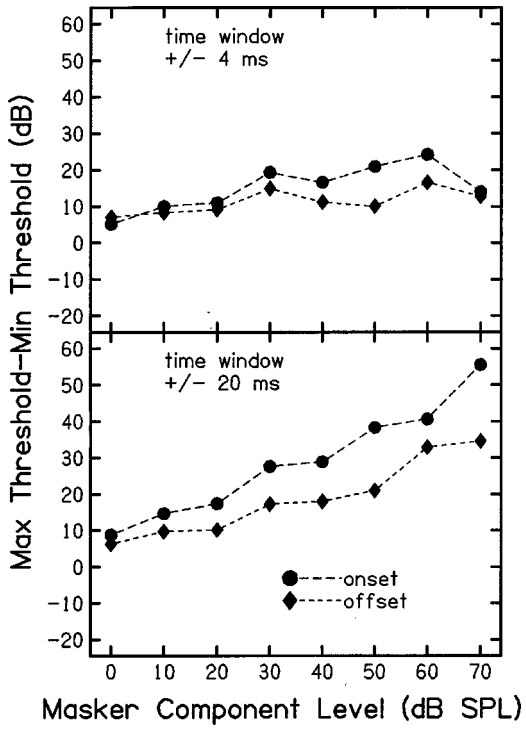

FIG. 6. Group average max–min threshold difference values at masker onset and offset were calculated from the respective values in Fig. 4 and are shown as a function of masker component level for the ±4-ms (top panel) and ±20-ms (bottom panel) temporal windows.

highest masker levels. The largest amount of temporal overshoot (17 dB) at masker onset was obtained for the highest masker component level within the larger time window. Temporal overshoot at masker offset was nominal, typically amounting to 5 dB or less across masker component level in both the ±4-ms and ±20-ms time windows.

Dynamic changes in the temporal masking functions at masker onset and offset were quantified by subtracting the min masked detection thresholds from the corresponding max masked detection thresholds (shown in Fig. 4). These max–min difference results are shown as a function of masker component level at masker onset (circles) and offset (diamonds) in Fig. 6 for the ±4-ms and ±20-ms temporal windows. Max–min differences were typically greater at masker onset than at offset and increased both as the time window was expanded and as a function of masker component level. An asymptotic effect was evident for the max–min difference values at the higher masker levels for the ±4-ms time window. The largest max–min difference values for this smaller time window were about 24 and 17 dB at masker onset and offset, respectively. By contrast, the max–min difference values for the ±20-ms time window increased systematically with increasing masker component level, with the largest value exceeding 55 dB at masker onset versus about 35 dB at masker offset.[1]

C. Discussion

The temporal masking functions measured in experiment 1 and presented in Fig. 3 are very different from the idealized representation of temporal masking depicted in Fig. 1. We are not aware that temporal undershoot patterns of the kind shown in Fig. 3 have been reported previously in the auditory literature. Nor is there much evidence in the classical literature for temporal masking functions with edges at masker onset and offset as steep as those reported here. In contrast, the patterns of temporal overshoot, which we routinely measured in the temporal masking functions at masker onset, and the ''overshoot bounce,'' which was common (but less well represented) at masker offset, are established auditory phenomena (although neither is depicted in the idealized textbook representation of temporal masking shown in Fig. 1).

One of the most remarkable findings in Fig. 3 was the very sizable fluctuation in the microstructure of the temporal masking functions for a given listener. In some panels, the masked detection thresholds varied widely over very small changes in the temporal location of the signal, especially near the onset and offset of the masker. Some of the variability is undoubtedly due to the use of a narrow-band masker, which is characterized by sizable random time-intensity fluctuations in the temporal envelope properties. These stimulus fluctuations are not large enough, however, to explain the behavior of the threshold microstructure.[2]

The large fluctuation in individual performance apparently is not random. This substantial, but orderly, variability can be demonstrated in two different ways. Consider first the pattern of the average standard deviation data for each individual listener and the composite data for the group. These data, shown in Fig. 7(a), are the standard deviation values averaged for all of the masked detection thresholds measured across all eight masker component levels at each of the 43 signal temporal positions. The behavior of both these individual and group standard deviation values closely mirrors the overshoot and undershoot effects that exaggerated the edges of the temporal masking functions shown for each listener in Fig. 3. A second way of representing this lawful variability is shown by the ''repeatability'' function in Fig. 7(b). This function highlights the contrasting ease and difficulty that our listeners encountered in achieving repeatable masked detection thresholds at different signal temporal locations. For some threshold points, as many as 10 or 11 blocks of trials were required for a given listener to obtain 3 consistent estimates. For other points, the threshold estimates were readily repeatable and only three or four blocks of trials were needed to achieve consistent performance for a given condition. To produce the reliability function, the total number of blocks required to achieve three consistent thresholds at each signal temporal position has been summed across all three listeners and across the eight masker component levels (0–70 dB SPL), and an average for the three listeners was calculated at each signal temporal position. The resulting repeatability function also shares the same general pattern of fluctuating microstructure evident in the standard deviation data and in many of the individual temporal masking functions shown in Fig. 3.

It is notable that the greatest overshoot values (17 dB) estimated from the summary data in Fig. 5 were roughly three-fold larger than the greatest undershoot values (about 6 dB) in Fig. 4. Thus in combination together, our listeners could potentially accrue an average maximum dynamic onset

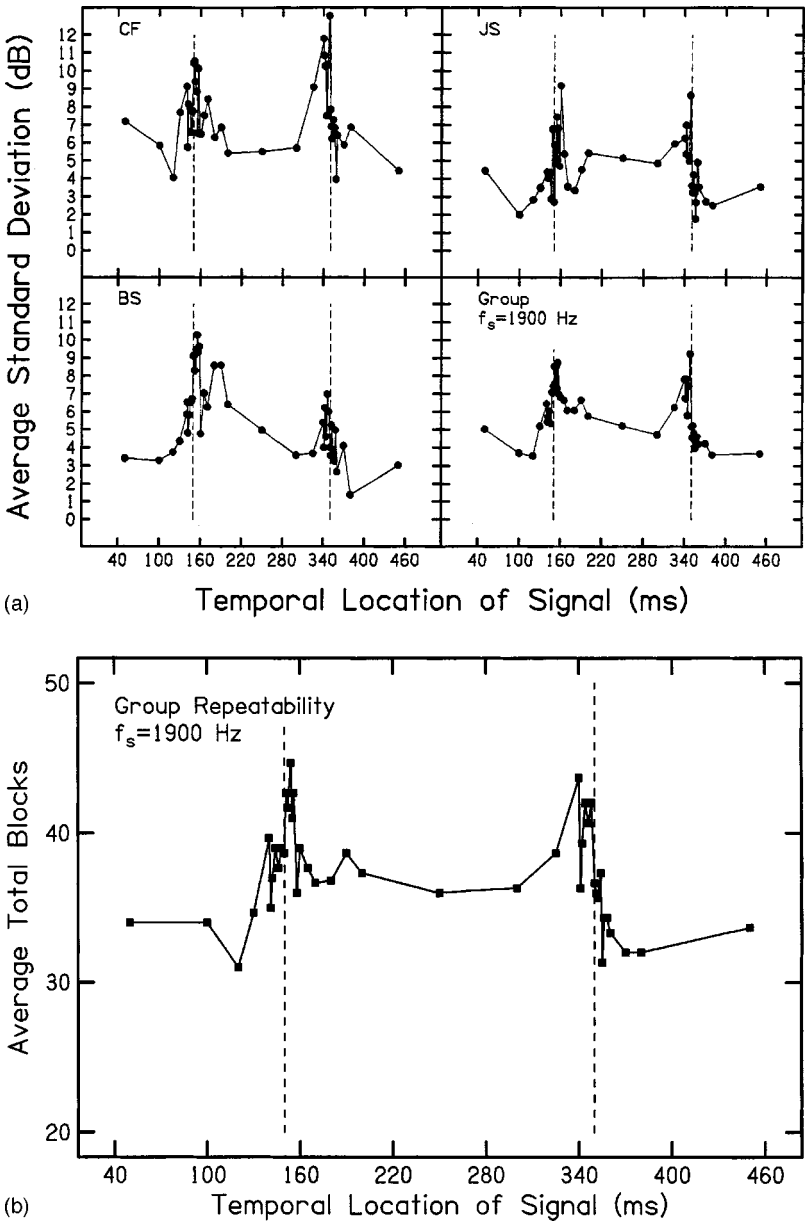

FIG. 7. Individual and group standard deviation values averaged for all of the masked detection thresholds measured in experiment 1 are shown in the top set of four panels in (a). The standard deviation values have been averaged across all eight conditions of masker component level (0–70 dB SPL) and are shown as a function of signal temporal position. The group repeatability function in the bottom panel (b) represents the total number of blocks that were measured on average for each of three listeners across all eight masker component levels (0–70 dB SPL) to achieve three consistent threshold estimates at each signal temporal position for the temporal masking results shown in Fig. 3. Dashed vertical lines in each panel indicate the nominal temporal onset and offset of the gated masker.

cue amounting to 23 dB from the undershoot and overshoot effects at masker onset. This 23-dB dynamic onset cue is in addition to the steady state masking response represented by the average threshold difference between the quiet and mid-point thresholds of the temporal masking function. In contrast, the largest dynamic cue available to our listeners at masker offset was only about half as large as that found at masker onset, and the contribution from the overshoot and undershoot components was roughly equivalent. Cues for dynamic change from overshoot and undershoot were therefore much more prominently represented in the temporal masking functions at masker onset than at masker offset, which is in agreement with reports of acoustic onsets consistently being more detectable than acoustic offsets (see Zera and Green, 1993). This result is in direct conflict with the standard deviation data and the repeatability function (see Fig. 7), which both revealed overshootlike patterns of comparable magnitude in the onset and offset microstructure.

Finally, the growth of the onset temporal masking response in Fig. 3 is highly nonlinear across the range of masker component levels from 0 to 70 dB SPL, and this nonlinearity can be monitored visually by comparing these masked detection thresholds with respect to the linear growth of the masker component levels represented by the shaded region in each panel. Overall, the growth trend of these temporal masking data suggests that the onset response to the masker is relatively more effective at low sound levels and less effective at intermediate levels. This nonlinear growth trend is consistent with a growing body of psychoacoustic data suggesting that normal cochlear function reflects fast-acting compressive properties of the basilar membrane response at moderate sound levels (Moore, 1995; Moore and Oxenham, 1998).[3] In contrast to the compressive behavior of the onset response, the steady state response estimated from the temporal mid-point values of the temporal masking functions reflects relatively linear growth of masking, with a slope of about 0.5 (see inverted triangles in Fig. 4).

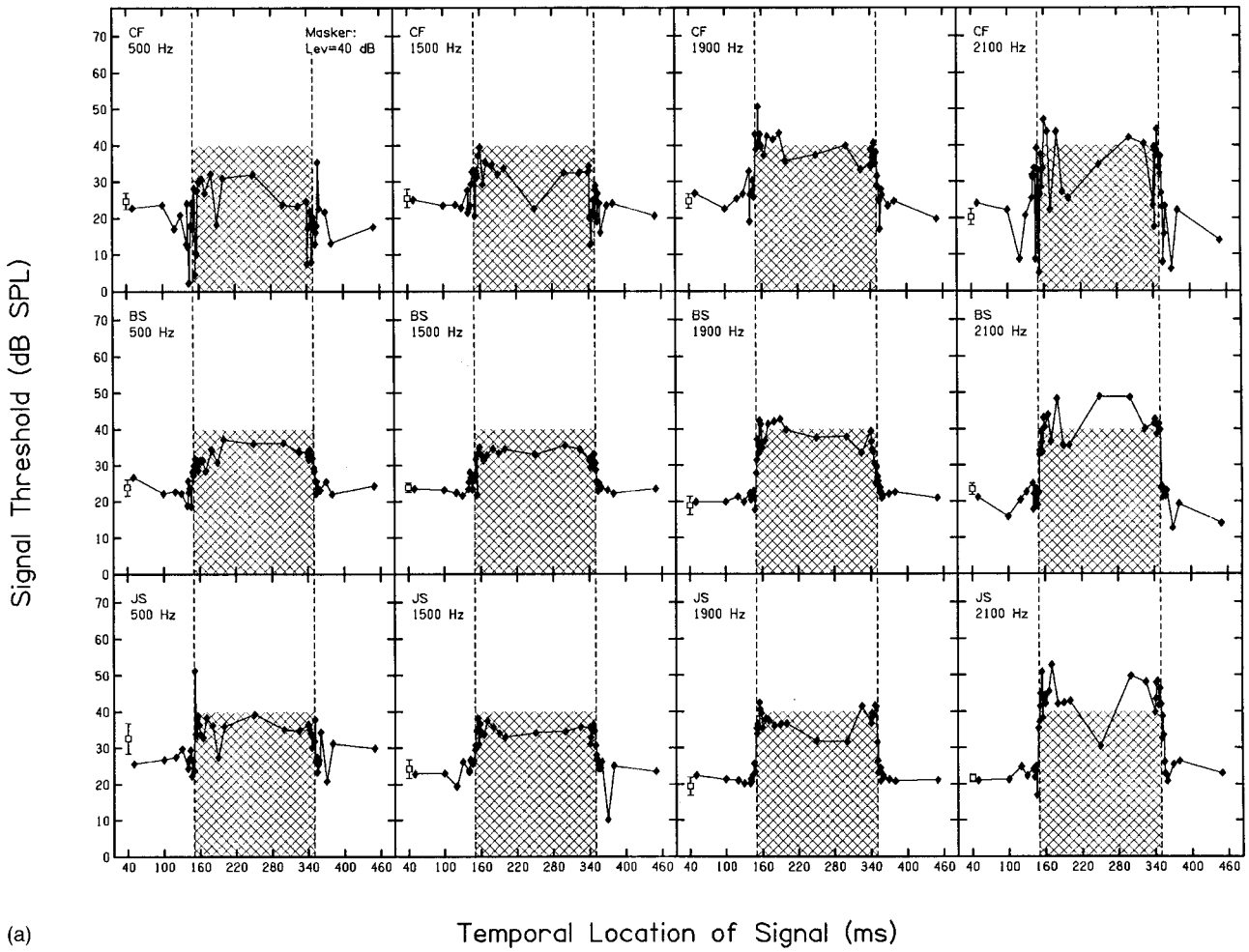

FIG. 8. Probe frequency effects in temporal masking for the critical-band masker centered logarithmically at 2500 Hz and presented at a masker component level of 40 dB SPL. The subject and the frequency of the probe signal, *fs*, are identified in the top left corner of each panel. Signal frequency increases systematically from left to right across the panels in each row. Results for the same *fs* condition are presented within a column. The average quiet detection threshold (and ±1 standard deviation bars) is shown in each panel for the respective listener and *fs* condition.

IV. EXPERIMENT 2: EFFECT OF SIGNAL FREQUENCY

A. Overview

The purpose of experiment 2 was to evaluate changes in the sharpness of the edges of temporal masking functions and the persistence and robustness of temporal overshoot and undershoot across an extended range of off- and on-frequency signal conditions (Formby *et al.*, 1998a). Temporal masking functions were measured for $fs = 500$, 1500, 2100, 2500, 2975, 3300, and 5000 Hz. The gated masker was presented at an intermediate sound level (40 dB SPL per component) for all measurement conditions. This masker was the same stimulus presented in experiment 1. The three listeners from experiment 1 again participated in these measurements.

B. Results

The temporal masking functions measured in experiment 2 are shown for the individual listeners in separate panels of Fig. 8 as a function of signal frequency. The temporal masking functions for the off-frequency signals ($fs = 500$, 1500, 2100, 2975, 3300, and 5000 Hz) are qualitatively similar to the temporal masking functions measured in experiment 1 (shown in Fig. 3). To facilitate comparison, the temporal masking functions measured for $fs = 1900$ Hz for the masker components presented at 40 dB SPL from experiment 1 are included in Fig. 8 for each listener. In every panel, masked detection thresholds were again greatest during the gated masker, particularly near masker onset. In general, the amount of temporal overshoot for these listeners was consistent with the ranges reported in experiment 1 for $fs = 1900$ Hz.

The listeners also exhibited varying amounts of temporal undershoot. These values may be estimated in each panel with reference to the corresponding quiet thresholds for *fs* (shown by the open square symbol). Listener CF routinely produced the most undershoot (in some conditions up to 15–20 dB) and JS the least. The temporal undershoot for CF often coincided with dramatic swings in his masked detection thresholds near masker onset and offset. For listener CF, small changes in signal temporal position of only a few milliseconds near the temporal onset and offset of the gated masker were associated with masked detection thresholds that in some instances oscillated markedly over a range of 20–30 dB. Listener BS exhibited similarly large fluctuations

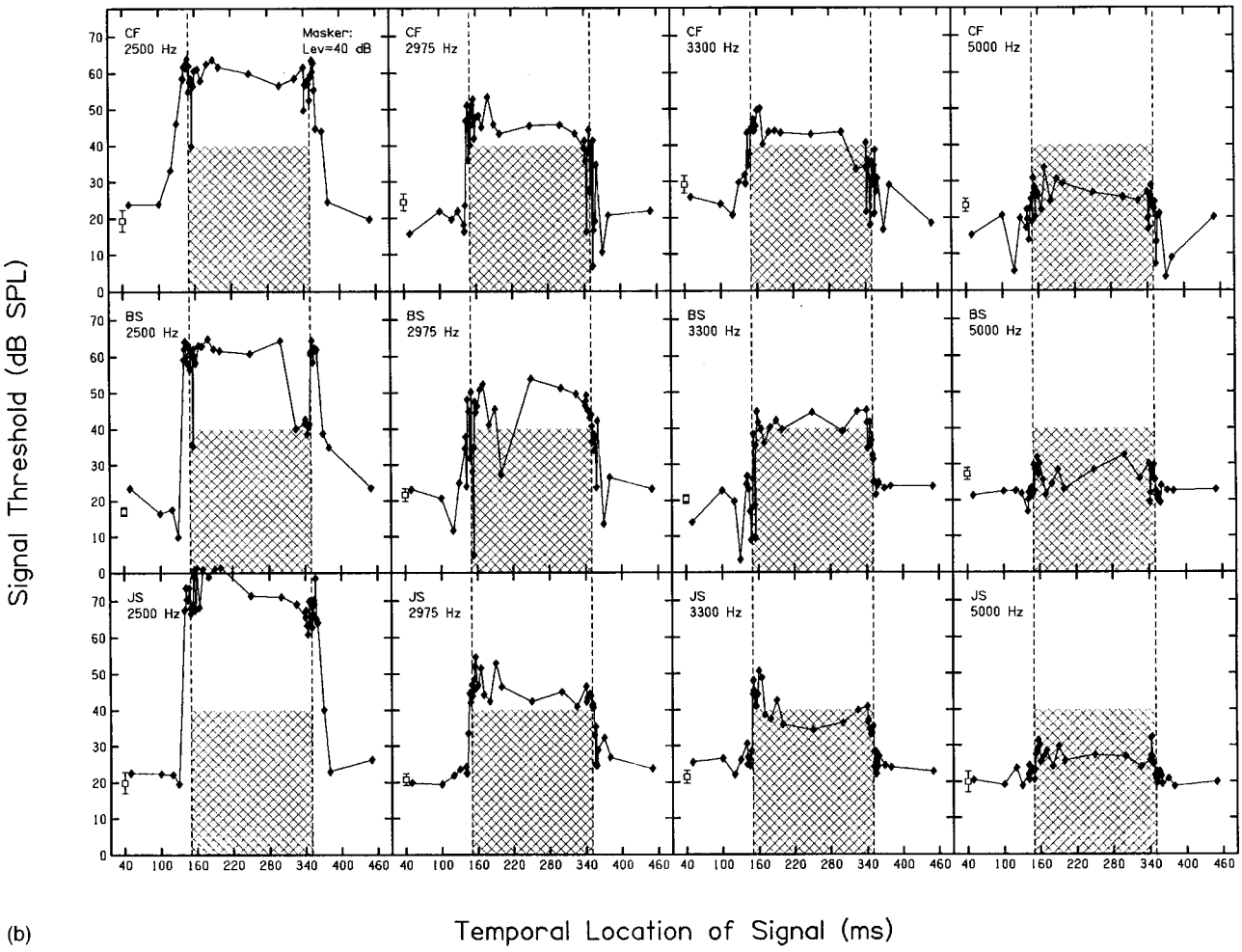

FIG. 8. (*Continued.*)

in masked detection performance near masker onset and offset, especially for $fs = 2975$ and 3300 Hz. As we found in experiment 1, these highly unstable judgements occurred in temporal transition regions associated with gating of the masker on and off.

As expected, the masked detection thresholds for each listener increased as the signal frequencey approached the masker frequencies. Masked detection thresholds for signal temporal positions within the gated masker were lowest for the extreme low ($fs = 500$ and 1500 Hz) and high ($fs = 5000$ Hz) signal frequencies, and were typically in the range of 30–40 dB SPL. The masked detection thresholds for the on-frequency signal ($fs = 2500$ Hz, the logarithmic center frequency of the masker) were the highest, exceeding 60 dB SPL for listeners CF and BS and more than 70 dB SPL for JS.

In addition to the much larger masked detection thresholds for $fs = 2500$ Hz, the temporal masking functions for this on-frequency signal condition were characterized by both backward and forward temporal spread of masking (i.e., preceding and following the gating on and off the masker). The temporal spread of masking was much less extensive in the temporal masking functions for our off-frequency signals in Fig. 8. This difference in temporal spread of masking for the on- and off-frequency conditions has perceptual implications that are considered in subsequent discussion.

C. Discussion

Two trends in these temporal masking functions merit further consideration. The first is that temporal masking functions measured for the off-frequency signals share the same basic structure for all three listeners. Namely, there is relatively minimal temporal spread of masking, and the onset and offset edges of the temporal masking functions are very steep. The steepness of the edges of the temporal masking functions is further exaggerated by the complex patterns of temporal overshoot and undershoot coinciding with masker onset and offset.

It is remarkable that these complex temporal overshoot and undershoot patterns were evident in the auditory temporal microstructure of the masking functions for signal frequencies at least 2000 Hz below and above the masker center frequency (2500 Hz). The significance of this finding is that the main temporal envelope characteristics of the gated masker, although sometimes greatly attenuated, were perceptible to our listeners across a range of signal frequencies spanning at least an order of magnitude. An experiment considered momentarily indicates that remote masking processes

are likely responsible for capturing the temporal envelope properties of the gated masker at frequencies below and distant from the masker frequencies. Traditional masking processes appear to account for the temporal masking results for signal frequencies higher than the masker frequencies.

The second major trend of note in experiment 2 was the poor relation between the leading and trailing edges of the temporal masking functions and the timing of the masker's onset and offset, respectively, for the on-frequency signal condition. There was no evidence of temporal overshoot for listener JS and only a weak semblance of temporal overshoot for listeners CF and BS for $fs = 2500$ Hz. This weak overshoot, however, was most apparent at temporal positions of the signal just prior to masker onset. Offset temporal overshoot was much more strongly represented in the temporal masking functions, especially for listener BS. His temporal masking function featured a 25-dB drop in threshold just before masker offset, and an equivalent threshold elevation just after masker offset. In fact, the ''bounce'' in the temporal masking functions for each listener occurred just after masker offset for $fs = 2500$ Hz. The only evidence of temporal undershoot (6–7 dB) for $fs = 2500$ Hz was obtained for listener BS (about 20 ms before masker onset). The implication of this peculiar general pattern of temporal masking is that the perceptual representation of the masker for $fs = 2500$ Hz appears to extend in time prior to and later than the actual times at which the masker was gated on and off. Thus temporal spread of masking smeared the sharp definition of the temporal edges of the masker.

V. EXPERIMENT 3: TEMPORAL MASKING AT FREQUENCIES REMOTE FROM THE MASKER FREQUENCIES

A. Overview

In an attempt to understand the perceptual processes that faithfully capture the temporal envelope of our gated masker at frequencies very distant from the masker frequencies, we measured new temporal masking functions for listener BS for $fs = 500$ and 5000 Hz for masker component levels of 50, 60, and 70 dB SPL. We included measurements at 13 additional signal temporal positions (shown in Table I) for these experiments. Otherwise the methods were identical to those used in experiment 2 for measuring the temporal masking functions for $fs = 500$ and 5000 Hz.

B. Results

The resulting temporal masking functions measured for $fs = 500$ Hz are shown in Fig. 9 for listener BS. The main effect of increasing masker level was to enhance and sharpen the definition of the edges of the temporal masking functions. The temporal edges of his masking function for the 70-dB masker component level were dramatically exaggerated by very prominent and well-defined undershoot patterns at both masker onset and offset. The temporal masking functions for BS were otherwise relatively invariant with masker level, reflecting virtually the same amount of masking found for $fs = 500$ Hz when the gated masker was presented at a component level of 40 dB SPL (see Fig. 3). In contrast to the level-invariant masking responses measured for $fs = 500$ Hz, the temporal masking functions for $fs = 5000$ Hz (not shown) were level-dependent and grew in magnitude with increasing masker level. For listener BS, overshoot was more prominently represented for $fs = 5000$ Hz than for $fs = 500$ Hz. As a consequence, the temporal edges of his masking functions were more exaggerated for $fs = 5000$ Hz than for $fs = 500$ Hz. This latter difference in the masking functions for $fs = 500$ and 5000 Hz may reflect known differences in the temporal response properties of the low- and high-frequency auditory filters through which these signals were processed.

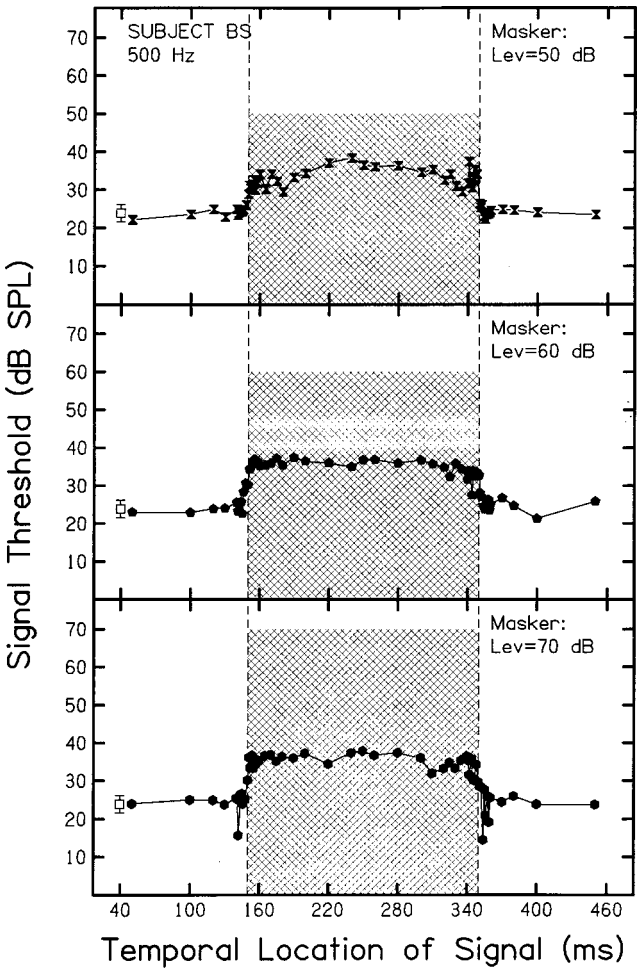

FIG. 9. Temporal masking functions for listener BS are shown for $fs = 500$ Hz for the critical-band masker centered at 2500 Hz and presented at masker component levels of 50 (top panel), 60 (middle panel), and 70 (bottom panel) dB SPL. Each temporal masking function represents masked detection sampled at 56 different temporal positions of the signal within the observation interval (see Table I).

C. Discussion

It is somewhat surprising that we obtained any temporal masking for $fs = 500$ Hz because the corresponding cochlear place was over two octaves below the masker center frequency and was not expected to respond to the masker. These results are consistent with remote masking phenomena described in a series of studies conducted at the Central Institute for the Deaf (CID) in the 1950's and 1960's (see

Bilger and Hirsh, 1956; Deatherage *et al.*, 1957a, b). For stimulus conditions similar to those described here, the CID investigators showed that masked detection thresholds for low-frequency signals measured in the presence of high-frequency noise bands were slightly elevated (by about 10 dB) above the quiet signal thresholds. Bilger and Hirsh (1956) found the amount of remote masking to be relatively invariant with overall masker level for maskers presented below about 80 dB SPL. At masker levels >80 dB SPL they observed remote masking to increase at roughly twice the rate of the increasing masker level and, at very high SPLs, the growth rate for remote masking decelerated. The CID investigators concluded that remote masking reflects a detection process that captures the temporal envelope properties of the masker at a remote cochlear site (Deatheridge *et al.*, 1957a).

The level-invariant temporal masking functions measured for BS for $fs = 500$ Hz provide strong perceptual evidence that the primary features of the temporal envelope of our gated masker were represented in the remote masking response. This level-invariant behavior virtually rules out the possibility that his remote masking response was due to subharmonic or intermodulation distortion processes. We would not expect these latter processes to be invariant with masker level. The level-dependent masking for $fs = 5000$ Hz appears to rule out remote masking processes, which are not thought to be a factor for signal frequencies above the frequencies of the masker.

VI. GENERAL DISCUSSION

A. Comparison with past measurements of temporal masking functions

The temporal masking functions measured in this study are remarkable in several ways. Most notably, in contrast with classical temporal spread of masking, our temporal masking functions for off-frequency signal conditions feature a pattern of restricted masking confined almost entirely to the masker duration. The edges of the temporal masking functions were routinely very steep and coincided closely with masker temporal onset and offset, especially for low to moderate masker levels. This precise acoustic stamping of the edges of the temporal masking functions was exaggerated by complex overshoot and undershoot patterns.

Although little evidence exists in the auditory literature for temporal masking functions with temporal edges as precipitous as those found in this study, the real surprise in our research was the finding of temporal undershoot near both onset and offset of the masker. Over the years, temporal unmasking phenomena have been reported under various labels. This includes backward ''unmasking'' results obtained for the special condition where two successive clicks are presented at very low sensation levels (Moore and Welsh, 1970). The temporal course of this unmasking effect, averaging about 3 dB, was reported to extend in time uniformly over at least a 600-ms range of durations between the two clicks. Forward ''unmasking'' effects have also been observed following exposure to a low-level masker (<40 dB SPL) for spectrally similar probe and masker conditions (Zwislocki *et al.*, 1959; Rubin, 1960; Moore and Welsh, 1970). This forward unmasking effect may extend in time to a period of 2 s after masker offset, with the maximum unmasking effect (about 6–7 dB) about 160 ms after masker offset. These unmasking effects have been variously termed ''facilitation'' and ''enhancement,'' and recently have been suggested to be a procedural artifact (Miskiewicz *et al.*, 1994). Whatever the processes may be, the time courses for the backward and the forward unmasking conditions noted above appear to be much longer than that for the temporal undershoot processes in this report.

In this context, it is important to review some temporal masking studies that were similar in design to the present investigation. These studies did not reveal evidence of undershoot nor did they characteristically find steep temporal edge effects. The study that is most akin to our experiment 1 was reported by Elliott (1969). She measured detection for a brief (5-ms) 1900-Hz tone presented within a silent gap between the offset and onset of an otherwise temporally continuous narrowband masker that contained a gap every 1500 ms. Elliott's masker was a 400-Hz-wide noise band with ''steep'' skirts. The masker was centered at 2550 Hz and presented at 70 dB SPL. Elliott's results reflect both offset and onset temporal overshoot and temporal spread of masking, but no evidence of temporal undershoot for silent gaps as large as 500 ms.

Another study that used a temporal masking paradigm similar to ours was reported by Soderquist *et al.* (1981). They measured masked detection thresholds for brief (10-ms) sinusoidal signals at times preceding, during, and following the presentation of a 250-ms, 1000-Hz sinusoidal masker delivered at 60 dB SPL. The signals and masker were both gated with 5-ms rise/fall ramps. Separate temporal masking functions were measured for eight sinusoidal signal frequencies between 400 and 1600 Hz. Their temporal masking functions revealed sharp leading edges, in some cases as steep as those we obtained at masker onset. Temporal overshoot at masker onset was prominent and contributed to the steep leading edges of their temporal masking functions. The offset bounce was also well represented in their results despite strong evidence for masker adaptation across the temporal masking functions [resembling closely the pattern of the standard deviation data in Fig. 7(a) for listener BS]. The trailing edges of their temporal masking functions at masker offset were characterized by extensive forward spread of masking. No consistent evidence of temporal undershoot was apparent in their data at either masker onset or offset. Results similar to Soderquist *et al.* (1981) were reported earlier by Leshowitz and Cudahy (1972) for a comparable range of sinusoidal signal and masker frequencies. Temporal overshoot at both masker onset and offset and the influence of adaptation across the duration of the masker were very prominently represented in their results, whereas undershoot was not apparent.

There are at least three possible reasons why the investigators may not have observed temporal undershoot in these past experiments. The first and most likely reason was temporal spread of masking associated with relatively high masker levels (≥60 dB SPL), a potential factor obscuring

temporal undershoot in each of the three studies reviewed above. Temporal spread of masking was an obvious factor in our experiment 1 at high levels of the masker. The elevated minima thresholds (i.e., poorer detection) within the ±4-ms time window (see Fig. 4 top panel) measured at high masker levels illustrate this effect. Undershoot was more prominent at low or moderate masker presentation levels for which temporal spread of masking was more limited. The second reason follows directly from the observation that the most prominent minima thresholds in experiment 1 were typically measured within a few milliseconds of masker onset or offset. In the three earlier studies, the spacing of the signal around the masker onset or offset times probably sampled detection too grossly to reveal these threshold minima. In the case of Soderquist *et al.* (1981), signal duration may also have obscured undershoot. Their 10-ms signals (exclusive of 5-ms rise/fall times) may have been too long to reveal changes in the temporal masking microstructure near masker onset and offset.

In experiment 2, we presented supporting data for a third reason why temporal undershoot may not have been evident in past studies. Namely, we showed that the spread of temporal masking for an on-frequency signal was greater than that measured for off-frequency signals. This trend is also evident in Elliott's (1969) results and in other temporal masking data from Osman and Raab (1963). Their data reflect extended temporal masking for click signals presented at temporal positions preceding the onset and following the offset gating of broadband noise burst maskers. Indeed, the temporal masking functions reported by Osman and Raab are very similar to the on-frequency temporal masking functions shown in Fig. 8 for listeners CF and JS. This pattern of temporal masking likely obscured undershoot effects in their data, as well as in our temporal masking functions.

Thus we surmise that because most temporal masking studies to date have focused on on-frequency measurement conditions for which the cochlear place of stimulation has been the same for both the signal and masker (see Moore, 1989), undershoot effects have likely been obscured. Probe signals presented off-frequency from the cochlear location of primary masker activity, in a nearby less strongly masked frequency region, apparently offer a better opportunity to measure unmasking of a brief signal in response to a transient reduction in masker effectiveness.

B. Explanations for temporal undershoot processes

Below we consider and eliminate some plausible *mechanisms* or *processes* that might contribute to the temporal undershoot measured in the present study.

1. Peripheral adaptation

Peripheral adaptation processes may account, at least in part, for the offset undershoot patterns that we obtained, but apparently cannot explain the onset undershoot patterns (Formby *et al.*, 1999). Thus peripheral adaptation can provide only a partial explanation for the present undershoot findings.

2. Enhancement and facilitation

Temporal unmasking attributed to facilitation or enhancement effects has previously been described only for on-frequency signal and masker conditions for which we found no consistent evidence of temporal undershoot. Moreover, we noted earlier that to achieve facilitation/enhancement effects in past studies the time intervals between the gating of the signal and the masker were much longer than those at issue in our measurements.

3. Stochastic resonance

Stochastic resonance is a nonlinear process by which the addition of a subthreshold background noise may enhance detection of a subthreshold periodic signal (Wiesenfield and Moss, 1995). Normal listeners have been shown to garner about a 2-dB benefit in detection for a 100-Hz sinusoidal signal in a subthreshold broadband noise (Zeng *et al.*, 1996). It is conceivable that our narrow-band masker, which was characterized by random temporal envelope fluctuations, might have enhanced detection in remote frequency regions for which the noise was subthreshold, such as $fs = 500$ and 1500 Hz. However, it seems unlikely that the narrow-band noise masker was subthreshold in the signal frequency region ($fs = 1900$ Hz) measured in experiment 1 for the 50-dB masker component level for which undershoot was observed.

4. Negative masking

Negative masking has been reported in a number of experiments for the special condition of a signal presented in a correlated or in-phase masker (see Hamer *et al.*, 1983). Negative masking in audition is an artifact of the definition of the test stimulus level. It is not obtained if the stimulus is considered in terms of the increment in energy arising from the addition of the signal to the masker (and the resulting detection threshold is reported in units of energy). Negative masking cannot account for the temporal undershoot obtained in this study because (1) the signal and masker were uncorrelated for those off-frequency conditions for which we measured temporal undershoot and (2) temporal undershoot was not found for the correlated on-frequency signal condition.

5. Suppressive unmasking

Traditional two-tone suppression, which is highly dependent on the relative frequency values of the experimental stimuli, probably cannot explain our findings of temporal undershoot over an order of magnitude range of signal frequencies (Houtgast, 1972; Shannon, 1976). It is conceivable, however, that a suppressive unmasking process of the kind described by Delgutte (1990) in his Fig. 1(d) might provide an explanation for some of our observations of temporal undershoot. His physiologically based argument was that when the level of a signal is raised near quiet threshold in the presence of a simultaneous off-frequency masker the resulting neural discharge rate to the signal plus masker will first decrease. This decrement in firing rate is due to suppression of the masker activity by the signal. For this special condition, the masked detection threshold will occur at the level at

which the neural discharge rate for the signal plus the masker is lower than the discharge rate for the masker alone by some probabilistic criterion. The resulting masked detection threshold will then be lower than the threshold in quiet, and unmasking will have occurred. Thus temporal undershoot could be explained by suppression of masker activity by the off-frequency signal during the weak masking transitional periods immediately pre- and post-gating of the masker. These special conditions correspond to periods of nominal simultaneous temporal overlap between the rise/fall ramps of the signal and masker. Suppressive unmasking effects might therefore provide a plausible explanation for temporal undershoot effects for at least some of the local off-frequency signal conditions.

A set of seemingly related physiological experiments from Hill and Palmer (1991) are especially noteworthy. They described suppressivelike unmasking in single-unit discharge rate responses when a gated 200-ms suppressor tone was presented in combination with a temporally continuous probe tone of different frequency. The resulting two-tone response was characterized by brief decrements in neural discharge rate coincident with the onset and following the offset of the test (suppressor) tone. Hill and Palmer also reported generally similar onset and offset decrements in rate responses measured for excitatory test tones presented in isolation. These surprising decrement responses to single-tone stimulation, however, were usually not as well represented as those observed in their two-tone responses and the response decrements were not evident for all fibers. Hill and Palmer noted that the responses to isolated single tones never reflected evidence of suppression bands next to the response area of the auditory nerve fiber and, therefore, traditional suppression processes probably cannot explain their observations. They concluded that the appearance of transient onset suppression in the rate responses to single tones provides evidence that, under certain conditions, excitatory stimuli can exert a short-latency suppression on peripheral neural spike generation. Thus their findings provide physiological evidence of both onset and offset suppression effects in the peripheral neural rate responses to two-tone off-frequency stimuli and to single tones.

6. Dual recovery processes

Nizami and Schneider (1994) presented evidence of nonmonotonic recovery patterns from forward masking for an on-frequency probe/masker paradigm. Notable in their data was a prominent supra-threshold improvement in detection occurring 5.5 ms after the masker was gated off. The timing of this enhancement occurred for a relative signal temporal position similar to that at which we often observed temporal undershoot following masker offset. Nizami and Schneider offered a tentative explanation for the nonmonotonic forward masking recovery pattern based upon the supposition that low-threshold high-spontaneous rate fibers and high-threshold low-spontaneous rate fibers recover from auditory activation (by the masker) at different rates. They assumed the effect to be analogous to the differential threshold recovery pattern to light adaptation reported in vision for rod and cone sensory cells within the retina. This explanation might be tenable for high-level maskers, but would not likely account for the temporal undershoot that we measured for the low-level maskers in experiment 1.

C. Temporal overshoot processes

The prominent patterns of temporal overshoot measured near masker onset and offset for the off-frequency signal conditions in this study are notable because most past reports have indicated that the amount of overshoot for tonal and narrow-band maskers is greater when $fm > fs$ than when $fm \leqslant fs$ (see Wright, 1991). It is not obvious in our temporal masking functions that the amount of temporal overshoot was appreciably greater for *fs* presented either above or below the frequencies of the masker. The results for all three listeners for $fs = 2500$ Hz are generally consistent with past findings, which reveal relatively little evidence of onset temporal overshoot for on-frequency signal and masker conditions (see Wright, 1991). Also it is notable that the amount of temporal overshoot measured at masker onset for $fs = 1900$ Hz generally increased with increasing masker level (Fig. 5). Some past reports, based on different stimulus conditions, indicate that the amount of onset temporal overshoot may either asymptote or decline at higher masker levels (Bacon, 1990; Fastl, 1976; Schmidt and Zwicker, 1991; Zwicker, 1965).

The mechanisms that are responsible for these temporal overshoot phenomena are not known (Bacon and Smith, 1991; Green, 1969). Onset overshoot is usually ascribed to a composite of physiological processes, including active cochlear processes, peripheral adaptation, and central neural effects (Bacon and Takahashi, 1992; Carlyon and Sloan, 1987; Champlin and McFadden, 1989; Kimberley *et al.*, 1989; McFadden, 1989; McFadden and Champlin, 1990). Other processes also likely contribute to onset overshoot, but these are poorly understood. Processes involved in offset overshoot are even more speculative and have been attributed to backward masking produced by central auditory neural offset responses (Elliott, 1965). There is evidence that some central auditory neurons increase their firing rates near stimulus offset, and these responses may be a factor in offset overshoot (e.g., Abeles and Goldstein, 1972; Evans and Nelson, 1973; Guinan *et al.*, 1972). Bacon and Moore (1986) speculated that the onset and offset temporal overshoot patterns are probably independent effects.

A number of acoustic factors have been identified that influence the amount of temporal overshoot. These factors and their interactions are complex and depend upon the particular condition of signal and masker parameters (see review by Wright, 1991). This complexity may explain some of the very large within- and across-subject variability that characterizes reports of temporal overshoot [see Overson *et al.* (1996) and also Chatterjee and Smith (1993) in Sec. VI E]. This response variability is readily evident in multiple ways in our temporal masking data.

Patterns of temporal overshoot coincident with masker onset and offset may be universal perceptual phenomena. The effects are most widely reported for audition, but have also been measured and described for both vision (Battersby and Wagman, 1964; Crawford, 1947) and vibrotaction (Ge-

scheider *et al.*, 1989). A pattern of onset overshoot and offset undershoot (i.e., reversal nystagmus) also is evident in the vestibular ocular reflex (VOR) that is elicited in response to either constant steps of acceleration (Malcolm and Melvill Jones, 1970) or to a caloric step of force (Formby and Robinson, 2000). In the case of the VOR, the response pattern can be explained by influences from vestibular adaptation. Vibrotactile temporal masking responses mediated by nonadapting and adapting skin receptors of the hand (i.e., Pacinian and non-Pacinian units, respectively) both exhibit temporal overshoot at masker onset and offset (Gescheider *et al.*, 1989). This fact suggests that if adaptation is a factor in vibrotactile temporal overshoot, then the site of the adaptation process must be central to the nonadapting fibers. Notably, temporal undershoot was not evident in the vibrotactile masking responses mediated by either the nonadapting or adapting fibers. Undershoot may have been obscured by temporal spread of masking (as discussed above). The stimulus parameters that were used by Gescheider *et al.* (1989) in their vibrotactile temporal masking measurements, especially their relatively long rise–fall times (37 ms), may also not have been ideal for revealing undershoot effects.

D. Cognitive processes: Listener uncertainty and attentional mechanisms

Listener uncertainty has been shown to be a confounding factor contributing to apparent increases in backward and forward masking measured with acoustically similar signal and masker stimuli (e.g., Moore and Glasberg, 1982; Puleo and Pastore, 1980). We suspect that listener uncertainty was a factor obscuring both temporal overshoot and undershoot in this study, and can account for the apparent backward and forward temporal spread of masking measured on-frequency for $fs = 2500$ Hz. These time-extended masking patterns, seemingly spreading backward in time just prior to gating of the masker on and forward in time just after gating of the masker off, respectively, may not arise from a ''real'' spread of temporal masking. Instead, the elevated thresholds may be a direct consequence of the listeners' inability to discriminate between spectrally similar properties of the signal and masker near masker onset and offset. This confusion between the signal and masker properties would result in elevated masked detection thresholds that otherwise would appear indistinguishable from threshold elevation due to traditionally conceived temporal masking. In turn, either the traditional temporal masking process or increased uncertainty could have obscured evidence of temporal undershoot for $fs = 2500$ Hz.

The peculiar oscillating patterns of masked detection that we measured in experiment 2 may also be a consequence of listener uncertainty and/or attentional mechanisms. Consider that the dramatic swings in performance in Fig. 8 often became increasingly prominent as the frequencies of the signal and masker stimuli became more similar and as the signal temporal position more closely approached the masker temporal onset or neared the masker temporal offset. These fluctuating masked detection threshold patterns may reflect the listener's inability to specify precisely the fluctuating amplitude and envelope properties of the narrowband masker. The masker stimulus fluctuation may, in turn, have contributed to temporal uncertainty about when to listen—with the masker onset (or offset) cueing the listener to be attentive, but providing information too late to be useable and possibly even detrimental to subsequent processing of the signal. In this context it is tempting to consider the possibility that marked threshold improvements in the microstructure of the temporal masking functions just after masker onset and offset (i.e., the temporal undershoot) might be explained by delayed cueing effects arising from gating the masker on and off, respectively.

In the future, temporal masking experiments using supplementary stimuli to cue the onset/offset timing of the masker may help minimize some of the uncertainty associated with fluctuating narrow-band noise stimuli (see Puleo and Pastore, 1980; Moore and Glasberg, 1982). Alternative strategies for studying listener uncertainty are to present low-noise noise (Hartmann and Pumplin, 1988) and frozen noise (von Klitzing and Kohlrausch, 1994) maskers to reduce masker energy fluctuations and control signal/masker phase relations, respectively, as sources of variability.

E. Off-frequency temporal masking

It is important here to re-emphasize that, in this study, we purposely used off-frequency signals to avoid strong activation of a common neural population by on-frequency signal and masker stimulation. This appears to have been a fortuitous decision. Otherwise, we probably would not have been able to probe the diminished masker effectiveness in time and to observe undershoot. Off-frequency nonsimultaneous stimulation is unusual in behavioral temporal masking studies and is even more rarely reported in physiological investigations. Perhaps the physiological data most directly relevant to this study are those recorded from gerbils by Chatterjee and Smith (1993). They described changes in the sensitivity of the compound action potential (CAP) of the auditory nerve in response to tone burst signals superimposed at various times on a pulse-train masker. Consistent with our observations of overshoot and undershoot, Chatterjee and Smith observed both overshoot- and undershoot-like response patterns for $fs \neq fm$. They, like us, however, found little or no evidence of these effects for $fs = fm$. Chatterjee and Smith reported that the state of neural adaptation and the overlap between the signal and masker response areas influenced the summed synchronized CAP response and, in turn, determined the signal-to-noise ratio and CAP sensitivity for their specific signal and masker conditions. Their physiological findings complement our psychoacoustic results by showing that complex interactions between different stimulated neural populations, in different states of adaptation, are conducive for revealing overshoot and undershoot effects.

Also relevant to this study is the distinctive pattern of response variability reported by Chatterjee and Smith for the CAP. They observed that the CAP response standard deviation was characteristically highest at response onset and dropped precipitously thereafter with adaptation. In general, Chatterjee and Smith found that this variability was related to the mean magnitude of the CAP response. Accordingly, the overshoot effect in their data, representing diminished

CAP sensitivity at masker onset, would necessarily be expected to have an associated greater response variability. This is entirely consistent with the large behavioral response variability that we found related to the onset overshoot in the temporal masking data (see Fig. 7). It is ironic and somewhat incongruous that, on one hand, such threshold overshoot patterns seem to enhance the sharp edges of our temporal masking functions and, on the other hand, correspond to listening conditions characterized by high response variability. This is a functional conundrum inasmuch as such inconsistent performance and high response variability would be expected to contribute to an ambiguous or ''fuzzy'' temporal boundary rather than to a perceptually sharp temporal edge.

F. Practical importance

The differences in the temporal masking functions measured for signals on- and off-frequency from the masker in experiment 2 were surprising and are potentially of practical importance for audition. Our findings suggest that temporal envelope information for a gated auditory stimulus is better represented (or at least more readily observed) off-frequency from the gated stimulus than on-frequency. The implication is that to achieve faithful perceptual representation of acoustic temporal edges at stimulus onset and offset and, therefore, optimum estimates of stimulus temporal properties, the listener may rely on off-frequency rather than on-frequency temporal cues for detection. Off-frequency listening and redundancy of temporal envelope information across a wide range of auditory frequencies may also help explain the relatively normal temporal resolution and acuity abilities reported for some hearing-impaired listeners with mild-to-moderate sensorineural deficits and high-frequency audiometric impairments (e.g., Bochner *et al.*, 1988; Dreschler, 1983; Dubno and Dirks, 1990). These suppositions will be interesting to evaluate in subsequent research.

Whatever processes are responsible for the complex patterns of temporal overshoot and undershoot measured in this study, they may be very significant perceptually for offering the listener prominent temporal edge cues for stimulus onset and offset. The temporal undershoot effects are particularly intriguing because they appear to be the perceptual counterpart to threshold undershoot phenomena associated with auditory lateral inhibition/suppression processes in the frequency domain (Houtgast, 1972; Shannon, 1976). These latter effects are believed to be important perceptually for enhancing and sharpening spectral edges. The functional roles of the temporal overshoot and undershoot phenomena in temporal processing tasks will be important to establish in future studies.

ACKNOWLEDGMENTS

This research was supported by a Multi-University Research Initiative award from the Office of Naval Research to the University of Maryland. M. G. Heinz developed the stimuli used in this study and provided acoustic analyses of these stimuli, and valuable criticism of this manuscript. We thank I. J. Hirsh, P. B. Nelson, and J. C. Rutledge for their constructive comments, and C. Champlain and an anonymous reviewer for their thoughtful reviews. We also thank Springer-Verlag and Elsevier Science for permission to use Figs. 1 and 2, respectively. We also gratefully acknowledge editorial assistance from A. Hammonds and J. Liverman.

[1]Another way of describing dynamic changes in temporal masking is to estimate the slopes of the temporal masking functions at masker onset (or offset) within each time window as a function of masker component level. We obtained slope estimates by dividing each of the max–min threshold difference values at masker onset in Fig. 6 by the corresponding time difference between these max and min values within each temporal window. The largest slopes (6–7 dB/ms) were measured for the ±4-ms time window at masker onset. These slope values were appreciably larger than those for the ±20-ms time window, which were only about 1–2 dB/ms. The corresponding analysis at masker temporal offset yielded slope values that were roughly half as steep as those estimated at masker temporal onset.

[2]To obtain an estimate of the masker amplitude variability in time, the masker energy fluctuation was simulated by generating 1000 repetitions of our 200-ms, 405-Hz-wide noise masker centered at 2500 Hz. The energy within 8- (±4 ms) and 40- (±20 ms) ms rectangular temporal windows was calculated across the duration of the masker for each of the 1000 repetitions. Histograms of the power within each temporal window revealed shapes closely approximating Gaussian, with similar means, and standard deviations of 2.3 dB and 0.8 dB for the 8-ms and 40-ms windows, respectively. These simulations indicate that the average energy fluctuations of our masker stimulus cannot account for the appreciably larger fluctuations in the threshold microstructure that are evident in our temporal masking functions.

[3]In the past, mid-level compression has usually been best observed psychophysically when the signals and maskers were presented nonsimultaneously so that each stimulus was compressed independently. Compression has also been observed for simultaneous masking under conditions for which the signal and masker frequencies were different (see Moore and Oxenham, 1998). Ideally, however, to probe compression of the masker response, the signal frequency should be within about one-half octave of the primary frequency activity of the masker (von Klitzing and Kohlrausch, 1994). Otherwise, as the probe location is moved more distant from the masker frequency activity, the physiological response of the basilar membrane is expected to become more linear. Based on these considerations and the nonlinear behavior of our temporal masking functions, the 1900-Hz signal condition appears to have been appropriate for observing the mid-range compression described here for signal temporal positions presented near masker onset.

Abeles, M., and Goldstein, M. H. (**1972**). ''Responses of single units in the primary auditory cortex of the cat to tones and to tone pairs,'' Brain Res. **42**, 337–352.

Bacon, S. P. (**1990**). ''Effect of masker level on overshoot,'' J. Acoust. Soc. Am. **88**, 698–702.

Bacon, S. P., and Moore, B. C. J. (**1986**). ''Temporal effects in masking and their influence on psychophysical tuning curves,'' J. Acoust. Soc. Am. **80**, 1638–1645.

Bacon, S. P., and Smith, M. A. (**1991**). ''Spectral, intensive, and temporal factors influencing overshoot,'' Q. Exp. Psychol. **43A**, 373–399.

Bacon, S. P., and Takahashi, G. A. (**1992**). ''Overshoot in normal-hearing and hearing-impaired subjects,'' J. Acoust. Soc. Am. **91**, 2865–2871.

Bacon, S. P., and Viemeister, N. F. (**1985a**). ''Simultaneous masking by gated and continuous sinusoidal maskers,'' J. Acoust. Soc. Am. **78**, 1220–1230.

Bacon, S. P., and Viemeister, N. F. (**1985b**). ''The temporal course of simultaneous tone-on-tone masking,'' J. Acoust. Soc. Am. **78**, 1231–1235.

Bacon, S. P., Hedrick, M. S., and Grantham, D. W. (**1989**). ''Temporal effects in simultaneous pure-tone masking in subjects with high-frequency sensorineural hearing loss,'' Audiology **27**, 313–323.

Battersby, W. S., and Wagman, I. H. (**1964**). ''Light adaptation kinetics: The influence of spatial factors,'' Science **143**, 1029–1031.

Bilger, R. C., and Hirsh, I. J. (**1956**). ''Masking of tones by bands of noise,'' J. Acoust. Soc. Am. **28**, 623–630.

Bochner, J. H., Snell, K. B., and MacKenzie, D. J. (**1988**). ''Duration discrimination of speech and tonal complex stimuli by normally hearing and hearing-impaired listeners,'' J. Acoust. Soc. Am. **84**, 493–500.

Carlyon, R. P., and Sloan, E. P. (**1987**). ''The ''overshoot'' effect and sensory hearing impairment,'' J. Acoust. Soc. Am. **82**, 1078–1080.

Carlyon, R. P., and White, L. J. (**1992**). ''Effect of signal frequency and masker level on the frequency regions responsible for the overshoot effect,'' J. Acoust. Soc. Am. **38**, 738–746.
Champlin, C. A., and McFadden, D. (**1989**). ''Reductions in overshoot following intense sound exposures,'' J. Acoust. Soc. Am. **85**, 2005–2011.
Chatterjee, M., and Smith, R. L. (**1993**). ''Physiological overshoot and the compound action potential,'' Hear. Res. **69**, 45–54.
Crawford, B. H. (**1947**). ''Visual adaptation in relation to brief conditioning stimuli,'' Proc. R. Soc. London, Ser. B **134**, 283–302.
Deatherage, B. H., Bilger, R. C., and Eldredge, D. H. (**1957a**). ''Remote masking in selected frequency regions,'' J. Acoust. Soc. Am. **29**, 512–514.
Deatherage, B. H., Davis, H., and Eldredge, D. H. (**1957b**). ''Physiological evidence for the masking of low frequencies by high,'' J. Acoust. Soc. Am. **29**, 132–137.
Delgutte, B. (**1990**). ''Physiological mechanisms of psychophysical masking: Observations from auditory nerve fibers,'' J. Acoust. Soc. Am. **87**, 791–809.
Dreschler, W. A. (**1983**). ''Impaired frequency/time resolutions and its effect on speech intelligibility,'' in *Hearing—Physiological Bases and Psychophysics*, edited by R. Klinke and R. Hartmann (Springer-Verlag, New York), pp. 364–371.
Dubno, J. R., and Dirks, D. D. (**1990**). ''Associations among frequency and temporal resolution and consonant recognition for hearing-impaired listeners,'' Acta Oto-Laryngol. Suppl. **469**, 23–29.
Eggermont, J. J. (**1985**). ''Peripheral auditory adaptation and fatigue: A model oriented review,'' Hear. Res. **18**, 57–71.
Elliott, L. L. (**1965**). ''Changes in the simultaneous masked threshold of brief tones,'' J. Acoust. Soc. Am. **38**, 738–746.
Elliott, L. L. (**1969**). ''Masking of tones before, during, and after brief silent periods in noise,'' J. Acoust. Soc. Am. **45**, 1277–1279.
Evans, E. F., and Nelson, P. G. (**1973**). ''The responses of single neurones in the cochlear nucleus of the cat as a function of their location and anaesthetic state,'' Exp. Brain Res. **17**, 402–427.
Fastl, H. (**1976**). ''Temporal masking effects: I. Broadband noise masker,'' Acustica **35**, 289–302.
Formby, C., and Robinson, D. A. (**2000**). ''Measurement of vestibular ocular reflex (VOR) time constants with a caloric step stimulus,'' J. Vest. Res. (in press).
Formby, C., Ferguson, S. H., and Heinz, M. G. (**1997**). ''Auditory temporal microstructure: Evidence of under- and over-shoot at onset and offset of a narrowband noise marker measured in an off-frequency masked detection task,'' J. Acoust. Soc. Am. **102**, 3161.
Formby, C., Rutledge, J. C., and Sherlock, L. P. (**1999**). ''A model of the component processes in human auditory adaptation,'' Proceedings of the International Bekesy Centenary Conference, Budapest, Hungary: Hungarian Academy of Sciences, pp. 59–63.
Formby, C., Heinz, M. G., Ferguson, S. H., and Sherlock, L. P. (**1998a**). ''Temporal over- and under-shoot effects accentuate temporal edges at onset and offset of a narrow-band masker,'' Abstracts of the 21st Midwinter Meeting of the Association for Research in Otolaryngology, p. 172.
Formby, C., Rutledge, J. C., Heinz, M. G., Sherlock, L. P., and Aleksandrovsky, I. V. (**1998b**). ''A descriptive model of under- and over-shoot patterns in the temporal masking function of a narrowband noise,'' J. Acoust. Soc. Am. **103**, 2811(A).
Gescheider, G. A., Bolanowski, S. J., and Verrillo, R. T. (**1989**). ''Vibrotactile masking: Effects of stimulus onset asynchrony and stimulus frequency,'' J. Acoust. Soc. Am. **85**, 2059–2064.
Green, D. M. (**1969**). ''Masking with continuous and pulsed sinusoids,'' J. Acoust. Soc. Am. **46**, 939–946.
Guinan, J. J., Guinan, S. S., and Norris, B. E. (**1972**). ''Single auditory units in the superior olivary complex. I. Responses to sounds and classification based upon physiological properties,'' Int. J. Neurosci. **4**, 101–120.
Hamer, R. D., Verrillo, R. T., and Zwislocki, J. J. (**1983**). ''Tactile masking of Pacinian and non-Pacinian channels,'' J. Acoust. Soc. Am. **73**, 1293–1303.
Harris, D. M., and Dallos, P. (**1979**). ''Forward masking of auditory nerve fiber responses,'' J. Neurophysiol. **42**, 1083–1107.
Hartmann, W. M., and Pumplin, J. (**1988**). ''Noise power fluctuations and the masking of sine signals,'' J. Acoust. Soc. Am. **83**, 2277–2289.
Hill, K. G., and Palmer, A. R. (**1991**). ''Time course of rate responses to two-tone stimuli in auditory nerve fibers in the guinea pig,'' Hear. Res. **33**, 167–176.
Houtgast, T. (**1972**). ''Psychophysical evidence for lateral inhibition in hearing,'' J. Acoust. Soc. Am. **51**, 1885–1894.
Kimberley, B. P., Nelson, D. A., and Bacon, S. P. (**1989**). ''Temporal overshoot in simultaneous-masked psychophysical tuning curves from normal and hearing-impaired listeners,'' J. Acoust. Soc. Am. **85**, 1660–1665.
Leshowitz, B., and Cudahy, E. (**1972**). ''Masking with continuous and gated sinusoids,'' J. Acoust. Soc. Am. **51**, 1921–1929.
Levitt, H. (**1971**). ''Transformed up-down methods in psychoacoustics,'' J. Acoust. Soc. Am. **49**, 467–477.
Malcolm, R., and Melvill Jones, G. (**1970**). ''A quantitative study of vestibular adaptation in humans,'' Acta Oto-Laryngol. **53**, 315–325.
McFadden, D. (**1989**). ''Spectral difference in the ability of temporal gaps to reset the mechanisms underlying overshoot,'' J. Acoust. Soc. Am. **85**, 254–261.
McFadden, D., and Champlin, C. A. (**1990**). ''Reductions in overshoot during aspirin use,'' J. Acoust. Soc. Am. **87**, 2634–2642.
Miskiewicz, A., Buus, S., and Florentine, M. (**1994**). ''Auditory facilitation: Procedural or sensory effect,'' J. Acoust. Soc. Am. **96**, 1429–1434.
Moore, B. C. J. (**1989**). *Introduction to the Psychology of Hearing*, 3rd ed. (University Park Press, Baltimore).
Moore, B. C. J. (**1995**). *Perceptual Consequences of Cochlear Damage* (Oxford University Press, New York).
Moore, B. C. J., and Glasberg, B. R. (**1982**). ''Contralateral and ipsilateral cueing in forward masking,'' J. Acoust. Soc. Am. **71**, 942–945.
Moore, B. C. J., Glasberg, B. R., Plack, C. J., and Biswas, A. K. (**1988**). ''The shape of the ear's temporal window,'' J. Acoust. Soc. Am. **83**, 1102–1116.
Moore, B. C. J., and Oxenham, A. J. (**1998**). ''Psychoacoustic consequences of compression in the peripheral auditory system,'' Psychol. Rev. **105**, 108–124.
Moore, T. J., and Welsh, J. R. (**1970**). ''Forward and backward enhancement of sensitivity in the auditory system,'' J. Acoust. Soc. Am. **47**, 534–539.
Nizami, L., and Schneider, B. A. (**1994**). ''Does recovery from forward masking reflect two or more neural channels?'' J. Acoust. Soc. Am. **95**, 2943.
Osman, E., and Raab, D. (**1963**). ''Temporal masking of clicks by noise bursts,'' J. Acoust. Soc. Am. **35**, 1939–1941.
Overson, G. J., Bacon, S. P., and Webb, T. M. (**1996**). ''The effect of level and relative frequency region on the recovery of overshoot,'' J. Acoust. Soc. Am. **99**, 1059–1065.
Plack, C. J., and Moore, B. C. J. (**1990**). ''Temporal window shape as a function of frequency and level,'' J. Acoust. Soc. Am. **87**, 2178–2187.
Puleo, J. S., and Pastore, R. E. (**1980**). ''Contralateral cueing effects in backward masking,'' J. Acoust. Soc. Am. **67**, 947–951.
Relkin, E. M., and Turner, C. W. (**1988**). ''A reexamination of forward masking in the auditory nerve,'' J. Acoust. Soc. Am. **84**, 584–591.
Rubin, H. (**1960**). ''Auditory facilitation following stimulation at low intensities,'' J. Acoust. Soc. Am. **32**, 670–681.
Schmidt, S., and Zwicker, E. (**1991**). ''The effect of masker spectral asymmetry on overshoot in simultaneous masking,'' J. Acoust. Soc. Am. **61**, 1298–1300.
Shannon, R. V. (**1976**). ''Two-tone unmasking and suppression in a forward-masking situation,'' J. Acoust. Soc. Am. **59**, 1460–1470.
Shannon, R. V. (**1990**). ''Forward masking in patients with cochlear implants,'' J. Acoust. Soc. Am. **88**, 741–744.
Smith, R. L. (**1977**). ''Short-term adaptation in single auditory nerve fibers: some poststimulatory effects,'' J. Neurophysiol. **40**, 1098–1112.
Smith, R. L. (**1979**). ''Adaptation, saturation, and physiological masking in single auditory-nerve fibers,'' J. Acoust. Soc. Am. **65**, 166–178.
Smith, R. L., and Zwislocki, J. J. (**1975**). ''Short term adaptation and incremental responses of auditory nerve fibers,'' Biol. Cybern. **17**, 169–182.
Soderquist, D. R., Carstens, A. A., and Frank, G. J. H. (**1981**). ''Backward, simultaneous, and forward masking as a function of signal delay and frequency,'' J. Aud Res. **21**, 227–245.
Turner, C. W., Relkin, E. M., and Doucet, J. (**1994**). ''Psychophysical and physiological forward masking studies: probe duration and rise-time effects,'' J. Acoust. Soc. Am. **96**, 795–800.
von Klitzing, R., and Kohlrausch, A. (**1994**). ''Effect of masker level on overshoot in running- and frozen-noise maskers,'' J. Acoust. Soc. Am. **95**, 2192–2201.
Wiesenfeld, K., and Moss, F. (**1995**). ''Stochastic resonance and the benefits of noise: from ice ages to crayfish and SQUIDs,'' Nature (London) **373**, 33–36.

Wright, B. A. (**1991**). ''Contributions of stimulus bandwidth, the reference condition, and individual differences to the auditory temporal effect: Evidence for within- and across-channel mechanisms,'' Ph.D. thesis, University of Texas.

Zeng, F. G., Chatterjee, M., Fu, O. J., and Morse, R. P. (**1996**). ''Stochastic resonance in normal-hearing and implant listeners,'' Abstracts of the 19th Midwinter Research Meeting of the Association for Research in Otolaryngology, p. 105.

Zera, J., and Green, D. M. (**1993**). ''Detecting temporal onset and offset asynchrony in multicomponent complexes,'' J. Acoust. Soc. Am. **93**, 1038–1052.

Zwicker, E. (**1965**). ''Temporal effects in simultaneous masking by white noise bursts,'' J. Acoust. Soc. Am. **37**, 653–663.

Zwicker, E., and Fastl, H. (**1990**). *Psychoacoustics: Facts and Models* (Springer-Verlag, New York).

Zwislocki, J., Pirodda, E., and Rubin, H. (**1959**). ''On some poststimulatory effects at the threshold of audibility,'' J. Acoust. Soc. Am. **31**, 9–14.

Contributions of suppression and excitation to simultaneous masking: Effects of signal frequency and masker-signal frequency relation

René H. Gifford and Sid P. Bacon[a)]
Psychoacoustics Laboratory, Department of Speech and Hearing Science, P.O. Box 871908, Arizona State University, Tempe, Arizona 85287-1908

(Received 22 July 1999; revised 24 August 1999; accepted 9 December 1999)

This study investigated the contributions of suppression and excitation to simultaneous masking for a range of masker frequencies both below and above three different signal frequencies (750, 2000, and 4850 Hz). A two-stage experiment was employed. In stage I, the level of each off-frequency simultaneous masker necessary to mask a signal at 10 or 30 dB sensation level was determined. In stage II, three different forward-masking conditions were tested: (1) an on-frequency condition, in which the signals in stage I were used to mask probes of the same frequency; (2) an off-frequency condition, in which the off-frequency maskers (at the levels determined in stage I) were used to mask the probes; and (3) a combined condition, in which the on- and off-frequency maskers were combined to mask the probes. If the off-frequency maskers simultaneously masked the signal via spread of excitation in stage I, then the off-frequency and combined maskers should produce considerable forward masking in stage II. If, on the other hand, they masked via suppression, they should produce little or no forward masking. The contribution of suppression was found to increase with increasing signal frequency; it was absent at 750 Hz, but dominant at 4850 Hz. These results have implications for excitation pattern analyses and are consistent with stronger nonlinear processing at high rather than at low frequencies. © *2000 Acoustical Society of America.* [S0001-4966(00)04203-5]

PACS numbers: 43.66.Ba, 43.66.Dc, 43.66.Mk [RVS]

INTRODUCTION

There are two likely peripheral mechanisms that could account for simultaneous masking,[1] namely spread of excitation and suppression. The spread of excitation produced by the masker to the place along the basilar membrane corresponding to the signal frequency has traditionally been held as the primary explanation for masking (Wegel and Lane, 1924; Egan and Hake, 1950). Alternatively, the presence of the masker may suppress the response to the signal even when there is little or no masker excitation at the signal place (Sachs and Kiang, 1968; Pickles, 1984; Ruggero *et al.*, 1992; Pang and Guinan, 1997). Suppression has been documented at both the neural (e.g., Sachs and Kiang, 1968) and mechanical (e.g., Ruggero *et al.*, 1992) levels of the auditory system. Because of the extensive similarities between suppression observed on the basilar membrane and that in the auditory nerve, neural rate suppression is thought to have a mechanical origin in the cochlea (Ruggero *et al.*, 1992). Some researchers have hypothesized that the underlying mechanism of suppression is closely related to that of the cochlear amplifier, in that the presence of the suppressor reduces the gain provided by the outer hair cells at the signal frequency place (Cooper, 1996; Pang and Guinan, 1997).

Investigators have attempted to examine the excitatory and suppressive contributions to masking with both physiological and psychophysical experiments. Pickles (1984) conducted a physiological study examining the suppressive and excitatory roles in simultaneous masking using a psychophysical tuning curve paradigm. He varied the levels of different tonal maskers so that a fixed sinusoidal signal equal to the characteristic frequency (CF) of a single auditory neuron would be simultaneously masked. The discharge rates for the masked thresholds were then compared with the discharge rates for the thresholds in quiet. The premise was that if masking were the result of a suppressive mechanism, then the discharge rates for the masked threshold and the threshold in quiet should be equivalent. For most masker frequencies, Pickles found that the discharge rates were higher for the masked thresholds, suggesting that masking was achieved, at least partly, by a swamping of the signal with excitation.

Delgutte (1990a, 1996) also evaluated the roles of excitation and suppression in simultaneous tone-on-tone masking. Working at the level of a single auditory neuron, he measured masked thresholds for both simultaneous and nonsimultaneous masking; the nonsimultaneous-masking paradigm was similar in concept to the pulsation threshold (e.g., Houtgast, 1972), and hence those thresholds are not truly ''masked thresholds.'' Because suppression requires the simultaneous presentation of at least two stimuli (Arthur *et al.*, 1971; Houtgast, 1972, 1973, 1974), it cannot contribute to nonsimultaneous masking as the masker and signal do not temporally overlap. Thus the effects of suppression can be revealed by comparing simultaneous- and nonsimultaneous-

[a)]Author to whom correspondence should be addressed; electronic mail: spb@asu.edu

masked thresholds. Delgutte (1990a, 1996) found that when the masker frequency (f_m) was well below the signal frequency (f_s), suppressive masking was strong, and that it increased in magnitude with increasing masker level. Excitatory masking was dominant when the masker was presented at low levels and when it was closer in frequency to the signal. Consequently, Delgutte concluded that suppression and excitation are not mutually exclusive. That is, simultaneous masking is the result of both suppressive and excitatory masking with each component contributing differentially depending upon masker level and masker-signal frequency separation. Because Pickles (1984) did not include nonsimultaneous masking, it is not possible to say whether the masking he observed included a suppressive component.

Most psychophysical studies that have addressed the role of suppression in simultaneous masking have compared the amount of simultaneous masking to the amount of nonsimultaneous masking, and taken the difference between them to reflect the contribution of suppression (Vogten, 1978; Moore and Glasberg, 1981, 1982b; Moore *et al.*, 1984; Sommers and Gehr, 1998; also see Oxenham and Plack, 1998, who corrected this difference for differences between simultaneous and nonsimultaneous masking *per se*). A different approach has been employed in three studies, each of which used a similar two-stage approach. In the first stage, off-frequency simultaneous maskers were used to mask a signal with frequency f_s. In the second stage, the levels from the first stage were used in a forward-masking paradigm to estimate the amount of excitation at the place corresponding to f_s in response to either the signal alone (on-frequency), the off-frequency masker alone, or the signal and the off-frequency masker combined. If the off-frequency masker masked the signal via excitation in stage I, then the combined (or the off-frequency) masker should produce considerable forward masking, close to the amount produced by the on-frequency masker. If, on the other hand, the off-frequency masker masked the signal via suppression in stage I, then the amount of forward masking produced by the combined (or the off-frequency) masker should be negligible. Finally, if the off-frequency masker masked the signal via both suppression and excitation, then the amount of forward masking produced by the combined (or the off-frequency) masker should be less than that produced by the on-frequency masker, but greater than 0 dB.

Both Moore and Glasberg (1982b) and Weber (1983) tested a narrow frequency range (for a fixed f_s of 1 kHz) using masker-signal pairs for which f_m/f_s ranged from 0.6–1.4 (Moore and Glasberg, 1982b) or 0.6-1.2 (Weber, 1983). Neither study consistently observed suppression. Furthermore, neither found a sufficient amount of suppression to account for simultaneous masking. Thus both Moore and Glasberg (1982b) and Weber (1983) concluded that simultaneous masking was primarily the result of an excitatory mechanism.

Based on the physiological results of Delgutte (1990a, 1996), Moore and Vickers (1997) argued that simultaneous masking via suppression might be more likely observed for maskers well below f_s. They employed a signal with a frequency of 2200 Hz and a masker with a frequency of 500 or 1800 Hz. For their 500-Hz masker, they found considerable amounts of suppression, although the results suggested that simultaneous masking by the 500-Hz masker also involved excitation. For their 1800-Hz masker, simultaneous masking appeared to reflect largely excitation. Consequently, their psychophysical results were in good agreement with Delgutte's (1990a, 1996) physiological results suggesting that simultaneous masking is a combination of suppression and excitation, but that suppressive masking is more likely to occur for masker frequencies well below f_s. As Moore and Vickers (1997) pointed out, however, the interpretation of their data [as well as the data of Moore and Glasberg (1982b) and Weber (1983)] is complicated by the likely presence of confusion effects in their forward-masking paradigm (Moore, 1981; Neff, 1985). Since confusion may have existed in the on-frequency condition, the addition of the low-frequency component in the combined conditions could have provided a salient cue allowing the subject to discriminate the offset of the masker from the onset of the probe. This could have led to an overestimation of the contribution of suppression, especially with the 1800-Hz masker where the amount of suppression was greater than would have been predicted given the low-to-moderate masker levels and the small masker-signal frequency separation (Delgutte, 1990a, 1996).

It is of particular importance to define the role of suppression in simultaneous masking because, as Moore and Vickers (1997) note, several perceptual models assume that simultaneous-masking patterns and excitation patterns are equivalent. Consequently, the framework of many excitation-pattern-based models may require modification based on the contributions of suppressive masking. Although previous studies have begun to describe the contributions of suppression and excitation to simultaneous masking, a considerable number of issues remain unresolved. This study is primarily concerned with two of these. The first deals with the frequency regions over which the two types of masking contribute to simultaneous masking at a given f_s. In particular, although suppression appears to play a major role for masker frequencies well below f_s (Delgutte, 1990a, 1996; Moore and Vickers, 1997; Oxenham and Plack, 1998), and little or no role for masker frequencies relatively close to f_s (Moore and Glasberg, 1982b; Weber, 1983), little is known regarding the extent of the frequency region where the two types of masking play a role. The present study addresses this by employing the two-stage paradigm used previously by Moore and Glasberg (1982b), Weber (1983), and Moore and Vickers (1997), and by using a wide range of masker frequencies for a given f_s, including frequencies both below and above f_s.

The second issue deals with the effect of overall frequency region. Many previous psychophysical papers concerned with the contributions of excitation and suppression to simultaneous masking have concentrated on the mid frequency range using a f_s of 1000 Hz (Moore and Glasberg, 1982b; Weber, 1983) or 2200 Hz (Moore and Vickers, 1997). There is reason to suspect, however, that the contribution of suppression may be dependent upon the frequency region. Studies have shown psychophysical suppression to

TABLE I. Shown here are the masker frequencies (f_m) for each signal frequency (f_s), as well as the cutoff frequency (f_c) and spectrum levels of the low-pass noise (L_{LPN}) used to mask the CDT. For each f_s, the maskers were located at −11.77, −7.19, −4.14, −1.84, and +1.53 ERB relative to f_s. The asterisks indicate a f_m too low to mask the signal.

	Signal frequency (Hz)								
		750			2000			4850	
Subject	f_m	f_c	L_{LPN}	f_m	f_c	L_{LPN}	f_m	f_c	L_{LPN}
S1	****			400			1057		
	223			800			2114		
	398			1200	450	−7, 13	3025	1250	−4, 16
	574	400	−5, 15	1600	1250	−7, 13	3938	3076	−9, 11
	926			2400			5759		
S2	****			400			1057		
	223			800			2114		
	398			1200	450	−9, 11	3025	1250	−9, 11
	574	400	−8, 12	1600	1250	−9, 11	3938	3076	−14, 6
	926			2400			5759		
S3	****			400			1057		
	223			800			2114		
	398			1200	450	−2, 18	3025	1250	−4, 16
	574	400	−1, 19	1600	1250	−1, 19	3938	3076	−8, 12
	926			2400			5759		
S4	****			400			1057		
	223			800			2114		
	398			1200	450	−2, 18	3025	1250	−1, 19
	574	400	−8, 12	1600	1250	−3, 17	3938	3076	−5, 15
	926			2400			5759		

be negligible or absent for signal frequencies below about 750 Hz, but clearly present for signal frequencies higher than that (Shannon, 1976; Lee and Bacon, 1998; Hicks and Bacon, 1999; but compare Duifhuis, 1980). Thus the present study examined the contributions of excitatory and suppressive masking over a wide range of signal frequencies.

I. EXPERIMENT

A. Design

The experiment used two stages similar to those used previously (Moore and Glasberg, 1982b; Weber, 1983; Moore and Vickers, 1997). In stage I, simultaneous-masked thresholds were measured for signal levels of 10- and 30-dB sensation level (SL). Three signal frequencies, 750, 2000, and 4850 Hz, were each paired with five masker frequencies spaced along an equivalent rectangular bandwidth (ERB) scale (Glasberg and Moore, 1990). The largest masker-signal spacing (−11.77 ERBs) could not be tested for the 750-Hz signal as it resulted in a f_m (47 Hz) that was too low to mask the signal (and thus only four masker frequencies were paired with the 750-Hz signal). A low-pass noise was included to mask the cubic difference tone (CDT), $2f_m - f_s$, for those masker-frequency separations in which the CDT would be most likely detected. Table I lists the masker frequencies for each f_s, as well as the cutoff frequencies and levels of the low-pass noise used to mask the CDT for signal levels of 10 and 30 dB SL. The cutoff frequency (f_c) of the low-pass noise was set 50 Hz above the frequency of the CDT, except for the 750-Hz signal, in which case the f_c was set 2 Hz above the CDT. The reason for this was that the proximity of the noise to the tonal masker resulted in a particularly difficult listening situation which was eased somewhat by lowering the f_c of the noise. The presentation level of the low-pass noise was determined by assuming conservatively that the CDT was 10 dB lower than the presentation level of the signal (Smoorenburg, 1972; Moore *et al.*, 1998), and then using critical ratio data (Hawkins and Stevens, 1950) to determine the spectrum level of the noise needed to mask the CDT. The spectrum level of the noise was 20 (398-, 400-, and 1200-Hz CDT) or 25 dB (3026-Hz CDT) below the estimated level of the CDT.

Stage II involved forward masking to reveal any effects of suppression that may have contributed to the simultaneous-masked thresholds in stage I. Forward-masked thresholds were obtained for three different masker situations:

(1) On frequency: The signal from stage I was the on-frequency masker in stage II. It was presented at 10 or 30 dB SL, and used to forward mask a probe of the same frequency. This yields an estimate of excitation produced at the signal frequency place in response to the signal alone.
(2) Off frequency: The off-frequency maskers from stage I were used to mask the probe. The masker levels were those levels determined to be necessary just to mask the 10- or 30-dB-SL signal in stage I. These forward-masked thresholds yield an estimate of excitation produced at the signal frequency place in response to the masker in simultaneous masking.
(3) Combined: The combined masker was comprised of the on-frequency masker, an off-frequency masker, and, when necessary, a low-pass noise. The on-frequency masker was set to 10 or 30 dB SL, and the off-frequency masker was set to the level necessary just to mask the 10- or 30-dB-SL signal (as determined in stage I). The low-pass noise, when present, was set to the same levels as in stage I (see Table I). Thus the on-frequency component of the combined masker was present, though masked by the off-frequency component as measured in stage I.

After the completion of these two stages, forward-masked thresholds were obtained for the on-frequency masker at levels of 0, 2, 4, 6, 8, and 10 dB SL (although the 10-dB-SL condition was run in stage II, it was repeated here). These data allow a more accurate interpretation of the magnitude of suppression for conditions in which there was little or no forward masking in stage II. Thus for example, if an on-frequency masker fails to produce any forward masking for a range of levels (at 0 dB SL and above), then an absence of forward masking for a combined condition in stage II could not be interpreted as unequivocal evidence for complete suppression of the signal in stage I. On the other hand, if a 0-dB-SL on-frequency forward masker produces a few dB of masking, then even if the signal were completely suppressed in simultaneous masking (stage I), some forward masking would likely be observed in stage II.

B. Subjects

Four subjects with normal hearing, ranging in age from 21 to 25 years, participated in the experiment. All subjects had absolute thresholds below 20 dB HL (ANSI, 1989) at octave frequencies from 250–8000 Hz in the test ear. Two subjects (S2 and S3) had extensive practice on simultaneous and forward masking, having been subjects in past experiments. The other two subjects each received a total of at least 4 h of training on simultaneous and forward masking prior to data collection. Subject S1 was the first author. The other subjects were paid for their participation.

C. Apparatus and stimuli

All stimuli were generated digitally using a digital array processor (TDT AP2) and output at a sampling rate of 50 kHz. The low-pass noise was generated in the frequency domain and transformed into the time domain via an inverse Fourier transform. It had a flat passband with components ranging from 1 Hz to f_c and an infinitely steep rolloff. In the simultaneous-masking paradigm, the sinusoidal signal and low-pass noise were output through one channel of a 16-bit digital-to-analog converter (DAC), whereas the masker was output through the second channel of the DAC (TDT DD1). The output of each channel was low-pass filtered at 8 kHz (TDT FT6-2), attenuated by separate programmable attenuators (TDT PA4), ultimately added together (TDT SMB) and routed to a TDH-49 headphone via a headphone buffer (TDT HB6). In the forward-masking paradigm, all stimuli (signal, masker, low-pass noise, and probe) were output through one channel of the DAC. For both simultaneous and forward masking, the levels of the stimuli were adjusted digitally via the array processor, and calibrated using a Stanford Research Systems SR760 fast Fourier transform (FFT) spectrum analyzer

For the simultaneous-masking conditions, the signal and masker had a total duration of 220 ms, including 10-ms $\cos^2$ rise/fall times. When present, the low-pass noise was gated synchronously with the masker and signal. For the forward-masking conditions, the on- and off-frequency maskers (and low-pass noise, when present) had total durations of 220 ms, and the probe had a total duration of 20 ms (all durations include a 10-ms $\cos^2$ rise/fall time). A masker-probe delay (0-voltage points) of 5 ms was incorporated, as it has been suggested that the addition of a temporal gap between masker offset and probe onset is one of the most effective ways to avoid confusion effects (Neff, 1985).

D. Procedure

Subjects were tested in a single-walled, sound-attenuating booth situated within an acoustically treated room. An adaptive, two-interval, forced-choice paradigm was used with an adaptive rule to track 79.4% correct (Levitt, 1971). The interstimulus interval was 300 ms. The observation intervals were indicated by lights on a response box. Quiet thresholds for the 220-ms signal were measured for each f_s to determine the presentation levels in SL for each subject. Additionally, quiet thresholds for the 20-ms probe were obtained for each probe frequency, so that the amount of forward masking could be calculated for each subject. Simultaneous-masked thresholds (stage I) were measured by varying the level of the tonal masker to mask a signal fixed in level at 10 or 30 dB SL. Those masker levels were then used in stage II, where forward-masked thresholds were obtained by varying the level of the tonal probe. The maximum level for the dynamically varying stimulus (masker in stage I, and probe in stage II) was fixed at 91 dB SPL. During a run, it was permissible for the threshold track to reach the ceiling value; however, if the track attempted to go above the ceiling, that particular run was discarded. If two runs for a particular condition were discarded on this basis, it was concluded that the signal (or probe) could not be masked for that particular condition.

The tonal signal (simultaneous masking) or probe (forward masking) was presented randomly in one of two intervals. Subjects responded by pressing the button on the response box corresponding to the signal (or probe) interval. Visual feedback was provided indicating whether the response was correct or incorrect. A run consisted of ten reversals; the threshold estimate was taken as the mean of the last eight reversals. The initial step size of 5 dB was decreased to 2 dB after the second reversal. On the rare occasion that an estimate had a standard deviation greater than 5 dB, that run was discarded. All reported thresholds represent the mean of at least three estimates. If the standard deviation of the mean of those estimates was greater than 3 dB, additional runs were completed and averaged up to a maximum of six. Out of the 506 thresholds obtained, 485 of those (95.9%) had standard deviations less than 3 dB and 411 of those (81.2%) had standard deviations less than 2 dB.

The four subjects were separated into the following two groups:

(1) Subjects S1 and S2 were tested in a way so that a given f_s was chosen and all quiet, simultaneous-masked (stage I), and forward-masked (stage II) threshold estimates were obtained over at least three test sessions with only one session, lasting approximately 2 to 2 1/2 h, occurring on any given day. During any given session, masked thresholds for all masker-signal pairs (for a given f_s) would be measured in a quasirandom order with respect to f_m and level. For example, if a subject were completing stage I for the 2000-Hz signal, during a given session, at least one estimate of simultaneous-masked threshold would be measured for all five masker-signal pairs at both signal levels. Upon completion of stages I and II for a given f_s, another f_s was chosen with testing completed in the same manner as described above.

(2) Subjects S3 and S4 were tested so that for a given masker-signal pair, all threshold estimates (quiet, stage I, and stage II) were obtained within a single test session lasting approximately 2 to 2 1/2 h. This method was included to control for any day-to-day variation in quiet or simultaneous-masked thresholds in stage I, as they are used for setting the masker levels in stage II. During each test session, three estimates of quiet threshold were obtained (for both signal and probe) and averaged to

TABLE II. Shown here are quiet thresholds in dB SPL for each signal frequency. Thresholds for stage I (220-ms signal) and stage II (20-ms signal) are separated by a comma. Thresholds for subjects S3 and S4 have been averaged across test sessions (see text for details).

	Signal frequency (Hz)		
Subject	750	2000	4850
S1	15, 23	13, 20	16, 21
S2	12, 17	11, 18	11, 21
S3	20, 26	19, 24	15, 27
S4	12, 23	17, 23	20, 30

calculate signal presentation levels in dB SL for stage I, and amount of forward masking in stage II.

Quiet thresholds are reported for each subject in Table II. Because there was very little day-to-day variation in quiet thresholds for subjects S3 and S4, their thresholds in Table II are the mean of all test sessions for a given f_s. For all subjects, data were collected for a given f_s before proceeding to the next f_s. The order in which f_s was tested was quasi-random for both groups of subjects.

II. RESULTS AND DISCUSSION

A. Simultaneous masking (stage I)

Table III summarizes the simultaneous-masking results obtained in stage I. Shown for each $f_m - f_s$ pair is the masker level necessary to mask the 10- or 30-dB-SL signal. These masker levels were used to obtain forward-masked thresholds in stage II. The horizontal dashed line indicates that the signal could not be masked at the highest masker level allowed[2] (91 dB SPL).

B. Forward masking (stage II)

As explained in the methods section, data were collected differently for subjects S3 and S4 (compared to S1 and S2) in an attempt to account for day-to-day variations in quiet threshold. In particular for S3 and S4, at least three estimates of each quiet threshold (signal and probe) and on-frequency forward-masked threshold were obtained during each testing session with a given f_s. For the 750-Hz signal, because neither S3 nor S4 could achieve a masked threshold for the lowest f_m (223 Hz), testing was completed over the course of three days (corresponding to three f_m), whereas testing required five days for 2000- and 4850-Hz signals. Because there was little to no day-to-day variation in quiet and on-frequency thresholds, those values were averaged across all test sessions for presentation here.

Although stage II was completed for all four subjects, and the overall trends in the data were similar across subjects, the on-frequency forward-masked thresholds for S2 were consistently higher than those for the other subjects. In fact, her thresholds were equal to or higher than the level of the on-frequency masker at both levels. This finding is consistent with the possibility that S2's results were influenced by confusion effects (Moore, 1981; Neff, 1985). Because confusion in the on-frequency condition can lead to an overestimation of the contribution of suppression, S2's forward-masking results are shown but not included in the calculation of mean data. A detailed description of S2's data, including evidence for confusion, is in the Appendix.

The results of the forward-masking data obtained in stage II are plotted in Figs. 1–3 for signal frequencies of 750, 2000, and 4850 Hz, respectively. The amount of forward masking for the on-frequency, off-frequency, and combined maskers are shown for all four subjects as well as for the mean across subjects S1, S3, and S4. The horizontal lines represent the results for the on-frequency masker, presented at 10 (solid) or 30 (dashed) dB SL. The symbols represent the results for the off-frequency masker alone (circles) or the off-frequency masker combined with the on-frequency masker (squares); for the most part, the off-frequency and combined maskers produced comparable amounts of forward masking. The filled symbols represent the results for the 10-dB-SL condition, whereas the unfilled symbols represent the results for the 30-dB-SL condition. Finally, the vertical dotted lines indicate f_s. Occasionally, a signal could not be masked in stage I for a particular subject (see Table III). In that case, the mean represents an average across two subjects and those points are not connected to the means of three subjects in Figs. 1–3. If a masked threshold for a given condition could not be obtained by two (or all three) of the subjects, that condition was excluded from the mean results.

1. 750-Hz signal

Suppression is thought to exist when the symbols fall below the respective horizontal line. As can be seen in Fig. 1, no suppression is apparent at either level for the 750-Hz signal (except for S2, whose results are likely influenced by confusion). Rather, both the off-frequency and combined maskers consistently produce as much or more forward masking than that observed in the on-frequency condition. These results suggest that simultaneous masking at 750 Hz is mainly due to excitation. It may seem somewhat surprising that the off-frequency (and combined) masker produced more forward masking than did the on-frequency masker, given that the level of the off-frequency masker was chosen to just mask the on-frequency masker (in stage I). Thus one might expect that the excitation produced by the off-frequency and on-frequency maskers should be comparable at the signal frequency place. Similar results have been observed in experiments employing a comparable f_s (Moore and Glasberg, 1982b; Weber, 1983). This finding could be accounted for by assuming that simultaneous-masked threshold is achieved at a negative signal-to-masker ratio in terms of excitation. It is reasonable to assume, for example, that simultaneous-masked threshold was achieved when the signal resulted in a 1-dB increment in excitation relative to that produced by the masker alone. Assuming a power summation of the signal and masker excitation, this corresponds to approximately a -6 dB signal-to-masker ratio in terms of excitation. Thus greater excitation produced by the off-frequency masker at the signal frequency place (in stage I) might be expected to result in more forward masking by the off-frequency than by the on-frequency masker. Another possibility is that the greater amount of forward masking for the off-frequency and combined maskers is due to off-

frequency listening in stage I. Although off-frequency listening in simultaneous masking would result in off-frequency maskers being higher in level than necessary, this would be offset, at least somewhat, by off-frequency listening in forward masking. Thus an explanation based on off-frequency listening seems unlikely.

There is a clear tendency for the largest amount of forward masking to exist when f_m is closest to f_s on the low-frequency side. There are several possibilities that could explain this finding. One is that the CDT may not have been masked in stage I of the experiment when f_m was 574 Hz. Thus the off-frequency masker would have been raised to a level higher than needed to mask the signal, producing excessive excitation at f_s, and hence greater forward masking. This explanation was tested by increasing the level of the low-pass noise by 20 dB and then remeasuring simultaneous-masked thresholds ($f_m = 574$ Hz) for subjects S1 and S3. The thresholds were essentially unchanged, suggesting that the CDT had been sufficiently masked in stage I, and thus that the peak in the forward-masking function at 574 Hz was not due to the detection of the CDT in stage I.

A second possibility deals with the detection of temporal envelope fluctuations, or beats, between the masker and signal. Moore *et al.* (1998) suggested that beating cues can influence simultaneous masking for masker-signal separations up to 250 Hz. If beats provided a salient cue in stage I when the masker was 574 Hz, then the masker level at threshold would have been higher than necessary to mask signal excitation at the signal frequency place. This would, in turn, result in more forward masking by the 574-Hz masker in stage II. This explanation was tested by obtaining simultaneous-masked thresholds for S1 using a 50-Hz-wide noise masker centered at 574 Hz, as beats have been shown to play little or no role with noise maskers (Fletcher and Munson, 1937; Egan and Hake, 1950; Moore *et al.*, 1998). The narrow-band-noise masker produced virtually the same masked threshold as the sinusoidal masker. That is, at masked threshold, the level of the narrow-band noise (expressed as overall level) was essentially equal to the level of the tone, suggesting that the peak in the forward-masking function at 574 Hz probably cannot be attributable to the detection of beats in stage I.

A third possibility is that, although not apparent in Fig. 1, there exists some degree of suppression for maskers well below and for the one above f_s. The peak at 574 Hz, then, might reflect a complete lack of suppression for that f_m.

TABLE III. Displayed here are the masker levels in dB SPL of a simultaneous masker necessary to mask a 10- or 30-dB SL signal. A dashed horizontal line indicates that the signal could not be masked at the highest level allowed (91 dB SPL). The asterisks indicate a f_m too low to mask the signal.

	Signal frequency (Hz)					
	750		2000		4850	
Subject	f_m(Hz)	L_m	f_m(Hz)	L_m	f_m(Hz)	L_m
S1	****		400	71, 85	1057	80, 88
	223	83, ⋯	800	61, 72	2114	76, 83
	398	74, 83	1200	55, 67	3025	61, 70
	574	63, 75	1600	48, 63	3938	42, 61
	926	58, ⋯	2400	40, 71	5759	58, 83
S2	****		400	70, 81	1057	71, 82
	223	82, 86	800	66, 72	2114	67, 77
	398	63, 74	1200	62, 68	3025	42, 71
	574	56, 74	1600	48, 59	3938	42, 57
	926	43, 80	2400	52, 66	5759	39, 86
S3	****		400	88, ⋯	1057	62, 83
	223	⋯, ⋯	800	73, 80	2114	58, 77
	398	79, 87	1200	52, 66	3025	56, 71
	574	63, 75	1600	51, 64	3938	54, 61
	926	65, 87	2400	45, 84	5759	31, 53
S4	****		400	80, 89	1057	85, ⋯
	223	⋯, ⋯	800	71, 79	2114	70, 83
	398	73, 84	1200	69, 77	3025	65, 76
	574	56, 75	1600	60, 74	3938	⋯, 71
	926	82, ⋯	2400	69, ⋯	5759	50, ⋯

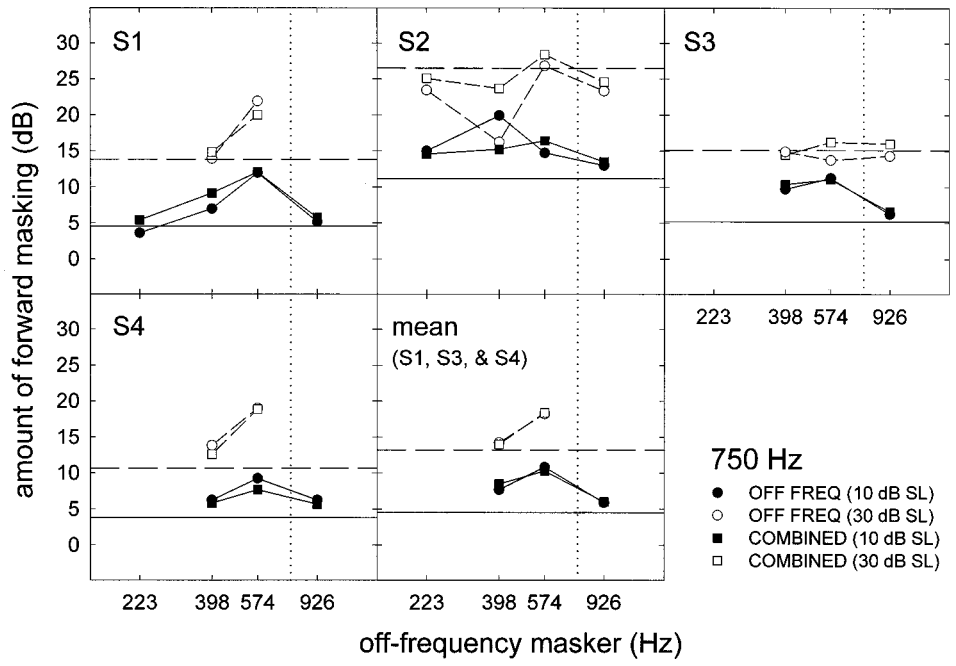

FIG. 1. Plotted here is the amount of forward masking at 750 Hz for all subjects as well as for the mean across subjects S1, S3, and S4. The horizontal lines represent the results for the on-frequency masker, presented at 10 (solid) or 30 (dashed) dB SL. The symbols represent the results for the off-frequency masker alone (circles) or the off-frequency masker combined with the on-frequency masker (squares). The filled and unfilled symbols represent the results using a masker level needed to mask a 10- or 30-dB-SL signal, respectively. The vertical dotted lines indicate f_s.

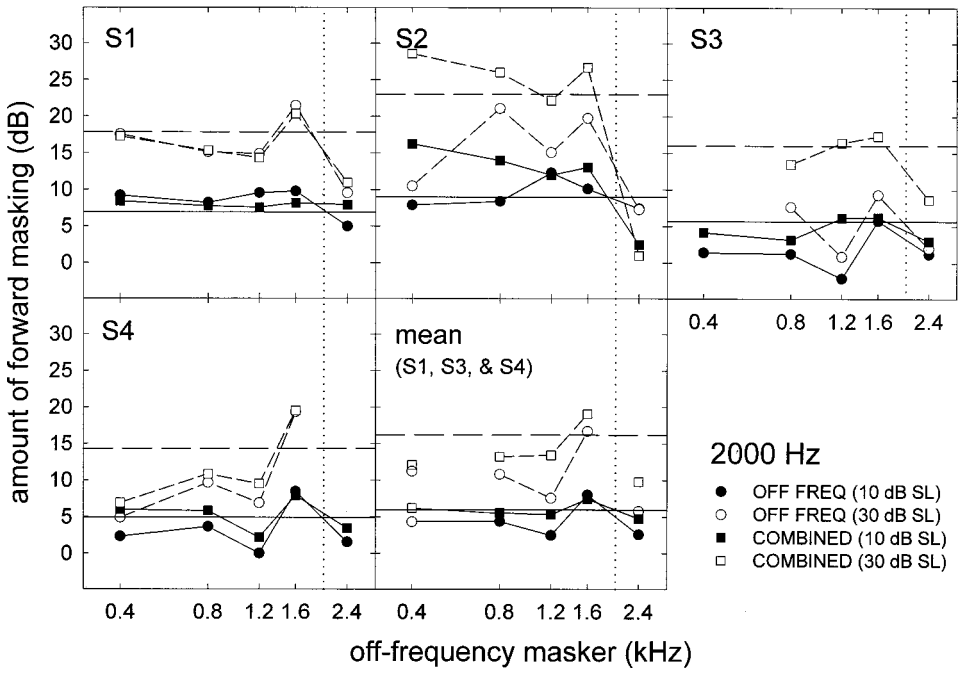

FIG. 2. As in Fig. 1, but for the 2000-Hz probe. The data points representing the mean of two subjects are not connected to those points representing the means of three subjects.

Seemingly at odds with this explanation is the fact that there is generally no evidence in Fig. 1 for suppression: the off-frequency or combined masker never produced less forward masking than did the on-frequency masker (except, again, for S2).

Finally, a fourth possibility is that spectral splatter of masker energy contributed to forward masking. Masking due to splatter would probably be most likely for maskers close to the signal on the low-frequency side. This explanation seems unlikely, however, given the relatively long (10-ms) rise/fall time, and that the same pattern of results was observed at the higher signal frequencies (see below) where splatter would be even less likely to contribute to forward masking.

2. 2000-Hz signal

Figure 2 shows the data for the 2000-Hz signal. This is the only frequency for which there was a clear and consistent difference between the amount of forward masking produced by the off-frequency and combined maskers, and it was confined to S2 and S3. At the lower level, there is evidence for small amounts of suppression, at least for subjects S3 and S4 (i.e., filled symbols typically lie somewhat below the solid horizontal line). At the higher level, all subjects show evidence of suppression (unfilled symbols fall below the dashed horizontal line), and the magnitude of suppression is generally greater than that observed at the lower level. The greatest amount of suppression generally occurred for the highest f_m. On average, off-frequency and combined maskers produced 3 dB or more forward masking, suggesting that—despite a probable influence of suppression—simultaneous masking in stage I was generally influenced by excitation. The amount of forward masking observed here with the 400-Hz masker was somewhat greater than that observed by Moore and Vickers (1997) with a 500-Hz masker (and a 2200-Hz signal), although they too suggested that excitation was involved in simultaneous masking. It is unclear why we observe generally less suppression than Moore and Vickers (1997) under comparable conditions, although it may reflect individual differences. Consistent with this is the fact that the results for S4 are similar to the results reported by Moore and Vickers (1997).

3. 4850-Hz signal

The results for the 4850-Hz signal are plotted in Fig. 3. Unlike the results for the lower frequency signals, there is evidence for significant amounts of suppression at all f_m for both masker levels. For S1 and S3, the functions are fairly flat, whereas for S2 and S4 they peak at the f_m (3938 Hz) closest to the f_s on the low-frequency side (at least at the higher level), as was generally observed with the lower frequency signals (Figs. 1 and 2). The difference here, however, is that there is evidence for suppression even at this peak. In many cases, the off-frequency or combined masker produced little or no forward masking, consistent with the possibility that simultaneous masking at 4850 Hz is due primarily to suppression.

C. Low-level, on-frequency growth of masking

If simultaneous masking were achieved completely via suppression, then one might expect that a combined (or off-frequency) masker would produce no forward masking. This assumes, however, that an on-frequency component—at simultaneous-masked threshold—would itself produce no forward masking. In other words, this assumes that an on-frequency masker at 0 dB SL produces no forward masking. To evaluate this possibility, and in general to determine how much forward masking is obtained by low-level on-frequency maskers, growth-of-masking functions were obtained for on-frequency maskers at levels from 0 to 10 dB SL. Although the 10-dB-SL condition was run in stage II (Sec. II B), it was also run here for comparison (the forward-

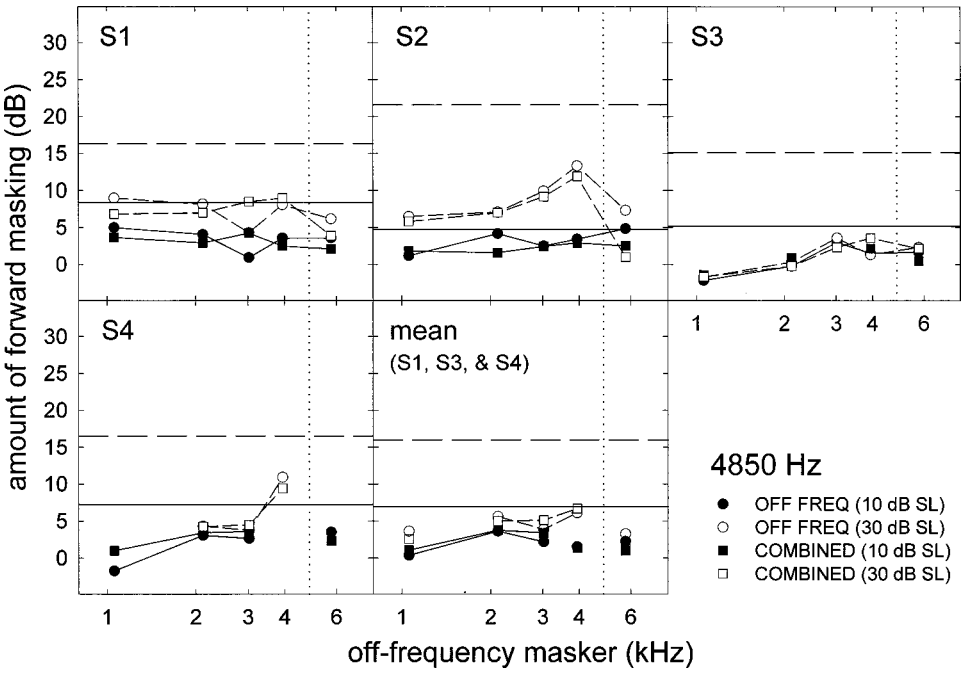

FIG. 3. As in Fig. 1, but for the 4850-Hz probe. The data points representing the mean of two subjects are not connected to those points representing the means of three subjects.

masked thresholds obtained here at 10 dB SL were approximately equal to those obtained in stage II, and thus we plotted only the threshold estimates obtained here[3]). All growth-of-masking functions were fitted with a least-squares linear regression. Although other functions may have provided better fits, the fits themselves were not of particular interest. Instead, of importance here is to determine approximately how much, if any, forward masking is produced by very low-level, on-frequency forward maskers. As was the case in Figs. 1–3, S2's results are shown but not included in the calculation of mean data, nor in the statistical analyses.

The results for the 750-Hz signal are shown in Fig. 4. The slope and r^2 values resulting from the fits are shown in each panel. The horizontal dotted line at 0 dB is provided for a visual reference. Noteworthy is that 0-dB-SL on-frequency maskers consistently produced 3–6 dB of forward masking. Straight-line regression analysis with masker level as the independent variable and amount of forward masking as the dependent variable was completed for these data. Utilizing the least-squares regression method, a t test for zero intercept was performed. This provides an indication of whether the amount of forward masking produced by a 0-dB-SL masker is significantly greater than 0 dB. Including the data from S1, S3, and S4 in the regression model, the test for zero intercept was significant for 750 Hz ($t=4.698$, $df=1$, $p=0.0002$). Thus the amount of forward masking provided by a 0-dB-SL masker is significantly greater than 0 dB.

The results for the 2000-Hz signal are shown in Fig. 5.

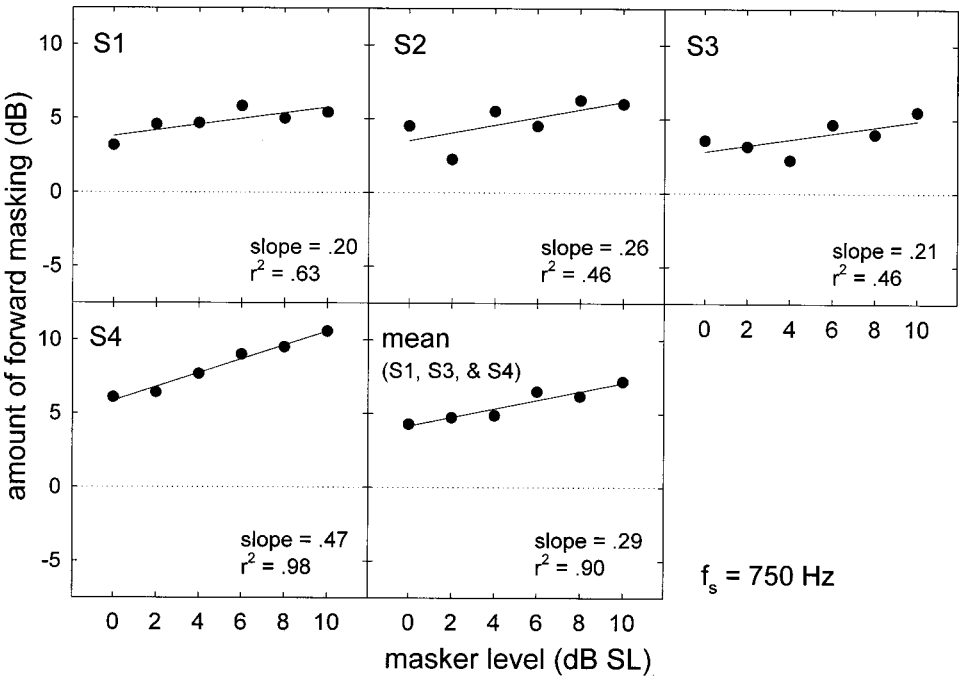

FIG. 4. Displayed here are on-frequency growth-of-masking functions at low masker levels for a masker and probe frequency of 750 Hz. The results are shown for all four subjects as well as for the mean across subjects S1, S3, and S4. The functions were fitted with a least-squares regression. Slope and r^2 values are given in each panel. The horizontal dotted line indicates 0 dB of forward masking.

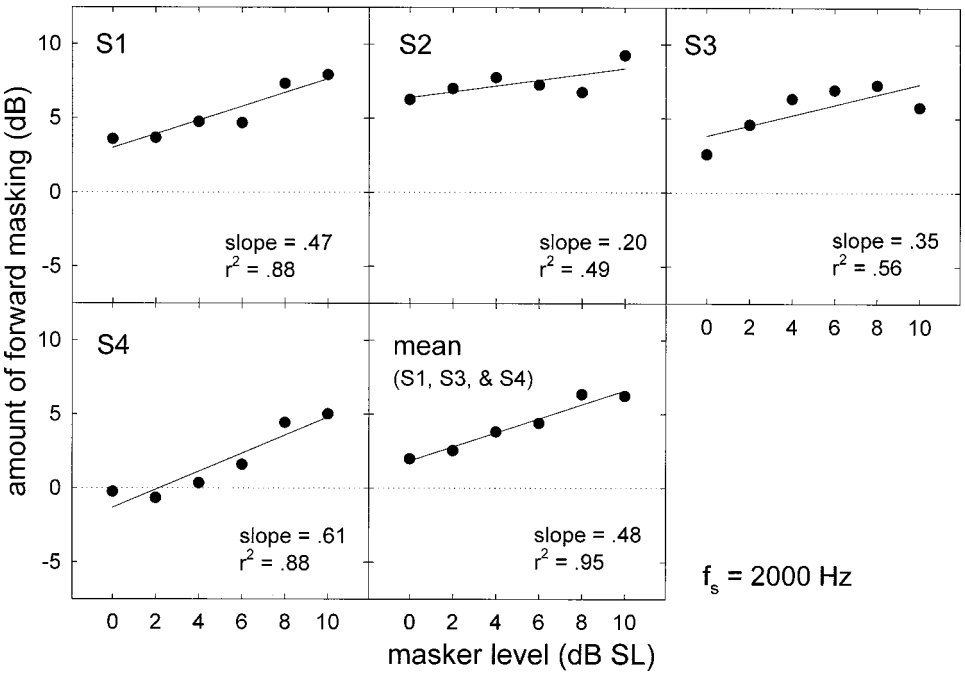

FIG. 5. As in Fig. 4, but for a 2000-Hz masker and probe.

A 0-dB-SL masker produces less masking here than for the 750-Hz signal, but nevertheless it does produce some forward masking for three subjects (S1, S2, and S3). This is similar to what Moore and Vickers (1997) observed for their 2200-Hz masker and probe. The test for zero intercept indicated that, overall, the amount of forward masking observed at 0 dB SL is not significantly greater than 0 dB ($t=2.098$, $df=1$, $p=0.0522$).

Finally, the results for the 4850-Hz signal are shown in Fig. 6. Overall, there is less forward masking here at a masker level of 0 dB SL than at the two lower frequencies. A 0-dB-SL masker does, however, produce about 2 dB of forward masking for S1 and S2, but negative amounts for S3 and S4. Overall, the test for zero intercept indicated that a 0-dB-SL masker does not produce a significant amount of forward masking ($t=-0.965$, $df=1$, $p=0.3491$).

The growth-of-masking functions in Figs. 4–6 indicate that, at least for 750 Hz, complete suppression in simultaneous masking (stage I) might not be evidenced by 0 dB of forward masking (stage II). Conversely, for 4850 Hz, 0 dB of forward masking may also not imply complete suppression in simultaneous masking; on average, masker levels from 0–4 dB SL produced almost no forward masking.

III. GENERAL DISCUSSION

The present study was concerned with two main issues. The first was the extent of the frequency region where exci-

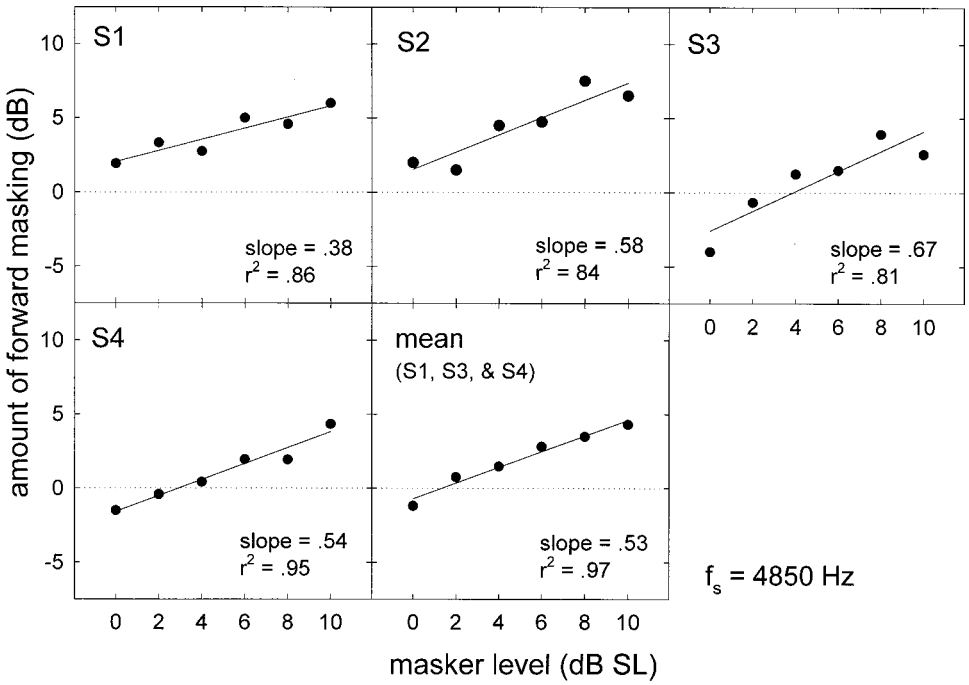

FIG. 6. As in Fig. 4, but for a 4850-Hz masker and probe.

tatory and suppressive masking contribute to simultaneous masking for a given f_s. The second was whether there is an effect of overall frequency region on the relative contributions of excitation and suppression to masking. Both issues are considered below.

A. Effect of relative masker frequency and effect of level

Previous physiological research (Delgutte, 1990a, 1996) has indicated that the contribution of suppression to simultaneous masking is maximal under conditions where f_m is well below f_s. In the present study, however, for the two signal frequencies (2000 and 4850 Hz) where suppression was apparent, there was a tendency for there to be as much or more suppression for the f_m above f_s than for any of the f_m below f_s. Moore and Glasberg (1982b) and Weber (1983) also generally observed more suppression in their psychophysical studies when $f_m > f_s$ than when $f_m < f_s$. It is worth noting, however, that neither Moore and Glasberg (1982b) nor Weber (1983) used masker frequencies well below f_s. The finding that suppression contributed to simultaneous masking in the present study when $f_m > f_s$ was not unexpected: we chose the masker-signal separation in ERBs such that $f_m/f_s \approx 1.2$, which is a nearly optimum ratio for psychophysical two-tone suppression (Houtgast, 1974; Shannon, 1976). Delgutte (1990a, 1996) did not observe suppression for conditions in which $f_m > f_s$, although he noted that one possible reason for this could be his choice of a relatively low f_m (1 kHz), given the generally small amounts of suppression for low-CF fibers (Arthur *et al.*, 1971; Harris, 1979; Fahey and Allen, 1985). Consistent with this is the finding that there is little or no psychophysical suppression at low overall frequencies (Lee and Bacon, 1998; Hicks and Bacon, 1999, present study). Thus had Delgutte used a higher f_m, he too may have observed suppression for conditions where $f_m > f_s$. This general lack of suppression at low frequencies may also account for why neither Moore and Glasberg (1982b) nor Weber (1983) observed much suppression for any $f_m - f_s$ pair tested, as both studies used a relatively low f_s (1 kHz).

The present study also found a clear tendency for suppression to be either absent (2000 Hz) or reduced (4850 Hz) when f_m was just below f_s. Consistent with this finding is that both Delgutte (1990a, 1996) and Moore and Vickers (1997) also observed less suppression when f_m was just below f_s.

In the present study, for those conditions in which suppression was observed, a greater contribution of suppression to simultaneous masking was found at the highest level tested (30 dB SL). This finding is consistent with the physiological results of Delgutte (1990a, 1996), who found that the contribution of suppression increased with increases in masker level over the range of 40–80 dB SPL. It is also consistent with the psychophysical results of Moore and Vickers (1997) and Oxenham and Plack (1998). Our results extend those of the previous studies, however, in showing that this occurs not only for conditions where $f_m < f_s$, but also for conditions where $f_m > f_s$.

B. Effect of overall frequency region

The results from the present study show a clear increase in the contribution of suppression to simultaneous masking as f_s increased from 750 to 4850 Hz. These are the first set of data (psychophysical or physiological) to address the issue of whether the contributions of excitation and suppression to simultaneous masking vary with overall frequency, and thus there are no data in the literature with which to compare. However, given that suppression reflects a cochlear nonlinearity (presumably that which results from normal outer hair cell function), these data are consistent with previous physiological findings indicating that the strength of the cochlear nonlinearity increases with frequency (Schmiedt *et al.*, 1980; Delgutte, 1990b; Cooper and Yates, 1994; Javel, 1994; Cooper and Rhode, 1995). The results are also consistent with psychophysical data showing an increase in nonlinear processing with increasing frequency (Shannon, 1976; Kidd and Feth, 1981; Rosen and Stock, 1992; Lee and Bacon, 1998; Bacon *et al.*, 1999; Hicks and Bacon, 1999).

C. Implications for the interpretation of masking patterns

Although simultaneous masking is probably rarely achieved solely via suppression (e.g., Delgutte, 1990a, 1996; Oxenham and Plack, 1998), the results from the present study show that suppression can contribute significantly to simultaneous masking, particularly at higher signal frequencies. It follows, then, that simultaneous-masked thresholds could yield an incorrect estimate of the masker's excitation along the basilar membrane. Consequently, as Moore and Vickers (1997) pointed out, perceptual models that equate simultaneous-masking patterns with excitation patterns are not completely accurate. Indeed, the framework of many excitation-pattern-based models may require modification based on the contributions of suppressive masking (Zwicker and Scharf, 1965; Zwicker and Fastl, 1990; Moore and Glasberg, 1996). The contribution of suppressive masking, however, has yet to be mapped-out in sufficient detail to allow modification of existing excitation-pattern-based models.

IV. SUMMARY

The results of the present study are consistent with the hypothesis that simultaneous masking results from both suppression and excitation, with each component contributing differentially depending upon overall frequency region and relative position of the masker. The results can be summarized as follows:

(1) Except for conditions in which f_m was closest to f_s on the low-frequency side (-1.84 ERBs), the contribution of suppression (when present) was relatively constant for the masker-signal separations -11.77, -7.19, -4.14, and $+1.53$ ERBs.
(2) Greater suppression was observed at higher levels.
(3) The contribution of suppression to simultaneous masking increased with increasing f_s over the range of 750–4850 Hz.

(4) Assuming that suppression is a product of nonlinear cochlear processing, it appears that the strength of the nonlinearity progressively increases with increasing frequency over the range of 750–4850 Hz.

ACKNOWLEDGMENTS

This research was supported by NIDCD Grant No. DC01376. We thank Dr. Li Liu and Dr. Jialong He for their assistance in programming, and Dr. Andrew Oxenham and Dr. Christopher Plack for their helpful comments on previous versions of this manuscript.

APPENDIX: PROBABLE INFLUENCE OF CONFUSION FOR S2

On-frequency forward masking is a condition for which confusion can affect the results. That is, the probe may be perceived as a continuation of the on-frequency forward masker, resulting in an artificially elevated threshold. Given that the interpretation of the present data is heavily dependent upon the amount of forward masking produced by the on-frequency maskers, any elevation due to this type of confusion in the on-frequency condition could greatly affect our conclusions. In particular, confusion would lead to an overestimation of suppression in the off-frequency or combined conditions. Neff (1985) suggested that the addition of a temporal gap between the masker offset and the probe onset is one of the most effective ways to avoid confusion effects. Hence, a 5-ms silent gap (0-voltage points) was inserted between the masker and the probe.

As mentioned in Sec. I B, S2's data were excluded from the mean as her results in the on-frequency forward-masking conditions were likely influenced by confusion. This conclusion was drawn from the results of her on-frequency forward-masked thresholds. Figure A1 displays the on-frequency forward-masked thresholds for the conditions where the masker was at 10 or 30 dB SL. The data for each individual subject are shown in a single panel for all three f_s. The filled circles represent 750 Hz, the unfilled circles represent 2000 Hz, and the inverted triangles represent 4850 Hz. The diagonal line across each panel represents a linear slope. For all subjects, thresholds for the 10-dB-SL signal are either equal to or greater than the masker level for all f_s. A similar trend was observed for the low-level on-frequency growth-of-masking functions shown in Figs. 4–6, although those data are plotted in terms of amount of masking and masker SL (quiet thresholds are given in Table I). On-frequency, forward-masked thresholds that are equal to or higher than the masker level have been associated with confusion effects (Moore, 1981; Moore and Glasberg, 1982a; Neff, 1985). However, this test for confusion is probably not valid at very low masker SLs, because the signal level generally will be higher than the masker level, given that the quiet threshold for the brief signal is usually higher than that for the longer duration masker. Thus a better test for confusion is at the higher masker level. Here the thresholds for the signal are lower than the masker level for all subjects except S2. This suggests that confusion was a problem only for S2.

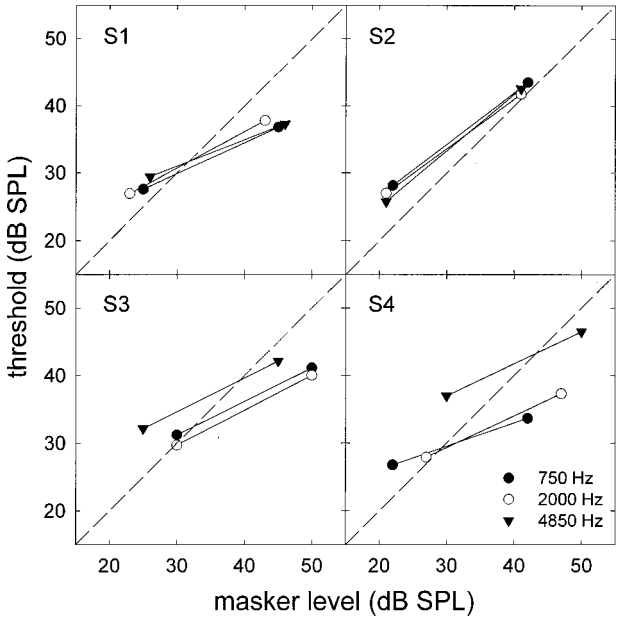

FIG. A1. Plotted here are the on-frequency forward-masked thresholds for all four subjects. The filled circles represent the 750-Hz signal, the unfilled circles represent the 2000-Hz signal, and the inverted triangles represent the 4850-Hz signal. The diagonal lines in each panel denote a slope of 1.

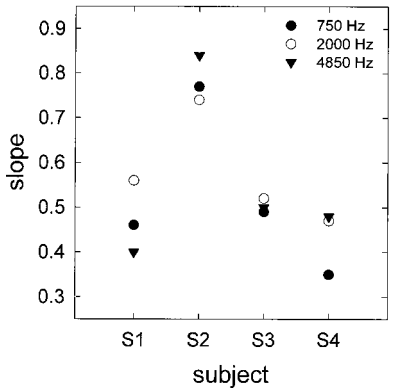

FIG. A2. Plotted here are the slope values for the straight lines drawn between the data points displayed in Fig. A1.

Further evidence that confusion was restricted to S2 comes from the slopes of the two-point masking functions in Fig. A1. Confusion is often evidenced by steep slopes, usually close to 1.0 (Neff, 1985). Slopes for the functions in Fig. A1 are shown in Fig. A2. The slope values are consistently higher for S2 than for the other three subjects for all f_s. A two-way ANOVA with subject and frequency as factors indicated a highly significant effect of subject ($F=19.90$, $df=3$, $p=0.0016$), but not of frequency ($F=0.83$, $df=2$, $p=0.4822$). An all-pairwise multiple-comparison procedure was completed using Tukey's honest significant difference method. A minimum significant difference between means of .1748 was considered to be significant at the .05 level. Subject S2 was found to be significantly different from all other subjects.

Further evidence that the other subjects probably were not affected by confusion comes from additional data collected from S1. We remeasured forward-masked thresholds in all on-frequency and one off-frequency (-4.14 ERBs f_m) condition for each f_s (30-dB-SL condition) with a 10-ms gap

between masker offset and signal onset. Additionally, the signal's duration was decreased to 10 ms, making it even less pitchlike, and hence less likely to be confused with the masker. Forward-masked thresholds were essentially identical to those obtained in stage II, suggesting that confusion had not influenced the results.

Furthermore, several researchers have found that the presence of a broadband noise gated with the masker provides a cue that helps avoid confusion effects (Moore and Glasberg, 1982a; Neff and Jesteadt, 1983; Neff, 1985). Hence, we remeasured all on-frequency forward-masked thresholds (at 30 dB SL) with the addition of an ipsilateral broadband noise (presented at a spectrum level of 0 dB SPL) that was gated synchronously with the masker. Thresholds were obtained for the 20-ms signal at a 5-ms delay and for the 10-ms signal at a 10-ms delay. The on-frequency forward-masked thresholds were essentially identical to those obtained in the main experiment, suggesting that confusion had not influenced the results obtained in stage II.

The results presented in this Appendix suggest that confusion was a problem only for S2. For this reason, S2's results were excluded from the mean results as well as the statistical analyses.

[1]Throughout, we use the term ''masking'' to refer to what might be referred to as ''energetic'' masking, as opposed to ''informational'' masking that might result from, say, signal or masker uncertainty (e.g., Neff *et al.*, 1993).

[2]This inability to mask the signal only occurred for a 30-dB-SL signal (see Table III). S4, however, could not perform the task for the 4850-Hz signal paired with the 3938-Hz masker at 10 dB SL. Several attempts were made to remeasure this threshold. S4 commented that she would ''lose'' the signal in the threshold track. This inexplicable finding was restricted to this one instance.

[3]Although masked thresholds were essentially the same, quiet thresholds for S4 for the 20-ms, 750-Hz probe were approximately 6 dB lower (17 vs 23 dB SPL) than in stage II despite the fact that thresholds in stage II represent nine estimates, and the range of those estimates was from 21 to 24 dB SPL. The reason for this change in threshold is unclear.

ANSI (**1989**). ANSI S3.6-1989, *Specifications for Audiometers* (American National Standards Institute, New York).

Arthur, R. M., Pfeiffer, R. R., and Suga, N. (**1971**). ''Properties of 'two-tone inhibition' in primary auditory neurones,'' J. Physiol. (London) **212**, 593–609.

Bacon, S. P., Boden, L. N., Lee, J., and Repovsch, J. L. (**1999**). ''Growth of simultaneous masking for $f_m < f_s$: Effects of overall frequency and level,'' J. Acoust. Soc. Am. **106**, 341–350.

Cooper, N. P. (**1996**). ''Two-tone suppression in cochlear mechanics,'' J. Acoust. Soc. Am. **99**, 3087–3098.

Cooper, N. P., and Rhode, W. S. (**1995**). ''Nonlinear mechanics at the apex of the guinea-pig cochlea,'' Hear. Res. **58**, 225–243.

Cooper, N. P., and Yates, G. K. (**1994**). ''Nonlinear input-output functions derived from the responses of guinea-pig cochlear nerve fibres: Variations with characteristic frequency,'' Hear. Res. **78**, 221–234.

Delgutte, B. (**1990a**). ''Physiological mechanisms of psychophysical masking: Observations from auditory-nerve fibers,'' J. Acoust. Soc. Am. **87**, 791–809.

Delgutte, B. (**1990b**). ''Two-tone rate suppression in auditory-nerve fibers: Dependence on suppressor frequency and level,'' Hear. Res. **49**, 225–246.

Delgutte, B. (**1996**). ''Physiological models for basic auditory percepts,'' in *Auditory Computation*, edited by H. L. Hawkins, T. A. McMullen, A. N. Popper, and R. R. Fay (Springer, New York).

Duifhuis, H. (**1980**). ''Level effects in psychophysical two-tone suppression,'' J. Acoust. Soc. Am. **67**, 914–927.

Egan, J. P., and Hake, H. W. (**1950**). ''On the masking pattern of a simple auditory stimulus,'' J. Acoust. Soc. Am. **22**, 622–630.

Fahey, P. F., and Allen, J. B. (**1985**). ''Nonlinear phenomena as observed in the ear canal and at the auditory nerve,'' J. Acoust. Soc. Am. **77**, 599–612.

Fletcher, H., and Munson, W. A. (**1937**). ''Relation between loudness and masking,'' J. Acoust. Soc. Am. **9**, 1–10.

Glasberg, B. R., and Moore, B. C. J. (**1990**). ''Derivation of auditory filter shapes from notched-noise data,'' Hear. Res. **47**, 103–138.

Harris, D. M. (**1979**). ''Action potential suppression, tuning curves and thresholds: Comparison with single fiber data,'' Hear. Res. **1**, 133–154.

Hawkins, J. E., Jr., and Stevens, S. S. (**1950**). ''The masking of pure tones and of speech by white noise,'' J. Acoust. Soc. Am. **22**, 6–13.

Hicks, M. L., and Bacon, S. P. (**1999**). ''Psychophysical measures of auditory nonlinearities as a function of frequency in individuals with normal hearing,'' J. Acoust. Soc. Am. **105**, 326–338.

Houtgast, T. (**1972**). ''Psychophysical evidence for lateral inhibition in hearing,'' J. Acoust. Soc. Am. **51**, 1885–1894.

Houtgast, T. (**1973**). ''Psychophysical experiments on 'tuning curves' and 'two-tone inhibition','' Acustica **29**, 168–179.

Houtgast, T. (**1974**). ''Lateral suppression in hearing,'' Ph.D. thesis, Free University of Amsterdam.

Javel, E. (**1994**). ''Shapes of cat auditory nerve fiber tuning curves,'' Hear. Res. **81**, 167–188.

Kidd, G., and Feth, L. L. (**1981**). ''Patterns of residual masking,'' Hear. Res. **5**, 49–67.

Lee, J., and Bacon, S. P. (**1998**). ''Psychophysical suppression as a function of signal frequency: Noise and tonal maskers,'' J. Acoust. Soc. Am. **104**, 1013–1022.

Levitt, H. (**1971**). ''Transformed up-down methods in psychoacoustics,'' J. Acoust. Soc. Am. **49**, 467–477.

Moore, B. C. J. (**1981**). ''Interactions of masker bandwidth with signal duration and delay in forward masking,'' J. Acoust. Soc. Am. **70**, 62–68.

Moore, B. C. J., Alacántara, J. I., and Dau, T. (**1998**). ''Masking patterns for sinusoidal and narrow-band noise maskers,'' J. Acoust. Soc. Am. **104**, 1023–1038.

Moore, B. C. J., and Glasberg, B. R. (**1981**). ''Auditory filter shapes derived in simultaneous and forward masking,'' J. Acoust. Soc. Am. **70**, 1001–1014.

Moore, B. C. J., and Glasberg, B. R. (**1982a**). ''Contralateral and ipsilateral cueing in forward masking,'' J. Acoust. Soc. Am. **71**, 942–945.

Moore, B. C. J., and Glasberg, B. R. (**1982b**). ''Interpreting the role of suppression in psychophysical tuning curves,'' J. Acoust. Soc. Am. **72**, 1374–1379.

Moore, B. C. J., and Glasberg, B. R. (**1996**). ''A revision of Zwicker's loudness model,'' Acust. Acta Acust. **82**, 335–345.

Moore, B. C. J., Glasberg, B. R., and Roberts, B. (**1984**). ''Refining the measurement of psychophysical tuning curves,'' J. Acoust. Soc. Am. **76**, 1057–1066.

Moore, B. C. J., and Vickers, D. V. (**1997**). ''The role of spread excitation and suppression in simultaneous masking,'' J. Acoust. Soc. Am. **102**, 2284–2290.

Neff, D. L. (**1985**). ''Stimulus parameters governing confusion effects in forward masking,'' J. Acoust. Soc. Am. **78**, 1966–1976.

Neff, D. L., Dethlefts, T. M., and Jesteadt, W. (**1993**). ''Informational masking for multicomponent maskers with spectral gaps,'' J. Acoust. Soc. Am. **94**, 3112–3126.

Neff, D. L., and Jesteadt, W. (**1983**). ''Additivity of forward masking,'' J. Acoust. Soc. Am. **74**, 1695–1701.

Oxenham, A. J., and Plack, C. J. (**1998**). ''Suppression and the upward spread of masking,'' J. Acoust. Soc. Am. **104**, 3500–3510.

Pang, X. D., and Guinan, J. J. (**1997**). ''Growth rate of simultaneous masking in cat auditory-nerve fibers: Relationship to the growth of basilar membrane motion and the origin of two-tone suppression,'' J. Acoust. Soc. Am. **102**, 3564–3575.

Pickles, J. O. (**1984**). ''Frequency threshold curves and simultaneous masking functions in single fibers of the guinea pig auditory nerve,'' Hear. Res. **14**, 245–256.

Rosen, S., and Stock, D. (**1992**). ''Auditory filter bandwidths as a function of level at low-frequencies (125 Hz–1 kHz),'' J. Acoust. Soc. Am. **92**, 773–781.

Ruggero, M. A., Robles, L., and Rich, N. C. (**1992**). ''Two-tone suppression in the basilar membrane of the cochlea: Mechanical basis of auditory nerve rate suppression,'' J. Neurophysiol. **68**, 1087–1099.

Sachs, M. B., and Kiang, N. Y. S. (**1968**). ''Two-tone inhibition in auditory nerve fibers,'' J. Acoust. Soc. Am. **43**, 1120–1128.

Schmiedt, R. A., Zwislocki, J. J., and Hamernik, R. P. (**1980**). ''Effects of

hair cell lesions on responses of cochlear nerve fibers. I. Lesions, tuning curves, two-tone inhibition, and responses to trapezoidal-wave patterns,'' J. Neurophysiol. **43**, 1367–1389.
Shannon, R. V. (**1976**). ''Two-tone unmasking and suppression in a forward masking situation,'' J. Acoust. Soc. Am. **59**, 1460–1470.
Smoorenburg, G. F. (**1972**). ''Audibility region of combination tones,'' J. Acoust. Soc. Am. **52**, 603–614.
Sommers, M. S., and Gehr, S. E. (**1998**). ''Auditory suppression and frequency selectivity in older and younger adults,'' J. Acoust. Soc. Am. **103**, 1067–1074.
Vogten, L. L. M. (**1978**). ''Low-level pure-tone masking: A comparison of 'tuning curves' obtained with simultaneous and forward masking,'' J. Acoust. Soc. Am. **63**, 1520–1527.
Weber, D. L. (**1983**). ''Do off-frequency simultaneous maskers suppress the signal?,'' J. Acoust. Soc. Am. **73**, 887–893.
Wegel, R. L., and Lane, C. E. (**1924**). ''The auditory masking of one sound by another and its probably relation to the dynamics of the inner ear.'' Phys. Rev. **23**, 266–285.
Zwicker, E., and Fastl, H. (**1990**). *Psychoacoustics—Facts and Models* (Springer-Verlag, Berlin).
Zwicker, E., and Scharf, B. (**1965**). ''A model of loudness summation,'' Psychol. Rev. **72**, 3–26.

Dichotic pitches as illusions of binaural unmasking. III. The existence region of the Fourcin pitch

John F. Culling[a)]
University Laboratory of Physiology, Parks Road, Oxford OX1 3PT, United Kingdom

(Received 19 December 1997; revised 10 August 1999; accepted 7 December 1999)

Two experiments explored the existence region of the Fourcin pitch. In each experiment, detectability was assessed by measuring listeners' ability to discriminate pitch changes. In the first experiment, the detectability of the pitch was measured as a function of the number of noises used to generate it. In the second experiment, the pitch was generated using two noises with equal and opposite interaural delays and detectability was measured as a function of the difference between these two delays, and thus of the perceived pitch height. In each case, the experimental results were compared with the predictions produced by a model of binaural unmasking, based on equalization cancellation, that had been designed to recover broadband sounds, such as speech, from interfering noise [Culling and Summerfield, J. Acoust. Soc. Am. **98**, 785–797 (1995)]. The model accurately predicted the results from experiment 1, but failed to show an adequate decline in performance for small differences in interaural delay (corresponding to higher perceived pitches) in experiment 2. A revised model, based on similar principles, but using data on listeners' sensitivity to interaural decorrelation, rather than an equalization-cancellation mechanism, was able to predict the results of both experiments successfully. © *2000 Acoustical Society of America.* [S0001-4966(00)04403-4]

PACS numbers: 43.66.Ba, 43.66.Dc, 43.66.Hg, 43.66.Pn [DWG]

INTRODUCTION

Dichotic pitches are heard when white noise is presented to the two ears under various binaural configurations. Listening to each earphone alone, the listener just hears noise, but when both earphones are used simultaneously a tone of some sort is heard standing out from the noise. Due to the tonal nature of each of these phenomena, they have been termed dichotic ''pitches,'' and have hitherto been investigated via pitch-matching experiments. However, one might more broadly describe them as dichotically evoked sounds.

Culling and co-workers (1998a, c) argued that the three most salient dichotic pitches, known as Huggins' pitch (Cramer and Huggins, 1958), the binaural edge pitch (Klein and Hartmann, 1986) and the Fourcin pitch (Fourcin, 1958, 1970) are all illusions produced by the mechanism of binaural unmasking. Durlach (1962) and Klein and Hartmann (1986) had previously invoked binaural unmasking as a mechanism for producing these pitches, but in the case of the Fourcin pitch, the suggestion was novel. As evidence for this claim, they showed that many features of each kind of pitch, both from the literature and from new experiments, could be predicted by a single model of binaural unmasking which had been designed to deal with the unmasking of complex sounds, without reference to dichotic pitches (Culling and Summerfield, 1995). The model was essentially a multichannel version of Durlach's equalization cancellation EC model (Durlach, 1960, 1962), although with the important caveate that the model should select equalization delays in each frequency channel independently. In many cases, Culling *et al.* (1998a, c) contrasted the performance of this model with the performance of competing models, based on selective direction of attention rather than on binaural unmasking (e.g., Bilsen, 1977; Raatgever, 1980; Raatgever and Bilsen, 1986) or different implementations of the EC model, which do not use different equalization delays in different frequency channels (e.g., Bilsen and Goldstein, 1974; Klein and Hartmann, 1986). In particular, Culling *et al.* (1998c) showed that the spectra which the model recovered from Fourcin-pitch stimuli corresponded to measurements of the perceived pitches which had been reported in the literature, while other models made qualitatively different predictions. A mathematical analysis showed that the model should produce the correct pitch for any configuration of two noises. Although this analysis showed that the model produces the correct pitches, it did not demonstrate that the model makes those predictions for all pitches which can be heard and for only those pitches. In other words, it did not predict the existence region of the Fourcin pitch.

The purpose of the current investigation was to extend the case developed in the earlier papers by exploring the existence region of the Fourcin pitch experimentally and comparing it with that predicted by Culling and Summerfield's modified EC (mEC) model. Notwithstanding a recent addition to the range of pitches that has been reported in Fourcin-pitch stimuli (Raatgever *et al.*, 1998), it is assumed throughout this article that the nature of the pitch which is evoked has been firmly established by others and that it is the detectability/salience of this dichotically evoked sound under different interaural configurations that most merits further investigation.

A. The Fourcin pitch

The Fourcin pitch can be demonstrated by presenting listeners with more than one (independent) broadband noise simultaneously and binaurally, over headphones. Each noise

[a)]Electronic mail: cullingj@cardiff.ac.uk

has a different interaural delay, and the differences in interaural delay between the different noises must be of the order of milliseconds. The perceived pitch is related to the difference in interaural delay between the different noises (Fourcin, 1958, 1970; Bilsen and Wesdorp, 1974; Bilsen, 1977) and decreases with increasing difference in delay. The pitch is ambiguous unless one of the two noises also has an interaural phase shift of 180°, whereupon the period of the pitch will be equal to the difference in delays. Since two or more noises are used and since they can each have different interaural delays, the Fourcin pitch has many parameters which may be varied. It was therefore necessary to constrain the current investigation to the most interesting manipulations. Those selected were (1) the number of noises employed and (2) the difference in interaural delay. These parameters were explored in experiments 1 and 2, respectively. Those aspects of the stimulus configuration which were not currently under test were always designed to make the pitch maximally clear (in the absence of empirical data on the effects of these parameters on the clarity of the pitch, assumptions were made based on the mechanism of the mEC model) and unambiguous; the delays were spaced evenly in interaural delay, with a symmetrical overall pattern (e.g., -2, 0 and $+2$ ms for 3 noises or -3, -1, $+1$, and $+3$ ms for four noises) and with alternate noises interaurally inverted. Since Fourcin (1970, p. 322) remarked that the phenomenon is most clearly heard when the pitch changes, the stimuli were also of an extended duration with continual or repeated movements in pitch, giving listeners time to pick the movements up.

Fourcin (1958, 1970) provides the only published reports of the use of more than two noises to generate the Fourcin pitch. Fourcin used up to five noises, which he spaced equally in interaural delay (e.g., -4, -2, 0, $+2$, $+4$ ms) with alternate noises inverted at one ear. Under these conditions, Fourcin observed that the clarity of the pitch did not improve with the number of noises. Experiment 1 provides the first formally presented data on this dimension of the existence region, using up to eight noises.

The extent of the existence region of the Fourcin pitch, in terms of the binaural configurations for which a pitch can or *cannot* be heard, has not been reported previously. However, various studies have shown that the pitch *can* be matched against other forms of pitch-evoking stimuli using differences in delays in the range 1–5 ms (Fourcin, 1958), 2–11 ms (Bilsen and Goldstein, 1974), and 2–9 ms (Bilsen and Wesdorp, 1974; Bilsen, 1977). Clearly the pitch exists in these regions, but the breakdown of the phenomenon outside them has not been documented. Experiment 2 seeks to explore the limits of the existence region.

B. The mEC model

Culling and Summerfield's (1995) mEC model is a modified version of Durlach's EC model. Briefly, the left- and right-channel wave forms are filtered by twin gammatone filterbanks (Patterson *et al.*, 1987, 1988) and processed by the Meddis (1986, 1988) hair-cell model. Then, corresponding frequency channels from the two sides are equalized first in level and then (so far as possible) in delay, before they are subtracted one from the other. Equalization delays of up to ± 5 ms are permitted and the best delays are selected independently in each frequency channel. The residual energy in each frequency channel is a measure of the binaural activity at that center frequency and a plot of rms residual energy as a function of center frequency forms the ''recovered spectrum''. See Culling *et al.* (1998a) for a more detailed description. The model gives a measure of the deviation in the interaural correlation from 1.0 at each frequency. Such deviations in interaural correlation are widely thought to be the percentual cues underlying binaural masking release (Gabriel and Colbum, 1981; Durlach *et al.*, 1986; Koehnke *et al.*, 1986; Jain *et al.*, 1991; Culling and Summerfield, 1995; Bernstein and Trahiotis, 1992, 1996a, b).

I. EXPERIMENT 1

Experiment 1 measured the detectability of the Fourcin pitch as a function of the number of noises used in generating the pitch, termed the ''order'' of the Fourcin pitch. Orders of 2–8 were used. Listeners were presented in each trial with an 11-pitch sequence, which traversed a wide range of frequencies in approximately half-octave steps, and were instructed to discriminate the direction of pitch movement.

A. Stimuli

To make a single Fourcin-pitch sequence, a series of Fourcin pitches were generated and then concatenated together. Each pitch was generated in the following way. Between two and eight 409.6-ms broadband noises (0–10 kHz) were generated digitally at a 20-kHz sampling rate. A copy of each of the noises was delayed, using frequency-domain filtering. The original and copy were combined into a stereo file. The left channel of every second stereo file was inverted and the files created for each noise were summed. The interaural delays were evenly spaced at intervals of the period of the desired pitch period and were symmetrically distributed about zero delay. These files could then be concatenated in both ascending and descending order of pitch, to create ascending and descending sequences with approximately half-octave steps between successive notes. After concatenation, the overall stimulus was gated with a 10-ms raised-cosine rise/decay function.

Since separately generated stimuli were directly concatenated, the transition between one pitch and the next was accompanied by a brief period (up to 5 ms) during which the noise in each channel was uncorrelated. This short period of interaural decorrelation was not noticeable in the finished stimuli and disrupted perception of the pitches less than gating the sound off and then back on between each pitch. Akeroyd and Summerfield (1999) have measured the threshold duration for the detection of burst a of decorrelation in otherwise correlated noise and found that only one of their six listeners could detect bursts of decorrelation shorter than 5 ms.

Figure 1 shows the broadband cross-correlation functions for Fourcin pitches of order 2–8, which demonstrates this arrangement. The maintenance of symmetry meant that for an odd order, one noise was at zero delay, whereas for an even order, two noises lay equally spaced on either side. In order to maintain maximal perceptual salience for an unam-

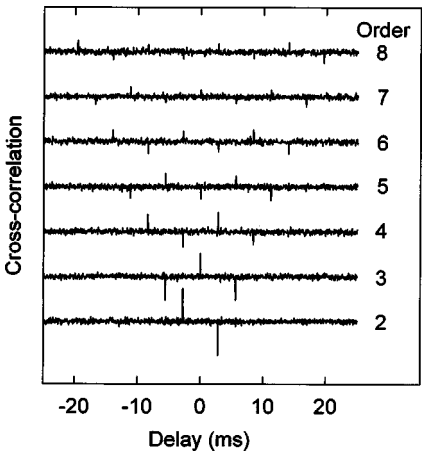

FIG. 1. Broadband cross-correlation functions for stimuli with between two and eight noises (order 2–8) in experiment 1. The interaural delays of the constituent noises are distributed at 5.6-ms intervals, corresponding to a perceived pitch of 179 Hz The cross-correlation used an exponentially tapering window with 50-ms time constant.

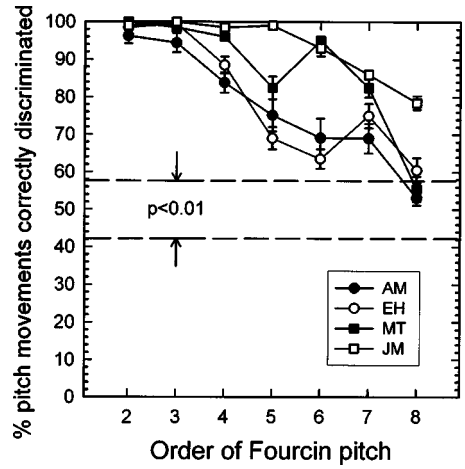

FIG. 2. Percentage of upward/downward pitch movements correctly discriminated as a function of the number of noises used to make the stimuli (the order). The data from four listeners is plotted separately with the different symbols. The error bars are standard errors of the mean for ten runs.

biguous pitch, every other noise was interaurally phase shifted by 180° (inverted). The levels of the constituent noises were adjusted so that each noise in a given stimulus was the same level and their combined power was the same for each condition. Five examples of each sequence were generated for each of the 7 conditions (orders 2–8) and, for each example, the 11 pitches were concatenated in both ascending and descending sequences. So, there were $5\times7\times2=70$ stimuli in all.

B. Procedure

Four listeners with no known hearing problems participated in experiment 1. They were trained without trial-by-trial feedback on Fourcin-pitch stimuli of the kind used in the experiment until they could discriminate ascending from descending sequences with 90% accuracy. Some listeners picked up the pitch quickly, while others were trained for many hours. Listeners were not selected for aptitude in the task. During the early stages of training, listeners were given sets of stimuli in which Fourcin pitches were interspersed with ''filler'' stimuli which were designed to sound similar, but be more perceptually salient than the Fourcin-pitch stimuli. Using these filler stimuli to assist listeners in training was found to be essential for two of the four listeners. Various filler stimuli were used, but the most effective were bases on the MPS pitch (Bilsen, 1977).

The listeners attended five 1-h sessions, during each of which they completed two experimental runs. All the stimuli were presented twice in a randomized sequence during each run, so that each run yielded a score out of 20 for each condition.

C. Results

Figure 2 shows the percentage of stimuli for which each of the four listeners correctly discriminated ascending from descending sequences as functions of the order of the Fourcin pitch. The figure also shows thresholds for statistical significance ($p<0.01$) for a single listener's data in a single condition [derived from binomial probability: 200 trials, $p(\text{correct})=0.5$]. All four listeners showed a progressive decline in discrimination accuracy with increasing order. By order 8, only two listeners performed significantly above chance ($p<0.01$).

D. Modeling

Figure 3 shows the spectra recovered by the mEC model from the stimuli used in experiment 2. The model was run on portions of the stimulus where the perceived pitch should be 179 Hz. The model correctly predicts that listeners will perceive a pitch of that frequency, but like the listeners, the model detects less evidence of a pitch as the order of the Fourcin pitch is increased. For order 2, the output of the model is well modulated, but, as the order of the pitch increases, the modulation decreases and the recovered spectrum becomes more and more ragged. For order 8 the output spectrum is virtually flat.

The most likely reason for the decline in salience is that unlike autocorrelation, the principle of superposition does

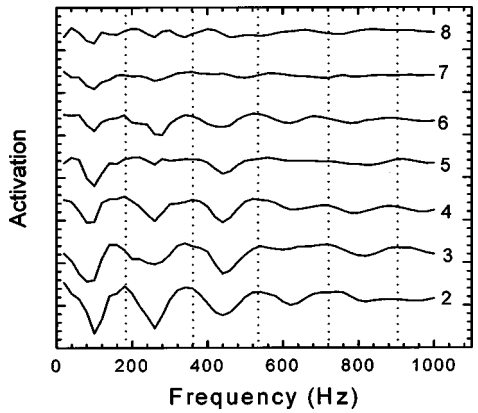

FIG. 3. Spectra recovered by the mEC model from the segment of noise whose Fourcin pitch has a perceived frequency of 179 Hz in experiment 1. Dotted vertical lines indicated the frequencies of harmonics of 179 Hz. Each spectrum is for a stimulus generated using a different number of noises (the order), indicated by the numeric labels 2–8.

not apply to the cross-correlation of finite-duration signals. That is to say that when two stimuli with different cross-correlation functions are added together, the cross-correlation of the resulting stimulus is *not* the sum of the two separate cross-correlation functions. The broadband cross-correlation functions shown in Fig. 1 show clearly that the consequence of adding extra noises with different interaural delays is that the cross-correlation (measured over a fixed interval of time) becomes weaker at the delays of the existing noises. By the time eight noises have been added, the spikes in the cross-correlation marking the delay of each individual noise are barely discernible from random fluctuations in the function. This situation contrasts with the monaural effect of echo pitch (also known as ''rippled noise'' or ''repetition pitch'') for which the addition of extra noises at regularly spaced delays increases pitch strength (e.g., Yost *et al.*, 1996).

II. EXPERIMENT 2

Experiment 2 investigated the classical existence region of the second-order Fourcin pitch, i.e., the range of pitches which can be heard. Investigating this aspect of the phenomenon was more difficult than the effect of order, since the stimulus could no longer be swept in an extensive sequence of pitches through several octaves. These pitch sequences were very helpful to listeners in enabling them to detect the pitch.

In pilot experiments, shorter sequences were employed that covered a smaller frequency range. However, even the most sensitive listeners had great difficulty detecting the pitch from such stimuli. As a result, the final design of experiment 3 included three features designed to help the listeners tune-in to the correct pitch while performing the task. First, the stimuli at each pitch frequency were presented in separate blocks, and the start of each block was preceded by a monaural repetition pitch stimulus with a pitch equal to the pitch frequency under test. Second, the Fourcin pitch stimuli in each block were interspersed with an equal number of modified multiple-phase-shift (MPS pitch) stimuli (Bilsen, 1976). These ''filler'' stimuli were designed to sound similar to, but be slightly more salient than, the Fourcin pitches. Third, the first two stimuli in a given block were always such MPS fillers.

A. Stimull

Fourcin pitches were generated in a similar manner to the second-order Fourcin-pitch stimuli from experiment 1. Each stimulus was constructed from eight 409.6-ms segments which had expected pitches 5% above and 5% below the pitch frequency under test. These segments were concatenated into sequences which either alternated through four cycles high–low–high–low... or low–high–low–high... . The stimuli were then gated with 10-ms raised-cosine onset/offset ramps. The same 11 pitches were tested as were used in Experiment 1, i.e., 31, 45, 63, 89, 125, 179, 250, 357, 500, 714 and 1000 Hz. Five examples of each stimulus were made. With 11 frequencies$\times$5 examples$\times$2 alternations, there were 110 Fourcin-pitch stimuli.

The filler stimuli were based on the MPS pitch described by Bilsen (1976). The MPS pitch is made by introducing a series of 360° interaural phase transitions at harmonic frequencies into otherwise diotic noise. In other words, it contains a harmonic series of Huggins' pitches (Cramer and Huggins, 1958). The pitch is highly salient if made with transition bandwidths which are 6% of the transition frequencies. In order to make the MPS pitches less salient they were created with 1% transition bandwidths. The narrower bandwidths reduced the strength of the pitch somewhat, but the pitch was still strong and the stimulus still differed from the Fourcin pitch perceptually; for the MPS pitch the noise is centered in the head while the pitch is either lateralized or diffuse, whereas for the Fourcin pitch, neither component of the percept is well localized. In order to diffuse the intracranial position of the noise, and also to reduce the pitch salience further, the noise was partially interaurally decorrelated: the phases of each component of the noise were offset at one ear form their original values by rectangularly distributed offsets in the range $\pm 30°$. The resulting stimuli were still easy to discriminate from Fourcin-pitch stimuli, but were sufficiently similar for the purposes of the experiment. In common with the Fourcin pitches, the resulting sounds were assembled into alternating-pitch stimuli and five examples of each stimulus were created. The cue tone which preceded each block was a single 409.6-ms monaural repetition pitch (Basset and Eastmond, 1964; Bilsen, 1966). This sound was generated by creating a 409.6-ms Gaussian noise, delaying a copy of this noise by the period of the pitch under test, and adding the delayed noise to the original. The resulting stimulus has a clear pitch with a noisy timbre.

B. Procedure

The same four listeners attended 11 1-h sessions, during each of which they completed two experimental runs. Each run was composed of 11 blocks of 20 stimuli. Each block was preceded by a single monaural-repetition-pitch cue tone. The noisy timbre of such a cue tone was thought more suitable than a pure tone as a cue for the stimuli which were to follow. The pitch used in successive blocks either ascended or descended throughout a run, except when the end of the scale had been reached whereupon the pitch jumped to the other end of the scale. The starting point varied progressively from one run to the next, so that each block would occupy each position in the sequence in different runs. For eleven runs the blocks ascended in pitch and for eleven it descended; two subjects did blocks of ascending pitch for the first eleven runs while the other two did blocks of descending pitch.

The 20 stimuli in a block were each of the 10 Fourcin-pitch stimuli (5 examples$\times$2 alternations) and each of the corresponding fillers. The listeners' task was to listen to the alternation of high and low pitch and determine whether the sequence was high–low–high–low..., or the reverse. The four cycles of alternation were important, because listeners rarely heard the entire sequence, and found the optimal strategy was to wait until they picked up the alternation and then decide whether the final sound was high or low.

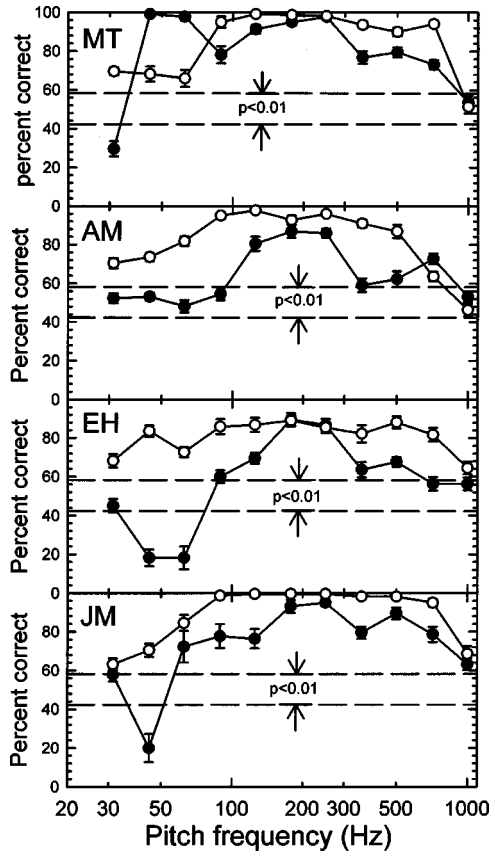

FIG. 4. Discrimination of high–low vs low–high alternation of Fourcin pitches (closed symbols) as a function of Fourcin pitch frequency for the four listeners in experiment 2. The dashed horizontal lines represent the thresholds of statistical significance ($p<0.01$) for individual data points.

C. Results

Figure 4 shows the effect of pitch frequency on listeners' ability to discriminate between high–low and low–high alternation of both the Fourcin pitch (closed symbols) and the modified MPS pitch (i.e., the fillers, open symbols). Each panel shows the results for one listener. The dotted lines show thresholds for significant deviations from chance ($p<0.01$) for each data point [from binomial probability: 220 trials, $p(\text{correct})=0.5$]. The MPS-pitch data are shown only to illustrate the fact that they were more easily discriminated than the Fourcin pitch stimuli.

Taking first the features of the Fourcin-pitch data which the listeners show in common, the pitch appears to be most salient around 125–250 Hz and is very difficult to hear for all listeners at the two extremes of the stimulus set (31 and 1000 Hz). All the listeners show a more or less monotonic decline in discrimination performance between 250 and 1000 Hz. The listeners performance at frequencies between 31 and 125 Hz is more variable. In particular, listeners MT, EH, and JM all show performance which is significantly *below* chance for one or more pitch frequencies.

D. Modeling

Figure 5 show the spectra recovered by the model for examples of the two Fourcin-pitch stimuli which were used in each condition of experiment 2. The two pitches should

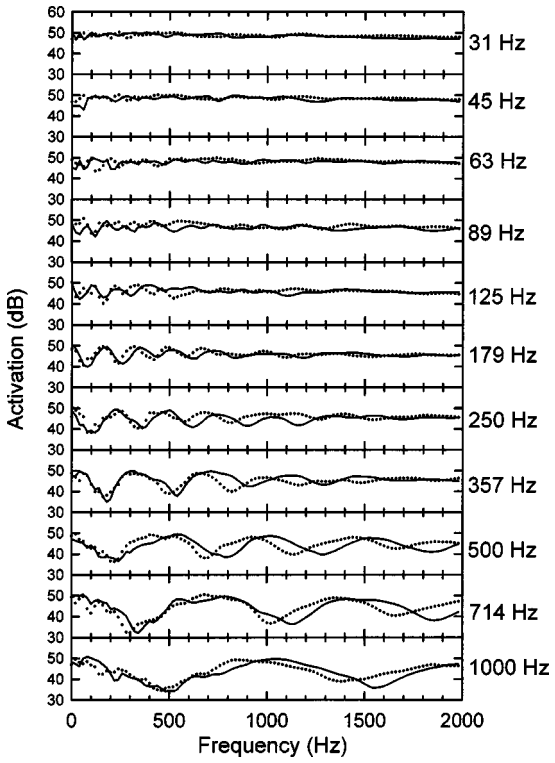

FIG. 5. Spectra recovered by the mEC model for Fourcin pitches at each pitch frequency used in experiment 2. Each panel shows the recovered spectra for the two Fourcin-pitch stimuli that listeners compared in experiment 2 for the indicated nominal pitch frequency. These stimuli had expected pitches 5% above (solid lines) and 5% below (dotted lines) the nominal pitch frequency.

differ by 10%, but listeners had difficulty detecting the direction of movement in experiment 2 when the pitch was lower than 89 Hz or higher than 357 Hz (the limits of this range varying across listeners). In order for the model to predict that the direction of a given pitch change should be discriminable, the corresponding panel of Fig. 5 should show peaks in the two curves which are displaced from each other in frequency, indicating harmonic series with different fundamental frequencies. The model recovers spectral peaks at appropriate harmonic frequencies for Fourcin pitches above about 100 Hz F_0. Unlike the listeners, no deficit in its performance is evident for pitch frequencies above 250 Hz.

III. DISCUSSION

A. The empirical existence regions

Experiment 1 shows that the Fourcin pitch becomes progressively less detectable as the number of noises used to generate it is increased (Fig. 3). Experiment 2 shows that pitches in the 125–250-Hz region (generated using interaural delays of 4–8 ms) are most easily detected, but that deviations from chance performance are displayed by the majority of listeners at all frequencies from 45 to 714 Hz. In the cases where listeners scored below chance, the most likely explanation is that the listeners were unable to hear all the harmonics of the pitch and that they picked up different harmonics during the high and low-pitch phases of the stimuli; if, for instance, decisions were based on single harmonics of different number, it is not surprising that the wrong pitch

movement was perceived. This explanation is supported by the fact that listeners reported a mismatch between the cue tones used in the conditions with low pitch frequencies and the pitches which they heard in the test stimuli. The test stimuli had much higher pitches, which were consistent with the detection of single high-numbered harmonics. Since listeners did detect evidence of the Fourcin pitch which influenced their decisions in a consistent manner, these deviations from chance may be regarded as detection of the pitch.

B. The predicted existence regions

With the exception of the decline in salience for high pitch frequencies in experiment 2, the spectra recovered by the model predicts the pattern of results displayed by the listeners in both experiments. The modulation of the model's output spectrum is affected by the order of the Fourcin pitch. The spectra become increasingly featureless as the number of noises is increased, mirroring the decline in the listeners' ability to discriminate different pitch movements in these conditions. The spectra produced by the model in response to very low pitch frequencies, where listeners have difficulty hearing the pitch, are quite flat (Fig. 5); they become better modulated at higher frequencies where listeners performance is at its best (125–250 Hz), but unlike the listeners, the model seems to work well (produce pairs of spectra with different harmonic structures) up to the highest pitch frequency used (1000 Hz). In contrast, the listeners show a gradual decline in their ability to discriminate different pitch movements at high pitch frequencies.

C. A revised model

The mismatch between model and data for high Fourcin pitches is probably attributable to the mEC model's lack of internal noise. The internal noise in Durlach's original formulation was principally intended to model the reduction in size of the binaural masking level difference with increasing frequency. The mEC model was designed for the purpose of making qualitative rather than quantitative predictions, and so does not feature internal noise as used in Durlach's original formulation of equalization cancellation. Consequently it performs too well at high frequency. Bernstein and Trahiotis (1992, 1996a, b) have recently shown that the decline in binaural masking release above 1500 Hz can be modeled by including peripheral nonlinearities which encode only the envelope of the stimulus wave form at higher frequencies. The model might be revised by adding internal noise or by changing its peripheral nonlinearities. [The existing peripheral nonlinearities, provided by the Meddis (1986, 1988) hair cell model, provide a degree of desynchronization to the carrier frequency at high frequencies, but this loss of synchrony is rather less than would be necessary for accurate predictions of binaural phenomena.] However, since contemporary models of binaural unmasking interpret binaural detection of masked sounds as resulting from the detection of interaural decorrelation of the stimulus, one can, equivalently, use empirical measurements of listeners' sensitivity to interaural decorrelation to predict their ability to detect sounds in noise and, in this case, to directly detect the interaural decorrelation which is present in dichotic-pitch stimuli.

Culling *et al.* (1998b, 2000) have collected data on listeners' sensitivity to interaural decorrelation. They measured listeners sensitivity to changes in correlation of one subband embedded within a broadband correlated noise. This sensitivity was expressed in terms of cumulative d' and a family of functions was derived which relate correlation to cumulative d' at each frequency (see the Appendix). These functions can be used to transform interaural correlations onto a perceptual salience scale. By measuring the interaural correlation of each frequency channel and calculating the cumulative d' for the difference between a correlation of 1 and each interaural correlation, ρ, $d'_{(1,\rho)}$ can be calculated. $d'_{(1,\rho)}$ represents the perceptual salience of the interaural decorrelation at that frequency, so a spectrum of values derived from different frequency channels constitutes a perceptually scaled binaurally recovered spectrum.

The revised model is similar to the mEC model in that it permits the application of delays of up to 5 ms, which are independently selected for each frequency channel. Like the mEC model, it assumes similar frequency selectivity to the monaural system (see Kohlrausch, 1988; Kollmeier and Holube, 1992). So the stimuli are still passed through a pair of gamma-tone filterbanks (Patterson *et al.*, 1987, 1988). As before, the wave forms are optimally delayed, but rather than canceling the corresponding left- and right-ear frequency channels these wave forms are correlated within an exponentially decaying window. [For the Fourcin-pitch stimuli used in experiment 2, a delay of $10^6/4f$ μs (where f is the channel center-frequency) must be applied to either the left- or right-hand channel in order to achieve maximal correlation. The side to be delayed alternates with increasing channel frequency, switching whenever f is a multiple of the pitch frequency.] The window was exponentially decaying with a 100-ms time constant. The equivalent rectangular duration of the window (also 100 ms) was thus brought into line with recent measurements of the binaural temporal window (Culling and Summerfield, 1998; Akeroyd and Summerfield, 1999). The resulting product–moment correlations can then be transformed according to the measured sensitivity of listeners to deviations in correlation from one ($d'_{(1,\rho)}$).

Figure 6 shows $d'_{(1,\rho)}$ as a function of frequency for examples of the two Fourcin-pitch stimuli which were used in each condition of experiment 2. The two pitches should differ by 10%, but listeners had difficulty detecting the direction of movement in experiment 2 when the pitch was lower than 89 Hz or higher than 357 Hz (the limits of this range varying across listeners). The d'-based model appears to make this prediction quite accurately. In order for the model to predict that the direction of a given pitch change should be discriminable, the corresponding panel of Fig. 6 should show peaks in the two curves which are displaced from each other in frequency, indicating harmonic series with different fundamental frequencies. None of these pairs of curves are identical, indicating that there may always be some audible difference between the two stimuli. However, systematic shifts in the peaks, indicating the correct differences in pitch, are only apparent for the middle range of pitch frequencies,

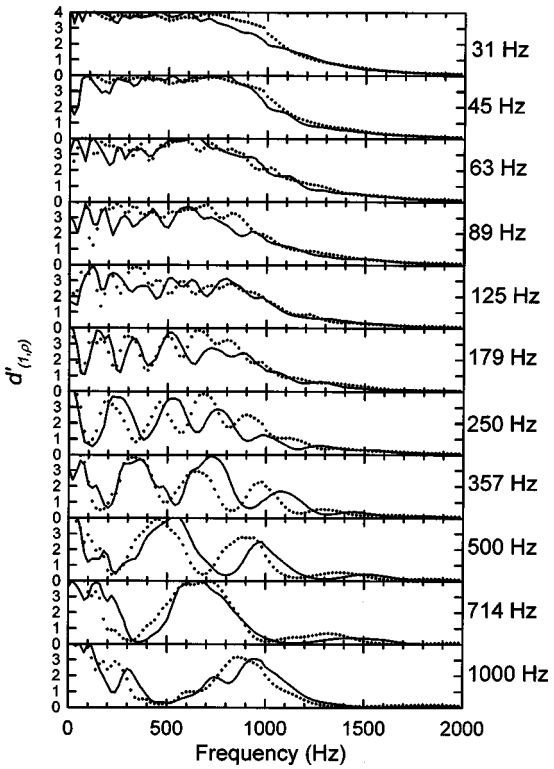

FIG. 6. As in Fig. 5, but showing perceptually scaled spectra for each Fourcin pitch in experiment 3. $d'_{(1,\rho)}$ is the expected sensitivity of listeners to the decorrelation of the stimulus within each frequency channel. The transform between ρ and $d'_{(1,\rho)}$ was taken from Culling *et al.* (2000). ρ was calculated on the corresponding frequency channels emerging from twin gammatone filterbanks (Patterson *et al.*, 1987, 1988) fed with the left- and right-hand channels of the stimuli.

where all the listeners were able to make the discrimination.

The revised model was also run on the stimuli from experiment 1 in order to check that it can still correctly predicted a decline in salience with increasing order. The results of this test are shown in Fig. 7 in identical format with Fig. 3 for easy comparison. The results are very similar in this case.

IV. CONCLUSIONS

The results of the two experiments reported here are in broad agreement with the predictions of the mEC model and are therefore consistent with the view that the Fourcin pitch is an illusion of binaural unmasking. Where disagreement between the mEC model and the data exists, a similar modeling method which incorporates measurements of the discriminability of different levels of correlation gives more accurate predictions.

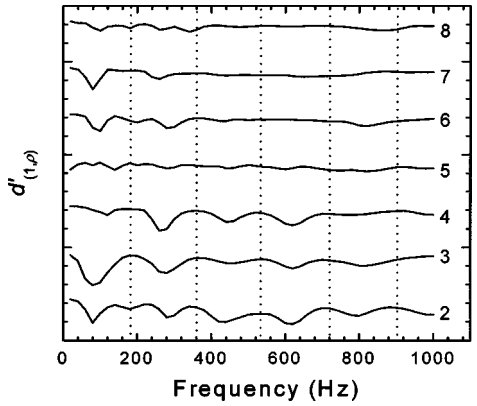

FIG. 7. As in Fig. 3, but showing perceptually scaled decorrelation spectra similar to those of Fig. 6.

ACKNOWLEDGMENTS

The author would like to thank Quentin Summerfield for comments on a previous draft of this manuscript and two anonymous reviews for their thorough and thoughtful reviews. Work supported by M.R.C.

APPENDIX

Sensitivity to interaural decorrelation has been summarized by Culling *et al.* (1998b, 2000) as follows. The growth in perceptual salience, measured using cumulative d', as a function of deviation in correlation from one, $d'_{(1,\rho)}$, can be described by

$$d'_{(1,\rho)} = e^{(k+n)} - e^{(k\rho+n)}. \tag{A1}$$

The parameters of this function varied with frequency according to the following logistic functions. The parameters of these logistic functions have been updated in line with additional data collected since Culling *et al.* (1998b).

$$k = \frac{4.68}{1+e^{0.0027(f-666)}} + 0.0027, \tag{A2}$$

$$n = \frac{3.17}{1+e^{-0.0047(f-560)}} - 2.75. \tag{A3}$$

Akeroyd, M. A., and Summerfield, Q. (**1999**). ''A binaural analog of gap detection: Gap thresholds,'' J. Acoust. Soc. Am. **105**, 2807–2820.

Basset, I. G., and Eastmond, E. J. (**1964**). ''Echolocation: Measurements of pitch versus distance for sounds reflected from a flat surface,'' J. Acoust. Soc. Am. **36**, 911–916.

Bernstein, L. R., and Trahiotis, C. (**1992**). ''Discrimination of interaural envelope correlation and its relation to binaural unmasking at high frequencies,'' J. Acoust. Soc. Am. **91**, 306–316.

Bernstein, L. R., and Trahiotis, C. (**1996a**). ''On the use of the normalized correlation as an index of interaural envelope correlation,'' J. Acoust. Soc. Am. **100**, 1754–1763.

Bernstein, L. R., and Trahiotis, C. (**1996b**). ''The normalized correlation: Accounting for binaural detection across center frequency,'' J. Acoust. Soc. Am. **100**, 306–316.

Bilsen, F. A. (**1966**). ''Repetition pitch: monaural interaction of a sound with the repetition of the same, but phase shifted sound,'' Acustica **17**, 295–300.

Bilsen, F. A. (**1976**). ''A pronounced binaural pitch phenomenon,'' J. Acoust. Soc. Am. **59**, 467–468.

Bilsen, F. A. (**1977**). ''Pitch of noise signals: Evidence for a 'central spectrum,''' J. Acoust. Soc. Am. **61**, 150–161.

Bilsen, F. A., and Goldstein, J. L. (**1974**). ''Pitch of dichotically delayed noise and its possible spectral basis,'' J. Acoust. Soc. Am. **55**, 292–296.

Bilsen, F. A., and Wesdorp, C. (**1974**). ''Dichotic pitch phenomena and their common basis,'' in *Eighth International Conference on Acoustics* (Goldcrest, London).

Cramer, E. M., and Huggins, W. H. (**1958**). ''Creation of pitch through binaural interaction,'' J. Acoust. Soc. Am. **30**, 858–866.

Culling, J. F., Colburn, H. S., and Spurchise, M. (**2000**). ''Interaural correlation sensitivity,'' unpublished.

Culling, J. F., Marshall, Q., and Summerfield, D. H. (**1998a**). ''Dichotic pitches as illusions of binaural unmasking II: The Fourcin pitch and the dichotic repetition pitch,'' J. Acoust. Soc. Am. **103**, 3527–3539.

Culling, J. F., Spurchise, M., and Colburn, H. S. (**1998b**). ''Interaural correlation sensitivity,'' J. Acoust. Soc. Am. **103**, 3081–3082.
Culling, J. F., and Summerfield, Q. (**1995**). ''Perceptual separation of competing speech sounds: Absence of across-frequency grouping by common interaural delay,'' J. Acoust. Soc. Am. **98**, 785–797.
Culling, J. F., and Summerfield, Q. (**1998**). ''Measurements of the binaural temporal window using a detection task,'' J. Acoust. Soc. Am. **103**, 3540–3553.
Culling, J. F., Summerfield, Q., and Marshall, D. H. (**1998c**). ''Dichotic pitches as illusions of binaural unmasking II: The Fourcin pitch and the dichotic repetition pitch,'' J. Acoust. Soc. Am. **103**, 3509–3526.
Durlach, N. I. (**1960**). ''Note on the equalization-cancellation theory of binaural masking level differences,'' J. Acoust. Soc. Am. **32**, 1075–1076.
Durlach, N. I. (**1962**). ''Binaural signal detection: Equalization and cancellation theory,'' J. V. Tobias (Ed.), *Foundations of Modern Auditory Theory*, Vol. II (Academic, New York).
Durlach, N. I., Gabriel, K. J., Colburn, H. S., and Trahiotis, C. (**1986**). ''Interaural correlation discrimination II: Relation to binaural unmasking,'' J. Acoust. Soc. Am. **79**, 1548–1557.
Fourcin, A. J. (**1958**). ''Speech perception and bandwidth compression,'' Signals Research and Development Establishment Report No. 1126.
Fourcin, A. J. (**1970**). ''Central pitch and auditory lateralization,'' R. Plomp and G. F. Smoorenburg (Eds.), *Frequency Analysis and Periodicity Detection in Hearing* (Sijthoff, The Netherlands).
Gabriel, K. J., and Colburn, H. S. (**1981**). ''Interaural correlation discrimination I: Bandwidth and level dependence,'' J. Acoust. Soc. Am. **69**, 1394–1401.
Jain, M., Gallagher, D. T., Koehnke, J., and Colburn, H. S. (**1991**). ''Fringed correlation discrimination and binaural detection,'' J. Acoust. Soc. Am. **90**, 1918–1926.
Klein, M. A., and Hartmann, W. M. (**1986**). ''Binaural edge pitch,'' J. Acoust. Soc. Am. **70**, 51–61.
Koehnke, J., Colburn, H. S., and Durlach, N. I. (**1986**). ''Performance in several binaural-interaction experiments,'' J. Acoust. Soc. Am. **79**, 1558–1562.
Kohlrausch, A. (**1988**). ''Auditory filter shape derived from binaural masking experiments,'' J. Acoust. Soc. Am. **84**, 573–583.
Kollmeier, B., and Holube, I. (**1992**). ''Auditory filter bandwidths in binaural and monaural listening conditions,'' J. Acoust. Soc. Am. **92**, 1889–1901.
Meddis, R. (**1986**). ''Simulation of mechanical to neural transduction in the auditory receptor,'' J. Acoust. Soc. Am. **79**, 702–711.
Meddis, R. (**1988**). ''Simulation of auditory-neural transduction: Further studies,'' J. Acoust. Soc. Am. **83**, 1056–1063.
Patterson, R. D., Nimmo-Smith, I., Holdsworth, J., and Rice, P. (**1987**). ''An efficient auditory filterbank based on the gammatone function,'' paper presented to the IOC speech group on auditory modeling at the Royal Signal Research Establishment, 14–15 December.
Patterson, R. D., Nimmo-Smith, I., Holdsworth, J., and Rice, P. (**1988**). ''Spiral vos final report, Part A: The auditory filter bank,'' Cambridge Electronic Design, Contract Report No. (APU 2341).
Raatgever, J. (**1980**). ''On the binaural processing of stimuli with different interaural phase relations,'' doctoral dissertation, Delft University.
Raatgever, J., and Bilsen, F. A. (**1986**). ''A central theory of binaural processing: Evidence from dichotic pitch,'' J. Acoust. Soc. Am. **80**, 429–441.
Raatgever, J., Bilsen, F. A., and Mungra, R. (**1998**). ''New experiments beyond the traditional Fourcin pitch range,'' J. Acoust. Soc. Am. **103**, 2767 (A).
Yost, W. A., Patterson, R., and Sheft, S. (**1996**). ''A time domain description for the pitch strength of iterated rippled noise,'' J. Acoust. Soc. Am. **99**, 1066–1078.

Auditory thresholds in a sound-producing electric fish (*Pollimyrus*): Behavioral measurements of sensitivity to tones and click trains

Peter Marvit[a] and John D. Crawford[b]
Department of Psychology, 3815 Walnut Street, Philadelphia, Pennsylvania 19104

(Received 23 September 1999; accepted for publication 11 January 2000)

In this report we present the first behavioral measurements of auditory sensitivity for *Pollimyrus adspersus*. *Pollimyrus* is an electric fish (*Mormyridae*) that uses both electric and acoustic signals for communication. Tone detection was assessed from the fish's electric organ discharge rate. Suprathreshold tones usually evoked an accelerated rate in naïve animals. This response (rate modulation $\geqslant$25%) was maintained in a classical conditioning paradigm by presenting a weak electric current near the offset of 3.5-s tone bursts. An adaptive staircase procedure was used to find detection thresholds at frequencies between 100 and 1700 Hz. The mean audiogram from six individuals revealed high sensitivity in the 200–900 Hz range, with the best thresholds near 500 Hz (66.5±4.2 SE dB *re*: 1 μPa). Sensitivity declined slowly (about 20 dB/octave) above and below this sensitivity maximum. Sensitivity fell off rapidly above 1 kHz (about 60 dB/octave) and no responses were observed at 5 kHz. This behavioral sensitivity matched closely the spectral content of the sounds that this species produced during courtship. Experiments with click trains showed that sensitivity (about 83-dB peak) was independent of inter-click-interval, within the 10–100 ms range.
 [S0001-4966(00)03704-8]

PACS numbers: 43.66.Gf, 43.80.Lb [WA]

INTRODUCTION

The African weakly electric fish (*Mormyridae: Pollimyrus spp*) produce elaborate communication sounds and also possess specializations of the auditory periphery for sound pressure detection (Crawford *et al.*, 1986). A tympanic gas bubble that is coupled to the sensory epithelium of the sacculus mediates sound pressure detection (Stipetic, 1939; Werns and Howland, 1976; Fletcher *et al.*, 2000). Previous studies have focused on the information-bearing characteristics of the communication sounds (Crawford *et al.*, 1986, 1997a) and the auditory neurophysiology of these sonic fish (Crawford, 1993, 1997a; Kozloski and Crawford, 1998). In this report, we present the first behavioral measurements of auditory sensitivity for *Pollimyrus*.

Pollimyrus produce a rich repertoire of sounds during social behavior (Crawford *et al.*, 1986; Bratton and Kramer, 1989). Males produce a succession of grunts and moans while courting females. Grunts are acoustic click trains (duration ≈250 ms) with an inter-click-interval of 18 ms, and are produced in alternation with moans (duration ≈800 ms). The moans are tonal with sharp spectral peaks at 240 and 480 Hz (Crawford *et al.*, 1997b). Thus these sounds can be approximated by sine tones or click trains—the stimuli we used here to measure detection thresholds.

In addition to producing sounds, *Pollimyrus* emit weak electric discharges (EODs) (typically 6–20 EOD/s at rest). EODs function in communication and orientation (Moller, 1995). The rate of EOD generation is modulated in response to a variety of sensory stimuli. During natural encounters with conspecifics, particular EOD temporal patterns (*social displays*) are produced in a context dependent fashion (Crawford, 1991; Moller, 1995). In addition, novel stimuli often result in an EOD suppression or acceleration (*novelty responses*). EOD modulations can be elicited by light (Moller, 1995; Ciali *et al.*, 1997), and sound (Kramer *et al.*, 1981), and have been used previously as conditioned responses in behavioral studies (Mandriota *et al.*, 1965, 1968; Ciali *et al.*, 1997).

In our experiments on *Pollimyrus*, we used a classically conditioned change in EOD rate as the behavioral assay for sound detection. We determined auditory sensitivity as a function of tone frequency and the inter-click-interval (ICI) of click trains, examined hearing in relation to the fishes' own natural sounds, and related the results to studies of auditory neural computation in this species. A preliminary account of this work has been presented previously (Marvit and Crawford, 1999).

I. METHODS

A. Animals

Pollimyrus adspersus were collected from the Niger River Basin in Nigeria, imported to the United States, and housed in laboratory aquaria at 26 °C. This study is based on ten adults (five male, standard length 63–80 mm, mean =73.2 mm, std=6.6; five female, standard length 56–84 mm, mean=67.0 mm, std=10.9). The animals were not breeding at the time of experiment. A total of 24 individuals were screened for consistent behavioral responses; animals that did not achieve, or retain, criterion performance (at least 75% correct) during training sessions were excluded.

[a]Electronic mail: marvit@psych.upenn.edu
[b]Electronic mail: crawford@psych.upenn.edu

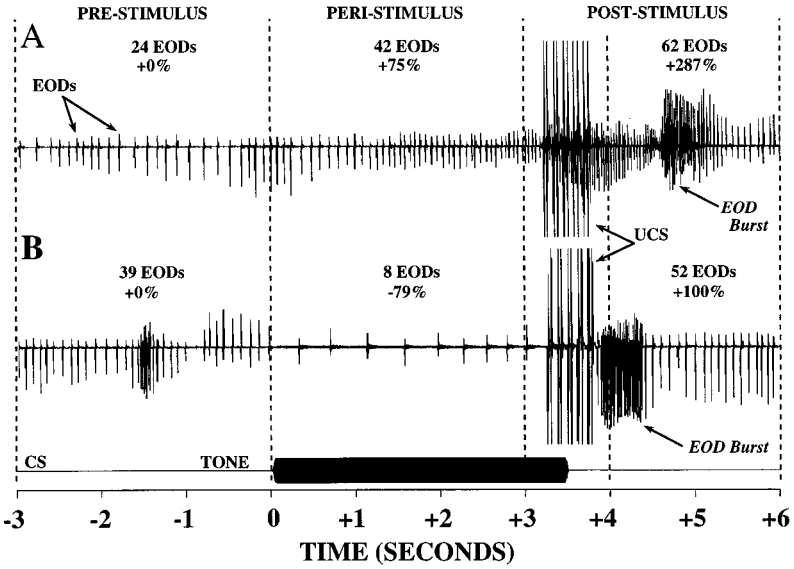

FIG. 1. The fish illustrated on top (a) accelerated its EOD rate in response to the tone, and the fish on the bottom decelerated in response to the tone. For each of the three periods (pre, peri, and post), the number of EODs produced is shown, and the percent change in rate (EOD/s) relative to the pre-stimulus period is shown. For the post-stimulus period, EODs were counted for only 2 s after the UCS.

B. Experimental tank

We used an experimental apparatus for underwater acoustic preparation that has been successfully employed in a number of previous studies of hearing in fish in other laboratories (e.g., Fay, 1989; Lu and Fay, 1993), and in our own for auditory neurophysiology (Crawford, 1993, 1997a; Kozloski and Crawford, 1998). Thus the acoustic environment of the current study facilitates comparison with previous behavioral and physiological investigations.

The fish were confined to a cylindrical holder centered 25 mm below the water surface in an acoustic tank. Each acoustic tank was located inside a sound attenuated chamber (IAC or Acoustic Systems). The water was kept at 26 °C ($\pm 1.5°$) and approximately 200-μS/cm conductivity. The holder was constructed from a length of polyvinyl chloride (PVC) pipe (l=80 mm, d=38 mm) that was machined to remove most of the material along its length, creating large elongate windows within a PVC frame. The windows were covered with fine fiberglass mesh cloth (1×1 mm squares). The fish were free to move within the small holder, but confined to the central acoustically calibrated portion of the tank. The holder was equipped with three Ag/AgCl electrodes ($d=1$ mm) along its length, above the fish, for differential recording of ongoing EOD activity. A pair of Ag/AgCl electrodes was also mounted on the sides of the holder in order to deliver a weak but aversive current (UCS described below).

C. Acoustic stimuli

Stimulus generation was done with hardware from Tucker–Davis Technologies (TDT) and microcomputers. Tones and click stimuli were synthesized on a computer and then output at a 50-kHz sample rate by a 16-bit digital to analog converter (TDT DA1), and low-pass filtered at 10 kHz (TDT FT5). The analog signals were fed to programmable attenuators (TDT PA4) and then to a power amplifier (Crown D-75). Sounds were presented through an underwater speaker (University UW-30), sealed in a thick rubber membrane and shielded within a grounded bronze mesh enclosure, at the bottom of the experimental tank. Tones had 30-ms raised cosine onset/offset ramps. The clicks were synthesized by passing 200-μs monophasic pulses through a band-pass filter set at 300 and 3000 Hz. The clicks recorded in the tank were about 5 ms in duration and had flat amplitude spectra in the 300–3000 Hz band.

All acoustic signals were characterized from the output of a pressure hydrophone (B&K 8103) positioned inside the fish holder, at the position normally occupied by the fish during testing. The output of the hydrophone was then amplified with BMA 202 amplifier, and digitized by a 16-bit analog to digital converter (TDT AD1). Tones were calibrated (dB rms *re*: 1 μPa) from their amplitude spectra. Clicks were calibrated dB peak *re*: 1 μPa from the digitized waveform.

D. Training and testing

We used sound-elicited modulations in EOD rate to measure acoustic detection in conditioned *Pollimyrus*. The novelty response will habituate with repeated sound presentations, but the response can be maintained with conditioning (e.g., Mandriota *et al.*, 1965). Temporal sequences of EODs were measured by computer from digitized records. EODs were recorded differentially (BMA 202 amplifier) with the recording electrodes in the wall of the fish holder. We used a TDT spike discriminator and event timer (SD1 and ET1) for time stamping the EODs to the nearest 1 μs. The EOD rate during a 3.0-s pre-stimulus period was compared to the rate during the subsequent 3.0-s peri-stimulus period, and changes in rate of 25% or more were taken as an indication that the fish detected the sound (Fig. 1). EOD rates during the pre-stimulus period were typically about 10 EODs/s (10.6 ± 6.1 SD EODs/s), and usually increased to 15 to 35 EODs/s during the pre-stimulus period (i.e., accelerated). Three of ten fish consistently decelerated during the acoustic stimulus, and the detection criterion used was again a 25% change. Individual fish responded to sound with either a consistent EOD rate acceleration or a consistent deceleration

(i.e., never changing direction). At present, we do not know the reason behind these individual differences in EOD modulation.

We used a classical conditioning paradigm for training and testing. The tone persisted through the 3.0-s peristimulus period, and continued for an additional 500 ms into a *post-stimulus period* where it overlapped for with the UCS (Fig. 1). The UCS was a series of five 80-ms DC pulses, 3–6 mA, delivered with a 40-ms inter-pulse-interval. The fish received this pairing of sound and the UCS on every training and testing trial. Training and testing sessions both consisted of 50 trials, and individuals were enlisted in single sessions no more than once per 24 h. Mean inter-trial interval was 2 min uniformly varied ±30 s.

Tone responses were obtained for six individuals by training them to a 500-Hz tone at 120 dB. This combination of sound pressure and frequency was naturalistic based on the fish's acoustic behavior. Click train responses were obtained for five fish (three of which were also used for tones) by initially conditioning them with trains having inter-click-intervals (ICI) that randomly varied from 10 to 100 ms, and with random levels between 110 and 130 dB. On any particular conditioning trial, the ICI and level of the train was fixed. The fish typically began performing at 75% correct, or better, within 2–5 training sessions with both tones and click trains (Fig. 2).

Auditory thresholds were obtained using a 1-up 2-down adaptive staircase procedure (Fig. 2), estimating thresholds at approximately 71% correct (Levitt, 1971). In this procedure, the stimulus level was determined by the fish's behavioral response. When the fish detected a sound, the sound was presented in the next trial at the same level. If the fish detected it again, the level was decreased for the subsequent trial (i.e., 2 down). When the fish missed the sound (i.e., no criterion EOD response), the stimulus level was increased to the previous level (i.e., 1 up). Changes in the direction of stimulus level change were referred to as *reversals* (Fig. 2).

The stimulus level step size was 6 dB for the first four reversals and these were not used in the threshold estimate. Subsequent steps were 3 dB. The threshold for a session was calculated as the average of the levels of the last even number of reversals. For the example shown [Fig. 2(b)], ten 3-dB reversals were used. Had there been an eleventh 3-dB reversal, it would have been used in combination with the previous nine reversals (i.e., omitting the first 3-dB reversal at trial 24). The standard error of each estimate was also calculated. Occasionally the SE was high (SE>3 dB) or there were too few usable reversals (less than 6), and the threshold for this frequency was estimated again on another day. In most test sessions, the threshold estimate was based on 8 to 12 reversals.

Each fish was used in only one test session on a given day, to obtain an estimate of threshold for a single frequency. The individual's audiogram was constructed by combining the threshold estimates for each of ten frequencies obtained over a period of about three weeks. An average audiogram for *Pollimyrus* was constructed by calculating the mean threshold, at each frequency, across all the individuals.

We selected the tested range of tone frequencies (100–

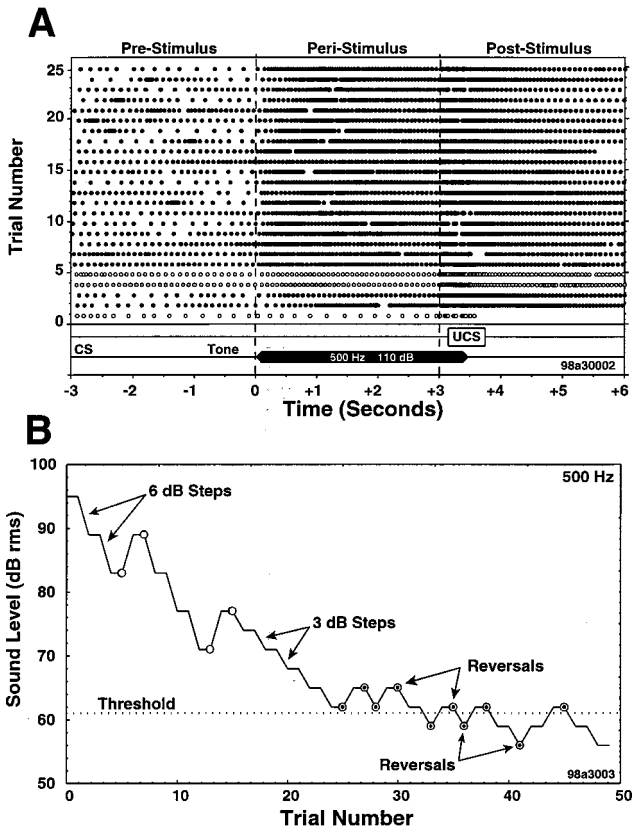

FIG. 2. The top panel (a) shows the first 25 training trials from a session of 50 trails. Each black dot indicates the time at which the fish made an EOD. In trials 1, 4, and 5, the dots are plotted as open circles because the fish did not show criterion accelerations on these trials. In most trials the fish showed a substantial EOD rate increase that was synchronized to the onset of the tone. The lower panel (b) shows a staircase testing session at 500 Hz. In this case, the threshold estimate of 61 dB was calculated from the ten reversals shown as circles with black centers. Sound levels are dB rms *re*: 1 μPa.

1700 Hz) and ICIs (10–100 ms) based upon characteristics of the sounds made by *Pollimyrus*. The courtship sounds have their peak energy in the 200–600 Hz range, and we thus expected that auditory sensitivity might be particularly high in this region. The click trainlike sounds are made with ICIs of approximately 20 ms (grunts) and 40 ms (growls), and therefore we spanned this range in click train ICIs. The trained fish were randomly tested at 100, 200, 300, 400, 500, 600, 900, 1200, 1400, and 1700 Hz to construct the audiograms. For click trains, fish were tested at 10-, 20-, 40-, 80-, and 100-ms ICI in randomized order.

In order to make sure that our criterion for detection (25% change in EOD rate) was reliable, we estimated the frequency with which each fish met criterion in the absence of an acoustic stimulus (i.e., *false positives*). In every trial, the EOD rate during the 3.0-s period preceding the pre-stimulus period (i.e., *the pre-pre-stimulus period*) was recorded, and compared to the pre-stimulus rate. The incidence of fish spontaneously reaching criterion was low, typically in the 20%–30% range (25±3% SE). In the two-down one-up adaptive procedure we used, this low rate of spontaneous responses had a negligible influence on the course of the staircase and the subsequent threshold estimate. We repeated one to five threshold estimates for each of seven fish, and the

results were reasonably consistent with an average threshold difference of 6 dB±2.5 dB SE. The low rate of spontaneous responses, the repeatability of threshold estimates, and the systematic dependence of threshold on sound frequency, all support the robustness of this method for estimating auditory thresholds.

We conducted several checks to be sure that our behavioral responses were mediated by the calibrated acoustic stimulus and not by an unidentified but correlated cue. First, we presented sounds well outside the expected auditory range (5 kHz) and confirmed that there was no detection. If the fish were, for example, detecting a minute electrical artifact, a 5-kHz signal would have been a better stimulus for the most sensitive high frequency electro-receptors (Hopkins, 1981), and the animals should have continued to respond to this stimulus. None of the fish responded to the 5-kHz stimulus.

Second, we re-measured auditory thresholds (at 500 Hz) in the presence of a continuous wide band pass masking noise (100–1000 Hz bandwidth) delivered from a speaker in air, suspended 1 m above the test tank. A separate hardware system (TDT and PC) was used to generate continuous noise during this control procedure. The spectrum of the broadcast noise was corrected so that the sound pressure signal was flat, as measured underwater at the position occupied by the fish. Noise delivered from the speaker in air should only have masked signal detection if detection was based on hearing. Four fish were used for this control procedure, including two previously tested with tones and click trains.

II. RESULTS

Trained *Pollimyrus* consistently modulated their EOD rate when they detected a sound, and then gave a pronounced burst of EODs in response to the applied current [Figs. 1 and 2(a)]. Testing with tone frequencies to which the fish were sensitive produced regular declining staircases, and then a sequence of reversals bracketing threshold [Fig. 2(b)]. The resulting audiograms showed that *Pollimyrus* were most sensitive to tones in the 200–900 Hz range (Fig. 3). The lowest thresholds were near 500 Hz, with an average threshold of 66.5 dB±4.2 SE at 500 Hz. Sensitivity declined slowly (about 20 dB/octave) above and below the sensitivity maximum. Above 1 kHz, sensitivity fell off sharply (about 60 dB/octave). Threshold estimates for tones did not differ significantly between males and females [$F(1,4)=0.153$, $p>0.71$].

The region of maximum sensitivity closely matched the dominant energy in the spectrum of the sounds these fish use in communication (Fig. 3). The high sensitivity at 500 Hz corresponded to the position of the prominent spectral peak in the *Pollimyrus* courtship display at about 490 Hz (Crawford *et al.*, 1997a). There was some individual variation in the thresholds of the six fish used to estimate the average audiogram for *Pollimyrus* (Fig. 3).

Pollimyrus produced the same kind of EOD modulations when trained on click trains, and their behavior during testing was similar to that described for tones. However, threshold was essentially independent of ICI in the 10–100 ms range (Fig. 4). The mean response function was nearly flat,

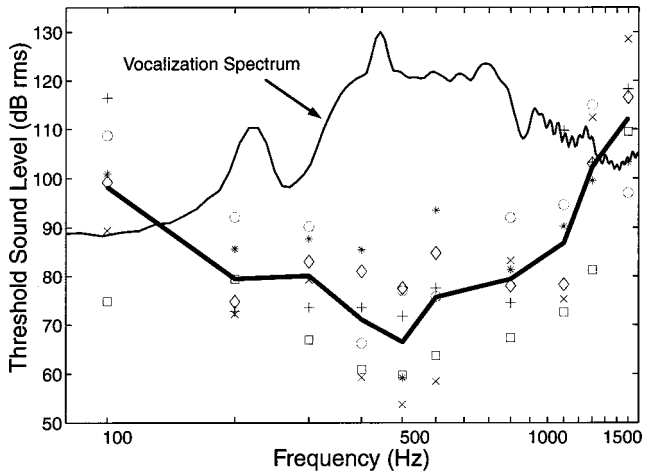

FIG. 3. The mean audiogram is indicated by the heavy line and is based on six individual *P. adspersus*. Thresholds for all six individuals are indicated at each frequency by various symbols. The composite vocalization sound spectrum is based on a courtship sequence including grunts, moans, and a growl (Crawford *et al.*, 1997a). Thresholds are dB rms *re*: 1 μPa.

with thresholds for five animals ranging from 81.0 to 86.9 dB peak, and averaging 83.3 dB±1.2 SE. The individual differences for the click data were relatively small. There was no significant difference between estimates from males and females [$F(1,2)=0.76$, $p>0.80$].

Masking noise, delivered from a speaker in air, resulted in systematically elevated thresholds. The degree of masking was dependent upon the sound pressure of the masking noise [$F(2,9)=13.2$, $p<0.002$]. Detection thresholds were measured with (1) no masking, (2) a moderate masking level (105-dB rms), and (3) a high masking level (120-dB rms). The mean unmasked threshold at 500 Hz was 59.2 dB±5.4 SE, and was not significantly different from the 500-Hz thresholds obtained while constructing the audiograms (i.e., 66.5 dB±4.2 SE, $t=2.3$, $df=8$, $p>0.31$). Thresholds were elevated by 14 dB (72.7 dB±5.7 SE) with the moderate

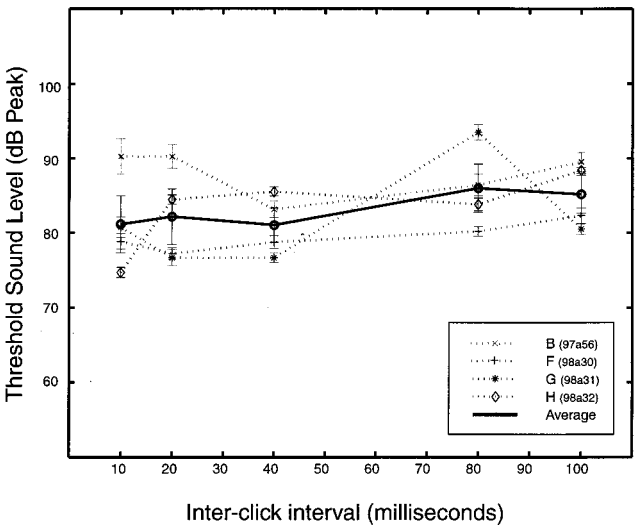

FIG. 4. The mean threshold for click trains differing in inter-click-interval, with SE, is shown for five adults by the thick black line. The data for each individual are presented as dashed lines keyed by different symbols shown at the lower right.

masking level, and by 40 dB (99 dB±5.6 SE) with the high masking level.

III. DISCUSSION

The acoustic behavior and auditory physiology of *Pollimyrus* have received considerable attention in recent years (e.g., Crawford, 1997b; Crawford *et al.*, 1997a). The relatively simple ear and acoustic social signals make this species particularly appealing for neuroethological studies of auditory processing. Nevertheless, prior to the present study we had no behavioral data on sound detection in *Pollimyrus*. The successful exploitation of natural EOD behavior for measuring sound detection is providing critical new information on hearing in this species, and has opened the door to ongoing studies of acoustic discrimination in mormyrids (Marvit and Crawford, 2000).

Hearing in *Pollimyrus* is beautifully matched to the acoustic energy in the communication sounds that this species produces (Fig. 3). During close-range sonic courtship, the sounds must be on the order of 70–90 dB above threshold (Crawford *et al.*, 1997b). The moans in the display introduce strong spectral peaks in the 225–275 Hz range, and in the 425–525 Hz range (Crawford *et al.*, 1997a). The best sensitivity revealed by our average audiogram corresponds closely with the higher of these two peaks, providing a clue that the second peak may be particularly important to the natural communication. Although less pronounced, the audiogram also suggests a second sensitivity maximum near the lower frequency spectral peak.

Although it is common practice in animal auditory psychophysics to train animals at a single audible frequency before measuring the audiogram, it is possible that the training stimulus might have influenced the shape of the audiogram. Results from ongoing studies with fish trained either at other frequencies or with a randomly varying set of frequencies suggest that there could have been a small influence of training on the shape of an individual's audiogram, but further work is needed to determine the significance of this effect. The close correspondence of our *Pollimyrus* audiogram to the audiograms of other species obtained with a variety of different methods (Fig. 5) suggests that if there was an influence of training, it was probably small.

The audiogram of *Pollimyrus* is similar to the audiograms of a variety of other species of fishes that also have peripheral adaptations for sound pressure detection (Fig. 5). The auditory sensitivity of *Gnathonemus petersii*, another mormyrid electric fish, differs by only 5–10 dB from *Pollimyrus*, with the largest differences appearing at high frequencies where *G. petersii* is apparently slightly more sensitive (McCormick and Popper, 1984). *G. petersii* is also a sound producer (Rigley and Marshall, 1973).

The hearing of these mormyrids is similar to that of the goldfish (*Carassius auratus*), with the general shape of the mormyrid audiograms corresponding closely to that of the goldfish (Fay, 1969, 1988). The frequencies for the best sensitivities of both goldfish (350 Hz; Fay, 1969) and *G. petersii* (400 Hz; McCormick and Popper, 1984) were quite close to what we found in *Pollimyrus*. However, goldfish are about 20 dB more sensitive than *Pollimyrus* at most frequencies.

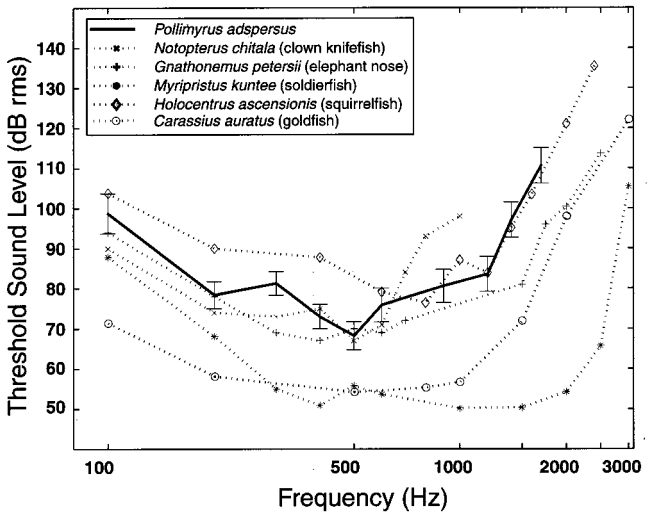

FIG. 5. The audiogram of *P. adspersus* compared to audiograms for several other fish species that have specializations for sound pressure detection. The *Pollimyrus* audiogram is duplicated from Fig. 3. The data for the other species was taken from Fay (1988).

Sensitivity differences are greatest at the lower frequencies, below about 1500 Hz. These differences may reflect true species differences. The goldfish data were obtained under the same acoustic conditions. However, different behavioral measures and criteria were used for the two species, and they may have also contributed to the differences in threshold estimates. The goldfish thresholds were measured based on respiratory suppression.

In our studies, and in comparisons with other species that have evolved coupling of auditory organs to gas-filled tympanic structures, we have assumed that the measured responses are determined by the pressure component of the acoustic stimuli. Although it is likely that there is at least some small contribution of particle motion detection in these species, several lines of evidence show that pressure detection dominates these responses. Removing the gas from the mormyrid's tympanic ear bladder reduces sensitivity profoundly (by about 32 dB; Fletcher *et al.*, 2000), and similar experiments with fish having other specializations that should mediate pressure detection have also produced large deficits (e.g., Fay *et al.*, 1982; Yan, 1998). These manipulations are only expected to influence pressure transduction. Our behavioral thresholds with *Pollimyrus* are also close to the best sensitivities measured electrophysiologically under identical acoustic conditions, but while the heads of the immobilized fish were rigidly fixed during physiology (Crawford, 1993; Suzuki and Crawford, 2000). At present it appears that even under conditions where there may be appreciable particle motion component of the sound field, mormyrid auditory responses are dominated by pressure detection. Further experiments will be needed for a complete understanding of the relative contributions of the various acoustic parameters, under various conditions, and in different regions of the audiogram.

So far as is currently known, goldfish do not produce communication sounds. Like mormyrids, goldfish and the cyprinid stock from which they are derived inhabit shallow

fresh water. These environments are usually acoustically quiet in the spectral region where these animals are sensitive to sound. The high acoustic sensitivity of fishes in these environments is probably advantageous because it allows them to detect the incidental sounds made by other fish while foraging, and while engated in courtship and mating, and other sounds that might facilitate orientation, the detection of prey, and the evasion of predators. Considering the similarities in hearing among species, especially those that are not sound producers, it may be reasonable to suppose that the evolution of hearing in mormyrids pre-adapted these animals for the subsequent evolution of acoustic signaling. Subsequent selection may have then driven an improved match between sound production and auditory sensitivity.

Even though there is similarity in the audiograms of many species, natural and sexual selection may well have yielded important species differences in hearing that will not be uncovered by simply measuring tone thresholds. It is perhaps more likely that important differences exist in the ability to make particular types of acoustic discriminations. For example, there are at least two sound producing species within the genus *Pollimyrus* living in the Niger River (Crawford *et al.*, 1997b). These fish must discriminate between similar sounds made by conspecific and heterospecific males. In ongoing experiments, we have extended the methodologies presented here to address new questions about acoustic discrimination (Marvit and Crawford, 2000).

The fish's grunts are essentially like trains of clicks, with ICI of 16–20 ms and a relatively flat spectrum between 100 and 1200 Hz. Nevertheless, *Pollimyrus* showed no particular sensitivity to the click trains that were most similar to grunts (ICI of 20 ms). It may be that *Pollimyrus* are more sensitive to small differences in click rate in the range used in natural communication, but this awaits new discrimination experiments. It is interesting that, even though the total energy in the click trains we used was greater at the shorter ICIs, the short ICI trains were no more detectable than the longer ICI trains.

ACKNOWLEDGMENTS

We are indebted to A. P. Cook, R. Rescorla, V. Richards, J. C. Saunders, and R. Seyfarth for their contributions to the development of the research presented here. This research was supported by grants from the NIH (DC01252), the PA Lions Hearing Research Foundation, and a grant from the University of Pennsylvania Research Foundation.

Bratton, B. O., and Kramer, B. (**1989**). ''Patterns of the electric discharge during courtship and spawning in the mormyrid fish, *Pollimyrus isidori*,'' Behavioral Ecology and Sociobiology **24**, 349–368.

Ciali, S., Gordon, J., and Moller, P. (**1997**). ''Spectral sensitivity of the weakly discharging electric fish *Gnathonemus petersi* using its electric organ discharge as the response measure,'' J. Fish Biol. **50**, 1074–1087.

Crawford, J. D. (**1991**). ''Sex recognition by electrical cues in a sound producing mormyrid fish, *Pollimyrus isidori*,'' Brain, Behav. Evol. **38**, 20–38.

Crawford, J. D. (**1993**). ''Central auditory neurophysiology of a sound-producing mormyrid fish: the mesencephalon of *Pollimyrus isidori*,'' J. Comp. Physiol. A **172**, 1–14.

Crawford, J. D. (**1997a**). ''Feature-detecting auditory neurons in the brain of a sound-producing fish,'' J. Comp. Physiol. A **180**, 439–450.

Crawford, J. D. (**1997b**). ''Hearing and acoustic communication in the mormyrid electric fishes,'' Marine & Freshwater Behavior & Physiology **29**, 65–86.

Crawford, J. D., Cook, A. P., and Heberlein, A. S. (**1997a**). ''Bioacoustic behavior of African fishes (*Mormyridae*): Potential cues for species and individual recognition in *Pollimyrus*,'' J. Acoust. Soc. Am. **102**, 1200–1212.

Crawford, J. D., Hagedorn, M. M., and Hopkins, C. D. (**1986**). ''Acoustic communication in an electric fish, *Pollimyrus isidori (Mormyridae)*,'' J. Comp. Physiol. A **159**, 297–310.

Crawford, J. D., Jacob, P., and Bénech, V. (**1997b**). ''Sound production and reproductive ecology of strongly acoustic fish in Africa: *Pollimyrus isidori, Mormyridae*,'' Behaviour **134**, 677–725.

Fay, R. R. (**1969**). ''Behavioral audiogram for the goldfish,'' Journal of Auditory Research **9**, 112–121.

Fay, R. R. (**1988**). *Hearing in Vertebrates: A Psychophysics Databook* (Hill-Fay Associates, Winnetka, IL).

Fay, R. R. (**1989**). ''Frequency discrimination in the goldfish (Carassius auratus): Effects of roving intensity, sensation level, and the direction of frequency change,'' J. Acoust. Soc. Am. **85**, 503–505.

Fay, R. R., Hillery, C. M., and Bolan, K. (**1982**). ''Representation of sound pressure and particle motion information in the midbrain of the goldfish,'' Comp. Biochem. Physiol. **71**, 181–191.

Fletcher, L.B., Cook, A. P., and Crawford, J. D. (**2000**). ''Acoustic detection by sound-producing fishes (Mormyridae): The role of tympanic ear-bubbles,'' Paper presented at the Midwinter meeting of the Association for Research in Otolaryngology, St. Petersburg, FL, February.

Hopkins, C. (**1981**). ''On the diversity of electric signals in a community of mormyrid electric fish in West Africa,'' Am. Zool. **21**, 211–222.

Kozloski, J., and Crawford, J. (**1998**). ''Functional neuroanatomy of auditory pathways in the sound producing fish *Pollimyrus*,'' J. Comp. Neurol. **401**, 227–252.

Kramer, B., Tautz, J., and Markl, H. (**1981**). ''The EOD sound response in weakly electric fish,'' J. Comp. Physiol. A **143**, 435–441.

Levitt, H. (**1971**). ''Transformed up-down methods in psychoacoustics,'' J. Acoust. Soc. Am. **49**, 467–477.

Lu, Z., and Fay, R. R. (**1993**). ''Acoustic response properties of single units in the torus semicircularis of the goldfish, *Carassius auratus*,'' J. Comp. Physiol. A **173**, 33–48.

Mandriota, F. J., Thompson, R. L., and Bennet, M. V. L. (**1965**). ''Classical condition of electric organ discharge rate in mormyrids,'' Science **150**, 1740–1742.

Mandriota, F. J., Thompson, R. L., and Bennet, M. V. L. (**1968**). ''Avoidance conditioning of the rate of electric organ discharge in mormyrid fish,'' Anim. Behav. **16**, 448–455.

Marvit, P., and Crawford, J. D. (**1999**). ''Behavioral measurements of auditory sensitivity in sound-producing electric fish: An audiogram for *Pollimyrus*,'' Paper presented at the Midwinter meeting of the Association for Research in Otolaryngology, Ft. Lauderdale, FL, February.

Marvit, P., and Crawford, J. D. (**2000**). ''Auditory discrimination in a sound producing electric fish: Tone frequency and click-rate difference detection in *Pollimyrus*,'' Paper presented at the Midwinter meeting of the Association for Research in Otolaryngology, St. Petersburg, FL, February.

McCormick, C. A., and Popper, A. N. (**1984**). ''Auditory sensitivity and psychophysical tuning curves in the elephant nose fish,'' J. Comp. Physiol. **155**, 753–761.

Moller, P. (**1995**). *Electric Fishes: History and Behavior* (Chapman & Hall, London).

Rigley, L., and Marshall, J. (**1973**). ''Sound production by the elephant noise fish, *Gnathonemus petersii (Pices, Mormyridae)*,'' Copeia **1973**, 134–135.

Stipetic, E. (**1939**). ''Über das Gehörorgan der Mormyriden,'' Zeitschrift für vergleichende Physiologie **26**, 740–752.

Suzuki, A., and Crawford, J. D. (**2000**). ''Characteristics of the primary auditory input to the brain of the sonic fish *Pollimyrus*,'' Paper presented at the Mid-Winter Meeting of the Association for Research in Otolaryngology, St. Petersburg, FL, February.

Werns, S., and Howland, H. C. (**1976**). ''Size and allometry of the saccular air bladder of *Gnathonemus petersii (Pisces: Mormyridae)*: Implications for Hearing,'' Copeia **1976**, 200–202.

Yan, H. Y. (**1998**). ''Auditory role of the suprabranchial chamber in gourami fish,'' J. Comp. Physiol. A **183**, 325–333.

Influence of spatial and temporal coding on auditory gap detection

Andrew J. Oxenham[a)]
Research Laboratory of Electronics, Massachusetts Institute of Technology, Cambridge, Massachusetts 02139

(Received 23 July 1999; revised 18 October 1999; accepted 4 January 2000)

This study investigated the effect on gap detection of perceptual channels, hypothesized to be tuned to spatial location or fundamental frequency (f_0). Thresholds were measured for the detection of a silent temporal gap between two markers. In the first experiment, the markers were broadband noise, presented either binaurally or monaurally. In the binaural conditions, the markers were either diotic, or had a 640-μs interaural time difference (ITD) or a 12-dB interaural level difference (ILD). Reversing the ITD across the two markers had no effect on gap detection relative to the diotic condition. Reversing the ILD across the two markers produced a marked deterioration in performance. However, the same deterioration was observed in the monaural conditions when a 12-dB level difference was introduced between the two markers. The results provide no evidence for the role of spatially tuned neural channels in gap detection. In the second experiment, the markers were harmonic tone complexes, filtered to contain only high, unresolved harmonics. Using complexes with a fixed spectral envelope, where the f_0 (of 140 or 350 Hz) was different for the two markers, produced a deterioration in performance, relative to conditions where the f_0 remained the same. A larger deterioration was observed when the two markers occupied different spectral regions but had the same f_0. This supports the idea that peripheral coding is dominant in determining gap-detection thresholds when the two markers differ along any physical dimension. Higher-order neural coding mechanisms of f_0 and spatial location seem to play a smaller role and no role, respectively. [S0001-4966(00)02204-9]

PACS numbers: 43.66.Mk, 43.66.Pn, 43.66.Hg [DWG]

INTRODUCTION

Gap detection has long been used as a measure of temporal resolution in the auditory system (Plomp, 1964b; Penner, 1977; Buus and Florentine, 1985; Moore *et al.*, 1993). Often, for sinusoids and broadband noise, silent gaps of 5 ms or less can be detected. This minimum detectable gap duration has been interpreted as revealing a fundamental ''sluggishness'' in the auditory system's response to very rapid changes in sound level. In another class of gap-detection experiments, the sounds before and after the gap, known as ''markers,'' differ along a certain physical dimension. For instance, using sinusoids, the two markers may have different frequencies. Previous studies have found that gap-detection thresholds increase as the frequency difference between the two markers increases, and that at large frequency differences, the minimum detectable gap increases to 20 ms or more, i.e., approximately an order of magnitude greater than when the two markers are at the same frequency (e.g., Williams and Perrott, 1972; Formby and Forrest, 1991; Formby *et al.*, 1998). A similar deterioration in performance, both in traditional gap detection (Phillips *et al.*, 1997) and in modulation gap detection (Grose *et al.*, 1999), is found when the two markers are presented to separate ears.

The effect of a difference in marker frequency has generally been attributed to the frequency selectivity established in the auditory periphery, and has also been modeled in this way (Forrest and Formby, 1996; Heinz *et al.*, 1996). When the two marker frequencies are the same or very similar, the markers stimulate the same region of the cochlear partition, which in turn leads to responses from the same population of auditory nerve fibers. Thus any perceived interruption (fluctuation, onset, or offset) in the stimulus is a reliable cue for detecting the gap. When the two markers have different frequencies, they are separated in the cochlea such that they maximally stimulate different places along the cochlear partition, which in turn leads to different populations of auditory nerve fibers responding to each frequency. In this case, the offset of the first tone and the onset of the second are always perceived, whether the gap is present or not. Thus the perceived onset or offset is no longer a reliable cue, and the gap can only be detected by a timing comparison across different neural channels (e.g., Hanekom and Shannon, 1998). These two cases are therefore often referred to as ''within-channel'' and ''between-channel'' gap detection, respectively.[1]

This explanation relies on the fact that stimulus frequency is a neurally and perceptually relevant dimension: If the auditory system were not frequency selective, then no discontinuity between the two markers would be perceived, regardless of the frequency difference. Similarly, gap detection might be used to probe other, higher-level, organizational principles in the auditory system. Two dimensions that are known to have neural representations established at a level higher than the cochlea are spatial location (Moore, 1991; Brainard, 1994) and periodicity (Langner, 1992). Recently, Phillips *et al.* (1998) reported finding an influence of spatial perceptual channels on gap detection. In their experiment, listeners were seated individually in a room with two

a)Electronic mail: oxenham@mit.edu

loudspeakers, positioned to the left and right of the listener. In one condition, listeners were required to detect a gap in a broadband noise emitted from one of the loudspeakers. As in studies using headphones, thresholds were generally less than 5 ms. In the second condition, the sound preceding the gap (marker 1) was played from one loudspeaker, while the sound following the gap (marker 2) was played from the other loudspeaker. Here, thresholds for gap detection were much worse, often by an order of magnitude. Phillips *et al.* suggested that this was due to the auditory system representing the two stimuli in different spatially tuned neural channels and that, as with the markers of different frequencies, the auditory system was not able to compare timing efficiently across these different channels.

While the study of Phillips *et al.* (1998) suggests that gap detection may indeed be a straightforward way of probing higher-order neural representations of sound, some questions remain. First, the localization of sound is generally achieved by combining information from the two ears in the form of interaural time differences (ITDs) and interaural level differences (ILDs) (Blauert, 1997). From the study of Phillips *et al.*, it is not clear which of these cues was dominant in producing the deterioration in gap detection. Second, presenting the markers from different locations results in monaural level differences between the two markers, at least for frequencies above about 500 Hz (Blauert, 1997). It has long been known that a monaural level difference between the two markers produces a deterioration in gap detection (Plomp, 1964b; Plack and Moore, 1991). Thus it is possible that the results of Phillips *et al.* (1998) do not represent an effect of spatial hearing at all, but rather reflect the monaural effect of introducing a level difference across the gap. These questions can be addressed by presenting the sounds over headphones. In this way, ITDs and ILDs can be manipulated independently to assess the relative contributions of each to changes in gap detection. Furthermore, the relative contribution of the monaural system can be assessed by comparing binaural and monaural performance using the same level differences.

Another acoustic dimension that seems to be represented in the higher levels of the auditory system is periodicity, or repetition rate (Langner, 1992). For complex sounds, this representation is believed to be orthogonal to the tonotopic representation of frequency, already established in the cochlea. It may be especially relevant for complex harmonic sounds, such as speech, where higher-order harmonics are no longer spectrally resolved in the auditory system, but where they combine within individual auditory filters to form periodic waveforms with a repetition rate equal to that of the fundamental frequency (f_0). Complexes comprising only high-order, unresolved harmonics can be used to dissociate the effects of spectral and temporal cues (Vliegen and Oxenham, 1999). Although the pitch of complexes containing only unresolved harmonics is weaker than that of resolved harmonic complexes, it remains reasonably clear and can be used to make judgments of musical intervals (Houtsma and Smurzynski, 1990).

If periodicity represents an important neural coding principle, and if gap detection reflects such coding, then gap detection should be worse for conditions where the f_0 of the two markers is different, even if the spectral envelope and overall level remain constant. This seems not to have been tested before, although some evidence suggests that gap *discrimination* deteriorates somewhat as the f_0 difference between the markers is increased (Vliegen *et al.*, 1999). Further evidence for the effect of periodicity on gap detection comes from a study of cochlear implant patients (Chatterjee *et al.*, 1998). In their experiment, Chatterjee *et al.* found that when stimulating a single electrode, performance was generally worst when the pulse rates of the two markers were very different. This is somewhat analogous to changing the f_0 while keeping the spectral envelope constant.

The experiments described here explore the effects of spatial and temporal cues on auditory gap detection. In the first experiment, the roles of ITDs, ILDs, and monaural level differences on gap detection in broadband noise were investigated. In the second experiment, unresolved harmonic complexes were used to separate the roles of spectral envelope and periodicity in gap detection.

I. EXPERIMENT 1. INFLUENCE OF SPATIAL PERCEPTUAL CHANNELS ON GAP DETECTION

A. Stimuli

Gap-detection thresholds were measured using broadband noise as markers. In the binaural conditions, the markers were either identical in the two ears (diotic), or had an ILD of 12 dB or an ITD of 640 μs. These differences were sufficient to fully lateralize the stimuli to one or the other side (Blauert, 1997). The following ITD conditions were tested: (1) Both markers lateralized to the left; (2) both markers lateralized to the right; (3) the first and second markers lateralized to the left and right, respectively; and (4) the first and second markers lateralized to the right and left, respectively. The ILD condition comprised marker 1 being lateralized to the left and marker 2 to the right. In two of the four monaural conditions, the ILD condition was repeated with either the left or the right headphone disconnected, such that a monaural level difference occurred between the two markers, with either the first marker (left ear only) or the second marker (right ear only) 12 dB higher. In the other two monaural conditions, the markers were at the same level and were both presented to either the left or the right ear. A schematic diagram of some of the stimulus configurations is shown in Fig. 1.

The spectrum level of the markers was 36 dB SPL, except in conditions involving a level difference. In such cases, the spectrum levels were 36 and 24 dB SPL (nominal overall levels of 79 and 67 dB SPL). The duration of the first marker was fixed at either 10 or 150 ms. Two durations were tested because Phillips *et al.* (1997, 1998) have reported that a short initial marker increases the difference in performance between within-and between-channel gap detection. The duration of the second marker was varied randomly in each interval from 100 to 300 ms, with uniform distribution. This was intended to render a possible cue of overall duration unreliable (Formby and Forrest, 1991). The markers were gated abruptly; because they were broadband, no audible

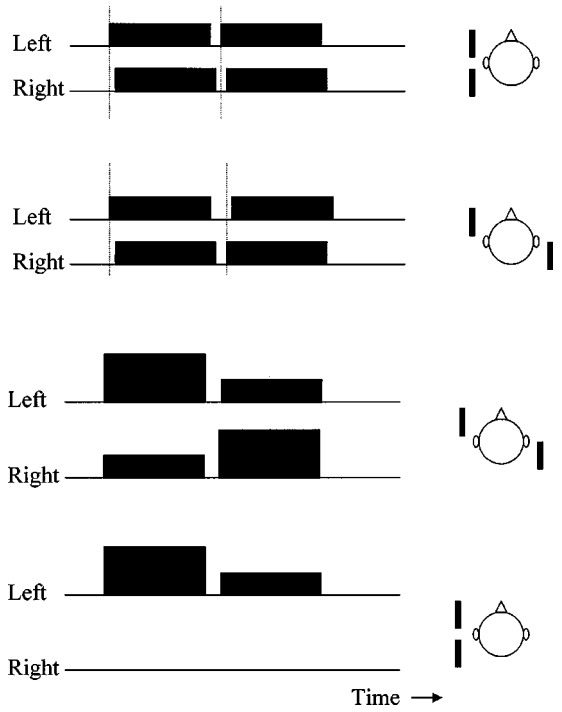

FIG. 1. Schematic diagram of the stimulus configurations for the ITD conditions and the binaural and monaural level differences (left column), and the perceived lateralization of the stimuli (right column). In the first panel, the left side leads by 640 μs for both the first and second marker; both markers are lateralized to the left. In the second panel, left leads right for the first marker, but right leads left for the second marker. This results in a shift in lateralization between the two markers. In the third panel, left is 12 dB higher in level than right for the first marker, and vice versa for the second marker, again leading to a shift in lateralization between the two markers. In the fourth panel, the stimulus is presented only to the left ear, but with the same level difference (12 dB) as used in the third panel.

spectral splatter was generated by this procedure. Before each trial, a new 655-ms sample of Gaussian noise was generated. The four noise bursts (markers 1 and 2 for both intervals) were cut independently and randomly with replacement from this long buffer.

All stimuli were generated digitally at a sampling rate of 50 kHz, and played out via a digital-to-analog converter (TDT DA2), The stimuli were lowpass filtered at 20 kHz (TDT FT5) and passed through a programmable attenuator (TDT PA4) before being presented to the listener via a headphone buffer (TDT HB6) and a Sony MDR-V6 headset.

B. Procedure

Thresholds for the minimum detectable gap were measured using a two-interval, two-alternative forced-choice method with a 3-down 1-up interleaved adaptive tracking procedure, which tracks the 79%-correct point on the psychometric function. Listeners were presented with two intervals, separated by an interstimulus interval of 400 ms, and were required to select the interval containing the gap. Correct-answer feedback was provided after each trial. In the ''no gap'' interval, the two markers generally abutted each other, such that there was no gap between the offset of marker 1 and the onset of marker 2. The exception to this was in the ITD conditions where the lateralization changed between markers. In these cases, even in the ''no gap'' interval, a gap of 1.28 ms ($2\times640\,\mu$s) was present in one of the two ears. This gap was not reported as being heard by any of the listeners, which is not surprising given that the minimum detectable gap is usually found to be between 2 and 3 ms. Thresholds in this condition are given as the duration of the longer of the two gaps.

The initial gap duration was set to 80 ms, or 20 ms in cases where it became clear in pilot experiments that thresholds were less than 10 ms. Three independent tracks were interleaved in each run, so that each trial within a run was selected randomly from one of the three tracks. The initial step size was an increase or decrease by a factor of 1.78. After three reversals, the step size in that track was reduced to an increase or decrease by a factor of 1.26. Each track was terminated after five reversals, and the (geometric) mean of the gap duration at the last two reversals from each of the three tracks was defined as threshold. Thus each track threshold was the mean of six values. Reported thresholds are the (geometric) mean of at least three such runs for each listener. In conditions involving a level difference, thresholds were found to be more variable and so a total of six runs were measured. The conditions were not run in any particular order and listeners were often presented with a number of different condition in one session.

C. Subjects

Six female listeners participated as subjects in this experiment. All had pure-tone thresholds of 15 dB HL or less at octave frequencies between 250 and 8000 Hz. All but one were college students and all were paid for their participation. The ages of the listeners ranged from 21 to 45 years (median age: 28.5). All listeners were given at least 2-h practice, spread across the different conditions, before data were collected. Two of the listeners had previous experience in psychoacoustic tasks.

D. Results

The pattern of results was similar for all listeners, and so only mean data are shown in Fig. 2. The error bars denote ±1 standard error of the mean across listeners. The left panel shows results from conditions in which there was no interaural or level difference between the markers. The filled squares represent the diotic condition and the circles and triangles represent results from the left and right ear only, respectively. The results are broadly in line with previous studies of gap detection in noise (Plomp, 1964b; Penner, 1977; Forrest and Green, 1987; Green and Forrest, 1989); thresholds for the 150-ms marker 1 are generally around 3 ms. Thresholds for the 10-ms marker are somewhat higher, with mean thresholds of between 6 and 7 ms. No general ear advantage is apparent, and there seems to be little if any benefit gained from having the stimuli presented to both ears. By pooling the monaural and diotic conditions for each listener and using a repeated-measures analysis of variance (ANOVA), the difference in thresholds between the two marker 1 durations was found to be significant ($F_{1,5}=11.05$; $p<0.05$).

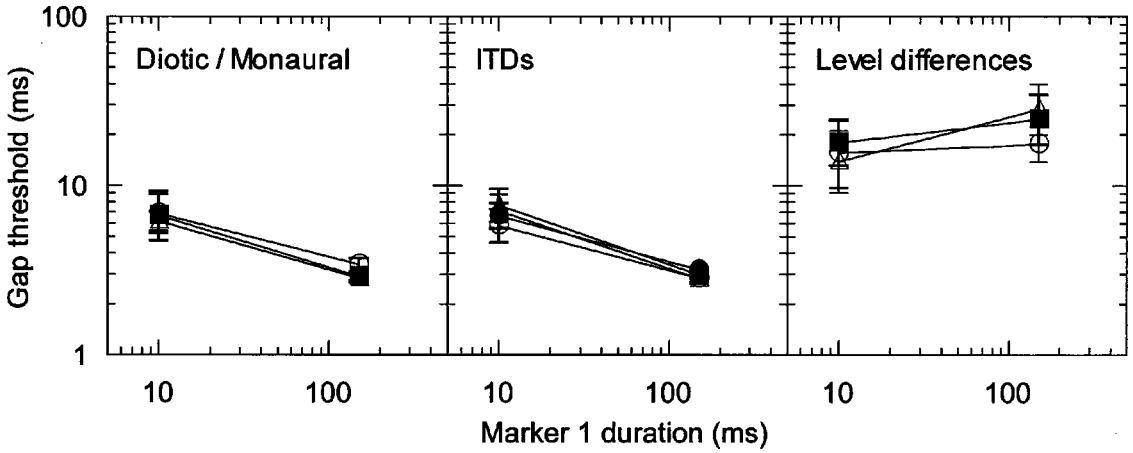

FIG. 2. Mean thresholds for detecting a gap between two broadband noise markers that were presented monaurally or diotically (left panel), with 640-μs interaural time differences (middle panel), or with 12-dB interaural or intermarker level differences (right panel). Error bars represent ± 1 standard error of the mean across six listeners. In the left panel, filled squares represent thresholds in the diotic condition, while the triangles and circles represent thresholds from stimuli presented monaurally, to the right and left ear, respectively. In the middle panel, circles denote conditions where left led right for marker 1; triangles denote conditions where right led left for marker 1. Open symbols represent conditions where the ITD was the same for both markers, and filled symbols represent conditions where the ITD was reversed for the second marker. In the right panel, circles denote the conditions presented to the left ear only, where marker 1 was 12 dB higher in level than marker 2. Triangles denote the conditions presented to the right ear only, where marker 1 was 12 dB lower in level than marker 2. Filled squares represent the binaural conditions, where the two previous conditions were presented together, producing an interaural level difference of 12 dB which was reversed between the two markers.

The middle panel of Fig. 2 shows data from binaural conditions with ITDs. Circles show conditions where marker 1 was lateralized to the left; triangles show where marker 1 was lateralized to the right. Open symbols represent conditions where both markers were lateralized to the same side; filled symbols represent conditions where the lateralization was reversed from marker 1 to marker 2. If perceived position had a large effect on gap thresholds, as proposed by Phillips *et al.* (1998), one might expect thresholds for conditions where the lateralization reverses across the gap to be higher than for conditions where the lateralization remains constant. In fact, the middle panel shows that changing the lateralization has essentially no effect on thresholds. This is despite the fact that all listeners reported hearing a large shift in the perceived location of the noise in these conditions. As with the monaural and diotic conditions, the difference in thresholds between the two marker 1 durations was found to be significant ($F_{1,5}=16.87$; $p<0.01$).

The right panel shows the effect of introducing monaural and binaural level differences. In many cases, performance was worse than in the diotic condition (squares in the left panel) by up to an order of magnitude. The mean threshold, pooled across all level-difference conditions, was 19 ms. The differences in thresholds between the monaural/diotic conditions and the level-difference conditions were highly significant for both the 10-ms marker 1 ($F_{1,5}=26.37$; $p<0.005$) and the 150-ms marker 1 ($F_{1,5}=50.38$; $p<0.001$). Listeners generally found these conditions more difficult and reported that the cues were different from those used in the other conditions. The idea that a different process may have been involved is supported by the somewhat higher variability associated with these thresholds, even when plotted on a log scale. There was, however, no noticeable difference in thresholds between the binaural and monaural level differences. In contrast to the previous two conditions, an ANOVA, again using individual mean data pooled across the three level-difference conditions, showed no significant effect of marker 1 duration ($F_{1,5}=3.13$; $p>0.1$).

E. Discussion

The data from the diotic and ITD conditions (left and middle panels of Fig. 2, respectively) show that thresholds for the 10-ms marker are generally higher than for the 150-ms marker. This is not consistent with the findings of Phillips *et al.* (1997, 1998), who found little or no effect of marker 1 duration in conditions where the markers had the same spectrum or location. The present results are also inconsistent with the results of most previous headphone studies, which have also reported little or no effect of marker duration (Abel, 1972; Penner, 1977; Forrest and Green, 1987). However, the results do seem to be consistent with a more recent study (Snell and Hu, 1999), in which gap detection was found to be poorest for a gap placed near the onset or the offset of a 150-ms broadband noise. It is not clear what accounts for these discrepancies. One consideration is that the amount of practice given to listeners in the present study was generally less than that reported in previous studies. It is possible that thresholds would have decreased further in the 10-ms conditions, if more extensive practice had been given. In support of this conjecture, He *et al.* (1999) also found an increase in gap thresholds as they decreased the overall marker duration from 400 to 100 ms. They used groups of young and aged listeners, all of whom had received only about 30 min practice on each condition. Also, Snell and Hu (1999) found that the effect of gap placement was greatest for their inexperienced listeners.

Unlike the monaural/diotic and ITD conditions, there was no consistent effect of marker 1 duration in the level difference conditions (Fig. 2, right panel). In contrast, Phillips *et al.* (1997, 1998) found that, for most of their listeners,

thresholds increased with decreasing marker 1 duration. Again, the reason for this discrepancy is not clear. However, some listeners reported that they were comparing the intervals between the *onsets* of the two markers to determine which interval contained the gap. If used at all, such a strategy would be more effective with the 10-ms marker, as the interval between the marker onsets is smaller for the shorter marker 1 than for the longer one.

Despite these relatively small differences, the main results of experiment 1 are clear: Gap detection is not affected by changing the ITD between marker 1 and marker 2 (Fig. 2, middle panel), suggesting that a change in perceived location does not necessarily elevate gap-detection thresholds. Although the ILD across the gap did have a large effect on gap-detection thresholds, essentially the same deterioration was produced by a monaural level difference between the two markers. Introducing binaural information produced no deterioration beyond that observed for the monaural level differences. This suggests that the binaural system plays little or no role in these tasks and that thresholds in all conditions can be understood solely by considering the signals presented to each ear separately. This in turn suggests that the spatial effect on gap detection reported by Phillips *et al.* (1998) may have been due to the monaural level differences introduced at each ear by presenting the stimuli from different sides of the head. Thus the effect of marker location reported by Phillips *et al.* is probably not a reflection of spatially tuned neural channels, but instead reflects the well-known consequence of presenting the two markers at different levels (Phomp, 1964b; Penner, 1977; Plack and Moore, 1991).

The finding that lateralization *per se* has no effect on gap thresholds is consistent with one condition tested by Phillips *et al.* (1997). In their experiment 4, they found that presenting marker 1 to the left ear only and marker 2 to both ears had only a small effect on gap thresholds, relative to the monaural condition. It therefore seems that if monaural information is available, listeners' performance is not greatly affected by binaural information.

The present results may also be useful in interpreting the results of Boehnke and Phillips (1999). As in Phillips *et al.* (1998), they measured gap detection using two loudspeakers. However, instead of fixing the speakers to the left and right of the listener, they measured gap-detection thresholds for a number of relative speaker locations. The results showed that performance depended primarily on whether the speakers were located ipsilaterally or contralaterally, and that the exact positions of the speakers on each side did not significantly affect thresholds. Boehnke and Phillips (1999) interpreted these results as providing evidence for two broadly tuned neural channels, roughly representing the left and right hemispheres. They related their findings to animal physiological and behavioral data showing fairly broad azimuthal tuning in auditory cortical regions, with each hemisphere best represented in contralateral cortical regions. In light of the present results, however, an alternative explanation can be made in terms of monaural level differences between the two markers. Large overall differences in ILD only occur when two stimuli are located in opposite hemispheres. Therefore, the pattern of results observed by Boehnke and Phillips (1999) is exactly what would also be predicted simply on the basis of monaural level differences.

The question remains as to why a level difference between the two markers has such a large effect on gap detection. It is interesting that threshold values and variability are more akin to a between-channel task than a within-channel one, despite the fact that the two markers are identical in everything but level. Plomp suggested that in the case of marker 1 being higher in level than marker 2, the onset of marker 2 was masked by marker 1. Thus the function relating gap threshold with the level of marker 2 may be treated as a measure of forward masking, or the ''decay of auditory sensation'' (Plomp, 1964b). Similarly, backward masking may govern conditions where marker 1 is lower in level than marker 2 (Plack and Moore, 1991). However, in this case it is difficult to reconcile the present results with our current understanding of backward masking, as it is generally accepted that little or no backward masking occurs for gaps longer than about 10 ms (e.g., Oxenham and Moore, 1994), and thresholds in the present experiment were often greater than 20 ms. It is possible that gap detection is generally performed by detecting an onset transient that is otherwise not detectable. In the case of marker 2 being higher in level than marker 1, the onset of marker 2 is always detectable, whether a gap is present or not. This makes the onset cue unusable for detecting a gap, and listeners may be forced to adopt another, less efficient, strategy involving temporal discrimination, rather than detection.

In summary, for gap detection in broadband noise, perceived changes in lateralization are neither necessary nor sufficient to produce elevated thresholds. At this stage, therefore, there seems to be little reason for postulating any additional influence of spatial coding on gap detection. It is more parsimonious to assume that the results of Phillips *et al.* (1998) and Boehnke and Phillips (1999) are due to monaural level differences between the two markers, rather than to spatially tuned neural channels.

II. EXPERIMENT 2. EFFECT OF F_0 AND SPECTRAL ENVELOPE ON GAP DETECTION

Experiment 1 showed that the effect of spatial separation on gap detection is probably due to monaural level differences, rather than a reflection of spatially tuned neural channels. The role of neural channels tuned to different repetition rates (or f_0s) remains open, although a study in cochlear implant patients (Chatterjee *et al.*, 1998) and a study of temporal discrimination in normal-hearing listeners (Vliegen *et al.*, 1999) both suggest that f_0 differences might have an effect on gap detection. This experiment investigated the separate influences of f_0 and spectral envelope on gap detection by using harmonic tone complexes consisting only of high harmonics, which are generally considered to remain unresolved in the auditory system.

A. Effect of fundamental frequency

1. Method

Equal-amplitude harmonic tone complexes with f_0s of 140 and 350 Hz were used as markers. The components were

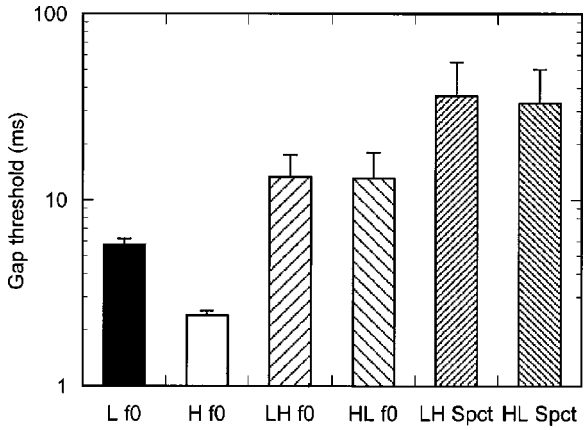

FIG. 3. Mean thresholds for detecting a gap between two harmonic complexes. Error bars represent ±1 standard error of the mean across six listeners. The first four bars (labeled ''f_0'') represent conditions in which the spectral envelope was held constant by bandpass filtering the complexes between 4 and 8 kHz. The f_0 of each marker was either 140 Hz (''*L*'') or 350 Hz (''*H*''). The f_0 s of the two markers were either the same (''*L*'' or ''*H*'') or different (''*LH*'' or ''*HL*''). The last two bars (labeled ''Spct'') represent conditions in which the f_0 was held constant at 140 Hz. One marker was bandpass filtered between 2 and 4 kHz (''*L*''), while the other marker was bandpass filtered between 4 and 6 kHz (''*H*''). The order of these two markers was interchanged to produce the two conditions ''*LH*'' and ''*HL*.''

added in sine phase. The duration of marker 1 was 150 ms; the duration of marker 2 was randomized between 100 and 300 ms. Each marker was gated abruptly and had a random starting phase. The random starting phase ensured that there was usually a phase discontinuity between the two markers in both the ''gap'' and ''no-gap'' intervals of a trial, even when the f_0 was the same. After gating, the stimuli were bandpass filtered with cutoff frequencies of 4000 and 8000 Hz (TDT PF1; attenuation slopes of 72 dB/octave). This eliminated any audible splatter due to gating, and also ensured that only components with harmonic numbers greater than 11 were at full amplitude. Plomp (1964a) has shown that generally only harmonics with numbers up to between 5 and 8 can be resolved by the auditory system.

The overall level of the complex tones after filtering was approximately 72 dB SPL. By keeping the overall level the same, both f_0s should have evoked the same loudness, as the overall bandwidth was also held constant. Four conditions were tested: (1) Both markers had an f_0 of 140 Hz, (2) both markers had an f_0 of 350 Hz; (3) the first and second markers had f_0s of 140 and 350 Hz, respectively; and (4) the first and second markers had f_0s of 350 and 140 Hz, respectively.

Stimuli were presented to the left ear only. Four repetitions of each conditions were measured, and the conditions were presented in random order. Otherwise, the method of stimulus generation, presentation, and measurement was the same as that in experiment 1. The same six listeners participated.

2. Results

Again, the individual patterns of results were fairly similar, and so the (geometric) mean data are plotted as the first four bars of Fig. 3. The first two bars show thresholds when both markers had the same f_0 of either 140 Hz (''Lf_0'') or 350 Hz (''Hf_0''). The next two bars show results for conditions where the f_0 changed across the markers from 140 to 350 Hz (''LHf_0'') or from 350 to 140 Hz (''HLf_0''). All six listeners showed an effect of f_0 for the two same-f_0 conditions (filled and open bars); the average gap threshold at 140 Hz was 5.7 ms compared with 2.4 ms at 350 Hz. Using a paired *t*-test, this difference was found to be highly significant $[t(5)=15.53;\ p<0.001]$.

Four of the six listeners and the mean data showed a deterioration in performance when the f_0 was altered across the gap. For the other two listeners, performance was similar to that of the lower f_0. The mean threshold, pooled across listeners and the two conditions, was 13.2 ms. This was significantly higher than the threshold for the 140-Hz same-f_0 condition $[t(13)=3.95;\ p<0.005]$. Thus it appears that changes in f_0 may have an effect on gap detection, even if the spectral envelope is held constant.

B. Effect of spectral envelope

The previous section showed an effect of f_0 on gap-detection thresholds, although the effect was generally not as large as has been reported for sinusoids of different frequencies (Formby *et al.*, 1998). This section examines whether a change in spectral region is sufficient to produce a deterioration in gap detection, even if the f_0 (and hence the pitch) stays constant.

1. Method

Complex tones with an f_0 of 140 Hz, generated in sine phase, were used as markers. Again markers were gated on and off abruptly, and the starting phase of each marker was randomized. The markers were filtered after gating with a 2-kHz-wide bandpass filter (TDT PF1; attenuation slopes of 72 dB/octave). The cutoff frequencies were either 2000 and 4000 Hz, or 4000 and 6000 Hz. The overall level of the complex after filtering was approximately 74 dB SPL. Markers 1 and 2 were always filtered into different spectral regions; both low-high and high-low conditions were tested. The two markers were generated and filtered separately and then combined (TDT SM3) before being passed to the headphone buffer. Stimuli were presented to the left ear only. Four repetitions of each condition were measured. All six listeners from experiment 1 participated.

2. Results

The mean results are shown as the last two bars of Fig. 3. It should be noted that the bandwidth of these conditions was 2 kHz instead of 4 kHz. The narrower bandwidth would be expected to produce somewhat higher thresholds even in the absence of a spectral difference between the markers. However, using noise markers, Eddins *et al.* (1992) found that thresholds increased by a factor of $\sqrt{2}$ for a halving in bandwidth. The mean increases observed here are closer to an order of magnitude. Individual thresholds range from around 10 ms for two listeners to over 100 ms for another listener. The mean threshold (pooled across low-high and high-low conditions) was 35 ms. This is significantly higher than both the same-f_0 and different-f_0 conditions with the fixed spectral envelopes ($p<0.005$). It is interesting to note

that the two listeners who showed virtually no effect of f_0, and the smallest effect of spectral region, were also the most experienced listeners, although by this stage all listeners had been exposed to at least 20-h gap detection.

C. Discussion

All listeners showed a larger gap threshold for the 140-Hz f_0 than for the 350-Hz f_0. This difference of more than a factor of two may be due to differences in the periodic fluctuations within each stimulated auditory filter. First, the fluctuations are slower for the 140-Hz complex, with a period of 7.14 ms (i.e., greater than the mean threshold) compared with 2.86 ms for the 350-Hz complex. The gaps may therefore be less discriminable from the inherent periodic dips in the filtered envelope. Second, the lower f_0 means that the components are spaced more closely together. Therefore, the waveform at the output of each auditory filter will be a combination of more components, giving a more modulated envelope than for the higher f_0 complex. A similar explanation in terms of random fluctuations (as opposed to the deterministic stimuli used here) has been proposed by Glasberg and Moore (1992) to account for poor gap detection in narrow-band noise.

The results in Fig. 3 show that the effect of changing spectral region was generally much greater than that of changing f_0. This supports the idea that the deterioration in gap detection observed with sinusoidal markers of different frequencies is primarily due to the effects of the frequency-to-place mapping in the cochlea. Changes in f_0 also have an effect, in line with the cochlear-implant study of Chatterjee *et al.* (1998). However, in line with the findings of Vliegen *et al.* (1999), spectral cues seem to have a stronger influence than f_0 cues in temporal discrimination tasks.

While the stimuli were designed to significantly reduce spectral cues in the different f_0 conditions, they cannot be totally ruled out of these experiments. In particular, it is possible that resolved combination tones (Goldstein, 1967; Smoorenburg, 1972a, b), spaced at harmonic integers below the stimulus passband, might have been audible and may have contributed to an overall spectral difference. It seems unlikely, however, that these low-level components had a strong influence on the results. Vliegen and Oxenham (1999) examined the role of resolved combination tones in a sequential streaming task, and found no change in the results when the combination tones were masked by low-pass noise. If combination tones did play a role, then the effect of f_0 on gap detection observed in this experiment may be greater than the ''true'' effect of f_0 alone. This is turn would strengthen the conclusion that spectral and/or level differences are of paramount importance in determining gap thresholds.

III. GENERAL DISCUSSION

Experiment 1 showed that spatial cues have no effect on gap detection, if monaural level differences between the markers are not present. This conflicts with a growing body of literature in which it is claimed that gap detection can be used to examine perceptual organization at levels higher than the cochlea (Phillips *et al.*, 1998; Boehnke and Phillips, 1999; Taylor *et al.*, 1999), a view that is also expounded in a recent review article (Phillips, 1999). Based on the results of experiment 1, it seems likely that all the results ascribed to effects of spatially tuned neural channels can in fact be explained in terms of the resulting monaural level differences between the two markers. In general, it seems that monaural information can be used to detect gaps, even if binaural information encourages perceptual segregation. Because of this, it is probably not possible to use gap detection to investigate the role of spatially tuned neural channels.

Based on data currently available, it seems that differences between the two markers in level and frequency spectrum can both have a strong effect on gap detection. Differences in periodicity (and hence pitch), independent of spectral envelope (or electrode for cochlear implants) also have an effect, but it seems to be weaker than that of spectrum, at least for normal-hearing listeners. This is consistent with recent results from a temporal discrimination task (Vilegen *et al.*, 1999).

A. The role of spatial coding in auditory streaming

At first sight, it may seem surprising that lateralization based on ITD's has no effect on gap detection, and that lateralization based on ILDs has no effect over and above that produced by the monaural level differences. On the other hand, it has been shown that ITDs play essentially no role in the perceptual grouping of concurrent sounds (Culling and Summerfield, 1995). Also, for sequential sounds, Deutsch (1974, 1975) found that frequency cues for pure tones overrode lateralization cues in forming ''auditory streams.'' This was true even though individual tones were presented to one ear at a time, producing an infinite ILD. Thus spatial cues may generally play a secondary role in the formation of auditory objects and streams (Darwin and Carlyon, 1995). If poor performance in gap detection is a reflection of stream segregation, then it follows that spatial cues should have a minimal effect.

B. Explaining within-and between-channel differences in gap detection

Gap detection generally seems poorest when the markers stimulate different peripheral frequency channels, regardless of the perceived pitch or location. There seems to be little consensus as to the mechanisms underlying this effect. Some previous studies have ascribed it to the cognitive load of attending to more than one perceptual channel. For instance, Fitgibbons *et al.* (1974) suggested that the shift of attention from one channel to another during the gap may impair performance. Phillips *et al.* (1997; see also Phillips, 1999) proposed that both channels may be attended to concurrently, but that attending to one channel may reduce the resources available for monitoring events in the other channel. Both these explanations seem unlikely for the following reasons. First, it has been shown for the detection of tones in noise that performance is only slightly degraded when the tone is presented randomly at one of four possible frequencies (Schlauch and Hafter, 1991), suggesting that it is possible to attend to at least four frequency channels without significant

attentional cost, at least in a detection paradigm. Second, detection of a multitone complex improves as the number of tones is increased from one to ten, consistent with the predictions of multiple observations in independent frequency channels, with no additional attentional load assumed (Buus *et al.*, 1998). Third, and most relevantly, gaps in multiple spectral bands are more detectable than a gap in a single band (Grose and Hall, 1988; Green and Forrest, 1989; Grose, 1991; Hall *et al.*, 1996), suggesting that listeners are able to efficiently combine information about gaps across frequency. Taken together, these results suggest that it is possible to attend to more than one frequency at a time, and that the sharing of attentional resources cannot explain the deterioration in gap thresholds by an order of magnitude or more when the markers are at different frequencies. Note that in all the studies cited above, the signals (or gaps) occurred at expected spectral locations. The situation is different when a signal has unexpected spectral (Greenberg and Larkin, 1968; Scharf *et al.*, 1987) or temporal (Wright and Dai, 1994) characteristics. However, in the case of all between-channel gap-detection studies so far undertaken, the spectral (or spatial) characteristics of both markers have not been randomized, and so can be treated as being expected by the listener.

In the Introduction, it was suggested that within-and between-channel gap detection may reflect very different detection strategies. For within-channel gap detection, with the markers at the same level, the detection of any transient (onset or offset) is sufficient to signal the presence of a gap, and no judgment of timing is necessary. Furthermore, the task can be done using a one-interval paradigm, where listeners are asked whether or not they detected a gap (He *et al.*, 1999). If the two markers are at different frequencies, transients are detectable whether a gap is present or not. Thus listeners are forced to make a judgment of timing, comparing either the two onsets or the offset of marker 1 with the onset of marker 2. This task is one of discrimination, rather than detection, and would be very difficult to perform in a one-interval paradigm without extensive prior training. This may also explain why performance deteriorates so dramatically in ''within-channel'' gap detection, when a level difference is introduced between the two otherwise identical markers.

In a study of increment and decrement detection, Oxenham (1997) suggested that onsets may provide a more salient cue than do offsets. This suggestion was made to account for the asymmetry between increment and decrement detection at very short durations, but it has some physiological support in the abundance of onset cells in the auditory system (Pickles, 1988). Onset cells are often broadly tuned, with bandwidths sometimes extending over several critical bands. This characteristic may help to explain some interesting results from the study of Formby *et al.* (1998). They found that the detection of a gap between two sinusoidal markers of equal frequency and level was impaired when an additional tone at a different frequency was gated with the second marker. In contrast, performance was hardly affected by gating an additional tone with the first marker. This suggests that the onset of the additional second marker tone made the gap more difficult to detect. It is therefore possible that the additional onset ''masked'' the onset of the second marker by stimulating neural units that would otherwise have provided information as to the presence of the gap. Similar neural mechanisms may be responsible for modulation detection interference, or MDI (Yost *et al.*, 1989).

IV. SUMMARY

In experiment 1, thresholds for detecting a gap between two broadband markers were measured for conditions in which interaural time, interaural level, or monaural across-marker level differences were introduced. Reversing the perceived lateralization of marker 2 with respect to marker 1 by varying the interaural time difference did not affect gap thresholds. Reversing the perceived lateralization by varying the interaural level difference did result in a deterioration in performance. However, the same deterioration was found in monaural conditions, when a level difference was introduced between marker 1 and marker 2. Thus perceived lateralization is neither necessary nor sufficient to produce a deterioration in gap-detection thresholds, while monaural level differences (Plomp, 1964b; Penner, 1977; Plack and Moore, 1991) are sufficient to produce as large an effect as is observed when the markers are presented from loudspeakers located on different sides of the head (Phillips *et al.*, 1998). The results do not support the idea that gap detection can be used to investigate the role of spatially tuned neural channels in temporal processing (Phillips *et al.*, 1998; Boehnke and Phillips, 1999; Phillips, 1999).

In experiment 2, the effect on gap detection of using harmonic-complex markers with different spectral envelopes or fundamental frequencies was investigated using complexes consisting of only high, unresolved harmonics. Changing the fundamental frequency across the gap significantly increased thresholds, but changes in the spectral envelope produced a larger deterioration in thresholds. This suggests that the initial frequency-to-place mapping in the cochlea is dominant in determining gap-detection thresholds for dissimilar markers, while temporal coding plays a secondary role (Vliegen *et al.*, 1999).

ACKNOWLEDGMENTS

This work was supported by NIH/NIDCD Grants Nos. R01 DC 00187 and R01 DC 03909 and was carried out while the author was at the Institute of Hearing, Speech, and Language at Northeastern University, Boston, MA. Karen Stafford assisted in collecting the data. Mary Florentine, Craig Formby, Dennis Phillips, and Chris Plack provided helpful comments on previous versions of this manuscript.

[1]Dichotic presentation, where the markers are presented to separate ears, may be regarded as ''between-channel,'' even if the two markers have the same spectral content, because separate peripheral pathways are being activated by the two markers.

Abel, S. M. (**1972**). ''Discrimination of temporal gaps,'' J. Acoust. Soc. Am. **52**, 519–524.

Blauert, J. (**1997**). *Spatial Hearing: The Psychophysics of Human Sound Localization* (MIT, Cambridge).

Boehnke, S. E., and Phillips, D. P. (**1999**). ''Azimuthal tuning of human perceptual channels for sound location,'' J. Acoust. Soc. Am. **106**, 1948–1955.

Brainard, M. S. (**1994**). ''Neural substrates of sound localization,'' Curr. Opin. Neurobiol. **4**, 557–562.
Buus, S., and Florentine, M. (**1985**). ''Gap detection in normal and impaired listeners: The effect of level and frequency,'' in *Time Resolution in Auditory Systems*, edited by A. Michelsen (Springer, New York).
Buus, S., Muesch, H., and Florentine, M. (**1998**). ''On loudness at threshold,'' J. Acoust. Soc. Am. **104**, 399–410.
Chatterjee, M., Fu, Q. J., and Shannon, R. V. (**1998**). ''Within-channel gap detection using dissimilar markers in cochlear implant listeners,'' J. Acoust. Soc. Am. **103**, 2515–2519.
Culling, J. F., and Summerfield, Q. (**1995**). ''Perceptual separation of concurrent speech sounds: Absence of across-frequency grouping by common interaural delay,'' J. Acoust. Soc. Am. **98**, 785–797.
Darwin, C. J., and Carlyon, R. P. (**1995**). ''Auditory organization and the formation of perceptual streams,'' in *Handbook of Perception and Cognition*, edited by B. C. J. Moore (Academic, San Diego), Vol. 6.
Deutsch, D. (**1974**). ''An auditory illusion,'' Nature (London) **251**, 307–309.
Deutsch, D. (**1975**). ''Two-channel listening to musical scales,'' J. Acoust. Soc. Am. **57**, 1156–1160.
Eddins, D. A., Hall, J. W., and Grose, J. H. (**1992**). ''Detection of temporal gaps as a function of frequency region and absolute noise bandwidth,'' J. Acoust. Soc. Am. **91**, 1069–1077.
Fitzgibbons, P. J., Pollatsek, A., and Thomas, I. B. (**1974**). ''Detection of temporal gaps within and between perceptual tonal groups,'' Percept. Psychophys. **16**, 522–528.
Formby, C., and Forrest, T. G. (**1991**). ''Detection of silent temporal gaps in sinusoidal markers,'' J. Acoust. Soc. Am. **89**, 830–837.
Formby, C., Sherlock, L. P., and Li, S. (**1998**). ''Temporal gap detection measured with multiple sinusoidal markers: Effects of marker number, frequency, and temporal position,'' J. Acoust. Soc. Am. **104**, 984–98.
Forrest, T. G., and Formby, C. (**1996**). ''Temporal gap detection thresholds in sinusoidal markers simulated with a single-channel envelope detector,'' Aud. Neurosci. **3**, 21–33.
Forrest, T. G., and Green, D. M. (**1987**). ''Detection of partially filled gaps in noise and the temporal modulation transfer function,'' J. Acoust. Soc. Am. **82**, 1933–1943.
Glasberg, B. R., and Moore, B. C. J. (**1992**). ''Effects of envelope fluctuations on gap detection,'' Hear. Res. **64**, 81–92.
Goldstein, J. L. (**1967**). ''Auditory nonlinearity,'' J. Acoust. Soc. Am. **41**, 676–689.
Green, D. M., and Forrest, T. G. (**1989**). ''Temporal gaps in noise and sinusoids,'' J. Acoust. Soc. Am. **86**, 961–970.
Greenberg, G. S., and Larkin, W. D. (**1968**). ''Frequency-response characteristics of auditory observers detecting signals of a single frequency in noise: The probe-signal method,'' J. Acoust. Soc. Am. **44**, 1513–1523.
Grose, J. H. (**1991**). ''Gap detection in multiple narrow bands of noise as a function of spectral configuration,'' J. Acoust. Soc. Am. **90**, 3061–3068.
Grose, J. H., and Hall, J. W. (**1988**). ''Across-frequency processing in temporal gap detection,'' in *Basic Issues in Hearing*, edited by H. Duifhuis, H. P. Wit, and J. P. Horst (Academic, New York).
Grose, J. H., Hall, J. W., and Buss, E. (**1999**). ''Modulation gap detection: Effects of modulation rate, carrier separation, and mode of presentation,'' J. Acoust. Soc. Am. **106**, 946–953.
Hall, J. W., Grose, J. H., and Joy, S. (**1996**). ''Gap detection for pairs of noise bands: Effects of stimulus level and frequency separation,'' J. Acoust. Soc. Am. **99**, 1091–1095.
Hanekom, J., and Shannon, R. V. (**1998**). ''Gap detection as a measure of electrode interaction in cochlear implants,'' J. Acoust. Soc. Am. **104**, 2372–2384.
He, N., Horwitz, A. R., Dubno, J. R., and Mills, J. H. (**1999**). ''Psychometric functions for gap detection in noise measured from young and aged subjects,'' J. Acoust. Soc. Am. **106**, 966–978.
Heinz, M. G., Goldstein, M. H., and Formby, C. (**1996**). ''Temporal gap detection thresholds in sinusoidal markers simulated with a multi-channel, multi-resolution cochlear model,'' Aud. Neurosci. **3**, 35–56.
Houtsma, A. J. M., and Smurzynski, J. (**1990**). ''Pitch identification and discrimination for complex tones with many harmonics,'' J. Acoust. Soc. Am. **87**, 304–310.
Langner, G. (**1992**). ''Periodicity coding in the auditory system,'' Hear. Res. **60**, 115–142.
Moore, B. C. J., Peters, R. W., and Glasberg, B. R. (**1993**). ''Detection of temporal gaps in sinusoids: Effects of frequency and level,'' J. Acoust. Soc. Am. **93**, 1563–1570.
Moore, D. R. (**1991**). ''Anatomy and physiology of binaural hearing,'' Audiology **30**, 125–134.
Oxenham, A. J. (**1997**). ''Increment and decrement detection in sinusoids as a measure of temporal resolution,'' J. Acoust. Soc. Am. **102**, 1779–1790.
Oxenham, A. J., and Moore, B. C. J. (**1994**). ''Modeling the additivity of nonsimultaneous masking,'' Hear. Res. **80**, 105–118.
Penner, M. J. (**1977**). ''Detection of temporal gaps in noise as a measure of the decay of auditory sensation,'' J. Acoust. Soc. Am. **61**, 552–557.
Phillips, D. P. (**1999**). ''Auditory gap detection, perceptual channels, and temporal resolution in speech perception,'' J. Am. Acad. Audiol. **10**, 343–354.
Phillips, D. P., Hall, S. E., Harrington, I. A., and Taylor, T. L. (**1998**). '' 'Central' auditory gap detection: A spatial case,'' J. Acoust. Soc. Am. **103**, 2064–2068.
Phillips, D. P., Taylor, T. L., Hall, S. E., Carr, M. M., and Mossop, J. E. (**1997**). ''Detection of silent intervals between noise activating different perceptual channels: Some properties of central auditory gap detection,'' J. Acoust. Soc. Am. **101**, 3694–3705.
Pickles, J. O. (**1988**). *An Introduction to the Physiology of Hearing* (Academic, London).
Plack, C. J., and Moore, B. C. J. (**1991**). ''Decrement detection in normal and impaired ears,'' J. Acoust. Soc. Am. **90**, 3069–3076.
Plomp, R. (**1964a**). ''The ear as a frequency analyzer,'' J. Acoust. Soc. Am. **36**, 1628–1636.
Plomp, R. (**1964b**). ''The rate of decay of auditory sensation,'' J. Acoust. Soc. Am. **36**, 277–282.
Scharf, B., Quigley, S., Aoki, C., Peachy, N., and Reeves, A. (**1987**). ''Focused auditory attention and frequency selectivity,'' Percept. Psychophys. **42**, 215–223.
Schluach, R. S., and Hafter, E. R. (**1991**). ''Listening bandwidths and frequency uncertainty in pure-tone signal detection,'' J. Acoust. Soc. Am. **90**, 1332–1339.
Smoorenburg, G. F. (**1972a**). ''Audibility region of combination tones,'' J. Acoust. Soc. Am. **52**, 603–614.
Smoorenburg, G. F. (**1972b**). ''Combination tones and their origin,'' J. Acoust. Soc. Am. **52**, 615–632.
Snell, K. B., and Hu, H. (**1999**). ''The effect of temporal placement on gap detectability,'' J. Acoust. Soc. Am. **106**, 3571–3577.
Taylor, T. L., Hall, S. E., Boehnke, S. E., and Phillips, D. P. (**1999**). ''Additivity of perceptual channel-crossing effects in auditory gap detection,'' J. Acoust. Soc. Am. **105**, 563–566.
Vliegen, J., Moore, B. C. J., and Oxenham, A. J. (**1999**). ''The role of spectral and periodicity cues in auditory stream segregation, measured using a temporal discrimination task,'' J. Acoust. Soc. Am. **106**, 938–945.
Vliegen, J., and Oxenham, A. J. (**1999**). ''Sequential stream segregation in the absence of spectral cues,'' J. Acoust. Soc. Am. **105**, 339–346.
Williams, K. N., and Perrott, D. T. (**1972**). ''Temporal resolution of tonal pulses,'' J. Acoust. Soc. Am. **51**, 644–647.
Wright, B. A., and Dai, H. (**1994**). ''Detection of unexpected tones with short and long durations,'' J. Acoust. Soc. Am. **95**, 931–938.
Yost, W. A., Sheft, S., and Opie, J. (**1989**). ''Modulation interference in detection and discrimination of amplitude modulation,'' J. Acoust. Soc. Am. **86**, 2138–2147.

Multichannel speech intelligibility and talker recognition using monaural, binaural, and three-dimensional auditory presentation

Rob Drullman[a] and Adelbert W. Bronkhorst
TNO Human Factors Research Institute, Department of Perception, P.O. Box 23, 3769 ZG Soesterberg, The Netherlands

(Received 13 January 1999; revised 19 July 1999; accepted 17 December 1999)

In a 3D auditory display, sounds are presented over headphones in a way that they seem to originate from virtual sources in a space around the listener. This paper describes a study on the possible merits of such a display for bandlimited speech with respect to intelligibility and talker recognition against a background of competing voices. Different conditions were investigated: speech material (words/sentences), presentation mode (monaural/binaural/3D), number of competing talkers (1–4), and virtual position of the talkers (in 45°-steps around the front horizontal plane). Average results for 12 listeners show an increase of speech intelligibility for 3D presentation for two or more competing talkers compared to conventional binaural presentation. The ability to recognize a talker is slightly better and the time required for recognition is significantly shorter for 3D presentation in the presence of two or three competing talkers. Although absolute localization of a talker is rather poor, spatial separation appears to have a significant effect on communication. For either speech intelligibility, talker recognition, or localization, no difference is found between the use of an individualized 3D auditory display and a general display. © *2000 Acoustical Society of America.* [S0001-4966(00)01104-3]

PACS numbers: 43.66.Pn, 43.66.Qp, 43.72.Kb [DWG]

INTRODUCTION

In various communication systems, such as those used for teleconferencing, emergency telephone systems, aeronautics, and (military) command centers, there may be a need to monitor several channels simultaneously. Conventional systems present speech over one or two channels, which may lead to reduced intelligibility in critical situations, i.e., when more than two talkers are talking at the same time. Alternatively, the signals can be presented by means of a 3D auditory display, where sounds presented over headphones are filtered binaurally in such a way that they seem to originate from virtual sources in a space around the listener. As in normal (nonheadphone) listening, the capacities of the human auditory system are used much better with such a 3D system, particularly with respect to sound localization and spatial separation. Spatial separation of the voices improves speech perception (''cocktail party effect,'' cf. Cherry, 1953) and may also facilitate the identification of the talkers.

Spatialized or 3D audio over headphones is obtained by filtering an incoming signal according to head-related transfer functions (HRTFs). These transfer functions are an essential part of a 3D auditory display, because they simulate the acoustic properties of the head and ears of the listener, on which spatial hearing is based. HRTFs are essentially a set of filter pairs that contain the directional information of the sound source as it reaches the listener's eardrums. When listening over headphones, substituting the transfer from headphone to eardrums by the HRTFs results in the perception of a virtual sound outside the head of the listener. Thus, an external sound source can be simulated for any direction for which the HRTFs exist.

Several studies on the efficacy of 3D auditory displays for speech communication have shown positive results. These results were obtained by both HRTF processing and more generic binaural listening techniques. Bronkhorst and Plomp (1992) used artificial-head (KEMAR) recordings of short sentences in frontal position and temporally modulated speech noise (simulating competing talkers) at various other azimuths in the horizontal plane. They evaluated intelligibility in terms of the speech-reception threshold (SRT), i.e., the speech-to-noise ratio needed for 50% intelligibility. For normal-hearing listeners, the gain occurring when one to six noise maskers were moved from the front to positions around the listener varied from 1.5 to 8 dB, depending on the number of maskers and on their positions.

Begault and Erbe (1994) used nonindividualized HRTF filtering for spatializing four-letter words (''call signs'') against a background of diotic multitalker babble. With naive listeners, an advantage of up to 6 dB in SRT was found for 3D presentation (60 and 90° azimuths) compared with diotic presentation. In a subsequent study, Begault (1995) used words against diotic speech noise. Again, at ±90° azimuth an average advantage of 6 dB in SRT *re* diotic presentation was found. Ricard and Meirs (1994) used nonindividualized HRTFs to measure the SRT of synthetic speech in the horizontal plane against a bandlimited white-noise masker in frontal position. They found an average maximum threshold decrease of 5 dB when the speech source was shifted to ±90° azimuth.

The question how intelligibility is affected when multiple talkers are presented at different (virtual) positions, in a

[a]Electronic mail: drullman@tm.tno.nl

way that each talker could be understood *per se*—a situation different and presumably more difficult than using noise as masker—was recently studied by a number of authors. Crispien and Eherenberg (1995) used HRTF filtering for four concurrent talkers, each at a different azimuth and elevation, pronouncing short sentences. While listeners knew the position of the desired talker and the same stimuli were presented three times, the intelligibility scores for words (not entire sentences) were on average 51%. In a simulated cocktail party situation, Yost *et al.* (1996) used bandlimited speech (words) uttered by up to three simultaneous talkers. Speech was presented over seven possible loudspeakers in a front semicircle around either a human listener, a single microphone, or a KEMAR. With three concurrent talkers, average word intelligibility for all utterances together were similar (about 40%) for live listening and listening to KEMAR recordings, whereas monaural listening scored only 18%. Peissig and Kollmeier (1997) measured subjective SRTs with HRTF filtering for sentences at 0°, masked by maximally three concurrent talkers at various azimuths. For normal-hearing listeners the maximum gains relative to presenting all talkers at 0° were 8 and 5 dB, for conditions with two and three competing talkers, respectively. Ericson and McKinley (1997) measured sentence intelligibility for two and four concurrent talkers in pink noise (65 and 105 dB SPL respectively), using a speech-to-noise ratio of 5–10 dB. Subjects had to reproduce sentences that contained a certain call sign (i.e., the talker to monitor was not fixed). Diotic, dichotic, and directional presentations (KEMAR recordings in the horizontal plane) were compared. With two talkers, scores were more than 90% for both dichotic and directional presentation when the two talkers were separated by at least 90°. With four talkers and low-level noise, the advantage from directional over diotic presentation with a mixed group of male and female talkers was maximally about 30% (90° separation of the talkers). Finally, Hawley *et al.* (1999) used up to four concurrent sentences from one talker presented over either loudspeakers or headphones (KEMAR recordings) in seven azimuths in the front horizontal plane. The azimuth configurations varied by taking different minimum angles between target and nearest competing speech. When all sentences originated from different positions, keyword scores for three competing sentences varied from about 65% (nearest competing sentence 30–90° from target) to about 90% (nearest competing sentence 120° or more from target).

In the present study, two types of speech material were used (words, sentences), spoken by up to five concurrent talkers, and the virtual positions of the talkers in the horizontal plane were varied systematically. The listener's task was to attend to a single target talker in the presence of one or more competing talkers. Presentation of the speech signals was done monaurally, binaurally, or via 3D audio. In addition, two modes of 3D presentation were used: one with individualized HRTFs and one with general HRTFs. Individualized HRTFs were adapted to the specific acoustic characteristics of the individual listener and had to be measured for each person, whereas general HRTFs were obtained from just one person and were used by all listeners. Several studies (Wightman and Kistler, 1989b; Wenzel *et al.*, 1993; Bronkhorst, 1995) have demonstrated that individualized HRTFs—and individualized headphone calibration (Pralong and Carlile, 1996)—are important for correct localization of virtual sound sources, but their use may be less relevant for speech intelligibility (cf. Begault and Wenzel, 1993).

Apart from speech intelligibility, two more aspects were investigated in this study, *viz.*, talker recognition and talker localization. These points are relevant within certain contexts (e.g., teleconferencing, military communication), as it is not only important to know *what* is being said, but also *who* and *where* the talker is. Except for Pollack *et al.* (1954), who used different combinations of two concurrent talkers, there has not to our knowledge been any study on the effect of multiple talkers on talker identification or verification, either with humans or machines.

In summary, the present study extends the approaches taken by previous studies with multiple talkers in a number of ways: (1) two types of speech material were employed to measure intelligibility; (2) testing was done with both individualized and general HRTFs (most of the earlier studies used KEMAR); (3) monaural (monotic) and binaural (dichotic) conditions were studied in addition to 3D conditions; and (4) talker recognition and talker localization were measured in addition to speech intelligibility.

Many of the applications employed for 3D audio, as mentioned in the first paragraph, make use of radio or telephone communication. Hence, listeners hear the speech signals through a limited bandwidth. Begault (1995) has shown positive results of 3D audio for both full (44.1-kHz sampling) and low (8-kHz sampling) bandwidth systems. Yost *et al.* (1996) used utterances low-pass filtered at 4 kHz. In order to obtain a reliable estimate of the performance of a 3D auditory display in critical situations, all speech signals in the present experiments were bandlimited to 4 kHz. This was the only restriction to the signals; no extra deteriorating effects such as speech coding were used.

I. HEAD-RELATED TRANSFER FUNCTIONS

A. Measurement of individual HRTFs

Prior to the speech intelligibility and talker recognition experiments, the HRTFs of each individual subject were measured. The HRTF measurement setup is situated in an anechoic room and consists of a chair for the subject and a rotatable arc with a movable trolley on which the sound source is mounted. The source is a Philips AD 2110/SQ8 midrange tweeter with a frequency transfer of 0.25–20 kHz. The distance from the source to the center of the arc is 1.14 m. The stimulus is a computer-generated time-stretched pulse (Aoshima, 1981), equalized to compensate for the nonlinear response of the tweeter.

The sound reaching the subject's ears was recorded by two miniature microphones (Sennheiser KE-4-211-2) in a foam earplug and inserted into the ear canals. This blocked-ear-canal method is different from measurements with miniature probe microphones (open-ear-canal measurement), where the sound is recorded close to the eardrum. Generally, either method can give good localization performance

(Wightman and Kistler, 1989a; Pralong and Carlile, 1994; Bronkhorst, 1995; Pösselt *et al.*, 1986; Møller *et al.*, 1995; Hartung, 1995). An advantage of the blocked-ear-canal method is the stability of the microphone position during the entire measuring process (including the subsequent headphone measurement), and a better signal-to-noise ratio for high frequencies compared to using probe microphones.

A subject was seated on the chair in the center of the arc (reference position). In order to assure the stability of the positions measured, head movements were monitored with a head tracker (Polhemus ISOTRAK). If the deviation from the reference position was more than 1 cm or 5°, the subject was instructed (by means of auditory feedback) to adjust his/her position. Angular deviations smaller than 5° were compensated for by adjusting the position of the sound source.

A total of 965 positions were measured (more than strictly needed for the present experiments), evenly divided over 360° azimuth and all elevations above −60° (60° below the horizontal plane), with a resolution of 5–6°. The test signal was generated and recorded at a sampling rate of 50 kHz (antialias filter at 18.5 kHz, 24 dB/oct roll-off) by a PC board with two-channel AD/DA and a DSP32C floating-point processor. The signal had a duration of 10.2 ms, and a time window was used in order to eliminate reflections. The level of the signals at the reference position was 70 dBA. The average of 50 signals per direction (played with 25-ms intervals in one measurement) was adopted as the HRTF of each ear.

After the free-field measurements the transfer function of the sound presented through headphones (Sennheiser HD 530) was determined. As the transfer from headphone to ear is somewhat dependent on the specific placement of the headphone on the subject's head, ten headphone measurements were performed and the average (calculated in the dB domain) was adopted as the headphone-transfer function.

For the implementation in the 3D auditory display, the free-field HRTFs for each subject were deconvolved by his/her headphone transfer function and adapted to the sampling rate of 12.5 kHz to be used in the listening experiments. Each HRTF was defined as a 128-tap convolution finite impulse response (FIR) filter.

B. General HRTFs

One of the goals of the present study was to assess the effect of the use of individualized HRTFs versus nonindividualized (general) HRTFs for speech intelligibility and talker recognition. Therefore, prior to the formal perceptual experiments described below, a pilot experiment was carried out in order to find the best general HRTF set among a set of eight (i.e., HRTFs from eight different persons). The selection was based on a relatively difficult localization task, presenting four directions on the left and four directions on the right that lie approximately on the cone of confusion, at a virtual distance of 1.14 m (the same task was used by Bronkhorst, 1995). Using computer-generated pink noise stimuli (50-kHz sampling, 18-kHz bandwidth, 500-ms duration), eight subjects had to indicate the direction of the stimuli by pressing labeled buttons on a hand-held box. The subjects were different from the persons whose HRTFs were used, and also different from those who participated in the listening experiments described in Secs. II and III. The results (in terms of absolute scores) showed the best set to have on average 53% correct localization. This was not significantly higher than the other seven, but it did have a significantly lower rate of front–back confusions. As a consequence, these HRTFs were selected as the general HRTFs to be used in the subsequent experiments. As with the individualized HRTFs, the general set was implemented as FIR filters with 128 taps at 12.5-kHz sampling frequency.

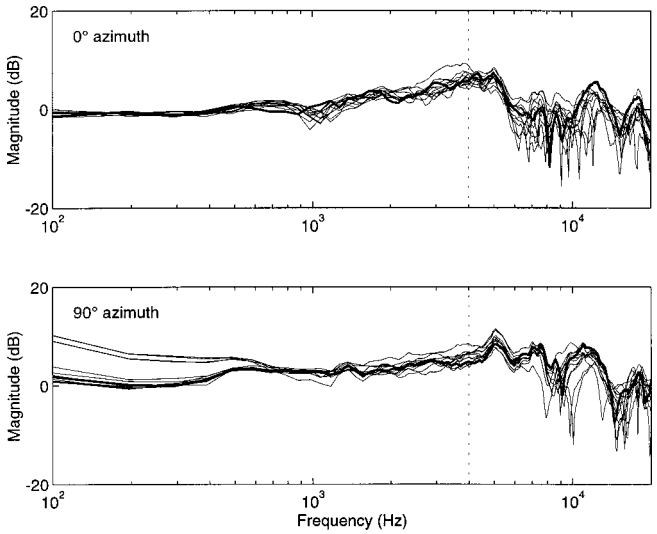

FIG. 1. Examples of 12 individual HRTFs (thin lines) and the general HRTF (heavy line) for the right ear in two different azimuth angles. The dotted vertical line marks the upper frequency of 4 kHz employed in the present study.

Figure 1 gives examples of the individual HRTFs of the 12 subjects that were used in the listening experiments (Secs. II and III) and of the general HRTF. The two panels refer to two different azimuths in the horizontal plane. Particularly up to 4 kHz (the upper frequency in the experiments), all HRTFs are quite similar.

II. SPEECH INTELLIGIBILITY IN A MULTITALKER ENVIRONMENT

A. Speech material

The experiment on the effect of presentation mode on speech intelligibility consisted of two parts: one with monosyllabic words and one with short sentences. In this way, the influence of the redundancy (absence or presence of a meaningful context) could be assessed.

1. Words

The word material consisted of 192 meaningful Dutch consonant–vowel–consonant (CVC)-syllables (Bosman, 1989). Recordings of the CVC syllables were made with four male talkers and one female talker (25–45 years old). The recordings were made on digital audiotape (DAT) in an anechoic room. One of the male talkers was used as target talker throughout the experiment, i.e., it was the task of the subjects to understand what he said. The other talkers were

competing talkers. Target and competing speech were always selected from the same set of CVC syllables.

The digital output from the DAT was stored via an Ariel DAT link into separate computer files (48-kHz sampling rate, 16-bits resolution). In order to equalize the levels of the different talkers, the words were grouped in 16 lists of 12 and the A-weighted speech level of each list was determined (i.e., speech parts that were more than 14 dB below peak level were discarded, cf. Steeneken and Houtgast, 1986). As this method is not applicable for single words, the levels were calculated for 12 concatenated words. The single words were then rescaled as to have the desired speech level. Any remaining variation in level between the words is to be attributed to the normal variation found in everyday speech. Finally, the words were downsampled to 12.5 kHz (using standard MATLAB software, including appropriate low-pass filtering), and digitally low-pass filtered at 4 kHz.[1]

2. Sentences

The sentence material for the target talker consisted of 540 everyday sentences of eight to nine syllables. They were read by a trained male talker in a soundproof room, recorded directly onto computer hard disk, using a sampling rate of 44.1 kHz, with a 16-kHz antialiasing low-pass filter, and 16-bits resolution.

The sentences for the competing talkers consisted of 65 similar sentences (Plomp and Mimpen, 1979), read by three male and one female talker. Recordings of these talkers were made on DAT in a soundproof room; the single sentences were stored in separate files via DAT link. For both the target talker and the competing talkers (ages 30–45), all sentences were individually equalized with respect to speech level. Subsequently, all sentences were downsampled to 12.5 kHz and low-pass filtered at 4 kHz.

B. Experimental design

The listening experiment consisted of two identical tests, *viz.* one with the words and one with the sentences as stimuli. Either listening test was set up in order to assess the following aspects:

(1) Presentation mode, i.e., monaural, binaural, and 3D with individual or general HRTFs;
(2) Number of competing talkers;
(3) In case of 3D presentation, the positions of the target talker and the competing talker(s).

Figure 2 shows a survey of all experimental conditions. The number of competing talkers varied from one to four. In the monaural presentation, this led to four conditions. In the binaural condition a selection of six conditions was made, with two varieties in the cases of three and four competing talkers. In the 3D presentations, the possible positions of the talkers were five directions in the horizontal plane: −90°, −45°, 0°, 45°, or 90° azimuth, where a negative sign refers to the left-hand side and a positive sign to the right-hand side. Thus, the talkers were placed in a virtual space on the front horizontal semicircle around the listener. The talker's utterances were mixed for presentation to the listeners; in the case of 3D, mixing was done after filtering each source separately with the appropriate HRTF. While varying the position of the target talker, the positions of the competing talkers were chosen in such a way that the angle from target to nearest competing talker was either 45°, 90°, or 135° (in one case, 180°). Figure 2 only displays conditions where the target talker is in the right quadrant.

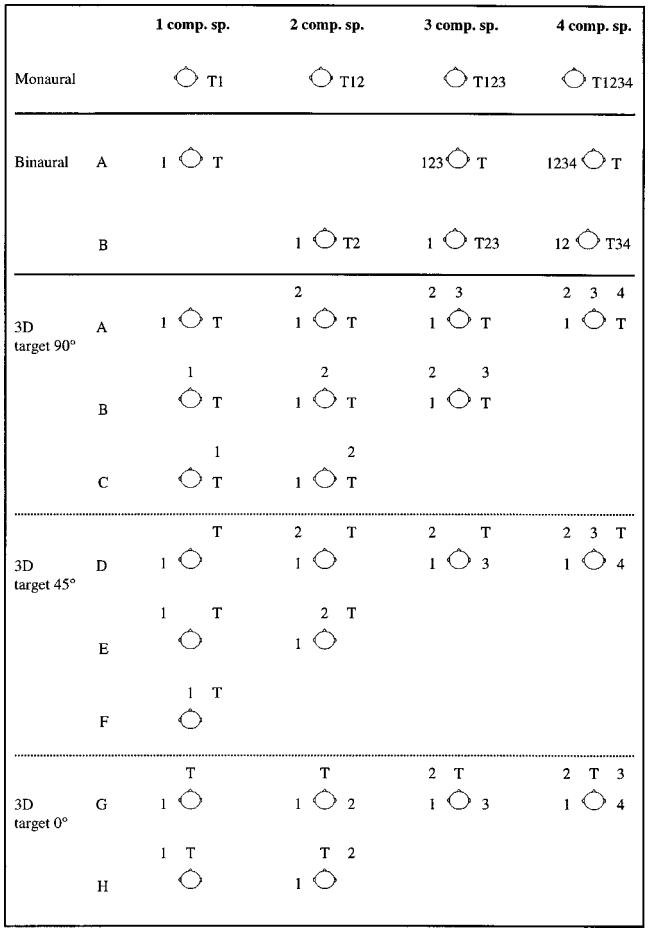

FIG. 2. Survey of the conditions for monaural, binaural, and 3D presentation (top view of subject looking ahead), with *T* as position of the target talker and 1–4 as positions of the competing talkers. Only conditions with the target talker in the frontal position or in the right quadrant are shown; conditions for the left quadrant were created by mirroring across the median axis.

In total, 4 (monaural)+6 (binaural)+22 (3D individualized HRTFs)+22 (3D general HRTFs)=54 conditions were considered per listening test. In each condition, 10 words/sentences were presented. There were not sufficient words to have a different stimulus per condition; most words were presented twice and some three times in order to meet the required 540 CVC stimuli. Single words have a low redundancy (and thus a low chance of being remembered), which is different for the sentences, of which 540 separate stimuli existed.

C. Procedure

A total of 12 students from the University of Utrecht, with ages ranging from 20 to 26 years, participated as sub-

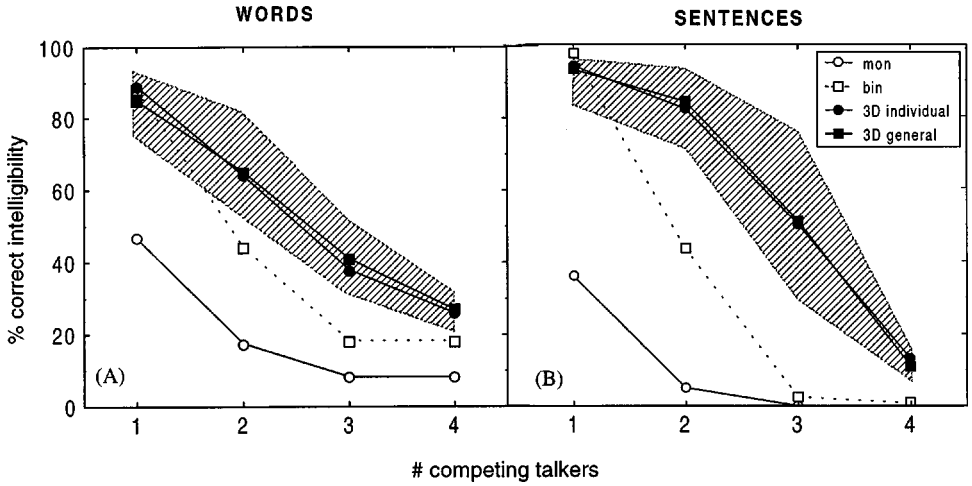

FIG. 3. Mean scores for words (panel A) and sentences (panel B) as a function of number of competing talkers, with presentation mode as a parameter. The curves for 3D give the averages of the different talker configurations; the hatched area around the 3D curves indicates the range of scores for the talker configurations (based on the pooled data for 3D with general and individual HRTFs).

jects. They did not report any hearing deficits and were not recently exposed to loud noises. The subjects were paid for their services.

Subjects were tested in a soundproof room in two sessions, one for the words and one for the sentences. Half of the subjects started with the words, the other half with the sentences. For each session and each subject a different sequence was made for the mode of presentation and talker configuration (Fig. 2). The order in which the stimuli were presented was fixed; the sequence of the presentation modes was varied according to a 4×4 Latin square, to avoid possible order and learning effects. Within each presentation mode the talker configurations were pseudorandomized, in the sense that trials with a fixed position for the target talker were presented in blocks and the number of competing talkers was assigned at random. The number of trials per block varied from 60 to 90, depending on the 3D condition (cf. Fig. 2, with ten words/sentences per condition). Competing talkers 1, 3, and 4 were men; competing talker 2 was a woman. This numbering corresponds to the order in which competing talkers were added. The words/sentences they pronounced were randomly selected in such a way that no two competing talkers pronounced the same word/sentence, which in turn were always different from the one pronounced by the target talker.

At the beginning of a block with a new position for the target talker, subjects would first hear three words/sentences from the target talker alone. This was done to make the subject aware of the target talker's position, so that he/she would focus on that voice and that position during the following trials in a block. These three words/sentences were always the same and did not occur as test trials.

Subjects received the target talker in the right quadrant in the word test and in the left quadrant in the sentence test, or vice versa. In 3D, the competing talkers could come from all directions, as shown in Fig. 2. In terms of Fig. 2, subjects got either conditions shown there or conditions mirrored across the median axis.

The stimuli were generated by two PC sound boards, each with a DSP32C processor and a two-channel DA convertor. The outputs from the sound boards were mixed (separately for left and right), led through a 4.5-kHz antialiasing low-pass filter (Krohn-Hite 3342) and presented to each subject through Sennheiser HD530 headphones. The level of presentation was approximately 65 dBA, as verified by measurements with an artificial ear (Brüel & Kjaer 4152).

Each stimulus was presented only once, and the task of the subject was to reproduce the word or the sentence of the target talker without a single error. Target talker and competing talkers started speaking at the same moment. Depending on the particular set of stimuli, the offset synchrony would vary up to a few hundred ms. No feedback as to the correctness of the subject's responses was given. Before the actual test, a practice round with 18 stimuli (from the same target talker, but with items that did not occur in the test) was presented in order to familiarize the subjects with the procedure. The practice round consisted of binaural presentations and 3D presentations with general HRTFs.

D. Results

For each condition the percentage of correctly received words/sentences was scored. Subsequent analysis of the results was done by means of an analysis of variance for repeated measures. Unless specified otherwise, tests were performed at the 5% significance level. For the sake of convenience, we will abbreviate the different conditions for monaural, binaural, and 3D presentation as mon, bin, and 3D, respectively, and write the number of competing talkers and the talker configuration in parentheses, with reference to Fig. 2. For example, mon(3) stands for monaural with 3 competing talkers; bin($4B$) stands for binaural with 4 competing talkers, configuration B; 3D($1E$) stands for 3D presentation, 1 competing talker, configuration E.

First of all, for both words and sentences there were no significant differences between the 3D conditions for individualized and general HRTFs. In view of the similarity in the HRTFs (cf. Fig. 1), this was not surprising. For the subsequent statistical analysis, the results of the two 3D presentations per condition were averaged.

Figure 3 shows the mean percentage of words (panel A) and sentences (panel B) correct for the different presentation modes as a function of the number of competing talkers. The scores decrease as the number of competing talkers increases, as expected. For binaural presentation, the results for three and four competing talkers only refer to conditions

bin(3*B*) and bin(4*B*), respectively. It appeared that bin(3*A*) and bin(4*A*) showed very high scores (at least 92% correct for words), similar to bin(1*A*). Hence, extra competing talkers in the ear opposite the target talker have no negative effect on intelligibility.

The data for 3D have been averaged over the different talker configurations. These average scores are represented by the black filled circles (individual HRTFs) or squares (general HRTFs) which are connected by a solid line. The hatched area around the 3D curves indicates the range of scores (averaged over individual and general) for the different talker configurations. On average, 3D presentation scores for sentences are 83% and 51% in case of two and three competing talkers, respectively, compared to 43% and 1% for binaural presentation.

The effects of presentation mode, number of competing talkers, and their interaction are significant. The trends for words and sentences are quite comparable: significantly higher intelligibility scores for 3D presentation, particularly with two and three competing talkers. Even with four competing talkers the benefit of 3D is there, although intelligibility remains rather low. As illustrated by the hatched areas in Fig. 3, the results with 3D presentation differ for the various talker configurations. A discussion of these results can be found in the Appendix.

III. TALKER RECOGNITION IN A MULTITALKER ENVIRONMENT

A. Speech material

The speech material for the talker-recognition experiment consisted of ten sentences which had been read out from Dutch newspaper articles by 12 male and 4 female talkers. The sentences were relatively long fragments, varying from 3.9 to 7.1 s with an average of 6.3 s. They had been recorded directly onto the computer hard disk via an Ariel Proport 565, sampled at 16 kHz with 16-bits resolution. The sentences were digitally low-pass filtered at 4 kHz and downsampled to 12.5 kHz. In the same way as for the intelligibility experiment, all sentences were equalized individually with respect to their A-weighted speech levels.

From the 12 male talkers, two were selected to be the target talkers. One of them had served as target talker of the CVC syllables in the previous intelligibility experiment. As the performance of talker recognition is expected to depend on the particular talker, the second talker was selected to have different objective (long-term average spectrum) and subjective characteristics (vocal effort, monotony, speaking rate). The target talkers read out ten extra sentences that were used to familiarize the subjects with the particular talkers ('talker-familiarization material'). These sentences were processed in the same way as the test material.

B. Experimental design

The experimental conditions were identical to those used in the intelligibility experiment. All ten sentences were used once in each condition. With respect to the relevant experimental factors employed (presentation mode, number of competing talkers, talker configuration in 3D), the question was whether the subjects could recognize the target talker and, if present, localize him among a number of concurrent talkers. The identification—or rather verification: target talker present or not—is actually no more than a simple yes/no detection task. Over all experimental conditions, six out of the ten sentences per condition were pronounced by the target talker and four by a different talker.

Apart from recognizing and localizing the target talker, the time listeners needed to come to their decision was recorded as well. In this way an extra differentiation could be made between the conditions, making it possible to test the hypothesis that 3D presentation would demand less time for recognition.

C. Procedure

The same 12 subjects as in the intelligibility experiment participated in this experiment. The order of the stimuli was randomized for each subject. The sequence of the presentation modes was varied according to 4×4 Latin squares, which were different for the two target talkers. Within each presentation mode the talker configuration and left/right presentation were randomized. As in the intelligibility experiment, competing talkers 1, 3, and 4 were men and competing talker 2 was a woman. For each trial, the male competing talkers were randomly selected from ten, the female talker from four. In the case that the target talker was not presented, a substitute was also selected out of the ten male talkers. It was not excluded that more than one talker (either target or competing talker) would pronounce the same sentence. On each trial all talkers started speaking at virtually the same time; mutual delays were within 20 ms.

The setup and equipment for generating the stimuli were the same as for the intelligibility experiment. The subject's responses were registered by means of a button box connected to a Tucker Davis PI2 module. This box had five ''target buttons'' for the five different directions and one button designated as ''not present.'' The task of the subjects was to decide whether the target talker was presented or not, and to press the appropriate button as soon as they were confident. Thus, the response/direction and the reaction time were registered for each condition. Measurement of the reaction time started at the onset of the target sentence.

The subjects were not informed about the presentation mode, nor was any feedback given as to the correctness of their response. The experiment was run in two sessions, one session per target talker. Half of the subjects started with the first target talker, the other half with the second one. Before the actual session, subjects had to listen carefully to the target talker, in order to ensure recognition of the correct talker. A voice-familiarization list of ten sentences (not included in the test) was presented twice, monaurally and via 3D with general HRTFs. After that, subjects were given a practice round of 48 sentences with competing talkers, presented binaurally and in 3D. During this practice round, feedback was given.

D. Results

As it was not the aim to draw conclusions on the recognizability of one particular talker, the data of both target

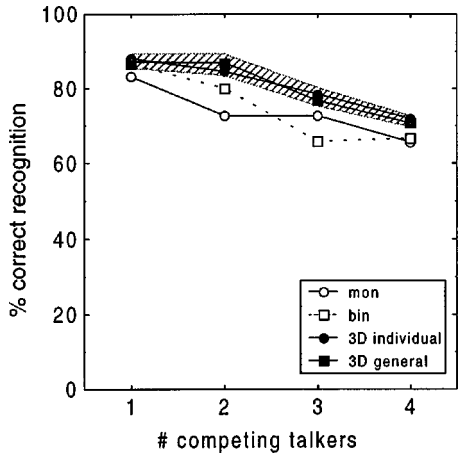

FIG. 4. Mean recognition scores for four presentation modes as a function of the number of competing talkers. The curves for 3D give the averages of the different talker configurations; the hatched area around the 3D curves indicates the range of scores for the talker configurations (based on the pooled data for 3D with general and individual HRTFs).

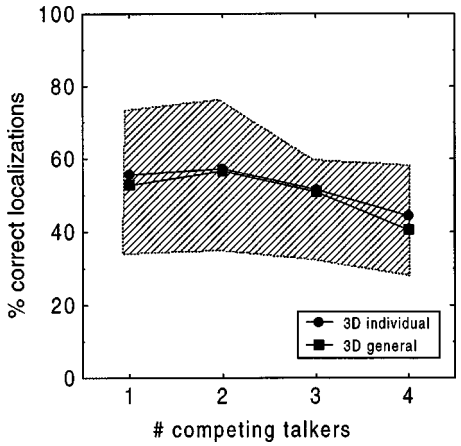

FIG. 5. Average localization scores for 3D presentation modes as a function of the number of competing talkers. The hatched area around the curves indicate the range of scores for the different talker configurations (based on the pooled data for 3D with general and individual HRTFs).

talkers were pooled before any further analysis of the results. This also has the advantage that more data points per condition were available, which increases the validity of the subsequent data processing. From the 12 subjects, one subject lost track of the target talker during the second test and one subject had been pressing continuously on one of the buttons during the first test. Their data were discarded.

1. Recognition

The examination of the recognition scores was done after the raw responses in each condition were transformed to an unbiased percentage of correct responses. This method uses the theory of signal detection (MacMillan and Creelman, 1991; Gescheider, 1997) for estimating the true recognition scores, i.e., corrected for guessing. The unbiased scores were used for the subsequent analyses of variance for repeated measures.

Figure 4 shows the recognition scores (direction not necessarily correct) for the four presentation modes as a function of the number of competing talkers. Again, as in the intelligibility experiment, the results for individualized and general HRTFs in the 3D conditions did not show a significant difference. The effects of presentation mode and number of competing talkers are significant, but their interaction is not. Compared to intelligibility (Fig. 3), the effect of competing talkers is (far) less pronounced for talker recognition. The slopes of the four curves are virtually identical. Going from one competing talker to four, the average decrease in performance is from about 88% to 69%.

Because of the virtually identical scores for the two 3D presentation modes, the results for general and individual HRTFs were pooled and the unbiased percent-correct recognition per condition was recomputed prior to the statistical analysis. Subsequent *post hoc* testing (Tukey HSD) of both factors revealed a slightly better performance for 3D than for monaural and binaural (81% vs 74/75%), and a gradual, significant decrease when going from one to two competing talkers (86% to 80%) and on to three or four competing talkers (72% or 68%). Overall, the configuration of the talkers in 3D presentation has no effect on the listeners' performance (see the Appendix).

2. Localization

In order to analyze the localization scores, only those responses were considered in which the target talker was indeed presented and recognized by the subject. Also for localization, no significant difference was found between the 3D conditions with individualized and general HRTFs, and the averages of the two were used for further analysis.

Figure 5 shows the localization performance for the 3D presentation modes as a function of the number of competing talkers. The main effect is significant, and *post hoc* analysis (Tukey HSD) revealed significantly decreasing steps going from two to four competing talkers (57% down to 43%). As with recognition (Fig. 4), the decrease in localization performance is quite gradual. Overall, the localization scores are rather poor, with relatively best performance when the target talker is at 0° azimuth (see the Appendix).

3. Reaction times

Analysis of the reaction times was performed on those responses where the target talker was indeed presented and recognized by the subject, but not necessarily correctly localized. Before going into the statistical analysis of the results, there is one aspect of the experimental design that should be mentioned first. The task given to the subjects consisted in fact of two subtasks which were executed more or less simultaneously. The subtasks were (1) recognizing the target talker and, if recognized, (2) determining his location. Pressing a button could only be done as soon as the second subtask was accomplished. In case of monaural presentation, this boils down to a simple yes/no task, since determining the location is trivial (all talkers are presented to one ear). There is a random factor of presenting the signals to the left or right ear, which would make it slightly less trivial. With binaural presentation there are three buttons to be considered (−90°, 90°, and not present), and with 3D presenta-

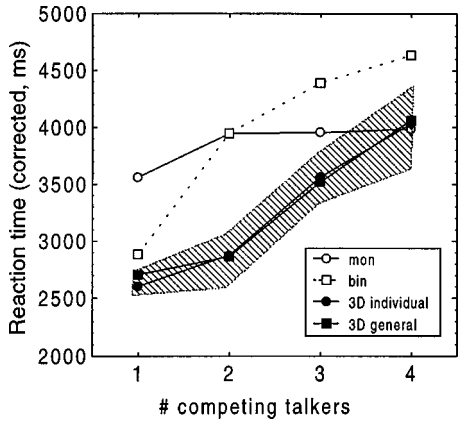

FIG. 6. Mean reaction times (with 600-ms correction for 3D) as a function of the number of competing talkers. The curves for 3D give the averages of the different talker configurations; the hatched area around the curve indicates the range of scores for the configurations (based on the pooled data for 3D with general and individual HRTFs).

tion six buttons (five directions and not present). It is known that reaction time increases as the number of response alternatives increase (cf. Wickens, 1984). This means that the reaction times of 3D will *a priori* be longer than those for monaural and binaural presentation. Therefore, no direct comparison between the three presentation modes is possible.

In order to get an estimate of the effect of having to make a choice out of two, three, or six buttons on the reaction times, a subset of the conditions was presented to six new subjects. This time the question was simply: Is the target talker present or not? The button box contained only 2 buttons assigned ''yes'' and ''no.'' Like in the original recognition test, subjects listened to the voice-familiarization sentences and got a practice round in order to familiarize themselves with the procedure. The conditions tested consisted of the following subset: mon(2), mon(4), bin(1*A*), bin(3*B*), bin(4*B*), 3D(1*A*), 3D(2*D*), 3D(2*F*), 3D(3*B*), 3D(4*A*), 3D(4*B*), and 3D(4*C*). For the 3D conditions, only those with general HRTFs were used.

The results of this experiment were compared with the results of the subset in the original experiment. It turned out that the differences in reaction times were on average 660 ms for monaural, 720 ms for binaural, and 1360 ms for 3D. These differences are merely a consequence of simplifying the task of the listener. It appears that this even applies to monaural presentation. A separate analysis of variance on the reaction-time differences showed that monaural and binaural were the same, but 3D was significantly higher. On the basis of these results, it was concluded that the *a priori* longer reaction time for 3D presentation in the original test was at least 600 ms. Therefore, 600 ms was subtracted from the original 3D results, so that the reaction time of mere recognition was obtained, and a comparison between the presentation modes could be made. The correction of 600 ms was fixed for all 3D conditions, as there was no statistical evidence that it depends on the number of competing talkers.

Figure 6 gives the corrected mean reaction times for the four presentation modes as a function of the number of competing talkers. There are significant effects of presentation mode, number of competing talkers, and the interaction between them. An analysis of the main effects per presentation mode revealed that the reaction times of binaural and 3D increase significantly as the number of competing talkers increases. Further analysis (planned comparisons) showed 3D to have the shortest reaction times for up to three competing talkers. Compared to binaural presentation with two to four competing talkers, 3D presentation gives on average 840-ms-shorter reaction times. There is hardly an effect of 3D talker configuration on the reaction times (see the Appendix).

IV. DISCUSSION

The effects of monaural, binaural, and 3D presentation of bandlimited speech were investigated with respect to intelligibility and talker recognition in situations with multiple concurrent talkers. The main question in this paper was to what extent a 3D auditory display can give benefits over monaural and binaural presentation in realistic, critical conditions. In summary, results show that for two or more competing talkers, 3D presentation yields better intelligibility than monaural and binaural presentation, and somewhat better and much faster talker recognition. Another important result is that there is no significant difference in performance between the use of individualized and nonindividualized HRTFs. This is true for all experimental findings in this paper: intelligibility, talker recognition, and talker localization. The absence of a difference is probably due to the bandlimited nature of the speech materials and, consequently, the use of low-pass filtered HRTFs. In addition, for spatial information in the horizontal plane, a detailed definition of the HRTFs is less critical for intelligibility and talker recognition. Hawley *et al.* (1999) also did not find differences between intelligibility scores of sentences presented in the front horizontal plane by means of loudspeakers or KEMAR recordings, the latter in fact being a kind of nonindividualized HRTFs. But, for localization they did find better absolute scores in the actual sound field than with virtual presentation.

A. Intelligibility

In the monaural condition with only one competing (male) talker, relatively low scores for both words and sentences are found. With an average speech-to-masker ratio of 0 dB, a score for sentences of only 36% (*all* words correct) indicates that subjects had great difficulty separating the two male voices. In a similar monaural test, Stubbs and Summerfield (1990) found a score of 57% for two concurrent male talkers. However, this score refers to the percentage of keywords reproduced correctly, not entire sentences, for which the score would clearly be lower. A keyword score of about 45% was reported by Hawley *et al.* (1999) for monaural virtual listening, i.e., monaural listening to KEMAR recordings of two concurrent sentences produced by one male talker at $\pm 90°$. Ericson and McKinley (1997) found a relatively high sentence-intelligibility score of 70%–75% for diotic presentation in pink noise [5–10 dB signal-to-noise ratio (SNR)] Festen and Plomp (1990) found an SRT for sentences of about +1 dB in the case of a male talker masked by his own voice, *viz.*, time-reversed speech. This implies a score below 50% for a speech-to-masker ratio of 0 dB. It should be noted

that much lower SRTs are normally obtained when target and competing talker are of opposite sex or when modulated noise is used (Festen and Plomp, 1990; Hygge *et al.*, 1992; Peters *et al.*, 1998). The monaural results for two and more competing talkers are consistent with the steepness of the intelligibility curve near threshold (10%–15%/dB). That is, with two competing talkers, the speech-to-masker ratio is −3 dB and the sentence score drops to 5%, eventually reducing to 0% for additional competing talkers.

The binaural curves for three and four competing talkers in Fig. 3 are based on the configuration bin($3B$) and bin($4B$), i.e., with two competing talkers at the same ear as the target talker. There is no significant difference between binaural scores for three and four competing talkers, indicating that two competing talkers instead of one at the other ear does not decrease performance. One can even state that the presence or absence of competing speech in the other ear does not influence intelligibility at all, in view of the results for the monaural conditions: comparing mon(1) with bin($2B$) and mon(2) with bin($3B$) or bin($4B$) justifies this conclusion.

We see that 3D presentation gives the highest intelligibility for more than one competing talker. For one competing talker, similar results can be obtained with binaural presentation. The findings for one and two competing speakers are essentially in agreement with results on spatial separation found by Yost *et al.* (1996) for three and two sources, respectively. Although there are situations in which binaural presentation with three or four competing talkers is superior (*viz.*, when only the target talker is presented to one ear and all competing talkers to the other ear), one can in general conclude, when drawing horizontal iso-intelligibility lines in Fig. 3, that binaural presentation with two or three competing talkers yields about the same intelligibility as 3D presentation with three or four competing talkers, respectively. So, 3D presentation allows for an extra competing talker compared to binaural presentation and for two more talkers compared to monaural presentation. Moreover, 3D presentation makes it possible to follow any of the talkers more easily (although certain azimuths have a slight advantage, see the Appendix).

In the present experimental design, the target talker and each of the competing talkers were given equal speech levels. This means that with two, three, and four competing talkers, the speech-to-masker ratio decreases, on average, by 3, 4.8, and 6 dB, respectively. Apart from the increase in background level, a second aspect plays a significant role, *viz.*, the change in spectro–temporal properties from a single voice to voice babble. Both factors increase the speech reception threshold (cf. Festen and Plomp, 1990). A number of 3D configurations of our experiment can be compared with the results for KEMAR recordings that Bronkhorst and Plomp (1992) obtained from normal-hearing subjects, i.e., their conditions with sentences presented at 0° azimuth and fluctuating speech noise at ±30° and ±90°. We used different sentence material (and a different talker) for the target speech and HRTFs instead of artificial-head filtering, but we may get some insight as to the effect of using real instead of simulated (modulated noise) speech. Correcting for the total level of competing speech, as mentioned above, Bronkhorst and Plomp found SRTs of −20.0 and −11.2 dB for configurations 3D(1G) and 3D(2G), respectively. In view of the psychometric curve of speech-to-noise ratio vs intelligibility which is also valid for fluctuating noise (Festen and Plomp, 1990), these SRTs imply sentence-intelligibility scores near 100% for equally loud target and competing speech. The scores found in the present study amount to 95% and 72%, respectively. Hence, one may tentatively conclude that having two talkers instead of noises [configuration 3D($2G$)] makes the task more difficult. This finding is corroborated when taking configuration 3D($4G$), for which Bronkhorst and Plomp (with two maskers at ±30° instead of ±45° in the present case) come to a level-corrected SRT of −4.0 dB, corresponding to a sentence intelligibility of about 65%.[2] This is much higher than the score of 16% we find with four competing talkers.

TABLE I. Comparison of the differences in scores between monaural and 3D presentation for selected conditions in the present study with the difference in estimated scores (based on differences in SRT) between frontal and spatialized presentation of KEMAR recordings in a study by Bronkhorst and Plomp (1992). Maskers refer to competing talkers or modulated noise, respectively.

			Bronkhorst and Plomp[a]	
# Maskers	Condition	Present study Diff. score	Diff. SRT (dB)	Est. diff. score
1	3D($1G$)	59%	7.0	>70%
2	3D($2G$)	67%	3.6	40%–55%
4	3D($4G$)	16%	0.9	10%–15%

[a]Differences in SRT including a 1-dB threshold increase for diotic instead of monaural presentation.

If we consider the gain of 3D compared to monaural presentation in the above three conditions, we get difference scores (for sentences) as shown in the third column of Table I. The same data for the fluctuating noise maskers of Bronkhorst and Plomp (1992) are shown relative to their conditions of frontal presentation. That is, the conditions for KEMAR recordings of all sources recorded at 0° azimuth presented binaurally to the listeners. The difference-SRT values are compensated for an assumed 1-dB gain for diotic vs monotic presentation. From these difference-SRTs, an estimate is made of the expected intelligibility score (right column), under the assumption of a slope of 10%–15% per dB. Given the differences between the two studies, variance in the data, and the assumptions made, we may conclude that the scores are more or less in line. One has to bear in mind, though, that the use of multiple fluctuating noise maskers is not always a good predictor for modeling multiple talkers, particularly when they are of the same sex. It does not account for segregation of voices and for the distraction that may occur due to simultaneous intelligibility of two or more talkers (cf. Festen and Plomp, 1990; but see Duquesnoy, 1983).

B. Talker recognition

For all presentation modes, the recognition scores depend less on the number of competing talkers than intelligi-

bility scores. The recognition scores we found for 3D presentation are slightly higher than for monaural or binaural presentation. They vary from 89% with one to 71% with four competing talkers (Fig. 4). These relatively high values indicate that talker recognition is an easier task than word or sentence reception.

Recognizing the target talker may be described as waiting for the moment that spectral and/or temporal dips occur in the competing voices. In a way this process is similar to understanding a message, but for talker recognition it may end at an earlier stage, as one does not need to capture the entire utterance of the target talker. As the number of competing talkers increases, the background level and the spectro–temporal ''filling'' increase, making recognition gradually more difficult.

While the effect of recognition *per se* (target talker present or not) appears not to be very dependent on the number of competing talkers, a different picture arises for the time needed for actual recognition (Fig. 6). For both binaural and 3D presentation, reaction times increase significantly when the number of competing talkers increases. Subjects apparently have to wait longer for the moment to ''catch a glimpse'' of the target talker. In other words, listeners still have a good chance to be sure they heard the target talker, but they take their time. The results on reaction times show there is a clear release from masking when three or more voices are spatially separated, yielding an average difference of over 800 ms compared with binaural presentation. With only one competing talker, 3D presentation with ultimate spatial separation, 3D(1*A*), does not do better than binaural presentation, bin(1*A*). The difference in reaction time of about 150 ms, as found in the original test (after 600-ms correction) and in the retest, appeared not to be statistically significant. In general, for one competing talker there is no significant difference between bin(1*A*) and the average of the 3D talker configurations (as plotted in Fig. 6).

For the monaural presentation, an asymptote in reaction time is already reached with two competing talkers. At first glance it looks like subjects probably had great difficulty recognizing the talker in these conditions and more or less ''gave up'' by pressing a button. But, this explanation is contradicted by the monaural recognition scores themselves (66% or more correct, Fig. 4), which are not significantly different from the binaural scores. An alternative explanation may be that recognition with monaural presentation involves a relatively easy task of selective attention, whereas with binaural or 3D presentation the listener uses divided attention (cf. Yost *et al.*, 1996). It should be noted that reaction times for 3D presentation found in this study underestimate those that will occur in realistic situations, since the location of the talker will then generally be known in advance.

C. Localization

Absolute localization of the target talker seems generally poor and becomes gradually more difficult as the number of competing talkers increases (Fig. 5). Having a closed-response set with five alternatives, the localization scores are on average around 50%. The finding that even for localization the use of either individualized or nonindividualized HRTFs does not yield significantly different results is not really surprising in view of the relatively low intersubject variability in HRTFs for frequencies below 4 kHz (cf. Fig. 1; see also Shaw, 1974; Møller *et al.*, 1995). The bandlimited nature of the speech signals and the consequent use of low-pass filtered HRTFs eliminates certain perceptual cues. These cues are primarily associated with the perception of elevation and externalization (cf. Bronkhorst, 1995). The former aspect is not particularly relevant in the present experiments, as all sources were presented on the horizontal plane. The latter point may however have played a role in the relatively poor localization scores, as some subjects mentioned hearing the voices close to their head and not at a distance.

Begault and Wenzel (1993) studied horizontal-plane localization of wideband speech stimuli of a single talker presented to inexperienced listeners, using nonindividualized HRTFs and open-set responses. They report that up to 46% of the stimuli were heard inside the head and found an average error angle of 28°. They conclude that most listeners can obtain useful azimuth information, the results being comparable with those for broadband noise stimuli. This conclusion was also drawn by Ricard and Meirs (1994) for synthesized, bandlimited speech, and by Gilkey and Anderson (1995), who used real sources and compared performance of speech and click stimuli. The latter study only reports left–right errors for four subjects, which were on average 16°.

In studies with simultaneous speech sources in the virtual horizontal plane, Hawley *et al.* (1999) found on average 72% correct for 2–4 concurrent sentences, having 7 response alternatives. In those experiments the listeners knew the sentence in advance and only had to pinpoint its location. In another study with bandlimited speech in the horizontal plane, Yost *et al.* (1996) had subjects localize all two or three words that were presented simultaneously. With a closed-response set of seven azimuths, scores were over 80% for two talkers and about 60% for three talkers. These are relatively high scores, but one has to keep in mind that the subjects could listen to the presentation as often as they liked. Our score of 51% (three competing talkers) seems comparatively low, but the task for our listeners was more complex, i.e., first detecting the target talker and subsequently determining his location.

In summary, localizing a target talker among a number of competing talkers when signals are bandlimited does yield relatively poor scores, but not to a dramatic extent in the light of the results reported in the literature. Besides, spatial separation as obtained in a 3D auditory display is more important for intelligibility and talker recognition than accurate localization.

V. CONCLUSIONS

From the results of the experiments in this paper, using bandlimited (4-kHz) speech signals and truncated HRTFs, the following conclusions can be drawn:

(1) There is no difference in performance between a 3D auditory display based on individualized HRTFs and general HRTFs. This conclusion applies to all scores assessed for speech intelligibility, talker recognition

(including the time required for recognition), and talker localization. This means that no individual adaptation of a bandlimited (4-kHz) communication system is needed in a practical application of an auditory display with many users.

(2) Compared to conventional monaural and binaural presentation, 3D presentation yields better speech intelligibility with two or more competing talkers, in particular for sentence intelligibility. Equivalent performance is achieved with 3D presentation compared to binaural presentation when one talker is added and compared to monaural presentation when two or three talkers are added. However, in specific conditions (all competing talkers on the side opposite the target talker) binaural presentation may be superior to 3D. Within the 3D configurations examined, intelligibility is highest when the target talker is at $-45°$ or 45° azimuth.

(3) Talker-recognition scores are higher for 3D than for monaural and binaural presentation, but the differences are small. Recognition scores depend less on the number of competing talkers than intelligibility scores. The virtual positions of the talkers in 3D are not a relevant factor.

(4) For binaural and 3D presentation, the time required to correctly recognize a talker increases with the number of competing talkers. For two or more competing talkers, 3D presentation requires significantly less time than binaural presentation.

(5) Absolute localization of a talker is relatively poor and becomes gradually more difficult as the number of competing talkers increases.

ACKNOWLEDGMENTS

This work was supported by the Royal Netherlands Navy. We wish to thank Dr. Niek Versfeld and colleagues of the Experimental Audiology Group at the ENT Department of the Free University Hospital in Amsterdam for providing part of the sentence material. The comments and suggestions of the three anonymous reviewers on earlier versions of this paper are greatly appreciated.

APPENDIX: EFFECT OF TALKER CONFIGURATION IN 3D PRESENTATION

In both the intelligibility and the recognition experiments, the configuration of the talkers in the case of 3D presentation was a factor in the design. In this Appendix we will discuss in more detail two situations with respect to the minimum angle between the target talker and the nearest competing talker, *viz.*, 90° or 45°. These conditions will be referred to as 45°-tca and 90°-tca, respectively (tca=target-competing talker angle). The second aspect in the talker configuration is the azimuth of the target talker, which could have an absolute value of 0°, 45°, or 90°. Planned comparisons at a 5% significance level were performed for the statistical analyses. Plots are shown only for the cases for which relatively substantial differences between configurations were found.

Figure A1 displays the mean scores for words and sentences, in 90°-tca and 45°-tca as a function of the azimuth of the target talker. The 90°-tca conditions only occurred with one or two competing talkers and for one azimuth (90°) with three competing talkers (filled single diamond). Both words and sentences show the same trend regarding the azimuth of the target talker. In the 90°-tca conditions with only one competing talker, the target talker's position is not relevant; with two competing talkers, a significantly worse score is found if the target talker is placed at 0°. The best target azimuth is 45°. In the 45°-tca conditions highest scores are found at 45° or 0° with one competing talker, at 45° with two competing talkers, at 45° or 0° with three competing talkers, and at any azimuth with four competing talkers. Hence, it would be best to place the target talker at 45°. Comparisons of the results of 90°-tca and 45°-tca for one and two competing talkers generally show that the scores are equal or higher for 90°-tca, depending on speech material and the azimuth of the target talker. Although there is no clear uniform result, enlarging the minimum angle between target talker and nearest competing talker can have a positive effect on speech intelligibility (cf. Peissig and Kollmeier, 1997).

For talker recognition and reaction times, no or minor effects of configuration are found, for which no plots are shown here. Only a small difference in recognition is found between 3D($3A$) and 3D($3B$). That is, when the target talker is at 90°, there is a slight benefit to have the nearest of three competing talkers 90° apart. Comparison between the 90°-tca and 45°-tca conditions for one or two competing talkers shows no significant differences. Hence, talker recognition is not critically dependent on the spatial segregation of target talker and competing talkers. As to the reaction times, only for 45°-tca with four competing talkers's a significantly shorter reaction time found for a target position of 90°. Comparison between the 90°-tca and 45°-tca conditions for one or two competing talkers shows no significant differences.

Figure A2 shows the localization scores in conditions 90°-tca and 45°-tca as a function of the azimuth of the target talker. For both 90°-tca and 45°-tca there is a significant effect of target position, with 0° giving the best performance.

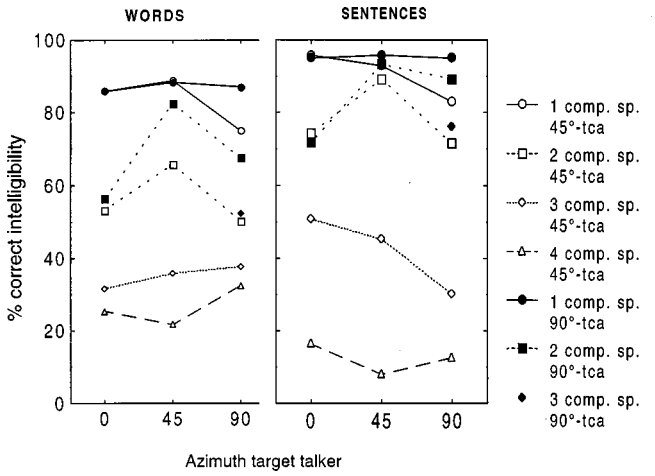

FIG. A1. Mean intelligibility scores for words and sentences as a function of the azimuth of the target talker, with number of competing talkers and 45°- or 90°-tca as parameters.

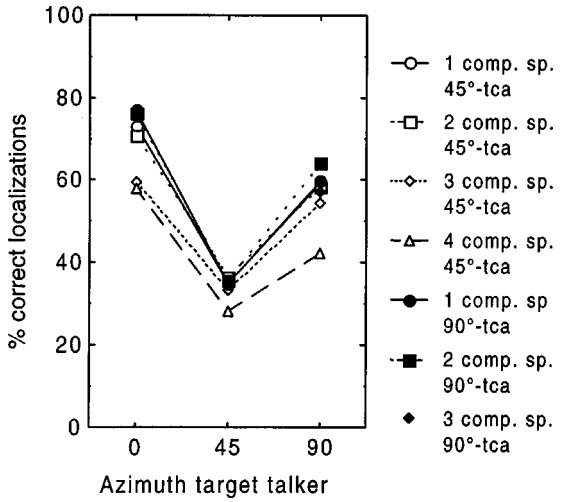

FIG. A2. Mean localization scores as a function of the azimuth of the target talker, with number of competing talkers and 45°-or 90°-tca as parameters.

The distribution of the localization errors did not show any response bias toward 0°. Comparison between the 90°-tca and 45°-tca conditions for one or two competing talkers shows no significant differences.

[1]Downsampling from 44.1 to 12.5 kHz was done by resampling with a ratio of 2/7. This actually results in a sampling rate of 12.6 kHz. Playing it at a rate of 12.5 kHz results in slight, negligible mismatch (0.8%).

[2]We assume an SRT for sentences in noise of −5 dB and a slope of the psychometric function of 15% per dB around the 50% point (Plomp and Mimpen, 1979). Hence, an SRT of −4 dB results in an intelligibility score of 65%.

Aoshima, N. (**1981**). ''Computer-generated pulse signal applied for sound measurement,'' J. Acoust. Soc. Am. **69**, 1484–1488.

Begault, D. R. (**1995**). ''Virtual acoustic displays for teleconferencing: Intelligibility advantage for telephone grade audio,'' *Audio Engineering Society 98th Convention Preprint 4008* (AES, New York).

Begault, D. R., and Wenzel, E. M. (**1993**). ''Headphone localization of speech,'' Hum. Factors **35**, 361–376.

Begault, D. R., and Erbe, T. (**1994**). ''Multichannel spatial auditory display for speech communication,'' J. Audio Eng. Soc. **42**, 819–826.

Bosman, A. J. (**1989**). ''Speech perception by the hearing impaired,'' Ph.D. dissertation, University of Utrecht.

Bronkhorst, A. W., and Plomp, R. (**1992**). ''Effect of multiple speechlike maskers on binaural speech recognition in normal and impaired hearing,'' J. Acoust. Soc. Am. **92**, 3132–3139.

Bronkhorst, A. W. (**1995**). ''Localization of real and virtual sound sources,'' J. Acoust. Soc. Am. **98**, 2542–2553.

Cherry, E. C. (**1953**). ''Some experiments on the recognition of speech, with one and with two ears,'' J. Acoust. Soc. Am. **25**, 975–979.

Crispien, K., and Ehrenberg, T. (**1995**). ''Evaluation of the cocktail-party effect for multiple speech stimuli within a spatial auditory display,'' J. Audio Eng. Soc. **43**, 932–941.

Duquesnoy, A. J. (**1983**). ''Effect of a single interfering noise or speech source on the binaural sentence intelligibility of aged persons,'' J. Acoust. Soc. Am. **74**, 739–943.

Ericson, M. A., and McKinley, R. L. (**1997**). ''The intelligibility of multiple talkers separated spatially in noise,'' in *Binaural and Spatial Hearing in Real and Virtual Environments*, edited by R. H. Gilkey and T. R. Anderson (Erlbaum, Mahwah, NJ), Chap. 32, pp. 701–724.

Festen, J. M., and Plomp, R. (**1990**). ''Effects of fluctuating noise and interfering speech on the speech reception threshold for impaired and normal hearing,'' J. Acoust. Soc. Am. **88**, 1725–1736.

Gescheider, G. A. (**1997**). *Psychophysics: The Fundamentals* (Erlbaum, Mahwah, NJ).

Gilkey, R. H., and Anderson, T. R. (**1995**). ''The accuracy of absolute localization judgments for speech stimuli,'' J. Vestib. Res. **5**, 487–497.

Hartung, K. (**1995**). ''Messung, Verifikation und Analyse von Aussenohrübertragungs-funktionen,'' in *Fortschritte der Akustik—DAGA '95* (DPG-GmbH, Bad Honnef, Germany), pp. 755–758.

Hawley, M. L., Litovsky, R. Y., and Colburn, H. S. (**1999**). ''Speech intelligibility and localization in a multi-source environment,'' J. Acoust. Soc. Am. **105**, 3436–3448.

Hygge, S., Rönnberg, J., Larsby, B., and Arlinger, S. (**1992**). ''Normal-hearing and hearing-impaired subjects' ability to just follow conversation in competing speech, reversed speech, and noise backgrounds,'' J. Speech Hear. Res. **35**, 208–215.

MacMillan, N. A., and Creelman, C. D. (**1991**). *Detection Theory: A User's Guide* (Cambridge University Press, Cambridge).

Møller, H., Sørensen, M. F., Hammershøi, D., and Jensen, C. B. (**1995**). ''Head-related transfer functions of human subjects,'' J. Audio Eng. Soc. **43**, 300–320.

Peissig, J., and Kollmeier, B. (**1997**). ''Directivity of binaural noise reduction in spatial multiple noise-source arrangements for normal and impaired listeners,'' J. Acoust. Soc. Am. **101**, 1660–1670.

Peters, R. W., Moore, B. J. C., and Baer, T. (**1998**). ''Speech reception thresholds in noise with and without spectral and temporal dips for hearing-impaired and normally hearing people,'' J. Acoust. Soc. Am. **103**, 577–587.

Plomp, R., and Mimpen, A. M. (**1979**). ''Improving the reliability of testing the speech reception threshold,'' Audiology **18**, 43–52.

Pollack, I., Pickett, J. M., and Sumby, W. H. (**1954**). ''On the identification of talkers by voice,'' J. Acoust. Soc. Am. **26**, 403–406.

Pösselt, C., Schröter, J., Opitz, M., Divenyi, P. L., and Blauert, J. (**1986**). ''Generation of binaural signals for research and home entertainment,'' in Proceedings of the 12th International Congress on Acoustics (Toronto, Canada), Vol. 1, B1–6 (Beauregard Press, Canada).

Pralong, D., and Carlile, S. (**1994**). ''Measuring the human head-related transfer functions: A novel method for the construction and calibration of a miniature in-ear recording system,'' J. Acoust. Soc. Am. **95**, 3435–3444.

Pralong, D., and Carlile, S. (**1996**). ''The role of individualized headphone calibration for the generation of high fidelity virtual auditory space,'' J. Acoust. Soc. Am. **100**, 3785–3793.

Ricard, G. L., and Meirs, S. L. (**1994**). ''Intelligibility and localization of speech from virtual directions,'' Hum. Factors **36**, 120–128.

Shaw, E. A. G. (**1974**). ''Transformation of sound pressure level from the free field to the eardrum in the horizontal plane,'' J. Acoust. Soc. Am. **56**, 1848–1861.

Steeneken, H. J. M., and Houtgast, T. (**1986**). ''Comparison of some methods for measuring speech levels,'' Report IZF 1986-20, TNO Institute for Perception, Soesterberg, The Netherlands.

Stubbs, R. J., and Summerfield, Q. (**1990**). ''Algorithms for separating the speech of interfering talkers: Evaluations with voiced sentences, and normal-hearing and hearing-impaired listeners,'' J. Acoust. Soc. Am. **87**, 359–372.

Wenzel, E. M., Arruda, M., Kistler, D. J., and Wightman, F. L. (**1993**). ''Localization using nonindividualized head-related transfer functions,'' J. Acoust. Soc. Am. **94**, 111–123.

Wickens, C. D. (**1984**). *Engineering Psychology and Human Performance* (Merrill, Columbus, OH), Chap. 10, pp. 337–376.

Wightman, F. L., and Kistler, D. J. (**1989a**). ''Headphone simulation of free-field listening: I. Stimulus synthesis,'' J. Acoust. Soc. Am. **85**, 858–867.

Wightman, F. L., and Kistler, D. J. (**1989b**). ''Headphone simulation of free-field listening: II. Psychophysical validation,'' J. Acoust. Soc. Am. **85**, 868–878.

Yost, W. A., Dye, R. H., and Sheft, S. (**1996**). ''A simulated cocktail party with up to three sound sources,'' Percept. Psychophys. **58**, 1026–1036.

Lip–jaw and tongue–jaw coordination during rate-controlled syllable repetitions

Ingo Hertrich[a] and Hermann Ackermann
Department of Neurology, University of Tübingen, Hoppe-Seyler-Str. 3, D-72076 Tübingen, Germany

(Received 21 February 1999; accepted for publication 21 January 2000)

The present study investigated the relationship between functionally relevant compound gestures and single-articulator component movements of the jaw and the constrictors lower lip and tongue tip during rate-controlled syllable repetitions. In nine healthy speakers, the effects of speaking rate (3 vs 5 Hz), place of articulation, and vowel type during stop consonant–vowel repetitions (/pa/, /pi/, /ta/, /ti/) on the amplitude and peak velocity of differential jaw and constrictor opening–closing movements were measured by means of electromagnetic articulography. Rather than homogeneously scaled compound gestures, the results suggest distinct control mechanisms for the jaw and the constrictors. In particular, jaw amplitude was closely linked to vowel height during bilabial articulation, whereas the lower lip component amplitude turned out to be predominantly rate sensitive. However, the observed variability across subjects and conditions does not support the assumption that single-articulator gestures directly correspond to basic phonological units. The nonhomogeneous effects of speech rate on articulatory subsystem parameters indicate that single structures are differentially rate sensitive. On average, an increase in speech rate resulted in a more or less proportional increase of the steepness of peak velocity/amplitude scaling for jaw movements, whereas the constrictors were less rate sensitive in this respect. Negative covariation across repetitions between jaw and constrictor amplitudes has been considered an indicator of motor equivalence. Although significant in some cases, such a relationship was not consistently observed across subjects. Considering systematic sources of variability such as vowel height, speech rate, and subjects, jaw–constrictor amplitude correlations showed a nonhomogeneous pattern strongly depending on place of articulation.
[S0001-4966(00)05204-8]

PACS numbers: 43.70.Aj, 43.70.Bk [AL]

INTRODUCTION

The concept of a ''phonetic gesture'' has been introduced as the basic functional unit of the speech motor system (Browman and Goldstein, 1986; Fowler and Saltzman, 1993). Even direct descriptions of articulatory movements in space over time, for example, in terms of measurable trajectories, were considered as the basis of phonological representations (Browman and Goldstein, 1986, p. 224). However, any definition of the functionally relevant gestures on the basis of motor data ends up with difficulties if articulation is considered in detail with respect to the complex relationships between compound gestures, on the one hand, and single-articulator movements, on the other. For example, the latter may show motor equivalence in terms of trading relations (Hughes and Abbs, 1976; Abbs, 1980; Perkell *et al.*, 1993a) and goal-directed compensation for perturbations (Abbs and Gracco, 1984; Gracco and Abbs, 1986; Munhall *et al.*, 1994; Savariaux *et al.*, 1995), that is, they seem to be linked with respect to superordinate functional aspects.

Regarding the neuronal mechanisms underlying articulation, gestures have been considered as more or less hard-wired coordinative structures (Kelso *et al.*, 1986, p. 55). While some authors subsume systems with relatively high flexibility under this concept allowing for on-line compensation for various kinds of perturbations (Kelso and Tuller, 1983, 1984; Kelso *et al.*, 1984; Saltzman, 1986), others conceive of synergies as more or less stereotypic and spatiotemporally coherent activities (Lee, 1984). Invariant scaling mechanisms can be considered a relevant criterion of neuronal synergies. For example, a largely linear relation between peak velocity and movement amplitude has been observed in compound lower lip/jaw or tongue/jaw gestures (Kuehn and Moll, 1976; Ostry and Munhall, 1985). On the basis of the mass-spring model, the slope of peak velocity/amplitude scaling can be interpreted as ''stiffness,'' representing an important control mechanism with respect to speech timing (Kelso *et al.*, 1985; Vatikiotis-Bateson and Kelso, 1993).

Both the ''motor equivalence'' and the ''coordinative structure'' view of speech motor control emphasize compound rather than component gestures to represent functional entities. In contrast, some studies provide evidence for a functional independence of the various subsystems such as the lower lip and the jaw. Whereas the constrictors (e.g., lower lip or tongue tip) primarily seem to be involved in consonant gestures, jaw opening has been supposed to represent a correlate of the syllabic sonority profile (Edwards and Beckman, 1988) and to be associated with vowel gestures (Gracco, 1994; Perkell, 1969; Tuller and Kelso, 1984). As compared to consonants, vowels, furthermore, tend to be more closely associated with opening than closing move-

[a]Electronic mail: ingo.hertrich@uni-tuebingen.de

ments (Gracco, 1994) and to be more sensitive to changes in speech rate in terms of articulatory undershoot or vowel reduction (Flege, 1988; Gay *et al.*, 1974; Gay, 1981; Lindblom, 1963; Miller, 1981).

As a consistent finding across various studies (Kelso *et al.*, 1985; Nelson *et al.*, 1984), smaller movement amplitudes have been reported under the condition of shorter movement durations. Besides aspects of physical energy (Nelson, 1983), idiosyncratic reorganization (Hughes and Abbs, 1976) as well as prosody-induced variation on a hypo–hyperarticulation scale (Vatikiotis-Bateson and Kelso, 1993) have been offered as an explanation for this phenomenon. So far, however, the differential rate effect on jaw and constrictor amplitudes has not systematically been assessed under strictly controlled rate conditions in a larger group of subjects.

During natural speech, articulatory gestures are modified by many interacting influences including various aspects of coarticulation and prosody. Due to such confounding effects, the variability of durational and displacement data thus cannot easily be decomposed into such underlying factors as phonological categories and speech rate. One possibility to assess more elementary articulatory gestures is to use simple speechlike material such as syllable repetitions instead of sentence utterances. Apart from the investigation of Westbury and Dembowski (1993), no systematic studies of multiarticulator movements during syllable repetition have been performed so far. The latter investigation, however, was designed as a maximum-rate performance test and, therefore, is supposed to document particular speaker strategies under temporal constraints rather than more general aspects of speech motor control. Furthermore, coordination of jaw, tongue, and lower lip solely was addressed in a descriptive way, and the test material (/pa/, /ta/, /ka/) only had comprised a single vowel category.

Considering the relatively weak database provided by previous studies on multiarticulator gestures, the present work aims at a further evaluation of jaw-constrictor coordination and its rate-induced changes. In order to avoid interference with higher-level effects such as linguistic boundaries, lexical stress, and sentence intonation, a syllabe repetition task comprising the stop consonant–vowel (CV) sequences /pa/, /pi/, /ta/, and /ti/ was selected as test material for the present investigation. For the sake of a quantitative assessment of speaking rate, two distinct tempo conditions (3 and 5 Hz) were induced. In particular, the following questions were addressed:

(a) Are compound gestures the result of superimposed single-articulator movements or are they controlled in a uniform way with respect to amplitude specification and peak velocity scaling?
(b) Does speech rate act as a global scaling factor or does it differentially change the characteristics of the various subsystems?
(c) Is rate-induced reduction of movement amplitudes more pronounced in vowel-related gestures as compared to consonants?
(d) Do jaw and constrictor movement amplitudes exhibit negative covariation?

I. METHODS

A. Subjects and recording procedure

Nine healthy subjects produced repetitions of the consonant–vowel sequences /pa/, /pi/, /ta/, and /ti/ each (see Footnote 1). Rates of three (slow condition) and five (fast condition) items per second were induced by binaural presentation of synthetic syllables over headphones (see Footnote 2). Articulatory movements were measured by means of electromagnetic articulography at a sampling rate of 400 Hz (EMA; AG100, Carstens Medizinelektronik, Lenglern, Germany; ten-channel system). Briefly, small transducer coils at selected fleshpoints within the midsagittal plane receive signals emitted by three transmitter coils mounted on a helmet; after demodulation, these signals are converted into two-dimensional trajectories (Gracco and Nye, 1993; Perkell *et al.*, 1992; Perkell, 1993b; Schönle, 1993; Schönle *et al.*, 1987). The present study considered seven receiver coils attached to the upper lip, lower lip, upper jaw (above the upper incisors), lower jaw (below the lower incisors), tongue tip (0.5 cm behind the tip of the tongue), tongue dorsum (about 4 cm posterior to the tongue tip), and nasion by means of a tissue glue (Histoacryl green, Braun, Melsungen, Germany). Using an additional coil, the contour of the palate was traced at the beginning of the recording session in order to have a display of this structure when monitoring the coil movements. For the purpose of the present study, only the lower lip, tongue tip, and lower jaw receivers were considered for analysis. Due to a defective sensor coil, the lower lip trajectories of subject N3 failed to be tracked. The nasion and the upper jaw receivers were used for inspection of the raw data in order to exclude major helmet displacements. Measurement accuracy amounts to about 0.5 mm under the conditions of the present study (Hertrich and Ackermann, 1997a; Hoole, 1993). In synchrony with the kinematic measurements, the acoustic signal was recorded at a sampling rate of 16 kHz. Each syllable train was repeated twice resulting in 16 ($=4$ syllables$\times 2$ rate conditions$\times 2$ repetitions) recordings. Five subjects performed a third trial of the entire material. As a rule, all subjects were able to synchronize their productions with the required rate within the first two syllables of a given train. Recording time amounted to 6 s per sweep with an intersweep interval of about 15 s. From each trial, ten syllables starting after the second syllable were considered for analysis.

B. Signal processing

Prior to parameter extraction, the kinematic signals were smoothed at 25 Hz (51-coefficient FIR low-pass hamming filter). Next, using principle component analysis, the predominant movement direction of the various articulators was determined separately for each repetition train and receiver coil (e.g., the lower lip coil during one sequence of /tatata..../). Since the speech material consisted of stop consonant–vowel sequences, the direction of the first princi-

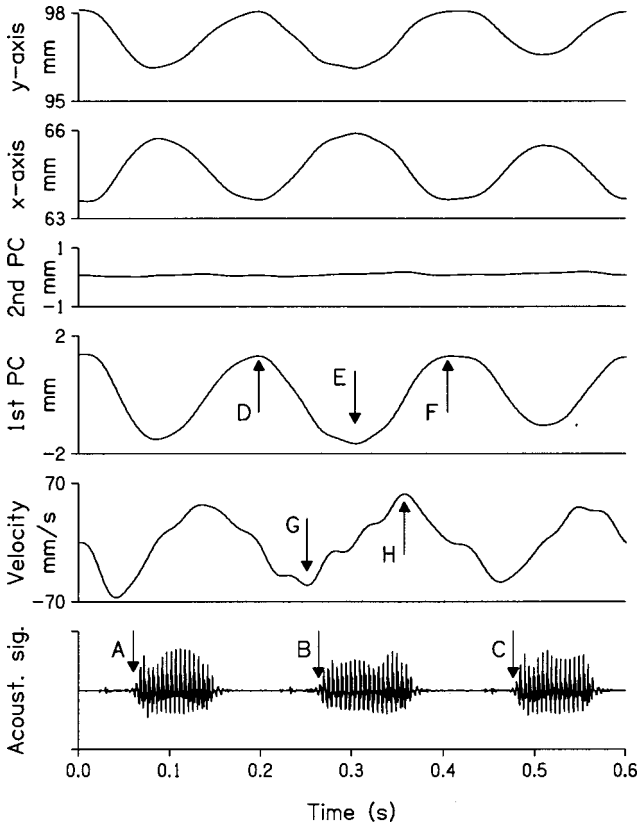

FIG. 1. Measurement of jaw displacement and peak velocity as exemplified by a /papapa/sequence at 5 Hz. The upper two panels show the original *x*- and *y*- coordinates, respectively, with reference to the EMA helmet; the fourth panel from top represents the time history of the first principal component (PC) of the original *x*/*y* data; the third panel from top displays the second principal component, that is, the movement component orthogonal to the first PC; the derivate (three-point difference) of the first PC is displayed in the fifth panel from top; the bottom panel shows the acoustic signal. Acoustic vowel onsets (A, B, C), displacement extrema (D, E, F), and velocity peaks (G, H) are marked by arrows.

pal component was assumed to reflect the oral opening and closing gestures (see Footnote 3). The projection of the original two-dimensional trajectory onto this direction provided a one-dimensional time course with the average position of a transducer during a syllable repetition train set to zero and the sign defined such that closed articulator positions had a positive value and open positions a negative value (see Fig. 1). Apart from a few trials that had to be discarded from analysis, the first principal component accounted for more than 70% of variance and showed a syllabic rhythm synchronized with the intensity contour of the acoustic signal.

In order to confine the intervals for automatic detection of displacement extrema, manual segmentation of the trajectories was performed with reference to acoustic vowel onsets. For each CV syllable, the onset of the opening gesture was defined as the highest value of the first principal component between vowel onsets of a given and the preceding syllable. The lowest value between two succeeding opening onsets was considered the closing onset. Movement amplitude was defined as the difference between two successive displacement extrema. Thus, no intermovement intervals were possible. Three-point differentiation of the time course of the first principal component yielded the velocity profile of the articulatory gestures. Peak velocity was determined as the highest absolute value of this parameter during a given opening or closing gesture (see arrows in Fig. 1 for illustration of the relevant events). Since, on average, opening and closing movements have the same size during syllable repetition, statistical analysis with respect to the movement amplitudes referred to the entire movement cycles, each defined as the mean of an opening and a following closing gesture. In contrast, when the scaling of amplitude and velocity was addressed, opening and closing movements were considered separately.

Differential constrictor values of movement amplitude and peak velocity were derived by simple subtraction of the respective jaw parameters from the compound data (see Footnote 4). The scaling of peak velocity and amplitude was assessed by linear regression for each rate condition and place of articulation. In order to obtain sufficient variability on the amplitude axis, data were pooled across the two vowels /a/ and /i/. In order to estimate the effects of vowel type, an additional analysis was performed using the simple quotient of peak velocity and amplitude (see Footnote 5).

II. RESULTS

A. Differential movement amplitude of the jaw and the constrictors

1. Analysis of variance

Evaluation of the systematic influence of place of articulation (/p/, /t/), vowel type (/a/, /i/), and rate condition (3 Hz, 5 Hz) on movement cycle amplitudes (mean of opening and closing amplitude) relied on repeated measures analyses of variance. Three ANOVAs were performed with the subject means across repetitions (see Table I) of the jaw, constrictor, and compound gesture amplitudes, respectively, entered as dependent variables (Table II). In order to compare the various effects and interactions, *F*-values may be considered a measure of effect strength in case of equal degrees of freedom. The subject means of jaw and compound amplitudes under the various conditions are displayed in Fig. 2. The jaw movements showed a predominant vowel and a minor rate effect only. Furthermore, jaw amplitudes did not differ across places of articulation and did not exhibit any significant interactions ($p>0.1$) among the factor variables. In contrast, the constrictor component amplitude failed a significant main effect of vowel type, but showed strong effects of place of articulation and speech rate as well as a vowel×place interaction. Furthermore, the interactions of vowel and speech rate as well as the three-way interaction achieved significance at the level of $p<0.05$. Considering the compound amplitude, all effects and interactions were highly significant with the exception of the place of articulation×rate interaction. The three-way interaction turned out to be the strongest effect in this data set, suggesting that the amplitude of compound trajectories is controlled in a more complex way than the excursion of its components.

In order to further analyze the observed interactions, *posthoc* ANOVAs were performed separately for each place of articulation. During /p/V articulation, jaw amplitude depended only on vowel type whereas the lower lip component

TABLE I. Subject means of jaw, constrictor, and compound movement cycle amplitudes (in mm).

		Slow			Fast		
Syllable	Speaker	Jaw	Constrictor	Compound gesture	Jaw	Constrictor	Compound gesture
/pa/	N1	1.6	5.6	7.3	2.0	4.4	6.4
	N2	4.6	6.3	10.8	3.4	5.2	8.5
	N3	…	…	…	…	…	…
	N4	2.4	8.3	10.7	5.4	3.9	9.3
	N5	4.3	7.3	11.6	3.4	5.6	9.0
	N6	1.2	6.6	7.8	1.8	3.1	4.9
	N7	5.7	4.0	9.7	4.0	3.9	7.9
	N8	5.9	8.1	14.0	4.8	5.9	10.8
	N9	3.3	5.3	8.6	2.8	5.0	7.8
Mean		3.6	6.4	10.1	3.4	4.6	8.1
/pi/	N1	0.8	7.1	7.9	0.6	5.6	6.2
	N2	1.6	7.8	9.4	0.8	6.0	6.9
	N3	…	…	…	…	…	…
	N4	0.7	9.7	10.4	1.1	6.9	8.0
	N5	1.0	7.8	8.7	1.1	5.3	6.3
	N6	0.5	7.5	8.0	0.7	2.7	3.4
	N7	3.2	4.3	7.5	1.9	2.9	4.8
	N8	1.1	8.9	9.9	1.3	6.3	7.6
	N9	0.3	7.6	7.9	0.3	7.1	7.4
Mean		1.1	7.6	8.7	1.0	5.4	6.3
/ta/	N1	3.1	6.0	9.1	2.4	4.3	6.7
	N2	7.1	4.4	11.5	4.3	2.2	6.5
	N3	3.6	4.8	8.4	1.3	2.8	4.1
	N4	4.8	4.9	9.7	1.5	5.2	6.7
	N5	3.5	9.0	12.4	3.4	3.7	7.1
	N6	3.4	7.1	10.5	4.1	0.6	4.7
	N7	4.0	5.6	9.6	3.4	4.3	7.6
	N8	8.5	3.6	12.1	3.8	2.8	6.6
	N9	5.6	4.8	10.5	3.8	2.2	6.0
Mean		4.8	5.6	10.4	3.1	3.1	6.2
/ti/	N1	1.3	2.8	4.1	0.6	3.7	4.4
	N2	2.5	1.1	3.6	1.8	0.4	2.2
	N3	0.6	3.3	3.9	0.6	2.5	3.1
	N4	1.5	1.7	3.1	1.0	0.8	1.8
	N5	0.7	3.2	3.9	0.9	1.6	2.4
	N6	0.7	6.1	6.8	0.6	3.4	3.9
	N7	2.0	2.4	4.4	1.4	2.5	3.9
	N8	1.5	3.2	4.7	1.1	2.3	3.4
	N9	2.4	2.2	4.5	1.5	2.7	4.2
Mean		1.5	2.9	4.3	1.1	2.2	3.3

showed a stronger effect of rate than of vowel. Furthermore, the latter effect exhibited an inverse pattern: the lower lip component amplitude for /i/ exceeded the one for /a/ (see group means in Table I). The compound amplitude showed a stronger effect of rate than of vowel type. No significant vowel×rate interaction was observed during /p/V articulation. Considering /t/V syllable repetitions, the jaw amplitude showed a strong vowel effect as well, but with respect to the remaining effects a somewhat different pattern emerged. Vowel type and speech rate imposed effects of comparable strength on the tongue tip component amplitude. Furthermore, the vowel×rate interactions were significant due to a nonlinearity in terms of larger rate effects in /ta/ as compared to /ti/ repetitions (see group means in Table I). This interaction was stronger in the constrictor component as compared to the jaw amplitude.

2. Individual variability

A variety of regularities emerged with respect to individual behavior (Table I): All subjects showed smaller jaw amplitudes during /i/ productions as compared to the respective /a/ items with the same place of articulation and under the same rate condition. During the slow condition, the constrictor component amplitude of /ta/ consistently exceeded the one of /ti/ productions whereas in /pa/ versus /pi/ the inverse pattern was observed. Apart from a few exceptions, the fast condition yielded a similar pattern. Compound am-

TABLE II. Repeated measures ANOVAs with respect to the influences of place of articulation (PLACE; /p/, /t/), vowel type (VOW; /a/, /i/), and syllable rate (RATE; 3 Hz, 5 Hz) on jaw, constrictor, and compound movement amplitudes.

	Jaw	Constrictor	Compound
(a) Three-way ANOVA, $F[1,8]$ values			
PLACE	2.05	18.43[a]	13.48[a]
VOW	66.25[a]	2.35	52.12[a]
RATE	6.83[b]	16.40[a]	50.32[a]
PLACE×VOW	1.02	15.75[a]	46.67[a]
PLACE×RATE	3.01	0.68	2.37
VOW×RATE	2.39	9.25[b]	16.85[a]
PLACE×VOW×RATE	2.47	6.49[b]	186.25[a]
(b) *Post hoc* analysis for /p/V articulation, $F[1,8]$ values			
VOW	44.05[a]	7.87[b]	10.88[b]
RATE	0.26	18.37[a]	43.48[a]
VOW×RATE	0.00	1.44	1.79
(c) *Post hoc* analysis for /t/V articulation ($F[1,9]$ values)			
VOW	63.61[a]	11.56[a]	80.06[a]
RATE	11.83[a]	10.14[b]	54.50[a]
VOW×RATE	5.46[b]	9.97[b]	79.26[a]

[a]Significance: $p<0.01$.
[b]Significance: $p<0.05$.

plitude was reduced in all but one (/ti/ productions of N1) fast item as compared to the slow cognates. As concerns the rate effect on the jaw and constrictor component amplitudes, consistency across subjects depended on place of articulation. During /pa/ repetitions, all subjects reduced the lower lip component under the fast condition but they were inconsistent with respect to jaw amplitude. In contrast, /ta/ utterances exhibited a more consistent rate effect on jaw amplitude as compared to the tongue tip component. Figure 3 exemplifies subject variability of differential jaw and constrictor amplitudes in three speakers. Each plot demonstrates strong influences of rate and vowel context on movement amplitudes, but the patterns differ across subjects and place of articulation. Speaker N6, for example, consistently modified jaw amplitude for vowel distinction, whereas the speech rate condition almost exclusively influenced the constrictor amplitude. A similar pattern was observed in N5's /p/V utterances, whereas this speaker's /t/V items showed vowel-induced modification of tongue tip amplitude as well. Subject N4, in contrast, exhibited considerable jaw amplitude overlap between fast /ta/ and /ti/ items, but a complete separation in the tongue tip component. During labial articulation, this subject used a different strategy, producing an even enlarged /a/–/i/ distinction in jaw amplitude under the 5-Hz condition as compared to the 3-Hz condition. Similar variability as shown in Fig. 3 could be observed for the remaining subjects not displayed here.

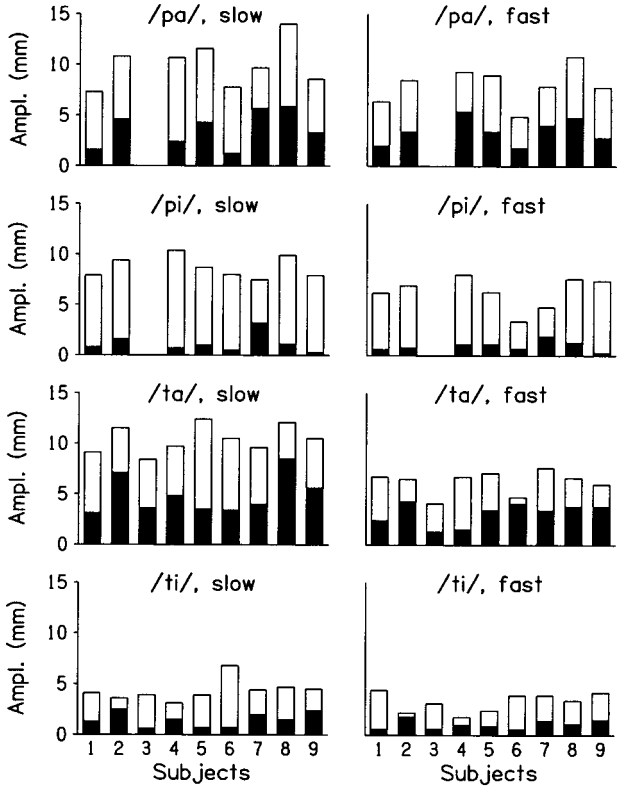

FIG. 2. Subject means of movement cycle amplitudes under the various conditions. The entire rectangles refer to the compound gestures, the jaw component is represented by the filled part of each rectangle.

3. Correlation analysis

Negative correlations between movement amplitudes of functionally complementary motor subsystems have been considered an indicator of motor equivalence. In order to obtain interpretable correlation coefficients, the nature of the variance underlying the data must be documented. In the present study, various sources of variance were tested using partial correlation analysis. The advantage of this technique is that, in order to obtain a sufficient sample size, data can be pooled across several subconditions after the particular statistical effects of these subconditions have been removed from the data set.

First, the jaw–constrictor correlations were computed for each subject separately after the systematic effects of speech rate and vowel type as well as their interaction had been removed. This was done by, first, performing a linear regression analysis of the three dummy variables VOW (/a/=0; /i/=1), RATE (slow=0; fast=1), and VOW×RATE on jaw and constrictor amplitude, respectively and, second, computing Pearson correlation coefficients from the residuals of this regression. Five of the 17 correlations shown in the upper part of Table III were significant at $p<(0.05/17)$, which is well above chance. With respect to sign, the correlation coefficients varied across subjects and place of articulation. Speaker N8, for example had positive correlations in /p/ and negative ones in /t/ utterances, whereas N9 showed the reverse tendency.

In a second step, a similar correlation analysis was performed with the subject means of jaw and constrictor amplitudes. Again, the main effects and interaction of speech rate and vowel category were partialled out, leaving intersubject variability as the residual source of variance. If all subjects organized their articulation in a similar way, but differed in a global size factor (Footnote 6), we would expect strong positive correlations between jaw and constrictor amplitude. In contrast, if subjects were comparable in the size of their

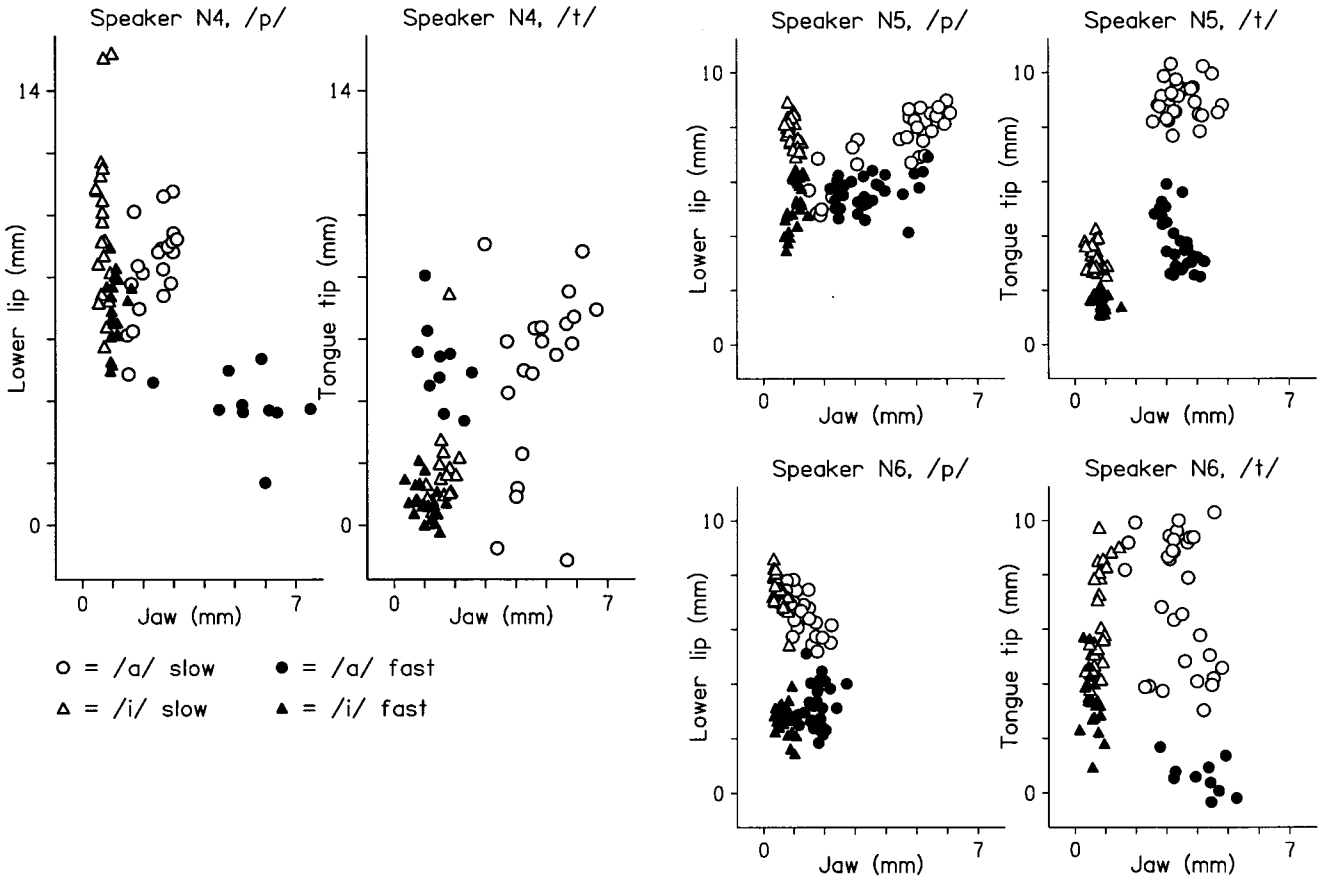

FIG. 3. Lower lip and tongue tip component movement amplitudes, respectively, plotted against jaw amplitude from three subjects. Each symbol represents a single movement cycle (mean of opening and closing amplitude).

compound trajectories, but used different strategies with respect to constrictor and jaw contribution, correlations would be strongly negative. As shown in the lower part of Table III, correlation across subjects tended to be negative and was significant for /t/ articulation, in spite of considerable compound amplitude differences across subjects (see Table I).

Two further correlation analyses of jaw and constrictor amplitude were performed with (a) vowel type and (b) speech rate as source of variability, respectively. In these analyses, subject variability, rate or vowel, and the subject×vowel or subject×rate interaction, respectively, were partialled out. Positive jaw–constrictor correlations

TABLE III. Correlation between jaw and constrictor amplitude in relation to various sources of variance. All systematic sources of variance not specified in the left column have been partialled out prior to computation of Pearson correlations.

Source of variance	Place of articulation			
	/p/		/t/	
	d.f.	*r*	d.f.	*r*
Repetitions, N1	80	−0.27	70	−0.08
N2	80	0.04	120	−0.46[a]
N3	⋯	⋯	110	−0.04
N4	70	0.10	70	0.21
N5	120	0.59[a]	120	−0.27
N6	110	−0.35[a]	90	−0.13
N7	80	0.30	70	−0.04
N8	110	0.53[a]	120	−0.37[a]
N9	70	−0.05	70	0.32
Subjects	32	−0.19	36	−0.62[a]
Vowel category	32	−0.70[a]	36	0.55[a]
Rate condition	32	−0.24	36	0.22

[a]Significance (a) for repetitions: $p<(0.05/17)$; for the remaining sources $p<(0.05/2)$.

would be expected if vowel type and speech rate affected both structures in terms of a common scaling parameter. In contrast, if these factors influence the two components differently, correlations would be negative. In both cases, the strength of the observed correlations depends on intersubject consistency. In case of vowel context as the source of variability, jaw–constrictor correlations were significantly negative for /p/V articulation, but significantly positive for /t/V items (Table III, second line from bottom). When syllable rate was the source of variance, the correlations showed a similar pattern, but were weaker and lacked significance (Table III, bottom line). The differences in sign indicate that the coordination between the jaw and the constrictor depends on place of articulation. In tongue tip articulation they seem to represent a synergy, whereas in bilabial articulation they show some kind of functional independence. The differences in absolute strength of the correlations between vowel- and rate-induced variability indicate that subjects were more consistent with respect to vowel effects on differential movement amplitudes as compared to rate-induced differences.

4. Comments

The results with respect to differential movement amplitudes indicate that—within some limits—the jaw and the constrictors have different functions and are independently controlled with respect to the demands of vowel context and speech rate. As concerns bilabial articulation, the compound amplitude of the lower lip trajectory could be decomposed into a rate-insensitive vowel-related jaw gesture and a rate-sensitive consonant-related lower lip constrictor component. During tongue tip articulation, the jaw showed a similar pattern with respect to vowel distinction, but interacted with the constrictor activity and seemed to be closer linked to it. The assumption that vowel gestures are predominantly reduced during fast speech cannot be corroborated on the basis of the present results. Considering jaw/constrictor covariation in movement amplitude, partial correlation analysis did not reveal consistent negative covariation across repetitions. With vowel type, syllable rate, or intersubject differences as sources of variability, the sign and significance of the computed correlation coefficients varied across these factors and interacted largely with place of articulation.

B. Dynamic movement specification

1. Individual patterns of peak velocity/amplitude scaling

On the basis of individual scatterplots, linear regression functions of peak velocity on amplitude were computed separately for each rate condition. Figure 4 shows some typical examples of the variability across subjects as observed in the data set. The mass-spring model suggests specific control mechanisms that, first, scale movement velocity in terms of a linear function of amplitude, and, second, vary stiffness for the adjustment of movement duration. Accordingly, the jaw closing gestures obtained from subject N4 (Fig. 4, the two rightmost upper panels) showed consistent rate-sensitive regression lines, in spite of different strategies of rate-sensitive amplitude scaling across places of articulation. Regarding /a/ and /i/ syllables, peak velocity was linearly scaled across vowel categories. Similar patterns were obtained from jaw data in more than half of all scatterplots across the speakers. However, different patterns were observed as well. Subject N1, for example, did not change jaw stiffness as a function of rate in his jaw opening gestures of /p/V items. The scatterplot displays a uniform velocity/amplitude scaling across vowels and rate conditions (leftmost top panel of Fig. 4). Subject N5, in contrast, showed largely rate-sensitive scaling and, in addition, a vowel effect. Although the regression lines were derived from the pooled /a/ and /i/ items, the triangles seem to show steeper scaling than the circles at visual inspection. An inverse vowel effect can be observed in this speaker's plots of constrictor and compound trajectory data where, under the fast condition, /a/ items exhibited a steeper peak velocity/amplitude slope (Fig. 4, second mid and bottom panel from left).

All four compound gesture plots displayed in Fig. 4 (lower panels) show marked rate-induced differences in peak velocity at a given amplitude. However, the mechanisms underlying this rate effect seem to differ across the four panels. In the mass-spring model, peak velocity is linearly scaled with movement amplitude and the intercept should be zero, whereas the presence of measurable intercepts may indicate more complex mechanisms of motor control, for example, in terms of intergestural timing. As concerns the closing gestures of subject N4's /t/V productions (rightmost panel), the speech rate conditions induced a difference in the slopes of the regression lines whereas the /p/V closing gestures were rather characterized by different intercepts. As a rule, the jaw data showed approximate zero intercepts in most cases, whereas particularly the compound gestures appeared less predictable by a nonintercept model.

2. Analysis of variance of peak velocity/amplitude scaling

In order to show systematic effects across subjects of gesture type (opening, closing), place of articulation (/p/, /t/), and speech rate (3 Hz, 5 Hz), these factors were entered in six repeated measures ANOVAS with the slopes and the intercepts of jaw, constrictor, and compound gesture velocity/amplitude scaling, respectively, as dependent variables (for cell means, see Fig. 5). Regarding the intercepts, the jaw as well as the constrictor data did not show any significant effects or interactions, whereas the compound gesture showed a rate effect ($F[1,7]=11.27$; $p<0.05$) and an interaction of gesture type and place of articulation ($F[1,7]=7.76$; $p<0.05$). With respect to the slopes, all three dependent variables showed a main effect of rate (jaw: $F[1,7]=90.02$, $p<0.01$; constrictor: $F[1,7]=10.82$, $p<0.05$; compound: $F[1,7]=510.78$, $p<0.01$). Furthermore, the compound slope depended on gesture type ($F[1,7]=27.09$, $p<0.01$), and a similar tendency was observed in the constrictor data ($F[1,7]=4.28$, $p<0.1$): On average, slopes were steeper in closing as compared to opening gestures.

For control reasons, a second series of analyses was performed in order to test for additional effects of vowel type on articulator stiffness. This part of the analysis used a nonintercept model since, unlike regression functions, simple quo-

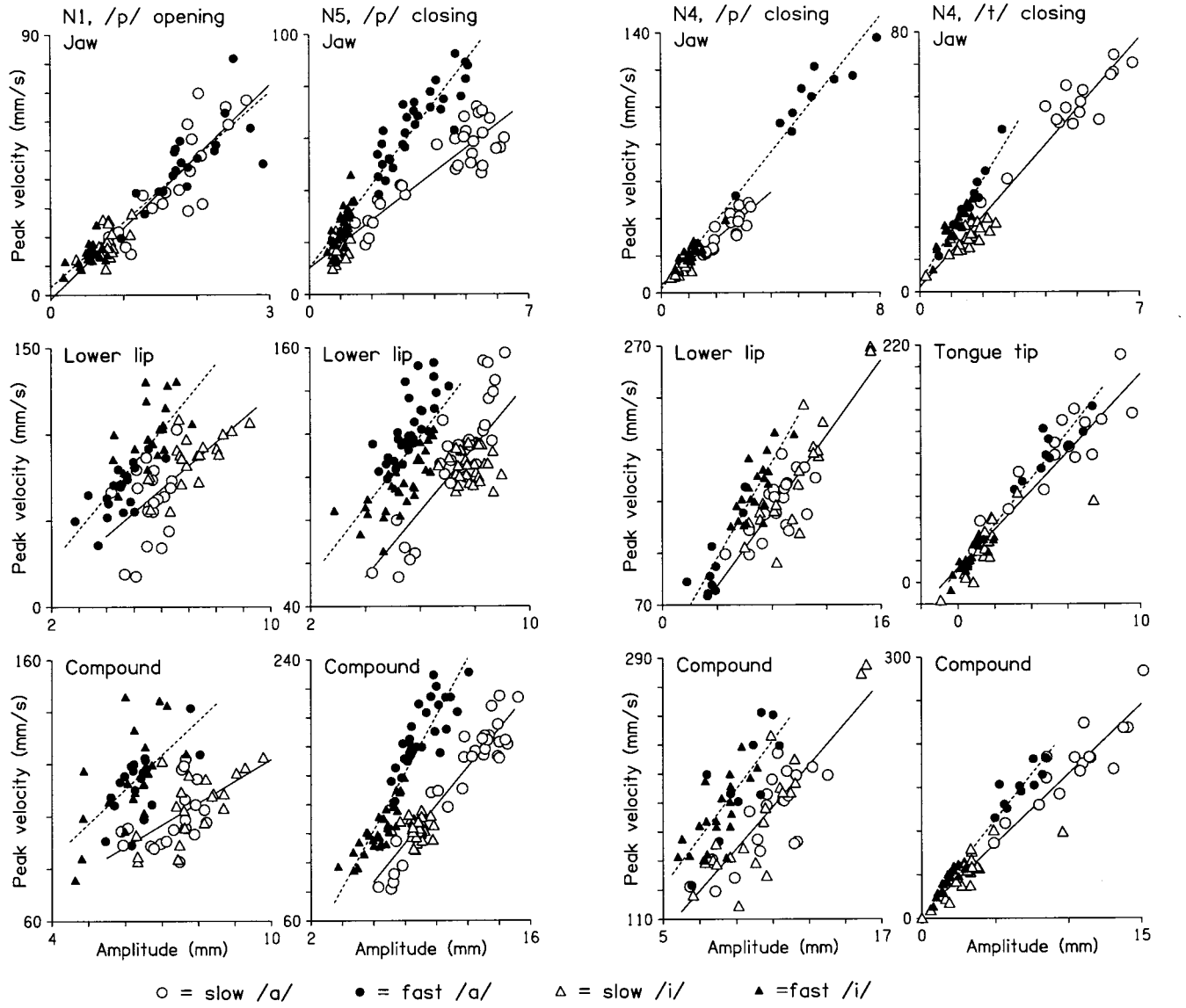

FIG. 4. Peak velocity plotted against movement amplitude as obtained from three subjects (N1, N4, N5). Each symbol represents a single gesture. Regression lines were computed across the pooled /a/ and /i/ items seperately for the slow (solid lines) and the fast conditions (dashed lines).

tients can be computed in the absence of any variation on the amplitude scale. Three repeated measures ANOVAS were performed testing the influences of place of articulation (/p/, /t/), speech rate (3 Hz, 5 Hz), vowel category (/a/, /i/), and gesture type (opening, closing) on the subject means of the peak velocity/amplitude ratio of (1) the jaw, (2) the constrictor, and (3) the compound trajectory, respectively. With respect to the jaw and the constrictor data, no significant vowel effects were observed, and the results were quite similar to the respective analyses of the slopes. The compound gesture, in contrast, showed a significant vowel effect as well as various interactions between vowel type and the remaining factors.

3. Quantitative effect of rate on the peak velocity/amplitude slope

If, as suggested by the spring model, the shape of the velocity profile is invariant across rate conditions and no additional mechanisms of intergestural timing are active, the peak velocity/amplitude slopes should directly reflect syllable rate, and the ratio of the two slopes corresponding to the 5- and the 3-Hz conditions, respectively, should amount to $5/3=1.66$. In contrast, a value of 1.0 is expected if the peak velocity/amplitude slope is kept constant across variation of speech rate. As shown in Fig. 6, most ratios lie between these two theoretical values, indicating that, on average, no full rate adaptation of stiffness was performed. While the jaw values were relatively close to the value of 1.66, constrictor stiffness turned out to be less rate sensitive. The difference between the jaw and constrictor data was significant ($F[1,5]=14.61$, $p<0.05$; repeated measures ANOVA performed with data from six subjects only; subjects with a nonsignificant [$p>0.1$] correlation between peak velocity and amplitude under at least one subcondition were considered as missing).

4. Comments

Although the present study revealed considerable variability across subjects with respect to peak velocity/

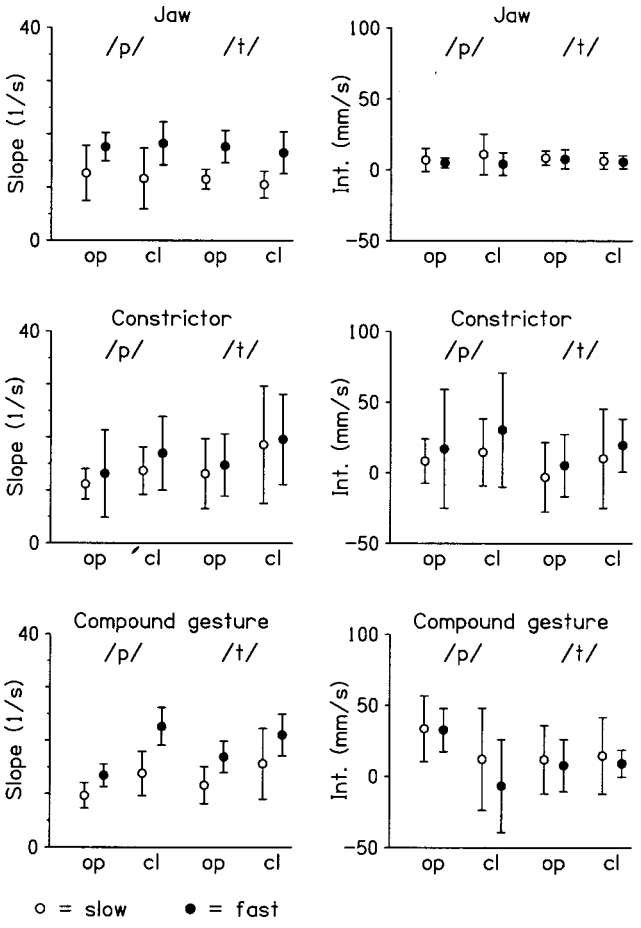

FIG. 5. Slopes (left panels) and intercepts (Int.; right panels) of the linear scaling of peak velocity and amplitude under the various conditions. Symbols and bars represent means and standard deviations across subjects, respectively. Abbreviations: op=opening; cl=closing.

amplitude scaling under the various subconditions studied, several statistical regularities could be observed. Both the jaw and the constrictor data were more or less compatible with a nonintercept model of peak velocity/amplitude adjustment whereas the compound gestures seem to be controlled in a more complex way. The jaw peak velocity/amplitude slopes showed rate-induced changes approximating the theoretical value for rate-sensitive proportional scaling. In contrast, the constrictors turned out to be less rate sensitive with respect to peak velocity/amplitude scaling. Opening and closing gestures did not consistently differ with respect to jaw slopes (Fig. 5, upper left panel). The constrictors, in contrast, exhibited steeper scaling in closing than in opening gestures. Neither the jaw nor the constrictors showed a significant vowel effect on the peak velocity/amplitude quotient. In contrast, the compound gestures did show complex vowel-induced interactions. With respect to peak velocity and amplitude scaling, thus, single articulators seem to be separately controlled, and the compound trajectories may be considered as the result of superimposed component structures rather than a functional entity.

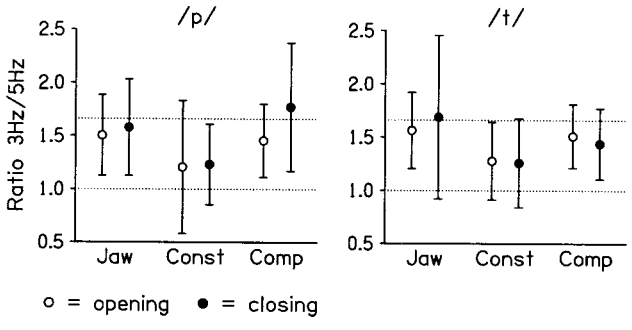

FIG. 6. Rate-induced changes in the slope of peak velocity/amplitude scaling: Linear slope of peak velocity/amplitude scaling at 5 Hz divided by the respective slope at 3 Hz. The lower and the upper dotted lines refer to theoretical values for rate-independent and rate-proportional scaling, respectively. Symbols and vertical bars represent means and standard deviations across subjects, respectively. Abbreviations: Const=constrictor component; Comp=compound gesture.

III. DISCUSSION

The present study investigated the effects of speech rate and vowel context on jaw–constrictor coordination. In spite of considerable intersubject variability, various regularities emerged with respect to both movement amplitude and peak velocity/amplitude scaling. The extent of jaw movements strongly depended on vowel height, whereas the constrictors (lower lip and tongue tip) failed a consistent pattern in this respect. Although compound amplitudes were reduced in fast as compared to slow speech, jaw movement amplitude was not consistently affected by syllable rate. With respect to velocity/amplitude scaling, the jaw showed a symmetrical pattern with respect to opening and closing gestures and more or less proportional changes of stiffness across speaking rates. The dynamic characteristics of the constrictors, in contrast, depended less on rate and exhibited steeper scaling of closing than opening gestures. Partial correlation analysis revealed covariation patterns among subsystems to vary largely across conditions and subjects.

In principle, an increase in speech rate can be achieved by two different strategies, either by a rise in movement velocity concomitant with rather unchanged excursions of articulatory trajectories or by reduced amplitude in the absence of major adjustments of velocity (Lindblom, 1990). The former strategy had been assumed to characterize constrictor gestures during consonant production, whereas the latter mainly seems to emerge during vowel-related jaw movements (Guenther, 1995; Miller, 1981). For example, Linville (1980) reported rate-induced reorganization of the various articulatory subsystems in terms of an increased lip and a decreased jaw amplitude during fast (>4 Hz) as compared to slow speech. Similar results were reported by Gay *et al.* (1974). The present data do not corroborate these findings. Although jaw displacement strongly depended on vowel height during /p/V syllable repetitions in accordance with previous studies (Gracco, 1994; Macchi, 1988; Tuller and Kelso, 1984), the effects of syllable rate were quite different. First, the lower lip component rather than the jaw excursion was reduced during fast rate and, second, jaw movement velocity showed proportional scaling with respect to the induced rate variations whereas the dynamic characteristics of the lower lip component did not change to a similar degree between the 3- and the 5-Hz conditions. In part, this discrepancy might be due to subject variability across studies and/or differences in stimulus material. For example,

the phenomenon of vowel reduction during propositional speech has turned out to be the result of complex interactions between phonological specifications, phonetic context, prosody, and speech rate (Fourakis, 1991; Rakerd *et al.*, 1980) rather than being a simple function of the time available to produce a vowel. Conceivably, rate-induced reduction of vowel gestures reflects higher-level processing during natural speech, whereas in a simple syllable repetition task the phonetic specification of vowels may be less rate sensitive.

As concerns the dynamic properties of articulatory gestures, stiffness has been considered an important control parameter with respect to the adjustment of speech rate (Kelso *et al.*, 1985). Accordingly, the present study revealed the ratio of peak velocity and amplitude to be, on average, higher in fast as compared to slow syllable rate. Some studies investigated compound jaw/lower lip or jaw/tongue gestures in order to derive the dynamic characteristics of articulatory movements in terms of peak velocity/amplitude scaling. The present study also found the velocity of compound trajectories to strongly depend on movement amplitude. Considering, however, both average patterns across subjects as well as particular strategies of individual speakers, the single-component data were more compatible with a linear nonintercept model than the compound gestures, whereas the latter seemed to represent the additive result of two more or less functionally independent subsystems. Thus, in accordance with previous studies reporting large variability of rate-induced alterations of articulatory dynamics (e.g., Sonoda, 1987), the present data suggest that control of speech rate comprises differential reparametrization of single subsystems rather than adaptation of a global scaling parameter.

Negative covariation between lip and jaw displacement has been suggested as a relevant aspect of motor equivalence, although experimental results are quite inconsistent across studies in this regard (Gracco and Abbs, 1986; Hughes and Abbs, 1976; Smith and McLean-Muse, 1987; Folkins and Brown, 1987). As concerns covariation among subsystems in general, the most important factor to be considered is the nature of the source of variability underlying the data. For example, if a speaker varies on a global dimension such as the hyper–hypoarticulation scale, two subsystems may exhibit positive covariation (DeJong, 1997). In contrast, if the source of variability is a kind of perturbation or imprecision within a single subsystem, the other might show a compensatory behavior, giving rise to negative covariation. For example, lip adjustments to jaw inaccuracy have been assumed to underly negative lip–jaw covariation (Hughes and Abbs, 1976; Gracco and Abbs, 1986). The present study yielded a nonhomogeneous picture across subjects and place of articulation, providing an argument against rather than in favor of generalizations as put forward in Hughes and Abbs (1976). A previous investigation by Smith and McLean-Muse (1987) measured lip/jaw correlations across repetitions in 24 subjects under 12 different conditions and obtained a wide range of—in most cases, nonsignificant—positive as well as negative correlation coefficients. Regarding the distribution of correlation values, the present results are in accordance with the latter study. The lower percentage of significant cases reported there can be explained by the small number of repetitions (only eight or five) underlying the computed correlation coefficients. The histogram of obtained correlation coefficients shown in Smith and McLean-Muse (1987) gives the impression of a bimodal distribution. Thus, although the average correlation may not significantly differ from zero, this may be due to the interaction of two competing mechanisms, one providing complementarity and the other representing variability on an external factor affecting both subsystems in the same direction.

In a broader sense, subject-specific strategies may also be considered as an aspect of motor equivalence. Despite considerable subject variability in compound amplitudes, the present study showed negative rather than positive correlations across subject variability, indicating individual differences with respect to the preferential use of the jaw and the constrictors for the production of opening–closing gestures. Considering jaw and constrictor amplitudes across variation of an external control variable that modifies amplitude, correlations are expected to be positive if the amplitude modification affects both subsystems in the same direction, negative if the subsystems are influenced differently, and zero if the influence of the factor is weak or inconsistent across subjects. Considering speech rate as the source of variability, correlations in the present study did not significantly differ from zero in spite of significant rate effects on amplitude, indicating subject variability rather than consistency. With respect to vowel category as a source of variability, in contrast, correlations were significant, but different in sign across places of articulation: in bilabial gestures jaw–lower lip correlations were negative, indicating vowel-induced reorganization. In contrast, apical gestures yielded positive jaw–tongue tip correlations indicating a common, vowel-induced scaling factor, confirming Lindblom and Sundberg (1971) that the jaw and the tongue represent a synergism for the production of vowel height.

Three main conclusions can be derived from the present results: First, the differential consideration of jaw and constrictor movements with respect to the effects of vowel height and speech rate provides evidence that, at least to some extent, the jaw is independently controlled from the two constrictors lower lip and tongue tip. Second, rate-induced modification of compound movement amplitudes affects the various subsystems quite differently and, therefore, cannot easily be understood as a general principle. Third, various aspects of motor equivalence as assessed by partial correlation analysis showed largely inconsistent patterns across subjects and places of articulation.

[1]In addition, the test material included the syllables /ka/ and /ki/. However, preliminary analyses revealed that principal component-based measurement of movement amplitudes failed in these items because the main movement direction did not always reflect the opening–closing dimension of the vocal tract. Furthermore, a pilot experiment in our laboratory using magnetic resonance imaging showed considerable vowel-induced variations in the exact place of tongue dorsum articulation and, therefore, EMA data using the same receiver placement for /ka/ and /ki/ items may not be valid with respect to the amplitude of opening–closing movements.

[2]Various aspects of rate variation can be considered when addressing influences of speech tempo, for example, rate variability across subjects, accidental variations within subjects, or evoked rate modifications in terms of

either verbal instructions such as ''conversational,'' ''fast,'' and ''slow'' or subjective scaling methods (see Adams *et al.*, 1993). Furthermore, an external pacing rhythm may be provided. Whereas conversational speech rate may be a reliable reference with respect to sentence utterances, previous experiences in our laboratory showed that ''convenient'' diadochokinetic syllable repetition rates sometimes are chosen quite arbitrarily. Some subjects may perform relatively fast, whereas others produce less than two syllables per second, which is considerably below their spontaneous speech rate. For diadochokinetic tasks, thus, external pacing is an easy and more reliable method of controlling syllable rate. With respect to articulatory dynamics as well as cycle-to-cycle regularity, no principal differences have been observed between self-selected and externally paced rates (Ackermann *et al.*, 1997; Konczak *et al.*, 1997). For the purpose of the present study, therefore, syllable repetition rate was induced by presentation of synthetic syllables over headphones.

[3]Various coordinate systems have been established for the assessment of articulatory kinematics. Commonly, the occlusal plane has been used as a reference (Westbury, 1994), but some studies considered the Frankfurt horizontal (Muller and Abbs, 1979) or a maxillay reference defined by the bridge of the nose and the upper incisors (Perkell *et al.*, 1992). For the sake of the present study, the essential demand was a set of one-dimensional time histories that optimally represent the opening-closing direction. Preliminary inspection of the kinematic data revealed that during stop consonant–vowel syllables the three coils (i.e., jaw, lower lip, and tongue tip) move approximately along a straight line, but that the exact direction of these movements may vary across speakers, articulators, and conditions. In some cases, all three trajectories were fairly parallel, whereas in others they differed somewhat with respect to movement direction. These differences may be due to either anatomical or behavioral differences between subjects. Instead of defining an invariant, anatomically defined dimension as the opening–closing direction, therefore, the opening–closing direction of the diadochokinetic movements was derived from the trajectories themselves. Similar approaches have been adopted in earlier studies (Adams *et al.*, 1993). In this way, the movement amplitudes of jaw and compound jaw-constrictor trajectories can easily be measured without an external reference system.

[4]For the assessment of the differential contribution of the constrictors to the compound lower lip and tongue tip movement amplitudes, a subtraction method had to be established. Ideally, a jaw-based coordinate system might be used to assess this aspect of motion. Since the jaw performs a combination of translational and rotational movements, two sensors fixed to the jaw in a reasonable distance from each other within the midsagittal plane would be required to represent this reference system, a condition which seems rather impossible within the framework of the EMA technique. Furthermore, computation of constrictor trajectories relative to the jaw would be considerably contaminated by random measurement noise since they had to be derived by mathematical operations on measured data from three sensor coils. In order to avoid these difficulties, a different approach was considered. Preliminary inspection of the raw data showed that during /tatata/ articulation, where the lower lip is supposed to be inactive, lower lip movements as well as their cycle-to-cycle variability in amplitude were very similar to jaw excursions. Similarly, in /papapa/ articulation the size of jaw movements appeared to be mirrored by the tongue tip trajectory. As a crude approximation, therefore, simple subtraction of the jaw amplitude from the compound amplitudes (derived from the respective principal component trajectories) represents a measure of the constrictors' differential contribution to the compound gestures. Admittedly, this method looks like an oversimplification of the actual complex biomechanical processes, but any attempt to measure the differential constrictor contribution more exactly, first, is much more effortful and, second, raises further problems of handling unknown variability, for example, with respect to the kind of biomechanical coupling between the bony structure and the fleshpoints of the measured trajectories. It should be emphasized, however, that the method adopted by the present study was applied to very simple sequences of opening–closing movements and that it is not recommended for the analysis of more complex speech utterances including front–back coarticulatory movements, lip rounding, or complex patterns of interarticulatory phasing.

[5]Previous studies indicate that peak velocity, by itself, does not represent a feasible parameter of functionally relevant variability of articulatory movements. For example, this measure rather depends on accidental variation of movement amplitude than on speech rate (Keller, 1987). Considering its relation to movement amplitude, however, peak velocity is a parameter that may contribute to our understanding of articulatory dynamics. Various methods have been introduced in order to assess the scaling of peak velocity and amplitude. While some authors relied on the peak velocity/amplitude quotient (Ostry and Munhall, 1985) as a measure of articulatory ''stiffness,'' others used more elaborated methods of regression analysis including an intercept term (Kelso *et al.*, 1985). The former procedure allows for the calculation of articulatory measures on the basis of individual utterances. In contrast, a regression model provides meaningful results only if a relatively large number of gestures, representing a homogeneous pool with respect to dynamic specification, is available. In particular, regression functions require sufficient variability on the amplitude axis. If a subject keeps movement amplitude constant across repetitions under a given subcondition, no regression function of peak velocity/amplitude scaling can be computed. One possibility of providing amplitude variation in opening–closing direction is variation of vowel height. A previous study has shown that, as a rule, linear scaling with respect to compound lower lip and jaw gestures is performed across different vowel categories (Hertrich and Ackermann, 1997b). Therefore, a similar approach was used in the present study. Since, however, vowel effects with respect to the differential use of the jaw and the constrictors may interfere with actual velocity/amplitude scaling, an additional analysis was performed using the simple peak velocity/amplitude quotient as a parameter of stiffness in order to particularly assess these vowel effects.

[6]When principal component analysis is performed on a variety of anthropometric variables, as a rule, the first principal component, accounting for a considerable amount of variance, represents a general size factor that is loaded with positive sign by all measures (Livshits *et al.*, 1995).

Abbs, J. H. (**1980**). ''Labial-mandibular motor equivalence in speech: A response to Sussman's evaluation,'' J. Speech Hear. Res. **23**, 702–704.

Abbs, J. H., and Gracco, V. L. (**1984**). ''Control of complex motor gestures: Orofacial muscle responses to load perturbations of lip during speech,'' J. Neurophysiol. **51**, 705–723.

Ackermann, H., Konczak, J., and Hertrich, I. (**1997**). ''The temporal control of repetitive articulatory movements in Parkinson's disease,'' Brain Lang. **56**, 312–319.

Adams, S. G., Weismer, G., and Kent, R. D. (**1993**). ''Speaking rate and speech movement velocity profiles,'' J. Speech Hear. Res. **36**, 41–54.

Brownman, C., and Goldstein, L. (**1986**). ''Towards an articulatory phonology,'' Phonology Yearbook **3**, 219–252.

DeJong, K. J. (**1997**). ''Labiovelar compensation in back vowels,'' J. Acoust. Soc. Am. **101**, 2221–2233.

Edwards, J., and Beckman, M. E. (**1988**). ''Articulatory timing and the prosodic interpretation of syllable duration,'' Phonetica **45**, 156–174.

Flege, J. E. (**1988**). ''Effects of speaking rate on tongue position and velocity of movement in vowel production,'' J. Acoust. Soc. Am. **84**, 901–916.

Folkins, J. W., and Brown, C. K. (**1987**). ''Upper lip, lower lip, and jaw interactions during speech: Comments on evidence from repetition-to-repetition variability,'' J. Acoust. Soc. Am. **82**, 1919–1924.

Fourakis, M. (**1991**). ''Tempo, stress, and vowel reduction in American English,'' J. Acoust. Soc. Am. **90**, 1816–1827.

Fowler, C. A., and Saltzman, E. (**1993**). ''Coordination and coarticulation in speech production,'' Lang. Speech **36**, 171–195.

Gay, T. (**1981**). ''Mechanisms in the control of speech rate,'' Phonetica **38**, 148–158.

Gay, T., Ushijima, T., Hirose, H., and Cooper, F. S. (**1974**). ''Effect of speaking rate on labial consonant-vowel articulation,'' J. Phonetics **2**, 47–63.

Gracco, V. L. (**1994**). ''Some organizational characteristics of speech movement control,'' J. Speech Hear. Res. **37**, 4–27.

Gracco, V. L., and Abbs, J. H. (**1986**). ''Variant and invariant characteristics of speech movements,'' Exp. Brain Res. **65**, 156–166.

Gracco, V. L., and Nye, P. W. (**1993**). ''Magnetometry in speech articulation research: Some misadventures on the road to enlightenment,'' Forschungsberichte des Instituts für Phonetik und sprachliche Kommunikation der Universität München **31**, 91–104.

Guenther, F. H. (**1995**). ''Speech sound acquisition, coarticulation, and rate effects in a neural network model of speech production,'' Psychol. Rev. **102**, 594–621.

Hertrich, I., and Ackermann, H. (**1997a**). ''Accuracy of lip movement analysis: Comparison between electromagnetic articulography and an optical two-camera device,'' Forschungsberichte des Instituts für Phonetik and sprachliche Kommunikation der Universität München **35**, 165–170.

Hertrich, I., and Ackermann, H. (**1997b**). ''Articulatory control of vowel length contrasts: Kinematic analysis of labial gestures,'' J. Acoust. Soc. Am. **102**, 523–536.
Hoole, P. (**1993**). ''Methodological considerations in the use of electromagnetic articulography in phonetic research,'' Forschungsberichte des Instituts für Phonetik and sprachliche Kommunikation der Universität München **31**, 43–64.
Hughes, O. M., and Abbs, J. H. (**1976**). ''Labial-mandibular coordination in the production of speech: Implications for the operation of motor equivalence,'' Phonetica **33**, 199–221.
Keller, E. (**1987**). ''Factors underlying tongue articulation in speech,'' J. Speech Hear. Res. **30**, 223–229.
Kelso, J. A. S., and Tuller, B. (**1983**). '' 'Compensatory articulation' under conditions of reduced afferent information: A dynamic formulation,'' J. Speech Hear. Res. **26**, 217–224.
Kelso, J. A. S., and Tuller, B. (**1984**). ''Converging evidence in support of common dynamical principles for speech and movement coordination,'' Am. J. Physiol. **246**, R928–R935.
Kelso, J. A. S., Saltzman, E. L., and Tuller, B. (**1986**). ''The dynamical perspective on speech production: Data and theory,'' J. Phonetics **14**, 29–59.
Kelso, J. A. S., Tuller, B., Vatikiotis-Bateson, E., and Fowler, C. A. (**1984**). ''Functionally specific articulatory cooperation following jaw perturbations during speech: Evidence for coordinative structures,'' J. Exp. Psychol. **10**, 812–832.
Kelso, J. A. S., Vatikiotis-Bateson, E., Saltzman, E., and Kay, B. (**1985**). ''A qualitative analysis of reiterant speech production: Phase portraits, kinematics, and dynamic modeling,'' J. Acoust. Soc. Am. **77**, 266–280.
Konczak, J., Ackermann, H., Hertrich, I., Spieker, S., and Dichgans, J. (**1997**). ''Control of repetitive lip and finger movements in Parkinson's disease: Influence of external timing signals and simultaneous execution on motor performance,'' Mov. Disord. **12**, 665–676.
Kuehn, D. P., and Moll, K. L. (**1976**). ''A cineradiographic study of VC and CV articulatory velocities,'' J. Phonetics **4**, 303–320.
Lee, W. L. (**1984**). ''Neuromotor synergies as a basis for coordinated intentional action,'' J. Motor Behavior **16**, 135–170.
Lindblom, B. (**1963**). ''Spectrographic study of vowel reduction,'' J. Acoust. Soc. Am. **35**, 1773–1781.
Lindblom, B. (**1990**). ''Explaining phonetic variation: A sketch for the H & H theory,'' in *Speech Production and Speech Modelling*, edited by W. J. Hardcastle and A. Marchal (Kluwer, Dordrecht), pp. 403–439.
Lindblom, B., and Sundberg, J. (**1971**). ''Acoustical consequences of lip, tongue, jaw, and larynx movement,'' J. Acoust. Soc. Am. **50**, 1166–1179.
Linville, R. N. (**1980**). ''Lip and jaw movements during altered speaking rates,'' J. Acoust. Soc. Am. **67**, S93.
Livshits, G., Otremski, I., and Kobyliansky, E. (**1995**). ''Genetics of human body size and shape: Complex segregation analysis,'' Ann. Hum. Biol. **22**, 13–27.
Macchi, M. (**1988**). ''Labial articulation patterns associated with segmental features and syllable structure in English,'' Phonetica **45**, 109–121.
Miller, J. L. (**1981**). ''Effects of speaking rate on segmental distinctions,'' in *Perspectives on the Study of Speech*, edited by P. D. Eimas and J. L. Miller (Erlbaum, Hillsdale, NJ), pp. 39–74.
Muller, E. M., and Abbs, J. H. (**1979**). ''Strain gauge transduction of lip and jaw motion in the midsagittal plane: Refinement of a prototype system,'' J. Acoust. Soc. Am. **65**, 481–488.
Munhall, K. G., Löfqvist, A., and Kelso, J. A. S. (**1994**). ''Lip-larynx coordination in speech: Effects of mechanical perturbations to the lower lip,'' J. Acoust. Soc. Am. **95**, 3605–3616.
Nelson, W. L. (**1983**). ''Physical principles for economies of skilled movements,'' Biol. Cybern. **46**, 135–147.
Nelson, W. L., Perkell, J. S., and Westbury, J. R. (**1984**). ''Mandible movements during increasingly rapid articulations of single syllables: Preliminary observations,'' J. Acoust. Soc. Am. **75**, 945–951.
Ostry, D. J., and Munhall, K. G. (**1985**). ''Control of rate and duration of speech movements,'' J. Acoust. Soc. Am. **77**, 640–648.
Perkell, J. S. (**1969**). *Physiology of Speech Production: Results and Implications of a Quantitative Cineradiographic Study* (MIT Press, Cambridge, MA).
Perkell, J. S., Matthies, M. L., Svirsky, M. A., and Jordan, M. I. (**1993a**). ''Trading relations between tongue-body raising and lip rounding in production of the vowel /u/: A pilot 'motor equivalence' study,'' J. Acoust. Soc. Am. **93**, 2948–2961.
Perkell, J. S., Svirsky, M. A., Matthies, M. L., and Manzella, J. (**1993b**). ''On the use of electromagnetic midsagittal articulometer (EMMA) systems,'' Forschungsberichte des Instituts für Phonetik and sprachliche Kommunikation der Universität München **31**, 29–42.
Perkell, J. S., Cohen, M. H., Svirsky, M. A., Matthies, M. L., Garabieta, I., and Jackson, M. T. T. (**1992**). ''Electromagnetic midsagittal articulometer systems for transducing speech articulatory movements,'' J. Acoust. Soc. Am. **92**, 3078–3096.
Rakerd, B., Verbrugge, R. R., and Shankweiler, D. P. (**1980**). ''Speaking rate, syllable stress, and vowel identity,'' Haskins Laboratories Status Report on Speech Research SR-62, pp. 149–159.
Saltzman, E. (**1986**). ''Task dynamic coordination of the speech articulators: A preliminary model,'' in Generation and Modelling of Action Patterns, edited by H. Heuer (Springer, New York), pp. 129–144.
Savariaux, C., Perrier, P., and Orliaguet, P. P. (**1995**). ''Compensation strategies for the perturbation of the rounded vowel [u] using a lip tube: A study of the control space in speech production,'' J. Acoust. Soc. Am. **98**, 2428–2442.
Schönle, P. W. (**1993**). ''The developmental genealogy of electromagnetic articulography (EMA),'' Forschungsberichte des Instituts für Phonetik and sprachliche Kommunikation der Universität München **31**, 83–90.
Schönle, P. W., Gräbe, K., Wenig, P., Höhne, J., Schrader, J., and Conrad, B. (**1987**). ''Electromagnetic articulography: Use of alternating magnetic fields for tracking movements of multiple points inside and outside the vocal tract,'' Brain Lang. **31**, 26–35.
Smith, B. L., and McLean-Muse, A. (**1987**). ''An investigation of motor equivalence in the speech of children and adults,'' J. Acoust. Soc. Am. **82**, 837–842.
Sonoda, Y. (**1987**). ''Effect of speaking rate on articulatory dynamics and motor event,'' J. Phonetics **15**, 145–156.
Tuller, B., and Kelso, J. A. S. (**1984**). ''The timing of articulatory gestures: Evidence for relational invariants,'' J. Acoust. Soc. Am. **76**, 1030–1036.
Vatikiotis-Bateson, E., and Kelso, J. A. S. (**1993**). ''Rhythm type and articulatory dynamics in English, French and Japenese,'' J. Phonetics **21**, 231–265.
Westbury, J. R. (**1994**). ''On coordinate systems and the representation of articulatory movements,'' J. Acoust. Soc. Am. **95**, 2271–2273.
Westbury, J. R., and Dembowski, J. (**1993**). ''Articulatory kinematics of normal diadochokinetic performance,'' Ann. Bull. RILP **27**, 13–36.

Piano hammers and their force compression characteristics: Does a power law make sense?

N. Giordano and J. P. Winans II
Department of Physics, 1396 Physics Building, Purdue University, West Lafayette, Indiana 47907-1396

(Received 22 April 1999; revised 29 December 1999; accepted 7 January 2000)

We have studied the force characteristics of a collection of piano hammers, through studies of the acceleration of the hammer head, the force due to the compression of the hammer felt, F_h, and the associated bending of the hammer shank which occurs when a hammer strikes a rigid object. By integration of the acceleration one can estimate the compression of the felt, and thus obtain a force-compression $F_h(z)$ relationship; our results for this function are compared with previous experiments and theoretical models. Close examination of our findings suggests that bending of the hammer shank, and also the time required for the force to be transmitted from the outer edge of the hammer to its core, play significant roles in the hammer dynamics. The data are used to estimate the quantitative impact of these effects on the derived $F_h(z)$ relation. The implications for physical modeling of a piano tone are briefly discussed.
 [S0001-4966(00)03304-X]

PACS numbers: 43.75.Mn [WJS]

INTRODUCTION

While piano hammers are essentially ''just'' felt covered wooden mallets, their design is the result of several centuries of evolution.[1] The manner in which the blow from such a hammer excites a piano string depends in large part on the force-compression characteristic of the hammer, $F_h(z)$. Here F_h is the force that the hammer exerts on a string when the hammer felt is compressed an amount z by virtue of its interaction with the string. Felt is a complicated material, and there is no ''first principles'' form for $F_h(z)$. It is tempting to assume that $F_h(z)$ has either a Hooke's law form, $F_h \sim z$, or that it is described by the Hertz result for an interaction involving a deformable elastic object, $F_h \sim z^{3/2}$.[2] However, much experimental work has shown that neither of these functional forms provides a reasonable description of real hammers.

Piano hammers have been the subject of a large number of experimental studies (see, e.g., Refs. 1, 3–16). Over the past several decades, many workers have asserted, shown, or assumed (or some combination of the three) that F_h follows a power law form

$$F_h = Kz^p. \tag{1}$$

Experiments have demonstrated that this functional form with an exponent p in the range 2.5–4 provides a much better description of real hammers than either the Hooke's law ($p=1$) or Hertz ($p=3/2$) forms.[1,7–10,12–14,16] The fact that the observed values of p are substantially larger than the Hooke and Hertz values is attributed to the way hammers are constructed.[1] The felt is applied in layers, with the innermost layers being stiffer than the outer ones. The common wisdom is that this makes the hammer effectively stiffer as the deformation is increased, thereby increasing the value of p.

Given that piano hammers have been much studied, one might wonder why a reader should welcome (or suffer through) another paper on the subject. The work described below was motivated by our ongoing efforts to construct a physical model of the piano. One goal of this project to apply Newton's laws to the hammers, strings, soundboard, etc., and proceed to calculate the sound produced by the instrument. In our initial modeling work[17] we treated the hammers using the power law form (1) with parameters K and p taken from the literature. However, certain aspects of the calculated tones led us to suspect that the hammer force characteristics were to blame for unsatisfactory results, especially for notes in the octaves above middle C. We therefore decided to conduct our own studies of the parameters K and p.

We had expected the measurements to be straightforward. Following previous workers, we attached an accelerometer to the hammer head and arranged for the hammer to strike a stationary force sensor. The results for the force and acceleration as functions of time were then used to obtain the force-compression relation, again following the analysis employed by previous workers (see, e.g., Refs. 11, 12). However, we found that the estimation of $F_h(z)$ from such measurements did not yield a simple power law; the results were in fact much more complicated. The purpose of this paper is to describe these complications in some detail, and suggest explanations. Similar complications have been observed in some previous experimental work, so our observations and conclusions should not be limited to the particular hammers that we have studied.

Our results suggest that bending of the hammer shank, and also the time delay associated with the propagation of compressional waves through the hammer felt, can both play significant roles in the force characteristic of a piano hammer. We will argue that a complete description of this characteristic requires more that a single hammer degree of freedom; knowledge of the felt compression z alone is not enough to calculate, characterize, or understand the dynamics of a piano hammer. Such a conclusion is not new, and many aspects of our results have been anticipated by previous workers (as we will reference in detail below). However, our analysis seems to be the first (as far as we know) to relate these internal degrees of freedom of the hammer to the hammer force characteristics in a quantitative way.

Where then does this leave the power law form for F_h? In a sense, we will come full circle at the end of this paper. While most of the paper will be concerned with deviations from, and shortcomings in, the simple power law form for $F_h(z)$, we will also show that for soft (*pianissimo*) hammer blows, deviations from a power law form are small, at least for some hammers. These deviations become larger for harder (*forte*) blows, but even then they are only of order 10% for the particular set of hammers that we have studied in the most detail. For such hammers, modeling with a power law many indeed be a reasonable approach, and lead to acceptable results. However, we have also encountered hammers (as have others in the literature) for which the deviations from a power law force characteristic are much larger. Realistic modeling of their behavior will be more complicated, but should still be feasible.

I. BACKGROUND

While the power law form (1) for the hammer force function has been widely used, examination of the literature shows that much of the experimental information on F_h is somewhat indirect. The experiments often involve quantities which can be derived from $F_h(z)$, such as the string velocity spectrum,[8–10,13] the hammer-string contact time,[13] or the residual shock spectrum.[16] Experimental results for such quantities are then compared to expectations based on the power law form (1), and the values of parameters such as p or K can then be deduced. While this approach has yielded much valuable information, it is clearly desirable to observe the functional form of F_h directly. This has been done in a number of cases, and it turns out that several careful measurements do *not* compare well with a power law. In some early work involving direct force and acceleration measurements, and also high speed photography, Yanagisawa and Nakamura[3,4,6] (see also the discussion of this work in Ref. 14) observed very large hysteresis of $F_h(z)$, with the force during decompression lying well below the value on compression. They attributed this, at least in part, to the finite response time of the felt; i.e., it takes some time for the felt to actually decompress. Boutillon[12] also found that F_h is a hysteretic function of z, and showed that the compression and decompression branches can be described by power laws with different exponents. On the theoretical side, Stulov[18] has proposed a very general approach to parameterizing this hysteresis. Hence, the experimental evidence supporting a simple power law (1) is fairly slim. Of course, one might argue that a power law captures the essential physics and is thus a good starting point. On the other hand, the measured deviations from a power law are often quite substantial and the meaning of the term ''essential physics'' is a bit slippery.

Our experiments are similar in spirit to some previous work, especially that of Yanagisawa and co-workers,[3,4,14] Boutillon,[12] and Suzuki,[5,7,11] but there are several important differences. First, in addition to measurements of the hammer acceleration and the hammer force, we have recorded simultaneous measurements of the strain associated with the bending of the hammer shank. Second, we have striven for very precise time resolution, approaching 4×10^{-5} s. Third, we present results for a number of hammers from the same piano; this is of particular value for modeling studies such as our own (see also Refs. 19, 20). Most importantly, we suggest a simple way to smoothly interpolate so as to obtain consistent values of the hammer parameters for all notes, a problem which has not been addressed (at least not adequately) until now.

We should hasten to add that many of our results or interpretations have been observed or touched on by previous workers (as we will note below). However, given the great importance of the hammer force characteristic to modeling work, it seems worthwhile to collect these observations in one place so that they can be placed quantitatively in the context of the corresponding experimental measurements.

II. EXPERIMENTAL PROCEDURE

The experiments employed a grand piano action obtained from Kimball, along with hammers and hammer shanks graciously supplied by a local piano technician. A piezoelectric accelerometer (PCB Piezotronics model 350A12, mass 4.2 g) was mounted on the wooden core of the hammer head, allowing the measurement of the acceleration of this part of the hammer; we will sometimes refer to this as simply ''the'' hammer acceleration, a_h, with the understanding that the acceleration of the felt surface of the hammer may in fact be different. Note that this accelerometer model is designed for ''shock'' measurements, and can thus easily handle the large acceleration values which are encountered, while maintaining a bandwidth of 20 kHz (according to the manufacturer's specifications). Tests with different mounting schemes, ranging from wax to epoxy, convinced us that the mounting method did not limit this bandwidth. A piezoelectric force sensor (PCB Piezotronics model 209C01; specified bandwidth 70 kHz) was mounted rigidly on a heavy aluminum block and supporting structure, so that it was impacted by the hammer. A brass edge (a narrow strip 1.0 mm wide) was attached to the face of the force sensor, so that the impact with the hammer occurred over an area similar to that of a real string. The bending of the hammer shank was measured using a strain gauge (Omega type KFG-10-120-C1; specified bandwidth greater than 100 kHz, length 1 cm) which was glued to the center of the shank. The strain gauge thus measured the fractional elongation over the central 1 cm of the shank. The shanks were typically 12.5 cm long, as measured from the hinge to the central axis of the hammer head.

The acceleration a_h, the force F_h, and the strain of the shank $\mathcal{S}$, were measured simultaneously as functions of time. The bandwidth of the measuring electronics was 44 kHz, which is higher than the bandwidth of the accelerometer (which was the slowest of the sensors). As noted above, the specified accelerometer bandwidth was 20 kHz, so our time resolution approached 5×10^{-5} s.

Most of the hammers we have studied were from a set from a Knabe piano. Other hammers gave similar results, although our most complete results to date are for the Knabe

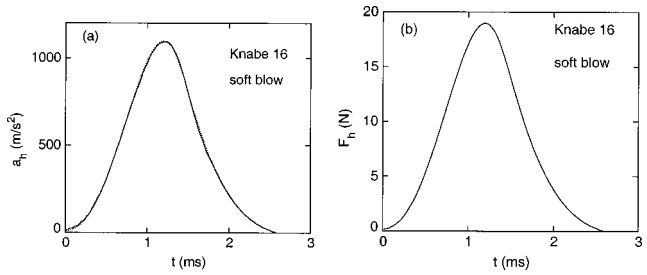

FIG. 1. The solid curves show (a) the hammer acceleration and (b) the hammer force as functions of time for Knabe hammer 16 for a soft blow. The hammer velocity just prior to impact was 0.6 m/s as determined by integration of the acceleration data (as described in the text). The dotted curve in (a) shows F_h/m_h, where m_h is a constant which we infer to be the hammer mass (see text for discussion).

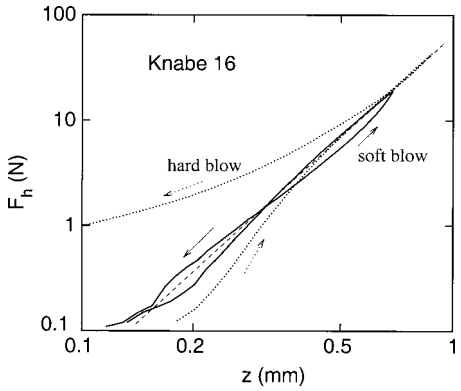

FIG. 2. Results for $F_h(z)$ for Knabe hammer 16, derived from the acceleration and force measurements in Figs. 1 (solid curve) and 3 (dotted curve). The dashed line shows a power law form Eq. (1).

set. All of the hammers were in like-new condition; they did not contain grooves from repeated string impacts, or any other discernible wear.

III. RESULTS

A. $F_h(z)$ for small hammer velocities

Figure 1 shows results for the hammer acceleration [the solid curve in part (a)] and the force [the solid curve in part (b)] as functions of time for a ''soft'' blow with a bass hammer; this blow would correspond to a note at a level of *p* or *mp*. In our notation, note 1 is the lowest bass note of the piano, so hammer 16 corresponds to the note two octaves below middle C. The zero on the time axis is arbitrary, but is the same in these two plots; the hammer made initial contact with the force sensor just prior to $t=0$ in the figure. It is observed that a_h and F_h have *very* similar shapes. This is seen from the dotted curve in Fig. 1(a) (which is barely distinguishable from the solid curve), which shows a plot of the force data from (b) normalized by a constant. That is, the dotted curve is a plot of F_h/m_h, where m_h is a constant which we will soon identify as the hammer mass (actually, it will be the effective mass of the hammer plus the mass of the accelerometer). The fact that a_h (the solid curve) and F_h/m_h (the dotted curve) are virtually identical is just a confirmation of Newton's second law, and allows us to surmise that m_h is the effective mass of the hammer. We use the term ''effective'' mass as we would expect m_h to deviate from the actual mass of the shank plus hammer (plus accelerometer) since the hammer is not a free mass (i.e., the hammer head moves in a circular arc, etc.). We should mention that different measurements with a given hammer yielded values of m_h which varied by no more than the experimental error ($<\pm 2\%$), regardless of how hard the key was pressed. It is also worth noting that the results in Fig. 1 provide at least a qualitative check on the actual measurement bandwidth. The fact that the acceleration and force signals are in such good correspondence, even though the sensors themselves have different inherent response times, and were mounted in completely different ways, implies that any time lags due to finite bandwidth are less than ~ 0.05 ms, which is the value estimated in Sec. II.

Following previous workers (e.g., Refs. 7 and 12), the results in Fig. 1 can be used to infer the force compression function. Integrating the acceleration once yields the velocity of the hammer head, $v(t)$. The constant of integration can be determined from the observation that $v=0$ when the hammer is most highly compressed, at which time the force and acceleration should be at their maximum values. The compression of the felt, z, can then be obtained by integrating $v(t)$. The constant of integration in this case is determined from the fact that z is zero when the hammer makes first contact with the force sensor. The time at which this occurs can be found by careful inspection of $F_h(t)$.

There are, of course, uncertainties in the determination of the time $t_{\max}$ at which a_h is a maximum, and in the time of first contact t_{contact}, and these will lead to uncertainties in the final results for $z(t)$. To assess the effects of these uncertainties, we have analyzed the data in Fig. 1 (and all of our other data sets as well) using different values for $t_{\max}$ and t_{contact}. We have found that any reasonable choices for these times yield essentially the same results for $F_h(z)$. That is, all reasonable choices for $t_{\max}$ and t_{contact} lead to the same basic functional form for $F_h(z)$, and the same final conclusions below.

The solid lines in Fig. 2 show the results for $F_h(z)$ obtained from the data in Fig. 1. There are two branches, corresponding to compression and then decompression of the felt, and they differ by approximately 10%. Enclosed by these two branches is the straight dashed line, which shows a power law from for comparison. While the deviations from a power law are here certainly noticeable, they are much smaller than was observed for the hammers studied and discussed in Refs. 12, 14, 3, 4, 6; their hammers exhibited much greater hysteresis, with a factor of 2 (or larger) difference between the two branches.

The physical origin for this hysteresis, and why it can vary so much from hammer to hammer, will be discussed in the next section, where we consider data for a much harder hammer blow. While our results for this soft blow can be described fairly well by a power law, we should note that there are several assumptions implicit in our analysis. First, we have assumed that the only force on the hammer is due to the felt compression. While gravity is certainly present, it is too small to have an effect on the scale important here. However, there will also be a force due to the flexing of the

hammer shank; we will estimate the magnitude of this force from the strain measurements presented below. Second, there is the assumption that the displacement of the hammer core (where the accelerometer was mounted) is equal to the displacement of the surface of the hammer, i.e., the compression of the felt. We will argue below that the impact at the edge of the hammer can, in some cases, take a significant time to propagate to the core, leading to a difference between the value of z derived above and the true compression of the surface of the felt. This effect is very small in Fig. 1, but we will soon see cases in which it is quite significant.

B. Behavior for hard blows: Bending of the hammer shank

One message from the previous section is that under some conditions, i.e., for a soft blow with this particular Knabe hammer, the force compression relation can be described approximately by a power law, with hysteresis at the $\sim$10% level. However, this relatively simple behavior did not persist to more forceful hammer blows. The dotted lines in Fig. 2 show results obtained for a hard blow with the same hammer. $F_h(z)$ again consists of two branches, corresponding to increasing and decreasing z. While the compression branch is not far from the power law (the dashed line) observed for the soft blow, the decompression branch lies much higher, and one might worry that F_h does not approach zero force as $z \rightarrow 0$.

The behavior seen in Fig. 2 was observed consistently for all of our hammers, with the difference between the upper and lower branches growing as the blows were made harder. This difference at small force levels is perhaps exaggerated by the logarithmic scales used here, but is well outside any experimental uncertainties. In terms of the maximum force during the entire blow, the difference between the two branches was still of order 10%–20% for the hardest blows, for which the hammer velocities just prior to impact were 1.5–2 m/s (such velocities correspond to *f* or *ff* levels[15,19,20]). Nevertheless, the behavior was quite systematic and striking, so it is interesting to consider its cause, especially since it is hard to see how this behavior can be accommodated by a single $F_h(z)$ function.

Acceleration and force data for the hard blow are shown in Fig. 3. In order to compare them in detail, we have normalized $F_h(t)$ by the value of the hammer mass obtained from the soft blow data. It is seen that $a_h(t)$ and $F_h(t)/m_h$ coincide fairly well, especially near their peaks, from which we conclude that the effective hammer mass m_h is indeed the same in the two cases (to within the experimental error of a few percent). However, careful examination of these data shows that at the longer times ($t > 1.0$ ms), F_h/m_h for the hard blow is slightly, but consistently, larger than a_h. This leads directly to the larger value of F_h found on the decompression branch in Fig. 2. It is striking that such a small difference in $F_h(t)$ can make such a significant difference in the force-compression characteristic, and shows that effects which seem small on the scale of the maximum force or acceleration can have a substantial effect on the final derived $F_h(z)$.

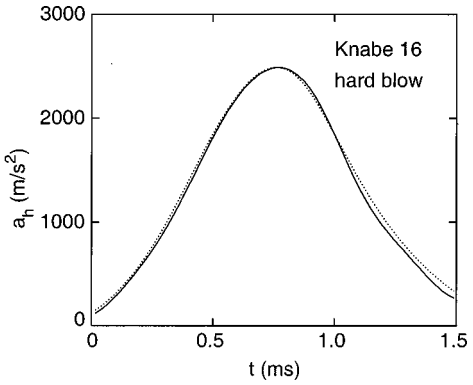

FIG. 3. Hammer acceleration (solid curve) and F_h/m_h (dotted curve) for Knabe hammer 16 for a hard blow. The hammer velocity just prior to impact was 1.0 m/s.

We believe that the effect responsible for this behavior is flexing of the hammer shank. As mentioned above, our analysis assumes that the only force on the hammer is due to the compression of the felt. There will clearly be an additional force due to the flexing of the hammer shank. This has been noted by several workers, and the vibrational modes of the shank have been observed and modeled by Askenfelt and Jansson.[15] However, so far as we know, a quantitative estimate of the magnitude of this flexural force has not yet been considered in the literature. To make such an estimate, we show some typical results for the shank strain in Fig. 4. These data, which correspond to the hard blow in Figs. 2 and 3, are shown on several time scales. In Fig. 4(a) the key was pressed at point A; before that time the shank strain was zero (only the instrumental noise was present before point A). After the keypress, the strain became positive, with the shank assuming the shape shown qualitatively in Fig. 4(d). Comparing with the work of Askenfelt and Jansson,[21] the sharp change in slope of the strain at point B signals when the

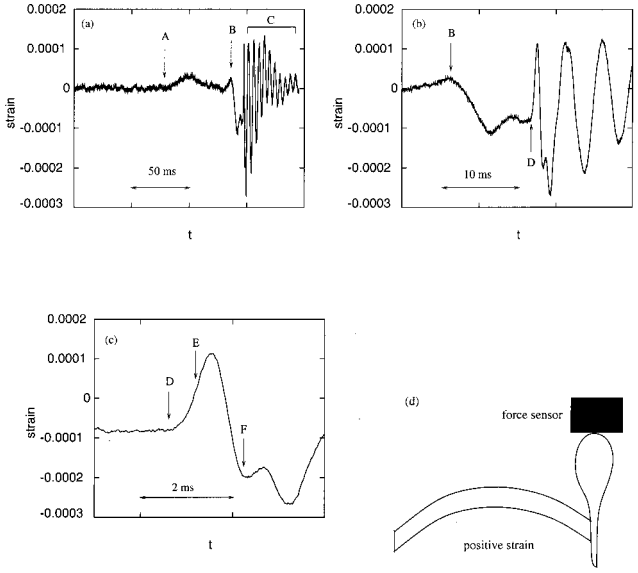

FIG. 4. Strain of the hammer shank measured for the hard blow of Fig. 3. The data are shown on different, successively magnified, time scales, and the letters label features discussed in the text. This labeling is consistent from figure to figure; i.e., point B in part (a) is the same as point B in (b). (d) shows qualitatively the shank deformation when the strain is positive.

roller lost contact with the jack. An expanded view of this region is shown in Fig. 4(b). Comparison with force-time data taken simultaneously (not shown here) showed that initial contact between the hammer and the force sensor was then made at point D. The oscillations at the end of this figure, and in region C in part (a), are shank oscillations which occurred after the hammer was caught by the backcheck. In part (c) of the figure we show a more expanded view. Point D is again when the hammer first contacted the force sensor. The hammer force attained its maximum value at point E, which is significantly earlier than the time of maximum strain. Contact with the force sensor ended at point F.

Let us now consider the strain results quantitatively, and estimate the force due to shank flexing. The strain $\mathcal{S} \equiv \Delta L/L$ is seen to take on maximal values of $\approx -0.9 \times 10^{-4}$ just before contact, and $\approx +1.1 \times 10^{-4}$ during contact. This is the strain at the middle of the shank; in order to estimate the associated force on the hammer head, we need to make some assumption about the shank profile. We will assume a deformation of the form

$$y = A \sin(\pi x/l), \tag{2}$$

where l is the length of the shank. This form is consistent with the modeling of Askenfelt and Jansson[15] (in particular, with their displacement profiles for the shank modes in the neighborhood of a few hundred Hz to 1 kHz), with the proper boundary conditions for a hammer hinged at one end,[22] and with common sense. We have found that other reasonable assumed forms for the displacement function would yield similar results for the magnitude of the force.

There are (at least) two ways to now estimate the importance of flexing on the force-compression characteristic. One is to compute the force required to bend a stiff rod[22]

$$F_{\text{shank}} = ESK^2 \frac{\partial^3 y}{\partial x^3}, \tag{3}$$

where E is the Young's modulus, S the cross-sectional area, and the radius of gyration $K = r/2$ for a cylindrical rod of radius r (the shank cross-section is not quite circular, but it is approximately so). The strain is related to the shank profile by[22]

$$\mathcal{S} = r \frac{\partial^2 y}{\partial x^2}. \tag{4}$$

With the shank radius of 3.0 mm, a measured strain of $\mathcal{S} \approx 1 \times 10^{-4}$, and the shank length of 12.5 cm we find [by using the profile Eq. (2) in Eq. (4)] $A \approx 6 \times 10^{-5}$ m. With the known Young's modulus for maple (the wood used for the shank) of 1×10^{10} N/m^2 (Ref. 23) we can then use Eq. (3) to obtain $F_{\text{shank}} \approx 1.1$ N. This should be compared with the maximum force due to the felt compression, which was approximately 45 N for this hammer blow. Comparing with the results for $F_h(z)$ in Fig. 2, we see that the difference between the two force-compression branches is indeed comparable to F_{shank}, confirming the importance of shank bending.

Another way to estimate the importance of shank flexing is to consider the deflection of the hammer head. For the sinusoidal profile assumed above, the deflection of the hammer head (from where it would have been if the shank were straight) is $\pi A = 0.18$ mm in our case. This is again quite comparable to the hysteresis when measured in terms of z, as seen for the hard blow in Fig. 2.

Our analysis shows that the (apparent) hysteresis observed in the derived $F_h(z)$ characteristic for hard blows can be accounted for quantitatively by shank flexing. This also means that, at the level of accuracy implicit in Fig. 2, a piano hammer cannot be modeled using a force-compression characteristic which is a function of z alone. Modeling of the hammer must also account for bending of the shank. This will require at least one additional parameter (such as the amplitude A defined above) associated with the degrees of freedom of the shank, but more parameters will likely be necessary in order to properly account for the several shank modes observed below 1 kHz.[15]

We have studied the behavior of several other hammer shanks, and found similar results. However, we do not have enough data to be able to comment on how the flexural properties vary across the keyboard range. Measurements of this kind could presumably shed light on the importance of a shank's ''tap tone'' on sound production.[15,1]

C. Hysteretic behavior for large F_h and its physical origin

In the previous section we presented evidence that flexing of the hammer shank leads to an apparent hysteresis in the derived $F_h(z)$. One should not necessarily think of this as hysteresis, since the irreversibility in $F_h(z)$ in Fig. 2 is a result of our assumption that the only force on the hammer is due to the compression of the felt. If the force due to flexing of the shank were included in the analysis used to obtain $F_h(z)$, the force-compression relationship for the felt alone might well be completely reversible.

In this section we will consider another source of hysteretic behavior in the force-compression relation, which we will argue originates in the behavior of the felt. An example of such hysteretic behavior is shown in Fig. 5. These data are for a midrange hammer from an unknown piano, not the Knabe instrument whose hammers were considered in the previous sections. The hammer velocity just prior to impact here was 2.9 m/s, corresponding to an approximately *ff* blow. For small z, the decreasing branch of the force-compression curve lies highest, an effect we again attribute to flexing of the shank, just as found for our Knabe hammers (Fig. 2) and discussed above. However, at large z the decreasing branch now lies lowest; this sign for the hysteresis agrees with that found previously,[3,4,12,14] and the magnitude of this hysteresis is quite comparable to that reported by those workers. Stulov[18] has proposed a functional form for describing such behavior. While one could view the theoretical modeling of Stulov as simply a mathematical construct, and not worry about the physics, we believe that it is worthwhile to try to understand where such hysteresis at large F_h actually comes from. Many previous discussions have assumed, or stated, that hysteresis can arise from irreversible slippage of the fibers of the felt, as they attempt to move past each other during compression and decompression (see, for example,

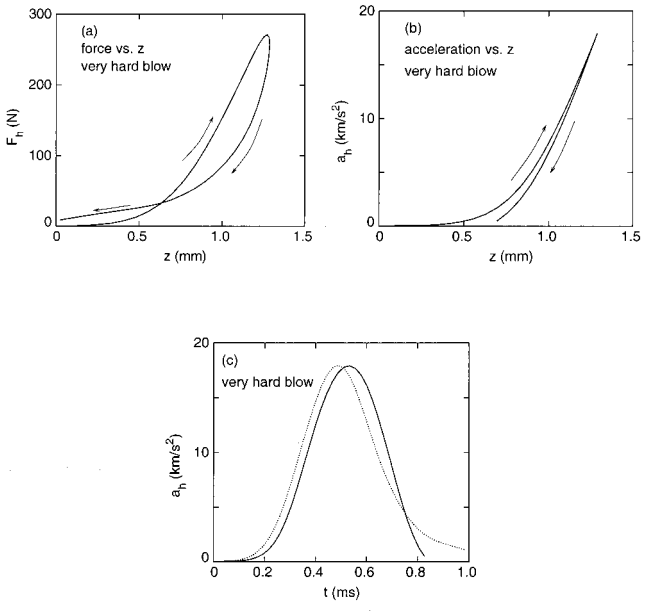

FIG. 5. Results for (a) $F_h(z)$, (b) acceleration as a function of z, and (c) a_h (solid curve) and F_h/m_h (dotted curve) as functions of time for a typical hammer (not from the Knabe set). The hammer velocity just prior to impact was 2.9 m/s.

Ref. 16). However, while this mechanism is certainly plausible and undoubtedly occurs in some cases, we believe that much of the hysteresis seen in Fig. 5(a) can be understood in a different way.

Figure 5(c) shows the results for the acceleration and F_h/m_h in this case. It is seen that from $t=0$ up to $t \sim 0.6$ ms the two have *very* similar shapes, but with a significant offset with respect to time, with the force curve leading the acceleration. We have observed this offset with a number of hammers, including our Knabe set, although it was not always as large as seen here. It seems quite natural to attribute this offset to the time required for the force to propagate from the outer edge of the hammer, which makes contact with the force sensor, to the inner core of the hammer, where the accelerometer is mounted. On impact this force is presumably carried by a compressional (shock) wave which propagates from the edge of the hammer to the inner core. The time delay seen in Fig. 5(c) implies a wave speed of $\approx$300 m/s, which seems like a very reasonable value for a soft material such as felt. Since other workers have also used accelerometers mounted in a similar place on the hammer, we would expect this hysteresis mechanism to be operative in many other experiments as well. Indeed, photographic studies of the time required for the felt to decompress[6] seem to have observed this effect, and those authors have discussed a multiple spring-dashpot model of such behavior.

It is interesting to consider what the force-compression relation would look like with the time delay removed. An approximate way to accomplish this is to *assume* that F_h is precisely equal to $m_h a_h$, so that the force and acceleration are proportional to one another. We can then use the measured acceleration to also deduce the force (apart from a constant factor) as a function of time. That is, we follow the same approach as in our previous calculations of $F_h(z)$, except that the force is taken to be proportional to $a_h(t)$. The results are given in Fig. 5(b); here we have plotted $a_h(z)$ so that we do not need to specify the value of m_h. It is seen that there is now much less hysteresis, particularly at the largest force levels, and the overall shape is quite different when the compression is largest. We believe that this result implies that a significant amount of the hysteresis commonly observed in ''measured'' $F_h(z)$ characteristics is in fact due to the time delay associated with force propagation within the hammer. It is in our opinion less plausible to attribute such behavior to slippage of the fibers of the felt, as it is difficult to see why this would give rise to such similar shapes for $a_h(t)$ and $F_h(t)$.

Besides suggesting a mechanism for the hysteretic behavior of F_h, our arguments imply that one might be able to construct a hammer model which does not have any ''intrinsic'' hysteresis. However, such a model would have to include some degrees of freedom associated with the hammer felt, so as to describe the propagation of the compressional wave which carries the force from the edge of the felt to the rest of the hammer; the model proposed by Yanagisawa and Nakamura[4] is one such possibility. While this seems to be a tractable problem, for many purposes (including physical modeling) it may be much more convenient to use a hammer model which ignores these degrees of freedom, such as the framework developed by Stulov.

D. Force law parameters

One message which could be drawn from the results given above is that piano hammers are complicated objects. A description of F_h (at the level of precision attained in our experiments) in terms of just a single parameter, i.e., the felt compression z, does not seem possible. This also suggests that accurate modeling of hammer dynamics will be much more involved than commonly assumed. However, returning to Fig. 2, we note that for this soft hammer blow, the force-compression curve displayed relatively little hysteresis from either the shank bending or the felt time delay. Hence, at least for some hammers, such as our Knabe set, and under certain conditions (soft blows, i.e., p or mp), it may still make sense to use a simple force function without hysteresis. Moreover, since the data for the soft blow in Fig. 2 enclose the dashed (power law) line, the form Eq. (1) should not be discarded quite yet.

So, it still seems worth studying the tones calculated using the power law force function Eq. (1). In order to do this, we need the power law force parameters K and p for a complete set of hammers. We have therefore carried out measurements like those in Figs. 1 and 2, for a number of Knabe hammers. For soft blows, the data for each hammer could be fit to a power law similar to the dashed line shown in Fig. 2. The results are given in Table I. Hammer 6 corresponds to the note nearly 3 octaves below middle C, while hammer 66 is two octaves above middle C. The effective hammer mass decreases systematically from bass to treble (as expected), with values in good accord with previous results in the literature.[10,1] The exponent values lie in the range $p=2.5-3.3$, which is also in good accord with previous measurements. The most interesting results in Table I concern the force constant K. There are actually very few results

TABLE I. Parameters measured for a set of Knabe hammers. The numbering scheme labels the lowest note as #1. The units for K are N/m$^{1/p}$. z^* is the value of the compression at which $F_h = 10$ N.

Hammer	m_h (g)	p	K	z^* (mm)
6	15.3	3.2	2.5×10^{11}	0.56
16	13.1	3.3	5.5×10^{11}	0.56
34	10.9	3.1	1.7×10^{11}	0.50
42	9.9	2.8	2.9×10^{10}	0.42
50	9.6	3.3	1.3×10^{12}	0.43
58	9.0	2.5	2.0×10^{9}	0.48
66	7.3	3.1	2.9×10^{11}	0.42

given in the literature for K; moreover, when attempting to compare with other workers, one must cope with large fluctuations in K from hammer to hammer.

For our physical modeling project we require parameters for all of the hammers. One approach would be to simply perform these measurements for *all* 88 hammers from a particular piano. Alternatively, one could extrapolate/interpolate the values of p and K in Table I, and we will now consider how this should be done. Since our exponent values vary relative little from hammer to hammer, and the variations which are observed do not appear to be systematic, we will assume that p is the same for all notes. It is often reported that p tends to increase as one goes from bass to treble,[12,10,16] but the reported variations of p seem to depend nearly as much on the particular brand of hammers as on their position on the keyboard. Hence, our results for p, and the assumption that p is a constant for all hammers from bass to treble, are probably consistent with previous work. For our particular set of Knabe hammers, it would be reasonable to choose $p = 3.0$ (which is close to the average of the values in Table I) for all notes. Our next problem is how to extrapolate/interpolate the values of K. Since the values of K in Table I fluctuate considerably, it is not initially obvious how to best choose values of K for the entire keyboard range.

A different way to view the variation of the hammer parameters is as follows. Let us define z^* to be the compression required to obtain a particular value of the force. We should emphasize that z^* does *not* depend on assumptions made concerning p, or on any fit to the data for $F_h(z)$; the value of z^* can be obtained directly from the *measured* $F_h(z)$ (assuming that the hysteresis is small). Table I lists the measured values of z^* for $F_h = 10$ N, and the results are plotted in Fig. 6, where we see that z^* varies quite smoothly from bass to treble. This indicates that the actual *magnitude* of the force for a given value of z varies rather smoothly and weakly from hammer to hammer. The large fluctuations in the fitted values of K are thus due to the variations in p. It is easy to see that when fitting to the power law from Eq. (1) a small change in p will be systematically coupled with a large change in K. The smooth variation observed for z^* can be used to make a reliable estimate for the force constant K in Eq. (1) across the keyboard. That is, once estimates have been made for p (in the previous paragraph we proposed using $p = 3.0$ for all of the hammers in our set), one should then choose K to produce a smooth and rather small variation of z^* across the keyboard like that shown in Fig. 6. We have employed this approach in our physical modeling work, and

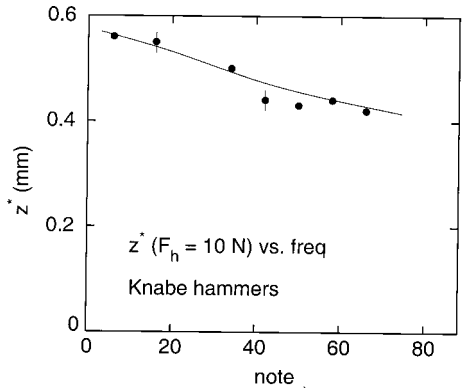

FIG. 6. Results for z^*, the value of the compression at which the hammer force is 10 N, for the Knabe hammers. The smooth curve is a guide to the eye. Typical error bars are shown.

the calculated tones with these values of K and p are encouraging.[17] This is a very different variation of K than found from other tabulations of hammer properties. For example, the values of K and p given in Ref. 20 yield values of z^* which vary by a factor of $\sim$2.5 from bass to treble, which is *much* greater than the $\approx$30% variation observed for our Knabe hammers in Fig. 6.

IV. DISCUSSION

The objective of the present work was to obtain high precision data for the properties of piano hammers. Our high time resolution has enabled us to directly observe the flexing of the hammer shank, and we have been able to quantitatively compare the magnitude of this flexural force with other forces on the hammer. We have also shown that for some hammers the time delay associated with shock propagation through the felt can cause an apparent and sizable hysteresis in the force-compression characteristics. Perhaps most importantly, we have obtained systematic results for the force law parameters for a collection of hammers. While our parameter values are in most cases similar to those reported by others, we find significant differences for the behavior of K, especially in the treble.

Since a primary motivation of this work has been our physical modeling project, it is appropriate to ask how much effect, if any, shank flexing, the $F_h(z)$ hysteresis, etc., have on the resulting piano sound. This is a topic which we are now exploring, and hope to discuss at length in a future paper. Results obtained using the power law force function Eq. (1) without any hysteresis are encouraging and will be reported shortly, along with a discussion of the computational aspects of our modeling project.[17]

ACKNOWLEDGMENTS

We are grateful to P. F. Muzikar for helpful comments and criticisms, B. Martin for invaluable experimental help along with a semi-infinite supply of hammers, T. Rossing, D. Russell, and H. Suzuki for helpful correspondence, and M. Jiang for valuable contributions to the modeling project and useful discussions. This work was supported in part by the NSF through Grant No. PHY-9722031.

[1] H. A. Conklin, Jr., ''Design and tone in the mechanoacoustic piano. Part I, Piano hammers and tonal effects,'' J. Acoust. Soc. Am. **99**, 3286 (1996).
[2] L. D. Landau and E. M. Lifshitz, *Theory of Elasticity* (Oxford University Press, Boston, 1986).
[3] T. Yanagisawa, K. Nakamura, and H. Aiko, ''Experimental study on force-time curve during the contact between hammer and piano string,'' J. Acoust. Soc. Jpn. **37**, 627 (1981).
[4] T. Yanagisawa and K. Nakamura, ''Dynamic compression characteristics of piano hammers,'' Transactions of Musical Acoustics Technical Group Meeting of the Acoustic Society of Japan **1**, 14 (1982).
[5] H. Suzuki, ''Vibration analysis of hammer-shank system,'' CBS Technology Center Report (1983).
[6] T. Yanagisawa and K. Nakamura, ''Dynamic compression characteristics of piano hammer felt,'' J. Acoust. Soc. Jpn. **40**, 725 (1984).
[7] H. Suzuki, ''Modeling of a piano hammer,'' CBS Technology Center Report (1985).
[8] D. E. Hall, ''Piano string excitation in the case of small hammer mass,'' J. Acoust. Soc. Am. **79**, 141 (1986).
[9] D. E. Hall, ''Piano string excitation II: General solution for a hard narrow hammer,'' J. Acoust. Soc. Am. **81**, 535 (1987).
[10] D. E. Hall, ''Piano string excitation III: General solution for a soft narrow hammer,'' J. Acoust. Soc. Am. **81**, 547 (1987).
[11] H. Suzuki, ''Model analysis of a hammer-string interaction,'' J. Acoust. Soc. Am. **82**, 1145 (1987).
[12] X. Boutillon, ''Model for piano hammers: Experimental determination and digital simulation,'' J. Acoust. Soc. Am. **83**, 746 (1988).
[13] D. E. Hall and A. Askenfelt, ''Piano string excitation: V: Spectra for real hammers and strings,'' J. Acoust. Soc. Am. **83**, 1627 (1988).
[14] H. Suzuki and I. Nakamura, ''Acoustics of pianos,'' Appl. Acoust. **30**, 147 (1990). This paper gives a nice description of work which had previously been available only in Japanese.
[15] A. Askenfelt and E. V. Jansson, ''From touch to string vibrations. II: The motion of the key and hammer,'' J. Acoust. Soc. Am. **90**, 2383 (1991).
[16] D. Russell and T. Rossing, ''Testing the nonlinearity of piano hammers using residual shock spectra,'' Acustica **84**, 967 (1998).
[17] N. Giordano, ''Physical modeling of the piano: First results for a simple monochord'' (in preparation).
[18] A. Stulov, ''Hysteretic model of the grand piano hammer felt,'' J. Acoust. Soc. Am. **97**, 2577 (1995).
[19] A. Chaigne and A. Askenfelt, ''Numerical simulations of piano strings. I. Physical model for a struck string using finite difference methods,'' J. Acoust. Soc. Am. **95**, 1112 (1994).
[20] A. Chaigne and A. Askenfelt, ''Numerical simulations of piano strings. II. Comparisons with measurements and systematic exploration of some hammer-string parameters,'' J. Acoust. Soc. Am. **95**, 1631 (1994).
[21] A. Askenfelt and E. V. Jansson, ''From touch to string vibrations. I: Timing in the grand piano action,'' J. Acoust. Soc. Am. **88**, 52 (1990).
[22] N. H. Fletcher and T. D. Rossing, *The Physics of Musical Instruments* (Springer-Verlag, New York, 1991).
[23] V. Bucur, *Acoustics of Wood* (CRC Press, Boca Raton, 1995).

Why pinnipeds don't echolocate

Ronald J. Schusterman and David Kastak
Long Marine Laboratory, University of California at Santa Cruz, 100 Shaffer Road, Santa Cruz, California 95060

David H. Levenson
Scripps Institution of Oceanography, La Jolla, California 92093-0208

Colleen J. Reichmuth and Brandon L. Southall
Long Marine Laboratory, University of California at Santa Cruz, 100 Shaffer Road, Santa Cruz, California 95060

(Received 30 July 1999; accepted for publication 3 January 2000)

Odontocete cetaceans have evolved a highly advanced system of active biosonar. It has been hypothesized that other groups of marine animals, such as the pinnipeds, possess analogous sound production, reception, and processing mechanisms that allow for underwater orientation using active echolocation. Despite sporadic investigation over the past 30 years, the accumulated evidence in favor of the pinniped echolocation hypothesis is unconvincing. We argue that an advanced echolocation system is unlikely to have evolved in pinnipeds primarily because of constraints imposed by the obligate amphibious functioning of the pinniped auditory system. As a result of these constraints, pinnipeds have not developed highly acute, aquatic, high frequency sound production or reception systems required for underwater echolocation. Instead, it appears that pinnipeds have evolved enhanced visual, tactile, and passive listening skills. The evolutionary refinement of alternative sensory systems allows pinnipeds to effectively forage, navigate, and avoid predators under water despite the lack of active biosonar capabilities. [S0001-4966(00)01804-X]

PACS numbers: 43.80.Ka, 43.80.Lb [WA]

INTRODUCTION

The most recent review of dolphin echolocation (Au, 1993) clearly shows that these animals have evolved sophisticated sonar systems to explore their environment. Echolocation performance depends on the evolution of specialized sound production, sound reception, and signal processing mechanisms. Active biosonar has enhanced the ability of odontocete cetaceans (dolphins and other toothed whales) to exploit underwater foraging environments where the visual sense is often of limited use. For this reason, echolocation has periodically been hypothesized to occur in other marine mammals, specifically the pinnipeds (seals, sea lions, and walruses).

Echolocation in bottlenose dolphins (*Tursiops truncatus*) was convincingly demonstrated about 40 years ago in experiments that required echolocating dolphins to perform obstacle avoidance or object discrimination tasks (Schevill and Lawrence, 1956; Kellogg 1958; Turner and Norris, 1966). To ensure that the dolphins were relying on biosonar and not visual cues while performing these operations, the dolphins completed the experimental tasks while swimming in murky or dark waters or while wearing rubber suction cups over their eyes (Schusterman, 1980). These subjects were able to orient in darkness by using a bistatic, active sonar system employing high frequency sounds. This system is used by many, if not all, odontocetes to detect and avoid obstacles and pursue prey. High frequency biosonar is selectively advantageous because of the increased resolving power of a system using signals with wavelengths smaller than the objects being targeted. This is especially important in water, in which sound speed is greater than sound speed in air by a factor of more than 4.

Like dolphins, pinnipeds forage at times in relatively dark waters. This ecological similarity eventually led to the proposition that most, if not all, pinnipeds had also evolved specialized sound emissions and hearing abilities in order to echolocate (Poulter, 1963). Indeed, Poulter (1963, 1966, 1967) reported that he had experimentally demonstrated sophisticated echolocation in California sea lions (*Zalophus californianus*) following observations and underwater recordings of captive animals approaching food items under a variety of conditions. Poulter (1967) additionally suggested that other otariid pinnipeds including the Steller sea lion (*Eumetopias jubatus*) and the northern fur seal (*Callorhinus ursinus*) used their normal in-air vocalizations for underwater echolocation signals. However, contrary to Poulter's (1963) observation that California sea lion underwater vocalizations ranged in frequency from 5 to 13 kHz while approaching fish in the dark, other investigators found that most of these sounds were of low frequency (<4 kHz), and were associated with social interactions rather than foraging activity (Schevill *et al.*, 1963; Schusterman, 1967). Systematic experimentation on the sonar ability of California sea lions has consistently yielded negative results (Evans and Haugen, 1963; Schusterman, 1967).

Poulter (1967) also hypothesized that some of the phocid seals, including bearded seals (*Erignathus barbatus*), Weddell seals (*Leptonychotes weddellii*), and leopard seals (*Hydrurga leptonyx*) had evolved highly specialized sonar

systems. In contrast to the otariids, which vocalize under water somewhat infrequently, most phocids routinely emit underwater signals that are thought to be related primarily to reproductive behavior. With few exceptions, these sounds are low in frequency (see Richardson *et al.*, 1995, for a review). Renouf and Davis (1982) hypothesized that the pulsatile sounds produced by harbor seals (*Phoca vitulina*) constitute active biosonar signals; however, their interpretations of a target discrimination experiment on this species were challenged based on alternative explanations for the seal's performance (Wartzok *et al.*, 1984). Other experiments testing for echolocation in phocids have been performed on gray seals (*Halichoerus grypus*) in controlled obstacle avoidance, maze learning, or target detection tasks. These experiments yielded negative results (Oliver, 1978; Scronce and Ridgway, 1980).

Despite the lack of supporting evidence, the pinniped echolocation hypothesis maintains a foothold in popular treatments of marine mammal acoustics, and has recently been resurrected based on earlier underwater observations on a single captive leopard seal that emitted high frequency signals while chasing fish under darkened conditions (Thomas *et al.*, 1983). The descriptions of the signals, along with the seal's behavior, have been expanded and updated (Awbrey *et al.*, in press). Awbrey *et al.* (in press), have joined Poulter (1967) in suggesting that Antarctic pinnipeds, which inhabit ice-covered areas and live in relative darkness during part of the year, are the most likely pinniped species to have evolved a specialized echolocation system, and that a variety of acoustic signals are used by these species in contexts of foraging and navigation.

Echolocation, defined in an evolutionary sense, is a specialized adaptation and not a generalized skill that may be used fortuitously when other sensory modalities are in some way prevented from being used. Examples of opportunistic echolocation include experimental evidence that blind and sighted humans can be trained to detect, locate, and discriminate targets by listening for reflected echoes (Rice *et al.*, 1965). In addition, rats are capable of using echoes from the sounds of their own movements to facilitate navigation through a maze (Riley and Rosenzweig, 1957). However, neither humans nor rats have evolved specialized mechanisms to detect objects or navigate via echolocation, even though such performance can emerge through experience (Schusterman, 1981). Indeed, the very notion that dolphins and microchiropteran bats perform complex tasks using sophisticated active biosonar is diminished by an expanded definition of echolocation that also includes the anomalous performance of nonspecialized animals. In a general sense, even though many, if not all, higher vertebrates can learn to use echoes to gain information about their environment in a crude or rudimentary fashion, most do not possess a specialized echolocation system [but see Tyack (1997) for a counter-argument].

In this paper, we consider the issue of whether some or all species of pinnipeds possess specialized acoustical abilities for underwater echolocation of the type shown by odontocete cetaceans. We will argue that, unlike the aquatic dolphins, pinnipeds have not developed active biosonar; rather, the amphibious lifestyle of pinnipeds has resulted in relatively nonspecialized underwater hearing abilities. We propose that many pinniped species depend on sensory capabilities other than active biosonar, including underwater hearing, enhanced vision, and acute hydrodynamic reception to explore their environment, particularly while foraging.

I. EARS AND HEARING

The typical mammalian ear is adapted to hear in air. The transition of certain vertebrates from water to land was accompanied by the evolution of the middle ear as an impedance matching mechanism, allowing the originally water-adapted ear to function in air. Impedance matching between the environment and the inner ear is achieved primarily by pressure amplification due to lever action and areal ratio transformation by the middle ear ossicles. Low pressure/high particle velocity sound waves in air are transformed into high pressure/low particle velocity waves in the inner ear fluid. The adaptive radiation of some mammalian lineages into the water introduced a new air–water interface separating the liquid environment and the air-filled middle ear. The middle ear, instead of performing its normal pressure amplifying function, would have suffered a severe loss of efficiency, because nearly 100% of incident acoustic energy is reflected at the air–water interface. In order to maintain auditory sensitivity under water, secondarily aquatic vertebrates needed to develop novel auditory adaptations; consequently, aquatic ears evolved independently and to different degrees in at least three lineages of marine mammals (carnivores, cetaceans, and sirenians). Organisms in only one of these groups (the odontocete suborder of the cetacea) are known to use echolocation. In roughly 60 million years of cetacean evolution, the outer and middle ears of odontocetes have become dramatically modified to facilitate reception of waterborne sound. The precise sound routes and sensory mechanisms involved in sound detection have not been elucidated; however, it is commonly accepted that the dolphin ear has become fully water-adapted in terms of best absolute sensitivity and differences between hearing in air and in water (see Ketten, 1992, for a review of the cetacean ear). The evolutionary restructuring of the dolphin ear for underwater use was possible in part because the cetacean lineage, in contrast to the secondarily aquatic carnivore lineages, has evolved entirely in water.

The first pinnipedlike animals appear in the fossil record about 27–25 million years ago and the closest living relatives to modern pinnipeds are other arctoid carnivores, most likely the ursids and mustelids (Tedford, 1976), and the ancestral pinniped ear was probably similar to that of a generalized carnivore. Indeed, apart from the presence of a layer of distensible vascularized tissue, the pinniped middle ear possesses few characteristics that cannot be found in certain other terrestrial mammals (Repenning, 1972). In contrast to cetaceans, pinnipeds spend a significant portion of their lives on land, and must attend to airborne as well as underwater sounds. Unlike the dolphin ear, the pinniped ear appears to have been constrained during its evolution by the necessity of functioning in two acoustically dissimilar media.

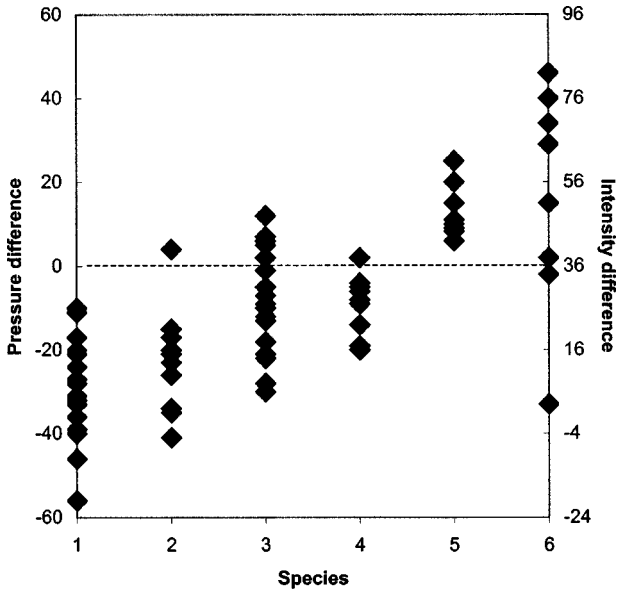

FIG. 1. Differences (in dB) between in-air and underwater sound pressure and intensity detection thresholds for five pinnipeds and one cetacean. Positive values indicate lower thresholds in water; negative values indicate lower thresholds in air. Species plotted are otariids: (1) northern fur seal, (2) California sea lion; generalized phocids: (3) harbor seal, (4) harp seal; and aquatic specialists, (5) northern elephant seal, (6) bottlenose dolphin. Statistically significant differences occur between all groupings: otariids and generalized phocids; otariids and water specialists; and generalized phocids and water specialists. Data summarized from Kastak and Schusterman (1998, 1999) and Richardson *et al.* (1995).

Early interpretations of amphibious functioning indicated that the seal ear was intermediate between a water adapted and an air adapted ear, given that a fully water-adapted ear would suffer a 30-dB loss in sensitivity in air and vice versa (Møhl, 1968). Later audiometric studies showed that, in general, the phocids appeared to be semi- or fully water adapted while the otariids, though able to hear with greater sensitivity under water than in air, did so with less facility than the phocids [see reviews by Schusterman (1981) and Richardson *et al.* (1995)]. In terms of the detection of acoustic energy, all pinnipeds tested thus far hear better in water than in air. However, in terms of acoustic pressure detection, the otariids appear to be primarily adapted to hear in air, while the phocids are generally adapted for amphibious hearing (Kastak and Schusterman, 1998). This trend holds for all phocids thus far studied except the deep-diving northern elephant seal, which detects acoustic pressure better under water than in air (Kastak and Schusterman, 1999). In Fig. 1, we demonstrate that the northern elephant seal shows differences in aerial and underwater sensitivity paralleling those of the bottlenose dolphin, implying aquatic specialization. The figure also shows that when pairwise comparisons of air–water sensitivity are made between pinnipeds, there are significant differences between phocids and otariids, and between the elephant seal and all other pinnipeds whose hearing has been tested both in air and under water. The patterns of air and water hearing sensitivity appear to correspond to the patterns of the life history of three pinniped assemblages: the otariids, the generalized phocids (*Phoca spp.*), and the northern elephant seal, a specialized phocid (Kastak and Schusterman, 1998, 1999). Except for the elephant seal, the pinnipeds have retained good airborne hearing sensitivity, and the necessity to hear well in air has constrained the development of the exceptional underwater sensitivity necessary for refined echolocation. However, even the elephant seal (in contrast to the dolphin) must detect conspecific signals in air in contexts related to social behavior and pup attendance (Kastak and Schusterman, 1999).

The refinement in the pinnipeds of sensory mechanisms other than echolocation for underwater orientation was due in part to selection pressures for maintaining auditory sensitivity in air, but also to phylogenetic constraints of the basic carnivore ear structure. These constraints are illustrated by a comparison between the aerial hearing sensitivity of the generalist pinnipeds and terrestrial carnivores. These taxa are similar in terms of best sensitivity (no more than 10–20 dB difference between pinnipeds and most nonfeline carnivores tested) and in terms of upper frequency limit (no more than 10–15 kHz difference between pinnipeds and most nonfeline carnivores; Fay, 1988). Differences in best sensitivity can be accounted for by the structure of the pinniped external meatus, which acts as a valve to keep water from entering the ear upon submersion. Differences in upper frequency limit of pinnipeds and fissipeds may be related to differences in body size (Rosowski, 1994). The conservation of the basic carnivore ear is evident not only in anatomy (Repenning, 1972) but in aerial function as well (e.g., Moore and Schusterman, 1987). Based on these factors, it is likely that both phylogenetic constraints and selective pressures acting to maintain airborne sensitivity precluded the development of very acute high frequency sensitivity necessary for efficient echolocation in the aquatic environment. The pinniped ear has instead evolved through natural selection to function amphibiously, perhaps at the cost of the evolution of an active biosonar system.

II. PASSIVE BIOSONAR

Laboratory experiments have shown that both phocid and otariid pinnipeds can localize underwater signals of low and intermediate frequencies up to about 16 kHz (reviewed by Schusterman, 1981) and therefore, by listening, may obtain a wealth of biologically significant information from their underwater environment. In addition to determining the location and status of conspecifics, certain pinnipeds may acoustically detect and localize predators such as sharks and killer whales. Sharks produce no communicative acoustic signals, but incidental sounds associated with their swimming or feeding may alert nearby pinnipeds. Killer whales do emit social and echolocation signals and there is some evidence suggestive of the ability of pinnipeds to detect them. A population of mammal-hunting killer whales in the north Pacific echolocate with fewer, more irregularly spaced clicks compared to another population that forages on fish (Barrett-Lennard *et al.*, 1996). These killer whale echolocation clicks have significant energy from 4 to 18 kHz, a span that falls within the most sensitive hearing range of most pinnipeds but is above the upper frequency hearing limit of most fish species (Popper and Fay, 1993). These observations are augmented by a report that killer whales in the

Indian Ocean are also acoustically cryptic when preying on southern elephant seals and king penguins (Guinet, 1992). In a captive setting, Schusterman and Kastak (1996) found that a northern elephant seal failed to habituate to, and in fact became sensitized to pulsatile sounds resembling killer whale echolocation clicks. These observations indicate that underwater hearing may play an important predator alerting function for the pelagic deep diving elephant seals that must spend more time resting at sea than more coastal species. This predator–prey system is analogous to the coevolution of the echolocation signals of some insectivorous bats and their detection by nocturnal moths (Fenton and Fullard, 1981).

Localization of prey by the sounds they produce may be an additional use of underwater hearing. Acoustic signals are produced under water by a wide range of organisms preyed upon by pinnipeds. Swimming, struggling, or foraging animals produce incidental sounds that may attract predators (Myrberg, 1981). Additionally, many invertebrates, teleost fish, and other marine animals produce communicative sounds in social, reproductive, and foraging contexts that may be detected over greater distances (Tyack, 1998). Interception of prey sounds by predators has been documented in several fish species (see Myrberg, 1981), and some cetaceans have been shown to acoustically detect prey items without using echolocation when they are experimentally blindfolded or are too far from prey for visual detection (Wood and Evans, 1980; Barrett-Lennard *et al.*, 1996). It is not known whether pinnipeds can detect prey by eavesdropping on the sounds they make; however, captive California sea lions can locate live fish, without emitting sound, in conditions of limited visibility (Schusterman, 1967). These findings may help to explain observations of apparently blind, free-ranging pinnipeds that survived for relatively long periods, thus supporting the notion that their hearing plays some role in prey detection (Schusterman, 1981).

In addition to facilitating predator avoidance and prey capture, hearing in pinnipeds may also function in spatial orientation and navigation. Many pinnipeds are active at night or in turbid water where vision is of reduced utility as an orientation mechanism. Others spend long periods diving deeply and continuously at sea where visual reference to coastal, bathymetric, and celestial features is limited. Efficient propagation of acoustic signals in water has prompted speculation by Norris (1967) that sounds produced by biotic or abiotic sources may function as a guidance mechanism for pinnipeds (for example, distant wave noise may demarcate the approximate location of a coastline). In the same vein, Norris (1967) suggested that sounds produced by marine animals characteristic of specific environments might convey depth as well as ecological information to an experienced passive listener.

The function of underwater hearing in free-ranging pinnipeds remains largely uninvestigated. However, experiments in the field by Wartzok *et al.* (1992) showed that blindfolded polar seals—ringed seals (*Phoca hispida*) and Weddell seals (*Leptonychotes weddellii*)—use acoustic cues provided by the experimenters to find novel holes cut through the ice. After these seals have oriented in the presence of acoustic cues, they rapidly acquire a cognitive spatial map of their environment that allows them to navigate under the ice in the absence of these acoustic cues. Based on the observation that these seals do not vocalize while searching for holes in the ice, echolocation is apparently neither required nor used for this task.

Hearing efficiency in a noisy environment depends on the ability to detect signals embedded in noise. Masking of biologically significant sounds reduces the range over which detection may occur. Some pinnipeds vocalize incessantly during the breeding season, presumably to increase the probability of signals being detected over high levels of noise common in coastal environments (Peterson and Bartholomew, 1969; Schusterman, 1978). Based on evidence from auditory masking experiments, pinnipeds perform quite well at extracting tonal signals from noise over a range of frequencies (reviewed in Richardson *et al.*, 1995; Southall *et al.*, 1998). This is likely a result of the naturally noisy environments they inhabit and the relatively wide bandwidths of biologically significant signals they must detect, which place a premium on efficient listening. The refinement of these listening skills in the pinnipeds may have at least partially offset the pressures to develop more sophisticated active biosonar.

III. SOUND PRODUCTION

Pinnipeds produce a wide variety of signals under water, including whines, grunts, roars, chirps, and pulsed sounds (reviewed by Richardson *et al.*, 1995). Many of these sounds are known to be related to social behavior and reproduction; however, the emission of high frequency and pulsed sounds has led some researchers to speculate about the existence of echolocation in pinnipeds. In this section, we outline the characteristics of dolphin echolocation sounds (reviewed by Au, 1993) and their presumed counterparts in pinnipeds, and argue that there is at present no evidence that pulsed and/or ultrasonic pinniped sounds are used for echolocation.

The bottlenose dolphin produces broadband echolocation clicks with significant energy at frequencies above 90 kHz. The clicks are extremely loud, with source pressure levels typically exceeding 200 $dB_{(pp)}$ *re*: 1 μPa. The production of loud signals probably compensates for signal and echo losses associated with sound absorption by water. The melon, a mass of fatty tissue located anterior to the braincase, is thought to enhance transmission of the echolocation pulse from the tissues of the head into the environment, as well as acting as a waveguide to focus the echolocation sound beam. As a result, the directionality of the transmitted pulse trains is extremely high. Dolphins exercise fine control over the temporal patterns of their echolocation signals; pulses are short (about 50–70 μs), and click intervals in detection tasks directly relate to the two-way transit time from source to target and back. Consequently, the dolphin has time to receive and process each echo before producing the next click. Dolphins approaching a target generally decrease the inter-pulse interval in proportion to the change in target range—individual pulses comprising click trains become more closely spaced as range decreases.

Given that pinnipeds also produce underwater sounds, it is a worthwhile question to ask whether these sounds could

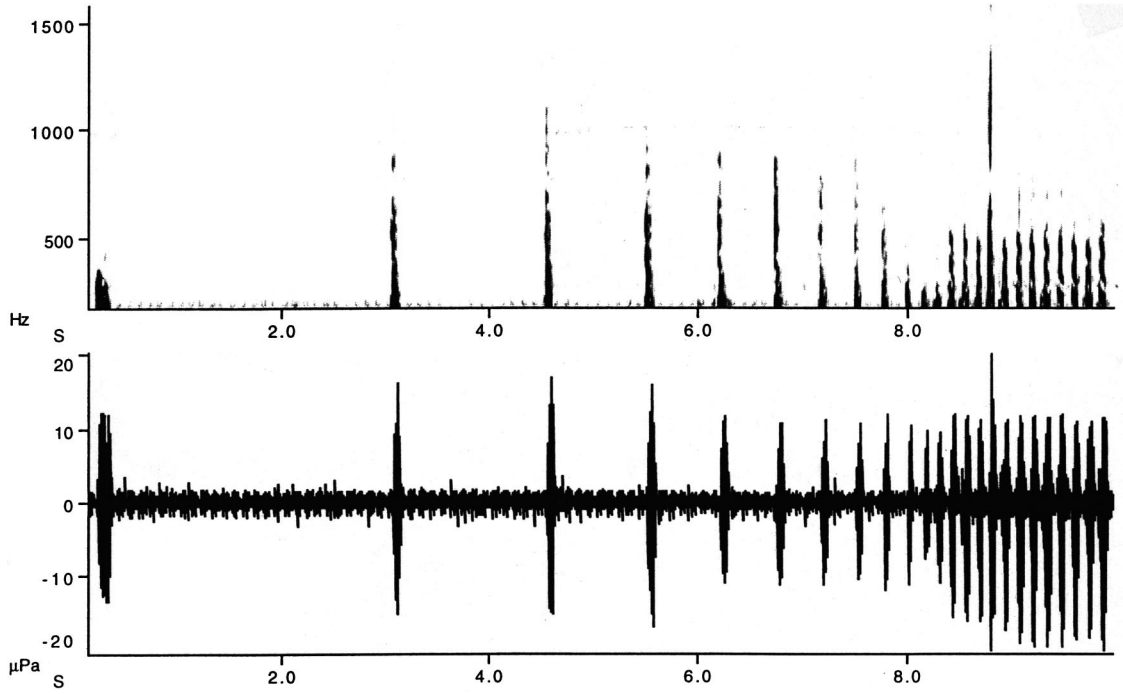

FIG. 2. Sound spectrogram and oscillogram of Weddell seal vocalizations produced while approaching an ice hole. The recording hydrophone was mounted on the seal's back (Davis *et al.*, 1999). Note the pulsatile nature and change in interpulse interval as the seal closed in on the ice hole. This figure is courtesy of Dr. William E. Evans.

function in a manner analogous to the echolocation pulses produced by odontocetes. What are the features of these sounds that make them appealing to proponents of the echolocation hypothesis? As Fig. 2 shows, many of them are pulsatile and repetitive, thus superficially resembling the click trains produced by dolphins, while some, such as those produced by the leopard seal, are ultrasonic and ought to provide detailed information about small targets. Further, many of these sounds have been recorded during foraging or navigation. Aside from the overall lack of experimental evidence for echolocation in pinnipeds, there are several uncertainties about pinniped vocalizations that have not been addressed by echolocation proponents. First, source levels are relatively low, ranging from only about 90 to 190 dB. In fact, the source levels of ultrasonic signals produced by leopard seals, perhaps the sounds most likely to be related to echolocation, have been described as ''low amplitude'' or ''weak'' (Richardson *et al.*, 1995; Thomas *et al.*, 1983). Some of these sounds, for example, FM sweeps, are also emitted almost continuously, with a duty cycle that does not appear to allow for detection and processing of echo returns between the production of subsequent outgoing pulses. Echoes from long duration FM sweeps would also be contaminated by background reverberation (especially under ice), making detection of small targets difficult. Even the shorter-duration pulses, which can be much longer than those of dolphin clicks (0.3 to >10 ms), while allowing detection of large objects, would not allow the fine target resolution seen in odontocetes. In contrast to the dolphins, pinnipeds do not appear to modify the temporal patterning of click signals according to target range in laboratory tests of echolocation performance (Schusterman, 1967). However, Evans *et al.* (in press, and as shown in Fig. 2) report that Weddell seal pulse rates changed as the seals approached ice holes. However, these authors conclude that the changes in interpulse interval might serve functions other than echolocation, for instance, arousal or advertisement (Evans *et al.*, in press). Additionally, the only pinniped tested in a temporal integration task performed relatively poorly; Terhune (1988) found that thresholds for brief pulses in a harbor seal were some 30–40 dB higher than thresholds for long tones at the frequency of best sensitivity. In contrast, the bottlenose dolphin threshold for high frequency brief pulses is only 10–20 dB higher than thresholds for long tones. Thus although the data are limited, it appears that the bottlenose dolphin, an echolocator, is better adapted to detect very brief acoustic signals than is the harbor seal. Given that best thresholds for long pure tones in the dolphin are some 20 dB lower than the best thresholds for the seal, the latter probably does not produce signals of sufficient intensity to detect prey at all but the shortest ranges, where other senses such as vision would accomplish the same task in a less energetically costly fashion. Further, the bottlenose dolphin has been shown to have a highly directional receiving beam, with a minimum audible angle of less than 1 degree for brief clicks, effectively increasing the signal-to-noise ratio of echo returns. Minimum audible angles for clicks in pinnipeds range from about 6 degrees in a California sea lion to about 4.5 degrees for a harbor seal—five to nine times poorer than the bottlenose dolphin. All of these observations suggest an acoustic system that is qualitatively different from that of the dolphin, in terms of sound production, sound reception, and orienting behavior.

Seasonal or geographic conditions of near or total darkness have been proposed as selective forces for the development of a pinniped active biosonar system. According to this hypothesis, pinnipeds that inhabit polar regions and/or dive

to extreme depths are the species most likely to echolocate. Attention has recently focused on the Antarctic leopard and Weddell seals, which are known to be extremely vocal under water (Awbrey *et al.*, in press; Evans *et al.*, in press). Although Evans *et al.* (in press) have proposed that Weddell seals echolocate in a foraging context, this proposition is contradicted in a recent study by Davis *et al.* (1999) who, on the basis of underwater observations of foraging seals, concluded that, '' . . . it seems unlikely that Weddell seals use active sonar to locate prey as some other marine mammals do (p. 995).'' Further, the primary prey items of Weddell seals, notothenioid fish (Davis *et al.*, 1999), lack swimbladders and thus scatter relatively little acoustic energy, especially at low frequencies. Given the generally low frequencies and source levels of Weddell seal calls, as well as the weak target strengths of typical prey items, it is reasonable to conclude at this time that this species is unable to detect prey using active biosonar.[1] Rather, the Weddell seal, as well as the leopard seal, probably relies mainly on vision to detect prey (Davis *et al.*, 1999).

In addition to foraging, it has been proposed that pinnipeds use active biosonar to navigate, for instance, in finding ice holes from underneath the Antarctic fast ice (Evans *et al.*, in press). However, in this study, only about half the seals produced clicks while approaching ice holes, and these authors concede that the sounds may be used as social or territorial signals broadcast to conspecifics. Although there is very little information on directionality in sound production, Schevill and Watkins (1971) concluded that the Weddell seal sound beam is directed forward and down. In order to best detect ice holes using active biosonar, these seals would have to swim and surface in an upside-down position. Considering the sensitivity of the pinniped visual system, it is far more reasonable to infer that these seals navigate by sight than by active biosonar.

So, what of the considerable circumstantial and anecdotal evidence for echolocation in seals and sea lions, such as pulsatile sounds recorded from pinnipeds in foraging or navigating contexts? Conclusions regarding the functions of such signals must by made with caution. For example, many species that produce the most intense underwater sounds produce them only in contexts related to social interactions and/or general arousal (Schusterman, 1967; Ballard and Kovacs, 1995). This makes interpretation of underwater sounds produced by a hungry animal feeding in darkness problematic—such sounds may be related to affect or motivation rather than prey detection. The influence of motivational factors on sound production in most pinnipeds is likely to remain unknown until more data on the underwater behavior of these animals are available. Until we gain a comprehensive picture of the sensory systems of species such as the Weddell and leopard seals, echolocation cannot be completely ruled out as a possibility. On the other hand, given the relative ease with which echolocation can be examined in many odontocetes, it is improbable that this ability is merely being overlooked in the pinnipeds.

IV. VISION

In the majority of reviews of pinniped sensory ecology, hearing is assumed to be of paramount importance to underwater foraging and navigation. Reliance on the acoustic sense seems to be a straightforward proposition, given the relative efficiency with which sound waves propagate under water. Light, on the other hand, is absorbed rapidly in the water column, and it is often assumed that complete or nearly complete darkness is characteristic of marine mammal foraging environments. However, a few authors (e.g., Schusterman, 1981) have attempted to reinforce the idea that pinnipeds forage visually, based on studies of anatomy (Walls, 1942) and behavior (Schusterman, 1981; Levenson and Schusterman, 1997, 1999) supporting the idea that the pinniped eye possesses adaptations allowing function in water and under dark conditions.

The first photorefractive studies of pinnipeds showed that the eyes of these amphibious mammals were primarily suited for vision in water rather than in air (Johnson, 1893). Like most aquatic vertebrates, pinnipeds possess large, round lenses to compensate for the absence of corneal refraction under water (Walls, 1942). In air, where refraction occurs at both the round lens and the cornea, pinnipeds are myopic (Piggins, 1970). However, their stenopaic (slitlike) pupils functions as pinhole apertures to reduce the effects of myopia in air and provide relatively clear vision, at least as long as the pupil remains relatively small (Walls, 1942). Behavioral studies have confirmed the pupil's role in aerial acuity when it was demonstrated that visual acuity drops off much faster in air than under water as ambient light levels decrease (Schusterman and Balliet, 1971).

While the pupil's role in compensating for myopia in air is clear, the pupillomotor mechanism itself is controlled primarily by ambient light levels, irrespective of medium (Lavigne and Ronald, 1972). Like other mammals adapted for vision in dim conditions, pinnipeds possess large lenses and pupils, and densely packed, rod dominated retinas with well-developed choroidal tapeta (Walls, 1942; Landau and Dawson, 1970). The ability to dramatically alter pupil size is almost certainly an adaptation to regulate illumination of the light-sensitive retinas and functions only secondarily to improve visual resolution. Indeed, the pupillomotor response is probably essential to maintaining appropriate levels of photoreceptor stimulation during the rapid changes in light levels experienced by diving animals. In support of this conclusion, substantial differences in pupillary dynamic range between shallow and deep diving pinnipeds have been observed (Levenson and Schusterman, 1997). The deepest-diving pinniped, the northern elephant seal, was found to be capable of an over 400 fold increase in pupillary area, while shallow and moderately deep divers possessed considerably smaller ranges of only 25–200 fold (Levenson and Schusterman, 1997).

The functional significance of differences in pupillary structure can be seen clearly in a comparison of the dark adaptation rates of pinnipeds. Figure 3 depicts these rates for three species. In the inset of Fig. 3, the time necessary to reach maximum sensitivity is seen to be substantially faster for the elephant seal than for the shallower diving California

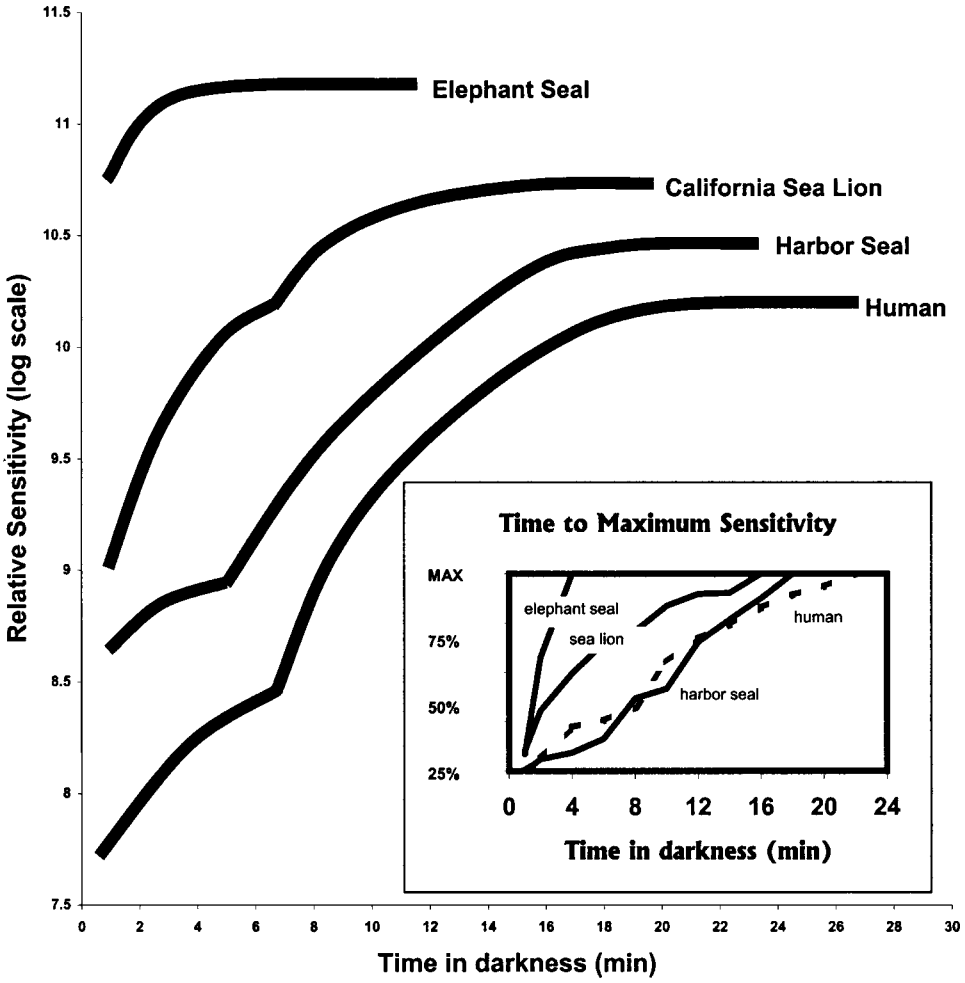

FIG. 3. Dark adaptation in three pinniped species and a human subject. Sensitivity values are reported on a relative log scale and were determined from the inverse of the each subject's white light threshold for each time interval. (Inset) Time to reach maximum sensitivity for three pinniped species and a human subject. Percentage values were calculated from sensitivity data as [(observed sensitivity/max sensitivity)*100]. Adapted from Levenson and Schusterman (1999).

sea lion and harbor seal. The 6-min dark adaptation time of the elephant seal (Levenson and Schusterman, 1999) matches the time it takes these seals to dive from the surface to foraging depths of 300–700 m (LeBoeuf and Laws, 1994), strongly implicating the visual sense in foraging ecology.

In addition to having rapid dark adaptation rates, elephant seals are highly light sensitive. This seal's extreme visual sensitivity directly relates to its ability to make long dives to great depths where ambient light levels are always low. Additionally, elephant seals possess specialized rod pigments that increase their sensitivity to the shorter wavelengths of light that predominate deep under water (Lythgoe and Dartnall, 1970). There are significant differences in maximum visual sensitivity between the elephant seal and shallow-diving species (Levenson and Schusterman, 1999), presumably because of the different conditions found in their respective foraging environments. Thus shallower diving harbor seals and California sea lions are less light sensitive than the elephant seal, and possess rod pigments that are only slightly short-wavelength shifted in sensitivity in comparison to those of terrestrial mammals (Lavigne and Ronald, 1975; Jacobs *et al.*, 1993).

These speculations about the importance of vision in foraging have recently been supplemented by observations of the Weddell seal, a deep diving phocid. Davis *et al.* (1999) obtained evidence that pinnipeds use backlighting to silhouette their prey while visually hunting. The researchers studied the hunting behavior of these seals beneath the Antarctic fast ice with a seal-borne video system. The seals were observed to stalk large Antarctic cod and smaller sub-ice fish whose silhouettes could be seen against the sunlight and ice above. During these observations of foraging in Weddell seals, these animals rarely vocalized, suggesting that echolocation was not the primary sensory system used for hunting fish prey beneath the ice.

Much remains to be learned about the visual capabilities of pinnipeds. However, the available evidence strongly suggests that their visual systems are primarily adapted for use under water. Pinnipeds have sacrificed the quality of their terrestrial vision in favor of enhancing their underwater capacities; natural selection in these animals has clearly favored the development of visual systems suited to foraging in an aquatic environment.

V. VIBRISSAE

Benthic-feeding dolphins have been observed to direct echolocation pulses into the substrate in order to detect prey (Rossbach and Herzing, 1997). These dolphins possess no apparent adaptation for benthic feeding, yet do so opportunistically using a biosonar system designed for use in the water. Pinnipeds that characteristically forage on the muddy sea floor tend to have modified vibrissae and facial structures used to detect and extract prey from the bottom (Reidman,

1990). The vibrissae of pinnipeds are apparently used to detect tactile and hydrodynamic stimuli very close to the source. The vibrissae of foraging Weddell seals were noted to become erect when they closed in on their fish prey (Davis *et al.*, 1999), suggesting that the vibrissae were used during the final stages of prey capture. Further, vibrissal function has been implicated in the short-range detection of ice holes by arctic phocids (see Reidman, 1990).

The extensive innervation of pinniped vibrissae, which can be up to ten times greater than that of terrestrial mammals (Hyvärinen and Katajisto, 1984), makes them well suited as a displacement detection mechanism (Dykes, 1975). Dehnhardt *et al.* (1998) experimentally demonstrated that a harbor seal was capable of detecting extremely weak hydrodynamic stimuli in the near field. These vibrations were several orders of magnitude below the particle velocities in the wake produced by a small swimming fish. Although probably useless for long range detection of prey or navigation, the vibrissae of pinnipeds likely function in close-range foraging and object detection when the visual sense is occluded or when prey is very close to the mouth and away from the line of sight.

VI. CONCLUSIONS

A highly sophisticated system of active biosonar has evolved only once in the marine environment, in a group of marine mammal predators—the odontocetes—that became completely tied to an aquatic existence early in their evolution. Echolocation in this group is linked to development of a high frequency signal production, reception, and signal processing system (Au, 1993). Because odontocetes were not evolutionarily constrained to give birth on land, the dolphin acoustic system became fully adapted for underwater functioning, allowing a refinement of the biosonar system not possible in amphibious mammals such as the pinnipeds. Because even the most aquatic pinnipeds must return to shore periodically and because airborne vocal communication appears to play an important role in most, if not all, pinniped social systems, selection pressures for highly sensitive, acute underwater hearing have not shaped the pinniped auditory system to as great an extent as they have in the dolphins.

All pinnipeds give birth on land or on ice, and terrestrial breeding activities have resulted in selection for retention of in-air hearing, primarily in the context of communication. Amphibious hearing ability has limited the sensitivity of hearing under water, where all pinnipeds must forage. Instead of developing a primarily sound-based system of underwater orientation, pinniped visual, tactile, hydrodynamic, and acoustic sensory systems were refined and incorporated into overlapping underwater perceptual channels that permit efficient underwater foraging and navigation without the use of active biosonar.

ACKNOWLEDGMENTS

This work was supported by Grant No. N00014-99-1-0164 from the Office of Naval Research to RJS. The authors thank the student volunteers of Pinniped Research in Cognition and Sensory Systems at Long Marine Laboratory for assistance with animal care and experiments in vision and audition. The ideas in this paper were augmented by detailed descriptions of experimental work with free-ranging seals provided by Doug Wartzok. Whit Au, Bill Evans, and Bertel Møhl provided constructive criticisms of an earlier version of this manuscript and helped us frame some of the issues regarding sound production. This paper is dedicated to the memories of Winthrop Niles Kellogg, Kenneth Stafford Norris, and the first international meeting on Animal Sonar Systems in Frascati, Italy, 1966.

[1]With pulse frequencies between about 10 and 100 kHz, the target strength of a 10-cm fish in side aspect would be between about −40 and −45 dB (Urick, 1983). A seal producing these pulses for the purpose of echolocation, at source levels of about 140 dB *re*: 1 μPa and having a detection threshold of about 65 dB *re*: 1 μPa should be able to detect such a fish in side aspect at a range of about 7.5 m. Similar calculations by Au (1990) for a bottlenose dolphin resulted in ranges of detectability for a fish of similar size of between 73 and 87 m. Given under-ice reverberation, ambient noise, the lack of a resonant swim bladder in Antarctic notothenioids, oblique target aspect, and relatively poor directional hearing in pinnipeds, the figure of 7.5 m is likely to overestimate the effective range of detection of a single fish by a Weddell or leopard seal.

Au, W. W. L. (**1990**). ''Echolocation in dolphins,'' in *Comparative Perception: Basic Mechanisms*, edited by M. A. Berkeley and W. C. Stebbins (Wiley, New York), pp. 315–350.

Au, W. W. L. (**1993**). *The Sonar of Dolphins* (Springer-Verlag, New York).

Awbrey, F. T., Thomas, J. A., and Evans, W. E. (**in press**). ''Ultrasonic underwater sounds from a captive leopard seal (*Hydrurga leptonyx*),'' in *Advances in the Study of Echolocation in Bats and Dolphins*, edited by J. Thomas, C. Moss, and M. Vater (University of Chicago Press, Chicago).

Ballard, K. A., and Kovacs, K. M. (**1995**). ''The acoustic repertoire of hooded seals (*Cystophora cristata*),'' Can. J. Zool. **73**, 1362–1374.

Barrett-Lennard, L. G., Ford, J. K. B., and Heise, K. A. (**1996**). ''The mixed blessing of echolocation: Differences in sonar use by fish-eating and mammal eating killer whales,'' Anim. Behav. **51**, 553–565.

Davis, R. W., Fuiman, L. A., Williams, T. M., Collier, S. O., Hagey, W. P., Kanatous, S. B., Kohin, S., and Horning, M. (**1999**). ''Hunting behavior of a marine mammal beneath the Antarctic fast ice,'' Science **283**, 993–996.

Dehnhardt, G., Mauck, B., and Bleckmann, H. (**1998**). ''Seal whiskers detect water movements,'' Nature (London) **394**, 235–236.

Dykes, R. W. (**1975**). ''Afferent fibres from mystacial vibrissae of cats and seals,'' J. Neurophysiol. **38**, 650–662.

Evans, W. E., and Haugen, R. M. (**1963**). ''An experimental study of the echolocation ability of a California sea lion, *Zalophus californianus* (Lesson),'' Bull. S. Calif. Acad. Sci. **62**, 165–175.

Evans, W. E., Thomas, J. A., and Davis R. W. (**in press**). ''Vocalization from Weddell seals (*Leptonychotes weddelli*) during diving and foraging,'' in *Advances in the Study of Echolocation in Bats and Dolphins*, edited by J. Thomas, C. Moss, and M. Vater (University of Chicago Press, Chicago).

Fay, R. R. (**1988**). *Hearing in Vertebrates: A Psychophysics Databook* (Hill-Fay Associates, Winnetka, IL).

Fenton, M. B., and Fullard, J. H. (**1981**). ''Moth hearing and the feeding strategies of bats,'' Am. Sci. **69**, 266–275.

Guinet, C. (**1992**). ''Comportement de chasse des orques (*Orcinus orca*) autour des iles Crozet,'' Can. J. Zool. **70**, 1656–1667.

Hyvärinen, H., and Katajisto, H. (**1984**). ''Functional structure of the vibrissae of the ringed seal (*Phoca hispida Schr.*),'' Acta Zool. Fennica **171**, 27–30.

Jacobs, G. H., Deegan, II, J. F., Crognale, M. A., and Fenwick, J. A. (**1993**). ''Photopigments of dogs and foxes and their implications for canid vision,'' Vis. Neurosci. **10**, 173–180.

Johnson, G. L. (**1893**). ''Observations on the refraction and vision of the seal's eye,'' Proc. Zool. Soc. Lond. 719–723.

Kastak, D., and Schusterman, R. J. (**1998**). ''Low-frequency amphibious hearing in pinnipeds: Methods, measurements, noise, and ecology,'' J. Acoust. Soc. Am. **103**, 2216–2228.

Kastak, D., and Schusterman, R. J. (**1999**). ''In-air and underwater hearing

sensitivity of a northern elephant seal (*Mirounga angustirostris*),'' Can. J. Zool. **77**, 1751–1758.
Kellogg, W. N. (**1958**). ''Echoranging in the propoise,'' Science **128**, 982–988.
Ketten, D. R. (**1992**). ''The marine mammal ear: Specializations for aquatic audition and echolocation,'' in *The Evolutionary Biology of Hearing*, edited by D. B. Webster, R. R. Fay, and A. N. Popper (Springer-Verlag, New York), pp. 717–750.
Landau, D., and Dawson, W. W. (**1970**). ''The histology of retinas from the pinnipedia,'' Vision Res. **10**, 691–702.
Lavigne, D. M., and Ronald, K. (**1972**). ''The harp seal, *Pagophilus groenlandicus* (Erxleben 1777). XXIII. Spectral sensitivity,'' Can. J. Zool. **50**, 1197–1206.
Lavigne, D. M., and Ronald, K. (**1975**). ''Pinniped visual pigments,'' Comp. Biochem. Physiol. **52**, 325–329.
LeBoeuf, B. J., and Laws, R. M. (Eds.) (**1994**). *Elephant Seals* (University of California Press, Berkeley).
Levenson, D. H., and Schusterman, R. J. (**1997**). ''Pupillometry in seals and sea lions: Ecological implications,'' Can. J. Zool. **75**, 2050–2057.
Levenson, D. H., and Schusterman, R. J. (**1999**). ''Dark adaptation and visual sensitivity in shallow and deep-diving pinnipeds,'' Mar. Mammal Sci. **15**, 1303–1313.
Lythgoe, J. N., and Dartnall, H. J. A. (**1970**). ''A 'deep sea rhodopsin' in a mammal,'' Nature (London) **227**, 955–956.
Møhl, B. (**1968**). ''Auditory sensitivity of the common sea in air and water,'' J. Aud. Res. **8**, 27–38.
Moore, P. W. B., and Schusterman, R. J. (**1987**). ''Audiometric assessment of northern fur seals *Callorhinus ursinus*,'' Mar. Mamm. Sci. **3**, 31–53.
Myrberg, A. A. (**1981**). ''Sound communication and interception in fishes,'' in *Hearing and Sound Communication in Fishes*, edited by W. N. Tavolga, A. N. Popper, and R. R. Fay (Springer-Verlag, New York), pp. 395–425.
Norris, K. S. (**1967**). ''Some observations on the migration and orientation of marine mammals,'' in *Animal Orientation and Navigation*, Proceedings of the 27th Annual Biology Colloquium (Oregon State University Press, Corvallis, OR), pp. 101–131.
Oliver, G. W. (**1978**). ''Navigation in mazes by a grey seal, *Halichoerus grypus* (Fabricius),'' Behaviour **67**, 97–114.
Peterson, R. S., and Bartholomew, G. A. (**1969**). ''Airborne vocal communication in the California sea lion, *Zalophus californianus*,'' Anim. Behav. **17**, 17–24.
Piggins, D. J. (**1970**). ''Refraction of the harp seal, *Pagophilus groenlandicus* (Erxleben 1777),'' Nature (London) **227**, 78–79.
Popper, A. N., and Fay, R. R. (**1993**). ''Sound detection and processing by fish: Critical review and major research questions,'' Brain Behav. Evol. **41**, 14–48.
Poulter, T. C. (**1963**). ''Sonar signals of the sea lion,'' Science **139**, 753–755.
Poulter, T. C. (**1966**). ''The use of active sonar by the California sea lion, *Zalophus californianus* (Lesson),'' J. Aud. Res. **6**, 165–173.
Poulter, T. C. (**1967**). ''Systems of echolocation,'' in *Les Systemes Sonars Animaux, Biologie et Bionique*, edited by R. G. Busnel (Laboratoire de Physiologie Acoustique, Jouy-en-Josas, France), pp. 157–185.
Renouf, D., and Davis, M. B. (**1982**). ''Evidence that seals may use echolocation,'' Nature (London) **300**, 635–637.
Repenning, C. A. (**1972**). ''Underwater hearing in seals: functional morphology,'' in *Functional Anatomy of Marine Mammals*, edited by R. J. Harrison (Academic, New York), Vol. 1.
Reidman, M. (**1990**). *The Pinnipeds: Seals and Sea Lions* (University of California Press, Berkeley).
Rice, C. R., Feinstein, S. H., and Schusterman, R. J. (**1965**). ''Echo-detection ability of the blind: Size and distance factors,'' J. Exp. Psychol. **70**, 246–251.
Richardson, W. J., Greene, C. R., Malme, C. I., and Thomson, D. H. (**1995**). *Marine Mammals and Noise* (Academic, San Diego).
Riley, D. A., and Rosenzweig, M. (**1957**). ''Echolocation in rats,'' J. Comp. Physiol. Psychol. **50**, 323–328.
Rossbach, K. A., and Herzing, D. L. (**1997**). ''Underwater observations of benthic feeding bottlenose dolphins (*Tursiops truncatus*) near Grand Bahama Island, Bahamas,'' Mar. Mamm. Sci. **13**, 498–504.
Rosowski, J. J. (**1994**). ''Outer and middle ears,'' in *Comparative Hearing in Mammals*, edited by R. R. Fay and A. N. Popper (Springer-Verlag, New York), pp. 172–247.
Schevill, W. E., and Lawrence, B. (**1956**). ''Food-finding by a captive porpoise (*Tursiops truncatus*),'' *Brevoria* (Mus. Comp. Zool., Harvard) **53**, 1–15.
Schevill, W. E., and Watkins, W. A. (**1971**). ''Directionality of the sound beam in *Leptonychotes weddelli* (Mammalia: Pinnipedia),'' in *Antarctic Pinnipedia*, edited by W. H. Burt (American Geophysical Union, Washington), pp. 163–168.
Schevill, W. E., Watkins, W. A., and Ray, C. (**1963**). ''Underwater sounds of pinnipeds,'' Science **141**, 50–53.
Schusterman, R. J. (**1967**). ''Perception and determinants of underwater vocalization in the California sea lion,'' in *Les Systemes Sonars Animaux, Biologie et Bionique*, edited by R. G. Busnel (Laboratoire de Physiologie Acoustique, Jouy-en-Josas, France), pp. 535–617.
Schusterman, R. J. (**1978**). ''Vocal communication in pinnipeds,'' in *Behavior of Captive and Wild Animals*, edited by H. Markowitz and V. J. Stevens (Nelson-Hall, Chicago), pp. 247–308.
Schusterman, R. J. (**1980**). ''Behavioral methodology in echolocation by marine animals,'' in *Animal Sonar Systems*, edited by R. G. Busnel and J. F. Fish (Plenum, New York), pp. 11–41.
Schusterman, R. J. (**1981**). ''Behavioral capabilities of seals and sea lions: A review of their hearing, visual, learning, and diving skills,'' Psychol. Rec. **31**, 125–143.
Schusterman, R. J., and Balliet, R. F. (**1971**). ''Aerial and underwater visual acuity in the California sea lion (*Zalophus californianus*) as a function of luminance,'' Ann. (N.Y.) Acad. Sci. **188**, 37–46.
Schusterman, R. J., and Kastak, D. (**1996**). ''Pinniped acoustics: habituation and sensitization to anthropogenic signals,'' 33rd Annual Meeting of the Animal Behavior Society, Flagstaff, AZ.
Scronce, B. L., and Ridgway, S. H. (**1980**). ''Grey seal, *Halichoerus*: Echolocation not demonstrated,'' in *Animal Sonar Systems*, edited by R. G. Busnel and J. F. Fish (Plenum, New York), pp. 991–993.
Southall, B. L., Schusterman, R. J., and Kastak, D. (**1998**). ''Low frequency masked hearing thresholds in two pinniped species,'' World Marine Mammal Conference (Abstract). Monaco, 20–25 January.
Tedford, R. H. (**1976**). ''Relationship of pinnipeds to other carnivores,'' Syst. Zool. **25**, 363–374.
Terhune, J.M. (**1988**). ''Detection thresholds of a harbour seal to repeated underwater high-frequency, short-duration, and sinusoidal pulses,'' Can. J. Zool. **66**, 1578–1582.
Thomas, J. A., Fischer, S. R., Evans, W. E., and Awbrey, F. T. (**1983**). ''Ultrasonic vocalizations of leopard seals (*Hydrurga leptonyx*),'' Antarct. J. U.S. **17**, 186.
Turner, R. N., and Norris, K. S. (**1966**). ''Discriminative echolocation in a porpoise,'' J. Exp. Anal Behav. **9**, 535–544.
Tyack, P. L. (**1997**). ''Studying how cetaceans use sound to explore their environment,'' in *Communication*, edited by D. H. Owings, M. D. Beecher, and N. S. Thompson (Plenum, New York), Vol. 12, pp. 251–296.
Tyack, P. L. (**1998**). ''Acoustic communication under the sea,'' in *Animal Acoustic Communication*, edited by S. L. Hopp, M. J. Owren, and C. S. Evans (Springer-Verlag, Berlin), pp. 163–220.
Urick, R. J. (**1983**). *Principles of Underwater Sound* (McGraw-Hill, New York).
Walls, G. (**1942**). *The Vertebrate Eye and its Adaptive Radiation* (Hafner, New York).
Wartzok, D., Schusterman, R. J., and Gailey-Phipps, J. (**1984**). ''Seal echolocation?'' Nature (London) **308**, 753.
Wartzok, D., Elsner, H., Stone, J., Barchak, J., and Burns, W. (**1992**). ''Under-ice movements and the sensory bias of hole findings by ringed and Weddell seals,'' Can. J. Zool. **70**, 1712–1722.
Wood, F. G., and Evans, W. E. (**1980**). ''Adaptiveness and ecology of echolocation in toothed whales,'' in *Animal Sonar Systems*, edited by R. G. Busnel and J. F. Fish (Plenum, New York), pp. 381–425.

Vocal control of acoustic information for sonar discriminations by the echolocating bat, *Eptesicus fuscus*

James Wadsworth
Harvard University, Department of Psychology, Cambridge, Massachusetts 02138

Cynthia F. Moss[a)]
University of Maryland, Department of Psychology, College Park, Maryland 20742

(Received 22 April 1999; accepted for publication 13 December 1999)

This study aimed to determine whether bats using frequency modulated (FM) echolocation signals adapt the features of their vocalizations to the perceptual demands of a particular sonar task. Quantitative measures were obtained from the vocal signals produced by echolocating bats (*Eptesicus fuscus*) that were trained to perform in two distinct perceptual tasks, echo delay and Doppler-shift discriminations. In both perceptual tasks, the bats learned to discriminate electronically manipulated playback signals of their own echolocation sounds, which simulated echoes from sonar targets. Both tasks utilized a single-channel electronic target simulator and tested the bat's in a two-alternative forced choice procedure. The results of this study demonstrate changes in the features of the FM bats' sonar sounds with echolocation task demands, lending support to the notion that this animal actively controls the echo information that guides its behavior. © *2000 Acoustical Society of America.* [S0001-4966(00)06103-3]

PACS numbers: 43.80.Ka, 43.80.Lb, 43.66.Gf [WA]

INTRODUCTION

An echolocating bat's vocal behavior directly influences the acoustic information carried by sonar echoes. In particular, changes in the bandwidth, duration, and timing of the bat's sonar transmissions determine the signal parameters available to its acoustic imaging system. Sonar/radar theory and its application demonstrate that broadband signals are best suited for target ranging, because each frequency in the returning echo provides a marker for arrival time, the parameter used to measure the distance of a sonar target (Woodward, 1964; Simmons and Stein, 1980; Skolnik, 1980). Narrow-band signals are well suited for target detection, because signal energy concentrated in a limited frequency band maximizes the signal-to-noise ratio in the returning echo (Woodward, 1964; Simmons and Stein, 1980; Møhl, 1988). Narrow-band signals are also well suited to carry velocity information through Doppler shifts in the returning echoes (e.g., Simmons and Stein, 1980; Skolnik, 1980; Altes, 1984).

Studies of echolocation behavior in the field provide indirect evidence that bats exercise active control over the echo information for changing sonar tasks (e.g., Griffin, 1958; Kalko and Schnitzler, 1998; Schnitzler and Kalko, 1998). Bats that typically hunt insects in open space use frequency modulated (FM) signals for echolocation, and these signals show distinct patterns of change at different phases of foraging (Griffin, 1953; Webster *et al.*, 1965; Simmons and Kick, 1984; Kalko and Schnitzler, 1998). During the search phase of insect pursuit, the big brown bat, *Eptesicus fuscus*, produces shallow FM signals, with the first harmonic sweeping from 25–22 kHz in 15–20 msec (Griffin, 1953, 1958). These sounds are well suited for target detection (Møhl, 1988), maximizing the signal-to-noise ratio in a narrow frequency band. Once the bat begins to approach a prey item, its sonar sounds shorten in duration, increase in bandwidth, and increase in repetition rate. The first harmonic sweeps from approximately 60 to 25 kHz in 2–5 msec during the approach phase of insect pursuit. Finally, at the end of the terminal phase of insect pursuit, the first harmonic of *Eptesicus*'s sonar sounds sweeps from approximately 25 to 12 kHz in less than a msec (Griffin, 1953; Simmons *et al.*, 1979; Schnitzler and Henson, 1980). The brief, broadband signals that are used in the approach and terminal phases are well suited to provide sharp registration of echo arrival time (Woodward, 1964; Simmons and Stein, 1980; Skolnik, 1980), the bat's measure of target distance (Hartridge, 1945; Simmons, 1973).

Reports from laboratory studies suggest that some bat species adapt the features of their sounds to influence the information available for specific sonar discriminations. For example, von der Emde and Menne (1989) report that the CF-FM bat, *Rhinolophus ferrumequinum*, increased the duty cycle of its sounds from about 40% at baseline to 70% when discriminating echoes from insect prey that differed in flutter rate. The increase in duty cycle provided the bat with more information about the fluttering insect's wingbeats over time.

Laboratory studies of bats using frequency modulated (FM) signals offer little data in support of the idea that bats show task-dependent vocal behavior. For example, negative evidence for active vocal control by FM bats was reported by Habersetzer and Vogler (1983), who trained *Myotis myotis* to discriminate targets with differing surface structure. They observed no changes in the parameters of the sonar signals used by bats performing in the task compared with those emitted by bats during free flight. It is possible that changes in sound features were present (and even perceptually salient

[a)]Author to whom correspondence should be addressed; electronic mail: cmoss@psyc.umd.edu

to the bats) but too small for the experimenters to identify using standard signal analysis techniques.

Most changes in vocal behavior reported in the literature are qualitative descriptions. For example, Simmons *et al.* (1975) noted that the FM bat, *Eptesicus fuscus*, modified its sounds in a range discrimination task when tested under noisy conditions. They describe the bat's addition of a short constant frequency (CF) component at around 23 kHz to the end of the FM sweep, which serves to improve the signal-to-noise-ratio. Kick (1982) reported that sounds produced by *Eptesicus fuscus* in a detection task were 4–8 msec in duration, longer than those recorded from bats performing in a ranging task (Simmons, 1973). Kick described a quasi-CF component at the end of the bat's FM sweep, similar to that reported by Simmons *et al.* (1975). The sounds described by Simmons *et al.* (1975) and Kick (1982) are suggestive of adaptive vocal control by FM bats under changing task conditions, but no quantitative measures were reported that directly compare sounds produced by the same bats under different task conditions.

One study of FM bat vocal behavior included extensive quantitative comparisons of signal features produced by bats performing in two distinct perceptual tasks; however, the results do not argue strongly for adaptive vocal behavior. Masters *et al.* (1991) measured small differences in the features of sonar signals produced by *Eptesicus fuscus* performing in echo detection and echo ranging tasks; however, they found larger differences between the sound features of individual bats performing in the same task than within a bat performing different tasks.

While sonar/radar theory demonstrates the utility of changing signal parameters with task demands, data on the FM bat's active role in echolocation performance is presently incomplete. In particular, laboratory studies of FM bats have not yet provided compelling data demonstrating active vocal control in bats that is specific to changing task demands. Given data from field recordings that suggest adaptive vocal behavior in FM bats (Griffin *et al.*, 1958; Kalko and Schnitzler, 1998; Schnitzler and Kalko, 1998), we propose that the appropriate task comparisons should yield corresponding vocal control data from the laboratory.

In the present study, we made quantitative comparisons of echolocation sounds produced by the FM bat, *Eptesicus fuscus*, in two distinct perceptual tasks: Target range discrimination and Doppler shift discrimination. These tasks were selected to maximize possible differences in vocal production patterns. Range discrimination requires signals that permit accurate measurement of echo arrival time, while Doppler discrimination requires signals that permit accurate measurement of echo frequency shifts. The results of our study provide clear evidence for task-dependent vocal behavior in the FM bat, *Eptesicus fuscus*.

I. METHODS

A. Animals

Three female FM bats of the species *Eptesicus fuscus* served as subjects in two different perceptual tasks. The animals were collected from private homes in Maryland during the summer of 1996 and housed in a colony room at the University of Maryland in College Park, Maryland. The temperature in the colony room was maintained at approximately 27 °C and the day/light cycle was reversed, with lights out between 7:00 a.m. and 7:00 p.m. Bats were given free access to water and maintained at about 85% of *ad lib* body weight. Food was available only as a reward during behavioral experiments, which were carried out 6–7 days/week over a period of 21 months.

B. Apparatus and target simulation

Behavioral experiments took place in a large ($6.2\times6.7\times2.5$ m) carpeted room, whose walls and ceiling were lined with acoustic foam (Sonex) that reduced the amplitude of ultrasonic reverberation by a minimum of 20–30 dB below what would be present if the room surfaces were hard and smooth.

Each bat was trained to rest at the base of an elevated Y-shaped platform (1.2 m above the floor) and to produce sonar sounds. The bat's sonar sounds were picked up by a vertically oriented 1/8″ Bruel and Kjaer condenser microphone (model 4138) that was centered between the arms of the platform at a distance of 17 cm from the bat. The bat's echolocation sounds were amplified, bandpass filtered at 20–99 kHz (Stewart filter, model VBF7), digitized with 12-bit accuracy at a rate of 496 kHz (see below), electronically delayed (custom DSP board, SPB2-Signal Data, installed in a '486 computer), attenuated (PA-4, Tucker-Davis Technologies), low-pass filtered (Krone-Hite), and broadcast back to the bat through a custom electrostatic loudspeaker (designed by Lee Miller, University of Odense, Denmark). The loudspeaker, positioned in front of the microphone (0.5 cm lower than the microphone grid) and 15 cm from the bat, was powered by a direct current (dc) amplifier (Ultrasound Advice) and had a frequency response that was flat within 3 dB between 25 and 95 kHz (see Fig. 1). Placement of the microphone behind the speaker eliminated feedback in the system, and the signals recorded were not distorted by the presence of the speaker.

A programmable function generator (Stanford Research Systems, model DS345) was connected to the DSP board in the '486 computer via an RS232 interface, allowing for Doppler shifts of the returning echoes by external control of the digital/analog (D/A) sample rate. For conditions in which no Doppler shift was introduced, the D/A sample rate was fixed at 496 kHz. Doppler shifts were introduced by adjusting the D/A sample rate, generating a percentage frequency shift in the playback echoes that was specified by the experimenter.

The total gain of the system feeding into the DSP board was approximately 60 dB, to bring the peak–peak amplitude of most bat sonar sounds to a level just below the 12-bit limit of the processor and for maximum signal-to-noise ratio. Digital attenuators (PA-4, Tucker-Davis Technologies) permitted adjustment of the playback level of the sounds returning to the bat's ears, which was set at approximately 80 dB SPL for all experiments.

Each sound produced by the bat resulted in a single sonar signal playback that simulated an echo from a target positioned directly in front of the bat, whose distance was

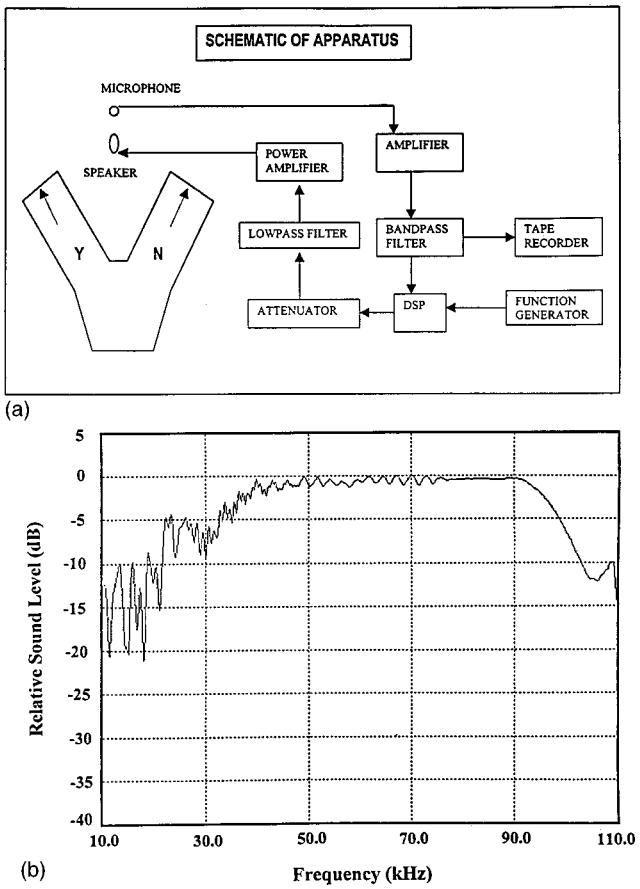

FIG. 1. (a) Schematic of sonar signal playback apparatus and response platform. The bat rested at the base of the Y-shaped platform, emitting echolocation sounds that were picked up by an 1/8″ Bruel and Kjaer microphone, filtered, amplified, digitized, electronically delayed, Doppler shifted (in some trials), and played back through an electrostatic loudspeaker. The bat received a food reward for crawling down the left arm of the platform when presented with stimulus Y (yes) and for crawling down the right arm of the platform when presented with stimulus N (no). For a description of stimulus Y and N, see text. (b) Standard calibration curve displays the frequency response of all equipment in the apparatus, except the 1/8″ Bruel and Kjaer microphone, which was tested separately.

determined by an electronic delay controlled by the experimenter. The shortest echo delay used was 4.3 msec, corresponding to a target distance of 74.0 cm. At this echo delay, the bat's sonar transmissions shorter than 3.3 msec did not overlap the simulated echoes.

Before each experiment, a calibration routine was run, to test each of the components of the target simulator. The electrostatic loudspeaker broadcast a linear 1-msec 10–100-kHz frequency modulated sweep that was picked up by a condenser microphone (QMC) positioned on the test platform. The signal received by the microphone was amplified, filtered (10–99 kHz), and delivered to the DSP board. The arrival time and power spectrum of the FM sound picked up by the microphone were measured and compared against standard values. Experimental data were collected only when the delay and power spectrum of the calibration signal matched the standard values, a 0.29-msec delay when the microphone was positioned 10 cm from the speaker (one-way travel delay, 2.9 ms/m) and a relatively flat spectrum [±3 dB at 25–95 kHz; see Fig. 1(b)].

C. Echolocation sound recordings

For each experimental session, the bats' echolocation sounds were recorded on tape at 30 in. per sec with a Racal Store-4 high-speed recorder. The sounds were later played back at 1/16 the recording speed, low-pass filtered and digitized (effective sample rate 240 kHz), analyzed and displayed spectrographically (Sona-PC, Waldmann©). Spectrograms were calculated using 256-point fast Fourier transforms (FFT's). Signal measurements included the duration, interpulse interval, duty cycle, and spectral characteristics of the bats' signals recorded under different task conditions.

D. Behavioral tasks

1. Experiment I: Range difference discrimination

Each of the bats was trained in a two-alternative forced-choice procedure to discriminate the echo delay difference of electronically simulated sonar targets. The bat learned to report whether the perceived target distance was at a shorter, standard delay by crawling down the left arm of the platform to indicate a ''yes'' (close target) response or at a longer delay by crawling down the right arm of the platform to indicate a ''no'' (far target) response. The echo delay of the standard target was set at 4.3 msec, simulating a target at 74.0 cm. The echo delay of the more distant target was variable, at values that ranged from 4.4 msec, simulating a target at 75.7 cm, to 5.1 msec, simulating a target at 87.7 cm. The echo delay values used in this experiment were all above discrimination threshold reported in other studies (see Moss and Schnitzler, 1995). The presentation of ''close'' (standard) and ''far'' targets followed a pseudorandom schedule (Gellerman, 1933), and the bat's response (yes/left or no/right) was recorded. For each correct response, the bat received a food reward (a piece of mealworm), and for each incorrect response, the bat experienced a 10–30-sec time out. No correction trials were introduced.

2. Experiment II: Doppler-shift discrimination

Each of the bats was trained in a two-alternative forced-choice procedure to discriminate the Doppler shift of electronically simulated sonar targets. On all trials, the echo delay was fixed at 4.3 msec (74.0 cm). For a given trial, the bat learned to report whether it perceived a Doppler shift in the echo, by crawling to the left to indicate ''yes'' and to the right to indicate ''no.'' The presentation of Doppler shifts in the playback echoes followed a pseudorandom schedule (Gellerman, 1933), and the bat's response (yes/left or no/right) was recorded. For each correct response, the bat received a food reward (a piece of mealworm), and for each incorrect response, the bat experienced a 10–30-sec time out. We tested both positive and negative Doppler shifts between 1% and 16%. No correction trials were introduced.

II. RESULTS

Behavioral data are reported here for the Doppler discrimination task, as performance in this task has not been previously described for bats using frequency modulated

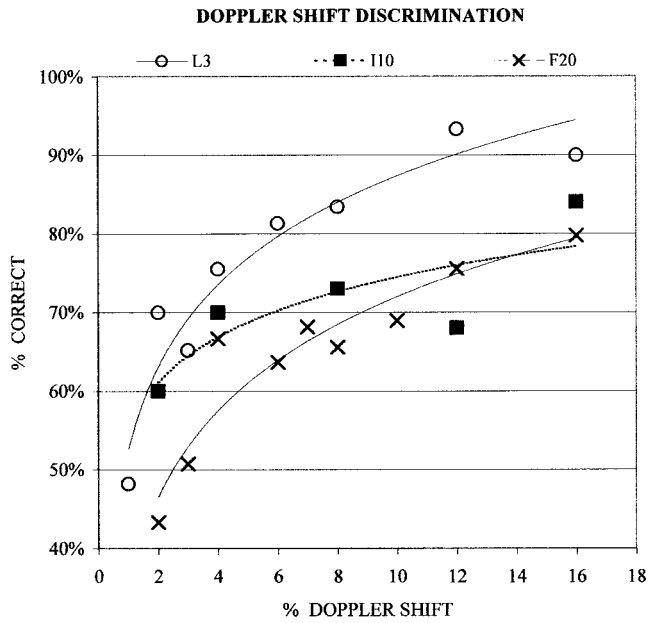

FIG. 2. Psychometric functions plotting percent correct performance for each of the three bats (L-3, I-10, F-20) tested across a range of Doppler shifts. Each data point represents the mean performance measure taken over an average of 60 trials.

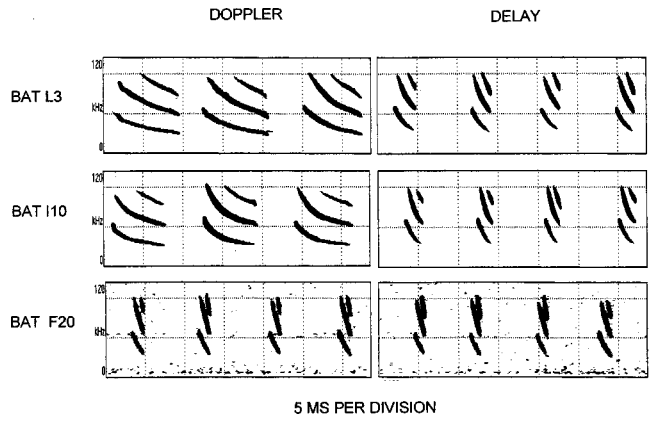

FIG. 3. Spectrograms of representative echolocation sounds produced by each of the three bats (L-3, I-10, F-20) under different task conditions. The left panel for each bat shows sounds recorded during a Doppler discrimination trial and the right panel shows sounds recorded during a delay discrimination trial. The figure does not represent actual sonar signal sequences. Sweeps are presented on the time axis at intervals convenient for display. The vertical axis divisions occur at 50-kHz intervals and the horizontal axis divisions occur at 5-msec intervals.

echolocation sounds. For all three bats studied, discrimination performance systematically increased with the magnitude of the Doppler shift; however, there were large individual differences. The data are plotted in Fig. 2, and each point summarizes mean performance over an average of 60 trials. One bat (L-3) performed at about 50% correct with a 1% Doppler shift, and showed a steady rise in performance for larger Doppler shifts, reaching about 90% correct for Doppler shifts at or above 12%. The other two bats (F-20 and I-10) also showed an increase in performance with Doppler shift, but overall discrimination levels were lower. While data were collected using both positive and negative Doppler shifts, all three bats died before complete psychometric functions with the positive Doppler shifts could be obtained. Therefore, the data reported here come from negative Doppler conditions, which the bat would experience, for example, when an insect wing moved away from it. Using 70% correct performance as an arbitrary criterion for threshold estimation, Doppler discrimination thresholds for L-3, I-10, and F-20 were 3.2%, 5.8%, and 8.8%, respectively.

For each of the bats, we analyzed the sonar vocalizations for Doppler-shift conditions that yielded behavioral discrimination performance at about 70% correct, our criterion for threshold in this study. We compared these sounds with those recorded from the same individual bat performing in the echo delay discrimination task. When the Doppler shift was close to the bat's threshold, we observed consistent changes in the features of the sounds produced by two of the three bats (L-3 and I-10). Interestingly, F-20 produced a different pattern of vocalizations in the two tasks and also showed the highest Doppler discrimination threshold of the three bats tested.

Representative examples of sounds produced by each of the three bats are displayed spectrographically in Fig. 3. The left panel for each bat shows sounds recorded during a Doppler discrimination trial, and the right panel shows sounds recorded during a delay discrimination trial. Though the order in which the sounds in each panel occurred has been preserved, the intervals between sounds were created for display purposes only. All bats produced FM sonar sounds; however, the time-frequency structure of the sounds depended on the task condition. In the delay discrimination task, the FM sounds of all three bats swept from approximately 60 kHz down to 28 kHz in approximately 1.7–3 msec. In the Doppler discrimination task, bat F-20's sounds showed a small decrease in sound duration and an increase in the end frequency of the sweep. By contrast, the two bats that showed the highest performance in the Doppler discrimination task showed the opposite trend, with an increase in signal duration (over 4 msec) and a drop in the end frequency of the sweep (25 kHz).

Duration data from individual Doppler and delay discrimination trials are summarized in Fig. 4. Data are presented in panels for each of the three bats, with the Doppler discrimination trial shown on the left and the echo delay discrimination trial shown on the right. Each of these panels displays data taken from sounds recorded sequentially during a single trial in which the bat made a correct response.

Figure 5 presents quantitative comparisons of several measures taken from signals produced by the bats in the delay and Doppler discrimination tasks. These measures are signal duration, duty cycle, interpulse interval, beginning frequency of the fundamental, ending frequency of the fundamental, and the total spectral bandwidth of the fundamental. This figure includes analysis of 720 sounds recorded from three bats. Data from 240 sounds are presented for each bat, half recorded in delay discrimination trials and half recorded during Doppler discrimination trials, yielding 120 sounds analyzed for each bat from the two task conditions. Histograms display the mean and standard deviations separately for each of the three bats, with the Doppler discrimination measures shown in solid bars and delay discrimination mea-

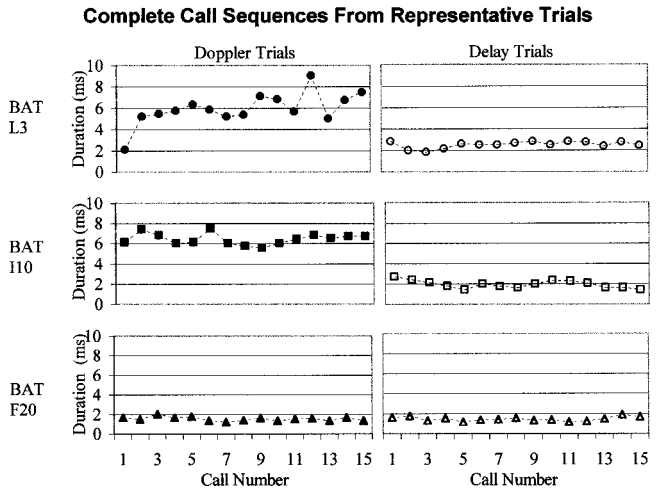

FIG. 4. Sound duration data taken from individual Doppler discrimination (left) and delay discrimination (right) trials for each of the three bats tested (L-3, I-10, F-20). Each panel displays duration measures taken from the first 15 sounds produced by the bat in the trial.

sures shown in open bars. All of the data summarized here come from the first 15 sounds produced by the bat in any given trial. Although some trials contained many more than 15 sounds, limiting the analysis to the first 15 sounds ensured that the data summaries did not include sounds produced by the bat as it crawled down the platform for its food reward

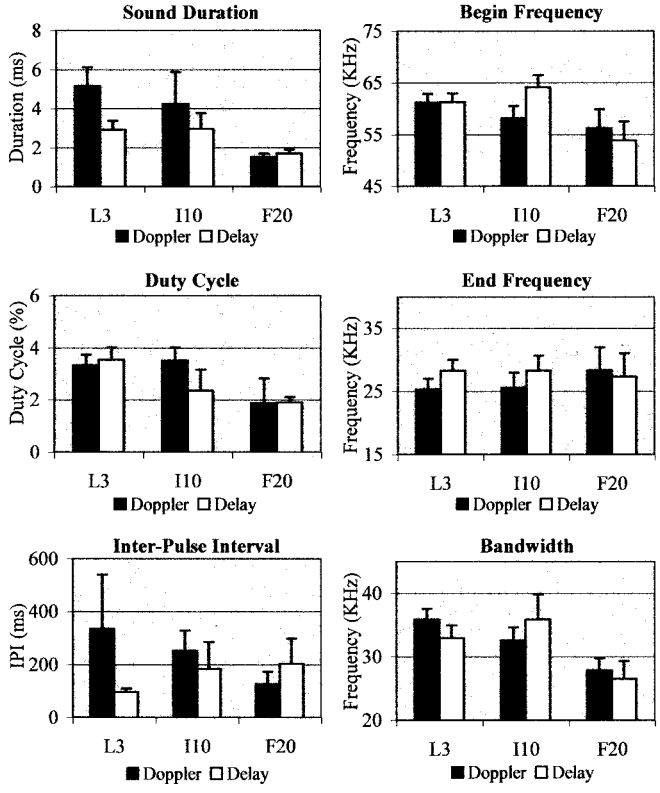

FIG. 5. Signal parameter measurements taken for each of the three bats (L-3, I-10, F-20) tested in an echo Doppler-shift discrimination task (filled bars) and in an echo delay difference discrimination task (open bars). Parameters summarized are signal duration, duty cycle, interpulse interval, beginning and end frequencies of the fundamental, and the bandwidth of the fundamental. Each histogram summarizes mean and standard deviation for 120 echolocation calls.

TABLE I. Results of the analysis of variance (ANOVA) on signal measures (duration, beginning and end frequencies of the fundamental, bandwidth of the fundamental, interpulse interval, and duty cycle) taken from sonar vocalizations produced in Doppler and delay discrimination test conditions. The degrees of freedom (df) for the ANOVA are shown in the table. Asterisks indicate statistically significant differences in signal measures in the two conditions, across subjects, and subject by condition interactions, with the corresponding *p* values.

	Condition df=1,714		Subject df=2,714		Interaction df=2,714	
	F	*P*-Value	*F*	*P*-Value	*F*	*P*-Value
Duration	206.21	<0.001*	368.62	<0.001*	83.27	<0.001*
Begin fund	10.29	0.001*	116.15	<0.001*	42.42	<0.001*
End fund	91.66	<0.001*	16.27	<0.001*	61.73	<0.001*
Bandwidth	0.65	0.419	127.36	<0.001*	19.67	<0.001*
IPI	2.99	0.001*	2.23	0.109	15.02	<0.001*
Duty cycle	10.78	0.084	32.12	<0.001*	6.24	0.002*

after making a decision. Data are reported only for trials in which the bat responded correctly.

An analysis of variance (ANOVA) performed on this data set shows that many of the parameters measured from the bats' sounds recorded under the two test conditions differed significantly. Signal duration, beginning and end frequencies of the fundamental sweep, and interpulse interval all differed significantly between the Doppler and delay discrimination trials. Statistically reliable differences between subjects appeared in all measures except IPI. Stimulus condition by subject interactions were statistically significant for all signal parameters (see Table I).

While individual differences account for the statistically significant subject and subject by condition interactions (consistent with data reported by Masters *et al.*, 1991), we wish to highlight the task-dependent differences in sonar signals and to relate these differences to the bats' Doppler discrimination performance. Bats L-3 and I-10 showed higher Doppler discrimination performance than bat F-20, and these two bats produced sonar signals in this task that were longer in duration, swept to a lower end frequency, and exhibited an increase in the interpulse interval, compared with sounds produced in the delay discrimination task. Bat F-20 showed the opposite pattern in its vocalizations, with shorter mean sound duration, shorter interpulse interval and higher end frequency in the Doppler discrimination task than in the delay discrimination task. Interestingly, this bat also showed the poorest performance in the Doppler discrimination task.

For bats L-3 and I-10, an increase in sonar signal duration accompanied a drop in the end frequency, as illustrated in Fig. 6 (left). Each panel shows data from each of the individual bats tested under the Doppler (crosses) and delay (open symbols) discrimination tasks. The data plotted in Fig. 6 are the same as those summarized in Fig. 4, with 240 signals measured for each bat (half in the Doppler and half in the delay discrimination tasks). In general, there is a tendency for the longest signals to also contain the lowest end frequencies, a trend that appears most clearly in the data from bat L-3, the bat with the lowest Doppler discrimination threshold. For bat F-20, sound duration and end frequency under the two behavioral test conditions cluster more closely.

Figure 6 (right) plots the relation between signal band-

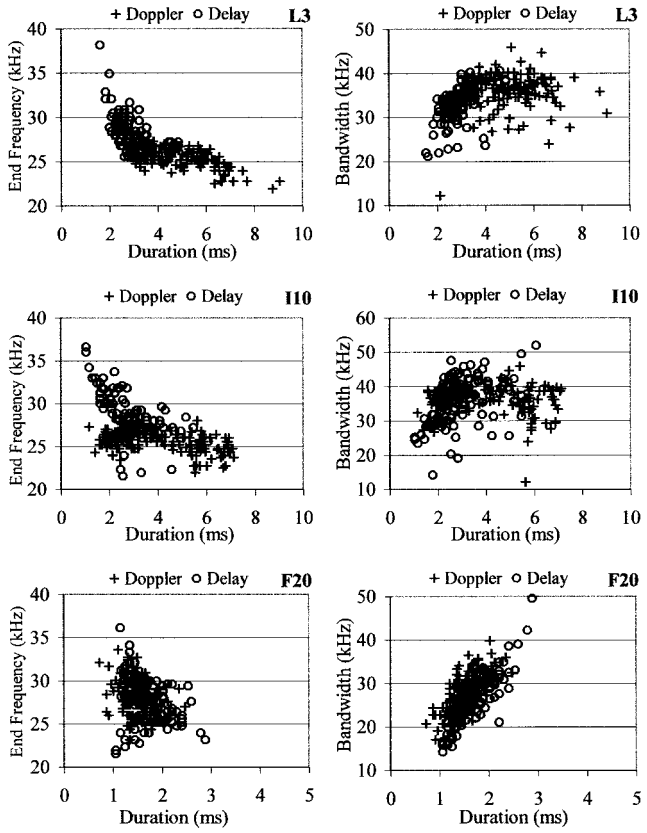

FIG. 6. Left panels: Signal end frequency (kHz) versus signal duration (msec). Right panels: Bandwidth of the fundamental (kHz) versus signal duration (msec). Both figures plot data separately for the three bats tested in the Doppler (crosses) and delay (open circles) discrimination tasks. Each bat's plot includes 240 data points, 120 measures taken from signals produced in each of the two task conditions.

width (fundamental frequency) and duration in the Doppler and delay discrimination tasks. Sounds produced by bats L-3 and I-10 show no correlation between bandwidth and duration. Bat F-20's signals show an overall increase in bandwidth with signal duration, and the sounds recorded in delay discrimination trials tend to contain the largest bandwidths.

III. DISCUSSION

The results of this study demonstrate adaptive vocal behavior in the FM-bat, *Eptesicus fuscus*, for shaping the acoustic information available in two distinct perceptual tasks. The sounds produced by bats in the echo delay discrimination task were brief and swept continuously from high to low frequencies. By contrast, the longer signals used by the bats for Doppler discrimination included a shallow FM tail from approximately 28–25 kHz, similar to the signal type described by Simmons *et al.* (1975) and Kick (1982). The differences in these sound characteristics produced by the bat under different task conditions correspond to those predicted by sonar/radar theory (Woodward, 1964; Simmons and Stein, 1980; Skolnik, 1980; Møhl, 1988).

An echo delay discrimination task requires that the bat register the echo arrival time with high accuracy, and sonar theory asserts that brief, broadband signals are best suited for this task. Each frequency in the FM sweep provides a marker for its time of arrival, and the broad bandwidth sharpens its time-domain representation (Woodward, 1964; Simmons and Stein, 1980; Skolnik, 1980; Menne and Hackbarth, 1986). Doppler discrimination requires that the bat detect frequency changes in the echo, and a signal that remains at a comparatively stable frequency over time is best suited for this task (Simmons and Stein, 1980; Skolnik, 1980; Altes, 1984). Thus the longer signals with the shallow FM tail, used by *Eptesicus fuscus* for Doppler discriminations, are better suited for frequency discrimination than the shorter FM sweeps used for echo delay discrimination.

The sounds produced by *Eptesicus fuscus* in this Doppler discrimination study are not typically observed in the laboratory. To our knowledge, the only other reports of similar sonar signals recorded from this species in the laboratory are those of Simmons *et al.* (1975) and Kick (1982). Both reports include qualitative descriptions of a shallow FM at the end of the sweep, noting that the bat's signals differed from those typically observed in the laboratory. However, these reports make no direct comparisons of signals produced by the same individual animals performing in different tasks.

In this study, the two bats showing better overall performance and lower thresholds in the Doppler discrimination task showed similar patterns in vocal production that differed in some respects from the third bat tested with the highest Doppler discrimination threshold. The two bats with the lower Doppler discrimination thresholds added the shallow FM tail to their signals in the Doppler task, and this tail resulted in a lower end frequency and longer duration signals. Bat L-3, the animal with the lowest Doppler discrimination threshold in this study, showed the strongest effect of task on signal duration and end frequency. While L-3 and I-10 showed similar, task-dependent patterns in signal duration and end frequency, they showed different patterns of change in total first harmonic bandwidth with task. L-3 produced sonar signals with higher bandwidth in the Doppler condition and I-10 produced signals with higher bandwidth in the delay discrimination condition, because the start frequencies of the FM sweeps used by these two bats in the different tasks changed in opposite directions. The individual differences in signal parameters used by the three bats in the two tasks is consistent with the report of individual vocal patterns presented by Masters *et al.* (1991).

Extensive field data from *Eptesicus fuscus* have not been published, but we speculate here that the longer sonar signals, with a shallow FM tail, produced by *Eptesicus* during the late search phase and early approach phase of insect pursuit (Griffin, 1958), may draw the same potential advantages as signals used by CF-FM bats, namely fluttering prey detection and discrimination (e.g., Schnitzler *et al.*, 1983; von der Emde and Menne, 1989; Kober and Schnitzler, 1990). In this context, it is worth noting that FM bats can discriminate between artificial wing beat stimuli that flutter at different rates (Grossetête and Moss, 1998; Roverud *et al.*, 1991; Sum and Menne, 1988). Sum and Menne (1988) first postulated that FM bats may perform this task by listening for a delay difference between echoes from the stationary and moving parts of the apparatus used to study flutter rate discrimination. The moving target produces a Doppler-induced echo

delay shift, whose magnitude varies with the target's velocity. The stationary parts of the apparatus return echoes at a fixed delay, and thus, the echo delay difference between moving and stationary target echoes increases with target velocity. Grossetête and Moss (1998) conducted acoustic studies of FM sonar echoes from an artificial wingbeat simulator and demonstrated that the magnitude of the Doppler-induced delay difference between the moving and stationary target echoes is influenced by the characteristics of the bat's sonar signals, in particular signal duration. Given the influence of signal duration on Doppler information, it is not surprising that the bat in this study that performed the best in the Doppler discrimination task also produced the longest sonar signals.

In summary, we present here quantitative comparisons of sonar signals produced by the same individual bats performing in distinct perceptual tasks. The data show task-dependent differences in sound duration and frequency structure of the bat's echolocation sounds, and the changes reported here for two bats are consistent with those predicted by sonar/radar theory. These results suggest that the sounds produced by echolocating bats may provide a window to understanding the information processing requirements of a given sonar task. Since we are limited by signal processing techniques that do not tap into the perceptual salience of signal changes to the bat, we can only speculate that more subtle changes in sonar sounds may also occur which reflect the bat's active enhancement of sonar images.

ACKNOWLEDGMENTS

This work was supported by NIMH Grant No. R01-MH56366. We thank Anne Grossetête and Willard Wilson for their contributions to the ideas developed in this paper and Amy Kryjak for assistance with the data analysis. We also thank Annemarie Surlykke and two anonymous reviewers for their helpful comments on an earlier version of this paper.

Altes, R. A. (**1984**). ''Echolocation as seen from the viewpoint of radar/sonar theory,'' in *Localization and Orientation in Biology and Engineering*, edited by D. Varju and H.-U. Schnitzler (Springer-Verlag, Berlin), pp. 234–244.

Gellerman, L. W. (**1933**). ''Chance orders of alternating stimuli in visual discrimination experiments,'' J. Gen. Psychol. **42**, 206–208.

Griffin, D. R. (**1953**). ''Bat sounds under natural conditions, with evidence for echolocation of insect prey,'' J. Exp. Zool. **123**, 435–465.

Griffin, D. (**1958**). *Listening in the Dark* (Yale University Press, New Haven, CT).

Grossetête, A., and Moss, C. F. (**1998**). ''Target flutter rate discrimination by bats using frequency modulated sonar sounds: Behavior and signal processing models.'' J. Acoust. Soc. Am. **103**, 2167–2176.

Habersetzer, J., and Vogler, B. (**1983**). ''Discrimination of surface-structured targets by the echolocating bat *Myotis myotis* during flight,'' J. Comp. Physiol. **152**, 275–282.

Hartridge, H. (**1945**). ''Acoustical control in the flight of bats,'' Nature (London) **156**, 490–494; **156**, 692–693.

Kalko, E. K. V., and Schnitzler, H-U. (**1998**). ''How echolocating bats approach and acquire food,'' in *Bat Biology and Conservation*, edited by T. H. Kunz and P. A. Racey (Smithsonian Institution, Washington, D.C.), pp. 197–219.

Kick, S. A. (**1982**). ''Target detection by the echolocating bat, *Eptesicus fuscus*,'' J. Comp. Physiol. A **145**, 431–435.

Kober, R., and Schnitzler, H-U. (**1990**). ''Information in sonar echoes of fluttering insects available for echolocating bats,'' J. Acoust. Soc. Am. **87**, 882–896.

Masters, W. M., Jacobs, S. C., and Simmons, J. A. (**1991**). ''The structure of echolocation sounds used by the big brown bat *Eptesicus fuscus*: Some consequences for echo processing,'' J. Acoust. Soc. Am. **89**, 1402–1413.

Menne, D., and Hackbarth, H. (**1986**). ''Accuracy of distance measurement in the bat *Eptesicus fuscus*: Theoretical aspects and computer simulations,'' J. Acoust. Soc. Am. **79**, 386–397.

Møhl, B. (**1988**). ''Target detection by echolocating bats,'' in *Animal Sonar Processes and Performance*, edited by P. E. Nachtigall and P. W. B. Moore (Plenum, New York), pp. 435–450.

Moss, C. F., and Schnitzler, H-U. (**1995**). ''Behavioral studies of auditory information processing,'' in *Springer Handbook of Auditory Research. Hearing by Bats*, edited by R. Fay and A. Popper (Springer-Verlag, Berlin), pp. 87–145.

Roverud, R. C., Nitsche, V., and Neuweiler, G. (**1991**). ''Discrimination of wingbeat motion by bats correlated with echolocation sound pattern,'' J. Comp. Physiol. A **168**, 259–263.

Schnitzler, H-U., and Henson, O. W. (**1980**). ''Performance of airborne animal sonar systems: I. Microchiroptera,'' in *Animal Sonar Systems*, edited by R. G. Busnel and J. Fish (Plenum, New York), pp. 109–181.

Schnitzler, H-U., Menne, D., Kober, R., and Heblich, K. (**1983**). ''The acoustical image of fluttering insects in echolocating bats,'' in *Neuroethology and Behavioral Physiology*, edited by F. Huber and H. Markl (Springer, Berlin), pp. 235–250.

Schnitzler, H-U., and Kalko, E. K. V. (**1998**). ''How echolocating bats search and find food,'' in *Bat Biology and Conservation*, edited by T. H. Kunz and P. A. Racey (Smithsonian Institution, Washington, D.C.), pp. 183–196.

Simmons, J. A. (**1973**). ''The resolution of target range by echolocating bats,'' J. Acoust. Soc. Am. **54**, 157–173.

Simmons, J. A., Howell, D. J., and Suga, N. (**1975**). ''Information content of bat sonar echoes,'' Am. Sci. **63**, 204–215.

Simmons, J. A., Fenton, M. B., and O'Farrell, M. J. (**1979**). ''Echolocation and pursuit of prey by bats,'' Science **203**, 6–21.

Simmons, J. A., and Stein, R. A. (**1980**). ''Acoustic imaging in bat sonar: Echolocation signals and the evolution of echolocation,'' J. Comp. Physiol. A **135**, 61–84.

Simmons, J. A., and Kick, S. A. (**1984**). ''Physiological mechanisms for spatial filtering and image enhancement in the sonar of bats,'' Annu. Rev. Physiol. **46**, 599–614.

Skolnik, M. I. (**1980**). *Introduction to Radar Systems*, 2nd ed. (McGraw-Hill, New York).

Sum, Y. W., and Menne, D. (**1988**). ''Discrimination of fluttering targets by the FM-bat Pipistrellus stenopterus?'' J. Comp. Physiol. A **163**, 349–354.

van Emde, Gvd., and Menne, D. (**1989**). ''Discrimination of insect wingbeat-frequencies by the bat Rhinolophus ferrumequinum,'' J. Comp. Physiol. A **164**, 663–671.

Webster, F. A., and Brazier, O. B. (**1965**). ''Experimental studies on target detection, evaluation and interception by echolocating bats,'' Aerospace Medical Res. Lab., Wright–Patterson Air Force Base, Ohio, AD 628055.

Woodward, P. M. (**1964**). *Probability and Information Theory with Applications to Radar*, 2nd ed. (Pergamon, NY).

Oscillations of polymeric microbubbles: Effect of the encapsulating shell

Lars Hoff
Norwegian University of Science and Technology, Department of Telecommunications, N-7491 Trondheim, Norway

Per C. Sontum
Nycomed Imaging AS, Research and Development Section, P.O. Box 4220, Torshov, N-0401 Oslo, Norway

Jens M. Hovem
Norwegian University of Science and Technology, Department of Telecommunications, N-7491 Trondheim, Norway

(Received 5 May 1999; revised 10 August 1999; accepted 9 December 1999)

A model for the oscillation of gas bubbles encapsulated in a thin shell has been developed. The model depends on viscous and elastic properties of the shell, described by thickness, shear modulus, and shear viscosity. This theory was used to describe an experimental ultrasound contrast agent from Nycomed, composed of air bubbles encapsulated in a polymer shell. Theoretical calculations were compared with measurements of acoustic attenuation at amplitudes where bubble oscillations are linear. A good fit between measured and calculated results was obtained. The results were used to estimate the viscoelastic properties of the shell material. The shell shear modulus was estimated to between 10.6 and 12.9 MPa, the shell viscosity was estimated to between 0.39 and 0.49 Pas. The shell thickness was 5% of the particle radius. These results imply that the particles are around 20 times more rigid than free air bubbles, and that the oscillations are heavily damped, corresponding to *Q*-values around 1. We conclude that the shell strongly alters the acoustic behavior of the bubbles: The stiffness and viscosity of the particles are mainly determined by the encapsulating shell, not by the air inside. © *2000 Acoustical Society of America.* [S0001-4966(00)04903-1]

PACS numbers: 43.80.Qf, 43.25.Yw, 43.35.Mr [FD]

INTRODUCTION

Use of gas bubbles as contrast agents for medical ultrasound imaging was proposed by Gramiak and Shah in 1968.[1] The interest in such agents has increased strongly during the last ten years, and the first ultrasound contrast agents are now on the market. Diameters of particles used in contrast agents are limited by the diameters of capillaries in the cardiac system[2] to about 10 μm, while the wavelength of diagnostic ultrasound is typically around 500 μm. Hence, the particles are much smaller than the acoustic wavelength. Gas-containing particles are used to obtain highly compressible particles, as these give very high scattering cross sections compared to other particles of the same size. In most agents, the gas is stabilized toward dissolution by an encapsulating shell or a membrane. This shell may stiffen the gas bubble, and alter its acoustic properties.

The basis for a theoretical description of gas bubble oscillations comes from Lord Rayleigh,[3] and gas bubbles in acoustic fields have later been the subject of many studies. Medwin[4] gives an overview of linearized models for scatter and absorption of sound from bubbles, while nonlinear bubble oscillations are summarized by Prosperetti[5] and in the book by Leighton.[6] Analytical[7] and numerical[8] studies have shown that gas bubbles behave nonlinearly at fairly low sound pressure amplitudes. This effect is used to detect bubbles by receiving scatter at the second harmonic of the transmit frequency, as proposed by Tucker and Welsby in 1968,[9] and later demonstrated by Miller[10] in 1981. Imaging at the second harmonic frequency is today commonly used in ultrasound contrast imaging.

Fox and Herzfield[11] showed how an encapsulating shell increases resonance frequency. Later, de Jong and Hoff[12,13] measured this increased resonance frequency when studying acoustic attenuation from the contrast agent *Albunex*®. Hoff and Sontum[14] investigated an experimental contrast agent from Nycomed, using a linear model based on bulk properties of the particles. Holm *et al.*[15] incorporated these studies into a model for the transmission and scatter of ultrasound pulses in tissue. A more well-founded, nonlinear theoretical model for shell-encapsulated bubbles was presented by Church[16] in 1995. Frinking and de Jong[17] have presented a phenomenological model describing the contrast agent *Quantison*. All these studies show that the shell increases the mechanical stiffness of the contrast agent particles, and that shell viscosity increases sound absorption.

The aim of this paper is to apply Church's well-founded theoretical model to a contrast agent consisting of polymer-shelled, air-filled particles, and to present a method to estimate values for the viscoelastic shell parameters. Church's model[16] is somewhat simplified, and calculations from this model are compared with acoustic attenuation measurements in the linear range. The results are used to estimate values for the viscoelastic parameters of the shell material, parameters that enter into the model but are not known *a priori*. It is further shown how the results can be used to calculate the stiffness of the whole particle, the bulk modulus. This links it

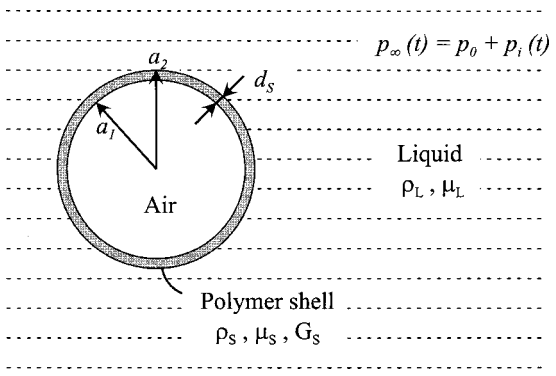

FIG. 1. Drawing of the investigated polymer-encapsulated air-filled particles.

to results reported in a previous, phenomenological study.[14]

A version of the methods described in this paper has also been applied to characterize the ultrasound contrast agent *Sonazoid* from Nycomed.[18]

I. COMPOSITION OF THE PARTICLES

The substance investigated in this study was prepared by Nycomed (Nycomed Amersham, Oslo, Norway) as an experimental contrast agent for medical ultrasound imaging. The substance consists of air bubbles enclosed in a thin polymer shell. Particle diameters are between 1 and 10 μm. Preparation and characterization of the particles are described by Bjerknes *et al.*[19] Figure 1 illustrates the composition of these polymeric microbubbles.

From the production process,[19] it is estimated that the ratio between polymeric shell material and total particle volume is constant, with 15% of the particle volume in the shell. This gives a constant ratio between shell thickness and particle radius, where the shell thickness is 5% of the particle radius.

II. THEORY

A. Equation of motion for the particles

The theoretical description of the particle oscillations is based on Church's model[16] for *Albunex*®. He described air bubbles enclosed in a solid, incompressible viscoelastic shell. The shell is described by a shear modulus G_S and a shear viscosity μ_S. The liquid surrounding the particles is modeled as incompressible and Newtonian, with shear viscosity μ_L. The shear modulus G_S and viscosity μ_S of a polymeric material are in general frequency dependent. The aim of this study was to characterize the contrast agent in the frequency range most commonly used in diagnostic medical imaging, from 1 to 8 MHz. It is assumed that G_S and μ_S are constant within this range. It is further assumed that the shell reduces surface tensions at the shell-liquid and shell–gas interfaces, so that surface tension can be neglected.

Under these assumptions, a nonlinear equation of motion for the particle surface is

$$\rho_L\left[\ddot{a}_2 a_2+\frac{3}{2}\dot{a}_2^2\right]+\rho_S\left[\ddot{a}_2 a_2\left(\frac{a_2}{a_1}-1\right)+\dot{a}_2^2\left(2\frac{a_2}{a_1}-\frac{1}{2}\left(\frac{a_2}{a_1}\right)^4-\frac{3}{2}\right)\right]=p_{ge}\left(\frac{a_{1e}}{a_1}\right)^{3\kappa}-p_\infty(t)-4\mu_L\frac{\dot{a}_2}{a_2}-4\mu_S\frac{V_S}{a_2^3}\frac{\dot{a}_1}{a_1}-4G_S\frac{V_S}{a_2^3}\left(1-\frac{a_{1e}}{a_1}\right), \tag{1}$$

where $a_1(t)$ and $a_2(t)$ are the inner and outer shell radii, ρ_S and ρ_L are the densities of the shell material and of the surrounding liquid, p_{ge} is the equilibrium pressure in the gas inside the bubble, a_{1e} and a_{2e} are the inner and outer shell radii at equilibrium, $p_\infty(t)$ is the pressure in the liquid far from the particle, κ is the polythropic exponent of the gas, $V_S=a_2^3-a_1^3$, and dots denote differentiation with respect to time.

Equation (1) is Church's Eq. (12). This has been rearranged to identify the different terms better, using the conservation of mass relation for an incompressible shell; $\dot{a}_1 a_1^2=\dot{a}_2 a_2^2$.

Equation (1) is the basis for the theoretical description of the polymeric microbubbles investigated in this paper, using shell thickness, viscosity, and shear modulus different from those of *Albunex*. According to this description, the thickness d_S of the shell varies as the particle oscillates, so that the shell volume is constant. The shell is thin compared to particle radius, and use of this, $d_S(t)\ll a_2$, allows simplification of Eq. (1).

The left side of Eq. (1) represents inertia: Terms multiplied with ρ_S represent inertia of the shell, terms multiplied by ρ_L represent inertia of the liquid, and ρ_S and ρ_L are of the same order of magnitude. The inertia terms are expanded in the small parameter d_S/a_2, keeping terms to the first order. This simplifies the left side of Eq. (1) to

$$\rho_L\left[\ddot{a}_2 a_2\left(1+\frac{\rho_S}{\rho_L}\frac{d_S}{a_2}\right)+\frac{3}{2}\dot{a}_2^2\right]. \tag{2}$$

Hence, the shell contributes to the inertia of the oscillating bubble through a term of order d_S/a_2, which can be neglected.

The right side of Eq. (1) represents restoring stiffness and damping viscous forces. The first three terms are known from the Rayleigh–Plesset equation for unshelled bubbles. The last two terms represent viscous and elastic forces due to movement and tension in the shell. The shell is thin, and terms of order d_S/a_2 are neglected. This reduces the last two terms in Eq. (1) to

$$4\mu_S\frac{V_S}{a_2^3}\frac{\dot{a}_1}{a_1}\approx 12\mu_S\frac{a_{1e}^2 d_{Se}}{a_2^3}\frac{\dot{a}_1}{a_1}, \tag{3a}$$

$$4G_S\frac{V_S}{a_2^3}\left(1-\frac{a_{1e}}{a_1}\right)\approx 12G_S\frac{a_{1e}^2 d_{Se}}{a_2^3}\left(1-\frac{a_{1e}}{a_1}\right), \tag{3b}$$

where d_{Se} is the shell thickness at rest. The shell viscosity and elasticity terms contain relative shell thickness d_{Se}/a_2

multiplied with viscous and elastic shell properties μ_S and G_S. The resulting terms may become large compared to other pressure terms. Hence, while the shell contribution to inertia is small and neglected, the contributions from the shell to stiffness and viscosity depend on G_S and μ_S, and must be considered.

The result of these simplifications is a version of Eq. (1), suitable when the encapsulating shell is thin compared to the particle diameter

$$\rho_L\left(\ddot{a}_2 a_2+\frac{3}{2}\dot{a}_2^2\right)=p_{ge}\left(\frac{a_{1e}}{a_1}\right)^{3\kappa}-p_\infty(t)-4\mu_L\frac{\dot{a}_2}{a_2}-12\mu_S\frac{a_{1e}^2 d_{Se}}{a_2^3}\frac{\dot{a}_1}{a_1}-12G_S\frac{a_{1e}^2 d_{Se}}{a_2^3}\left(1-\frac{a_{1e}}{a_1}\right). \tag{4}$$

Equation (4) contains both inner radius a_1 and outer radius a_2 of the shell. It is reduced to an equation in outer radius $a=a_2(t)$ alone by setting

$$\frac{a_{1e}}{a_1}\approx\frac{a_{2e}}{a_2}\left(1+\left(\frac{d_{Se}}{a_{2e}}-\frac{d_S}{a_2}\right)\right)\approx\frac{a_{2e}}{a_2}=\frac{a_e}{a}. \tag{5}$$

At equilibrium, the pressure in the gas inside the bubble is assumed to be equal to the hydrostatic pressure in the surrounding liquid, $p_{ge}=p_0$. This means that there is no tension in the shell at equilibrium. The pressure p_∞ far from the bubble is the sum of the atmospheric pressure p_0 and the incoming acoustic pressure $p_i(t)$.

All these assumptions lead to the following reduced equation of motion, containing outer particle radius $a(t)$ as the only variable,

$$\rho_L\left(\ddot{a}a+\frac{3}{2}\dot{a}^2\right)=p_0\left(\left(\frac{a_e}{a}\right)^{3\kappa}-1\right)-p_i(t)-4\mu_L\frac{\dot{a}}{a}-12\mu_S\frac{d_{Se}a_e^2}{a^3}\frac{\dot{a}}{a}-12G_S\frac{d_{Se}a_e^2}{a^3}\left(1-\frac{a_e}{a}\right). \tag{6}$$

To simulate bubble oscillation $a(t)$ as a response to an applied acoustic pressure field $p_i(t)$, the elastic and viscous shell parameters G_S and μ_S must be determined. The shell material is not easily made in bulk quantities that allow conventional measurements of elastic properties. Instead, G_S and μ_S are estimated from measurements of ultrasound absorption in a particle suspension.

B. Linearization

The parameters G_S and μ_S are estimated from acoustic measurements at low pressure amplitudes. Here, the oscillation is linear and Eq. (6) is solved analytically. The particle radius $a(t)$ is written

$$a(t)=a_e(1+x(t)),\quad |x(t)|\ll 1. \tag{7}$$

Equation (6) is expanded in the radial displacement $x(t)$, keeping terms to the first order in x. This gives a simple linear equation for the forces acting on the surface of the particle

$$ma_e\ddot{x}+Ra_e\dot{x}+sa_e x=-4\pi a_e^2 p_i(t), \tag{8}$$

with coefficients

$$m=4\pi\rho_L a_e^3,\quad s=4\pi a_e\left(3\kappa p_0+12G_S\frac{d_{Se}}{a_e}\right),\quad R=4\pi a_e\left(4\mu_L+12\mu_S\frac{d_{Se}}{a_e}\right). \tag{9}$$

Equation (8) is best handled in the frequency domain. Fourier transformation yields

$$(\omega_0^2-\omega^2+i\omega\omega_0\delta)\hat{x}(\omega)=-\frac{1}{\rho_L a_e^2}\hat{p}_i(\omega), \tag{10}$$

with coefficients

$$\omega_0^2=\frac{s}{m}=\frac{1}{\rho_L a_e^2}\left(3\kappa p_0+12G_S\frac{d_{Se}}{a_e}\right), \tag{11a}$$

$$\delta=\frac{R}{\omega_0 m}=\delta_L+\delta_S,\quad \delta_L=\frac{4\mu_L}{\omega_0\rho_L a_e^2},\quad \delta_S=\frac{12\mu_S\dfrac{d_{Se}}{a_e}}{\omega_0\rho_L a_e^2}. \tag{11b}$$

In previous work, several slightly different definitions of the damping constant δ are found. The definition used here is the same as that used by Church, but differs by a factor ω/ω_0 from those used by Medwin[4] and Leighton.[20]

The linear resonance frequency f_0 of the shell-encapsulated bubble is

$$f_0=\frac{\omega_0}{2\pi}=\frac{1}{2\pi a_e}\sqrt{\frac{1}{\rho_L}\left(3\kappa p_0+12G_S\frac{d_{Se}}{a_e}\right)}. \tag{12}$$

Compared to the free bubble, the shell increases resonance frequency through the shear modulus G_S, by increasing the stiffness of the bubble. Without a shell, when $d_{Se}=0$, and under adiabatic conditions, when $\kappa=\gamma$, Eq. (12) reduces to the well-known Minnaert resonance frequency[21] for gas bubbles.

From Eq. (10) the radial oscillation $\hat{x}(\omega)$ as function of acoustic pressure $\hat{p}(\omega)$ is found,

$$\hat{x}(\omega)=\frac{1}{\Omega^2-1-i\Omega\delta}\frac{\hat{p}_i(\omega)}{\rho_L\omega_0^2 a_e^2},\quad \Omega=\frac{\omega}{\omega_0}. \tag{13}$$

C. Acoustic attenuation and scatter

The increased attenuation caused by adding contrast agent particles to a liquid is given by the extinction cross section σ_e defined by

$$\sigma_e(a,\omega)=\frac{P_A(a,\omega)}{I_i(\omega)}=\frac{P_A(a,\omega)}{|\hat{p}_i(\omega)|^2/(2\rho_L c)}, \tag{14}$$

where $P_A(a,\omega)$ is the power absorbed by the oscillating particle, and $I_i(\omega)$ is the intensity of the incoming acoustic

field. The power absorbed by the particle is found from Eqs. (8), (10), and (11b) to be

$$P_A(a,\omega)=\tfrac{1}{2}m\omega_0\omega^2a_e^2\delta|\hat{x}(\omega)|^2. \tag{15}$$

Insertion of the expression for $\hat{x}(\omega)$ from Eq. (13) gives the extinction cross section $\sigma_e(a,\omega)$ of one particle,

$$\sigma_e(a,\omega)=4\pi a_e^2\frac{c\delta}{a_e\omega_0}\frac{\Omega^2}{(1-\Omega^2)^2+\Omega^2\delta^2}. \tag{16}$$

At low concentrations, the oscillations of the different particles do not interact. The power absorbed by a particle suspension is the sum of the power absorbed by the individual particles. This gives acoustic attenuation $\alpha(\omega)$ per unit distance in decibels,

$$\alpha(\omega)=10\log_{10}(e)\int_0^\infty\sigma_e(a,\omega)n(a)da[dB], \tag{17}$$

where $n(a)da$ is the number of particles per unit volume with radius in $(a,a+da)$.

Medwin[4] and Church[16] give expressions for the scattering cross sections of bubbles. Applied on these thin-shelled bubbles, this gives the scattering cross section $\sigma_S(a_e,\omega)$ as

$$\sigma_S(a_e,\omega)=4\pi a_e^2\frac{\Omega^4}{(\Omega^2-1)^2+\Omega^2\delta^2}. \tag{18}$$

Both normalized frequency Ω and damping constant δ depend on the viscoelastic properties of the shell, as defined in Eqs. (13), (11a), and (11b).

D. Thermal and acoustic damping

The calculations have assumed an incompressible liquid, not including losses from acoustic radiation and from thermal conduction in the gas. More complete treatments of oscillating bubbles, including such damping terms, are available for bubbles without a shell.[22–25] Church[16] provides simplified expressions for these terms in the frequency domain.

Devin[22] calculated the viscous, acoustic, and thermal damping constants of bubbles oscillating at small amplitude at resonance. These calculations also give an expression for the polythropic exponent κ. Eller[26] extended this work to give expressions for the damping constants off resonance.

The polythropic exponent and thermal damping constant of the shell-encapsulated particles are found from Devin's Eqs. (49) and (50). These give the relation between the driving acoustic pressure $\hat{p}_i(\omega)$ and the volume change $\hat{v}(\omega)$ for a gas bubble as

$$\frac{\hat{v}(\omega)}{\hat{p}_i(\omega)}=-\frac{V_e}{p_0}\Phi(a_e,\omega), \tag{19}$$

where

$$\Phi(a_e,\omega)=\frac{1}{\gamma}\left(1+\frac{3(\gamma-1)}{X^2}(X\coth X-1)\right), \tag{20a}$$

$$X(a_e,\omega)=a_e\sqrt{\frac{i\omega\rho_gC_p}{K_g}}, \tag{20b}$$

and V_e is the equilibrium volume of the bubble. $X(a_e,\omega)$ depends on the thermodynamic properties of the gas: ρ_g is the density, C_p is the heat capacity at constant pressure, K_g is the thermal conductivity, and γ is the adiabatic constant of the gas.

The thermal damping constant δ_{th} and the polythropic gas exponent κ are identified from Eq. (19). The acoustic damping constant δ_c is found from Eller.[26] The total damping constant δ_{tot} is the sum of all damping terms. This gives the following expressions for the polythropic exponent and the total damping constant,

$$\kappa=\text{Re}\left(\frac{1}{\Phi(a_e,\omega)}\right),\quad \delta_{th}=\frac{1}{\omega\omega_0}\frac{3p_0}{\rho_La_e^2}\text{Im}\left(\frac{1}{\Phi(a_e,\omega)}\right), \tag{21a}$$

$$\delta_c=\frac{\omega}{\omega_0}\frac{\omega a_e}{c},\quad \delta_{\text{tot}}=\delta_L+\delta_S+\delta_c+\delta_{th}. \tag{21b}$$

Damping from liquid viscosity δ_L and from the shell δ_S are defined in Eq. (11b).

The thermal damping constant δ_{th} was derived for a bubble without a shell, looking at temperature variations in the gas, with the liquid acting as a heat reservoir of constant temperature.[22] Using this model on the shelled bubble means assuming the shell to have the same constant temperature as the liquid. Hence, heat generation in the shell during oscillations is neglected. This assumption seems fair, as the heat capacity per volume of the shell is of the same order of magnitude as water, and about three orders of magnitude greater than the heat capacity per volume of air.[27]

Thermal and acoustic damping were not part of the derivation of the equations of motion, Eqs. (6) and (10). These extra damping terms can be added to the linearized expressions for extinction and scattering cross sections, Eqs. (16) and (18), by replacing δ from Eq. (11b) with δ_{tot} from Eq. (21b).

III. EXPERIMENTAL METHOD

A. Particle size distribution

Particle size distributions were measured using a *Coulter Multisizer* (Coulter Electronics, Luton, UK). The effect of varying particle size was investigated by removing the larger particles by a flotation technique. Particle samples were injected into a glass tube and left at rest for a specified time. The flotation speed of gas bubbles increases with diameter. By extracting particles from the bottom of the tube after varying flotation times, samples of varying size distribution were obtained. Particle samples were harvested after 30, 60, 120, and 180 min flotation time. The resulting size distributions, measured with the *Coulter Multisizer*, are plotted in Fig. 2, showing how the procedure produced particle samples of successively smaller size.

B. Acoustic attenuation spectra

Acoustic attenuation was measured using a method similar to that described by de Jong *et al.*[12] The measurement setup is shown in Fig. 3. The equipment consists of a pulser/receiver (Panametrics 5800PR, Panametrics, Inc., Waltham,

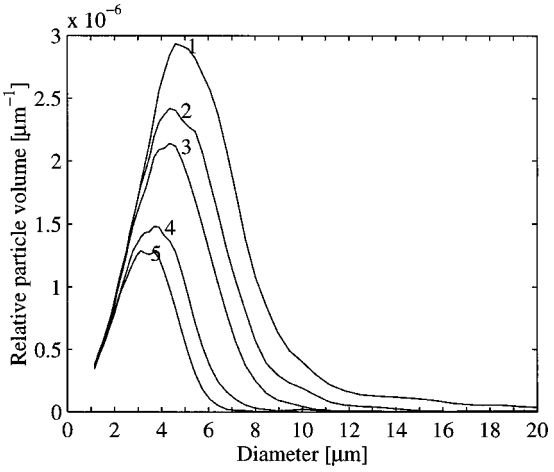

FIG. 2. Size distribution of particle samples, plotted as relative volume of particles per μm. (1) is the original particle distribution, (2) to (5) are samples extracted from the bottom of a glass tube after flotation: (2) is after 30 min, (3) after 60 min, (4) after 120 min, and (5) after 180 min flotation time.

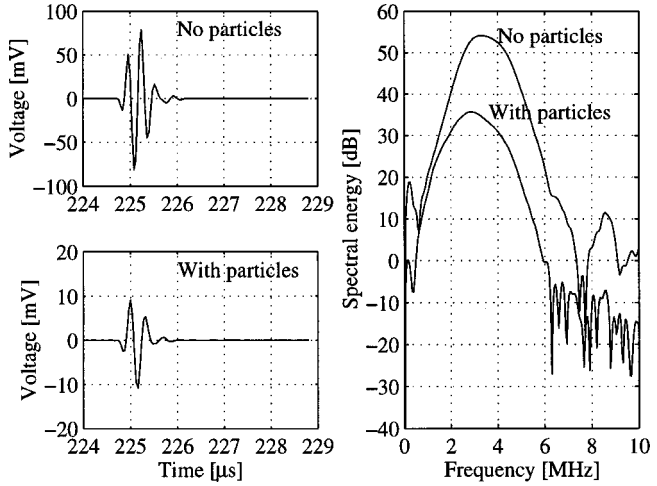

FIG. 4. Example of pulses measured with the 3.5-MHz transducer. The left diagrams show pulses received after reflections from the back wall, traversing the sample cell twice: The upper pulse is from a reference measurement with no particles in the sample cell, the lower pulse is received with a contrast agent sample present in the sample cell. The right diagram shows the power spectra of the two pulses. This 3.5-MHz transducer was used to evaluate spectra in the frequency range from 1.5 to 5.0 MHz.

MA), a coaxial cable relay for selecting transducers (CX-600N, Toyo Tsusho Electric Co. Ltd., Japan), two transducers (Panametrics Videoscan V382-SU and V326-SU), and a digital oscilloscope (LeCroy9410, LeCroy Corporation, Chestnut Ridge, NY). The pulser/receiver and oscilloscope were connected to a PC-type computer via a GPIB board (National Instruments, Inc., Austin, TX). The coaxial relay was controlled over a PC-DIO24 digital in/out board (National Instruments, Inc.). The measurement system was controlled and digitized results were acquired using LABWINDOWS software (National Instruments, Inc.).

The two transducers were broadband and unfocused, one with center frequency 3.5 MHz and 13 mm aperture diameter, the other with 5.0 MHz center frequency and 10 mm aperture. They were mounted in parallel in a water tank made of Perspex. A sample cell with thin rubber membranes acting as acoustic windows was placed 10 cm from the transducer faces. The back wall of the water tank was used as an acoustic reflector, at a distance 15 cm from the transducer faces. The length of the sample cell was 3.15 cm. The sample cell was filled with 55 ml *Isoton II* (Coulter Electronics Ltd.), and samples of contrast agent were diluted in this. Sensitivity and signal-to-noise ratio were optimized by varying the dilution, depending on the size distribution of the sample investigated. Best results were obtained for dilutions giving acoustic attenuation around 3 dB/cm. This resulted in dilution factors between 1:2500 and 1:250, depending on the particle sample. Acoustic attenuation was verified to vary linearly with particle concentration, and all results were scaled to a standardized dilution of 1:1000.

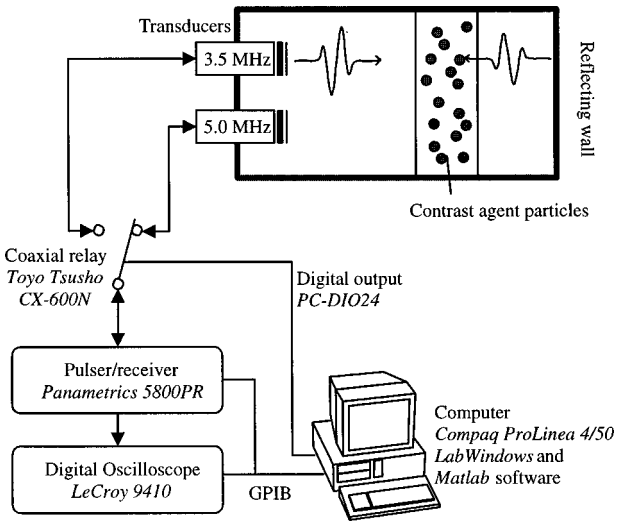

FIG. 3. Setup for measuring acoustic attenuation spectra.

The measurement sequence was as follows: The transducers were excited by short pulses from the pulser/receiver, sending broadband ultrasound pulses through the sample cell at 50 pulses per second. The pulses were reflected at the back wall of the water tank, and received by the transmitting transducer after traversing the sample cell twice. This gives a total sound path length through the sample cell of 6.3 cm. The received signals were amplified in the receiver section of the pulser/receiver and transferred to the oscilloscope. The oscilloscope was set to display only the reflection from the back wall of the chamber, by using delayed trigger and time gating. The pulses were digitized in the oscilloscope at a sampling rate of 25 Msa/s, averaged over 50 successive pulses, and transferred over the general purpose interface bus (GPIB) to the computer. Figure 4 shows an example of received pulses and their power spectra, without and with contrast agent particles in the sample cell.

Signal processing of the received pulses was done in the computer using MATLAB software (The Math Works, Inc., Natick, MA). Power spectra were calculated from fast Fourier transform (FFT) and the part of the spectrum containing useful information for each transducer was singled out: The 3.5-MHz transducer was used between 1.5 and 5.0 MHz, the 5.0-MHz transducer between 2.5 and 8.0 MHz. The overlap region, where both transducers provided spectral informa-

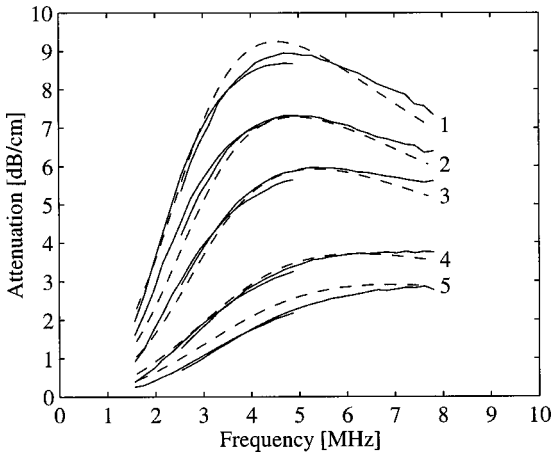

FIG. 5. Acoustic attenuation spectra measured on the samples displayed in Fig. 2. Solid lines are measured attenuation. Dashed lines show acoustic attenuation spectra calculated from size distributions, using the described theory. The viscoelastic properties G_S and μ_S were adapted to the best fit between measured and calculated attenuation spectra. This result is for batch (a), see Table I.

tion, gave a test of the validity of the results, as the different transducers should give equal results here. The power spectra measured with contrast agent particles present were normalized by dividing them with the spectra measured without contrast agent in the sound path. This corrected for the frequency responses of the transducers and for propagation path characteristics.

IV. RESULTS

A. Attenuation spectra

Acoustic attenuation spectra were measured on the particle samples shown in Fig. 2. The results are plotted in Fig. 5. The attenuation spectra are normalized to standardized dilution 1:1000. These results show how the overall attenuation level is reduced, the resonance frequency increased, and the spectrum broadened as the larger particles are removed. In the region covered by both transducers, from 2.5 to 5.0 MHz, the curves from the different transducers overlap.

B. Estimation of shell parameters

The viscoelastic parameters G_S and μ_S of the shell were estimated by comparing theoretically calculated acoustic attenuation spectra with the measured spectra plotted in Fig. 5.

The theoretical spectra were calculated from the linearized model described above, using the measured size distributions shown in Fig. 2. Acoustic attenuation $\alpha(\omega)$ in decibels was calculated from Eqs. (16) and (17), using the total damping constant from Eq. (21b). The integral in Eq. (17) was replaced by a sum over the 64 logarithmically spaced *Coulter Multisizer* channels, spanning diameters from 1 to 30 μm,

$$\alpha(\omega) = \log_{10}(e) \sum_{k=1}^{64} \sigma_e(a_k, \omega) n_k \ [\mathrm{dB}]. \tag{22}$$

TABLE I. Values for parameters estimated for the three different batches of polymer-encapsulated air bubbles, (a), (b), and (c). Shell thickness d_{Se} was estimated from production process parameters and electron microscopy (Ref. 19) to 5% of particle radius for all samples. The viscoelastic shell parameters G_S and μ_S and the particle bulk modulus K_p were estimated from acoustic measurements.

Batch	Shear modulus G_S[MPa]	Shear viscosity μ_S[Pas]	Bulk modulus K_p[MPa]
(a)	10.6±1.0	0.39±0.04	2.2±0.3
(b)	11.6±1.2	0.48±0.05	2.4±0.3
(c)	12.9±0.9	0.49±0.03	2.7±0.2

Here, a_k is the geometric mean radius of *Coulter Multisizer* channel k and n_k is the number of particles per unit volume counted in channel k.

The equation of motion, Eq. (6), contains the viscoelastic shell parameters G_S and μ_S only as products of the parameters and the relative shell thickness, $G_S d_{Se}/a_e$ and $\mu_S d_{Se}/a_e$. The shell thickness was estimated to 5% of the particle radius, as described in Sec. I, giving

$$\frac{d_{Se}}{a_e} = 0.05 = \text{constant}. \tag{23}$$

The exact value of the ratio d_{Se}/a_e is not critical for the modeling; it enters into the calculations as a simple scaling of G_S and μ_S. It is assumed that all particles are equal, that is, have the same shell material properties G_S and μ_S and relative thickness d_{Se}/a_e.

The values of G_S and μ_S were estimated by adjusting their values to minimize summed square difference between the measured and calculated spectra. The parameter values were then varied around these first estimates, and measured and calculated spectra were compared by visual inspection and by calculating the residual. The values of G_S and μ_S were adjusted until the fit between measured and calculated spectra was judged unacceptable. This corresponded to a doubling of the summed square error between measured and calculated spectra, and was selected as limits for the confidence intervals of G_S and μ_S.

This procedure was repeated for three different production batches of the polymeric microbubbles. Results for the individual batches are given in Table I. The differences between the three batches are close to the uncertainty estimates for each batch. The differences are judged as significant, and may be caused by variations in production parameters between the batches.

The theoretically calculated attenuation spectra for one of the batches is plotted in the same graph as the measured spectra, Fig. 5. The theoretical spectra for the four larger particle samples, (1) to (4), fit very well to the measured spectra. The attenuation calculated for the smallest sample (5) is higher than the measured value. Microscopic images and comparisons of polymer and particle volume[19] indicate that the samples contain a very small fraction of small fragments of solid polymer material. These fragments will show up as small particles on the *Coulter Multisizer*, but have minimal effect on the attenuation. This may explain the reduced attenuation of the smallest size fraction.

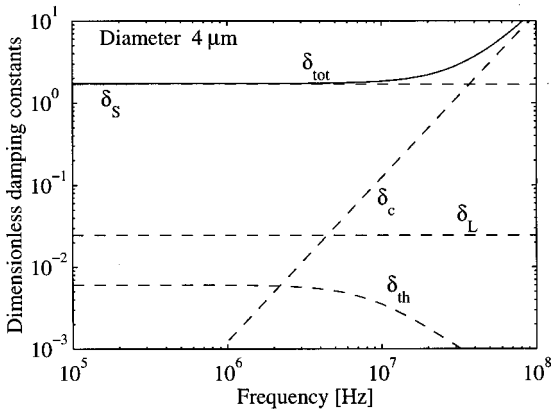

FIG. 6. Dimensionless damping constants for a polymeric microbubble with diameter 4 μm as function of frequency. Contribution from liquid viscosity δ_L, shell viscosity δ_S, acoustic radiation δ_c, thermal conduction in the gas δ_{th}, and the total damping $\delta_{\text{tot}}=\delta_L+\delta_S+\delta_c+\delta_{th}$. The shell viscosity was set to $\mu_S=0.48$ Pas.

C. Damping constants

The total damping constant δ_{tot} is the sum of several damping terms, see Eq. (21b). The contribution from each of these terms is plotted in Figs. 6 and 7, for particle diameters 4 and 8 μm. The value of δ_S is calculated from the value of μ_S estimated from the measurements. The curves show that shell viscosity is the dominating damping mechanism for frequencies below 10 MHz.

Contributions from acoustic and thermal damping were not included in the derivation of the equation of motion (6). The curves in Figs. 6 and 7 indicate that these are not very important at frequencies below about 10 MHz. Acoustic damping starts to play a role only for frequencies above about 10 MHz for particles with diameter below 8 μm.

D. Particle stiffness

The bulk modulus K_p expresses the stiffness of the whole particle, composed of gas-filled interior and surrounding shell. It is informative to compare this particle stiffness

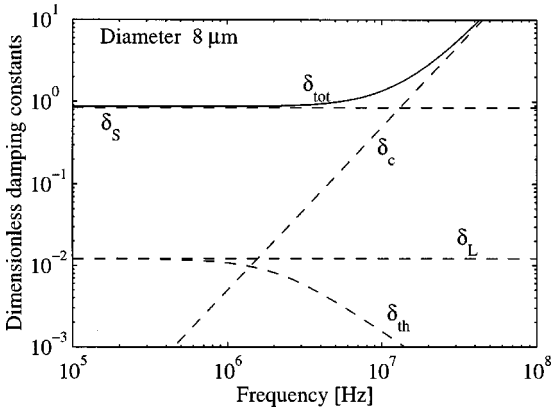

FIG. 7. Dimensionless damping constants for a polymeric microbubble with diameter 8 μm as function of frequency. Contribution from liquid viscosity δ_L, shell viscosity δ_S, acoustic radiation δ_c, thermal conduction in the gas δ_{th}, and the total damping $\delta_{\text{tot}}=\delta_L+\delta_S+\delta_c+\delta_{th}$. The shell viscosity was set to $\mu_S=0.48$ Pas.

TABLE II. Particle stiffness. Bulk modulus of the investigated polymer-shelled particles compared with other substances.

Substance	Bulk modulus K [MPa]
Air (isothermal)	0.10
Air (adiabatic)	0.14
Polymer-shelled air bubbles	2.5
Water	2250
Steel	160 000

with the bulk moduli of known materials. Bulk modulus K_p and bulk viscosity μ_p are defined from the relation

$$\Delta p=-K_p\frac{\Delta V}{V_e}-\mu_p\frac{d}{dt}\left(\frac{\Delta V}{V_e}\right), \tag{24}$$

were Δp is the applied pressure, ΔV is the change in particle volume, and V_e is the equilibrium volume. For the polymeric microbubbles, expressions for K_p and μ_p are found from Eq. (8) to

$$K_p=\kappa p_0+4G_S\frac{d_{Se}}{a_e},\quad \mu_p=4\mu_S\frac{d_{Se}}{a_e}. \tag{25}$$

The bulk modulus for a polythropic gas is $K_g=\kappa p_0$. Compared to the free gas bubble, the bulk modulus of the shell-encapsulated particles increases due to the shear modulus of the shell. Bulk moduli for the polymeric microbubbles are estimated by inserting the values for G_S into Eq. (25). This results in values for K_p of around 2.5 MPa, see Table I. K_p and μ_p are independent of the particle diameter when the ratio between shell thickness and particle diameter is constant. The value of K_p estimated for the polymeric microbubbles is compared with other materials in Table II. According to these results, the polymeric microbubbles are approximately 20 times stiffer than free gas bubbles. The stiffness of the particles is mainly determined by the shell, not by the air inside. The polymeric microbubbles are, however, 1000 times more compressible than water.

When the particles are described by their bulk modulus K_p, the resonance frequency f_0 from Eq. (12) can be expressed in a simple form analogous to the result by Minnaert,[21]

$$f_0=\frac{1}{2\pi a_e}\sqrt{\frac{3K_p}{\rho_L}}. \tag{26}$$

E. Resonance frequency and scattering cross section

Increased particle stiffness from shell elasticity causes the resonance frequency to increase. Increased damping from shell viscosity broadens the resonance peak and increases sound absorption. The resonance frequency calculated from Eq. (12) is compared with results for free gas bubbles; results are plotted in Fig. 8. The resonance frequency of the polymeric microbubbles was found to be approximately four times higher than what is expected for air bubbles of the same diameter.

The scattering cross section is calculated from Eq. (18). Figure 9 shows dependence on diameter, at frequency 3.5 MHz, while Fig. 10 shows dependence on frequency for par-

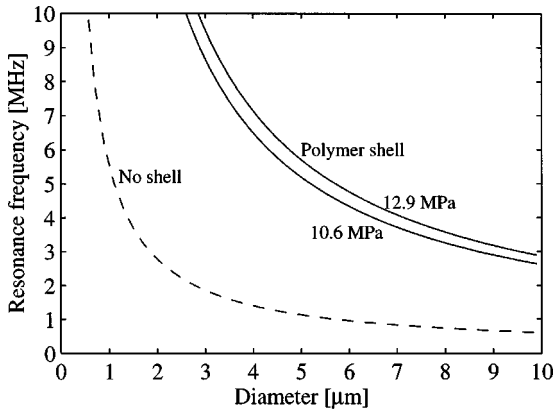

FIG. 8. Calculated resonance frequency as function of particle diameter. The solid lines show the values found for the bubbles encapsulated in a polymeric shell, while the dashed line shows values calculated for free air bubbles. The two curves for the polymeric microbubbles correspond to the parameter values $G_S = 10.6$ and $G_S = 12.9$ MPa. See Table I.

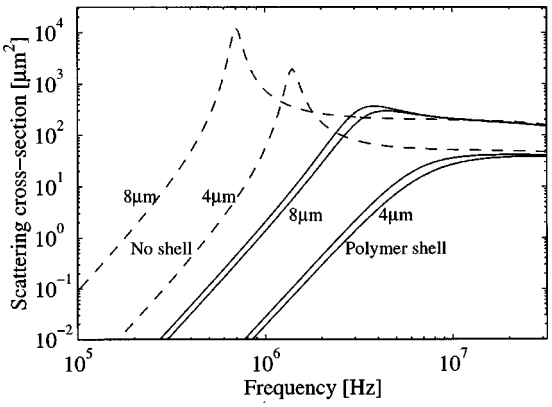

FIG. 10. Scattering cross section as function of frequency. Calculated for polymer-encapsulated air bubbles (solid lines) and for air bubbles without shells (dashed lines) with diameters 3 and 8 μm. The two curves for the polymeric microbubbles correspond to the parameter combinations $G_S = 10.6$ MPa, $\mu_S = 0.39$ Pas and $G_S = 12.9$ MPa, $\mu_S = 0.49$ Pas. See Table I.

ticles with diameters of 4 and 8 μm. Scattering cross sections of air bubbles without shells are plotted in the same diagrams for comparison. Figure 9 corresponds to Fig. 8 in Church's article.[16] Figures 9 and 10 show how the resonance frequency increases and the resonance peak broadens and almost disappears, due to the viscoelastic polymeric shell.

V. DISCUSSION

Shell thickness

A critical assumption for the estimation of the viscoelastic shell parameters is that the ratio between shell thickness and particle radius is constant. The basis for this assumption is the production process for the particles:[19] A droplet with a constant fraction of dissolved polymeric material is converted to one air-filled, polymer-shelled microbubble, with proportionality between initial droplet size and resulting microbubble size. The good agreement between experimental and theoretical attenuation spectra supports this assumption.

The model was tested by assuming a constant shell thickness instead of constant ratio between shell thickness and radius. This gave poor agreement between measurements and calculations for any combination of G_S and μ_S, supporting the assumption that shell thickness varies with particle diameter.

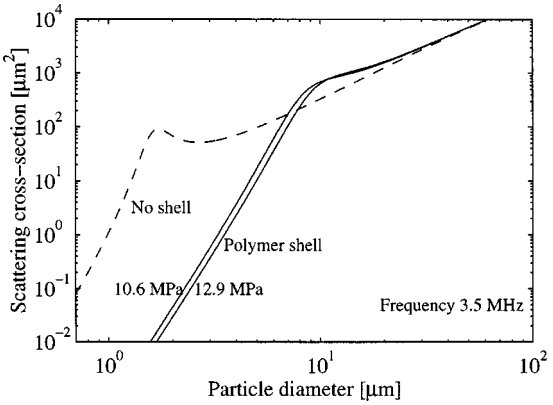

FIG. 9. Scattering cross section for polymer-encapsulated air bubbles (solid lines) compared with air bubbles without shells (dashed line). Curves are calculated for frequency 3.5 MHz. The two curves for the polymeric microbubbles correspond to the two parameter combinations $G_S = 10.6$ MPa, $\mu_S = 0.39$ Pas and $G_S = 12.9$ MPa, $\mu_S = 0.49$ Pas. See Table I.

Another critical assumption is that all particles of the same size are equal: the shell thickness is uniquely determined by particle diameter, and the values of the viscoelastic material parameters of the shell are equal for all particles. Particle characterization methods[19] have not shown variations in shell thickness between particles of the same size. This supports the assumption. If there are variations in shell thickness or viscoelastic parameters, this would typically cause overestimation of the shell viscosity μ_S: the resulting broadening of the resonance peak could be interpreted as being caused by an increased damping of the oscillating particle.

VI. SUMMARY

A model has been developed describing oscillations of gas bubbles encapsulated in a thin polymer shell. The model depends on viscoelastic parameters of the shell material that are not known *a priori*. A linearized version of the model was used to estimate the shell material properties shear modulus and shear viscosity from acoustic attenuation spectra. Good agreement between experimental and theoretical results was found. The results show that the polymer shell increases particle stiffness 20 times compared to a free gas bubble.

ACKNOWLEDGMENTS

We wish to thank Nycomed Imaging AS for providing the contrast agent and experimental equipment used in these experiments. We also thank Andrew Healy for many helpful comments during the preparation of this paper. This work was supported by the Research Council of Norway.

[1] R. Gramiak and P. Shah, ''Echocardiography of the aortic root,'' Invest. Radiol. **3**, 356–388 (1968).
[2] J. Hogg, ''Neutropil kinetics and lung injury,'' Physiol. Rev. **67**, 1249–1295 (1987).
[3] Lord Rayleigh, ''On the pressure developed in a liquid during the collapse of a spherical cavity,'' Philos. Mag. **34**, 94–98 (1917).

[4] H. Medwin, ''Counting bubbles acoustically: A review,'' Ultrasonics **15**, 7–13 (1977).
[5] A. Prosperetti, ''Bubble phenomena in sound fields: Part one,'' Ultrasonics **22**, 69–77 (1984).
[6] T. G. Leighton, *The Acoustic Bubble*, 1st ed. (Academic, London, 1994), Chap. 4.2, pp. 301–311.
[7] A. Prosperetti, ''Nonlinear oscillations of gas bubbles in liquids: Steady-state solutions,'' J. Acoust. Soc. Am. **56**, 878–885 (1974).
[8] W. Lauterborn, ''Numerical investigation of nonlinear oscillations of gas-bubbles in liquids,'' J. Acoust. Soc. Am. **59**, 283–293 (1976).
[9] D. Tucker and V. Welsby, ''Ultrasonic monitoring of decompression,'' Lancet **I**, 1253 (1968).
[10] D. Miller, ''Ultrasonic detection of resonant cavitation bubbles in a flow tube by their second harmonic emissions,'' Ultrasonics **22**, 217–224 (1981).
[11] F. Fox and K. Herzfield, ''Gas bubbles with organic skin as cavitation nuclei,'' J. Acoust. Soc. Am. **26**, 984–989 (1954).
[12] N. de Jong, L. Hoff, T. Skotland, and N. Bom, ''Absorption and scatter of encapsulated gas filled microspheres: Theoretical considerations and some measurements,'' Ultrasonics **30**, 95–103 (1992).
[13] N. de Jong and L. Hoff, ''Ultrasound scattering properties of Albunex microspheres,'' Ultrasonics **31**, 175–181 (1993).
[14] L. Hoff and P. C. Sontum, ''Acoustic properties of shell-encapsulated, gas-filled ultrasound contrast agents,'' in *1996 IEEE Ultrasonics Symposium Proceedings* (IEEE, New York, 1997), pp. 1441–1444.
[15] S. Holm, M. Myhrum, and L. Hoff, ''Modelling of the ultrasound return from Albunex microspheres. Ultrasonics,'' Ultrasonics **32**, 123–130 (1994).
[16] C. C. Church, ''The effects of an elastic solid surface layer on the radial pulsations of gas bubbles,'' J. Acoust. Soc. Am. **97**, 1510–1521 (1995).
[17] P. Frinking and N. de Jong, ''Acoustic modelling of shell-encapsulated gas bubbles,'' Ultrasound Med. Biol. **24**, 523–533 (1998).
[18] P. C. Sontum, J. Østensen, K. Dyrstad, and L. Hoff, ''Acoustic properties of NC100100 and their relationship with the microbubble size distribution,'' Invest. Radiol. **34**, 268–275 (1999).
[19] K. Bjerknes, P. Sontum, G. Smistad, and I. Agerkvist, ''Preparation of polymeric microbubbles: Formulation studies and product characterisation,'' Int. J. Pharm. **158**, 129–136 (1997).
[20] T. G. Leighton, *The Acoustic Bubble*, 1st ed. (Academic, London, 1994), Chap. 3.4, pp. 172–190.
[21] M. Minnaert, ''On musical air-bubbles and the sounds of running water,'' Philos. Mag. **16**, 235–248 (1933).
[22] C. Devin, ''Survey of thermal, radiation and viscous damping of pulsating air bubbles in water,'' J. Acoust. Soc. Am. **31**, 1654–1667 (1959).
[23] L. Trilling, ''The collapse and rebound of a gas bubble,'' J. Appl. Phys. **23**, 14–17 (1952).
[24] J. B. Keller and M. Miksis, ''Bubble oscillations of large amplitude,'' J. Acoust. Soc. Am. **68**, 628–633 (1980).
[25] H. G. Flynn, ''Cavitation dynamics. I. A mathematical formulation,'' J. Acoust. Soc. Am. **57**, 1379–1396 (1975).
[26] A. I. Eller, ''Damping constants of pulsating bubbles,'' J. Acoust. Soc. Am. **47**, 1469–1470 (1970).
[27] J. Österman and C. Nordling, *Physics Handbook*, 4th ed. (Studentlitteratur, Lund, Sweden, 1987), Chap. F-1.5, pp. 35–39.

Experimental investigation of the pulse inversion technique for imaging ultrasound contrast agents

Xander A. A. M. Verbeek, Léon A. F. Ledoux, Jean M. Willigers, Peter J. Brands, and Arnold P. G. Hoeks

Department of Biophysics, Cardiovascular Research Institute Maastricht (CARIM), Maastricht University, The Netherlands

(Received 15 July 1999; revised 26 October 1999; accepted 15 December 1999)

The application of ultrasound contrast agents aims to detect low velocity blood flow in the microcirculation. To enhance discrimination between tissue and blood containing the contrast agent, harmonic imaging is used. Harmonic imaging requires the application of narrow-band signals and is obscured by high levels of native harmonics generated in an intervening medium. To improve discrimination between contrast agent and native harmonics, a pulse inversion technique has been proposed. Pulse inversion allows wide-band signals, thus preserving the axial resolution. The present study examines the interference of native harmonics and discusses the practical difficulties of wide-band pulse inversion measurements of harmonics by a single transducer. Native harmonics are not eliminated by pulse inversion. Furthermore, only even harmonics remain and are amplified by 6 dB, alleviating the requirement for selective filtering. Finally, it is shown that the contaminating third harmonic contained in the square wave activation signal leaks through in the emitted signal. The spectral location of the contaminating third harmonic is governed by the transducer spectral characteristics while the location of the native and contrast agent second harmonics is not. Thus the contarninating third harmonic and the native and contrast agent second harmonics may overlap and interfere. Optimal discrimination requires a balance between maximal sensitivity for the second harmonic at reception and minimal interference from the contaminating third harmonic. © *2000 Acoustical Society of America.* [S0001-4966(00)06003-3]

PACS numbers: 43.80.Vj, 43.80.Qf, 43.58.Ry, 43.60.−c [FD]

INTRODUCTION

Conventional ultrasound techniques have shown their value in many clinical and diagnostic applications. The techniques provide excellent information about both anatomy and blood flow. Because of the low echogenicity of blood compared to tissue, however, blood flow can only be measured with ultrasound if there is a clear velocity or spatial differentiation between blood and tissue. This is obviously not the case for perfusion of tissue or tumors, which involves slow flow in the smallest vessels of the microcirculation, beyond the resolution of the ultrasonic equipment.

In the past, the assessment of tissue perfusion with ultrasound has been an objective for many studies.[1–3] None of the proposed methods, however, has demonstrated to be as promising as the methods employing ultrasound contrast agents. Next to tissue[4,5] or tumor[6–10] perfusion assessment, which is the ultimate aim in the application of ultrasound contrast agents, these agents have proven their value in many other applications, e.g., the enhancement of Doppler signals,[11] small vessel delineation[12] or the delineation of heart cavities.[4]

It is an established fact that a successful use of the contrast agents for tissue perfusion assessment requires new techniques and processing based on radio frequency (RF) signals.[13–15] All of these techniques aim at an even better discrimination between blood containing the agent and tissue.

Maybe the most familiar technique nowadays is harmonic imaging,[16–18] which is already incorporated in a number of commercial scanners. This technique uses the property of nonlinear scattering, which a microbubble exhibits when excited at its resonance frequency with sufficiently high pressure amplitudes, which are well within the diagnostic range. Nonlinear scattering introduces harmonics in the ultrasound signal. These harmonics, the second harmonic in particular, are claimed to be of considerable strength.[16,17,19–21] The concept of harmonic imaging is to display selectively the amplitude of the second harmonic signal, which is supposed to reveal the presence of the contrast agent. Although theoretical studies indeed report of a remarkable physical harmonic response of the contrast agent,[22,23] recent studies show that this response will be limited when using a single transducer ultrasound system due to transducer sensitivity limitations,[24] not even when wide-band transducers are used. Moreover, tissue distorts the propagating ultrasound nonlinearly and the subsequently appearing native harmonics interferes with the contrast agent intrinsic harmonics.[24–26] In fact, the native harmonic is of such a strength that a new technique, called native or tissue harmonic imaging,[27–30] has evolved in which the amplitude of the generated native harmonic signals is displayed. Although the contrast agent intrinsic harmonics is commonly higher than the native harmonics and hence does improve contrast, the formation of native harmonics limits the power of the harmonic imaging technique to discriminate between tissue and blood and to analyze the data quantitatively.

One of the latest technical improvements for harmonic imaging is called pulse inversion. Pulse inversion claims to

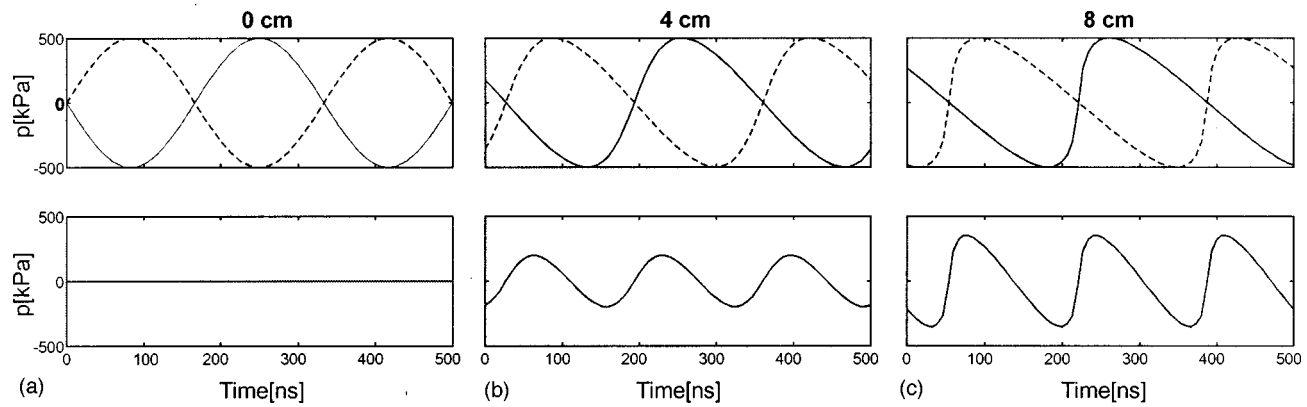

FIG. 1. Gradual distortion of an initial sinusoidal plane wave (solid line) and inverted sinusoidal wave (dashed line) as a function of time measured at a fixed location from the source. (a) At the source, (b) at 4 cm, and (c) at 8 cm from the source. Also shown, at the bottom of each figure, is the pulse inversion residue signal, which is the sum of the inverted and noninverted distorted waves.

solve two important limitations of harmonic imaging. First of all, pulse inversion should provide a better discrimination between tissue and blood.[25] Second, it overcomes the requirement of the application of a narrow-band signal for harmonic imaging in order to be able to distinguish and separate the fundamental and harmonic components from each other. As a consequence also the axial resolution is preserved.

The present paper focuses on the practical aspects of the pulse inversion technique, taking into account properly amongst others (1) interference from other sources of harmonics and (2) single transducer measurement of the RF signal response to pulse inversion insonification. In the first section, concepts will be discussed to illustrate the practical aspects. First the different sources of harmonics are briefly reviewed. Next, the attribution of the harmonics originating from nonlinear distortion of ultrasound by tissue is explained. Finally, the limitations of wide-band transducer activation and proper interpretation of the received harmonic signal response is addressed. In the following sections, the concepts will be validated by experiments. In the last sections the results are presented and discussed, and finally, the conclusions of the present study are summarized.

I. CONCEPTS

Sources of harmonics

In the present study three different types of harmonics will be distinguished, which originate from different processes: (1) contrast agent intrinsic harmonics, (2) native or tissue harmonics, and (3) contaminating harmonics. The contrast agent intrinsic harmonics is due to the nonlinear scattering by the microbubbles,[22] which occurs if a microbubble is excited near its resonance frequency at sufficiently high pressure amplitudes. Native harmonics is caused by nonlinear distortion of the ultrasonic wave when it propagates through a medium. The positive half cycles of this wave experience a different acoustic velocity than the negative half cycles, which causes the wave to become deformed.[31–33] Finally, the contaminating harmonics is contained in the emitted signal itself. Most commercial scanners use a square wave to activate the transducer in order to attain sufficiently high pressure amplitudes. The odd harmonics in the square wave activation signal leaks through in the emitted signal, especially for wide-band transducers used nowadays.[24]

Native harmonics and pulse inversion

To show the influence of the native harmonics to the pulse inversion concept the nonlinear distortion of an acoustic wave propagating in a medium is analyzed based on elementary considerations for a plane wave approximation. The plane wave approximation is suitable for the focal region of more realistic ultrasonic beams. Equation (1) shows the wave equation, describing the particle displacement $\xi(x,t)$ in a medium for the linear case for one dimension,

$$\frac{\partial^2 \xi}{\partial t^2} = c_0^2 \frac{\partial^2 \xi}{\partial x^2}. \tag{1}$$

In this equation c_0 is the acoustic wave propagation velocity in the medium and t and x denote time and place, respectively. In the nonlinear case the acoustic velocity no longer can be regarded as a constant. Disregarding dissipation, the acoustic velocity $c(t)$ is a function of the particle velocity $u(x,t)$, with $u=(\partial\xi)/(\partial t)$, given by Eq. (2),[32,33]

$$c(t) = c_0 \cdot \left(1 + \frac{B}{2A} \cdot \frac{u(x,t)}{c_0}\right)^{1+(2A/B)}. \tag{2}$$

Here, B/A is the nonlinearity parameter of the medium.[34] Substitution of Eq. (2) in Eq. (1) provides a nonlinear differential equation. In the nondissipative case and for an initial sinusoidal motion, given by the boundary condition $u(0,t) = u_0 \cdot \sin(\omega \cdot t)$, the explicit solution of this equation is given by[33]

$$u(t,x) = 2u_0 \cdot \sum_{n=1}^{\infty} \frac{J_n(nx/L)}{nx/L} \cdot \sin[n(\omega t - kx)] \quad x < L, \tag{3}$$

with $k=\omega/c_0$, J_n the Bessel function of the first kind of order n, and L the discontinuity distance given by

$$L = \frac{2c_0^2}{\left(\frac{B}{A}+2\right) \cdot \omega \cdot u_0}. \tag{4}$$

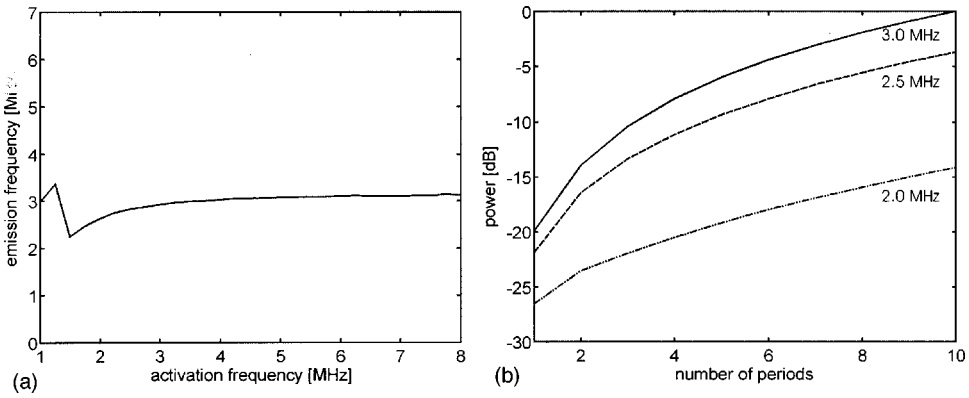

FIG. 2. (a) Emission frequency, as a function of the activation frequency for a square wave activation pulse of one period. (b) Relative power at the emission frequency, as a function of number of periods in the activation pulse, at different activation frequencies. The results are based on computer simulations for a 3.0-MHz transducer with assumed Gaussian spectral characteristics and a −6-dB roundtrip bandwidth of 30%.

Figure 1(a) shows an initial sinusoidal wave, traveling in water ($c_0 = 1480$ m/s, $B/A = 5.2$), with a frequency of 3 MHz and a particle velocity amplitude based on a pressure amplitude of $p_0 = 500$ kPa. Figure 1(b) and (c) show the gradual distortion of this wave, at distances of 4 and 8 cm from the source. Also shown in each figure are the same results for an initially inverted sinusoidal wave and the sum of this and the noninverted signal. As can be observed, this residue signal equals zero at the source, which is to be expected. However, as the wave becomes gradually distorted a residue signal evolves. This residue signal has a carrier frequency that is doubled with respect to that of the distorted pulses. Consequently, it appears as though the residue signal contains only the even constituents of the harmonics that appears in the distorted signal itself. Because of the summation, the amplitude of the even harmonics is amplified by a factor 2 (6 dB) in the residue signal. As can be observed in Fig. 1(b) and (c), the level of the residue signal is substantial, indicating that a considerable native harmonic contribution has to be expected in pulse inversion experiments if contrast agents are employed.

Limitations to transducer wide-band excitation

In addition to the distinction in contrast agent intrinsic, native, and contaminating harmonics, another difference has to be made, namely the difference between the physical level and actual observed level of these harmonics. Many studies focus on the physical response of a microbubble based on theoretical predictions,[19,22,23] which might not be obtained in practice.[22,24] In most experimental studies, the harmonic response is measured with separate transducers for emission and reception.[5,19,22,35,36] Then each transducer may have an optimal sensitivity for the frequency of interest, thus giving the most reliable representation of the physical harmonic response. In more realistic measurements using a single transducer,[17,18,20] however, the spectral sensitivity characteristics of the transducer govern the harmonic response that can be observed.[24]

Pulse inversion aims at the application of wide-band signals in order to maintain the axial resolution. For wide-band activation (single period) another problem arises which is also due to the transducer spectral characteristics. In order to obtain a sufficiently high harmonic response at reception it is necessary to drive the transducer below its resonance frequency.[24] For wide-band activation signals, however, it is not possible to drive the transducer effectively at a frequency that differs substantially from the transducer resonance frequency.

To clarify the above problem, computer simulations are performed for a 3-MHz transducer with an assumed Gaussian-shaped spectral sensitivity distribution and a −6-dB roundtrip bandwidth of 30% (0.9 MHz) of the resonance frequency (42% single trip). This is approximately identical to the transducer employed in the experimental part of the present study. A single period, square wave activation pulse is simulated and filtered by the simulated transducer spectral sensitivity distribution, resulting in the emitted pulse. The spectrum of the emitted pulse is analyzed. Considering the wide band and possible asymmetric nature of the pulse spectrum, the emission frequency refers to the dominant frequency in the emitted pulse spectrum. For the square wave activation pulse, the activation frequency will be defined as the reciprocal of the time period.

Figure 2(a) shows the emission frequency as a function of the activation frequency. Because of the transducer spectral characteristics, the emission frequency does not match the activation frequency. It is clear that it is not possible to obtain emission frequencies outside the range from 2.2 to 3.1 MHz. Below an activation frequency of approximately 1.3 MHz the graph peaks. This peak is caused by the third harmonic, which at this point becomes dominant.

Although Fig. 2 shows it is not feasible to obtain emission frequencies outside the range 2.2–3.1 MHz, lower frequencies are still present in the emitted pulse, due to its wide-band nature. Thus the above finding does not really impede the requirement that a contrast agent needs to be driven near its resonance frequency in order to behave as a nonlinear scatterer. Moreover, contrast agents nowadays conveniently have a relatively wide resonance band, which is related to the size distribution of the microbubbles.[37,38]

The problem with wide-band activation, however, dwells in the power of the emitted signal. Figure 2(b) depicts the spectral power at the emission frequency, as a function of the number of periods in the activation signal for corresponding activation frequencies of 2, 2.5, and 3 MHz. When increasing the number of periods, not only the absolute power increases but also this larger amount of power is concentrated in a smaller frequency band. Increasing the power of the activation signal can provide a solution for this problem, but might not be feasible in practice.

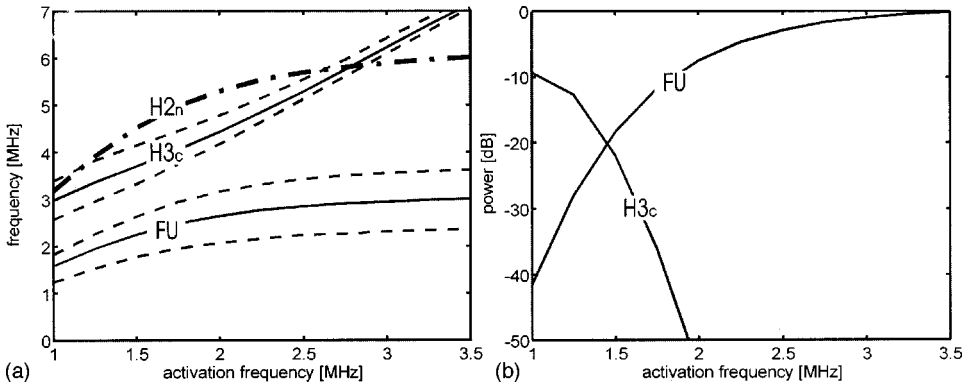

FIG. 3. (a) Location of the dominant frequency (solid lines) and −6-dB bandwidth limits (dashed lines) of the fundamental (FU) and contaminating third harmonic ($H3_c$) components in the emitted pulse spectrum and expected location of the frequency of the native second harmonic ($H2_n$) as a function of the activation frequency. (b) Power of the fundamental (FU) and contaminating third harmonic components ($H3_c$) in the emitted pulse spectrum, normalized to the maximum power of the fundamental component as a function of the activation frequency. These results are based on computer simulations for a 3.0-MHz transducer with assumed Gaussian spectral characteristics and a −6-dB single trip bandwidth of 42%, activated by a one period square wave signal.

Another difficulty might arise when analyzing the second harmonic response in single transducer experiments applying wide-band activation. Unlike the fundamental and the contaminating harmonic, the location of native second harmonic is not determined by the transducer spectral characteristics, but solely by the fundamental frequencies present. As can be observed in Fig. 3(a), the expected location of the native second harmonic ($H2_n$) and the contaminating third harmonic ($H3_c$) overlaps within a large range of frequencies.

Fortunately, at activation frequencies higher than approximately 1.8 MHz, the contaminating third harmonic is more than 30 dB smaller than the fundamental component [Fig. 3(b)]. For this particular transducer, interference may be minimized by application of activation frequencies higher than 1.8 MHz. In practice, transducers may have bandwidths that are much larger than the transducer simulated here and interference might be unavoidable. Moreover, for activation frequencies higher than 1.8 MHz the emission frequencies are higher than 2.5 MHz (with a −6-dB range from 2 to 3 MHz), indicating that the transducer is rather insensitive to the native or contrast agent second harmonics, which accordingly have frequencies higher than 5 MHz. The latter illustrates another restriction of the emission frequency in single transducer, wide-band activation.

II. EXPERIMENT

A focused 3.5-MHz transducer (KB Aerotech, MLA 35 DM), with a diameter of 13 mm and a focal region from 4 to 10 cm, was used in the pulse inversion experiments. The actual resonance frequency of this transducer was at 3 MHz. The −6-dB roundtrip bandwidth of the transducer was approximately 30% (0.9 MHz) (42% single trip) of the resonance frequency. The transducer is used for both emission and reception.

The transducer was activated by a custom-made ultrasound transmitter board with pulse inversion capabilities, generating a square wave with an adjustable number of periods and a (stepwise) adjustable frequency. For all measurements, the effective activation voltage was fixed at 20 V peak-to-peak. The maximum pressure amplitude at a distance of 5 cm (maximum intensity within the focus region) depends on the frequency and number of periods in the activation signal and is given in Table I.

Pulse shapes were measured with a polyvinylidenefluoride (PVDF) needle hydrophone (NP-1000, model number NTR-TNU001A, MTR Systems Inc., Seattle). This needle hydrophone has a 0.5-mm-diameter aperture and a bandwidth of 1–20 MHz.

The transducer and hydrophone RF signals were digitized either by a custom-built analog-to-digital converter (ADC) board or by an 8-bit digital oscilloscope (FLUKE, PM 3394B, 200 MHz), both connected to a personal computer. The custom-built ADC board has a dynamic range of 72 dB (12 bit) and a maximum sample frequency of 30 MHz. The sample clock signal, provided by the transmitter board, is synchronous with the emission pulse and has a frequency of eight times the emission frequency. For comparison of pulse shapes, RF signals' response and calculation of residue signals in the pulse inversion experiments, synchronous sampling is essential.

For experiments involving contrast agents, the transducer was mounted in a small container, with a volume of approximately 100 ml, filled with an air-saturated buffer solution with a pH=7.4 (8.00g NaCl, 2.38 g Na_2HPO_4, 0.19 g $KH_2PO_4^*H_2O$ diluted with distilled water to obtain a volume of 1000 ml). Approximately 5 ml of the contrast agent Levovist (SHU508A, Shering AG, Berlin) was dissolved in this solution. Levovist is composed of air-filled microbubbles, with a mean diameter of 3 μm, encapsulated in a galactose shell which is stabilized by a small amount (0.1%) of palmatic acid.[37] The contrast agent was prepared according to prescription to obtain a concentration of 200 mg/ml. Levovist resonates at frequencies between 1.5 and 5 MHz.[37] In

TABLE I. Maximum pressure amplitudes attained at a distance of 5 cm with the 3.0-MHz transducer driven by an effective power of 20 V peak-to-peak.

Frequency (MHz)	Periods	Pressure (kPa)
3.375	4	243
3.375	1	112
2.5	4	100
2.5	1	77

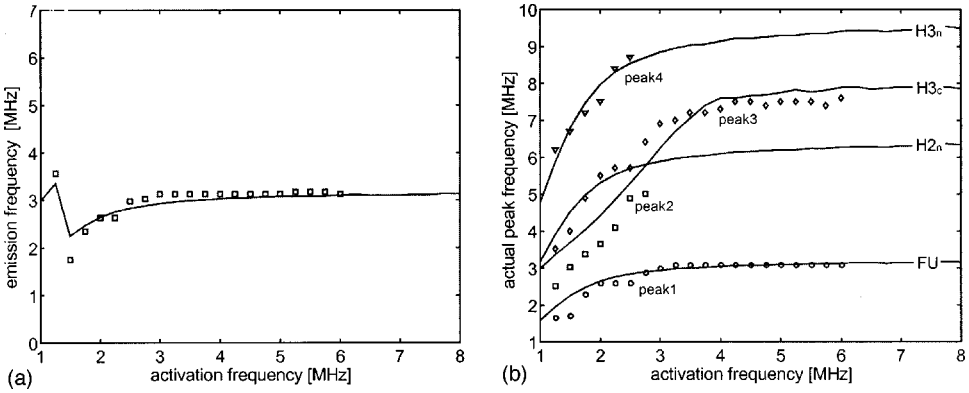

FIG. 4. (a) Simulated and measured relation between emission and activation frequency. (b) Predicted locations of fundamental (FU), native second ($H2_n$) and third ($H3_n$) harmonic and contaminating third harmonic ($H3_c$) components, and location of first four peaks in the spectra of the actually measured pulse as a function of the activation frequency. In both figures the solid lines give the expected value based on computer simulations.

another study,[38] this range was found to be slightly narrower from 1.5 to 3.5 MHz with a peak at 2 MHz.

For reference measurements, Carborundum particles were used, which are composed of silica carbide and have a diameter of approximately 5 μm. The Carborundum particles act as linear scatterers of ultrasound. Carborundum particles were suspended in Agarose (Life Technologies, Paisley, Scotland) in order to eliminate motion artefacts in the reference measurement. The solid Agarose Carborundum suspension was obtained by rapid cooling of an 80 °C water mixture of Agarose and Carborundum particles both in a 1% mass concentration.

III. RESULTS

Limitations to transducer wide-band excitation

Verification of the concepts concerning wide-band activation of a single transducer is found in the results presented in Fig. 4. The pulse emitted by the 3.5-MHz transducer was measured with the needle hydrophone and digitized by the oscilloscope for different activation frequencies. For calculation of the spectra, RF segments of 512 sample points (sample frequency $f_s = 25$ MHz) were used. Measured values are corrected for hydrophone sensitivity. Figure 4(a) depicts the measured emission frequency while in Fig. 4(b) the frequencies of the first four peaks appearing in the observed pulse spectra are plotted, both as a function of the activation frequency. The second and fourth peak could only be identified for activation frequencies up to 2.75 and 2.5 MHz, respectively, above which the second peak merges with the third peak and the level of the fourth peak drops below the noise level.

Both figures also depict the theoretical expected values for the fundamental (FU), native second ($H2_n$) and native ($H3_n$) and contaminating ($H3_c$) third harmonic components, based on the computer simulations which were described before. The expected simulated values were already presented in Figs. 2(a) and 3(a).

Native harmonics and pulse inversion

In order for pulse inversion to work accurately, the normal and inverted square wave activation pulses should not be a source of significant residue signals themselves. The pulses were both measured at the transmitter-board output, which was loaded with the 3.5-MHz transducer. Sampling was performed with the PCI-ADC board, synchronously to the activation pulse, with a sample frequency of eight times the activation frequency. Figure 5 shows the normal (solid line) and inverted (dashed line) square wave activation pulses of one period at a frequency of 3.375 MHz. The spectrum of the normal and the inverted pulses did not expose any differences and only one of them is displayed. Also shown is the spectrum of the residue signal. Similar results are presented in Fig. 6; however, now for the emission pulses measured with the hydrophone at a distance $z = 50$ mm from the transducer surface.

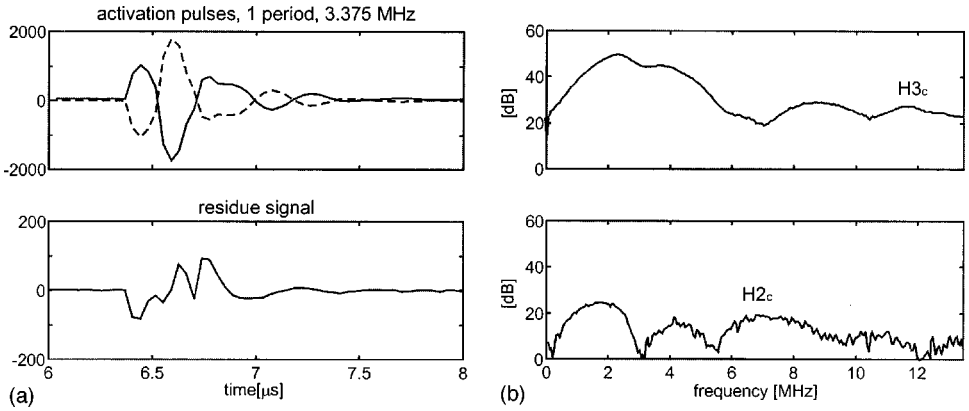

FIG. 5. Normal (solid line) and inverted (dashed line) activation pulses, their residue signals and corresponding spectra. Measurements were performed at the transmitter-board output, which was loaded with the 3.5-MHz transducer, for a square wave activation pulse of (a) one period and a frequency of 3.375 MHz. Synchronous sampling was performed at frequencies of 27 MHz. The spectra (b) reveal the contaminating second ($H2_c$) and third ($H3_c$) harmonics. Note the difference in vertical scale between the normal/inverted pulses and the residue signal.

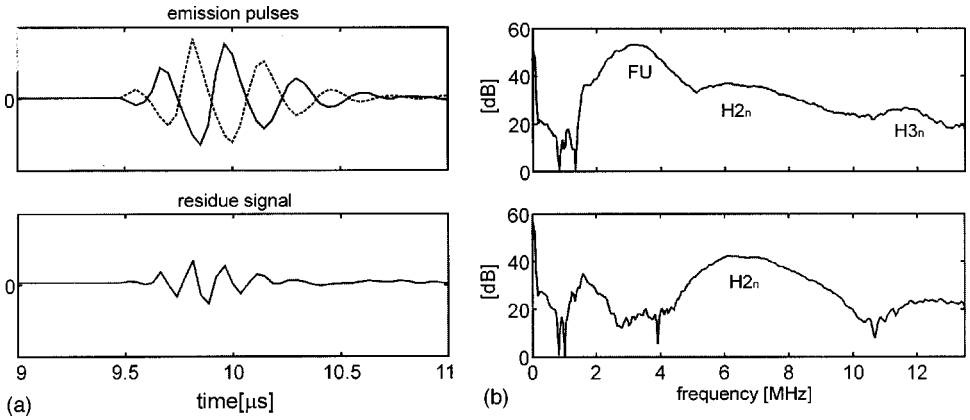

FIG. 6. (a) Normal (solid lines) and inverted (dashed lines) pulse emitted by the 3.5-MHz transducer measured by the hydrophone in water, at a distance of 5 cm from the transducer surface. Also given (b) are the corresponding pulse spectra. Results are presented for a one period, 3.375-MHz square wave activation signal.

Pulse inversion with Levovist

In Fig. 7 the results of the Levovist measurements are given. Spectra are presented for both RF signals and pulse inversion residue signals, which were obtained by summation of subsequently received RF signals. Activation frequency and number of periods were varied (one or four period square wave pulses with 3.375 and 2.5 MHz activation frequencies, respectively). The pulse repetition frequency depended on the activation frequency of the transducer and was 1.3 kHz and 956 Hz for activation frequencies of 3.375 and 2.5 MHz, respectively. The sample frequency was a factor eight times the activation frequency (27 and 20 MHz, respectively). For calculation of the spectra, 100 RF segments of 1168 and 864 sample points (for activation frequencies of 3.375 and 2.5 MHz, respectively) were averaged to reduce spectral variance. The size of the RF segments corresponds to a depth range of 36 mm. Measurements started at a distance of 38 mm from the transducer surface. The results of the corresponding reference measurements with suspended Carborundum, under the same conditions, are presented next to each Levovist spectrum.

IV. DISCUSSION

The experiments confirm the concepts discussed in the first chapter of this paper. The attribution of the native harmonics to the pulse inversion residue signal is clearly demonstrated. It is found that pulse inversion does not suppress the native even harmonics, but does provide the means for wide-band activation. Pulse inversion enhances the even harmonics by 6 dB. Furthermore, experiments validate the possible difficulties of wide-band activation in single transducer measurements. Unlike the native and contrast agent intrinsic harmonics, the location of the contaminating harmonics is governed by the transducer spectral characteristics. Because of the possible overlap of contaminating and native or contrast agent harmonics, interpretation of the received RF sig-

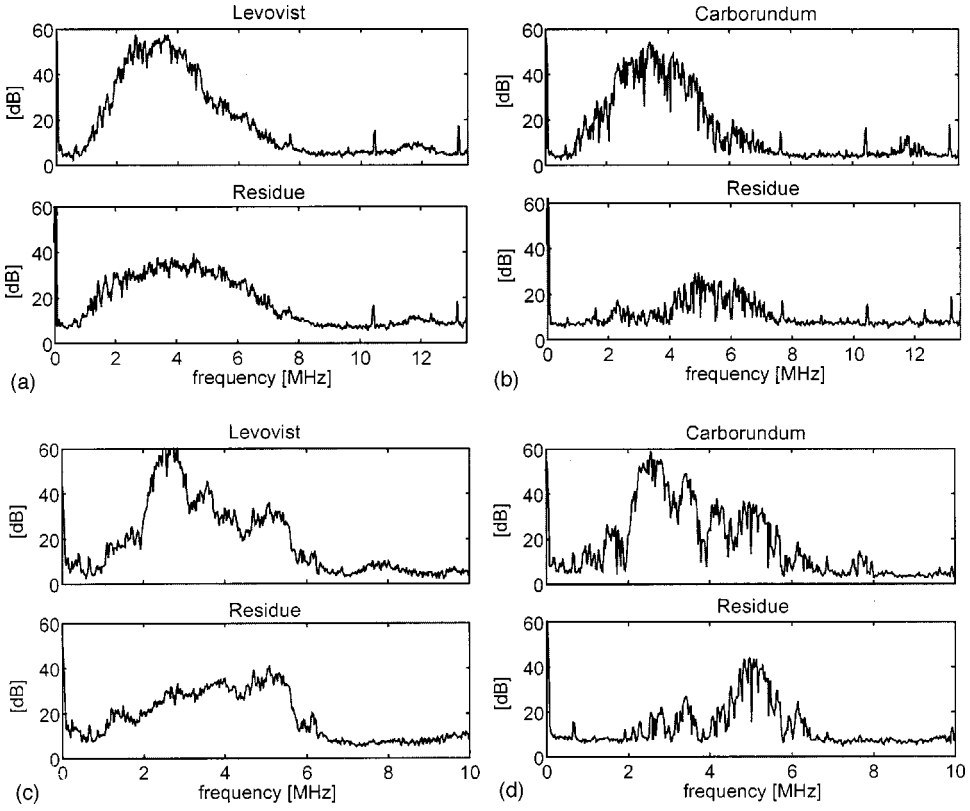

FIG. 7. Spectra of Levovist and reference measurements for different frequencies and number of periods of the square wave activation pulse. (a) and (b) one period, 3.375-MHz, and (c) and (d) four periods, 2.5-MHz.

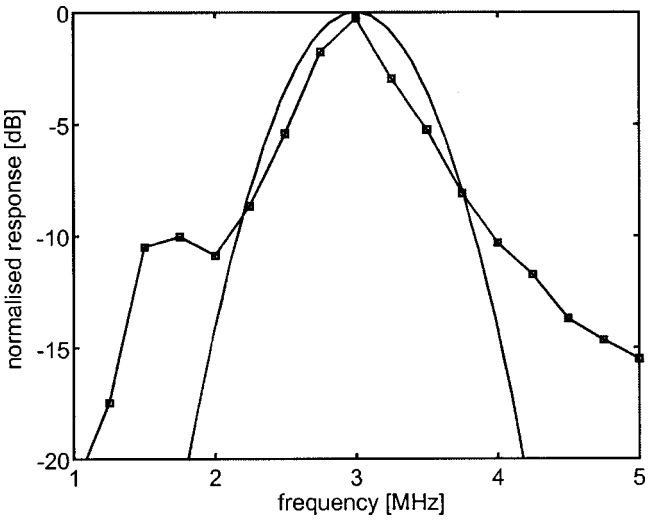

FIG. 8. Measured single trip spectral characteristics and assumed Gaussian distribution with approximately the same bandwidth (42% of the resonance frequency).

nals may be complicated. Interference of the contaminating harmonics, however, also depends on the power of this component, which can be limited by proper choice of the activation frequency.

The results in Fig. 4 basically confirm the concepts of wide-band transducer activation. Deviations between theory and experiment can be explained by the assumption of a Gaussian spectral sensitivity distribution. Figure 8 shows that this is not the case for the transducer used in the experiments, especially at frequencies far from the transducer resonance frequency, where an increased efficiency is observed. The single trip spectral sensitivity distribution of the transducer is derived from measurements of the fundamental frequency in the emission pulse for a square wave activation pulse with different frequencies, constant amplitude, and composed of five periods.

Figure 4(b) clearly illustrates the difficulty that arises in the interpretation of the peaks in the measured spectra. The reason for this difficulty is the different processes the harmonics originates from. The dominant frequency of the contaminating harmonics is primarily governed by the transducer characteristics while the spectral location of native and contrast agent intrinsic harmonics is not. Given the expected values, based on the simulations, it appears as though the second peak in the measured spectra can be identified as the contaminating third harmonic. The native second harmonic appears at frequencies exceeding the location of the third harmonic. Above 2.75 MHz the contaminating third harmonic and the native second harmonic merge and interpretation of the peak location is not feasible, though simulations predict that the level of the contaminating third harmonic should drop rapidly [Fig. 3(b)]. Although the real spectral sensitivity distribution deviates from the assumed Gaussian distribution, the level of the contaminating third harmonic in practice will still be very low compared to the second harmonic.

For sufficiently high amplitudes of the incident ultrasound, the spectra should also reveal a native third harmonic, of which the location deviates from that of the contaminating third harmonic. Indeed the fourth peak in the spectra [Fig. 4(b)] coincides with the expected location of the native third harmonic. Again, sensitivity limitations determined that the fourth peak could only be measured for activation frequencies up to 2.75 MHz.

Analyses of the normal and inverted activation pulses (Fig. 5) and their corresponding spectra reveal a second harmonic residue signal. This residue signal may be a source of contamination to the native or contrast agent intrinsic second harmonic. With respect to the contaminating second harmonic in the spectrum of the normal or inverted pulse, the contaminating second harmonic in the residue signal is 6 dB larger in power. This corresponds to a factor 2 in amplitude, which can be explained by the summation of the normal and inverted pulses. Figure 8 shows that for an activation frequency of 2.5 MHz and a corresponding second harmonic frequency of 5.0 MHz, the contaminating second harmonic will be downgraded by 15 dB at emission. For an activation frequency of 3.375 MHz, with the second harmonic at 6.75 MHz, this effect will be even larger. Thus the transducer spectral characteristics prevent the contaminating second harmonic to leak through into the emission signal.

The spectra presented in Fig. 6 confirm the concept of pulse inversion. The results are given for a wide-band pulse (one period) at a frequency of 3.375 MHz. The pulse inversion residue signal clearly has a dominant frequency that is doubled with respect to that of the original pulse. The residue signal spectra nicely show that the even harmonics remains and the odd harmonics cancels. The level of the remaining even harmonics in the residue is approximately 6 dB higher compared to that in the spectra of the normal or inverted pulses. Again, this corresponds to a factor 2 in amplitude, caused by summation of the normal and inverted pulses. Notwithstanding this increased harmonic response, the pulse inversion technique is still sensitive to the same interference of native harmonics as normal harmonic imaging.

A validation of the problems arising from wide-band activation is only found partially in these results [Fig. 6(a) and (b)]. The clear absence of the odd harmonics in the residue signal in Fig. 6(b) confirms that these peaks are indeed correctly identified as the fundamental and native third harmonic components in the normal of inverted pulse. Because the contaminating third harmonic should cancel as well the appearance of the wide band, the second harmonic component in the spectrum of residue signal should be different compared to the spectrum of the distorted pulses. There are, however, several reasons why this is not apparent. The most significant reason is that the contaminating third harmonic at this point has probably dropped far below the noise level and therefore exhibits no interference. Also, the effect of the coincidence of the native second harmonic and the contaminating third harmonic is unknown.

The spectra from the Levovist and Carborundum reference measurements, presented in Fig. 7, exhibit the same basic properties that apply to the spectra of the distorted pulses given in Fig. 6. The most important difference is the roundtrip measurement of the RF signals these spectra are based upon, while for Fig. 6 single trip signals were consid-

ered. Thus in Fig. 7, native and contrast agent intrinsic harmonics are also affected by the transducer spectral characteristics. Possible overlap between harmonics from different sources has, however, already occurred before reception. The remainder of native even harmonics in the residue signal of Levovist and Carborundum confirms that pulse inversion has to deal with similar interference as harmonic imaging.

In general, the Carborundum spectra exhibit a spectral variance that is much larger than that of the Levovist spectra. Because of flow motion of Levovist microbubbles in the water, the averaging process reduces the spectral variance of the Levovist spectra. For the Carborundum measurement this is not the case, given the static embedded nature of the particles. Even though relative high pulse repetition frequencies (approximately 1 kHz) are used, motion or structural changes of the microbubbles in between two successively emitted inverted pulses cause the subsequent received RF signals to carry slightly different information. That is why the Levovist spectra show a remainder of the fundamental component in the residue signal that is much larger than that in the reference spectra. The motion artefacts are a difficulty of the pulse inversion technique. For perfusion assessment of static structures the influence of motion artefacts is limited, but for myocardium motion artefacts will occur.

Unfortunately, an apparent additional harmonic response from Levovist could not be established. Such an additional harmonic response, although small, is visually observed in *in vivo* pulse inversion experiments and quantitatively verified in normal harmonic imaging experiments.[18,22,24] There are several complications that provide an explanation for the apparent absence of an additional harmonic response in the experiments of the present study. First of all, it was not practically feasible to adjust the concentration of Carborundum particles in such a way that a power level of the fundamental component equal to that in the Levovist measurement could be accomplished. This is further complicated by the wide-band nature of the signals. Second, the Carborundum measurements show a spectral variance that is much larger than observed in the Levovist spectra. Accordingly, it is not possible to make reliable quantitative comparison of the second harmonic power levels between the Levovist and the reference measurement.

Another reason for the apparent absence of an additional response is the low number of periods in the emission signal. Several studies indeed report on an onset delay of the second harmonic response from microbubbles.[19,21] Also, the pressure amplitude of the emitted pulse is a limiting factor. Although pressures of 112 kPa at 3.375 MHz and 77 kPa at 2.5 MHz are sufficient to induce an observable contrast agent intrinsic harmonic response when narrow-band pulses are applied,[19,20,22,23] this might not be the case or wide-band pulses, since the actual power of the pulse is spread over a much larger frequency range [Fig. 2(b)]. It is known that microbubbles only show a harmonic response if they are driven near their resonance frequency at sufficiently high power levels.[19,20,22,23] Finally, the sensitivity to the second harmonic component is seriously reduced because of the transducer spectral characteristics. This is particularly significant for an activation frequency of 3.375 MHz, where the native and contrast agent intrinsic second harmonics emerge at approximately 6.75 MHz. Although this applies to both native and contrast agent intrinsic harmonics, it also reduces the difference that can be measured between native and contrast agent intrinsic harmonic response. In conclusion, a contrast agent harmonic response additional to the native harmonic response could not be observed due to experimental limitations in the single transducer measurement.

One might question the application of a transducer with -6 dB roundtrip bandwidth of 30%, when wide-band activation is intended. Practical limitations concerning the power that can be obtained with wide-band transducers, however, prohibit the use of transducers with a much larger bandwidth. Nevertheless, application of such a transducer will not affect the results significantly. This is confirmed by concept and experiment, which were performed for both wide and small band activation pulses and did not show significant differences in the RF signal response to pulse inversion insonification (Fig. 7).

Finally, as all experiments are performed in water, the role of attenuation is neglected in the present study. In tissue, attenuation will affect the level of all harmonics. Since attenuation depends on frequency, third harmonics is more attenuated than second harmonics. Also compared to the fundamental component, the second harmonic response will be decreased due to attenuation. For the native second harmonic, an optimum occurs at distances at which a balance between native harmonic generation and attenuation is reached. At a large distance from the transducer, attenuation will play a dominant role, while close to the transducer the native harmonic will not have formed yet. It is not unlikely that contrast agents do respond differently to pulse inversion insonification than tissue does. Recent studies[25] show that the signal responses of single bubbles in water, at a distance of approximately 5 cm, differ from each other when inverted pulses are applied and exhibit a relative delayed response and a frequency shift. The presented results corroborate the theory but unfortunately no reference measurement is given. Since no information is provided about pressure amplitude, predictions regarding a contribution due to nonlinear distortion of the emitted pulses can not be made. Also, the measurements are performed with separate transducers for emission and reception, thus avoiding the difficulties that arise in wide-band experiments with a single transducer. As the transducers used for reception are optimally sensitive for second harmonic frequencies, also the effects of pulse inversion will be larger than can be observed with a single transducer.

Other techniques that might be more successful in providing a better discrimination between tissue and contrast agent are found in a combination of pulse inversion and Doppler processing (pulse inversion Doppler)[39] which exploit both the nonlinear properties and motion of the microbubbles.

V. CONCLUSION

The results of the present study indicate several practical difficulties that are encountered in pulse inversion experiments, performed with a single transducer in water. This

study shows the interference of native harmonics and provides an explanation of the mechanism of the pulse inversion residue signals of these native harmonics.

First of all, when wide-band signals are applied it is not possible to drive a transducer at frequencies desired to induce and measure harmonics optimally. This is determined and governed by transducer spectral sensitivity characteristics and limits the harmonic response that can be measured. The wide-band nature of the signal also affects the emitted power and, consequently, the contrast agent intrinsic harmonic response that can be induced.

Furthermore, it was illustrated and verified experimentally that the locations of contaminating and native harmonics of the same order do not match. The location of the contaminating harmonics in the spectrum of the emitted pulse is determined by transducer spectral characteristics, while the location of the native and contrast agent harmonics is independent of the transducer properties. It was shown that the contaminating third harmonic appears at frequencies below or equal to those of the native second harmonic. Thus the contaminating third harmonic and native or contrast agent intrinsic second harmonics overlap. The real interference is limited for narrow-band transducers but can be substantial for wide-band transducers for which the contaminating third harmonic leaks through in the emission signal at sufficiently high powers. Optimal experimental conditions are governed by the balance between minimal interference from the contaminating third harmonic and maximal sensitivity for the contrast agent intrinsic and native second harmonic.

It was demonstrated conceptually and experimentally that the native harmonics is not suppressed by pulse inversion. Thus it is attributed equally to pulse inversion and harmonic imaging. Further studies are required to indicate whether contrast agents possess the potential to show higher harmonic responses in wide-band pulse inversion experiments compared to normal harmonic imaging experiments. If not, pulse inversion can not improve discrimination between tissue and contrast agents compared to harmonic imaging. For these reasons, this study once more emphasizes the requirement of reliable reference measurements.

One of the great advantages of pulse inversion is that it provides the means for wide-band activation, thus preserving axial resolution. Furthermore, the second harmonic response in the residue signal is enhanced by 6 dB. Consequently, the demand for filtering of the signal to retrieve the (second) harmonic signal falls. Pulse inversion suffers, however, from motion artefacts.

ACKNOWLEDGMENT

This work was financially supported by the Dutch Department of Economic Affairs (IBV97.001).

[1] D. A. Christopher, P. N. Burns, J. Armstrong, and F. S. Foster, ''A high-frequency continuous-wave Doppler ultrasound system for the detection of blood flow in the microcirculation,'' Ultrasound Med. Biol. **22**(9), 1191–1203 (1996).

[2] A. Buhrer, U. T. Moser, P. M. Schumacher, T. Pasch, and M. Anliker, ''Substraction procedure for the registration of tissue perfusion with Doppler ultrasound,'' Ultrasound Med. Biol. **22**(56), 651–658 (1996).

[3] R. Eriksson, H. W. Persson, S. O. Dymling, and K. Lindstrom, ''Blood perfusion measurement with multifrequency Doppler ultrasound,'' Ultrasound Med. Biol. **21**(1), 49–57 (1995).

[4] A. L. Strauss and K. D. Beller, ''Contrast ultrasonography for 2-D opacification of heart cavities, peripheral vessels, kidney and muscle,'' Ultrasound Med. Biol. **23**(7), 975–982 (1997).

[5] B. A. Schrope and V. L. Newhouse, ''Second harmonic ultrasonic blood perfusion measurement,'' Ultrasound Med. Biol. **19**(7), 567–579 (1993).

[6] P. Hauff, T. Fritzsch, M. Reinhardt, W. Weitschies, F. Luders, V. Uhlendorf, and D. Heldmann, ''Delineation of experimental liver tumors in rabbits by a new ultrasound contrast agent and stimulated acoustic emission,'' Invest. Radiol. **32**(2), 94–99 (1997).

[7] Y. Kono, F. Moriyasu, Y. Mine, T. Nada, N. Kamiyama, Y. Suginoshita, T. Matsumura, K. Kobayashi, and T. Chiba, ''Gray-scale second harmonic imaging of the liver with galactose-based microbubbles,'' Invest. Radiol. **3**(2), 120–125 (1997).

[8] H. Madjar and J. Jellins, ''Role of echo enhanced ultrasound in breast mass investigations,'' Eur. J. Ultrasound **5**, 65–75 (1997).

[9] C. Frischke, J. R. Lindner, K. Wei, N. C. Goodman, D. M. Skyba, and S. Kaul, ''Myocardial perfusion imaging in the setting of coronary artery stenosis and acute myocardial infarction using venous injection of a second-generation echocardiographic contrast agent,'' Circulation **96**, 959–967 (1997).

[10] D. Rovai, E. M. Ferdeghini, A. Mazzarisi, M. Paternui, V. Lubrano, C. Vassalle, L. Serasini, and A. L'Abbate, ''Quantitative aspects in myocardial contrast echocardiography,'' Eur. Heart J. **16** (Suppl. J), 42–45 (1995).

[11] G. J. Hartley, J. Cheirif, K. R. Collier, J. S. Bravenec, and J. K. Mickelson, ''Doppler quantification of echo-contrast injections in vivo,'' Ultrasound Med. Biol. **19**(4), 269–278 (1993).

[12] G. Seidel and M. Kaps, ''Harmonic imaging of the vertebrobasilar system,'' Stroke **28**, 1610–1613 (1997).

[13] R. Leischik, J. Rose, G. Caspari, A. Skyschally, G. Heusch, and R. Erbel, ''Contrast echocardiography for assessment of myocardial perfusion,'' Herz **22**(1), 40–50 (1997).

[14] M. J. Monaghan, J. M. Metcalfe, S. Odunlami, A. Waaler, and D. E. Jewitt, ''Digital radiofrequency echocardiography in the detection of myocardial contrast following intravenous administration of Albunex,'' Eur. Heart J. **14**, 1200–1209 (1993).

[15] B. Wilson, K. K. Shung, B. Hete, H. Levene, and J. L. Barnhart, ''A feasibility study on quantitating myocardial perfusion with Albunex, an ultrasonic contrast agent,'' Ultrasound Med. Biol. **19**(3), 181–191 (1993).

[16] P. N. Burns, ''Harmonic imaging with ultrasound contrast agents,'' Clin. Radiol. **51**(1), 50–55 (1996).

[17] P. H. Chang, K. K. Shung, S. Wu, and H. B. Levene, ''Second harmonic imaging and harmonic Doppler measurements with Albunex,'' IEEE Trans. Ultrason. Ferroelectr. Freq. Control **42**(6), 1020–1026 (1995).

[18] B. Schrope, V. L. Newhouse, and V. Uhlendorf, ''Simulated capillary blood flow measurement using a nonlinear ultrasonic contrast agent,'' Ultrason. Imaging **14**, 134–158 (1992).

[19] P. D. Krishna and V. L. Newhouse, ''Second harmonic characteristics of the ultrasound contrast agents albunex and FS069,'' Ultrasound Med. Biol. **23**(3), 453–459 (1997).

[20] J. E. Powers, P. N. Burns, and J. Souquet, ''Imaging instrumentation for ultrasound contrast agents,'' in *Advances in Echo Imaging using Contrast Enhancement*, edited by N. C. Nanda, R. Schlief, and B. B. Goldberg (Kluwer Academic, Dordrecht, 1997), pp. 139–170.

[21] W. Zheng and V. L. Newhouse, ''Onset delay of acoustic second harmonic backscatter from bubbles or microspheres,'' Ultrasound Med. Biol. **24**(4), 513–522 (1998).

[22] N. de Jong, ''Acoustic properties of ultrasound contrast agents,'' Erasmus University Rotterdam, 1993.

[23] S. Meerbaum, ''Microbubble fluid dynamics of echocontrast,'' in *Advances in Echo Imaging using Contrast Enhancement*, edited by N. C. Nanda, R. Schlief, and B. B. Goldberg (Kluwer Academic, Dordrecht, 1997), pp. 3–38.

[24] X. A. Verbeek, J. M. Willigers, P. J. Brands, L. A. Ledoux, and A. P. Hoeks, ''Measurement of the contrast agent intrinsic and native harmonic response with single transducer pulse waved ultrasound systems,'' Ann. Biomed. Eng. **27**(5), 670–81 (1999).

[25] K. Morgan, M. Averkiou, and K. Ferrara, ''The effect of the phase of transmission on contrast agent echos,'' IEEE Trans. Ultrason. Ferroelectr. Freq. Control **45**(4), 872–875 (1998).

[26] K. Q. Schwarz, X. Chen, S. Steinmetz, and D. Phillips, ''Harmonic im-

aging with Levovist,'' J. Am. Soc. Echocardiogr **10**(1), 1–10 (1997).
[27] T. Christopher, ''Finite amplitude distortion-based inhomogeneous pulse echo ultrasonic imaging,'' IEEE Trans. Ultrason. Ferroelectr. Freq. Control **44**(1), 125–139 (1997).
[28] T. Christopher, ''Experimental investigation of finite amplitude distortion-based, second harmonic pulse echo ultrasonic imaging,'' IEEE Trans. Ultrason. Ferroelectr. Freq. Control **45**(1), 158–162 (1998).
[29] B. Ward, A. C. Baker, and V. F. Humphrey, ''Nonlinear propagation applied to the improvement of resolution in diagnostic medical ultrasound,'' J. Acoust. Soc. Am. **101**(1), 143–154 (1997).
[30] M. A. Averkiou, D. N. Roundhill, and J. E. Powers, ''A new imaging technique based on the nonlinear properties of tissues,'' IEEE Ultrason. Symp. Proc., 1561–1566 (1997).
[31] D. H. Evans, W. N. McDicken, R. Skidmore, and J. P. Woodcock, *Doppler Ultrasound, Physics, Instrumentation and Clinical Applications* (Wiley, Chichester, 1989).
[32] J. A. Jensen, *Estimation of Blood Velocities using Ultrasound*, 1st ed. (Cambridge University Press, Cambridge, 1996).
[33] R. T. Beyer, ''Nonlinear acoustics,'' in *Physical Acoustics*, edited by W. P. Mason (Academic, New York, 1965), Vol. II, part B, pp. 231–263.
[34] F. A. Duck, *Physical Properties of Tissue*, 1st ed. (Academic, London, 1990).
[35] P. H. Chang, K. K. Shung, and H. B. Levene, ''Quantitative measurements of second harmonic Doppler using ultrasound contrast agents,'' Ultrasound Med. Biol. **22**(9), 1205–1214 (1996).
[36] J. Wu and J. Tong, ''Measurement of the nonlinearity parameter B/A of contrast agents,'' Ultrasound Med. Biol. **24**(1), 153–159 (1997).
[37] R. Schlief, ''Echo-enhancing agents: Their physics and pharmacology,'' in *Advances in Echo Imaging using Contrast Enhancement*, edited by N. C. Nanda, R. Schlief, and B. B. Goldberg (Kluwer Academic, Dordrecht, 1997), pp. 85–113.
[38] J. Wu and J. Tong, ''Experimental study of stability of a contrast agent in an ultrasound field,'' Ultrasound Med. Biol. **24**(2), 257–265 (1998).
[39] D. Simpson and P. Burns, ''Pulse inversion Doppler: A new method for detecting nonlinear echos from microbubble contrast agents,'' Proc. IEEE Ultrason. Symp., 1597–1600 (1997).

LETTERS TO THE EDITOR

This Letters section is for publishing (a) brief acoustical research or applied acoustical reports, (b) comments on articles or letters previously published in this Journal, and (c) a reply by the article author to criticism by the Letter author in (b). Extensive reports should be submitted as articles, not in a letter series. Letters are peer-reviewed on the same basis as articles, but usually require less review time before acceptance. Letters cannot exceed four printed pages (approximately 3000–4000 words) including figures, tables, references, and a required abstract of about 100 words.

Profile analysis of harmonic complexes: Effects of mistuning the target

Nicholas I. Hill[a] and Peter J. Bailey
Department of Psychology, University of York, York YO10 5DD, United Kingdom

(Received 1 October 1999; accepted for publication 6 January 2000)

The effect of mistuning a single target component of a harmonic complex on listeners' ability to detect an increment in the relative level of the target was investigated. In the baseline condition, the complex consisted of the first 20 harmonics of 200 Hz, with harmonic 3 designated the target. In the mistuned condition, the third harmonic was shifted down in frequency by 8%. To control for possible within-channel cues, versions of the above stimuli were also included in which harmonics 2 and 4 were removed. The results suggest that mistuning the target component does not impair across-frequency intensity comparisons. © *2000 Acoustical Society of America.* [S0001-4966(00)02104-4]

PACS numbers: 43.66.Ba, 43.66.Fe [SPB]

INTRODUCTION

A number of profile studies have investigated the effect of manipulations that promote perceptual segregation of the target and nontarget components. These manipulations include presenting the target and nontarget components (a) to different ears (e.g., Green and Kidd, 1983; Bernstein and Green, 1987), (b) with different relative onsets and/or offsets (e.g., Green and Dai, 1992; Hill and Bailey, 1997, 1998), and (c) with different patterns of amplitude modulation (e.g., Green and Nguyen, 1988; Dai and Green, 1991). Generally, these manipulations have led to an elevation in threshold relative to the corresponding conditions in which the target and nontarget components were perceptually fused into a single auditory object. These results have led to speculation that relative intensity comparisons between concurrent frequency components are optimal when the components being compared are perceived as a single sound (Bacon and Smith, 1996; Dai, 1996). Some evidence for this view was provided by the study of Hill and Bailey (1997), who found that the deleterious effects of onset asynchrony on profile comparisons could be partially reversed by reducing the tendency of the target component to segregate from the remainder of the complex.

The present experiment sought to test further the hypothesis that grouping cues can influence profile discrimination by investigating the dependence of threshold on the spectral relationship between the target and nontarget components. When all the components of a complex are either logarithmically or harmonically spaced, there are no spectral cues that would lead to a single component being perceptually segregated from the remainder of the complex. However, when a low-numbered component of an otherwise harmonic complex is sufficiently mistuned, perceptual segregation of that component does occur. Previous studies have shown that a low-numbered harmonic mistuned down in frequency by 8% makes a significantly reduced contribution to both the periodicity pitch of a complex (Moore *et al.*, 1985), and to the quality of a vowel (Darwin and Gardner, 1986). If profile comparisons are optimal when the target and nontarget components are fused, and in particular, if the perceptual cue underlying a change in the relative level of a single target component is timbral in nature, one might expect a mistuning of similar magnitude imposed on the target component to result in an elevation in threshold relative to the case when all components are harmonic.

I. EXPERIMENT

A. Listeners

Five male listeners, aged between 20 and 34 years, participated in the experiment. All listeners had normal audiometric thresholds over the range of frequencies used in the experiment. Listener NH was the first author and had considerable experience in profile analysis tasks. The remaining listeners were students at the university and received payment. Listener TB had participated in a previous profile

[a]Author to whom correspondence should be addressed. Electronic mail: nih1@york.ac.uk

analysis experiment, while listeners MR and GP had participated in unrelated auditory experiments. Listener TS had no previous experience of auditory tests.

B. Stimuli and equipment

Four stimuli were employed: a multitone complex consisting of the first 20 harmonics of 200 Hz, a mistuned complex in which the third harmonic (target) was at 552 Hz (−8% mistuning), and two 18-component stimuli which were derived from the 20-component stimuli by removing harmonics 2 and 4. The latter pair of stimuli was included as a control for the possibility that within-channel interaction between the target and adjacent nontarget components may provide a cue to discrimination with the 20-component stimuli. The third harmonic was selected as the target because use of a low-numbered harmonic reduces the likelihood that discrimination can be based on within-channel cues, and because in a harmonic complex with fundamental frequency of 200 Hz, thresholds for hearing out a mistuned component and thresholds for detecting an increment in the level of a single component are lowest for harmonic 3 (Moore *et al.*, 1986; Zera *et al.*, 1993).

All components had a duration of 400 ms, including a 10-ms $\cos^2$ onset and offset ramp. The overall level of the stimuli was selected randomly on each presentation from a uniform distribution spanning a range of 20 dB. At the midpoint of this range, the level of each component (with the exception of the incremented target) was 55 dB SPL. The third harmonic was always gated on in sine phase, while the phases of the remaining components were selected randomly on each presentation. In all four conditions, the signal was an increment in the relative level of the third (possibly mistuned) harmonic.

Stimuli were synthesized in real time at a sampling rate of 44.1 kHz using custom software running on an IBM-compatible PC. The resulting waveforms were converted to voltages using a 16-bit soundcard (Soundblaster Awe64 Gold), and amplified by 10 dB using the boost mode of a programmable signal switcher (Tucker-Davis Technologies model SS1). The overall level of the stimuli was controlled using a pair of programmable attenuators (TDT model PA4) having a resolution of 0.1 dB. The level of the target component relative to the nontarget components was adjusted in software. Stimuli were presented monaurally over Sennheiser HD414 headphones to the listeners' right ear. Listeners were run individually in a sound-attenuating enclosure.

C. Procedure

Thresholds for detecting an increment in the level of component 3 relative to the remainder of the complex were determined using an adaptive, two-interval, two-alternative, forced-choice procedure. The level increment was achieved by software addition of a sinusoidal signal having identical frequency and phase to component 3. The level of this signal relative to component 3 (and hence the size of the level increment) was varied adaptively using a 3-down, 1-up rule which targeted the level corresponding to a 0.794 probability of correct detection (Levitt, 1971). At the beginning of an adaptive run, the signal was set to be 8 dB above the level of component 3. The size of the signal was varied in 4-dB steps until three reversals had occurred, from which point on the step size was reduced to 2 dB. Errors on the first trial of each run were not treated as a reversal, and the signal level was therefore unchanged. The threshold for a single run was defined as the average level over an even number of reversals excluding the first three or four as appropriate. The level of the signal relative to component 3 was restricted to the range +20 to −40 dB.

At the beginning of each trial, a visual alerting signal was presented in the center of a visual display for 200 ms. The first sound was presented 500 ms after the offset of the alerting signal, and there was a silent interval of 650 ms between the offset of the first sound, and the onset of the second. These intervals were defined visually by the presentation of the Arabic numerals ''1'' and ''2'' in the center of the display. Listeners were required to indicate the interval in which component 3 was incremented in level, and were given an unlimited time in which to respond. Immediately following their response, listeners were provided with visual feedback as to the correctness of their response, with the next trial beginning 1 s after the termination of feedback.

Listeners typically completed one session per weekday with a single session lasting approximately 45–50 min. Each session consisted of eight 80-trial runs, four repetitions of one of the two harmonic conditions, and four repetitions of the corresponding mistuned condition. The eight runs were presented in a random order determined by the computer. The conditions were alternated across sessions to ensure that listeners had equivalent exposure to the four stimuli during the course of the experiment. All listeners completed a total of 16 sessions (32 runs per condition), with the threshold for each condition being defined as the average of the final 12 runs.

D. Results

Individual thresholds (signal-to-pedestal ratio in dB) for the two harmonic and mistuned conditions are displayed in Fig. 1. Error bars denote ± 1 standard error. Consider first thresholds for the 20-component harmonic stimulus (open squares). For the two most sensitive listeners, NH and TB, thresholds are about 1–2 dB greater than those reported by Zera *et al.* (1993) using a similar stimulus and procedure. By contrast, the two least sensitive listeners, MR and GP, clearly had great difficulty with this stimulus. For a 3-down, 1-up procedure and a level rove of 20 dB, the theoretical lower limit on threshold for a listener basing his/her decision purely on the level of the target component is 2.1 dB (Green, 1988). Thresholds for both MR and GP were above this limit, suggesting that they were not able to make effective use of across-channel cues in this condition.

Comparing performance in the 20-component harmonic condition with that in the corresponding mistuned condition (solid squares), it is apparent that negatively mistuning the target component by 8% did not impair detection of an increment in its relative level. Indeed, listeners MR and GP displayed substantially lower thresholds in the mistuned condition and were clearly making use of across-frequency com-

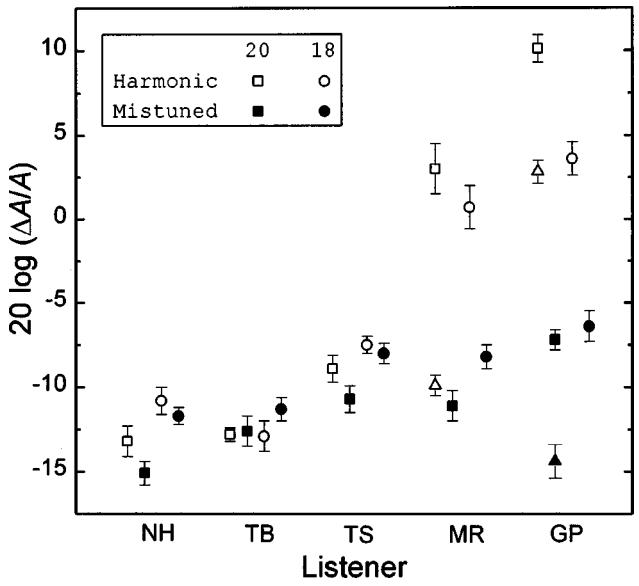

FIG. 1. Individual thresholds for the 20-component (squares) and 18-component (circles) conditions. The target was either harmonic (open symbols) or mistuned (solid symbols). Also shown are supplementary data for MR and GP (triangles). Error bars indicate ±1 standard error.

parisons of level. The pattern of data for the two 18-component stimuli (open and solid circles) was similar to that for the 20-component stimuli, with again no evidence that mistuning led to a significant increase in threshold. The similarity in the pattern of data for the 20-component and 18-component conditions suggests that the absence of a deleterious effect of mistuning on profile discrimination in the 20-component condition was not due to listeners having access to within-channel cues. This conclusion is supported by the results of a study of profile discrimination using two-tone complexes (Versfeld and Houtsma, 1995). They found that for frequency separations greater than about two semitones, profile discrimination appears to be based on across-channel level comparisons. In the 20-component mistuned condition of the present experiment, the frequency separation between the target and most proximal nontarget component is over five semitones.

Given the poor performance of listeners MR and GP in the harmonic conditions, additional data were collected for these two listeners to explore whether (a) using a four-interval, two-alternative procedure (with the signal added in interval two or three), and (b) blocking the presentation (so that the harmonic and mistuned stimuli were not presented in the same session) would lead to a lowering of thresholds. For these supplementary conditions the number of runs per session was reduced from 8 to 6.[1] The thresholds for these additional harmonic and inharmonic conditions are shown in Fig. 1 as open and solid triangles, respectively. For MR, additional data were collected only for the 20-component harmonic complex, and the reported threshold is the mean of the fifth and final session. For GP, data were collected for both the harmonic and inharmonic 20-component complexes. The data for the harmonic condition showed no consistent trend across nine sessions and the reported threshold was therefore determined by averaging across all 56 runs. GP completed two sessions of the inharmonic condition. The reported threshold is the mean of the final six runs, which was approximately 1.5 dB lower than the mean threshold obtained in the first session. Both MR and GP showed improvements in performance in the supplementary tests relative to the main experiment. MR's threshold in the harmonic condition improved by approximately 13 dB, although this was still more than 1 dB above the threshold obtained in the corresponding mistuned condition of the main experiment. GP's thresholds improved by about 7 dB in both conditions.

E. Discussion

The results of the present experiment indicate that mistuning the target component down in frequency by 8% does not impair relative intensity discrimination. Such a mistuning is well above the threshold of around 2% required for perceptual segregation of the third harmonic of 200 Hz (Moore *et al.*, 1986), and all listeners indicated that they were able to hear out the target component in the mistuned conditions. The results suggest that perceptual segregation of the target and nontarget components *per se* is not sufficient to disrupt profile comparisons. A similar conclusion was drawn by Bacon and Smith (1996), who found that moderate amplitude modulation of the nontarget components actually resulted in a slight lowering of threshold. Only when the modulation depth was 100% were the thresholds for their listeners clearly elevated.

The fact that perceptual segregation need not, by itself, impair profile discrimination is consistent with results from pitch perception studies. For example, Moore *et al.* (1985) found that a mistuned harmonic made a full contribution to the pitch of the complex for mistunings of up to around 3%, beyond that required for perceptual segregation. In contrast with the present results, however, a harmonic that is mistuned by 8% makes a substantially reduced contribution to both periodicity pitch and vowel quality (Moore *et al.*, 1985; Darwin and Gardner, 1986).

The failure to find an effect of mistuning on profile discrimination in the present experiment is not necessarily inconsistent with the hypothesis that at least some of the effects reported in previous profile studies may be due to perceptual organization. For example, it may be that the mechanism underlying profile analysis is insensitive to harmonicity cues since natural sounds are not always harmonic. On the other hand, it may be that profile analysis of the type studied in the present experiment does not require that the target and nontarget components be perceptually fused. Indeed, it is possible that listeners are just as effective at making explicit comparisons of the level of concurrent but distinct auditory objects, as they are at discriminating a change in the spectral profile of a single fused object on the basis of timbral cues. If this is the case, profile analysis would clearly not be an effective tool for investigating grouping processes. However, before such a conclusion could be reached, alternative explanations would need to be found for the observed effects of onset asynchrony, dichotic presentation, and amplitude modulation on profile discrimination.

When questioned during the main experiment about their difficulties with the harmonic stimuli, both listeners MR and GP reported that in the mistuned conditions their deci-

sions were based on a comparison of the prominence of target component (cf. Gockel, 1996). In the harmonic conditions, however, both listeners expressed difficulty hearing out the target component, and indicated that they were unable to find a reliable strategy. Both these subjective reports and the pattern of data for listeners MR and GP are consistent with the idea that drawing attention to the target component by means of mistuning assisted these listeners in adopting a suitable listening strategy (e.g., Berg and Green, 1990).

ACKNOWLEDGMENTS

The authors would like to thank the two anonymous reviewers for their constructive comments on an earlier version of this manuscript. Financial support was provided by the BBSRC, Grant No. 87/S09839.

[1]Listener GP's first session in the harmonic condition consisted of eight runs of the adaptive procedure.

Bacon, S. P., and Smith, M. A. (**1996**). ''Profile analysis with amplitude-modulated nontarget components,'' J. Acoust. Soc. Am. **99**, 1653–1659.

Berg, B. G., and Green, D. M. (**1990**). ''Spectral weights in profile listening,'' J. Acoust. Soc. Am. **88**, 758–766.

Bernstein, L. R., and Green, D. M. (**1987**). ''The profile-analysis bandwidth,'' J. Acoust. Soc. Am. **81**, 1888–1895.

Dai, H. (**1996**). ''Effect of perceptually separating spectral components on profile discrimination,'' J. Acoust. Soc. Am. **100**, 2681.

Dai, H., and Green, D. M. (**1991**). ''Effect of amplitude modulation on profile detection,'' J. Acoust. Soc. Am. **90**, 836–845.

Darwin, C. J., and Gardner, R. B. (**1986**). ''Mistuning a harmonic from a vowel: Grouping and phase effects on vowel quality,'' J. Acoust. Soc. Am. **79**, 838–845.

Gockel, H. (**1998**). ''On possible cues in profile analysis: Identification of the incremented component,'' J. Acoust. Soc. Am. **103**, 542–552.

Green, D. M. (**1988**). *Profile Analysis: Auditory Intensity Discrimination* (Oxford University Press, Oxford).

Green, D. M., and Dai, H. (**1992**). ''Temporal relations in profile comparisons,'' in *Auditory Physiology and Perception*, edited by Y. Cazals, L. Demany, and K. Horner (Pergamon, Oxford), pp. 471–477.

Green, D. M., and Kidd, Jr., G. (**1983**). ''Further studies of auditory profile analysis,'' J. Acoust. Soc. Am. **73**, 1260–1265.

Green, D. M., and Nguyen, Q. T. (**1988**). ''Profile analysis: Detecting dynamic spectral changes,'' Hearing Res. **32**, 147–164.

Hill, N. I., and Bailey, P. J. (**1997**). ''Profile analysis with an asynchronous target: Evidence for auditory grouping,'' J. Acoust. Soc. Am. **102**, 477–481.

Hill, N. I., and Bailey, P. J. (**1998**). ''Relative intensity comparisons between a tone and spectrally remote noise: Effects of onset asynchrony,'' J. Acoust. Soc. Am. **103**, 1075–1079.

Levitt, H. (**1971**). ''Transformed up–down methods in psychoacoustics,'' J. Acoust. Soc. Am. **49**, 467–477.

Moore, B. C. J., Glasberg, B. R., and Peters, R. W. (**1985**). ''Relative dominance of individual partials in determining the pitch of complex tones,'' J. Acoust. Soc. Am. **77**, 1853–1860.

Moore, B. C. J., Glasberg, B. R., and Peters, R. W. (**1986**). ''Thresholds for hearing mistuned partials as separate tones in harmonic complexes,'' J. Acoust. Soc. Am. **80**, 479–483.

Versfeld, N. J., and Houtsma, A. J. M. (**1995**). ''Discrimination of changes in the spectral shape of two-tone complexes,'' J. Acoust. Soc. Am. **98**, 807–816.

Zera, J., Onsan, Z. A., Nguyen, Q. T., and Green, D. M. (**1993**). ''Auditory profile analysis of harmonic signals,'' J. Acoust. Soc. Am. **93**, 3431–3441.

On the decline in overshoot at high masker levels

Sid P. Bacon[a] and Li Liu
Psychoacoustics Laboratory, Department of Speech and Hearing Science, Arizona State University, Tempe, Arizona 85287-1908

(Received 18 October 1999; revised 21 December 1999; accepted 28 December 1999)

The purpose of the present study was to determine whether the decline in overshoot at high masker levels might be due to the slow recovery of the onset response of low-spontaneous rate (sr) fibers. Overshoot was measured for a 4000-Hz signal at a relatively low (20 or 30 dB) and at a relatively high (50 dB) masker spectrum level in both an adaptive, two-interval forced-choice (2IFC) paradigm and in a fixed-level, yes–no paradigm. In the 2IFC paradigm, there was only 500 ms of silence between the two masker bursts of a trial; in the yes–no paradigm, there was 4 s of silence between each burst (i.e., between each trial). The timing of the trial sequences of these two paradigms was such that the 2IFC paradigm probably would not ensure complete recovery of the onset response of low-sr fibers, whereas the yes–no paradigm would. Nevertheless, for both paradigms, there was an average of about 9 dB of overshoot at the lower masker level and 2 dB at the higher masker level. These results suggest that the decline in overshoot at high masker levels is not due to the protracted recovery from adaptation of the onset response of low-sr fibers. © *2000 Acoustical Society of America.* [S0001-4966(00)01304-2]

PACS numbers: 43.66.Dc, 43.66.Mk, 43.66.Ba [DWG]

INTRODUCTION

The threshold for a brief signal tends to decline as it is moved temporally through a longer duration, broadband noise masker (e.g., Zwicker, 1965; Elliott, 1965; Fastl, 1976). Zwicker (1965) referred to the elevated threshold near masker onset as an ''overshoot'' of masking. The amount of overshoot is often defined as the difference between the threshold obtained at two points in time: one near the beginning and one near the center of the masker. Although it is still unclear how to account for overshoot, one possibility is that at least some of overshoot is due to peripheral adaptation (e.g., Smith and Zwislocki, 1975). In this account, the elevated thresholds near masker onset are due to the relatively large onset response of auditory-nerve fibers at the beginning of the masker (for a discussion, see Bacon and Smith, 1991).

Overshoot tends to increase and then decrease with increasing masker level (Bacon, 1990; Carlyon and White, 1992; Klitzing and Kohlrausch, 1994; Overson *et al.*, 1996); indeed, at high levels, overshoot is often negligible. One possible explanation for this decline in overshoot at high levels is that the neural response to the masker is now dominated by low-spontaneous rate (sr), high-threshold fibers (see McFadden and Champlin, 1990). The onset response of low-sr fibers can take considerably longer to recover from prior stimulation than does the onset response of high-sr, low-threshold fibers (Relkin and Doucet, 1991; also see Rhode and Smith, 1985). Indeed, it can take at least 2 s for the onset response of low-sr fibers to recover. Thus, the timing sequence of a typical two-interval forced-choice (2IFC) procedure may preclude complete recovery of the onset response of low-sr fibers, and hence preclude the observance of large amounts of overshoot at high levels. The purpose of the present experiment was to examine this possibility.

[a]Electronic mail: spb@asu.edu

I. METHOD

A. Apparatus and stimuli

All stimuli were digitally generated and produced at a 20-kHz sampling rate using a digital array processing card (TDT AP2) and presented via one channel of a digital-to-analog converter, or DAC (TDT DD1). The output of the DAC was low-pass filtered at 8 kHz (TDT FT6), attenuated (TDT PA4), and routed via a headphone buffer (TDT HB6) to a TDH-49P headphone mounted in an MX/51 cushion.

The signal was a 4000-Hz tone; its duration was 10 ms. The masker was broadband noise that was generated in the frequency domain and transformed into the time domain via an inverse Fourier transform. It had components from 0 to 8 kHz, and a duration of 100 ms. A new noise sample was used for each masker presentation. Two masker spectrum levels were used: a relatively low level (20 or 30 dB) and a relatively high level (50 dB). The choice of which lower level to use for a given subject was based on previous overshoot results in these subjects (Bacon and Liu, 1999); the level yielding the larger overshoot was chosen. The signal was presented at a delay of 0 or 70 ms; the difference between those two thresholds is the amount of overshoot. All durations include 5-ms $\cos^2$ rise/fall times, and all durations and delays are determined from 0-voltage points.

B. Procedure

Testing was completed in a single-walled, sound-attenuating chamber located within an acoustically treated room. The procedure was either adaptive, 2IFC or fixed-level, yes–no. The testing with the 2IFC procedure was completed first. For both procedures, subjects responded by pressing one of two buttons on a response panel. Lights were used to indicate when the signal might occur and to provide correct-answer feedback. The 2IFC procedure employed a

TABLE I. Shown here are individual and mean threshold values expressed as the signal level relative to the masker spectrum level (in dB) for the 0-ms and 70-ms delay conditions for both the lower (20 or 30 dB) and higher (50 dB) masker spectrum levels. The difference between those thresholds (i.e., the amount of overshoot) is also shown.

		Lower masker level			Higher masker level		
	Subject	0 ms	70 ms	Overshoot	0 ms	70 ms	Overshoot
2IFC	S1	50.0	42.0	8.0	46.0	41.2	4.8
	S2	51.7	42.1	9.6	38.9	37.6	1.3
	S3	52.9	45.5	7.4	43.3	41.3	2.0
	S4	51.8	42.6	9.2	43.0	41.6	1.4
	Mean	**51.6**	**43.1**	**8.5**	**42.8**	**40.4**	**2.4**
Yes–No	S1	55.0	41.5	13.5	43.8	40.3	3.5
	S2	51.8	45.3	6.5	41.1	38.3	2.8
	S3	50.3	45.8	4.5	43.9	40.4	3.5
	S4	52.7	42.0	10.7	38.0	39.5	−1.5
	Mean	**52.5**	**43.7**	**8.8**	**41.7**	**39.6**	**2.1**

three-down, one-up decision rule that tracked 79.4% correct (Levitt, 1971). The (silent) time between the two observation intervals was 500 ms, the time between trials included a subject-dependent response time and a 500-ms warning interval. A run consisted of 12 reversals; the threshold estimate for a given run was the mean of the signal levels at the last 10 reversals. The initial step size of 5 dB was reduced to 2 dB after the second reversal. Three or four threshold estimates were averaged to produce a threshold for a given condition. The standard deviation of this average was always less than 3 dB and usually less than 2 dB. Testing was completed within a single 2-h session, where runs for the two masker levels and two signal delays were interspersed. In the yes–no procedure, the signal level was fixed throughout a block of 50 trials. Signal levels were chosen to provide levels of performance between about 60% and 90%, based on the results with the 2IFC procedure. The time between trials was fixed at 4 s, with 3 s allotted for subject response; the subjects always responded within that time. The *a priori* probability of a signal occurring on a given trial was 0.5, although the number of signal trials for a given block was not constrained to be equal to 25. Overall, 50.7% of the trials contained a signal. Usually four, but as many as six, blocks of 50 trials were completed per signal level. For two of the subjects (S2 and S4), complete psychometric functions for a given condition (masker level and signal delay) were obtained within a single 2-h session. For the other two subjects (S1 and S3), the psychometric function for a given condition was obtained over at least 2 days (the exception being for S1 in the 0-ms condition at the lower level). For all subjects, conditions for the yes–no procedure were tested in quasirandom order, and all testing required four 2-h sessions.

C. Subjects

Four individuals participated; two were female (S1 and S4) and two were male (S2 and S3). They ranged in age from 26–35 years, and had thresholds of 15 dB HL or lower (ANSI, 1989) for octave test frequencies from 500 to 8000 Hz. All had participated previously in overshoot experiments (Bacon and Liu, 1999). Except for S1, the second author, the subjects were paid for their participation.

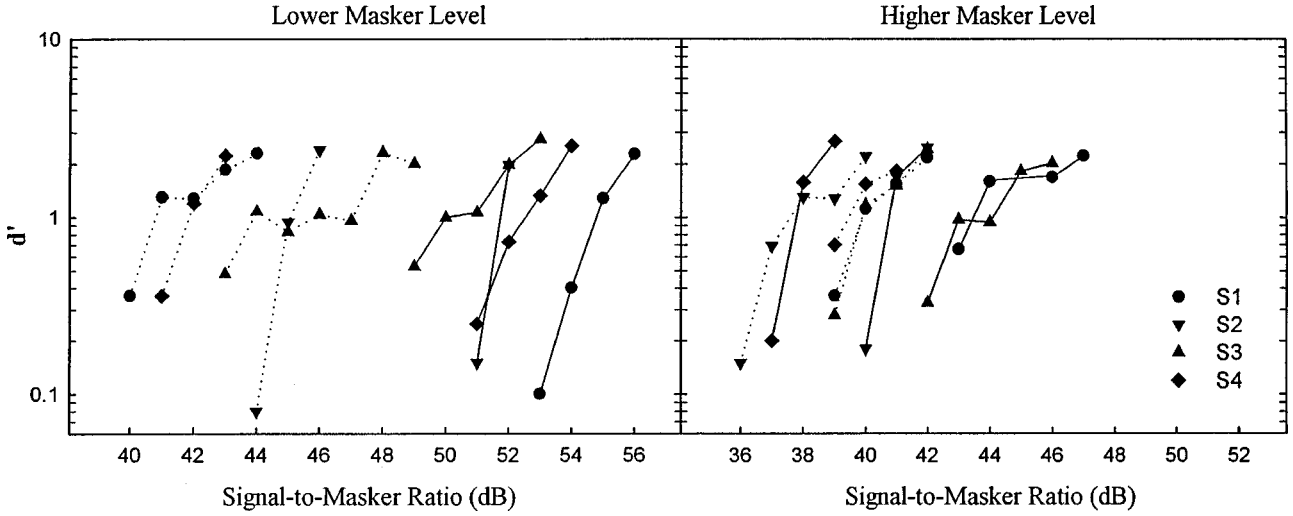

FIG. 1. Shown here are the psychometric functions obtained in the single-interval, yes–no procedure. The left panel shows the results for the lower masker spectrum level (20 or 30 dB) and the right panel shows the results for the higher masker spectrum level (50 dB). The functions obtained with a 0-ms delay are connected by a solid line, and those with a 70-ms delay are connected by a dotted line.

II. RESULTS

The results from the 2IFC paradigm are shown in the top half of Table I. The results for the lower masker level are shown on the left, and those for the higher masker level on the right. The results are reported both as the signal level relative to the masker spectrum level at threshold (i.e., as the signal-to-masker ratio or SMR) for the two signal delays and as overshoot. As shown previously in 2IFC paradigms (e.g., Bacon, 1990; Carlyon and White, 1992), the amount of overshoot decreases at high levels; in this case, it decreases from an average value of 8.5 to 2.4 dB.

The psychometric functions obtained in the yes–no paradigm are shown in Fig. 1, where d' is plotted as a function of SMR. The results for the lower level are in the left panel, and those for the higher level are in the right panel. Within a given panel, the results are shown for each individual at both signal delays. For a given subject, the results for the 70-ms delay (dotted lines) are located to the left of those for the 0-ms delay (solid line), indicating better performance at the 70-ms delay (i.e., overshoot). These functions were fitted with a least-squares straight line ($\log d'$ vs SMR); the r^2 values ranged from 0.74 to 0.98 (mean of 0.88), excluding the one function (S2, lower level at a 0-ms delay) that contained only two points. There were no systematic differences in the slopes at the two delays or two masker levels. Excluding the one two-point function, the average slope on these coordinates was 0.32. From these fits, the threshold for a given condition was estimated as the SMR yielding a d' of 1.0. These are shown in the bottom half of Table I, along with the overshoot values. There are generally only small differences in threshold and overshoot values between the 2IFC and yes–no procedures within a given subject; averaged across subjects, there is almost no difference at all. For both procedures, the mean overshoot value decreases from about 9 to 2 dB as the masker spectrum level increases from either 20 or 30 dB to 50 dB.

III. DISCUSSION

The purpose of this study was to determine whether the decline in overshoot at high levels might be related to the slow recovery of high-threshold, low-sr fibers (Relkin and Doucet, 1991). The onset response of those fibers can require as long as 2 s or so to recover, and it has been suggested that those fibers are responsible for the (long) recovery of the compound action potential in humans following intense acoustic stimulation (Murnane *et al.*, 1998). Thus, we wished to determine whether the timing sequence of a typical 2IFC procedure, where there is usually no more than about 500 ms between observation intervals, might preclude the complete recovery of the onset response of those fibers, and hence reduce overshoot. We implemented a single-interval, yes–no procedure with 4 s between observation intervals, thus providing sufficient time for complete recovery. Nevertheless, a nearly identical decline in overshoot with level was observed in the yes–no procedure as in the 2IFC procedure. Although we cannot be certain that low-sr fibers dominated the response at the higher masker level, we probably can assume that, at a given level, the same group of fibers dominated the response in the two paradigms. Thus, the results of the present study strongly suggest that the decline in overshoot at high levels is not due to low-sr fibers being in a state of adaptation. Whether it is instead related to some other factor, such as the basilar-membrane input–output function changing from compressive to linear, remains to be determined.

ACKNOWLEDGMENT

This research was supported by NIDCD Grant No. DC01376.

ANSI (**1989**). ANSI S3.6-1989, *Specifications for Audiometers* (American National Standards Institute, New York).

Bacon, S. P. (**1990**). ''Effect of masker level on overshoot,'' J. Acoust. Soc. Am. **88**, 698–702.

Bacon, S. P., and Liu, L. (**1999**). ''Effects of ipsilateral and contralateral precursors on overshoot,'' J. Acoust. Soc. Am. (submitted).

Bacon, S. P., and Smith, M. A. (**1991**). ''Spectral, intensive, and temporal factors influencing overshoot,'' Q. J. Exp. Psychol. **43A**, 373–399.

Carlyon, R. P., and White, L. J. (**1992**). ''Effect of signal frequency and masker level on the frequency regions responsible for the overshoot effect,'' J. Acoust. Soc. Am. **91**, 1034–1041.

Elliott, L. L. (**1965**). ''Changes in the simultaneous masked threshold of brief tones,'' J. Acoust. Soc. Am. **38**, 738–746.

Fastl, H. (**1976**). ''Temporal masking effects I. Broad band noise masker,'' Acustica **35**, 287–302.

Klitzing, R., and Kohlrausch, A. (**1994**). ''Effect of masker level on overshoot in running- and frozen-noise maskers,'' J. Acoust. Soc. Am. **95**, 2192–2201.

Levitt, H. (**1971**). ''Transformed up-down methods in psychoacoustics,'' J. Acoust. Soc. Am. **49**, 467–477.

McFadden, D., and Champlin, C. A. (**1990**). ''Reductions in overshoot during aspirin use,'' J. Acoust. Soc. Am. **87**, 2634–2642.

Murnane, O. D., Prieve, B. A., and Relkin, E. M. (**1998**). ''Recovery of the human compound action potential following prior stimulation,'' Hearing Res. **124**, 182–189.

Overson, G. J., Bacon, S. P., and Webb, T. M. (**1996**). ''The effect of level and relative frequency region on the recovery of overshoot,'' J. Acoust. Soc. Am. **99**, 1059–1065.

Relkin, E. M., and Doucet, J. R. (**1991**). ''Recovery from prior stimulation. I. Relationship to spontaneous firing rates of primary auditory neurons,'' Hearing Res. **55**, 215–222.

Rhode, W. S., and Smith, P. H. (**1985**). ''Characteristics of tone-pip response patterns in relationship to spontaneous rate in cat auditory nerve fibers,'' Hearing Res. **18**, 159–168.

Smith, R. L., and Zwislocki, J. J. (**1975**). ''Short-term adaptation and incremental responses in single auditory-nerve fibers,'' Biol. Cybern. **17**, 169–182.

Zwicker, E. (**1965**). ''Temporal effects in simultaneous masking by white-noise bursts,'' J. Acoust. Soc. Am. **37**, 653–663.

Erratum: "3aBB4. Ultrasound contrast agents retain acoustic activity post phagocytosis by leukocytes" [J. Acoust. Soc. Am. 106, 2192(A) (1999)]

Paul Dayton, James Chomas, and Katherine Ferrara
University of California, Davis, One Shields Avenue, Davis, California 95616

Jonathan Lindner and Matthew Coggins
University of Virginia, Charlottesville, Virginia 22908

A corrected abstract from the 138th Meeting of the Acoustical Society of America is printed here.

9:45

3aBB4. Ultrasound contrast agents retain acoustic activity post phagocytosis by leukocytes [J. Acoust. Soc. Am. 106, 2192(A) (1999)]

Paul Dayton, James Chomas, and Katherine Ferrara
University of California, Davis,
One Shields Avenue, Davis, California 95616

Jonathan Lindner and Matthew Coggins
University of Virginia,
Charlottesville, Virginia 22908

It has been observed that ultrasound contrast microbubbles are phagocytosed intact by activated leukocytes in regions of inflammation. In order to determine if microbubbles remain acoustically active following phagocytosis, the physical responses of phagocytosed and free microbubbles to acoustic pulses were measured optically and acoustically. The rate of microbubble destruction at each acoustic pressure is lower for phagocytosed compared to free microbubbles. Destruction of phagocytosed microbubbles at −1600 kPa occasionally results in disruption of the leukocyte cell membrane. The phenomena of leukocyte destruction by insonified microbubbles was assessed with a high-speed imaging system and appeared to be due to rapid, extreme fluctuations in microbubble diameter (up to 300%) during pressure rarefaction. Analysis of the echoes returning from phagocytosed microbubbles demonstrated similarity to the nonlinear responses produced by free microbubbles. Primary radiation force is observed to displace phagocytosed microbubbles a distance of 100 microns (−240 kPa, 10 kHz PRF) thus providing further evidence of acoustic activity. It can be concluded that phagocytosed microbubbles maintain their susceptibility to acoustic destruction and can generate nonlinear echoes. These results indicate that contrast-enhanced ultrasound may be used to identify and assess regions of inflammation by detecting acoustic signals from microbubbles that are phagocytosed by activated leukocytes.

 0001-4966/2000/107(4)/2298/1/$17.00

Erratum: "Thermal diffusion and mixture separation in the acoustic boundary layer" [J. Acoust. Soc. Am. 106, 1794–1800 (1999)]

G. W. Swift and P. S. Spoor
Condensed Matter and Thermal Physics Group, Los Alamos National Laboratory, Los Alamos, New Mexico 87545

(Received 14 December 1999; accepted for publication 6 January 2000)

[S0001-4966(00)02004-X]

Our arbitrary decision to let c represent the mass fraction of the *lighter* component was very unfortunate, because it caused k_T' to be *negative* for typical gas mixtures such as He–Ar, in contradiction to the sign convention for k_T used in most publications and in our own numerical examples. Hence, for consistency within this paper and with most publications: In the third paragraph of Sec. II and the first two paragraphs of Sec. IV, the words ''lighter'' and ''heavier'' should be interchanged, and ''lower'' should be ''higher.'' Subscripts H and L should be interchanged in and near Eqs. (39), (40), (43), (44), and (52). [Equations (41), (42), and (45) are unchanged because $n_H = 1 - n_L$.]

 0001-4966/2000/107(4)/2299/1/$17.00